NORTH ATLANTIC TREATY ORGANIZATION

RESEARCH AND TECHNOLOGY ORGANIZATION

BP 25, 7 RUE ANCELLE, F-92201 NEUILLY-SUR-SEINE CEDEX, FRANCE

RTO MEETING PROCEEDINGS 11

System Identification for Integrated Aircraft Development and Flight Testing

(l'Identification des systèmes pour le développement intégré des aéronefs et les essais en vol)

Papers presented at the RTO Systems Concepts and Integration Panel (SCI) Symposium held in Madrid, Spain, 5-7 May 1998.

19990413 070

Published March 1999

Distribution and Availability on Back Cover

RTO MEETING PROCEEDINGS 11

System Identification for Integrated Aircraft Development and Flight Testing

(l'Identification des systèmes pour le développement intégré des aéronefs et les essais en vol)

Papers presented at the RTO Systems Concepts and Integration Panel (SCI) Symposium held in Madrid, Spain, 5-7 May 1998.
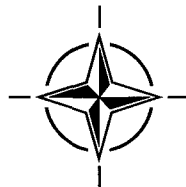
AQF99-07-1290

The Research and Technology Organization (RTO) of NATO

RTO is the single focus in NATO for Defence Research and Technology activities. Its mission is to conduct and promote cooperative research and information exchange. The objective is to support the development and effective use of national defence research and technology and to meet the military needs of the Alliance, to maintain a technological lead, and to provide advice to NATO and national decision makers. The RTO performs its mission with the support of an extensive network of national experts. It also ensures effective coordination with other NATO bodies involved in R&T activities.

RTO reports both to the Military Committee of NATO and to the Conference of National Armament Directors. It comprises a Research and Technology Board (RTB) as the highest level of national representation and the Research and Technology Agency (RTA), a dedicated staff with its headquarters in Neuilly, near Paris, France. In order to facilitate contacts with the military users and other NATO activities, a small part of the RTA staff is located in NATO Headquarters in Brussels. The Brussels staff also coordinates RTO's cooperation with nations in Middle and Eastern Europe, to which RTO attaches particular importance especially as working together in the field of research is one of the more promising areas of initial cooperation.

The total spectrum of R&T activities is covered by 6 Panels, dealing with:

- SAS   Studies, Analysis and Simulation
- SCI   Systems Concepts and Integration
- SET   Sensors and Electronics Technology
- IST   Information Systems Technology
- AVT   Applied Vehicle Technology
- HFM   Human Factors and Medicine

These Panels are made up of national representatives as well as generally recognised 'world class' scientists. The Panels also provide a communication link to military users and other NATO bodies. RTO's scientific and technological work is carried out by Technical Teams, created for specific activities and with a specific duration. Such Technical Teams can organise workshops, symposia, field trials, lecture series and training courses. An important function of these Technical Teams is to ensure the continuity of the expert networks.

RTO builds upon earlier cooperation in defence research and technology as set-up under the Advisory Group for Aerospace Research and Development (AGARD) and the Defence Research Group (DRG). AGARD and the DRG share common roots in that they were both established at the initiative of Dr Theodore von Kármán, a leading aerospace scientist, who early on recognised the importance of scientific support for the Allied Armed Forces. RTO is capitalising on these common roots in order to provide the Alliance and the NATO nations with a strong scientific and technological basis that will guarantee a solid base for the future.

System Identification for Integrated Aircraft Development and Flight Testing

(RTO MP-11)

Executive Summary

Over the last decades flight vehicles such as aircraft and helicopters entering service and requiring increased operational effectiveness have with few exceptions experienced prolonged flight test development to achieve full certification. In many cases the original requirements had later to be reduced to enable release to service. The impact on the customer, and manufacturer has been considerable leading to increased costs and or reduced operational capabilities. These costly experiences are largely a result of the flight vehicle not behaving as modelled and designed.

The evaluation of flight test data can be used as a tool for validating windtunnel results and mathematical models describing the flight dynamical behaviour. In this sense the uncertainty of important aerodynamic stability and control parameters can be reduced and the confidence of aircraft mathematical models improved. An additional important factor comes from the implementation of active control systems offering the promise of significantly increased flight vehicle performance and operational capability. This approach extends the traditional trade-offs between aerodynamics, structures and propulsion systems to include full-time, full-authority fly-by-wire/light systems. It is imperative that the aerodynamic stability and control parameters of such integrated flight and propulsion control systems have to turn out inflight as predicted, since inherent stability margins will be lower and the flight control system must correct these deficiencies to provide flight critical redundancy and safety.

With the methodology of system identification from flight tests it is possible to sense the control inputs and the flight vehicle reactions such as accelerations, rates and attitudes. The mathematical model, e.g. the model structure and parameters, has to be determined from the relationship of the measured control inputs and the system's responses.

The aim of this symposium was to review the present state of the art of flight vehicle system and parameter identification techniques, and to provide a critical appraisal of current methods developed and applied to flight test data in a number of NATO nations. Particular emphasis was placed on practical aspects and lessons learned in order to generate information useful to the flight test community in industry and government agencies.

The technical papers share invaluable experience and emphasize the advances of flight vehicle system identification over the last years to the point where confidence and robustness level is now reasonably high. The symposium covered overviews of identification methodologies, flight test techniques, recent aircraft and helicopter application programs, and a session of short papers covering up-to-the-minute flight test results. A final discussion included prepared comments from experts and concluded with key issues learned in the application of system identification and future research needs.

The essential benefits to NATO nations can be condensed as follows:
- More accurate mathematical models for high bandwidth flight control systems,
- Improved assessment and evaluation of flying qualities,
- High fidelity mathematical models for flight vehicle development and mission training simulators, and generally,
- Reduced flight test time and costs.

L'identification des systèmes pour le développement intégré des aéronefs et les essais en vol

(RTO MP-11)

Synthèse

Pour les aéronefs à voilure fixe et tournante, pour lesquels on demande toujours plus d'efficacité opérationnelle, il a été noté, au cours des dernières décennies un rallongement quasi-général des essais en vol avant de pouvoir obtenir la certification complète pour mise en service. Dans beaucoup de cas, cette certification est passée par une réduction des spécifications initiales. Pour les clients et pour les constructeurs, les conséquences sont considérables car elles entraînent une augmentation des coûts et/ou une diminution des capacités opérationnelles. Ces expériences coûteuses s'expliquent largement par le fait que l'aéronef ne se comporte pas en vol comme prévu lors de la conception et modélisation.

Les résultats des essais en vol peuvent valider les essais en soufflerie, ainsi que les modèles mathématiques de la dynamique du vol. Ainsi, l'incertitude associée à certains paramètres de stabilité et de contrôle aérodynamiques peut être atténuée et la fiabilité des modèles mathématiques d'aéronefs, améliorée. De plus, l'installation de systèmes de contrôle actif offre la possibilité d'une amélioration considérable des performances et des capacités opérationnelles des véhicules aériens. Cette approche élargit le domaine des compromis traditionnels entre l'aérodynamique, les structures et les systèmes de propulsion pour inclure des systèmes de commandes de vol électriques/à fibres optiques à autorisation permanente et sans restriction. Il est indispensable que les paramètres de stabilité et de contrôle aérodynamiques de tels systèmes intégrés de commande de propulsion et de vol, se comportent en vol comme prévu, puisque les marges de stabilité propre seront plus faibles et le système de commandes de vol doit compenser ces carences, afin d'assurer la redondance et la sécurité indispensables.

Avec la méthodologie d'identification des systèmes, utilisée lors des essais en vol, on peut enregistrer les données relatives aux commandes de pilotage et les réactions du véhicule aérien, telles que positions, accélérations et vitesses. Le modèle mathématique, c'est à dire la structure et les paramètres du modèle, doit être déterminé à partir du rapport entre les commandes de pilotage et les réponses du système.

Ce symposium a eu pour objectif de faire le point des connaissances actuelles en techniques de systèmes de commandes de vol et d'identification de paramètres, et de fournir une évaluation critique des méthodes qui ont été développées et appliquées aux données des essais en vol par bon nombre de pays de l'OTAN. Un accent particulier a été mis sur les aspects pratiques et les enseignements tirés, afin de donner des informations utiles aux responsables des essais en vol de l'industrie et des agences gouvernementales.

Les communications techniques présentées sont le fruit d'une expérience inestimable et soulignent les avancées réalisées au cours des dernières années en matière d'identification des systèmes de pilotage, qui profitent maintenant d'un niveau de confiance relativement élevé. Le symposium a donné un aperçu général des méthodologies d'identification, des techniques d'essais en vol, des programmes d'application récents pour aéronefs à voilure fixe et à voilure tournante. Une session a été consacrée à de courtes présentations sur les derniers résultats des essais en vol. Lors de la dernière session, les spécialistes ont présenté des commentaires et la séance a été conclue par une discussion des questions clés soulevées par l'application des techniques d'identification des systèmes, ainsi que par l'identification des futurs besoins en matière de recherche.

Les principaux avantages pour les pays membres de l'OTAN peuvent être résumés ainsi :
- Des modèles mathématiques plus précis pour les systèmes de pilotage à bande supérieure,
- Estimation et évaluation des qualités de vol améliorées,
- Des modèles mathématiques de haute fidélité pour le développement des véhicules aériens et pour les simulateurs de mission, et, en général,
- La diminution des coûts et des délais des essais en vol.

Contents

---

† Paper not available at time of printing.

---

† Paper not available at time of printing.

Preface

System identification is becoming a tool of continually increasing importance within the processes of design and clearance of engineering systems. Many systems, and especially aircraft, are becoming increasingly complex, such that it can be difficult and expensive to verify the total system performance by demonstration alone. This applies whether the aircraft being considered is for military or civilian purposes.

Verification of the performance of a total system is increasingly reliant upon calculation, particularly for these highly integrated systems. Demonstration on its own is no longer an adequate tool to verify performance. To achieve verification of performance by calculation, it is essential to utilise models derived from prediction and verified by test. The methods used for identification of the system that enable these comparisons are referred to as the System Identification processes.

For use in this purpose, it is necessary that the processes and techniques have been proven to be correct by use of data derived from experiment. This data is then analysed and correlated with the expected performance, before being used in simulation of the total system. The use of system identification tools is the cornerstone upon which this philosophy is based. Successful application of these tools represents a major step in the integration of the overall system.

The objectives of the current symposium, sponsored by the Systems Concepts and Integration Panel of the Research and Technology Organization, can be described in the following way:

- A brief overview of the methods that are available for use, without delving too deeply into the mathematical background, such that an engineer might be able to consider the method most applicable to his purpose.
- The sharing of experience from the development of the system and practical application of system identification techniques.
- The understanding of lessons learned when the applications of the techniques have been unsuccessful, and what lay behind these events.

Systems Concepts and Integration Panel

Chairman:

Dr Edwin B. STEAR
Vice President Technology Assessment
The BOEING Company
P.O. Box 3999
Mail Stop 85-93
Seattle, WA 98124-2499
United States

Vice-Chairman:

Prof. Luis M.B. da Costa CAMPOS
Instituto Superior Tecnico
Torre-6o Pais
1096 Lisboa Codex
Portugal

TECHNICAL PROGRAMME COMMITTEE

Dr Mark B. TISCHLER
Rotorcraft Group Leader
AMES Research Center
MS N211-2
Moffett Field
CA 94035-1000
USA

Prof.Dr.-Ing. Peter HAMEL
Director
Institut für Flugmechanik
DLR
Postfach 3267
38022 Braunschweig
Germany

Prof.Dr.Ir. J.A. MULDER
Delft University of Technology
Faculty of Aerospace Engineering
1. Kluyverweg
P.O.Box 5058
2600 GB Delft
Netherlands

HOST NATION COORDINATOR

Prof. Jose-Luis LOPEZ-RUIZ
SENER, Ingenieria y Sistema, S.A.
Parque Tecnologico de Madrid
Calle Severo Ochoa s/n
28760 Tres Cantos (Madrid)
Spain

PANEL EXECUTIVE

Thomas E. ROBERTS, LTC, USA

Acknowledgements

Words of Don Pedro Morenés, Secretary of State for Defense

Good morning Ladies and Gentlemen,

As Secretary of State for Defense, it is my pleasure to welcome to Spain all those attending this Symposium on "System Identification for Integrated Aircraft Development and Flight Testing" organized by the "Systems Concepts and Integration Panel" of the NATO Research and Tecnology Organization, known by its initials RTO.

As many of you will know, the RTO is the result of the fusion of two other organizations, both with a long tradition in NATO. One is the AGARD, whose mission was dedicated to the aerospace world, and whose work has been a reference point for any other organization belonging to tthe aerospace world. The other, the DRG covers the land and naval aspects in particular. With this union, NATO intends to promote the activities of both, by taking the best from each. Likewise this is a sample of the importance that technology holds in NATO's plans vis a vis the changing world which has arisen since the end of the cold war.

Everyone is well aware of the profound changes that not only NATO, but all activities related to defense are undergoing.. Budget needs and restrictions have modified not only the Armed Forces, which find themselves more reduced in all countries, but also their missions, which are more multi-purpose, mobile and flexible. These changes promote and enhance the role of technology, as the only means of reconciling the needs and the restrictions.

On the other hand, nowadays we also bear witness to the use of the Armed Forces as means of pacification and humanitarian aid. This is in consonance with the Declaration of Rome in 1991 on Peace and Co-operation, in which the NATO countries base their principles of action on three elements: dialogue, co-operation and the maintenance of a collective defense capability.

Spain has participated in the activities of the AGARD and the DRG since it joined NATO in 1982. Almost every year we have hosted synposiums of the various panels, and our technical experts have particpated in the panels and work groups, with a degree of activity in consonance with our capabilities. It is our intention to continue the same degree of particpation in the RTO at all levels.

Regarding the symposium we are about to inaugurate, "System Identification for Integrated Aircraft Development and Flight Testing", I shall not insist further, as all of you present are experts in the matter. I only wish to point out that it is an example of how technology collaborates in improving the quality and price of modern aircraft.

Lastly, to round off my words, I would like to express my desire that the work sessions prove fruitful and that you will have an enjoyable stay in Madrid.

System Identification

for Integrated Aircraft Development and Flight Testing.

Technical Evaluation Report

K. McKay
British Aerospace, Military Aircraft and Aerostructures
Warton Aerodrome,
Warton, Preston, PR4 1AX, UK

Abstract

System identification is becoming a tool of continually increasing importance within the processes of design and clearance of engineering systems. Many systems, and especially aircraft, are becoming increasingly complex, such that it can be difficult and expensive to verify the total system performance by demonstration alone. This applies whether the aircraft being considered is for military or civilian purposes.

Verification of the performance of a weapon system is increasingly reliant upon calculation methods that have been proven to be correct and by use of data derived from experiment. This data is then analysed and correlated with the expected performance, before being used in simulation of the total system. The use of system identification tools is the cornerstone upon which this philosophy is based. Successful application of these tools represents a major step in the integration of the overall system.

The objectives of the current symposium, sponsored by the Vehicle Systems & Concepts Integration Panel of the Research and Technology Organisation, and as described in the pilot paper upon which the symposium is based, can be described in the following way:

- A brief overview of the methods that are available for use, without delving too deeply into the mathematical background, such that an engineer might be able to consider the method most applicable to his purpose.

- The sharing of experience from the development of the system and practical application of system identification techniques.

- The understanding of lessons learned when the applications of the techniques have been unsuccessful, and what lay behind these events.

My personal interest in this symposium, as the writer of this Technical Evaluation Report, reaches back many years. One of my earliest duties, as a member of the preceding Flight Mechanics Panel of AGARD, was to rewrite the pilot paper upon which the current activity is based. Personally, one of my key objectives was the sharing of the practical experience of application of these tools, as bitter experience had shown me that there were a number of pitfalls awaiting the inexperienced user. Whilst sharing of experience cannot prevent such problems, it is clear that not sharing knowledge and experience deprives everybody the opportunity to benefit from the experience of others.

1 Overview of the Symposium

The symposium featured a generally high standard of paper, both in content and presentation, with a number of the presenters showing the work performed to verify their modelling and ensure that their derived system models had an understandable, physical interpretation. Some of the techniques show the potential to derive models that match the experiment, but, should they be required for use in diagnosis of engineering fixes, then they will give rise to problems as they have a less physical meaning. The papers presented strongly indicate which techniques are currently being employed in a "production" environment by industry, as a preference for just this reason.

Many of the presenters confirmed the role of the engineer in interpretation of any results obtained. This is a crucial aspect. It is becoming increasingly clear that, if a physically realistic model is to be obtained, then the trained engineering interpretation

is needed. It is possible to automate the system identification processes, to ease the workload, but it will remain an essential that the overall engineering understanding is still in place.

Failure to achieve this would have the potential to arrive at models that have no physical meaning and cannot be used for other than predicting the responses from which they are derived. Clearly, this relates back to the issue of which system identification techniques are employed and will place a responsibility on the developers on new methods to deliver capabilities that allow this goal to be attained.

The symposium highlighted the rapid development of the analysis techniques that are now available for use in rotorcraft design and analysis. Ten years ago, such tools were only just being derived, predominantly featuring frequency domain techniques, in order to reduce the sensitivity to the high noise levels found with rotorcraft.

At the same time, there has been continued development of the fixed wing methods. These are now capable of analysis in very non-linear flight regimes, such as high angles of attack. However, there are uses for the frequency domain processes even with fixed wing, and it is clear that both fixed and rotary wing engineering teams can learn from each other.

There are a wealth of very demanding drivers for the use of these tools. The tools are now capable of delivering their full potential, not just in engineering terms, but also in terms of allowing flight test programmes to be reduced, with all the associated cost and timescale benefits that can result. The benefits obtainable need to be firmly demonstrated, whilst not allowing a reduction in the product quality. This is a major lesson that needs to be understood by all involved in projects where the tools are to be employed.

It will be interesting to compare the tools derived for aircraft purposes with those used in other fields. System identification tools are used increasingly within other applications outside of aerospace, and there is a potential for cross-fertilisation that has yet to be really followed up.

The papers present a wealth of information on the various techniques and the innovative applications being found for them and would provide both experienced system identification users and new users a good foundation of knowledge upon which to work. Some of the potential pitfalls associated with the tools are also indicated, and this will be a major benefit to new users and developers, alike.

2   The Keynote Addresses

The first address, by Charlie Crawford of Georgia Technical Research Institute, stressed the use of system identification in the development and qualification of rotary wing aircraft. Historically, the need arose from the problems that had been encountered in past products, resulting in the need to enhance the tools available and reduce the risks associated with new aircraft projects.

The major issue identified was the relative immaturity of the processes for predicting the behaviour and analysing the behaviour of rotorcraft, compared to the capabilities shown in fixed wing development programmes. The consequence of this immaturity was the need for extensive design changes in the aircraft after their first flights, even on the aircraft that won their respective design competitions.

The results showed a need to go back to basics, refining the modelling, including the use of wind tunnels, and the development of appropriate flight analysis techniques for use with rotorcraft. The result was the development of a frequency response test method, capable of providing information relating to most of the dynamic aspects of the airframe in flight.

The methods are capable of being used interactively, to allow analysis during flight, such that the test results are available at debrief of a test flight. Extensive use is being made of these techniques in the progression of the YRAH-66 flight test programme.

A key need, that was identified, relates to the ability to be rapidly assess the data quality for utilisation within the frequency response analysis, and then to be able to assimilate the results of the analysis and be able to provide simple explanations of the findings.

The second keynote address, by Prof. E. Varela Arroyo, Director General of INTA, stressed the use of the modelling as a means of reducing costs, whilst being better able to examine the real boundary conditions than is possible purely by flight test. The experience within INTA has developed from a means of correlation of wind tunnel measurements with flight, to a mathematical technique for system identification developed to support the qualification and certification of aircraft built and certified within Spain.

The activities included checking the results obtained from the processes developed against the flight data of known aircraft, in order to prove the system was performing correctly. These developed tools are now in use for the production of data relating to flight mechanics, performance and flutter on both the CASA CN235 and Eurofighter programmes. The key message was to recognise the significance of the tools, but also that they would never be able to replace the testing of the aircraft in flight.

3 System Identification - Applications in Recent Aircraft Programmes.

The objective of this session was to highlight the uses that have been found for system identification in current aircraft projects, including both experimental and prototype aircraft programme applications. Four papers described the breadth of applications in military, civil, fixed and rotary wing vehicle applications.

Paper 1, presented by John Hodgkinson, set out to present the airframe manufacturer's view of system identification. The tools used are either frequency or time domain and the use is chosen according to the application. The time domain methods used are derived from the US Navy Athena tool, a regression based technique. The frequency domain methods have their origins in the methods developed by the US Army for analysis of rotary wing aircraft.

Whatever tool is being used, it is essential that the engineer is always aware of state of the analysis. The tools are designed to assist an engineer with knowledge of aircraft increase his knowledge, and can never be regarded as "push-button". It is the engineering skill that underlies the successful use of the tools, supported by the process of always checking the measured data and designing the flight experiments properly to enable the data to be extracted properly. The paper contains a wealth of detail information relating to the practical experience from application of the tools on a range of projects, including transport aircraft, fighters and helicopters.

The paper forecasts that affordability would increase in significance as a driver for the systems identification process improvement and utilisation. For use within the civil transport market, there is already a well-defined and established utility that feeds into the verified models for simulators, etc. The military applications are working into higher angles of attack, with proven capability to deal with the problems that can be encountered due to non-linearity of the aerodynamics.

Paper 2, presented by Peter Hamel, addressed the key roles for system identification in relation to the model validation and the integration of the overall aircraft systems. It includes a review of a number of project applications within the experience of DLR, who have been major developers of system identification techniques for both fixed and rotary wing applications. The fidelity of the answer that is obtained is a crucial aspect, especially when defining the information for use in flight simulators. The paper describes the process as "Given the answer, what are the questions?" This gives the simplest view of the utility of system identification, which can be readily understood. A co-ordinated approach is necessary, based around the principles of the "Quad M" approach, i.e. Motion, Measurements, Methods and Models.

The paper stressed the need for automated generation of inputs that allow the correlated effects to be resolved. Correlations occur when the pilot input results in the motions of more than one control surface simultaneously, or response in two or more parameters at the same time. Experience with aircraft, such as the X-31, shows the need for individual excitation of the control surfaces to allow the resolution of the individual terms with the required accuracy.

The system identification techniques have been developed to cope with the effects of unsteady aerodynamics, and the paper showed the application of the resulting combined models to the stall of the Dornier 328.

Whilst DLR are considering developing technologies based upon neural nets, the presenter stressed the need to be able to relate the results back to a physical understanding. Without this, then it would be difficult to apply the results obtained, especially if the results are to be applied for certification. The general use of neural nets was considered to be one which will offer some significant problems for the certification process.

Paper 3 of the session reviews the use of system identification throughout the aircraft design cycle, using the experiences with fly-by-wire flight control systems for rotorcraft development and integration. In these applications, the main thrust has been the application of frequency domain representations, which can then be related directly back to the aircraft handling qualities and the design requirements. The specific tool that has been developed at the US Army Ames Research Centre

is CIFER – Comprehensive Identification from Frequency Responses. The paper includes a number of examples of the application of the system identification process to a number of different aircraft project applications, including both fixed and rotary wing. These applications have been made at various points in the design, certification and verification processes for the projects.

The key message related to the ability to extract an appropriate linear model that can be used for control system design purposes, rather than the difficulty of dealing with a fully non-linear model. The frequency sweep technique, adopted with the CIFER process, is preferred to a numerical perturbation technique, and was demonstrated to give better fits to the flight test data.

The tool has also been applied to the analysis of wind tunnel data relating to full-scale rotor tests performed in the NASA Ames tunnels. This was performed with a view to understanding the key physical parameters of the rotor, prior to building these parameters back into the prediction models of the full vehicle.

Frequency domain techniques, such as those described are, in the opinion of the author, particularly suited to the design process for flight control system developments.

4 System Identification Methodologies.

The first paper of this second session, Paper 4, addressed the application of output error identification techniques to the flight mechanics of Airbus aircraft. The requirement was to be able to update the pre-flight prediction for the aircraft within four months of first flight, using A-319 as an example. This stresses the importance of a good database to start from combined with the need to utilise the skills of the engineer to interpret the data. The results of the analysis were to be used in the formal certification of the aircraft.

Due to the non-linear aerodynamics involved, especially with the spoilers, the flight tests had to be specially designed to obtain a range of different data from different manoeuvres at close to the same angles of attack. These manoeuvres included dynamic inputs, steady sideslips and engine out of trim cases. All of these tests then contribute to the analysis of the lateral aerodynamics of the aircraft. Again, the presentation showed the need for the engineer to understand the process in order to be able to generate answers which would be physically

understandable and capable of re-predicting the aircraft motion satisfactorily.

It was noted, in response to a question, that the aircraft control laws in the approach mode had been modified to take account of the results obtained.

The second paper, Paper 5, dealt with the need to update aerial refuelling training aids to be more representative of the flight environment and behaviour actually encountered in this close control task. The paper described the extensive programme of tests necessary to derive the data updates to cover the possible tanker - receiver pairs. The result was an upgraded understanding of the tanker flow fields and their effects on the receiver aircraft. The process adopted made extensive use of GPS information to provide accurate positional data of the receiver relative to the tanker, essential for the determination of the tanker flow field and the effect that the receiver has on this as it approaches the refuelling boom.

The basic model structure chosen for the analysis was derived from a Dryden turbulence model. Using this approach, it was possible to generate a model that then reflected the aircraft behaviour. The validation of the derived model related to the analysis of the power spectral density information and no further validation was found to be necessary.

Simple model representations were adequate to provide a satisfactory model of the situation, based upon multi-dimensional look-up tables, which eased the implementation of the models.

The third paper, Paper 6, addressed the use of system identification applied to ground vibration testing and the supporting finite element structural models and the aerodynamic models, with a view to ensuring the aircraft is free from flutter within its flight envelope. The paper concentrates upon (a) the ground vibration test analysis and the subsequent updating of the Finite Element structural Model (FEM), together with an overview of the different aircraft support systems that are commonly used in ground test and (b) the resolution of the damping data from flight test. The presentation described the various techniques that are used, but mainly associated with transport aircraft, with the damping levels appropriate to this class of aircraft being considered. The conclusions are that further work is required to understand the effects of non-linearity, due to structural effects, flight control systems, etc.

The final paper of the session, Paper 7, outlined the applications of system identification techniques to the V-22 aircraft, with particular reference to the structural modes and their treatment by self-adaptive notching. The standard approach, as outlined by the previous speakers, was taken, with the chosen process being used to identify the model structure necessary.

The paper includes a description of the DSRA process. It concludes with describing the application to the V-22 structural mode analysis. Up to 21 modes were identified simultaneously. As with the previous paper, the main difficulty appeared to be identification of the damping with confidence. Using the techniques, adaptive notching, capable of dealing with abrupt frequency changes, was developed. This appears to be necessary as the mode frequencies vary with the applied load levels on this vehicle.

The paper concluded with an initial examination of the use of Kalman filtering to replace the notches. This technique was stated to be robust to changes in the modal frequencies and the associated damping. However, further work remains to be done with this technique in simulation, before moving to flight trials.

5 Flight Testing, Instrumentation and Data Gathering.

This session concentrated on the design of the experiments, and the associated instrumentation, to support the system identification requirements. One of the lessons to be drawn from these presentations is the need to be sure of what has been measured and to what accuracy, and to ensure that the flight experiments are designed to allow the necessary data to be extracted.

The first paper of the session, Paper 8, described the design of appropriate experiments to deal with both the bare airframe, i.e. considering just the response to the control surface inputs, and the aircraft with the FCS included in the loop. An optimal input has been designed, based upon a square wave of varying frequency, which gives a minimal output error. The resulting control inputs have been applied to the experimental F-18 HARV, implemented by an on-board excitation system. The presented results indicate that the optimal input always produced a final answer with better overall accuracy and lower variance. Also, the resulting models were more robust to errors in the apriori modelling of the system.

Design of this type of input has also been utilised in the assessments of other aircraft, including X-31 drop models, Active F-15 and will be applied to the Hyper-X.

There was a concern that too much effort could be placed in the design of the optimal inputs, especially when the effects of the amplitudes of the inputs have to be accounted for. There is a need to ensure that the exercise does not become one of academic purity, but retains its sense of purpose and application to an engineering task.

The second paper, Paper 9, described the validation of structural coupling stability, in flight, with a full authority, high gain flight control system. The example used within the paper is the Eurofighter 2000 aircraft project. The problem was that for this aircraft project, the traditional conservative approach of gain stabilisation is not viable for the range of configurations to be covered with the design. Hence, a phase stabilisation approach has been adopted, which required in-flight measurements to verify the process and ensure the safety of the aircraft.

In the process described, the structural aspects of the model validation have been proven via ground tests performed before the aircraft flew. This leaves the aerodynamic terms as the outstanding data to be determined in flight to validate the predictive model. To this end, specific inputs were designed for inclusion within the aircraft Frequency and Bias Injection system, using frequency sweeps between 2 and 15 Hz. A key requirement, to be able to utilise the facility and design the inputs correctly, was the determination of the detail effects of the flight control system and the data acquisition system.

With the understanding generated, it was possible to demonstrate the necessary validation of the design philosophy. The use of phase stabilisation is now an accepted part of the Eurofighter design philosophy.

The paper concluded with a view of where the further work was necessary and future research should be concentrated.

The third paper, Paper 10, of this session dealt with the identification of the dynamics of a helicopter with an underslung load. This is of significance as the load can cause degradation of the stability and performance of the system and there have been a number of accidents and incidents relating to this task. The task is complex, as the modes associated with the underslung load are added to the complex modes associated with the carrying helicopter.

A frequency domain analysis was employed, utilising the US Army CIFER process. The instrumentation packages were fitted to both the carrier and to the load, with the data being telemetered from both to a ground station for analysis.

The results presented clearly showed the changes in behaviour that can be experienced with the underslung loads. Depending on the margins that exist for the basic airframe, then this may become very critical for the aircraft and load combination. The remaining development issues relate to the understanding of the motions of the load under hover conditions, associated with the rotor downwash effects and limited information on the load aerodynamics.

The final paper of the session, Paper 11, discussed the use of integrated software tools as a means to expedite the production of analysed solutions. A wide variety of tools are available, but in the past, it has not been easy to transfer information between the tools, with consequent loss of time and additional cost. As a consequence, the US Navy had set out to integrate a number of these tools, updating as necessary, making the software portable and user friendly. A key initial step in the processes is the consistency checking which is undertaken before starting to determine the structure of the model, utilising an equation error based algorithm. Work on developing this system is now addressing the use of on line analysis and the generation of an expert system capable of making real time identification decisions.

6 Applications to Fixed and Rotary Wing Aircraft

This session of the symposium was by far the largest in terms of the number of papers describing applications of the techniques for system identification to fixed wing aircraft. Eight papers describe the applications to a wide range of fixed wing aircraft projects and with different applications for the resulting analysis. A further five papers describe the application of system identification techniques to rotary wing aircraft. Two papers, Paper 20 and 24, were withdrawn before the start of the symposium.

6.1 Fixed Wing Applications

The first paper, Paper 12, reviewed the system identification techniques and results generated within the Eurofighter consortium from tests performed at each of the flight test centres. The four partners use different identification processes,

all based upon well established techniques, but tailored to their individual needs and adapted to be able to cope with the highly unstable nature of the aircraft. The paper provides brief descriptions of the different processes and adaptations in use, with sample data showing the effectiveness of the techniques.

The paper showed a high degree of consistency between the different techniques, but indicated initially different data from the flight analysis compared to expectation in some areas. More detailed analysis indicated this was due to non-linearity in the sideslip data, for which no allowance had been made at the beginning of the process. Allowance for this could be made in some of the techniques and some examples of the results are included. Examples of use of the analysed results to confirm that the modelling gave believable and consistent results were shown.

A key message from the presentation was the close agreement of the results to the basic description of the aircraft and that the process has become one of confirming that the aircraft lies within the expected tolerance bands.

The second paper, Paper 13, dealt with the use of identification on large flexible transport aircraft, e.g. Boeing 777, with the intent of controlling the aircraft structural modes of this class of aircraft. For these aircraft, the problem is the low frequency of the structural modes with which the pilot can interact. Use of notch filters is not favoured due to the effects on phase loss that would result. The chosen solution is to develop modal suppression control laws to eliminate or reduce the effects of these modes on the aircraft control and motions. The starting point for the process is a structural model derived for flutter and dynamic load purposes, which is then matched for use within the controller design process. The identification process is complicate by the interaction of a number of modes within the structure, which can adversely affect the coherence data. A time domain model is developed for use in the controller design, based upon the identified behaviours. The presenter described how the process was refined, showing how it was necessary to modify the model to better fit specific modes and improve the ride response at different fuselage stations. The outcome has been a validated model used in the certification process of the Boeing large aircraft.

In response to a question on the effects of fuel state on the structural modes, the presenter stated that there were no problems of the controller robustness, but that checks had been performed, using sweeps,

at the extremes of the possible loading to confirm the robustness.

The third paper, Paper 14, describes the development of a database for use within a Level D flight simulator. This type of simulator, by definition, has to have the highest levels of fidelity to the aircraft being simulated. In this activity, DLR were acting as contractors to the aircraft manufacturer to supply their models to the simulator manufacturers. For these purposes, DLR chose to identify the aircraft from flight data, rather than derive corrections to existing wind tunnel data. The paper demonstrates that two different aircraft types required very different approaches to the modelling of the single engine effects.

Differences in propeller slipstream required considerably different approaches and experimental data to enable the resolution of the effects adequately for use in the simulation. A major conclusion of the work was the near impossibility of deriving a friction model for the control system that could cope with static control checks, dynamic control checks and modelling of the aircraft phugoid motion. A good set of learned lessons is included.

The fourth paper, Paper 15, dealt with a similar subject, deriving a model for a simulator from flight test identification. The work was performed as a co-operative research between NLR and University of Delft, with involvement of DLR Braunschweig. The particular aspect of interest was the objective relating to the development of an on-line data analysis capability, for use on the test aircraft. This required the development of techniques capable of determining the local winds, calibrating the air-data system and then deriving the aerodynamic model. It was noted, but not presented, that the model is now being extended to cover the effects of fuel slosh, with significant improvement being noted in the identification of some terms. The paper concluded that on-line analysis was possible, with consequent speed up of the flight test programme, but required good preparation and careful off-line processing to arrive at the final model.

The fifth paper, Paper 16, highlights some of the work performed at NASA with the HARV F/A-18 research vehicle applying system identification techniques for control law design and handling qualities evaluation. The vehicle features conventional controls, but has additional thrust vectoring and actuated nose strakes. The design of the flight control laws utilised a low order equivalent systems approach, and was shown to

give an adequate representation when the design ensured that high frequency modes were well separated and did not interact with the low frequencies.

The identification was found to give significantly different results from prediction at some conditions, which highlighted the very non-linear aerodynamics to be found at some conditions. The choice of amplitude for linearisation was a major factor. Also, the handling qualities assessments gave surprising variation, indicating that one pilot used significantly different amplitudes and bandwidth to his colleagues. A key finding is the need for running the tests at a range of amplitudes and frequencies to allow for the different dynamics that can result from the non-linear behaviour of the aircraft or control system. Some of the issues encountered are attributed to a combination of the control system gains and the characteristics of the aircraft actuators.

The sixth paper, Paper 17, examines the generation of a model for application in the aircraft stall, including unsteady effects.

The model form was derived from consideration of data from theory, and then this was applied to data from wind tunnel test measurements. The approach relates the aerodynamics to the flow separation point on the wing. The derived model structure was then used as the basis for flight test analysis, and results were shown comparing the results of both steady and unsteady stall models. The models clearly show the large hysteresis effects that occur due to the time delays inherent in the flow breakdown and redevelopment as the stall is recovered. As a final check, responses were estimated for flight tests which had not been used within the identification process, with good quality of the overall match. This gives added confidence in the quality of the identified model.

The paper caused some debate, as the simplicity of the modelling surprised a number of delegates with its ability to predict a complex situation, especially as it handles the wing drop behaviour at the stall. The test lies in the quality of the results produced.

The seventh paper, Paper 18, of the session dealt with developments of the techniques for application to high performance aircraft. These aircraft pose some unique problems, due to their ability to operate at extreme conditions for prolonged periods, their manoeuvrability and often, high levels of instability. This latter aspect makes the separation of control effects particularly difficult and is reflected in the co-linearity that leads to poor

conditioning of the analysis. The best way to deal with this is the use of single surface excitation inputs, rather than pilot inputs, implemented directly into the aircraft control system.

The results presented indicated the differences that are obtained from analysis of the same aircraft using pilot inputs, a least squares technique and a computer generated input with a regression technique. The paper provides good insight into the problems to be overcome and some of the ways for dealing with the problems encountered. Clear benefits are shown from having the single surface excitation fed in to the flight control system, even when all the control loops are still fully functional.

The final paper, Paper 19, of the fixed wing session described the system identification processes that have been developed and applied to analysis of the X-31, throughout the flight envelope of the aircraft, and including the effects of thrust vectoring. The presenter expressed the view that a deviation from a linear model based on a Taylor series is to be expected and that this was a driver to develop a more capable tool. The observed errors clearly confirmed this statement.

The addition of the thrust vector system produces some additional effects, due to the vectoring relying upon paddles around the nozzle. Flow visualisation, from the F-18 HARV confirmed these effects, which led to additional terms being included in the modelling. The thrust vector effectiveness is different depending on the direction of the vector, either up or down.

The apparent differences between this and the previous presentation for the thrust vector effectiveness were put down to differences in the initial prediction model. DLR had used the data from within the X-31 FCS look-up tables as a basis, knowing that these had been updated by flight test. Modelling of the thrust vector system required knowledge of the structure of the exhaust jet structure that helped contribute to the knowledge of the source of non-linearity.

It was suggested that the system identification process was suitable for calibrating the thrust vector efficiency.

6.2   Rotary Wing Applications

The first of the rotary wing application papers, Paper 21, related to the application of system identification in the time domain to helicopters. This application utilises a Kalman filter/eigensystem approach to derive an appropriate mathematical model of the system

under investigation, for use in the preliminary design of a flight control system. The process had to be capable of dealing with the effects of system noise, under circumstances where it may not always have been possible to even be sure of the feedback signals. The objective was to establish the capability to derive a model for a simulator build.

The process was applied to a model of the Lynx to demonstrate the capability and to an unstable radio controlled model helicopter. At present, the maturity of the approach remains to be better established, as this work is still in its early stages.

The second paper, Paper 22, presented the work on identification of a helicopter model in low speed flight. The test vehicle was the CEV Dauphin test vehicle, specifically dedicated to establishing the performance, acoustics and wake interactions. The FTI fit was highly redundant, working in fixed frame sensors, and a rotating frame to examine the blade flapping. These two systems were synchronised by using the azimuth of blade 1 as a reference. Again, the inputs were made via an automated system, whilst the pilot concentrated on trim and flight envelope control. Data processing included consistency checks and state reconstruction, using output error identification and extended Kalman filtering.

Whilst it was possible to produce adequate fits to the measured data, there were issues that need improvement. The response is insensitive to some parameters, the speed range was too great, the test amplitude too small. An improved model structure is needed with dedicated test manoeuvres defined to excite the aircraft.

The third paper, Paper 23, addressed the modelling techniques being developed at DLR with the objectives of identifying the vehicle with an accuracy that meets the requirements of the FAA for simulation fidelity. Both linear and non-linear modelling techniques are examined, together with a technique that combines both linear and non-linear methods.

The inclusion of the rotor dynamics increases the complexity of the model, even when considering the linearised model. In non-linear modelling, it is usual to build a modular model, each module representing a major component, giving rise to the overall forces and moments.

When combining the approaches, the model includes the main rotor and its motions, the tail rotor, downwash models for the main and tail rotors, fuselage and empennage parametric

formulations and a representation of the engine. The final model generation relies entirely on having a complete flight test database for the generation of the component terms, together with knowledge of all components of the helicopter. High fidelity representation is believed to be achievable.

The next paper, Paper 25, describes the work performed at NRC to include the higher order rotor dynamics in the modelling of a helicopter in the hover, based upon data from their Bell 412HP. This vehicle is to be used as an in-flight simulator, requiring a high fidelity model of the vehicle. The techniques were developed from work on the previous Bell 205, using sweep techniques. However, the process had to be modified to account for the behaviour of the Bell 412 at the lower sweep frequencies. A maximum likelihood estimation method was used, with a simplified rotor dynamics model. This demonstrated the need to modify the test input to achieve satisfactory flight characteristics.

Analysis was performed using CIFER, with generally good results, although there were discrepancies at some frequencies. This was identified as being associated with mast torque effects, which influences the dynamics, and gave a coherence problem. Also, the yaw and heave motions were difficult to reproduce, indicating the existence of higher order modes and an under damped modelling of the engine governor behaviour. Experiments were performed to confirm the validity of the identified models, confirming the validity between 0.1 and 30 Hz.

The final paper of the session, Paper 26, describes work performed to model the rotor flap inflow effects and the effects of the distortion of the wake. Again, the objective was to generate a model for use in simulation of the vehicle. Problems had been identified in predicting the off-axis dynamics of the vehicles, with the effects in flight even being of the opposite sign to prediction. A range of possible explanations exists; some of which improve the modelling, but may have limited physical meaning. The consequence is the need for extensive system identification tests to arrive at a description.

A generalised wake model was chosen as there was a wish to understand better the structure of the wake, rather than just arrive at a simplified representation that would not have a more general application. Comparisons of the model based predictions with wind tunnel measurements were presented. Inclusion of the wake distortion modelling greatly improved the off-axis responses, without influencing the on-axis response, which

was adequately predicted. The paper concluded with a view of the future work required to refine the understanding of the wake distortion effects and to add some of the higher order dynamics.

7 Special Applications and Future Trends

The seven papers within this section deal with unusual applications of system identification, or with novel techniques being developed. The section deals with a number of innovative applications, and contains two presentations of particular note for their novelty, these being Papers 27 and 31.

The first paper, Paper 27, describes the work performed on the Pathfinder solar powered research aircraft. The aircraft is the first of a series of research aircraft aimed at extreme duration flight at very high altitude. Flight duration of several months is being considered for the final vehicle. The very light vehicle, weighing around 500 lbs, is extremely flexible and flies at very low speeds, as low as 15 m.p.h. equivalent air speed, with operating altitudes up to 71500ft. Modelling of this system posed interesting challenges, associated with its apparent mass, similar to a blimp, its flexibility and the power effects due to the high thrust line and the slipstream effects from the propellers. Engine power effects are complicated by the power dependency on sunlight strength and direction.

Analysis of the aircraft was based upon programmed sweeps that were analysed to determine the aircraft stability margins with the control system included. CIFER was used as the tool to determine the margins, allowing a rapid flight envelope expansion and the adaptation of the control system gains.

The second paper, Paper 28, describes the application of system identification to updating a database of aerodynamic coefficients derived from wind tunnel tests. The work uses the data from the X-31 project.

The objective was to determine where there were deficiencies in the database, updating only where it was necessary, and including the thrust effects within the model at the same time as the aerodynamics. The technique used was a regression algorithm, avoiding the need for any integration. The basic database is used only once, and the updates are provided as increments to this. The presentation stressed the need to ensure the data is compatible and that accurate information for the effects of fuel state are obtained. Considerable

effort was spent in deriving the true fuel quantity, and this was subject to its own estimation process.

Demonstrations of the model match are provided, as are verifications of the model using comparisons with manoeuvres not included from within the identification manoeuvre set. The possibility of extending the identification to cover the dynamic flow separation effects at high angle of attack are being considered, as are improved thrust interference effects.

The third paper, Paper 29, presented an adaptive hybrid genetic algorithm for identification of the aerodynamics of a UAV. The driver for the work related to the design of the control system for the UAV, which required the application of identification techniques to generate a model for design. The presenter suggested that maximum likelihood process suffer from a number of well known problems, which can be overcome by the use of "genetic algorithms". This terminology correctly reflects the origins of the technique in the modelling of biological evolution. Advantages and disadvantages associated with the algorithms are assessed. The key advantage claimed is that the system is better capable of finding the global minimum for non-linear systems. Unfortunately, due to the loss of the test vehicle, it has not been possible to show the results with real flight data. Also, it was unclear whether a physical model would result.

The next paper, Paper 30, describes the aerodynamic identification using linear aeroballistic theory, an analysis technique derived in the 1920's. This theory was developed to describe the motions of rolling and non-rolling missiles in flight. The paper describes the basis of theory and concludes with comparisons of the simulated responses with the results from the estimation method. The technique is shown to be sensitive to noise, but can still provide adequately accurate initial estimates of the aerodynamics of the key parameters.

The fifth paper, Paper 31, examined the application of system identification to gyroplane stability and control. The key driver was the understanding of the airworthiness issues surrounding gyroplane or autogyro vehicles and their control characteristics at low airspeed, in support of the Bristish civil airworthiness authorities. Currently, there are no commercial applications and most use is in the homebuilt aircraft category. The work resulted from the accident rate experienced with the vehicle type.

The trials undertaken posed special problems, arising from the size of the aircraft and the very light weight, combined with operating under the necessary regulations within the UK. The analysis employed frequency domain techniques with an equation error approach. Frequency sweeps were used, but the key to successful identification lay in the use of engineering judgement if the results obtained.

Rotor speed couples significantly with the rigid body modes in this type of vehicle, which gave rise to significant variations in rotor speed as the pitch stick is cycled during its frequency sweep. A significant relation between vertical c.g. position and the propeller thrust line were identified as a major contributor to the low speed pitch stability.

Again, the presenter showed the verification of his derived model against the flight test data.

From the data gathered in these trials and the subsequent analysis performed, the statutory requirements have been updated.

The sixth paper, Paper 32, examines the release of weapons from aircraft. Here, the objective is to ensure as large a release envelope as possible whilst ensuring the safety of the aircraft, especially when considering modern weapons which tend to be stealthy and aerodynamically unstable. The prediction process was outlined, looking at the store and the aircraft motions, using information derived from CFD methods, captive store trajectories and flight trials analysis. Structural interfaces are considered within the modelling. Allowances are made for uncertainty in the aerodynamics and the ejection devices in preparation for the flight release trials.

Two examples are discussed, the release of a missile (Apache) from the Mirage 2000 and a tank from the underwing station of Rafale. The presentation showed the use that had been made of the CFD tool in understanding some of the roll aerodynamic interactions between the aircraft and the tank, even after separation from the aircraft.

The final paper of both the session and the symposium, Paper 33, addressed the use of neural networks to adaptive controls and control system failure identification. The vehicles of interest have included the high altitude unmanned research aircraft, spacecraft and UAVs. The attraction of the neural net approach lies in the ability of a neural net to recognise patterns and classify these. They are of particular use for systems involving uncertainty. They inherently are suitable for

parallel processing, which are then highly fault tolerant, and have an ability to learn from previously recorded information. Examples of application to simulated data, including injected failures of sensors and actuators were presented. The process identified the failure correctly, up to which point the system was still learning. The presenter recognised that the certification issues had not be addressed, but that had not been on of the declared objectives.

8 Latest Results

This final session of the symposium was aimed at sharing some of the latest results obtained from the application of the various techniques available, for which no formal presentations had been prepared. The presenters gave short briefs on their latest information and key messages for the symposium attendees.

The first presentation related to an experimental analysis of wing rock. The experiment involved a free to roll model with an 80° leading edge sweep, tested in a low speed wind tunnel. The objective was to produce a database for further analysis.

The second presentation dealt with the correlation of flight and wind tunnel data from the Eurofighter high angle of attack programme. The presentation highlighted the power of the output-error regression analysis technique in dealing with non-linear aerodynamic behaviour. It also illustrates the quality that can be achieved in the wind tunnel. The wind tunnel indicated very non-linear rolling moments at certain combinations of foreplane angle and angle of attack, and this related closely to the data extracted from flight. The question was posed as to how many of the non-linear problems described by other presenters were associated with this type of aerodynamic phenomenon, and had this been identified?

The third presentation examined the identification of unsteady aerodynamics from wind tunnel data, using the F-16XL. The formulation introduced a frequency dependency into the modelling for high angle of attack. The driver was the difference observed between static test data and oscillatory test data. Significant unsteady effects were identified, which were dependent on both the frequency and the amplitude, raising a question as to how this should be modelled. The result was a model using the static term combined with a damping term from small perturbation oscillatory data and the additional indicial functions that represent the effects of frequency and amplitude.

This was shown to be able to predict the characteristics at varying amplitude satisfactorily.

The fourth presentation related to the update of the powered approach database utilised in the training simulation for the F-18. The brief covered the origin of the database and the work undertaken by the Navy to derive the update for the model. The investigation concluded that control effectiveness had been over predicted and that there were significant errors in the damping terms. The consequence was that the simulation model gave very pessimistic behaviour compared to the aircraft in flight. Some of the effects read across to the F/A-18E/F roll damping problem.

The final presentation covered work performed at INTA on an RPV using a state estimator to provide estimates of the vehicle attitudes, rates, air-data information and navigation data inputs. These inputs are then used in the control of the vehicle, which is somewhat demanding, as it requires sustained flight close to the vehicle stall speed. This places a tight requirement on the speed data and angle of attack signals. With the chosen approach, the result is a fault tolerant system with the possibility of continued operation following a sensor failure.

9 Concluding Remarks – The Future Needs

Overall, the symposium achieved the objectives that were declared in the original pilot paper. A wide range of possible system identification techniques were presented and discussed, with a lot of examples of the practical application of the techniques being provided.

It is clear that there has been very significant development taking place since the last AGARD activity on this subject, with a wide range of tools, albeit of comparatively standard types, being employed throughout the engineering community.

This is especially true of the rotary wing applications, where an extreme need had been identified, some time ago, to be able to extract data for use in design of helicopters. Until this happened, the designers had almost no database, other than past experience upon which to work. The result has been the development and use of frequency domain techniques, which allow the inherent signal noise problems to be circumvented. Now, time domain methods are being looked at to cope with models needing increasing complexity and non-linearity.

For fixed wing vehicles, the major developments have been in extending the capabilities to be able to analyse the vehicles at high angles of attack, in the presence of extreme aerodynamic non-linearity. Also, some application is now being made of the frequency domain techniques the identification of the structural elastic modes of the aircraft in flight. Examples of this were shown for civil and military applications.

From the information presented, the following conclusions have been drawn: -

1   System identification tools have achieved a level of power and maturity where their application should now provide significant gains in terms of reduced flight test programmes and, hence, project timescales and costs.

2   Tools appropriate to both the time and frequency domain are available and are robust and validated.

3   The flight test experiments have to be properly designed, if maximum use is to be made of the data gathered. It is essential that time is taken to prepare the data adequately prior to its use with the chosen technique.

4   The role of the engineer in using the various system identification tools will remain a key factor in the successful use of the tools.

5   Whilst it is possible to automate the processes involved in data preparation, data handling and display of the results, it is difficult to see how the interpretation will be automated.

6   Associated with this, there are some concerns over techniques that will provide models that cannot be related to the physical characteristics of the vehicle or system being modelled.

7   These concerns are alleviated if the engineer has a clear view of what the model is intended for. A non-physical model can be appropriate for some applications.

The future needs relate more to the development of the appropriate models to work with the existing techniques, rather than the search for new techniques for system identification.

Having said that, there are techniques being worked upon that would appear to have potential as analysis techniques, but which certainly require significant validation using real flight data, together with all of the problems that this will bring. Currently, these techniques, such as the application of neural networks, have a low level of maturity and an associated difficulty of interpretation.

It is clear that industry will seek for improved, faster processes which support their activities, but only if the cost of development will produce the reward of reduced project costs, whilst maintaining or enhancing the current levels of product quality.

NATO Research & Tech Org ———————— **Georgia Tech** Research Institute

POTENTIAL for ENHANCING the ROTORCRAFT DEVELOPMENT / QUALIFICATION PROCESS USING SYSTEM IDENTIFICATION

Presented by:
Charles C. Crawford, GTRI ∗

SYS IDENTIFICATION for INTEGRATION
AIRCRAFT DEVEL & FLT TESTING
5 - 7 May 98

Sys Concepts & Integration Panel ———— **Madrid Spain** ————

NATO Research & Tech Org ———————— **Georgia Tech** Research Institute

ORDER of PRESENTATION

✔ **BACKGROUND**
➢ *1989 Alexander Nikolsky Lecture*
➢ *Back to Basics*

✔ **ROTORCRAFT FLYING QUALITIES OPTIMIZATION PRIOR to SYS IDENTIFICATION METHODS**

✔ **ENHANCING DEVELOPMENT / QUAL PROCESS**
➢ *a New Basic, Frequency Response Testing*

✔ **BENEFITS of SYSTEMS IDENTIFICATION METHODS for MODIFICATION and / or UPGRADE PROGRAMS**

✔ **SUMMARY**

Sys Concepts & Integration Panel ———— **Madrid Spain** ————

∗ Aerospace & Transportation Lab.
Georgia Technic. Research Institute
7220 Richardson Rd., Bldg 2-160
Smyrna, GA 30080, USA

AHS 1989 NIKOLSKY LECTURE

"ROTORCRAFT ANALYTICAL, IMPROVEMENT NEEDED to REDUCE DEVELOPMENT RISK"

✔ ANALYSIS of 4 MAJOR HELO DEVELOPMENTS

UTTAS		AAH	
UH-60	SIKORSKY	YAH-63	BELL
YUH-61	BOEING	AH-64	HUGHES

✔ INTERDISCIPLINARY COMPLEXITIES of ROTORCRAFT

✔ ANALYTICAL PREDICTION SHORTFALLS

➤ Vibration Levels   – Aerodynamic Performance

➤ Vibratory Loads   – Weight Estimating Realism

✔ LACK of SIGNIFICANT ROTORCRAFT WINDTUNNEL TESTING

✔ MAJOR AIRVEHICLE DESIGN CHANGES in FLT TEST

✔ INABILITY of TOOLS to FACILITATE DESIGNS which FLY ADEQUATELY "OFF the DRAWING BOARD"

Sys Concepts & Integration Panel ————————— Madrid Spain

ROTORCRAFT MULTI-DISCIPLINE INTERACTIONS
Main Lifting Rotor Only

Sys Concepts & Integration Panel ————————— Madrid Spain
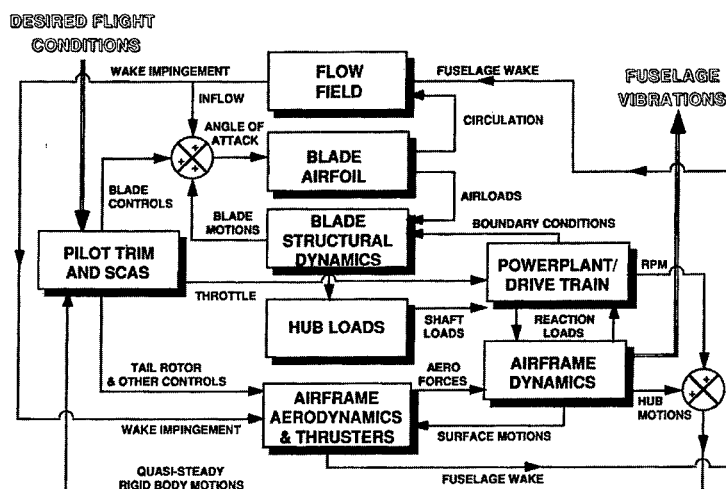
NATO Research & Tech Org ——————————— Georgia | Research
Tech | Institute

MOST COMPLETE US DEVEL / QUAL PROG
UH-60 SERIES

Sys Concepts & Integration Panel ——————— Madrid Spain

YUH-60A DESIGN CHANGES AFTER 1st FLT

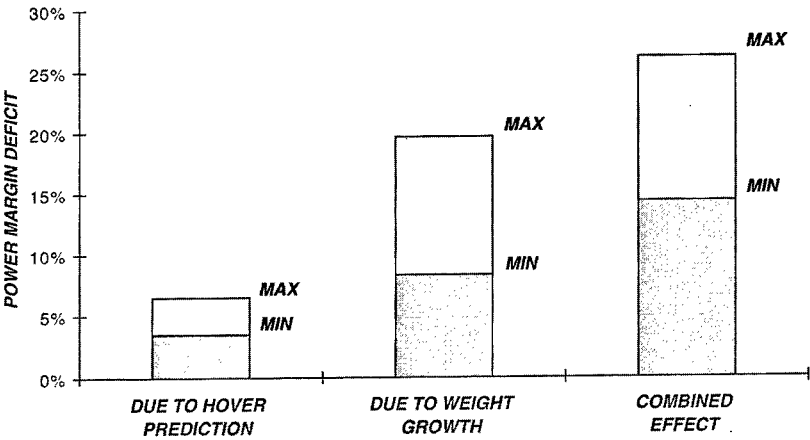| TOPIC	FLT TEST PROBLEM	DESIGN CHANGE
• BASIC AIRFOIL	• MAX LOAD FACTOR LOW	• ADDED DROOP SNOOT
• MAIN ROTOR BLADE	• HOVER CAPABILITY LOW	• TIP CAP EXTENDED 4 INS/BLADE
• ROTOR HEIGHT	• HIGH VIBRATION HIGH ROTOR BLADE LOADS	• ROTOR MAST INCREASED 15 INS
• STABILATOR CONFIG	• AIRCRAFT ATTITUDES IN LOW SPEED FLT REGIMES • HIGH SHAFT BENDING	• LOW FIXED STABILIZER RAISED • MADE MOVABLE OVER A 43 DEG RANGE THRU AUTO CONTROLS
• VERTICAL FIN AREA	• LARGE TRIM CHANGE UNSTABLE SIDEWARD FLT	• REDUCED FIN AREA WITH CUT-OUT
• TAIL ROTOR MOUNT & CONTROL	• HIGH FLT LOADS	• ROTOR SHAFT, SUPPORT STRUCT, & CONTROLS REDESIGNED FOR INCREASED STRENGTH
• LANDING GEAR SPONSON	• HIGH DRAG	• CHANGED INCIDENCE ANGLE TO ALIGN WITH FUS FLOW
• TAIL ROTOR GEARBOX	• UNDETECTED OVERTEMP	• REPLACED GREASE LUB WITH OIL
• CONTROL SYSTEM AUTHORITY	• POOR CONTROL HARMONY	• LAT SENSITIVITY INCREASED YAW/ROLL MECHANISM INCORPOR
• MAIN ROTOR SERVOS	• HIGH FLT LOADS	• REDESIGNED FOR INC STRENGTH
• MAIN ROTOR DAMPERS	• HIT DAMPER STOPS IN HIGH SPEED AUTOROTATION	• MOVED INBOARD DAMPER OUTBOARD BY 3.5 INS
• MAIN TIRES	• MECHANICAL GROUND INSTABILITY	• INCREASED SIZE & PRESSURE TO INCREASE STABILITY MARGINS
• AIRSPEED SYSTEM	• EXCESSIVE ERROR	• FLEW OVER 100 FLTS TO OPTIMIZE
• AFT NACELLE CONFIG	• HIGH TAIL VIBRATION & BUFFET	• REDESIGNED TO IMPROVE AIRFLOW PATH
• STABILITY AUG SYS	• VARIABLE FLT CONTROL SYS CHARS W/ EXTREME TEMPS	• CHANGED FROM FLUIDIC TO ELECTRICAL/MECHANICAL

Sys Concepts & Integration Panel ——————— Madrid Spain

YUH-60A DESIGN CHANGES AFTER 1st FLT

TOPIC	FLT TEST PROBLEM	DESIGN CHANGE
• BASIC AIRFOIL	• MAX LOAD FACTOR LOW	• ADDED DROOP SNOOT
• MAIN ROTOR BLADE	• HOVER CAPABILITY LOW	• TIP CAP EXTENDED 4 INS/BLADE
• ROTOR HEIGHT	• HIGH VIBRATION HIGH ROTOR BLADE LOADS	• ROTOR MAST INCREASED 15 INS
• STABILATOR CONFIG	• AIRCRAFT ATTITUDES IN LOW SPEED FLT REGIMES • HIGH SHAFT BENDING	• LOW FIXED STABILIZER RAISED • MADE MOVABLE OVER A 43 DEG RANGE THRU AUTO CONTROLS
• VERTICAL FIN AREA	• LARGE TRIM CHANGE UNSTABLE SIDEWARD FLT	• REDUCED FIN AREA WITH CUT-OUT
• TAIL ROTOR MOUNT & CONTROL	• HIGH FLT LOADS	• ROTOR SHAFT, SUPPORT STRUCT, & CONTROLS REDESIGNED FOR INCREASED STRENGTH
• LANDING GEAR SPONSON	• HIGH DRAG	• CHANGED INCIDENCE ANGLE TO ALIGN WITH FUS FLOW
• TAIL ROTOR GEARBOX	• UNDETECTED OVERTEMP	• REPLACED GREASE LUB WITH OIL
• CONTROL SYSTEM AUTHORITY	• POOR CONTROL HARMONY	• LAT SENSITIVITY INCREASED YAW/ROLL MECHANISM INCORPOR
• MAIN ROTOR SERVOS	• HIGH FLT LOADS	• REDESIGNED FOR INC STRENGTH
• MAIN ROTOR DAMPERS	• HIT DAMPER STOPS IN HIGH SPEED AUTOROTATION	• MOVED INBOARD DAMPER OUTBOARD BY 3.5 INS
• MAIN TIRES	• MECHANICAL GROUND INSTABILITY	• INCREASED SIZE & PRESSURE TO INCREASE STABILITY MARGINS
• AIRSPEED SYSTEM	• EXCESSIVE ERROR	• FLEW OVER 100 FLTS TO OPTIMIZE
• AFT NACELLE CONFIG	• HIGH TAIL VIBRATION & BUFFET	• REDESIGNED TO IMPROVE AIRFLOW PATH
• STABILITY AUG SYS	• VARIABLE FLT CONTROL SYS CHARS W/ EXTREME TEMPS	• CHANGED FROM FLUIDIC TO ELECTRICAL/MECHANICAL

Sys Concepts & Integration Panel ——————— Madrid Spain

POWER MARGIN DEFICIENCIES
Excludes VROC Consideration

Sys Concepts & Integration Panel ——————— Madrid Spain

BACK to BASICS

✔ **BUILDING STRONGER THEORETICAL METHODS to ENSURE that ROTORCRAFT PERFORM as PREDICTED**

✔ **RESULTING ANALYTICAL CODES, (Partial List)**
  ➢ *Second Gen Comprehensive Helicopter Analysis Sys - - (2GCHAS)*
  ➢ *Comprehensive Analytical Model of Rotorcraft Aerodynamics & Dynamics - - (CAMRAD / JA & CAMRAD / II)*
  ➢ *University of Maryland Advanced Rotorcraft Code (UMARC)*

✔ **APPROACH WIND TUNNEL TESTING as UTILIZED by FIXED-WING DEVELOPERS**

✔ **NASA / ARMY UH-60A ROTORCRAFT AIRCREW SYS CONCEPTS AIRBORNE LAB (RASCAL) FLT TEST PROG**

Sys Concepts & Integration Panel ————————— Madrid Spain

COMPREHENSIVE ANALYSIS

✔ **MUST COVER for ALL ROTORCRAFT CONFIGS**
  ➢ *Aerodynamic, Structural, and Kinematic Nonlinearities*
  ➢ *Arbitrary Large Motion of Components*
  ➢ *Multiple Load Paths*

✔ **MUST be CAPABLE at ALL STAGES of DEVEL CYCLE**
  ➢ *Research*   ➢ *Detailed Design*
  ➢ *Conceptual Design*   ➢ *Development*

✔ **MUST PROVIDE MULTI-DISCIPLINARY ANALYSIS**
  ➢ *Performance*   ➢ *Vibration*
  ➢ *Loads*   ➢ *Stability*
  ➢ *Dynamic Response (Handling Qualities)*

Sys Concepts & Integration Panel ————————— Madrid Spain

FLYING QUALITIES OPTIMIZATION PRIOR to SYS IDENTIFICATION METHODS

✔ **SIGNIFICANT STABILITY & CONTROL FLT TEST HRS**
  - ➤ *Method of Operation - - Test, Fix, Retest*
  - ➤ *Some Simulation Used; Little Before Late 1980's for Rotorcraft*
  - ➤ *AFCS Knobs only Easy Tuner*

✔ **EXAMPLES:**

	Total Devel / Qual	HQ / AFCS / VIB
YUH / UH-60A	1275 flt hrs	470 flt hrs
YUH - 61	893 flt hrs	523 flt hrs

✔ **FREQUENCY RESPONSE TESTING SIMPLY NOT DONE**
  - ➤ *Single Frequency Pilot Induced Stick Stirs Potentially Risky*
  - ➤ *Jigs Used to Control Input Sizes*
  - ➤ *Data Analysis Techniques not yet Matured*

Sys Concepts & Integration Panel ———— *Madrid Spain*

JVX and LHX BEGAN SIGNIFICANT CHANGES
Advent of Fly-by-Wire Flt Controls

✔ **A NEW "BASIC", FREQ RESPONSE TESTING**
  - ➤ *A Means of Correlating Theory and Experimentation*
  - ➤ *Applies to HQ Analysis, Model Validation, & Control Law Design*

✔ **ULTIMATE GOALS:**
  - ➤ *Decrease Devel Cost by Reducing Flt Test & Redesign Efforts*
  - ➤ *Capitalize on Multiplex Tech for Increased Sensors Reqts*
  - ➤ *Capitalize on High-Bandwidth Digital Flight Control Sys*
  - ➤ *Increased Safety During Developmental Flt Testing*
  - ➤ *Avoid Structural Modes - Control Sys Coupling*

✔ **FIRST APPLICATIONS in MID 1980's:**
     Boeing ADOCS & Bell XV-15

Sys Concepts & Integration Panel ———— *Madrid Spain*

NATO Research & Tech Org ———————— **Georgia Tech** Research Institute

CURRENT ADVANCE DEVELOPMENT PROG
RAH-66 COMANCHE

Sys Concepts & Integration Panel ———————— *Madrid Spain*

NATO Research & Tech Org ———————— **Georgia Tech** Research Institute

RANGE of APPLICATIONS for
FREQ RESPONSE TESTING

VIBRATION SPECTRAL ANALYSIS

SAFETY & RELIABILITY

HANDLING QUALITIES

SIMULATION VALIDATION

AIRCRAFT DYNAMICS — FREQUENCY SWEEPS — FREQUENCY RESPONSE DATABASE → STRUCTURAL DYNAMICS

AEROELASTIC ANALYSIS

TRANSFER FUNCTION MODELS

CONTROL SYSTEM DESIGN

STATE SPACE MODELS
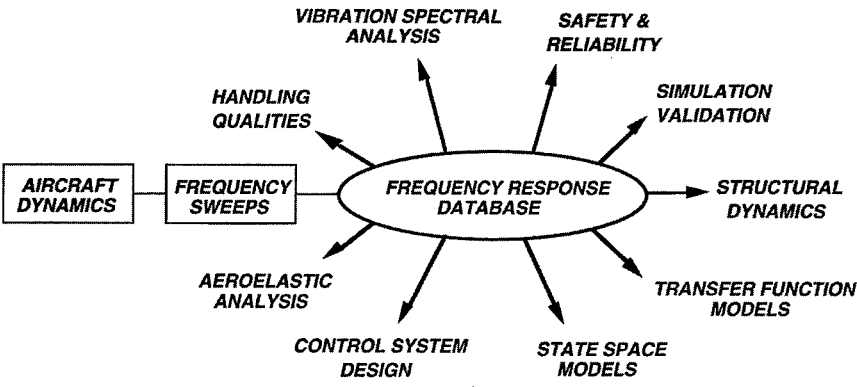
Sys Concepts & Integration Panel ———————— *Madrid Spain*

YRAH-66 TEST INSTRUMENTATION
First Aircraft to Test

	Approx No Parameters
Flt State Parameters	20
Rotary Airspeed System	85
Structural Measurements	190
Vibration Accelerometers	45
Thermocouples	310
Pressure Measurements	150
Flt Control Computer Parameters	750
Multiplex Bus Parameters	300
Mission Equipment Package	1050
	2900

INSTRUMENTATION PACKAGE WEIGHT = 1986 lbs

NOTES:
1) 79 Flts for 87.4 hrs thru 27 April 1998
2) Avg Test Flt = 1.1 hrs
3) Total Planned Prog = 3400 flt hrs

Sys Concepts & Integration Panel ——————— *Madrid Spain*

FLT CONTROL SYS INTEGRATION LAB
FCSIL - Features Provide

✔ **INTERFACE to RAH-66 FCS & RELATED COMPONENTS**

✔ **HYDRAULIC & ELECTRIC POWER to FCS HARDWARE UTILIZING AIRCRAFT PUMPS, HPMGS & PROVISIONS for GENERATORS**

✔ **SYSTEM SPECIFIC TEST EQUIPMENT**

✔ **FCSIL is USED to VERIFY & VALIDATE ALL FCS COMPONENTS & SOFTWARE PRIOR to FLT**

✔ **FREQ RESPONSE TESTING has BEEN USED TO:**

➤ *Validate that Actuators Perform to Spec*

➤ *Sensors Perform to Spec*

➤ *FCS End-to-End Response Performs to Spec*

Sys Concepts & Integration Panel ——————— *Madrid Spain*

TYPICAL YRAH-66 FREQ SWEEP

1-4 H_Z Lat Sweep, HOGE @ 13,300 lbs, 95% N_R
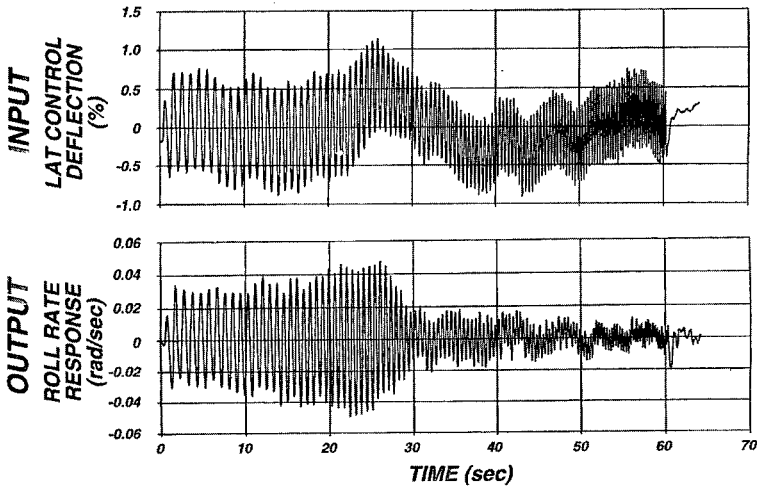
Sys Concepts & Integration Panel ——————— Madrid Spain

TYPICAL YRAH-66 FREQ SWEEP

1-4 H_Z Lat Sweep, 140 KIAS @ 13,300 lbs, 100% N_R
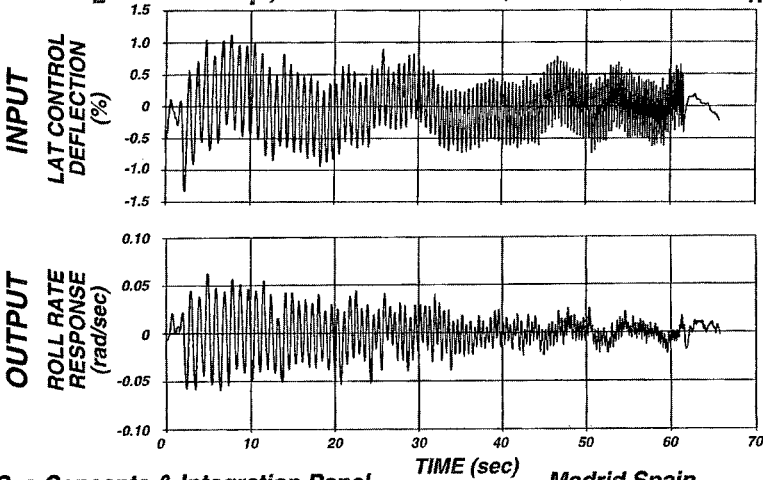
Sys Concepts & Integration Panel ——————— Madrid Spain

NATO Research & Tech Org ———————————— **Georgia Tech** Research Institute

FREQ RESPONSE TESTING for YRAH-66

✓ *DIRECTIONAL AXIS STAB MARGIN INVESTIGATIONS*

✓ *AIRSPEED SCHED STATIC MIXING MATRIX IDENTIFIED*

✓ *FLIGHT CONTROL SYS / STRUCTURAL COUPLING EVAL*

✓ *FLIGHT SIMULATION MODEL VALIDATION*

✓ *REGRESSING LAG MODE IDENTIFICATION*
   ➤ *Modified Pitch-Lag Coupling Model*
   ➤ *Updated Snubber Damper Properties*

✓ *ELASTIC AIRFRAME MODE IDENTIFICATION*
   ➤ *Validate or Adjust NASTRAN Predicted Modes*

Sys Concepts & Integration Panel ————— *Madrid Spain*

NATO Research & Tech Org ———————————— **Georgia Tech** Research Institute

MAJOR SOF HELICOPTER UPGRADE
MH-53J PAVELOW

Sys Concepts & Integration Panel ————— *Madrid Spain*

NATO Research & Tech Org ————————————— **Georgia Tech** Research Institute

SYS ID for MOD / UPGRADE PROGS
A Worked Example

✔ **DEFINED by STABILITY MARGINS (GAIN and PHASE) of FLT CONTROL SYSTEM SERVO-LOOP**

✔ **MARGINS REQUIRED to ALLOW for REDUCED STABILITY due to:**
  ➤ *Hysteresis, Control System Slop, Servo Wear, A/C Variability*
  ➤ *Increased Pilot Gain (ex. Precision Tracking)*
  ➤ *Configuration Changes (ex. Sling Loads)*

✔ **OPEN LOOP from CONTROL INPUT to AFCS OUTPUT**

✔ **MARGINS MEASURED from BODE PLOTS**
  ➤ *Phase Margin - Dist to 180° at 0 dB Gain*
  ➤ *Gain Margin - Dist to 0 dB at 180° Phase*

Sys Concepts & Integration Panel ———— *Madrid Spain*

NATO Research & Tech Org ————————————— **Georgia Tech** Research Institute

FCS / STRUCTURAL COUPLING

AIRFRAME FIRST VERTICAL BENDING MODE

GYRO LOCATIONS · ANTI-NODE · BENDING MODE · FUS. STA. · FWD · MID · AFT
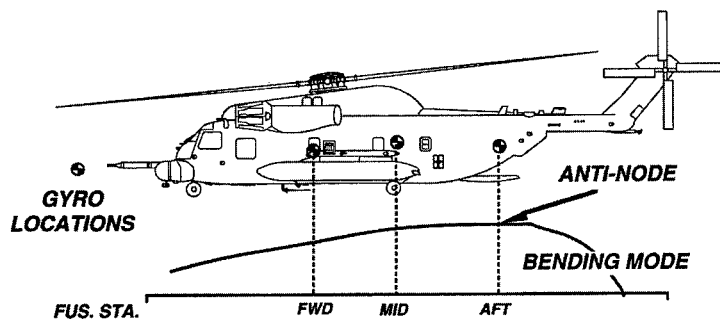
✔ **FCS SENSOR PICKS UP FUSELAGE ELASTIC RESPONSE**
✔ **RESULTS in REDUCED STABILITY MARGINS**
✔ **BIODYNAMIC FEEDBACK ALSO IMPACTS STABILITY**

Sys Concepts & Integration Panel ———— *Madrid Spain*

NATO Research & Tech Org ———————— **Georgia Tech** Research Institute

SAFETY CONSIDERATIONS

✔ *TESTING INVOLVES an OVERLAP of DISCIPLINES:*
  (HANDLING QUALITIES - FLT CONTROLS - STRUCT)

✔ *HISTORY of ACCIDENTS INVOLVING STRUCTURAL*
  FAILURES DURING TESTS

✔ *STRUCTURAL DAMPING CAN BE VERY LOW (1-2%)*

✔ *CRITICAL STRUCTURAL RESPONSES MUST BE*
  MONITORED REAL-TIME

✔ *PRE-TEST ANALYSIS and TEST BUILD-UP REQ'D*

Sys Concepts & Integration Panel ——————— *Madrid Spain* ———

NATO Research & Tech Org ———————— **Georgia Tech** Research Institute

FREQUENCY RESPONSE TEST TECHNIQUE

Sys Concepts & Integration Panel ——————— *Madrid Spain* ———

Slide 1
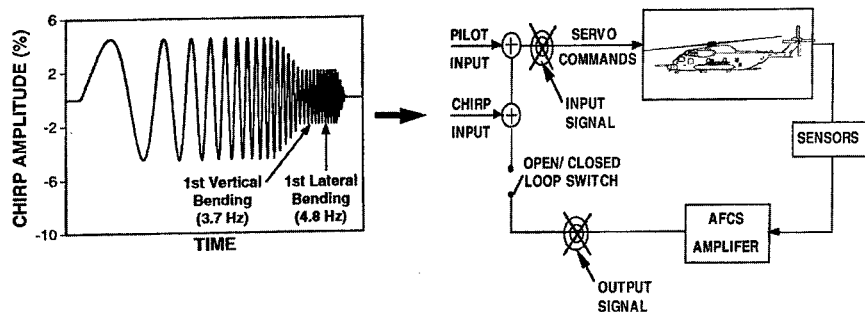
STABILITY MARGIN ANALYSIS
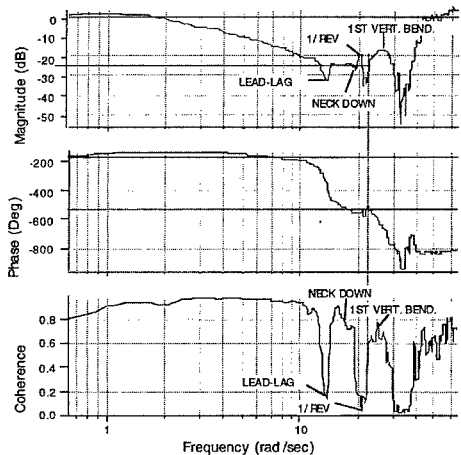
✔ **STABILITY AFFECTED by GYRO LOCATION**

✔ **LARGEST GAIN MARGIN at ANTI-NODE**

Vertical Gyro Location	Gain Margin (dB)	Phase Margin (deg)
FS "FWD"	7.95	31.0
FS "MID"	6.33	30.3
FS "AFT"	15.08	28.2

Sys Concepts & Integration Panel ———— Madrid Spain

Slide 2

SUMMARY

✔ **SYSTEM IDENTIFICATION METHODOLOGY BENEFITS**

➤ Results in Massive Quantity of Data for Rapid Prob / Mishap Analysis & Facilitates Definition of Design Fixes

➤ Accurate Definition of Aircraft Response for Validating/Updating Models Including an Understanding of Vehicle Dynamics not Previously Possible

➤ Basic Technology for Handling Qualities & Flt Control Dev &Validation Which is Equally Useful for Modernization of Older Aircraft

✔ **NEEDED TECHNOLOGY/ MGT ENHANCEMENTS**

➤ Tools for Rapid Assessment of Data Quality/Identification Results Inflight

➤ Wider Dissemination of Sys Identification Tools, Techniques & Training

✔ **BEST USED with FLT CONT INTEGRATION LAB in DEVEL**

✔ **CHALLENGE - - - STANDARDIZE PROCEDURES and SIMPLIFY EXPLANATIONS for PROJ MGT PERSONNEL**

Sys Concepts & Integration Panel ———— Madrid Spain

Keynote Address

System Identification: Its Application in Aerospace Development, The Spanish Experience

Prof. Emilio VARELA ARROYO
General Director, INTA
Catra. de Ajalvir, Km4
28850 Torrejon de Ardoz (Madrid), Spain

Excellencies, Ladies and Gentlemen: It is a great honour for me to address this select audience in the Keynote Addresses of this symposium on "System Identification for Integrated Aircraft Development and Flight Testing".

The symposium's subject is in itself a topic with a great future since it helps us to obtain a better knowledge of aerospace systems and enables us to improve their operational capability before initial operation of the units of the series.

INTA, the Spanish Institute in charge of the development of aerospace technologies cannot isolate itself from these techniques that study the behaviour of aerospace systems and which are a good complement to the flight test programs. The use of these techniques results in a reduction of the number of flight tests required before certification of an aerospace system, with the corresponding saving in time and money. This is done using mathematical models which allow a more exact control of boundary conditions than in the real flight tests.

Since the forties, the Spanish aerospace industry has used several precedents of these techniques. Wind tunnels and mathematical simulation were applied for several projects carried out by Spanish firms as CASA, SENER, GMV, INDRA as you may see in the keynote address.

During the 90's, parameter identification has been promoted in Spain by CASA and INTA.

CASA uses these techniques in three main domains:

* ❖ Flight Mechanics
* ❖ Runway Performances
* ❖ Flutter Analysis

In flight mechanics, CASA has developed its own software packages with different methodologies including equations error and statistical methods. The runway performances are fundamental to develop the proper take off and landing techniques, specially for STOL aircraft. The interest of flutter analysis lies in the identification of the modal, structural parameters. All these techniques have been used in the CN-235, CN-295 and in FE 2000 aircrafts using CASA flight centre telemetry facilities.

A group of INTA engineers are currently working in the development of software applicable to parameter identification in the following aspects:

- Stationary Conditions
- Modal analysis
- Identification of equivalent models
- Adaptive Estimator for navigation, guidance and flight control system.

The software developed by INTA in these areas has been applied to parameter identification of SIVA, an Unmanned Aircraft Vehicle developed by the Spanish aerospace industry.

As you can see, the interest of the Spanish aerospace in this subject is very great, since we wish to continue to be present in future aerospace developments, cooperating with all the other countries which are present here today.

In the future, parameter identification techniques will be a common application in the development process of aerospace systems, with the corresponding reduction of flight tests. But, may I say that my opinion is that in aerospace technoloyg, flight tests will continue to be present for many years. Among other reasons, because flight tests are the basis of these new parameter identification technologies, and finally because the model, however exact it may be will never replace the real aircraft testing.

I thank you for your attention and I wish you a fruitful work during this symposium and a pleasant stay in Spain during these days.

An Aircraft Manufacturer's View of Parameter Identification

John Hodgkinson
Joseph R. Boland
Meredith Q. Brandt
Eugene Lavretsky
Kenneth F. Rossitto
A. Thomas Stephens
Scott W. Stevenson
Thomas L. Thompson

The Boeing Company
Mail Stop C078-0420
2401 East Wardlow Rd.
Long Beach, CA 90807-5309, USA

ABSTRACT

Boeing adopts an eclectic approach to parameter identification methods. Time-domain methods for stability and control parameter estimation are used alongside frequency-domain methods which are chiefly used for determining lumped flying qualities parameters. Example applications described include use of identification to develop training simulators for transport aircraft, determining parameters and sensor corrections for fighter/attack aircraft, reconstructing an event for which partial data were available, determining the flying qualities changes due to helicopter modifications, and validating the dynamics of an in-flight simulator.

INTRODUCTION

Parameter identification is a technology with especially wide relevance to an aircraft manufacturer. This paper describes only some of the parameter identification approaches being used in some of Boeing's activities because an exhaustive coverage of all related company activities would be impractical. Examples of additional activities appear in Reference 1. The methods described in this present paper consist of time-domain methods for stability and control parameter estimation, and frequency domain methods for determining lumped flying qualities parameters. The time domain methods have their origins in software developed for fighters, and the frequency domain methods were originally developed by the US Army for helicopters.

APPLICATIONS AND APPROACHES FOR PARAMETER IDENTIFICATION

Applications

In this paper, we will specialize the term 'parameter identification' (PID) as any method that infers the parameters of a dynamic mathematical model from the responses of an aircraft. Our company has a wide range of aircraft products, examples of which appear in Figure 1. The following Table indicates some applications of PID as practiced in various components of the Boeing company.

Product or Application	Example	Motivation for PID	PID Features/Challenges
Fighters	F-18 C/D/E, F-15/E, AV-8B, X-36	Update of control laws. Implementation of training simulation. Documentation of configurations. Effects of stores.	High order control dynamics with heavily damped modes Operation at high angles of attack (where the model is nonlinear)
Large transports	B747, B757, B767, B777, MD-11, C-17,	Update of control laws. Implementation of training simulation.	High order control dynamics with heavily damped modes. Flexibility. Relaxed static

	MD-10,	Verify effects of mods (stretches, new surfaces etc)	stability. Power effects including powered-lift effects.
Medium transports	B737, B717	Implementation of training simulation. Verify effects of mods (stretches, new surfaces etc)	Instrumentation commensurate with simple flight controls.
Attack helicopters	AH-64	Update of control laws. Implementation of training simulation	Rotor/power effects. High order control dynamics with heavily damped modes
In-flight simulators	Total In-Flight Simulator (TIFS) C-17 T-1 test-bed	Validation of flying qualities model-following.	High order control dynamics. Excellent instrumentation.
Research aircraft	Drop models, X-36	Determine parameters at edge of the envelope	Scaling effects
Generic	All	Incident/accident investigation	Reconstructing events from sparse data

Methods

In this paper, we report on various methods which draw on the most appropriate PID technology for the task at hand. We will describe time domain techniques applied to fighter aircraft, and frequency domain methods applied to helicopters and to flying qualities research aircraft.

Time domain methods

Most of our fighter/attack PID experience is with time domain methods. Methods used generally include an equation error (regression) approach combined with flight trajectory/signal reconstruction, and a filter error estimation approach. The PID program PRISM has been developed over the last eight years. It contains the capabilities for either of these two methods. The specific method used depends on many factors like the angle of attack range, the types of maneuvers available for PID, and the type of data measurements available. The filter error method is generally more successful in the low AOA region where the aerodynamic behavior of the aircraft is linear and the PID model is relatively small (less than 30-50 parameters). In this method an optimization scheme is used to estimate parameters to achieve matches between flight test and simulated time history signals.

The integrated signals are filtered back to the flight test measured signals. One significant advantage of the filter error approach includes not having to perform extensive airdata or signal reconstruction of maneuvers prior to PID. Many airdata and instrumentation errors can be identified and corrected at the same time as the desired aerodynamic parameters. A disadvantage of the filter error method is its inability to handle neutrally stable or unstable aircraft. When applied to unstable aircraft, high filter gains must be used to prevent the integrated time histories from diverging. These high gains often have an adverse effect on parameter estimates.

The most widely used PID method applied to fighter aircraft is the equation error method combined with flight test signal reconstruction/validation. The equation error method is fundamentally very simple. It consists of performing a regression to fit a PID data model to time histories of the six aerodynamic coefficients computed from flight test. Advantages of this method include its ability to handle relatively large PID data models (200-250 parameters), and its ability to combine large numbers of maneuvers. These two factors make the equation error method well suited for use in

the medium-high AOA regions of the flight envelope.

Here, the PID model is non-linear. Though PID is often thought of as a fundamentally linear technique, with engineering judgement it can be extended to nonlinear data. Starting with "consistently reduced" flight test data, we perform a non-linear least-mean square regression of the differences between the flight test aerodynamic coefficients and the aero model predicted coefficients. The regression is iterative, where the engineer is trying different regression models, piecewise-linear break points, spline functions, etc. to minimize the overall mismatch. Different maneuvers are combined into one large data set to achieve the needed information content. We often create nonlinear data models using piecewise linear or spline basis functions.

Frequency domain methods

Most of our frequency domain experience has been with the Comprehensive Identification from FrEquency Responses (CIFER) computer code. Very briefly, the code is essentially a fast Fourier transform of time history data followed by a fit of the resulting frequency responses with a rational transfer function. The method was originally developed for helicopter applications but has also been widely applied to fixed-wing aircraft. Some advantages and disadvantages of the CIFER frequency domain method (which is described in detail by Tischler (References 2, 3) have been discussed by Harding (Reference 4).

Advantages:

Bode plot presentation
This presentation allows bandlimiting to accommodate the desired model structure. For example, Harding used this feature to exclude effects of the relatively high-frequency first rotor flapping mode and modes beyond so that he could focus on rigid-body modes.

Weighting with frequency
Low and high frequency dynamics are weighted more equally. Time domain methods tend to place more weight on low frequency dynamics.

Initial accelerations and reference shifts
These items must be handled by time domain methods, but in frequency domain methods they are unnecessary.

Database buildup
The database can be built up from different test data. This is more involved in time-domain methods which require time synchronization with a common number of inputs and outputs.

Lumped parameter approach
In addition to the above factors mentioned by Harding, the lumped parameter form of equivalent systems can be obtained directly in the frequency response matching segment of the method.

Disadvantages:

Computational effort
Frequency response estimation, compared with time response methods, has the additional step of estimating frequency responses before the parameter estimation matching process itself is performed.

Insight
The physical understanding of how the state-space model parameters affect the frequency responses is somewhat lost compared to matching time histories. However the validity of this statement depends somewhat on the background of the analyst and the objective of the identification exercise. In particular, if the purpose of the exercise is to examine the flying qualities of the vehicle, many analysts prefer the Bode presentation.

Treatment of high frequency modes
If the high frequency modes are of particular interest, the frequency response method is generally superior because the Bode presentation unfolds the high frequency response rather than collapsing it into the initial response of a time history. Again, flying qualities analysts are looking for lag/delay effects at high frequencies, and as we shall illustrate, helicopter analysts are particularly interested in higher frequency modes generated by rotor dynamics.

SPECIFIC APPLICATIONS

Heritage Boeing Commercial Aircraft Applications

From the foregoing, it is evident that considerable computational power and sophistication is available to the analyst at Boeing. Nevertheless, we place a large premium on engineering insight and this is reflected in our choice of methods. Bearing this in mind, our first example describes the approach adopted by the heritage Boeing Commercial Airplane Group, the former Boeing commercial aircraft unit prior to the merger with McDonnell Douglas.

Aerodynamic simulation model development at the heritage Boeing Commercial Airplane Group is focused on producing high-quality, full flight envelope simulation databases which support both crew training and engineering design/analysis. Desired simulation fidelity is currently not achievable without performing a flight-test update to the predicted aerodynamic models. The processes and tools used to perform a flight update to a simulation model have evolved over several years to a level which produces excellent aerodynamic databases (Reference 5). An overview of the current process is presented below.

While the specific implementation and level of automation may vary, the basic steps required to produce a satisfactory flight test update to a simulation database are similar. These steps are outlined below.

- Understand airplane instrumentation and resulting measurements
- Determine flight test maneuver set
- Obtain acceptable flight test data
- Prepare flight test data for analysis
- Calculate aerodynamic coefficient errors
- Distribute coefficient errors to appropriate model buildup terms
- Validate updated model via proof-of-match
- Document the simulation model, data, verification and validation

A brief description of the heritage Boeing Commercial implementation of each of these steps follows.

Understand airplane instrumentation and resulting measurements
A detailed understanding of how the data get from the sensor to the analysis program is essential to a successful flight test update process (Reference 6). Complete information on measurement filtering, time skew, calibrations and post-flight processing is often difficult to obtain. It is essential, however, for adequate data conditioning. Information obtained for each flight test measurement used is coded into the software tools (see Flight Data Processor below) to ensure consistent, universal interpretation of the measurements.

Determine flight test maneuver set
Heritage Boeing Commercial obtains simulator-specific flight test data for:
1) validation of the simulation to high standards of fidelity
2) information to aid in aerodynamic coefficient error extraction and allocation.
It is important to determine a flight test maneuver set that optimizes the information content for the aerodynamic coefficient extraction process and covers the required/desired maneuvers for simulation validation while minimizing the flight test time required.

Maneuvers which support crew training simulator qualification are selected to include appropriate tests from the Flight Simulator Validation Tests of the ICAO Simulator Qualification Manual (Reference 7) and the IATA Simulator Data Requirements (Reference 8). Selected data from these tests will ultimately appear in the Approval Test Guide which is provided by each training simulator operator to the appropriate regulatory authority.

Coefficient extraction maneuvers are obtained primarily from expansion of the flight envelope around ICAO simulator qualification tests. Since the simulation is used for both engineering and crew training purposes throughout most of the flight envelope, it is important to update and validate as much of the flight envelope as possible. To this end, maneuvers are performed at a variety of altitudes, Mach numbers, center-of-gravity positions and configurations (e.g. flaps, gear, spoilers,

etc.) above and beyond those called out for simulator qualification.

The ideal design of flight maneuvers for aerodynamic coefficient extraction would have independent parameter variation in only one parameter at a time. This is never completely accomplished in flight, but attempts are made to isolate effects on coefficients as much as possible. Some maneuver procedures may be modified to improve coefficient extraction analysis. One example is leaving the landing gear extended throughout a normal takeoff/climbout maneuver to remove gear transition effects.

A few maneuvers are designed and flown specifically for coefficient extraction. Examples of these include shallow approach to landing, decelerations with various airplane configurations and stabilizer/elevator trades.

Obtain acceptable flight test data
Flight testing for simulation requires careful planning. Test conditions, maneuver types, and pilot techniques must be well defined. Onboard instrumentation must be specified along with the requirements for measurement accuracy. All of this planning requires close coordination between aerodynamics engineering, flight-test support groups and flight test pilots. Boeing test pilots are highly skilled and often provide valuable insight and suggestions for how a test should be performed.

While pre-certification and certification testing is used wherever possible, approximately 30-80 hours of simulator-specific flight testing is required for each new airplane program. Simulator-specific flight testing is required for several reasons:

- Simulator-specific flight testing needs to occur late in the flight test program to ensure that the configuration represents the production airplane. This is not possible for pre-certification testing.
- The requirement for modified procedures to support coefficient extraction for some maneuvers would preclude the use of non-simulation maneuvers.

- It is not possible, with current technology, to account accurately for the effects of a turbulent wind field on the aircraft response. Therefore, an important requirement for each test is that the atmosphere be as free of turbulence as possible.

Prepare flight test data for analysis
Simulation validation and aerodynamic coefficient extraction analysis require highly accurate, kinematically consistent flight test measurements throughout the flight test operating envelope. This requires a thorough knowledge of each flight test measurement so that all known errors may be removed prior to use in engineering analysis. The Flight Data Processor (FDP) is the primary software tool used to prepare flight test data for engineering analysis. The primary functions are:
1) formatting parameters (e.g. flap, slat, gear positions) to be compatible with engineering analysis tools,
2) filtering Euler angles and rates, linear accelerations and ground speeds,
3) calculating an altitude and static pressure time history based on kinematically corrected inertial accelerations (i.e. flight path reconstruction),
4) using these static pressures to calculate airspeeds,
5) calculating angle of attack from either inertial data or by using a detailed alpha vane calibration, and
6) calculating the winds and gusts acting on the airplane.

Calculate aerodynamic coefficient errors
Our update process uses measured flight data to determine the incremental coefficient values which must be applied to the existing simulation aerodynamic model to satisfy the equations of motion (Reference 6). We calculate these incremental coefficient values in a software tool known as the Coefficient Extraction Program (CEP). The CEP takes the output from the flight data processor and
1) computes total flight test aerodynamic coefficients based on flight test accelerations and airplane state,
2) computes current simulation model aerodynamic coefficients given the flight

test airplane state and control system inputs and

3) computes incremental aerodynamic coefficients required to match the simulation and flight test outputs (i.e. the difference between 1) and 2) above).

The program will also compute the resulting table values for each of the selected tables assuming all of the coefficient error is put into the selected table.

Distribute coefficient errors to appropriate model buildup terms

This step of the process can be one of the most challenging. If the simulation model were only used to replicate flight test results over a fairly restricted flight envelope for which data were available, the task of updating the model would be greatly simplified. However, the simulation is used as an engineering design tool to make new design decisions, is used outside the flight test validated flight envelope, and must be capable of supporting a wide range of training applications. This requires the total aerodynamic coefficient errors identified in the previous step be correctly distributed to the appropriate individual components of the aerodynamic buildup equations.

Our method for aerodynamic coefficient error allocation relies on considerable interpretation and engineering judgment in conjunction with carefully flown maneuvers which aid in the isolation of individual components. The flight test update is undertaken by a team of engineers who have extensive knowledge of the aerodynamic effects on aircraft stability and control. The team is divided into a Longitudinal and Lateral/Directional group who work each axis in parallel. Each axis group may further focus on specific areas (e.g. high speed, low speed, ground effects, etc.). The team must carefully coordinate its efforts to produce a consistent model which satisfies the requirements of all types of maneuvers throughout the flight envelope.

The sequence in which each aerodynamic coefficient is updated is important. For example, in the longitudinal axis the best results are obtained by first updating stabilizer effectiveness using longitudinal trims. The next term to be modified is the elevator effectiveness based on

stabilizer/elevator trades. Once the updated tail effectiveness has been established, the basic wing-body terms may be determined using deceleration and stall maneuvers. This process continues through each of the coefficient components. Several iterations of this update sequence may be required to converge on a flight test update coefficient set.

Advantages of this method include:
1) produces excellent simulator databases,
2) can be visualized in physical terms making it easy to explain,
3) engineers gain an understanding of the fundamental characteristics of the airplane which may be useful in future analyses,
4) "physically correct" data constraints may be applied throughout the update process.

Disadvantages include:
1) very labor intensive,
2) requires a long flow time to create a simulation update,
3) not guaranteed to be a repeatable process.

There are significant pressures to decrease engineering and flight test related costs including those related to the flight test update of the simulation database. At the same time, there is a continual need to improve simulation fidelity to satisfy both external customers (e.g. training simulator operators and regulatory agencies) and internal customers (e.g. engineering design groups) in expanding roles. This combination of conflicting requirements is leading us to search for improved alternative coefficient update methods and increased automation wherever possible throughout the update process.

Validate updated model via proof-of-match

Quantitative validation of the aerodynamics model is achieved by showing a match between the simulation and flight test data for a variety of maneuvers and flight conditions. To perform such a match, the engineering simulator is driven by actual measured values of control surface position and engine thrust, as well as wind speed and direction throughout the time history. The use of mathematical pilot models is acceptable for certain applications. The

simulator response is overlaid with the measured airplane time history.

Document the simulation model, data, verification and validation
Documentation of the process outputs is very important and is a requirement of the simulator manufacturers to aid in the qualification of the flight simulator under development. The simulation aerodynamic model and data are provided in the Data Document, the verification data in the Checkout Document and proof-of-match data in the Validation Document. Each of these documents are an important internal reference and are provided to the simulation manufacturers in both hard copy and electronic media format.

Summary of Heritage Boeing Commercial Experience
The simulation flight update process has evolved to a point where high-quality, full-flight envelope mathematical models may be consistently produced. Basic steps similar to all update methods are used in the heritage Boeing Commercial update process. While each step of the process is important, the most challenging step is the allocation of total coefficient errors among the appropriate individual components of the aerodynamic buildup equations. This requires considerable interpretation and engineering judgment. The conflicting requirements of reduced costs while improving simulation fidelity are encouraging the search for improved alternative coefficient update methods and increased automation wherever possible throughout the update process.

Fighter/Attack PID Experience
Time domain PID methods have been used on all of Boeing's fighter aircraft programs over the last ten years to update flight simulation aerodynamic data models. Areas of application have included the low, medium, and high Angle of Attack (AOA) regions across the entire Mach envelope. An objective in all these regions is to improve the simulation data model fidelity and thus flying qualities predictions. Other objectives include loads predictions in the low AOA/ high-speed regions, departure characteristics in the medium AOA region, and spin and spin recovery characteristics in the high AOA region.

F/A-18E/F example
The Super Hornet is 25 percent larger than its predecessor. The fuselage features a 34-inch extension, and the wing has an additional 100 square feet, again being 25 percent larger. The F414-GE-400 engine, with larger air inlets, produces 35 percent more thrust.

An example of the improvement to the simulation model achieved with PID is demonstrated in the F/A-18E/F coefficient match of a rolling maneuver at moderate AOA shown in Fig 2. In the figure, flight test total rolling moment is calculated directly from the roll acceleration measured in flight. The baseline database is calculated from the wind tunnel basis using the value of the pertinent independent variables along the flight test trajectory. When PID estimates are included in the database, significant improvement in matching the flight test data is seen. In this case, estimates made of roll damping were the primary factor in improving the model in the roll axis, Fig 3.

Improving the coefficient match of a particular time history is not the only goal of the PID analysis, however. Integrated time history matches can also be generated by use of a six degree-of-freedom program. Fig 4 shows a comparison of a flight test trajectory to the simulated trajectory of an F/A-18E/F upright spin. In the figure, the simulated trajectory is generated by initializing the six degree-of-freedom program at the flight test conditions, then driving the program with the pilot inputs from the flight test maneuver. The oscillatory-divergent characteristics of the spin are improved with the addition of PID estimates to the aerodynamic database. In this case, the modeling of the non-linearity of directional stability with sideslip was improved in the PID model, Fig 5.

AV-8 example
The main disadvantage to the equation error (regression) method is its sensitivity to data inaccuracies. The method requires a high degree of data accuracy and repeatability from a combined set of maneuvers. Small biases in AOA, slideslip, control surface positions, or other measurements can have

a significant impact on results. Data accuracy requirements of the equation error method require that the data be validated and/or reconstructed prior to its inclusion. This validation/reconstruction step often becomes 80% of the effort when performing PID analyses.

Some recent high-speed loads analysis on the AV-8B aircraft revealed a significant source error correction to the production AOA sensor. To estimate the source error correction, a filter error method was used to reconstruct flight test AOA and compare this reconstructed signal with the production AOA measurement. In this method, inertial velocities and reconstructed winds are transformed through a series of kinematic equations to compute an estimated (reconstructed) AOA. An optimization loop wrapped around these kinematic equations determines the AOA bias and scale factor necessary to make the flight test production AOA measurement best match the estimated AOA. Figure 6 is an example of a typical AOA reconstruction from a wind-up turn maneuver. This figure provides a comparison of the production AOA measurement, the estimated (reconstructed) AOA, and the production AOA corrected with the estimated bias and scale factor. In this example, applying the AOA bias and scale factor estimates causes the measured AOA to match closely the estimated AOA.

Then, a least squares regression of all of the AOA biases and scale factors from a large set of maneuvers is performed to arrive at the final AOA upwash correction as a function of Mach number and production AOA. Figure 7 shows the final upwash correction identified during the recent AV-8B high-speed loads analysis. This plot indicates that the production angle of attack measurement was in error by as much as 10% at the higher Mach numbers.

Performing PID anlyses without identifying and compensating for data measurement errors of this nature would cause these measurement errors to translate directly into aerodynamic coefficient errors, thereby significantly lessening the value and effectiveness of the PID effort.

Heritage Douglas Commercial Experience

Background

Compared with its predecessor, the DC-10, the MD-11's aerodynamic improvements include winglets and a redesigned wing trailing edge, a smaller horizontal tail with integral fuel tanks and an extended tail cone. These features reduce drag, save fuel and add range.

The MD-11 certification program included an increase in the automation of the traditional PID development process. The motive was to be able to meet the requirements for the Level-D (the highest level) FAA simulator qualification. This qualification involved matching flight test data for more than eighty maneuvers throughout the flight envelope using the in-house developed six-degree-of-freedom simulation program. The PRISM software was adopted to supplement the MMLE maximum likelihood method. PRISM was designed to perform a non-linear regression and was able to estimate the incremental tables while the MMLE was geared towards the linear derivatives.

The PRISM software is designed to perform two major tasks:

1. Flight test data reduction. This capability has been employed extensively as an aircraft incident/accident investigation and analysis tool. Its components are:
   - kinematics consistency check This task is based on the function minimization (optimizer) routine. Currently the Levenburg-Marquardt method is employed
   - data calibration
   - data filtering
   - wind reconstruction.
2. Identification of aerodynamic parameters
   - estimation of the incremental aerodynamic data tables based on the existing aircraft-specific aerodynamic database and aero model structures.

We applied the above processes during the MD-11 and MD-90 certification programs. Both motion base simulators were qualified on time to Level D.

Example ValuJet Flight 592 Flight Path Reconstruction

The PID package was used to estimate missing data from the flight data recorder, as well as to perform kinematic consistency check on the available data. Though the acceleration data were available at 8Hz, the remaining data were available at only 1Hz. Nevertheless, the flight path of the aircraft was reconstructed consistent with other known aspects of the flight (see Figure 8). The results were used by the US National Transportation Safety Board (NTSB) and the FAA during the case hearing. This data reconstruction/smoothing method has since been standardized for our investigations of aircraft accident/incidents for the NTSB. The method also offers an ability to estimate the wind profile if it is suspected that the incident is wind/turbulence-related.

Rotary-Wing Experience

Much recent rotary wing identification has utilized the CIFER program developed by Tischler. This program bases its identifications on CHIRP (Continuous Harmonic Intermediate Range Progression) frequency responses.

In the study we will describe, frequency response data were obtained for a prototype AH-64D Longbow Apache aircraft as part of a handling qualities survey test. The responses and the identified parameters were obtained for comparison with existing AH-64A data. The AH-64D is the next-generation version of the combat-proven AH-64A Apache. The Apache Longbow's fire control radar and advanced avionics suite give combat pilots the ability to rapidly detect, classify, prioritize and engage stationary or moving enemy targets at standoff ranges in near all weather environments. The AH-64D configuration has greater pitch and roll inertia and greater mass compared with the AH-64A, and it will be seen that the identification quantified the dynamic differences that would be expected from these changes.

One value of this comparison was to estimate the effects of the changed configuration on the dynamic response of the vehicle. Data were acquired in hover and level forward flight at 75 and 120 knots true air speed at 2300 feet density altitude,

and in climbing flight at 1500 ft/minute at 80 knots at 5000 feet altitude. The input was a pilot-generated frequency sweep in one axis from below 0.2 Hz to about 3.5 Hz, beginning and ending with the aircraft in trim. A frequency sweep typically took between 90 to 120 seconds to complete. The pilot was able to achieve a fairly constant rate of change of frequency by listening to a small tape player which sounded different notes at each half cycle point. This signal was recorded several times over and enabled the pilot to perform a succession of repeatable frequency sweeps. The stability augmentation system was turned off. The pilot was instructed to make any inputs necessary in the remaining three control axes to maintain the aircraft near the trim condition. The control sweeps were conducted three times in each axis. An example sweep for the directional axis is illustrated in Figure 9, along with the primary and secondary responses (yaw and roll rate respectively).

Data Acquisition

All the frequency responses were derived from time histories acquired at 58.2 Hz (0.017 seconds resolution). Data were then reduced off-line using the CIFER (Comprehensive Identification from FrEquency Responses) program (References 2 and 3). CIFER operated on responses concatenated from ones like Figure 9, giving 4 or 5 minutes of vehicle excitation to reduce variance in the responses. Five windows with intervals of 60, 40, 20, 10, and 5 seconds were used. The effects of secondary control inputs were removed by conditioning the frequency responses determined in each of the windows. The conditioned responses resulting from this process are the same as would have been obtained had no secondary control inputs been present. A CIFER composite window algorithm was then used to combine responses from each of the five windows, which increased the accuracy of the final set of extracted responses over a wide range of frequencies. Plots of log-magnitude, phase and coherence were then generated as a function of log-frequency using a CIFER plotting utility.

Identification

Once the amplitude and phase characteristics had been gathered, the responses were fitted with simple low order transfer functions. The fitting process uses routines originally developed at Boeing for order reduction of fixed-wing flying qualities responses (for example, see References 10 and 11). The matching routine utilizes a search algorithm. The algorithm minimizes the sum of the squared amplitude and phase differences between the frequency response data and the data for a low order transfer function. Thus, the algorithm seeks the low order transfer function parameters that produce the best match. For example, the heave degree of freedom was matched with

$$a_z(s) / \delta_{col}(s) = \frac{sZ_{col}}{(s - Z_w)}$$

where Z is the vertical force, Z_w is the vertical damping derivative, and Z_{col} is the vertical control derivative

The aircraft pitch dynamics in hover were modeled in a similar fashion. For this case, it was useful to include an equivalent time delay, τ, in the equation to approximate the effects of the actuator and the rotor response at high frequency:

$$q(s) / \delta_{lon}(s) = \frac{M_{lon}e^{-s\tau}}{(s - M_q)}$$

where M is the pitching moment (positive nose up), M_{lon} is the pitching moment control derivative, M_q is the pitch damping derivative, and τ is the time delay.

The CIFER method also allows for identification of a state-space model given by the usual form

$$\dot{x} = Ax + Bu$$

where $x^T \equiv (u, v, w, p, q, r, \theta, \phi)$

and $u^T \equiv (\delta_{lon}, \delta_{lat}, \delta_{col}, \delta_{dir})$.

The procedure followed was to determine the error between the measured flight test frequency responses and the model responses. Following 200-400 iterations of the solution procedure, the frequency response pair with the highest cost was eliminated, and the iterations resumed. When all cost functions for all remaining

frequency responses were 'reasonable', as defined by Tischler (Reference 2), stability and control derivatives which the model determined to be insensitive were eliminated (fixed to a value of zero) on a one-by-one basis and another 200-400 iterations were executed. This process was continued until the insensitivity and standard deviation of the identified derivative was acceptably small. This was a relatively time-consuming process on a VAX 4000-300 which required about an hour for 100 iterations. Figure 10 is an example of the responses obtained in hover.

We have found correct identification of high frequency dynamics by CIFER to be very helpful in control system design. For example, in determining the roll rate feedback gain, the delay due to computational frame time and actuator lag must be modeled. If these terms are ignored, an apparently reasonable roll rate gain in fact drives the lag mode unstable. The instability would be missed using lower order models that contain neither terms for blade lag dynamics nor for system time delays. (Figure 11, from Harding, Reference 4). It is evident that we must include low frequency rigid body modes plus higher frequency rotor dynamics. Modeling and control studies on today's increasingly flexible, highly augmented fixed wing aircraft are also seeing similar effects in their aerodynamic/structural/control interaction.

Our identification of M_q is approximately twice the analytical prediction, and L_p and N_r are around 14% greater than the analytical values. Since the Cramer-Rao bounds indicate accurate identification, the prediction methods would appear to require modification. (This was found also by Molusis in Reference 12). Pitch and roll coupling derivatives (M_p and L_q) which represent main rotor coupling are opposite in sign to their analytical predictions. Since again our identification matches were excellent, re-examination of the analytical methods appears necessary.

Experience with Flying Qualities Research Simulators

As part of our efforts to explore and document flying qualities criteria for active control transports, we have performed several simulations using the USAF/Calspan Total In-Flight Simulator (TIFS, Figure 12). This aircraft uses a model-following control system and six mechanical degrees of control freedom so that motions at the evaluation pilot's station in the nose replicate the motions of some developmental or notional aircraft. By varying the dynamic parameters in the model, the dynamics of TIFS change and the corresponding pilot ratings and comments can be used to build data bases to support flying qualities criteria and requirements.

An important aspect of this type of research is; how accurate is the model following? We tackled this question using a CHIRP-like frequency sweep of the longitudinal control column, shown in Figure 13. Figure 14 compares frequency responses (from the CIFER program) of an example model with the actual TIFS response. The pitch response match from 0.1 to 4.0 radians/second is excellent. This is not strictly an application of PID of course until we extract parameters from the responses, but it shows how we use a PID tool, CIFER in this case, as an experimental validation tool. Because the frequency responses are now available from CIFER, it is a straightforward step to use PID to extract equivalent systems parameters from the responses. Figure 15 is an example of a match, comparing the pitch response to pilot's longitudinal column input with the transfer function form shown below. This form uses the shorthand (root) and [damping:frequency] for the first and second order roots;

$$\frac{\theta(s)}{\delta(s)} \approx \frac{K_\theta (1/T_{\theta_1})(1/T_{\theta_2})e^{-\tau s}}{[\varsigma_{sp}:\omega_{n_{sp}}][\varsigma_p:\omega_{n_p}]}.$$

Notice that this low order form, as for the helicopter example, contains a term $e^{-\tau s}$ to approximate high frequency phase effects. Otherwise it is the classical form for an unaugmented aircraft pitch response (see discussion in Reference 12).

Notice too in Figure 16 that we accept an apparently poor match in the low frequency (phugoid) region. Actually, we had reliable time history data for the phugoid oscillation, so the phugoid parameters were fixed in the frequency response matching process. Because our frequency response test method had resulted in somewhat low coherence at low frequencies, we preferred substituting the time history data in the low frequency region. We then used the mismatch frequency response envelopes from the Flying Qualities Military Standard to check the overall quality of the match (Figure 16), realizing that these envelopes are not yet validated for aircraft classes other than fighters. The mismatch appears acceptable except in the phugoid region, as expected.

Because our application is to an in-flight simulation, we actually do not care about the aerodynamic parameters of the NC-131H aircraft upon which TIFS is based. Nevertheless the PID tools are of great utility for our application. Our example shows also that we can combine time- and frequency response-derived data for different frequency ranges.

We have also used the CIFER data to diagnose and measure high frequency effects in TIFS. Though space limitations prevent us from showing examples of this, we have used CIFER and PID via equivalent systems, to gain better understanding of how data are measured and presented in TIFS experiments, and how better to specify the powerful flying qualities effects of high frequency terms like equivalent time delays.

SUMMARY AND LESSONS LEARNED

General

The PID process is not push-button and does not take the engineer out of the design loop. It merely provides a software tool to assist engineers while requiring a great deal of aircraft-related knowledge as well as some mathematical background in statistics and optimization. The process requires patience, and for any aircraft class, time must be spent sorting the flight test data before the identification process even begins. Practitioners feel that sorting the

data in preparation for the identification requires experience that can best be gained by moving from one aircraft project to the next. However, generally each project produces unique problems. The individuals performing this work must draw on considerable creativity to surmount the new problems.

Fixed-Wing Transports
A well-ordered identification process is needed to support regulated requirements for simulations and for incident/accident investigation. The insight of the organization is a vital component of the identification. If necessary, human intervention will take precedence over intensive computation. This need for human intervention is increased for derivative aircraft, for which a backlog of experience has been built. At the same time, as the PID technology matures, and as completely new configurations are developed, the need for affordability will encourage constant reevaluation of the computational approaches.

Fixed-Wing Fighter/Attack Aircraft
PID has been successfully applied to the large flight envelopes and agile maneuvers associated with this class of aircraft. The computational methods have gained wider acceptance for this class of aircraft than for transports.

Our examples showed that PID can be used to identify and compensate for data measurement errors and inconsistencies. It can significantly improve the fidelity of six-degree-of-freedom simulation models, even at high angles of attack where aircraft aerodynamic characteristics are highly nonlinear.

Rotary-Wing
The frequency response approach, which separates phenomena at different frequencies, appears well-suited to helicopters. Higher frequency modes, particularly those associated with rotor dynamics, must be included in the model or the subsequent flight control loop closures may be erroneous. Predictions of key derivatives like M_q, L_p and N_r have been significantly different from the identified values, and since the identification has been accurate, the prediction methods would appear to require re-examination.

Research simulation
We chose to show in-flight simulation data, but of course PID is very valuable for ground-based simulator validation also. Many of the points noted in the rotary-wing frequency response work have their parallels in the fixed-wing arena also, notably the significance of high frequency effects.

FUTURE WORK

Acceptance
PID, both time-and frequency-domain, has gained wide acceptance and we have much validating data. However, the cautious acceptance of highly computational PID for some aircraft is the most interesting lesson learned. For the heritage Boeing commercial applications, this reluctance stems from familiarity of the engineering team with a stable of aircraft that are basically similar. However, our C-17 models, with their nonlinearities and strong thrust coupling, are also based on identification that involved much human intervention. Clearly the insight of the engineering team is of overriding importance, and when budget allows, there has been a preference for intensive human intervention. The developers of PID therefore have the challenge of producing tools that contribute to fast, affordable

design and test cycle times, and yet retain the needed insight. These developers will perhaps need to emphasize graphical user interfaces (for example, see Reference 13), analyst's associates, and very fast interactive computation rather than increased mathematical sophistication.

Other trends
Though PID approaches like neural nets exhibit promise, the need for engineering insight into the PID process presents a challenge for neural net approaches.

One consequence of NASA's interest in safety in commercial air travel is the need to establish accurate simulations that accurately reflect the behavior of commercial transports at high angles of attack and sideslip. Fighter/attack experience with PID in these flight regimes will be of enormous value.

REFERENCES

1. Najmabadi, K., and Fritchman, B., "A Process for Model Identification and Validation of the Dynamic Equations for a Flexible Aircraft", RTO/SCI Symposium on System Identification for Integrated Aircraft Development and Flight Testing, Madrid, Spain, 5-7 May 1998

2. Comprehensive Identification from Frequency Responses- An Interactive Facility for System Identification and Verification, Volume 2-User's Manual NASA Conference Publication 3188, April 1992

3. Tischler, M., "System Identification Methods for Aircraft Flight Control Development and Validation" Paper no. 3, Symposium of the AGARD Flight Vehicle and Integration Panel on System Identification for Integrated Aircraft Development and Flight Testing, 5-7 May 1998, Madrid, Spain

4. Harding, Jeffrey W., "Frequency-Domain Identification of Coupled Rotor/Body Models of an Advanced Attack Helicopter" 48th Annual Forum of the American Helicopter Society, Washington

5. Neville, K.W., Stephens, A.T., "Flight Update of Aerodynamic Math Model", AIAA Technical Paper 93-3596, Proceedings of AIAA Flight Simulation Technologies Conference, Monterey, CA, 1993.

6. Maine, R.E., Iliff, K.W., "Application of Parameter Estimation to Aircraft Stability and Control - The Output-Error Approach", NASA RP-1168, June 1986.

7. International Civil Aviation Organization, "Manual of Criteria for the Qualification of Flight Simulators", Document 9625-AN/938, 1st Edition, 1995.

8. International Air Transport Association, "Flight Simulator Design & Performance Data Requirements", 4th Edition, 1993.

9. Thompson, T., and Shanthakumaran, P., "Longbow Apache Requency Response Flight Test Data Reduction and Analysis" McDonnell Douglas Helicoper Systems Report, Contract no. DAAJ09-89-C-A086, June 1995.

10. Hodgkinson, J., "Equivalent Systems Criteria for Handling Qualities of Military Aircraft". AGARD-CP-333, 1982.

11. Wunnenberg, H. et al, "Handling Qualities of Unstable, Highly Augumented Aircraft". AGARD AR-279, May 1991.

12. Molusis, J.A., "Rotorcraft Derivative Identification from Analytical Models and Flight Test Data" AGARD CP172, 1974

13. Lavretsky, E., "High Speed Civil Transport (HSCT) Flight Simulation and Analysis Software Development" AIAA Paper 98-0173, 36th Aerospace Sciences Meeting and Exhibit, January 1998, Reno, NV.
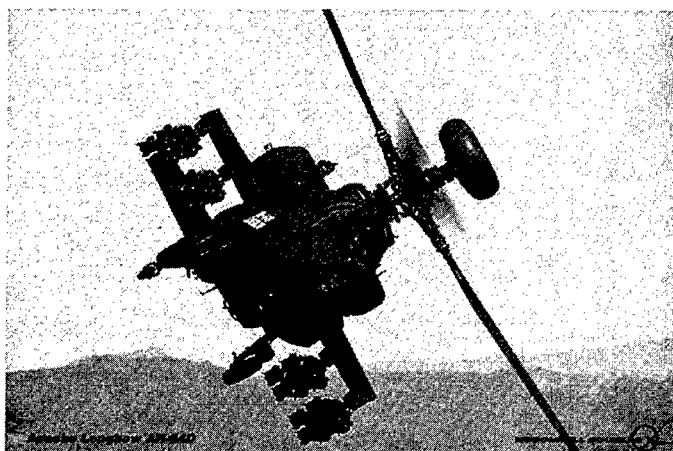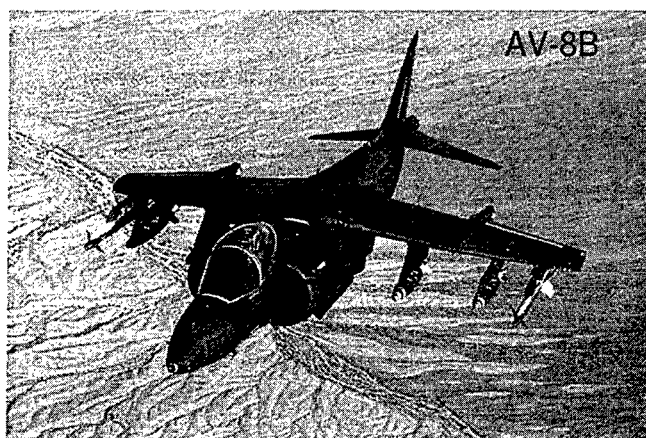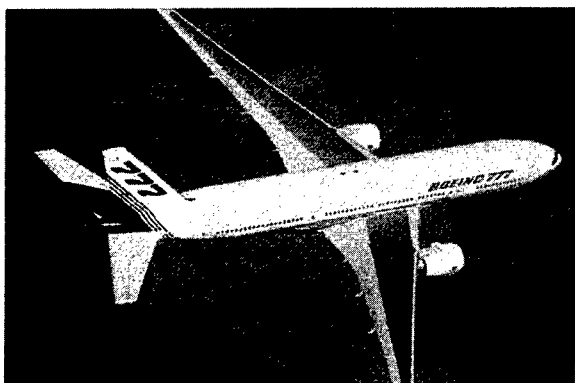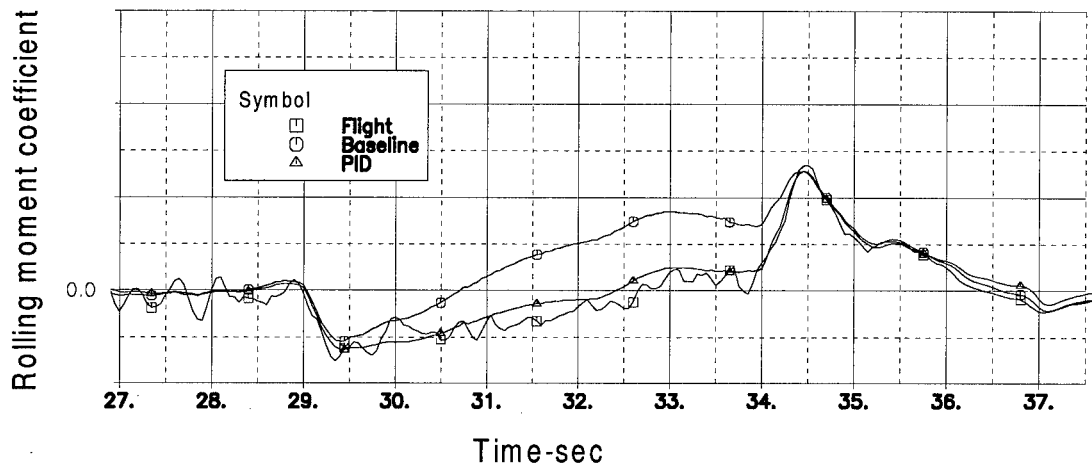
Figure 1 Some Boeing Company Products

Figure 2 PID allows improved matching of total rolling moment coefficient
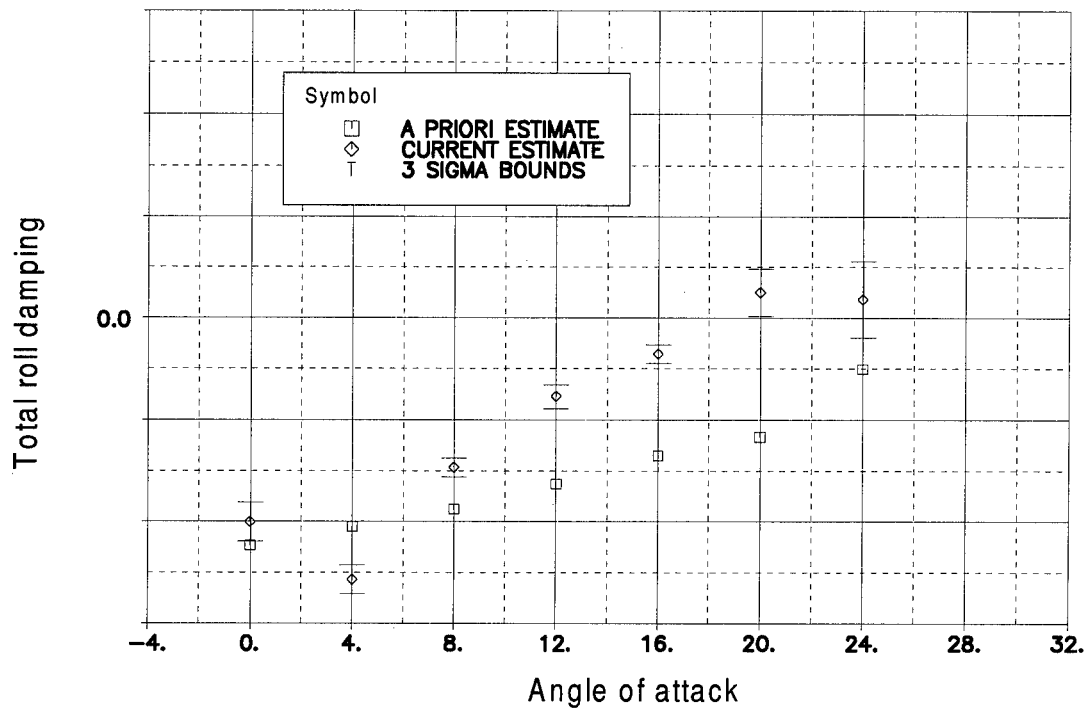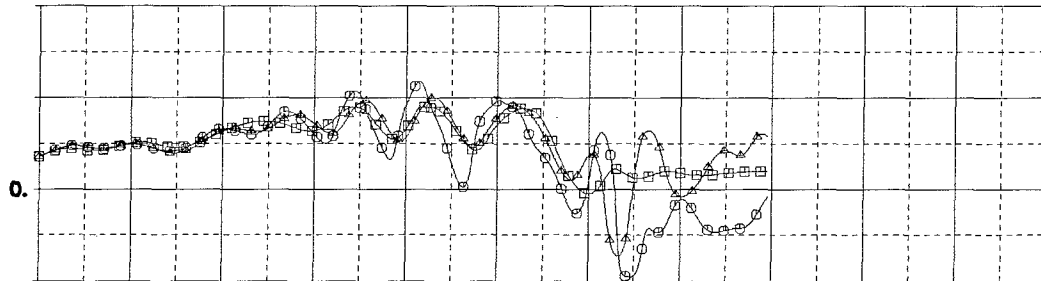in F/A-18 E/F rolling maneuver.

Figure 3 PID estimates of roll damping compared with
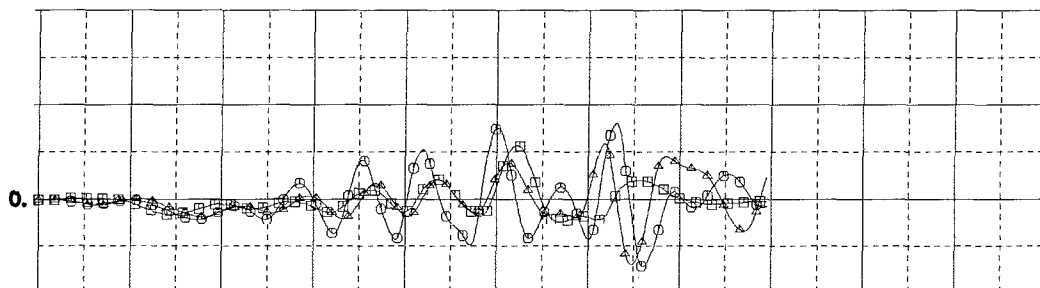a priori estimates

Symbol
  □   UPRIGHT SPIN, RIGHT, HALF FWD/FULL RIGHT
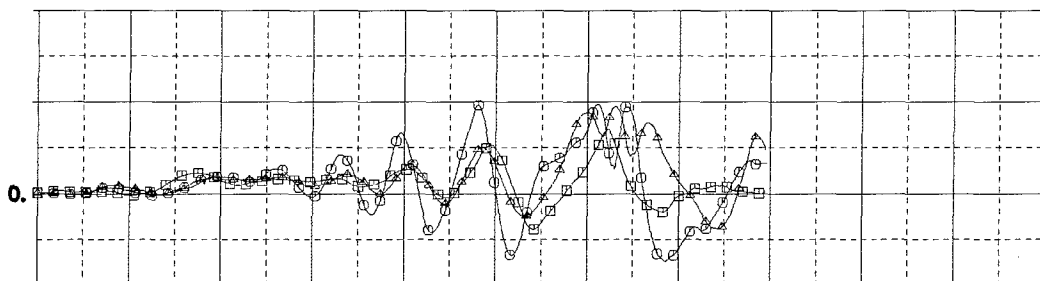 ○   DATABASE CALCULATIONS
  △   PID

Angle of attack, degrees

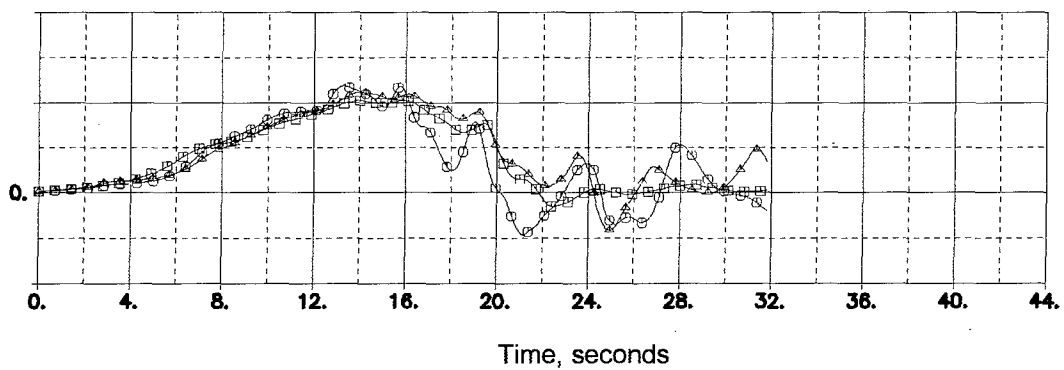Sideslip angle, degrees

Roll rate, degrees/sec

Yaw rate, degrees/sec

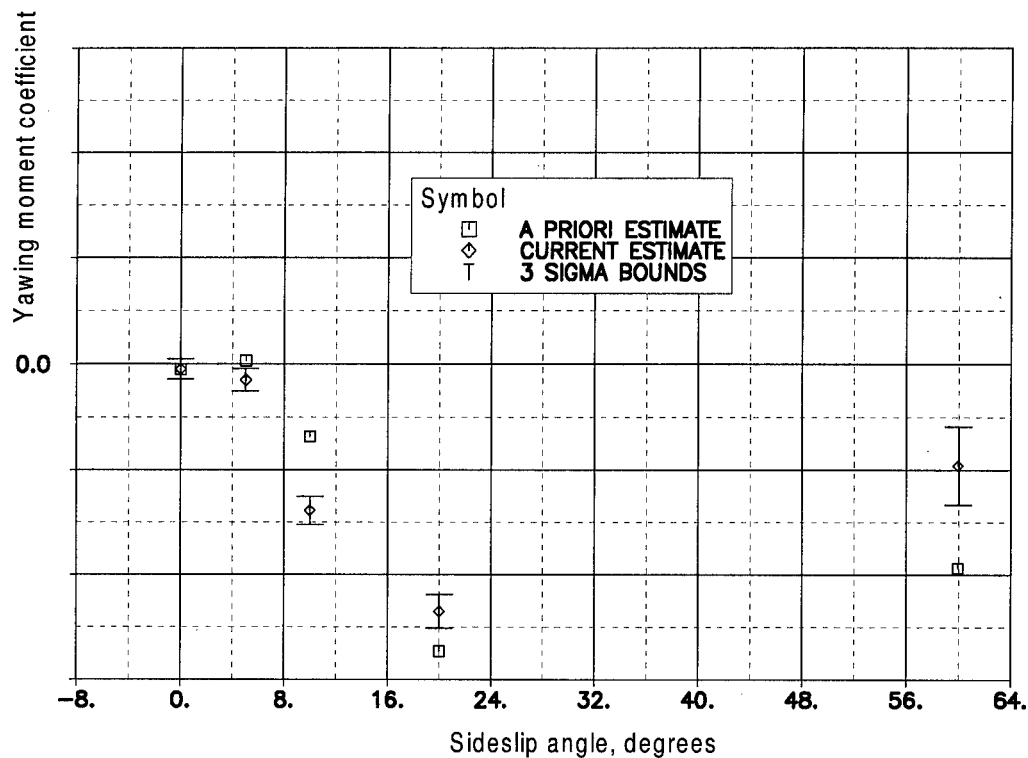Time, seconds

Figure 4 PID improves match to spin responses

Figure 5 PID-modified values of directional stability (yawing moment versus sideslip) at moderate/high angle of attack (F/A-18 E/F aircraft)
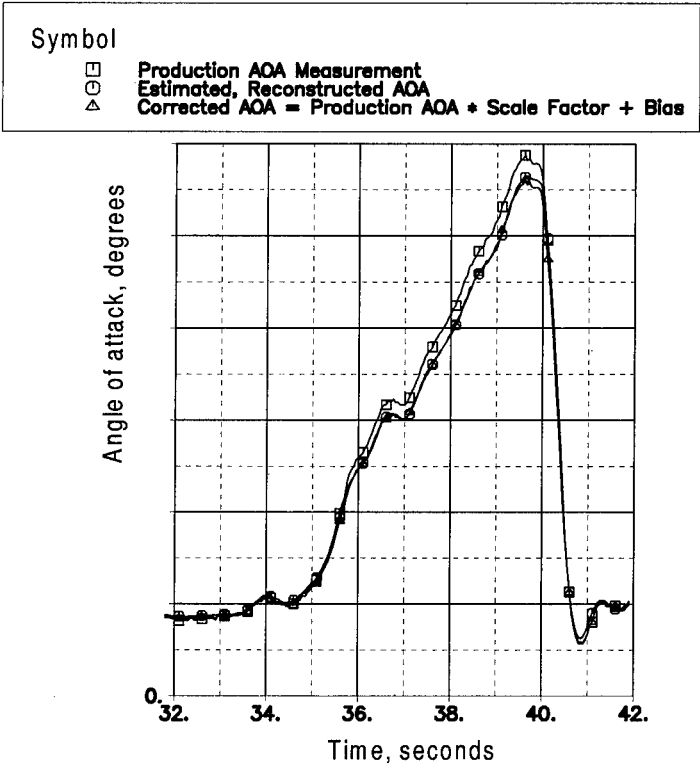

Figure 6 Angle of attack reconstruction from windup turn maneuver (AV-8B aircraft)

Symbol	Mach
⊡	**0.60**
⊙	**0.70**
△	**0.80**
◇	**0.85**

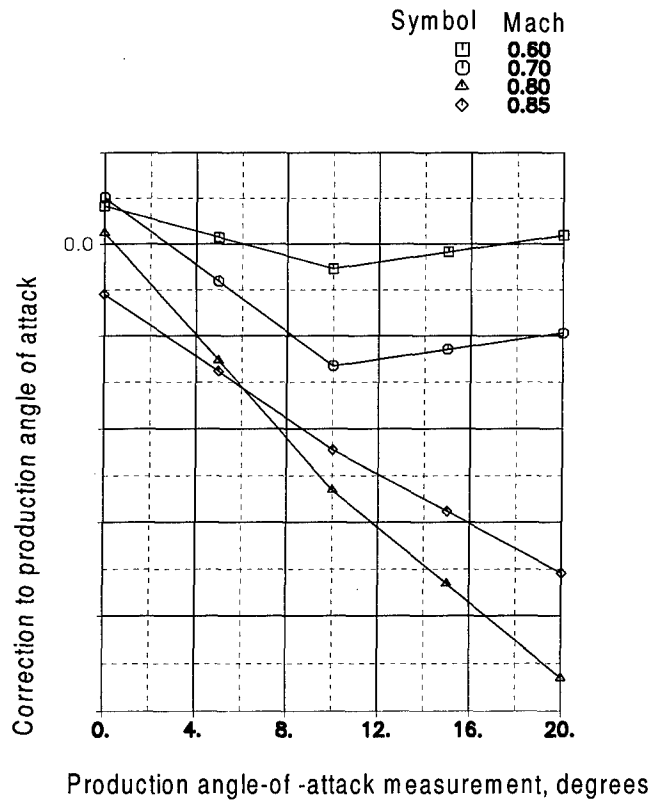**Production angle-of-attack measurement, degrees**

Figure 7   Upwash correction to angle of attack (AOA) measurement.
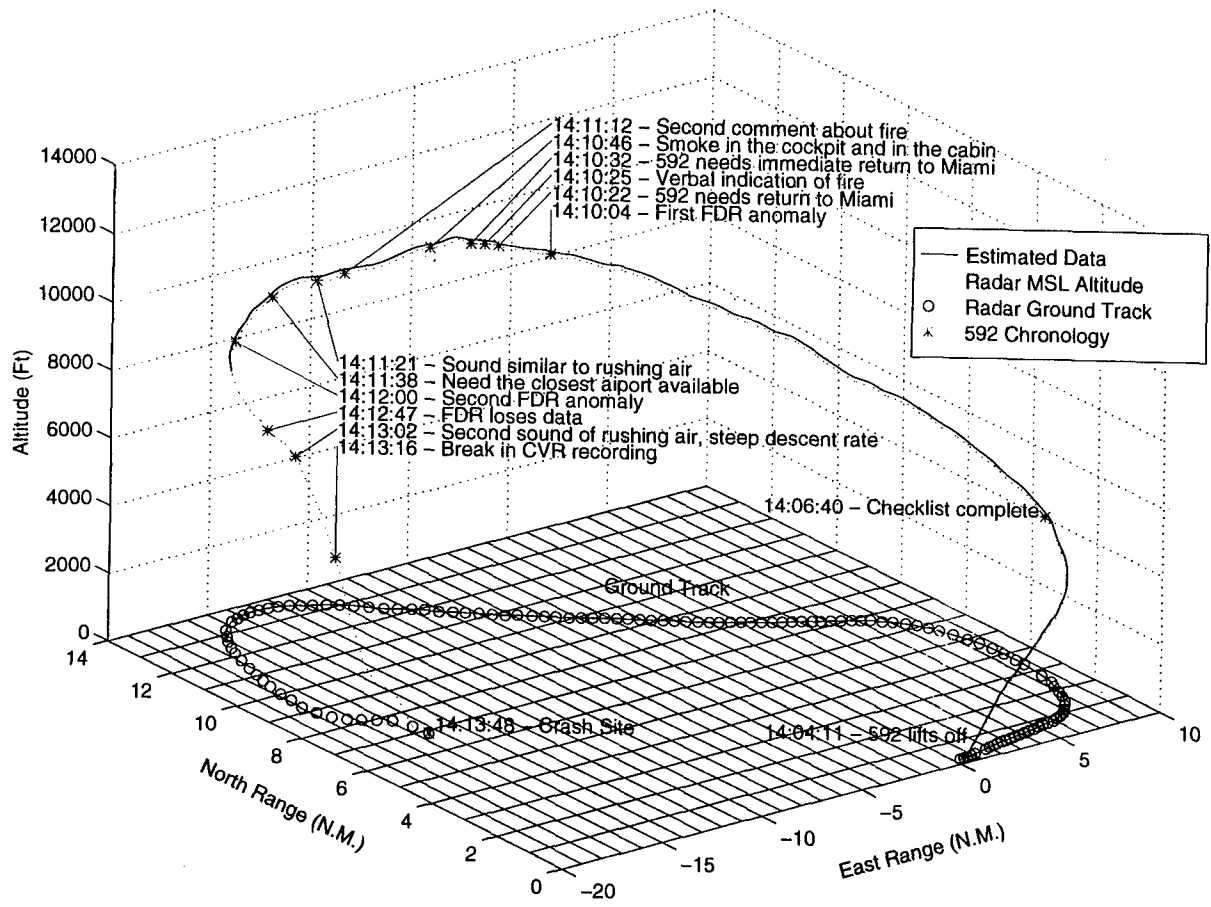AV-8B Aircraft.

Figure 8   Reconstruction of inertial vertical flight path of ValuJet Flight 592
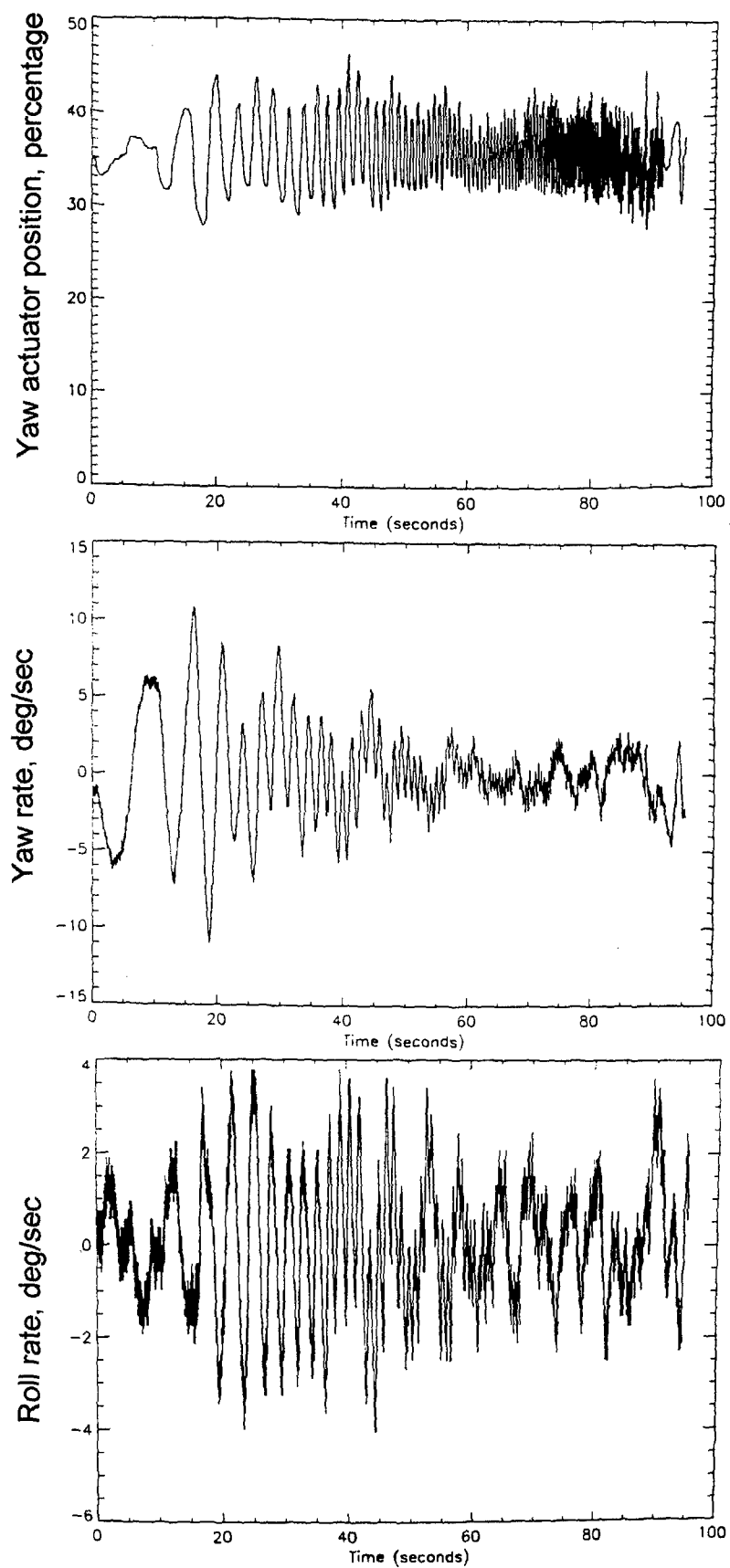
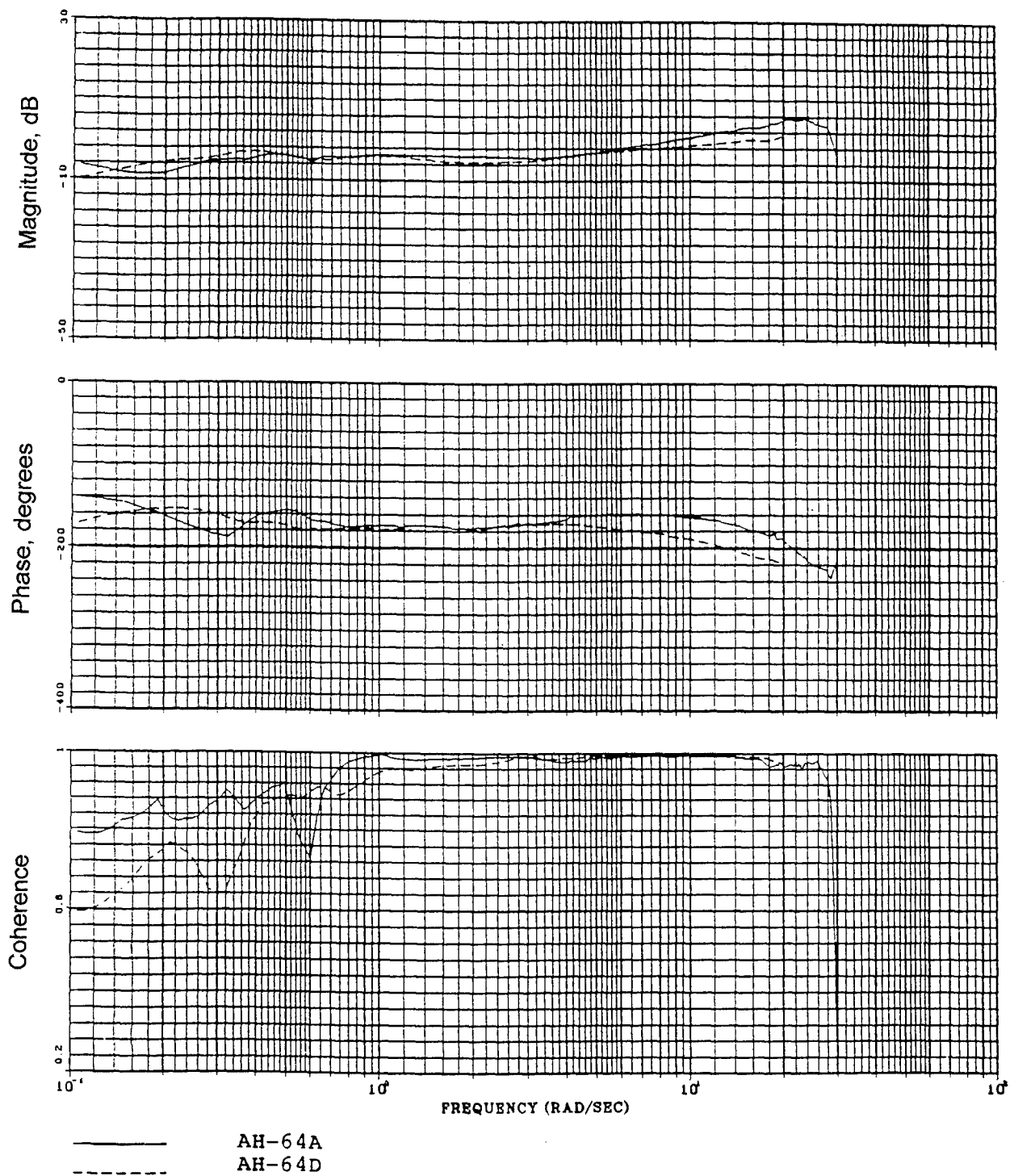Figure 9 Time history responses of yaw actuator, yaw rate and roll rate from directional axis CHIRP testing

Figure 10 Comparison between AH-64A and AH-64D normal
acceleration frequency responses in hover

Imaginary (rad/sec)

no time delay

20 —

time delay 0.04 sec

regressing
lag

×

○

regressing
flap

.10 —

unstable

×

roll

⊗

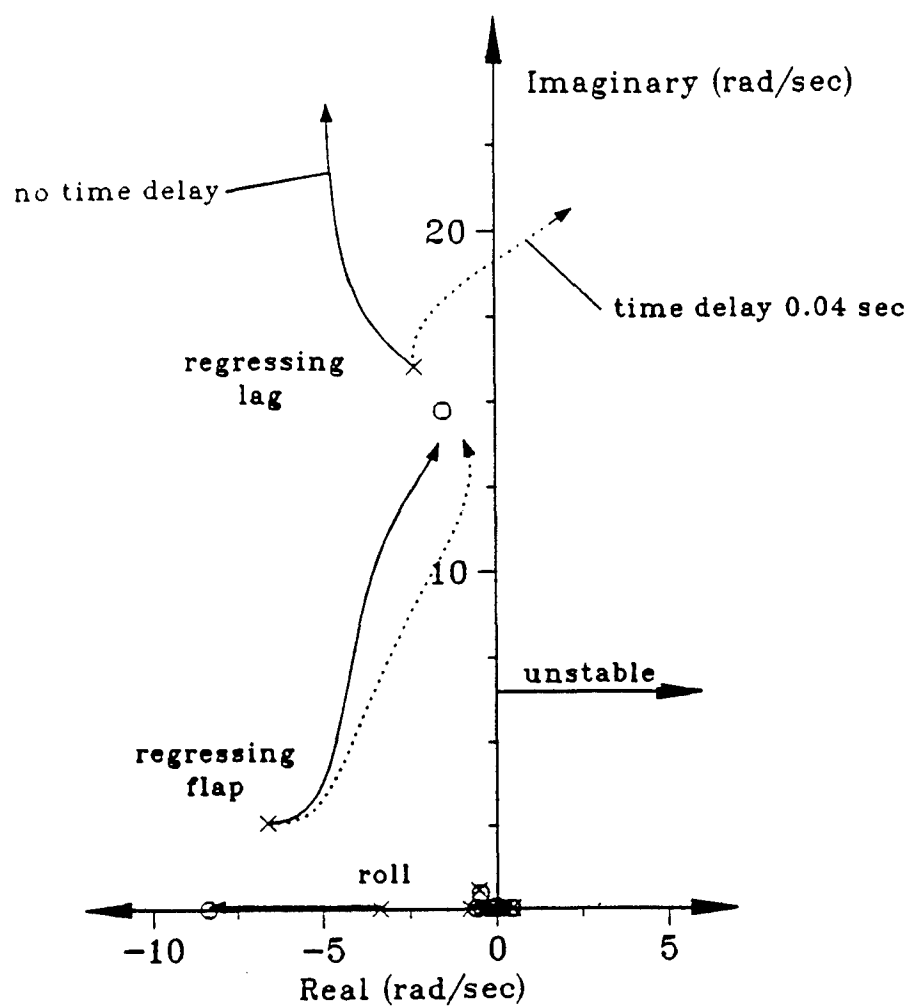-10   -5   0   5

Real (rad/sec)

Figure 11   Root-locus of 10-degree-of-freedom- plus- lag model for roll rate
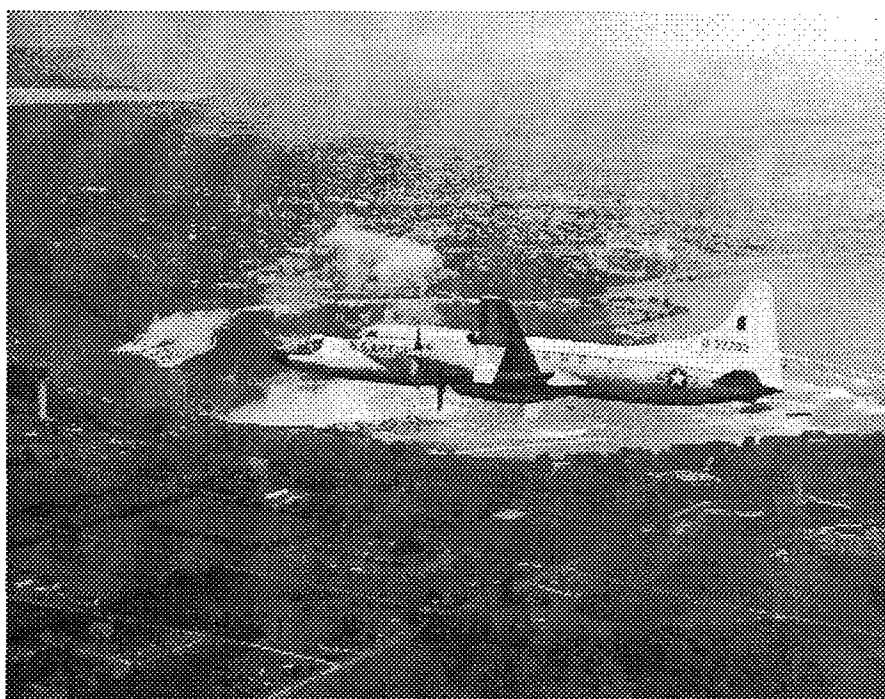gain variation, with and without added time delay of 0.04 seconds

Figure 12.   USAF/Calspan Total In-Flight Simulator (TIFS)

Note: Noisier signal is TIFS
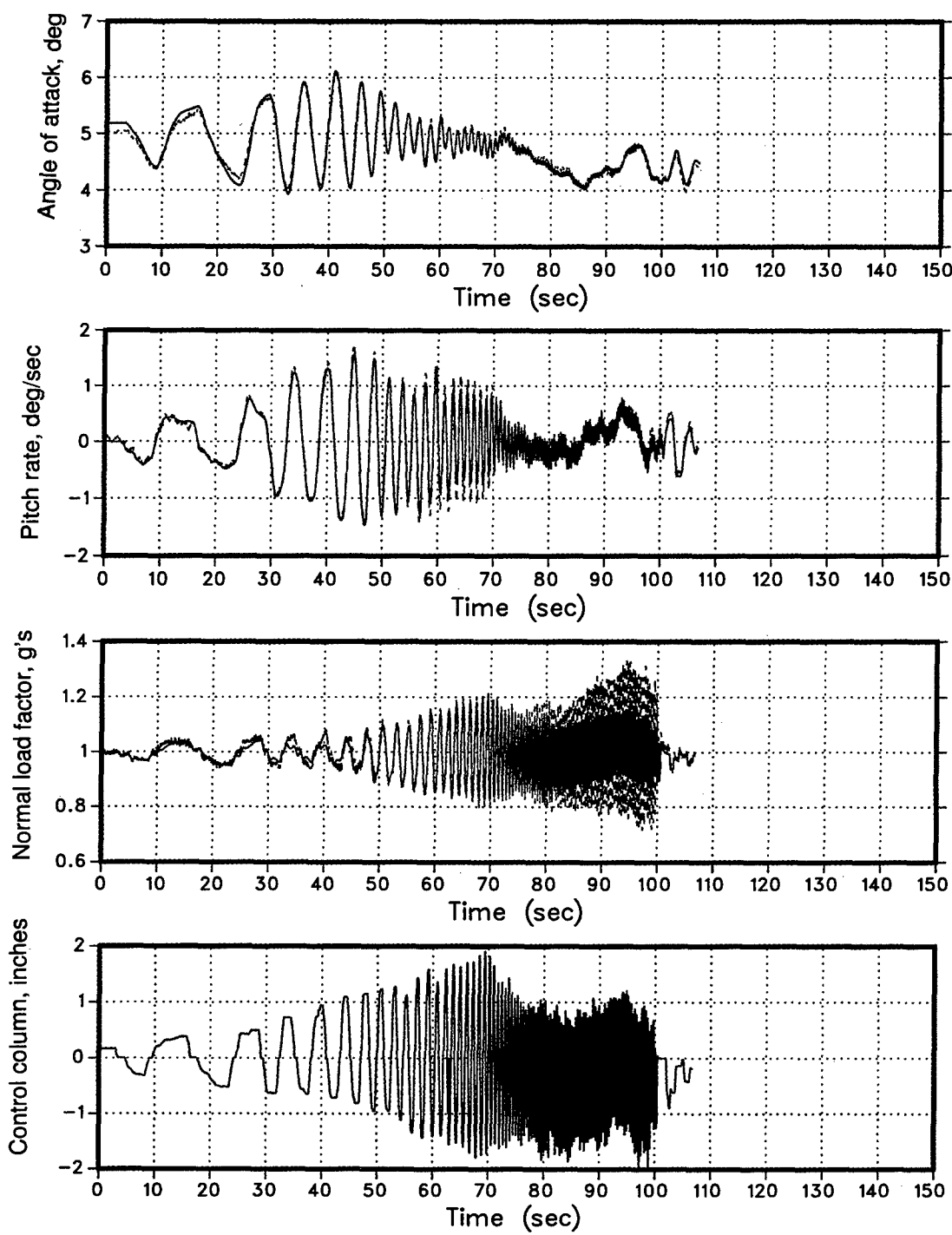   Normal load factor is measured at the pilot's station

Figure 13 Comparison of model versus Total In-Flight Simulator (TIFS)
responses: longitudinal, approach and landing

CIFER V2

MAGNITUDE(DB)

PHASE(DEG)

COHERENCE

FREQUENCY (RAD/SEC)
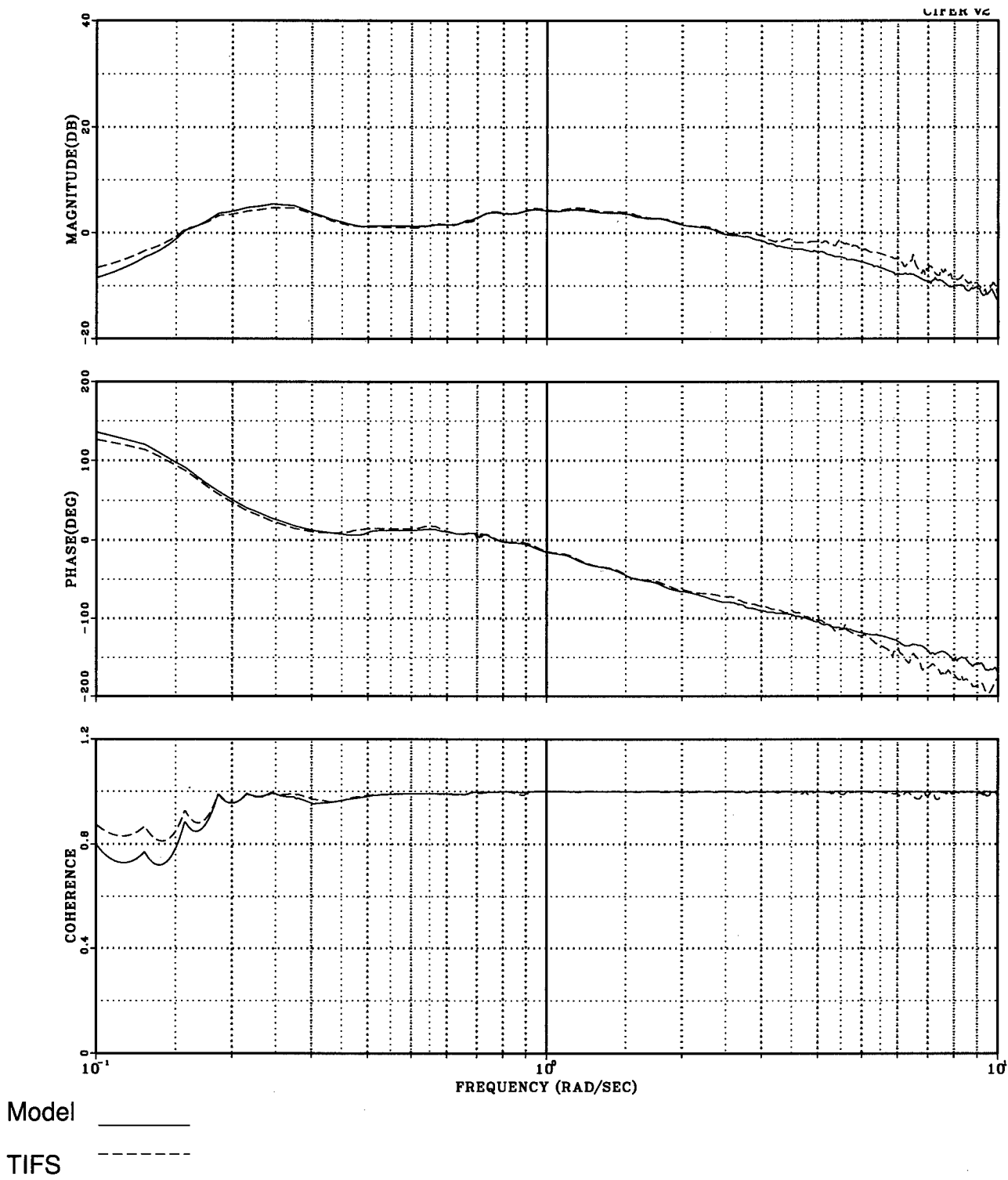
Model _____

TIFS -------

Figure 14 Frequency response com parison between model and TIFS pitch rate
to pitch column stick

LINE CODE

———————— HOS
------------ LOS

LOS =Low Order System
HOS =High Order System
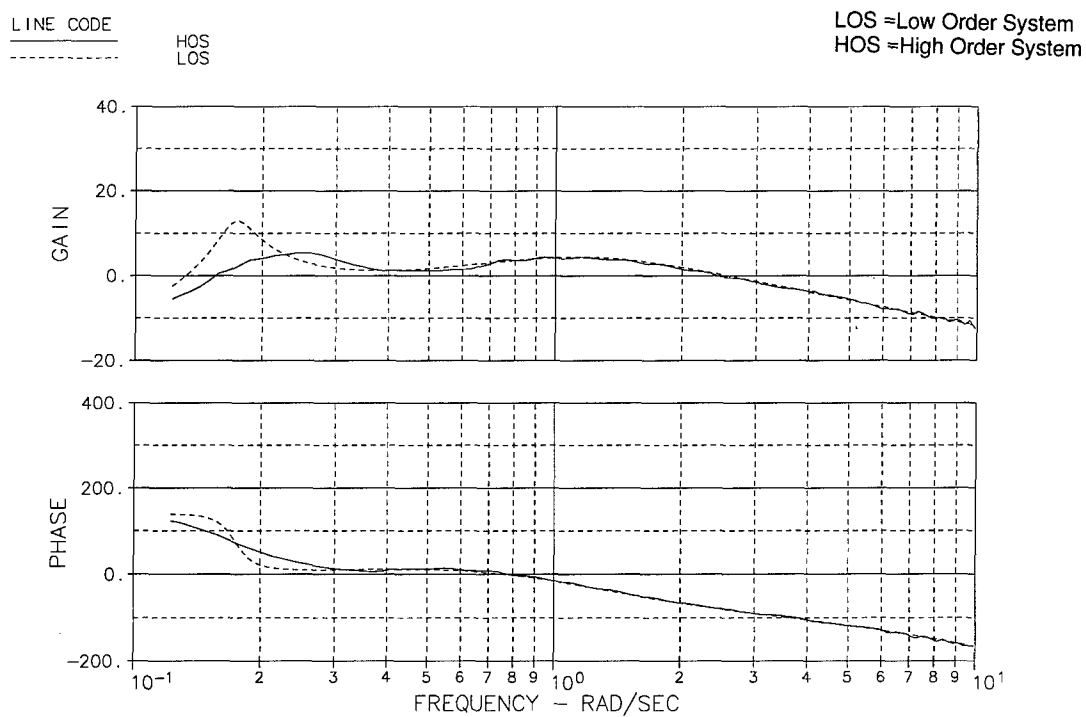
Figure 15. Equivalent Systems HOS/LOS Comparison Frequency Response for Model Pitch Rate to Pitch Stick
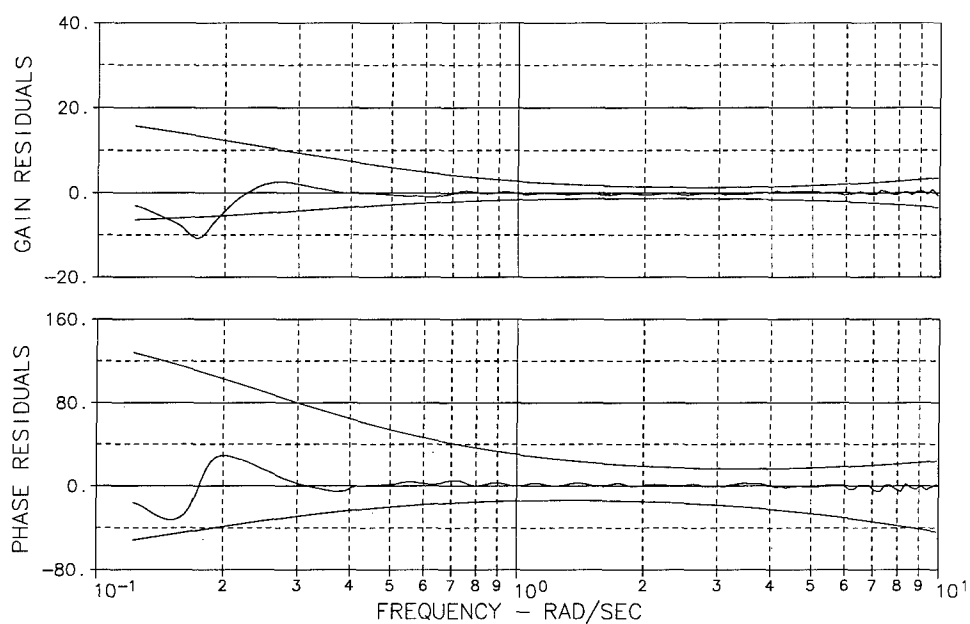
Figure 16. Equivalent Systems Residual Frequency Response with MUAD Envelopes for Model Pitch Rate to Pitch Stick

The Role of System Identification for Flight Vehicle Applications - Revisited

P. G. Hamel and R. V. Jategaonkar

Institut für Flugmechanik
DLR - Deutsches Zentrum für Luft- und Raumfahrt e.V.
Lilienthalplatz 7, D-38108 Braunschweig,
Germany

1. SUMMARY

During the last few decades system identification methodology has been extensively used for flight vehicle modeling. This paper provides an overview of the basic methodology, highlighting the classical approaches and indicating a few current trends. Successful application of advanced aircraft parameter estimation methods has been demonstrated on a few challenging examples such as determination of aerodynamic effects of secondary importance, identification of highly augmented unstable or flexible aircraft, and high bandwidth rotorcraft modeling. The selected examples demonstrate that the system identification methods have reached a maturity level that makes them a powerful and indispensable tool to support not only research but also the industry activities in various key areas such as model validation, handling qualities evaluation, control law design, and flight vehicle design. Thus, it contributes significantly to risk and cost reduction in the optimal deployment of existing aircraft and in the development of new generation flight vehicles.

2. INTRODUCTION

During the last few decades there has been a constant effort in determining static as well as dynamic characteristics from flight test measurements. The coordinated approach encompassing flight test instrumentation, flight test techniques, and flight data analysis leads to a Quad-M (Motion, Measurements, Methods, and Models) concept of system identification [1]. It has resulted in generating sufficient practical experience to apply these techniques to diversified flight vehicle applications on a routine basis [1-3]. Today, the scope of applications ranges from the classical purpose of data correlation for increasing the confidence in flight mechanical prediction techniques to generating high fidelity aerodynamic databases, flight envelope expansion, high performance unstable aircraft, and high bandwidth rotorcraft modeling [1].

The full-fledged flight crew training simulators for commercial transport as well as high performance aircraft, in general, should demonstrate high fidelity, often meeting the Level D fidelity standards specified by the Federal Aviation Administration (FAA) [4,5]. Fidelity of flight simulation depends to a large extent on the accuracy of the aerodynamic database representing the aircraft. Furthermore, the demands of high-performance characteristics have led to aerodynamically unstable aircraft configurations, which can be flown only with the aid of flight controllers based on modern control concepts. In this case, it is mandatory that the aerodynamic characteristics used for control law design are representative of the actual aircraft.

To minimize the overall developmental costs, it is necessary to minimize the amount of costly and time consuming flight testing necessary for aircraft specification and certification requirements. Furthermore, the new aerodynamic design concepts such as, for example, thrust vectoring [6] or quasi-tailless aircraft [7], require careful expansion of the flight envelope through i) data correlation between the prediction and flight identified aerodynamic characteristics and ii) isolation and identification of non-anticipated aerodynamic effects. This is also true in the case of large flexible aircraft, where the structural modes can influence the aircraft response and the accuracy of flight mechanical models [8,9].

The philosophy of model-following control based on feed forward regulation provides safer and more accurate mode control; the performance, however, depends strongly on the validated mathematical model of the host flight vehicle [1,10]. For such an application, the rotorcraft flight control has to meet the high bandwidth requirements, demanding augmentation of the rigid-body model through higher-order rotor dynamics.

Thus, the present challenge to flight vehicle system identification may be formulated as to determine a high-fidelity aerodynamic model of a high performance, highly augmented vehicle from rapid, large amplitude maneuvers. Such a global model is, in general, of unknown structure, highly nonlinear, and affected by elastic modes, unsteady aerodynamics, and erroneous air data measurements. Although a general single shot solution to this problem may be difficult, significant advances have been made both in terms of aerodynamic modeling and aircraft parameter estimation methods. A brief account of the Quad-M approach is presented in this paper, indicating a few current trends and bringing out the salient features through typical examples for each of the four M. Model validation issues are briefly addressed. The paper then demonstrates that for each of the aforementioned flight vehicle applications the current system identification tools provide an adequate solution, enabling either an update of the predicted database or even generation of a comprehensive database/model valid over the operational flight envelope meeting the high accuracy de-

mands. These examples bring out clearly the role of system identification for flight vehicle applications. It is evident from Fig. 1 that today these tools are an integral part of any aircraft development and assessment program.

3. PRINCIPLES OF SYSTEM IDENTIFICATION

The general approach used in aircraft system identification is shown in Fig. 2. During the flight tests, specifically designed control inputs are applied to excite the characteristic aircraft motions. The applied control inputs and aircraft responses are measured and recorded. A suitable model is postulated for the phenomenon being investigated and the model parameters are so determined as to match the model predicted response with the flight measured aircraft response.

A coordinated approach to flight vehicle system identification can be divided into three major parts [1]:

- **Instrumentation and Filters** which cover the entire flight data acquisition process including adequate instrumentation and airborne or ground-based digital recording equipment. Effects of all kinds of data quality have to be accounted for.

- **Flight Test Techniques** which are related to the selected flight vehicle maneuvering procedures. The input signals have to be optimized in their spectral composition in order to excite all response modes from which parameters are to be estimated.

- **Analysis of Flight Data** which includes the mathematical model of the flight vehicle and an estimation criterion which devises some suitable computational algorithm to adjust some kind of starting values or a priori estimates of the unknown parameters until a set of best parameter estimates is obtained which minimizes the response error.

Corresponding to these strongly interdependent topics, four important aspects of the art and science of system identification have to be carefully treated, Fig. 2.

- Design of the control input shape in order to excite all modes of the vehicle dynamic **motion**.

- Selection of instrumentation and filters for high accuracy **measurements**.

- Type of flight vehicle under investigation in order to define the structure of a possible mathematical **model**.

- Quality of data analysis by selecting the most suitable time or frequency domain identification **method**.

These **"Quad-M"** requirements must be carefully investigated for each flight vehicle from a physical standpoint, and are the key to the successful flight vehicle system
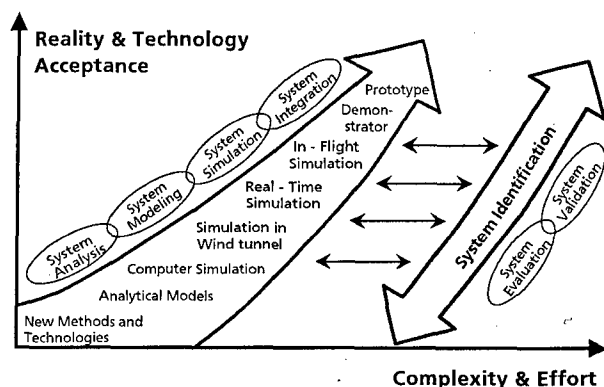
Application Spectrum:
- **Data Base Generation for**
  - Flight Vehicle Design
  - Flight Simulator Development
- **Flying Qualities Evaluation**
- **Flight Envelope Expansion**

- **Flight Control System Optimization**
- **Structural Modeling, Flutter Testing**
- **Aeroservoelastic Model Validation**

Fig. 1: The key role of system identification

identification. A systematic treatment of these key-issues has been provided by Hamel [11], and Mulder et al [12] Maine and Iliff [2,13], and Klein [3]. A survey of contributions to flight vehicle system identification up to 1980 has been provided by Iliff [14] and more recently by Hamel and Jategaonkar [1].

4. OPTIMAL INPUTS FOR DYNAMIC MOTION

The accuracy and reliability of parameter estimates depend heavily on the amount of information available in the vehicle response. Hence, a proper experiment design is important. In general, an optimal input is that which best excites the frequency range of interest. Purely from this view point, the direct choice may appear to be a frequency sweep input. However, it leads to relatively long maneuver times, is mostly restricted to single axis excitation and has a tendency to depart from the nominal trim. Based on these practical considerations, several signals have been designed in the past, for example 1) doublet, 2) multistep 3211, 3) Mehra, 4) Schulz, 5) DUT, and 6) Langley input [15-20]. Although the 3211, Mehra, DUT, and Langley inputs are more efficient, the doublet input is often used due to its simplicity. Amongst the
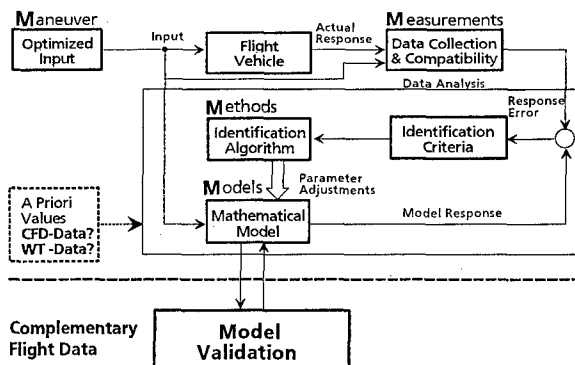

Fig. 2: The Quad-M basics of flight vehicle system identification

above indicated inputs signals, the multistep 3211 signal is easily realizable and relatively easy to fly manually by pilots [18]. It is for this reason that the 3211 signal remains as the one most accepted by the flight test community. Fig. 3 shows the 3211 input and its spectrum in comparison to step and doublet input signals.

More recently the emphasis has been on improving the hitherto designed input signals and on expanding the design techniques based on additional practical considerations. For example, Fig. 3 shows an improved 3211 signal, which has different amplitude levels for each step, resulting in a better spread of the frequency spectrum compared to the conventional 3211 signal, and also having zero energy content in the low frequency range which alleviates the tendency to depart from the nominal trim [21]. A derivative of the Mehra's signal has also been designed by minimizing the number of elementary sine functions used to optimize the signal [22]. In yet another application, dynamic programming technique has been used to generate an input signal by optimally combining square waves only [23]. This approach is applicable to nonlinear models and also enables to account for feedback control and actuator dynamics in the optimization. These recent designs have improved properties and have been applied in a few practical cases; however, they are difficult to fly manually and can be best realized through onboard computer implementation. Thus, although it may appear that the current trend is towards more complex computerized control inputs, the simpler input signals like doublet or 3211 will continue to be as accepted in the future as in the past.

Although the dynamic programming technique allows an input design accounting for the feedback control, it does not overcome the control-surface correlation which may be dominant in highly augmented aircraft. In such cases the separate surface excitation (SSE) yields the best parameter estimates [1,24,25]. In this approach the standard doublet or 3211 inputs are fed after the controller to directly deflect the control surfaces. As a typical example, Fig 4 shows the estimates of the canard control effectiveness obtained from the X-31A flight test data for two cases, namely the pilot input maneuvers and the separate surface excitation. As evident from Fig. 4a, the pilot input maneuvers yield estimates with large standard deviations and moreover the scatter is also large. This is
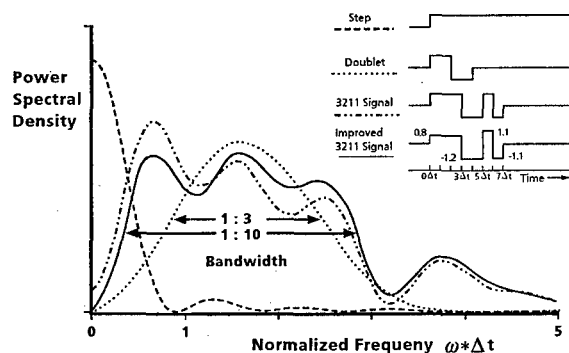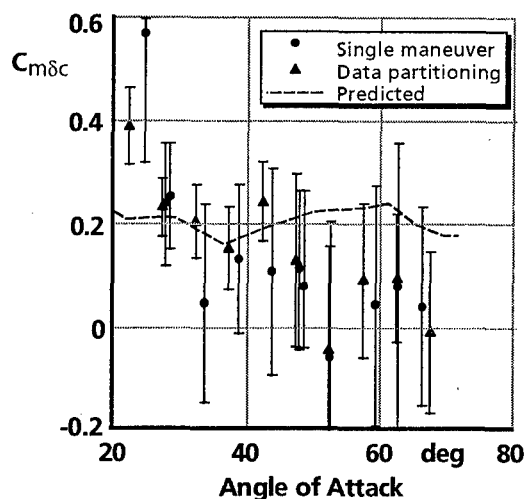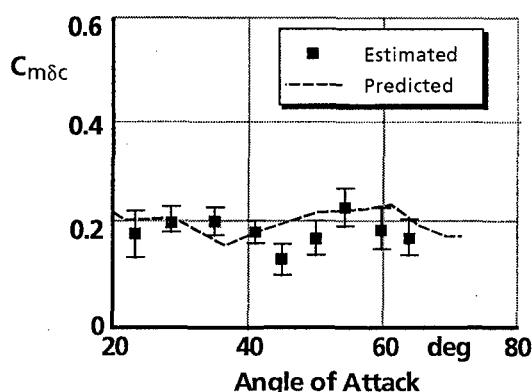

a) Pilot input maneuvers

b) Separate surface excitation maneuvers

Fig. 4: Estimates of canard control effectiveness from X-31A flight data

definitely attributed to the difficulties of insufficient information content and of correlated variables. On the other hand, the separate surface excitation maneuvers yield well identifiable estimates, Fig. 4b.

For rotorcraft system identification, frequency sweep test techniques and multistep signals like doublet or 3211 are popular. Both these test techniques are found to provide comparable results. Frequency sweep testing is better suited for identification of transfer function models and is necessary when the estimation algorithm is based on frequency domain techniques [26,27]. In several of the cases it has been observed that the pilot flown sweeps, which tend to contain sharp superimposed inputs, yield better estimates compared to those from the pure sweep inputs applied from an onboard computer. Care needs to be exercised during the sweep testing to avoid critical flight incidence resulting from aero-servoelastic interactions or due to exceeding the permissible loads.

Fig. 3: Frequency domain comparison of input signals

5. FLIGHT TEST MEASUREMENTS

The accuracy of the parameter estimates is directly dependent on the quality of flight measurements, and, hence, high accuracy measurements of the control inputs and aircraft responses is of paramount importance. Typi-

cally, measurements of i) linear accelerations a_x, a_y, a_z, ii) angular rates p, q, r, iii) attitude angles ϕ, θ, ψ, iv) control surface deflections, v) air flow angles α, β, vi) airspeed, vii) engine parameters, viii) static and dynamic pressures, and ix) control column and wheel forces are necessary for parameter estimation.

Significant number of parameters, for example linear accelerations, angular rates, attitude angles, and control surface deflections, are generally available from the existing flight data recorder. In such cases it is necessary to check for the source from where the signals are tapped, for signal processing which mostly includes filters, and for calibration. This is usually done in a data pre-processing step through flight path reconstruction. The measurements of control column and wheel forces may require additional installation and flight certification. These measurements are, however, of importance only in the case of reversible flight controls; they are required for modeling of flight controls and for simulator certification, but not for rigid-body aerodynamic model identification.

Measurement of air flow angles, namely the angle of attack and angle of sideslip, is more tedious. The fuselage mounted vanes are used for pilot monitoring purposes, but they are not accurate enough for parameter estimation. Flight logs or five hole probes provide reasonably good measurements of these flow angles. The common practice is to mount these sensors on a long enough noseboom. In certain cases of database generation, particularly those for commercial aircraft, the time constraint may be a severe limitation on design and flight certification of a noseboom. In such cases, mounting the five-hole probe on the aircraft radome may offer an alternative option [28,29]. The standard flight path reconstruction techniques enable proper calibration of these measurements.

The current developments in the Global Positioning System (GPS) and Differential GPS (DGPS) are also likely to be useful in flight vehicle system identification [29,30]. More reliable information regarding the inertial position, climb or sink rate, wind, and gust levels may be derived from the GPS/DGPS measurements.
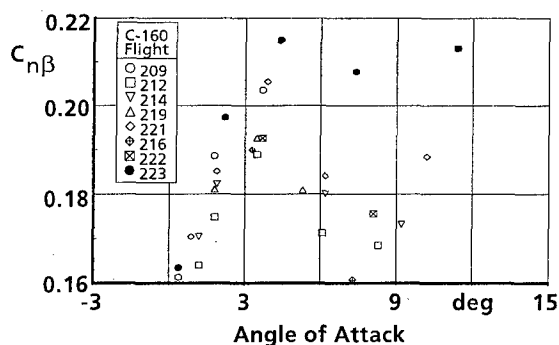
6. ESTIMATION METHODS

The classical methods, starting from those used by Gauss in the 18th century up to the first half of this century, were deterministic, graphical based on the use of paper and pencil, mostly in frequency domain or based on analog computations. In contrast, the modern methods of parameter estimation are based on statistical analysis and require automatic data processing capabilities provided by digital computers. An overview of the systematic development of these methods is found in Ref. 1.

For conventionally stable flight vehicles, the most commonly and widely applied parameter estimation methods are: i) regression analysis and ii) output error method. Regression analysis is based on linear models for the aerodynamic phenomena and requires error free and

compatible measurements [3,13]. The output error method, which has several desirable statistical properties, is applicable to general nonlinear systems and accounts for measurement noise [1-3]. However, it yields biased estimates when random process noise excites the system, for example flight data gathered in the presence of atmospheric turbulence. In such cases the filter error methods are necessary [1,31].

Fig. 5 shows that even in the case of flight maneuvers in smooth air, the filter error methods could lead to better estimation results, because some of the unavoidable modeling errors are then treated as process noise characterized by low-frequency contents rather than as measurement noise [31,32]. The C-160 data analyzed here was gathered from eight flights carried out during a span of less than two weeks, seven of them being in a seemingly steady atmosphere whereas one encountered moderate amount of turbulence. It is clearly visible that the estimates provided by the output error method, particularly those for flight 223 during which moderate turbulence was encountered, differ much from those of other flights at the same nominal flight conditions [1,32]. Moreover, a fair amount of scatter is observed in the estimates from other flights in a seemingly steady atmosphere making a final conclusion regarding the nature of the nonlinearity or fairing of data difficult. On the other hand, the filter error method yields clearly grouped estimates with much less scatter and the estimates from flight 223 match well with the other estimates. The nonlinear dependency of the weathercock stability on the angle of attack is now to be observed much better.

a) Output error method
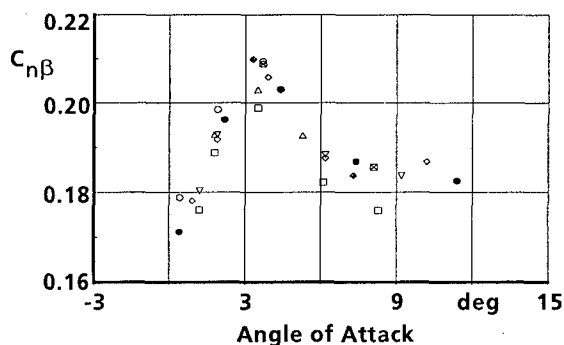
b) Filter error method

Fig. 5: Flight estimates of weathercock stability

For high performance aircraft of unstable aerodynamic configuration, the commonly applied methods are regression analysis, filter error method, and extended Kalman filter technique based on state augmentation [33]. The artificially stabilized output error method has also been used in a few applications; however, it does not have a strong theoretical basis, involves engineering judgement, and the estimates are affected by the stabilization introduced to overcome the numerical divergence resulting from integration of an unstable system [34].

A characteristically different approach to aerodynamic modeling is provided by artificial neural networks. Through a flexible set of basic functions having certain properties, neural networks provide a means of nonlinear mapping the given input/output subspace resulting in an overall characterization of a system. The classical or global neural networks have found limited applications in flight vehicle system identification for database generation, model validation, and for cases where the aerodynamics is primarily linear. Neural networks have been used for a few applications like sensor failure detection and for modeling of highly nonlinear phenomena such as stall hysteresis and unsteady separated flow fields [35-38]. However, to extend the validity of a trained model to regions not covered during the training, an incremental update or fine tuning of part models may be difficult. Also, the recent advances in aerodynamic modeling have yielded analytical models for stall hysteresis accounting for the unsteady aerodynamics. Such models are more versatile, readily adaptable in simulation and conventional approach based on the equations of aircraft motion, and provide physical insight into the phenomenon being investigated.

7. MATHEMATICAL MODELS

The equations of flight vehicle motion are derived from the Newtonian mechanics which is fairly well understood. The typical assumptions made are of rigid-body, a flat and non-rotating earth, and the time rate of change of mass and inertia are neglected. In the case of fixed-wing aircraft, usually the symmetry allows to decouple the longitudinal and lateral-directional motion. For the time domain methods, the equations of motion result in a state space representation. These equations, defining the characteristic motion, involve the fundamental assumption that the forces and moments acting on the flight vehicle can be synthesized. Validity and utility of the mathematical models depend to a large degree on the adequacy and accuracy with which these external forces and moments acting on the flight vehicle can be modeled. Adequate model postulates are necessary to derive the benefits from the powerful tools of system identification methodology.

The classical approach to aerodynamic modeling is based on the Taylor series expansion, resulting in a linear aerodynamic model. For example, the rolling moment coefficient C_l may be modeled as:

$$C_l = C_{l\beta}\ \beta\ + C_{lp}\ p + C_{lr}\ r + C_{l\delta a}\ \delta_a + C_{l\delta r}\ \delta_r \qquad (1)$$

where β is the angle of sideslip, p is the roll rate, r is the yaw rate, δ_a is the aileron deflection, and δ_r is the rudder deflection. Based on such linear model postulates, point identification yields a model related to a specific trim condition. Repeating the point identification at all of the points flight tested, the entire operational flight envelope is covered. As a typical example, Fig. 6 shows the results obtained from the X-31A flight data analysis covering the angle of attack range up to 70°. Based on such results database update is generally possible.

In many cases the linear models are inadequate to represent the aerodynamic effects. For example, unsteady aerodynamics including the stall hysteresis, lift generated by direct-lift control surfaces, and the control effectiveness for large control surface deflections [39-42]. Eq. (2) shows a typical nonlinear model for the elevator control effectiveness identified from C-160 flight data [40].

$$C_{LT} = C_{L\alpha T}\ \alpha_T + [\ C_{L\delta c} + C_{L\delta c\alpha}\ \alpha_T \qquad (2)$$
$$+ C_{L\delta c\alpha 2}\ \alpha_T^2 + C_{L\delta c3}\ \delta_c^2\ ]\ \delta_c$$

where C_{LT} is the lift due to the tail, α_T is the angle of attack at the tail, and δ_c is the elevator deflection.

Many of the derivatives vary with angle of attack. This dependency on the angle of attack can also be nonlinear, for example, the weathercock stability of C-160 shown in Fig. 5 or the aileron effectiveness of X-31A shown in Fig. 6. If such dependencies are to be estimated through multi-point identification by concatenating several trim conditions, the nonlinear effects need to be properly modeled.

Recent advances in aerodynamic modeling have led to analytical models for complex processes such as ground effects and separated flow including stall hysteresis, making identification from flight data more amenable. For example, from quasi steady stall maneuvers an unsteady aerodynamic model for high lift including flow separation and stall was identified. Based on the Kirchhoff's theory of flow separation, the wing lift can be modeled as a function of angle of attack α and flow separation point X [41,42]:
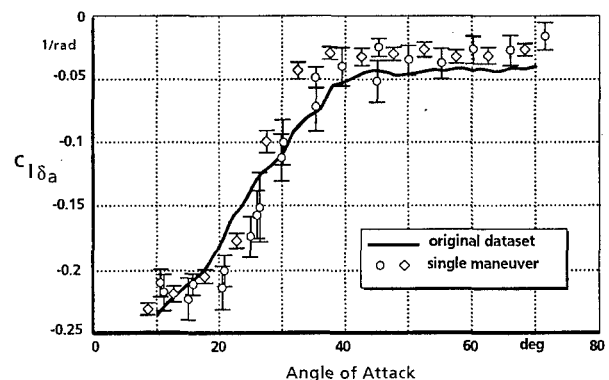

Fig. 6: Estimates of aileron effectiveness from point identification

2-6

$$C_L(\alpha, X) = C_{L\alpha} \left(\frac{1 + \sqrt{X}}{2} \right)^2 \alpha \qquad (3)$$

where $C_{L\alpha}$ is the lift curve slope and X ($0 \leq X \leq 1$) is a dynamic variable describing the instantaneous location of the flow separation point along the chord on the upper surface of the wing, $X = 1$ and $X = 0$ correspond to attached and fully separated flow respectively.

The flow separation point X may be determined from wind-tunnel tests or can also be identified from flight test data using the approximation:

$$X = \frac{1}{2} \left\{ 1 - \tanh \left[a_1 (\alpha - \tau_2 \dot{\alpha} - \alpha^*) \right] \right\} \qquad (4)$$

where $\dot{\alpha}$ is the rate of change of angle of attack, τ_2 is the time constant accounting for the unsteady aerodynamic effects, α^* is the breakpoint corresponding to $X = 0.5$, and a_1 is the static stall characteristics of the airfoil. The time constant τ_2 depends on airfoil section and wing configuration. The three parameters a_1, τ_2, and α^* are completely adequate to model the stall hysteresis.

Fig. 7a shows a comparison of the lift coefficient C_L as a function of angle of attack obtained from measured stall flight data (shown by solid lines) with those identified in the database (shown by dashed lines). Fig. 7b shows a comparison between the flight measured and model predicted time responses for α the angle of attack, a_Z the vertical acceleration, θ the pitch attitude, and V the true airspeed; δ_e is the elevator deflection. Adequacy of the identified model is apparent from the time history plots and the efficacy of the analytical model postulate is evident from the hysteresis in the lift coefficient [42,43].

Different approaches to account for the downwash lag effect have also been investigated for parameter estimation [44,45]. The conventional approach approximates the downwash lag through derivatives due to $\dot{\alpha}$, the rate of change of angle of attack. It is also possible to account explicitly for the downwash lag effect by considering wing-body and tail separately and postulating a two-point aerodynamic model. Such models, although more oriented towards physics of the phenomenon, require estimation programs capable of handling models which are nonlinear in the parameters being estimated, whereas estimation of the derivatives with respect to the rate of change of angle of attack requires special flight tests. In general, both the approaches yield comparable results as far as model fidelity is concerned.

To generate high-fidelity databases for flight simulators, there are two viable approaches. The first approach is to update the wind-tunnel predictions through incremental coefficients obtained from flight data analysis [46-48]. The second approach is to generate a new database from flight data through a systematic procedure starting from a basic model for symmetric flight and extending it to include special effects like landing gear, high angle of attack regime, unsteady aerodynamics, ground effects, engine-out effects [40,43]. In both the approaches the
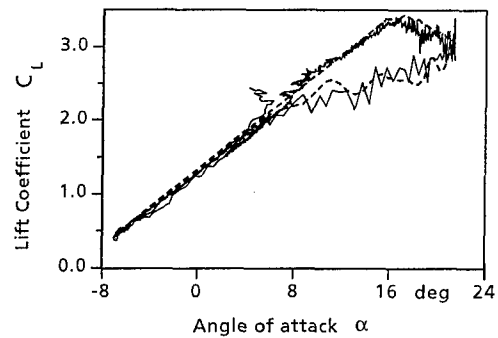
a) Crossplot of C_L versus α
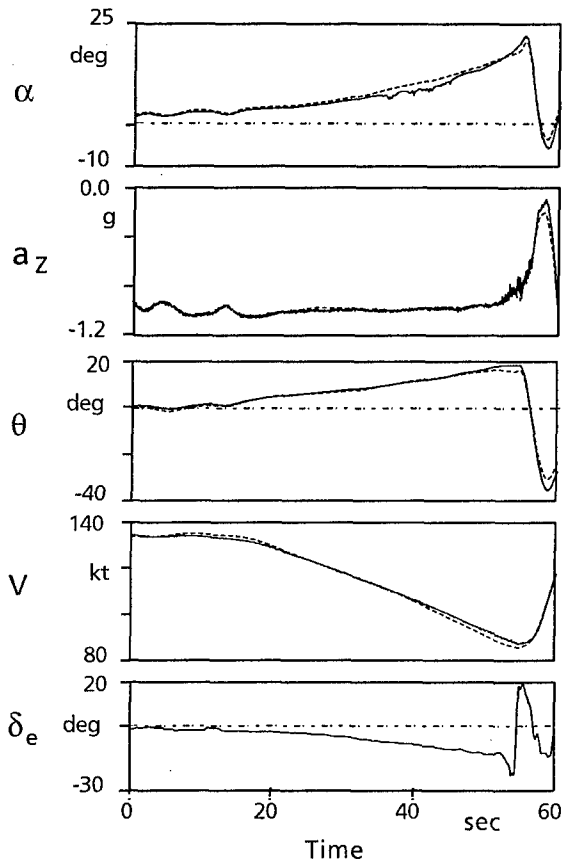
b) Response time histories

Fig. 7: Modeling and identification of stall hysteresis - Dornier 328 (—— Flight measured; - - - - Estimated)

task is formidable, the process iterative, requiring model structure determination, and can be equally complex. In general, the primary aerodynamic derivatives can be extracted well; determination of aerodynamic effects of secondary order requires some considerations. Particularly in such cases care needs to be taken to avoid over-parameterization, which yields better response match but not necessarily physically justifiable estimates. It needs to be ensured that the identified model is parsimonious.

8. MODEL VALIDATION

As depicted in Fig. 2, the parameter estimation and the model validation are integral parts of system identifica-

tion. Several criteria, to be used in conjunction with each other, help to validate the model: i) standard deviations of the estimates (i.e. estimation uncertainties in terms of Cramer-Rao bounds), ii) goodness of fit (i.e. value of the cost function being minimized, for example, the determinant of the covariance matrix of the residuals), iii) correlation coefficients among the estimates, iv) plausibility of the estimates from physical understanding of the system under investigation or by comparison with other predictions such as wind-tunnel or analytical methods, and v) model predictive capability.

The predictive capability of the identified model is determined by comparing the flight measured aircraft responses with those predicted by the model for the same control inputs keeping the aerodynamic model fixed. This proof-of-match process is an important part of flight simulator certification and acceptance. To eliminate subjective evaluation, the FAA has specified guidelines in terms of tolerances for each variable depending upon the nature of the validation test [4,5]. Although the majority of the validation tests are verified in time domain through a comparison of time histories, it is also possible to extend the verification to the frequency domain, which may bring out more clearly the range of applicability of the identified model [1,49]. This is particularly important for high authority flight control systems or in cases where aeroservoelastic effects may be dominant. For aircraft with reversible flight controls, importance is given to an end-to-end match using an integrated model, i.e. model incorporating six degree-of-freedom equations of aircraft motion coupled with dynamic models of flight controls using the identified rigid-body and hinge moments databases.

As a typical example of proof-of-match, Fig. 8 shows the end-to-end match obtained from a force driven integrated model for a normal landing with a Dornier 328 propeller aircraft having reversible flight controls, where V is the airspeed, h is the altitude above ground level, θ is the pitch attitude, ϕ is the bank angle, δ_e is the elevator deflection, and δ_r is the rudder deflection. The applicable FAA tolerances for each parameter are shown as vertical bars. The match between the model predicted and the flight measured responses for this high activity task, which is a critical area for pilot training, is well within the tolerances and demonstrates adequacy of the flight identified database for a flight simulator. It may also be pointed out that proof-of match based on a force driven integrated model incorporating the identified rigid-body and hinge moments databases is significantly more complex than models driven through control surface position inputs [43,50].

9. SELECTED EXAMPLES

To bring out the salient features of the four legs of the Quad-M approach, several examples have already been presented in the foregoing sections. The identified models ranged from linear models to highly nonlinear ones including unsteady aerodynamic effects. In this section additional examples are presented to bring out the wide applicability of these tools.
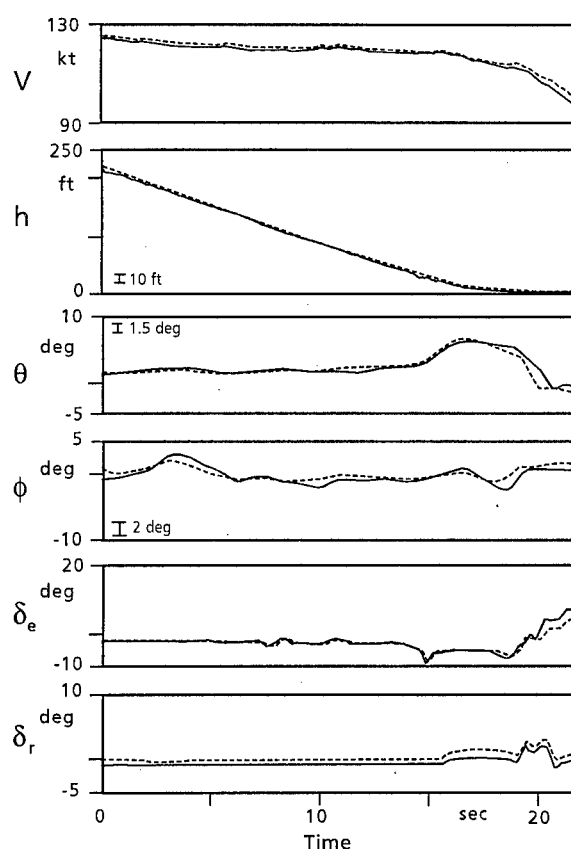

Fig. 8: End-to-end match for high activity task of normal landing, Dornier 328

(——— Flight measured; - - - - Estimated)

9.1 Aerodynamic Effects of Secondary Order

As already pointed out in the foregoing section, determination of primary derivatives does not pose any serious difficulties. For high-fidelity databases for flight simulators, however, it is necessary to properly model the aerodynamic effects of secondary order as well. This is particularly true when the model fidelity has to meet the Level D standards specified by the FAA. The ramp door and landing gear effects, or the downwash due to speed brakes are some typical examples of this class [51].

Fig. 9 shows two flight maneuvers flown with extended landing gear; the first maneuver is a short period motion excited by a 3211 input and the second is an aileron and rudder input maneuver resulting in rolling and yawing motion. The basic aerodynamic model identified from the clean configuration, i.e. neglecting the landing gear effects, yields the response match shown in Fig. 9a, where a_x is the longitudinal acceleration, r is the yaw rate, θ is the pitch attitude, α is the angle of attack, and β is the angle of sideslip. The discrepancies in the longitudinal acceleration are demonstrative of additional drag being introduced. The lateral-directional variables, angle of sideslip β and yawing rate r, also show some discernible differences.

Through a systematic approach, and keeping in mind the principle of parsimony, additional parameters were identified to model the incremental effects due to landing

a) Neglecting landing gear effects

b) Accounting for landing gear effects
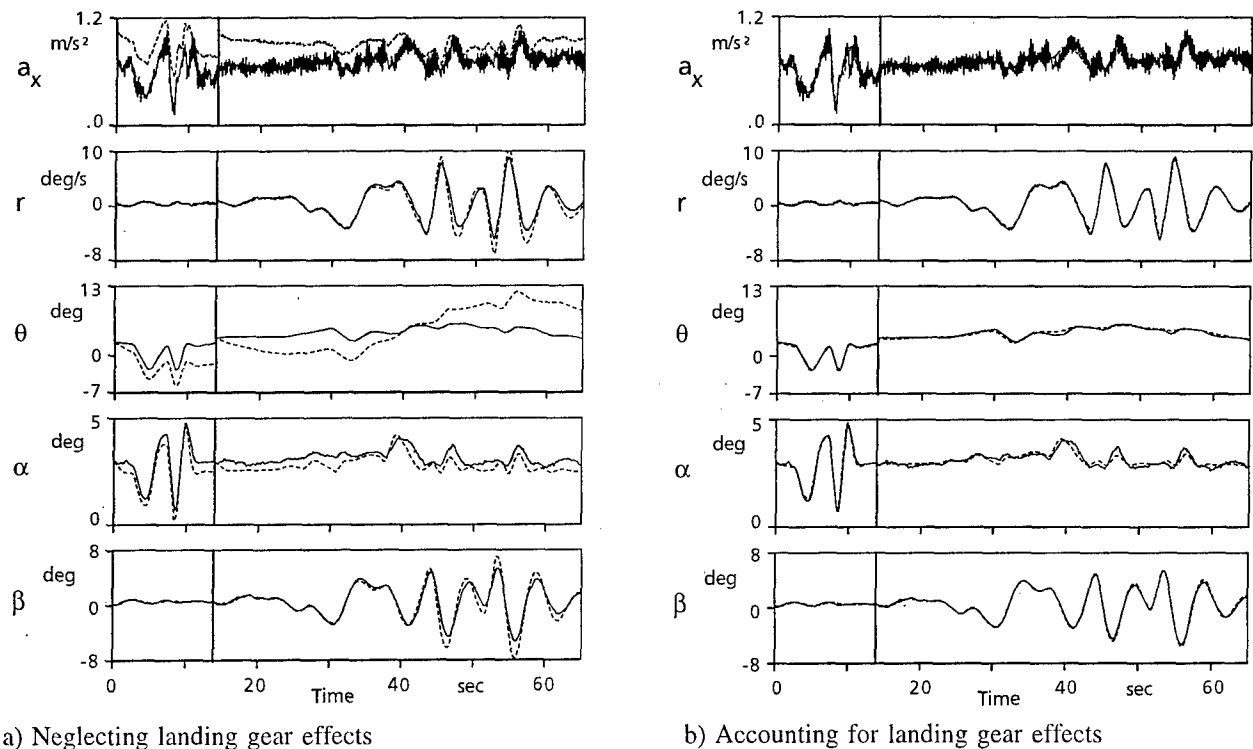
Fig. 9: Estimation of aerodynamic effects of secondary order - C-160 Landing gear effects

(——— Flight measured; - - - - - Estimated)

gear [51]. The identified value of ΔC_{DLG}, the incremental change in the drag coefficient C_D due to landing gear (subscript LG), suggests increased drag and the derivative $C_{n\beta LG}$ increased weathercock stability. The resulting model yields the response match shown in Fig. 9b, which is significantly better compared to that in Fig. 9a. The landing gear effects are typically in the range of 5% to 10% of the total, but still important for simulator fidelity. Proper test techniques and a systematic modeling approach enabled accurate identification of such aerodynamic effects of secondary order.

9.2 X-31A System Identification

The U.S./German experimental aircraft X-31A is a highly control augmented fighter with enhanced maneuverability. Post-stall maneuvering is enabled by applying advanced technologies such as high angle-of-attack aerodynamics and flight control system integrated thrust vectoring. System identification methods were employed to predict aerodynamic behavior at new flight conditions and to validate and update the predicted aerodynamic database.

The X-31A posed several challenges in aircraft system identification mainly because the aircraft is inherently unstable, and because the integrated flight control laws lead to correlated deflections of the control surfaces and of the thrust vector vanes. However, diligent modeling and a wide variety of estimation techniques provided flight validated aerodynamic characteristics, including post-stall regime and thrust vector control. Furthermore, the crux of the problem pertaining to highly augmented aircraft was the data correlation and insufficient excita-

tion, and as already pointed out in Fig. 4, an efficient solution to this problem was provided by separate surface excitation.

The results of X-31A system identification have been used to validate and in several cases update the wind-tunnel predicted database. As a typical example, Fig. 10 shows the dihedral effect. It can be clearly observed that the flight estimates did not confirm the predicted large value of dihedral effect between 30° and 45° of angle of attack [1,24]. System identification provided improved results for flight test planning, flight envelope expansion, and a database for simulation and control law modifications and validation, and thus catered to actual needs of the aircraft industry.
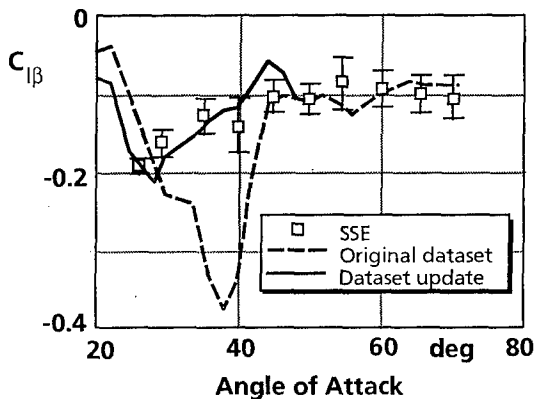

**Fig. 10: X-31A Dihedral effect - database update**

9.3 Identification of Flexible Aircraft

Elasticity effects, particularly for large aircraft, are known to affect the aerodynamic derivatives such as lift curve slope, dihedral effects, control surface effectiveness, and pitch as well as roll damping. In general, quasi-steady influences of the most important structural degrees of freedom on the aerodynamic derivatives are accounted for through flex factors, provided the rigid-body and structural frequencies are sufficiently separated. Predicted flex factors are usually based on analytical computations and structural in-vacuo frequencies [8,9,52]. Recent results demonstrate that through linear model postulates and by combining several flight maneuvers at judiciously chosen flight conditions, the dynamic pressure dependent quasi-steady effects due to structural deformation and rigid-body aerodynamic derivatives can be separated and identified using system identification methods [53].

For a large transport aircraft, the data correlation between the prediction and flight estimated values of several derivatives, for example lift curve slope $C_{L\alpha}$ in Fig 11a and elevator effectiveness $C_{m\delta e}$, was good for both the rigid-body and the flexible aircraft [53]. However, in
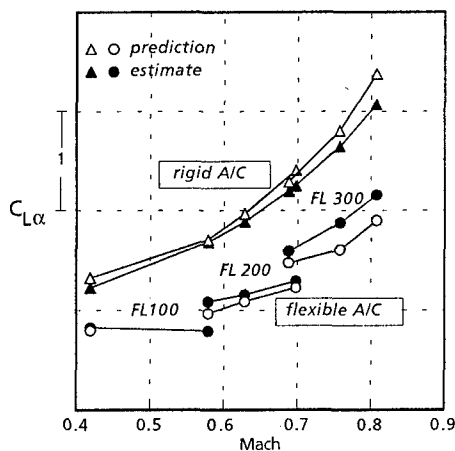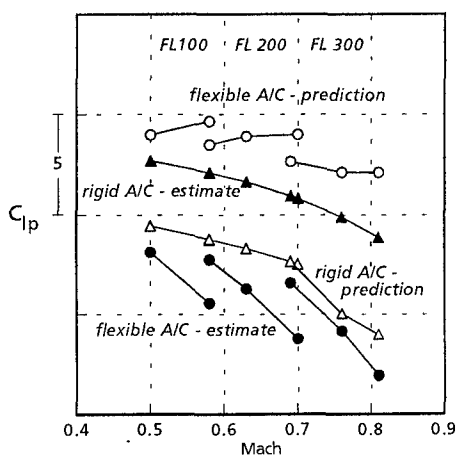
a few cases significant differences were observed. For example, Fig. 11b shows the predicted and the flight identified roll damping derivatives C_{lp}. It is observed that the estimated roll damping of the rigid aircraft is slightly lower than the prediction. More interestingly, the flexibility results in an increased roll damping whereas the prediction had indicated reduction.

9.4 Rotorcraft High Bandwidth Modeling

The application spectrum of rotorcraft modeling spans over several models of different complexities. In terms of the increasing effort they are: i) MIL-spec compliance, ii) vibration spectral analysis, iii) transfer function models, iv) state space models for handling qualities evaluation, v) high-fidelity simulation models in state space, and vi) aeroservoelastic models, see Fig. 12; the abbreviations SID and SIM are used for system identification and simulation respectively. In the context of rotorcraft modeling, the two key problem areas are model parameter uncertainty and model structure uncertainty. These two uncertainties are typically associated with low-order and higher-order dynamics; they can result in the first case due to inaccurate configuration parameters such as interactional aerodynamics and in the second case due to unmodeled rotor or control dynamics respectively [1,54].

As already pointed out, high fidelity rotorcraft simulation demands high bandwidth models. Such high bandwidth requirements can be met only through augmentation of the rigid-body model with higher-order rotor dynamics. The conventional approach to rotorcraft identification incorporates nonlinear equations of motion and linear aerodynamic models based on derivatives [55-57]. Such models are primarily used for stability and control analysis, as well as for control system design. Extensive flight data is necessary in this case to identify derivatives.

The conventional approach to rotorcraft simulation is, however, based on generic models incorporating element-by-element characteristics. Such models, used for simulation, performance analysis, and vehicle design, are mostly characterized by nonlinear aerodynamics. Flight data in such a case is needed only for validation purposes.
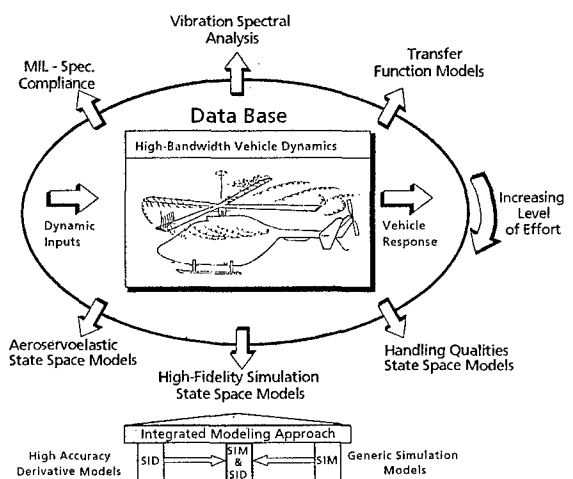
a) Lift curve slope $C_{L\alpha}$

b) Roll damping derivative C_{lp}

Fig. 11: Flight estimated and predicted aerodynamic derivatives of a large flexible aircraft

Fig. 12: Application spectrum of high bandwidth rotorcraft modeling

Incorporation of flight identified derivative-models in rotorcraft simulation was hitherto a bottleneck, mainly because of the differences in the modeling art, namely derivative models versus generic models. The recent thrust has been towards expanding the scope by combining the classical identification and simulation approaches, see Fig. 13. In such an integrated modeling approach, generic models are considered as the base-line models and discrepancies in the model fidelity are reduced through an identification procedure incorporating parametric or derivative models. This approach allows to retain the advantages of the generic models, but at the same time refine them through the expertise available from the classical approach of rotorcraft identification and thereby minimize the inherent uncertainties and tolerances present in the generic model. Viability of such an approach is demonstrated in Fig. 14a which shows the results of an identification run for a doublet input. Fig. 14b shows the validation for a sweep input using complementary data not used in identification [58]. From Fig. 14, it is evident that the BO-105 model meets the requirements specified for helicopter simulators [59].

10. CONCLUDING REMARKS

In the recent years there has been an explosion of system identification applications to flight vehicles. Besides the classical applications, the current focus seems to be on modeling complex phenomena which generally result in highly nonlinear aerodynamics, on high fidelity models, on minimization of inherent uncertainties and tolerances, and on unstable aircraft identification. In light of this scenario, the present paper attempts to take stock of the capabilities provided by system identification methodology. The Quad-M key issues are recapitulated, highlighting the classical approaches and bringing out the current trends. An overview of a few recently concluded flight vehicle applications is provided. From the several examples provided in this paper, it appears that over the last few years the basic tools of parameter estimation have remained more or less the same, but the application spectrum has widened significantly. The confidence gained in the use of these powerful techniques have made them an indispensable tool for the various key activities of the aeronautical research establishments, military flight test
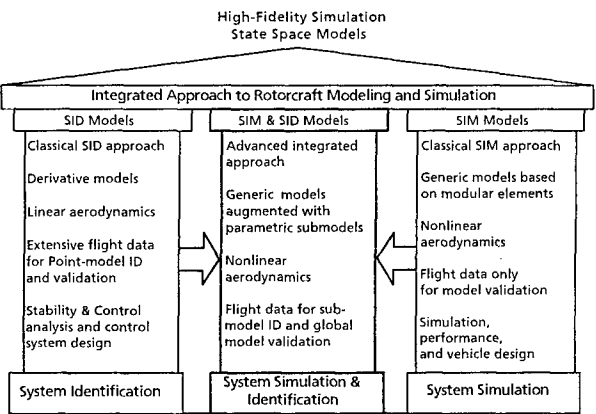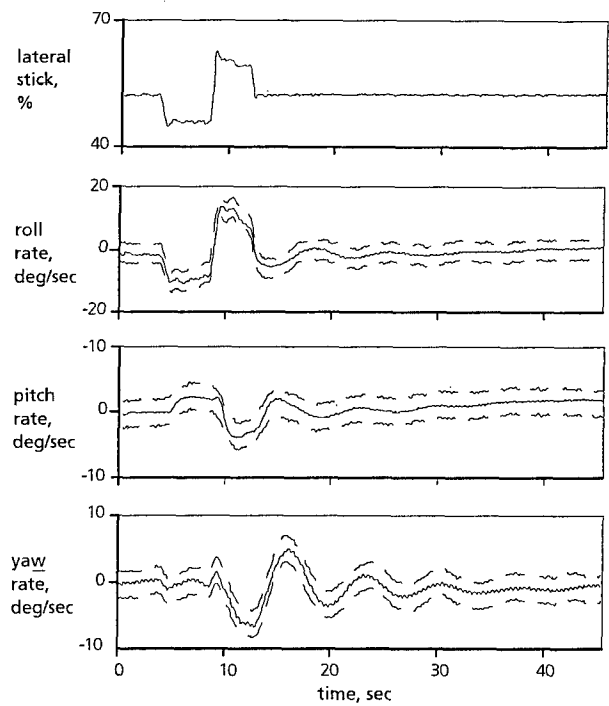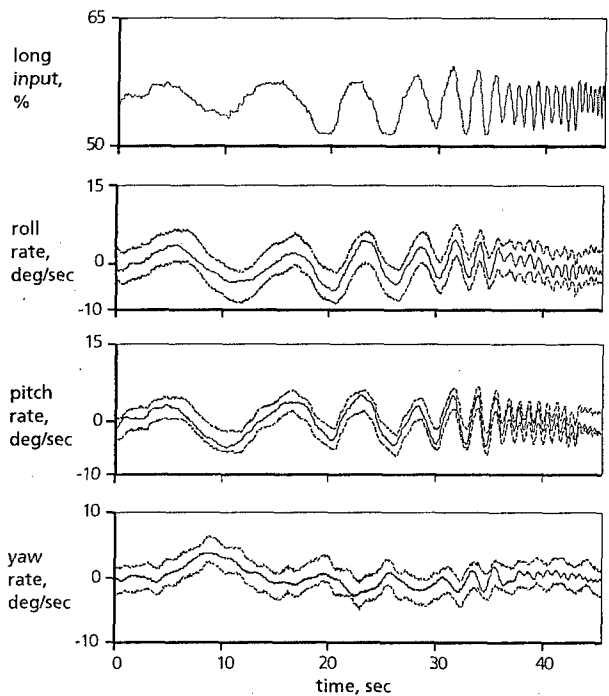

Fig. 13: Integrated approach to rotorcraft modeling and simulation

a) Doublet input

b) Proof-of-match for sweep input - complementary data

Fig. 14: Nonlinear modeling and identification of BO-105
(- - - - flight measured ± FAA tolerances; —— estimated)

centers, and aircraft industry. In the future, system identification will play an ever-increasing role in the sophisticated complex of modeling and Simulation (M&S) during the flight vehicle design and evaluation phase. The integrated utilization of system identification tools and expertise will provide ultimate answers to unmasking modeling deficiencies, reducing development risks, and improving flight safety issues.

11. REFERENCES

[1] Hamel, P. G. and Jategaonkar, R. V., "Evolution of Flight Vehicle System Identification", Journal of Aircraft, Vol. 33, No. 1, Jan.-Feb. 1996, pp. 9-28.

[2] Maine, R. E. and Iliff, K. W., "Identification of Dynamic Systems - Applications to Aircraft. Part 1: The Output Error Approach", AGARD AG-300-Vol. 3, Part 1, Dec. 1986.

[3] Klein, V., "Estimation of Aircraft Aerodynamic Parameters from Flight Data", Progress in Aerospace Sciences, Pergamon Press, Oxford, Vol. 26, 1989, pp. 1-77.

[4] Anon., "Airplane Simulator Qualification", FAA Advisory Circular, AC 120-40B, Interim Version, Feb. 1991.

[5] Anon., "Airplane Flight Simulator Evaluation Handbook", The Royal Aeronautical Society, London, Feb. 1995.

[6] Ross, H., "X-31 Enhancement of Aerodynamics for Maneuvering beyond Stall", AGARD CP-497, Nov. 1991, Paper 2.

[7] Huber, P., "Control Law Design for Tailless Configurations and In-Flight Simulation Using the X-31 Aircraft", AIAA Guidance, Navigation, and Control Conference, Baltimore, MD, Aug. 6-10, 1995, Paper 95-3199.

[8] Rynaski, E. G., Andrisani II, D., and Weingarten, N. C., "Identification of the Stability Parameters of an Aeroelastic Airplane", AIAA 78-1328, 1978.

[9] Chevalier, H. L., Dornfeld, G. M., and Schwanz, R. C., "An Analytical Method for Predicting the Stability and Control Characteristics of Large Elastic Airplanes at Subsonic and Supersonic Speeds - Part II: Application", NASA TM-X-66378, Jan. 1968.

[10] Hamel, P. G. and Kaletka, J., "Rotorcraft System Identification - An Overview of AGARD FVP Working Group 18", AGARD CP-552, Aug. 1995, Paper 18.

[11] Hamel, P. G., "Aircraft Parameter Identification Methods and Their Applications - Survey and Future Aspects", AGARD LS-104, Nov. 1979, Paper 1.

[12] Mulder, J. A., Jonkers, H. L., Horsten, J. J., Breeman, J. H., and Simon, J. L., "Analysis of Aircraft Performance, Stability and Control Measurements", AGARD LS-104, Nov. 1979, Paper 5.

[13] Maine, R. E. and Iliff, K. W., "Identification of Dynamic Systems", AGARD AG-300, Vol. 2, Jan. 1985.

[14] Iliff, K. W., "Parameter Estimation for Flight Vehicles", Journal of Guidance, Control, and Dynamics, Vol. 12, No. 5, Sept.-Oct. 1989, pp. 609-622.

[15] Mehra, R. K. "Optimal Inputs for Linear System Identification", Preprints, JACC, Stanford, California, 1972.

[16] Stepner, D. E. and Mehra, R. K., "Maximum Likelihood Identification and Optimal Input Design for Identifying Aircraft Stability and Control Derivatives", NASA CR-2200, March 1973.

[17] Gupta, N. K and Hall, W. E. Jr., "Input Design for Identification of Aircraft Stability and Control Derivatives", NASA CR-2493, Feb. 1975.

[18] Koehler, R. and Wilhelm, K., "Auslegung von Eingangssignalen für die Kennwertermittlung", DFVLR-IB 154-77/40, Dec. 1977.

[19] Plaetschke, E. and Schulz, G., "Practical Input Signal Design," AGARD LS-104, Nov. 1979, Paper 3.

[20] Morelli, E. A. and Klein, V., "Optimal Input Design for Aircraft Parameter Estimation Using Dynamic Programming", AIAA Atmospheric Flight Mechanics Conference, Portland, OR, Aug. 20-22, 1990, Paper 90-2801.

[21] Friehmelt, H., Weiss, S., Rohlf, D., and Plaetschke, E., "Using Single Surface Excitation for X-31 System Identification at High AoA", Proceedings of the 26th Annual Symposium of the Society of Flight Test Engineers, Berlin, June 19-23, 1995, pp. 4.51-4.62.

[22] van der Linden, C. A. A. M., Mulder J. A., and Sridhar, J. K., "Recent Developments in Aircraft Parameter Identification at Delft University of Technology - Optimal Input Design", in Cook M. V. and Rycroft, M. J. (Eds), Aerospace Vehicle Dynamics and Control, Clarendon Press, Oxford, 1994, pp. 259-284.

[23] Morelli, E. A., "Flight Test Validation of Optimal Input Design and Comparison to Conventional Inputs", AIAA Atmospheric Flight Mechanics Conference, New Orleans, LA, Aug. 11-13, 1997, Paper 97-3711.

[24] Weiss, S., Friehmelt, H., Plaetschke, E., and Rohlf, D., "X-31A System Identification Using Single-Surface Excitation at High Angles of Attack", Journal of Aircraft, Vol. 33, No. 3, May-June 1996, pp. 485-490.

[25] Gates, R. J., Bowers, A. H., and Howard, R. M., "A Comparison of Flight Input Techniques for Parameter Estimation of Highly Augmented Aircraft", AIAA Atmospheric Flight Mechanics Conference, San Diego, CA, Aug. 11-13, 1996, Paper 96-3363.

[26] Tischler, M. B., Fletcher, J. W., Diekmann, V. L., Williams, R., A., and Cason, R. W., "Demonstration of Frequency-Sweep Testing Techniques Using a Bell 214-ST Helicopter", NASA TM-89422, April 1987.

[27] Tischler, M. B. and Cauffman, M. G., "Frequency-Response Method for Rotorcraft System Identification: Flight Applications to BO 105 Coupled Rotor/Fuselage Dynamics", Journal of the American Helicopter Society, Vol. 37, No. 3, July 1992, pp. 3-17.

[28] Krag, B., Jategaonkar, R. V., Mönnich, W., and Fischenberg, D., "Estimation of an Aerodynamic Data Base for a New C-160 'Transall' Flight Simulator from Flight Data", Proceedings of the RAeS Symposium on 'Data Issues for Flight Simulators - An On-Going Problem?', Nov. 10-11, 1993, London, pp. 7.1-7.12.

[29] Baillie, S. W., Hui, K., Srinivasan, R., and DeLeeuw, J. H., "Aerodynamics for Flight Simulators: A Look at Data Collection, Reduction and Model Development", Proceedings of the RAeS Symposium on 'Data Issues for Flight Simulators - An On-Going Problem?", Nov. 10-11, 1993, London, pp. 16.1-16.13.

[30] Vörsmann, P., Haverland, M., and Schänzer, G., "High Precision Navigation for Flight Testing (AERONAV)", AGARD CP-519, Oct. 1992, Paper 20.

2-12

[31] Maine, R. E. and Iliff, K. W., "Formulation and Implementation of a Practical Algorithm for Parameter Estimation with Process and Measurement Noise", SIAM Journal of Applied Mathematics, Vol. 41, Dec. 1981, pp. 558-579.

[32] Jategaonkar, R. V., "A Comparison of Output Error and Filter Error Methods from Aircraft Parameter Estimation Results", In: DLR-Mitt. 93-14, Dec. 1993, pp. 63-87.

[33] Jategaonkar, R. V. and Thielecke, F., "Parameter Estimation Methods for Unstable Aircraft", Journal of Aircraft, Vol. 31, No. 3, May-June 1994, pp. 510-519.

[34] Maine, R. E. and Murray, J. E., "Application of Parameter Estimation to Highly Unstable Aircraft", Journal of Guidance, Control, and Dynamics, Vol. 11, No. 3, May-June 1988, pp. 213-219.

[35] Napolitano, M. R., Neppach, C., van Casdorph, Naylor, S., Innocenti, M., and Silvestri, G., "Neural-Network-Based Scheme for Sensor Failure Detection, Identification, and Accommodation", Journal of Guidance, Control, and Dynamics, Vol. 18, No. 6, Nov.-Dec. 1995, pp. 1280-1286.

[36] Linse, D. J. and Stengel, R. F., "Identification of Aerodynamic Coefficients Using Computational Neural Networks", Journal of Guidance, Control, and Dynamics, Vol. 16, No. 6, Nov.-Dec. 1993, pp. 1018-1025.

[37] Rokhsaz, K. and Steck, J. E., "Use of Neural Networks in Control of High-Alpha Maneuvers", Journal of Guidance, Control, and Dynamics, Vol. 16, No. 5, Sept.-Oct. 1993, pp. 934-939.

[38] Schreck, S. J., Faller, W. E., and Luttges, M. W., "Neural Network Prediction of Three-Dimensional Unsteady Separated Flowfields", Journal of Aircraft, Vol. 32, No. 1, Jan.-Feb. 1995, pp. 178-185.

[39] Jategaonkar, R. V., "Identification of Actuation System and Aerodynamic Effects of Direct-Lift-Control Flaps", Journal of Aircraft, Vol. 30, No. 5, Sept.-Oct. 1993, pp. 636-643.

[40] Jategaonkar, R. V., Mönnich, W., Fischenberg, D., and Krag, B., "Identification of C-160 Simulator Data Base from Flight Data", Proceedings of the 10th IFAC Symposium on System Identification, Copenhagen, Denmark, July 1994, pp. 3.67-3.74.

[41] Goman, M. and Khrabrov, A., "State-Space Representation of Aerodynamic Characteristics of an Aircraft at High Angles of Attack", Journal of Aircraft, Vol. 31, No. 5, Sept.-Oct. 1994, pp. 1109-1115.

[42] Fischenberg, D. and Jategaonkar, R. V., "Identification of Aircraft Stall Behavior from Flight Test Data", RTO SCI Symposium on 'System Identification for Integrated Aircraft Development and Flight Testing', May 5-7, 1998, Madrid, Spain, Paper 17.

[43] Jategaonkar, R. V. and Mönnich, W., Identification of DO-328 Aerodynamic Database for a Level D Flight Simulator, AIAA Atmospheric Flight Mechanics Conference, New Orleans, LA, Aug. 11-13, 1997, Paper 97-3729.

[44] Jategaonkar, R. V. and Gopalratnam, G., "Two Complementary Approaches to Estimate Downwash Lag Effects from Flight Data", Journal of Aircraft, Vol. 28, No. 8, Aug. 1991, pp. 540-542.

[45] Maine, R. E. and Iliff, K. W., "Maximum Likelihood Estimation of Translational Acceleration Derivatives from Flight Data", Journal of Aircraft, Vol. 16, No. 10, Oct. 1979, pp. 674-679.

[46] Neville, K. W. and Stephens, A. T., "Flight Update of Aerodynamic Math Model", AIAA Flight Simulation Technologies Conference, Paper 93-3596, Monterey, CA, Aug. 9-11, 1993.

[47] Trankle, T. L. and Bachner, S. D., "Identification of a Nonlinear Aerodynamic Model of the F-14 Aircraft", Journal of Guidance, Control, and Dynamics, Vol. 18, No. 6, Nov.-Dec. 1995, pp. 1292-1297.

[48] Rohlf, D., "Direct Update of a Global Simulator Model with Increments via System Identification", RTO SCI Symposium on 'System Identification for Integrated Aircraft Development and Flight Testing', May 5-7, 1998, Madrid, Spain, Paper 28.

[49] Tischler, M. B., "System Identification Methods for Aircraft Flight Control Development and Validation", NASA TM 110369, Oct. 1995.

[50] Mönnich, W. and Jategaonkar, R. V., "Database Development for Level D Simulators - Lessons Learned", RTO SCI Symposium on 'System Identification for Integrated Aircraft Development and Flight Testing', May 5-7, 1998, Madrid, Spain, Paper 14.

[51] Jategaonkar, R. V., Mönnich, W., Fischenberg, D., and Krag, B., "Identification of Speed Brake, Ramp Door, Air-Drop, and Landing Gear Effects from 'Transall' Flight Data", Journal of Aircraft, Vol. 34, No. 2, March-April 1997, pp. 174-180.

[52] Ghosh, A. K. and Raisinghani, S. C., "Parameter Estimates of an Aeroelastic Aircraft as Affected by Model Simplifications", Journal of Aircraft, Vol. 31, No. 2, March-April 1994, pp. 452-454.

[53] Fischenberg, D. and Rohlf, D., "Identifizierung der Einflüsse von Kompressibilität und Strukturelastizität auf die aerodynamischen Derivative eines Widebody-Verkehrsflugzeugs", DLR-IB 111-98/03, Jan. 1998.

[54] Hamel, P. G. (Editor), "Rotorcraft System Identification", AGARD AR-280, Sept. 1991.

[55] Kaletka, J. and von Grünhagen, W., "System Identification of Mathematical Models for the Design of a Model Following Control System", Vertica, Pergamon Press, Oxford, Vol. 13, No. 2, 1989, pp. 213-228.

[56] Tischler, M. B., "Identification Requirements for High-Bandwidth Rotorcraft Flight Control System Design", Journal of Guidance, Control, and Dynamics, Vol. 13, Sept.-Oct. 1990, pp. 835-841.

[57] Hamel, P. G. and Kaletka, J., "Advances in Rotorcraft System Identification", Progress in Aerospace Sciences, Pergamon Press, Oxford, Vol. 33, 1997, pp. 259-284.

[58] Rohlfs, W., von Grünhagen, W., and Kaletka, J., "Nonlinear Rotorcraft Modeling and Identification", RTO SCI Symposium on 'System Identification for Integrated Aircraft Development and Flight Testing', May 5-7, 1998, Madrid, Spain, Paper 23.

[59] Anon, "Helicopter Simulator Qualification", FAA Advisory Circular, AC 120-63, Oct. 1994.

System Identification Methods for Aircraft Flight Control Development and Validation

Mark B. Tischler

Army/NASA Rotorcraft Division
Aeroflightdynamics Directorate (AVRDEC)
US Army Aviation and Missile Command
Ames Research Center, Mail Stop N210-5
Moffett Field, California 94035-1000
USA

1. SUMMARY

System-identification methods compose a mathematical model, or series of models, from measurements of inputs and outputs of dynamic systems. The extracted models allow the characterization of the response of the overall aircraft or component subsystem behavior, such as actuators and on-board signal processing algorithms. This paper discusses the use of frequency-domain system-identification methods for the development and integration of aircraft flight-control systems. The extraction and analysis of models of varying complexity from nonparametric frequency-responses to transfer-functions and high-order state-space representations is illustrated using the Comprehensive Identification from FrEquency Responses (CIFER®) system-identification facility. Results are presented for test data of numerous flight and simulation programs at the Ames Research Center including rotorcraft, fixed-wing aircraft, advanced short takeoff and vertical landing (ASTOVL), vertical/short takeoff and landing (V/STOL), tiltrotor aircraft, and rotor experiments in the wind tunnel. Excellent system characterization and dynamic response prediction is achieved for this wide class of systems. Examples illustrate the role of system-identification technology in providing an integrated flow of dynamic response data around the entire life-cycle of aircraft development from initial specifications, through simulation and bench testing, and into flight-test optimization.

2. INTRODUCTION

System identification is a procedure for accurately characterizing the dynamic response behavior of a complete aircraft, subsystem, or individual component from measured data. This key technology for modern fly-by-wire flight-control system development and integration provides a unified flow of information regarding system performance around the entire life cycle from specification and design through development and flight test (fig. 1). A similar "roadmap" for application of system-identification methods to rotorcraft development was previously proposed by Schrage in a comprehensive report dedicated to this topic (Anon. 1991). An excellent historical summary and overview of system identification is given by Hamel (1995). System identification has been widely utilized in recent aircraft programs including many of those described in a recent volume on aircraft flight control (Anon. 1994). Common applications for flight-control system development include:

definition of system requirements, specification and analysis of handling qualities, evaluation of proposed control-law concepts, validation and improvement of complex simulation models, validation of subsystem components and development facilities, and flight-test optimization of control laws.
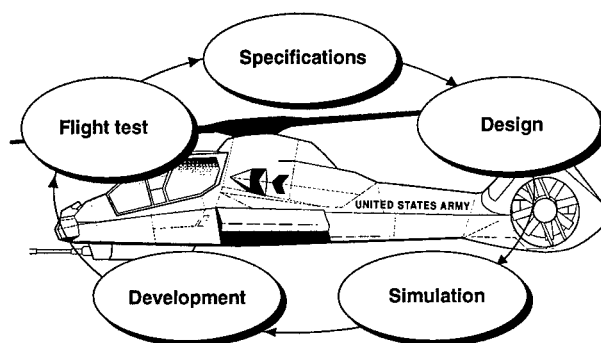

Figure 1. Road map for fly-by-wire flight-control system development and integration.

Frequency-domain identification approaches are especially well suited to the development and validation of flight-control systems. Feedback stability and noise amplification properties are determined from the broken-loop frequency response, and characterized by metrics such as crossover frequency, and associated gain and phase margins. Command tracking performance is determined from the closed-loop frequency-response, and characterized metrics such as bandwidth and time-delay, and equivalent system eigenvalues. Frequency-domain identification approaches allow the direct and rapid (including real-time) identification of these frequency responses and metrics, without the need to first identify a parametric (state-space) model structure such as is required in applying time-domain methods. Careful tracking of the broken-loop and end-to-end closed-loop frequency-response behavior from the preliminary design studies through detailed design and simulation and into flight test provides an important "paper trail" for documenting system performance and solving problems that may appear in the later phases of development.

The availability of comprehensive and reliable computational tools has substantially enhanced the acceptability of frequency-

domain techniques in the flight-control and flight-test community. Benefits from applying these techniques include the reduction of flight-test time required for control system optimization and handling-qualities evaluation, especially for complex control-law architectures, and improvements in the final system performance. Frequency-domain methods offer a transparent understanding of component and end-to-end response characteristics that can be critical in solving system integration problems.

This paper reviews frequency-domain system-identification methods for development and integration of aircraft flight-control systems. These methods were developed under a long-term research activity at the Ames Research Center by the Army Aeroflightdynamics Directorate (AFDD), the NASA and Sterling Software. Many of the flight applications have been to rotorcraft, which pose an especially difficult challenge to system identification (Tischler 1990). The dynamics of these aircraft are highly coupled, and unstable. Additionally, the rotorcraft dynamics include lightly-damped fuselage and rotor modes. Vibration and low excitation signal content, especially near hover, results in typically low signal-to-noise ratios. Experience in developing and applying system-identification methods to the rotorcraft problem has produced a set of tools that has proven highly reliable for the broad scope of applications reviewed in this paper. The first section presents a summary of the frequency-domain approach and the CIFER® comprehensive analysis facility. The remainder of the paper is organized into five sections following the flight-control development flowchart of figure 1 from specifications and design through flight-test optimization. Each section illustrates important techniques with examples based on fixed and rotary-wing projects at the Ames Research Center.

3. OVERVIEW OF AFDD/NASA SYSTEM-IDENTIFICATION TECHNIQUES

The AFDD/NASA frequency-domain system identification procedure is shown in figure 2, and in reviewed in this section. Details of the procedure are found in Tischler and Cauffman (1992). System-identification methods and requirements for specific application to high-bandwidth rotorcraft flight-control system design are given by Tischler (1990).

Aircraft or subsystem component dynamics are excited by a pilot-generated or computer-generated frequency-sweep input. The dynamic responses are generally measured by dedicated sensors, and the data are either recorded on-board or telemetered to the ground for processing. Kalman filtering techniques (or simple numerical integration) are used to check data compatibility and eliminate spurious instrumentation system biases, scale factors, and drop-outs. Here, unmeasured signals may be estimated from the available measured states.

The foundation of the AFDD/NASA approach is the high-quality extraction of a complete multi-input/multi-output (MIMO) frequency-response database. These responses fully characterize the linearized coupled characteristics of the system without a priori assumptions. Advanced multivariable spectral analysis using the Chirp-Z transform and composite optimal window techniques have been developed and exercised over many flight applications. These methods provide significant improvement in identification quality relative to standard fast Fourier transform (FFT) methods. The frequency-response database directly supports important flight-control system
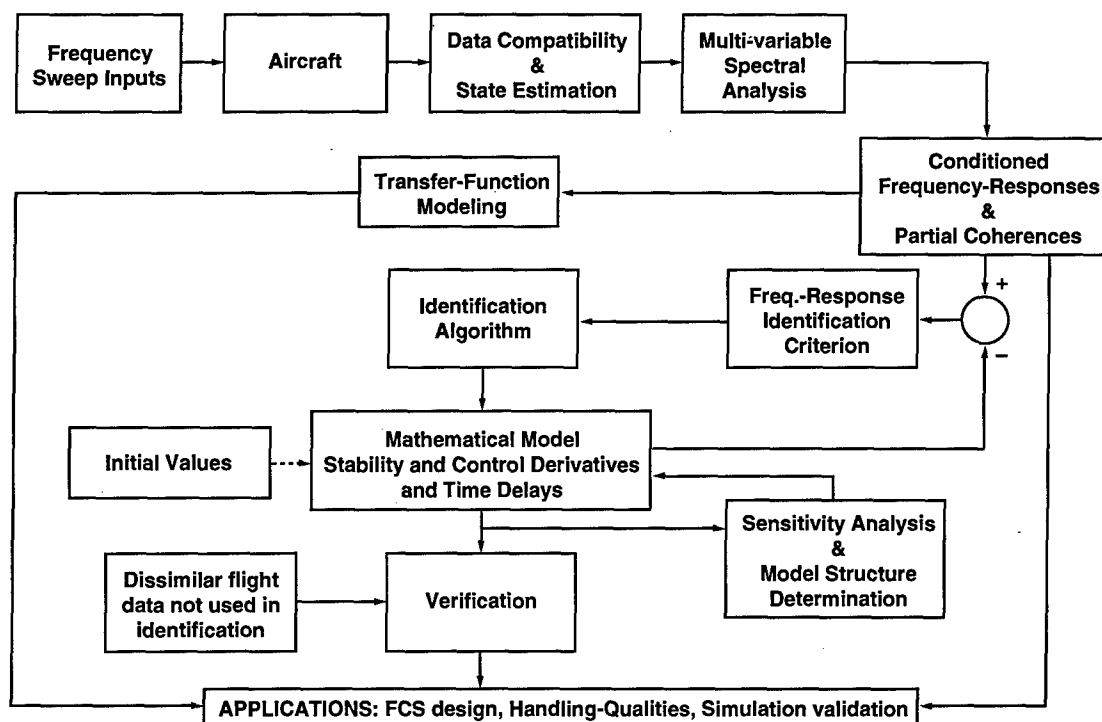

Figure 2. Frequency-domain system identification procedure.

applications including: handling-qualities analysis and specification compliance testing, simulation validation, and servo-loop stability analysis.

Transfer-function fitting is a rapid procedure for extracting simple single-input/single-output parametric models of specific frequency-responses pairs. These transfer-function models define the lower-order equivalent systems (LOES) of the fixed wing handling-qualities specifications (MIL-STD-1797) and directly support root-locus techniques for flight-control system design.

Accurate MIMO state-space models are often needed to support multivariable control-law design, simulation model validation and improvement, and validation of aerodynamic theory or wind tunnel results. Here, sophisticated nonlinear search algorithms are used to extract a general state-space model that matches the complete MIMO input/output frequency-response database. A significant advantage of identifying parametric models from frequency responses is the capability to individually define the appropriate frequency range for each response pair based on the associated coherence function—a valuable accuracy and linearity metric. The coherence function is also useful for automatically selecting error weighting in the cost function independent of the model structure. A methodical and integrated model structure determination procedure simplifies the model to a minimum set of reliable parameters that accurately characterizes the MIMO frequency-response database. Finally, the identified state-space model is validated by comparing predicted time responses with the actual flight responses for test inputs not used in the identification procedure.

The frequency-domain system-identification procedure is incorporated in a sophisticated interactive computational facility known as CIFER®–Comprehensive Identification from FrEquency Responses. Integrated data-basing and extensive user-oriented utilities are distinctive features of CIFER® for organizing and analyzing the large amounts of data which are generated for flight-test identification projects. A screen-driven interface is tied to the database for rapid user interaction. Previous program set-ups and analysis results are retrieved by simply referencing case names. Then, changes can be easily made by moving the cursor around on the user screens and modifying the default or previously saved program parameter values. The changes are then updated in the database with a single key stroke. Utilities are available for quick inspection, searching, plotting, or tabulated output of the contents of the database. Extensive analysis modules within CIFER® support: 1) rapid identification of transfer-function models; 2) signal spectral analysis; 3) handling qualities and classical servo-loop analysis; and 4) time and frequency-domain comparisons of identification and simulation model predictions with flight data. Aircraft applications of CIFER® have included the full life-cycle of flight-control system development depicted in figure 1. The Deutsche Forschungsanstalt für Luft- und Raumfahrt (DLR) Institute for Flight Mechanics (Braunschweig, Germany) has also developed and widely applied excellent methods for frequency-domain system identification. Applications to flight-mechanics and flight-control studies at the DLR include rotorcraft, transport aircraft, and high-performance aircraft (Kaletka and von Grunhagen 1989, Kaletka and Fu 1993).

4. DESIGN SPECIFICATIONS AND SPECIFICATION ACCEPTANCE TESTING

Formulating design specifications is the starting point for flight-control system development, while validating the achievement of these design goals is the concluding step in the process (fig. 1). Dynamic models of expected system behavior are determined in the design process using system identification and are tracked and updated throughout the aircraft development and flight testing. This documentation provides an important "paper trail" that minimizes flight-control development time and reduces the need for costly flight-test tuning. This section presents system-identification methods for defining and verifying design specifications. Flight test examples illustrate the analysis of handling qualities and servo-loop stability characteristics.

Early handling-qualities specifications for fixed-wing aircraft (MIL-F-8785A, Anon. 1954), and for rotary-wing aircraft (MIL-H-8501A, Anon. 1961) were based on simple dynamic modeling concepts and time-domain metrics. These specifications were suitable to aircraft in which stability augmentation systems (SAS) did not significantly alter the character of the (classical) bare-airframe flight-mechanics responses. Compliance testing techniques depended on standard step and doublet inputs long used in the flight-test community, with little requirement for sophisticated post-flight-data processing.

Modern fly-by-wire aircraft employ high-bandwidth digital flight-control systems to achieve greatly increased agility and disturbance rejection across a significantly widened operational flight envelope as compared with the older generation of aircraft. The flight control includes complex feedback and feedforward shaping and advanced control moment devices that profoundly alter the bare-airframe characteristics and invalidate the classical stability and control modeling concepts and testing methods. For example, modern combat aircraft achieve independent pitch pointing and flightpath control with direct lift devices and vectored thrust, rather than the coupled attitude-path response to elevator for conventional aircraft. This capability greatly enhances weapon pointing and air-to-air combat maneuvering. Another common feature of advanced aircraft is side-stick controllers which reduce weight, space, and cockpit complexity compared to standard center-sticks. Classical static stick-stability testing is an invalid method for determining speed stability since the side-sticks possess automatic trimming at neutral stick position and feedback loops provide the required stability independent of the trim gradient.

A new concern that arises for modern fly-by-wire aircraft is the potential for the accumulation of effective time delays due to digital flight-control computations, flight-control system filters, and fly-by-wire actuators. Actuator rate-limiting can also contribute large equivalent time delays in modern aircraft (Buchholz et al. 1995). Excessive delays have been repeatedly cited as a key cause for handling-quality problems and stability-loop margin degradation in modern aircraft, yet equivalent time delay can not be reliably measured using the standard testing

techniques. Clearly the dynamics modeling concepts, specifications, and testing techniques must be appropriate to the unique characteristics of modern highly-augmented aircraft.

System identification provides an accurate, rapid, and reliable approach for defining design specifications and for validating aircraft flight performance for highly-augmented flight-control systems. The modern U.S. fixed-wing specification (MIL-STD-1797; Anon. 1987) and rotorcraft specification (ADS-33C; Anon. 1989) are based on extensive frequency-domain system-identification analyses of flight-test and simulation responses. Numerous examples from these and comparable European handling-qualities specifications are presented in the aircraft control volume (Anon. 1994) and in the references of this paper. Two common handling-quality specifications are the bandwidth/phase-delay criteria and the LOES criteria. The former is checked directly from frequency-response identification, and the latter is checked from a transfer function fit of the frequency-response result. An illustration of flight-test and handling-qualities analyses based on these specifications is now presented.

The Advanced Digital Optical Control System (ADOCS) demonstrator (fig. 3), developed by Boeing's Helicopters Division under contract to the U.S. Army, was a UH-60A helicopter highly modified with redundant processors, instrumentation, and side-stick controllers (Glusman et al. 1987). The overall program objective of the ADOCS was to provide the technology base for the engineering development of an advanced battlefield-compatible flight-control system that: 1) enhanced aircraft mission capability; 2) improved handling qualities; and 3) decreased pilot workload. System identification flight tests and analyses using CIFER® were conducted to document the response characteristics and to compare handling-qualities characteristics with the (proposed at that time) ADS-33 design specifications (Hoh et al. 1988). Aircraft excitation was achieved via piloted frequency sweeps using the side-stick controller as shown in figure 4. Real-time telemetry of pilot inputs and aircraft responses ensured that pre-established aircraft flight limits were not exceeded.
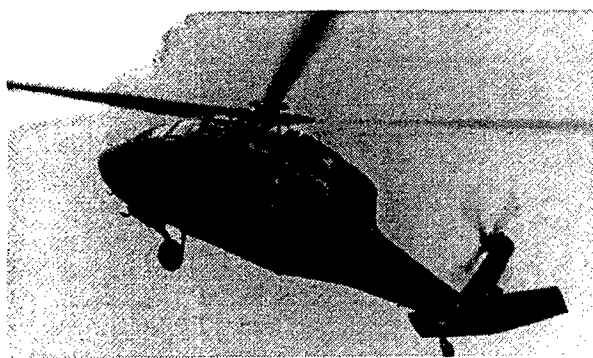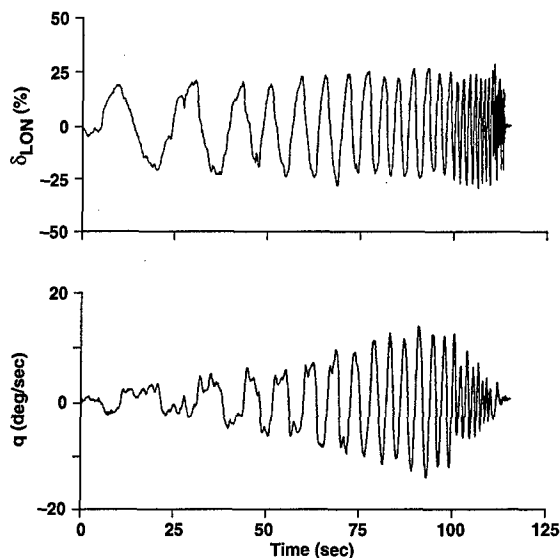

Figure 4. Longitudinal side-stick frequency-sweep in hover; (a) pitch input, (b) pitch rate.

The ADOCS frequency response for pitch response due to longitudinal input is shown in figure 5, along with the determination of bandwidth and phase delay as required by the ADS-33 specification. The value of the coherence function (fig. 5) is consistently above 0.8 for the frequency range of 0.2–8 rad/sec indicating excellent identification. At higher frequencies, the coherence drops, which reflects the intentionally reduced piloted inputs. The pitch bandwidth and phase delay values obtained from the hover identification results are shown on the ADS-33 specification boundary in figure 6. Level I (satis-factory) handling qualities for moderate pilot-gain tasks such as the helicopter "bob-up" are predicted, which is consistent with the Cooper-Harper pilot rating displayed next to the data symbol. A good correlation of pilot rating and the predicted handling qualities result was also indicated in pitch for the 80 kt flight condition.

Figure 3. Advanced digital optical control system (ADOCS) demonstrator.

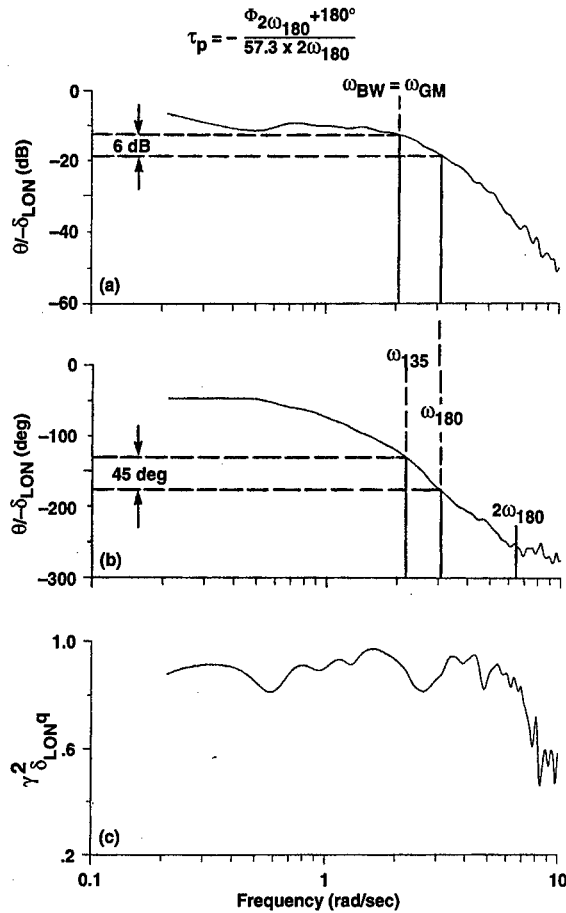$$\tau_p = -\frac{\Phi_{2\omega_{180}} + 180°}{57.3 \times 2\omega_{180}}$$

Figure 5. Identification of ADOCS pitch-rate response in hover.

Transfer-function (LOES) models of the key on-axes responses were generated from single-input/single-output fits of the identified ADOCS frequency responses. The LOES pitch response in hover is:

$$\frac{\theta}{\delta_{LON}} = \frac{-0.876(s + 0.229)e^{-0.238s}}{s[0.539, 1.82]} \tag{1}$$

The response is dominated by a well-damped second-order mode with a frequency of 1.8 rad/sec. The LOES handling-qualities specification boundaries of figure 7 have been established based on system-identification analyses of an extensive flight-test and simulation data base (Hoh and Ashkenas 1979). The ADOCS characteristics are seen to lie well within the Level I region. A second important characteristic of
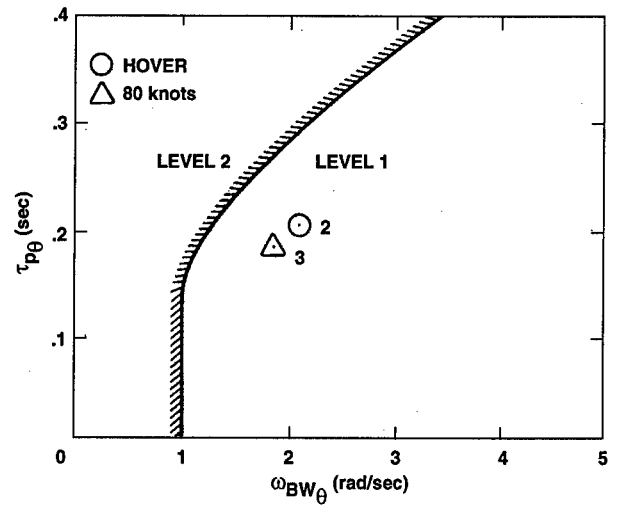
Figure 6. Handling-qualities correlation of ADOCS small amplitude pitch response in hover and 80 kt; average pilot ratings are shown next to the data.
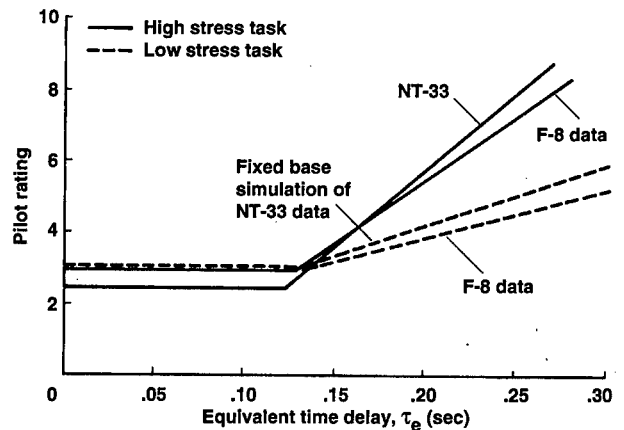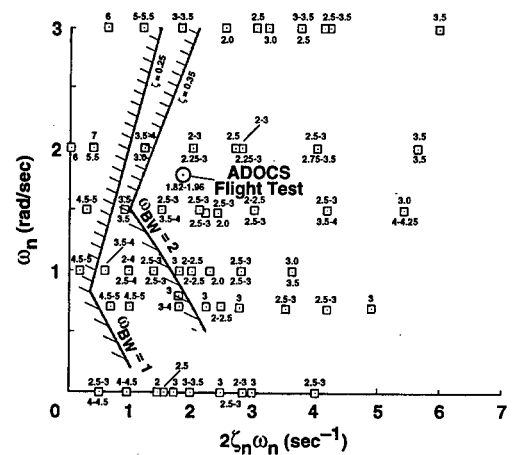
Figure 7. Correlation of ADOCS LOES pitch response with handling-qualities data.

the LOES pitch response is the relatively large equivalent time delay, $\tau = 238$ msec. Handling-qualities experience indicates that the equivalent time delay should not greatly exceed $\tau = 120$ msec, thereby suggesting ADOCS handling-qualities degradation for "high-gain" tasks. Comparable levels of equivalent time delay in the roll axis were considered to be a key contributor to pilot-induced oscillations (PIO) for "high-gain" piloting tasks such as slope landing (Tischler et al. 1991). Additional examples of handling-qualities analyses using lower-order equivalent-system modeling are presented in the 1994 volume (Anon. 1994).

The stability characteristics of aircraft rigid-body and structural dynamics may be greatly affected by the feedback loops of the flight-control system. Feedback may degrade the flutter margin stability at the same time it improves the rigid-body stability and handling qualities. Military specification 9490D (Anon. 1975) defines minimum levels of control system gain and phase margin as determined from a broken servo-loop frequency-response analysis. The specifications are given as a function of frequency range, with larger gain margins required for the structural elastic modes (table 1). Figure 8 shows the broken servo-loop frequency response of a large single-rotor helicopter as obtained by computer-generated frequency-sweep flight-test procedures. The rigid-body response crossover frequency is 2.0 rad/sec with an associated phase margin of 28 deg. This margin is slightly below the recommended specification value. The gain margin is checked at each crossing of the 180 deg ($\pm n360$) phase line as shown in the figure. The critical margin is the minimum value (GM_5), which is 15 dB at a frequency of 23.5 rad/sec. This frequency corresponds to the first vertical bending mode for the tail boom of this aircraft. Reference to table 1 indicates this gain margin to be well within accepted design specifications. The coherence function of figure 8 shows excellent identification accuracy for this flight test across the broad frequency range of interest (1–30 rad/sec). Sharp drops ("holes") or peaks in the coherence function reflect structural anti-nodes and nodes respectively. Examples of fixed-wing programs using frequency-domain system identification for elastic mode stability-margin evaluation include the X-29 (Clarke et al. 1994) and EAP (Caldwell 1994) aircraft.
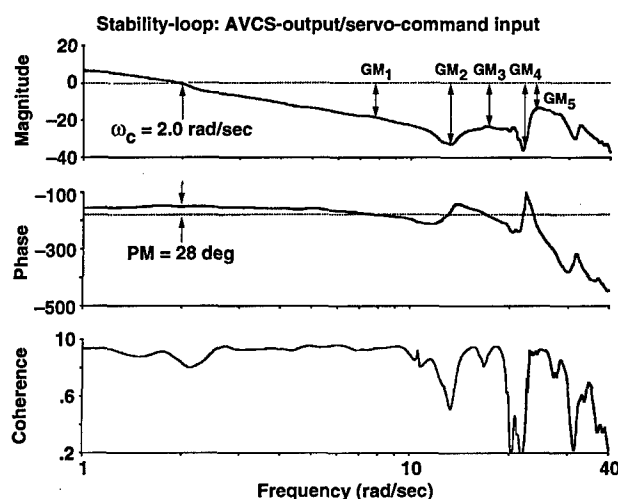

Figure 8. Rotorcraft servo-elastic stability margin testing.

5. DESIGN

The design process establishes control system loop architecture and associated control-law parameters that achieve desired handling-qualities and servo-loop stability specifications. During the conceptual design phase, system-identification procedures are applied to simple linear-design models to establish a baseline description of the proposed control system approaches and an initial check of specification compliance. At the detailed design stage, system-identification methods can extract highly-accurate linear-control system design models from complex simulation models or wind-tunnel data. These applications of system identification in the design process are illustrated in this section.

Conceptual control-system design studies are commonly based on simple stability and control derivative descriptions and transfer function of the airframe dynamics as obtained from first-principles aerodynamic theory. Control-law architectures are conceived and the initial system is modeled in a computer-aided design (CAD) environment such as MATLAB® (1992). System identification provides LOES models which are very useful in characterizing the end-to-end system dynamics and delays, and for an initial check against the design specifications. Flight-control system design parameters are then adjusted until the identified LOES characteristics satisfy the design requirements. In the F-15 S/MTD demonstrator project, a numerical optimization design tool was developed to automatically adjust control-law parameters to meet LOES specifications (Moorhouse and Citurs 1994).

Detailed flight-control design efforts are based on very complex high-order and nonlinear-simulation models. Force and moment descriptions are developed for each of the aircraft elements such as the wings, propulsion system, and flight-control systems based on wind tunnel look-up tables, component bench-test data, and analytical theory. The simulation of multiple rigid-body systems, or flexible bodies involves sets of dynamic equations of motion linked by constraint conditions. In many simulations these sets of equations are numerically integrated in serial form

Table 1. MIL-F-9490D gain and phase margin requirements (dB, deg) from Caldwell (1994)

Airspeed Mode Freq. Hz	Below $V_{o\ min}$	$V_{o\ min}$ to $V_{o\ max}$	At Limit Speed V_L	At $1.15 * V_L$
$f_M < 0.06$	GM = 6dB No Phase Reqt. below $V_{o\ min}$	GM = ± 4.5 PM = ± 30	GM = ± 3.0 PM = ± 20	GM = 0.0 PM = 0.0 Stable at Nominal Phase and Gain
$0.06 \le f_M < 1st ASE$		GM = ± 6.0 PM = ± 45	GM = ± 4.5 PM = ± 30	
$1st ASE < f_M$		GM = ± 8.0 PM = ± 60	GM = ± 6.0 PM = ± 45	

to reduce the complexity of deriving a fully-coupled multibody simulation. The distributed or serial nature of these complex simulations thus may preclude the extraction of an integrated high-order linear model of the fully-coupled system as is needed for accurate control-design studies.

Even when the simulation architecture allows for the direct extraction of higher-order linear models using classical numerical perturbation methods, the assumption of independent perturbations results in incorrect phasing of the state variables within the multidimensional look-up tables. For example, the look-up table for aerodynamic pitching moment may depend both on angle of attack and pitch rate, so $C_{m_q} = f(\alpha)$. Thus, the correct determination of phugoid dynamics depends on maintaining representative phasing of q and α within the linearization process. Selection of perturbation size can also strongly influence the linearization results. These effects can significantly degrade the predictive accuracy of the extracted linear model. Much more accurate linear models are obtained by simulating piloted frequency-sweep inputs and extracting state-space models using system identification just as if from flight-test data.

Engelland extracted accurate stability and control derivative models of a conceptual A/STOVL aircraft from a complex nonlinear off-line simulation (Engelland et al. 1990) to support control-system design studies. The excitation input consisted of computer-generated frequency sweeps and white noise. In a procedure described by Ballin and Dalang-Secretan (1991), artificial feedback control loops were included to keep the aircraft flight condition near the reference trim point during the inputs. Starting from the perturbation derivative results CIFER® was used to identify a more accurate 6 DOF bare-airframe model. The perturbation and CIFER® derivatives are compared in table 2. Longitudinal-frequency responses of the two linear models are compared with the complete simulation responses in figure 9 for a flight condition of 120 knots. The linear model obtained using system identification is seen to be much more accurate than the numerical perturbation model for the high-frequency (3.0–20 rad/sec) pitch-rate response q/δ_θ, and for the low-frequency (0.1–1.0 rad/sec) longitudinal-acceleration response a_x/δ_θ. The models are essentially identical in the mid-frequency range. A time domain comparison of the two-linear models with the nonlinear-simulation response is shown in figure 10 for a small (1 deg) pitch-doublet input. The system-identification model is seen to track the non-linear behavior much more closely than the numerical perturbation model. The improvements are most noticeable for the long-term response (low-frequency) behavior, which is consistent with the frequency-response comparison of figure 9.

Table 2. Comparison of ASTOVL perturbation derivatives and CIFER® results

| Derivative	Perturb. Value	CIFER Value	C.R. (%)	Insens. (%)
X_u	−0.03471	−0.03602	−5.662	2.289
X_w	0.03958	0.02852	6.910	2.840
$X_{\dot{w}}$	6.764E-04	6.764E-04†	—	—
X_q	0.2451	0.2451†	—	—
X_{PCD}	−7.690E-03	−8.303E-03	−7.504	3.584
X_{PLA}	0.02270	0.02229	3.731	1.835
X_{Θ_N}	−0.5150	−0.5586	−2.353	1.005
Z_u	−0.04596	−0.03312	−13.62	4.579
Z_w	−0.3704	−0.2817	−4.386	1.377
$Z_{\dot{w}}$	−0.01023	−0.01023†	—	—
Z_q	−3.754	−3.754†	—	—
Z_{PCD}	0.1389	0.1551	5.571	2.698
Z_{PLA}	−0.3800	−0.3305	−2.254	1.016
Z_{Θ_N}	−0.01724	−0.03055	−4.646	2.242
M_u	1.661E-04	−1.059E-03	−6.016	1.745
M_w	1.222E-03	3.715E-03	5.263	1.283
$M_{\dot{w}}$	−1.286E-03	−1.286E-03†	—	—
M_q	−0.4971	−0.6852	−5.561	1.873
M_{PCD}	0.02494	0.02818	2.517	0.9822
M_{PLA}	4.993E-04	4.993E-04 †	—	—
M_{Θ_N}	2.502E-04	4.953E-04	10.16	4.257

† Perturbation value used.
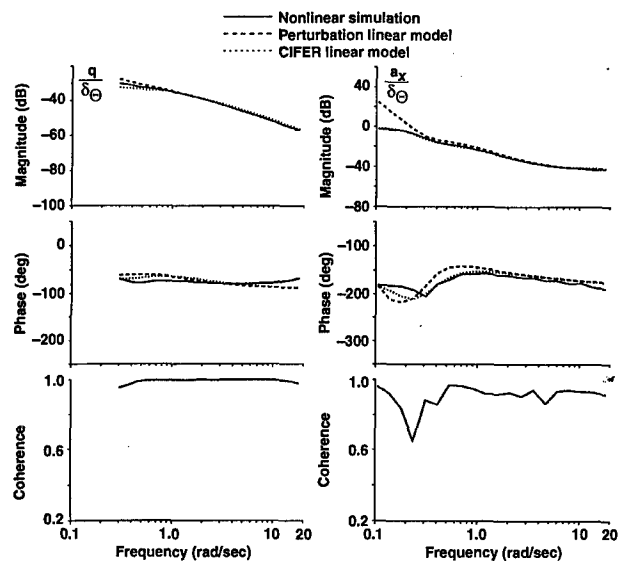
Figure 9. Frequency-response comparison of perturbation and identification models with nonlinear ASTOVL simulation.

These results show that system identification provides an A/STOVL linear model that will be much more accurate than models extracted using numerical perturbation methods. The improvement obtained by "flying" the frequency-sweep input is especially apparent at low frequencies where the dynamic responses are larger, and correct phasing of the representative motion variables for entry into the multidimensional look-up tables is important. A cursory time-domain comparison of the

numerical perturbation results with the nonlinear-simulation response would suggest the presence of strong nonlinearities in the A/STOVL aircraft dynamics. However, the very close agreement of the system-identification model with the nonlinear simulation shows that the method of linear model extraction is much more important in this case than the nonlinear characteristics of the simulation.
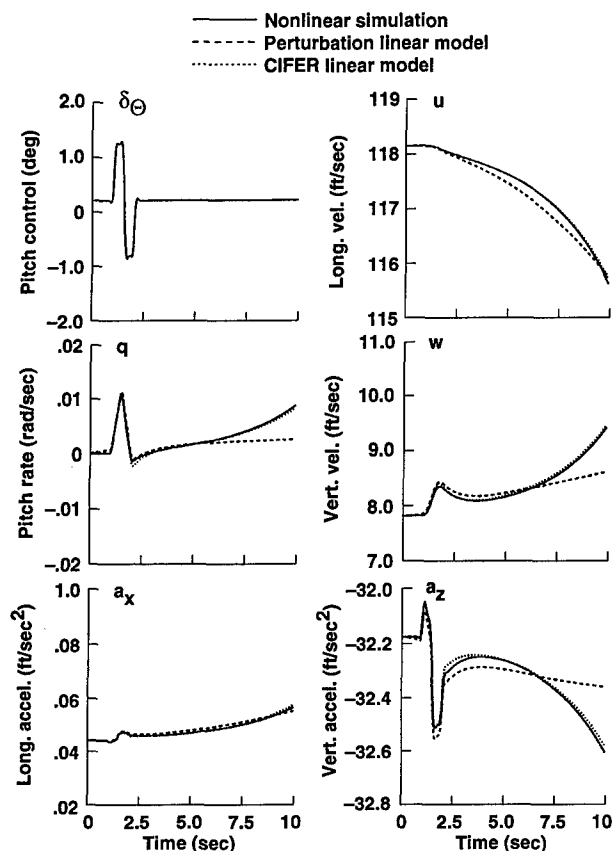

Figure 10. Time-domain comparison of perturbation and identification models with nonlinear simulation of ASTOVL aircraft.

Success in achieving maximum control-system performance and robustness in flight depends heavily on the predictive accuracy of the linear-design models. The system identification approach provides highly-accurate design models for design at specific flight conditions, but it is clearly more time intensive than the simple numerical perturbation method. This is not a practical approach for checking control system behavior at the tens or hundreds of off-nominal conditions.

6. SIMULATION

The detailed implementation of the control-system design is evaluated in comprehensive real-time piloted simulation trials. System-identification techniques are exercised to validate the real-time math model implementation of nonlinear digital control laws. Also, these techniques are used to document simulator motion and visual systems. Once flight-test data are available, system identification provides an important tool for validating and updating the simulation math models. This

section illustrates system-identification techniques for validating simulation math models and simulator validation using XV-15 tilt-rotor (airplane mode) and UH-60A helicopter results. A companion frequency-domain format is proposed for specifying simulation model fidelity for the on-axis responses. Finally, an analysis based on an A/STOVL piloted simulation study illustrates the use of system identification for determining actuator authority requirements.

Direct frequency-response comparison of the end-to-end performance of the complex simulation model with the conceptual design models and specifications constitutes an important "dynamic check" which often exposes unexpected processing delays such as in the numerical integration procedures, or errors in the digital (Z-plane) implementation of control laws. This technique is also useful in exposing degradation in control system performance due to high-order structural or other hardware dynamics modeled in the advanced design simulation model that may not have been taken into account in the conceptual studies.

Simulator visual and motion systems should track the math-model response as accurately as possible to ensure that the pilot's cueing environment is correct and that the handling-qualities evaluation obtained in the simulator reflect what may be expected in flight. Nonlinear compensation algorithms have been developed by McFarland (1988) that offset visual system delays, thereby minimizing the mismatch between the simulator visual system response and the math model. In work reported by Atencio (1993) and illustrated in figure 11, there is nearly perfect agreement of the DIG-1 visual system image (with McFarland compensation) and the UH-60A helicopter simulation math model. Math-model commands to the simulator motion drive are attenuated using wash-out logic. The wash-out parameters are selected to preserve the dynamic behavior in the frequency range of most concern to the pilot (e.g., 1–10 rad/sec for pitch and roll tasks), while accommodating the restricted motion environment of the simulator. Figure 12 from Atencio (1993) compares the (washed-out) cab roll-motion to stick input with the math-model response for the UH-60A simulation in the Ames Vertical Motion Simulator (VMS). In the 1–10 rad/sec frequency range, the simulator motion drive response follows the math model, although the motion is less than one-to-one as seen by the vertical shift in the magnitude curves. The motion drive wash-out logic is designed to minimize phase distortions in this frequency range as can be seen in the figure. At low frequencies the large motion is washed-out, and considerable errors are encountered in the magnitude and phase response as expected. At high frequency, the motion drive is unable to follow rapid commands to the aircraft model, resulting in larger phase lags of the motion follow-up as seen in the figure.
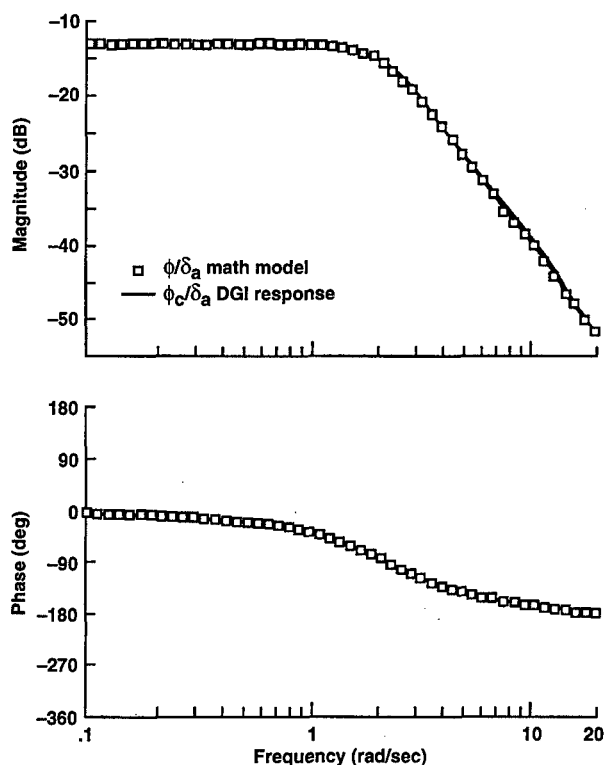
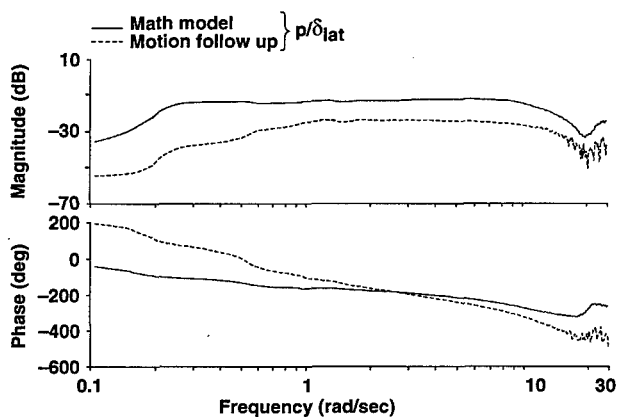Figure 11. Validation of DIG-1 visual-system response.

Figure 12. Documentation of VMS motion follow-up for UH-60A roll response in hover.

Once flight-test data are available, system-identification tools are exercised to validate and update the simulation math models. The direct comparison of frequency-response behavior provides a clear picture of model fidelity as a function of frequency. This is critical for validating piloted simulations since the requirements on pilot cueing accuracy are also frequency dependent. The separate display of the magnitude and phase responses allows the sources of simulation discrepancies to be more easily determined. For example, an excessive time delay (τ) in the simulation math model or hardware causes a linear phase shift with frequency ($\phi = -\tau\omega$). Scaling errors in the simulation model appear as a clear vertical shift (in dB) in the magnitude curve. These effects are all combined in the time-domain and therefore are not easily discernible in the traditional

time-response comparison methods for validation. Further, the procedure of overlaying time histories is often not very accurate since the flight responses rarely begin in a trim quiescent condition.

Tischler (1987) conducted an extensive flight-test program and simulation math-model validation study on the XV-15 tilt-rotor aircraft shown in figure 13. This tilt-rotor math model is based on comprehensive look-up tables of full-scale wind-tunnel test data, and detailed theoretical models of the rotor-system behavior and rotor-on-airframe aerodynamic interference effects. Figure 14 compares the flight and simulation roll responses for a flight condition of 170 kts. Excellent dynamic response fidelity is seen in the close match of the simulation prediction and the measured flight response. Figure 15 replots these results in terms of magnitude and phase errors as a function of frequency. Here 0 dB magnitude and 0 deg phase indicate perfect tracking of the flight and simulation results. Also shown in the figure are math model mismatch boundaries proposed herein for the highest fidelity training simulations (FAA Level D). These boundaries correspond to the LOES mismatch criteria from the fixed-wing handling-qualities criteria (Hoh et al. 1982). The XV-15 simulation math model complies with the proposed Level D (high-fidelity) criteria. This result is consistent with the very favorable pilot comparison of simulator and flight behavior (Churchill and Dugan 1982). The same approach of mismatch boundaries in the frequency-domain has also been independently proposed and applied by DLR researchers to detect the effects of unnoticeable dynamics in the case of helicopters (Hamel and Jategaonkar 1995), and for evaluating the fidelity of in-flight simulation (Buchholz et al. 1995).
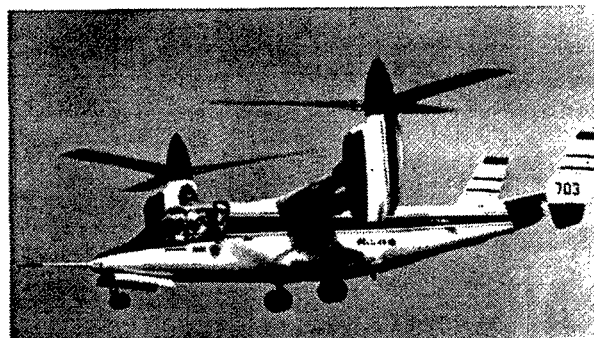
(a)
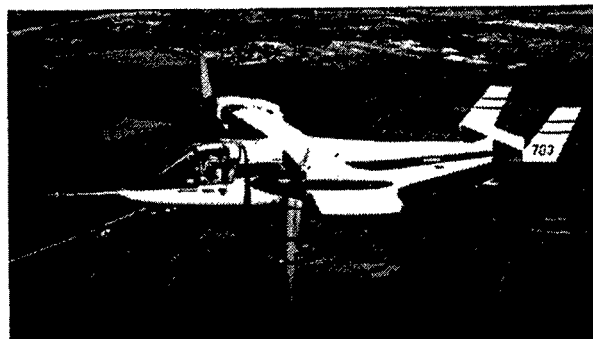
(b)

Figure 13. XV-15 tilt-rotor aircraft; (a) hover configuration, (b) cruise configuration.
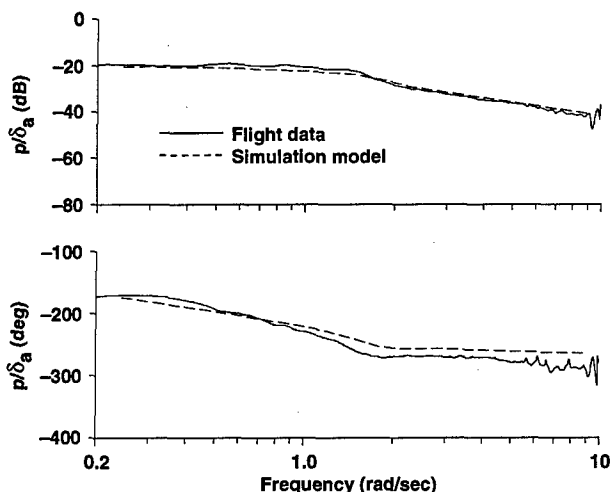
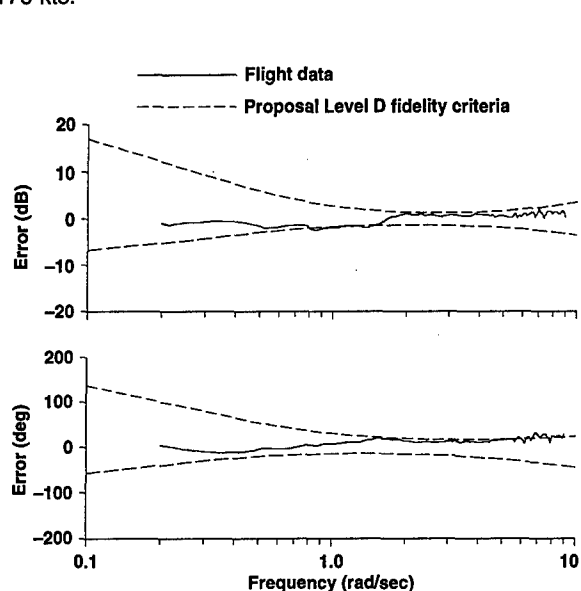Figure 14. XV-15 tilt-rotor simulation model validation for 170 kts.

Figure 15. Tilt-rotor math model error functions and proposed fidelity criteria for Level D simulators.

Direct comparisons of stability and control derivatives identified from flight tests with values identified from simulation math models can be used to derive correction factors for significantly improving the model fidelity. For example,

$$L_{corrected} = f(nonlin.sim.eqns)$$

$$+ [(L_p)_{flight} - (L_p)_{sim}]\,p$$

$$+ [(L_{\delta_{lat}})_{flight} - (L_{\delta_{lat}})_{sim}]\,\delta_{lat} + ...$$

$$(2)$$

Identification tools provide a systematic and accurate approach to determine these correction factors which are routinely used by the simulator industry to improve dynamic fidelity.

Comprehensive simulation studies are often used to define flight-control system hardware requirements such as actuator and sensor filter bandwidths. Franklin et al. (1991) used

CIFER® to determine actuator bandwidth requirements for a conceptual A/STOVL aircraft. The spectral characteristics of the stabilization and command augmentation system (SCAS) commands to the aircraft control surfaces were obtained for ensemble analyses of simulated flight tasks, and are shown in figure 16. The results indicate a SCAS command signal bandwidth (frequency at −3dB amplitude) of about 4 rad/sec in pitch and roll, with a significantly lower command bandwidth for the thrust (vertical) axis. Actuator hardware response bandwidths should be 5–10 times the respective SCAS command bandwidths to avoid introducing significant phase lag in the control loops (Franklin et al. 1991). Similar analysis techniques were used by Blanken to determine the effect of control-system design on changes in pilot control bandwidth (workload) and handling qualities. This study included an interesting comparison of pilot workload for the simulation and flight-test environments (Blanken and Pausder 1994).
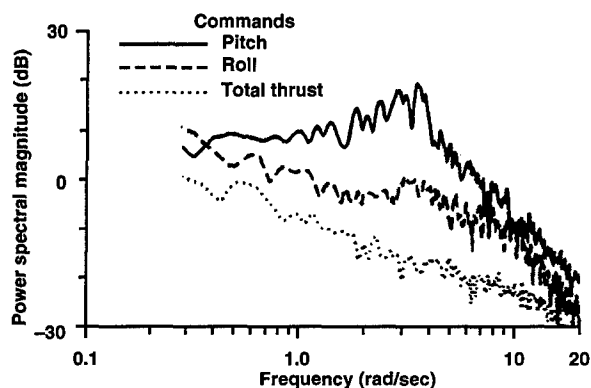

Figure 16. Power spectra of ASTOVL propulsion system commands.

7. DEVELOPMENT

At the development stage, flight-control system hardware and software components and subsystems undergo bench testing to verify that the performance characteristics meet the design specifications. Sophisticated flight-control development facilities (DF) or "hot-benches" allow the test of prototype flight software and hardware integrated with the simulated aircraft dynamics. In helicopter development, model or full-scale rotors are dynamically tested in the wind tunnel and the responses are validated against design requirements and comprehensive analysis models. This section presents system-identification techniques to support development stage validation. Examples are drawn from the NASA VSRA project, helicopter actuator tests, and the Sikorsky Bearingless Main Rotor (SBMR) full-scale rotor wind-tunnel tests.

Figure 17. NASA V/STOL system research aircraft (VSRA).

An extensive development facility has been used in the NASA vertical/short takeoff and landing (V/STOL) systems research aircraft (VSRA) project, which equipped a YAV-8B Harrier aircraft with a fly-by-wire research flight-control system (Foster et al. 1987) (fig. 17). The overall flight-control goals of the VSRA program are to assess critical technology elements for advanced short takeoff/vertical landing (STOVL) aircraft, including: integrated flight/propulsion control, advanced control and display laws, and reaction-controlled bleed-flow requirements. The role of the DF has been for verification of control-law flight software, system software, and safety monitoring. Actual flight computers and flight hardware were included in the DF to validate flight systems during the final development stage. The aircraft dynamics are simulated by the VSRA math model, with inputs from a test console or a rudimentary pilot-cockpit station. CIFER® was exercised extensively to validate broken-loop and end-to-end closed-loop frequency responses of the DF flight systems against the design models and theoretical analyses. Signal processing and conditioning algorithms and digital timing were also verified during DF testing.

Actuator system dynamics comprise an important component of the overall high-frequency phase lag in modern flight-control systems. Therefore, flight-control system stability margins and overall closed-loop performance and handling qualities can be significantly degraded if the actuator dynamics do not meet the design specifications. System-identification bench testing of aircraft actuators ensures that expected performance is achieved and that costly modifications can be avoided at the flight-test stage. Frequency-response identification and transfer-function modeling from a typical helicopter actuator test are shown in figure 18. Excellent coherence is achieved over a broad frequency range (0.2–40 rad/sec) using a computer-generated frequency-sweep excitation. The actuator dynamics are well characterized by the damped second-order response obtained by CIFER® (fig. 18). These component system results are used to update simulation math models and to optimize flight-control system gains prior to first flight.
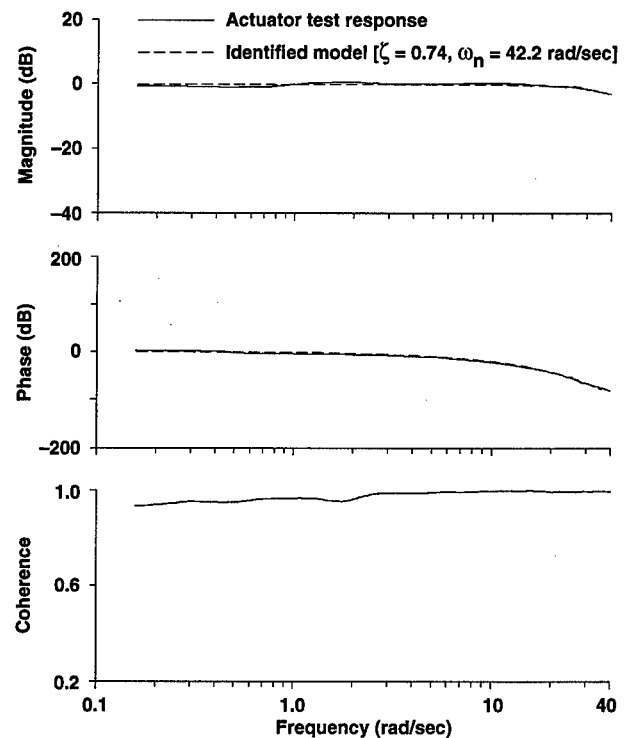

Figure 18. Helicopter actuator response identification and modeling.

Structural analysis programs such as NASA structural analysis (NASTRAN) are rarely able to accurately predict the flexible response beyond the first elastic modes of a new aircraft. Therefore, structurally-scaled models or full-scale structural test vehicles are evaluated in special rigs to verify the elastic characteristics and make final adjustments to the structural compensation (e.g., notch filters) in the control system prior to first flight. Automated test/analysis facilities excite the individual structural modes of the aircraft with shakers and then use system-identification methods to determine model characteristics. For modern rotorcraft development, system identification has also been effective in extracting dynamic response model of subscaled or full-scale rotor systems from dynamic wind-tunnel test data. The control response dynamics of the SBMR were determined in a joint NASA/Sikorsky test in the Ames 40- by 80-Foot Subsonic Wind Tunnel (fig. 19) (Tischler et al. 1994). Computer-generated frequency-sweep excitation signals to the SBMR swashplate actuator were carefully designed to ensure adequate identification within the limitations of the rotor and wind-tunnel stand. Rotor blade and hub moment frequency responses were then extracted using CIFER® and were compared to comprehensive simulation models of the SBMR. CIFER® was also used to extract the rotor's physical parameters based on a linearized 14 DOF analytical formulation of the SBMR dynamics (Tischler et al. 1994).

Figure 20 shows the identified on-axis roll moment response to a lateral stick input. The simulation math model and 14 DOF identified model agree closely with measured responses. The off-axis pitching moment to lateral stick input is shown in figure 21. Here, the simulation model phase response deviates

significantly from both the measured response and identified parametric model, indicating a poor prediction of rotor cross-coupling.

Figure 19. Sikorsky Bearingless Main Rotor (SBMR) test in NASA Ames 40- by 80-Foot Subsonic Wind Tunnel.
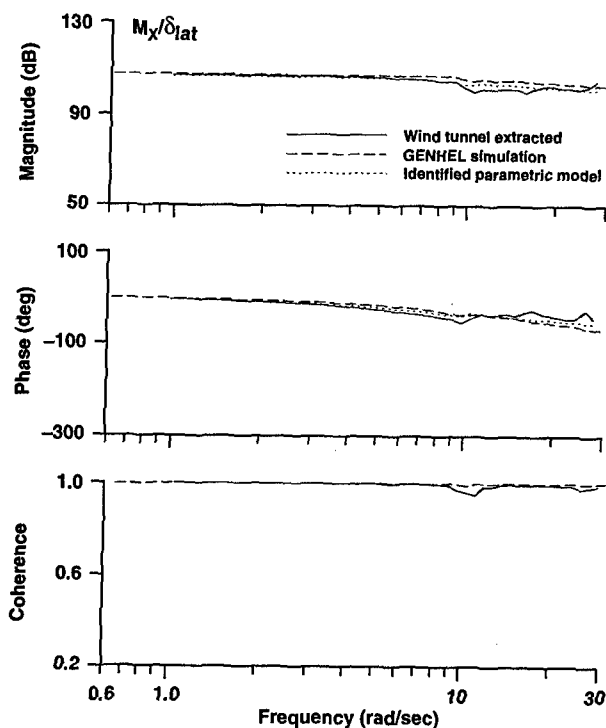

Figure 20. SBMR roll-moment response to lateral-stick input (40-kts flight condition).
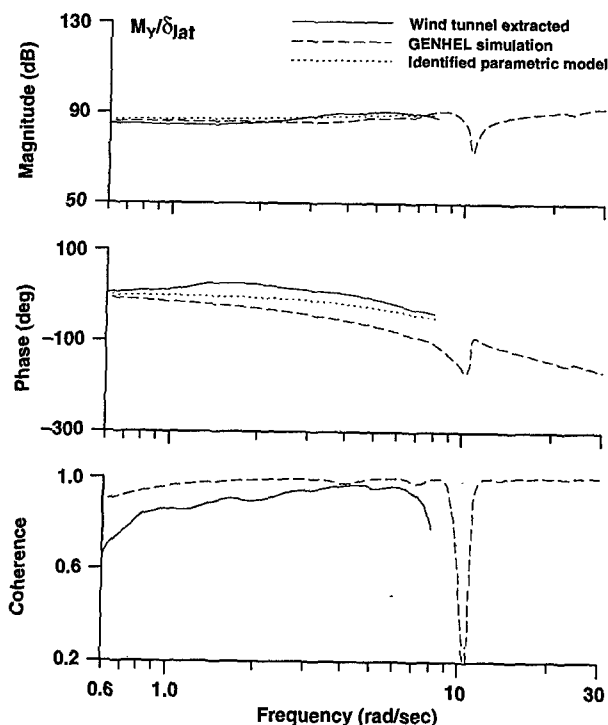

Figure 21. SBMR pitching-moment response to lateral-cyclic-stick input (40 kts).

The key identified physical parameters of the rotor system are compared with the GenHel simulation values in table 3 (both are updated from the earlier results of Tischler et al. 1994). Many of the important rotor parameters such as Lock number, blade inertia, and effective hinge off-set compare very favorably, and reflect the good on-axis response prediction of the simulation model. The important difference between the identified model and the GenHel simulation is the control-phase angle. This parameter has a known geometric value of -14 deg in the wind-tunnel tests, but the identified value needed to capture the measured off-axis response of figure 21 is -23.4 deg. This discrepancy in control phasing indicates a fundamental problem in the aerodynamic modeling of the rotor. Follow-on analysis of these results have yielded a new approach for correcting the simulation math model and improvements in the identification methods for free-flight results (Takahashi et al. 1995). Accurate cross-coupling prediction is especially important for the design of decoupling compensators in modern rotorcraft flight-control systems. Corrections to the flight-control laws prior to final flight software installation and vehicle testing reduces development flight-test costs and improves the final performance of the system.

Table 3. Comparison of SBMR identified parameters with GENHEL values

Rotor Parameter	Symbol	Units	GENHEL value	Identified value
Lock number[1]	γ	ND	7.46	7.82
Lift-curve slope	a	1/rad	5.73	5.33
Blade inertia[1]	I_b	slug-ft^2	552.81	489.8
Blade 1st mass moment[1]	S_b	slug-ft	38.76	48.78
Blade weight	$m_b g$	lbs	115	142.68
Flapping frequency	ν_β	per rev	1.081	1.080
Effective hinge-offset	e	ND	0.097	0.095
Lag frequency	ν_ζ	per rev	0.699	0.697
Lag damper	C_ζ	ft-lb-sec/rad	372	473.29
Collective-lag/shaft freq.	ν_{ζ_0}	per rev	—	0.474
Collective-lag/shaft damping	C_{ζ_0}	ft-lb-sec/rad	—	1631.49
Trim coning angle	β_T	rad	0.0768	0.0654
Pitch-flap coupling	K_{P_β}	rad/rad	0	0
Pitch-lag coupling	K_{P_ζ}	rad/rad	-0.0225	-0.184
Control phase angle	Δ_{SP}	deg	-14.0	-23.4

IMPORTANT NOTE:
[1]Mass moment parameters and Lock number are referenced to the hub center and not to the hinge-axis.

8. FLIGHT TESTING

The flight-test program for flight-control and handling-qualities validation and optimization has a significant impact on the overall development schedule and cost for modern fly-by-wire aircraft. System identification provides a critical technology for tracking aircraft dynamic response performance into flight, solving problems that arise in flight tests, and rapidly optimizing control system parameters. This section presents system-identification methods for control system flight testing. Flight data results are presented for the VSRA and UH-60A Rotorcraft Aircraft Systems Concept Airborne Laboratory (RASCAL) projects.

Flight test verification of aero-servo-elastic stability margins is an important concern for modern fly-by-wire aircraft, where dynamic coupling of the high-gain flight control system with light-weight structural dynamics can degrade flutter stability. Flutter margin verification using system identification has been adopted by British Aerospace in the development of a series of fly-by-wire high-performance aircraft, as described by Caldwell (1994). Near real-time system identification was employed during the X-29 aircraft flight testing (Clarke et al. 1994) for on-line verification of stability margins in a highly-efficient flight envelope expansion program. Piloted frequency sweeps were used to excite the vehicle structural modes at each test condition, and the telemetered data were then analyzed using high-speed array processing computers. Once the stability margins were verified, the pilot was cleared to proceed to the next flight condition, avoiding the normally time-consuming test technique of clearing one flutter test point per flight. In a similar application of near real-time identification techniques, CIFER® was used to support flight tests of the "Pathfinder," a large high-altitude solar Unmanned Air Vehicle (UAV) (Dornheim 1995). Servoloop stability margins were extracted based on telemetered data from computer-generated frequency-sweep tests, and then compared with simulation predictions. When the CIFER® results indicated a loss of stability margins at a high altitude flight condition, the ground station pilot executed real-time switching commands to adjust the Pathfinder control law gains.

Theoretical analyses of the XV-15 tilt-rotor aircraft (fig. 13) predicted that the reduction of whirl mode flutter stability margins with increasing flight speed would limit the aircraft's usable flight envelope. An extensive flight-test program was conducted to verify the expected margins. Early testing using the traditional dwell-delay method proved time-consuming and resulted in considerable data scatter. Acree and Tischler (1993) conducted automated frequency-sweep tests using wing flaperon excitation and subsequently analyzed the data using the CIFER® identification tools. The frequency-domain test technique proved to be much more time-efficient, and the results showed both a reduction in the scatter at specific conditions and an improvement in consistency across flight conditions.

Automated frequency-sweep flight testing was also conducted on the VSRA YAV-8B aircraft (Foster et al. 1987) (fig. 17) to determine the locations of the (open-loop) first and second structural wing-bending modes, and to verify actuator and sensor processing dynamics. The parametric model shown in figure 22 was obtained from CIFER®, and includes the rigid-body response and second-order representations of the two structural modes. Notch filters, included to avoid coupling of the flight-control and aeroelastic dynamics, and control-law gains were subsequently updated based on these identification results. Piloted frequency-sweep flight testing was also conducted in the VSRA program to document the final stability margins and closed-loop response for a number of flight conditions. The broken-loop pitch response for 120 knots as obtained from CIFER® is shown in figure 23. The figure shows that the dynamics are conditionally stable, with a minimum crossover frequency of 1 rad/sec required for closed-loop vehicle stability. The nominal crossover frequency of 4 rad/sec yields a phase margin of 40 deg (acceptable). A gain margin of about 8 dB is indicated over the broad frequency range 15–30 rad/sec were the phase curve has a nearly constant value of about–180 deg.

The identified closed-loop response dynamics are shown in figure 24. In the frequency range of 0.3–5 rad/sec the response is accurately modeled by a well-damped second-order system:

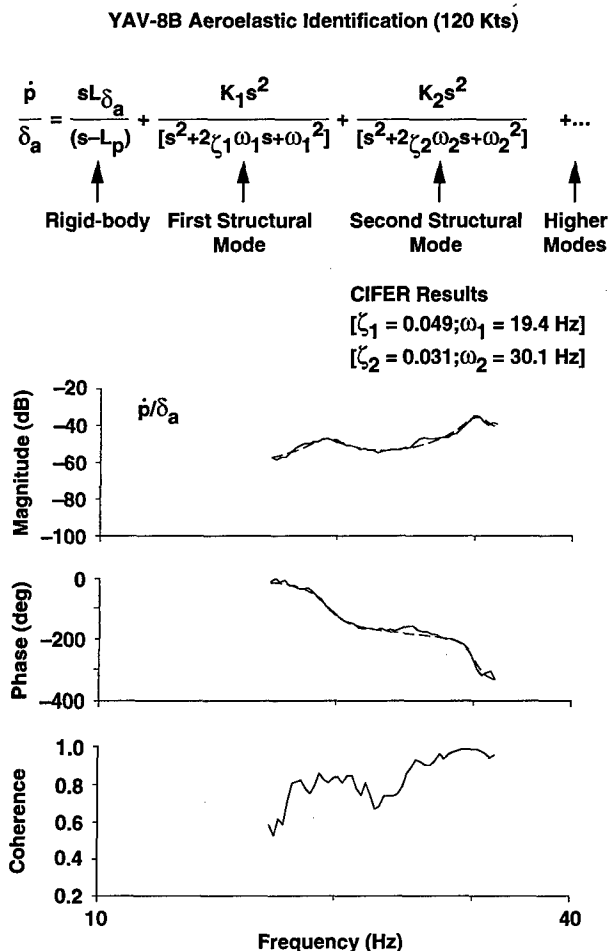$$\frac{\theta}{\theta_{com}} = \frac{6.35\,e^{-0.048s}}{[0.953, 2.47]} \tag{3}$$

YAV-8B Aeroelastic Identification (120 Kts)

$$\frac{\dot{p}}{\delta_a} = \frac{sL_{\delta_a}}{(s-L_p)} + \frac{K_1 s^2}{[s^2+2\zeta_1\omega_1 s+\omega_1^2]} + \frac{K_2 s^2}{[s^2+2\zeta_2\omega_2 s+\omega_2^2]} + \ldots$$

Rigid-body   First Structural   Second Structural   Higher
Mode   Mode   Modes

CIFER Results
$[\zeta_1 = 0.049; \omega_1 = 19.4 \text{ Hz}]$
$[\zeta_2 = 0.031; \omega_2 = 30.1 \text{ Hz}]$

Figure 22. YAV-8B aero-elastic wing-bending identification (120 kts).

Figure 23. VSRA broken-loop pitch response (120 kts).

These dynamics closely match the design response of:

$$\frac{\theta}{\theta_{com}} = \frac{4.0}{[1.0, 2.0]} \tag{4}$$

The small equivalent time delay of $\tau = 48$ msec reflects the VSRA high-bandwidth fly-by-wire actuators and rapid digital calculations, and suggests no time-delay related handling-qualities problems.

In some applications, simulation math models are not sufficiently accurate for control-law design prior to first flight. For example, the current state-of-the-art of rotorcraft flight dynamics simulation yields a fair prediction of the on-axis characteristics, but usually an inadequate prediction of the cross-coupling response as in the baseline simulation result of figure 21, often not even correct in sign (Curtiss 1992).
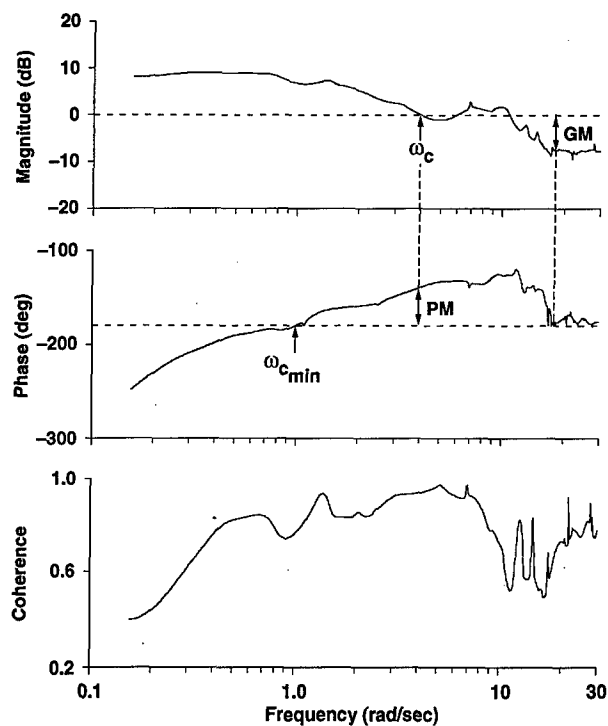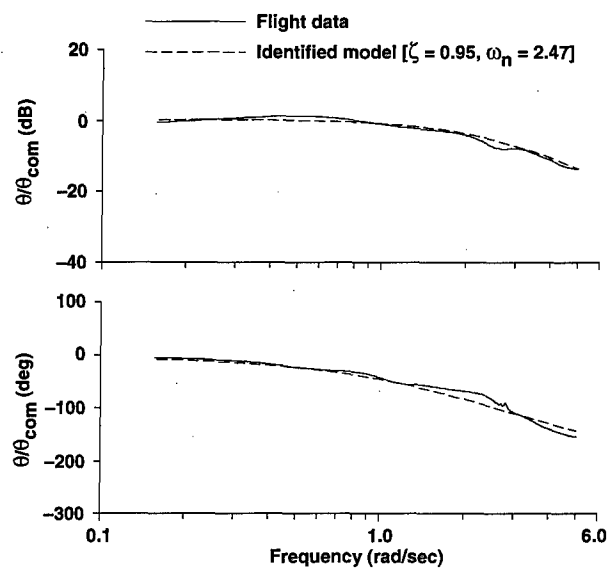
Figure 24. VSRA closed-loop pitch response (120 kts).

Rotorcraft math models are still useful for initial simulation and development efforts, but are less satisfactory for the final determination of stability margins and decoupling controller gains.

Initial flight tests with the SCAS-OFF or with reduced control system gains can be conducted to identify new aircraft dynamics or to update the simulation for final control-law parameter selection. The DLR developed a high-bandwidth flight-control system for the Bo-105 variable-stability aircraft (ATTHeS) based directly on bare-airframe state-space models extracted

from flight data using frequency-domain system identification (von Grunhagen et al. 1994). This direct use of flight-identified state-space models for control-law design represents the most sophisticated and demanding application of system-identification tools.

An approach similar to that of the DLR has been adopted by the AFDD/NASA in the development of an advanced fly-by-wire flight-control system for the RASCAL UH-60A helicopter (Takahashi et al. 1995), which uses the same airframe as the ADOCS demonstrator (fig. 3). Extensive theoretical studies of combat rotorcraft control-law concepts for application to RASCAL have been conducted by Takahaski (1994) and Cheng et al. (1995) based on UH-60A simulation math models. At the same time, Fletcher (1995) has conducted UH-60A flight tests and comprehensive frequency-domain identification studies to extract high-order state-space models of the aircraft for hover and cruise flight conditions. These efforts were brought together in the RASCAL control-law study described in Takahashi et al. (1995). Figures 25 and 26 compare two flight-mechanics-simulation math models ("A" and "B") used for the control-law designs with the bare-airframe flight-test data. The on-axis roll response agreement between the math models and the flight-test data is reasonable at mid-frequency (0.8–10 rad/sec), but is inadequate beyond 10 rad/sec due to errors in the prediction of the in-plane rotor response. Large errors are also seen at low frequency. The simulation models show poor predictive capability for the cross-coupling response of roll rate to longitudinal stick input, with large phase errors in the critical frequency range of 1–10 rad/sec (fig. 26). While the simulation models were sufficient for the preliminary flight-control and simulation studies, they are clearly inadequate for selecting final flight gains—especially for the response decoupling parameters.

The identified higher-order linear model is compared with the flight data and the simulation models in Figures 25 and 26. Significant improvement in the on-axis prediction is seen for both the high-frequency (rotor response) and lower-frequency dynamics. The identified model also tracks the off-axis magnitude and phase very closely, showing clear improvement compared to the two simulation models. The excellent predictive capability of the identified model is also seen in the time response comparison of figure 27.
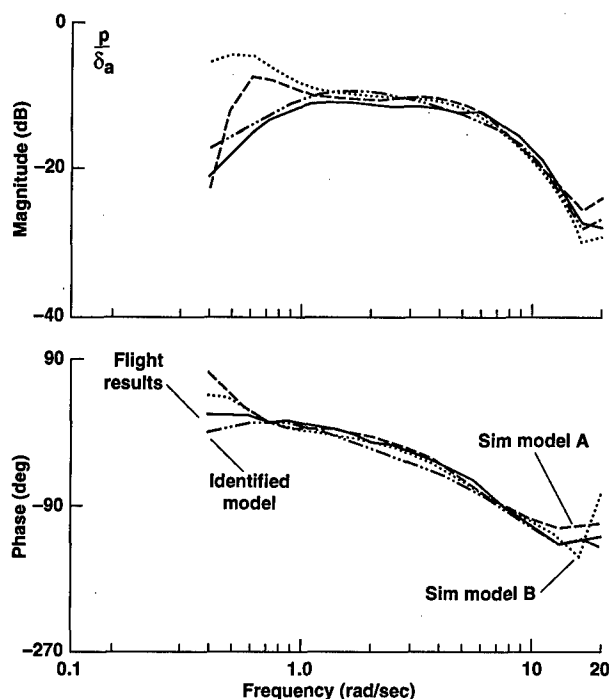

Figure 25. UH-60A on-axis roll-rate response to lateral stick (hover); comparison of simulation and identified state-space model with flight data.
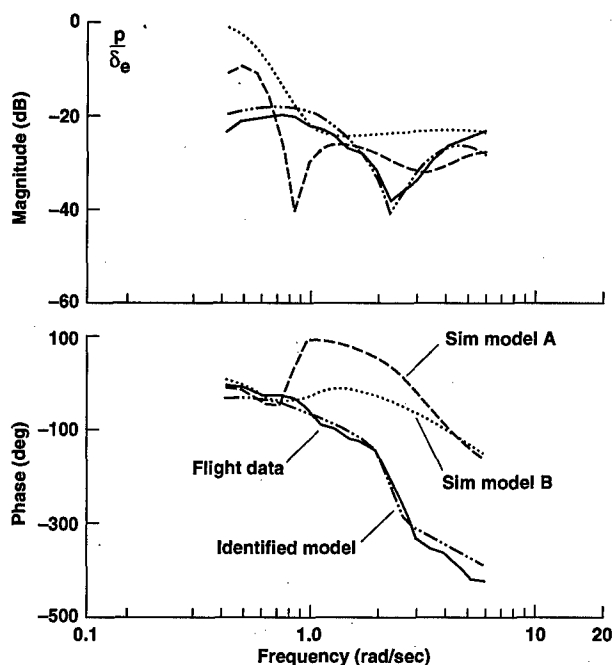

Figure 26. UH-60A off-axis roll-rate response to longitudinal stick (hover); comparison of simulation and identified state-space model with flight data.
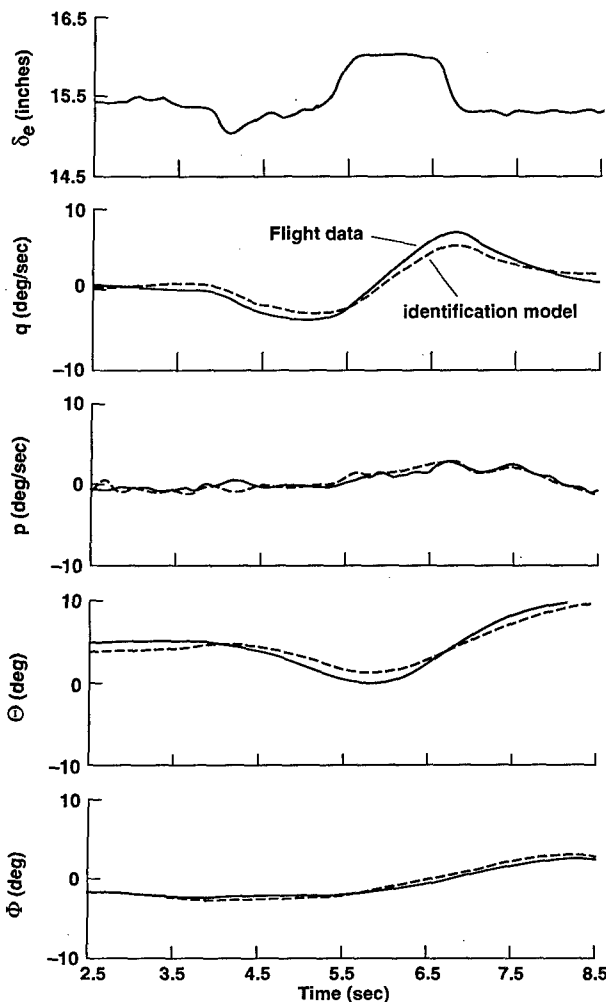
Figure 27. Time response comparison of UH-60A identi-
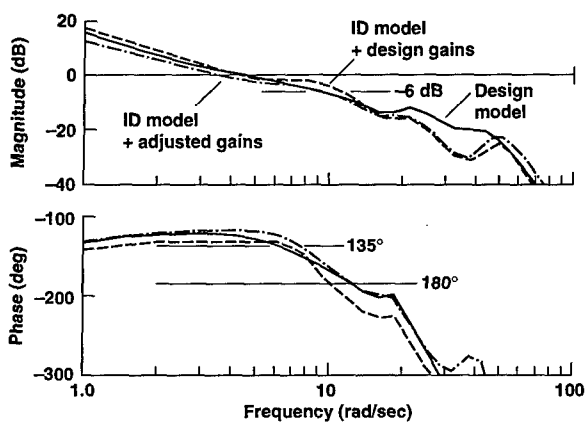fication model and flight data.

Figure 28. RASCAL UH-60A broken-loop roll response in
hover.

The identified state-space model was then substituted into the
model-following control system block diagram in place of the
original simulation model ("A") response to check the expected

flight characteristics. Figure 28 shows The identified state-space
model was then substituted into the model-following control
system block diagram in place of the original simulation model
("A") response to check the expected flight characteristics.
Figure 28 shows that the design phase margin is significantly
degraded when the identified model is incorporated. Further, the
level of closed-loop cross-coupling (fig. 29) increases by 20 dB
(a factor of 10) in the critical handling-qualities frequency range
of 1–10 rad/sec. The control-system design parameters were
then retuned for the identified model response. Figure 28 shows
that the original design crossover frequency, phase margin, and
gain margin are recovered. Also, the cross-coupling level for the
retuned system closely tracks the coupling levels for the original
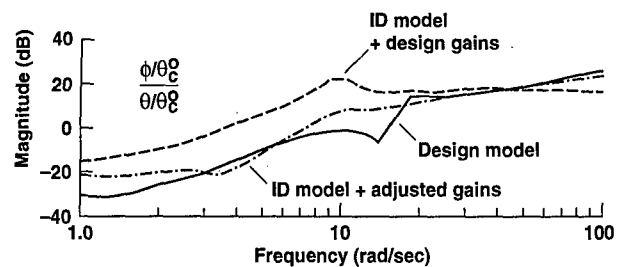control-system design (fig. 29).

Figure 29. RASCAL UH-60A coupling response of roll-rate
due to longitudinal input for hover.

The full exploitation of system-identification tools early in the
flight-test development and control system optimization effort
has been illustrated for the Bo-105 (ATTHeS) and UH-60A
(RASCAL) programs. This approach will significantly reduce
flight-test development time for new aircraft, and will expedite
the optimization of flight-control system performance and
handling qualities.

9. CONCLUDING REMARKS

1. System identification is a full life-cycle technology that
supports aircraft flight-control system development from design
specification through flight-test optimization. Significant
reductions in development time and costs are realized by
tracking open and closed-loop dynamic response characteristics
through the development process.

2. Frequency-domain system-identification methods are well
suited to aircraft flight-control development since many current
design specifications, design and analysis techniques, and
acceptance flight-test techniques are based in the frequency
domain.

3. Reliable computational tools for system identification are
available and have been successfully employed in many recent
aircraft programs.

4. System identification is especially effective in providing a
transparent and integrated understanding of handling-qualities
characteristics and system stability. Considerable improvements
in system performance are facilitated by the rapid availability of
accurate end-to-end and subsystem dynamic models.

10. REFERENCES

Acree, C. W., Jr.; and Tischler, M. B.: Determining XV-15 Aeroelastic Modes from Flight Data with Frequency-Domain Methods. NASA Technical Paper 3330, ATCOM Technical Report 93-A004, 1993.

Anon.: Military Specification, Flying Qualities of Piloted Airplanes, MIL-F-8785 (ASG), 1954.

Anon: Helicopter Flying and Ground Handling Qualities; General Requirements for MIL-H-8501A, 1961.

Anon.: Military Specification, Flight Control Systems-General Specification for Design, Installation, and Test of Piloted Aircraft, MIL-F-9490D (USAF), 1975.

Anon.: Military Standard, Flying Qualities of Piloted Vehicles, MIL-STD-1797 (USAF), 1987.

Anon.: Aeronautical Design Standard, Handling Qualities Requirements for Military Rotorcraft, ADS-33C (AVSCOM), 1989.

Anon.: Rotorcraft System Identification. AGARD AR 280, 1991.

Anon.: International J. Control: Special Issue. Aircraft Flight Control, vol. 59, no. 1, 1994.

Atencio, A.: Fidelity Assessment of a UH-60A Simulation on the NASA Ames Vertical Motion Simulator. NASA TM-104016, 1993.

Ballin, M. G.; and Dalang-Secretan, M. A.: Validation of the Dynamic Response of a Blade-Element UH-60A Simulation Model in Hovering Flight. J. Amer. Hel. Soc., vol. 36, no. 4, 1991, pp. 77–88.

Blanken C. L.; and Pausder, H. -J.: Investigation of the Effects of Bandwidth and Time Delay on Helicopter Roll-Axis Handling Qualities. J. Amer. Hel. Soc., vol. 39, no. 3, 1994, pp. 24–33.

Buchholz, J. J.; Bauschat, J. M.; Hahn, K. U.; and Pausder, H. J.: ATTAS & ATTHeS In-Flight Simulators: Recent Application Experiences and Future Programs, AGARD Flight Vehicle Integration Panel Symposium "Simulation: Where are the Challenges," Braunschweig, Germany, 1995.

Caldwell, B. D.: The FCS-Structural Coupling Problem and its Solution. AGARD-CP-560, Paper 16, 1994.

Cheng, R. P.; Tischler, M. B.; and Biezad, D. J.: Rotorcraft Flight Control Design Using Quantitative Feedback Theory, Symposium on Quantitative Feedback Theory, 2-4 August, Purdue University, West Lafayette, Ind., 1995.

Churchill, G. B.; and Dugan, D. C.: Simulation of the XV-15 Tilt Rotor Research Aircraft. NASA TM-84222, 1982.

Clarke, R.; Burken, J. J.; Bosworth, J. T.; and Bauer, J. E.: X-29 Flight Control System: Lessons Learned. International J. Contr., vol. 59, no. 1, 1994, pp. 199–219.

Curtiss, H. C., Jr.: On the Calculation of the Response of Helicopter to Control Inputs. 18th European Rotorcraft Forum, Avignon, France, 1992.

Dornheim, Michael A.: Aviation Week and Space Tech., Sept. 18, 1995, p. 67.

Engelland, S. A.; Franklin, J. A.; and McNeill, W. E.: Simulation Model of a Mixed-Flow Remote-Lift STOVL Aircraft. NASA TM-102262, 1990.

Fletcher, J. W.: Identification of UH-60A Stability Derivative Models in Hover from Flight Test Data. J. Amer. Hel. Soc., vol. 40, no. 1, 1995.

Foster, J. D.; Moralez, E, III; Franklin, J. A.; and Schroeder, J. A.: Integrated Control and Display Research for Transition and Vertical Flight on the NASA V/STOL Research Aircraft (VSRA). NASA TM-100029, 1987.

Franklin, J. A.; Stortz, M. W.; Engelland, S. A.; Hardy, G. H.; and Martin, J. L.: Moving Base Simulation Evaluation of Control System Concepts and Design Criteria for STOVL Aircraft. NASA TM-103843, 1991.

Glusman, S. I.; Dabundo, C.; and Landis, K. H.: Evaluation of ADOCS Demonstrator Handling Qualities. Proceedings of the 43rd Annual National Forum of the American Helicopter Society, Washington, D.C., 1987.

Hamel, P. G.; and Jategaonkar, R. V.: The Evolution of Flight Vehicle System Identification. AGARD Structures and Materials Panel Specialists' Meeting on Advanced Aeroservoelastic Testing and Data Analysis, Rotterdam, The Netherlands, 1995.

Hoh, R. H.; and Ashkenas, I. L.: Development of VTOL Flying Qualities Criteria for Low Speed and Hover. Systems Technology, Inc., Hawthorne, Calif., TR-1116-1, 1979.

Hoh, R. H.; Mitchell, D. G.; Ashkenas, I. L.; Klein, R. H.; Heffley, R. K.; and Hodgkinson, J.: Proposed MIL Standard and Handbook-Flying Qualities of Air Vehicles. AFWAL-TR-82-3081, vol. 2, 1982.

Hoh, R. H.; Mitchell, D. G.; Aponso, B. L.; Key, D. L.; and Blanken, C. L.: Proposed Specification for Handling Qualities of Military Rotorcraft. Vol. 1— Requirements. U.S. Army Aviation Systems Command, TR 87-A-4, 1988.

Kaletka, J.; and Fu, K. -H.: Frequency-Domain Identification of Unstable Systems Using X-31 Aircraft Flight Test Data. AIAA-93-3635, AIAA Atmospheric Flight Mechanics Conference, Monterey, Calif., 1993.

Kaletka, J.; and von Grunhagen, W.: Identification of Mathematical Derivative Models for the Design of a Model Following Control System. 45th Annual Forum of the American Helicopter Society, Boston, Mass., 1989.

MATLAB®: High-Performance Numeric Computation and Visualization Software. The Math Works, Inc., Reference Guide, 1992.

McFarland, R. E.: Transport Delay Compensation for Computer-Generated Imagery Systems. NASA TM-100084, 1988.

Moorhouse, D. J.; and Citurs, K. D.: The Control System Design Methodology of the STOL and Maneuver Technology Demonstrator. International J. Contr., vol. 59, no. 1, 1994, pp. 221–238.

Takahashi, M. D.: Rotor-State Feedback in the Design of Flight Control Laws for a Hovering Helicopter. J. Amer. Hel. Soc., vol. 39, no. 1, 1994, pp. 50–62.

Takahashi, M. D.; Fletcher, J. W.; and Tischler, M. B.: Development of a Model Following Control Law for Inflight Simulation Using Analytical and Identified Models. American Helicopter Society, 51th Annual Forum, Fort Worth, Tex., 1995.

Tischler, M. B.: Frequency-Response Identification of XV-15 Tilt-Rotor Aircraft Dynamics. NASA TM-89428, 1987.

Tischler, M. B.: System Identification Requirements for High-Bandwidth Rotorcraft Flight Control System Design. J. Guid., Contr., and Dyn., vol. 13, no. 5, 1990, pp. 835–841.

Tischler, M. B.; and Cauffman, M. G.: Frequency-Response Method for Rotorcraft System Identification: Flight Applications to BO 105 Coupled Rotor/Fuselage Dynamics. J. Amer. Hel. Soc., vol. 37, no. 3, 1992, pp. 3–17.

Tischler, M. B.; Driscoll, J. T.; Cauffman, M. G.; and Freedman, C. J.: Study of Bearingless Main Rotor Dynamics from Frequency-Response Wind Tunnel Test Data. American Helicopter Society Aeromechanics Specialists Conference, San Francisco, Calif., 1994.

Tischler, M. B.; Fletcher, J. W.; Morris, P. M.; and Tucker, G. E.: Flying Quality Analysis and Flight Evaluation of a Highly Augmented Combat Rotorcraft. J. Guid., Contr., and Dyn., vol. 14, no. 5, 1991, pp. 954–963.

von Grunhagen, W.; Bouwer, G.; Pausder, H. -J., Henschel, F.; and Kaletka, J.: A High Bandwidth Control System for a Helicopter In-Flight Simulator. International J. Contr., vol. 59, no. 1, 1994, pp. 239–261.

Outils d'identification de la mécanique du vol latérale des Airbus

D.Liot
AEROSPATIALE
A/BTE/EG/MDVS
316 Route de Bayonne
31093 - Toulouse
France

A.Bucharles
ONERA-DCSD
Département Commande des Systèmes et Dynamique du vol
2 avenue Edouard Belin (BP 4025)
31055 Toulouse Cedex 4
France

1. RÉSUMÉ

Pour chaque avion développé, AEROSPATIALE se dote d'un modèle de mécanique du vol pour :

- assurer l'analyse des qualités de vol de l'avion,
- aider à la définition, la mise au point et la validation des lois de commande de vol (automatiques et manuelles),
- permettre l'entraînement des équipages des compagnies aériennes.

Ce modèle doit couvrir l'ensemble du domaine de vol de l'avion (normal, périphérique, cas de pannes,...) avec la meilleure représentativité possible.

En pratique, il se construit progressivement. Les calculs théoriques alliés à l'expérience acquise, puis les essais en soufflerie permettent d'élaborer un modèle prévisionnel déjà très satisfaisant. Toutefois, la précision demandée ne peut être atteinte qu'en le recalant à partir de l'analyse du comportement en vol des avions d'essai.

AEROSPATIALE, en collaboration avec l'ONERA a développé deux outils d'identification, IDLAT_NL et COR_NL, permettant de recaler les modèles aérodynamiques latéraux prévisionnels dans les zones linéaires et non-linéaires. Ceux-ci ont été mis en oeuvre avec succès sur les derniers programmes Airbus.

Nomenclature

m : masse de l'avion
V : vitesse aérodynamique
l, S : corde et surface de référence
α : angle d'incidence
β : angle de dérapage
θ : assiette longitudinale
ϕ : assiette latérale
ψ : angle de cap
p,q,r : vitesses de roulis, de tangage et de lacet
CY : coefficient aérodynamique de force latérale
CL : coefficient aérodynamique de moment de roulis
CN : coefficient de moment de lacet
P_d : pression dynamique
η : correction aéroélastique
δq : braquage de la profondeur
i_H : braquage du plan horizontal
δr : braquage de la gouverne de direction
δp : braquage des ailerons
δsp : braquage des spoïlers
A,B,C : inerties de l'avion en roulis, tangage, lacet

E : inertie croisée de l'avion
TY : projection de la force de propulsion sur l'axe latéral avion
L_T, N_T : moments de roulis et de lacet dus à la force de propulsion

2. CONTEXTE

Dans le cadre du GIE Airbus Industrie, AEROSPATIALE a la responsabilité du système de pilotage des avions. Cette activité fait un large appel à la modélisation de la mécanique du vol de l'avion :

- conception, mise au point des lois de pilotage,
- analyse des qualités de vol
- validation des systèmes,
- étude sur simulateur piloté des cas de pannes trop risqués à réaliser en vol.

Or la connaissance prévisionnelle des efforts aérodynamiques (soufflerie essentiellement) n'est pas suffisante pour assurer ces tâches avec efficacité au cours de la campagne d'essais, de réglage et de certification de l'avion. De plus, AEROSPATIALE doit fournir ce modèle aux fabricants de simulateurs pour permettre l'entraînement des équipages.

Le modèle de mécanique du vol doit donc être recalé sur l'avion avec précision dans tout le domaine de vol et dans les plus brefs délais après le premier vol. 500 à 600 essais doivent ainsi être identifiés en 4 à 5 mois couvrant les phénomènes longitudinaux, latéraux, les effets de sol, le roulage,...

Depuis 7 ans, AEROSPATIALE et l'ONERA ont réuni leurs compétences pour développer des outils d'identification robustes et efficaces dans un contexte industriel contraignant.

La mécanique du vol latéral a demandé la mise en place de moyens spécifiques qui font l'objet de cette communication.

3. PROCESSUS GENERAL DE L'IDENTIFICATION LATÉRALE

3.1. Le modèle de mécanique du vol latéral

AEROSPATIALE s'est doté pour le développement des lois de pilotage, les analyses de qualités de vol, la validation des systèmes et la simulation d'entraînement, d'un outil de simulation de la mécanique du vol appelé OSMA (Outil de Simulation des Mouvements Avion). Il exploite les équations classiques de la mécanique rationnelle exprimées dans un référentiel galiléen en faisant l'hypothèse d'une

terre plate et immobile. Pour les mouvements latéraux, les équations s'expriment dans les axes liés à l'avion :

$$mV\cos\beta\left[\dot\beta - p\sin\alpha + r\cos\alpha\right] = \frac{1}{2}\rho SV^2 CY$$
$$+ mg\cos\theta\,\sin\Phi + TY$$

$$A\dot p - E\dot r - (B-C)\,qr - Epq = \frac{1}{2}\rho SlV^2 CL + L_T$$

$$\dot\Phi = p + tg\,\theta\left(q\sin\Phi + r\cos\Phi\right)$$

$$-E\dot p + C\dot r - (A-B)\,pq + Eqr = \frac{1}{2}\rho SlV^2 CN + N_T$$

$$\dot\psi = (q\sin\Phi + r\cos\Phi)/\cos\theta$$

3.2. Modèle aérodynamique latéral des Airbus

La démarche adoptée pour conduire une identification à son terme dépend avant toute chose de la nature des phénomènes à observer. Concernant le modèle aérodynamique latéral, les essais conduits en soufflerie ont permis de déterminer les paramètres influant sur les efforts et leurs éventuels couplages. Ils ont finalement permis de structurer le modèle en dégageant les différents effets et en distinguant les comportements linéaires et non-linéaires. Rappelons que ce modèle est destiné à répondre aux besoins des simulateurs d'entraînement (respect de la norme IATA), des études de qualités de vol et de développement des lois de pilotage.

A titre d'illustration, nous donnons ci-dessous la structure fondamentale du modèle relatif au coefficient de force aérodynamique latérale dans une configuration de vol hypersustentée

$$CY = Cy\beta.\beta + \Delta Cy\beta_{NL} + Cyp.\frac{pl}{V} + Cyr.\frac{rl}{V} + Cy\dot\beta.\frac{\dot\beta l}{V}$$
$$+ Cy\delta r.\delta r + \Delta Cy\delta r_{NL} + \Delta Cy_{spoïlers} + \Delta Cy_{ailerons}$$

$$Cy\beta = Cy\beta_{SEH}(\alpha) + \eta_\beta(Pd)\,Cy\beta_D(\alpha)$$

$$\Delta Cy\beta_{NL} = \Delta Cy\beta_{NL}(\alpha,\beta)$$

$$Cyp = Cyp_{SEH}(\alpha) + \eta_p(Pd)\,Cyp_D(\alpha)$$

$$Cyr = Cyr_{SEH}(\alpha) + \eta_r(Pd)\,Cyr_D(\alpha)$$

$$Cy\dot\beta = Cy\dot\beta(\alpha)$$

$$Cy\delta r = \eta_{\delta r}(Pd)\,Cy\delta r(\alpha)$$

$$\Delta Cy\delta r_{NL} = \Delta Cy\delta r_{NL}(\alpha,\beta,\delta r,\delta q,i_H)$$

$$\Delta Cy_{spoïlers} = \eta_{sp}\left\{\Delta Cy_{sp}(\alpha,\delta sp_{gauche}) - \Delta Cy_{sp}(\alpha,\delta sp_{droit})\right\}$$

$$\Delta Cy_{ailerons} = \eta_{ail}\left\{\Delta Cy_{ail}(\alpha,\delta p_{gauche}) - \Delta Cy_{ail}(\alpha,\delta p_{droit})\right\}$$

SEH désigne la participation de l'avion sans empennage et D celle de l'empennage.

3.3. Protocole d'identification

L'expression précédente issue des études conduites en soufflerie, appelle les remarques suivantes :

- tous les coefficients et autres tables aérodynamiques dépendent de l'incidence,
- en configuration hypersustentée, les corrections aéroélastiques statiques sont faibles, mais non négligeables
- les efforts d'amortissement sont découplés des autres termes et s'expriment linéairement (approximation suffisante sur avion de transport),
- les efforts induits par les gouvernes de gauchissement (ailerons et spoïlers) dépendent du braquage de façon non- linéaire,
- les efforts induits par le dérapage comportent une plage de fonctionnement linéaire, corrigée à fort dérapage de non-linéarités,
- les effets induits par la gouverne de direction comportent eux aussi une plage de fonctionnement linéaire corrigée à fort braquage par une non-linéarité très complexe faisant intervenir le dérapage et l'incidence mais aussi les braquages du plan horizontal et de la gouverne de profondeur.

Le modèle aérodynamique de référence inclus dans OSMA est donc d'une grande complexité. Les remarques précédentes permettent toutefois de retirer des enseignements précieux quant à la stratégie à mener pour recaler au mieux les coefficients du modèle :

- les essais doivent être faits par "lot d'incidence",

- les corrections aéroélastiques ne seront pas recalées,

- des essais stabilisés à différentes dérapages (vitesses de lacet et de roulis nulles) permettront de réduire le nombre d'inconnues,

- des sollicitations de type créneau pour chaque gouverne seront faites à différents braquages. La large zone linéaire existant sur les effets de dérapage, d'amortissement et de la gouverne de direction permet d'envisager une optimisation paramétrique des coefficients $Ci\beta$, Cip, Cir, $Ci\delta r$ (i=y, l, n) à partir des essais dynamiques de direction. Or, $Ci\beta$, Cip, Cir interviennent aussi dans la réponse de l'avion lors des essais dynamiques de gauchissement. Il convient donc de traiter ensemble les essais dynamiques de direction d'aileron et de spoïler en prenant en compte le fait que les efforts induits par le braquage des gouvernes de gauchissement sont non-linéaires.

La bonne connaissance du modèle moteur autorise d'autre part à exploiter des essais réalisés avec des poussées dissymétriques. Les équilibres un moteur en panne réalisés à faible dérapage complétés des dérapés stabilisés à fort dérapage, permettront de recaler les effets de la direction à grand braquage (non-linéarités). Les pannes moteur contrées qui sont des essais dynamiques faisant de faibles excursions dans les zones non-linéaires seront analysées avec les autres essais dynamiques (créneaux gouverne).

Au delà de l'identification, les essais décrits ici servent à la certification des simulateurs d'entraînement selon la norme IQTG (International Qualification Test Guide). C'est pourquoi nous nous sommes limités pour les essais dynamiques à des entrées de type créneau.

Pour une incidence donnée, le protocole d'identification est donc le suivant :

- exploiter les dérapés stabilisés de façon à connaître les grandes tendances dans les zones linéaires : $Cn\beta/Cn\delta r$ et $Cl_{gauchissement}/Cl\beta$.

- exploiter simultanément les essais dynamiques de direction, de gauchissement et de panne moteur contrée, ceci permettra de déterminer les recalages des zones linéaires en dérapage, direction, vitesses de lacet et de roulis et ceux des non-linéarités d'aileron et de spoïler. Cette identification sera conduite en respectant les rapports issus du traitement des dérapés stabilisés

- exploiter in fine les équilibres un moteur en panne et les dérapés stabilisés à grand dérapage de façon à corriger les non-linéarités de direction et de dérapage.

4. BESOINS POUR L'IDENTIFICATION LATÉRALE

4.1. Les outils d'identification nécessaires

• *Exploitation des "dérapés stabilisés"*

Pour chaque palier de dérapage, les équilibres en lacet et roulis s'écrivent en première approximation :

$$0 = Cn\beta \cdot \beta + Cn\delta r \cdot \delta r + \Delta Cn\beta_{NL}$$

$$0 = Cl\beta \cdot \beta + \Delta Cl_{spoilers} + \Delta Cl_{ailerons}$$

En se limitant à des dérapages inférieurs à 10° et en prenant en compte l'ordre global de gauchissement δl qui induit les braquages des spoilers et des ailerons, on obtient les deux relations suivantes :

$$\delta r = - \frac{Cn\beta}{Cn\delta r} \cdot \beta \quad \text{et} \quad \delta l = - \frac{Cl\beta}{Cl\delta l} \cdot \beta$$

Le tracé du braquage de direction et de l'ordre de gauchissement obtenus pour chaque palier de dérapage permet donc d'avoir une bonne estimation des rapports $\frac{Cn\beta}{Cn\delta r}$ et $\frac{Cl\beta}{Cl\delta l}$ de l'avion.

Le second rapport reste toutefois délicat à exploiter car le gauchissement conjugue simultanément les effets spoilers et ailerons. Il fournit néanmoins une information précieuse quant à la tendance du recalage.

Un outil a donc été développé qui permet de relever les paramètres stabilisés. La visualisation graphique $\delta r = f(\beta)$ et $\delta l = f(\beta)$ de ces mesures permet d'atteindre les rapports précédents.

• *Exploitation des essais dynamiques*

Les essais dynamiques sollicitent simultanément les neuf coefficients : Ciβ, Cip, Cir ; s'y ajoutent d'une part les trois coefficients Ciδr pour les essais de direction, d'autre part les six tables Cisp(δsp) et Ciδp(δp) pour les essais spoilers et ailerons. Trois braquages spoïler et six braquages aileron sont en général observés, ce qui conduit au total à 39 valeurs numériques à ajuster au travers de 15 essais environ. Un outil d'optimisation paramétrique IDLAT_NL a donc été naturellement développé pour aider l'ingénieur à résoudre ce problème.

• *Exploitation des équilibres non-linéaires*

Les dérapés stabilisés aux grands dérapages et les équilibres un moteur en panne font intervenir des non-linéarités complexes couplant les effets liés au dérapage et à la gouverne de direction, mais aussi à l'incidence, au plan horizontal et à la gouverne de profondeur. Nous ne disposons pas de suffisamment d'essais pour identifier complètement ces non-linéarités. Il s'agit donc de décaler ou déformer les réseaux issus des essais en soufflerie de façon à recouper les quelques essais en vol disponibles.

Dans ce cadre, nous avons développé un outil graphique "COR_NL" capable de représenter directement le déficit non-linéaire.

4.2 - Objectifs et contraintes des outils d'identification

Les outils d'identification IDLAT_NL et COR_NL doivent *s'inscrire dans l'environnement industriel* déjà présent. Ils ont donc à communiquer efficacement avec la base de données d'essais qui assure la gestion, la traçabilité et la pérennité des mesures. Les recalages produits doivent être compatibles avec l'outil de simulation de référence OSMA de façon à assurer leur diffusion rapide et cohérente vers tous les autres outils construits à partir d'OSMA (simulateurs d'intégration, d'entraînement,...).

D'autre part, *les recalages doivent avoir un caractère physique* ; ceci permet d'avoir une plus grande confiance dans le modèle, au delà de sa représentativité, et permet de l'exploiter sans craintes hors du domaine couvert par les essais en vol. Enfin, cette connaissance physique permet une transposition du modèle pour obtenir une représentation prévisionnelle valable des avions dérivés suivants (allongement fuselage, changement de moteur,...).

Un autre objectif de ces outils est bien sûr *d'accroître la productivité et de réduire les cycles*. Il est demandé à l'équipe de mécanique du vol de fournir un modèle recalé dans les configurations atterrissage, seulement 3 à 4 mois après le premier vol. Un modèle représentatif sur tout le domaine de vol est requis 3 mois avant la date de certification pour soutenir l'analyse de certains cas de pannes sur les simulateurs d'intégration. Dans cette période environ 350 essais "latéraux" sont traités pour recaler le modèle.

En résumé, les outils d'identification doivent avoir les qualités suivantes :

- compatibilité avec l'environnement industriel,
- efficacité / robustesse,
- assurance de la vraisemblance des recalages.

Pour atteindre ces objectifs, nous avons fait le choix d'algorithmes simples et robustes mais pilotables aisément par l'ingénieur au travers d'une interface homme-machine la plus ergonomique possible. Les transferts d'information entre l'environnement d'identification, la base de données d'essais et OSMA ont été automatisés. Nos outils d'identification ont été développés avec le souci de décharger l'ingénieur de toutes les manipulations informatiques fastidieuses et sources d'erreur , de lui présenter les informations nécessaires de façon pertinente pour soutenir efficacement son jugement et lui permettre de retoucher aisément les paramètres de l'identification. Ces outils permettent à nos ingénieurs d'exprimer et de développer leur expertise pour produire rapidement des modèles représentatifs et vraisemblables.

5. IDLAT_NL

5.1. Principe

Le caractère fortement structuré du modèle latéral conduit à choisir la technique dite de minimisation des erreurs de sortie pour recaler sur un point de vol et à partir d'essais dynamiques les effets linéaires induits par le dérapage, les vitesses de roulis et de lacet et le braquage de direction conjointement avec les efficacités non-linéaires de gauchissement Cette approche itérative nécessite à chaque pas un grand nombre de simulations pour évaluer le gradient du critère d'erreur, nécessaire au calcul de l'optimum. L'exploitation directe du modèle de référence

OSMA conduirait à des coûts de calcul prohibitifs. C'est pourquoi un modèle simplifié, déduit du précédent, a été développé pour IDLAT_NL en recherchant le meilleur compromis représentativité / coût calcul.

5.2 - Modèle simplifié

Le modèle est restreint à 3 degrés de liberté. Les évolutions longitudinales (q, θ, α, V) sont celles mesurées sur l'avion au cours des essais.

Les effets d'incidence, présents dans le modèle OSMA sont linéarisés au voisinage de l'incidence du point de vol considéré. Le gradient prévisionnel d'incidence n'est pas recalé au cours de l'optimisation, mais il permet de prendre en compte les disparités d'incidence entre essais d'un même lot et les variations d'incidence au cours des manoeuvres.

Les effets moteur (traînée de captation, dissymétries de poussée) sont renseignés en fonction du temps après une simulation préalable avec le modèle moteur de référence dans les conditions de vol mesurées sur l'avion.

Les non-linéarités de dérapage et de direction sont renseignées en fonction du temps selon le même processus que pour les moteurs. Ceci permet de prendre en compte des essais faisant de brèves excursions dans les zones non-linéaires sans biaiser l'identification de la zone linéaire.

Les coefficients à identifier sont relatifs à l'avion complet et intègrent les corrections aéroélastiques supposées peu varier au cours des essais. La répartition avion sans empennage / empennage est faite a posteriori lors de l'affectation des recalages du modèle simplifié aux données du modèle de référence.

Les non-linéarités d'aileron et de spoiler sont considérées comme des tableaux de coefficients dont chacun est susceptible d'être recalé. Les valeurs intermédiaires sont obtenues par interpolation linéaire. La discrétisation des tableaux est rigoureusement celle du modèle de référence.

Cet ensemble de simplifications conduit pour le coefficient aérodynamique de force latérale à l'expression suivante :

$$CY = \left\{ Cy\beta_{\alpha=\overline{\alpha}} + Gy\beta . (\alpha_{EV} - \overline{\alpha}) \right\} \beta$$
$$+ \left\{ Cyp_{\alpha=\overline{\alpha}} + Gyp . (\alpha_{EV} - \overline{\alpha}) \right\} \frac{p.l}{V}$$
$$+ ...$$
$$+ \left\{ Cy\delta r_{\alpha=\overline{\alpha}} + Gy\delta r . (\alpha_{EV} - \overline{\alpha}) \right\} \delta r_{EV}$$
$$+ \Delta Cy\delta sp_{\alpha=\overline{\alpha}}(\delta sp_{EV}) + Gy\delta sp(\delta sp_{EV}) . (\alpha_{EV} - \overline{\alpha})$$
$$+ ...$$
$$+ \varepsilon(t)$$

où l'indice EV désigne la valeur mesurée lors de l'essai , $\overline{\alpha}$ l'incidence moyenne du lot d'essais et $\varepsilon(t)$ rassemble les effets non-linéaires et moteur prévisionnels directement calculés à partir des mesures d'essai en vol.

Plutôt que de travailler directement sur les coefficients du modèle simplifié, il a paru plus judicieux d'identifier des corrections additives ou multiplicatives de ces mêmes coefficients. Cette formulation offre l'avantage de conserver en permanence les coefficients prévisionnels comme référence. Par ailleurs, une représentation par splines a été adoptée pour les corrections affectant les efficacités non-linéaires de gauchissement. Elle permet de choisir librement les abscisses de correction des efficacités en fonction de l'information présente dans les essais et d'assurer a posteriori une bonne continuité des recalages après projection sur la grille de discrétisation du modèle de référence.

5.3. Algorithme d'identification

L'estimation des corrections des coefficients aérodynamiques est réalisée par la technique classique de minimisation des erreurs de sortie dont le principe général est rappelé ci-dessous :
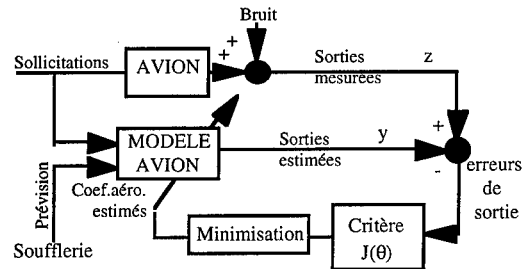
Le critère à minimiser représente la somme pondérée des énergies des erreurs de sortie sur l'horizon de l'essai :

$$J(\theta) = \frac{1}{2} \sum_{i=1}^{N} [Z(t_i) - Y(t_i)]^T M_i^{-1} [Z(t_i) - Y(t_i)]$$

Une technique efficace pour minimiser le critère est la méthode de Gauss-Newton. Partant d'une estimation initiale $\hat{\theta}_0$, elle consiste à calculer itérativement les paramètres selon l'expression :

$$\hat{\theta}_{j+1} = \hat{\theta}_j - \left[\frac{\partial^2 J}{\partial\theta\partial\theta^T} \right]_{\theta=\hat{\theta}_j}^{-1} \left[\frac{\partial J}{\partial\theta} \right]_{\theta=\hat{\theta}_j}$$

avec

$$\frac{\partial J}{\partial\theta} = -\sum_{i=1}^{N} \left[\frac{\partial Y(t_i)}{\partial\theta} \right]^T M_i^{-1} [Z(t_i) - Y(t_i)]$$

et

$$\frac{\partial^2 J}{\partial\theta\partial\theta^T} \sim \sum_{i=1}^{N} \left[\frac{\partial Y(t_i)}{\partial\theta} \right]^T M_i^{-1} \left[\frac{\partial Y(t_i)}{\partial\theta} \right]$$

Ces calculs font intervenir le gradient des sorties du modèle par rapport aux paramètres qui est évalué par différences finies.

5.4. Mise en oeuvre

Du fait de l'utilisation de procédures d'optimisation non-linéaire, la technique précédente, pour bien fonctionner, nécessite de disposer d'une bonne initialisation des coefficients du modèle. Pour tous les avions de la gamme Airbus, l'initialisation fournie par les données aérodynamiques prévisionnelles s'est toujours avérée de qualité suffisante pour qu'il ne soit pas nécessaire de recourir à une procédure spécifique d'initialisation, de type moindres carrés par exemple.

Les essais à exploiter se composent de sollicitations des gouvernes à différents braquages (créneaux mono et bi-ailerons, créneaux spoïlers, créneau et doublet direction) et d'essais de type panne moteur contrée.

L'état du modèle latéral (β, p, Φ, r, ψ) est entièrement mesuré ainsi que le facteur de charge latéral (ny) et les accélérations de roulis et de lacet (ṗ et ṙ). Pour un point de vol, les données correspondant à l'ensemble des essais sont simultanément traitées par minimisation du critère global :

$$J(\theta) = \frac{1}{2} \sum_{k}^{essais} \frac{1}{N(k)} \sum_{i} \left\{ [Z(t_i) - Y(t_i)]^T M_i^{-1} [Z(t_i) - Y(t_i)] \right\} W(t_i, k)$$

où N(k) désigne le nombre d'échantillons temporels du kième essai. La normalisation par N(k) donne à chaque essai un poids identique dans le critère indépendamment de sa longueur. W est un terme de pondération complémentaire qui permet de privilégier soit globalement un essai vis à vis des autres, soit une zone de temps particulière d'un essai par rapport au reste de l'essai pour garantir un équilibre initial par exemple.

Les paramètres à identifier se composent d'une part des corrections des coefficients aérodynamiques prévisionnels, d'autre part des biais d'état et de sortie propres à chaque essai. L'état initial du modèle est fixé à la valeur du premier point de mesure de l'essai.

De façon générale, pour un point de vol standard rassemblant 15 essais, 39 termes de correction des coefficients aérodynamiques sont mis en recherche auxquels il faut ajouter 6 biais par essai, soit au total 129 paramètres à identifier. Cinq à six itérations sont en moyenne nécessaires pour atteindre l'optimum.

5.5. Ergonomie

L'environnement d'identification se présente à l'ingénieur au travers de trois fenêtres :

1/ - extraction des essais de la base de données et classement par lots (même incidence en configuration hypersustentée, même Mach en configuration croisière),

2/ - manipulation des données aérodynamiques, pilotage de l'algorithme et gestion des recalages,

3/ - visualisation graphique des simulations.

La deuxième fenêtre est donnée planche 1. L'ensemble des coefficients aérodynamiques recalables sont présentés à l'ingénieur, organisés par axes (roulis, lacet, latéral) et par effet aérodynamique (vitesses de roulis, de lacet, dérapage, braquages des gouvernes). Les valeurs prévisionnelles sont présentées en permanence, soit sous forme d'une valeur numérique quand l'effet considéré est linéaire (exemple $Cn\beta$) soit sous forme d'une courbe pour les effets non-linéaires (exemple $\Delta Cl\delta p(\delta p)$).

Dans le cas de coefficients scalaires (effets linéaires), l'ingénieur peut en cliquant sur la case faire apparaître un dialogue de sélection lui permettant au choix :

- de mettre en recherche le coefficient et de choisir sa valeur initiale (prévisionnelle ou autre),

- d'imposer le coefficient à la valeur de son choix (prévisionnelle, recalage précédent ou autre),

- d'exprimer ses choix en termes de valeur ou de recalage additif ou multiplicatif à sa convenance.

Un code de couleur lui permet de connaître à tout moment l'état d'un coefficient : vert en recherche, rouge bloqué.

Dans le cas d'effets non-linéaires des braquages de gouverne, l'ingénieur clique sur la zone pour accéder à une fenêtre "plein écran" (voir planche 2) où lui sont présentés:

- la courbe prévisionnelle,
- le recalage fonction du braquage
- un diagramme donnant les braquages présents dans le lot d'essais considéré.

L'ingénieur pilote la courbe de recalage en cliquant sur chacun des points. Il peut ainsi :

- mettre un point en recherche. Cette décision est prise en fonction du diagramme inférieur qui lui précise la répartition de l'information.

- bloquer un point. Il lui donne la valeur voulue en le tirant à la souris (concept "click & drag").

- rendre un point dépendant de ses voisins. Il n'est pas en recherche ni bloqué mais défini par interpolation spline en fonction de ses colatéraux.

La courbe aérodynamique est remise à jour instantanément en fonction de l'évolution de la courbe de recalage. Ceci permet le lissage "manuel" de la courbe recalée et donne des informations sur la vraisemblance du recalage.

L'ingénieur a en outre la possibilité d'imposer aux coefficients $Cy\delta r$ ou $Cl\delta r$ de prendre le même recalage que $Cn\delta r$. Ceci lui permet de garder une cohérence physique entre ces coefficients (points d'application des efforts sur la dérive) pour pallier à une faible discrimination des effets de force latérale et de roulis induits par la gouverne de direction.

Après avoir configuré son optimisation et choisi les essais à traiter, l'ingénieur déclenche une optimisation (bouton "résolution"). Celle-ci demande, sur les calculateurs actuels d'AEROSPATIALE, en moyenne trois minutes de calcul pour 15 essais traités.

Les résultats sont affichés en regard des valeurs prévisionnelles. Ils sont sauvegardables, ce qui permet d'étudier différentes combinaisons pour chercher la solution la plus vraisemblable.

Le critère optimisé est affiché et l'utilisateur a accès à sa décomposition par essais et par axe. Ceci lui permet de détecter des essais atypiques (erreurs de mesure, excursions non-linéaires,...) ou de statuer sur certaines solutions sous-optimales.

A tout moment, l'utilisateur peut accéder à la simulation pour comparer, essai par essai, la réponse de l'avion à celle du modèle recalé (cf planche 3).

IDLAT_NL offre donc une grande souplesse d'utilisation sans contraindre l'ingénieur à un processus figé d'identification. Il peut ainsi "dégrossir" un recalage sur la base de nombreux essais ou au contraire se focaliser sur un phénomène local ne mettant en jeu que peu d'essais ou de coefficients aérodynamiques.

En règle générale, tous les essais disponibles sont dans un premier temps identifiés simultanément et presque tous les coefficients mis en recherche. L'ingénieur observe ainsi les tendances ; il verrouille alors aux valeurs recalées plausibles, sinon prévisionnelles, les coefficients de moindre poids sur le critère. Les coefficients fondamentaux ($Cn\delta r$, $Cn\beta$, $Cl\beta$, $\Delta Cl(\delta p)$)... sont laissés en recherche et progressivement bloqués à des valeurs raisonnables de l'avis de l'ingénieur. Une fois ces coefficients définis, les coefficients de moindre poids sont optimisés localement et lissés.

5.6. Intégration industrielle

Au delà de l'interface homme-machine, IDLAT_NL est un outil autonome qui ne s'interface avec la base de données d'essai et l'outil de simulation de référence OSMA qu'en début et en fin de traitement (cf planche 4).

Initialement, IDLAT_NL extrait les essais de la base de données et pour chacun stimule OSMA avec les braquages de gouverne et les états longitudinaux et latéraux du vol. OSMA fonctionne alors dans un mode particulier où les intégrateurs sont inhibés. IDLAT_NL obtient ainsi d'OSMA:

- les effets secondaires en fonction du temps (non-linéarités, effets moteurs, souplesses,...),

- la valeur moyenne des coefficients aérodynamiques globaux ; par exemple :

$$Cy\beta = Cy\beta_{SEH}(\overline{\alpha}) + \eta_\beta(\overline{Pd}) \cdot Cy\beta_D(\overline{\alpha})$$

- les gradients en incidence.

L'interface homme-machine permet de donner un statut (à recaler ou bloqué) aux coefficients aérodynamiques.

L'ensemble de ces informations (coefficients + statut, gradients, effets secondaires f(t)) sont transmis au noyau numérique constitué du modèle latéral simplifié et du moteur d'optimisation qui met en oeuvre l'algorithme.

Les recalages obtenus sont renvoyés à l'interface homme-machine pour visualisation et analyse par l'utilisateur. Les biais sont stockés.

Si une visualisation est demandée, le moteur d'optimisation est mis en action dans un mode particulier qui ne produit qu'une simple simulation.

Le retour dans le monde "officiel" OSMA se fait par l'intermédiaire d'une opération de traduction. Les recalages sont formatés pour pouvoir se coupler aux données aérodynamiques de référence (par exemple le recalage sur $Cy\beta$ est distribué sur $Cy\beta_D$ et $Cy\beta_{SEH}$). Les biais sont traduits en retouches des conditions initiales de chaque essai.

Le noyau numérique d'IDLAT_NL a été développé en Fortran par l'ONERA. L'implémentation des autres fonctions (gestion des données, activation des tâches, interface homme-machine...) a été réalisée dans le langage LE-LISP.

6. COR_NL

6.1. Principe

L'outil COR_NL est basé sur le principe suivant :

- la mesure des accélérations linéaires et angulaires à bord de l'avion permet de connaître directement la somme des forces et moments qui s'appliquent à l'appareil :

$$\sum \vec{F}_{r\acute{e}el}, \sum \vec{\mathcal{M}}_{r\acute{e}el}$$

- la mesure des états et des braquages donne au travers des modèles prévisionnels des forces aérodynamique et moteur la somme des forces et moments attendus :

$$\sum \vec{F}_{mod\grave{e}le}, \sum \vec{\mathcal{M}}_{mod\grave{e}le}$$

- la différence entre les deux termes :

$$\sum \vec{F}_{r\acute{e}el} - \sum \vec{F}_{mod\grave{e}le} \text{ et } \sum \vec{\mathcal{M}}_{r\acute{e}el} - \sum \vec{\mathcal{M}}_{mod\grave{e}le} \text{ représente}$$

donc l'erreur de modélisation globale à chaque instant

$$\delta\vec{F}(t), \delta\vec{\mathcal{M}}(t)$$

- l'erreur de modélisation peut être corrélée graphiquement à un paramètre d'évolution jugé pertinent pour l'essai considéré. Par exemple, au cours d'un essai de décrochage où la prise d'assiette avant l'abattée est très lente, on peut tracer δF_z ou plutôt

$$\delta C_z = \frac{\delta F_z}{\frac{1}{2}\rho SV^2}$$

en fonction de l'incidence. On obtient directement le recalage de la courbe de portance.

- la juxtaposition de plusieurs essais permet d'avoir une approche statistique et ainsi de mieux définir le recalage.

6.2. Mise en oeuvre industrielle

La mesure directe sur avion des accélérations, de tous les états et des braquages permet une mise en oeuvre très simple.

Le processus d'intégration d'OSMA est inhibé de façon à positionner en entrée des modèles aérodynamique et moteur les états et braquages mesurés sur l'avion. Leurs sorties sont retranchées aux efforts directement déduits des accélérations. Ainsi aucune approximation n'est faite.

L'utilisateur de COR_NL a la possibilité de demander le traitement de plusieurs essais. Une fenêtre graphique (cf planche 5) lui permet :

- de définir le résidu d'effort à visualiser et le paramètre évolutif à lui corréler,
- d'éliminer les points gênants (forte dynamique, dépassement de la zone d'étude, hystérésis,...),
- de tracer le résidu d'effort en fonction du paramètre choisi pour les essais de son choix.

Un code de couleur associé à un deuxième paramètre défini par l'utilisateur permet d'apprécier d'éventuels effets secondaires ou interactions.

Les tables numériques des modèles aérodynamique ou moteur peuvent être directement retouchées depuis la fenêtre graphique. La réédition du traitement avec ces recalages permet de contrôler dans des délais très courts la réduction de l'erreur du modèle.

6.3. Limitations

Cet outil est limité par sa simplicité même :

• les essais à forte dynamique sont peu exploitables car ils supposent des mesures d'accélération, d'état et de braquage absolument synchrones, ce qui est rarement le cas. L'outil ne disposant d'aucun filtrage est, par conséquent, vite mis en défaut,

• les essais sollicitant simultanément de nombreux effets aérodynamiques sont peu exploitables. Basés sur une analyse graphique, les interactions entre paramètres sont difficilement mises en évidence par l'outil, à moins d'utilisateurs perspicaces.

Ces limitations ne sont pas un réel obstacle à l'utilisation de COR_NL. Il est en effet possible de définir des essais de faible dynamique mettant en valeur des phénomènes aérodynamiques spécifiques comme les dérapés stabilisés et les équilibres un moteur en panne.

7. PERSPECTIVES

Dans le cadre de l'identification aérodynamique latérale des avions Airbus, AEROSPATIALE a développé en collaboration avec l'ONERA des outils complémentaires. La robustesse des algorithmes et l'ergonomie des interfaces ont permis de réduire significativement les cycles de production des modèles de qualité de vol recalés sur l'avion, tout en améliorant leur vraisemblance physique. Ces gains ont accompagné ceux réalisés sur la mise au point de l'avion lui-même (cycle et maturité à la mise en service).

AEROSPATIALE et l'ONERA poursuivent leurs efforts pour permettre l'identification conjointe d'essais latéraux réalisés à diverses incidences. L'ergonomie de ces futurs outils sera bien sûr conçue pour aider les experts à élaborer rapidement des modèles pertinents.
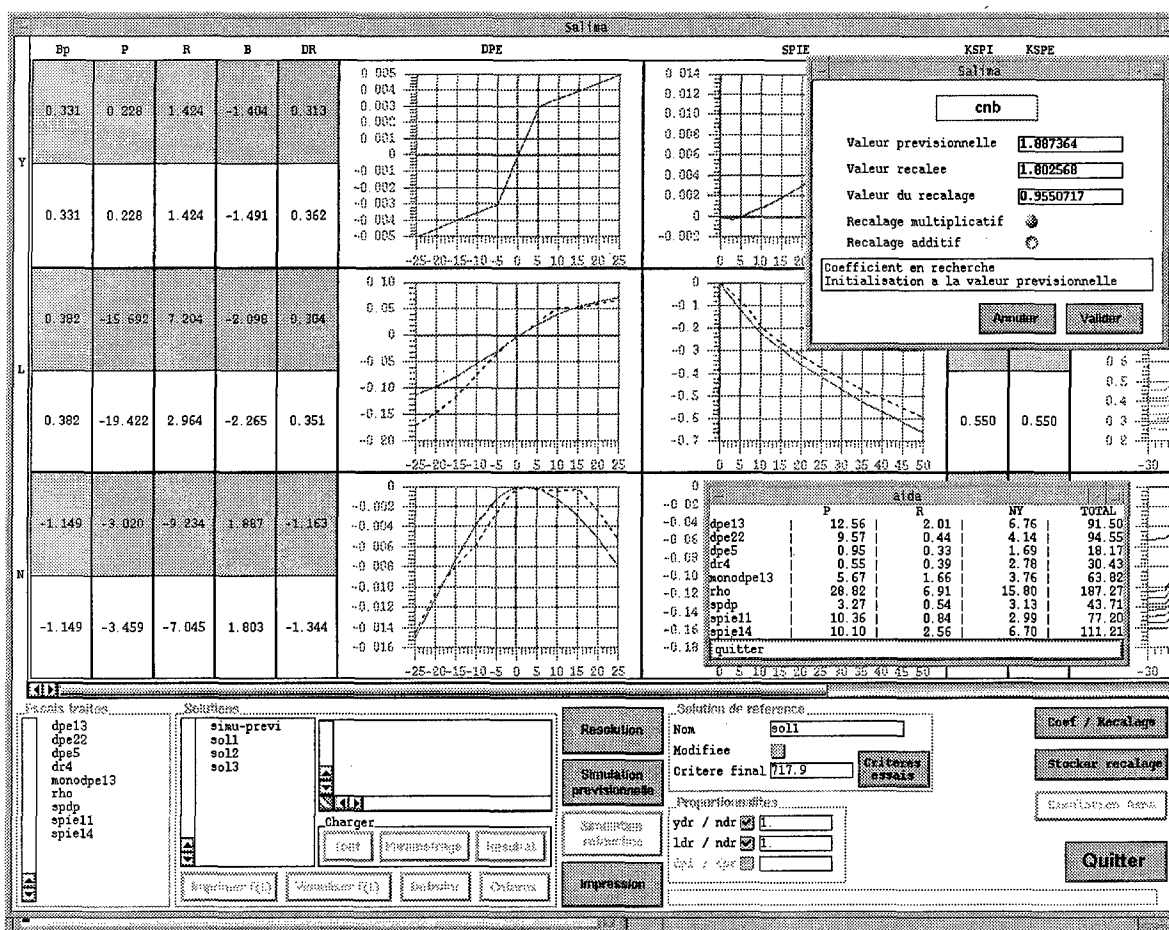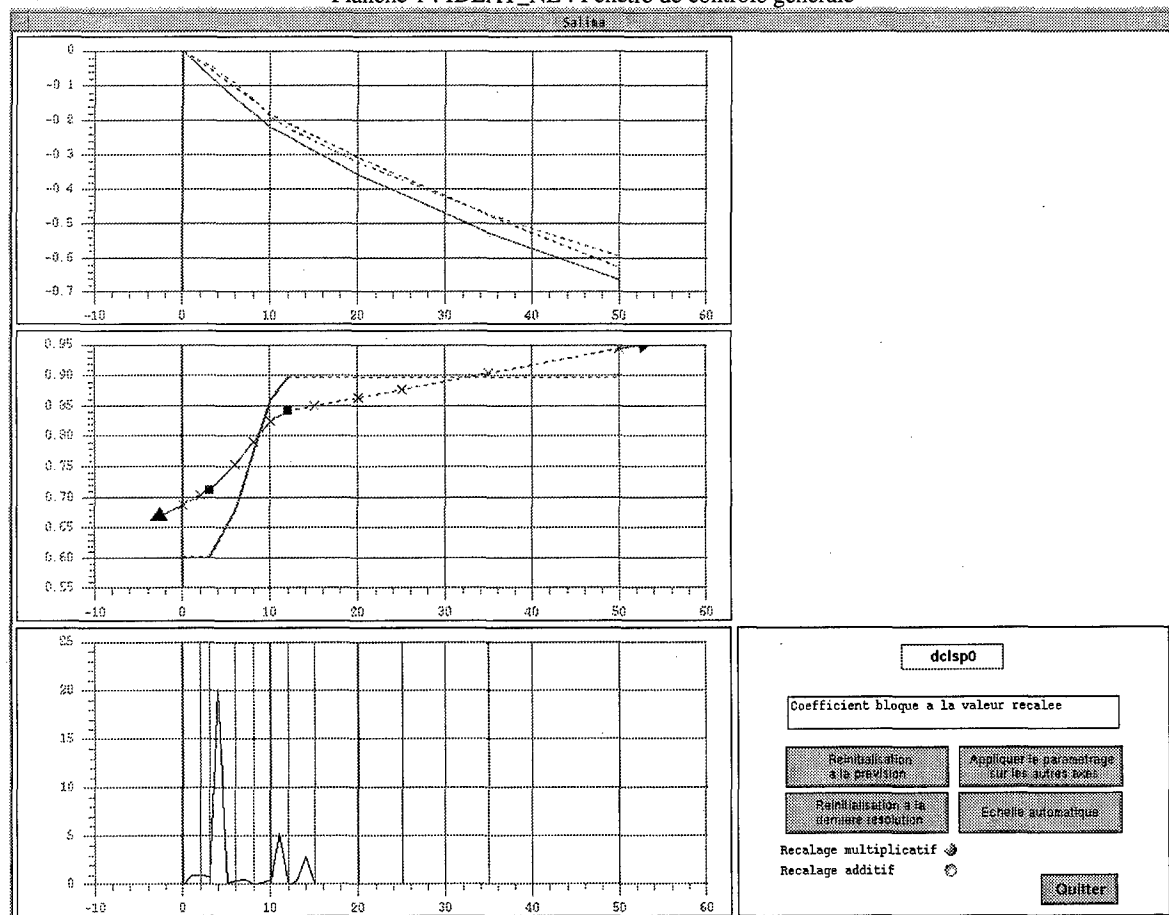
Planche 1 : IDLAT_NL : Fenêtre de contrôle générale
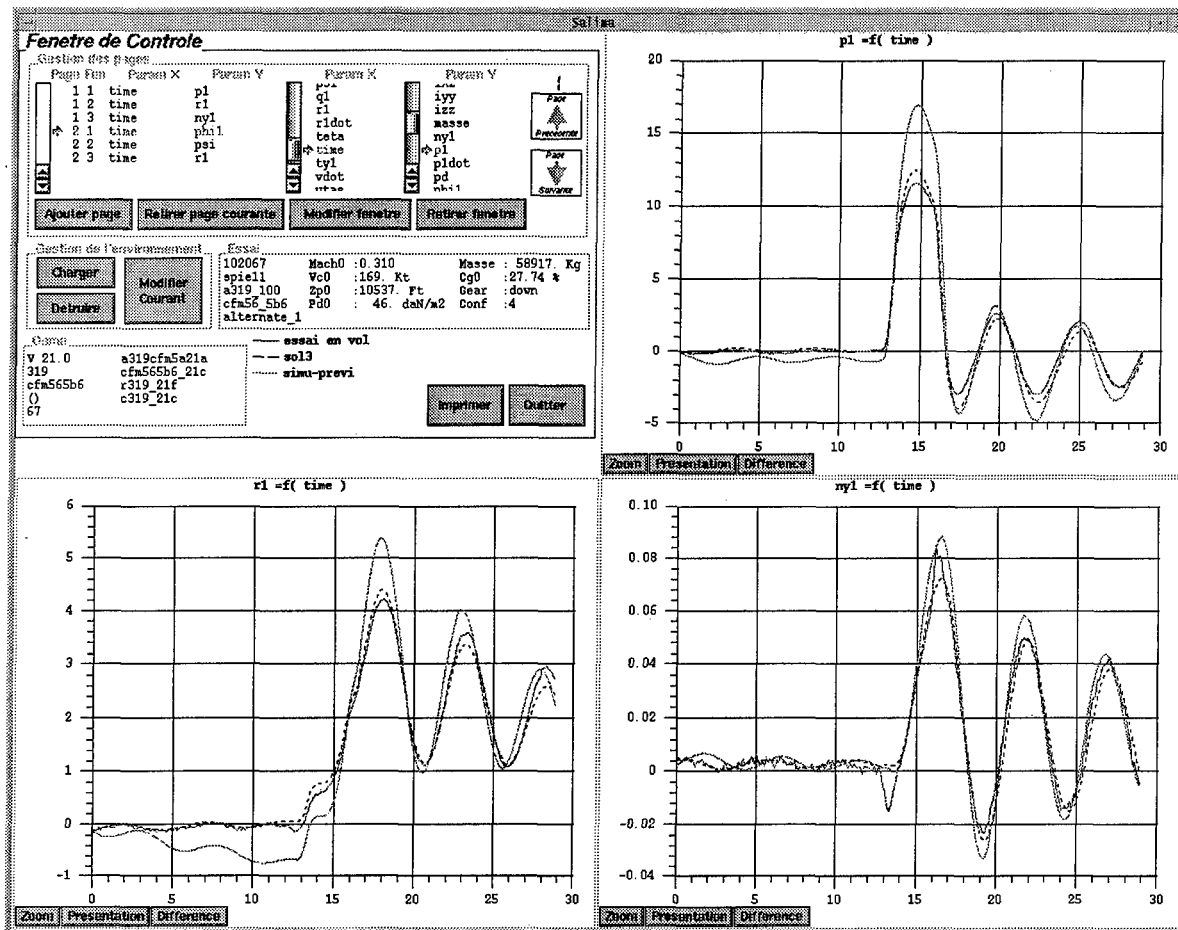

Planche 2 : IDLAT_NL : Fenêtre de contrôle spoïlers
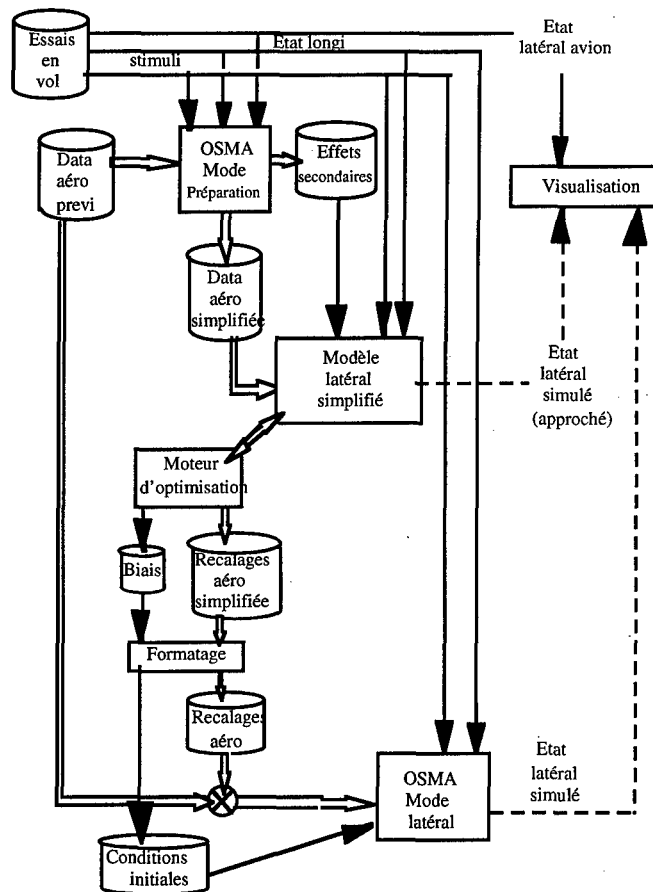
Planche 3 : IDLAT_NL : recoupement modèle/essai
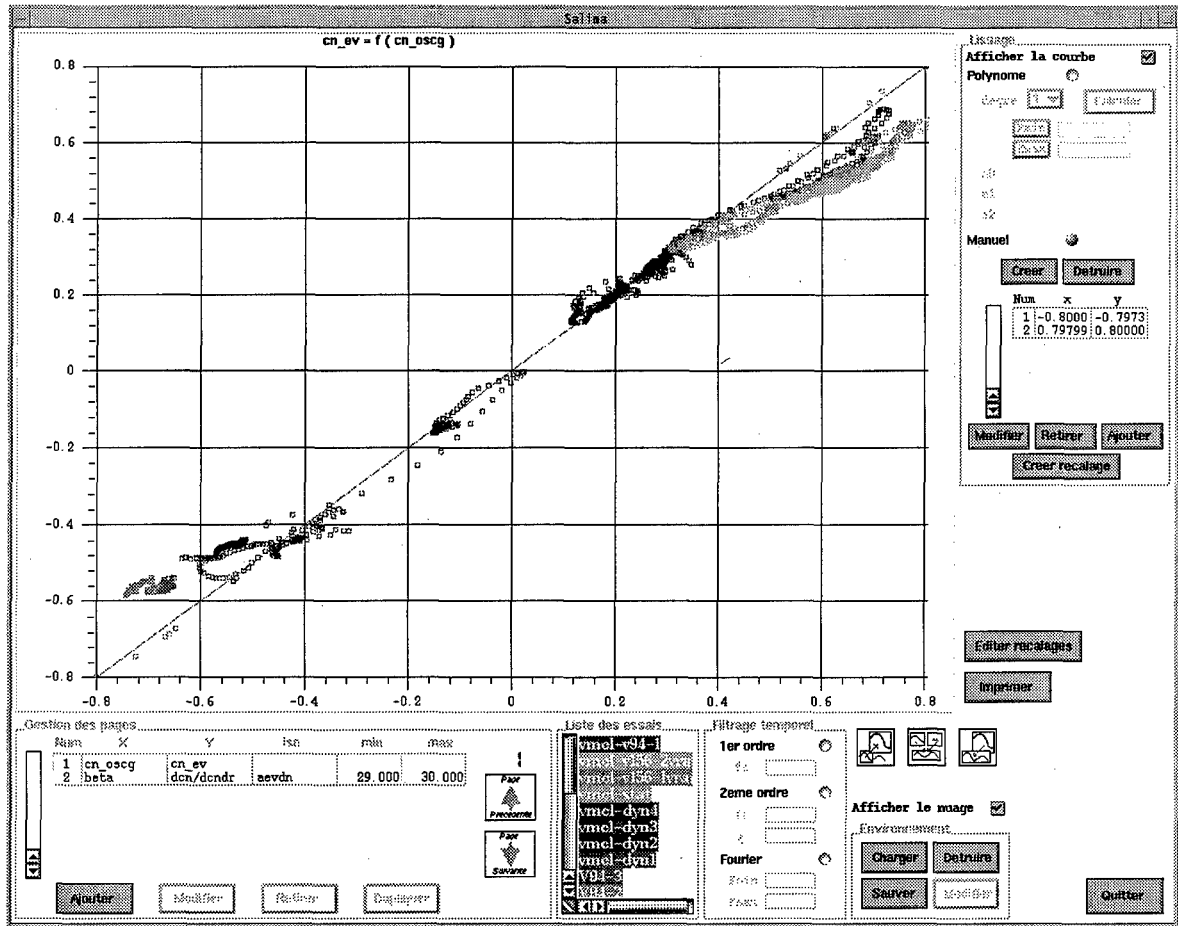
Planche 4 : IDLAT_NL : Organisation informatique

Planche 5 : COR_NL : non-linéarité de direction

DEVELOPING AERIAL REFUELING SIMULATION MODELS
FROM FLIGHT TEST DATA USING ALTERNATIVE PID METHODS

George Wesley Ryan III
Stewart J. Platz
Kohlman Systems Research
319 Perry Street
Lawrence, Kansas 66044
USA

SUMMARY
To improve existing aerial refueling training devices, a flight test program was completed for several tanker/receiver pairs for the United States Air Force Air Mobility Command, by Kohlman Systems Research (KSR) and SIMTEC, Inc. (Ref 1) These flight tests were designed to record accurate quantitative measurements of the aerodynamic changes and random turbulence acting on both the tanker and receiver during refueling, including accurate real-time relative position measurements of the aircraft. Because the aerial refueling environment is a quasi-steady state environment, flight test data reduction presented some unique problems. The lack of strong forcing function relationships in the data prohibited traditional parameter identification algorithms from working efficiently. Two separate alternative PID methods were developed during the production of an aerial refueling simulation of a C-141B reciever and a KC-135R tanker. The first was designed to identify the large aerodynamic changes associated with refueling. The second was designed to identify the random turbulence associated with the tanker flow field. This paper presents the results of the two methods. The first method is based on trimming the six equations of motion to match the simulation and flight test data. Aerial refueling coefficient deltas and a down-wash term identified from the data as a function of relative position were used to account for the large aerodynamic influences present. The second parameter estimation method was used to identify coefficients from recorded acceleration data. These coefficients were used in a random turbulence model to reproduce the power spectrum of the random turbulence associated with the aerial refueling environment. The end result is a simulation capable of reproducing the response of both aircraft during aerial refueling within tolerances similar to those used for single aircraft training device acceptance.

NOMENCLATURE

A_z	Aircraft vertical acceleration
AR	Aerial refueling
C_D	Drag force coefficient
C_L	Lift force coefficient
C_l	Rolling moment coefficient
C_M	Pitching moment coefficient
C_N	Yawing moment coefficient
C_Y	Side force coefficient
F	Force, lbs
FFT	Fast Fourier Transform
g	Gravitational constant
GPS	Global Positioning System
i_H	Horizontal stabilizer incidence, deg
I	Moment of inertia, slug ft^2
L	Aircraft lift force, lb
L_u, L_v, L_w	Gust scale length, ft (x,y, and z axis)
m	Aircraft mass, slugs

M	Aircraft pitching moment, ft lb
N	Aircraft yawing moment, ft lb
P	Aircraft roll rate, rad/s
PID	Parameter Identification
PSD	Power Spectral Density
qbar	Dynamic pressure, lb/ft^2
Q	Aircraft pitch rate, rad/s
RMS	Root Mean Square
RPMS	Relative Position Measurement System
R	Aircraft yaw rate, rad/s
S	Aircraft reference wing area, ft^2
U	Longitudinal velocity, ft/sec
X	Longitudinal axis, positive forward
x_rpms	x position behind the tanker - ft
Y	Lateral axis, positive out right wing
y_rpms	Y position behind the tanker - ft
Z	Vertical axis, positive downward
z_rpms	Z position behind the tanker - ft.
α	Aircraft angle of attack
δ_e	Deflection angle, deg
Δ	Delta or change to coefficient
θ	Aircraft pitch angle, deg
$\sigma_u, \sigma_v, \sigma_w$	RMS Gust Intensity (x, y, and z axes)
ϕ	Aircraft roll angle, deg
Φ	Turbulence Spectrum
Ω	Spatial frequency, 1/ft

SUBSCRIPTS

A	Aerodynamic Force
T	Thrust component
o	Zero angle of attack

1. INTRODUCTION
Aerial refueling is a closed-loop, high-gain, station-keeping task with large aerodynamic influences and random turbulence effects constantly disturbing the receiver aircraft, making it one of the most difficult tasks that pilots must perform. Improvements in refueling systems and in aircraft handling qualities have made aerial refueling less hazardous, but pilots must constantly practice the task in flight to become proficient.

To lower training costs associated with aerial refueling training, a simulation that accurately reproduces the refueling environment for a given tanker/receiver pair is highly desirable. Most existing training devices lack the needed fidelity to accurately reproduce the refueling environment. Flight test programs have been performed in the past to collect qualitative data associated with refueling and to evaluate flight test techniques. However, qualitative data allows the large aerodynamic changes to be modeled in training devices only after long hours of pilot evaluation and model revision. Also, without an accurate measurement of the relative positions between the tanker and receiver, it is difficult to determine exactly where certain aerodynamic effects take place.

With the use of highly accurate carrier phase differential GPS measurements, the relative position of the tanker and receiver can be known in real-time and correlated to recorded flight test data. By using this accurate relative position measurement, it is possible to correlate flow field disturbances to the position of the receiver behind the tanker.

Even with an accurate position measurement and recorded aircraft flight test parameters, it is difficult to identify the aerodynamic relationships that exist in the data. Because aerial refueling is a quasi-steady state position keeping task, the dynamic movements of the receiver are small in magnitude. This makes the identification of aerodynamic coefficients from flight test data difficult using standard parameter identification methods.

Traditionally, PID methods require that a clearly identifiable relationship exist between pilot inputs and the response of the aircraft. Control doublets, and other pilot inputs are traditionally used to provide a strong forcing function for parameter identification tools to work properly. However, these types of inputs are not feasible for the refueling environment for safety reasons.

To extract the needed aerodynamic coefficients from recorded flight test data, two unique and independent PID methods were developed by KSR as alternatives to traditional methods. The first is based upon trimming the equations of motion in the simulation models to match the recorded flight test values of the forces and moments acting on the tanker and receiver. This technique accounts for the large aerodynamic changes that are present during refueling. This is referred to in this paper as the Coefficient Trim method.

The second parameter estimation method, which was based on machine learning techniques, was used to identify a random turbulence model that accurately reproduces the random disturbances encountered during aerial refueling. It is possible for a highly trained refueling pilot to trim the receiver aircraft in the Contact position and maintain the position. However, once the trim state is achieved, it is usually disturbed by random flow field effects, causing the pilot to adjust the controls during refueling. These disturbances make station keeping difficult and need to be properly reproduced in the simulation.

Frequency domain comparisons between the flight test and simulation acceleration data provided the objective function that was used in the machine learning genetic algorithm search to identify the coefficients in the random turbulence model. This will be referred to as the Turbulence Identification method.

2. RELATIVE POSITION MEASUREMENT
One unique aspect of the flight test program was the use of a carrier-phase, moving base, differential GPS system to measure the relative position between the two aircraft in real time. The sign conventions and axis definitions for the system, referred to as the Relative Position Measurement System (RPMS), are shown in Figure 1. Figure 2 shows the refueling envelope that was tested.

A GPS base station located on the tanker acted as the
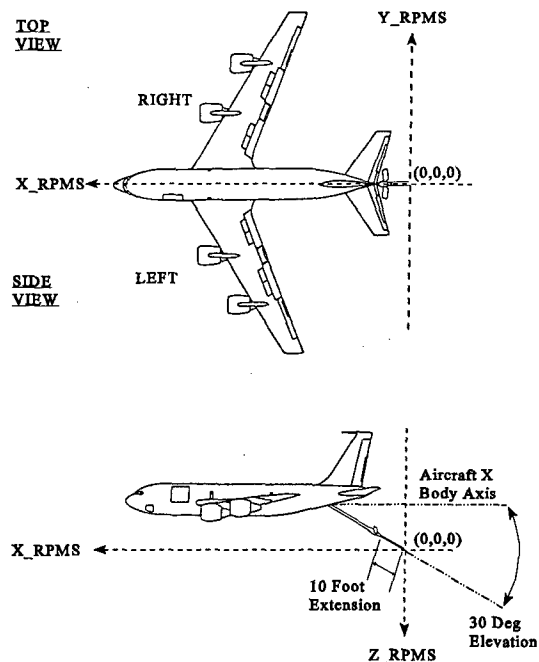
Note: RPMS Measurements Are From The Boom Tip In Trail Position to the UARRSI of the Receiver Aircraft. Trail Position = 0° Azimuth, 30° Elevation, and 10 ft Extension.

Fig 1 - RPMS Coordinated System Definition

moving base for the differential GPS position calculations. A similar system on the receiver aircraft was used to determine its position using a common set of satellites for the two aircraft. By using carrier phase GPS measurements, two to five cm accuracy levels can be achieved for position measurements after proper system initialization. More detail on differential GPS techniques and carrier phase calculations can be found in References 2 and 3, respectively.

The GPS relative position was translated through a coordinate transformation into coordinates relative to the distance from the tip of the boom (std ref pos) and the refueling receptacle on the receiver. Data, including GPS and attitude data from the tanker, necessary for this transformation was exchanged between the two aircraft through the use of a radio modem link. The resulting relative position data was displayed in real time on the receiver with a 4 Hz update rate. A small lag in the system of only a quarter of a second was present due to data transfer time and calculation time.

3. COEFFICIENT TRIM METHOD
By matching the trim condition at each simulation time segment using flight test recorded states and surface positions, it is possible to determine the total residual force or moment values that are needed to match the simulation to the flight test data. This method attributes all the variation between the simulation and the flight test data into one aerial refueling delta coefficient for each force and moment. Provided that the free-air simulation model for each respective aircraft matches free-air recorded flight test points, it is an accurate measure of the gross aerodynamic changes influencing the tanker or the receiver during aerial refueling.
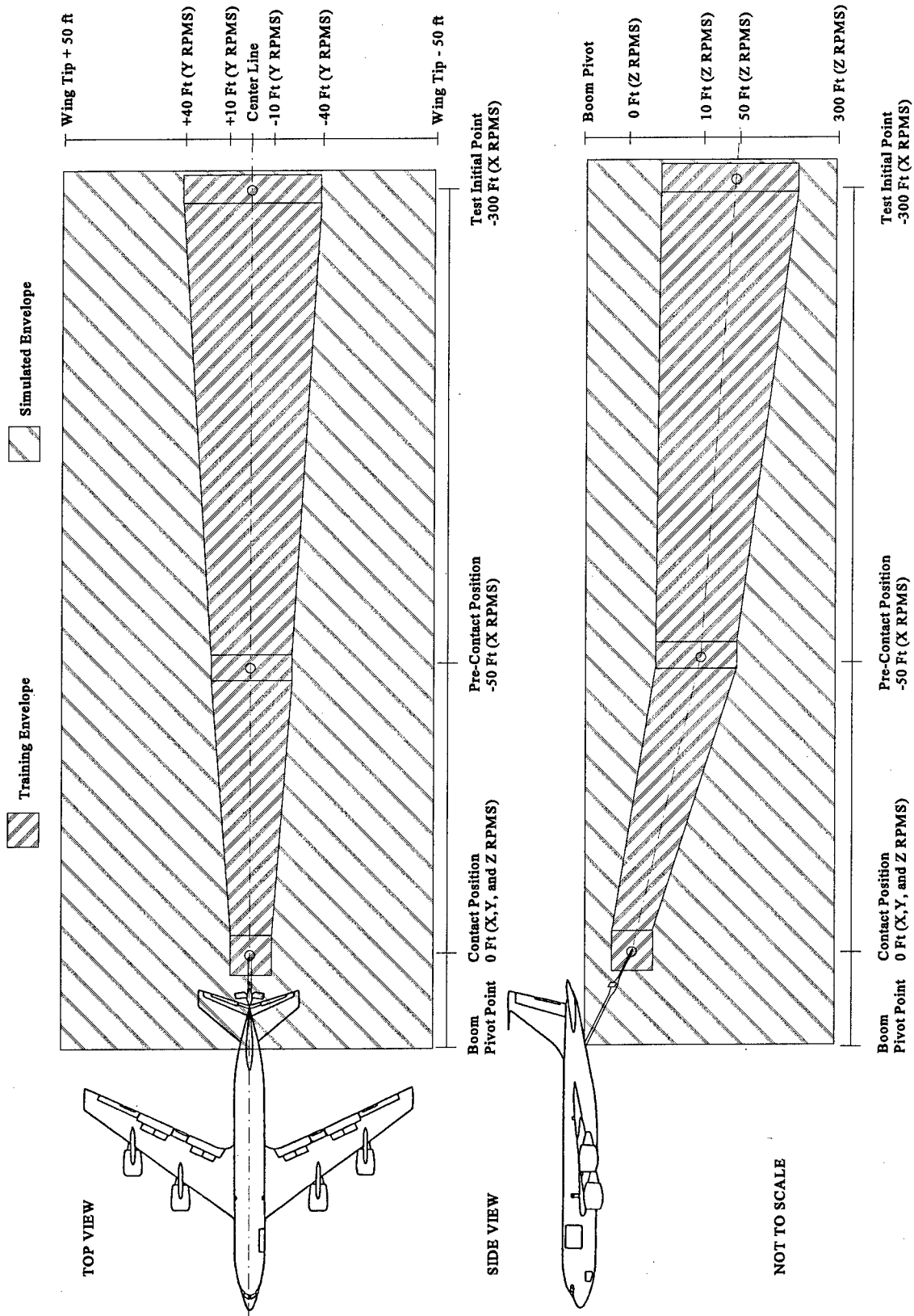
TOP VIEW

SIDE VIEW

NOT TO SCALE

Wing Tip + 50 ft

+40 Ft (Y RPMS)

+10 Ft (Y RPMS)

Center Line

-10 Ft (Y RPMS)

-40 Ft (Y RPMS)

Wing Tip - 50 ft

Boom Pivot

0 Ft (Z RPMS)

10 Ft (Z RPMS)

50 Ft (Z RPMS)

300 Ft (Z RPMS)

Simulated Envelope

Training Envelope

Test Initial Point
-300 Ft (X RPMS)

Pre-Contact Position
-50 Ft (X RPMS)

Contact Position
0 Ft (X, Y, and Z RPMS)

Boom
Pivot Point

Fig 2 - Typical Aerial Refueling Envelope

The standard Newtonian expressions for the conservation of angular and linear momentum yield the following standard set of equations of motion for a rigid aircraft in motion:

$$m(\dot{U}-VR+WQ)=-mg\ \sin(\theta)+F_{A_x}+F_{T_x} \qquad drag \quad (1)$$

$$m(\dot{V}+UR-WP)=mg\ \sin(\varphi)\ \cos(\theta)+F_{A_y}+F_{T_y} \quad sideforce(2)$$

$$m(\dot{W}-UQ+VP)=mg\ \cos(\varphi)\ \cos(\theta)+F_{A_z}+F_{T_z} \quad lift \quad (3)$$

$$I_{xx}\dot{P} - I_{xz}\dot{R} - I_{xz}PQ + (I_{zz} - I_{yy})RQ=L_A+L_T \quad roll \quad (4)$$

$$I_{yy}\dot{Q} + (I_{xx} - I_{zz})PR + I_{xz}(P^2 - R^2)=M_A+M_T \quad pitch \quad (5)$$

$$I_{zz}\dot{R} - I_{xz}\dot{P} + (I_{yy} - I_{xx})PQ + I_{xz}QR=N_A+N_T \quad yaw \quad (6)$$

The sum of the forces and moments on the right side of equations 1-6 above can be broken into functional dependencies for the different aircraft states and control surface deflections. For example, the dependencies for the aerodynamic pitching moment, M_A, can be written as follows:

$$M_A = C_M \ \bar{q} \ S \qquad (7)$$
where:
$$C_M = C_{M_o} + C_{M_\alpha}\alpha + C_{M_{i_H}}i_H + C_{M_{\delta_e}}\delta_e \qquad (8)$$

By adding an additional aerial refueling delta coefficient to each equation of motion it was possible to identify residual forces and moments that would allow the simulation trim condition to match the flight test data trim state. For example, pitching moment equation 7 now becomes:

$$C_M = C_{M_o} + C_{M_\alpha}\alpha + C_{M_{i_H}}i_H + C_{M_{\delta_e}}\delta_e + \Delta C_{M_{AR}} \qquad (9)$$
where:
$$\Delta C_{M_{AR}} Caused \ by \ AR \ Flowfield$$

Before determining the large aerodynamic influences present during aerial refueling, the free air model for each aircraft was compared to recorded free air flight test data points. Simulation and flight test data for the free air points were overlaid and evaluated with a proof of match criteria similar to those used for acceptance of existing simulation training devices, such as presented in Reference 4.

After the tanker and receiver free air simulation models were determined to be accurate representations of the aircraft, data from the aerial refueling flight test points were analyzed. Several effects were present during refueling on both the tanker and receiver that needed to be quantified.

Initially, the receiver flight test data from the refueling points indicated that there was a steady downwash component present, as indicated by a mismatch between the trim angle of attack calculated by the simulation and the recorded data. The receiver trimmed in flight as if it were in a climb, despite having a zero rate of climb. This downwash was quantified using the SMACK program (Ref 5) and implemented into the simulation by adding a z velocity component to the trim condition as a function of the receiver position behind the tanker. The result was a match between the simulation and flight test recorded trim angle of attack, pitch angle, and climb rate.

After identifying the proper downwash components and

implementing them into the simulation models, the other large aerodynamic effects were analyzed. They included bow wave effects from the receiver on the tanker, tanker flow field effects on the receiver, and boom aerodynamic effects on both aircraft.

The process used to identify the large aerodynamic coefficients needed to mimic the flow field effects on both the tanker and receiver is conceptually presented in Figure 3.
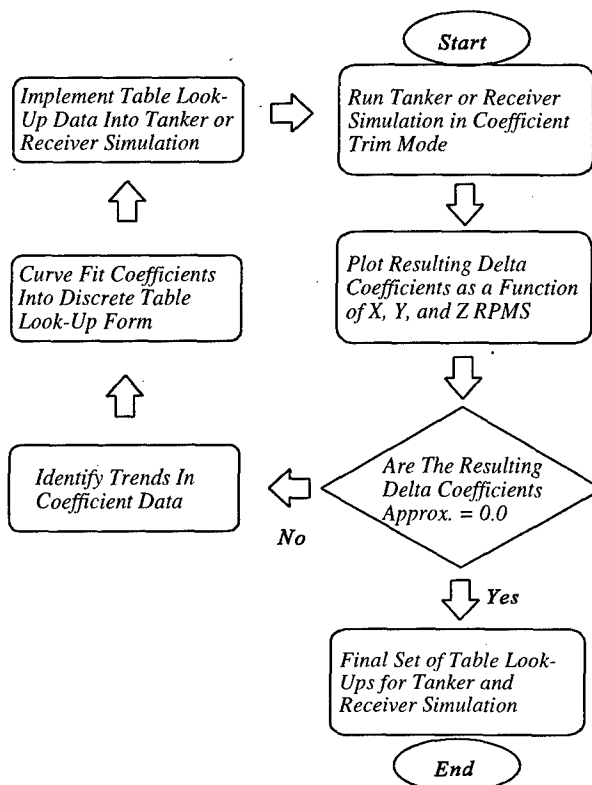

Fig 3 - Coefficient Trim Process Flow Diagram

First, the tanker or receiver simulation was used to trim the equations of motion at 5 second intervals for the duration of each recorded flight test maneuver. From these trim windows, values of residual forces and moments were calculated from the equations of motion. The residual forces and moments were non-dimensionalized into aerodynamic delta coefficients and were sorted and plotted as a function of position in the flow field and aircraft test configuration.

After sorting the data, plots were used to study the data and identify trends in the data. Clear trends were identifiable in the data. The trends allowed coefficient tables to be created and implemented as look-ups in the simulation. By implementing the deltas back into the simulation, the desire was to re-run the piece-wise equation of motion trims and iterate until the identified delta values were all zero.

Figure 4 shows the calculated values of AR induced ΔCM for the tanker for a closure maneuver where the receiver closes from 300 ft aft of the tanker into the contact position.
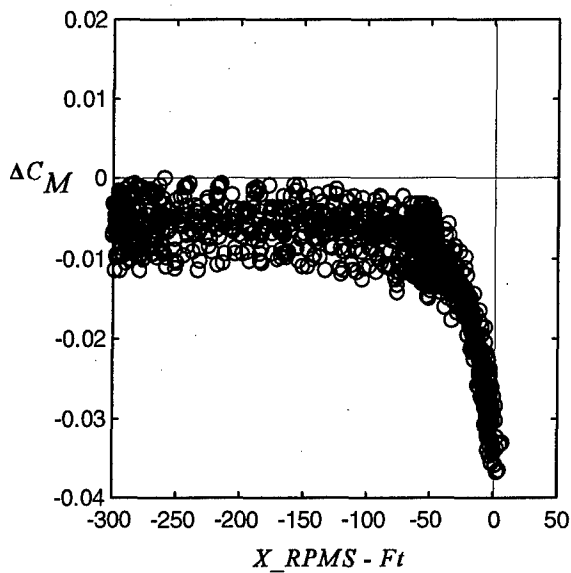
Fig 4 - ΔC_M due to bow wave effects
(Tanker)

The trend in pitching moment as a function of x_rpms shows that the bow wave of the receiver induces a nose down pitching moment on the tanker at about 100 ft aft. As the receiver closes, the influence gets stronger. The bow wave effects are caused by up-wash from the receiver that changes the angle of attack of the tail surfaces on the tanker.

Figure 5 shows the resulting ΔCM after the iterative process shown in Figure 3 was used to arrive at the final set of table look-ups that were then added back into the simulation.
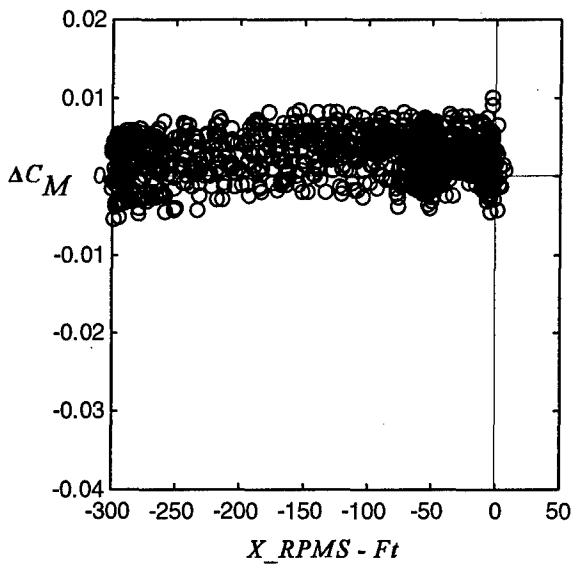
Fig 5 - ΔC_M After Table Implementation
(Tanker)

The final result is a near-zero value for all the ΔCM values, with some scatter due to the flight test data being taken by different pilots on several flights.

Similarly, Figure 6 shows ΔCl values identified from recorded data on the receiver during lateral flow field sweeps behind the tanker.
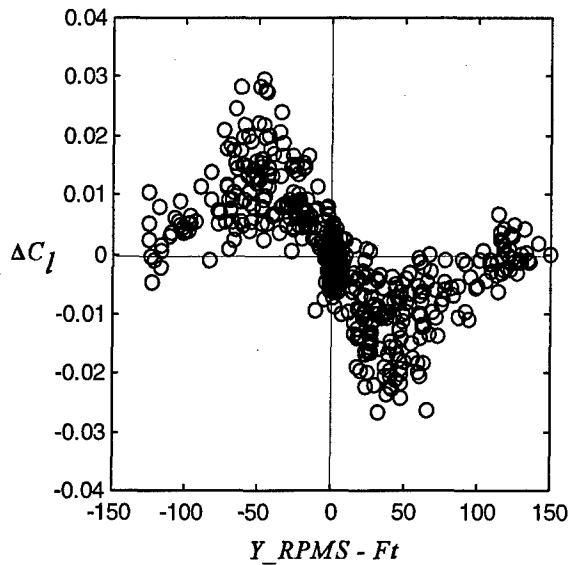
Fig 6 - ΔC_l During a Lateral Sweep
(Receiver)

The plot shows that there is a rolling moment towards the center of the flow field. This rolling moment is strongest near the wing tip of the tanker at +/-65 ft y_rpms. The flow field rolling moment effects are induced by the tanker wing tip vorticies changing the lift distribution on the wing of the receiver.

By curve fitting the data into table look-ups and implementing them back into the simulation as a function of relative position, the flow field effects are accounted for. Figure 7 shows the same set of data after the ΔCl coefficient tables are added back into the simulation using the iterative process outlined in Figure 3.
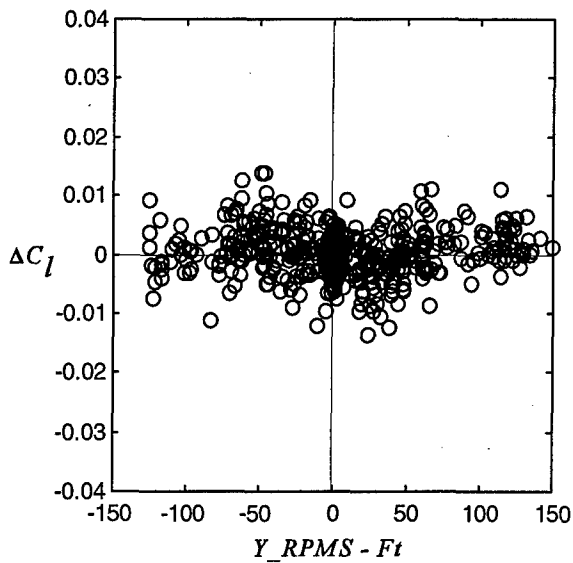

Fig 7 - ΔC_l After Table Implementation
(Receiver)

A similar process was used to identify values for other force and moment influences on both the receiver and the tanker during refueling.

4. TURBULENCE IDENTIFICATION METHOD

To identify the proper power spectrum of random velocity components present in the flow field during refueling, acceleration data was recorded at a 300 Hz sample rate during the flight test program. This data was then analyzed using frequency domain analysis techniques. A random turbulence model in the simulation was used to reproduce the same power spectrum for each of the measured accelerations. Machine learning software was used to automate the search process to identify the proper model coefficients in the simulation random turbulence model.

The random turbulence model used was based on the standard NASA Dryden turbulence model. More detail on the Dryden model is available in Reference 6. It is listed as follows in spatial frequency form, Ω:

$$\Phi_u(\Omega) = \sigma_u^2 \frac{2}{\pi} L_u \frac{1}{1+(L_u \Omega)^2} \qquad X \ Axis \ Turbulence \quad (10)$$

$$\Phi_v(\Omega) = \sigma_v^2 \frac{L_v}{\pi} \frac{1+3(L_v \Omega)^2}{[1+(L_v \Omega)^2]^2} \qquad Y \ Axis \ Turbulence \quad (11)$$

$$\Phi_w(\Omega) = \sigma_w^2 \frac{L_w}{\pi} \frac{1+3(L_w \Omega)^2}{[1+(L_w \Omega)^2]^2} \qquad Z \ Axis \ Turbulence \quad (12)$$

These random turbulence equations were converted into the Laplace domain and then into the time domain, with scaling in the resulting equations to account for the simulation sample rate. Though the Dryden model was originally designed to model isotropic atmospheric turbulence, it can also be used to model anisotropic turbulence, which is why the models are broken into an equation for each axis.

The turbulence equations were implemented by adding the velocity components from the random turbulence model to the simulation body axis velocity components at every simulation time step. The magnitude and frequency of the resulting gust component field depends on the values of the RMS gust intensity, σ, and the gust scale length, L, for each axis.

It is possible to verify the magnitude and frequency of the random turbulence components by using FFT methods to calculate a PSD of the flight test and simulation recorded accelerations. The PSD is defined as the modulus-squared of the FFT, therefore the FFT is calculated by:

$$F[x(n)] = \sum_{n=0}^{N-1} X(n)e^{k} \qquad (13)$$

where:

$$k = \frac{-i2\pi n}{N} \qquad (14)$$

The modulus-squared is:

$$R_x(i) = \sum_{n=0}^{N} x(n) \ x^*(n) \qquad (15)$$

where the x^* represents the complex congugate of x

The resulting PSD data was then compared to similar data calculated by the simulation for each axis. This method is commonly used to validate frequency response of aircraft training devices, such as presented in Reference 7.

By finding an optimal set of turbulence equation coefficients for the simulation turbulence models, it is possible to match the power spectra for the acceleration data from both sources. It can then be assumed that the simulation random turbulence model is accurately reproducing disturbances present during the flight test.

A genetic algorithm search method was used to identify the optimum RMS gust intensity, σ, and the gust scale length, L, for each axis that reproduced the power spectrum of the measured acceleration data from flight test.

5. GENETIC SEARCH TECHNIQUE

Genetic algorithms lend themselves well to complex optimization problems because they operate on probabilistic rules of convergence and not on deterministic ones. In other words, it is not necessary to calculate objective function derivative information with respect to the independent variables present in a given optimization problem. This simplifies the complexity of the type of calculations that must be done for a given problem. Genetic algorithms search a solution space in a quasi-random fashion using numerous simulation iterations. They have been extensively applied to complex optimization problems related to aerospace. References 8 and 9 are just two examples. A complete presentation of genetic algorithm theory is available in Reference 10

The implementation of the genetic algorithm for the turbulence coefficient identification involved coding the three gust intensity and three scale length values into a binary format that could be operated on by the algorithm. The range for RMS gust intensity and gust scale solutions was chosen to sufficiently cover all reasonable turbulence levels, from zero turbulence to severe thunderstorm turbulence levels. The genetic algorithm loop used to identify the intensity and scale length values for each flight test point is conceptually presented in Figure 8.

After coding independent variables into a binary format, an objective function was designed to "teach" the program what a good solution was. This involved doing FFT evaluations on the accelerations from each axis. The resulting PSD data was used in the evaluation of the objective function to be optimized.

The receiver simulation was run over the entire length of a recorded flight test run, using flight test states and control deflections. The simulation evaluated the possible solutions present in each generation of the genetic search and passed the results on to the next generation. Selection, crossover, and mutation were all used in the genetic algorithm to create a new population of possible solutions. Subsequent generations resulted in an improved set of solutions until a final optimal set of solutions was reached. The final solution resulted in a set
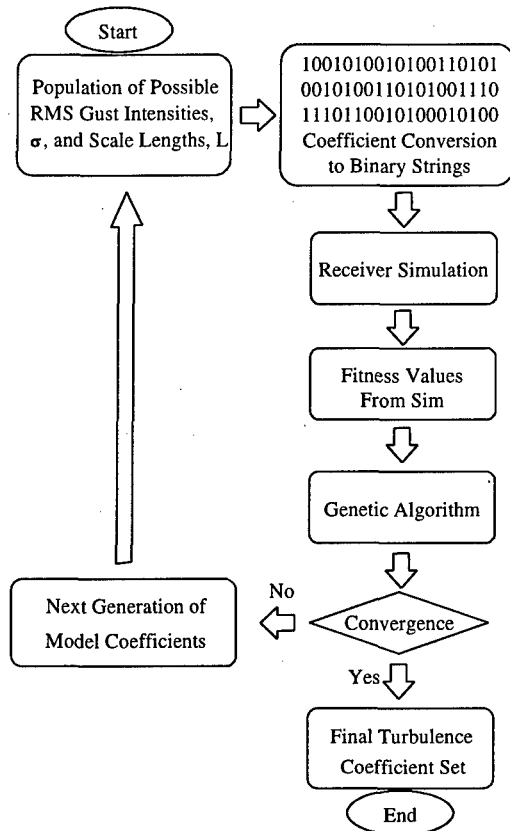
Fig 8 - Genetic Algorithm Search Block Diagram

The plot shows a comparison of flight test and simulation data. It is clear from this plot that there is a significant amount of activity that is not represented by the basic simulation model.

Similarly, Figure 10 shows the same flight test run and simulation data with the random turbulence model turned on. A comparison between the two sets of data shows that the random turbulence model is capable of reproducing a similar spectrum of recorded acceleration data as was recorded during flight test.
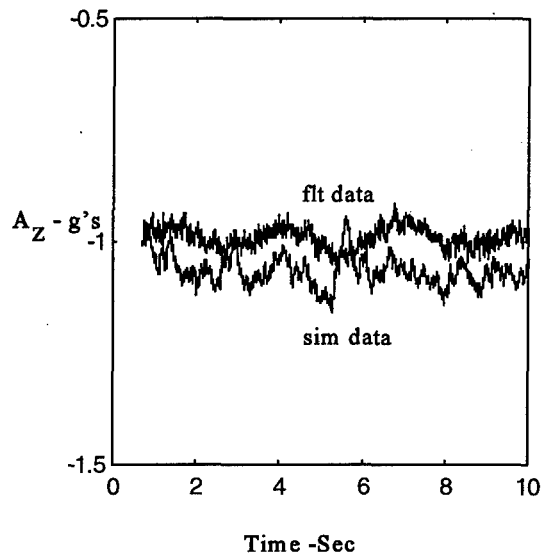
Fig 10 - Acceleration Data With Turbulence ON
(Receiver)

of gust intensity and scale length coefficients that closely reproduced the power spectrum of random turbulence present in the recorded flight data for each simulation run.

The identified coefficients were then implemented back into the simulation as a function of position in the flow field, which allowed the modeled turbulence level to change as the receiver moves through the flow field.

Figure 9 shows a receiver acceleration trace recorded during a pre-contact position (50 ft aft) refueling point.

6. RESULTS AND DISCUSSION

The resulting models implemented in the simulations of both the tanker and receiver aircraft provided very good matches between the recorded flight test data and each simulation. The data shown in Figures 11 through 14 demonstrate that the Coefficient Trim method was capable of identifying the large aerodynamic deltas needed to reproduce the effects of the receiver bow wave on the tanker and the tanker flow field effects on the receiver.

Figure 11 shows tanker time history data for a closure run from the pre-contact position at 50 ft aft into the contact position. The plot represents the simulation results before implementation of the AR delta coefficients back into the simulation. The time history traces show that the elevator deflection is not within the required one degree tolerance, which indicates that the bow wave effect is not properly accounted for.

Figure 12 shows the same run after table look-ups are added in to account for ΔCM_{AR} due to the receiver bow wave. The tanker elevator time history is now within tolerance and the trends match those recorded during flight test.

Figures 13 and 14 show receiver time history data of a lateral flow field sweep before and after the aerodynamic deltas have been added. The time history data in Figure 13 shows that the rolling moment effects induced on the receiver by the tanker wing vortex sheet are not accounted

Fig 9 - Acceleration Data Without Turbulence
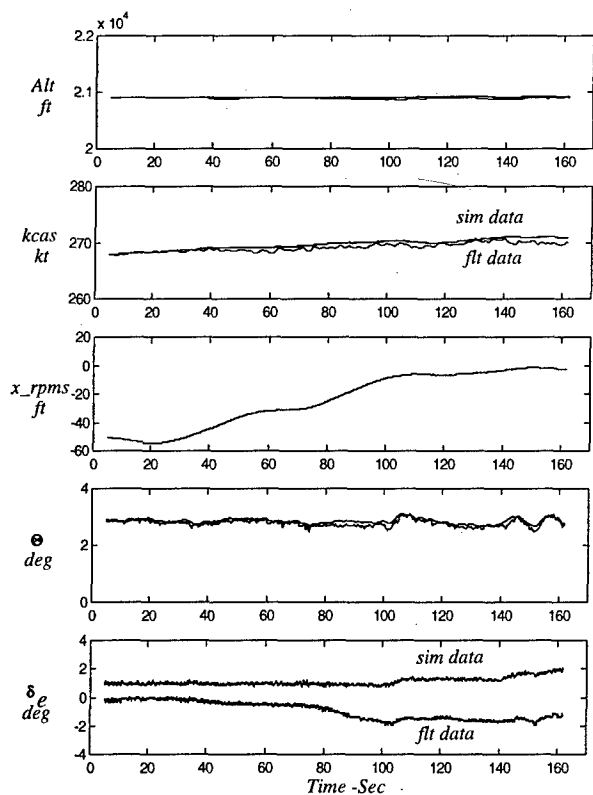(Receiver)

Fig 11 - Closure Data Before Deltas Added
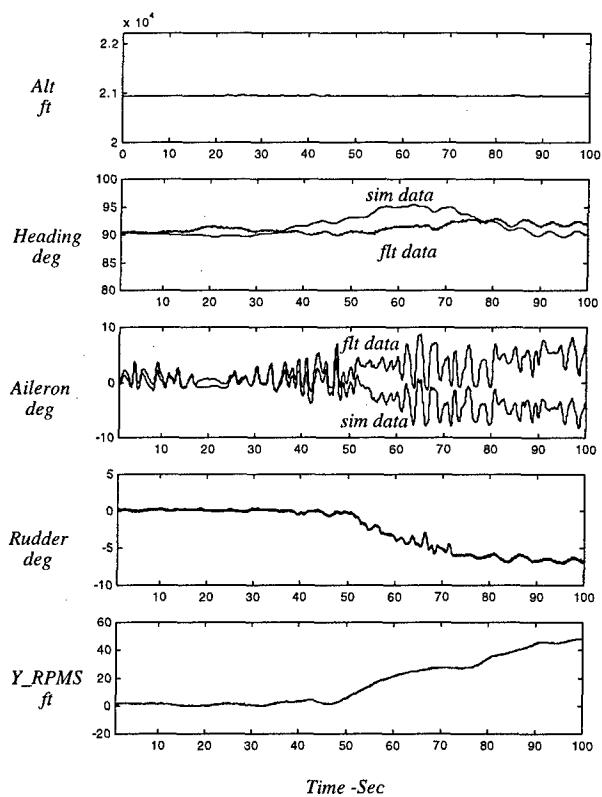(Tanker)

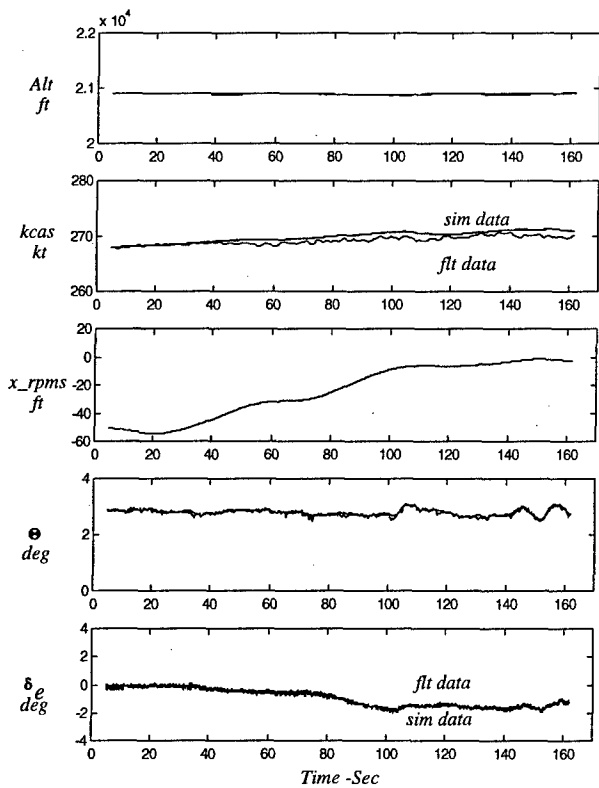Fig 13-Lateral Data Before Deltas Added
(Receiver)

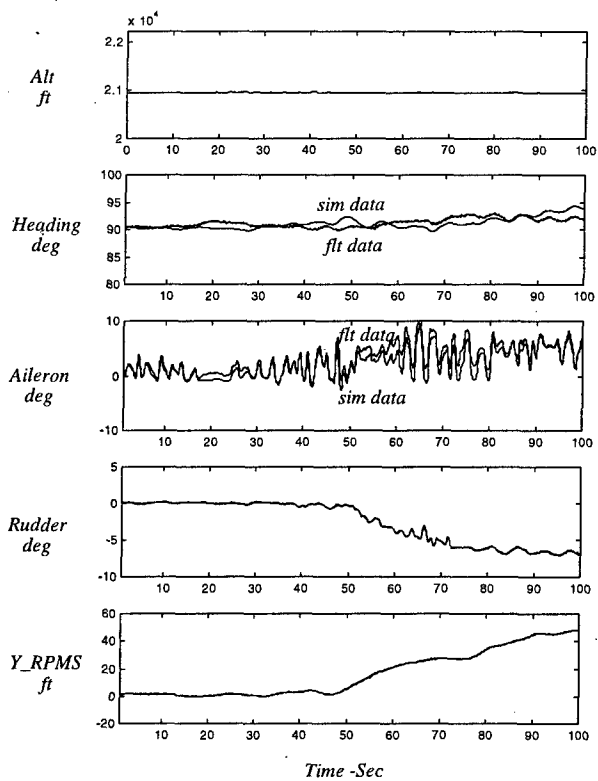Fig 12 - Closure Data After Deltas Added
(Tanker)

Fig 14-Lateral Data After Deltas Added
(Receiver)

for properly. This is evident from the large differences in aileron deflection as the receiver moves to higher Y_RPMS positions.

After identifying the proper aerodynamic deltas and implementing them in the receiver simulation, Figure 14 shows that the rolling moment effects were properly accounted for, as evidenced by improved match in the aileron trace during the sweep.

The turbulence models implemented in the simulation also provided excellent reproduction of the flight test data. Figure 15 shows the PSD of normal load factor, or a_z, on the receiver for a pre-contact position point. It is evident from the plot that the higher frequency data that was present during refueling is not reproduced by the basic simulation.
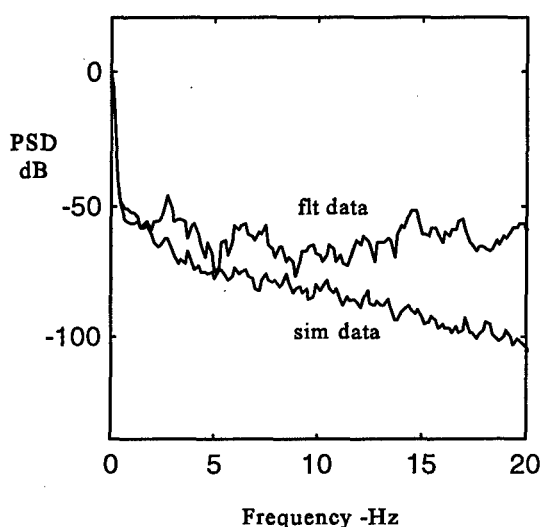
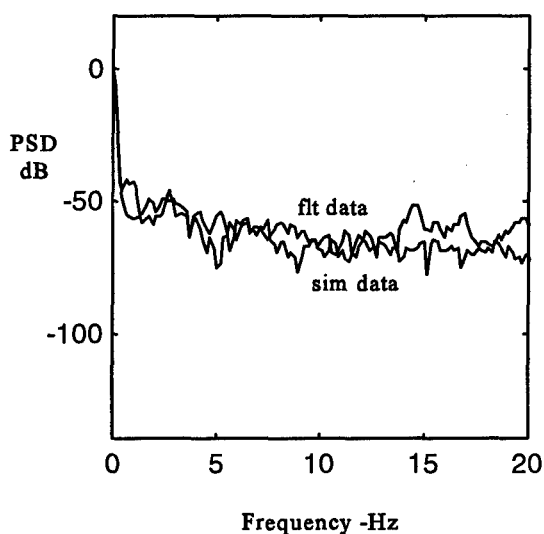Fig 15 - PSD of A_z Data - No Turbulence Model (Receiver)

Fig 16 - PSD of A_z Data - With Turbulence Model (Receiver)

Figure 16 shows that the PSD of the simulation data matches that of the recorded flight test data after implementing the turbulence model with the proper gust scale length and intensity factors for each position,

7. CONCLUSIONS AND RECOMMENDATIONS

The Figures presented show that the PID methods presented are capable of identifying the large aerodynamic changes and random turbulence components associated with aerial refueling as an alternative to traditional PID methods. The following conclusions can be drawn from the results presented:

1. Quasi-steady state recorded flight test data can be analyzed by evaluating the equations of motion in an iterative fashion to identify aerodynamic information from the data.

2. Random turbulence recorded during flight test can be reproduced accurately in simulation by using relatively simple model equations.

3. The complex aerodynamic effects from aerial refueling can be described by simple multi-dimensional table look-ups, making implementation into existing simulation training devices simple and portable.

3. Advances in computational power for computers have made it possible to develop iterative analysis tools that can solve problems that formerly required a large number of man-hours to accomplish. For example, the use of a genetic algorithm search to identify the turbulence coefficients from recorded accelerometer data exploited computer power and required very little intervention to achieve a final solution once the tool was mature.

The following recommendations are made as a result of this study:

1. The identified models for both the aerodynamic changes and turbulence associated with aerial refueling need to be implemented into existing training devices for pilot evaluation.

2. The Coefficient Trim method and the Turbulence Identification method should be applied to other aircraft combinations to validate the approach and determine if the approach is robust.

8. REFERENCES

1. Shaw, Jay; Gerken, Fred; "Fight Data Collection and Analysis for KC-135R/C-141B Aircraft Pair - Volume IV - Executive Summary" Simtec Inc., Manassas, Virginia, Sept 15, 1997.

2. Wells, David, *Guide to GPS Positioning*, Canadian GPS Associates, Ottawa, Canada, 1987.

3. Cosandier, D. and Martell, H., "Moving Base GPS Surveys", Waypoint Consulting, Inc., March, 1996.

4. "Airplane Simulator Qualification, FAA Advisory Circular AC 120-40B", Federal Aviation Administration, US Dept. Of Transportation, July 29, 1991.

5. Bach, Ralph E., "State Estimation Applications in Aircraft Flight-Data Analysis, A Users Manual for SMACK", NASA Reference Publication 1252, NASA Ames Research Center, Moffett Field, California, 1991.

6. Houbolt, John C., Stiener, Roy, Pratt, Kermit G., "Dynamic Response of Airplanes to Atmospheric Turbulence Including Data on Input Response", NASA Technical Report, TR R-199, June 1964.

7. Miller, C and Vandervliet, G., "Shipboard Mission Training Effectiveness of the Naval Air Warfare Center's V-22 Government Test Pilot Trainer", AIAA 92-4130, Aug. 1992.

8. Dike, B.A. and Smith, R.E., Application of Genetic Algorithms to Air Combat Maneuvering, The Clearinghouse for Genetic Algorithms, report no. 93002, U. of Alabama, Aug. 23, 1993.

9. Ryan, G.W., A Genetic Search Technique for Identification of Aircraft Departures, NASA CR-4688, 1995.

10 Koza, J.R., *Genetic Programming: On the Programming of Computers by means of Natural Selection*, MIT Press, Cambridge, Mass., 1992.

ADVANCES IN EXPERIMENT DESIGN
FOR HIGH PERFORMANCE AIRCRAFT

Eugene A. Morelli

Dynamics and Control Branch
MS 132, NASA Langley Research Center
Hampton, Virginia 23681 - 2199 USA

SUMMARY

A general overview and summary of recent advances in experiment design for high performance aircraft is presented, along with results from flight tests. General theoretical background is included, with some discussion of various approaches to maneuver design. Flight test examples from the F-18 High Alpha Research Vehicle (HARV) are used to illustrate applications of the theory. Input forms are compared using Cramér-Rao bounds for the standard errors of estimated model parameters. Directions for future research in experiment design for high performance aircraft are identified.

LIST OF SYMBOLS

a_y, a_z	linear accelerations, g's
$E\{\ \}$	expectation operator
J	cost function
L, M, N	body axis aerodynamic moments
M	information matrix
N	total number of sample times
p, q, r	body axis angular velocities, rad/sec
R	discrete noise covariance matrix
$S(i)$	output sensitivity matrix at time $i\Delta t$
T	maneuver duration, sec
u	n_i-dimensional control vector
V	airspeed, ft/sec
x	n_s-dimensional state vector
y	n_o-dimensional output vector
$y(i)$	output vector at time $i\Delta t$
$z(i)$	measured output vector at time $i\Delta t$
Y, Z	body axis aerodynamic forces
α	angle of attack, rad
β	sideslip angle, rad
δ_{ij}	Kronecker delta
Δt	sampling interval, sec
δ_a	aileron deflection, rad
δ_r	rudder deflection, rad
δ_s	stabilator deflection, rad
ϕ, θ, ψ	Euler angles, rad
η_e	longitudinal stick deflection
η_a	lateral stick deflection
η_r	rudder pedal deflection

μ_j	jth input amplitude constraint
$v(i)$	ith discrete measurement noise vector
θ	n_p-dimensional parameter vector
θ_j	jth model parameter
σ_j	Cramér-Rao bound for the jth parameter
τ_a	lateral stick equivalent time delay, sec
τ_r	rudder pedal equivalent time delay, sec
ξ_k	kth output amplitude constraint
$\forall$	for all, for every
Tr	trace

Superscripts

T	transpose
-1	matrix inverse

Subscripts

o	average or trim value
s	stability axis

1. INTRODUCTION

Aircraft flight tests designed to collect data for modeling purposes are generally motivated by one or more of the following objectives:

1. The desire to correlate aircraft aerodynamic characteristics obtained from wind tunnel experiments and aerodynamic calculations with flight test data.

2. Refinement of the aircraft model for control system analysis and design.

3. Accurate prediction of the aircraft response using the mathematical model, including flight simulation and flight envelope expansion.

4. Aircraft acceptance testing.

The design of an experiment to achieve any of the above objectives involves specification of the instrumentation, the signal conditioning, the flight test operational procedure, the inputs for the flight test maneuver, the model structure, and the data analysis methods. In this work, the maneuver design – specifically, design of flight test input signals – will be studied independently of the other aspects which impact the success of the flight test.

The flight test maneuver (equivalently, the flight test input) has a major impact on the quality of the data for modeling purposes. Designing an input for accurate model parameter estimation requires rich excitation of the system, which is frequently at odds with various practical constraints. One such practical constraint is the requirement that output amplitude excursions (e.g., in angle of attack or sideslip angle) about the flight test condition be limited in order to assure the validity of an assumed model structure. Input amplitudes must be constrained for the same reasons, and to avoid nonlinearities such as mechanical stops and rate limiting when the model is linear. These practical constraints translate to amplitude constraints on the inputs and outputs during the flight test.

Tests for high performance aircraft often involve flight at high angles of attack, sometimes using drop models. In these cases, flight test time is extremely limited due to rapid altitude loss, and it is imperative that information content in the data per unit of flight time be maximized for effective use of expensive flight test time. Such considerations highlight the importance of optimizing the flight test inputs.

In general, an aircraft model contains multiple response variables, multiple aircraft model parameters, and one or more inputs. The overall goal is to design a maneuver that produces data from which model parameters can be estimated accurately. This translates into exciting the system modes so that the sensitivities of the model outputs to the parameters are high and correlations among these sensitivities are low. Frequency sweep inputs[1] can be used to do this, requiring little more than knowledge of the frequency range of interest for the modeling. This technique is restricted to moving a single input at a time, so that off-axis responses or coupled motions are generally not well modeled from frequency sweep data. Frequency sweeps also require relatively long maneuver times (i.e., 1-2 minutes) to run through the frequency range of interest. Low frequency components of the frequency sweep contribute to long maneuver times, and also increase the tendency for the aircraft to depart from the desired flight test condition. For high performance aircraft, limited flight test time, multiple control effectors, and flight conditions such as high angle of attack make the frequency sweep approach difficult to use and expensive.

An alternate approach is to take advantage of *a priori* knowledge about the dynamics of the aircraft to focus the input energy at frequencies near the system modes. An *a priori* model can be assembled using wind tunnel aerodynamic data and knowledge of rigid body dynamics and the control system. With the *a priori* model, a short flight test maneuver can be designed to produce data with high information content. Resulting flight test data can be analyzed using a variety of methods in the time and frequency domains. A paradox occurs here, in that very good inputs will be designed when the *a priori* model is very good; however, in this case the experiment is less needed. Obviously, the input design technique must be robust to errors in the *a priori* model.

Designing an input that excites the aircraft dynamic response as much as possible when modal frequencies are imperfectly known, while simultaneously satisfying practical constraints, is a difficult problem. Several researchers have studied the problem of finding optimal inputs for aircraft parameter estimation[2-11]. The most serious obstacles to using the results of these studies in flight have been practical implementation issues. These include unrealizable optimal input forms, and failure to account for closed-loop control, actuator dynamics, or constraints on input and output amplitudes. Computationally, the difficulties have been selection of an appropriate optimality criterion, inadequate numerical optimization techniques for finding global optimal solutions, and difficulties associated with multiple input design.

Recent research[12-16] has produced an optimal input design technique which addresses the above issues. The technique generates square wave inputs which are globally optimal in the sense that information content in the data is maximized for a fixed flight test time, or, alternatively, specified parameter accuracy goals are achieved in minimum flight test time.

The global optimal square wave input design technique has been shown to be theoretically sound[12,13], has been validated in flight for aerodynamic model parameter estimation experiments using pilot implementation, including demonstrated higher parameter accuracies compared to compound doublet inputs[14], has been used successfully to specify flight test maneuvers for closed loop model identification at high angles of attack[15], has shown improved parameter accuracy in comparison to doublet and 3-2-1-1 inputs in flight tests[16], and has compared favorably to other techniques in the literature for a standard test problem[17]. In Ref. [17], the global optimal square wave input produced the lowest value of the sum of estimated parameter variances, even though the maneuver time allotted for this design was the smallest of any of the techniques studied (see Table 3 of Ref. [17], p. 281). This fact, though not pointed out by the authors of Ref. [17], demonstrates the effectiveness of the global optimal square wave input design technique.

The purpose of this work is to give an overview of NASA research on optimal input design for high performance aircraft, and to present relevant flight test results. The next section outlines the theory involved in optimal input design, and discusses the choices made in developing the global optimal square wave input design technique. Next, the F-18 High Alpha Research Vehicle (HARV) test aircraft and some details of flight test procedure are described. Following this, results from selected flight tests are presented and discussed.

2. THEORETICAL DEVELOPMENT

Airplane dynamics can be described by the following linear model equations:

$$\dot{x}(t) = Ax(t) + Bu(t) \tag{1}$$

$$x(0) = x_o \tag{2}$$

$$y(t) = Cx(t) + Du(t) \tag{3}$$

$$z(i) = y(i) + v(i) \quad i = 1, 2, \ldots, N \tag{4}$$

Linear models are used in Eqs. (1) and (3) because of the common practice of estimating stability and control derivatives from flight test data collected at a chosen flight condition. Elements of the system matrices A, B, C, and D contain stability and control derivatives, which are the unknown model parameters to be estimated from flight test data. If the maneuver is designed for small perturbations of the inputs and outputs about a chosen flight condition, the stability and control derivatives can be assumed constant. Measurement noise $v(i)$ is assumed Gaussian with

$$E\{v(i)\} = 0 \text{ and } E\{v(i)v(j)^T\} = R\delta_{ij} \tag{5}$$

Eqs. (1)-(5) can be used to characterize bare airframe dynamics, where the inputs are control surface deflections and the outputs can include air data (V, α, β), body axis angular velocities (p, q, r), Euler angles (ϕ, θ, ψ), and translational accelerations (a_x, a_y, a_z). The same general model structure can be used to characterize closed loop dynamics, where the inputs are pilot stick and rudder deflections and the outputs are selected from the same list as before. For closed loop modeling, the input includes a pure time delay τ, called the equivalent time delay, to account for phase lag effects from sources such as high order control system dynamics, digital sampling delay, and actuator dynamics. For either bare airframe or closed loop modeling, longitudinal and lateral cases are treated separately, with the linear model structure shown above resulting from the usual small perturbation assumptions.

Constraints arising from practical flight test considerations can be represented as limits on all input amplitudes and selected output amplitudes. Input amplitudes are limited by mechanical stops, flight control software limiters, rate limits, or linear control effectiveness. Selected output amplitudes must be limited to avoid departure from the desired flight test condition and to ensure validity of the assumed linear model structure. In addition, constraints may be required on aircraft attitude angles for flight test operational considerations, such as flight safety and maintaining line of sight from the downlink antenna aboard the aircraft to the ground station. These constraints are specified by

$$\left| u_j(t) \right| \leq \mu_j \quad \forall t \quad j = 1, 2, \ldots, n_i \tag{6}$$

$$\left| y_k(t) \right| \leq \xi_k \quad \forall t \quad k \in (1, 2, \ldots, n_o) \tag{7}$$

where μ_j and ξ_k are positive constants.

Some researchers have implemented practical flight test constraints using an energy constraint on the input,

$$\int_0^T u(t)^T u(t)\, dt = E \tag{8}$$

where E is some fixed value of the allowable input energy, chosen by experience or intuition. This constraint is intended to limit input and output amplitudes, but it is also chosen for convenience in the optimization. Input energy is typically introduced as a constraint on the input form, while the cost function quantifying achievable model parameter accuracy based on the data is optimized using variational calculus to arrive at an optimal input design. In practice, there is no direct constraint on the amount of input energy which can be applied during the flight test, since neither the pilot nor the control system have inherent energy limitations. The practical flight test situation dictates that the constraints be directly on the amplitudes of both the input and the output variables, as given by Eqs. (6) and (7), respectively. The constraint in Eq. (8) limits the input and output amplitudes indirectly with an integral expression.

When estimating model parameter values from measured data, the minimum achievable parameter standard errors using an asymptotically unbiased and efficient estimator (such as maximum likelihood) are called the Cramér-Rao lower bounds[12,18,19]. The Cramér-Rao lower bounds for the parameter standard errors are computed as the square root of the diagonal elements of the dispersion matrix $\mathcal{D}$ [12,18,19]. The dispersion matrix is defined as the inverse of the information matrix M, the latter being a measure of the information content of the data from an experiment. The expressions for these matrices are

$$M = \sum_{i=1}^{N} S(i)^T R^{-1} S(i) \tag{9}$$

$$\mathcal{D} = M^{-1} \tag{10}$$

where $S(i)$ is the matrix of output sensitivities to the parameters,

$$S(i) = \left. \frac{\partial y(i)}{\partial \theta} \right|_{\theta = \hat{\theta}} \tag{11}$$

and $\hat{\theta}$ denotes the parameter vector estimate.

The information matrix can be loosely interpreted as signal-to-noise ratio for multiple output, multiple parameter linear systems. In this interpretation, the signal is the sensitivity of the outputs to the parameters. If these sensitivities are large relative to the noise level (3 to 1 ratio or greater) and are

uncorrelated with one another, then the output dependence on the parameters is strong and distinct for each parameter. Parameter values can then be estimated with high accuracy when adjusting each of the parameters so that model outputs match measured outputs in a least squares sense. Elements of the information matrix also depend on the measurement sampling rate and the measurement noise characteristics, which are determined when specifying the instrumentation system.

The output sensitivities for the jth parameter appear as the jth column of the sensitivity matrix, and are computed from

$$\frac{d}{dt}\left[\frac{\partial x}{\partial \theta_j}\right] = A\frac{\partial x}{\partial \theta_j} + \frac{\partial A}{\partial \theta_j}x + \frac{\partial B}{\partial \theta_j}u \qquad (12)$$

$$\frac{\partial x}{\partial \theta_j}(0) = 0 \qquad (13)$$

$$\frac{\partial y}{\partial \theta_j} = C\frac{\partial x}{\partial \theta_j} + \frac{\partial C}{\partial \theta_j}x + \frac{\partial D}{\partial \theta_j}u \qquad (14)$$

for $j = 1, 2, ..., n_p$. Eqs. (12)-(14) follow from differentiating Eqs. (1)-(3) with respect to θ_j, combined with the assumed analyticity of x in the model equations. Note that it is necessary to have nominal (*a priori*) values for the model parameters to solve Eqs. (12)-(14). The output sensitivities $S(i)$ can also be computed using finite difference perturbations from the nominal parameter values and Eqs. (1)-(3).

From Eqs. (9)-(14), it is clear that the information matrix elements (and therefore the Cramér-Rao bounds) depend on the input through the sensitivity equations (12)-(14). The input u influences the sensitivities both directly as a forcing function in the sensitivity equations and indirectly as an influence on the states, which also force the sensitivity equations. The dependence of the Cramér-Rao bounds on the input is nonlinear in the input amplitude, regardless of whether or not the system equations (1) and (3) are linear, because of the nonlinear character of Eqs. (9) and (10).

Eq. (9) is a discrete approximation to a time integral over the maneuver duration $T = N\Delta t$. Therefore, when comparing the effectiveness of various input designs using some function of the dispersion matrix $\mathcal{D}$ as the criterion for comparison, the input designs being compared should have the same maneuver duration, and in light of the last paragraph, also the same allowable maximum input amplitude. This approach contrasts with comparisons presented in previous works[9,10,11,17], which were based on constant input energy. If only constant input energy is imposed on all inputs, a comparison among the inputs using a criterion which is a function of $\mathcal{D}$ is inherently unfair because a wide range of values for maximum allowable input amplitude and maneuver duration can give the same input energy.

Similarly, the dispersion matrix $\mathcal{D}$ depends nonlinearly on the states, which are often the same as the outputs. Therefore, output amplitudes must be comparable if an input design comparison is to be focused only on the merits of the input forms. For this reason, as well as to ensure validity of the assumed model structure, the inputs should be designed to produce comparable output amplitudes. If the maneuver duration, input amplitudes, and output amplitudes are not the same for all input designs being compared, it is possible to arrange matters so that almost any chosen input form will appear to be the best, based on a criterion function that depends on $\mathcal{D}$.

For the global optimal square wave input design, the flight test maneuver duration $T = N\Delta t$ might be fixed *a priori* due to practical time constraints of the flight test or an analysis of the rate of decrease of the Cramér-Rao bounds with increasing maneuver time using the optimized input. For the flight test examples included in this work, the cost function to be minimized for a fixed maneuver duration was the sum of squares of the Cramér-Rao bounds for the parameter standard errors,

$$J = \sum_{j=1}^{n_p} \sigma_j^2 = Tr\left[M^{-1}\right] = Tr[\mathcal{D}] \quad \text{for a given } T \quad (15)$$

Another formulation of the cost can be defined to design the input for minimum flight test time to achieve specific goals for the Cramér-Rao bounds[12]. This is a minimum time problem, so that the cost is given by

$$J = T \quad \text{when } \sigma_k \le \xi_k \quad \forall k = 1, 2, ..., n_p \quad (16)$$

For the flight test examples included here, the optimal input applied to the dynamic system described by Eqs. (1)-(5) minimized the cost function in Eq. (15), subject to the constraints in Eqs. (6) and (7).

3. OPTIMAL INPUT SOLUTION

The optimization problem posed in the last section is difficult to solve in general. For the particular problem of optimal input design for aircraft parameter estimation, there are good reasons to restrict the allowable input form to full amplitude square waves only. Among these are analytical work on a similar problem[6], which indicated that the optimal input should be "bang-bang" (i.e., a full amplitude switching input). Square wave inputs are simple to implement for either an onboard computer or the pilot. Finally, several flight test evaluations[10,14,16,17] have demonstrated that square wave inputs were superior to sinusoidal and doublet inputs for parameter estimation experiments, largely due to richer frequency spectra.

For the above reasons, and to make the optimization problem tractable, input forms were limited to full amplitude square waves only; i.e., only full positive, full negative, or zero amplitude was allowed for any input at any time. Full input amplitude was used in

order to excite the system as much as possible. Choice of the pulse timing and having zero amplitude available gave the optimizer the ability to use full input amplitudes without exceeding output amplitude constraints. With the above restrictions on the input form, the problem becomes a high order combinatorial problem involving output amplitude constraints, which is well-suited to solution by the method of dynamic programming.

Dynamic programming is essentially a very efficient method for doing a global exhaustive search. Arbitrary dynamics such as control surface actuator dynamics, feedback control, and general nonlinear models can therefore be included inside the optimization without difficulty. The result obtained is a globally optimal square wave input obtained in a single pass solution. The technique includes provisions to adjust the input possibilities at certain times in order to account for practical limitations on frequency content of the input, such as avoiding structural resonance frequencies. The dynamic programming solution smoothly handles the multiple input problem, since this just changes the number of square wave input possibilities. Keeping the system responses within the output space for which the assumed model structure is valid can be handled directly with dynamic programming by discarding any input sequence whose output trajectory exceeds the constraint limits. More details on the dynamic programming solution method can be found in Refs. [12] and [13].

4.   AIRCRAFT AND TEST PROCEDURES

The F-18 High Alpha Research Vehicle (HARV) is a modified F/A-18 fighter[20]. The flight test inputs were implemented by the pilot, and also by a computer-controlled On-Board Excitation System (OBES).

The pilot initiated each maneuver by first trimming the aircraft at the specified flight condition. For the piloted square wave inputs, the pilot signaled the ground controllers to send the square wave input sequence via the uplink from a computer on the ground. The maneuver was described by required stick and rudder deflections, represented to the pilot as movements of a cockpit indicator in real time. Accurate implementation of the input was achieved if the pilot accurately tracked the indicator movement with his own stick and rudder inputs. Using this procedure, the pilot was able to produce a high fidelity realization of the desired square wave inputs.

For square wave inputs implemented by the OBES, the pilot first selected a pre-programmed maneuver using buttons on a Digital Display Interface (DDI) inside the cockpit. The aircraft was then brought to the desired trimmed flight condition and an engage/disengage button on the DDI was pressed to initiate the maneuver. Square wave perturbation inputs from the OBES were added directly to the appropriate control surface actuator commands (for bare airframe modeling) or to pilot stick and rudder commands (for closed loop modeling), with the

feedback control system still operating. The pilot held stick and rudder deflections constant at the trimmed values until the maneuver was complete. The maneuver could be disengaged manually by the pilot toggling the engage/disengage button, or automatically by the research flight control system, based on g-limits, etc. The pre-programmed square wave perturbation inputs were standard 3-2-1-1 inputs, doublets, or square waves obtained from the optimal input design technique described above.

Various downlink data transmission rates were employed on the F-18 HARV aircraft, but all of the data used for analysis was converted to a common sampling rate of 40 Hz. Corrections were applied to the angle of attack, sideslip angle, and linear accelerometer measurements to account for sensor offsets from the center of gravity, and the angle of attack measurement was corrected for upwash. Data compatibility analysis[21] revealed the need for a scale factor correction on the angle of attack and sideslip angle measurements from the wing tip vane, and small bias error corrections on the measurements from the rate gyros and accelerometers.

5.   FLIGHT TEST RESULTS

For bare airframe short period longitudinal dynamics, the state vector x, input vector u, and output vector y in Eqs. (1)-(4) are defined by

$$x = \begin{bmatrix} \alpha & q \end{bmatrix}^T \quad u = \begin{bmatrix} \delta_s & 1 \end{bmatrix}^T \quad y = \begin{bmatrix} \alpha & q & a_z \end{bmatrix}^T \quad (17)$$

System matrices containing the model parameters are:

$$A = \begin{bmatrix} Z_\alpha & 1 + Z_q \\ M_\alpha & M_q \end{bmatrix} \quad B = \begin{bmatrix} Z_{\delta_s} & Z_o \\ M_{\delta_s} & M_o \end{bmatrix} \quad (18)$$

$$C = \begin{bmatrix} 1 & 0 \\ 0 & 1 \\ \dfrac{V_o}{g} Z_\alpha & \dfrac{V_o}{g} Z_q \end{bmatrix} \quad D = \begin{bmatrix} 0 & 0 \\ 0 & 0 \\ \dfrac{V_o}{g} Z_{\delta_s} & a_{z_o} \end{bmatrix} \quad (19)$$

For bare airframe lateral-directional dynamics,

$$x = \begin{bmatrix} \beta & p & r & \phi \end{bmatrix}^T \quad u = \begin{bmatrix} \delta_r & \delta_a & 1 \end{bmatrix}^T \quad (20)$$

$$y = \begin{bmatrix} \beta & p & r & \phi & a_y \end{bmatrix}^T \quad (21)$$

System matrices A, B, C, and D contain the model parameters:

$$A = \begin{bmatrix} Y_\beta & Y_p + \sin\alpha_o & Y_r - \cos\alpha_o & \dfrac{g}{V_o}\cos\Theta_o \\ L_\beta & L_p & L_r & 0 \\ N_\beta & N_p & N_r & 0 \\ 0 & 1 & \tan\Theta_o & 0 \end{bmatrix} \quad (22)$$

$$B = \begin{bmatrix} Y_{\delta_r} & Y_{\delta_a} & Y_o \\ L_{\delta_r} & L_{\delta_a} & L_o \\ N_{\delta_r} & N_{\delta_a} & N_o \\ 0 & 0 & \dot{\phi}_o \end{bmatrix} \qquad (23)$$

$$C = \begin{bmatrix} 1 & 0 & 0 & 0 \\ 0 & 1 & 0 & 0 \\ 0 & 0 & 1 & 0 \\ 0 & 0 & 0 & 1 \\ \dfrac{V_o}{g}Y_\beta & 0 & 0 & 0 \end{bmatrix} \qquad (24)$$

$$D = \begin{bmatrix} 0 & 0 & 0 \\ 0 & 0 & 0 \\ 0 & 0 & 0 \\ 0 & 0 & 0 \\ \dfrac{V_o}{g}Y_{\delta_r} & \dfrac{V_o}{g}Y_{\delta_a} & a_{y_o} \end{bmatrix} \qquad (25)$$

For closed loop lateral-directional dynamics in stability axes, the model is

$$x = \begin{bmatrix} \beta & p_s & r_s & \phi \end{bmatrix}^T \qquad (26a)$$

$$u = \begin{bmatrix} \eta_r(t-\tau) & \eta_a(t-\tau) & 1 \end{bmatrix}^T \qquad (26b)$$

$$y = \begin{bmatrix} \beta & p_s & r_s & \phi & a_y \end{bmatrix}^T \qquad (27)$$

$$A = \begin{bmatrix} Y_\beta & Y_p & Y_r - 1 & \dfrac{g}{V_o}\cos\Theta_o \\ L_\beta & L_p & L_r & L_\phi \\ N_\beta & N_p & N_r & N_\phi \\ 0 & \dfrac{\cos\Gamma_o}{\cos\Theta_o} & \dfrac{\sin\Gamma_o}{\cos\Theta_o} & 0 \end{bmatrix} \qquad (28)$$

$$B = \begin{bmatrix} Y_{\eta_r} & Y_{\eta_a} & Y_o \\ L_{\eta_r} & L_{\eta_a} & L_o \\ N_{\eta_r} & N_{\eta_a} & N_o \\ 0 & 0 & \dot{\phi}_o \end{bmatrix} \qquad (29)$$

$$C = \begin{bmatrix} 1 & 0 & 0 & 0 \\ 0 & 1 & 0 & 0 \\ 0 & 0 & 1 & 0 \\ 0 & 0 & 0 & 1 \\ \dfrac{V_o}{g}Y_\beta & \dfrac{V_o}{g}Y_p & \dfrac{V_o}{g}Y_r & 0 \end{bmatrix} \qquad (30)$$

$$D = \begin{bmatrix} 0 & 0 & 0 \\ 0 & 0 & 0 \\ 0 & 0 & 0 \\ 0 & 0 & 0 \\ \dfrac{V_o}{g}Y_{\eta_r} & \dfrac{V_o}{g}Y_{\eta_a} & a_{y_o} \end{bmatrix} \qquad (31)$$

The L_ϕ and N_ϕ terms are present in the closed loop lateral-directional model equations because the control law used bank angle feedback for gravity compensation to coordinate stability axis rolls. Closed loop model parameters are in general different from the bare airframe parameters, because the closed loop model parameters include the dynamics of the control system in addition to the bare airframe. Model equations could also be written using non-dimensional parameters[18].

A priori linear models used for the input design cases included here were derived from a nonlinear batch simulation of the F-18 HARV[22], which uses a wind tunnel database for the aerodynamics. Noise variance estimates for the a priori models were obtained from previous flight test data records using an optimal Fourier smoothing technique[23]. The models used for parameter estimation from flight test data were identical in structure to the a priori models, except that the a priori models did not include linear accelerometer outputs.

All flight test data analysis was done using output error maximum likelihood parameter estimation[18,19,24]. For the closed loop modeling, the equivalent time delays were estimated as the pure time delay from pilot input to control surface deflection. The equivalent time delay can be estimated very accurately this way because the signals involved have very low noise levels and the pilot inputs were square waves. Equivalent time delay was then held fixed at this estimated value during the maximum likelihood estimation. The Cramér-Rao bounds for the parameter standard errors were the square root of the diagonal elements of the dispersion matrix $\mathcal{D}$ computed from Eq. (10). In the time domain, a correction for colored output residuals from maximum likelihood estimation is necessary if the Cramér-Rao bounds are to accurately represent the error in the parameter

estimates[19,25]. The correction was not applied to the time domain results given here, because the input comparison results were unaffected by it, and also because the Cramér-Rao bounds used in the optimal input design assumed white Gaussian measurement noise. The same white noise assumption is made in computing the Cramér-Rao bounds from flight test data using output error maximum likelihood estimation. For flight test data analysis in the frequency domain, the correction is not necessary. Refs. [19] and [25] address this issue in detail. Model structure was held constant for the compared maneuvers, so that the number of parameters estimated from each data record was identical. All data analysis and parameter estimation was done using angle measurements in radians, but the plots were made using degrees.

The first input design was a bare airframe lateral-directional case using the OBES to implement sequential rudder and aileron inputs. The flight condition was 5 deg angle of attack, Mach 0.6, and altitude of approximately 25,000 ft. The model was given by Eqs. (1)-(5) and (20)-(25). Perturbation input and output amplitude constraints resulting from various practical flight test constraints were:

$$|\delta_r| \leq 4.0 \text{ deg} \qquad |\delta_a| \leq 2.5 \text{ deg} \qquad (32a)$$

$$|\beta| \leq 5.0 \text{ deg} \qquad |\phi| \leq 32.0 \text{ deg} \qquad (32b)$$

The 3-2-1-1 input form has been shown to be very effective for aircraft parameter estimation in previous flight test investigations[9,10], so this input was chosen to compare with the globally optimal square wave input design. Standard 3-2-1-1 inputs and globally optimal square wave inputs were designed using the same input amplitude constraints in (32a), the same maneuver duration, the same a priori model, and the same output amplitude constraints in (32b).

The 3-2-1-1 inputs were designed by matching the frequency of the "2" pulse to the frequency of the dominant oscillatory mode for the a priori model, and adjusting amplitudes and control sequence timing so that the chosen output amplitude constraints were satisfied. Optimal inputs were designed with a computer program that implemented the optimal input design procedure described above[12]. The duration of each maneuver was 24 seconds.

Figures 1 and 2 show the input and output time histories measured in flight for the OBES lateral-directional 3-2-1-1 and optimal inputs at 5 degrees angle of attack. The solid lines on the left side of Figures 1 and 2 are the commanded inputs from the OBES, and the dashed lines are the actual measured control surface positions. The desired input forms were distorted by the feedback control system, as can be seen in the figures. The distortion of the input forms by the lateral-directional feedback control system was not accounted for in the design process for either input design. Figures 1 and 2 show that the maximum input and output amplitudes for these two maneuvers were very nearly the same, and the length of each maneuver was the same. The maneuvers were

run in immediate succession on the same flight. With the model structure held fixed for the data analysis on each maneuver, any differences in the resulting model parameter accuracies can be attributed to effect of the input form.

Parameter estimation results for the OBES lateral-directional 3-2-1-1 and optimal inputs at 5 degrees angle of attack are given in Table 1. Column 1 in Table 1 lists the model parameters, column 2 contains the a priori values of the parameters used for the input design, column 3 contains parameter estimates and Cramér-Rao lower bounds for the parameter standard errors using the 3-2-1-1 input. Column 4 contains the corresponding results for the optimal square wave input. The dashed lines on the right side of Figures 1 and 2 are the model responses computed using the measured inputs and the estimated model parameters from columns 3 and 4 of Table 1. The match is very good in both cases.

Values in column 5 of Table 1 are the percent change in the Cramér-Rao bound for each model parameter standard error for the optimal input maneuver compared to the 3-2-1-1 maneuver, based on the 3-2-1-1 value. The optimal input reduced parameter standard errors (equivalently, increased parameter accuracy) by an average 20%, with lower parameter standard errors for every estimated parameter. Parameter estimates in columns 3 and 4 of Table 1 are generally in good agreement.

The percent error of the a priori parameter values relative to the parameter values estimated from flight test data (computed as the average of values in columns 3 and 4 of Table 1) varied from 4.2% to 65.1%, with an average value of 24.2%. Nevertheless, both input design methods based on the a priori model produced experimental data with excellent information content, as evidenced by the low standard error bounds in Table 1.

Symmetric stabilator input designs implemented by OBES for longitudinal model identification are shown in Figures 3 and 4. In this case, the distortion of the input forms by the feedback control was accounted for in the a priori model by including a linear model of the feedback control identified from the nonlinear simulation. The same a priori design model was used to design both inputs shown in Figures 3 and 4. The flight condition was again 5 deg angle of attack, Mach 0.6, and altitude of approximately 25,000 ft. The model used for the parameter estimation is given by Eqs. (1)-(5) and (17)-(19). The same methods were used for the input designs and the data analysis, except that the optimal input design was allowed a higher input amplitude than the 3-2-1-1 input. This was done to investigate the capability available with the optimal input design routine to use higher input amplitudes for increased parameter accuracies while maintaining the same output amplitude constraints. Such flexibility is not available with the 3-2-1-1 input because of its fixed form. Perturbation input and output amplitude constraints were:

$$\left| \delta_s \right| \le 3.0 \text{ deg} \qquad \text{for the 3-2-1-1 input}$$
$$\left| \delta_s \right| \le 4.0 \text{ deg} \qquad \text{for the optimal input} \tag{33a}$$

$$\left| \alpha \right| \le 3.0 \text{ deg} \tag{33b}$$

Each maneuver lasted 26 seconds, and the maneuvers were run in immediate succession on the same flight. The left sides of Figures 3 and 4 show the significant distortion of the stabilator commands resulting from the longitudinal feedback control. Parameter estimation results are given in Table 2 using the same format as Table 1. The parameter accuracies are now improved by an average 72% using the optimal input compared to the 3-2-1-1 input. The optimal input maneuver produced larger α perturbations than the 3-2-1-1, although maximum α amplitude was the same for both inputs in the design phase using the *a priori* model. The reason for this discrepancy was that the control law removed most of the "3" pulse for the 3-2-1-1, and this effect was not well modeled in the *a priori* model. The optimal input used shorter pulses in general, and thus was less affected. The dashed lines on the right sides of Figures 3 and 4 indicate a good match between the measured outputs and the model responses using the measured inputs and the estimated model parameters from columns 3 and 4 of Table 2. The estimates of pitching moment parameters in columns 3 and 4 of Table 2 do not agree. Lower parameter standard error bounds for the optimal input indicate that the pitching moment parameter estimates from the optimal input should be more accurate. To check this, a different maneuver at the same flight condition was used to investigate the prediction capability of the models using the parameters in Table 2. Figure 5 shows measured and predicted pitch rate response using the model parameters from Table 2 with the same model structure used before. The stabilator input (not shown) was a perturbation input with amplitude approximately ±5 deg from the trim value of 2 deg. The stabilator input was applied to both models to produce the prediction responses plotted with the measured response in Figure 5. The prediction using the parameters estimated from the 3-2-1-1 input (shown on the left side of Figure 5) was less accurate than the prediction using the parameters from the optimal input (shown on the right side of Figure 5), both in frequency and amplitude. This result gives confidence that the parameters estimated from the optimal input maneuver are indeed more accurate, as indicated by the computed Cramér-Rao bounds.

Next, two longitudinal maneuvers flown at 20 deg angle of attack, Mach 0.4, and approximately 25,000 feet altitude are studied to compare the optimal square wave input design to a sequence of doublets. The maneuvers were implemented by the pilot in this case, using the procedure described in section 4 above. The objective was accurate modeling of the bare airframe short period dynamics. Perturbation input and output amplitude constraints were:

$$\left| \eta_e \right| \le 1.0 \text{ in} \tag{34a}$$

$$\left| \alpha \right| \le 4.5 \text{ deg} \tag{34b}$$

Each maneuver lasted 14 seconds. The left side of Figure 6 shows the pilot longitudinal stick deflection for the doublet sequence. The right side of Figure 6 shows the target optimal square wave input (dashed line) with the pilot's realization of that target input in flight (solid line). The pilot's realization of the optimal square wave input is highly accurate in frequency, but somewhat inaccurate in amplitude. The inputs shown in Figure 6 have similar maximum input amplitudes. Table 3 contains the results of maximum likelihood parameter estimation using the same longitudinal model structure as before. Compared to the doublet sequence input, the optimal square wave input maneuver produced lower parameter standard errors (higher accuracy) for every model parameter, despite distortion in the pilot's implementation of the optimal square wave input. The average improvement was 47%, based on the standard error value from the doublet sequence maneuver. This example demonstrates that the optimal square wave input design is robust to distortion, and can be successfully implemented by a pilot in flight.

The next optimal input design example is a closed loop modeling case executed using the OBES at 60 deg angle of attack, Mach 0.25, and average altitude approximately 24,000 ft. At this high angle of attack, the aircraft sink rate was approximately 150 feet per second, as altitude dropped from 25,500 feet to 21,900 feet during the 24 second maneuver. Perturbation input and output amplitude constraints imposed for the input design were:

$$\left| \eta_r \right| \le 80 \text{ lbf} \qquad \left| \eta_a \right| \le 2.5 \text{ in} \tag{35a}$$

$$\left| \beta \right| \le 5.0 \text{ deg} \qquad \left| \phi \right| \le 20.0 \text{ deg} \tag{35b}$$

The solid lines in Figure 7 show the measured input and output time histories from flight for the lateral-directional optimal square wave inputs at 60 deg angle of attack. Since the square wave perturbation inputs were implemented by the OBES, the inputs realized in flight matched desired optimal inputs exactly; therefore, only one trace is shown for each input on the left side of Figure 7.

The data analysis was done using output error maximum likelihood parameter estimation in the frequency domain[24]. The model used for the parameter estimation is given by Eqs. (1)-(5) and (26)-(31).

Results for the OBES lateral-directional optimal inputs at 60 degrees angle of attack are given in Table 4. Column 1 in Table 4 lists the closed loop parameters, column 2 contains the *a priori* parameter values, and column 3 shows the parameter values estimated from flight test data. Column 4 contains the Cramér-Rao lower bounds for the parameter standard errors using flight test data from the optimal

square wave input maneuver. The dashed lines on the right side of Figure 7 indicate the model responses using the estimated closed loop model parameters from column 3 of Table 4 and the measured inputs. The match is good considering that the aerodynamic dependencies are generally nonlinear at this flight condition. The input and output amplitude constraints imposed during the input optimization restrained these nonlinearities throughout the maneuver, so that the assumed linear model structure could be used.

Comparing columns 2 and 3 of Table 4, the *a priori* model parameters were significantly different from the parameter values estimated from the flight test data. The percent error of the *a priori* parameter values relative to the parameters estimated from flight test data varied from 3.1% to 226.5%, with an average value of 41.9%. Nevertheless, the optimal input design based on the *a priori* model produced experimental data with excellent information content, as evidenced by the low standard error bounds in column 4 of Table 4. All pairwise correlations between estimated parameters were less than 0.8, with most below 0.2. This example demonstrates the robustness of the optimal input design technique to errors in the *a priori* model, as well as the applicability of the technique to closed loop flight test maneuver design at high angles of attack.

Figure 8 shows a prediction case at roughly the same flight condition as the last maneuver. The solid lines in Figure 8 represent measured flight test data. The dashed lines in Figure 8 were generated using the measured flight test inputs in Figure 8 and the closed loop model estimated from the flight test data of Figure 7 (i.e., model parameters from column 3 of Table 4). The plots in Figure 8 show the excellent prediction capability of the closed loop model estimated from flight test data generated by the optimal square wave inputs. This result gives confidence that the linear model can be usefully employed at high angles of attack, and moreover that such models can be accurately estimated from short data records using optimized square wave inputs.

Figure 9 shows flight test data for a lateral-directional optimal square wave input design implemented by the pilot. The maneuver was flown at 30 deg angle of attack, Mach 0.28, and average altitude of approximately 24,000 ft. The inputs were optimized with the square wave pulses constrained to be integer multiples of 0.5 second, and including a constraint that one second of zero input separate the rudder pedal and lateral stick input square waves (see Figure 9). These constraints were included to help the pilot accurately realize the optimal input form using the rudder pedals and the lateral stick in sequence. Such constraints can be easily incorporated into the dynamic programming optimization for the optimal square wave input design. Ref. [12] describes this feature of the optimal input design technique in detail. Perturbation input and output amplitude constraints imposed for the piloted optimal input design were:

$$|\eta_r| \leq 102 \text{ lbf} \qquad |\eta_a| \leq 1.5 \text{ in} \qquad (36a)$$

$$|\beta| \leq 6.0 \text{ deg} \qquad |\phi| \leq 20.0 \text{ deg} \qquad (36b)$$

Table 5 contains the maximum likelihood estimation results for the piloted optimal input, obtained in the same manner and presented in the same format as before for the OBES closed loop optimal input maneuver. The dashed lines on the left side of Figure 9 show the target optimal input, and the solid lines indicate the pilot's implementation in flight. The pilot inputs are again highly accurate in frequency (i.e., the square wave switching times were reproduced well), with some error in the amplitudes. The dashed lines on the right side of Figure 9 are the model responses using estimated closed loop model parameters from column 3 of Table 5 and the measured pilot inputs. As in the OBES closed loop optimal input case, the match is good despite higher order dynamics and nonlinearities in the physical system. The high accuracy of the estimated parameters shown in column 4 of Table 5 indicates that the optimal input design technique is robust to errors both in the *a priori* model, and in the implementation of the optimal square wave input form.

The parameter standard errors for this 30° α pilot implementation case were lower that those seen for the computer-implemented optimal input at 60° α, mainly due to the severe amplitude distortion by the pilot. If the distortion in the implementation of the optimal input (by the pilot or the feedback control system) can be characterized by linear dynamics (an excellent assumption in the case of the feedback control system distortion), then the effect of the input distortion on the flight test results is similar to the effect of errors in the *a priori* design model.

6. CONCLUDING REMARKS

The expense associated with flight testing high performance aircraft dictates that flight test data for modeling purposes be collected as efficiently as possible. This work reviewed some recent research in maneuver design for high performance aircraft, including examples from F-18 HARV flight tests.

Single and multiple input design cases were studied for bare airframe and closed loop modeling over a range of angles of attack, including fair comparisons of global optimal square wave inputs to conventional 3-2-1-1 and doublet input forms. The impact of the different input forms on estimated parameter accuracy was quantified through these investigations. For a flight test comparison done on an equal basis, the optimal square wave input decreased estimated parameter standard errors (equivalently, increased estimated parameter accuracy) by an average 20% compared to the 3-2-1-1 input. The decrease in estimated parameter standard errors improved to an average 72% using higher input amplitudes in the optimal input design while maintaining flight condition. Compared to a compound doublet sequence, the optimal input

decreased estimated parameter standard errors by an average 47% in a piloted flight test. For all the comparisons, every individual parameter was estimated more accurately using the optimal square wave input. These results were obtained with optimal square wave inputs implemented successfully by both the pilot and an onboard computer system.

The results of this investigation indicate that a properly designed 3-2-1-1 input can give good performance relative to the optimal square wave. Optimal square wave input designs demonstrated increased data information content in all cases studied, but the optimal input design technique is perhaps most valuable because of its ability to address practical design issues. Examples include an automated ability to limit output amplitude excursions during the flight test maneuver, good robustness to errors in the *a priori* model and to distortions in the realized input form, and the design flexibility to investigate the impact of changes in the conditions or constraints of the input design, such as available maneuver time, control surface rate limits, or input/output amplitude constraints. Such changes can be evaluated in terms of estimated parameter accuracies, using the single pass global optimizer in the optimal input design procedure. Some of these capabilities were demonstrated in this work using flight test results.

In the future, optimal design of maneuvers to collect data for dynamic modeling purposes should move off the engineer's workstation and onto the aircraft. This is possible because of increasing capabilities of flight control computers and improved understanding of the important aspects of the input optimization. Initial studies in this area are already underway[26]. In addition, research in the area of optimal input design for model parameter estimation should influence real time parameter estimation schemes that are required for adaptive and reconfigurable control. More areas to explore include optimal input design for nonlinear models, unsteady aerodynamic effects, and structural dynamics.

7. ACKNOWLEDGMENTS

8. REFERENCES

1. Williams, J.N., Ham, J.A., and Tischler, M.B., "Flight Test Manual, Rotorcraft Frequency Domain Flight Testing", U.S. Army Aviation Technical Test Center, Edwards AFB, CA, AQTD Project No. 93–14, September 1995.

2. Stepner, D.E. and Mehra, R.K., "Maximum Likelihood Identification and Optimal Input Design for Identifying Aircraft Stability and Control Derivatives", NASA CR-2200, March 1973.

3. Mehra, R. K., "Optimal Input Signals for Parameter Estimation in Dynamic Systems - Survey and New Results", IEEE Transactions on Automatic Control, *AC-19*, 6, December 1974, pp.753-68.

4. Gupta, N.K. and Hall, W.E., Jr., "Input Design for Identification of Aircraft Stability and Control Derivatives", NASA CR-2493, February 1975.

5. Mehra, R. K. and Gupta, N. K., "Status of Input Design for Aircraft Parameter Identification", AGARD-CP-172, May 1975, paper 12.

6. Chen, R. T. N., "Input Design for Aircraft Parameter Identification: Using Time-Optimal Control Formulation", AGARD-CP-172, May 1975 paper 13.

7. Gupta, N.K. and Hall, W.E., Jr., "Model Structure Determination and Test Input Selection for Identification of Nonlinear Regimes", Office of Naval Research, Arlington, VA, Report ONR-CR215-213-5, February 1976.

8. Gupta, N.K., Mehra, R.K. and Hall, W.E., Jr., "Application of Optimal Input Synthesis to Aircraft Parameter Identification", Journal of Dynamic Systems, Measurement and Control, *98*, 2, June 1976, pp. 139-45.

9. Plaetschke, E. and Schulz, G., "Practical Input Signal Design", AGARD-LS-104, November 1979, paper 3.

10. Plaetschke, E., Mulder, J.A., and Breeman, J.H., "Flight Test Results of Five Input Signals for Aircraft Parameter Identification", in Proceedings of the Sixth IFAC Symposium on Identification and System Parameter Estimation, Pergamon Press, Vol. 2, June 1982, pp. 1149-1154.

11. Mulder, J. A., Sridhar, J.K., and Breeman, J.H., "Identification of Dynamic Systems – Applications to Aircraft, Part 2: Nonlinear Analysis and Manoeuvre Design", AGARD-AG-300, Vol. 3, Part 2, May 1994.

12. Morelli, E. A., "Practical Input Optimization for Aircraft Parameter Estimation Experiments", NASA CR-191242, May 1993.

13. Morelli, E. A. and Klein, V., "Optimal Input Design for Aircraft Parameter Estimation Using Dynamic Programming Principles", AIAA paper 90-2801, AIAA Atmospheric Flight Mechanics Conference, August 1990.

14. Morelli, E.A., "Flight Test Validation of Optimal Input Design using Pilot Implementation", in Proceedings of the 10th IFAC Symposium on System Identification, Danish Automation Society, Vol. 3, July 1994, pp. 43-8.

15. Morelli, E.A., "Optimal Input Design for Closed Loop Modeling at High Angles of Attack", AIAA paper 96-3418, AIAA Atmospheric Flight Mechanics Conference, July 1996.

16. Morelli, E.A. "Flight Test Validation of Optimal Input Design and Comparison to Conventional Inputs", AIAA paper 97-3711, AIAA Atmospheric Flight Mechanics Conference, August 1997.

17. van der Linden, C.A.A.M., Mulder, J.A., and Sridhar, J.K., "Recent Developments in Aircraft Parameter Identification at Delft University of Technology - Optimal Input Design", *Aerospace Vehicle Dynamics and Control*, Clarendon Press, Oxford, 1994, pp. 259-84.

18. Maine, R.E. and Iliff, K.W., "Application of Parameter Estimation to Aircraft Stability and Control - The Output-Error Approach", NASA RP 1168, June 1986.

19. Morelli, E.A. and Klein, V., "Determining the Accuracy of Maximum Likelihood Parameter Estimates with Colored Residuals", NASA CR 194893, March 1994.

20. Kempel, R. "F-18 High Alpha Research Vehicle Description", Internal Document, NASA Dryden Flight Research Facility, Edwards, CA.

21. Klein, V., and Morgan, D.R. "Estimation of Bias Errors in Measured Airplane Responses using Maximum Likelihood Method", NASA TM-89059, January 1987.

22. Messina, M.D., et al., "Simulation Model of the F/A-18 High Angle-of-Attack Research Vehicle Utilized for the Design of Advanced Control Laws", NASA TM-110216, May 1996.

23. Morelli, E.A., "Estimating Noise Characteristics from Flight Test Data using Optimal Fourier Smoothing", Journal of Aircraft, *32*, 4, July-August 1995, pp. 689-695.

24. Klein, V. "Aircraft Parameter Estimation in Frequency Domain", AIAA paper 78-1344, AIAA Atmospheric Flight Mechanics Conference, August 1978.

25. Morelli, E.A. and Klein, V., "Accuracy of Aerodynamic Model Parameters Estimated from Flight Test Data", Journal of Guidance, Control, and Dynamics, *20*, 1, January-February 1997, pp. 74-80.

26. Morelli, E.A. "In-Flight System Identification", AIAA paper 98-4261, AIAA Atmospheric Flight Mechanics Conference, August 1998.

Table 1 Maximum Likelihood Results for Lateral-Directional OBES Maneuvers F-18 HARV, 0.6 / 25K, $\alpha = 5°$

Parameter	a priori Estimate	3-2-1-1 Estimate ±Std. Error	Optimal Estimate ±Std. Error	Std. Error Percent Change
Y_β	-0.1316	-0.0970 ±0.0013	-0.0859 ±0.0012	-7.2
Y_{δ_r}	0.0285	0.0304 ±0.0009	0.0327 ±0.0008	-14.1
Y_{δ_a}	0.0053	0	0	†
L_β	-11.56	-11.376 ±0.048	-10.764 ±0.037	-22.8
L_p	-1.592	-1.8120 ±0.0070	-1.7998 ±0.0055	-21.1
L_r	0.5462	0.3396 ±0.0224	0.1727 ±0.0200	-10.4
L_{δ_r}	1.910	2.3074 ±0.0398	1.8768 ±0.0316	-20.7
L_{δ_a}	-15.81	-19.480 ±0.0623	-17.470 ±0.0441	-29.3
N_β	2.139	1.2807 ±0.0039	1.3120 ±0.0028	-27.9
N_p	-0.0085	0	0	†
N_r	-0.0940	-0.1027 ±0.0021	-0.0436 ±0.0019	-11.7
N_{δ_r}	-1.223	-1.3924 ±0.0056	-1.3450 ±0.0043	-23.5
N_{δ_a}	0.2444	0.1738 ±0.0038	0.2383 ±0.0028	-26.6

† = parameter dropped in model structure determination

Table 2 Maximum Likelihood Results for Longitudinal OBES Maneuvers F-18 HARV, 0.6 / 25K, $\alpha = 5°$

Parameter	a priori Estimate	3-2-1-1 Estimate ±Std. Error	Optimal Estimate ±Std. Error	Std. Error Percent Change
Z_α	-0.5832	-0.5940 ±0.0126	-0.6050 ±0.0047	-62.8
Z_q	0.0	0	0	†
Z_{δ_s}	-0.1093	-0.0378 ±0.0063	-0.0789 ±0.0032	-49.3
M_α	-2.2600	-4.543 ±0.080	-2.195 ±0.012	-85.1
M_q	-0.2927	-4.746 ±0.109	-1.341 ±0.014	-86.8
M_{δ_s}	-6.0380	-5.482 ±0.104	-4.597 ±0.024	-76.4

† = parameter dropped in model structure determination

Table 3 Maximum Likelihood Results for Longitudinal Pilot Maneuvers F-18 HARV, 0.4 / 25K, $\alpha = 20°$

Parameter	Compound Doublet Std. Error	Optimal Std. Error	Std. Error Percent Change
Z_α	0.0069	0.0027	-61.4
Z_q	0.0044	0.0028	-35.1
Z_{δ_s}	0.0038	0.0031	-17.0
M_α	0.0114	0.0033	-70.6
M_q	0.0086	0.0039	-54.0
M_{δ_s}	0.0094	0.0052	-45.2

Table 4 Maximum Likelihood Results
for Lateral-Directional Closed Loop OBES Maneuvers
F-18 HARV, 0.25 / 24K, $\alpha = 60°$

Parameter	A Priori Value	Optimal Estimate	Std. Error
Y_β	-0.062	-0.044	0.0018
Y_p	0.002	0	†
Y_r	-1.059	-0.989	0.001
Y_{η_r}	0.336	-0.00252	0.00012
Y_{η_a}	-0.796	-0.1908	0.0034
L_β	-1.705	-2.103	0.070
L_p	-0.730	-0.643	0.024
L_r	0.309	0.684	0.048
L_ϕ	-0.005	0	†
L_{η_r}	-3.022	-0.0387	0.0044
L_{η_a}	26.99	7.293	0.146
N_β	2.435	4.066	0.040
N_p	0.122	0.389	0.027
N_r	-1.293	-1.334	0.032
N_ϕ	0.083	0	†
N_{η_r}	17.88	0.176	0.004
N_{η_a}	-4.876	-3.579	0.103
τ_r	0	0.037	*
τ_a	0	0.038	*

† = parameter dropped in model structure determination
* = fixed parameter

Table 5 Maximum Likelihood Results
for Lateral-Directional Closed Loop Pilot Maneuvers
F-18 HARV, 0.28 / 24K, $\alpha = 30°$

Parameter	A Priori Value	Optimal Estimate	Std. Error
Y_β	-0.043	-0.102	0.004
Y_p	0.018	0.044	0.002
Y_r	-1.015	-0.918	0.004
Y_{η_r}	0.142	-0.00080	0.00015
Y_{η_a}	-1.121	-0.2818	0.0084
L_β	-2.800	-7.708	0.296
L_p	-1.669	-2.519	0.0817
L_r	-0.101	0	†
L_ϕ	0.080	0.895	0.079
L_{η_r}	-20.36	-0.3415	0.0096
L_{η_a}	81.16	11.66	0.42
N_β	1.638	6.331	0.124
N_p	0.142	0	†
N_r	-1.703	-2.600	0.066
N_ϕ	0.140	-0.515	0.039
N_{η_r}	13.18	0.2104	0.0057
N_{η_a}	-7.183	1.671	0.182
τ_r	0	0.046	*
τ_a	0	0.022	*

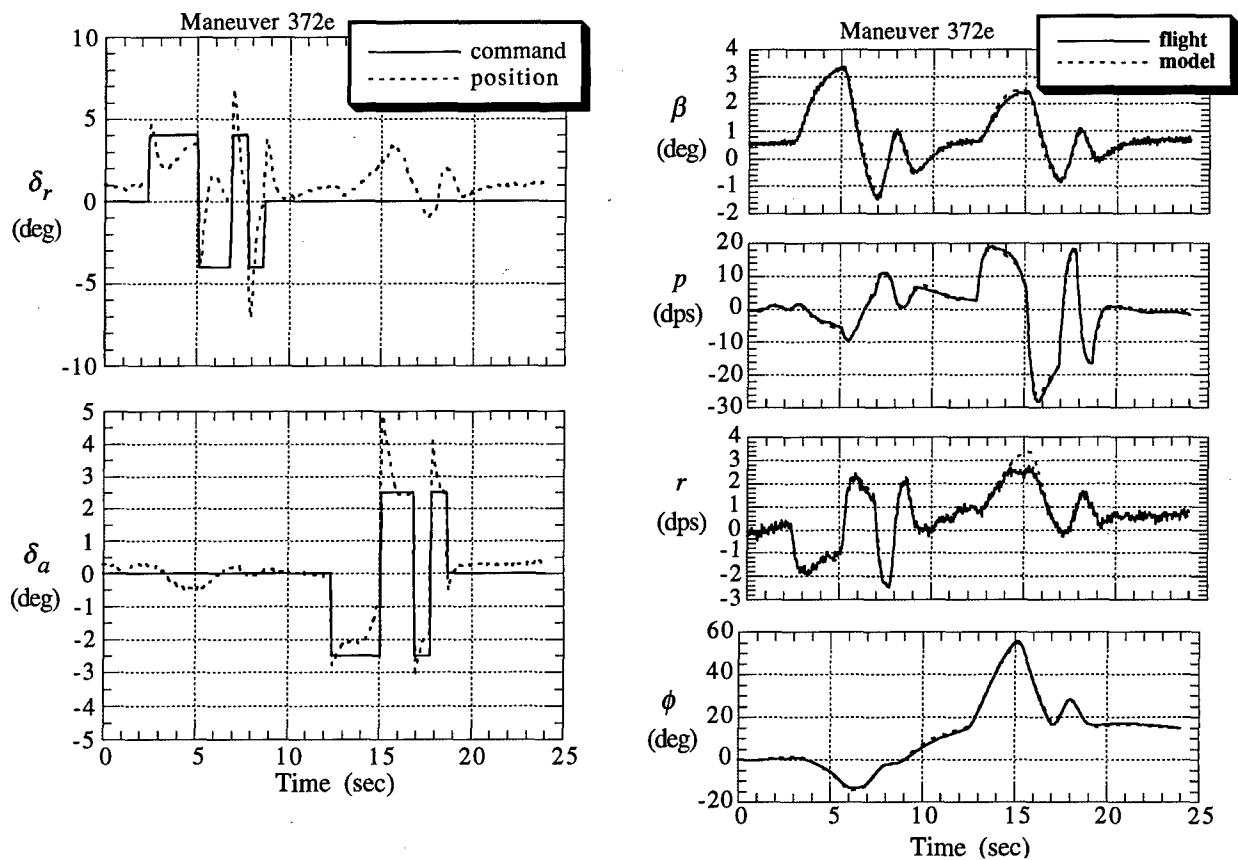† = parameter dropped in model structure determination
* = fixed parameter

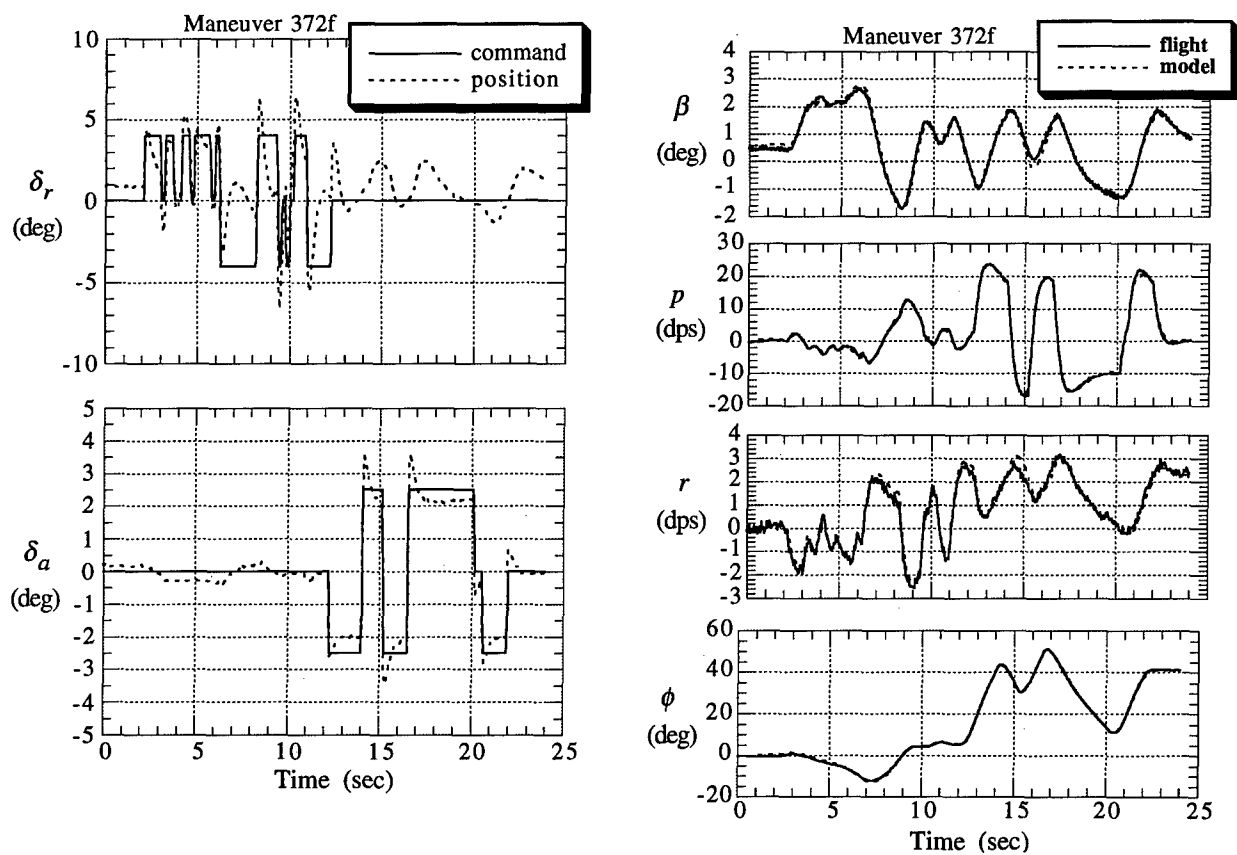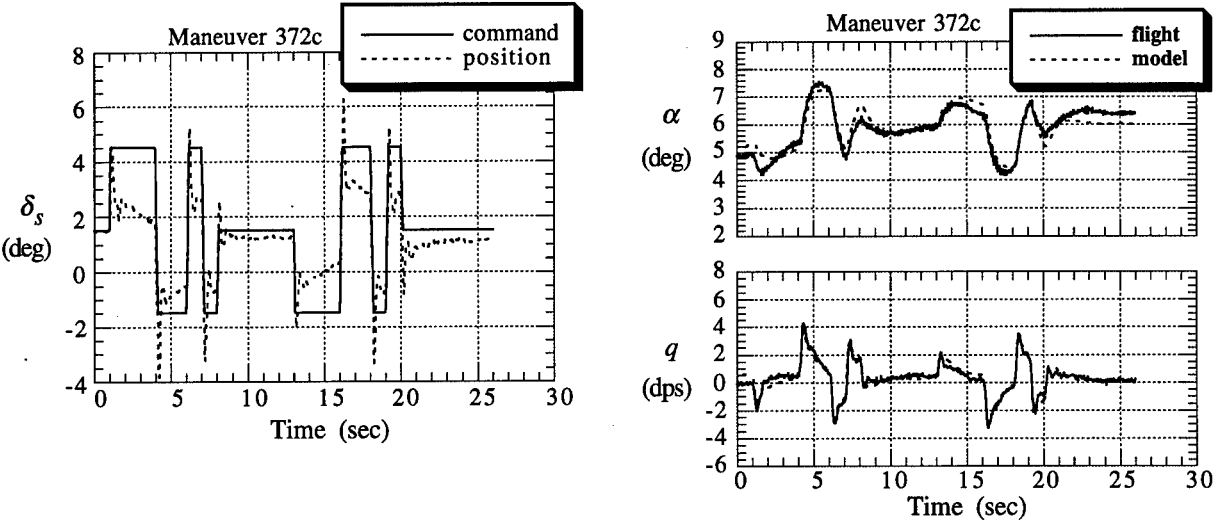Figure 1 Lateral-Directional OBES 3-2-1-1 Input
F-18 HARV, 0.6 / 25K, a = 5°

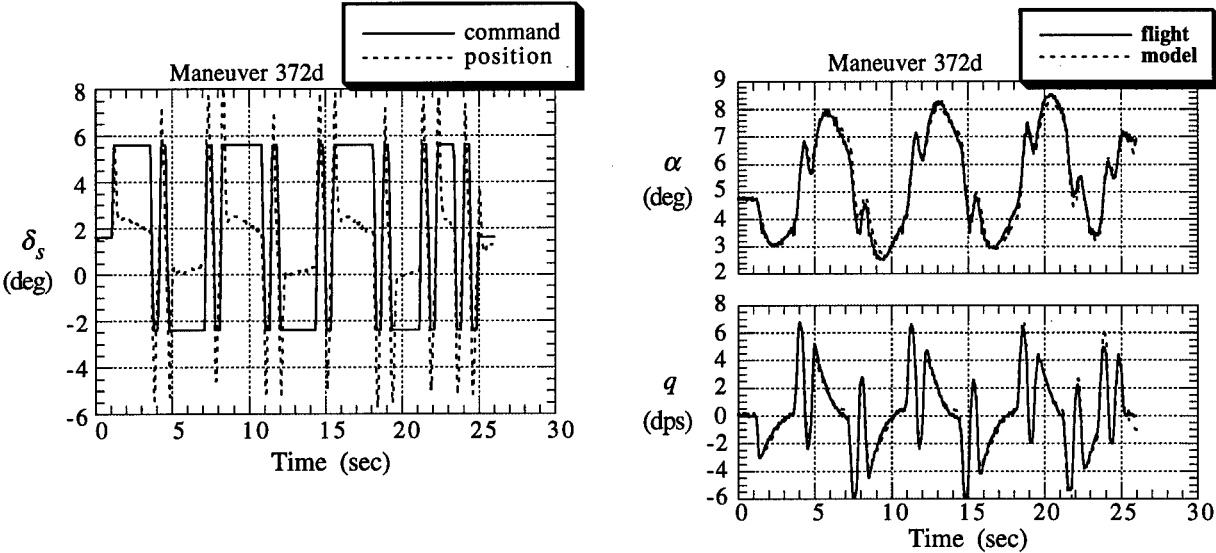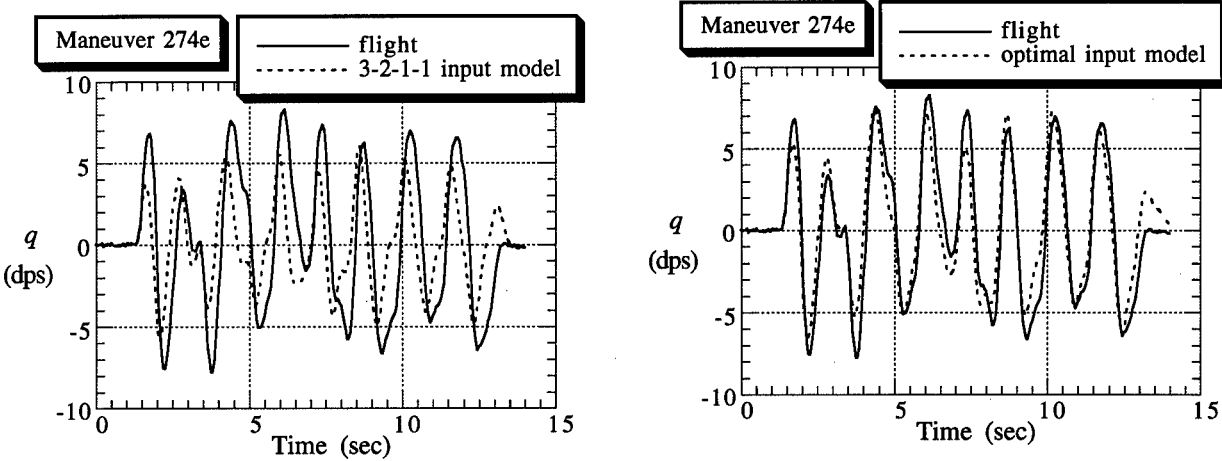**Figure 2** Lateral-Directional OBES Optimal Input
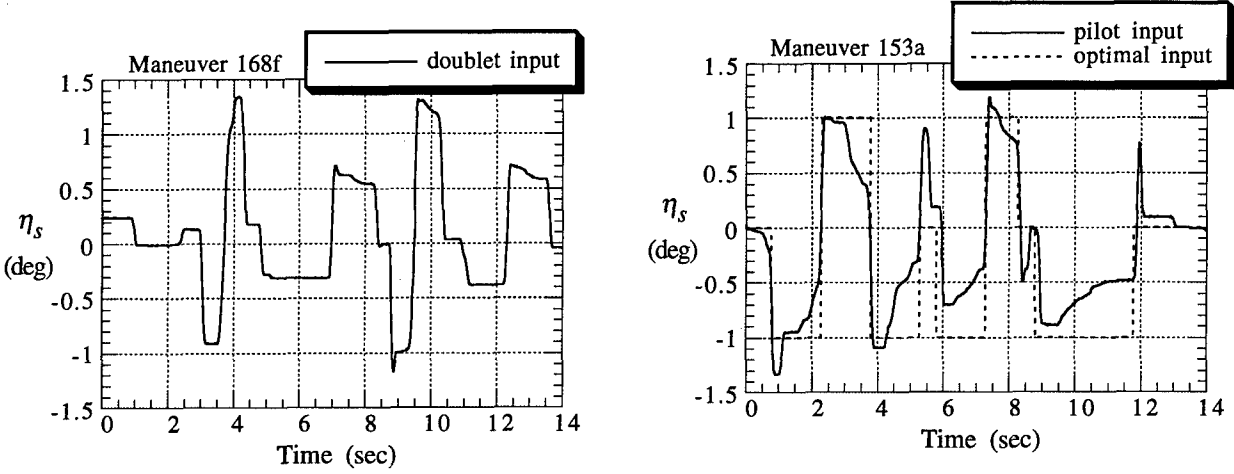F-18 HARV, 0.6 / 25K, α = 5°

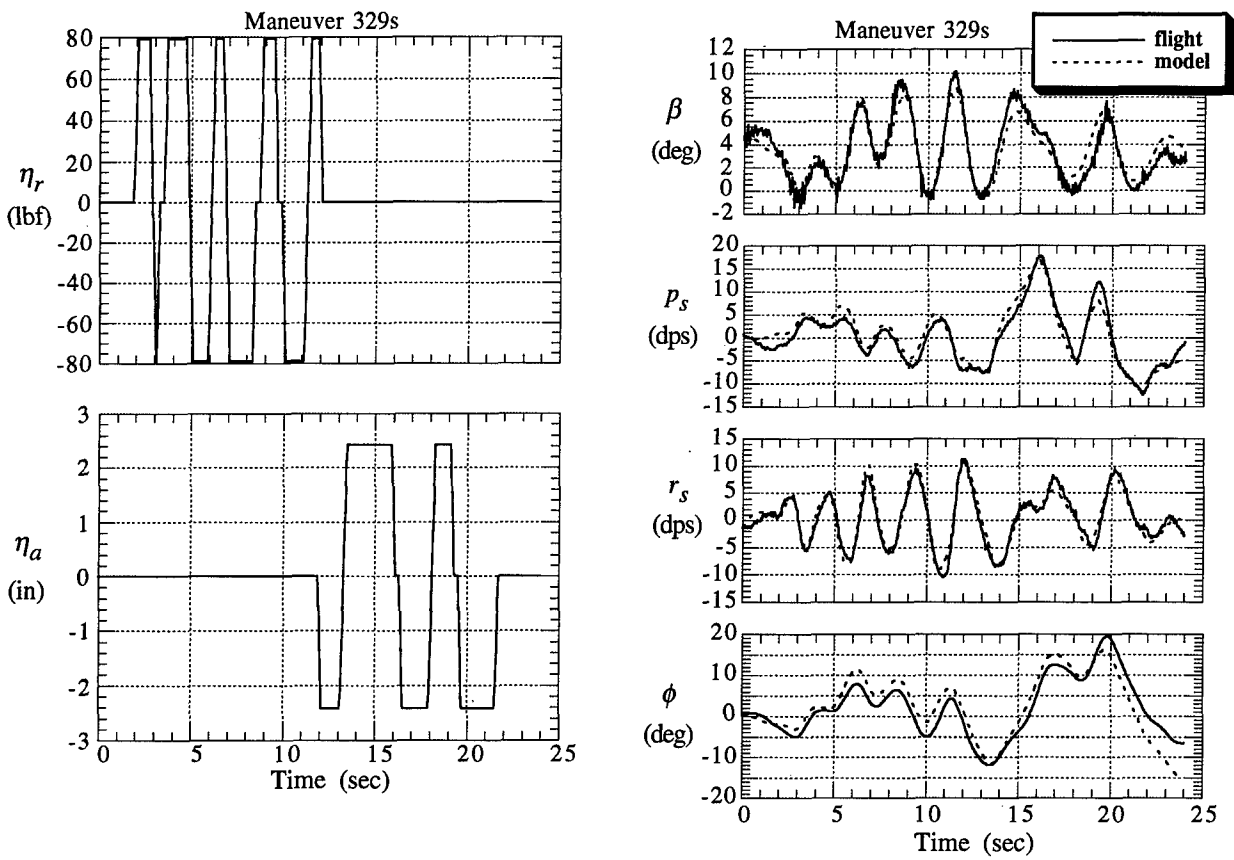**Figure 3** Longitudinal OBES 3-2-1-1 Input
F-18 HARV, 0.6 / 25K, $\alpha = 5°$

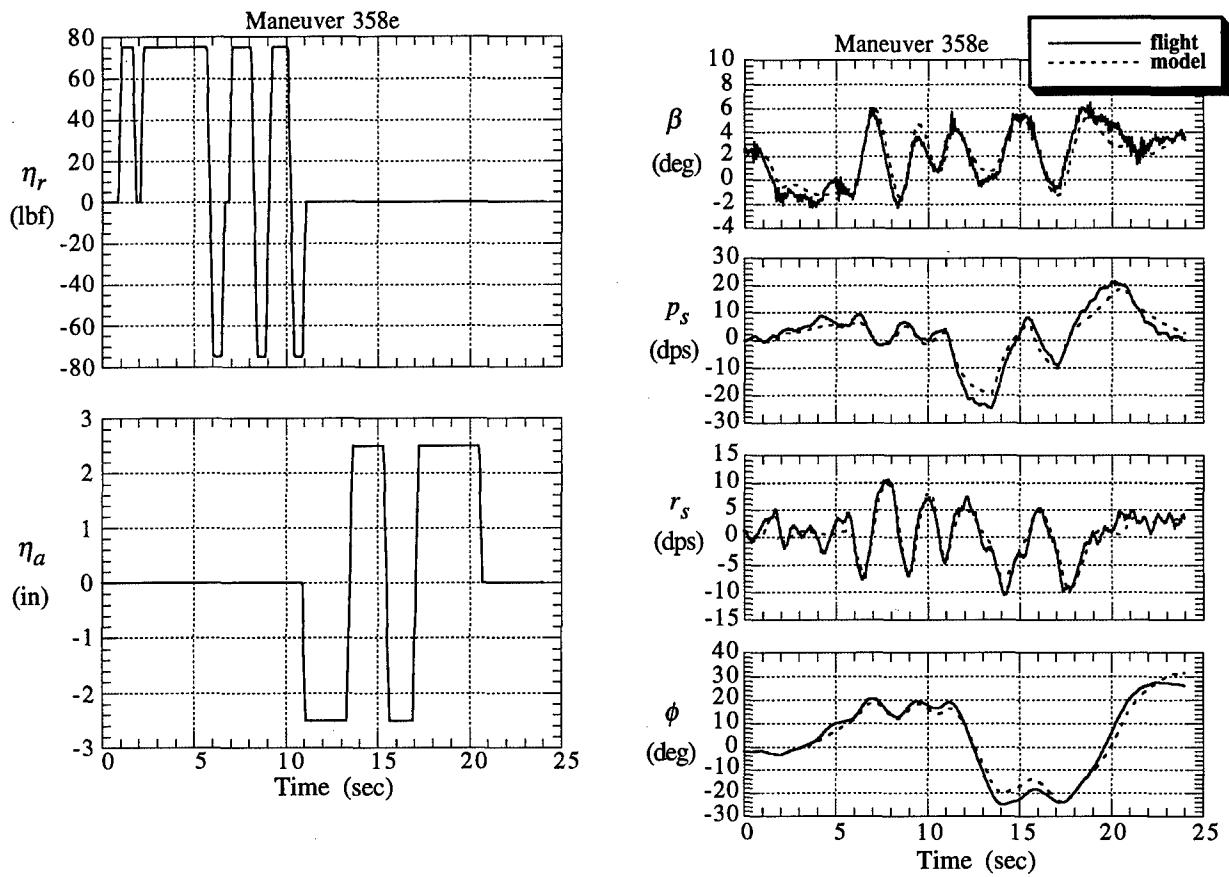**Figure 4** Longitudinal OBES Optimal Input
F-18 HARV, 0.6 / 25K, $\alpha = 5°$

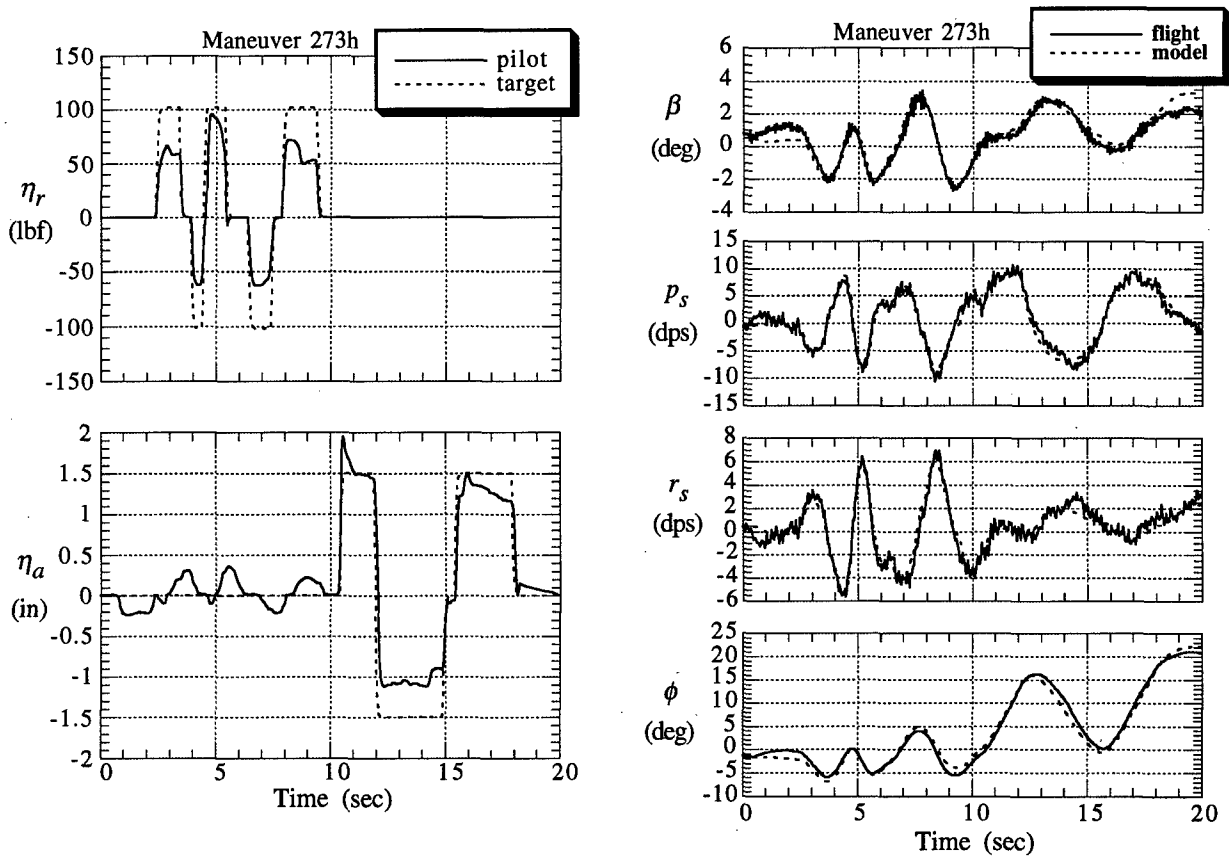**Figure 5** Longitudinal Prediction Case
F-18 HARV, 0.6 / 25K, $\alpha = 5°$

Figure 6 Longitudinal Pilot Inputs
F-18 HARV, 0.4 / 25K, $\alpha = 20°$

Figure 7 Lateral-Directional Closed Loop OBES Optimal Input
F-18 HARV, 0.25 / 24K, $\alpha = 60°$, TV Mode

Figure 8 Lateral-Directional Closed Loop OBES Prediction Case
F-18 HARV, 0.25 / 24K, $\alpha = 60°$, TV Mode

Figure 9 Lateral-Directional Closed Loop Pilot Optimal Input
F-18 HARV, 0.28 / 24K, $\alpha = 30°$, TV Mode

VALIDATION OF FCS STRUCTURAL COUPLING STABILITY CHARACTERISTICS THROUGH IN-FLIGHT EXCITATION

Brian Caldwell and Richard Felton
British Aerospace (Operations) Plc.
Military Aircraft and Aerostructures
Aerodynamics W310P
Warton Aerodrome
Preston, Lancashire PR4 1AX, UK
brian.caldwell@bae.co.uk

SUMMARY.
The Paper will outline the background to the Structural Coupling 'problem', and the motivation for the development of the in-flight excitation system, analysis methodologies and tools for the Eurofighter project. The influence of the flight clearance requirements on the choice of a frequency domain approach to system identification and thence the system design will be noted. In this application, accuracy and reliability of the structural response phase measurement is of prime importance, and it has been necessary to understand every detail of the system time delays and dynamics interposed between the recorded input and output signals and the corresponding actual parameters, such that these effects can be modelled, and a true representation of in-flight flexible aircraft dynamics obtained. The process of building the required models is described, illustrated with example results from ground and flight tests. The paper will recommend further development and integrated design of the excitation and analysis methods to ensure full value is obtained from the costly flight test campaign.

LIST OF SYMBOLS

AFCS	Automatic Flight Control System
ASE	Aero Servo Elasticity
C/L	(Flight Control System) Control Law
D&C	Design and Clearance
DSP	Digital Signal Processing
EAP	Experimental Aircraft Programme
FAM	Flexible Aircraft Model
FBI	Frequency and Bias Injection (System)
FCC	Flight Control Computer
FFT	Fast Fourier Transform
GRT	Ground Resonance Test
H/W	(FCS) Hardware
IMU	Inertial Measurement Unit
NF	Notch Filter
PSQS	Preliminary System Qualification Statement
SC	Structural Coupling
SCT	Structural Coupling Test
U/S	Unsteady (Aerodynamics)
WB1	Fundamental Wing Bending Mode
W/T	Wind Tunnel
q	Aircraft Pitch Rate
α	Aircraft Aerodynamic Incidence
δ	Trailing Edge Control Surface Deflection

1. INTRODUCTION

Structural Coupling, (or AeroServoElasticity) is a phenomenon associated with the introduction of an Automatic Flight Control System into a flexible aircraft. An essential part of such an AFCS is a sensor, required typically to measure aircraft actual pitch rate for comparison with a desired value commanded by the pilot. However, the FCS motion sensors detect not only the rigid-body motion of the aircraft, but also the superimposed higher frequency oscillations due to the dynamics of the flexible structure. If the high frequency component of the sensor output is not attenuated, it will propagate through the control system and drive the aircraft's flying control surfaces. The inertial and aerodynamic forces generated by the oscillating control surfaces may excite the structural dynamics, such that a coupled, closed loop, system involving AFCS, structure and aerodynamics is formed with attendant potential for instability. The conventional means of assuring FCS/Structural Coupling stability is to provide notch filtering in the control system to attenuate the high frequency signal component of the sensor signal, but these filters introduce additional phase lag to the AFCS which may compromise system, and therefore aircraft, performance. In broad terms FCS 'performance' is associated with high control laws gain, which exacerbates SC, and necessitates additional filtering and phase lag. Thus there is a design trade off to be made, closely involving structural dynamicists and control laws design engineers.

The Eurofighter unstable canard-delta is typical of configurations where the aircraft SC characteristics are dominated by the control surface aerodynamic, rather than inertial, excitation forces, and a high gain, full authority AFCS (Reference 1). In such cases, a ground SC test (SCT) alone cannot provide all of the information required for notch filter design and SC clearance, and Flexible Aircraft Modelling (FAM) must be used to predict in-flight SC characteristics. Where this situation arises, the accuracy and reliability of the FAM becomes a critical issue, and means must be found to generate the confidence necessary for flight clearance.

Confident clearance will be achieved in the most cost-efficient manner when a suitable balance is established between design and clearance (D&C) requirements which reflect the perceived level of uncertainty in system modelling or measurement, the form, scope and depth of the analysis required for D&C, and the programme of validation to bound the uncertainty and derive the necessary clearance evidence. In applications with tightly defined and specific design goals, parameters and characteristics (for example the EAP technology demonstrator, which shares structural, aerodynamic and active control concepts with the current Eurofighter project and exhibited the same type of SC problems, but was a single example with

limited stores carriage capabilities), it may be possible to push the balance toward conservative D&C processes and requirements, saving cost and time as a result, since only the specific set of SC characteristics has to be addressed. For a complex, series production, Weapons System aircraft such as Eurofighter, however, this approach would lead to NFs with phase lag characteristics which might jeopardise the fundamental design concept of the vehicle, fundamentally because of the notch filtering required to cover the wide variation in structural dynamics with changing stores configuration, and the subtle variations in build across a fleet of aircraft.

It was therefore imperative for Eurofighter that conservatism was reduced to enable a reasonable balance between NF and FCS design to be reached. Figure 1 compares the EAP and Eurofighter SC stability gain and phase margin requirements, expressed in Nichols diagram form as is appropriate to the frequency domain, control system stability approach to SC adopted. The 'EAP' margins are conservative in that the 9dB gain margin must be maintained across all phase, avoiding the need to generate confidence in predicted phase, and reducing the modelling and validation effort required considerably. For Eurofighter, the 'relaxation'.of requirements, to permit reduced open loop *gain margins* where adequate *phase margin* could be demonstrated (referred to as 'phase stabilisation'), clearly entailed the use of the FAM in a more demanding role; that is to predict the system gain and phase characteristics on the ground and in flight in a 'stand alone' mode, in a situation where errors in predicting phase might have direct implications for stability and therefore flight safety.

The noted relaxation of requirements, reduction of conservatism and explicit reliance on model accuracy, required that additional evidence be brought to the process to maintain the confidence level at that necessary for clearance. Specifically, flexible aircraft model reliability at the critical in-flight conditions required support. Some theoretical / wind tunnel work for validation of FAM unsteady aerodynamics has been done (e.g. Reference 2) but none is supported by full-scale verification and none was specific enough for immediate assimilation into the Eurofighter D&C process. Thus the need for direct model validation through in-flight excitation of the structural modes emerged.

A direct approach, focused specifically on FAM validation was selected, instead of measurement of the SC stability of the whole system, since the latter scheme would logically have required re-test following any change to the FCS part of the SC 'loop'. Together with the frequency-domain basis for the FCS and SC design and clearance process, this philosophy drove the design of the Eurofighter Frequency and Bias Injection (FBI) and supporting recording and analysis systems shown schematically in Figure 2, featuring injection of test signals at the FCS control surface actuators, and measurement of response at the Inertial Measurement Unit (IMU) input to the Flight Control Computer (FCC) control laws.

The cost of the dedicated testing required, and of the design and validation of the excitation. recording and analysis systems mean that the less conservative option will be taken only where there is exceptional need, and only after assessment of alternative routes to clearance. The high cost also indicates the need to maximise the efficiency of the flight test by careful design of the 'experiment' as a whole. It is also clear that applicability of the 'relaxed' D&C requirements will be limited to structural resonances, or 'modes', for which in-

flight validation evidence can be gained, and this is determined in the Eurofighter case by the capabilities of the FBI. In practice, extension of phase stabilisation to modes much above 12Hz was not considered economic in terms of the NF phase lag saving against the cost of FBI system capability.

Having established the need for the in flight validation, the paper will outline describe the position of the flight testing in the overall SC validation process, leading to definition of the excitation / recording / analysis system design and Flight Test programme requirements. The FBI in-flight excitation and recording systems developed for EF2000 will be described together with the data analysis and special Flight Test techniques applied. Specimen results will be shown to illustrate the conclusions reached in EF2000 validation to date. Finally difficulties faced and observations made during the programme will lead to recommendations for future work and for future applications of in-flight excitation.

2. THE EUROFIGHTER SC CLEARANCE PROCESS & THE ROLE OF IN FLIGHT MEASUREMENTS

Since key components of the additional validation evidence required for application of 'relaxed' requirements were only available from flight, it was immediately obvious that a staged clearance programme was required. Initial clearance was based on the conservative approach and D&C requirements evolved for EAP, to allow the evidence needed to support the next stage to be gained safely in the initial flight test phase, and to allow other aspects of the flight test programme to progress in parallel. Figure 3 shows schematically the staged process and development of the 'stand alone' model.

At 'Stage 1' in the Figure 3 process, basic, unmatched flexible aircraft model data is supported by SCT results, in the Stage 1 clearance to the more conservative 'EAP' type Stage 1 requirements. Stage 1 clearance supports the essential FBI Flight Test phase. In parallel with the Stage 1 flight test activities, the modelling is developed progressively through matching to SCT, FCS hardware rig tests and on-ground FBI to Stage 1a), and at this point information from SC flight test is assimilated into the process, to validate, in particular, the unsteady aerodynamics part of the FAM and culminating in modelling suitable for stand alone use in the Stage 2 clearance to the relaxed, Stage 2 criteria. Much improved NF lag characteristics result, permitting the variation in SC characteristics across a range of stores configurations to be accommodated without penalising the FCS.

This staged procedure integrated easily with the phased release of Eurofighter FCS functionality, facilitating updates to the NF specification, and also fitted in with the demands of the Flight Test Programme, which began with basic aircraft handling and aerodynamic parameter identification and later progressed to stores-related testing. This approach also frees SC testing from the need for real time analysis, since the Stage 1 Flight Test results are for application at a later date, in Stage 2.

3. SYSTEM MODELLING & VALIDATION

The elements of the system models correspond to the blocks in Figure 2; the modelling applied and validation indicated in Figure 3 are briefly expanded below.

3.1 FAM Structural Elements

The structural elements of the FAM comprise the 'Modal Dynamics' and (control surface) 'Inertial Excitation' elements

of Figure 2, and was adapted for SC analysis from the 'flutter' model, which was itself derived from a high order Finite Element Model. The FAM is refined prior to Stage 1 use through input of information from dynamic test and modal analysis of airframe components together with final estimates of flight standard mass distribution, as indicated in Figure 3. For Stage 1a) the model was further matched based on GRT and, in particular, ground SCT data. Issues in matching to SCT are noted below:

• Great care must be taken to understand the effects of structural and other non-linearities on the test data. For Eurofighter this was facilitated by;

    − step-sine, sine-dwell ground SCT techniques,

    − maximisation of ground-SCT actuator demand excitation amplitude to 'break out' the structure, and

    − understanding and avoiding the non-linearities of the actuators at low and high demand amplitudes.

• Upgrade to match all combinations of excitation and response in a single model may be difficult or impossible - specific matching to address particular problems may be required, and the overall 'quality' of the match must be accounted for throughout the D&C process.

• There may be a number of plausible means of matching. For example, a gain mismatch in a response peak may be due to an error in excitation, i.e. control rotation mode inertia cross-terms, or response, i.e. mode damping or fuselage mode shape local to the FCS sensors. The implications must be anticipated and the consequences accounted for downstream in the process.

Fuselage modelling may not be a critical issue for traditional flutter investigations, but is clearly of central importance for SC, and is increasingly important for all structural dynamics studies where the FCS forms a part of the system. The influence of the fuselage was one of the factors in deciding limits on the application of relaxed D&C stability criteria.

3.2 FAM Aerodynamics

The FAM Aerodynamics are represented by the (control surface) 'Aero. Excitation' and 'Modal Aerodynamics' blocks of Figure 2.

The unsteady (U/S) aerodynamics are derived from linear potential flow theory and hence suffer the following limitations:-

• Rigid body aerodynamics are poor because of the absence of fuselage interference effects.

• Thickness and viscous effects are absent.

• Vortical flows are not modelled.

In this application, rigid mode aerodynamics were replaced with terms derived from the Stability and Control Dataset, such that a match with rigid aircraft analyses was achieved. The second point means that the effectiveness of trailing edge control surfaces is consistently over-estimated, a fact well documented and demonstrated by wind tunnel testing (e.g. Reference 2), and the latter two points indicate that incidence effects on the current canard-delta planform will not be predicted, and the model strictly represents SC characteristics at low incidence.

Given the conservatism of the D&C requirements applied at Stage 1, the unsteady aerodynamics are considered adequate for Stage 1 clearance. Validation of the FAM in flight, and quantification of the basic and incidence-induced overprediction of control surface effectiveness at Stage 1a) forms the basis for advancement to Stage 2.

3.3 Actuation System

The actuation system is represented by a high-order transfer function model, matched in gain and phase to on-aircraft test measurements. Loading, failure etc. effects are included as tolerances on the final result, and, for the frequency range under consideration, it has not been found necessary to include complex actuator modelling into the system in the manner of Brenner (Reference 3).

3.4 FCS Hardware Model

The 'hardware' includes the digital FCC, IMU and the interconnecting digital databus. As for the Actuation System, the FCS hardware is represented by simple linear transfer function models for the digital input/output processes, for the IMU & FCC computation delays, for the transmission and asynchronous delays associated with IMU / databus / FCC communication, and for the dynamics associated with the IMU transducers. Modelling of incidence sensors is not required here since the inherent attenuation in this control laws path means it has no contribution to the FCS / SC loop (Reference 1).

The appropriate models are developed from those used in the control law design, and will thus be thoroughly validated by rig test. Care must be taken to obtain typical values of the delays etc., with upper and lower bounds, rather than worst case or specification characteristics, and the frequency range over which the model is valid may also need to be extended, where appropriate, to cover the flexible aircraft regime.

3.5 Control Laws

The control laws are represented by combinations of linear gains and linear modelling of notch and other control laws filters. The model is obtained directly from the control law designers. The filter representation may need to be improved for validity over the wider frequency range to be investigated here, compared with the control laws design. In particular, the true 'digital' frequency response characteristics of the notch filters should be modelled.

3.6 FBI Input / Output Hardware Modelling

The preceding sections have concerned modelling and validation of elements within the SC loop of Figure 2. For FBI predictions and aerodynamics validation in Stage 1a), it is equally important to include the correct representation of additional processes associated with excitation signal injection to, and response signal extraction from the FCS, and with the buffering and routing of the generated and measured signals to the aircraft tape for recording. In the digital recording system provided for Eurofighter, even the relative location of each variable within the recorded 'frame' of data must also be understood, since the effect on the apparent phase of the response may be significant at the frequencies of interest.

The modelling of these aspects is validated through rig tests and through on ground execution of the FBI system. The results are compared with FBI predictions, and with data from ground SCT, which is a tightly controlled test and considered to give a true representation of aircraft SC characteristics.

4. DESIGN OF THE FBI SYSTEM AND FLIGHT TEST PROGRAMME

Section 2 has outlined flight clearance programme and the supporting development of the FAM for its enhanced role. As has been stated, the intention of the SC FBI Flight Testing was to gain direct validation evidence for the FAM rather than to measure SC stability margins, with the objective of building confidence in the FAM such that a complete validated SC system model can be built.

In line with this approach, validation experiments were designed with the primary aim of measuring IMU response, and particularly response *phase*, to control surface excitation across a range of Mach and height. In view of the known conservatism of the unsteady aerodynamics methods used, further aims were to quantify the over-prediction of control surface effectiveness, and the supplementary effect of aerodynamic incidence on this effectiveness at flexible mode frequencies. These effects can then be accounted for in the clearance process.

The importance of the logical, stepwise model development activity implicit in the process shown in Figure 3, and outlined later in Section 5, now becomes apparent; it is vital that the source of a response over-prediction can be correctly attributed, such that advantage may justifiably be taken and *appropriate* modifications made to the model. It is also clear that the test methods used must be capable of providing the required measurement of system characteristics with an adequate and known degree of accuracy. These considerations formed major constraints on the application of the relaxed D&C requirements, and, as noted below, strongly influenced the system design.

4.1 System Design Considerations

Consideration of the frequency range for which application of the relaxed criteria would have most benefit, and of modelling and excitation system capabilities suggested that the validation effort should be confined to the low frequency (less than 15Hz), pitch axis (symmetric) modes only. Accordingly, pitch rate and normal acceleration IMU output in response to inboard and outboard elevon excitation was measured and recorded, together with actuator position and wing tip acceleration.

The required results for FAM validation were transfer function measurements relating IMU outputs to control surface actuator excitation, for frequency domain comparison with predictions at Stage 1a) of the clearance process. The additional information relating to actuator and wing-tip responses allowed confirmation of the actuator modelling under actual test conditions, and gave additional information for FAM matching.

4.2 Flight Test Programme & Techniques

For validation of predicted response phase and quantification of the expected control effectiveness over-prediction, a grid of Flight Test points was specified at M0.4, 0.8 & 1.2 and various heights corresponding to conditions addressed in the flight clearance work, and including the critical flight conditions for this clearance phase. At selected points, the basic 1g trim tests were supplemented by FBI executions at a number of steady αs to allow quantification of the control effectiveness variation with α. The α's programmed were chosen on the basis of examination of the rigid aircraft control power vs. α trends.

The steady α tests demanded special techniques to maintain the required flight conditions for the duration of the FBI test. First the aircraft was stabilised at 1g, at the required Mach but above the specified height. The test excitation was then initiated, and a descending turn commenced, aiming to stabilise at the required α and passing the test altitude just prior to the excitation sweep reaching the mode frequency of interest.

To facilitate the matching process, time histories of Mach, height and alpha were included in the data delivered from each flight, along with details of fuel state before and after each test. This enabled re-prediction to be made at the correct test conditions.

4.3 Excitation System

The Eurofighter FBI excitation system is mechanised as a sub-system of the FCS, within the FCC. The FBI generates a digital demand signal at 320 samples per second. For the purposes of this exercise, where the maximum frequency of interest is 15Hz, this rate is high enough to avoid any aliasing and harmonic generation problems. The excitation demand is output in synchronisation with the actuator digital outer loop closure and applied to the summation point with the control law output, as shown in Figure 2.

The SC excitation signal is a swept frequency sinusoid with parameters selected from software memory by the pilot via a cockpit interface. The parameters are stored in sets defining specific combinations of start and stop frequency, duration, amplitude profile and actuator to be driven.

A deterministic test signal was preferred to aid visualisation, and to facilitate the 'profiling' of the excitation amplitude as a function of frequency. In order to maximise the test signal to noise ratio, the profiles were designed to match the limits of linearity of the actuators where this was the limiting factor (at low dynamic pressure), and to match response amplitude with structural dynamic loads limitations at higher speeds.

From EAP and ground test experience, and in line with the constraints on application of the relaxed criteria noted in 4.1, 2-15Hz logarithmic sweeps with a duration of 60 sec have been used. The long duration was intended to minimise the distorting effects of high sweep rates observed in ground test comparisons with 'single sine' test results, and the logarithmic frequency profile to give a better distribution of power through the sweep range.

4.4 Response Measurement & Recording System

As shown in Figure 2, measurements were obtained by the Flight Test Instrumentation (FTI) Recording System from the FCS IMU via the FCS databus and an FCC 'buffer' area of memory.

Note that data is recorded for post flight analysis; real time analysis is not required under the staged clearance procedure adopted.

The FCC buffer is updated at 160Hz (a multiple of the basic FCC iteration rate of 80Hz), is read by the FTI at 128Hz (a multiple of the binary basic iteration rate of the FTI), and loaded into a 'frame' of data on the digital tape. Post-test, the tape is processed and time histories required for analysis constructed. While FCS data is recorded at 128s/s, which is already high enough, compared with the maximum frequency of interest of 15Hz, to avoid aliasing problems, the data is padded with interpolated intermediate values to an effective

rate of 512s/s, for compatibility with data from airframe mounted accelerometers.

In all of this processing prior to analysis, there is clearly potential for the relative phase of the excitation and response signals to become distorted. Since this is the essential output of the flight testing for model validation and application of the phase stabilisation criteria, all of these operations had to be identified and accounted for in the model development process, as outlined in Section 3.6.

4.5 Analysis

In the application of FFT methods to the analysis of the data, a strong desire was to both maximise and understand the quality of the results obtained. To this end, some of the ideas regarding FFT analysis procedures outlined in Reference 4 & 5 were applied.

The weighted, overlapped, segmented averaging method first proposed by Welch (Reference 6) was employed. In this approach, the excitation and response time series are divided into a number of overlapping segments, which are then multiplied by a window function to force periodicity and reduce the statistical dependence of adjacent segments, and filtered to remove zero-frequency offsets. The FFTs of the individual segments are then averaged to form the result. The transfer function between input and output is formed from (Reference 4);

$$\hat{H}_{xy}(k) = \frac{\hat{G}_{xy}(k)}{\hat{G}_{xx}(k)}$$

Where $\hat{G}_{xy}$ is the cross spectral density estimate;

$$\hat{G}_{xy}(k) = \frac{1}{Kf_s n} \sum_{j=1}^{K} X_j^*(k) Y_j(k)$$

and $\hat{G}_{xx}$ is the auto spectral density estimate of the input signal time history;

$$\hat{G}_{xx}(k) = \frac{1}{Kf_s n} \sum_{j=1}^{K} \left| X_j(k) \right|^2$$

where;

K is the number of segments, f_s is sampling frequency, n is the number of data points/segment, k is the Discrete Frequency Variable, and X_j, Y_j are the FFTs for input and output for the *jth* segment,

The bias and variance errors inherent in the processing are controlled by increasing the length of individual segments, and increasing the number of segments averaged, respectively. Clearly, with a fixed overall quantity of data available, these requirements are in conflict.

Overlapping segments allows more segments to be averaged for a fixed overall data length, but the improvement is limited by the statistical dependence of successive segments. Carter (Reference 7) has shown that 62.5% overlap gives good results, but since transformation computation time is not an issue here, an overlap of 95% was adopted. Data windowing reduces statistical dependence of the segments, and reduces leakage in the spectral estimates, but also reduces resolution

and so offsets the bias error improvements gained by overlapping longer segments.

The following basic steps were followed:-

An appropriate analysis resolution was selected in order to achieve an acceptable level of bias error. This value of resolution was then used to decide the segment size, which was then used to calculate the random error of the transfer function estimates.

The resolution necessary is related to the bandwidth of the resonance peak being analysed - typified by the half power bandwidth where;

$$\left| H(f) \right|^2 = \tfrac{1}{2} \left| H(f_{PEAK}) \right|^2$$

From Bendat & Piersol (Reference 5) it may be inferred that the normalised bias error for transfer function estimation is of the order of:-

$$\varepsilon_b = \frac{2}{3} \left(\frac{B_e}{B_r} \right)^2$$

where B_e is the required analysis bandwidth and B_r is the half power bandwidth.

Thus: $$B_e = B_r \sqrt{\frac{3}{2} \varepsilon_b}$$

For a normalised error of, say, 5%, this gives:-

$$B_e = 0.27 B_r, = \frac{1}{3.7} B_r$$

This compares well with the recommendation of Young (Reference 4), but does not account for loss of resolution which later windowing of the data will cause: Young suggests halving the resolution to cover this;-

$$\Rightarrow B_e = 0.137 B_r, = \frac{1}{7} B_r$$

Wallace (Reference 8) recommends:-

$$B_e < \frac{1}{5} B_r$$

From Eurofighter ground test the first Wing Bending (WB1) mode has a half power bandwidth of approximately;

$$B_r = 0.15 \text{Hz}$$

$$\Rightarrow 0.02 \text{Hz} < B_e < 0.04 \text{Hz}$$

In flight, aerodynamic damping will increase the modes' half power bandwidth, so values of B_e of 0.06Hz and 0.03Hz were selected.

Since: $$B_e = \frac{1}{T}$$

where T is the Length of the data series analysed, and

$$T = n\Delta t$$

where n is the Number of Data Points in the series, and Δt is the Sample Interval, it follows that;-

$$B_e = \frac{f_s}{n}$$

where f_s is the Data Sample Rate $\frac{1}{\Delta t}$, or;

$$n = \frac{f_s}{B_e}$$

Here, $f_s = 512Hz$, and for

$$B_e = 0.03Hz \quad n = 17066,$$

or for $B_e = 0.06Hz \quad n = 8533$

Close binary values, for which the FFT is most economical were 8192 and 16384, giving bias errors (by the above definition) of:-

$$n = 8192 \Rightarrow B_e = 0.0625Hz \Rightarrow \varepsilon_b = 11.5\%$$

$$n = 16384 \Rightarrow B_e = 0.03125Hz \Rightarrow \varepsilon_b = 3\%$$

The number of overlapping blocks which cover the entire data is given by:-

$$K = \frac{N - n * P}{n(1 - P)}$$

Where N is the Total number of points available and P is the overlap ratio

For 95% overlap; $n = 8192 \Rightarrow K = 62$,

$$n = 16384 \Rightarrow K = 21$$

Wellsted (Reference 9) gives the random error (variance) as:-

$$\frac{Var(|H(k)|)}{|H(k)|^2} = Var(Arg(H(k))) = \frac{1}{2K}\left(\frac{1}{\gamma_{xy}^2} - 1\right)$$

Where γ_{XY}^2 is the 'ordinary' coherence function:

$$\gamma_{xy}^2(k) = \frac{|G_{xy}(k)|^2}{G_{xx}(k)G_{yy}(k)}$$

Insertion of the proposed analysis parameters predicts very small random errors for values of coherence greater than 0.8

Analyses were conducted with both sets of parameters, for comparison. The alternative analysis parameters and associated Bias and Random errors (ε_b and Var) are summarised in the table below.

n	B_e	ε_b	K	Var
8192	.0625Hz	11.5%	62	0.002
16384	.03125Hz	3%	21	0.006

5. RESULTS

5.1 Model Match to SCT

Progression from Stage 1 to Stage 1a) in the Figure.3 process requires validation of the FAM structural elements, i.e. the inertial excitation and modal dynamics parts of the Figure 2 flexible aircraft schematic, and of the FCS hardware representation, i.e. the linear modelling of the actuation system and the IMU and FCS data bus. Figure 4 shows the end result of this phase of work, showing test-measured and matched-model predicted IMU pitch rate response to outboard symmetric flap excitation. The SC test was carefully conducted using the benchmark stepped-sine 'correlation' technique, and is regarded as definitive over most of the tested range.

Of particular note are the excellent phase match through to 11.5Hz, indicating well-modelled FCS hardware. The gain match at frequencies below WB1 (6Hz) is less good, perhaps due to interference from the SCT pneumatic soft-support system.

Beyond 11.5Hz the match deteriorates, probably because of the influence of the relatively poor fuselage model, and its contribution to the higher frequency modes.

5.2 Model Match to On Ground FBI

To verify understanding of the FBI input / output, and to validate its representation in the SC System Model, Figure 5 shows the matched-to-SCT FAM with added FBI input / output modelling, plotted against results from an on ground execution of the FBI. The FBI results plotted are for the lower resolution, 8192 point-per-segment analysis. The coherence loss at 6Hz indicates that finer resolution is required in this frequency range, which was confirmed by the analysis with 16384 points. Results for the higher frequency mode at 11Hz deteriorated however, indicating the 8192 point analysis presented here is better balanced between resolution and variance for this mode. Again the excellent phase match is notable, indicating well matched FBI hardware models. The 2.5 and 3Hz modes in the test are undercarriage dynamics not included in the model. Note also the frequency sweep effects (similar between 8192 and 16384 analyses) on the WB1 mode peak, pushing it towards higher frequencies.

5.3 Model Match to In Flight FBI

In Stage 1a) in the Figure 3 process, the now validated FAM structural components, FCS hardware and FBI System models are combined and used to re-predict SC FBI Flight Test results. Comparison of test and prediction then leads to validation of model predicted response phase and allows evaluation of the conservatism in the modelled control surface effectiveness.

Figure 6a) shows predicted and measured SC results for M0.4 20,000ft. 1'g'. FBI analysis parameters were similar to Figure 5. The WB1 peak displays the same test-method effects as the on-ground comparison, but with additional loss of model / test peak amplitude, attributable to the noted deficiencies in modelling of control effectiveness. The good coherence at sub-WB1 frequencies indicates that the relatively poor match between 2 & 5Hz is not due to test technique, but may be due to mis-matched flight conditions or fuel state between the test and prediction.

After accounting for the above effects, and considering the excellent representation of phase trends with frequency, the Figure indicates that the FAM is providing a good

representation of SC characteristics; the Nichols presentation Figure 6b), which de-emphasises test method effects on peak frequency, demonstrates this.

6. CONCLUSIONS AND RECOMMENDATIONS

The results have shown that the FBI system and mathematical modelling give good results over the frequency range of interest. Extensive investigation and model matching work has lead to a good understanding of the FBI/FTI/Analysis System and formed a solid base from which flight clearances based on 'relaxed', phase stabilisation SC stability criteria have been developed in the Eurofighter consortium.

While it has been shown that the current methods of excitation and analysis give acceptable results, it is clear that further investigation of alternative excitation schemes (e.g. faster, multiple sweeps, or Schroeder Phased excitation, Reference 4) and analysis methods (e.g. Chirp z-Transform (Reference 10) is warranted, in order to maximise benefit gained from the costly flight testing.

7. ACKNOWLEDGEMENTS

Eurofighter is a collaborative programme, and the authors wish to acknowledge the contributions of the partners from Deutsche Aerospace, Alenia and CASA to the work described in this paper.

8. References

1 Caldwell,B.D., "The FCS/Structural Coupling Problem and its Solution", AGARD CP-560, Paper 16, 1994

2 Lambourne,N.C., Wight,K.C., and Welsh,B.L., "Measurements of Control Surface Oscillatory Derivatives on a Sweptback, Tapered Model Wing in Two Transonic Tunnels", MoD PE Aeronautical Research Council R&M No.3806, 1977

3 Brenner,M.J., "Actuator and Aerodynamic Modelling for High Angle of Attack", AIAA 93-1419, April 1993

4 Young,P., "An Assessment of Techniques for Frequency Domain Identification of Helicopter Dynamics", D.Phil. Thesis, Dept.of Electronics, University of York, 1993

5 Bendat,J.S., and Piersol,A.C., "Engineering Applications of Correlation and Spectral Analysis", John Wiley & Sons, New York, NY, 1993

6 Welch,P.D., "The Use of the Fast Fourier Transform for the Estimation of Power Spectra: A Method Based on Time Averaging Over Short Modified Periodograms", IEEE Transactions in Audio and Electro acoustics, Vol.AU-15, No.2, 1967 pp70-73

7 Carter,G.C., Knapp,C.H.,and Nuttall,A.H., "Estimation of the Magnitude Squared Coherence Function Via Overlapped Fast Fourier Transform", IEEE Transactions in Audio and Electro acoustics, Vol.AU-21,No.4, 1973 pp337-344

8 Wallace,R., Gabri,B., Mathews,J., and Tomlinson,A., "Course Notes - Basic Practical Signal Processing", Signal Processing and Applications Group, Cranfield Institute of Technology, Bedford, 1979

9 Wellsted,P.E., "Spectral Analysis and Its Applications", Control Systems Centre Report No.411, UMIST, Manchester University, 1978

10 Tischler,M.B., "Frequency Response Identification of XV-15 Tilt Rotor Aircraft Dynamics", NASA TM-89428, 1987
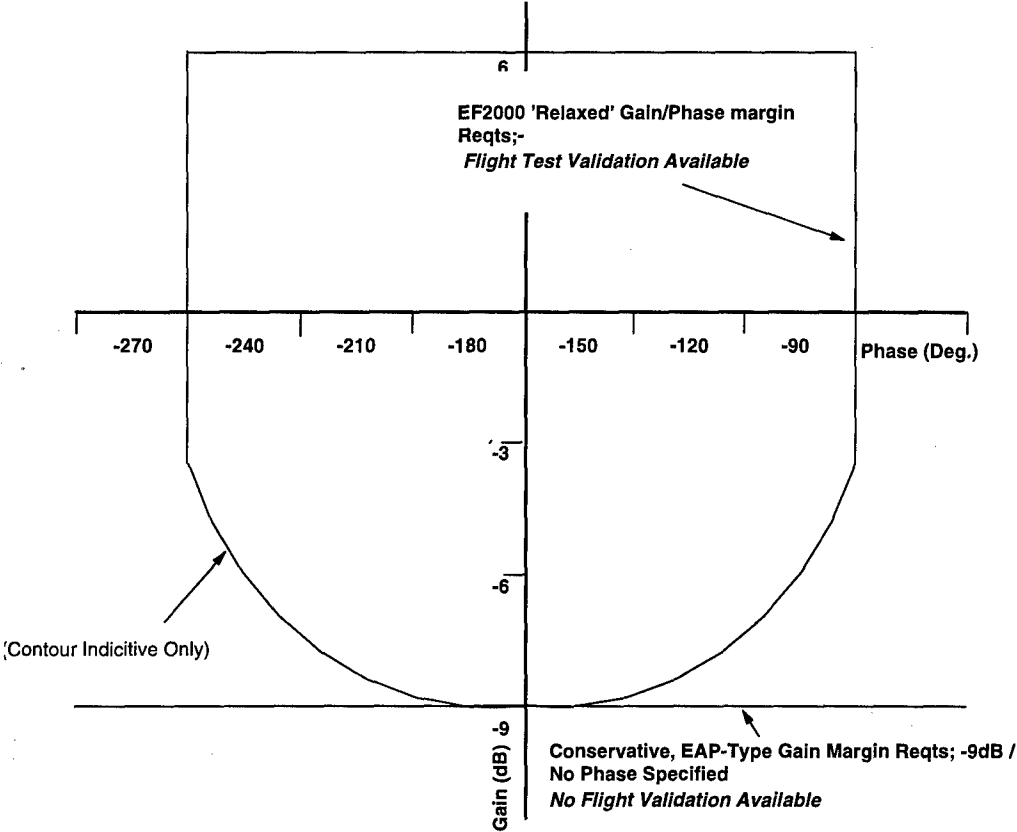
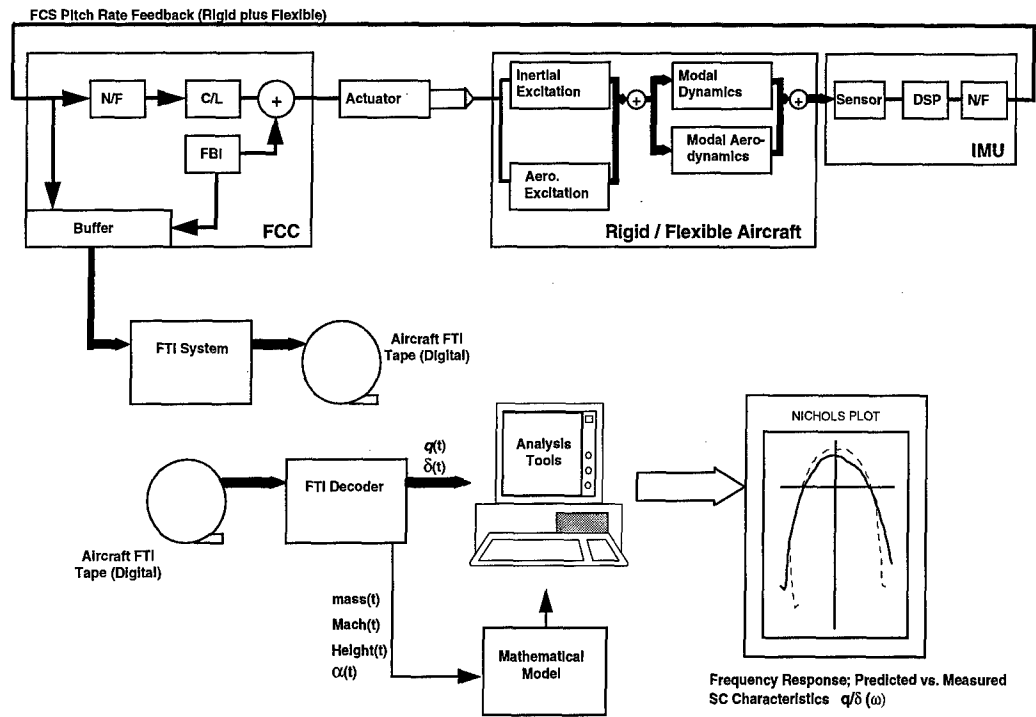Figure 1. SC Stability Margin Requirements
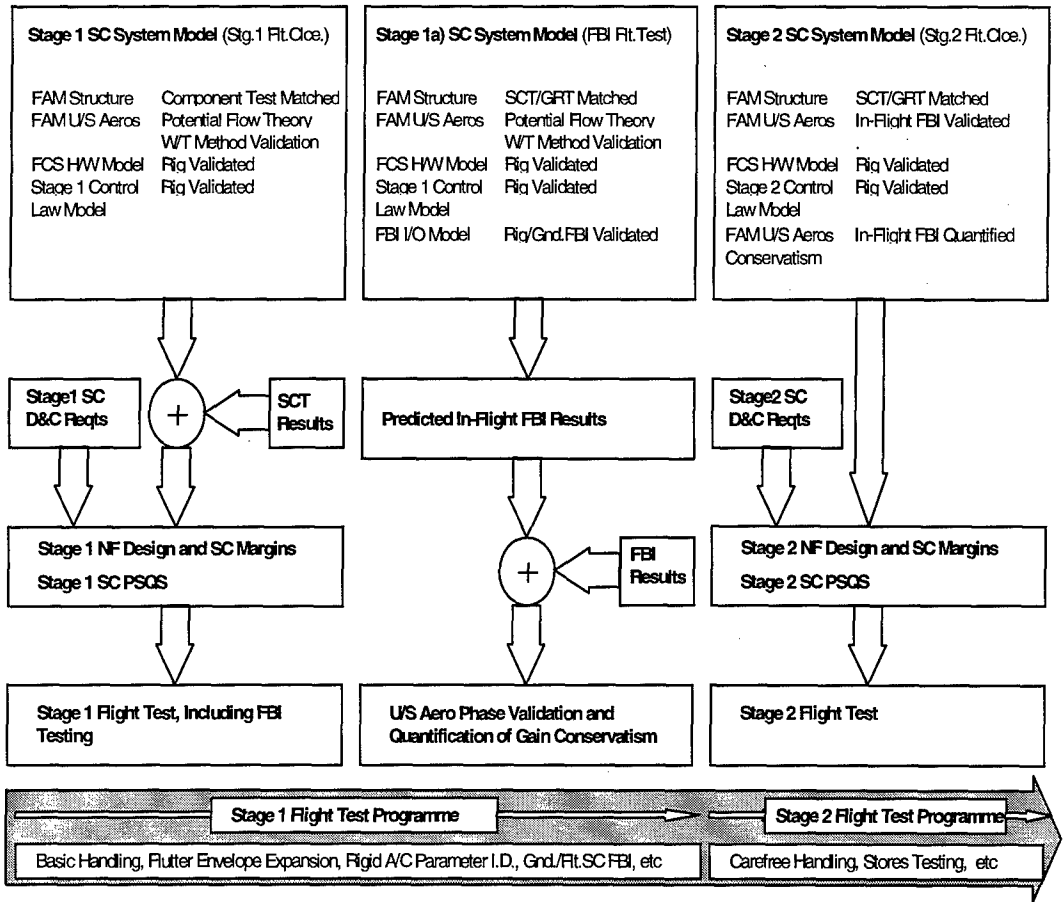
Figure 2. SC System Schematic
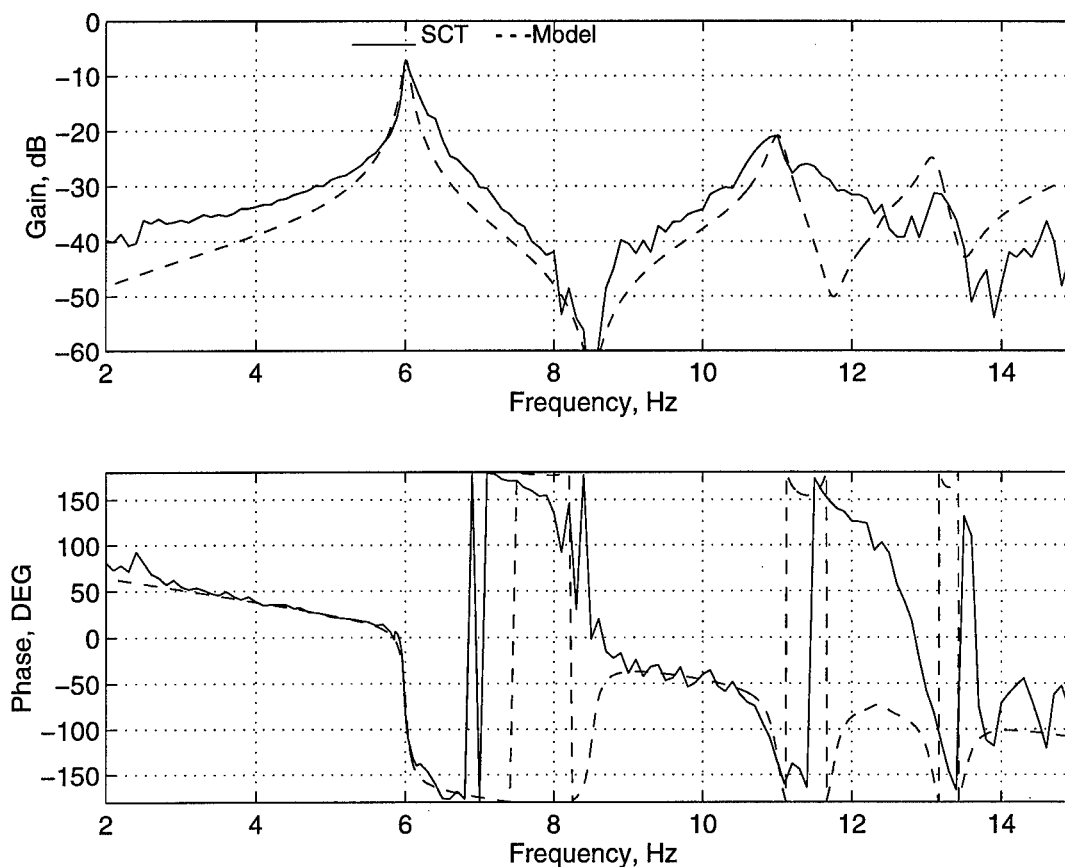

Figure 3. SC D&C Process Schematic

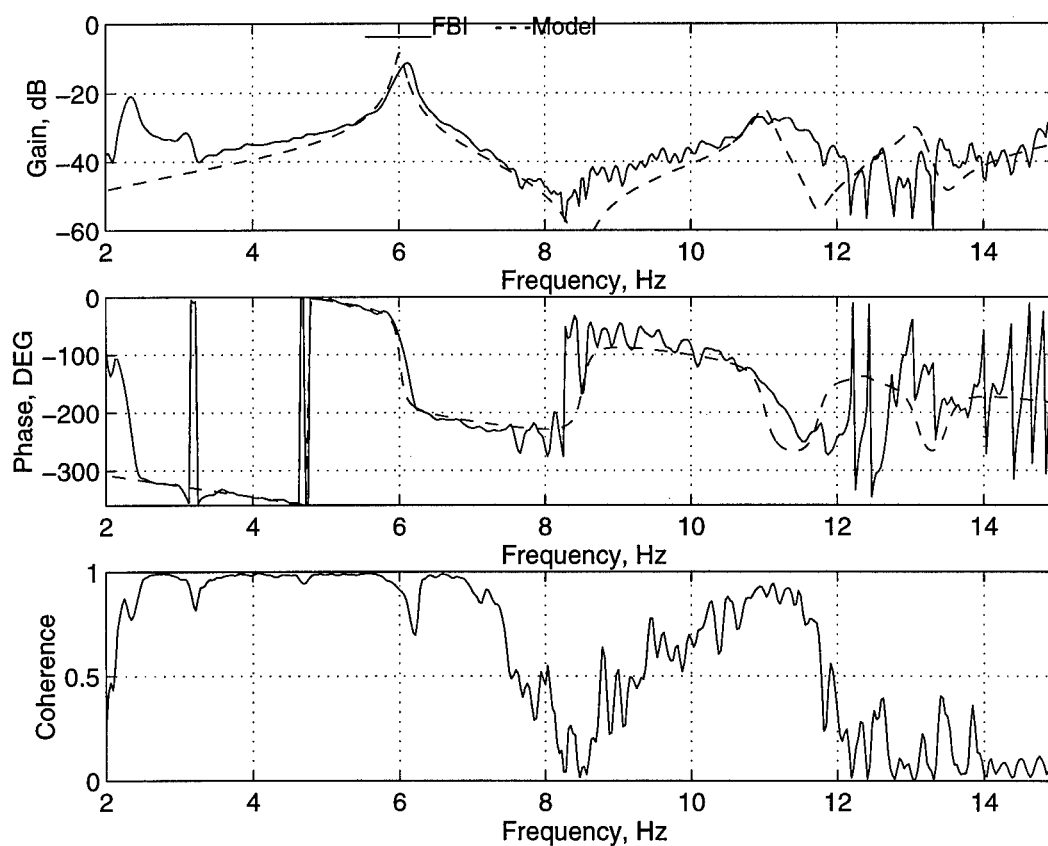Figure 4 Comparison:- Ground SCT/Model Prediction

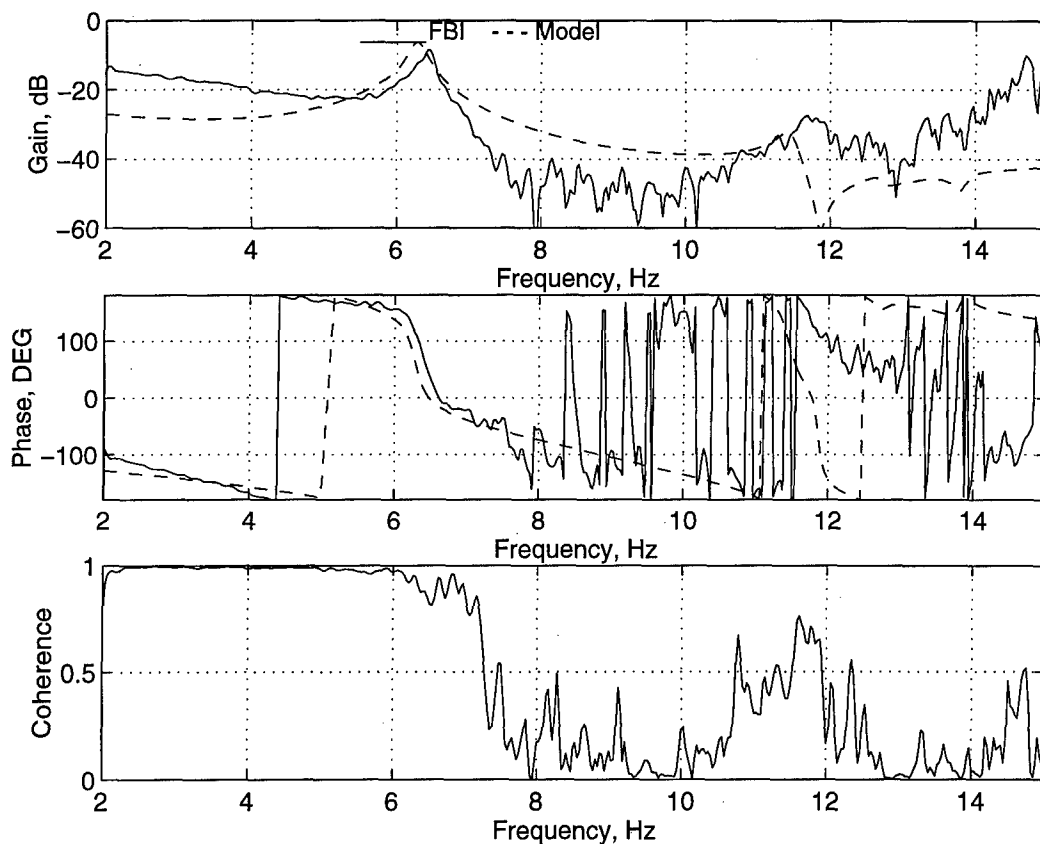Figure 5 Comparison:- Ground FBI/Model Prediction
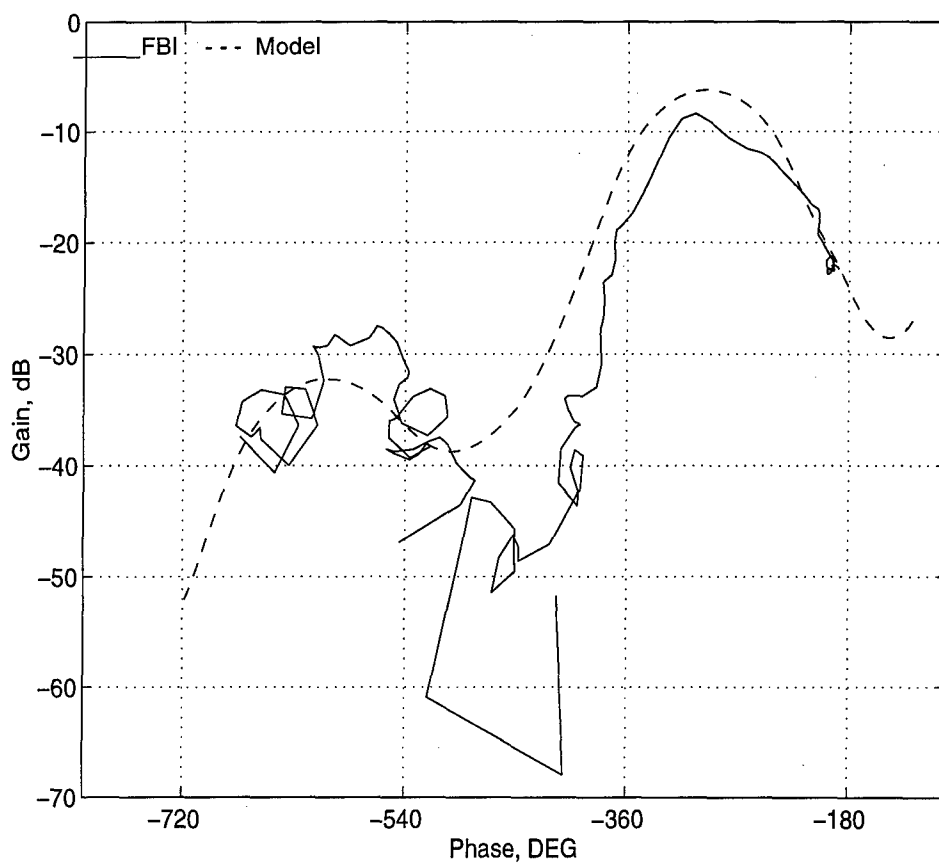
Figure 6a) Comparison:- In-Flight FBI/Model Prediction

Figure 6b) Comparison:- In-Flight FBI/Model Prediction (Nichols Plot)

Flight-Time Identification of a UH-60A Helicopter and Slung Load

Luigi S. Cicolani

Army/NASA Rotorcraft Division
Ames Research Center, MS N211-2
Moffett Field, CA 94035-1000, USA

Allen H. McCoy

U.S. Navy Post Graduate School
Monterey, CA, USA

Mark B. Tischler

ARMY/NASA Rotorcraft Division
Aeroflightdynamics Directorate (AVRDEC)
US Army Aviation and Missile Command
Ames Research Center, Mail Stop N210-5
Moffett Field, CA 94035-1000, USA

George E. Tucker

Advanced Air Transportation Technology Office
Ames Research Center, Mail Stop 262-5
Moffett Field, CA 94035-1000, USA

Pinhas Gatenio

Dani Marmar

Israel AF Flight Test Center, Instrumentation Dept., Israel

SUMMARY
This paper describes a flight test demonstration of a
system for identification of the stability and handling
qualities parameters of a helicopter-slung load
configuration simultaneously with flight testing, and the
results obtained. Tests were conducted with a UH-60A
Black Hawk at speeds from hover to 80kts. The principal
test load was an instrumented 8x6x6ft cargo container.
The identification used frequency domain analysis in the
frequency range to 2Hz, and focussed on the longitudinal
and lateral control axes since these are the axes most
affected by the load pendulum modes in the frequency
range of interest for handling qualities. Results were
computed for stability margins, handling qualities
parameters and load pendulum stability. The
computations took an average of 4 minutes before
clearing the aircraft to the next test point. Important
reductions in handling qualities were computed in some
cases, depending on control axis and load-sling
combination. A database, including load dynamics
measurements, was accumulated for subsequent
simulation development and validation.

1. INTRODUCTION
Helicopter slung load operations are common in both
military and civil contexts. The slung load adds load rigid
body modes, sling stretching, and load aerodynamics to
the system dynamics, which can degrade system stability
and handling qualities and reduce the operating envelope

of the combined system below that of the helicopter alone.

Military helicopters and loads are often qualified for these operations via flight tests which can be expensive and time consuming. These activities include certification of loads for the multi-service Helicopter External Air Transport (HEAT) manual [1], in which pilots evaluate specific load-helicopter combinations for flying qualities and airspeed limits without analytical support and without generating quantitative stability data. There can also be extended tests, including analyses, to certify a helicopter load carrying capacity, [2]. However, stability and envelope can vary significantly among the large range of loads, slings, and flight conditions which a utility helicopter will encounter in its operating life, and flight tests cannot practicably encompass the entire operating range of configurations.

A recent industry paper [2] has advocated the accumulation of quantitative stability data from slung load certification flight tests and pointed out the potentially significant reductions in cost and risk available from using a validated simulation to predict stability for a variety of sling-load combinations and to predict the critical cases for flight test evaluation. Towards these objectives, an exploratory project was initiated at Ames in which flight tests were conducted to demonstrate identification of aircraft stability and handling qualities and load pendulum stability simultaneously with the flight test. Such a capability would have potential for significant reductions of qualification tests in comparison to point-by-point testing. Stability evaluations were made after each test airspeed before going on to the next. A database was also accumulated for subsequent simulation development and validation efforts.

This paper describes the flight test method and results. The test aircraft was a UH-60A Black Hawk, and the principal test load was an instrumented 8x6x6 ft CONEX cargo container. The CONEX is a low-density load with significant aerodynamics such that load stability limits the system flight envelope. The load instrumentation included accelerometers, angular rate sensors, and fluxgate compass, and was provided by the Israel Flight Test Center under a US/Israel memorandum of agreement for cooperative research on rotorcraft aeromechanics and man-machine integration technology [3]. Under this agreement the US would provide the aircraft, load, and test range and Israel would provide an instrumentation package and wind tunnel testing. The load instrumentation allowed computation of load stability parameters during flight tests, and documented details of the load dynamics not previously available for simulation validation.

Tests focused on the longitudinal and lateral axes in which the load pendulum motions have their principal effects on aircraft control. Tests were conducted at airspeeds between hover and 70kts. The identification computations used the CIFER® software previously developed by the Army group at Ames [4], [5].

The paper begins with a discussion of the parameters to be identified and the required computations for that, followed by descriptions of the test configurations, the test instrumentation, the flight test profile, and the data acquisition system and computational procedure for flight time identification. Identification results for all parameters are presented. The paper ends with a brief comparison of load motions from flight and simulation, and an assessment of simulation development issues. Reference [6] provides more extensive documentation of the test equipment and results.

2. IDENTIFICATION COMPUTATIONS

2.1 Dynamic System

The dynamic system (fig 2.1) consists of helicopter and load. A stability augmentation system is closed around this, and the pilot closes another loop around that combination to regulate the system to a desired flight path. The plant element is rich in dynamics which include the helicopter's rigid body modes, rotor modes, engine and drive train modes, and structural modes; and the load adds its rigid body and elastic sling modes to this set.
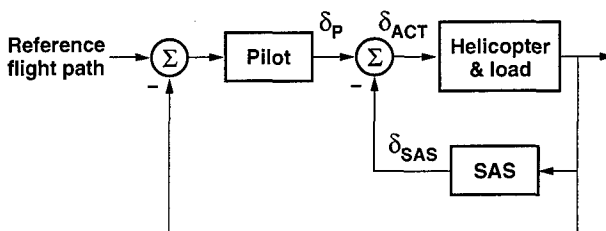

Figure 2.1 Dynamic System.

Over the years, the US military has developed handling qualities requirements that the closed loop system must meet to avoid PIO tendencies when the pilot exercises control [7], and stability margins that the stability augmentation system (SAS) must meet to avoid potentially destructive resonance with the plant dynamics [8]. The clearance of loads is concerned with evaluating these handling qualities and stability margins for the combined system and the stability envelope of the load. Quantitative assessment of stability and handling qualities is based on frequency domain analysis of the dynamic system.

Flight condition: hover, lateral axis, 4K CONEX
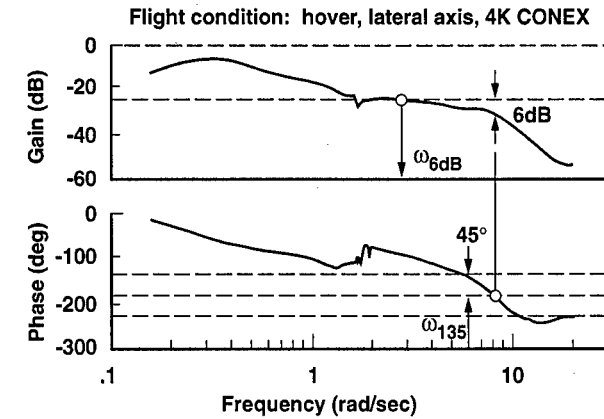
Bandwidth: $\omega_{BW} = \min\{\omega_{6dB}, \omega_{135}\}$

Phase delay: $\tau_{PD} = -\dfrac{\Phi(2\omega_{180}) + 180}{2\omega_{180}}$ or $-\dfrac{1}{2}\left(\dfrac{d\Phi}{d\omega}\right)_{\Phi=180}$
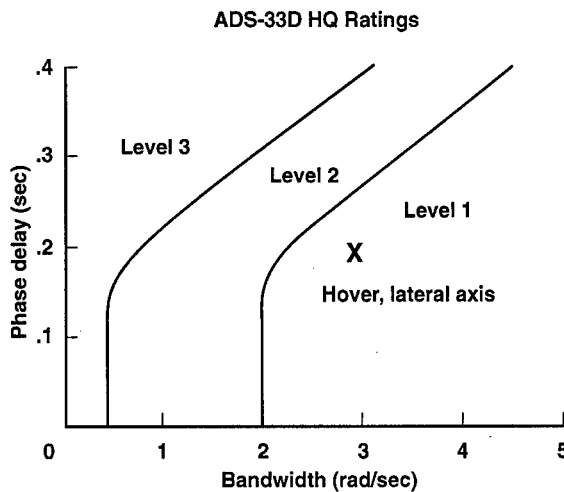
ADS-33D HQ Ratings

Figure 2.2. Handling Qualities Parameters from Attitude Response.

2.2 Handling Qualities

The handling qualities parameters are properties of the closed loop attitude frequency response. Two primary parameters are bandwidth and phase delay (fig 2.2). Bandwidth is measured as the maximum input frequency for which 6db of gain margin and 45 deg of phase margin can be obtained. Fig 2.2 indicates the required computations are to determine the two frequencies where these margins are obtained and then bandwidth is taken as the smaller of the two. Instances occur in which phase is below -135deg at all frequencies, in which case bandwidth is zero. Phase delay is the rate at which phase changes at the frequency where the phase shift is 180deg, and can be computed from a two-point estimate or a least squares fit at that frequency.

Phase delay indicates how rapidly the system is going unstable as the input frequency approaches the point of 180 deg phase shift. Larger values imply a rapid loss of pilot-vehicle stability margins, and result in pilot complaints about PIO tendencies.

Army specifications for these parameters are defined in an Aeronautical Design Standard document, ADS-33D [7]. A satisfactory system is required to have its combination of bandwidth and phase delay within a specified region, termed level 1, where simulation and flight tests indicate satisfactory pilot ratings are obtained (fig 2.2). Additional regions are level 2 (satisfactory with improvements) and level 3 (unsatisfactory). At phase delays below .15 sec the specifications require a minimum bandwidth of 2rad/sec for level 1. For phase delays above .15 sec, increased phase delay requires more bandwidth.

The ADS-33D specifications for handling qualities were defined to serve the Comanche (RAH-66) procurement, with the object of providing acceptable behavior for a suite of tasks appropriate to scout attack rotorcraft. It includes requirements for other motion parameters in addition to the on-axis attitude response parameters computed in this study. ADS-33D is based on simulation data and flight data from several helicopters including the UH-60. Although slung load tasks were not included in the ADS-33D specification, the ADS-33D levels 1-3 will be used as the reference specifications for the present discussion. Another Army project at Ames is currently in progress to extend that specification to cover cargo helicopters and slung load operations in support of the improved cargo helicopter procurement [9].

2.3 Stability Margins

Stability margins define the stability robustness of the aircraft/SAS feedback loop to changes in gain (gain margin) and phase (phase margin). Typical requirements from MIL-F-9490D [8] are for 6db of gain margin (a factor of 2) and 45 deg of phase margin. These margins also ensure well-damped responses to turbulence and pilot inputs. The UH-60 has roll, pitch and yaw SAS channels, and stability margins can be computed for these channels.

The control system stability margins are properties of the control loop computed from the broken-loop frequency response of the SAS signal to the inputs to the primary actuators as shown in fig 2.3. The phase margin is computed at the crossover frequency where the gain crosses through 0db, and is the margin from 180deg of phase shift there. There can be multiple crossings, as in the sample case, in which case the phase margin (PM) is taken as the smallest phase margin for crossings in the frequency range of interest [.05, 2.0]Hz. Cases occur in which gain never crosses below 0db, in which case phase margin is infinite and instability cannot occur. The gain margin (GM) is computed where the phase angle goes through 180deg.
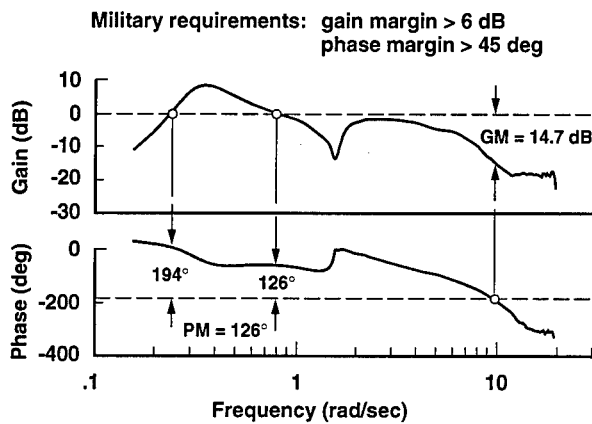
Military requirements: gain margin > 6 dB
phase margin > 45 deg

Figure 2.3. Stability margins from control response $\dfrac{\delta_{SAS}(s)}{\delta_{ACT}(s)}$.

2.4 Load Pendulum Modes

Linear analysis indicates the load adds a number of modes to those of the helicopter alone; these are two pendulum modes, two yaw modes, and 3 oscillatory sling stretching modes. Of these, only the pendulum modes interact with the helicopter in the frequency range of interest. The pendulum frequencies can be estimated from a point mass dumbbell approximation of the system as

$$\omega_p = \sqrt{\frac{g}{\ell}\left(1+\frac{W2}{W1}\right)}$$

where ℓ, W1, W2 are sling length, and the helicopter and load weights, respectively. Pendulum frequencies of 1 to 1.5 rad/sec can be estimated for the current configurations.

Simulation model analysis indicates that the pendulum modes at hover are decoupled lateral and longitudinal pendulum motions relative to the helicopter and that these are readily excited by lateral and longitudinal control inputs, respectively. Consequently, each mode can be identified by fitting a second order pole to the frequency response of the load angular rate in the region around the pendulum frequency. A typical frequency response is shown in fig 2.4; gain peaks near the expected load pendulum frequency, and the fitted 2nd order system is seen to achieve a close fit to the flight data.

3. FLIGHT TEST CONFIGURATIONS

3.1 Test Configurations

Flight tests were performed with an instrumented UH-60A and with several test external loads and slings (fig 3.1). It is noted that the UH-60 without a load has significant stability margins from the minimums allowed and is thus a safe aircraft for slung load research where margins can be reduced by the load. The load-sling combinations tested are drawn to scale in fig 3.2. These

included an instrumented CONEX (CONtainer EXpress) cargo container, a steel plate, and a steel block suspended with single and multi-cable slings. The plate and block were well-behaved out to the power-limited level flight speed of the aircraft (about 140 kts) and were used in the first phase of the work. The CONEX was an easily available load with nontrivial and complex aerodynamics which limit its operational envelope to 60kts.

Hover lateral pendulum mode: $\zeta = 0.166$ $\omega_p = 1.53$ rad/sec
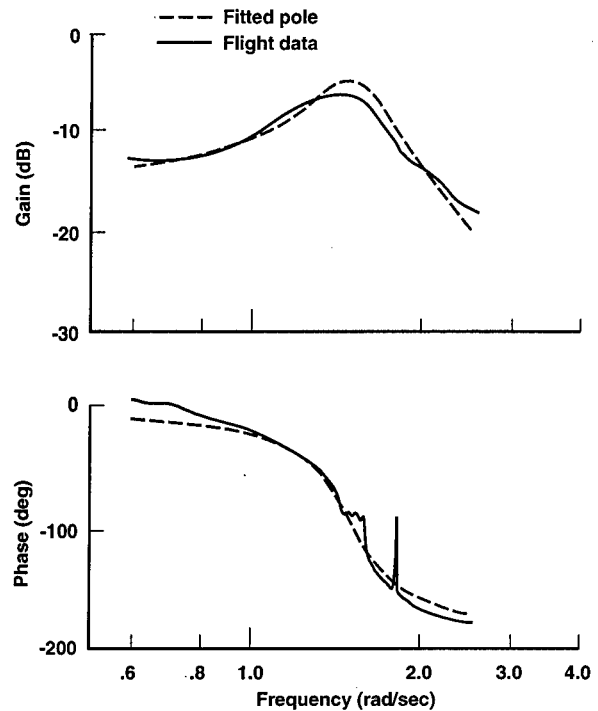
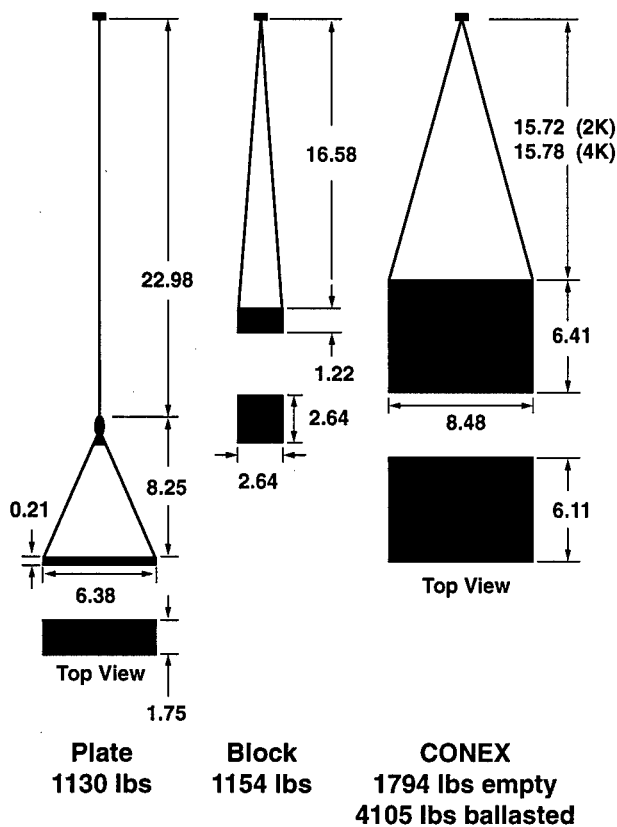Figure 2.4. Identification of load pendulum roots.
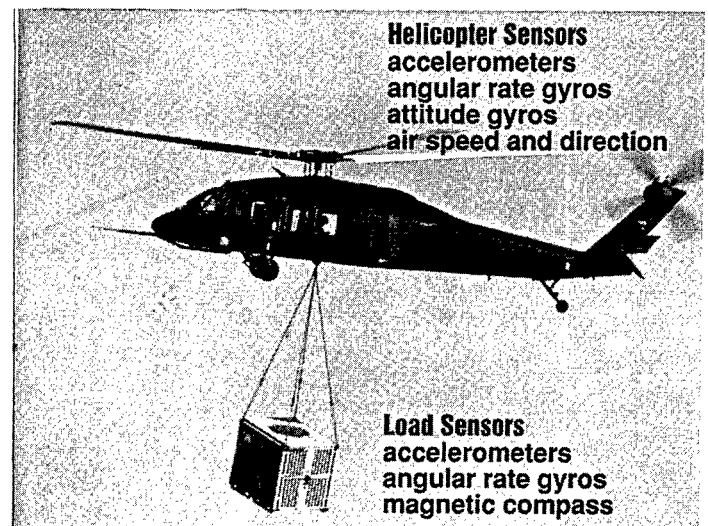
Figure 3.1. UH-60 with CONEX load.

Figure 3.2. Load-sling test configurations.

Note: All dimensions in ft

Plate   **Block**   **CONEX**
1130 lbs   **1154 lbs**   **1794 lbs empty**
                              4105 lbs ballasted

Slung load configurations can be viewed as two rigid bodies connected by a sling. In general, the configuration can be defined by all the fixed parameters of the helicopter, the load, and the sling for which numerical values are required in the system's equations of motion. All of these parameters play some more or less important role in the motions of the 2-body system which can be studied in simulations. Out of the existing range of such systems, the present tests are limited to one helicopter, and a small sample of slings and loads, but this suffices for our immediate objectives.

3.2 Helicopter Parameters

The helicopter's basic rigid body parameters are listed in fig 3.3. The gross weight and cg location are standard takeoff values for this aircraft with slung load crew (2 pilots and crew chief). Approximately 1800lbs of fuel (2 hrs of flight) is available for use during a test, with corresponding changes in gross weight and with forward movement of the cg by 9 in. Aerodynamic and other information for the UH-60 can be found in [10] - [13].

The UH-60A hook (fig 3.4a) is mounted in the floor of the helicopter and can be released manually at the hook or from the right seat stick. It is gimbaled only in roll so that the load-sling combination swings laterally about this axis, and longitudinally at the hook load beam about 8in lower. The hook is offset 4.3ft below the aircraft cg and up to 1 ft forward of the cg depending on fuel weight, and is rated at 8000lbs carrying capacity.

Figure 3.3 Helicopter and Load Rigid Body Parameters.

(a) Helicopter

Takeoff Weight	14,601 lbs.	
Max External Load	8,000 lbs.	

Coordinates	Takeoff cg	Hook
station	363.5	352.6 in
butt line	0	0
water	247.2	195.5 in

(b) Loads

Load	Plate	Block	Empty CONEX	Ballasted CONEX
Weight	1130	4154	1794	4105 lbs.
Density	456	488	5.4	12.5 lbs./ft^3
Ixx	108	91	785	1876 slg-ft^2
Iyy	212	91	569	1482
Izz	121	150	766	1377
Zcg	-.4	0	0	1.4 ft.

Notes:
- Inertias, Ixx, ..., are computed about the load cg.
- Axes used for inertias are:
  plate: x along the long dimension, z down
  block: x along a horizontal edge, z down
  CONEX: y along longest dimension, z down
- Zcg = vertical distance from geometric center to cg, positive down
- Empty CONEX data includes installed instrumentation

3.3 Load-Sling Parameters

Flight test data was obtained for the aircraft alone and with the sling-load combinations shown in fig 3.2. Load weights ranged from 1000lbs to 4000lbs (up to 50% of the hook capacity and 28% of helicopter weight). The CONEX weight was varied by ballasting it with bags of gravel-like material of density 43 lbs / ft^3, and it was flown empty at about 2K lbs. and ballasted at 4K lbs.

The dimensions of these load-sling combinations are noted in fig 3.2, and mass-inertia data for these loads is listed in fig 3.3. Fig 3.2 gives an impression of the differences in sling length and geometry. These differences are moderate, but quite different results were obtained at hover among these loads, probably due to these geometric differences.

The 1K plate load consisted of a steel plate (1070 lbs.) and wire bridle with swivel and ring (60 lbs.). It was suspended with a standard 20ft military sling comprised of 2 loops of flat nylon webbing, and attached at the ends with nylon rings (fig 3.4b). Such slings are described in

[1] and occur in the US military inventory in various lengths from 3 to 140 ft.

The remaining test loads were suspended with a standard military 4-legged sling set rated at 10K lbs. and weighing 52 lbs. Each leg of this sling is a 12 ft braided nylon rope connected to an 8ft steel chain which is passed through a load lift point and returned to a grabhook at the end of the rope (fig 3.4c). The details of rigging this sling to certified loads such as the CONEX, are specified in the HEAT manual [1]. Similar sling sets with ratings up to 40K lbs. occur in the military inventory and can be rigged with 2 to 6 legs, depending on the load as seen in the HEAT manual, [1]. This sling was flown in the present tests with and without a swivel, and the resulting load yaw motions at airspeed were quite different.

Sling stretch properties will not be discussed in detail since stretching occurs at frequencies well above the range of interest in handling qualities studies. The slings are fairly stiff and stretching was estimated at a fraction of 1 ft in all cases. The sling lengths given in fig 3.2 are for the loaded sling.

3.4 Load Aerodynamics

The available aerodynamic data for slung loads is limited to a few specific loads. Load aerodynamics are unimportant for very dense loads such as the steel plate and block loads ($450 \, lbs \, / \, ft^3$). These can be flown over the power-limited speed range of the helicopter without generating significant aerodynamic specific forces and moments. The CONEX is much less dense ($5\text{-}12 \, lbs \, / \, ft^3$ average density in the present tests) and can generate sufficient aerodynamics to affect load motions. The effects include a load trail angle in proportion to the drag specific force, and modification of the load pendulum motions in various ways as airspeeds increases, including coupling of the yaw degree of freedom with the load lateral and longitudinal pendulum motions and a speed limit for stability well below the helicopter's power–limited speed. The CONEX drag can be estimated at $D/Q = 75 \, ft^2$ which yields trail angles of 19.5 deg and 8.8 deg for the empty and ballasted CONEX at 50kts, respectively, and these loads reach .5g specific drag at 60, and 90kts, respectively.

The principal parameters affecting load motions are as follows. The load pendulum frequency is set principally by sling length and load relative weight, while helicopter cg-to-hook offset couples the load motions to the helicopter attitude dynamics which then are a source of damping in accordance with helicopter aerodynamics and inertias. Load aerodynamic forces and moments increase with airspeed and have an increasing effect on load dynamics depending on the magnitude of the specific forces and moments produced.

(a) UH-60A Cargo Hook with Weigh System
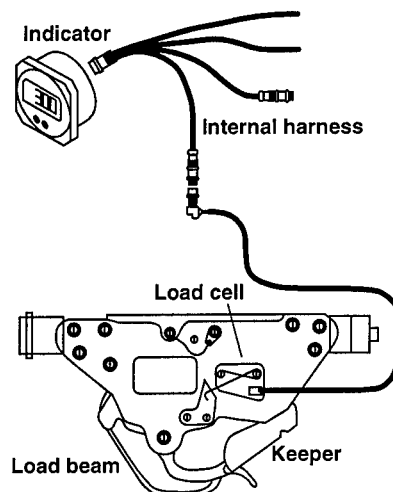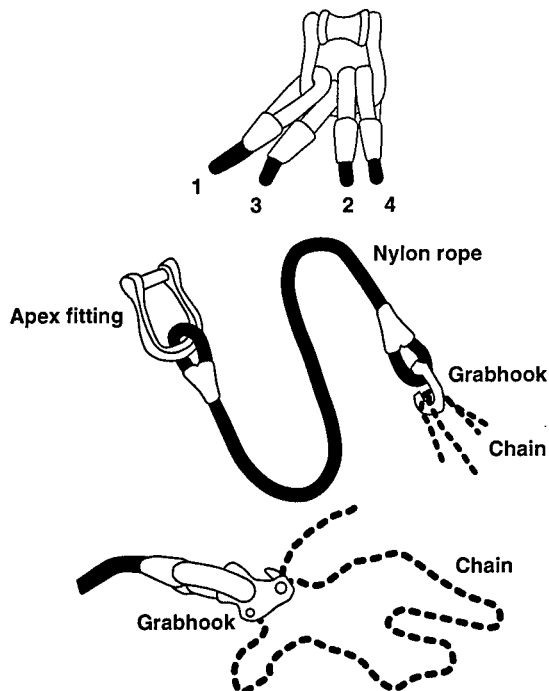

(b) Nylon Web Sling
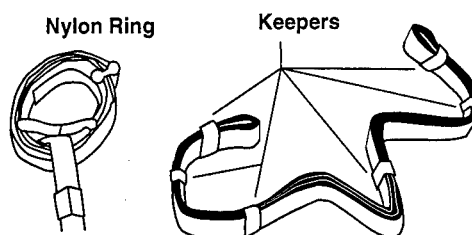
(c) Nylon Cord Sling Set

Figure 3.4. Suspension Details ([1], [17]).

4. INSTRUMENTATION AND SIGNALS

4.1 Helicopter and Load Sensors

The test aircraft was heavily instrumented for an earlier airloads study at Ames, as described in [14]. The sensors recorded for the slung load tests were those measuring the aircraft rigid body states and control deflections. These are listed in fig 4.1 along with sensor ranges and the data sampling rates for recording and telemetry (209 HZ). The hook was also instrumented with a strain gauge load weight cell [15].

The load instrumentation is listed in fig 4.1. This included a gimballed magnetic fluxgate compass [16] mounted on

an aluminum boom extending 2.5ft from the CONEX (fig 4.2) to minimize magnetic interference from the steel CONEX. The remaining load instrumentation [17] was contained in a single package mounted on an aluminum crossbeam installed in the CONEX near the geometric center (fig 4.2). The instrumentation package (fig 4.3) contained 3-axis accelerometers and angular rate sensors, and also pitch and roll inclinometers. This package, including power supply, filters, PCM encoder, and telemetry transmitter was assembled at an estimated cost of $40K, and weighed 119 lbs. including the mounting.

Figure 4.1 Instrumentation

| Helicopter sensors sample rate = 209 Hz	Range	Load sensors sample rate = 260 Hz	Range
Longitudinal stick position	[0, 100] %	Roll Inclinometer	[-90, 90] deg
Lateral stick position	[0, 100] %	Pitch inclinometer	[-90, 90] deg
Pedals	[0, 100] %	Fluxgate compass	[0, 360] deg
Collective	[0, 100] %	Roll rate gyro	[-60, 60] deg/sec
Longitudinal SAS output	[0, 100] %	Pitch rate gyro	[-60, 60] deg/sec
Lateral SAS output	[0, 100] %	Yaw rate gyro	[-120, 120] deg/sec
Directional SAS output	[0, 100]%	Longitudinal accelerometer	[-2, 2] g
Longitudinal mixer input	[0, 100] %	Lateral accelerometer	[-2, 2] g
Lateral mixer input	[0, 100] %	Vertical accelerometer	[-1, 3] g
Directional mixer input	[0, 100] %		
Roll angle	[-90, 90] deg		
Pitch angle	[-90, 90] deg		
Directional gyro	[0, 360] deg		
Roll rate gyro	[-50, 50] deg/sec		
Pitch rate gyro	[-50, 50] deg/sec		
Yaw rate gyro	[-50, 50] deg/sec		
Longitudinal accelerometer	[-2, 2] g		
Lateral accelerometer	[-2, 2] g		
Vertical accelerometer	[-2, 4] g		
Angle-of-attack vane	[-100, 100] deg		
Sideslip vane	[-100, 100] deg		
Dynamic pressure	[0, 2] in. Hg		
Static pressure	[20, 32] in. Hg		
Stagnation temperature	[-20, 50] deg C		
Longitudinal low airspeed	[-35, 165] kts		
Radar altimeter	[0, 1,500] ft		
Hook load	[0 10,000] lbs.		
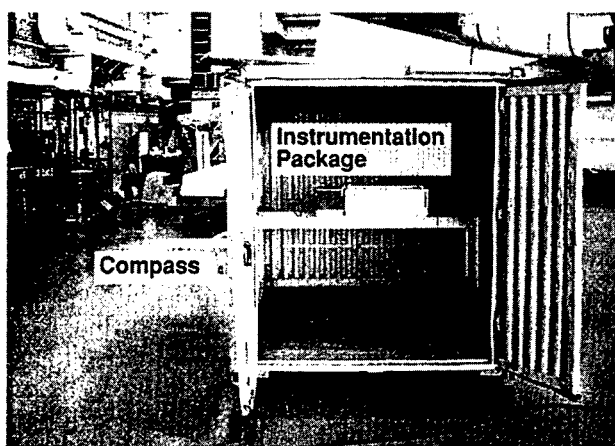
Figure 4.2. CONEX Instrumentation
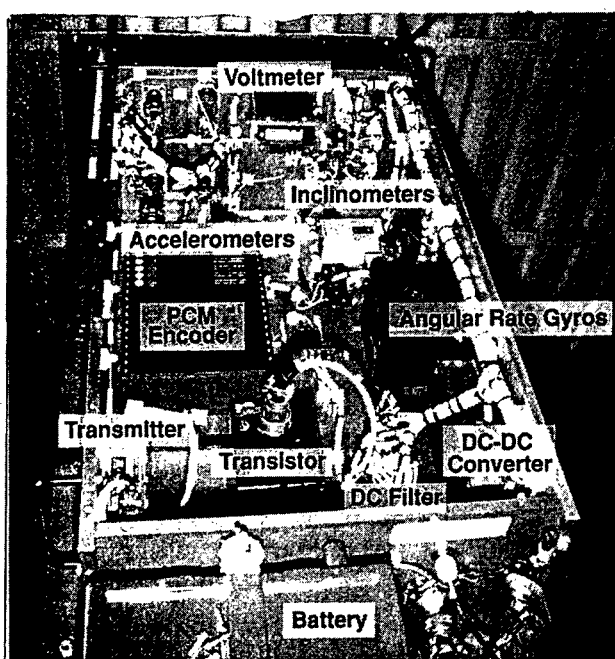
Figure 4.3. CONEX Instrumentation Package

4.2 Overview of Sensors

This sensor set is more than is needed for the identification computations, which require only the helicopter and load angular rates and heading, and the control positions. The set is somewhat short of measuring all the rigid body states of the two bodies and the forces and moments at the hook; and short of what's needed to measure the load aerodynamics. Omitted states and variables include load velocity vector and the hook force direction angles. Further, the inclinometers and hook load cell are devices designed for static conditions and were subject to significant uncorrectable errors under dynamic pendulum motions, so that variations in load pitch and roll angles and hook force magnitude were not adequately sensed.

The load dynamic range was larger than anticipated in yaw, where yaw rates above 100 deg/sec occurred for airspeeds above 50kts. This resulted in saturation of the load yaw rate gyro 120 deg/sec limit and corresponding large dynamic lags in the fluxgate compass at the higher test airspeeds.

The present load sensors provide good access to the pendulum dynamics up to 50kts airspeed and limited access to the load aerodynamics for the simulation validation effort.

4.3 Signals

The helicopter sensors are standard types whose signal properties are already familiar in the flight test literature. The sensors of principal interest are the rate and heading gyros. The helicopter angular velocity signals from a typical frequency sweep (fig 4.4) contain a moderate amount of vibration at 2-3 deg/sec amplitude and frequencies of 1-4 per revolution, plus biases up to 6deg/sec. Vibrations are well above and biases are well below the frequency range of the identification computations and have no effect on the results. The directional gyro was not slaved and had a random startup bias as well as a drift which required calibration at the start and end of each flight.
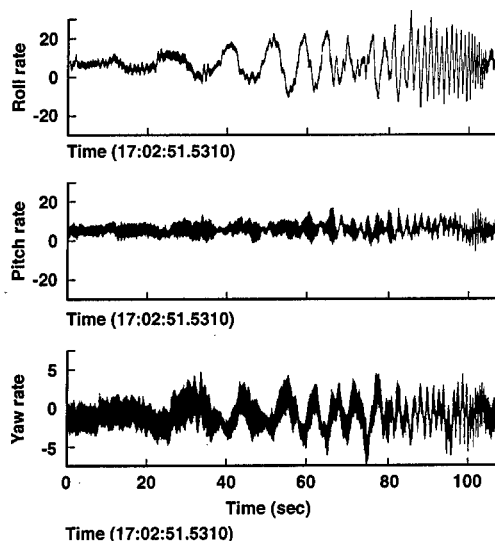

Figure 4.4. Helicopter rate gyro signals (deg/sec) 30kts, lateral sweep, flight 172, record 26.

The load accelerometer signals (fig 4.5) don't contain the vibrations that dominate the helicopter accelerometer signals. There is some small amplitude high frequency content, probably from sling stretching or helicopter vertical modes. The low frequency variations in the x, y accelerometers in this record (taken at 30 kts) are the signature of the steady load trail angle due to load drag combined with yaw motions which distribute the specific drag to the x and y accelerometers according to the yaw time history. It turns out that the pendulum swinging motions are not detectable by the x-y accelerometers
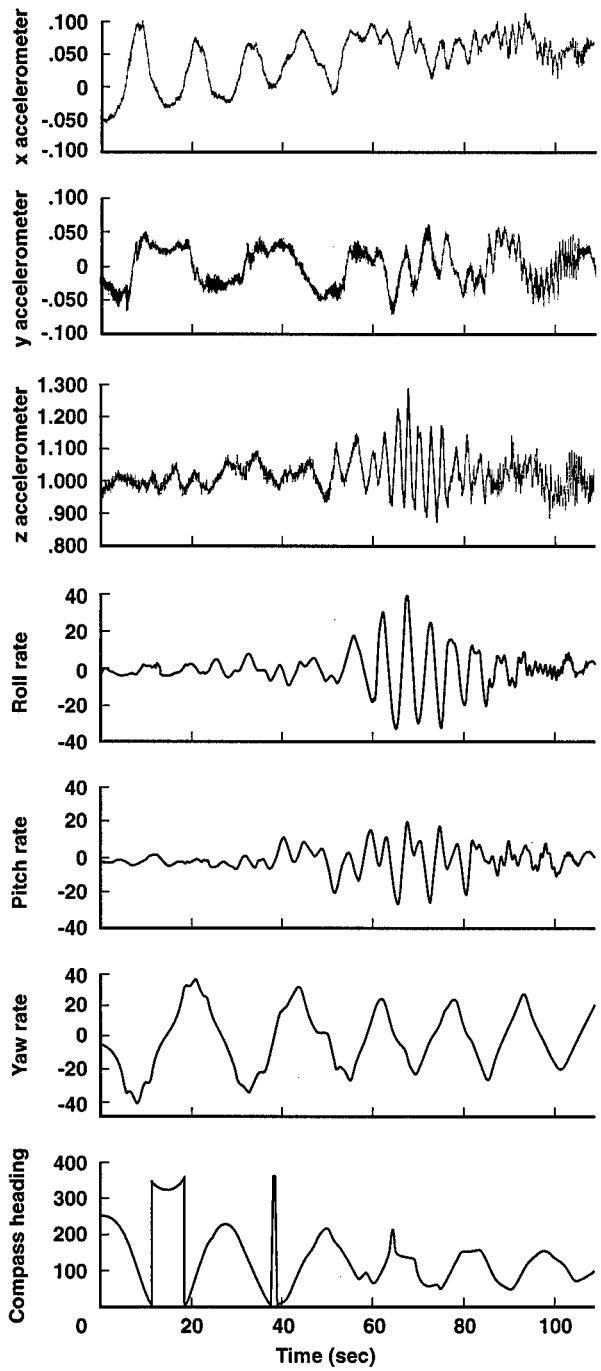
Figure 4.5. Load sensor signals (g, deg/sec, deg).

because the apparent gravity associated with pendulum swinging is always close to the load vertical axis and along the sensitive axis of the vertical accelerometer.
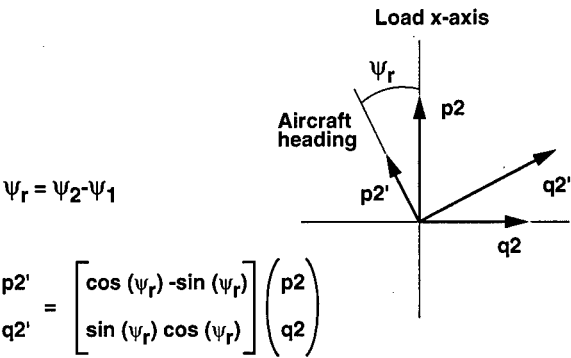
The load angular velocity signals in fig 4.5 are free of high frequency content or noise to the resolution of the plot. The yaw history in this record indicates periodic yawing of the load by 80deg. The pitch and roll rate histories represent the angular velocity associated with load lateral pendulum motions which is distributed to the

load pitch and roll rate sensors according to the load yaw history.

The fluxgate compass was subject to several systematic and dynamic errors. These included (1) transients at each crossing of the limits of its range at 0 and 360deg, (2) geometric errors due to misalignment from the true vertical during pendulum motions, and (3) large dynamic lags for load yaw rates above 90 deg/sec. The first of these was correctable. Correction of the second error requires measurement of the load pitch and roll attitude. However, analysis indicated the geometric error was moderately small in size for the load pendulum motions of the test, and could be ignored in the identification computations.

4.4 Signal Processing

Relatively little processing of the received signals was required for the identification computations. The helicopter stability margins and handling qualities parameters could be computed almost directly from the helicopter control and angular velocity signals.

$$\psi_r = \psi_2 - \psi_1$$

$$\begin{bmatrix} p2' \\ q2' \end{bmatrix} = \begin{bmatrix} \cos(\psi_r) & -\sin(\psi_r) \\ \sin(\psi_r) & \cos(\psi_r) \end{bmatrix} \begin{pmatrix} p2 \\ q2 \end{pmatrix}$$

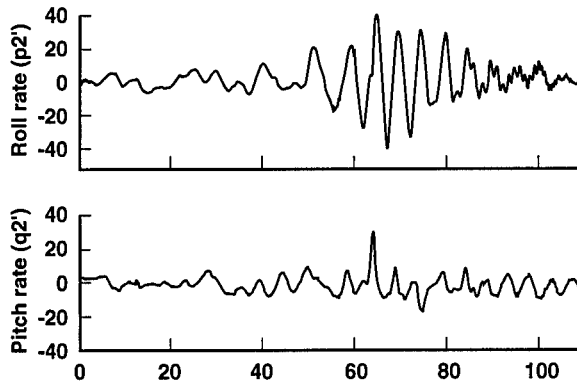Transformed rates: lateral sweep, flight 172, record 12

Figure 4.6. Transformed load angle rates.

Computation of load stability parameters required transformation of the load pitch and roll rate signals to axes aligned with the helicopter heading (fig 4.6) to get sufficient correlation of the load angular rates with the control inputs for identification of the load pendulum

roots. This was required because the load underwent arbitrary yawing which distributed the angular rates due to pendulum swinging to the pitch and roll rate gyros according to the yaw time history. The transformed signals for the record shown in fig 4.5 is included in fig 4.6, and shows that the load angular rates resolve principally into rotation about the helicopter longitudinal axis.

5. FLIGHT TEST PROFILE

5.1 Take-off Procedure
Flight tests were preceded by a briefing of the test team, including the aircrew, load handlers, telemetry staff and test engineers, to review test procedures, test points, load hook-up procedures and safety considerations.

Subsequently, the aircraft was powered up on the ramp and control calibrations were performed along with telemetry communications checks with the ground station, and directional gyro calibration. The load handlers waited near the load and, for the CONEX, powered up the load instrumentation and secured the doors.

The plate and block loads were hooked up with the aircraft on the ground. For the CONEX, the aircraft approached, stabilized over the load, and lowered to the desired height with guidance from the crew chief who was prone on the deck with a view through the hook hatch. Two load handlers stood on top of the CONEX, one to ground the hook and a second to lift the sling shackle onto the cargo hook (fig 5.1). The rotor downwash carried a significant amount of airborne debris and buffeted the load handlers as the helicopter approached, but this lessened considerably with the helicopter directly overhead. After hookup, the handlers dismounted the load with the help of a handhold that was welded onto the CONEX near the top. Generally, the load hook-up procedures and equipment specified in the HEAT manual [1] were used.

5.2 Test Records
The flight data was taken with the stability augmentation system (SAS) on and the flight path stabilization system (FPS) off. The FPS would otherwise superpose control inputs on that of the pilot.

Flight test inputs at each flight condition usually consisted of a trim record, followed by 3 repeated frequency sweep records, and ending with pairs of steps and doublets in opposite directions. The identification computations used only the frequency sweep records and the remaining records were used for independent checks. This sequence was performed principally with the longitudinal and lateral controls and at speeds of hover, 30kts, 50kts along with some data at higher speeds. A total of 11 data flights (11.5 flight hours) were performed during 1996-97 at Moffett Field with calm winds. A detailed listing of flights, loads, and data records is given in [6].
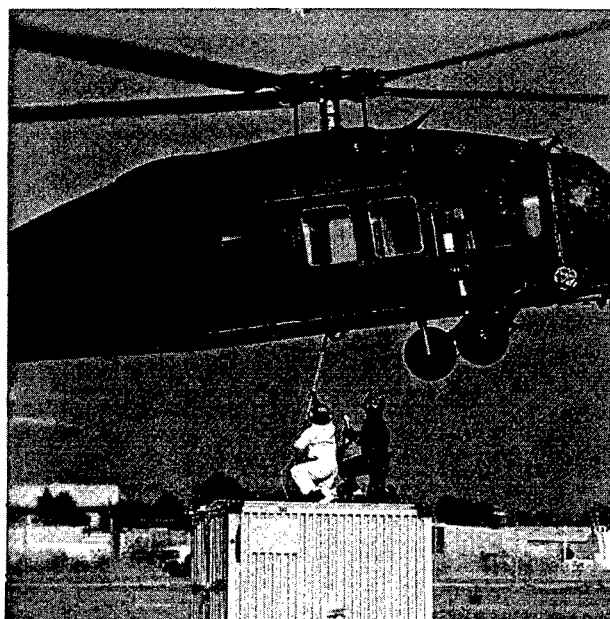

Figure 5.1. CONEX Hookup

5.3 Frequency Sweep Records
Identification based on frequency sweep flight test data has been developed over the past decade or more, and numerous examples have been reported in the literature. The design and execution of pilot-generated frequency sweep inputs has been considered in detail in [18], [19]. The main considerations in generating good data are to remain generally centered about the reference trim flight condition; and to avoid large correlated secondary control inputs, gust disturbances, and excessive excitation of lightly damped modes in the frequency range of the test. Each aircraft and test frequency range have their own unique considerations, but the UH-60 at frequencies to 2Hz presented no special problems.

A sample lateral axis control sweep is shown in fig 5.2. The pilot begins with a short period of trim, then starts with two cycles at the minimum frequency (20sec period in this case), and increases frequency smoothly to 2 Hz, with the assistance of the copilot who calls out quarter cycles for the first two cycles and every 15secs thereafter. The test monitor indicates when 2 Hz has been reached and the complete sweep record is about 90secs long. The frequency range from .05 to 2 Hz is considered appropriate for handling qualities studies. The minimum value avoids large aircraft motions that can result from low frequency inputs and pilot input amplitude is reduced in this range as seen in fig 5.2, and otherwise amplitude is selected to maintain linearity. The maximum frequency is low enough to avoid resonance with the lowest structural and rotor modes. The load pendulum modes of interest in this study are well within this range at .25Hz.

The off-axis controls departed very little from their trim values, although there is a small amount of correlated pedal input at low frequencies. In general, correlated

secondary control inputs reduce data quality, and the pilot endeavor to maintain the reference conditions with occasional uncorrelated low frequency off-axis inputs.

In fig 5.2, the helicopter roll rate response is held to about 10deg/sec maximum amplitude, and the (transformed) load roll rate is seen to have its principal response around resonance with the predicted pendulum frequency and with peak amplitude of 20deg/sec. The helicopter roll angle has its largest response at low frequencies and reaches 10deg. The reference pitch attitude and airspeed are well maintained in this sample. Generally, airspeed variations up to 10 kts around the reference speed can be tolerated without significant loss of linearity, and excursions of that size were common.
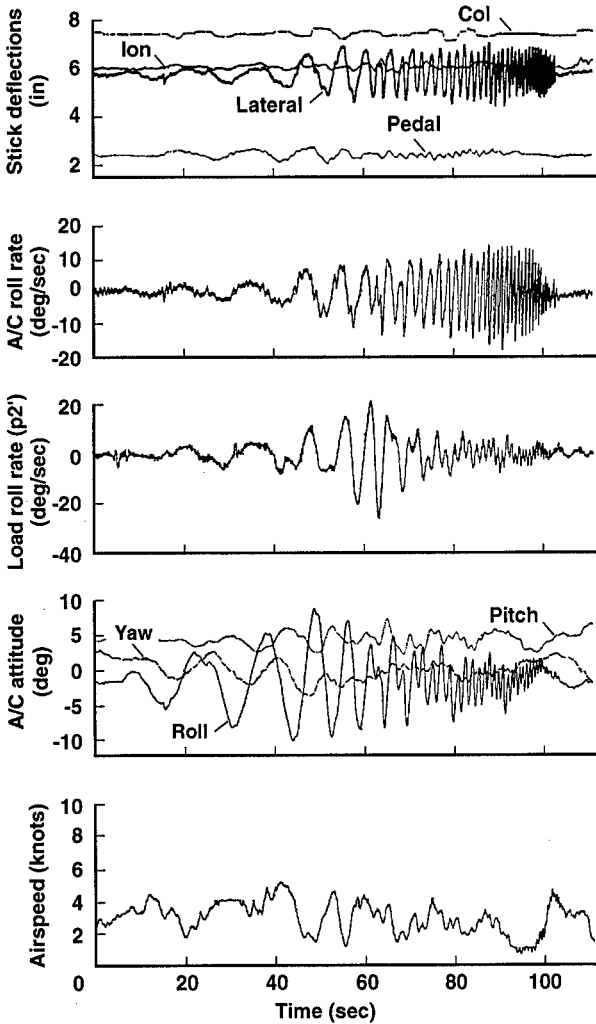

Figure 5.2. Sample lateral frequency sweep.

6. DATA ACQUISITION AND IDENTIFICATION PROCEDURE

6.1 Data Acquisition
The data acquisition system is shown in fig 6.1. All sensor signals were recorded on board the aircraft and telemetered simultaneously to the ground station, which

was equipped for real time strip chart displays, data recording, and video monitoring of the aircraft when it was within range of the ground station cameras. The ground station and telemetry support was provided by the Western Aeronautical Test Range facility at Moffett Field.

A camera was also mounted in the aircraft looking down through the hook hatch at the load. This was successfully recorded on board but reception of the load video at the ground station was always poor. This video provided a visual record of load motions relative to the aircraft to augment the time histories from the instrumentation.
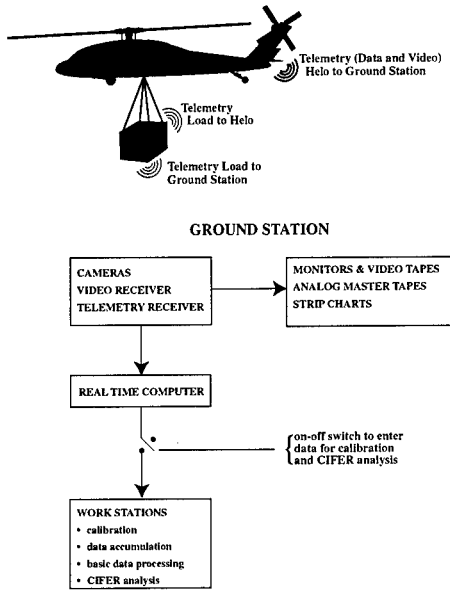

Fig 6.1 DATA ACQUISITION AND FLIGHT TIME CIFER ANALYSIS

Figure 6.1. Data Acquisition and flight time CIFER analysis.

6.2 Flight Time Identification System
The flight time computations used a system of three workstations and required complex data communications across several networks from the real time telemetry receivers to the workstations. The system was implemented by the telemetry support group [20].

Data was input to the workstations using an on-off switch which allowed the test engineer to store and concatenate the three frequency sweep records obtained at each test condition. The required computations were then carried out using the CIFER® software [3], [4] for interactive frequency domain analysis. This software has received wide application in the past decade to both helicopters and fixed wing aircraft, including instances of flight time identification [21]. The CIFER® computations took an average of 4 minutes to perform. The workstations also contained logic to carry out and store the required initial calibration of the helicopter heading gyro and to process the controls and load signals prior to the CIFER® computations.

6.3 Identification Procedure .

The frequency domain identification procedure determines the frequency response functions between given input and output flight records. When the plant dynamics are nonlinear this produces a frequency response that best represents the first harmonic approximation of the dynamics. The residual signal associated with the higher order dynamics is seen as noise in this procedure. The quality of this approximation is measured by the coherence function, which is the linear correlation between input and output as a function of frequency and has values in the interval [0,1]. Turbulence and measurement errors also produce reductions in coherence. An objective of the computations is to maintain adequate coherence (above .6) at all frequencies in the frequency range of interest, and there are numerous devices aimed at doing this, both in shaping the input control histories appropriately and in the computational procedure.

The CIFER® computational steps in the slung load identification are outlined in fig 6.2. First, the available frequency sweep records are concatenated so as to maximize the information for the flight condition. Second, the single-input-single-output (SISO) Bode plots are computed. The concatenated record is divided into overlapping time intervals or windows for the computations and the final frequency responses are obtained as averages of the results from these windows. The window size is a selectable parameter in the process and it determines the lowest frequency for which the frequency response can be given (1/T Hz, T = window size). Coherence also depends in part on window size, and smaller (larger) windows give better coherence at higher (lower) frequencies. For the flight time identification only one window size was used (20secs) to reduce the computation time. In postflight analysis, the computations can be repeated for multiple window sizes and the results combined to optimize coherence at all frequencies using CIFER®'s COMPOSITE utility.

Third, the effects of off-axis control inputs on the SISO frequency response can be removed by computations based on multiple inputs using CIFER®'s MISOSA utility. However, the effects of small off-axis control activity were found to be small and this step was omitted.

Finally, the handling qualities parameters and stability margins were computed from the Bode plots, and load pendulum roots were determined by fitting a second order pole to the load's frequency response in the neighborhood of the pendulum frequency using CIFER®'s NAVFIT utility. This utility also measures the quality of the fit, and the frequency range over which the fit is made can be adjusted to optimize its quality for the given record.

Figure 6.2 Identification Procedure.

(a) Computational Steps
1. Concatenate Frequency Sweep Records
2. Compute Single-Input-Single-Output Bode Plots
   - select window size(s)
   - compute Fourier integral
   - compute spectral functions
   - compute Bode plots
3. Multi-window optimization (postflight only)
4. Remove effects of correlated secondary control inputs (omitted).
5. Compute stability margins and handling qualities parameters from Bode plots.
6. Compute load pendulum roots by fitting 2nd order pole to load Bode plot.

(b) Flight-Time vs. Postflight Procedure

Flight-Time:
   - 50 Hz data rate
   - TM data dropouts
   - Directional gyro bias correction
   - Concatenate 3 records each case
   - 1-Window averaging (T = 20 seconds)
   - SISO analysis

Postflight:
   - 100 Hz data rate ·
   - No data dropouts
   - Directional gyro bias and drift corrections
   - Concatenate all available records each case
   - Optimized multi-window averaging (T = 10, 20, 25, 30, 40 seconds)
   - SISO analysis

6.4 Flight Time Identification Computations

The flight time computations used a number of simplifications and was subject to some difficulties which may not occur in postflight computations (fig 6.2). The data records were decimated to 50 Hz while the postflight work used 100 Hz. This reduced computation time significantly but satisfies the working rule of 16 times frequency out to 3Hz. The telemetered data was occasionally subject to extended dropout owing to antenna shadowing while the on-board recorded data used in postflight analysis had almost no data dropouts. Extended dropouts were treated by reorienting the aircraft and repeating the record. CIFER® sees the inevitable data spikes and momentary dropouts as high frequency noise which have no significant effect on the data quality.

The flight time computations used 1-window averaging while postflight work could use 5 window sizes to optimize coherence at all frequencies. The flight time computations also used only 3 concatenated records each case, while postflight computations could concatenate all available records from multiple flights for each case. Last, the analysis was based on on-axis records only, that is, single input/single output. Despite these simplifications,

the flight time estimates were close to the best postflight results in all cases.

7. IDENTIFICATION RESULTS

7.1 Handling Qualities

Some results for handling qualities are shown in fig 7.1. First, a comparison of the ballasted CONEX with the helicopter alone for the lateral axis indicates a reduction of handling qualities parameters at all airspeeds. Points move toward the Level 1-2 boundary, losing bandwidth or gaining phase delay with the addition of this load, depending on airspeed. Hover is the flight condition closest to the boundary. In addition, it is seen that other loads can have more significant losses in handling qualities as shown by the hover results for the 1K plate for longitudinal control, and for the 4K block for lateral control. These points are in the Level 2 region owing mostly to a significant loss of bandwidth from that of the helicopter alone. Thus, the effects of the load on handling qualities appear to be highly variable with ordinary differences among slings and loads, even for a very light load.
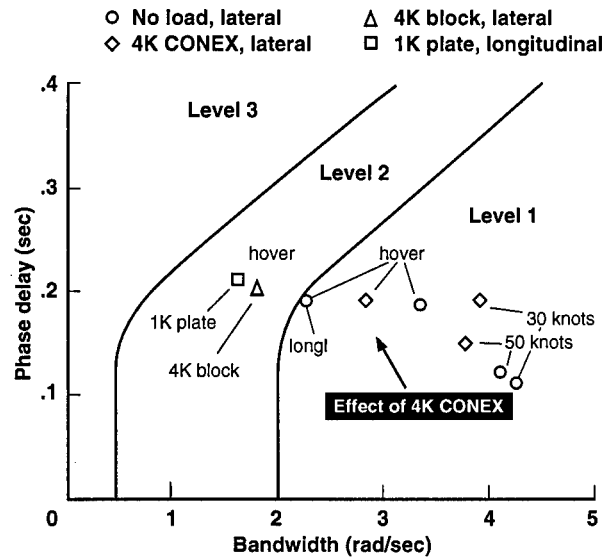

Figure 7.1. Handling qualities parameters.

Handling qualities parameters are plotted vs airspeed in fig 7.2. The lateral axis results repeat those already seen in fig 7.1. For the longitudinal axis, bandwidth is in the range of 2-3 rad/sec in almost all cases, and actually improves somewhat due to the load. An exception is the 1K plate for which bandwidth is reduced below 2rad/sec at hover. Phase delays are between .15 and .2 sec and degraded (increased) by the load in most cases.

The effect of load weight on lateral axis attitude control is shown in fig 7.3, which shows Bode plots for no load, 2K CONEX and 4K CONEX. A dip occurs in gain and phase in the neighborhood of the pendulum frequency due to the effect of the load dipole on the helicopter transfer

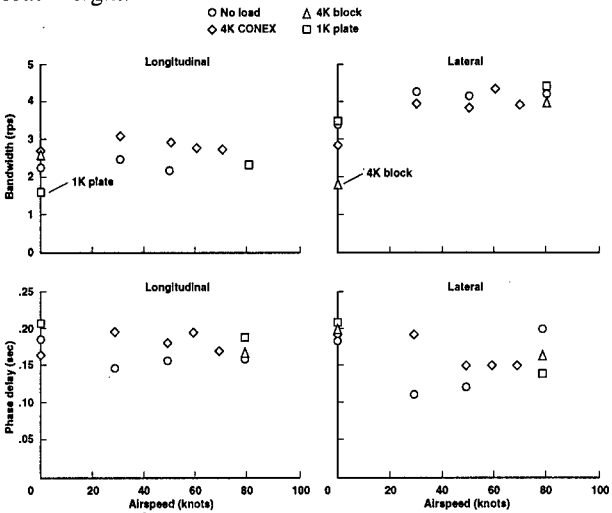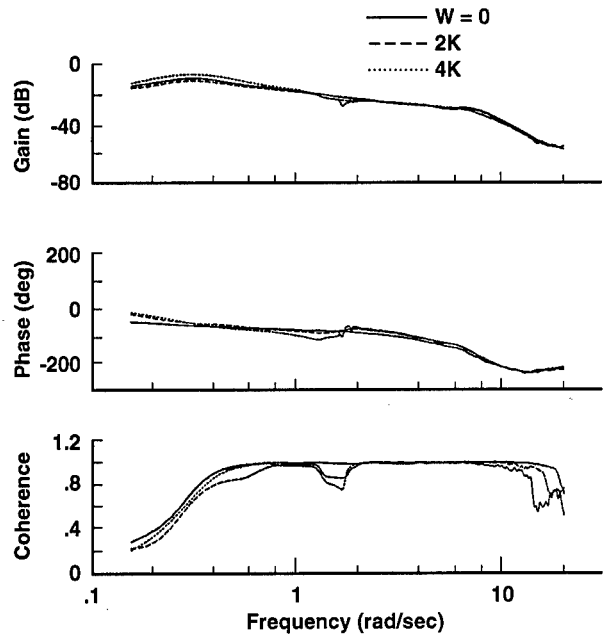function, and this dip in all three quantities increases with load weight.

Figure 7.2. Handling qualities vs. Airspeed.

Load weight (lbs)	Bandwidth (rad/sec)	Phase delay (sec)
0	3.33	0.186
2K CONEX	2.87	0.181
4K CONEX	2.82	0.190

Figure 7.3. Effect of load weight on attitude response.

This reflects a loss of helicopter attitude response at the load pendulum frequency as load weight increases. Simulation work at Ames [9] with the CH47 and larger

relative load weights than in this study indicates that for sufficiently large weight the bandwidth drops significantly to a value below the pendulum frequency and the pilot then controls the load with much lower frequency inputs. That same work indicates a similar effect of increasing sling length.

7.2 Control System Stability Margins

Some stability margin results are shown in fig 7.4. A comparison of the lateral axis results for the 4K CONEX with the helicopter alone shows a loss of both gain and phase margin at all airspeeds. Margin losses at hover are 4db and 16deg for the CONEX, and larger losses occur for the 1K plate and 4K block. The UH-60A is seen to have large margins from the minimums so that moderate losses in margin due to the load don't threaten stability. However, other aircraft can have different base margins and such losses would be more critical. An example is the MH-53J [22] which is shown in fig 7.4 to have margins near the minimums.

Control system stability margins are plotted vs. airspeed in fig 7.5. Longitudinal axis margins for the 4K CONEX show almost no effect of the load on both margins up to 50kts. There are more significant effects on margins with the block and plate loads for the available comparison points at hover and 80kts. The lateral axis margins indicate a loss in both margins at nearly all airspeeds. This is consistent with industry experience that the lateral axis is the one for which stability is normally degraded by the load [2].

The effect of load weight on lateral axis stability margins is seen in fig 7.6. Dips occur in gain and phase owing to the load dipole in the helicopter transfer function, and the effect increases with load weight.
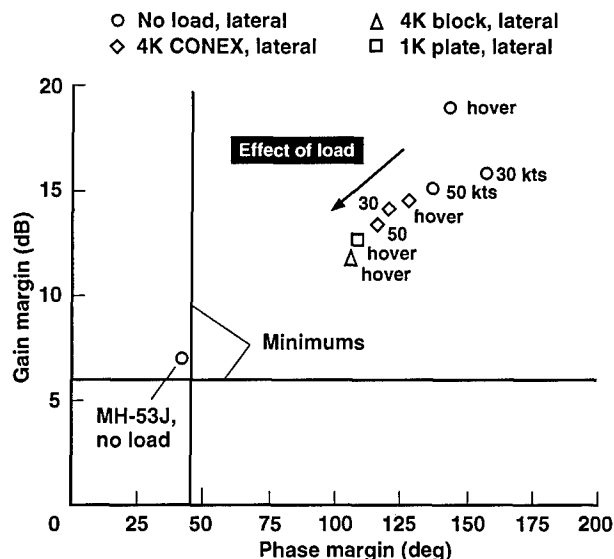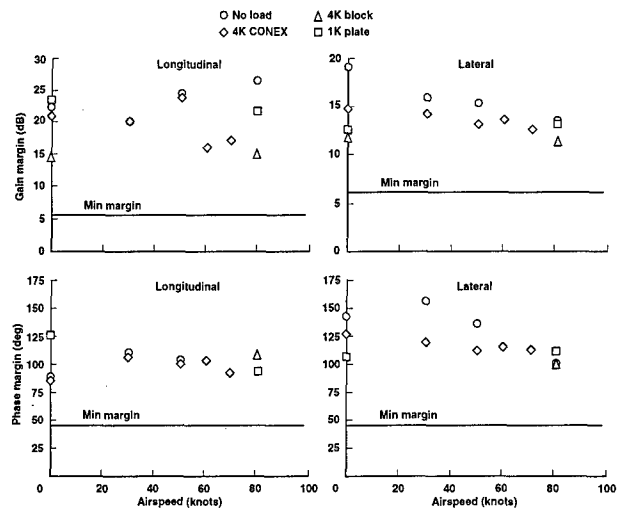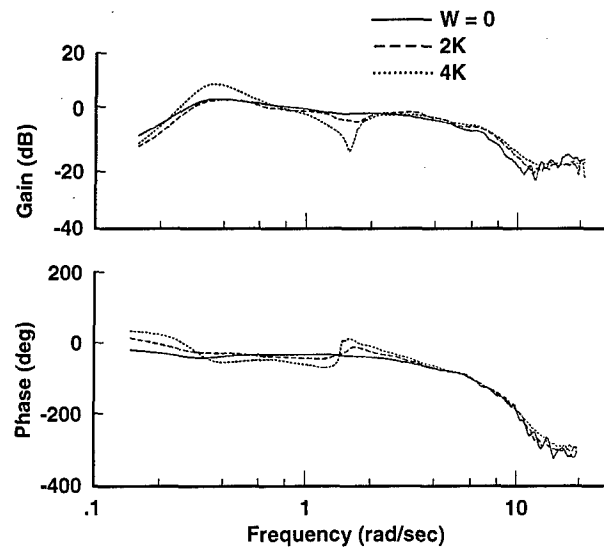
Figure 7.4. Stability margins.

Figure 7.5. Stability margins vs. airspeed.

Flight condition: hover, lateral axis, CONEX load

Load weight (lbs)	Gain margin (dB)	Phase margin (deg)
0	19.0	142
2K CONEX	16.5	137
4K CONEX	14.7	126

Figure 7.6. Effect of load weight on control response.

7.3 Load Pendulum Roots

Damping and natural frequency of the load pendulum modes at hover are shown in fig 7.7, which includes a comparison with simulation results. Frequency is very nearly identical for both modes, around 1.5 rad/sec, and is very well predicted by simulation models. The flight data

show moderate damping between .1 and .2 on both axes, while the simulation predicts the longitudinal pendulum to be lightly damped, about 5%, and the lateral pendulum to have twice the measured damping. Thus there is significant disagreement between simulation and flight data on pendulum damping.

Damping and natural frequency are also plotted vs. airspeed in fig 7.7. The pendulum roots are nearly constant with airspeed in these results. Considerable load yaw motion developed with airspeed for the ballasted CONEX but without coupling to the pendulum modes; that is, the load aerodynamics principally influenced the yaw degree of freedom without modifying the pendulum modes. However, the empty CONEX exhibited considerably more coupling among these degrees of freedom as airspeed increased to 50-60kts, and tests with the empty CONEX at higher speeds might give quite different results.

7.4 Comparison of Flight Time and Postflight Analysis

Adequate coherence was routinely obtained for the helicopter parameter identifications with the flight time procedure. The postflight procedure normally expanded the frequency range with adequate coherence, and increased coherence at most frequencies including at the dipole dip near the pendulum frequency, as seen in the sample case in fig 7.8. These improvements ranged from marginal to significant depending on the case.

For the load response, adequate coherence was difficult to obtain owing to the interference of the load yaw motions in measuring the pendulum swinging motions, the limited range of input frequencies which excite load response, and the suppression of the pendulum mode response to control inputs at higher airspeeds. Identifications were made at hover and 30kts, and these indicated that coherence was marginally acceptable for the longitudinal axis, and much better for the lateral axis.

The flight time procedure provided identifications with adequate coherence for all cases and parameters where this could be done by the postflight procedure.

Improvements of the flight time procedure and system are under consideration. This includes a more efficient user interface, improved computational efficiency and performance, and implementation with a single workstation in conjunction with a portable ground telemetry station.
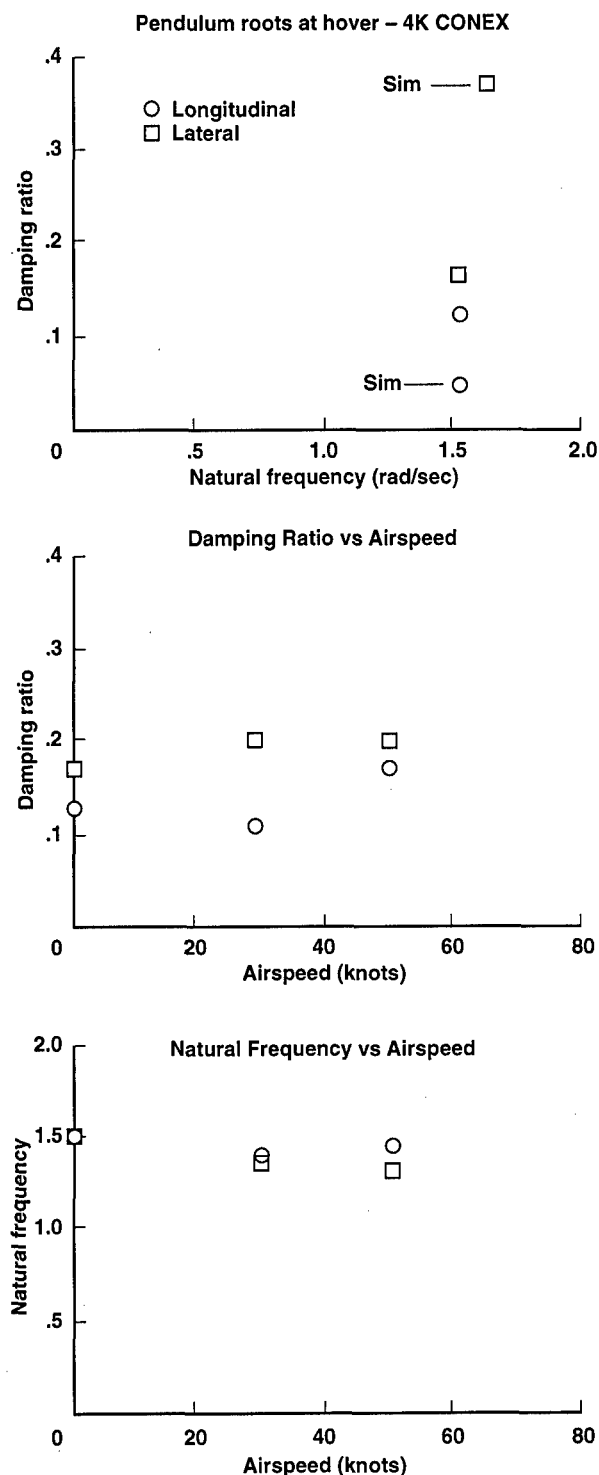

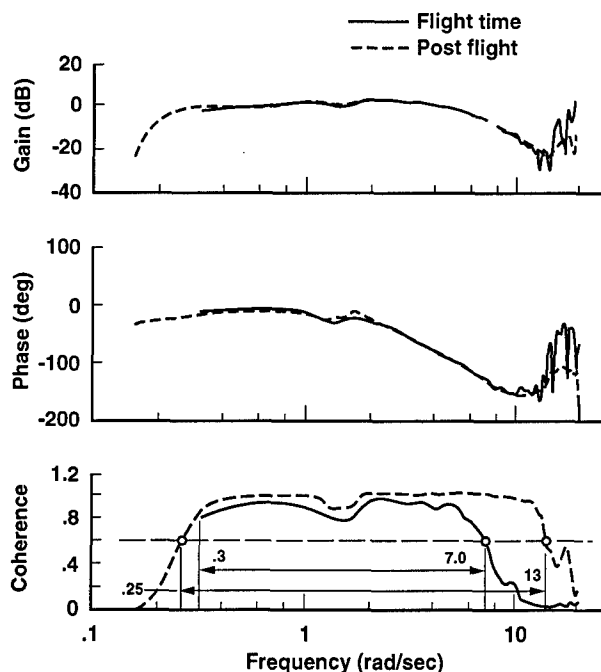Figure 7.7. Load pendulum modes for 4K lbs. CONEX.

Figure 7.8. Comparison of flight time and post flight analysis. Attitude response, hover, longitudinal axis, 4K CONEX.

8. SIMULATION OF LOAD DYNAMICS

8.1 Comparison of Flight and Simulation Load Motions

A simulation model for slung loads is currently under development at Ames. Flight and simulation time histories can be compared by entering the flight test control input histories into the simulation. The simulation contains exact rigid body dynamics for elastic or inelastic slings [23]. The UH-60 aerodynamics are currently represented by a stable linear approximation [24], and the load aerodynamics are currently limited to drag only.

Results at hover for lateral and longitudinal control frequency sweeps are shown in figs 8.1, and 8.2 for the on-axis angular rates. The sling is modeled as inelastic in the simulation results. The approximate helicopter model is seen to reproduce the helicopter rates fairly well over the test frequency range. The load roll rate history shows good agreement in phase and damping. The load pitch rate history exhibits reasonably good phase agreement but the simulation history shows larger amplitude and longer persistence of the longitudinal pendulum mode than in flight. This is consistent with the difference in damping ratio previously noted for the longitudinal pendulum mode.
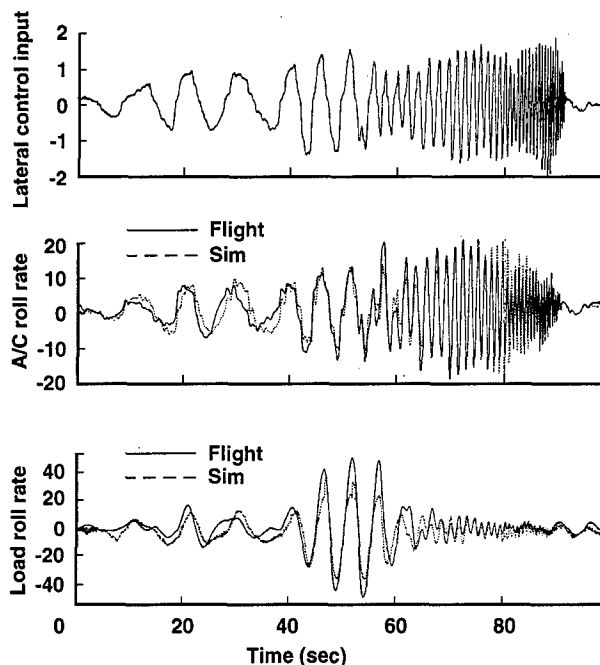
Figure 8.1. Comparison of flight and simulation. Lateral control sweep, hover, 4K CONEX.
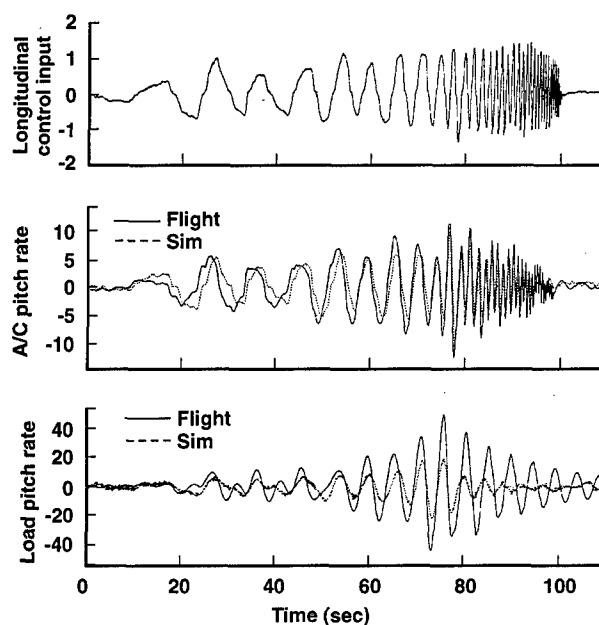
Figure 8.2. Comparison of flight and simulation. Longitudinal control sweep, hover, 4K CONEX.

8.3 Slung Load Simulation Development Issues

Since helicopter model validation has been well advanced in the last decade out to high frequencies (e.g., [2], [4]) the main challenge for validation of a slung load simulation is in modeling the load-sling dynamics. The

current flight experience and prior experience with simulations indicate the following points for study and development:

First, there are significant differences in the damping of the pendulum modes between flight and simulation.

Second, the CONEX with swiveled suspension was observed to reach steady yaw rates at hover. This indicates the existence of measurable rotor downwash effects on load motions at/near hover.

Third, load yaw motions differed for swiveled and unswiveled sling. Modeling complexities for the unswiveled sling include sling windup and corresponding variable sling geometry, and yaw resistance moment at the hook.

Fourth, the standard model of the elastic sling as a lightly damped spring which supports only tension was rated by pilots as unrealistic in recent moving based simulation studies at Ames underlying [9]. This model generates significant excursions in hook force when pilot control inputs excite elastic stretching, and corresponding vertical cg motions which were rated unrealistic. Possible causes are unmodeled sling hysteresis, and interactions of sling stretching with the rotor coning dynamics that were not represented in the simulation rotor model.

Last, only limited load aerodynamic data is available. Load aerodynamics can be grouped into static, rotary, and unsteady aerodynamics. The static aerodynamics are, in principle, easiest to measure and model, and are expected to account for the load yaw motions and yaw-pendulum coupling. Prediction of load instability, however, depends on unsteady effects [26].

A simulation model of the static aerodynamics requires definition of six force and moment components over the complete range of angle of attack [-90,90] and sideslip [-180,180]. Complete coverage is available for the MILVAN [27], [28] and the CONEX. Otherwise, the available wind tunnel data is restricted to partial coverage and information. The potential for measuring load aerodynamics from flight test data with an instrumented load remains to be examined.

9. CONCLUSIONS

1. A system for computing control system stability and handling qualities parameters for a helicopter and external load during flight testing has been demonstrated. This capability is useful for slung load certification tests owing to the uncertain stability and envelope of the system, and can potentially result in significant reductions in the cost and time.

2. Good agreement was obtained between the simplified flight-time computations and the refined postflight analysis. The flight-time computational procedure achieved sufficient coherence for a reliable identification

in all cases where sufficient coherence was obtained by the post-flight procedure.

3. Although the set of load-sling combinations tested at hover was small in number, significant variations in helicopter handling qualities parameters among these combinations were computed. This suggests a large range of effects on stability and handling qualities among common loads and slings.

4. The sensor requirements to identify load pendulum stability were met without difficulty at low airspeeds. However, flight experience indicated yaw rates increase strongly with airspeed to sufficiently high levels that the selected compass and yaw rate sensors did not function adequately above 50kts. Load dynamic range can exceed that of the helicopter in slung load testing and a corresponding sensor dynamic range is required. Additional sensors for load attitude and the hook force vector would allow identification of the load static aerodynamics from flight data.

5. Simulation development issues include significant differences in load pendulum damping from flight values, modeling of rotor downwash effects on load aerodynamics at/near hover, modeling of sling windup and yaw resistance at the hook, sling stretching dynamics, and limited load aerodynamic data.

10. ACKNOWLEDGEMENTS

11. REFERENCES

1 Multiservice Helicopter External Air Transport: Vols. I, II, III. US Army FM-55-450-3, 4, 5. Feb. 1991.

2 Lawrence T., Gerdes W., Yakzan S.: Use of Simulation for Qualification of Helicopter External Loads. Proceedings, AHS 50th Annual Forum, May 1994

3 Ten Years of Cooperation on Rotorcraft Aeromechanics and Man-Machine Integration Technology. M. Tischler, A. Kuritsky, editors. Ames Research Center, Oct 1996.

4 Tischler M., Cauffman M.: Frequency-Response Method for Rotorcraft Identification: Flight Applications to BO-105 Coupled Rotor/ Fuselage Dynamics. JAHS, vol. 37, no3, July 1992.

5 Tischler M., Cauffman M.: Comprehensive Identification from Frequency Responses (CIFER®): An Interactive Facility for System Identification and Verification. Vols. 1, 2. NASA Conference Publication 10149, USAATCOM TR-94-A-017. Sept, 1994

6 McCoy A.: Flight Testing and Real Time System Identification Analysis of a UH-60A Black Hawk Helicopter with an Instrumented External Sling Load. NASA CR 1998-196710, April 1998.

7 Handling Qualities Requirements for Military Rotorcraft. US Army Aeronautical Design Standard ADS-33D-PRF. USAATC/AVRDEC, US Army Aviation and Troop Command, St Louis, Mo. May 1996.

8 General Specification for Flight Control Systems: General Specification for Design, Installation, and Test of Piloted Aircraft. MIL-F-9490D. (USAF) June, 1995

9 Key D., Hoh R., Blanken C.: Tailoring ADS-33 for a Specific End Item. 52nd Annual AHS Forum, Wash DC, May 1998.

10 Hilbert K.: Math Model of the UH-60 Helicopter. NASA TM 85890. April 1984.

11 Howlett J.: UH-60A Black Hawk Engineering Simulation Program NASA CR 166309, Dec 1981.

12 Fletcher J.: A Model Structure for Identification of Linear Models of the UH-60 Helicopter in Hover and Forward Flight. NASA TM 110362, Aug 1995.

13 Operator's Manual for Army Models UH-60A, UH-60L, EH-60A Helicopters. Army technical manual TM-1-1520-237-10, 31 Aug 1994

14 Kufeld R., Balough D., Cross J., Studebaker K., Jennison C.,Bousman W.: Flight Testing the UH-60A Airloads Aircraft. AHS Forum Washington DC, May 1994.

15 Black Hawk Slung Load Instrumentation Package: Development Report and User Manual. IAF Flight Test Center, Instrumentation Dept Report for the MOA. Oct 1996

16 Owner's Manual, C100 Electronic Compass. KVH Industries Inc, Middletown, Rhode Island.

17 Owner's Manual, E-79 Electronic Load Weigh System. Onboard Systems, Portland, Oregon, May 1996

18 Tischler M., Fletcher J., Diekman J., Williams V., Cason R.: Demonstration of Frequency Sweep Test Techniques Using a Bell-214-T Helicopter. NASA TM-89422, Apr 1987.

19 Willams J., Ham J., Tischler M., Flight Test Manual: Rotorcraft Frequency Domain Flight Testing. AQTD Project 93-14, US Army Aviation Technical Test Center. Sept 1995.

20 Wei M., Ng S.Y., Somes A., Aoyagi M., Leung J.: Real-Time Server-Client System for the Near Real-Time Research Analysis of Ensemble Data. Paper to be given at International Telemetry Conference, San Diego, Oct 98.

21 Lisoski D., Tischler M.: Solar Powered Stratospheric Research Aircraft Flight Test and System Identification. RTA Symposium on System Identification for Integrated Aircraft Development and Flight Testing. Paper #27, May 1998, Madrid

22 MH-53J AFCS Evaluation. Project A-8867 Final report. Georgia Tech Research Institute, Nov 1993 (for Warner Robins Air Logistics Center, Robins AF Base, Ga. Contract F09603-89-G-00077-0008).

23 Cicolani L., Kanning G., Synnestvedt R.: Simulation of the Dynamics of Slung Load Systems. Journal of the American Helicopter Society, Oct 1995.

24 Whalley M., Carpenter W.: A Piloted Simulation Investigation of Forward Flight Handling Qualities Requirements for Air-to-Air Combat. NASA TM 103919, May 1992.

26 Simpson A., Flower J.: Unsteady Aerodynamics of Oscillating Containers and Application to the Problem of Dynamic Stability of Helicopter Underslung Loads. AGARD CP-235, May 1978.

27 Laub G., Kodani H.: Wind Tunnel Investigation of Aerodynamic Characteristics of Scale Models of Three Rectangular Shaped Cargo Containers. NASA TM X-62169, July 1972

28 Cicolani L., Kanning G.: A Comprehensive Estimate of the Static Aerodynamic Forces and Moments of the 8x8x20 ft Cargo Container. NASA TM 89433. May 1987.

Aircraft System Identification using Integrated Software Tools

Dennis J. Linse
Senior Engineer
SCIENCE APPLICATIONS INTERNATIONAL CORPORATION
44417 Pecan Court, Suite B
California, MD 20619
USA

1. SUMMARY

System identification is a complicated, multi-step process requiring considerable expertise to perform. In a traditional flight test program, the elapsed time from flying the aircraft and gathering data until the simulation is updated can be months or even years. The primary reasons behind the long times between flight test and simulation update are the labor-intensive processes of data processing and system identification. Too much time is spent manipulating data and models to the format needed by the disparate programs. The Integrated Data Evaluation and Analysis System (IDEAS) gathers existing software into a distributed client/server architecture that integrates all of the tools required to process flight test data. Using consistent data handling routines and a networked communication scheme, IDEAS can distribute tasks among heterogeneous processors while maintaining an integrated working environment. Tools are available for data preprocessing, filtering, consistency checking, aircraft simulation, equation error and output error identification as well as communication paths to other existing programs such as frequency domain identification routines. An innovative modeling technique provides uniform access to complex, nonlinear model representations. A single, intuitive description of the identification model is processed by each of the different system identification methods with no recoding or rehosting required.

As a demonstration of the capabilities of the integrated system, an analysis of flight test data from a twin turbofan military aircraft is conducted. The aerodynamic and engine models of the current operational flight trainer (OFT) are hosted under the IDEAS framework. Using both equation error and output error techniques, the simulation models are updated using the gathered flight data and validated against independent data. Where possible, nonlinear increments are added to augment the aerodynamics and engines to best match the available data. The updated simulation shows significant improvement in fidelity of the OFT across the flight envelope.

2. INTRODUCTION

2.1 The Problem

Decisions made during aircraft development and operation depend heavily on an accurate representation of capabilities that aircraft. Aircraft system identification is a rigorous, multi-step process that analyzes the data gathered during a flight test program and produces a mathematical description of the vehicle. Figure 1 shows some of the details of the aircraft system identification process.
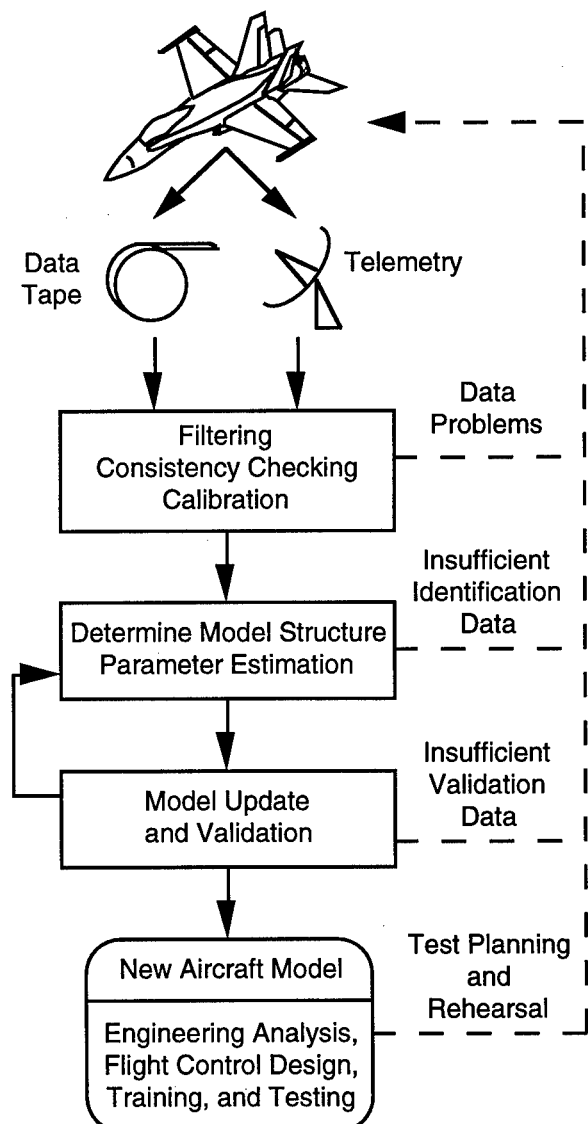

Figure 1. The Aircraft System Identification Process

In addition to the primary processing of data by a variety of tools, there are a number of decision points at which the data are evaluated to determine suitability for the overall goal of the task. Multiple steps and distinct procedures are performed on the stream of data produced by the testing.

The primary difficulty with this process to date is the length of time it takes to generate useful results after the data are collected. In many cases this can be months or years. This delay has a significant impact on safety decisions, development decisions, and aircrew training.

2.2 Background

There are nearly as many computer programs to perform the data preprocessing, system identification, and simulation update process as there are people performing these operations. In general each organization has developed in-house methods that work well for the projects at hand. Some methods have achieved more wide-spread use including MMLE3[1,2] by Maine and Iliff, one of the most well-known maximum likelihood estimation algorithms for aircraft identification; SMACK[3], a smoothing and data consistency checking program; and CIFER[4,5], an integrated system for frequency response identification.

At SAIC, a number of advanced system identification and data analysis methods have been developed. These include Athena[6], an equation error identification algorithm using principal components regression analysis; NAVIDNT[7], a filter error identification program running a navigation equations algorithm for flight data filtering and data consistency checking; and SCIDNT[8], an output error identification program for nonlinear aerodynamic modeling. These programs have been used individually and jointly with a great deal of success updating aircraft simulations ranging from the F-4[8] to the C-130[9]. Notwithstanding the success of these programs, too much of the overall project time was spent converting to the particular data formats needed by each program, learning the method of operation of disparate programs, and reengineering simulation models from one program to the next.

2.3 Overview of Paper

This paper discusses an integrated system for analysis of flight test data. First, the architecture of an integrated suite of tools is described, with an emphasis on the data structure design and the flexibility offered by that design. Next, the tools required for flight test data analysis are detailed. This is followed by an example system identification using the described system. Finally, real-time identification guided by an expert system is discussed briefly. This is a current area of expansion of IDEAS.

3. INTEGRATED DATA EVALUATION AND ANALYSIS SYSTEM

IDEAS is an analysis system designed for manipulation of flight test data emphasizing the creation, identification, and validation of complex nonlinear simulations from recorded flight data. From the initial design, this system has been built for end-to-end processing of large portions of dynamic data. Stream-lined data paths and efficient access methods are included as well as flexible processes that readily handle computationally intensive tasks.

3.1 Integrated Tools

The IDEAS environment is a distributed architecture that separates individual functions into distinct tools. The function of an individual tool is well defined as is its place in the overall architecture. A common connection to a single database and a straight-forward programming interface ensures that all tools interact uniformly. Communication among tools is performed using a platform independent, networked scheme that allows IDEAS to run on a single machine or multiple machines in a heterogeneous network. The communication mechanism is optimized for large data transfer, as is common in test data analysis.

The current processes of IDEAS are displayed in Fig. 2. Each box represents a distinct tool; system level tools are shaded gray and user tools are white. All processes make requests through the Information Gateway that provides routing of messages to the appropriate tool. The gateway forms the backbone of a client-server architecture.

New user tools are easily added to IDEAS through a well-defined application programming interface. Each tool processes history vectors. All input, output, and data storage of history vectors is handled by existing IDEAS processes (the user interface, plot interface, and database manager respectively). New tools are released from these duties and free to concentrate on the task at hand. Existing simulations and analysis tools are readily interfaced into IDEAS.

While a common interface structure integrates the various tools, the distributed processing requires some coordination for repeated operation. A multi-level scripting capability is available to store common sequences of repeated commands.

3.2 Data Storage and Access

A single data base manager stores all permanent data in IDEAS. The data base is designed to store aircraft flight test data, although it is general enough to store response data from any dynamic system. Individual processes retrieve and store data through a uniform interface.

A multi-layer data storage and access architecture is used to provide logical grouping of information. Each layer provides further restriction of the data and allows for storage of additional details about the data. A
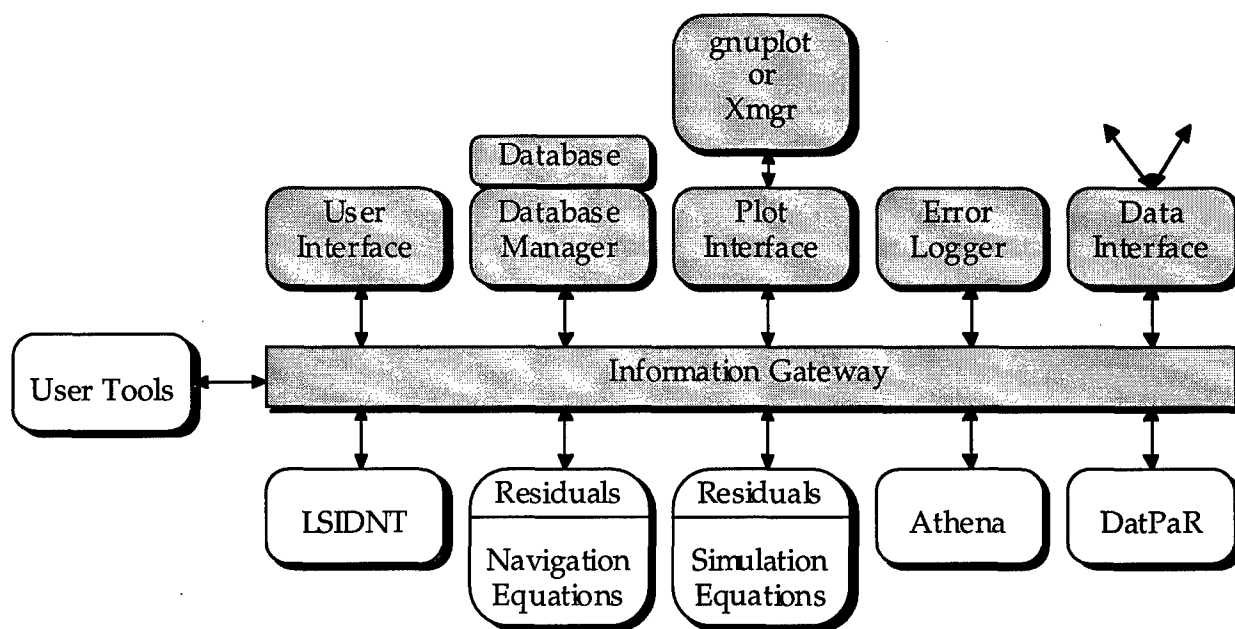
Figure 2. Integrated Identification Tools

distinct separation is made between data storage and data access to further encourage flexibility. This separation is shown in Fig. 3.

3.2.1 History Vectors

The lowest level data element in IDEAS is the history vector (indicated as HV in Fig. 3). Conceptually, a history vector is the time response of one signal stored as a N by 2 matrix where each row is one time and value pair for the signal. The only requirement on the time column is that the elements be monotonically increasing. There is no requirement for uniform sampling. In addition to the time response data, each history vector has descriptive information associated with it including the unit of measure, sign convention, and the date of last modification.

The history vector is the primary unit of manipulation in IDEAS in the same manner that vectors and matrices are the primary units of manipulation in many control system design programs. History vectors may be added and filtered as well as used as inputs and outputs for identification, simulation, and validation tools. Since the number of history vectors for a single flight program grows large very quickly, there is an additional hierarchy imposed to ensure easy operation.

3.2.2 Data Structures for Storage

Data are stored into the database using flights, records, and history vectors (Fig. 3). A flight test program is generally broken into a series of flights. A *flight* is the highest level data storage area for a single mission from the start of data gathering before take-off until the end of data gathering after landing. Associated with each flight are number of descriptive features such as aircraft number, crew, date of flight, time of flight, overall atmospheric conditions, and basic aircraft configuration.

The data recorded for each flight are further divided into *records*. Each record contains the data for a contiguous length of time (although small time drop-outs are handled seemlessly). Associated with each record is another set of descriptive data that is unique to the record. This would contain items such as unique configuration changes (dropping of stores) and localized atmospheric phenomena affecting the recorded data.

Within each record of a flight are the stored history vectors for each signal recorded by the instrumentation system. This is the primary storage location for all data. It is expected that the flight data are stored with no corrections or manipulations applied.

When new data are generated by manipulation of existing history vectors within a record, the new history vectors are stored back to the same record. The new data are stored as new vectors within the record. The original flight data is never overwritten, but processed vectors may be replaced or overwritten as needed.

3.2.3 Data Structures for Processing

While flights, records, and history vectors provide an excellent hierarchical storage mechanism, they do not provide an efficient and logical access method for analyzing the flight data. For analysis, the data are accessed using groups and segments (Fig. 3). A *segment* is a fixed length of time from a single record. A segment may be thought of as a single *maneuver*, but the latter term already has multiple, sometimes conflicting, uses. A segment provides no data storage space of its own (other than descriptive information), but rather it references a particular segment of time within a record. A record may contain data from a number of events (such as step responses, doublets, or wind-up turns) performed in sequence. A single event, such as a doublet including a
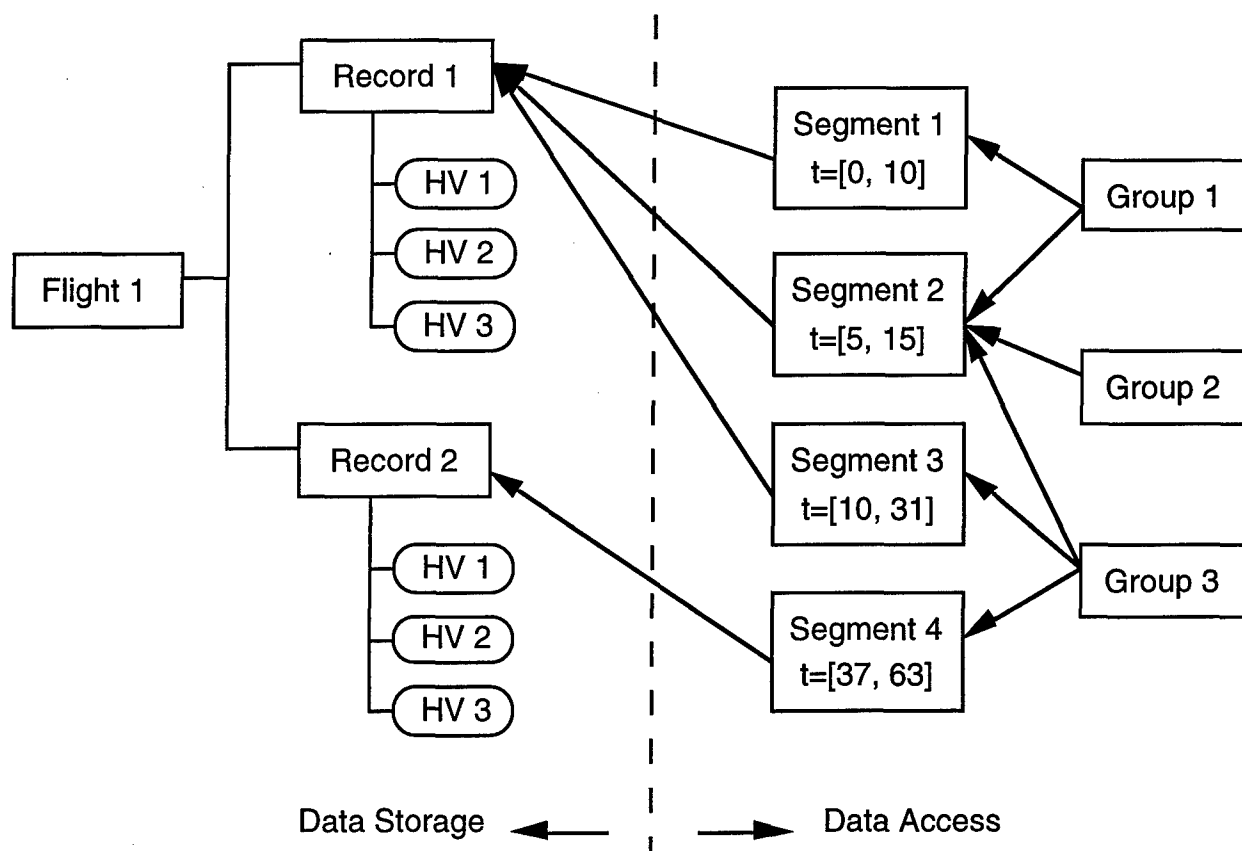
Figure 3. IDEAS Data Storage and Access

portion of time preceding and following the actual motion, is noted as a segment. In Fig. 3, Segment 2 indicates all of the history vectors from Record 1 are available between times 10 seconds and 31 seconds.

A *group* is a collection of one or more segments. The segments may be from a single record, from different records in a single flight, or from different records in separate flights. There is no explicit relationship required between the segments of a group. The group, like the segment, provides no primary data storage. It only contains the names of the segments and a small amount of identification information. Typically, there are three types of groups: single segment groups, single maneuver type groups, and integrated test block groups. For example, an integrated test block group would contain all of the events performed at a single altitude and airspeed. The group provides a coherent structure so that the flight data are manipulated in a uniform manner.

4. INTEGRATED AIRCRAFT SYSTEM IDENTIFICATION

Designed for aircraft system identification from flight test data, all of the common data processing tools are provided in the standard suite. Figure 4 shows the detailed data flow for a typical simulation update process. An initial set of data processing steps produce the single, uniform set of data required by model

structure and identification processes. These same steps are also required for the flight data set aside for verification and validation. With the data prepared, the system identification is performed. This includes both model structure determination and parameter estimation for the selected models. The final step is validation of the final models with independent V&V data. Figure 4 also shows the IDEAS tools that perform each of these processes. These include DatPaR, the data processing and reconstruction tool; LSIDNT, a least-squares optimization tool; NAVEQNS, the navigation equations of motion simulation; and Athena, an equation error identification tool.

4.1 Data Processing

The first step in the aircraft system identification process of Fig. 4 is processing the raw flight test data into a form suitable for model structure determination and parameter identification. This preprocessing involves steps such as conversion of measured values to a common coordinate system (including unit of measure, origin location, and sign convention), kinematic consistency checking, filtering, and calibration.

4.1.1 Simple Data Manipulation
The common data manipulation tools include

- simple mathematical operations such as addition, subtraction, and scalar multiplication

- units conversions (angles, velocities, temperatures)
- filtering, smoothing, and differentiation
- wild point editing
- axis rotation and translation
- time synchronization and shifting

Several specialized tools are also included to directly address common aircraft flight test data manipulations. These include

- translation of accelerations to the center of gravity
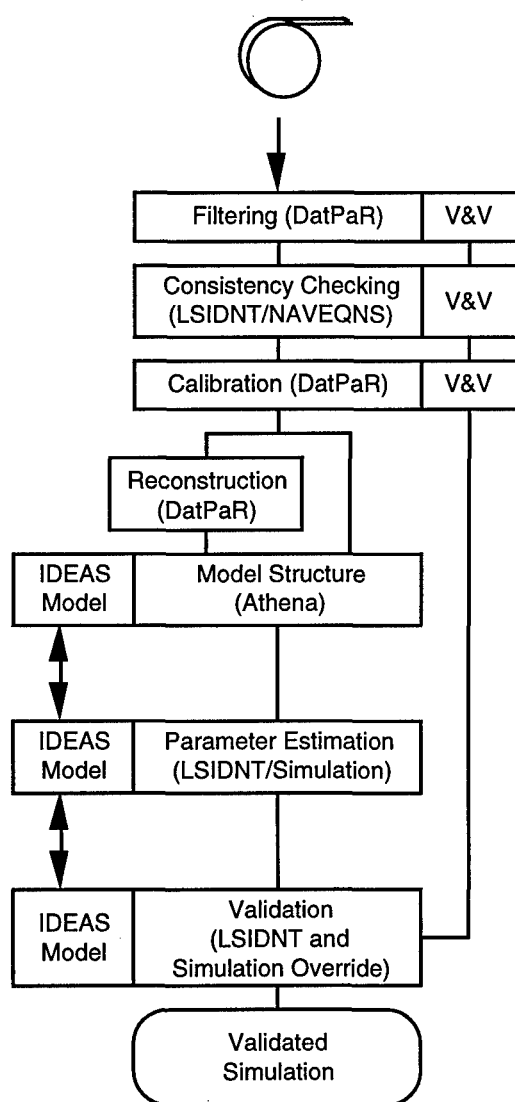- translation of air data measurements to the center of gravity
- axes translations of aerodynamic coefficients

Figure 4. Detailed Aircraft System Identification for Simulation Update

4.1.2 Wind Estimation and Sensor Calibration for Data Consistency

In general, recorded flight data come from a number of different sensors. Separately, each of these sensors records the data subject to its own calibration. In addition, air data sensors are corrupted by atmospheric winds. Taken together, all of the recorded data forms a description of a single dynamic system. For accurate system identification, it is vital that these data form a coherent set. To address wind estimation, sensor calibration, and kinematic consistency the NAVEQNS and LSIDNT tools are used.

NAVEQNS is a high-fidelity simulation of the inertial navigation equations of a rigid aircraft flying over an oblate, rotating Earth. NAVEQNS integrates flight measured linear accelerations and angular rates to generate the motion of the rigid aircraft. It incorporates parameterized sensor models for all of the inputs and outputs, including air data measurements.

LSIDNT (Least-Squares Identification) is a general, bounded, nonlinear least squares optimization routine. It is based on the N2F family of algorithms[10]. Splitting the optimization algorithm from the identification tool represents a distinct change from the NAVIDNT[7] and SCIDNT[8] tools. Rather than tightly coupling the optimizer to a particular set of residual equations, it is separated and used to address several different problems. The single LSIDNT tool is used with different residual calculations in consistency checking, parameter estimation, trim and initialization, and validation.

Using NAVEQNS and LSIDNT, calibration constants are determined that combine measured data into a single set subject to the required kinematic constraints. This ensures that accelerations, rates, and positions are mathematically consistent.

4.1.3 Data Reconstruction

The final step of data preprocessing reconstructs any additional channels from measured data. For example, Mach number is often not measured directly, but can easily be determined from known data. At this point, all of the data required for effective system identification is available.

4.2 Model Structure Determination

One of the most difficult tasks in system identification is to determine a suitable representation of the nonlinear dynamic system under examination given only recorded data. The problem is easier for aircraft system identification as years of experience by many researchers has developed large families of suitable representations depending upon the required degrees of fidelity and accuracy.

The primary tool for model structure determination within the IDEAS environment is the Athena equation error tool (described in Section 4.3). This interactive tool provides quick response to variations on quite

complex models. Using the IDEAS model within environment allows for seamless transfer of candidate model structures from the simpler identification algorithms to more detailed, but slower, algorithms.

4.2.1 IDEAS Model

The IDEAS model is a parameterized nonlinear model compatible with all identification tools. It further speeds up the identification and simulation update process by removing the need to recompile an identification program for each change of model. This model, stored as an easily readable ASCII file, is used to approximate complex aerodynamic, engine, gear, and other functions. The IDEAS model is constructed with polynomial functions of the flight data, tables, and polynomial basis splines, all of which depend upon user-defined parameters. In most instances, it is used as an incremental model to augment and correct the existing simulation values. Incremental models are especially useful during a simulation update as the effect of the increment can be easily switched off by setting the corresponding term to zero. This returns the simulation to the prior model. For example, assume that an incremental model for the pitching moment coefficient (using standard notation) is

$$\Delta C_m = C_{m_0}(M) + C_{m_\alpha}(M)\,\alpha + C_{m_q}\frac{q\bar{c}}{2V} + C_{m_{\delta_E}}\delta_E$$

where the basic moment and the moment due to angle of attack are splined functions of Mach number. The IDEAS model for this coefficient is given in Table 1.

By using a general model format accessed through a simple programming interface, each identification algorithm uses the same model so that multiple algorithms can quickly be employed to identify a process. For example, an equation error algorithm could be used for quick model structure determination with further refinement of the model parameters coming from an output error process.

4.3 Parameter Identification

Both equation error and output error identification are available in the IDEAS environment. Equation error is performed by the Athena process[6]. Athena uses a principal component regression algorithm using singular value decomposition to provide accurate estimates. The IDEAS model is used to describe the identification model in Athena. While equation error methods are limited to linear parameters, complex nonlinear models are available within Athena using cubic basis spline representations.

With minimal modification (and rehosting if necessary) any dynamic simulation process may be placed within the IDEAS environment. This includes installation of the IDEAS model. Under control of LSIDNT, a powerful, nonlinear, output error identification process is formed. There are not explicit limitations on the complexity of the IDEAS identification model within the output error process.

4.4 Verification and Validation

Verification and validation of the final results are extremely important in a system identification program.[11] As any complete system identification problem is a solution to a complex, multi-dimensional optimization problem (either directly or indirectly), there is a requirement to verify that the resulting model truly represents the dynamic system under study. In complete programs, data are gathered that are not used for primary system identification. These data (indicated as V&V in Fig. 4) must still be processed to a format suitable for comparison, but they are not used within the parameter identification programs. Within IDEAS existing tools allow for accurate comparison of independent validation data to updated simulations. Optimized simulation initialization and input biasing provides for equivalent comparisons between simulation and flight test data.

Table 1. Example IDEAS Model

```
%-----------------------
% Pitching Moment Model
%-----------------------

% -- Define spline break points
brkpt mach_bpts   0.25 0.35 0.45 0.55

% Cmo   -- Basic moment
param Cmo_m1 -0.01 free
param Cmo_m2  0.01 free
param Cmo_m3  0.01 free
param Cmo_m4  0.01 free
cbspline Cmo(mach_bpts) Cmo_m1 Cmo_m2
Cmo_m3 Cmo_m4

% Cma   -- Angle of attack
param Cma_m1 -0.006 free
param Cma_m2 -0.014 free
param Cma_m3 -0.013 free
param Cma_m4 -0.010 free
cbspline Cma(mach_bpts) Cma_m1 Cma_m2
Cma_m3 Cma_m4

param Cmq -0.2 free
param Cmde -0.015 fixed

% -- Define output equation
output cm_hat =    Cmo(mach)
                 + Cma(mach) * alpha
                 + Cmq * qb*cbar/(2*V)
                 + Cmde * delev
```

5. APPLICATION OF IDEAS

As a demonstration of some of the benefits of using an integrated software suite for aircraft system identification, some results of an on-going flight test data analysis project are presented. The purpose of the

project is to improve the flight fidelity of an operational flight trainer for, a twin turbofan military aircraft.

5.1 Data Preprocessing

After the raw flight data were stored into IDEAS, a significant amount of initial processing was required. The most important tasks were sensor calibration and wind estimation. Using NAVEQNS and LSIDNT to form an output-error estimation tool, estimates of the biases on the accelerations, angular rates, and air data sensors as well as estimates of the horizontal winds were generated. The analysis group consisted of the following maneuvers from a single integrated test block (275 Kts, 10,000 ft):

- 2 minute turn

- Longitudinal stick input: doublet and 3211

- Lateral stick input: doublet and 3211

- Directional pedal input: doublet and 3211

Figures A.1 through A.3 compare the air data measurements from the boom for one of the eight maneuvers: the lateral stick doublet input. The corresponding aileron deflection is shown in Fig. A.4. The flight data values are directly from the instrumentation system. The uncorrected values were developed from the NAVEQNS simulation driven by the flight measured accelerations and angular rates. The corrected values include optimized biases on the instruments as well as estimates of the constant winds. The results show that significant corrections are necessary to obtain a consistent set of data.

5.2 Existing Simulation Response

To assess the performance of the existing OFT simulation, the flight dynamics elements (aerodynamics, engines, and equations of motion) were hosted under IDEAS. The simulation was driven with the measured control surface positions and engine controls. The lateral response of the simulation for the same doublet maneuver as above are shown in Figures B.1 through B.4. The lateral-directional model in this simulation was known to not be representative of the aircraft, and this is well demonstrated. The simulation shows excessive roll performance and a poor match of sideslip. Both the control effectiveness values and the aerodynamic values associated with the Dutch roll mode need to be corrected.

5.3 Model Structure Determination and Initial Parameter Identification

To correct the deficiencies of the existing model, a new model for the rolling moment coefficient was developed using Athena. Again, a large group is analyzed for each identification to create a complete model. Twenty four maneuvers were combined with Mach numbers ranging from 0.26 to 0.56 and altitudes of 6000 and 10,000 feet. At each test condition, six maneuvers were included

- Lateral stick inputs: doublet and 3211

- Directional pedal input: doublet and 3211

- 60° bank-to-bank with ailerons and spoiler

- 60° bank-to-bank with ailerons only

Excellent matches at each condition are typified by Fig. 5. Similar procedures were performed for each of the other aerodynamic coefficients to generate an updated model for the aerodynamics of the aircraft. In this case, a complete model rather than an incremental model was used as the OFT model had significant nonlinearities that could not be overcome using increments only.

The results of the initial model structure determination and parameter identification are displayed in Figures C.1 through C.4 for the same maneuver as shown previously. The updated simulation shows significantly better performance for the sideslip and roll rate with the Dutch roll frequency and damping correctly matching the flight
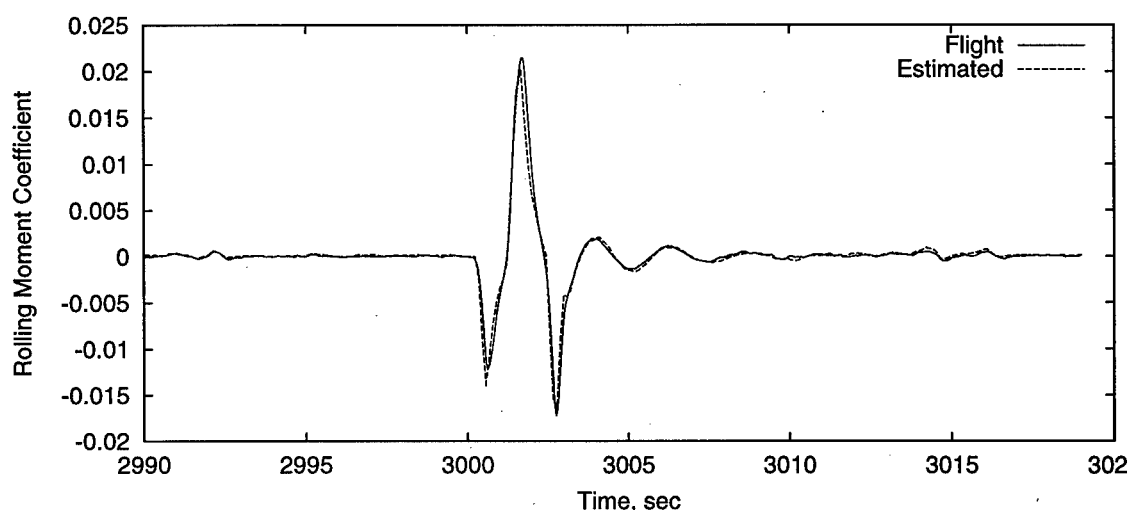

Figure 5. Rolling Moment Coefficient Comparison

data. The roll angle is particularly sensitive to initialization, and this results in an offset at the end of the maneuver. The velocity response is not yet matched as well as it could be. Detailed parameter identification using an output-error approach is under way to further refine the aerodynamic and engine models.

6. REAL TIME IDENTIFICATION

Often a flight test program is completed well before the analysis of the collected data is finalized. The knowledge gained from the analysis is not available to affect the on-going flight tests. The integrated environment of IDEAS provides a framework for efficient analysis, but lacks the speedy tools and integrated knowledge to perform all of the analysis as quickly as the data are collected. Current research into real-time and near-real-time aerodynamic identification expands on the integrated environment of IDEAS. Two coordinated methods are being used to speed up the process: fast identification and automated identification. Before discussing the methods, there is a brief examination of the goals of real-time identification.

6.1 Real Time vs. Near Real Time

Two closely related time frames are under investigation. Real-time identification seeks to provide analysis of the flight test data *as it is collected*. This provides immediate feedback to the test engineers with enhanced information regarding aircraft safety. Real-time identification also allows for data collection over a short segment of the flight (for example, a test block) and analysis of the data to allow decisions to be made regarding continuation of testing while the aircraft is still in the air. Such identification requires completely autonomous operation through the entire identification process. There is no time for operator intervention.

Near-real-time identification attempts to analyze gathered data between flights of a single program. This may mean in several hours, overnight, or within several days. Near-real-time identification seeks to address the overall progression of a flight test program. For example during flight envelope expansion, newly collected and analyzed data are compared in detail to current data. Upcoming flights can be practiced using the most up-to-date simulation, and test points can be reassigned based on knowledge, or lack thereof, of regions of interest. Repeated measurements of well-known data are avoided, and additional data are collected in areas of the most uncertainty.

6.2 Fast Identification

To speed up aircraft system identification, both hardware and software techniques are being pursued. Modern processing power has accelerated with parallel computation well within reach for a large number of problems. The power of these super computers is increasingly being applied to areas outside the traditional problems (such as computational fluid dynamics). For example, the High Performance Computing Distributed Center located at the Naval Air Warfare Center Aircraft Division, Patuxent River, Maryland operates a Silicon Graphics Power Challenge Array providing over 50 GFLOPS Peak, 24 GB memory, and 800 GB total hard disk storage. This center is dedicated to the investigation of real-time tasks of all varieties.

A number of software methods are being investigated for fast identification as well. Most techniques center on recursive methods that provide immediate updates to parameters as new data become available. For example, the square root information filter[12] has shown some promise. Of particular interest are those algorithms that can be remapped into parallel algorithms, that is, algorithms that are suitable for efficient operation on a parallel computer.

6.3 Expert System Identification

To enable real-time or near-real-time analysis, even with high performance computational capability and fast identification algorithms, a high-level coordination of tasks is required. A system identification expert system is under development that monitors data quality, selects identification methods, alerts the analyst of data and identification problems, provides alarms if flight safety is jeopardized, and prioritizes identification tasks. Connected as a separate process into IDEAS (Fig. 2), the expert system has full use of all available tools.

The typical identification process involves the analyst trying a variety of model structures and comparing the results to determine the best solution. While considering the results, the computer sits idle. Using a distributed concurrent processing approach, an expert system distributes and controls candidate models and estimation tasks among available computational resources. Tasks are monitored for feasibility of completion within the time allotted. Task distribution is done at a number of levels including running separate models on different processors, running separate algorithms with the same data, and distributing complex algorithms across multiple machines.

7. CONCLUSIONS

Integrating the tools of system identification into a uniform framework frees the engineer to tackle the difficult problems associated with identification of a complex nonlinear model. A database tailored for flight test data analysis with the base unit of a history vector encourages coherent processing. A flexible model definition, which is included in all identification and simulation tools, simplifies structure determination and parameter estimation by eliminating complex recoding tasks. The integrated architecture significantly speeds up overall data processing and opens the possibility of real-time aircraft identification. Operating on work stations or personal computers, IDEAS offers a significant advancement to the process of system identification for complex nonlinear aircraft.

8. ACKNOWLEDGMENTS

The support of all of those working on the IDEAS program is gratefully acknowledged. The identification work of Joelle Loretta and Al Paris has been particularly beneficial to this paper and to IDEAS.

9. REFERENCES

1. Maine, Richard E. and Iliff, Kenneth W., "User's Manual for MMLE3, A General FORTRAN Program for Maximum Likelihood Parameter Estimation," NASA TP-1563, 1980.
2. Maine, Richard E., "Programmer's Manual for MMLE3, A General FORTRAN Program for Maximum Likelihood Parameter Estimation," NASA TP-1690, 1981.
3. Bach, R. E., Jr., "State Estimation Applications in Aircraft Flight Data Analysis," A User's Manual for SMACK, NASA RP-1252, March 1991.
4. Tischler, Mark B., and Cauffman, Mavis G., "Comprehensive Identification from FrEquency Responses, Vol. 1 — Class Notes," NASA Conference Publication 10149, September, 1994.
5. Tischler, Mark B., and Cauffman, Mavis G., "Comprehensive Identification from FrEquency Responses, Vol. 2 — User's Manual," NASA Conference Publication 10150, September, 1994.
6. Anderson, Laurence C., "Robust Parameter Identification for Nonlinear Systems Using a Principal Components Regression Algorithm," AIAA-85-1766, AIAA 12th Atmospheric Flight Mechanics Conference, August 1985, pp 28–36.
7. Trankle, T.L., Rabin, U.H., and Vincent, J.H., "Filtering Flight Data Prior to Aerodynamic System Identification," AIAA Atmospheric Flight Mechanics Conference, August 1983.
8. Trankle, T.L., Vincent, J.H., and Frankin, S.N., "System Identification of Nonlinear Aerodynamic Models," Advances in the Techniques and Technology of the Application of Nonlinear Filters and Kalman Filters, AGARD-AG-256, Paper 7, March 1982.
9. Alaverdi, Omeed, Warner, Michael S., and Abanero, Jose N.T., "Development of a Flight Test Database for the MC-130E Aircrew Training Device," Proceedings of the 14th Interservice/Industry Training Systems and Education Conference, November 1992, pp. 197–204.
10. Dennis, J.E. Jr., Gay, D.M., and Welsch, R.E., "An Adaptive Nonlinear Least-Squares Algorithm," ACM Transactions on Mathematical Software, Vol. 7, No. 3, September 1981, pp 348–368.
11. Bonner, M.S., and Gingras, D.R., "Status of a Comprehensive Validation of the Navy's F/A-18A/B/C/D Aerodynamics Model," AIAA-96-3529-CP, AIAA Flight Simulation Technologies Conference, July 1996.
12. Maybeck, P.S., Stochastic Models, Estimation, and Control, Vol. 1, Academic Press, New York, 1979.
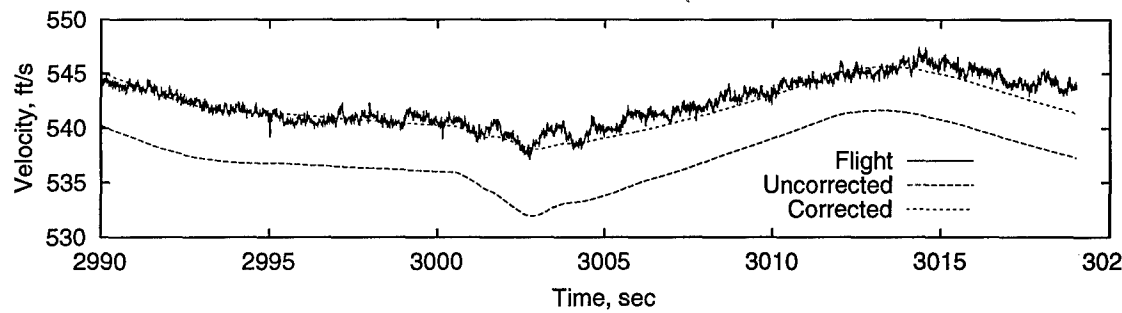
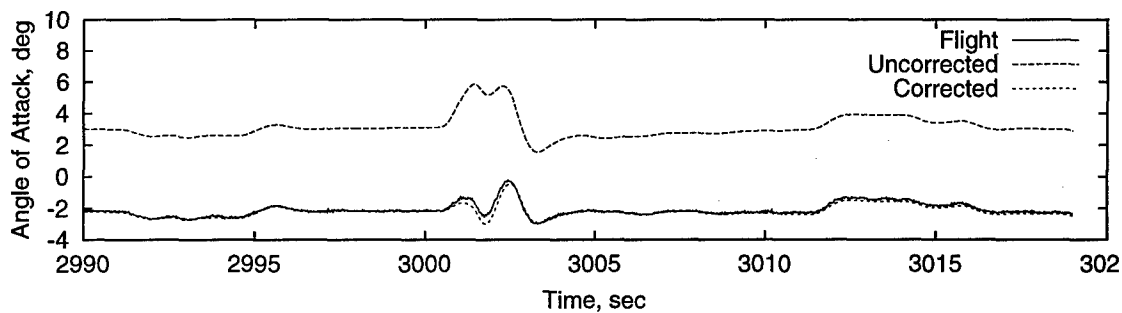Figure A.1. Comparison of Boom Velocity Corrections

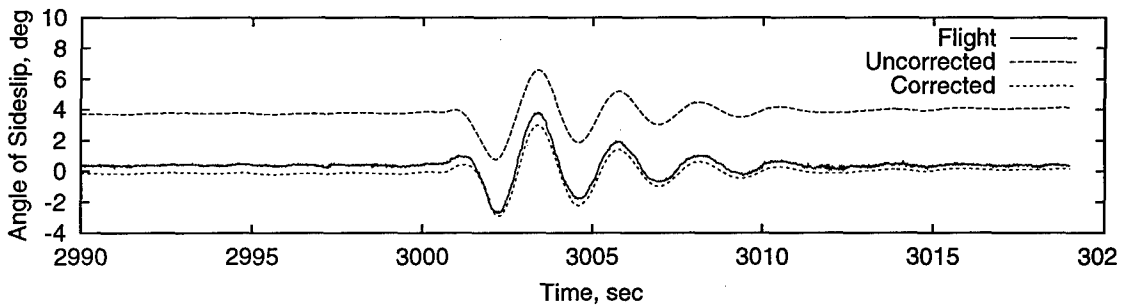Figure A.2. Comparison of Boom Angle of Attack Corrections

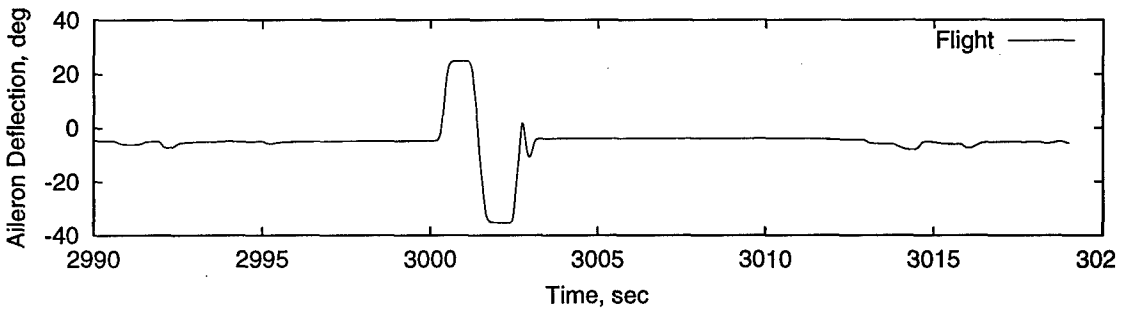Figure A.3. Comparison of Boom Angle of Sideslip Corrections

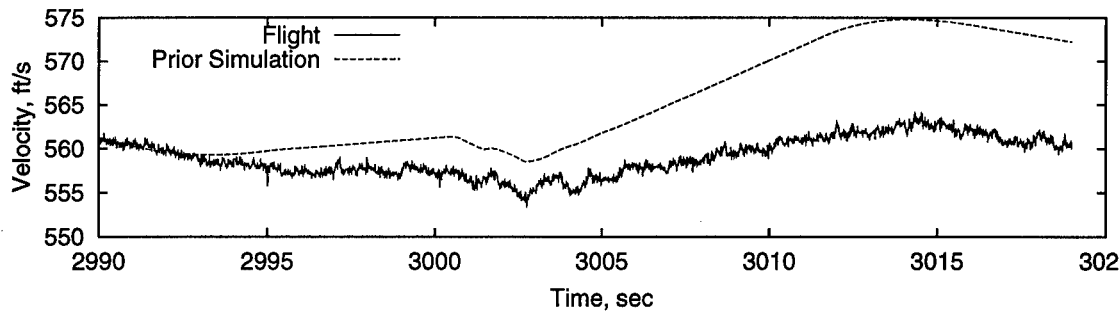Figure A.4. Lateral Command Input

Figure B.1. Existing Simulation Velocity History
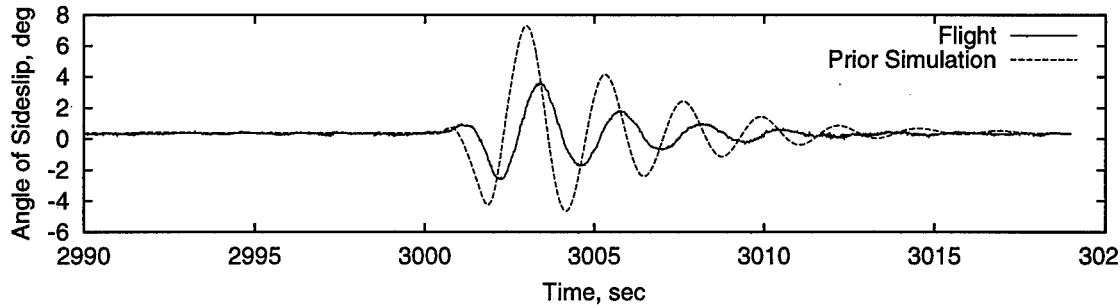

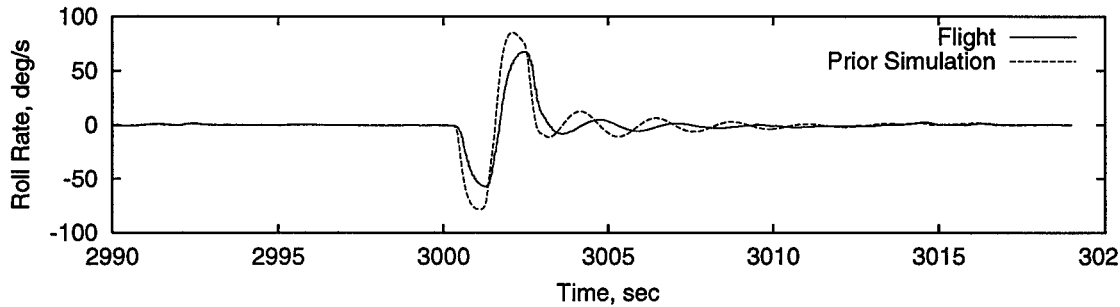Figure B.2. Existing Simulation Angle of Sideslip History

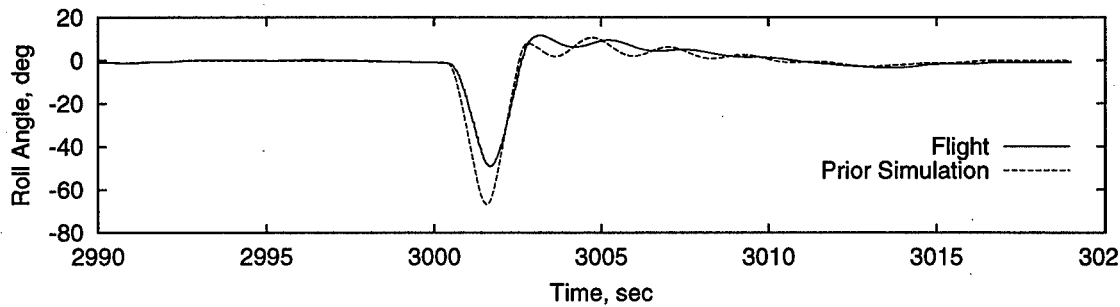Figure B.3. Existing Simulation Roll Rate History

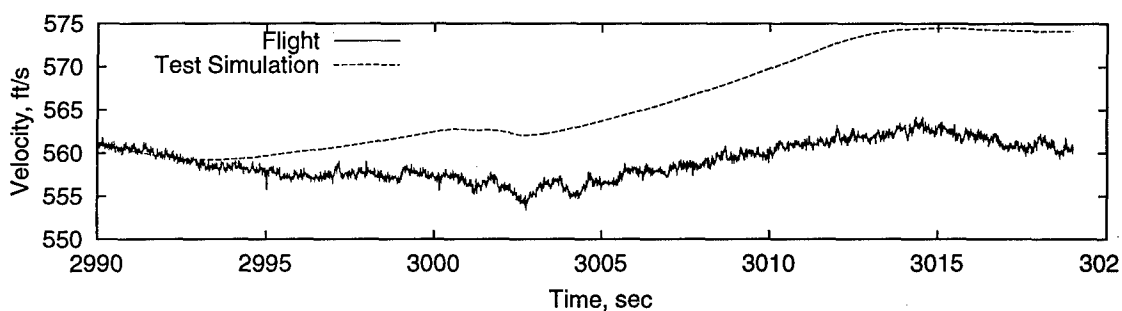Figure B.4. Existing Simulation Roll Angle History
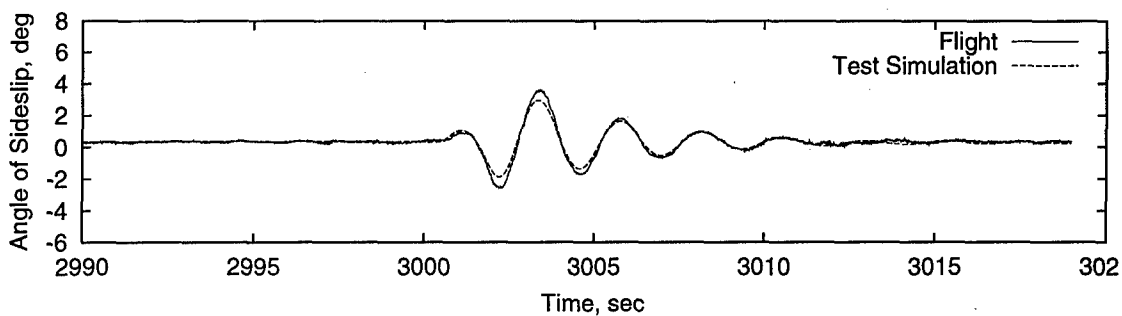
Figure D.1. Velocity History for Preliminary Model

Figure D.2. Angle of Sideslip History for Prelminary Model
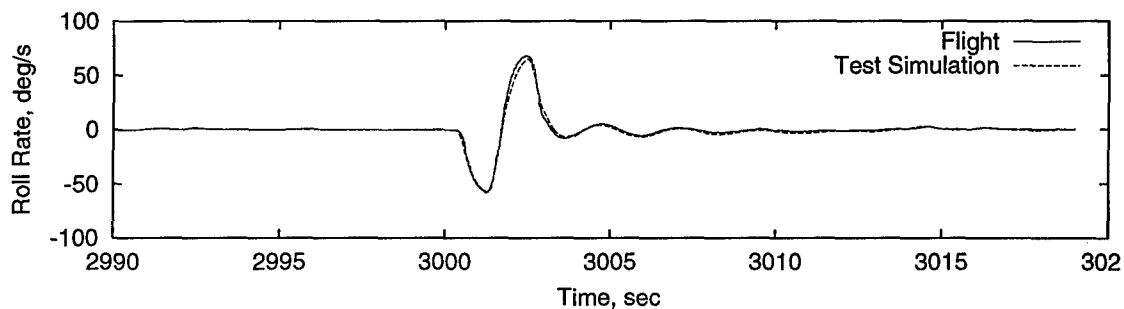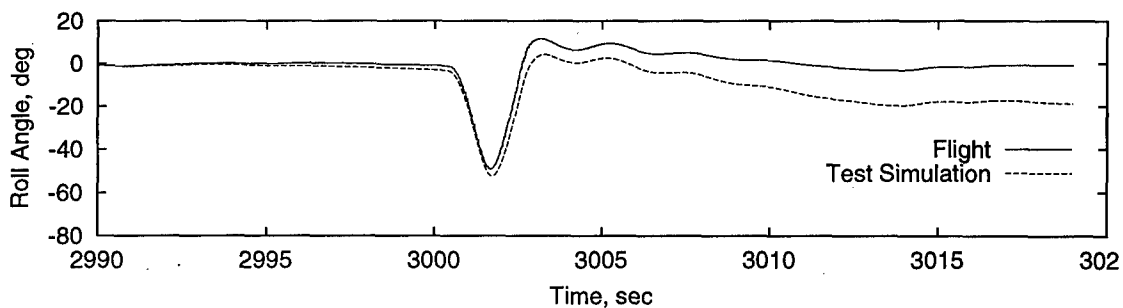

Figure D.3. Roll Rate History for Preliminary Model

Figure D.5. Roll Angle History for Preliminary Model

Recent Experiences on
Aerodynamic Parameter Identification
for EUROFIGHTER at
Alenia, British Aerospace, CASA and Daimler-Benz Aerospace

by

Renzo Bava[*], Graham T. Hoare[†], Gabriel Garcia-Mesuro[‡], Hans-Christoph Oelker[§]

Abstract

EUROFIGHTER, a very agile configuration, which incorporates a high level of inherent longitudinal instability, will be the new fighter aircraft for the airforces of Italy, United Kingdom, Spain and Germany in the next century. It is being developed jointly by industrial partners of these four nations (Alenia, British Aerospace, Construcciones Aeronauticas S.A. and Daimler-Benz Aerospace).

For flight test evaluation of the aerodynamic properties of this aircraft at four different partners confidence had to be established in different methods as well as in comparison between results of different development aircraft. The present paper gives an overview of company specific aerodynamic parameter identification methods. All methods are based on well known theories. Each method, though, incorporates some specific tailoring in order to cope with the characteristics of the basically unstable airframe.

Results are given for four principal examples. At first a problem of the aircraft's weathercock stability is discussed. Discrepancies could be confirmed with all methods on different aircraft. The procedure of correcting the dataset is described and illustrated. The second example deals with the twin-seater. Certain increments representing the twin-seater could not be verified in flight test, it is shown how and why they were omitted. Presentation of time history matching illustrates the capabilities of all methods to deal with large perturbation manoeuvres. Finally identifying and reducing tolerances of the dataset leads to an improved flight clearance.

1. Introduction

EUROFIGHTER will be the new fighter aircraft for the airforces of Italy, United Kingdom, Spain and Germany in the next century. It is being developed jointly by industrial partners of these four nations, these are: Alenia (ALN) for Italy, British Aerospace (BAe) for the United Kingdom, Construcciones Aeronauticas (CASA) for Spain and Daimler-Benz Aerospace (DASA) for Germany. The aircraft is based on a very agile configuration, which incorporates a high level of inherent longitudinal instability. An overview of the basic geometry is given in Fig. 1. The characteristic feature is the canard, generating the inherent instability. Due to this fact the aircraft is controlled by a digital, full authority, quadruplex redundant flight control system (FCS).

The current status of the programme is well ahead in the development flight test evaluation. A total of seven development aircraft (DA's) are flying and working the way to a full operational clearance of the aircraft.

In order to guarantee a progressive and cost efficient exploration of the flight envelope flight test tasks have been split up between the four EUROFIGHTER partner companies (EPC's). This applies also to the rather complicated subsystem „aerodynamics" in all development phases. For flight test evaluation at four different partner companies confidence had to be established in different flight data analysis methods as well as in comparison between results of different development aircraft. The one development aircraft considered to be the „data gathering aircraft" for validation of the aerodynamic data set, is DA1, operated at the DASA Manching facility. Supporting basic data gathering, especially in the high angle of attack regime for the carefree envelope expansion, is done on DA2, operated at the BAe Warton facility. Aerodynamics of tank configurations is mainly investigated on DA3 and DA7, which are both operated at the ALN Caselle facility. Again support from other DA's will be present, namely DA1, DA2 and DA5, operated at DASA Manching, for the single seater and DA6 for the twin seater. Basic twin seater aerodynamics are

[*] Renzo Bava, Flight Mechanics Specialist, Flight Mechanics Group, Alenia, Corso Marche, 10146 Torino, Italy

[†] Graham T. Hoare, Group Leader EUROFIGHTER Flight Mechanics, British Aerospace Military Aircraft, Warton Aerodrome, Preston, Lancashire, PR4 1AX, United Kingdom

[‡] Gabriel Garcia-Mesuro, Head of EUROFIGHTER Aerodynamic Technology, Construcciones Aeronauticas S. A., P. John Lennon, s/n, 28906 Getafe (Madrid), Spain

[§] Dr.-Ing. Hans-Christoph Oelker, Senior Flight Test Engineer, Flight Test Handling Group, Daimler-Benz Aerospace AG, Military Aircraft, Postfach 1149, D-85073 Manching, Germany

being investigated on DA6, operated at the CASA Getafe facility. Supporting work is done on DA4, the second twin seater flying, and operated at BAe Warton. From these explanations it can be seen that none of the work can be done on a single aircraft, partners are dependent on each other. This challenging task will be illustrated in this paper with the example of four different aerodynamic parameter identification methods used by the four partners.

During the course of this paper at first a brief overview of the methods will be given, highlighting the individual peculiarities. Typical results for each method will be given as well as an example how results from each company are being pooled to aid the overall validation process of the aerodynamic model. The main purpose of this paper will be to show how results from tools with different properties are being harmonised and used to validate and to update one common single data base, that is the aerodynamic stability and control data set.

2. Aerodynamic Parameter Identification Methods

All four involved EPC's use different methods for aerodynamic parameter identification (APID). All methods incorporate some company specific „tailoring", which is mainly based on the need to analyse a highly unstable and non-linear configuration. All methods are based on well known theories, therefore only the company specific tailoring will be treated here.
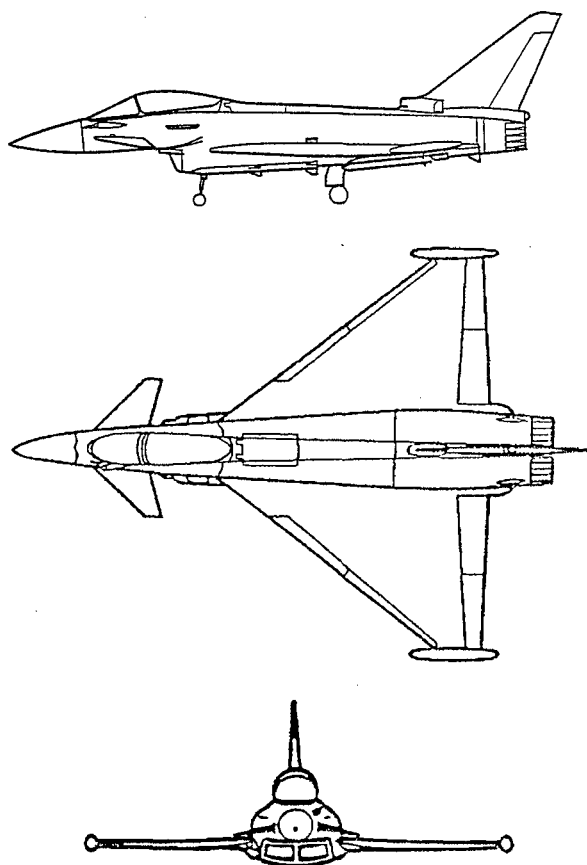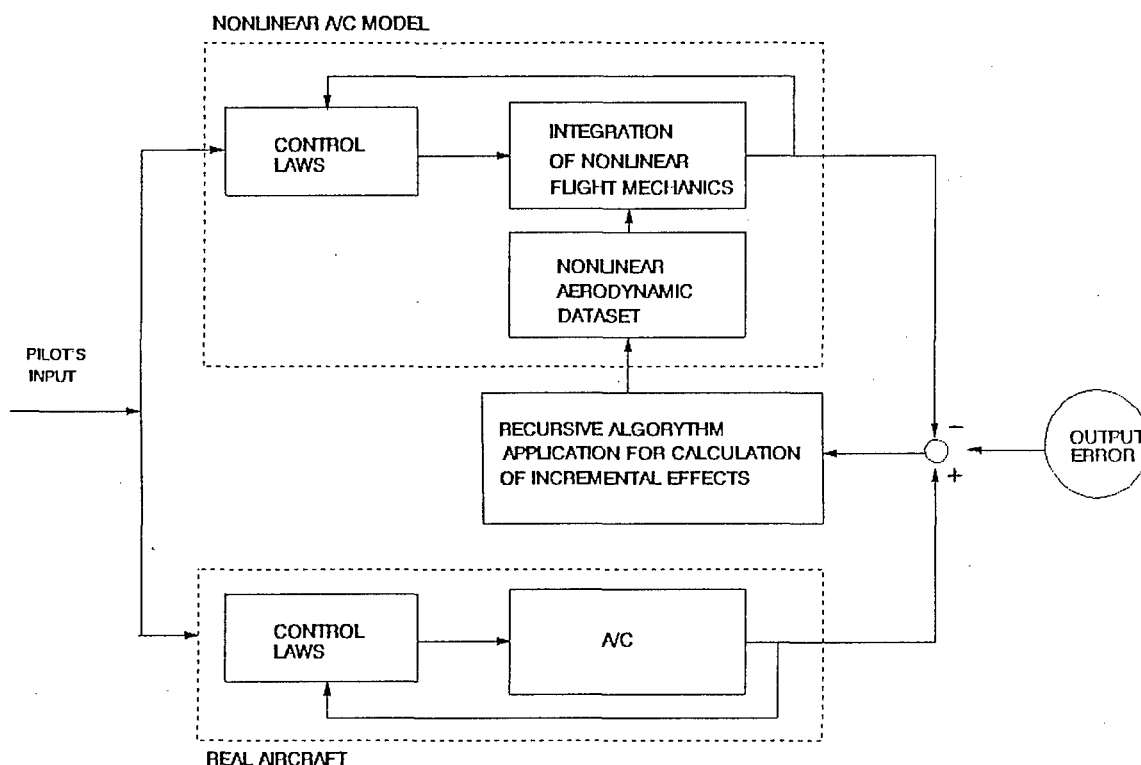

Fig. 1: EUROFIGHTER Geometry

Fig. 2: Schematic Overview of Alenia's Identification Method.

2.1 Method at Alenia

The Alenia method is based on an extension of the classical output error description in conjunction with a maximum likelihood estimation. In the basic well known realisation this method fails for unstable aircraft because the integration of the flight mechanical equations will generally diverge to infinite values, among many other publications see e.g. [1] and [2]. The basic idea at ALN for repairing this defect is the inclusion of the full non-linear aircraft model with controller into the method. A schematic overview of this new process is given in Fig. 2.

Besides the inclusion of the control law algorithms into the code also a special treatment of the non-linear aerodynamic model was introduced. For EURO-FIGHTER the aerodynamic coefficients generally are modelled with non-linear increments as follows in the aerodynamic data set:

$$c_x = c_x(\alpha = 0) + \Delta c_x(\alpha) + \Delta c_x(\text{control surfaces})$$
$$+ \Delta c_x(\text{damping}) + \dots \tag{1}$$

where x can be any one of the six degrees of freedom. Now for incorporation into the ALN method an additional set of aerodynamic terms has been included. The example is given for the pitching moment equation:

$$c_m = c_m(\alpha = 0) + \Delta c_m(\alpha) + \Delta c_m(\text{control surfaces})$$
$$+ \Delta c_m(\text{damping}) + \dots + \dots$$
$$+ \Delta c_{m\alpha} \cdot \alpha + \Delta c_{m\delta} \cdot \delta + \Delta c_{m\eta} \cdot \eta \tag{2}$$
$$+ \left(\Delta c_{mq} \cdot q + \Delta c_{m\dot\alpha} \cdot \dot\alpha \right) \cdot \frac{\bar{c}}{V_\infty} + \Delta c_{m0}$$

These additional terms show a mathematically linear structure. Now the non-linear aerodynamic model can be updated via the application of the maximum likelihood estimator. In a recursive algorithm, as indicated in Fig. 2, the output error is being minimised.

According to ALN the following advantages can be taken with this tool, especially with respect to linear methods:

- This method accounts for all non-linear aerodynamic and FCS scheduling effects.

- All linearisation approximations have been avoided (e.g. aeroelastic, gyroscopic, cross coupling or other secondary terms are considered).

- The estimated corrections are directly verified on the full, non-linear aircraft model.

- Open loop artifices required to deal with the divergence of the integration process for the unstable aircraft is avoided. In the present method the „real" FCS operates to stabilise the aircraft.

- The method could be incorporated into a code with the same interactive structure of the usual simulation programme.

According to ALN the following disadvantage could be relevant:

- Uncertainties of the FCS model could impair the estimate of the derivatives.

- Strong non-linearities can influence the convergence process.

The principal structure of the optimisation model, as given in Eq. 2, allows also for identification of other systems of EUROFIGHTER. So ALN has identified successfully EUROFIGHTER tyre characteristics and updated the relevant model.

2.2 Method at British Aerospace

The technique for aerodynamic parameter identification at BAe is based on the equation error approach. This method can be readily applied to systems that are described by non-linear equations. As it attempts to balance the left and right hand sides of the equations involved, no integration is involved, and hence the method is readily applicable to unstable aircraft.

The programme used at BAe, called Athena, was developed by SD Scicon, a UK software house, and is an update of an earlier version successfully applied on a number of different aircraft (e.g. Harrier, Tucano). It uses a principal components regression algorithm. The method is well defined in [3], a brief overview follows: To allow regression methods to be applied, the non-linear system description is first made linear in the terms to be identified, by expressing them as a series expansion. Solution to the ensuing least squares problem would normally involve inversion of matrices. However, as that is not necessarily straight forward, or even possible, the problem is mathematically manipulated to yield a diagonal (the principle components) matrix. The terms within the model structure are then identified by carrying out regression analysis. Only terms above a user defined threshold are identified, those below the threshold are set to apriori levels. The user is given an indication of the information content within the flight data, as a basis for setting the threshold.

As this method operates at equation level, flight data under consideration need not be time continuous. Consequently flight data can be ranged (i.e.: filtered). This allows the user to eliminate variability in one or multiple parameters in order to aid the solution or simplify the model structure to be identified. However, because this methods operates at equation level, flight data quality is of paramount importance. This is considered to be a drawback.

A key feature of the method is the ability of the user to define the model structure to be identified. The user iterates to the optimum solution by altering the model structure, selected model elements, the ranges of the supplied variables, and the weighting given to a priori data. An output error predictor allows comparisons between flight measured aircraft responses and calculated responses based on the updated model.

The overall suite, developed over several years, is given in a schematic overview in Fig. 3, it involves a number of routines developed by either SD Scicon (e.g. data pre-processor, output error predictor) or in-house (e.g. prior programme, kinematics compatibility programme).
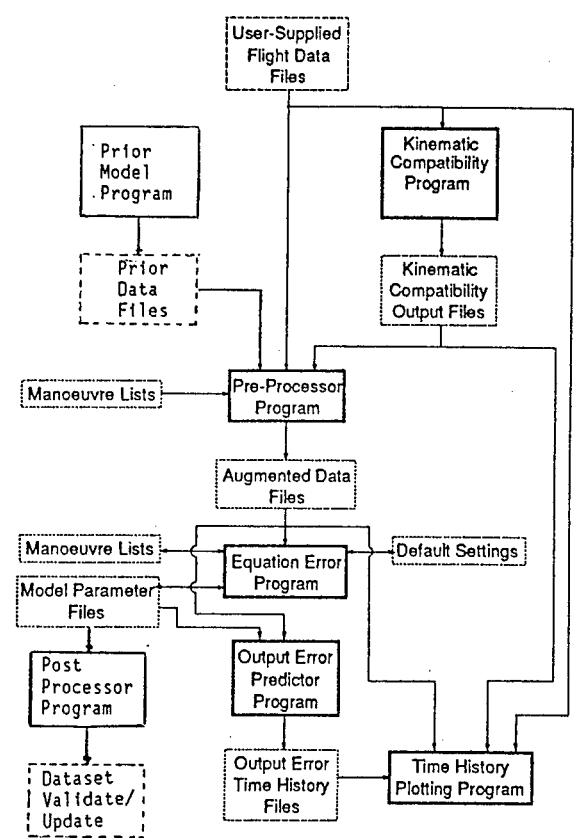
Fig. 3: Schematic Overview of Aerodynamic Parameter Identification Process at BAe

2.3 Methods at CASA

At CASA two methods are being used for aerodynamic parameter identification. One method is based on the well known output error approach in conjunction with the equation decoupling algorithm. This method will be presented as DASA's method further down.

The other method in use at CASA is based on the well known equation error approach in conjunction with a regression analysis parameter estimator. This method is called Dynamic Detrimming (DDT), since it involves also detrimming during the calculation process. The DDT method was set up for the EUROFIGHTER flight test programme, taking advantage of the structure and quality of the wind tunnel based data to be validated (Stability and Control as well as Tolerances Data Set).

Using aircraft measurements (α, β, δ, p, q, r, n_z, n_x, n_y, ...) and elaborated (computed) parameters ($\dot{p}$, $\dot{q}$, $\dot{r}$, mass properties, engine data,...) inertial and propulsive forces and moments are calculated. Then the so-called global coefficient error is calculated, as function of time, as follows:

$$\left\{ [\text{Inertial} + \text{Propulsive}]_x(t) \right\}_{Flight} - \left\{ [\text{Aerodynamic}]_x(t) \right\}_{Dataset} = \Delta C_x(t) \tag{3}$$

being:

X   generic force or moment

$\Delta C_x(t)$ Observation vector .

On the basis of the theoretical wind tunnel data the vector of aerodynamic forces and moments is calculated and used in Eq. 3, the resulting observation vector (global coefficient error) is then corrected to zero controls, also with the data from the aerodynamic model, and a dynamic compatibility check,
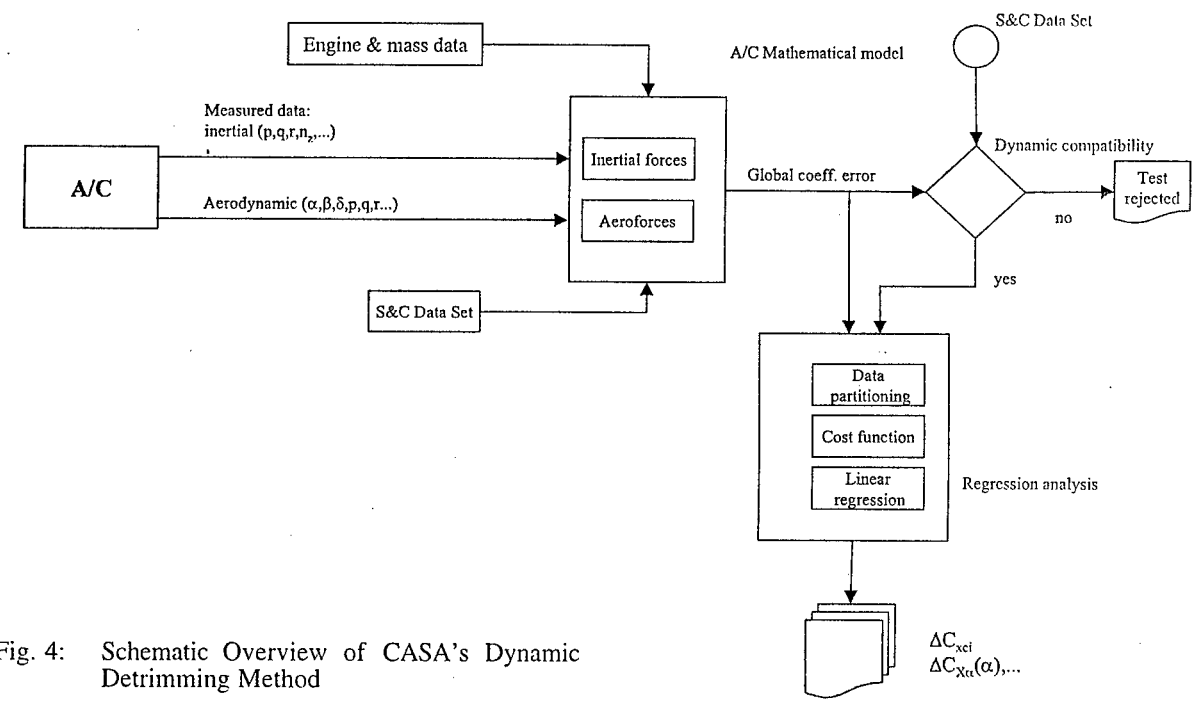

Fig. 4: Schematic Overview of CASA's Dynamic Detrimming Method

based on engineering know-how, is performed, which is the key part of the method. It allows either to decide about the suitability of the DDT for the manoeuvre to be identified or the acceptance or rejection of the test result.

It is worth to note that DDT is an excellent method if the wind tunnel based data to be flight validated are of very good quality and if the measurements are as well of good quality. Time shifts or delays, sensors effects, etc. shall be accounted for in the measured data to assure high fidelity in the flight parameters.

Mathematically speaking DDT is an equation error method that implements a linear regression analysis using the following cost function to be minimised:

$$J = \left[\Delta C_{x0} + \Delta C_{x\alpha}\alpha + \Delta C_{x\beta}\beta + \sum_i \Delta C_{x_{c_i}} c_i \right] - \Delta C_x \qquad (4)$$

being:

X   generic force or moment

c_i generic control input (controls, angular velocities, etc...)

α angle of attack

β angle of sideslip.

Due to its form DDT can be called as an equation error method in „derivative errors" (see Eq. 3). The advantage of this approach is that it allows to measure the error in derivatives scaled in „tolerance units", therefore allowing direct comparison with the tolerance dataset.

With the identification module, which consists in a data partitioning and time slicing module, cost function computing and linear regression algorithm routines as well as different data partitioning can be used depending on the type of derivative or non-linearity to be identified; here the engineering judgement is of vital importance for the success of the analysis. An overview of the whole process is given in Fig. 4 in the form of a block diagram.

The main advantage of this method is the fact, that it is a non-iterative procedure with high numeric stability. Therefore it is appropriate for highly unstable aircraft. Due to the fact that it identifies the model coefficients for a difference, the usually possible equation error bias can be avoided. Finally the presentation of the result in tolerance units immediately allows for interpretation of the suitability of the aerodynamic model used in the entire process.

2.4 Method at DASA

At DASA flight test an extended version of the well known output error approach in conjunction with a maximum likelihood estimator has been used highly successful for many years. Due to the mathematical nature of this algorithm the involved simulation step has to be based on a linearised aerodynamic model. For stable aircraft this procedure is well known and well established. For unstable aircraft this procedure fails because integration of the flight mechanical equations will generally diverge to infinite values, as already mentioned above. Therefore an output error comparison cannot be performed anymore. Ref. 1 gives a procedure, which introduces artificial stabilisation during integration of the equations. The method requires additional computational effort. At DASA flight test another approach has been followed, the equation decoupling technique as introduced by H. Schäufele [4].

The basic idea of the equation decoupling techniques is based on the introduction of flight measured aircraft state variables into the integration of the flight mechanical equations. The usual state equation

$$\dot{\tilde{x}} = \underline{A}(\underline{\xi})\tilde{x} + \underline{B}(\underline{\xi})\underline{u} \qquad (5)$$

with $\tilde{x}$ = simulated state vector

$\underline{u}$ = control vector

$\underline{\xi}$ = parameter vector

$\underline{A}$ = system matrix

$\underline{B}$ = control matrix

$$\dot{\tilde{x}} = \underline{KOI}\ \underline{A}(\underline{\xi})\ \underline{x} + \underline{KO}\ \underline{A}(\underline{\xi})\ \tilde{x} + \underline{B}(\underline{\xi})\ \underline{u}$$
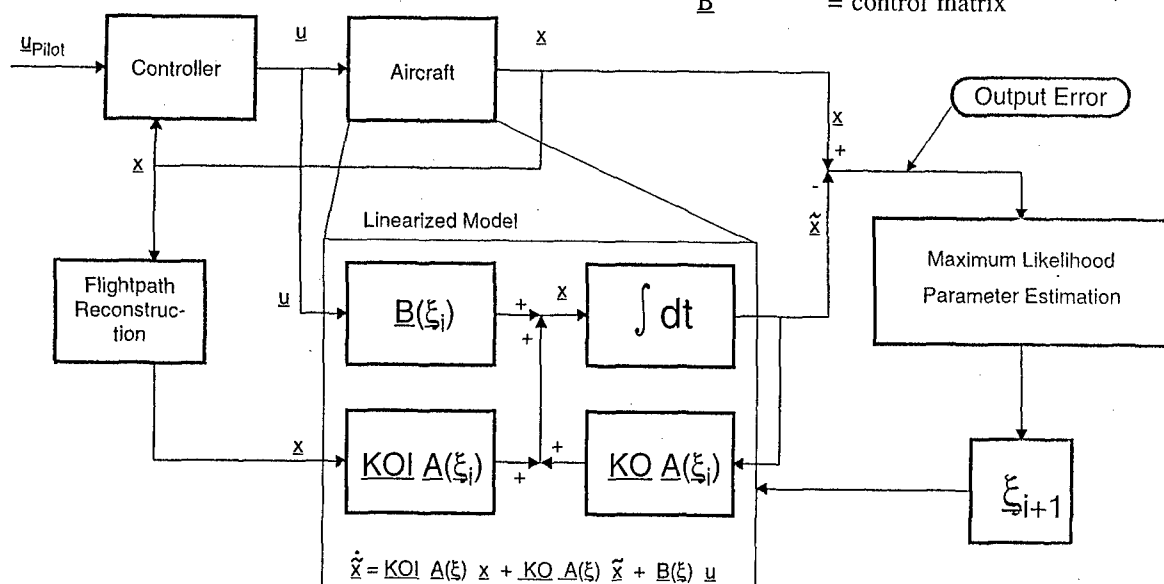
Fig. 5:   Schematic Overview of DASA's Equation Decoupling Method

is then changed to

$$\dot{\underline{x}} = \underline{KOI} \; \underline{A(x)} \underline{x} + \underline{KO} \; \underline{A(x)} \dot{\underline{x}} + \underline{B(x)} \underline{u} \qquad (6)$$

with $\underline{KOI}, \underline{KO}$ = decoupling matrices

$\underline{x}$ = measured state vector.

The decoupling matrices, introduced in [4], are complementary, which means that at equal positions one matrix contains a '1' whereas the other contains a '0' at this position. The entire process, output error approach and equation decoupling, is summarised in Fig. 5. For general use at DASA also a flight path reconstruction is part of the process. The final result is a set of flight validated aerodynamic parameters, which now can be used to calculate the flight mechanical properties of the aircraft.

The given APID procedure has been successfully used at DASA flight test for different aircraft of stable and unstable basic airframe characteristics. The main programme of the past years was TORNADO, also experience on unstable aircraft has been gained, e.g. the German F-104 CCV (Control Configured Vehicle) in the early eighties and EAP (Experimental Aircraft Programme) in the late eighties. Also helicopters have been investigated successfully.

3. Results

The above given methods amongst others are being used during the process of flight envelope expansion. The tasks related to this process are split up between EPC's and thus development aircraft. Results of tests are being evaluated jointly, regularly during meetings. The first example of joint evaluation stems from the very early period of envelope expansion flying.

3.1 Weathercock Stability

Rather early already during flight test some discrepancies in weathercock stability, $c_{n\beta}$, had been discovered. At this time mainly DA1 and DA2 were flying for data gathering. A typical result from DA1 derived with the DASA method is given in Fig. 6. In this figure the weathercock stability is plotted as a function of angle of attack. It is evident that the values identified from flight are considerably lower than those given from the data set. The difference increases with angle of attack. Independently, at the same time, similar results were found on DA2 at BAe Warton. A typical example of their findings is given in Fig. 7. There also the weathercock stability derivative is plotted versus angle of attack. Again it is evident that the identified values for $c_{n\beta}$ are smaller than those given in the dataset, and also the discrepancies increase with angle of attack. Since in both figures given here, for clearance reasons, numbers have been taken off the ordinates, it must be mentioned that the identified reduction of $c_{n\beta}$ is in the same order of magnitude. Fig. 8 gives an equivalent result obtained also with the BAe method. Here the ability of this method to deal with non-linear aerodynamic behaviour is being utilised. It shows weathercock stability as a function of angle of sideslip at a given angle of attack. The result indicates a weak non-linearity around zero angle of sideslip.

At first it was thought there is a reduction of weathercock stability on these DA's due to the different afterbodies, compared to the windtunnel models. At that
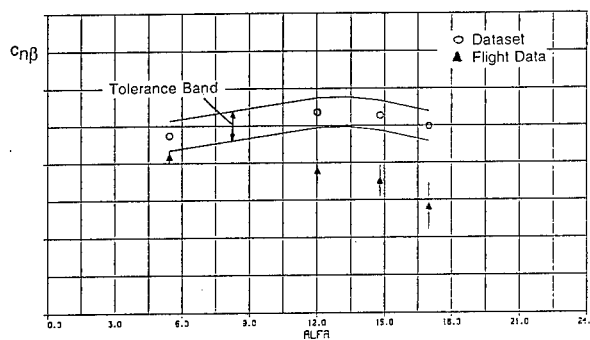

Fig. 6:   Comparisons of Identified Weathercock Stability with Dataset Values versus Angle of Attack (DASA's Equation Decoupling Method for DA1 Data)
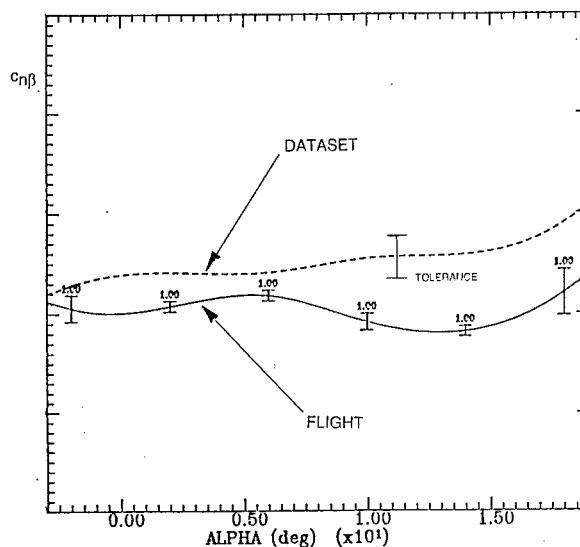

Fig. 7:   Comparison of Identified Weathercock Stability with Dataset Values versus Angle of Attack (BAe's Equation Error Method for DA2 Data)
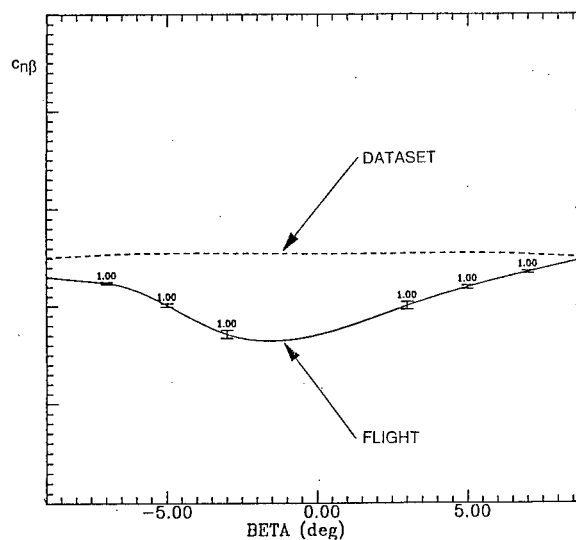

Fig. 8:   Comparison of Identified Weathercock Stability with Dataset Values versus Angle of Sideslip for a given Angle of Attack (BAe's Equation Error Method for DA2 Data)
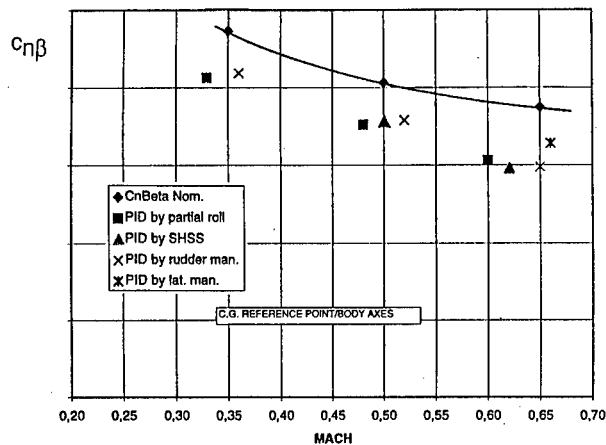
$c_{n\beta}$

Fig. 9: Comparisons of Identified Weathercock Stability with Dataset Values versus Mach Number (Alenia's Output Error Method for DA3 Data)
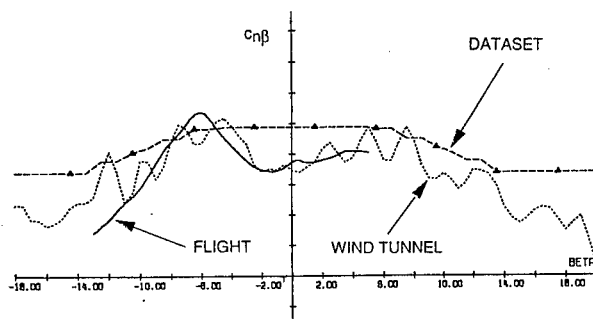

Fig. 10: Comparison of Identified Weathercock Stability with Dataset Values and Windtunnel Data versus Angle of Sideslip for a given Angle of Attack (BAe's Detrimming Method for DA2 Data)

time DA1 and DA2 were equipped with the interim engine RB199, which is shorter than the final EJ200 engine. Due to this fact the windtunnel model is relatively longer than the real aircraft and a reduction of $c_{n\beta}$ in flight could have been concluded. Therefore supporting results from DA3 were requested. This aircraft was already equipped with the EJ200 engine at that time. But also results from this aircraft show a reduction in $c_{n\beta}$, as given in Fig. 9 from the Alenia method. Here the results are presented as a function of Mach number and for different manoeuvres, showing that the behaviour found on DA1 and DA2 is consistent for the subsonic speed range also on DA3.

Having already identified a weak non-linearity of $c_{n\beta}$ for small angles of sideslip, compare Fig. 8, a reassessment of the windtunnel data confirmed its existance, as illustrated in Fig. 10. Here windtunnel measurements from a BAe model of $c_{n\beta}$ versus sideslip at a given angle of attack are compared to those of the dataset. The figure indicates an unmodelled non-linear decrease in $c_{n\beta}$ for small angles of sideslip. Also indicated is an excellent agreement between windtunnel

and flight data, as derived from a detrimming method in use at BAe. The reason the local loss was not modelled stems from the way in which the datset is structured. It consists of a basic $c_{n\beta}$ term, constant with angle of sideslip, plus a non-linear Δc_n term that is a function $f(\alpha,\beta)$. In modelling the non-linearity as Δc_n some detail found in the wind tunnel data was lost.

The reason why the measured results from flight revealed the non-linear decrease of weathercock stability for angles of sideslip around zero lies in the way the system was excited. Due to the nature of this augmented aircraft the controller hardly allows the build up of angles of sideslip as large as 5°, even for full pedal doublet or 3211 excitations. Therefore parameter identification results could deliver the $c_{n\beta}$ for smaller angles of sideslip only. This explains the found discrepancies. Steady Heading Sideslip manoeuvres however did provide data at high angles of sideslip and allowed the non-linearity to be assessed by BAe (Fig. 10). - Based on these findings the dataset was modified, existing non-linear terms have been changed for small angles of sideslip.

3.2 Twin-Seater Experience

For training purposes EUROFIGHTER will also fly as a twin-seater variant. Two development aircraft, DA4 and DA6, are twin-seaters. The main data gathering aircraft is DA6, operated by CASA.

In the structure of the overall dataset the twin-seater is being handled as an increment to the original single-seater data. Fig. 11 shows now results derived from CASA's DDT method for $c_{m\alpha}$. In Fig. 11a flight measured data are being compared with the twin-seater dataset (single-seater data plus twin-seater increment) as a function of angle of attack. It is evident from these results that the difference of longitudinal instability between flight data and predictions becomes larger with angle of attack. The flight data lie in the upper tolerance band or above it.

A thorough investigation of the dataset revealed that the flight data follow the predictions much better if one compares solely with the single-seater data omitting the twin-seater increment, this comparison is given in Fig. 11b. Now an even scatter of flight measured data around the nominal predicted value of $c_{m\alpha}$ is present. - Again, the reason for this finding is based on the structure of the aerodynamic model. In order to keep the necessary testing costs as low as possible, the twin seater was treated as a store increment to the single seater. The resulting increment in the dataset stems from the difference of two large numbers of the same magnitude, e.g. (c_m single - c_m twin), which each may be confined with measurement noise. The difference between these two large numbers is small but the measurement noise is still present and now, relatively, much larger. For this reason the twin-seater increment may only represent the measurement noise for certain areas of the envelope. Thus flight results follow better the single-seater predictions. For the identified „problem area" the twin-seater increment to the basic dataset was set to zero. This result was confirmed with existing windtunnel data.

The second example for the twin-seater is related to the known $c_{n\beta}$ discussion. Fig. 12 gives CASA DDT results for the twin-seater compared with the already corrected single-seater dataset plus twin-seater increment. The comparison reveals a rather good agreement between database and flight data, indicating that the corrections, discussed in the previous section, work in the right direction.

3.3 Time Histories

In this section some results of time history matching will be presented in order to illustrate the capabilities of the different methods. Time history matching is being used to check the plausibility of the identification results. For the classical methods this comparison is the basis for the cost function calculation.

At first a result from Alenia for a pilot performed lateral frequency sweep will be given. Fig. 13a shows the matching for the aircraft states as given before the identification run with the nominal data from the dataset. Fig. 13b then gives the corresponding comparisons after aileron effectiveness and damping derivatives have been identified. The model was made up in accordance with the example model given in Eq. 2. Comparing both figures a considerable increase in matching quality can be observed. This proves the validity of the identification result. It also shows that the given method is capable of dealing with complicated manoeuvres over such long time intervals.

Whereas the previous example may well fall under the category of a „small perturbation" manoeuvre the next example stems from a „large perturbation" manoeuvre. These types of manoeuvres are under consideration in order to test the reliability of the results obtained with the given methods. Fig. 14 gives the matching for a 360° roll manoeuvre, also from the Alenia method. For this case the matching for the initial „nominal dataset" simulation and the final „identified dataset" simulation are given in one figure in comparison to the measured flight data. Also here the identification process with the fully non-linear Alenia method significantly improves the comparison. Thus confirming the validity of the identification results. A similar result is given in Fig. 15 for the BAe regression analysis method. Also this method is capable of identifying large perturbation manoeuvres and leading to acceptable identification results.

The equation decoupling method, as used by CASA and DASA, is the method of those presented here which is most restricted to small perturbation manoeuvres. It is nevertheless also used when identifying large perturbation manoeuvres. A typical result is given in Fig. 16. It shows an almost perfect matching for a roll at a supersonic Mach number. These results illustrate that the presented method is well capable of treating large perturbation manoeuvres.
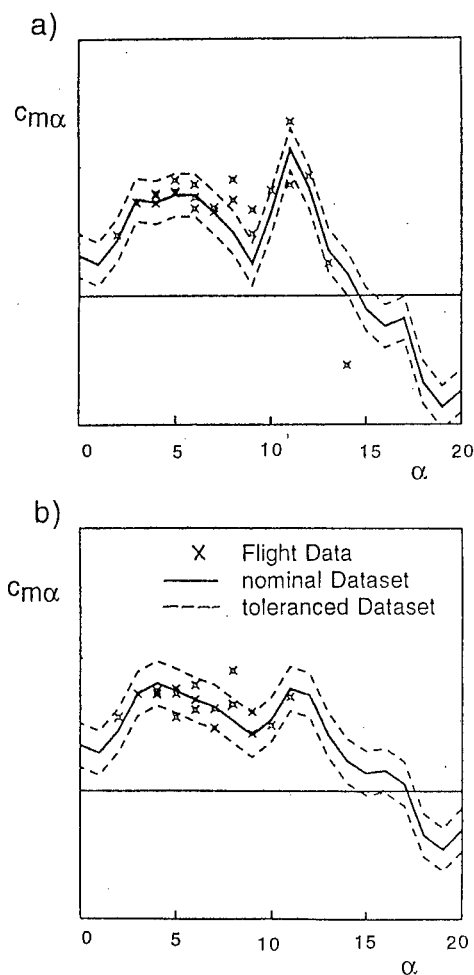
a)

b)

Fig. 11: Comparisons of Identified Longitudinal Stability Derivativ with a) Twin-Seater and b) Single-Seater Dataset Values (CASA's Dynamic Detrimming Method for DA6 Data)
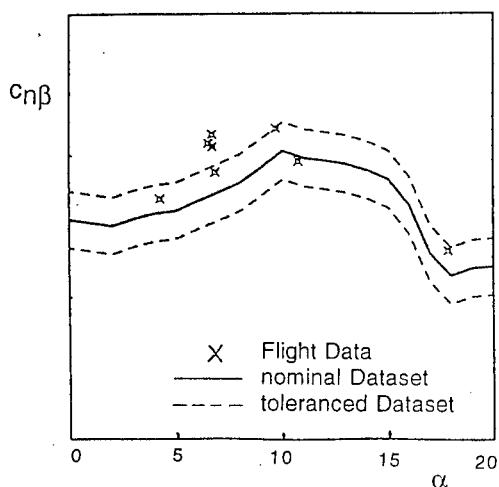

Fig. 12: Comparisons of Identified Weathercock Stability with updated Twin-Seater Dataset Values versus Angle of Attack (CASA's Dynamic Detrimming Method for DA6 Data)
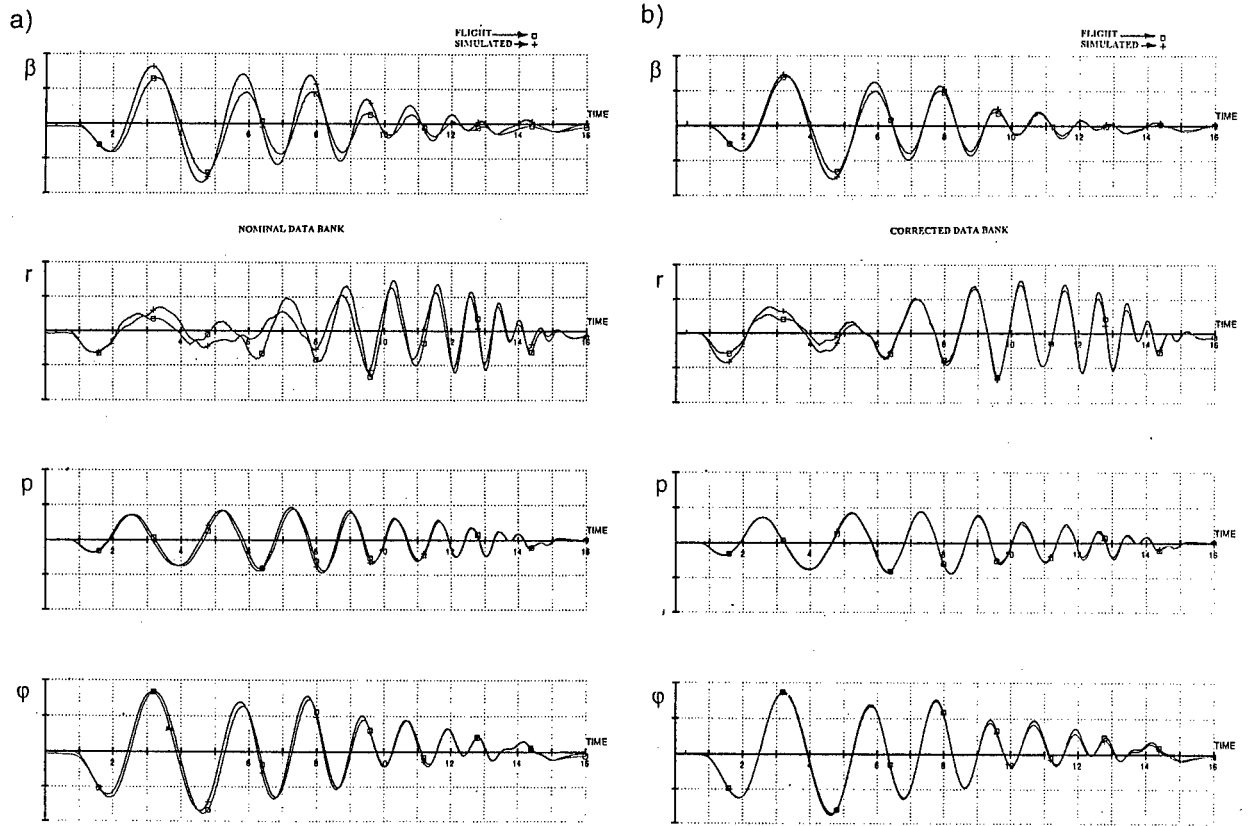
a)

b)

Fig. 13: Time History Matching for a Frequency Sweep with a) nominal and b) updated Dataset Values (Alenia's Output Error Method for DA3 Data)
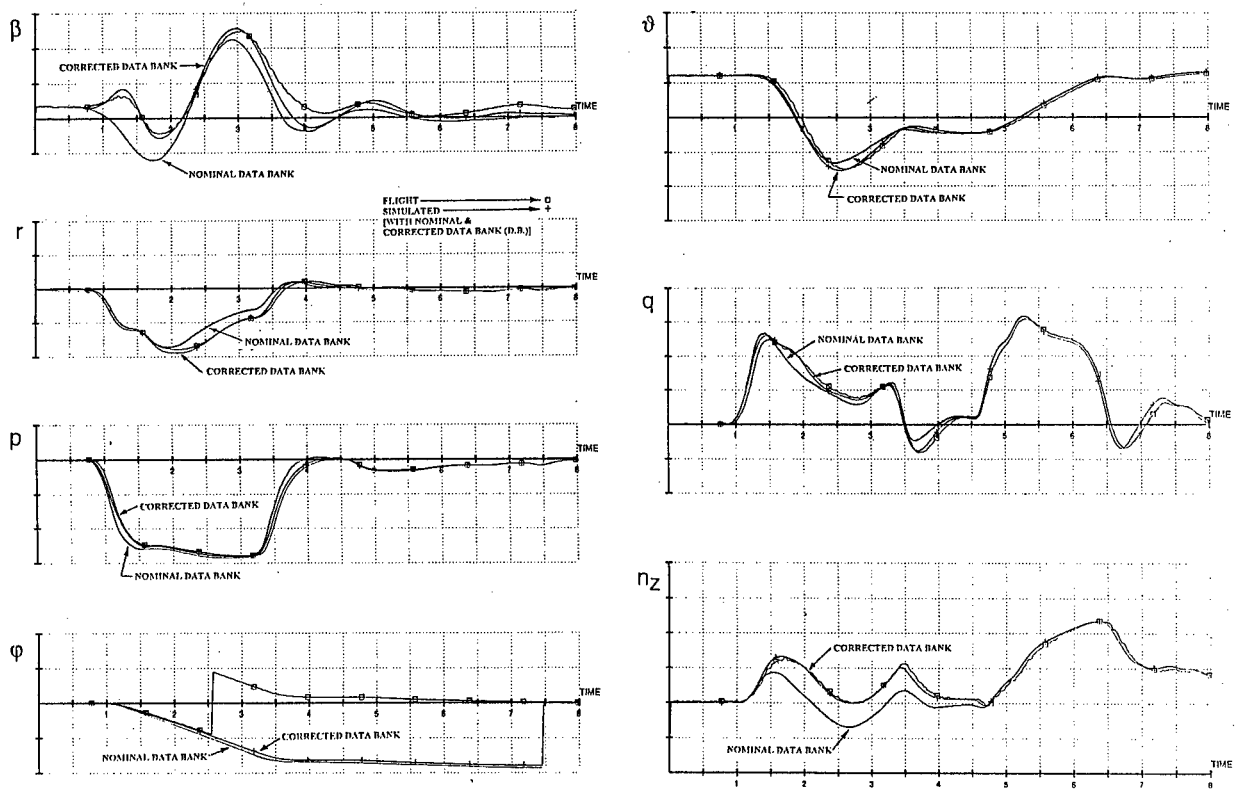

Fig. 14: Time History Matching for a 360° Roll versus nominal and updated Dataset Values (Alenia's Output Error Method for DA3 Data)
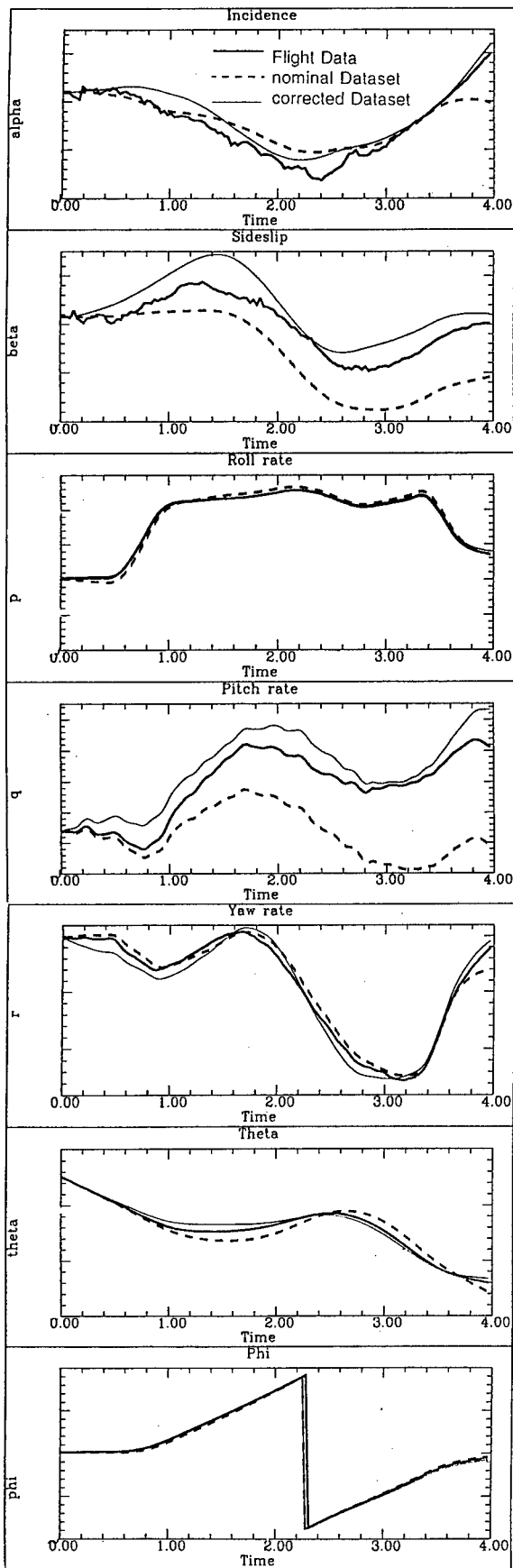
Fig. 15: Time History Matching for a 360° Roll versus nominal and updated Dataset Values (BAe's Equation Error Method for DA2 Data)
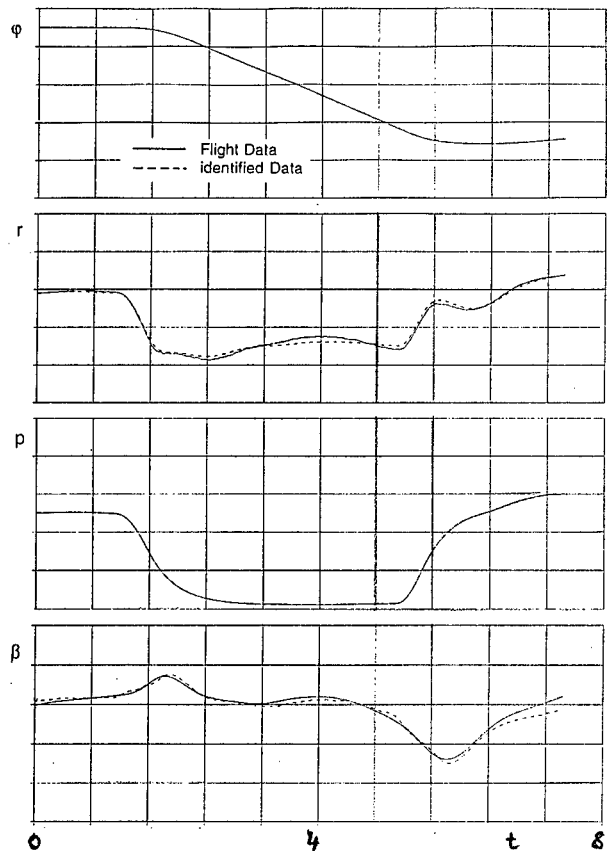

Fig. 16: Time History Matching for a 360° Roll versus updated Dataset Values (DASA's Equation Decoupling Method for DA1 Data)

3.4 Tolerances

During the envelope expansion process at each company a multitude of manoeuvres has been examined with the presented methods. Due to the generally very good quality of the dataset „surprises" seldom occur! Two cases where corrections to the dataset on the basis of flight data had been necessary have been documented above. The usual „daily" work is less thrilling than these two cases. It consists mainly of comparisons with respect to the tolerance band of the dataset. A typical example of this process is presented in Fig. 17 from DASA, giving results for $c_{m\alpha}$ obtained on DA5. Over a large band of Mach numbers the identified values for $c_{m\alpha}$ lie very close to the predictions, well within the 2σ tolerance band.

These rather „boring" results generally prove the excellent quality of the given dataset. They are very important for the development process, and they allow the overall tolerance level of the dataset to be reduced. This eases the clearance process of the flight mechanical clearance of the aircraft. If tolerances can be reduced successfully on the basis of flight data, the clearance can be performed also for a smaller tolerance band and possibly be improved through this method, thus clearing a larger portion of the flight envelope. This again documents how important parameter identification methods are in the development process of an aircraft.
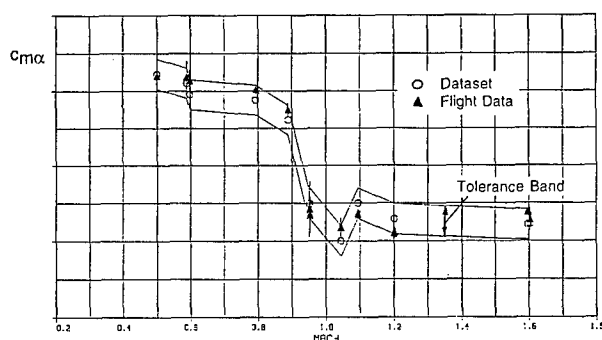
Fig. 17: Comparisons of Identified Longitudinal Stability with Dataset Values versus Mach Number (DASA's Equation Decoupling Method for DA5 Data)

4. Conclusions

EUROFIGHTER will be the new fighter aircraft for the airforces of Italy, United Kingdom, Spain and Germany in the next century. It is being developed jointly by industrial partners of these four nations. The aircraft is based on a very agile configuration, which incorporates a high level of inherent longitudinal instability. The characteristic feature is the canard, generating the inherent instability. Due to this fact the aircraft is controlled by a digital, full authority, quadruplex redundant flight control system (FCS). Within the development flight test program seven development aircraft are flying, flight test tasks have been split up between the four EUROFIGHTER partner companies (EPC's).

For flight test evaluation of the aerodynamic properties of this aircraft at four different partners confidence had to be established in results from different flight data analysis methods as well as in results from different development aircraft. All methods are based on well known theories, nevertheless these methods are tailored with some company specific extensions in order to cope with the non-linear characteristics of EUROFIGHTER. The Alenia method is based on an extension of the classical maximum likelihood estimation in conjunction with an output error description. The basic idea at ALN for repairing the defect of this method not to be able to cope with unstable aircraft is the inclusion of the full non-linear aircraft model with the actual controller into the method. In the original non-linear aerodynamic model additional terms with a linear structure are included, so the model can be updated via a maximum likelihood algorithm. The identified terms directly give the difference between full model and aircraft. The method at BAe is based on the classical equation error approach coupled with a regression analysis. The key feature of this regression algorithm is a principal components approach. This allows the user to define the model structure to be identified since it provides him with an indication of the information content within the flight data. The user iterates to the optimum solution by altering the model structure, selected model elements, the ranges of the supplied variables, and the weighting given to a priori data. At CASA a dynamic detrimming method is used which is also based on the equation error method together with a regression analysis. An observation vector, representing the equation error, is cor-

rected for zero controls. A dynamic compatibility check based on engineering know how is performed. Then the observation vector is modelled with the principal influences. These are identified with the regression analysis. The fourth method is being used at DASA and at CASA. It is based on the output error approach in conjunction with an equation decoupling technique providing this method with the capability of dealing with unstable aircraft.

Results are given for four principal examples. At first a problem of the aircraft's weathercock stability was discussed. Flight test analysis revealed a reduced weathercock stability in comparison with the dataset. These discrepancies could be confirmed with all methods on different aircraft. A solution to this problem was found in the structure of the dataset. In modelling the non-linearity as Δc_n some detail found in the wind tunnel data was lost. In flight, due to the nature of the controller, only smaller angles of sideslip could be reached compared to those used for the windtunnel measurements. Thus revealing a non-linear behaviour for small angles of sideslip. Successive corrections could be made to the dataset, curing this problem. The second example deals with the twin-seater. Here it was found that certain increments representing the twin-seater could not be verified in flight test. They were subsequently removed from the dataset. The third example deals with the time history matching which is an important tool to check the credibility of identified parameters. Examples for a frequency sweep and for several rolls are given. These examples document the capability of all methods to deal with large perturbation manoeuvres. Finally the fourth example documents the „dry" daily work dealing with tolerances. This way leads to an overall reduction of dataset tolerances which is intended to improve the overall dataset credibility as well as speed up the clearance process in order to arrive at an improved flight clearance.

It was shown how results obtained from different aircraft with different tools with different properties are being harmonised. It was then shown how one common single data base, that is the aerodynamic stability and control data set, is being validated and how it is updated.

5. References

[1] E. Plaetschke: Identifizierung instabiler flugmechanischer Systeme mit einem Ausgangsfehlerverfahren, Zeitschrift für Flugwissenschaften und Weltraumforschung 12 (1988), 166 -177.

[2] H. Preissler, H. Schäufele: Equation Decoupling - A new Approach to the Aerodynamic Identification of Unstable Aircraft, J. o. Aircraft 28 (1991), 146 -150.

[3] L.C. Anderson: Robust Parameter Identification for Non-linear Systems using a Principal Components Regression Algorithm, AIAA Paper 85 - 1766.

[4] H. Schäufele: Parameteridentifikation mit einem modifizierten Maximum-Likelihood-Verfahren, Fortschrittberichte der VDI Zeitschriften, Reihe 8 Nr. 40, 1981.

A Process for Model Identification and Validation of Dynamical Equations for a Flexible Transport Aircraft

Kioumars Najmabadi, Bruce Fritchman and Chuong Tran
The Boeing Company
P.O. Box 3707, Seattle, WA 98124, USA

Abstract

This paper introduces a process for identification and validation of a single-input/multi-output model for a flexible aircraft based on in-flight control-surface frequency sweeps. This model is used to develop a compensator for active control of aircraft structural modes. The output of the system contains parameters used in the controller design cost function and those used as the feedback signals modified to include appropriate system time delays. The identification method parameterizes the system as a partial fraction expansion and solves a weighted, non-linear least square problem to determine the numerator and denominator coefficients. The initial values of the denominator coefficients are determined based on the higher order aeroelastic model. Once the initial values for the denominator coefficients are known, the initial values for the numerator terms are obtained by the linear least square technique.

Two approaches are employed to prove the fidelity of the model for control law design. The first method uses the output signals of the model to provide a closed-loop description of the system for which an in-flight response characteristics exists. Comparison of the in-flight response characteristics with those of the model provides the confidence for the fidelity of the identified model. The second approach utilizes a newly developed compensator and compares the frequency response characteristics of the closed-loop system based on the in-flight sweep data and those based on the model. The closeness between the two frequency responses is treated as a measure of the fidelity of the model. An example of this process for identification and validation of a model for the lateral motion of a commercial transport aircraft is presented.

1.0 Introduction

Active control of an aircraft's flexible modes may play a significant role in providing flutter stability margins, reducing dynamic loads on structure and providing better ride quality for passengers and pilots. To design control systems for the above applications, an aircraft model with high fidelity at both low (rigid body) and high frequency (structural modes of interest) is required. This model should include:

1) Dynamics of rigid body modes,
2) Dynamics of aircraft's structural modes,
3) Accurate representation of rigid body and flexible modes coupling,
4) Dynamics of sensors and actuators,
5) Dynamics of control surface and actuator coupling,
6) System transport and computational delays,
7) Effects of non-linearities.

One method to obtain such a high fidelity model is to conduct a control surface frequency sweep in flight and compute the gain and phase relationships between the control surface and the selected output signals. This frequency representation can be employed in design of the controller for a given objective. However, the design of such a controller may only be supported by frequency based design techniques. To use the modern control techniques (e.g., LQR/LQG) a time domain model is required. The objective of this paper is twofold:

1) To present a method to generate a high fidelity time domain model, and

2) To provide a validation process to ensure that the required level of fidelity is met.

2.0 Description of an Example

The example selected here to facilitate the discussion deals with the control of lateral motion of a large flexible aircraft. Figure 1. presents a simplified diagram of the system of interest. This system consists of the airplane actuators, sensors at various stations, yaw damper and modal suppression control laws. The sensor signals are transported via digital data buses. The transport and the computational time delays are also shown. The analog to digital (A/D) converters and their associated sample and hold delays are not shown to keep the diagram simple. However, their effects are included in the estimate of time delays. FFG denotes the Frequency Function Generator input which provides the input during the surface frequency sweep.

The yaw damper control law's objective is to provide sufficient damping for the Dutch roll mode having a typical frequency between 1 to 2 rad/sec. The quasi-steady aeroelastic model is appropriate for use in this design as long as sufficient attenuation to limit the activity of the control law in the structural modes frequency range is provided.

The modal suppression control law's objective is to improve the ride quality in turbulence by reducing the lateral acceleration due to excitation of the structural modes at specified locations without increasing lateral acceleration at other locations. The increase in any other location's lateral acceleration may be a concern because of ride quality deterioration and/or dynamic loads increase. Furthermore, this control law is expected to have no appreciable effect over the rigid body dynamic response.

To meet the modal suppression control law's requirements, a high fidelity model that includes dynamic characteristics of the Dutch roll mode, structural modes, system's non-linearities and accurate knowledge of the system delays is required.

2.1 Time Domain Model Option

To generate the time domain model for use in modal suppression, two options are available:

1) Develop the time domain model for the open-loop aircraft and integrate it with the control law (i.e., yaw damper) and the appropriate time delays to form the closed-loop model,

2) Use the closed-loop surface-frequency sweep data to generate the time domain model for the closed-loop system.

The second approach is selected in our example, because it does not require the extra step of integrating the open-loop aircraft and the control law models to form the closed-loop model. However, for other applications where the inner-loop control law, in this example the yaw damper, is to be changed, the first method would be more appropriate.

3.0 Identification of the Modal Aeroelastic Model

This section presents a method employed to identify the time domain model based on the in-flight control-surface frequency sweep data.

3.1 Air Transport Modal Identification Problem

To use modern control techniques in the design process of a controller which provides additional damping to structural modes, the identification of modal aeroelastic models from in-flight data is necessary. This may require identification of the first ten to fifteen bending modes of the aircraft in either the lateral or longitudinal axes. In this context, identification of fundamental structural parameters of an aeroelastic model, e.g. inertia, stiffness, damping, etc., is not required. However, the identified modal model must be consistent with the corresponding modal form of the fundamental aeroelastic models so that the

designed controller reflects minimal conflict with models used for aircraft certification by Dynamic Loads and Flutter organizations. Eigenvalues for a such a typical model are shown in Figure 2.

3.1.1 Sensor Locations

Bending modes of a large transport aircraft involve simultaneous and complex combined motion of all parts of the airframe, e.g. wings, empennage, fuselage, engine nacelles, etc. Accurate identification of the various flexible modes of an aircraft therefore requires appropriate sensor placement to measure these complex motions. Our experience has shown that a set of several appropriately located sensor measurements is adequate to identify the desired ten to fifteen first flexible modes of a transport aircraft. For example, for a typical lateral axis model of a large air transport, using these sensor locations, the first twelve bending modes can be identified exactly. Figure 3 depicts frequency response functions between the rudder to accelerations at the seven sensor locations. When system identification is performed, as shown in Figure 4, the first twelve flexible modes can be almost exactly identified from these data. A comparison of typical frequency response functions for the actual model and the realized model are shown in Figure 5.

3.1.2 In-Flight Test Data

In-flight data for large commercial transports are gathered through excitation of the various control surfaces with sinusoidal sweeps of the controller in the frequency range of interest. This data is subsequently transformed into sets of frequency response functions (FRF) via the Fast Fourier Transform. The coherence function

$$\gamma_{xy}^2(\omega) = \frac{|\Phi_{xy}(\omega)|^2}{\Phi_{xx}(\omega)\Phi_{yy}(\omega)}$$

where $\Phi_{xx}(\omega)$, $\Phi_{yy}(\omega)$ and $\Phi_{xy}(\omega)$ are the FRF input and output power spectra and cross spectra respectively, is also computed for each

FRF. The coherence function provides a measure of the "goodness" or quality of the data. A coherence of 1.0 reflects high linearity and a high signal-to-noise ratio whereas low coherence may reflect non-linearities or more commonly a low signal-to-noise ratio. Figure 6 presents typical FRF's between the rudder control surface and lateral acceleration at various locations in a cruise condition. The corresponding coherences are shown in Figure 7. It is typical that at a given location, low coherences for FRF's over a frequency range are found if the rudder is not adequately exciting any mode, sensor is located on a modal node or modes are excited by a disturbance in that frequency band.

3.2 Modal Aeroelastic Identification Method

System identification results in an optimization problem of finding the parameters of a linear system that best fit the measured data. For a structural or aeroelastic model, the order of the identified system is proportional to the number of flexible modes that must be identified. For fifteen flexible modes, the order of the system will be thirty or more. The minimum number of parameters or minimal parametric representation of the system is the standard real-modal form where the system matrix A and the input matrix B are of the form

$$A = \begin{bmatrix} \begin{bmatrix} 0 & \omega_1^2 \\ 1 & 2\zeta_1\omega_1 \end{bmatrix} & 0 & 0 & 0 & 0 & 0 & 0 \\ 0 & \begin{bmatrix} 0 & \omega_2^2 \\ 1 & 2\zeta_2\omega_2 \end{bmatrix} & 0 & 0 & 0 & 0 & 0 \\ 0 & 0 & \dots & 0 & 0 & 0 & 0 \\ 0 & 0 & 0 & \dots & 0 & 0 & 0 \\ 0 & 0 & 0 & 0 & \dots & 0 & 0 \\ 0 & 0 & 0 & 0 & 0 & \dots & 0 \\ 0 & 0 & 0 & 0 & 0 & 0 & \begin{bmatrix} 0 & \omega_n^2 \\ 1 & 2\zeta_n\omega_n \end{bmatrix} \end{bmatrix}, B = \begin{bmatrix} \begin{bmatrix} 1 \\ 0 \end{bmatrix} \\ \begin{bmatrix} 1 \\ 0 \end{bmatrix} \\ \dots \\ \dots \\ \dots \\ \dots \\ \begin{bmatrix} 1 \\ 0 \end{bmatrix} \end{bmatrix}$$

To obtain this real-modal form we start with the partial-fraction parameterization of the FRF's given by Spanos and Mingori [1] and perform

the nonlinear least squares minimization of the
the cost function

$$J(x) = \sum_{i=1}^{P} w_i |G(j\omega_i) - \hat{G}(j\omega_i, x)|^2$$

where $G(j\omega)$ is the measured complex FRF

data, $\hat{G}(j\omega)$ is the identified model response
and w_i is a frequency-dependent weighting on
the error. We typically choose the weighting
function to w_i defined as

$$w_i = \gamma(\omega_i) \frac{|G(j\omega_i) - \hat{G}(j\omega_i)|}{|G(j\omega_i)|^2}$$

This choice of weighting function serves three
purposes. Obviously, using the coherence
function deemphasizes the poor data with
respect to good data. Secondly, using the error
as a weight drives the optimization harder in the
direction of the error. Thirdly, normalizing by
the square of the norm of the FRF's provides for
a relative weighting on the error in order to fit
data that may range in amplitude over many
orders of magnitude.

The parameterization which is a partial-fraction
expansion is chosen so that

$$\hat{G}(j\omega, x) = \sum_{k=1}^{m} \frac{a_k + j\omega b_k}{\alpha_k^2 + j\omega \beta_k^2 - \omega^2} + d$$

for even-order systems, or

$$\hat{G}(j\omega, x) = \sum_{k=1}^{m} \frac{a_k + j\omega b_k}{\alpha_k^2 + j\omega \beta_k^2 - \omega^2} + \frac{a_{m+1}}{\alpha_{m+1}^2 + j\omega} + d$$

for odd-order systems, where x is defined as

$$x = [a\, b\, \alpha\, \beta\, d]$$

Once the denominator parameters α and β are
determined, finding the initial numerator
parameters that minimize the cost function
$J(x)$ becomes a linear least-squares problem
that can be solved in one iteration. From this
initial point, numerator and denominators are
solved simultaneously using quasi-Newton
iteration. Once the partial-fraction expansion of
the system is determined it is converted to real
modal form. Thus, a typical identification of a

30th-order system with a single input and seven
measurements results in an optimization
problem of about 250 parameters. This method
is available for single-input/multi-output use as
one of the tools for the control system design
and analysis bundled with the EASY5 Matrix
Algebra Tool [2]. A new tool based on this
approach has recently been developed to handle
mult-input/multi-output systems.

3.3 Example Aeroelastic Model Identification

In this section we present a typical example of
this aeroelastic system identification method
applied to in-flight test data shown in Figures 6
and 7, taken from a large transport aircraft. In
this example we fit a system to four FRF's
between rudder input and lateral acceleration
measurements from four location denoted by S1,
S2, S3 and S4. We start our fit with an initial
set of eigenvalues obtained from an aeroelastic
model similar to the flight and aircraft loading
conditions of the test. These eigenvalues
correspond to the Dutch roll rigid-body mode,
the first fifteen flexible modes and a second
order aerodynamic lag mode and they span the
frequency range from 0.0 to 10 Hz. Figures 8
through 11 show comparisons of the identified
system response with the measured data. Thus
the identified aeroelastic model is a 34th-order
model containing the Dutch roll mode, fifteen
flexible modes and a second order aerodynamic
lag mode which fits the data well through the
range of 10.0 Hz.

4.0 Model Validation Process

In this section, validation of the time domain
model will be discussed and application of this
process will be illustrated. There are three parts
in the validation process:

1) Validation of the phase and gain relationships
obtained from the in-flight control sweep data,

2) Validation of the time domain model,

3) Verification of the system transport and
computational time delays.

4.1 Validation of the Computed Phase and Gain Relationships

To validate the phase and gain relationships obtained from the flight test data and to verify the estimate for the system transport and computational delay, the following steps are taken:

1) Integrate the open-loop airplane transfer function ,G1(s), with a known control augmentation, H1(s), and appropriate system delay, D1(s), to form the analytical phase and gain relationship for the closed-loop system denoted by G2(s) where

G2(s)= G1(s) / (1+G1(s)*H1(s)* D1(s))

2) Compare the phase and gain relationships of the G2(s) with those obtained from the in-flight sweep data referred to as G3(s). Having a close match between the phase and gain characteristics of G2(s) and G3(s) is a measure for the validation of phase & gain relationships developed from the in-flight sweep data and for the verification of the system computational and transport delays.

In our example, G1(s) is the aircraft's open-loop transfer function matrix, H1(s) is the yaw damper control law transfer function matrix, D1(s) is transfer function matrix for the system's delays and G3(s) is the phase and gain relationships obtained based on the in-flight sweeps conducted with the yaw damper feedback loop closed.

The above steps of the process are required before the identification technique is used to generate the time domain model.

4.2 Validation of the Time Domain Model

The validation of the time domain model is performed by utilizing the following approaches:

1) Compare the open-loop frequency response characteristics (phase and gain) of the time domain model with those obtained based on in-flight sweep data and require a close match between the two representations over the frequency range of interest,

2) Compare the closed-loop frequency response characteristics of the time domain model and those obtained using the in-flight sweep data and require a close match between the two representations over the frequency range of interest. The frequency response characteristics include the transfer function matrix, loop gain and phase or the Nyquist plot.

In our example, validation of a time domain model for use in the design of a modal suppression controller is considered. The system identification method is applied to provide a model over the frequency range of 1 to 6 Hz. The PSD plots of acceleration and the phase relationship between the rudder and acceleration at four stations are presented in Figures 12. The identified model matches the flight test data very closely over the frequency range of interest.

A controller to reduce the acceleration level at station S3 is designed and integrated with the model and the flight test data to provide the closed loop response of the system. Figure 13 presents the comparison for the closed-loop system. The PSD plots are selected because they are usually used to show the performance of the control law. A comparison of the loop gain based on the model and the flight test data is presented in figure 14. Based on these comparisons, the fidelity of the model over the frequency of range of interest and estimation of the system's time delays are validated.

Figure 15 presents the performance of the controller by comparing the acceleration levels at S1 and S3 locations for the open-loop and closed-loop systems.

In a second example, a controller is developed to further reduce the acceleration at the S1 location. This controller includes feedback from additional sensors. Figure 16 presents the performance of the controller based on the flight test data. This controller destabilizes two modes at 6.5 and 7 Hz . This is shown in the acceleration plot for the S4 station. Figure 17 depicts the loop gain comparison based on the model and the flight test data. As shown the loop gain in the frequency range of 6 to 8 Hz is significantly higher when flight test data is used. Obviously, the additional feedback paths increases the loop gain significantly over the frequency range in which the model is not valid.

5.0 A Brief Description of the Control Design Method

The control law design method employs LQR/LQG technique. The cost function consists of acceleration at different stations with appropriate weighting and frequency weighted input to provide the desired roll-off characteristics in both low and high frequency bands. The desired performance using full-state feedback is established by adjusting the weighting of terms in the cost function. Then, an observer is designed to recover the full-state feedback loop gain using the available sensor outputs.

For the first controller discussed in section 4.2, comparison of the performance of the control laws using full-state feedback and output feedback are shown in figure 18. As seen, the full-state feedback performance is mostly recovered using the available output feedback.

6.0 Conclusion

A systematic process to generate and validate a time domain model based on in-flight frequency response characteristics has been introduced. An application of this method to design a modal suppression controller to improve the ride quality has been illustrated. This approach has been successfully employed in the design of a modal suppression system for the Boeing family of airplanes which served as the final validation of the process.

References

[1] Spanos, J.T., and Mingori, D.L., "Newton Algorithm for Fitting Transfer Functions to Frequency Response Measurements," Journal of Guidance, Control and Dynamics, Vol. 16, No. 1, Jan-Feb 1993

[2] Miller, S.A., Tollefson, J.C., and Ummel, B.R., EASY5 Matrix Algebra Tool User's Guide, The Boeing Co., March, 1995
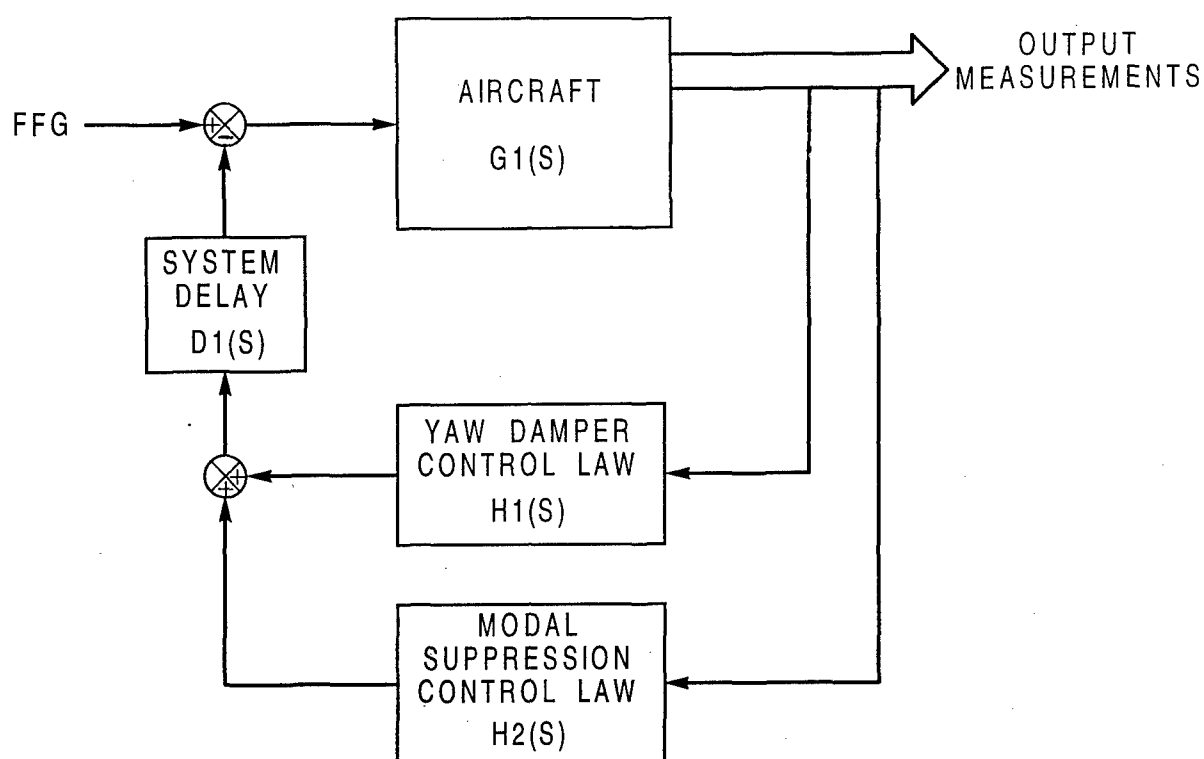
Figure 1.   Simplified Diagram of the Closed-Loop System
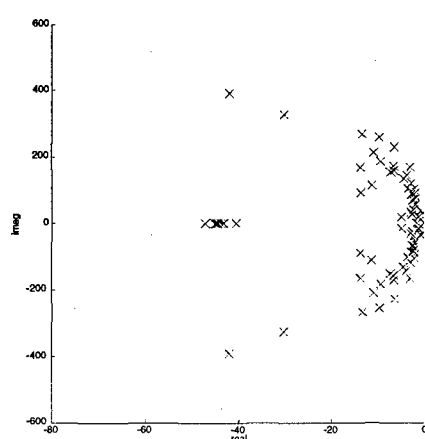
Figure 2. Typical Eigenvalues
of an Aeroelastic Airtransport Model
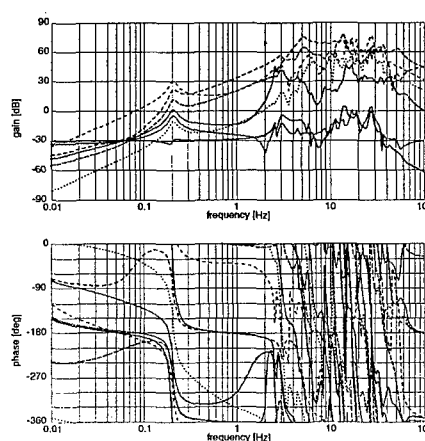
Figure 3. Typical Aeroelastic model FRFs
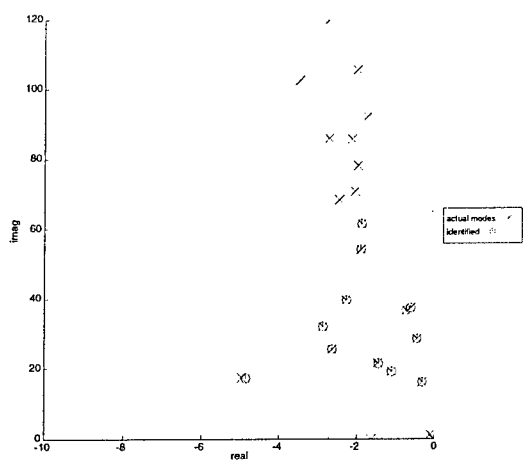for Rudder to Lateral Acceleration
at Various Stations

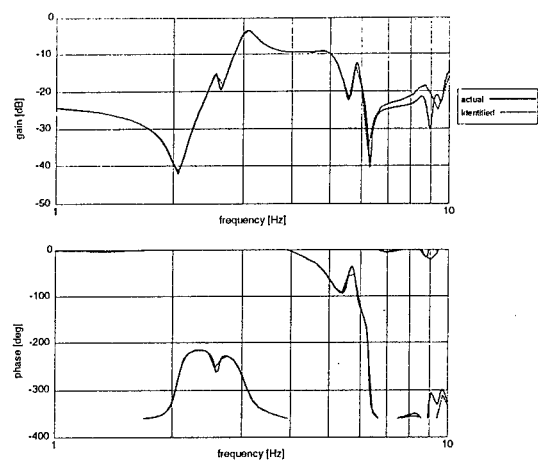Figure 4. Comparison of the Identified Modes
and Aeroelastic Model's Modes

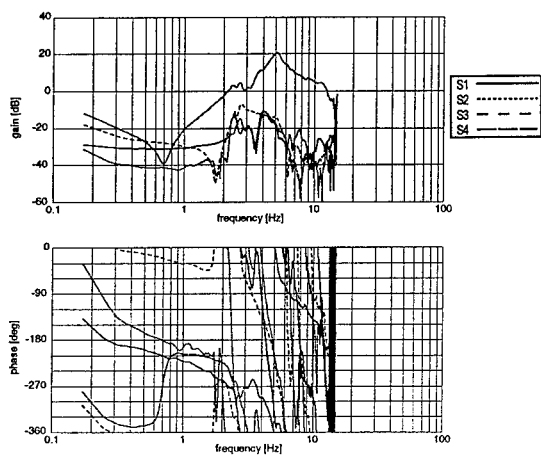Figure 5. Comparison of a Typical
Frequency Response Function

Figure 6. Typical Flight Test FRFs
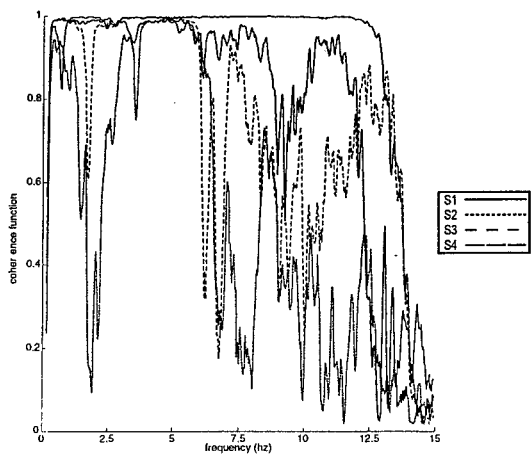for Rudder to Lateral Acceleration
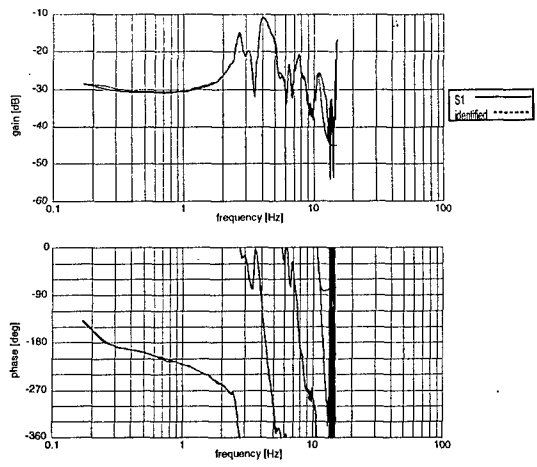at Four Stations

Figure 7. Typical Coherence
Functions for Flight Test FRFs

Figure 8. Comparison of the FRFs
for the Rudder to Lateral Acceleration
at Location S1
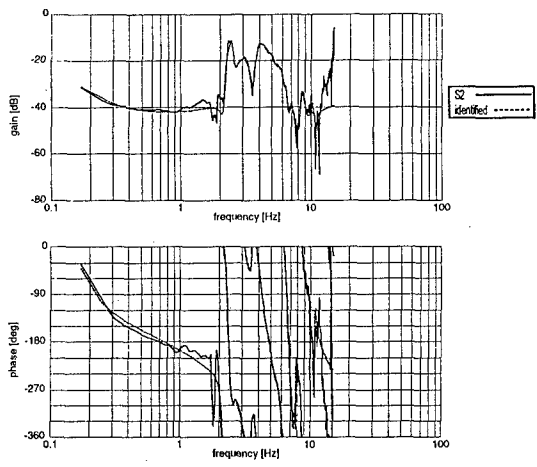
Figure 9. Comparison of the FRFs
for the Rudder to Lateral Acceleration
at Location S2
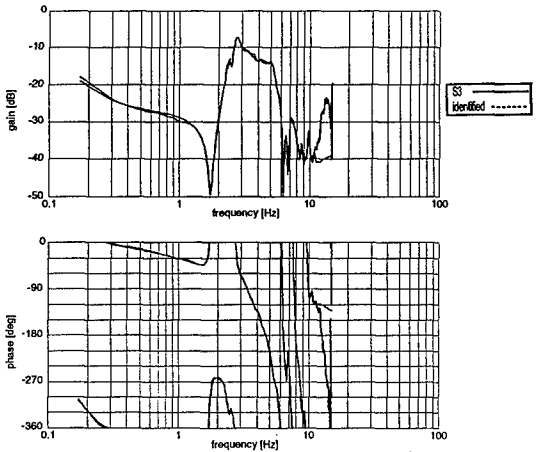
Figure 10. Comparison of the FRFs
for the Rudder to Lateral Acceleration
at Location S3
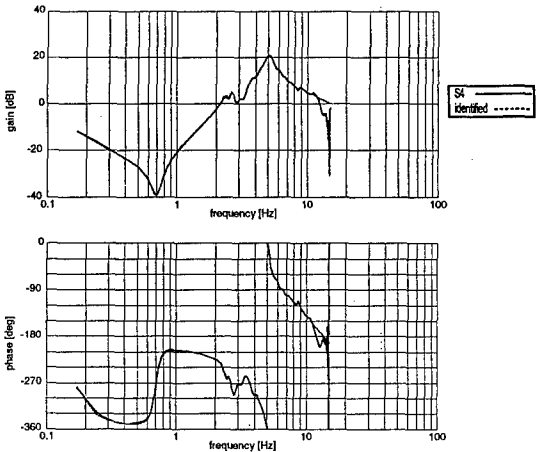
Figure 11. Comparison of the FRFs
for the Rudder to Lateral Acceleration
at Location S4
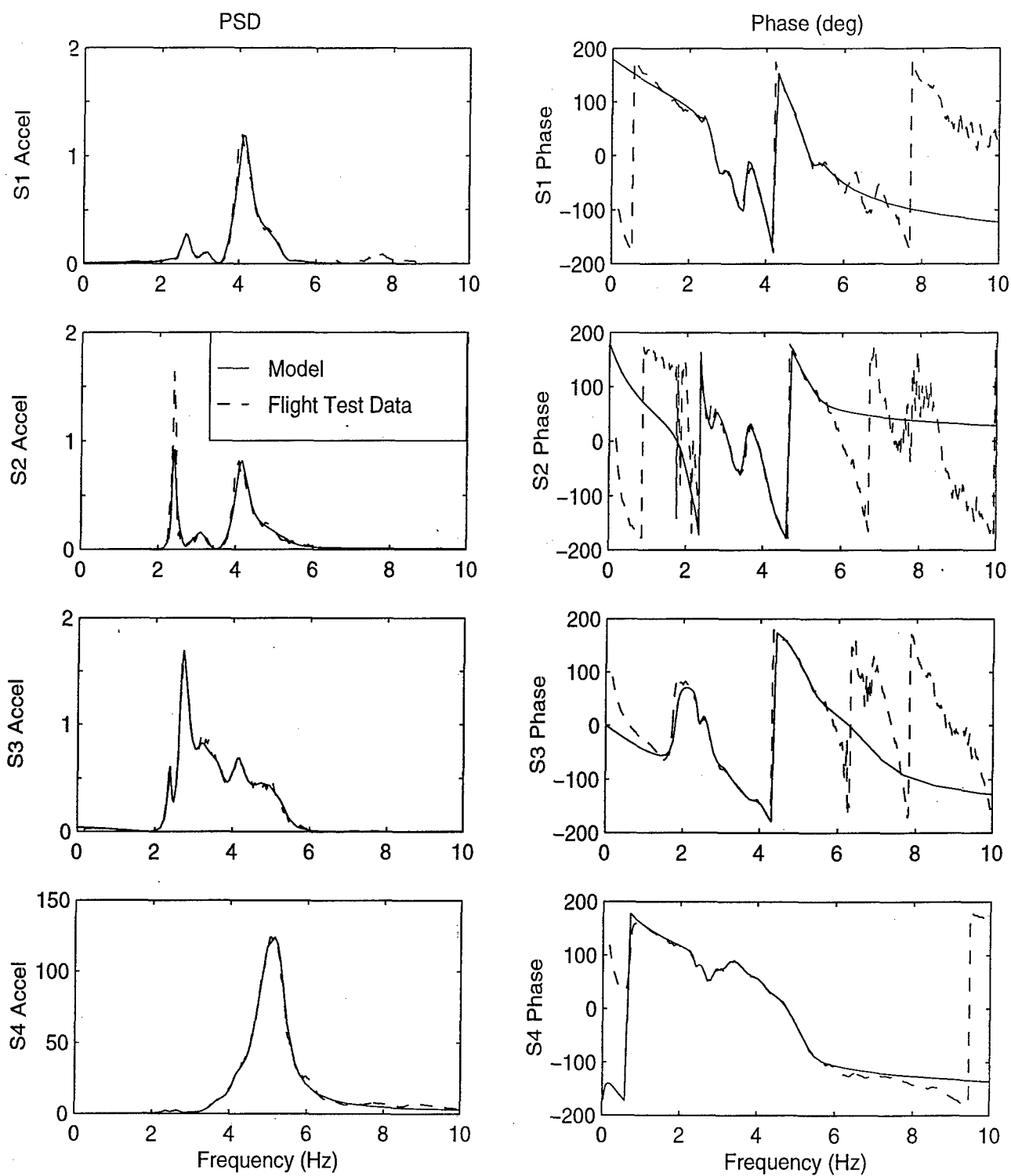
Figure 12. Comparison of the Identified Model and the Flight Test Data
(PSD values are not actual)
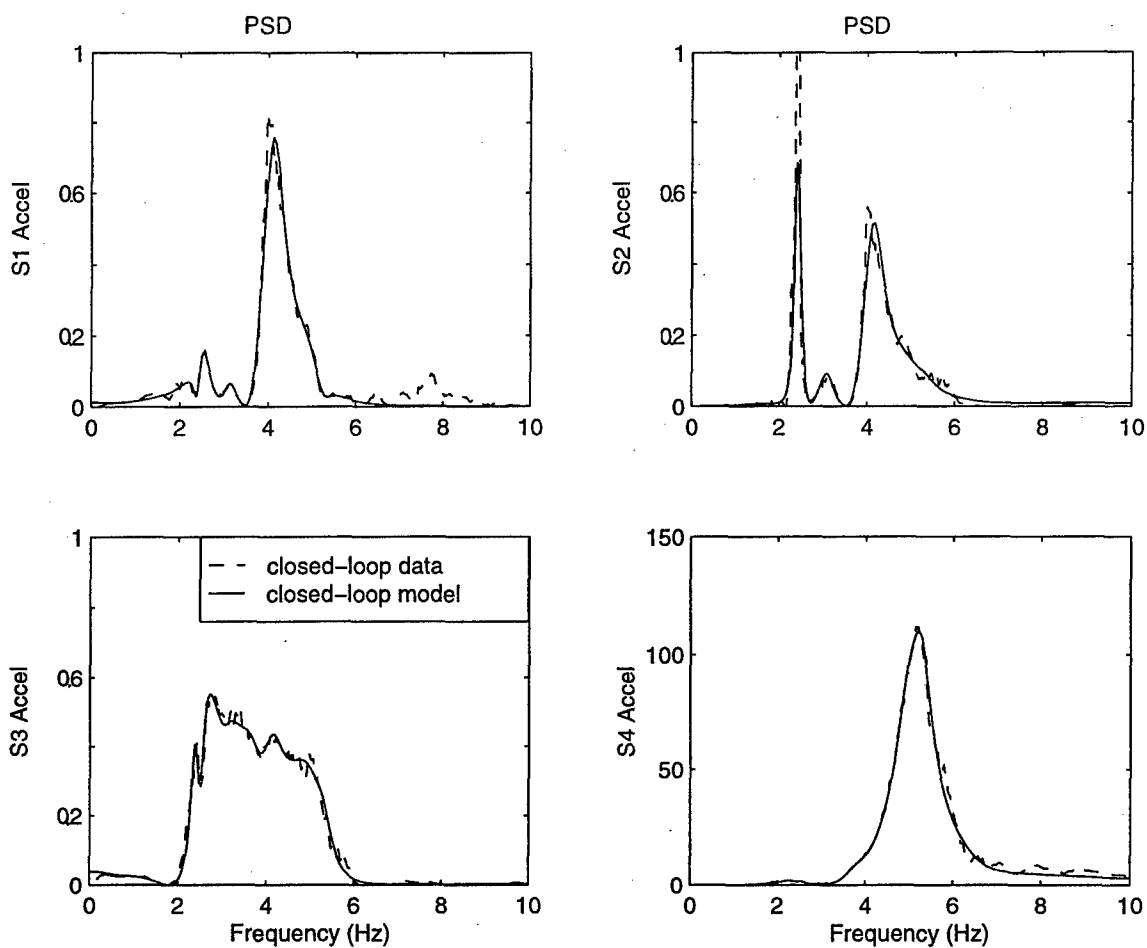
Figure 13. Comparison of the Closed-loop Response based on the Identified Model and the Flight Test Data   (PSD values are not actual)
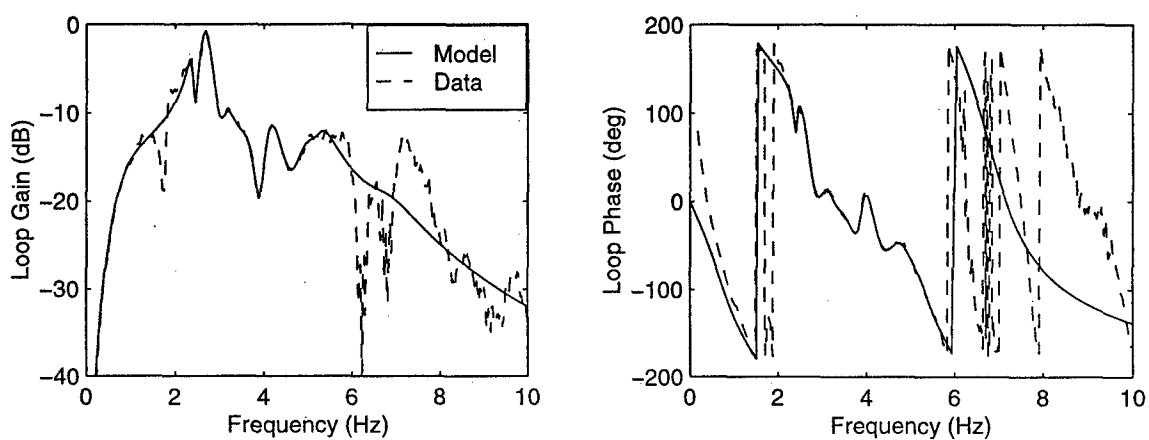
Figure 14. Comparison of the Loop Phase and Gain Characteristics (PSD values are not actual)
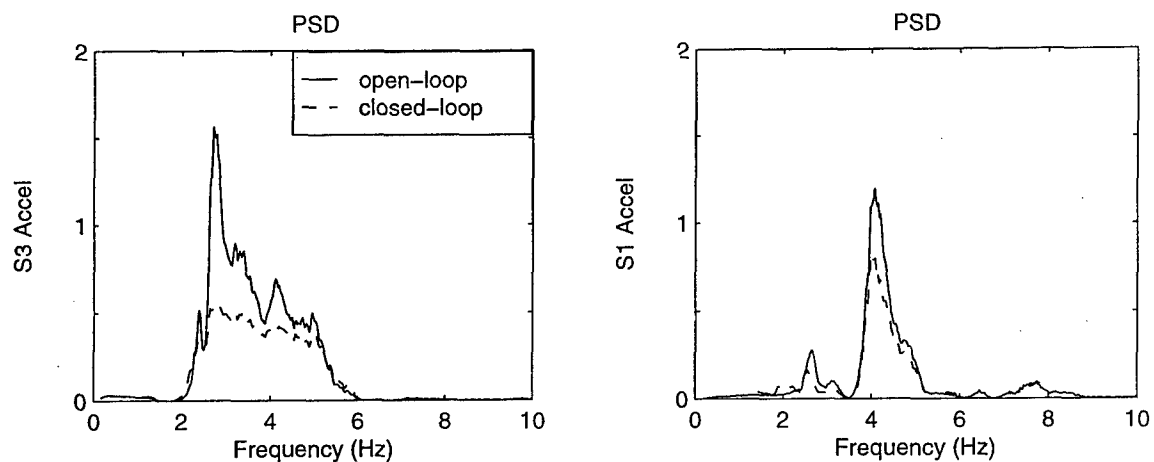
Figure 15. Comparison of the Lateral Acceleration Levels For the Open-Loop and Close-loop systems at S1 and S3 Locations   (PSD values are not actual)
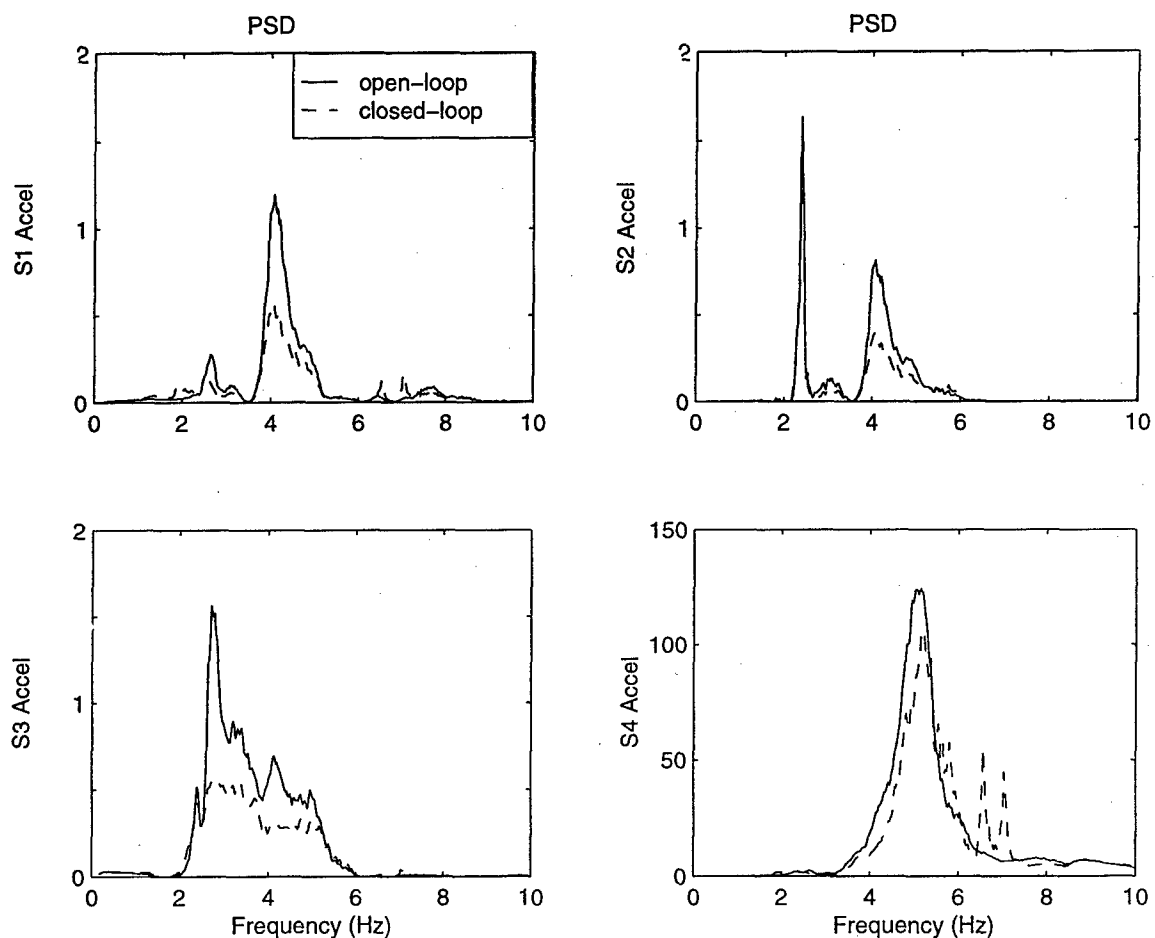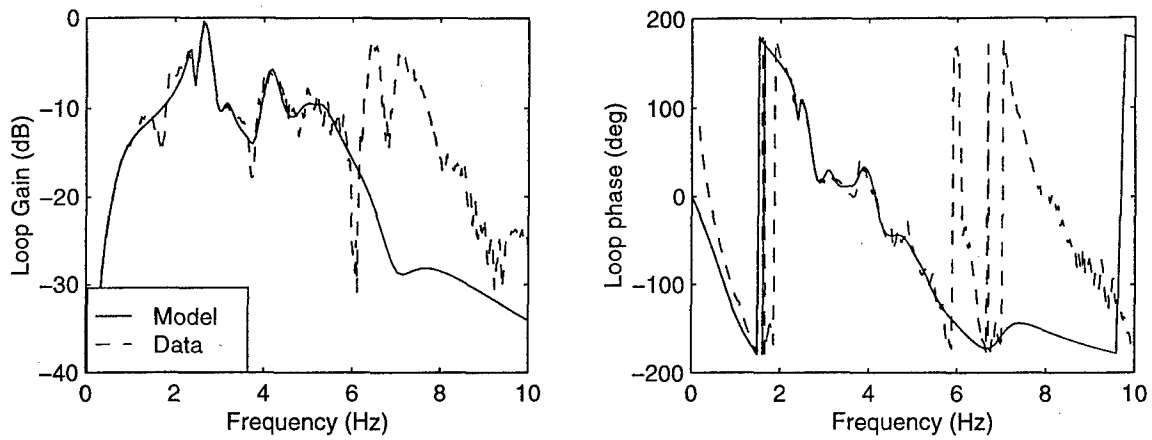

Figure 16. Comparison of the Acceleration Levels for the Closed- loop and Open-loop Systems at Various Stations   (PSD values are not actual)

Figure 17. Comparson of the Loop Gain and Phase Characteristics   (PSD values are not actual)
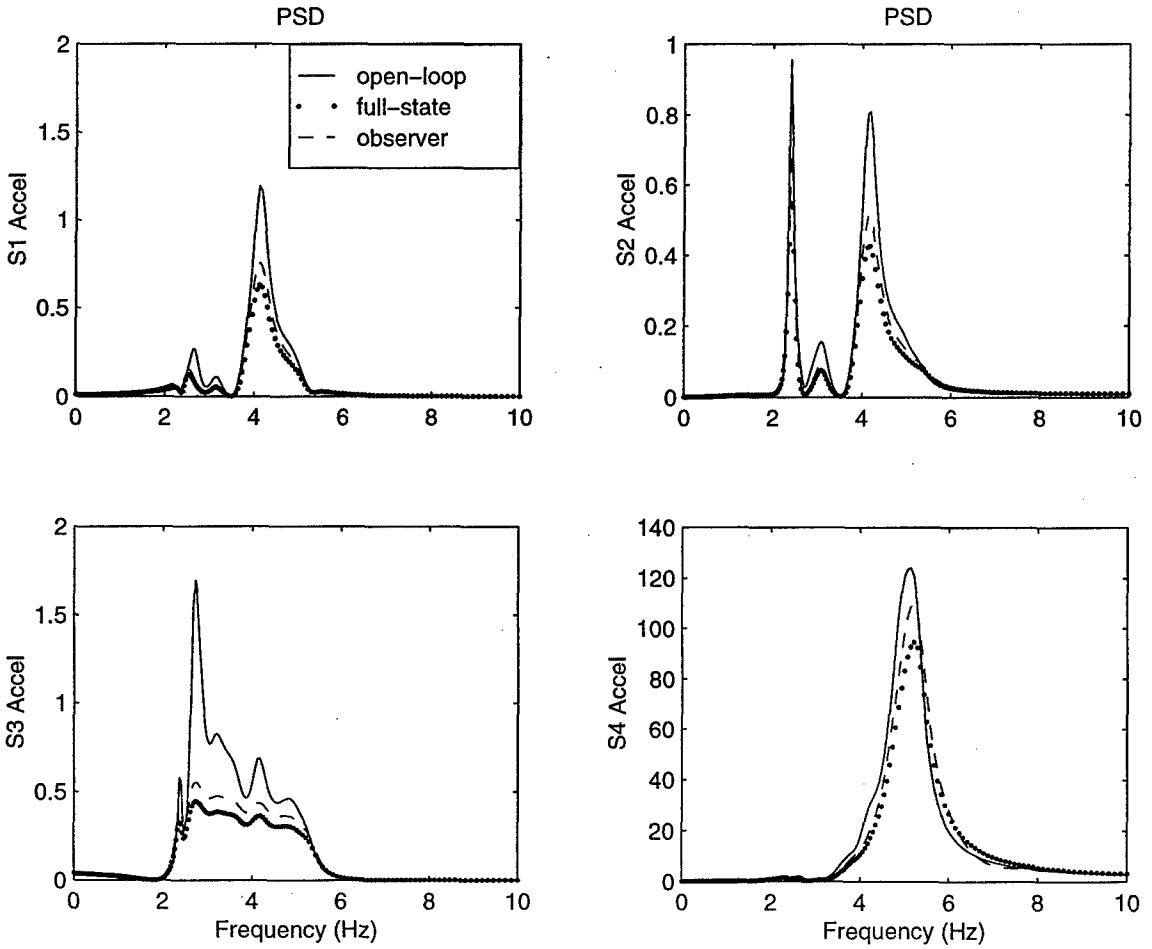

Figure 18. Comparison of the Acceleration levels with Full-state and output Feedback
(PSD values are not actual)

DATA BASE DEVELOPMENT FOR LEVEL D SIMULATORS - LESSONS LEARNED

W. Mönnich and R. V. Jategaonkar
Institut für Flugmechanik
DLR - Deutsches Zentrum für Luft- und Raumfahrt
Lilienthalplatz 7, D-38108 Braunschweig
Germany
Email: wulf.moennich@dlr.de, jategaonkar@dlr.de

1. SUMMARY

In the recent past aerodynamic data bases meeting the stringent accuracy requirements of Level D flight simulators have been generated at the DLR Institute of Flight Mechanics for two propeller aircraft, namely the C-160 military transport aircraft and the Dornier 328 commercial passenger transport aircraft. In the case of Dornier 328 having reversible flight controls, in addition to the rigid body aerodynamics, it was required to generate the hinge moment data base. Furthermore, it was also necessary to demonstrate the end-to-end match resulting from an integrated model with pilot's force inputs (i.e. 6-DOF equations of aircraft motion incorporating the identified aerodynamic data base coupled with the dynamic models of the flight control systems driven through pilot applied forces and incorporating the identified hinge moments data base). In contrast to the usual approach of demonstrating the adequacy based on a model driven through control surface inputs adopted in the case of C-160, the force driven models of the Dornier 328 turned out to be significantly more complex. This paper highlights the approach adopted for generating the data bases, the difficulties encountered in the data generation, and the lessons learned therefrom.

2. BACKGROUND

In the recent past the DLR Institute of Flight Mechanics has been contracted to develop mathematical aircraft models for application in Level D simulators in two cases

1. C-160 military transport aircraft and
2. Dornier 328 commercial passenger transport aircraft.

2.1 Level D Simulator

The definition of a Level D simulator that had to be applied by DLR in both the cases is found in the Advisory Circular AC 120-40B[1] of the Federal Aviation Administration (FAA). This document defines four simulator levels, i.e. A, B, C, and D, where D is the highest fidelity level. The quality requirements for the mathematical aircraft models to be developed by DLR are mainly found in Appendix 2, "SIMULATOR VALIDATION TESTS". Therein 53 validation test types are defined for which the quality of the mathematical aircraft model has to be proven against actual flight test data by comparing the simulated response with the measured response (proof-of-match or POM simulations). The errors for the main parameters have to be within specified tolerance limits. The minimum number of maneuvers to be flown and proven is about 120, since some of the validation test types require more than one maneuver.

2.2 The C-160 Project

In the early nineties the German military procurement organization decided to procure a modern flight simulator for the C-160 "Transall" aircraft, Fig. 1, Table 1, to replace the old simulator at Wunstorf airbase.
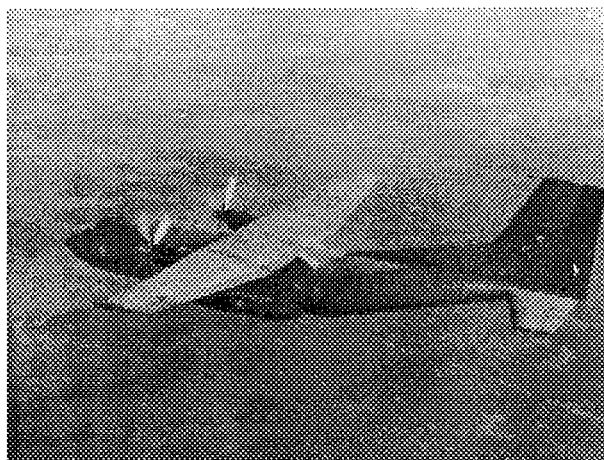

Figure 1. C-160

Table 1. Geometry and mass data

	C-160	Dornier 328
Max. take-off weight	51,000 kg	13,990 kg
Wing span	40 m	21 m
Max. speed	277 KIAS	270 KIAS

The main contractor was the French simulator manufacturer Thomson-CSF, as a subcontractor DLR Institute of Flight Mechanics was responsible for

1. instrumentation of the test aircraft,
2. execution of the flight tests, and
3. development of the mathematical model including the aerodynamic data base.

DLR's work started with the instrumentation in May '92. The main flight test campaign was conducted in November and December '92, supplemented by some flight tests in February '93. The model development phase lasted from December '92 to July '93. The total number of maneuvers to be evaluated was about 1,000.

The model to be delivered by DLR is a so called rigid body model using measured control surface deflections as input. Several papers covering modeling and instrumentation aspects have already been published [2-7].

2.3 The Dornier 328 Project

Under contract to the aircraft manufacturer Dornier (now Fairchild Dornier) DLR Institute of Flight Mechanics developed the mathematical model of the Dornier 328-110, Fig. 2, Table 1, to be implemented by the British simulator manufacturer Thomson Training & Simulation.
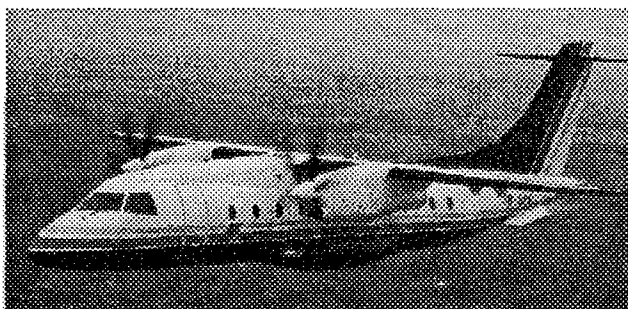

Figure 2. Dornier 328

The work started in December '95 and was finished in December '96. Because of the reversible flight controls, not only a rigid body model as in the case of the C-160 but also models of the primary flight control systems (i.e. elevator, ailerons, and rudder) had to be developed. The control system models consist of a mathematical model of the control system dynamics and the corresponding aerodynamic hinge moments. The POM simulations had to demonstrate the end-to-end match resulting from an integrated model with force inputs (i.e. 6-DOF equations of aircraft motion incorporating the identified aerodynamic data base coupled with the dynamic models of the flight control systems driven through pilot applied forces and incorporating the identified hinge moments data base).

All the flight test data were provided by Dornier, DLR was neither involved in the instrumentation nor in the flight testing. The total number of maneuvers to be evaluated was about 1,300. Further information regarding the Dornier 328 data base development project can be found in references 8 and 9.

2.4 DLR's Model Development Approach

For both cases, C-160 and Dornier 328, it was considered appropriate to generate a new data base from flight data applying modern system identification methods instead of determining increments to the existing wind tunnel data base. DLR uses the output error method in the time domain with a maximum likelihood cost function[10].

Although the final validation tests have to be carried out as end-to-end tests, the actual identification is done with so called stand-alone models for the rigid body and each of the primary flight control systems (Fig. 3).

a) Stand-alone

b) Integrated

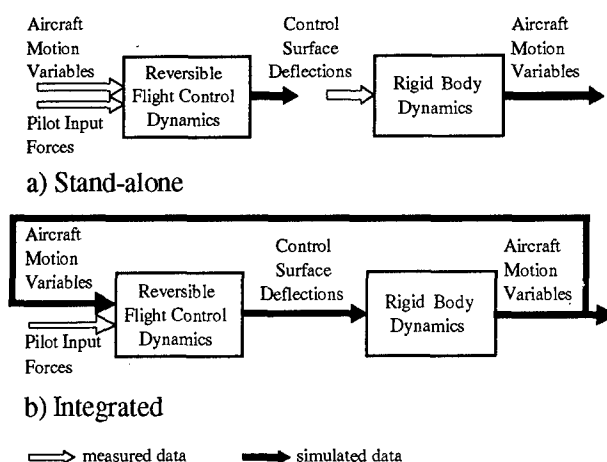⇒ measured data   ➤ simulated data

Figure 3. Stand-alone and integrated models

A separate set of parameters is estimated for each nominal flap setting (C-160: 0°, 20°, 30°, 40°, 60°; Dornier 328: 0°, 12°, 20°, 32°). Flap change dynamics are simulated by linear interpolation between these different sets.

The identification starts with point-identification runs, evaluating a set of standard dynamic maneuvers at nominal flight conditions throughout the flight envelope to identify primary aerodynamic parameters without yet accounting for Mach number, thrust setting or landing flap effects.

Collating the point-identification results, the structure of the aerodynamic model valid over a broader range is determined and a model incorporating dependencies on angle-of-attack, Mach number, angle of sideslip, and thrust coefficient is postulated. Maneuvers from several flight conditions are concatenated in a multi-point identification to arrive at a single set of parameters describing these linear and nonlinear dependencies. This is done for the symmetrical flight configuration with two engines on, landing gear retracted, at a fixed landing flap setting.

The models are then extended to include ground effect and single engine effects. For the rigid body aerodynamics also effects due to landing gear and the stall have to be considered.

At this stage for each flap setting a comprehensive set of aerodynamic parameters is available. These sets are finally combined in a single data base incorporating a linear interpolation procedure for flap position only. This so-called "derivative model" is implemented in the C-160 simulator. It is, however, rarely used in flight simulators mainly because the data base in the so-called "table model" form was hitherto mostly generated from wind tunnel measurements. For the Dornier 328 the identified derivative model was converted into a tabular format comparable to a "classical" wind tunnel based data base. It is noteworthy that at least in this case the resulting data base is much bigger than a conventional wind tunnel based data base, for example the rigid body part of the data base alone contains 14 five-dimensional and 28 four-dimensional tables.

If flight control system dynamics have to be considered, the previously developed stand-alone models for rigid body and flight controls are combined to form an integrated model for end-to-end validation.

3. LESSONS LEARNED

The two aforementioned projects on data base development had several aspects in common (twin prop configuration, Level D fidelity required, number of maneuvers, ...). Based on this commonality and aiming at minimizing the effort for future similar projects, it is next attempted to crystallize the lessons learned. Out of the many lessons learned during the course of these two projects, only the most important ones are presented here.

3.1 Lesson I

*The development of an integrated
model is much harder than the development of stand-alone models.*

Of course, it was clear at the very start of the Dornier 328 project that the development of an integrated model will require more effort than the development of two stand-alone models. However, it was a surprise how much more effort it required.

The intricacies resulting from combination of the stand-alone models are brought out in Fig. 4. Fig. 4a shows the match for the stand-alone models for a stall approach. The primary input into the elevator model is the measured pilot force, the primary input into the rigid body model is the measured elevator angle plus a trim offset. The output of the elevator model is the simulated elevator angle, whereas the output of the rigid body model is the pitch angle. The match appears to be quite good in both the cases and is well inside the tolerances. The elevator offset required to trim the rigid body stand-alone model is visible in the plot and is less than 1°. However, integrating these two models and running an end-to-end test results in an unsatisfactory match (see Fig. 4b). As a consequence the elevator hinge moment model had to be extended in the high-α region.

3.2 Lesson II

The amount of effort required to arrive at a suitable model depends on the types of maneuvers and the propeller slipstream interference effects.
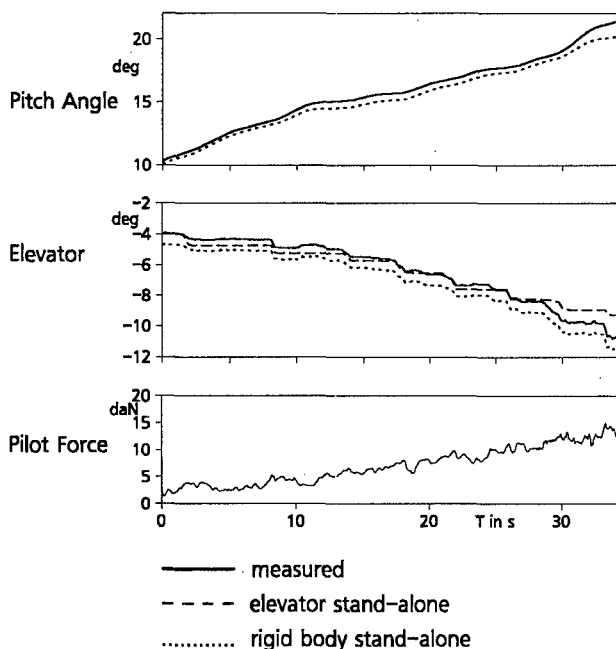
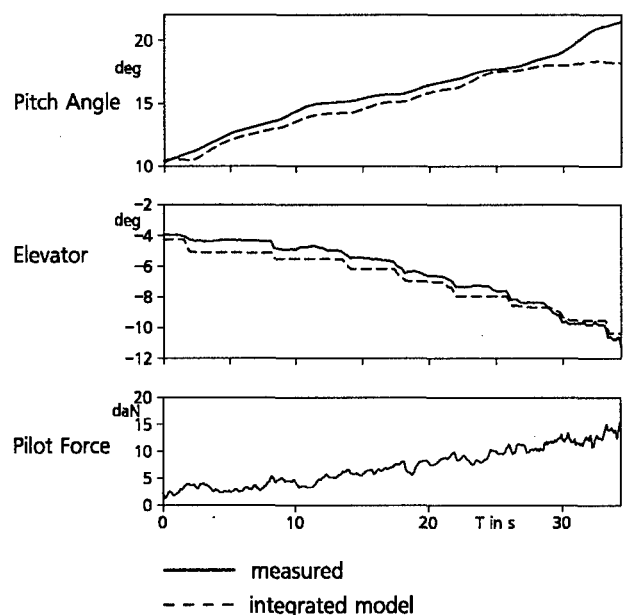Figure 4a. Stall approach with stand-alone models

Figure 4b. Stall approach with integrated model

As mentioned above the number of maneuvers to be evaluated was about the same for C-160 and Dornier 328 (1,000 vs. 1,300 including about 300 mistrims that are of primary importance only for the flight controls). Therefore it was expected that the development of an adequate rigid body model for the Dornier 328 would take about the same effort as for the C-160, maybe even a little less, because of the experience gained in the C-160 project. This expectation turned out to be wrong. In the end about twice the C-160 effort has been put into the Dornier 328 rigid body model development. Subsequent analysis showed that there were three primary reasons for this:

Although the absolute number of maneuvers was very similar, the distribution and the type of the maneuvers was quite different. In the case of the C-160 the bulk of the maneuvers consisted of a sequence of six standard maneuvers performed at up to 17 trim points in the flight envelope (horizontal, symmetric flight at various airspeeds and altitudes) for each of five flap settings. The standard sequence consisted of a 3211 elevator input[11], exciting the short period motion, an elevator pulse input exciting the phugoid motion, a bank-to-bank maneuver exciting the rolling motion, a rudder input exciting the dutch roll, and finally a power lever doublet to enable identification of slipstream interference effects. In addition, whenever permissible a level turn maneuver with superimposed elevator doublets in the banked position was carried out. It provides more information to accurately estimate the downwash parameters.

For the Dornier 328 the standard set of maneuvers consisted of elevator step inputs in both directions, an elevator doublet, aileron pulse inputs in both directions, a bank-to-bank maneuver, rudder step inputs in both directions, a rudder doublet, and steady sideslips in both directions, amounting to a total of eleven maneuvers. This standard set was flown at only three airspeed/altitude combinations, but at three different thrust levels (flight idle, power for level flight, and max. power). Also there were only four flap settings.

The most severe difference in the two sets of standard maneuvers is that for the Dornier 328 steady-state maneuvers were used instead of resp. in addition to the dynamic maneuvers for the identification of thrust (slipstream) and sideslip influences:

- steady sideslips in addition to dynamic rudder inputs and
- different thrust levels instead of power lever inputs.

Also for the C-160 quite large angles of sideslip have been reached during the rudder input maneuvers. However, these are reached only temporarily for a brief time. For the Dornier 328 both types of maneuver were available (dynamic rudder inputs and steady sideslips) and it proved much more difficult to come up with a model

that matched not only the dynamic maneuvers but also the steady state maneuvers.

With regard to slipstream interference effects the execution of the complete set of standard maneuvers at different thrust levels proved to be much more challenging than a power lever doublet with an amplitude of 20% around a trim point and a total duration of 10 s.

However, the problems encountered during the Dornier 328 model development are probably not only due to the maneuver types to be matched, but also due to more severe propeller slipstream interference effects compared to the C-160. An indication for this is the fact that, if no slipstream effects are modeled, the required aileron trim biases for single engine trims are by a factor of three greater for the Dornier 328 than for the C-160. The reason for that is currently not clear. It seems to be a combination of several small effects going in the same direction and adding up to a quite significant difference. The relative position of the propellers is more outward and more forward for the Dornier 328 than for the C-160, also the slipstream is closer to the vertical tail for the Dornier 328 and the thrust to weight ratio of the Dornier 328 is higher.

Fig. 5 gives an example from the identification of single engine effects on aircraft motion. For the C-160 three parameters were found to be sufficient to match all single engine maneuvers. Identification of the same three parameters for the Dornier 328 yields the match shown in Fig. 5a. The aileron maneuver shown is part of a point-identification run combining five maneuvers in one evaluation. Clearly three parameters are not adequate to cover all the effects. It was found that a minimum of eleven parameters is necessary to obtain a good match for all the maneuvers of the point-identification run; the resulting match for the aileron input is shown in Fig. 5b. Many more parameters are needed to come up with a model covering single engine effects for the entire flight envelope.

3.3 Lesson III

The development of a FAA-adequate friction model for flight control systems seems to be impossible (for pilot force driven end-to-end testing).

Due to the fact that pilot forces are the primary inputs to the control system models, friction has to be taken into account. As no further information was available about the friction in the system, it was modeled as an additional moment acting at the corresponding control surface axis.

Friction was modeled with a very simple model including static and sliding (Coulomb) friction (see Fig. 6).
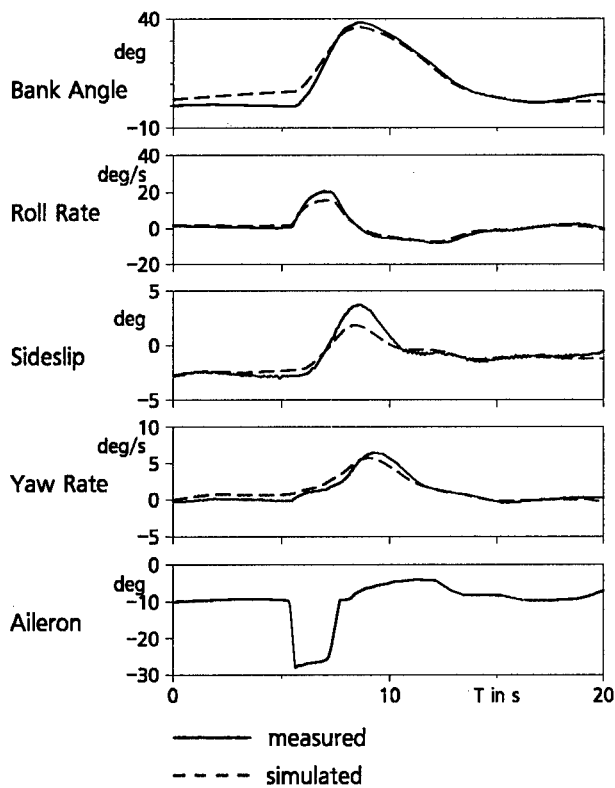
Figure 5a. Single engine aileron step - Dornier 328
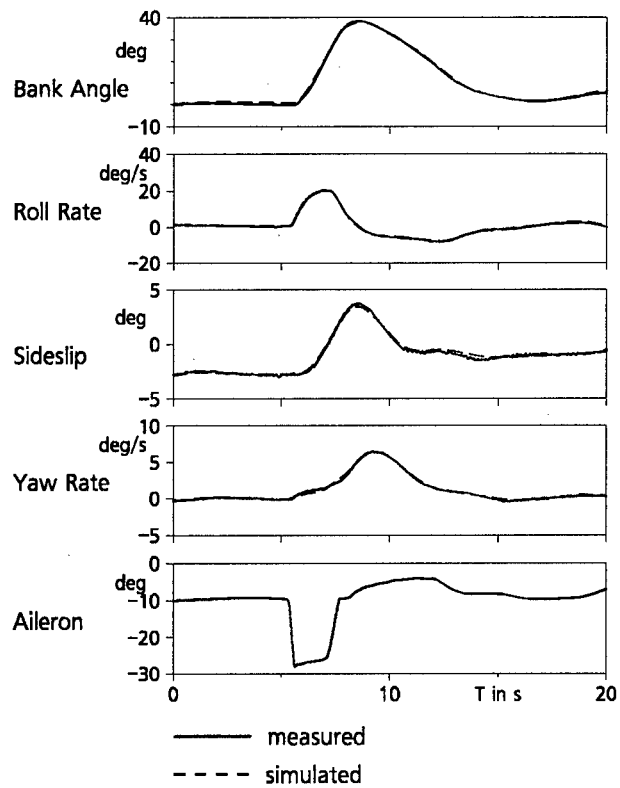Match with three SE parameter model

Figure 5b. Single engine aileron step - Dornier 328
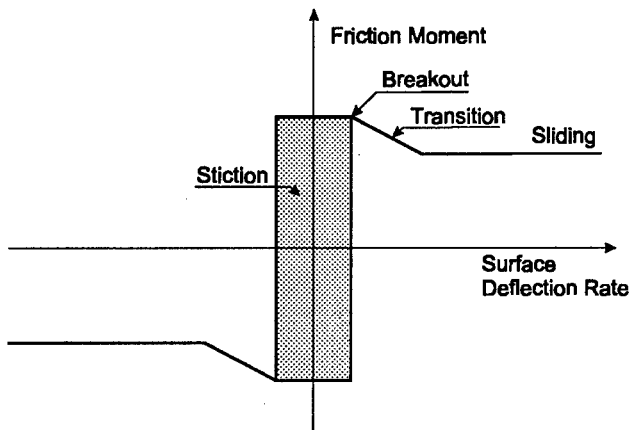Match with eleven parameter model

Figure 6. Friction model

With the respective control surface in standstill, static friction causes stiction until the external moments exceed the static friction moment (breakout). Once the control surface is in motion, there is a transition from static to sliding friction, which depends on deflection rate.

The structure of this model is sufficient for the static control checks (FAA validation tests 2a(1), 2a(2), and 2a(3)). However, even for these tests the variation of friction coefficients with temperature and maintenance state cannot be accounted for.

More severe problems with this type of friction model occurred in all the other validation tests where the en-

gines are running and the whole aircraft is vibrating depending mainly on propeller rpm and difference in left/right propeller rpm. Research in robotics indicates that the effective static friction is zero in systems with vibration[12]. However, for the Dornier 328 the same friction model with stiction has been used for maneuvers with and without running engines. This caused problems in small amplitude maneuvers, e.g. accounting correctly for elevator floating during phugoids.

As can be seen from Fig. 7, in the phugoid validation test with the integrated model the simulated elevator is at a standstill most of the time, whereas the real elevator is floating with a very small amplitude of about 0.1°.
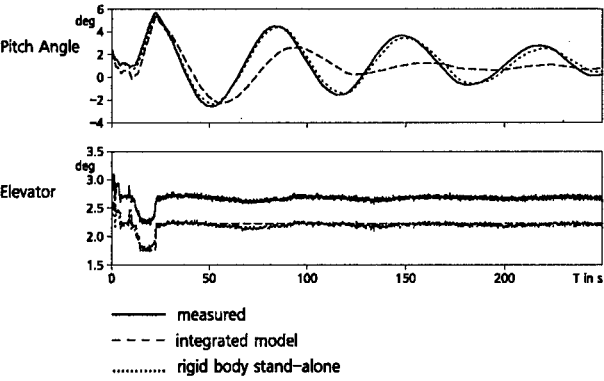

Figure 7. Phugoid

The elevator match itself is well inside a 1° tolerance. Unfortunately this is not true for frequency and damping of the phugoid, the main parameters to be evaluated in this validation test (cf. time histories of simulated and measured pitch angle in Fig. 7). Additionally shown is the match for the rigid body stand-alone model that is driven by the measured elevator deflection plus a trim offset. Comparison of the three cases shows that frequency and damping of the phugoid are very sensitive to even small elevator movements.

Other tests that proved to be quite sensitive with respect to the friction model are the dynamic control checks (FAA validation tests 2b(1), 2b(2), and 2b(3)).

It seems to be practically impossible to come up with a friction model that covers the static control checks, the dynamic control checks, and the phugoid simultaneously and satisfactorily in end-to-end validation using pilot force inputs and trimming by force offsets held constant for the whole maneuver.

The experience gained from the Dornier 328 project confirms the statement by Neville[13]: "Realistic end-to-end matching requirements may require increases in data tolerance values.".

3.4 Lesson IV

A gradient based optimization method is not very well suited to handle systems with static friction in an identification context.

DLR's identification software uses a Gauss-Newton optimization algorithm to determine the optimal values of the parameters to be identified. The required gradients of the cost function with respect to the parameters are determined numerically taking the ratio of the variation in the cost function to the corresponding variation of the parameter.

Numerical problems caused by static friction are most often encountered in the secondary degrees of freedom during proof-of-match calculations, e.g. in the aileron and rudder systems for a short period validation test with elevator input only. Our test technique for end-to-end validation with pilot force inputs is to identify pilot force offsets to trim the aircraft. If for example during an elevator input maneuver the aileron is all the time standing still due to static friction, a small change in the wheel force to determine the gradient with respect to the wheel force offset may be too small to cause the aileron to leave the static friction band and move. So nothing happens, the cost function is unchanged and the gradient is zero. But that means for the optimization algorithm that the parameter, in this case the wheel force offset, is not identifiable. In such a case DLR's current identification software version stops the program execution with-out having reached the optimal match. In other cases the calculated gradient may not be zero but incorrect, leading to convergence problems and/or local minima solutions.

Due to this problem the proof of match runs required very time consuming optimization by hand in many cases.

3.5 Lesson V

The direct identification approach works, but there are some inherent, practical limitations.

By developing mathematical models that meet the respective tolerances for two aircraft, DLR has shown that in general system identification and the approach outlined above is a viable method for data base development for Level D simulators. There are, however, some inherent, practical limitations associated with the approach adopted here that should be mentioned:

The parameters are identified for each flap position separately. The simulation of flap change dynamics is, therefore, not possible before all the parameters have been identified. If the flap change dynamics do not match within the tolerances, most of the time a complete new identification iteration has to be performed for at least one flap position. Sometimes a nonlinear interpolation between the two parameter sets is sufficient. But usually the models for the separate flap positions are good enough, i.e. they are in the tolerances for all the maneuvers with that particular flap deflection. They just require different trim offsets before and after the flap change itself, because the unavoidable modeling errors are not the same for the two flap positions. Since the trim offsets are required to be constant during the maneuver, it is not possible to fulfill the trim requirements at the start and at the end of the flap change maneuver simultaneously. In such cases the aerodynamic zero coefficients have to be reiterated.

Using stand-alone models for the actual identification leads to problems with the integrated model. That is due to the fact that for identification of the flight control systems the measured rigid body variables are used as inputs (e.g. angle of attack, airspeed, ...) and for the identification of the rigid body the measured control surface deflections are used as inputs. In the simulation with the integrated model in both the cases simulated values are used instead of the measured values. These simulated values usually deviate from the measured values resulting in a poorer match than in the stand-alone cases. This could at least partly be avoided by identifying all the parameters in one identification run, but that is currently prohibited by the size of the estimation problem as it would require the identification of more than 1,000 parameters.

The identification of the flight control systems on ground proved to be a problem, because of the limited quality of the measurements of the rigid body variables, especially the angle of attack, the angle of sideslip, and the airspeed. It was required to set up a special model mode driving the rigid body by measured control surface deflections and using the simulated rigid body variables as inputs for the identification of the flight control system parameters.

A general problem with a model that is determined solely by identification is that its validity is only ensured for the flight envelope covered by the flight tests that have been used for the identification. Any extrapolation of the model may lead to incorrect results, especially if nonlinear terms have been introduced in the model. Unfortunately for the final model used on the simulator usually some extrapolation is necessary. This should be done very carefully and at least the physical plausibility should be checked. Another possibility is to extend the model based on wind tunnel data, if these are available.

3.6 More Lessons Learned

Without going into much some other lessons learned that may be of general interest are listed in the sequel:

- Flight tests for simulator model development should be performed in a limited time frame (e.g. eight weeks) utilizing just one aircraft.

- Enough time should be allocated for checking of flight test data and determining suitable maneuver time segments.

- Due to cpu-time and memory limitations usually only a limited number of maneuvers can be used for an identification run. Once a good model for this subset of maneuvers is obtained, its appropriateness for all other maneuvers it is supposed to cover should be checked.

- Although this may be difficult for complicated model structures with hundreds of parameters, the identified values for each of these parameters should be checked for physical plausibility. Otherwise there is a certain danger of overparameterization and development of models that cannot be applied to cases that have not been evaluated. Physically meaningless values may also be an indication of a local minimum.

- Derivation of an equivalent table model from a derivative model is possible, but takes considerable effort and may result in huge tables. In DLR's environment the derivative model runs about ten times faster than the table model.

- At the very beginning of a simulator model development project the aircraft manufacturer, the simulator

manufacturer, and the data base developer should have a good mutual understanding of

- required flight tests,
- model development methods and their limitations, ·
- models and model structures required by the simulator manufacturer, and
- test techniques for model validation.

4. CONCLUSIONS

This paper gives a brief introduction into the FAA requirements for Level D Flight Simulators relevant to the development of the mathematical aircraft model, provides an overview of two data base development projects, which were successfully completed in the recent past, and highlights the main lessons learned therefrom. These are

1. The development of an integrated model is much harder than the development of stand-alone models.
2. The amount of effort required to arrive at a suitable model depends on the types of maneuvers and the propeller slipstream interference effects.
3. The development of a FAA-adequate friction model for flight control systems seems to be impossible (for pilot force driven end-to-end testing).
4. A gradient based optimization method is not very well suited to handle systems with static friction in an identification context.
5. The direct identification approach works, but there are some inherent, practical limitations.

5. ACKNOWLEDGEMENTS

6. REFERENCES

1. Anon., "Airplane Simulator Qualification", FAA Advisory Circular AC 120-40B, Interim Version, Feb. 1991.
2. Zach, A. and Klewe, H.-J., "Flight Test Instrumentation for Transall C-160 Simulator Data Gathering", in Proceedings of the European Test and Telemetry Conference ETTC '93, Arcachon, France, June 1993, pp. 1107-1119.
3. Krag, B., Jategaonkar, R. V., Mönnich, W., and Fischenberg, D., "Estimation of an Aerodynamic Data Base for a New C-160 "Transall" Flight Simulator from Flight Data", RAeS Symposium on "Data Issues for Flight Simulators - An On-going Problem", Paper No. 7, London, UK, Nov. 1993.
4. Jategaonkar, R. V., Mönnich, W., Fischenberg, D., and Krag, B., "Identification of C-160 Simulator Data Base from Flight Data", in Proceedings of the

10th IFAC Symposium on System Identification, Copenhagen, Denmark, Elsevier Sciences Ltd., IFAC Publications, Oxford, UK, 1994, pp. 1031-1038.

5. Jategaonkar, R. V., Mönnich, W., Fischenberg, D., and Krag, B., "Identification of Speed Brake, Air-drop, and Landing Gear Effects from Flight Data", Journal of Aircraft, Vol. 34, No. 2, March-April 1997, pp. 174-180.

6. Fischenberg, D., Mönnich, W., Krag, B., and Jategaonkar, R. V., "Aspects of C-160 Simulator Model Determination and Validation On and Close to the Ground", AIAA Flight Simulation Technologies Conference, Paper No. 94-3404, Scottsdale, AZ, Aug. 1-3, 1994.

7. Fischenberg, D. and Mönnich, W "C-160 Ground Handling Model Update Using Taxi Test Data", in "Flight Simulation - Where are the Challenges", AGARD-CP-577, Paper No. 12, Neuilly-sur-Seine, France, 1996.

8. Jategaonkar, R. V. and Mönnich, W., "Identification of DO-328 Aerodynamic Database for a Level D Flight Simulator", AIAA Modeling and Simulation Technologies Conference, Paper No. 97-3729, New Orleans, LA, Aug. 11-13, 1997.

9. Weiss, S., Gockel, W. Mönnich, W., and Rohlf, D., "Identification of Dornier-328 Reversible Flight Control systems", AIAA Modeling and Simulation Technologies Conference, Boston, MA, Aug. 10-12, 1998 (to be published).

10. Hamel, P. G. and Jategaonkar, R. V., "Evolution of Flight Vehicle System Identification", Journal of Aircraft, Vol. 33, No. 1, Jan.-Feb. 1996, pp. 9-28.

11. Koehler, R. and Wilhelm, K., "Auslegung von Eingangssignalen für die Kennwertermittlung" (in German), DFVLR-IB 154-77/40, Braunschweig, Germany, 1977

12. Cheok, K. C., Hu, H., and Loh, N. K., "Modeling and Identification of a Class of Servomechanism Systems with Stick-Slip Friction", ASME Transactions, Journal of Dynamic Systems, Measurement and Control, Vol. 110, pp. 324-328, 1988.

13. Neville, K. W., " Simulator-to-Flight Validation – Methods, Problems and Dilemmas", RAeS Symposium on "Data Issues for Flight Simulators - An Ongoing Problem", Paper No. 14, London, UK, Nov. 1993.

IN-FLIGHT MODEL IDENTIFICATION RESEARCH
AIMED AT DEVELOPING A FLIGHT SIMULATOR MODEL
by

J.H. Breeman, H. Kannemans, M. Laban
National Aerospace Laboratory NLR
P.O. Box 90502, 1006 BM Amsterdam, The Netherlands

SUMMARY

In the last decade NLR and Delft University of Technology have conducted an cooperative research program using the Swearingen Metro II laboratory aircraft. Topics studied in this program are a/o instrumentation techniques, flight test techniques and the modeling of aerodynamics, engine thrust and flight controls. As one of the topics it was decided to investigate the feasibility of in-flight on-line aerodynamic model identification. This paper summarizes the main results of the on-line identification project and then goes on to describe the following off-line analysis, which should lead to a complete flight simulator model for the Metro.

NOMENCLATURE

b	wing span	S	wing area
$\bar{c}$	mean aerodynamic chord	T	thrust
D	drag	T_c	thrust coefficient
F	force	V	airspeed
G	gearing coefficient	Y	side force
H	hinge moment	α	angle of attack
I	moment of inertia	β	angle of sideslip
L	lift	δ_a	aileron deflection
$\mathcal{L}$	rolling moment	δ_e	elevator deflection
l	length	δ_r	rudder deflection
M	Mach number	Δp_t	total pressure increase
$\mathcal{M}$	pitching moment	ζ	damping ratio
m	mass	η	propeller efficiency
$\mathcal{N}$	yawing moment	θ	pitch angle
n	rotations per second	μ	friction coefficient
p	roll rate	τ	sideforce function
Q	shaft torque	ρ	air density
q	pitch rate	ϕ	roll angle
q_c	dynamic pressure	φ	control deflection
r	yaw rate, radius		

$$C_D \quad \frac{D}{\frac{1}{2}\rho V^2 S} \qquad C_l \quad \frac{\mathcal{L}}{\frac{1}{2}\rho V^2 Sb}$$

drag coefficient   rolling moment coefficient

$$C_L \quad \frac{L}{\frac{1}{2}\rho V^2 S} \qquad C_n \quad \frac{\mathcal{N}}{\frac{1}{2}\rho V^2 Sb}$$

lift coefficient   yawing moment coefficient

$$C_m \quad \frac{\mathcal{M}}{\frac{1}{2}\rho V^2 S\bar{c}} \qquad C_Y \quad \frac{Y}{\frac{1}{2}\rho V^2 S}$$

pitching moment coefficient   side force coefficient

Subscripted variables of the form $C_{D_{()}}, C_{L_{()}}, C_{l_{()}}, C_{m_{()}}, C_{n_{()}}$, $C_{Y_{()}}$ denote partial derivative of coefficients with respect to (•).

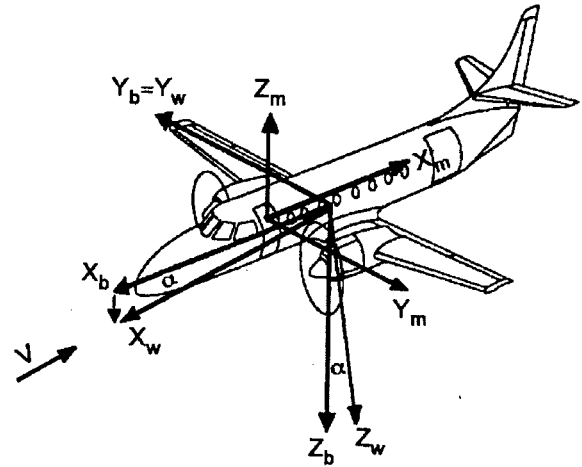The subscript p denotes the propeller thrust and j denotes the jet thrust.

Figure 1: Metro II aircraft and definition of body, wind and measurement axes

1. INTRODUCTION

The NLR has a long history in flight test data acquisition and developing measurement and analysis techniques to determine the performance and handling characteristics of the aircraft. In order to develop mathematical models numerous flight test programs were carried out with a variety of aircraft, including Hawker Hunter Mark VII, Fokker F-28, Fokker F-27 Maritime, Cessna Citation 500, Lockheed Orion, Fokker 50, Fokker 100 and Fokker 70 (Refs. 1-8).

To obtain a mathematical model of the turboprop Metro II research aircraft of the NLR (National Aerospace Laboratory) a number of flight test campaigns have been executed in close cooperation with the DUT (Delft University of Technology). During the flight tests use was made intensively of dynamic flight test techniques. The analysis of the test data was done using the NSM (Nonstationary Measurement) technique which is also referred to as the Two Step method (Ref. 9). This method starts by reconstructing the aircraft flight path. The second step is the calculation of model coefficients using regression analysis techniques.

The advantage of the NSM method is its capability to allow analysis of a great number of alternative models within a short time at low cost without increase of flight test hours. Special attention is paid in determining the turboprop thrust. The modelling of the control motion and control force system as well as the undercarriage modelling was done in close co-operation with the TU Braunschweig (TUBs).

2. TEST AIRCRAFT

The flight tests were conducted with the NLR research aircraft Fairchild Metro II, PH-NLZ (Figure 1). This aircraft is a transport type aircraft equipped with two wing mounted turboprop engine of the type AiResearch TPE-331-3UW-304G. Each engine drives a three bladed pitch regulated constant speed Hartzell propeller.

3. MEASUREMENT SYSTEM

The aircraft has been equipped with special flight test instrumentation. The measurement system of this aircraft consists of the following main components:

- A basic data acquisition system used for a large number of various projects, including:
  - Digital Air Data Computer
  - signal conditioning unit
  - anti-aliasing filters
  - remote multiplexer digitiser unit
  - 14-track tape recorder
  - time code generator
- Extra equipment for gathering data for model identification:
  - an Inertial Reference System sensing the body acceleration and body attitude rates
  - Global Positioning System receiver
  - elevator, aileron and rudder control surface and stabilizer deflections
  - wing flap angle
  - column, wheel and rudder pedal control forces and displacements
  - power lever angles
  - nose mounted boom for measurement of angle of attack and angle of sideslip
  - pressure rakes located at a short distance behind the propeller.
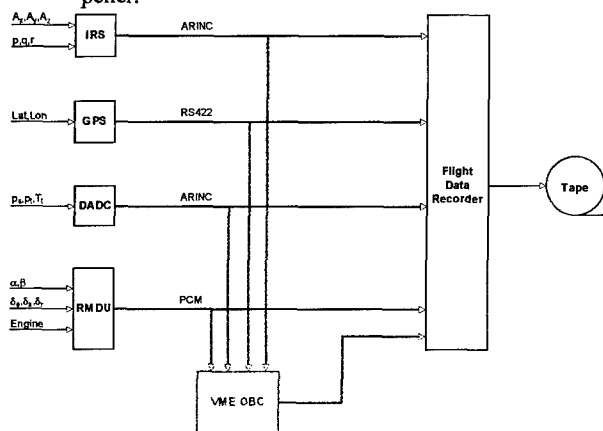
Figure 2: Instrumentation block diagram

Figure 2 shows a block diagram of the instrumentation system. Note the link to the on-board computer.

4. FLIGHT TEST PROGRAM

The objective of the flight test programme was the execution and measurement of different kinds of flight test manoeuvres for the identification of an aircraft model.

In total 550 manoeuvres were flown distributed over 15 test flights. Each flight test campaign was devoted to a particular research item as follows:

1985	3	flights aero-model clean configuration
1988	3	flights aero-model clean configuration and thrust determination from total pressure rakes
1990	1	flight aero-model for air traffic control
1991	5	flights aero-model take-off, cruise, approach and landing configuration and on-line parameter identification
1995	3	flights control force system, Proof-of-Match

The flight test program for model identification was carefully designed in the sense that flight test manoeuvres were evenly distributed within the flight envelope. All the manoeuvres were flown by hand and most of them were block shaped.

The following types of manoeuvres were flown:

- block shaped elevator inputs: 3211, 4411 and doublets
- aileron doublets

- rudder doublets
- level acceleration/decelerations
- thrust doublets, symmetric and asymmetric
- sideslip sweeps
- stalls
- climbs and descents
- frequency sweeps, symmetric and asymmetric
- quasi-steady sideslips
- phugoids
- aileron responses
- go-arounds
- stabilizer-elevator exchanges
- special combinations of manoeuvres

5. DATA ANALYSIS TECHNIQUES

The Two-Step method as used by NLR was developed by the Department of Aerospace Engineering of the Delft University of Technology. The basics of this method are extensively described in Ref. 9. Figure 3 gives an flow diagram of the method.
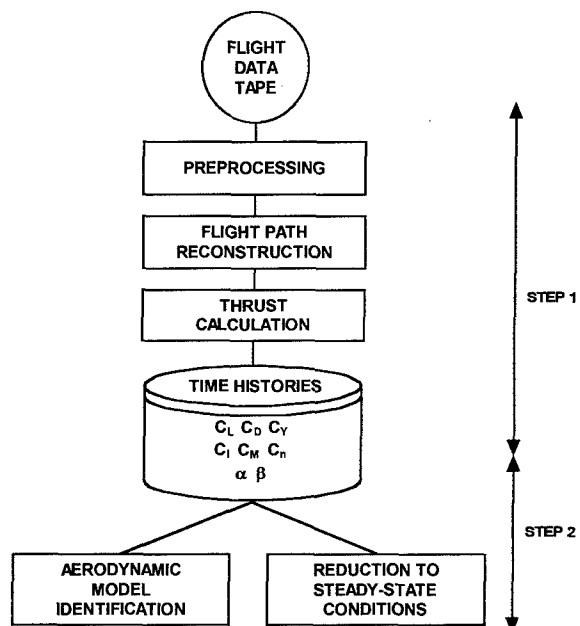

Figure 3: Data reduction flow diagram

The first phase of the first step is called "pre-processing" and involves a/o. the application of the sensor calibrations and position error corrections, the correction of pressure measurements for time lags and the transformation of the acceleration measurements to the centre of gravity. After pre-processing, the state trajectory of the aircraft with respect to the surrounding air mass is reconstructed applying the well-known Kalman filter methodology. The exact algorithm is described in detail in Ref. 9. As will be discussed in this paper, at this stage of data processing, attention must be paid to the wind velocity. This is due to the fact that the actual measured aircraft specific forces and moments are sensitive to the wind components as well, which is of random nature and therefore cannot be modelled in a simple way. The last phase is the calculation of the engine thrust components. Correction of the inertial measurements for the thrust components yields the aerodynamic forces and moments. The end result of the first step is the smoothed time histories of the nondimensional aerodynamic forces and moments and of the aircraft state variables.

In the second step an interactive parameter identification program based on linear regression techniques allows the determination of the coefficients of an aerodynamic model.

Due to its low computer requirements and the possibility of recursive implementation, the Two-Step method is eminently suited for real-time applications as will be discussed in the next section.

6. IN-FLIGHT PARAMETER IDENTIFICATION

6.1 Introduction

In-flight parameter identification potentially offers significant benefits. The identification results are available for inspection immediately during flight. This allows a high level of quality assurance, because unsuccessful manoeuvres can be repeated immediately and the manoeuvres can be improved iteratively. In addition no ground-based processing time is lost between flights and the overall program duration can be shortened significantly.

But there are also obvious disadvantages. All up-to-date sensor calibration information must be available before the flight. Off-line data analysis is potentially more accurate due to standard techniques such as data smoothing and glitch removal and iterative improvements. Finally the data analyst must always be present on-board and without special measures his workload is considerable.

On-line identification is of course also possible with telemetry. However, the on-board approach has no range limitations and is much cheaper to operate. The corresponding disadvantage is that the workload of the flight test engineer/analyst during an intensive test flight is considerable.

The objective of the on-line identification project was to demonstrate the feasibility of on-line aerodynamic model identification, but there were significant limiting conditions. There was to be minimal interference with the on-going flight test program and the existing instrumentation system should be used unaltered. The results should be generated in near real-time, displayed in the aircraft for inspection and should be the same as those of the standard off-line analysis. The software should be robust, highly automated and include facilities for graphical presentation and allow selectable model structures. Each flight test manoeuvre should be self-contained, i.e. should not use information from other tests. Finally the results should be stored in a database that can be inspected in flight.

The project was started with a detailed theoretical study of all aspects of the whole aerodynamic model identification process, such as instrumentation, computer hardware, flight test technique, analysis software and a priori aerodynamic models. For each of these aspects a recommendation was made for an on-line method that would be as accurate as the currently used off-line method.

Based on these recommendations the on-line identification was implemented and tested in flight. The system operated successfully during two flight test series conducted in the ongoing Metro flight test program. The on-line and off-line results were compared and the results were found to be practically identical. This allows the conclusion that on-line aerodynamic model identification has proven to be a viable approach, which allows a considerable speed-up in flight test program. More details can be found in Refs. 10-11.

6.2 Instrumentation

The existing instrumentation system met all requirements as to accuracy, delays, bandwidth and sample rates. However, it was decided to add the Global Positioning System (GPS) data to facilitate the on-line estimation of wind components and sensor calibration coefficients.

The only additional hardware consisted of two INMOS T800 transputer cards. One transputer card was a VME card which fitted in a spare slot in the existing data acquisition computer(see Figure 2). The measurement data is acquired by 'bus snooping' on the VME bus. The other was a PC card in a Toshiba T3200 laptop computer which communicated with VME card using the processor-to-processor channel and uses the laptop screen to display the graphical results.

On-line identification naturally requires that up-to-date calibrations must be available before flight. Although this is also the goal during normal test flights, it is not always easy to achieve in practice. In addition additional corrections are needed. such as corrections for PEC, dynamic effects and accelerometer bias. The air data calibration coefficients were modelled with aerodynamic theory and based on this model a limited but sufficient set of sensor calibration coefficients was defined. The air data calibration and accelerometer bias coefficients were estimated on-line during the dynamic manoeuvre together with the wind components. The GPS information was essential for this.

6.3 Data analysis algorithms

As stated earlier the Two-Step method is ideally suited for real-time implementation. For the state estimation an extended Kalman filter in UD form was chosen. The parameter estimation algorithms chosen were recursive, which allowed the real-time monitoring of the parameter estimates. The techniques implemented were Mixed-Mode Least-Squares and Principal Component Total Least-Squares.

The complete on-line data processing, state estimation and parameter identification program was written in OCCAM and ran distributed over the two transputers.

6.4 Flight test manoeuvre

A special combined flight test manoeuvre was designed (see Figure 4). The first part is a calibration manoeuvre, which consists of an 180 degrees turn, followed by first an angle of attack variation and then a sideslip variation. This first part yielded sufficient information to cause the Kalman state estimator to converge, setting the stage for accurate parameter identification.
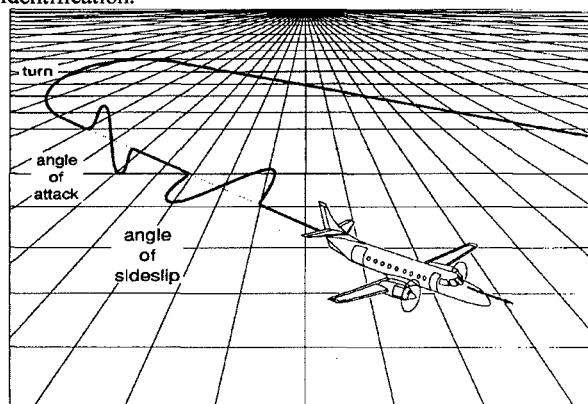

Figure 4: Calibration part of the flight test manoeuvre

The second part is the parameter identification manoeuvre (Figure 5). First, a symmetric excitation was applied, consisting of either a doublet or a 3211 elevator input followed by a thrust lever doublet. Then an asymmetric excitation was applied which consisted of an aileron doublet followed by a rudder doublet.
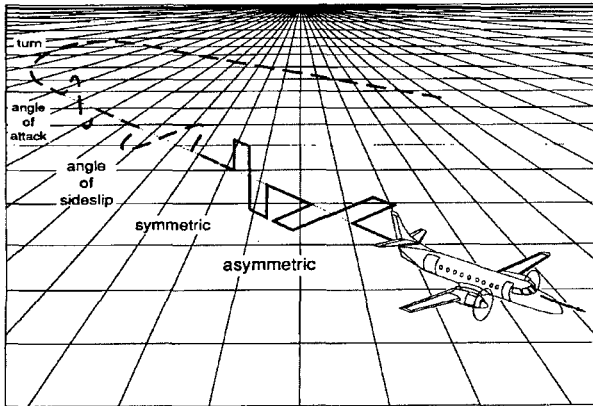

Figure 5: Parameter identification part of the flight test manoeuvre

The second part of the manoeuvre yielded enough information to allow good parameter estimates as attested by the convergence of the standard deviations of the on-line parameter identification algorithm to low values. This behaviour can be clearly seen in the on-board display (see Figure 6).

6.5 A priori aerodynamic model

During on-line identification the maximum extent of the models must be fixed a priori, in other words all important terms should be known in advance. During flight terms that turn out to be insignificant can be deleted. An extensive analysis based on aerodynamic theory led to the following a priori propeller aircraft aerodynamic model:

$$C_D = C_{D_0} + C_{D_\alpha}\alpha + C_{D_{\alpha^2}}\alpha^2 + C_{D_q}\frac{q\bar{c}}{V} + \tag{1}$$
$$C_{D_{\delta_e}}\delta_e + C_{D_{T_c}}T_{c_p} - T_{c_j}$$

$$C_L = C_{L_0} + C_{L_\alpha}\alpha + C_{L_q}\frac{q\bar{c}}{V} + C_{L_{\delta_e}}\delta_e + \tag{2}$$
$$C_{L_{\alpha T_c}}\alpha T_{c_p} + \alpha T_{c_j}$$

$$C_m = C_{m_0} + C_{m_\alpha}\alpha + C_{m_q}\frac{q\bar{c}}{V} + C_{m_{\delta_e}}\delta_e + \tag{3}$$
$$C_{m_{\alpha T_c}}\alpha T_{c_p} + \frac{z_{cg} - z_j}{\bar{c}}T_{c_j}$$

$$C_Y = C_{Y_0} + C_{Y_\beta}\beta + C_{Y_p}\frac{pb}{2V} + C_{Y_r}\frac{rb}{2V} + \tag{4}$$
$$C_{Y_{\delta_a}}\delta_a + C_{Y_{\delta_r}}\delta_r + C_{Y_{\beta T_c}}\beta T_{c_p} - \beta T_{c_p}$$

$$C_l = C_{l_0} + C_{l_\beta}\beta + C_{l_p}\frac{pb}{2V} + C_{l_r}\frac{rb}{2V} + \tag{5}$$
$$C_{l_{\delta_a}}\delta_a + C_{l_{\delta_r}}\delta_r + C_{l_{\Delta T_c}}T_{c_p}$$

$$C_n = C_{n_0} + C_{n_\beta}\beta + C_{n_p}\frac{pb}{2V} + C_{n_r}\frac{rb}{2V} + \tag{6}$$
$$C_{n_{\delta_a}}\delta_a + C_{n_{\delta_r}}\delta_r + C_{n_{\Delta T_c}}\Delta T_{c_p} + \frac{|y_j|}{b}\Delta T_{c_j}$$

The engine thrust calculation was based on propeller torque measurements using the propeller efficiency charts from the

manufacturer. The jet thrust calculation used the engine operating condition charts from the manufacturer. Based on aerodynamic theory, the propeller-airframe interference was incorporated into the above model with a minimal set of influence coefficients involving the propeller thrust coefficient T_{c_p}. Note that some of the last terms involving the thrust are known terms and do not have coefficients.
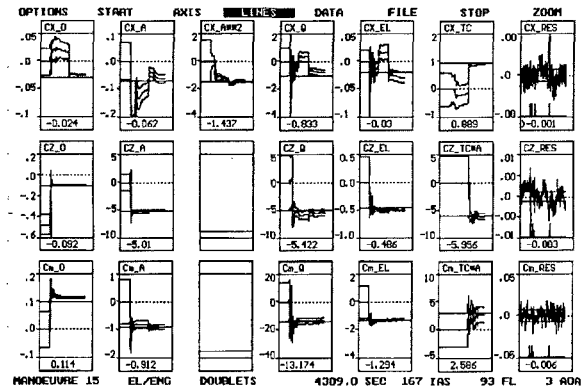

Figure 6: On-line display of identification results

6.5 Example result

Figure 6 is a screen dump from the on-board computer display. It shows the parameter values and the theoretical error bounds as they evolve in time during the second part of the combined manoeuvre. From this display it is immediately clear whether the required accuracy is being achieved by looking at both the error bounds and at the way the estimated parameters converge to a stable value.
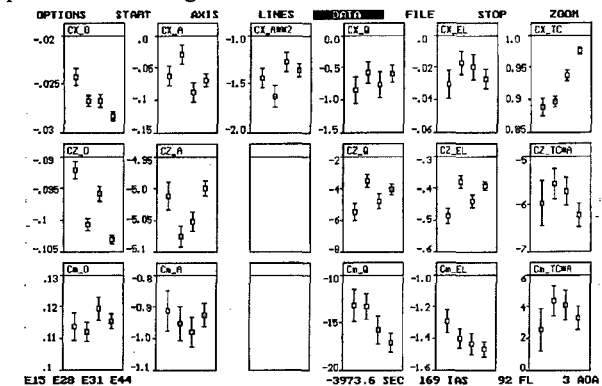

Figure 7: On-line display of results database

7. OFF-LINE AERODYNAMIC ANALYSIS

7.1 Aerodynamic model development

An essential first step in developing a model of the aircraft is the construction of a mass property model. The position of the centre of gravity of the Metro II was measured by electronic balances placed under the nose and the main gear. By weighting the load with different pitch angles, the horizontal as well as the vertical position of the centre of gravity became available. The moments of inertia were obtained through meticulous bookkeeping of all components of the aircraft. The actual centre of gravity location as well as the actual moments of inertia were corrected in according to the actual fuel loading by means of polynomial functions. The effects of fuel excursions due to body accelerations and rotations have been neglected so far.

An important objective of the flight test programme was the development of a mathematical model of the aerodynamic forces and

moments which would apply to all aircraft configurations and all admissible flight conditions. It is common practice to model the dimensionless aerodynamic force and moment coefficients in terms of linear or non-linear polynomials in variables as angle of attack, sideslip angle, body rotation rates and surface deflections, e.g. see Ref. 12. The parameters in the polynomials, the so-called aerodynamic derivatives, will in general depend on aircraft configuration and flight condition.

The aerodynamic model identification is based on linear regression technique, which can be used interactively. The program contains graphical facilities to evaluate the results very quickly. In this way the analyst is capable of evaluating a large number of alternative models until the resulting models are accurate and consistent. The same model identification procedure was applied to the control force and undercarriage modelling.

The analysis of the aerodynamic model was based on six dimensionless coefficients for each of the rigid body degrees of freedom of the aircraft. The force coefficients (C_D, C_L, C_Y) were chosen in the air-trajectory reference frame. The moment coefficients (C_l, C_m, C_n) were chosen in the body axes frame (see Figure 1). In order to obtain the aerodynamic drag C_D a thrust model is required. This thrust model will be discussed in the chapters 7.2 and 7.4.

The derivatives with respect to $\dot\alpha$ and q are usually strongly correlated and, as a result, difficult to determine and the same is true for the $\dot\beta$ and r derivatives, therefore the coefficients for $\dot\alpha$ and $\dot\beta$ were set equal to zero. The model is applied to small manoeuvres about trim flight conditions so that a linear aerodynamic model can be assumed. The numerical values of the coefficients are functions of the condition and the aircraft configuration.
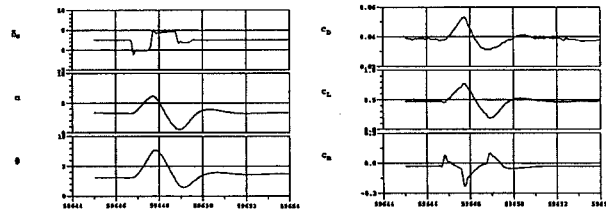

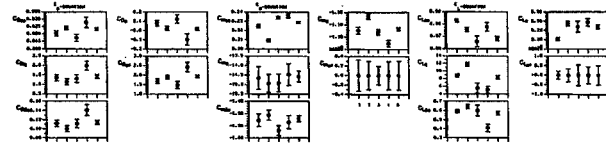Figure 8: Time history of elevator doublet manoeuvre

Figure 9: Repeatability of the longitudinal stability and control derivatives

7.2 Longitudinal model

A typical example of model identification based on elevator doublet manoeuvres is presented. Figure 8 shows traces as a result of this manoeuvre. Parameter estimation results are shown in Figure 9. Each figure shows a number of elementary plots, each visualising aerodynamic derivative results, as related to the following equations:

$$C_D = C_{D_0} + C_{D_\alpha}\alpha + C_{D_q}\frac{q\bar{c}}{V} + C_{D_{\delta_e}}\delta_e + \\ C_{D_{\alpha^2}}\alpha^2 \qquad 7$$

$$C_L = C_{L_0} + C_{L_\alpha}\alpha + C_{L_q}\frac{q\bar{c}}{V} + C_{L_{\delta_e}}\delta_e \qquad 8$$

$$C_m = C_{m_0} + C_{m_\alpha}\alpha + C_{m_q}\frac{q\bar{c}}{V} + C_{m_{\delta_e}}\delta_e \qquad 9$$

The thrust effect can be analysed by extending the mathematical model by introducing a propulsion term as follows:

$$C_D = C_{D_0} + C_{D_\alpha}\alpha + C_{D_q}\frac{q\bar{c}}{V} + C_{D_{\delta_e}}\delta_e + \\ C_{D_{T_c}}T_c + C_{D_{\alpha^2}}\alpha^2 \qquad 10$$

$$C_L = C_{L_0} + C_{L_\alpha}\alpha + C_{L_q}\frac{q\bar{c}}{V} + C_{L_{\delta_e}}\delta_e + \\ C_{L_{T_c}}T_c \qquad 11$$

$$C_m = C_{m_0} + C_{m_\alpha}\alpha + C_{m_q}\frac{q\bar{c}}{V} + C_{m_{\delta_e}}\delta_e + \\ C_{m_{T_c}}T_c \qquad 12$$

with the thrust coefficient:

$$T_c = \frac{T}{\frac{1}{2}\rho V^2 S} \qquad 13$$

and

$$T = \eta\frac{2\pi nQ}{V} \qquad 14$$

where η is the propeller efficiency computed from an efficiency table delivered by the propeller manufacturer.

Combining manoeuvres of different power settings the coefficients $C_{D_{T_c}}$, $C_{L_{T_c}}$ and $C_{m_{T_c}}$ can be estimated. Note that these coefficients can successively be interpreted as the mismatch in propeller efficiency (the corrected overall efficiency is $\eta_c = \eta - \eta C_{D_{T_c}}$), the increase of lift due to the propeller slipstream over the wing and an approximation of the lever arm of the thrust with respect to the centre of gravity location.
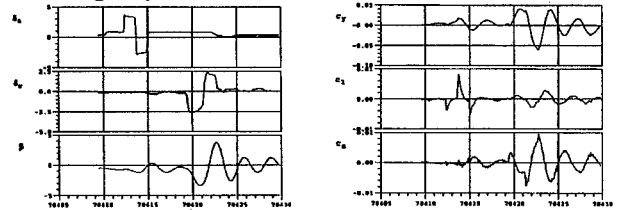

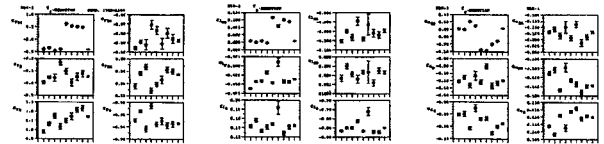Figure 10: Time history of combined aileron doublet and rudder doublet manoeuvre

Figure 11: Repeatability of the lateral-directional stability and control derivatives

7.3 Lateral-directional model

The model identification has been based on combinations of rudder doublet and aileron doublet manoeuvres (see Figure 10). A typical example of parameter estimation results is shown for the condition 170 kts, flight level 10000, power setting for level flight and clean configuration (Figure 11). Each figure shows a number

of elementary plots each visualising aerodynamic derivative results as related to following equations:

$$C_Y = C_{Y_0} + C_{Y_\beta}\beta + C_{Y_p}\frac{pb}{2V} + C_{Y_r}\frac{rb}{2V} +$$
$$C_{Y_{\delta_a}}\delta_a + C_{Y_{\delta_r}}\delta_r$$

15

$$C_l = C_{l_0} + C_{l_\beta}\beta + C_{l_p}\frac{pb}{2V} + C_{l_r}\frac{rb}{2V} +$$
$$C_{l_{\delta_a}}\delta_a + C_{l_{\delta_r}}\delta_r$$

16

$$C_n = C_{n_0} + C_{n_\beta}\beta + C_{n_p}\frac{pb}{2V} + C_{n_r}\frac{rb}{2V} +$$
$$C_{n_{\delta_a}}\delta_a + C_{n_{\delta_r}}\delta_r$$

17

7.4 Total pressure increase over the propeller

Precise determination of turboprop thrust in-flight is of much interest as it allows to verify the specified engine performance and propeller characteristics as well as to quantify the lift and drag characteristics of the airframe.

Various in-flight propeller force measurement techniques are analysed by Muhammad (Refs. 13, 14). Two of these will be discussed here, the shaft torque with propeller efficiency model and the slipstream total pressure model. The measurement method practised in the actual study is based on the use of a flexible torsion shaft, splined into the aft end of the turbine shaft end of the turbine-compressor shaft, generating an oil pressure difference exhibiting linear relationship with the shaft torque. This relation is calibrated by means of load cells during a ground based experiment. The torque is besides the propeller efficiency losses a direct measure of the propeller force. The propeller efficiency data are provided by the propeller manufacturer.

The alternative method, proposed in the Refs. 13-14, is based on the measurement of the total pressure rise over the propeller disc.
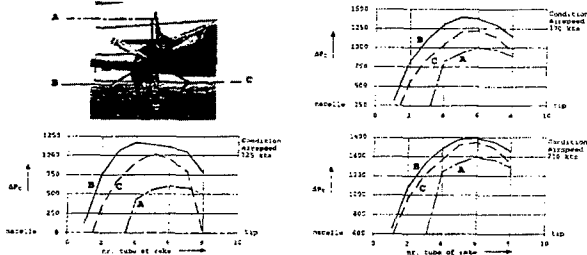
Figure 12: Distribution of total pressure increase behind propeller measured by three rakes

The measured total pressure rise at steady trimmed conditions are shown in Figure 12 as function of speed and radial position. Three total pressure rakes were used with tubes at 35, 45, 55, 65, 75, 85, 90 and 95% of the tip radius. Only the engine at the right wing was measured this way.

In the Refs. 13, 14 the thrust was supposed to be approximately equal to the integration of the total pressure increase over the propeller area. Following equation is used:

$$T_P = \frac{2\pi}{N_r}\sum_{i=1}^{N_r}\sum_{j=1}^{N_p}\Delta P_{T_{i,j}} r_p \Delta r_j$$

18

where Δr_j is the step size of the ith rake, i.e. the distance between two total head tubes.

It should be noted however that acceptable accuracy can only be realised if the pressure measurements are closely spaced and

cover the entire propeller disc. Especially the areas near the propeller tip must be measured in detail.
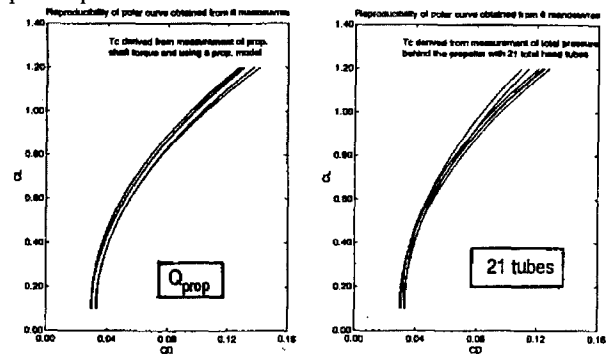
Figure 13: Reproducibility of polar curve

Figure 13 shows the reproducibility of the polar curve obtained from the analysis of 6 data sets obtained during quasi-steady manoeuvres. Comparison of the total pressure measurement (left plot) with the torque measurement results (right plot) show (a) more spread at high angles of attack and (b) minimum drag at about $C_L=0.15$ instead of zero lift. From this it is concluded that the torque measurement is of higher accuracy.

In Ref. 14 it is concluded that the pressure distribution method is to be considered as an independent alternative for the torsion shaft measurement method. The overall conclusion is that the thrust obtained from measurements of the propeller shaft torque and engine speed and using the propeller model, or from the measurement of total pressure in the propeller slipstream using total head tubes, resulted in consistent polar drag curves.

7.5 Longitudinal slipstream effects

Propeller slipstream effects are considered here the effects presented in the aerodynamic model, expressed as functions of the thrust (the thrust is determined here by the Equs. 13-14 of chapter 7.2). To be able to extend the Equs. 10-12 further by adding the so-called slipstream effects sufficient variations in the measurement data of these effects must be present. This can be realised by combining a large number of manoeuvres taken at various conditions throughout the flight envelope.

In a first attempt the Equs. 10-12 were written more generally as follows:

$$C_D = C_{D_{viscous}} + C_{D_{induced}} + C_{D_{slipstream}}$$

19

$$C_L = C_{L_{condition}} + C_{L_{dynamic}} + C_{L_{slipstream}}$$

20

$$C_m = C_{m_{condition}} + C_{m_{dynamic}} + C_{m_{slipstream}}$$

21

The drag equation was considered to be build up of viscous effects, induced effects and slipstream effects. The influence of thrust on the drag is assumed to be a part of the slipstream effect. The following list gives an overview of all the influencing effects considered for Equs. 19-21, together with their physical interpretation. They are grouped into three general categories.

	effect of condition:
0	basic coefficient
α	influence of angle of attack
α^2	see α
δ_e	influence of elevator deflection
δ_s	influence stabilizer
$\delta_e \delta_s$	see δ_e en δ_s
C_L^2	induced drag

dynamic effect:

q	influence of pitch rate
α'	time delay in the influence of down wash on the horizontal tail
αq	influence of down wash on the pitch rate effect

slipstream effect:

T_c	influence of thrust after subtraction of the thrust
$T_c\alpha$	slipstream effect
$T_c\alpha\delta_e$	change in elevator effectiveness due to slipstream
$T_c\alpha\delta_s$	change in stabilizer effectiveness due to slipstream
$T_c\alpha\delta_e\delta_s$	see $T_c\alpha$ and $\delta_e\delta_s$

It was found that the pitching moment equation model can be improved in accuracy significantly by determining the ratio between the stabilizer and elevator effectiveness first. Therefore a number of so-called stabilizer-elevator exchange manoeuvres were flown at different conditions. The following linear regression equation result was obtained:

$$\frac{C_{m_{\delta_s}}}{C_{m_{\delta_e}}} = 1.713 - .35 \ \delta_s - .56 \ M^2 \qquad 22$$

From 19 combined elevator doublet manoeuvres following equations were identified after withdrawal of all insignificant terms:

$$C_D = C_{D_0}(T_c, M) + C_{D_{C_L^2}}C_L^2 \qquad 23$$

$$C_L = C_{L_0}(T_c, M) + C_{L_\alpha}\alpha + C_{L_q}\frac{q\bar{c}}{V} + C_{L_{\delta_e}}\delta_e + \qquad 24$$
$$C_{L_{\delta_s}}\delta_s + C_{L_{\delta_e\delta_s}}\delta_e\delta_s + C_{L_{T_c\alpha}}T_c\alpha$$

$$C_m = C_{m_0}(T_c, M) + C_{m_\alpha}\alpha + C_{m_q}\frac{q\bar{c}}{V} + C_{m_{\delta_e}}\delta_e + \qquad 25$$
$$C_{m_{\delta_s}}\delta_s + C_{m_{\delta_e\delta_s}}\delta_e\delta_s + C_{m_{T_c\alpha}}T_c\alpha +$$
$$C_{m_{T_c\alpha\delta_e}}T_c\alpha\delta_e + C_{m_{T_c\alpha\delta_s}}T_c\alpha\delta_s +$$
$$C_{m_{T_c\alpha\delta_e\delta_s}}T_c\alpha\delta_e\delta_s$$

Time selections of the data are applied to guarantee that the dynamic part of the manoeuvre containing the major part of the information is used for parameter identification.
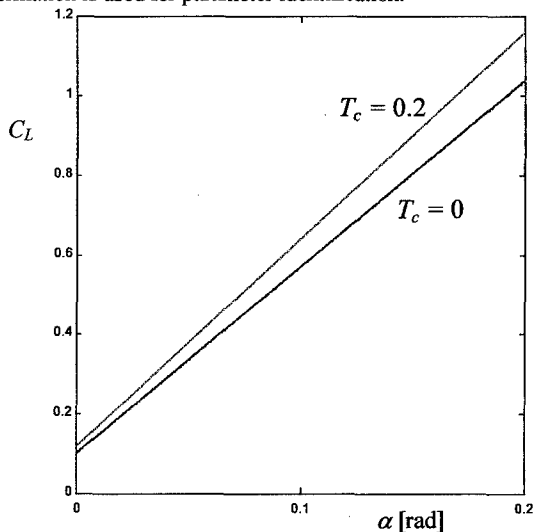

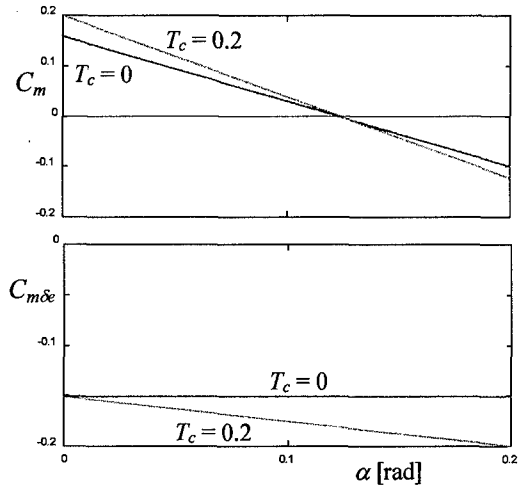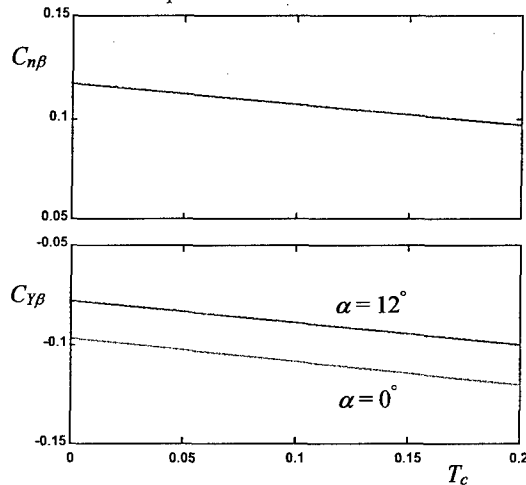Figure 14: Increase in lift due to propeller slipstream

Figure 15: Effect of propeller slipstream on C_m and $C_{m\delta e}$

The identified slipstream effects are plotted in Figure 14 for the lift and in Figure 15 for the pitching moment. Figure 14 shows that the slipstream causes an increase in lift. From Figure 15 it becomes clear that the propeller slipstream causes an increase in tail effectiveness once the tail moves downward into the propeller slipstream. Note that only linear behaviour is plotted because only first order effects were identifiable.

7.6 Lateral-directional slipstream effects

In principal the same basic approach as for the longitudinal-directional propeller slip stream effects holds for analysing the lateral-directional effects. To be able to extend the Equs. 15-17 by adding propeller slipstream effects, also here, sufficient variations in the measurement data of these effects must be present. This can be realised by combining a large number of manoeuvres taken at various conditions throughout the flight envelope.

The Equs. 15-17 were written more generally as follows:

$$C_Y = C_{Y_{condition}} + C_{Y_{dynamic}} + C_{Y_{slipstream}} \qquad 26$$

$$C_l = C_{l_{condition}} + C_{l_{dynamic}} + C_{l_{slipstream}} \qquad 27$$

$$C_n = C_{n_{condition}} + C_{n_{dynamic}} + C_{n_{slipstream}} \qquad 28$$

All the terms considered for Equs. 26-28 are listed below, together with their physical interpretation. They are grouped into three general categories.

effect of condition:

0	basic coefficient
β	influence of angle of sideslip
$\alpha\beta$	change in influence of angle of sideslip
δ_a	influence of aileron deflection
δ_r	influence of rudder deflection

dynamic effect:

p	influence of roll rate
r	influence of yaw rate
β'	time delay in the influence of sideslip on the vertical tail

slipstream effect:

T_c	asymmetrical slipstream effect
$T_c\alpha$	asymmetrical slipstream effect
$T_c\beta$	slipstream effect
$T_c\alpha\beta$	slipstream effect

Combining 16 rudder doublet manoeuvres with 7 aileron doublet manoeuvres following equations were identified after withdrawal of all insignificant terms:

$$C_Y = C_{Y_0}(T_c, M) + C_{Y_\beta}\beta + C_{Y_p}\frac{pb}{2V} +$$

$$C_{Y_r}\frac{rb}{2V} + C_{Y_{\delta_a}}\delta_a + C_{Y_{\delta_r}}\delta_r + \qquad\qquad 29$$

$$C_{Y_{\alpha\beta}}\alpha\beta + C_{Y_{T_c\beta}}T_c\beta$$

$$C_l = C_{l_0}(T_c, M) + C_{l_\beta}\beta + C_{l_p}\frac{pb}{2V} +$$

$$\qquad\qquad\qquad\qquad\qquad\qquad 30$$

$$C_{l_r}\frac{rb}{2V} + C_{l_{\delta_a}}\delta_a + C_{l_{\delta_r}}\delta_r$$

$$C_n = C_{n_0}(T_c, M) + C_{n_\beta}\beta + C_{n_p}\frac{pb}{2V} +$$

$$\qquad\qquad\qquad\qquad\qquad\qquad 31$$

$$C_{n_r}\frac{rb}{2V} + C_{n_{\delta_a}}\delta_a + C_{n_{\delta_r}}\delta_r + C_{n_{T_c\beta}}T_c\beta$$

Time selections of the data are applied to guarantee that the dynamic part of the manoeuvre containing the major part of the information is used for parameter identification.

Figure 16: Effect of propeller slipstream on $C_{Y\beta}$ and $C_{n\beta}$

The identified slipstream effects are plotted in Figure 16. It turned out that the C_{Y_β} and Cn_β derivatives are functions of the thrust. The figure shows that the slipstream causes an increase in sideslip force while the tail effectiveness reduces. Note that only linear behaviour is plotted because only first order effects were identifiable. More information can be found in Ref. 15.

8. CONTROL SYSTEM MODELLING

8.1 Introduction
The flight controls of the Metro II are operated manually and they incorporate a cable and/or push-pull tube system with aerodynamic as well as spring balancing.
In this paper both a model equation for the motion and a model equation for the control forces will be discussed. The identification of the coefficients in these model equations will be based on flight test data.
In a first attempt various approaches have been tried in identifying the elevator control model (different sets of variables, different model equations, different time selections). It turned out that identification from sweep manoeuvres with frequencies varying up to 1 Hz results into far more accurate models than from doublet

manoeuvres. Most likely explanation of this finding is the fact that the lowest elastic eigen mode of the aircraft structure is 3 Hz; it is believed that the mechanical control system interferes strongly in case of resonance of the aircraft structure. Note that a doublet excitation contains all frequencies and as a consequence also the elastic eigenmodes of the whole structure. The eigen frequencies of e.g. the mechanical elevator control system was observed to be 5 Hz as became clear from a ground test. Another additional explanation for the fact that sweeps result in a more accurate control model is concluded from the finding that Coulomb forces turned out to be significant while they are not clearly visible in the resulting control force of a block shaped doublet input. A more detailed analysis of the Metro II elevator system is reported in Ref. 16 and of the rudder and aileron system in Ref. 17.

8.2 Elevator control motion and control force modelling
In the following a mathematical model for the Metro II elevator will be established. Three models have to be established to describe the elevator behaviour. The three models are as follows:

1. The ground model:
   A simple model for the elevator behaviour on the ground can be derived from a ground test.

2. The relation between the column- and elevator movement:

$$\delta_e = f(\varphi_e, \dot{\varphi}_e, \ddot{\varphi}_e, \delta_e, \dot{\delta}_e, \ddot{\delta}_e, \alpha, q, q_c) \qquad 32$$

   This equation is required to make the input into the aerodynamic model sufficiently accurate.

3. The equation describing the control forces:
   For the control forces, a separate equation was identified describing the control force as function of all relevant mechanical and aerodynamic variables:

$$F_e = f(\varphi_e, \dot{\varphi}_e, \ddot{\varphi}_e, \delta_e, \dot{\delta}_e, \ddot{\delta}_e, \alpha, q, q_c) \qquad 33$$

Note that the force F_e is in reality input of the control function and may be removed to the right hand side and replaced by e.g. δ_e as will be discussed later on.

8.2.1 *The ground model*
A ground test was performed on the Metro II allowing the determination of following characteristics of the elevator-mechanics:
- The static spring behaviour, i.e. the spring constant of the mechanical linkage between column and elevator.
- The eigen frequency of the elevator-cable system and the column cable system.
- The moment of inertia of the column-cable-elevator system.
- The maximum possible excitation frequency on the ground.
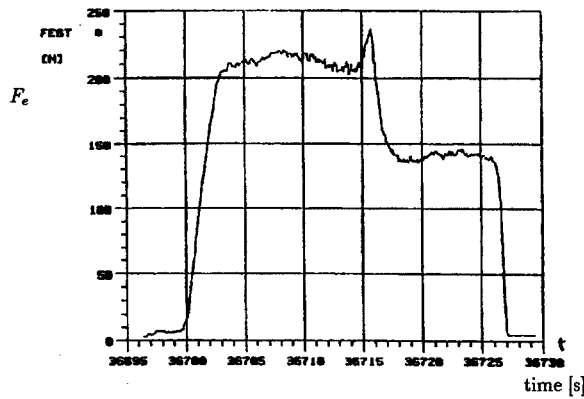- The elevator deflection range

Figure 17: Control force during ground test

For the behaviour of the control forces on the ground, a very simple model can be derived, without aerodynamic forces, based on ground tests. The plot in Figure 17 is made from one limit (fully forward) to the opposite limit (fully backward) and back. Due to the elevator downspring the control force is positive everywhere. The remarkable big difference between the force that is required to pull the column compared to the force to release the column results from static friction. The simple model for the elevator force on the ground was found to be:

$$\delta_e = F_{down} \quad for \ \dot{\varphi}_e \geq 0$$
$$F_e = F_{up} \quad for \ \dot{\varphi}_e < 0$$

$$34$$

8.2.2 The kinematic column elevator model

No dynamic behaviour could be identified in the frequency range up to 3 Hz. All influencing variables except φ_e, α and δ_s were proven to be negligible. For one flown condition the identified equation is of the form:

$$\delta_e = C_0 + C_{\varphi_e}\varphi_e + C_\alpha\alpha + C_{\delta_s}\delta_s \qquad 35$$

8.2.3 Control force model

Different approaches were tried to identify a control force model:

- identification of two acceleration equations
- identification of two position equations

Identification of two acceleration equations
The first approach was to identify a model consisting of two second order differential equations. Since there are two spring-mass systems an attempt is made to identify these two systems:

$$\ddot{\delta}_e = f(F_e, \ \delta_e, \ \dot{\delta}_e, \ \alpha, \ q, \ q_c)$$
$$\ddot{\varphi}_e = f(F_e, \ \dot{\varphi}_e, \ \varphi_e, \ \alpha, \ q, \ q_c, \ \delta_e, \ \dot{\delta}_e) \qquad 36$$

From a mechanical point of view Equ. 36 may be written by the following set of Equs. (37 through 41):
column system:

$$I_{col}\ddot{\varphi}_e = F_e l_{e_1} + F_1 l_{e_2} + F_c l_{e_2} \qquad 37$$

elevator system:

$$I_e\ddot{\delta}_e = H_e - F_2 l_{\delta_e} + F_3 l_{\delta_e} \qquad 38$$

cable stretch:

$$F_1 = F_2 = C_{ke}(l_{\delta_e}\delta_e - l_{e_2}\varphi_e) \qquad 39$$

hinge moment:

$$H_e = C_{h_e} q_c S_e \bar{c}_e (C_{h_0} + C_{h_\alpha}\alpha + C_{h_q}\frac{q\bar{c}_e}{V} + C_{h_{\delta_e}}\delta_e +$$
$$C_{h_{\dot{\delta}_e}}\frac{\dot{\delta}_e\bar{c}_e}{V} + C_{h_{\delta_s}}\delta_s) \qquad 40$$

It was experienced that it was practically impossible to achieve a sufficient accurate identification of model Equ. 36.

The goal is to obtain at least a model which describes well the slow motion and the static behaviour as appear during "everyday" flight operation. This can easily achieved by modelling the variables δ_e and φ_e instead of their time derivatives or accelerations. Moreover, it is important to obtain an accurate model for δ_e since it is one of the control parameters of the aerodynamic model generating, on its turn, the aircraft response.

Identification of two position equations
The model describing the static behaviour is of the following form:

$$\delta_e = f(F_e, \ \dot{\delta}_e, \ \ddot{\delta}_e, \ \delta_s, \ \alpha, \ q, \ q_c)$$
$$\varphi_e = f(F_e, \ \delta_e, \ \dot{\delta}_e, \ \ddot{\delta}_e, \ \alpha, \ q, \ q_c) \qquad 41$$

It turned out that it was not possible to achieve a sufficient accurate model for the high frequency part of the sweep above 3 Hz. Equ. 41 has been identified as follows:

$$\delta_e = C_0 + C_{q_c}(q_c S_e)^{-1} + C_{\dot{\delta}_e}\frac{\dot{\delta}_e}{q_c S_e} + C_{\ddot{\delta}_e}\frac{\ddot{\delta}_e}{q_c S_e} +$$
$$C_{F_e}\frac{F_e}{q_c S_e} + C_{\delta_s}\delta_s + C_\alpha\alpha + C_q\frac{q\bar{c}_e}{V} \qquad 42$$

together with φ_e which is defined by using Equ. 35. An example of the model fit is shown in Figure 18.
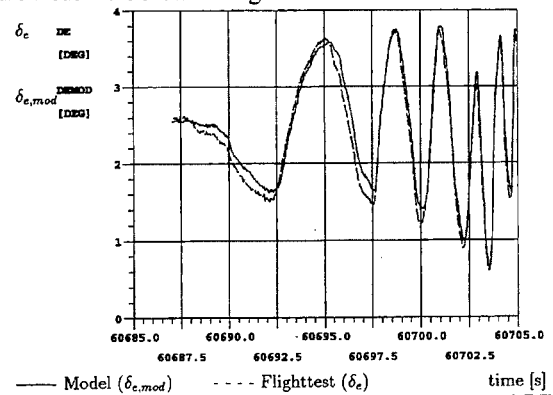

Figure 18: Match of elevator control model

The final models are derived by forming tables of the identified coefficients as functions of thrust setting and flap setting.

8.3 Rudder control motion and control force modelling

During stationary flight conditions there is a constant ratio between the pilot control force F_r and the rudder hinge moment H_r :

$$F_r G_r = H_r$$

The constant G_r is called the "rudder gearing coefficient". During non stationary flight conditions the influence of inertia can be included:

$$F_r G_r = H_r + I_r \ddot{\delta}_r \qquad 44$$

where I_r represents the inertia of the whole rudder control system. Friction and Coulomb friction may be required as well resulting in the equation:

$$F_r G_r = H_r + I_r \ddot{\delta}_r + C_{h_{visc_r}} \dot{\delta}_r + C_{h_{coul_r}} \text{sign}(\dot{\delta}_r) \qquad 45$$

In order to identify the mechanical behaviour of the rudder steering control, only ground tests are needed. Following parameters were identified by analysing ground test data.
- rudder deflection range
- pedal displacement range
- pedal-rudder gearing
- moments of inertia and damping by analysing a ground sweep

The aerodynamic influences on the rudder have to be analysed and added to Equ. 45, which is a second order differential equation. Following aerodynamic influences were investigated:
- rudder deflection
- angle of sideslip
- rate of yaw
- rate of roll

The pilot control force F_r has been split into two separate forces:

$$F_r = F_{r_{ground}} + F_{r_{aero}} \qquad 46$$

$F_{r_{ground}}$ is already known from the ground test identification. Assuming that inertia and damping do not change during flight, the in-flight measured pilot force can be corrected for the mechanical force to obtain the aerodynamic influence:

$$F_r - F_{r_{ground}} = F_{r_{aero}} \qquad 47$$

$F_{r_{aero}}$ represents the aerodynamic influences and was used to identify following equation:

$$F_{r_{aero}} = q_c S_r (C_0 + C_{\delta_r} \delta_r + C_{\dot{\delta}_r} \frac{\dot{\delta}_r \bar{c}_r}{2V} + C_\beta \beta + \qquad 48$$
$$C_p \frac{p \bar{c}_r}{2V} + C_r \frac{r \bar{c}_r}{2V})$$

The influences of the parameters $\dot{\delta}_r$, p and r were found to be negligible so that Equ. 48 simplifies to:

$$F_{r_{aero}} = q_c S_r (C_0 + C_{\delta_r} \delta_r + C_\beta \beta) \qquad 49$$
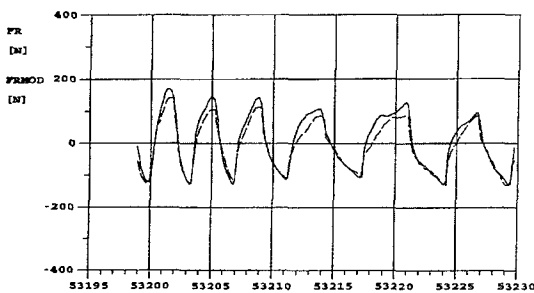

Figure 19: Match of rudder control force

Figure 19 shows a comparison of the measured and modelled control force. Significant asymmetrical behaviour is visible which seems to be typical for this individual aircraft.

8.4 Aileron control motion and control force modelling

During stationary flight conditions there is a constant ratio between the pilot control force F_a and the aileron hinge moment H_a:

$$F_a G_a = H_a \qquad 50$$

The constant G_a is called "aileron gearing coefficient".

During non stationary flight conditions the influence of I_a which represents the inertia of the whole aileron control system can be included by adding the term $I_a \ddot{\delta}_a$.

Influence of friction
Friction is a force proportional to velocity. A cross plot of the steering-wheel deflection against the pilot force shows a gap between positive and negative aileron motion caused by Coulomb friction. It can be described by a constant $C_{h_{coul_a}}$ times the sign of the motion. Viscous friction and Coulomb friction are thus both required, resulting in the equation:

$$F_a G_a = H_a + I_a \ddot{\delta}_a + C_{h_{visc_a}} \dot{\delta}_a + C_{h_{coul_a}} \text{sign}(\dot{\delta}_a) \qquad 51$$

In order to identify the mechanical behaviour of the aileron steering control, only ground tests are needed. Following parameters were identified by analysing ground test data.
- aileron deflection range
- wheel displacement range
- wheel-aileron gearing
- moments of inertia and damping by analysing a ground sweep

The aerodynamic influences on the aileron have to be analysed and added to the second order differential equation (Equ. 51). The following aerodynamic influences were checked:
- aileron deflection
- angle of sideslip
- rate of yaw
- rate of roll

The pilot control force F_a has been split into two separate forces:

$$F_a = F_{a_{ground}} + F_{a_{aero}} \qquad 52$$

The in-flight measured pilot force can be corrected for the mechanical force to obtain the aerodynamic influence:

$$F_a - F_{a_{ground}} = F_{a_{aero}} \qquad 53$$

$F_{a_{aero}}$ represents the aerodynamic influences and was used to identify following equation:

$$F_{a_{aero}} = q_c S_a (C_0 + C_{\delta_a} \delta_a + C_{\dot{\delta}_a} \frac{\dot{\delta}_a \bar{c}_a}{2V} + C_\beta \beta + \qquad 54$$
$$C_p \frac{p \bar{c}_a}{2V} + C_r \frac{r \bar{c}_a}{2V})$$

The influences of the parameters $\dot{\delta}_r$, p and r were found to be negligible so that Equ. 54 simplifies to:

$$F_{a_{aero}} = q_c S_a (C_0 + C_{\delta_a}\delta_a + C_\beta\beta) \qquad 55$$
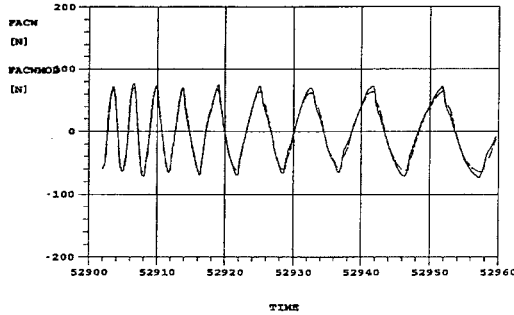
Figure 20: Match of aileron control force

Figure 20 shows a comparison of the measured and modelled control force.

9. UNDERCARRIAGE MODELLING

This chapter describes the identification of an undercarriage model of the Swearingen Fairchild Metro II. The undercarriage model includes the modelling of components like gear, tires, breaks, damper and steering equipment. The model is based on measurements and on theoretical considerations. Basic assumptions and simplifications will be discussed. A more detailed analysis of the Metro II undercarriage is reported in Ref. 18.

The Metro II has three gears (nose gear, left main gear and right main gear). The force and moment vectors on the gears are defined in the body co-ordinate system:

$$\vec{F}_{UC} = \sum_{i=1}^{3} \vec{F}_{UC_i}$$

$$\vec{M}_{UC} = \sum_{i=1}^{3} (\vec{F}_{UC_i} \otimes \vec{l}_i) \qquad 56$$

The z component of the lever arm l depends on the vertical deflection of the gear:

$$l_{z_i} = l_{z_{i_0}} + \delta_i \qquad 57$$

Assuming a rigid fuselage, the following relationship holds:

$$\delta_i = l_{z_i} - h_{cg} - l_{x_i}\sin\theta + l_{y_i}\cos\phi \qquad 58$$

So far, the basic interaction of the gear struts with the runway are described. These interactions have to be numerically expressed as functions of there physical behaviour resulting in a set of elementary models. These elementary models will briefly be explained as related to the direction of the force components.

Since the horizontal force models need the normal force as an input, the z-model is examined first. The side force model requires a brake force as input, therefore the second section examines the x-force and finally the third section deals with the side force.

9.1 Forces in z direction

The gears can be modelled assuming a spring-damper system. Generally, the vertical force from a gear can be described by:

$$F_{z_i} = f_{spring_i}(\delta_i) + f_{visc_i}(\dot{\delta}_i) + f_{coul_i}\text{sign}(\dot{\delta}_i) \qquad 59$$

A possibility to measure the spring behaviour of the gear struts and the tires is to put the aircraft on jacks. Three jacks need to be placed near each of the three gear struts. The deflection of each gear can be varied by varying the altitudes of the corresponding jacks. Electronic balances under each gear measure the force of each individual strut. The measurements were made for both a gradual increase and a gradual decrease of the individual deflections. The actual deflection of the tire and the strut spring are measured separately. Figure 21 shows the spring measurements for one of the main gears. The maximum spring force in the measurements corresponds to a load factor of n=1. During landing however, the undercarriage has to support a higher load factor and therefore those measurements have to be extrapolated.
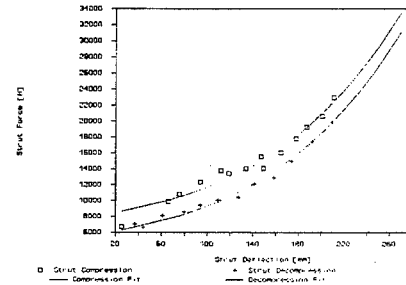
Figure 21: Spring characteristics for the left main gear

To be able to do this an accurate model equation is required which has been identified as follows:

$$F_{z_i} = F_{\delta^3_i}\delta^3_i + F_{\delta_i}\delta_i + F_0 + F_{coul_i}\text{sign}(\dot{\delta}_i) \qquad 60$$

The third power term accounts for the non-linear pneumatic spring.

The damping behaviour of the gear struts has been identified from measurement results obtained during manually induced eigen-oscillations of the aircraft pitch angle. The numerical value of the damping has been computed from the ratio of the vanishing oscillations after excitation. The force in z direction thus reads:

$$F_{z_i} = F_{\delta^3_i}\delta^3_i + F_{\delta_i}\delta_i + F_{\dot{\delta}_i}\dot{\delta}_i + F_0 + F_{coul_i}\text{sign}(\dot{\delta}_i) \qquad 61$$

9.2 Forces in x direction

Two forces are considered: friction of the tires and the brake force. The friction is defined by:

$$F_{roll_i} = \mu_{roll_i}F_{z_i} \qquad 62$$

The friction coefficient is a function of the velocity, the condition of the runway and condition of the tire.

The actual amount of the brake force is commanded by the pilot via the brake pedal deflection. The brake torque is then produced by an hydraulic system. A delay between the change in brake pedal deflection and the change in brake force exist and depends on the sign of this change and of the whether condition.

9.3 Forces in y direction

The side force results from a non zero yaw angle of the tires. A non zero yaw angle of the nose wheel is used to steer the aircraft on the ground. A number of relatively complex approaches for the calculation of this side force can be found in the literature. The side force can be calculated from:

$$F_{y_i} = F_{z_i}\mu_{side}\tau_i \qquad 63$$

where τ is a rather complicated function of the yaw angle, the condition of the surface and the speed. The physics of this relation is fairly complex. The equations describing this complex behaviour are based on theoretical considerations and not on parameter identification and therefore will not be discussed here. The applied theoretical background is extensively described in e.g. Refs. 18, 19 and 20.

The measurement data for the side force as a function of tire ground slip are derived from turns at different speeds. The theoretical model has been trimmed to those data.

10. CONCLUSIONS

The in-flight identification project has successfully demonstrated the feasibility of determining accurate aerodynamic models in real-time. However, the on-line procedure only yields a linear model valid for each individual test condition. The subsequent off-line analysis has shown that there is still a lot of work to be done before a complete simulator model is obtained. A model has to be developed that is valid for a large range of conditions and this can only be done by carefully piecing together information from a large number of different flights. In this analysis a large number of sometimes subtle effects have to be taken into account. This can be done by analysing a large number of combined manoeuvres distributed over a range of conditions. In this paper the effect of propeller slipstream has been treated extensively, but subsequent analysis has shown that a further considerable improvement in model consistency can be obtained by incorporating the effect of fuel slosh, moments of inertia errors and elasticity into the models. This research will be reported separately.

The relations between the pilot control forces and control surface deflections have been identified with sufficient accuracy. Special attention was paid to the identification of a model that reacts in a realistic way for flight conditions that appear often in "everyday" flight traffic. It was experienced that only in-flight low frequency sweep manoeuvres were useful for the identification of the control system, which is most likely due to elastic eigen-modes of the aircraft. The determination of the control models and the undercarriage model involved a number of static an dynamic ground tests where on-line identification is of no benefit.

Finally, the NSM technique has proven to be an accurate and cost effective tool both for on-line and off-line analysis.

11. REFERENCES

1. Gerlach, O.H. The determination of stability derivatives and performance characteristics from dynamic manoeuvres. Delft University of Technology, Report VTH-163, 1971.

2. Breeman, J.H., Simons, J.L. Evaluation of a method to extract performance data from dynamic manoeuvres for a jet transport aircraft. NLR MP 78021 U, 1978.

3. Mulder, J.A., Jonkers, H.L., Horsten, J.J., Breeman, J.H., Simons, J.L. Analysis of aircraft performance, stability and control measurements. AGARD lecture series no. 104 on parameter identification, 1979.

4. Breeman J.H., Erkelens L.J.J., Nieuwpoort, A.M.H. Determination of performance and stability characteristics from dynamic manoeuvres with a transport aircraft using parameter identification techniques. AGARD FMP Symposium on Flight Test Techniques, Lisbon, 1984.

5. Nieuwpoort, A.M.H., Breeman, J.H., Erkelens, L.J.J., Geest, P.J. v.d. Correlation between flight simulation and processing of flight tests based on inertial measurements. NLR MP 85058 U, 1985.

6. Baarspul, M., Mulder, J.A., Nieuwpoort, A.M.H., Breeman, J.H. Mathematical model identification for flight simulation, based on flight and taxi tests. DUT Report LR-550, April 1988.

7. Mulder, J.A., Baarspul, M.,Breeman, J.H., Nieuwpoort, A.M.H., Verbraak, J.P.T., Steeman, P.S.J.M. Determination of the mathematical model for the new Dutch Government Civil Aviation School flight simulator. SFTE paper, 18th Annual Symposium, Amsterdam.

8. Nieuwpoort, A.M.H., Breeman, J.H., Baarspul, M., Mulder, J.A. Phase II flight simulator mathematical model and datapackage, based on flight test and simulation techniques. 16th ICAS-Congres, Jerusalem, 1988.

9. Mulder, J.A., Breeman, J.H., Sridhar, J.K. on Identification of Dynamic Systems-Applications to Aircraft, Part 2: Nonlinear Analysis and Manoeuvre Design. AGARDograph 300 Vol.3, 1994.

10. Laban, M., On-Line Aircraft Aerodynamic Model Identification. Ph.D. dissertation Delft University of Technology, 1994.

11. Breeman, J.H., Laban, M., Mulder, J.A. NLR/DUT Experience with On-Line Aerodynamic Model Identification. SFTE European Chapter Symposium, Toulouse, 1997.

12. Klein, V. Estimation of aircraft aerodynamic parameters from flight data. Prog. Aerospace Sci. Vol. 26, p. 1-77, 1989.

13. Muhammad, H., Mulder, J.A., Identification of turboprop thrust from flight test data. SFTE, Amsterdam, 1994.

14. Muhammad, H., Identification of turboprop thrust from flight test data. Ph.D. dissertation Delft University of Technology, 1995.

15. Kannemans, H. Recent experience in modelling the NLR Metro II research aircraft. NLR TP 95457 U, 1995.

16. Tröndle, G. Modelling of the flight control system of the regional airliner Metro II. TUBs OA 95/175.

17. Langenbach, H. Modelling of the flight control system of the regional airliner Metro II. TUBs OA 96/ to be published.

18. Gräber, M. Design of the Undercarriage Model of the Regional Airliner Swearingen Fairchild Metro II. TUBs OA 95/362.

19. Waki, M.K., Yourkowski, F.M. 757-200 crew training simulator - Ground handling data. Boeing Commercial Aircraft Company, Seattle.

20. Anon. Boeing landing gear mathematical models and data for flight training simulators. (B707, 727, 737, 747), June 1976.

CLOSED-LOOP SYSTEM IDENTIFICATION EXPERIENCE FOR FLIGHT CONTROL LAW AND FLYING QUALITIES EVALUATION OF A HIGH PERFORMANCE FIGHTER AIRCRAFT

Patrick C. Murphy
NASA Langley Research Center, Mail Stop 132
Hampton, Virginia 23681-2199, USA

SUMMARY

This paper highlights some of the results and issues associated with estimating models to evaluate control law design methods and design criteria for advanced high performance aircraft. Experimental fighter aircraft such as the NASA High Alpha Research Vehicle (HARV) have the capability to maneuver at very high angles of attack where nonlinear aerodynamics often predominate. HARV is an experimental F/A-18, configured with thrust vectoring and conformal actuated nose strakes. Identifying closed-loop models for this type of aircraft can be made difficult by nonlinearities and high-order characteristics of the system. In this paper only lateral-directional axes are considered since the lateral-directional control law was specifically designed to produce classical airplane responses normally expected with low-order, rigid-body systems. Evaluation of the control design methodology was made using low-order equivalent systems determined from flight and simulation. This allowed comparison of the closed-loop rigid-body dynamics achieved in flight with that designed in simulation. In flight, the On Board Excitation System was used to apply optimal inputs to lateral stick and pedals at five angles of attack: 5, 20, 30, 45, and 60 degrees. Data analysis and closed-loop model identification were done using frequency domain maximum likelihood. The structure of the identified models was a linear state-space model reflecting classical 4th-order airplane dynamics. Input time delays associated with the high-order controller and aircraft system were accounted for in data preprocessing. A comparison of flight estimated models with small perturbation linear design models highlighted nonlinearities in the system and indicated that the estimated closed-loop rigid-body dynamics were sensitive to input amplitudes at 20 and 30 degrees angle of attack.

NOMENCLATURE

b	number of eigenvector elements specified
C_{lp}	nondimensional aerodynamic rolling moment coefficient due to roll rate
$C_{n\beta}$	nondimensional aerodynamic yawing moment coefficient due to sideslip
d	number of measurements
m	number of controls
n	number of states
n_z	normal acceleration, g's
n_y	lateral acceleration, g's
p_{max}	maximum roll rate, deg/sec
p_s	stability-axis roll rate, rad/sec
r_s	stability-axis yaw rate, rad/sec
α	angle of attack, rad.
β	sideslip, rad.
ϕ	bank angle, rad
λ	eigenvalue

η_{ped}	pilot pedal input, lbs./105.38
η_{stick}	pilot lateral stick input, in./3.57
ω	frequency, rad/sec
ζ	damping ratio
τ_a	lateral stick input time delay
τ_r	rudder pedal input time delay

A/B	afterburner
ANSER	Actuated Nose-Strakes for Enhanced Rolling
AOA	Angle of Attack
CHR	Cooper-Harper flying qualities rating
CRAFT	Control Power Robustness Agility and Flying Qualities Tradeoffs
DEA	Direct Eigenspace Assignment
DR	Dutch Roll
HARV	High Alpha Research Vehicle
HATP	High Alpha Technology Project
HIL	Hardware-in-the-loop
MDA	McDonnell Douglas Aerospace
Mil-Std	Military Standard Specifications
MIMO	multi-input/multi-output
NL	nonlinear
OBES	On-Board Excitation System
PIO	pilot induced oscillation
PsC	Psuedo Controls
RMS	root mean square
S	Strake mode of ANSER control law
SID	System Identification
STV	Strake and Thrust-vectoring mode of ANSER control law
TV	Thrust-vectoring mode of ANSER control law

INTRODUCTION

An important step in flight control law development is a rigorous flight test program to test system performance, stability and control. As part of the flight test evaluations test pilots are typically required to assess the quality of manual control during specified maneuvers usually in terms of the Cooper-Harper rating scale [1]. Obtaining favorable pilot ratings may lead a designer to believe that the control design methodology was effective. However, without models identified from flight test data, representing the closed-loop dynamics of the system, there is only qualitative evidence that the design method was successful. Using system identification techniques to identify closed-loop models provides direct evidence as to whether the intended dynamics were achieved and can explain the cause of unexpected pilot ratings or aircraft behavior. To be completely successful, however, an important part of the identification process must also address the high-order and typically nonlinear characteristics of modern high performance aircraft systems.

This paper will provide some results of the closed-loop modeling effort performed during the NASA High-Alpha Technology Program (HATP) [2]. One goal of this program was to develop advanced control law design

methodologies for fighter aircraft with high levels of agility and high angle-of-attack (high-α) capability. This effort has provided the Actuated Nose Strakes for Enhanced Rolling (ANSER) control law [3]. The ANSER control law was designed for the NASA High Alpha Research Vehicle (HARV) and was flight tested over a three year period from 1994 to 1996. HARV is a highly modified F/A-18, configured with two novel control effectors: thrust vectoring and conformal actuated nose strakes. More details of these control effectors can be found in [4,5]. The lateral-directional control law was designed to use yaw thrust vectoring and forebody strakes individually or in combination. The longitudinal control law [6] uses pitch thrust vectoring throughout the flight envelope.

Control design methods and control design criteria were integral parts of the overall control design approach studied in the HATP program. The design methods used were a combination of CRAFT (Control Power, Robustness, Agility, and Flying Qualities Tradeoffs) [7] and Pseudo Controls (PsC) [8,9]. The combination of CRAFT and PsC is a hybrid design technique that combines both linear and nonlinear design methods. The design criteria used to develop the ANSER control law were taken from several sources covering a spectrum of design guidelines from those flight-validated and commonly used at low-α to high-α guidelines that are currently a subject of research. The goal of this hybrid technique was to develop a control law that would provide the HARV with agile maneuvering capability and Level 1 flying qualities in high-α flight. In addition, a complete set of nonlinear design guidelines [10] was used to design the final ANSER control law. Although the nonlinear design guidelines are an important aspect of the research in HATP, only linear flying qualities specifications are considered in this paper.

One goal of the system identification effort in HATP was to evaluate control design methods and control design guidelines for their success in developing the ANSER lateral-directional control law. To perform evaluations of both design method and design criteria, low-order equivalent systems (LOES) were estimated from both flight data and from nonlinear simulation data for comparison. These models are identified in the form of 4th-order state-space representations of the closed-loop system. Estimated state-space models were required for the control law evaluation since the control law design method directly defined the eigenspace for the low order, multi-input/multi-output (MIMO), closed-loop system. This approach allows comparison of low-order desired dynamics determined in the control law design process using CRAFT with low-order dynamics achieved in nonlinear simulation and in flight. Merit of the design methodology was determined by the degree of success in achieving the desired closed-loop dynamics. Flying qualities criteria was assessed by comparison of achieved dynamics with pilot ratings obtained in flight. This paper presents some of the system identification problems and issues that arose during the evaluation of the design methods and flying qualities design guidelines. The evaluation is restricted to the lateral-directional ANSER control law in thrust-vector (TV) mode without nose strakes activated.

CONTROL LAW OVERVIEW

A key set of objectives for the lateral-directional control law was to provide good flying qualities, robustness, and agility appropriate for an advanced fighter aircraft while respecting the control power limitations of the experimental vehicle. This included optimal blending of control effectors and management of system changes as the novel control effectors, thrust-vectoring and forebody strakes, are included in the control mix or as the conventional aerodynamic controls become ineffective at high α.

In the ANSER control system, lateral stick commands stability axis roll rate and pedals command a conventional body yaw rate response. The control law is designed for "feet on the floor" control by the pilot for normal coordinated flight. The feedback gains and pilot input gains were designed at twelve flight conditions (α: 5 to 60 degrees for every 5 degrees, $n_z=1g$, altitude=25K feet). Feedback gains were designed using the CRAFT method. In the control law the pilot input gains are scheduled with α, n_z, and altitude; and the feedback gains are scheduled with α. The measurements used for inner-loop feedback control are body axis roll rate, body axis yaw rate, lateral acceleration, and an estimated sideslip rate. The controls are aileron, rudder, differential stabilator, yaw thrust vectoring and actuated forebody strakes. Differential leading and trailing edge flaps were not used.

CRAFT and PsC were integrated to synthesize the lateral-directional control law for HARV. The Pseudo Controls method was applied to HARV as a way of allocating pilot commands to all the lateral-directional controls. For the HARV, an envelope was defined over a wide range of angle of attack, Mach number, and engine thrust settings. Pseudo Controls allows feedback design for a reduced problem, since it maps multiple control inputs into a minimum orthogonal set of control inputs. This maximizes the coordinated use of the available control power. In addition, the control law is simplified by substantially reducing the number of feedback gains. With this reduced system, CRAFT was used efficiently to determine the "optimum" eigenspace for a measurement feedback control law.

The CRAFT design approach determines linear, multivariable feedback gains by using Direct Eigenspace Assignment (DEA) [11] and a graphical framework to trade-off multiple and often conflicting design requirements. DEA provides a mechanism to determine measurement feedback control gains that produce an achievable eigenspace for the closed-loop system. It has been shown [12] that for a system that is observable and controllable with n states, m controls, and d measurements, one can exactly place d eigenvalues and m elements of their associated eigenvectors in the closed-loop system. DEA provides feedback gains that place b elements ($m<b<n$) of d eigenvectors associated with d eigenvalues through a least squares fit of the desired eigenvectors to the achievable eigenspace. The CRAFT method satisfies a need to incorporate multiple design requirements into the flight control design process. Design requirements that can be quantified are readily included. Generally, these requirements fall into one of four categories of design metrics: 1) control power, 2) robustness, 3) agility, and 4) flying qualities. Details of the CRAFT design process are presented in [7].

In the design process for HARV, due to the frequency separation between the rigid-body and higher-order modes the feedback design was performed on 4th order rigid-body lateral-directional models only. However, stability

analysis (gain and phase margin calculations) was done using full 26th order linear system model of the plant and control law. The 26th order model included actuator models, sensor models, compensation filters, aeroelastic models and corresponding notch filters. Nonlinear simulation allowed designers to uncover any limitations inherent in the linear analysis and allowed tuning of critical elements such as command gains. This portion of the development was followed by extensive piloted simulation and hardware-in-the-loop tests.

The flying qualities design criteria used to develop the ANSER lateral-directional control law are drawn from several sources. For low α, the commonly used Mil-STD 1797A [13] and the fighter-specific study of Moorhouse-Moran [14] were used. Moorhouse-Moran criteria was used as the preferred criteria. These criteria are shown in figures 1 and 2. The Cooper-Harper level 1 and level 2 regions of the Mil-Std criteria represent the largest areas and the Moorhouse-Moran the smallest areas. The desirable regions used in the Moorhouse-Moran study are much smaller than the Mil-Std because of the restricted nature of the tasks considered; these tasks were specifically tailored to modern high-performance fighter missions.

At the beginning of the control design effort, NASA sponsored McDonnell Douglas Aerospace (MDA) to develop flying qualities criteria at three stall and post-stall angles of attack. This work did not define Dutch Roll mode criteria, therefore the Moorhouse-Moran criteria was used except when control power limitations at $\alpha = 60$ degrees prevented the criteria from being met. The early MDA work was done concurrently with the HARV control law development and was reported in [15] and [16]. Lateral criteria were developed for stability-axis roll rate command systems. Figure 3 show flying qualities specifications [15] for desirable roll mode dynamics at high α for a lateral-directional fine-tracking maneuver. These criteria, presented in both low-order equivalent system modal parameter and bode envelope formats, have been refined and are summarized in reference [17].

CONTROL LAW DESIGN METHOD EVALUATION

For this report, the method evaluation will primarily focus on a comparison of desired versus achieved closed-loop rigid-body eigenvalues. This is a very focused view considering the wide variety of linear and nonlinear design guidelines affecting any control system design. For evaluation of the CRAFT-PsC design method, however, using the achieved linear dynamics as a primary evaluation metric is appropriate since an important result of the CRAFT design process is the determination of the best linear rigid-body dynamics for the aircraft. One design goal for the ANSER control law was to provide desirable rigid-body dynamics in fine-tracking maneuvers over a large range of α. Fine-tracking maneuvers require relatively small pilot inputs and therefore tends to produce linear responses, which supports using linear analysis of both flight and simulation results. Fine-tracking maneuvers, used in the HARV experiment, were designed to allow development of high-α flying qualities criteria and associated evaluation tasks. This work was done in simulation by McDonnell Douglas Corporation under task order contract to NASA LaRC and detailed task descriptions can be found in reference [17].

Linear Design Rigid-Body Dynamics

Rigid-body dynamics were defined over the entire range of α in conjunction with analysis of HARV capabilities, mission requirements, linear guidelines, and nonlinear guidelines that were also part of HATP research. The results of this analysis produced the HARV ANSER design goals for the rigid-body dynamics. These dynamics are shown in figure 4 as solid lines. Only the roll mode and Dutch Roll mode frquency and damping ratio are shown. Although the spiral mode was also included in the ANSER control law design, it is not a dominant mode and will not be shown in this paper. Dutch Roll mode specifications for low α, defined by Mil-Std 1797A level 1 requirements and Moorhouse-Moran, were assumed to be valid for high α. Mil-Std 1797A requires the product of Dutch Roll frequency and damping ratio to be greater than 0.4. As shown in figure 4, design goals of $\zeta_{DR}=0.7$ and $\omega_{DR} \geq 1.0$ are indicated over the entire range of α for HARV. MDA criteria, developed in simulation, were used as a guide for roll mode dynamics at α equal to 30, 45, and 60 degrees.

For the ANSER control law, the CRAFT design process used 4th-order linear plant models extracted from nonlinear simulation using a small perturbation approach to obtain the Jacobian matrices. Small perturbation models may be used for design purposes if the full nonlinear system has relatively mild nonlinearities and the linear models adequately describe the nonlinear system responses to small inputs. As the degree of nonlinearity increases, the small perturbation models can produce dramatically different models with only small changes in the trim operating point or in the size of perturbation. For the HARV simulation used in design, some substantial nonlinearities exist in the aerodynamic model, especially for α between 20 and 30 degrees. These nonlinearities found in wind tunnel studies have been flight validated by Klein [18].

The feedback gains used in the ANSER control law applied to the 4th-order design models of HARV in TV mode produce the dynamics indicated in figure 4 as the "low order linear" case. The differences between the design goals and the low order case are completely due to intentional changes in feedback gains to accommodate the S (nose strakes only) and STV (strakes and TV) modes. Although CRAFT provides a design tool that allows matching of design specifications, in this case, it does not lend itself to matching 3 distinct aircraft configurations, simultaneously, with one set of feedback gains. The movement of the rigid-body dynamics with the introduction of higher order dynamics is shown in figure 4 as the difference between the "low order" and "high order" cases. The results of increasing order of the system were a slight increase the speed of the Roll subsidence mode and Dutch Roll mode frequency as well as a small increase in Dutch Roll damping.

Rigid-Body Dynamics Achieved in Flight And Nonlinear Simulation

Low-order equivalent systems of the MIMO closed-loop system for ANSER-HARV in TV mode were estimated from flight data to provide a direct comparison with the corresponding design models estimated from simulated data. Both flight data and simulated data were sampled at

80 Hz. Corrections for sensor offsets from the center of gravity were applied to angle of attack, sideslip angle and accelerometer signals from flight. Angle of attack was corrected for upwash and small data compatibility corrections were also applied to the flight data.

Optimal inputs were designed for this study as a series of square waves optimized to maximize information content for a fixed time period [19]. The inputs are documented in references [20-22]. This method was chosen because only very short maneuver times were available. This constraint resulted from the limited time the test aircraft could remain at a given flight condition when testing at high α. Although modest changes in altitude did not dramatically change the system dynamics, the test aircraft had very large sink rates at high α and thus could significantly change the test condition if long test times were allowed. The input optimization technique also limited output amplitudes to avoid large deviation from the test condition. Test inputs were executed at the pilot station by a computerized On-Board Excitation System (OBES) after the pilot trimmed the aircraft at the specified test condition.

The estimated closed-loop models were linear, 4th order, lateral-directional models in state-space form. System states, $x = [\beta \; p_s \; r_s \; \phi \;]$, were sideslip angle, stability axis roll rate, stability axis yaw rate and bank angle. OBES inputs, $u = [\eta_{ped}(t-\tau_r) \; \eta_{stick}(t-\tau_a)]$, were rudder pedal force and lateral stick deflection normalized by factors of 105.38 and 3.57, respectively. Equivalent time delay parameters τ_r and τ_a were estimated to be 0.042 sec. and 0.038 sec., respectively, for the $\alpha=45°$ case. These values are representative over the α range studied. Equivalent time delay parameters were estimated separately in the time domain using the approach recommended in reference [13]. Final values for these parameters were formed by averaging response delays found for individual surfaces to the commanded input. Time delay parameters were applied to the inputs in the frequency domain before estimation and held fixed during estimation of the state-space systems to avoid parameter correlation problems. System outputs, $y = [\beta \; p_s \; r_s \; \phi \; n_y]$, were the four states and lateral acceleration. This form of the model allowed determination of the system eigenspace and thus direct comparison of design eigenvalues and eigenvectors achieved in nonlinear simulation versus the corresponding flight-achieved values. The closed-loop system eigenspace was the primary metric for verification of the CRAFT design methodology. The system matricies can be written as

$$
A = \begin{bmatrix}
Y_\beta & Y_{p_s} & Y_{r_s}-1 & \dfrac{g\cos(\theta_o)}{V_o}+Y_\phi \\
L_\beta & L_{p_s} & L_{r_s} & L_\phi \\
N_\beta & N_{p_s} & N_{r_s} & N_\phi \\
0 & \dfrac{\cos(\gamma_o)}{\cos(\theta_o)} & \dfrac{\sin(\gamma_o)}{\cos(\theta_o)} & 0
\end{bmatrix}
\tag{1}
$$

$$
B = \begin{bmatrix}
Y_{\eta_r} & Y_{\eta_a} \\
L_{\eta_r} & L_{\eta_a} \\
N_{\eta_r} & N_{\eta_a} \\
0 & 0
\end{bmatrix}
\tag{2}
$$

$$
C = \begin{bmatrix}
1 & 0 & 0 & 0 \\
0 & 1 & 0 & 0 \\
0 & 0 & 1 & 0 \\
0 & 0 & 0 & 1 \\
\dfrac{V_0}{g}Y_\beta & \dfrac{V_0}{g}Y_{p_s} & \dfrac{V_0}{g}Y_{r_s} & \dfrac{V_0}{g}Y_\phi
\end{bmatrix}
\tag{3}
$$

$$
D = \begin{bmatrix}
0 & 0 \\
0 & 0 \\
0 & 0 \\
0 & 0 \\
\dfrac{V_0}{g}Y_{\eta_r} & \dfrac{V_0}{g}Y_{\eta_a}
\end{bmatrix}
\tag{4}
$$

These system equations are very similar to the open-loop system equations except for parameters L_ϕ, N_ϕ, and Y_ϕ. These parameters account for a small feedback gain applied to bank angle by the control system. The controller provided gravity compensation during large bank angle rolls or multiple rolls by the aircraft.

Estimation of the closed-loop models was accomplished using a maximum likelihood method in the frequency domain after the model structure was determined using stepwise regression [23]. The frequency domain approach improved two steps in the identification process: (1) simplifies application of input time delays, and (2) automatically adjusts parameter error bounds to reflect the possibility of colored noise on the measurements [24].

Assuming a state-space model of the system, without process noise, the system can be written in the time-domain as

$$
\begin{aligned}
\dot{x} &= Ax + Bu, \qquad x(0) = 0 \\
y &= Cx + Du \\
z_i &= y_i + v_i
\end{aligned}
\tag{5}
$$

where z_i is the discrete ith measurement of the output vector y and v_i is the ith measurement noise vector that is assumed to be from a zero mean Gaussian random process.

In the frequency domain, the system given by equation (5) can be written as

$$
\begin{aligned}
\tilde{x} &= [i\omega I - A]^{-1} B\tilde{u} \\
\tilde{y} &= C[i\omega I - A]^{-1} B\tilde{u} + D\tilde{u} \\
&= G\tilde{u} \\
\tilde{z}_n &= G_n \tilde{u}_n + \tilde{v}_n
\end{aligned}
\tag{6}
$$

where G represents the system transfer function matrix in the frequency domain. The measurement noise statistics can be written as

$$
E(\tilde{v}_n) = 0; \qquad E(\tilde{v}_n \tilde{v}_n^*) = S_{vv}
\tag{7}
$$

where S_{vv} represents the spectral density of the measurement noise. The cost function, J, minimized to estimate the maximum likelihood parameters is

$$
J = \frac{1}{2}[z_n - G_n u_n]^* S_{vv}^{-1} [z_n - G_n u_n]
\tag{8}
$$

where parameter estimates are obtained by minimizing $J(\theta)$ with respect to unknow parameters, θ. Because of the resulting nonlinear estimation problem a modified Newton-Raphson technique was used to find the minimum of $J(\theta)$. This approach is described in references [25] and [19].

System Identification maneuvers were performed at α =[5 20 30 45 60] degrees. Parameter estimates at $\alpha=45°$ are shown in the following table

Parameter Estimates for System at $\alpha=45°$

parameters	estimate	error bound
Y_β	-0.0600	0.0045
Y_{p_s}	0.0091	0.0017
$Y_{r_s}-1$	-0.9881	0.0030
Y_ϕ	-0.0053	0.0013
Y_{η_r}	-0.0072	0.0004
Y_{η_a}	-0.0104	0.0004
L_β	-3.1214	0.1213
L_{p_s}	-0.6685	0.0462
L_{r_s}	0.8559	0.1167
L_ϕ	-0.2467	0.0338
L_{η_r}	-0.1447	0.0177
L_{η_a}	0.0967	0.0118
N_β	2.7912	0.0506
N_{p_s}	0	*
N_{r_s}	-1.8258	0.0462
N_ϕ	0.2157	0.0222
N_{η_r}	0.4594	0.0107
N_{η_a}	0.2516	0.0078

* parameter excluded during model structure determination

Errors for the flight identified system matrix elements were typically 5% to 10% of their mean values and all parameters had error bounds less than 15%, except for Y_{p_s} and Y_ϕ. The relatively small values of these terms likely made accurate identification difficult and small values of $\phi(t)$ also made the Y_ϕ term less identifiable. Very large bank angles were avoided to maintain linear responses to inputs. Figures 5 and 6 show time histories for the flight data and estimated model at 45 degrees angle of attack. To produce time history comparisons a second estimation is required to obtain bias parameters. A time-domain maximum likelihood estimation was performed with the estimated model parameters held fixed at the values shown while bias parameters were allowed to vary.

Figure 7 shows the rigid-body dynamics from flight estimated models. The poles show a classical airplane distribution as was intended by design. For comparison with flight estimated values, the corresponding dynamics estimated from nonlinear simulation are presented in figure 7. The parameters in nonlinear simulation models were estimated in exactly the same manner as the flight models. For the simulation problem, the actual optimal inputs used in flight were applied to nonlinear simulation and the time histories were then treated as simulated flight data.

Reasonably good agreement between flight and simulation is shown in figure 7. The poles from simulation and flight follow the same trends as a function of α although some small differences occurred at certain points, such as, at α equal to 30 and 60 degrees for Dutch Roll frequency and 5 and 20 degrees for Dutch Roll damping. The roll mode shows good agreement. Nonlinear simulation was performed without measurement noise in order to determine the best case design results and to establish a benchmark for comparison with flight results.

One and two sigma error bounds for the flight-estimated pole locations are shown in figure 8 as light and dark shades around the pole mean values. Error bounds were obtained by using Monte Carlo simulation in which each estimated parameter of the system was allowed to vary with a uniform probability distribution over a range defined by the corresponding error bound for that parameter. The Monte Carlo simulation was run 5000 times to ensure coverage of all possible combinations and the eigenspace was determined for each new system to produce the plots in figure 8. One and two sigma boundaries provide a 68% and 95% confidence levels that the true value is contained within the indicated bounds. For $\alpha > 5$ degrees the two sigma bounds allow a range of roll and spiral poles that produces a complex mode with roll-spiral coupling. For the high-α range relatively small error bounds were obtained. In general, these results indicate reasonably accurate system identification.

In a formal evaluation of CRAFT, assessment of the complete system eigenspace achieved in flight would be required. However, for brevity, this paper will present rigid-body pole locations as the primary evaluation metric of both CRAFT and the high-α design criteria. Eigenvectors estimated from flight data matched those in simulation with accuracy comparable to that found for the eigenvalues. As an example, figure 9 shows eigenvectors achieved in flight compared with those achieved in nonlinear simulation at $\alpha = 30$ degrees. Eigenvectors are shown as bar graphs, where the dominant eigenvector element is used to normalize the eigenvector. The element magnitudes are plotted for models estimated from flight and from nonlinear simulation. The four bars represent the four eigenvector elements corresponding to the four states [β (rad) p_s (rad/sec) r_s (rad/sec) ϕ (rad)]. The eigenvector comparison shows that the design modal shaping (from simulation) was achieved in flight reasonably well and that the shapes have a desirable aircraft form as intended.

System Identification Models vs Small Perturbation Models

Part of the design process for the ANSER lateral-directional control law required high-order linear models representing design points over the entire HARV flight envelope; these models were the primary tool for assessing stability margins. Creation of these models was accomplished by combining 4th-order, linear plant models with a linear model of the control law. In this form, a 26th-order linear perturbation model was obtained.

Figure 10 compares the rigid-body dynamics from high-order linear models with rigid-body dynamics from low-order equivalent systems obtained through system identification (SID) of flight and nonlinear simulation data. The low-order models identified from flight and

simulation are not obtained from small perturbations. They show the effects of system nonlinearities, such as rate limiting, that are not present in the small perturbation models. In addition, other nonlinearities, such as aerodynamic nonlinearities, will be expressed differently between the SID and small perturbation models. For both SID models and small perturbation models the nonlinearities create input-amplitude dependent variations in the models. However, because the amplitudes considered are quite different between the two approaches the resultant models can also be dramatically different. Careful assessment of nonlinearities is critical for any linear analysis of nonlinear systems.

Figure 10 shows reasonably good agreement between the SID models identified from flight and from nonlinear simulation. However, fairly large disagreement occurred between the SID models and the small perturbation models at $\alpha = 20$ and $\alpha = 30$ degrees. Since input amplitudes are orders of magnitude different between the two methods, nonlinearity must be investigated. Identifying SID models from simulation using a range of input amplitudes, allowed determination of a threshold input amplitude below which the estimated models' dynamics stopped changing. Figure 10 shows the poles from SID models where the input amplitudes were set at this threshold; the poles are identified as "low Amp NL Sim". These results were obtained by reducing the input amplitudes by 50% at $\alpha = 20$ degrees and by 40% at $\alpha = 30$ degrees. At $\alpha = 30$ degrees, the new SID model matches the small perturbation model. At $\alpha = 20$ degrees, further reduction of the input amplitude did not produce a significantly different model. The difference shown between these two cases at $\alpha = 20$ degrees is not resolved by adjusting SID input amplitude.

System Nonlinearities At $\alpha = 20$ Degrees

Two sources of error due to nonlinearity appear to exist since only a portion of the mismatch between SID and small amplitude models is explained by reducing input amplitude for the SID models. Another source of nonlinearity must explain the remaining mismatch at $\alpha = 20$ degrees. The difference between the reduced amplitude SID model and the small perturbation model at $\alpha = 20$ may be explained by considering the underlying plant aerodynamic model. Figure 11 shows C_{lp} and $C_{n\beta}$ as a function of α. This data was taken from Klein [18] where wind tunnel data for the HARV was flight validated by comparison with flight estimated aerodynamic parameters. These two aerodynamic parameters are strongly responsible for defining the roll mode and Dutch Roll mode frequency, respectively. At $\alpha = 20$ degrees, $C_{n\beta}$ exhibits a dramatic nonlinearity directly affecting the Dutch Roll frequency and at slightly under $\alpha = 22$ degrees, C_{lp} also exhibits a sharp nonlinearity affecting the roll mode. The variation of α during the flight experiment was approximately ±4 degrees from trim for all test points greater than $\alpha = 5$ degrees. This ensures that the nonlinearities at $\alpha = 20$ degrees were experienced during flight. Unless a flight experiment is designed specifically to capture a nonlinearity this sharp and the small perturbation model is developed respecting this characteristic, it is very difficult to achieve a match between SID and small perturbation models. Additional

unknown nonlinearities may have been introduced since β perturbations were slightly larger than expected during the flight experiment.

A second source of nonlinearity is predominantly due to rate limiting of the control surfaces. Rate limiting can produce a strong nonlinearity in the response data. In the simulation of the ANSER HARV system the no-load rate limit of the rudders is 82 deg/sec and under the loads experienced maneuvering at $\alpha = 20$ degrees, the loaded rate limit was approximately 75 deg/sec. For the same α maneuver in flight, the rudders rate limited at approximately 72 deg/sec for the right rudder and 67 deg/sec for the left rudder. To assess the effects of rate limiting, a metric defining the percent of time the surfaces experienced rate limiting was defined. The percent-of-time metric is computed as the percent of time during maneuver that the surface rate exceeds a specific threshold appropriate for that surface. The threshold for rudders, ailerons, and vanes was set at 60 deg/sec. The threshold for stabilators, which have substantially slower actuators, was set at 30 deg/sec. These thresholds reflect the loaded rate-limit capability of the stabilators and rudders, in particular.

Figure 12 shows the percent of time the surfaces experienced rate limiting for each α case considered. As shown in the figure, both rudder surfaces spent more than 35% of maneuver time in rate limit for the $\alpha = 20$ degrees case and more than 27% of maneuver time in rate limit for the $\alpha = 30$ degree case. By reducing the input amplitudes to the low amplitude thresholds, discussed previously, the percent time metrics were reduced to 18% and 9% for the cases where α was 20 and 30 degrees, respectively. It appears that a modest amount of rate limiting can be tolerated in flight and still allow reasonable dynamic matching of linear models between small perturbation models and SID models from flight. With rate limit metric values in the range of 10-15% the small perturbation models and SID models from flight have a reasonable match.

An Experiment Design Issue

A concern in designing the experiment for identification of closed-loop models from flight was finding input amplitudes that would strike a balance between being small enough to keep the responses in the linear range but large enough to keep response levels adequate for SID. Early in the flight test program, test pilots were asked to apply optimal inputs manually to the stick and pedals. OBES was not available during this testing. Although manual inputs have been used successfully in other flight test experiments, the spectrum and sequencing of the inputs are limited. These early flight tests were done using optimal inputs with lateral stick input amplitudes of approximately 1.5 inches and full pedal input amplitudes of 100 lbs. These tests were repeated using the same input form but with half the amplitude. The results indicated that half amplitude manual inputs were insufficient to produce adequate response information for SID. Unfortunately, the half amplitude inputs were representative of the amplitudes used by the pilots in fine-tracking maneuvers. In light of these results, more aggressive, full-amplitude inputs were designed for use with OBES to ensure good signal to noise ratios and adequate system excitation for SID. These inputs

were intentionally designed to maximize the response of the system and even allow a small amount of rate limiting.

The results in figure 10 and 12 indicate that the inputs for the test points at α equal to 20 and 30 degrees were too aggressive. Two factors contributed to this result. First, the control law command gains were large in this region in order to satisfy agility requirements. Second, the rate limits of the rudder actuators in flight were slower than expected. Limited test time prevented further testing to determine if OBES inputs could be reduced to provide adequate data with smaller input amplitudes. Fortunately, the match between simulation and flight models is reasonably good when comparable inputs are used to estimate models. This gives some confidence that the SID models determined with the lower amplitudes from simulation may represent the correct dynamics for the system. In addition, the match between simulation and flight time histories during fine-tracking is very good. In light of this, the dynamics experienced by HARV pilots during fine-tracking maneuvers is best represented in figure 10 by the flight and simulation models for all α except at α =[20 30] degrees. For these two cases, the best available representation of system dynamics is more likely given by "low Amp NL Sim" model dynamics.

System Dynamics: Variation With Normal Acceleration

An issue that arises when evaluating the high-α flying qualities design criteria is whether the SID models estimated from 1g flight correctly predict the dynamics corresponding to that occurring during fine tracking of a turning target aircraft. Although pilots are using relatively small inputs during fine tracking and therefore should be in the linear response range, fine tracking does occur in a loaded condition. Time histories for fine tracking maneuvers at α = 30 degrees show the flight loads are approximately 2 g's. For fine tracking at α equal to 45 and 60 degrees, the flight loads fall to approximately 1.5, g's. To address this question, the closed-loop rigid-body dynamics from models trimmed at 1 and 2 g's are presented in figure 13. This comparison is made using the low-order, closed-loop, linear design models (small perturbation models) for 1 and 2 g's. The results indicate that the roll mode is only slightly affected by g load over most of the α range. There is an increase in roll mode eigenvalue for α = 5 degrees and a modest decrease in value for α = 60 degrees. The Dutch Roll mode, on the other hand, is generally affected uniformly over the entire α range considered. Dutch Roll mode frequency is increased with an increased g load and Dutch Roll damping ratio is decreased.

The high-α design criteria provides roll mode specifications only at α equal to 30, 45, and 60 degrees [17]. The roll mode dynamics given in figure 10 were determined from 1g flight data and 1g simulation data using SID techniques at 5 α's. These roll mode dynamics can be compared with the high-α design criteria and should correctly represent that experienced in flight during fine tracking maneuvers. However, at α = 30 degrees, the most plausible estimate for roll mode during fine tracking is given by the low amplitude simulation value. Comparison of 1g model dynamics with the design criteria can be done for the following reasons: (1) the roll mode is not substantially changed under a 2g load for a range of α

extending from 10-50 degrees; and (2) although figure 13 indicates some reduction in roll mode eigenvalue at α = 60 degrees with a 2g load, the fine tracking maneuvers of interest at this α reach only 1.5 g's.

Dynamics Achieved in Flight vs Design Dynamics: Flying Qualities Summary

Achieving good flying qualities during fine-tracking maneuvers was an important design goal for the ANSER lateral-directional control law. To help judge the success of the control law, figures 14 and 15 display closed-loop rigid-body poles for ANSER (TV mode) in relation to the flying qualities criteria. The variation of these dynamics with α is also shown. The poles displayed are from three sources: (1) design goals; (2) flight-achieved dynamics; and (3) rate-limited dynamics.

Design goals (1) are the intended dynamics defined by high-order linear perturbation models. Flight-achieved dynamics (2) represent the rigid-body dynamics estimated from flight data, except at α equal to 20 and 30 degrees where excessive rate limiting occurred during the SID maneuvers. At these two α's, the best estimates of the flight-achieved dynamics, when rate-limiting is not occurring, is given by the "low Amp NL Sim" models. These models are estimated using nonlinear simulation responses to flight SID inputs with reduced amplitudes. This provides the best estimate of the dynamics experienced by pilots during fine tracking maneuvers in lieu of actual low input-amplitude flight data. During fine tracking maneuvers pilots are using sufficiently small inputs that actuator rate limiting is minimized and linear responses are obtained. Rate-limited dynamics (3), at α equal to 20 and 30 degrees, define the dynamics obtained with relatively large inputs. These are estimated from fight data where full-amplitude SID maneuvers resulted in excessive actuator rate limiting.

Figure 14 provides the Dutch Roll criteria from Mil-Std 1797A and the Moorhouse-Moran study. The boundaries indicated are for Level 1 flying qualities during Class IV, Category A flight at low α. For this study it was assumed to be valid over the entire α range. Superimposed on this graphic are the Dutch Roll poles for the 5 flight test points from α = 5 to 60 degrees. The plot shows that all the criteria were satisfied except for the flight-achieved Dutch Roll damping ratio at α = 60 degrees. At this flight condition the damping ratio fell below the design goal of 0.4 to 0.31. This was likely caused by a lack of control power since at this α the stabilator is position limited (differential stabilator provides some yaw control) and thrust-vectoring pitch priority logic is used.

Figure 15 provides the roll mode criteria from Moorhouse-Moran for low α and from MDA for α = 30 degrees. Roll pole locations representing the flight-achieved dynamics are plotted on this chart as roll mode time constants for each of the 5 test points. The corresponding design goals are also shown for these five points as well as two additional values at α equal to 10 and 35 degrees. All the low-α ($\leq 10°$) roll poles are well within the Moorhouse-Moran design criteria. The high-α roll poles from α = 20 to 35 degrees, although somewhat low relative to the criteria, still satisfy the requirements. Although no criteria

is provided for α equal to 45 and 60 degrees, the design values and achieved values are shown for comparison. Both design and flight-achieved poles are plotted with very low roll rate sensitivity values reflecting the low control power (relative to the criteria) available to the HARV vehicle at high α. Also shown is the substantial effect of rate-limiting on roll mode characteristics at α equal to 20 and 30 degrees. At both α's the roll mode time constant was approximately doubled in response to the rudders rate limiting more than 25% of the maneuver time. This moved the poles well out of the desirable regions for α equal to 20 and 30 degrees and into the α = 60 degrees region.

SID Issues Presented by Stick Characteristics

The MDA criteria uses stability axis roll rate sensitivity as a means of capturing both the roll rate capability and stick characteristics in one metric. Stick characteristics play an important roll in the pilot's perception of aircraft flying qualities, and since relatively small commands are used for fine-tracking maneuvers, roll rate sensitivity is a more appropriate metric than, for example, maximum roll capability. In the HARV-ANSER control system a nonlinear stick shaper is used to optimize the pilot's handling qualities. The shaper is a smooth parabolic function which allows full command authority by rapidly increasing stick sensitivity for relatively large input commands and reduces stick sensitivity for relatively small commands.

The stick shaper is not a dynamic element in the control law; it does, however, modify the pilot's commands. Because of these characteristics the stick shaper is a double-edged sword for the SID problem. The nonlinear shaper makes designing excitation inputs more difficult by modifying inputs, however, since it is not a dynamic element it does not change estimated system eigenvalues. A key concern for both the control law designer and the SID input designer is that the command inputs are not large enough to produce nonlinear responses such as rate-limiting. This type of nonlinear response will dramatically change the dynamics of the closed-loop system, as shown in figure 15.

Since the estimated eigenvalues are independent of the nonlinear stick shaper an assumption of 1 inch stick inputs is made to determine roll rate sensitivity and make all the plots with respect to the MDA flying qualities criteria. This value represents the size of maximum inputs normally required by pilots to perform fine-tracking maneuvers. This assumption is also supported by the shaper being approximately linear for small inputs.

CONTROL LAW DESIGN CRITERIA EVALUATION

High-α design criteria were developed in fixed-base piloted simulation with a variety of tracking tasks reflecting the gross acquisition and fine tracking. Control power and actuator limitations were not addressed in that study. In order to properly compare the flight estimated models and pilot ratings of this flight experiment with the design criteria it is necessary to use the "low Amp NL Sim" models for the 20° and 30° α cases. This should provide the best estimate of system dynamics experienced by the pilots. Although the "low Amp NL Sim" models are estimated from the nonlinear simulation, these models match flight time histories. In addition, the simulation and flight-estimated

model dynamics also matched well under rate-limited conditions.

Pilot ratings were determined using a Cooper-Harper scale [1] for tasks specifically designed to address the fighter fine-tracking task. This task, although well defined, still allows pilot's discretion as to the piloting method to achieve the goals of fine tracking. Consequently, it is possible to have different input characteristics for the same task. To demonstrate this, the statistics of three pilot's inputs were computed by estimating the mean, standard deviation, and maximum input over each pilot's flights. As shown in figure 16, a sample of three pilots performing the same fine tracking task at 30° α, indicates quite different input statistics. The figure shows a bar chart of the pilot's mean input (absolute value) during fine tracking. Pilots are indicated by the research program's pilot labels of D, E, and A, respectively. The mean values are small as would be expected for a fine tracking maneuver where the pilot frequently returns to a steady position on a smoothly turning target. The standard deviation bar chart characterizes the amplitude of each pilot's stick motion. Pilot E has substantially larger stick inputs during these maneuvers. The bandwidth of these inputs (not shown) was also dramatically higher compared with pilots D and A. The maximum deflection chart highlights the magnitude of the inputs for each pilot. Pilot E chose an approach for tracking with almost full command and at very high frequency. This would be more in line with a gross acquisition task or a task requiring very rapid maneuvering. Discussions with pilot E indicated a strong interest in detecting sensitivity to PIO. The result of large amplitude inputs, as was shown for the aggressive SID models, is severe rate limiting in the rudders. Consequently, substantially different dynamics were experienced by pilot E. In light of this result, pilot E's ratings must be associated with the rate-limited dynamics and not with the design values.

Figure 17 shows the linear design criteria for both low and high α, the best estimates of the roll mode dynamics experienced by pilots D, E, and A during fine-tracking, and the corresponding pilot's Cooper-Harper ratings. For the α = 30 degrees case where pilot E used large enough inputs to experience significant rudder rate-limiting the pole location is indicated with a * and the corresponding CHR is shown. No pilot ratings were obtained at low α. However, the low-α roll mode dynamics are indicated to show their relative position to the high-α results. For cases where rate limiting was not an issue, the pilot ratings shown in brackets represent an average rating from each pilot. Pilots D and A are shown at 30 α, pilots D, E, and A are shown at 45 α, and pilots D and E are shown at α = 60 degrees. One of the pilots flew the maneuvers at least three times for the cases with α equal to 30 and 45 degrees. The pilot rating for the rate-limited dynamics at α = 30 degrees was obtained from a single run using pilot E.

It appears that the dynamics achieved in flight resulted in a system that is mostly near the lower boundaries of the MDA criteria. At α = 30 degrees, the average pilot rating of CHR=3 agrees with the MDA level 1 boundary. The rate-limited pole location obtained in flight at α = 30 degrees suggests a level 2-3 boundary. CHR's of 3 and 4 by pilots D and A using low amplitude inputs, at α = 45 degrees,

suggests this may be near a level 1-2 boundary. At $\alpha = 45$ degrees, pilot E's CHR of 7 for the lateral-directional axis may have reflected deteriorated dynamics in the longitudinal axis which was rated by pilot E as CHR=8. Pilot E's large amplitude inputs caused rate limiting in the longitudinal axis causing poor dynamic response and may have caused cross contamination of the ratings. At $\alpha = 60$ degrees, a CHR=7 by two pilots clearly suggests the dynamics were undesirable, however, the Dutch Roll damping ratio was not within level 1 requirements and may have caused the poor ratings. This pole location may define a boundary between level 2 and level 3.

CONCLUDING REMARKS

Estimating linear, closed-loop, low-order equivalent systems facilitated evaluation of both the control law design method and the high angle-of-attack flying qualities design criteria. However, the results highlight several issues that should be considered before adopting this approach. Strong agreement existed between dynamics identified from flight and simulation at all α. However, at α equal to 20, 30 and 60 degrees the flight achieved dynamics were not as closely matched to the design goals determined by small perturbation models from simulation. At $\alpha = 20$ degrees, this was most likely due to a combination of rate limiting and very nonlinear plant aerodynamics. Errors due to rate limiting were removed from the simulation results by reducing input amplitudes. The remaining difference between the small perturbation model and the estimated model using system identification is believed to be related to the nature of small pertrubation models. Errors in small perturbation models can be magnified depending on the size of small perturbations selected to obtain Jacobian matrices from nonlinear systems. At $\alpha = 30$ degrees the difference between flight and simulation estimated models with the small perturbation model was completely accounted for by reducing input amplitude and correspondingly reducing the amount of rate limiting. A likely cause of mismatch at $\alpha = 60$ degrees may be lower levels of control power in flight than predicted by the small perturbation model. The small perturbation models in this study highlighted the nonlinear effects from rate limiting and from the basic aircraft aerodynamic model, particularly at α equal to 20 and 30 degrees.

These results highlight the fact that for flight test experiments of high performance aircraft several issues need to be considered in the experiment design. One issue concerns the degree of nonlinearity of the system under study. Careful experiment design, flight test, and data analysis are required but some a priori knowledge of the system may be required to account for certain system nonlinearities, especially strong nonlinearities that are not well modeled by classical rigid-body airplane models. Planning for linear, LOES identification experiments should include multiple input amplitudes to provide a basis for testing the degree of nonlinearity. Identifying the limits of validity the LOES is also needed when nonlinear responses are possible. Finding the limits of estimated linear models is similar in importance to estimating error bounds for the model parameter estimates. Separate analysis and identification of the control law and aerodynamic model might be required to determine the sources of some errors or nonlinearities. The same consideration should be applied to less classical higher

order systems, although that issue was not experienced with the lateral-directional system presented in this study due to the large frequency separation between the controller dynamics and the closed-loop, rigid-body dynamics. For this study, it was shown that these potential error sources can be overcome and accurate models can be identified from flight test if certain measures are taken to compensate for the various sources of error. Parameter error bounds of up to 10% on the estimated model parameters were estimated. The highest error bounds were associated with parameters which are typically very small and do not contribute significantly to the response.

An observation from this study is the importance of checking the validity of small perturbation models taken from full nonlinear simulatons. These models are typically used in control design and analysis to model the open-loop and closed-loop plant characteristics. Whether used in design or analysis a series of perturbation amplitudes for generating these models should be used to test the sensitivity of the plant dynamics to perturbation size. Linear models obtained from small perturbations can produce dynamics significantly in error depending on the degree of nonlinearity of the basic aerodynamic model. A check of the linear model responses against nonlinear simulation or the flight vehicle responses should be made at expected nominal operating input and response amplitudes. If nonlinearities exist, system identification methods may be preferred over small perturbation techniques to obtain linear design models. This would allow estimation of linear models that represent the nonlinear system as it operates with nominal input and response amplitudes. However, some strong nonlinearities may preclude the use of LOES altogether.

The percent of time actuators spend in rate limit was used effectively to highlight the nonlinear effect on linear dynamics. Although this was an effective metric for this study, it is not clear that the rate limit metric could be universally applied to any maneuver. The maneuvers used in this study were of the same duration and the optimal inputs had similar power spectrums designed to excite rigid-body dynamics. Comparing maneuvers with dramatically different input types may lead to errors in the comparison of percent time in rate limit. However, it may be useful to determine the appropriate benchmark value for each case or use the percent time metric with a specific input design specifically to test for such nonlinearity.

Another issue related to experiment design is to account for the sometimes different piloting techniques used by test pilots. In this study, the variation of input amplitude and frequency spectrum among the pilots produced dramatically different flying qualities evaluations. For modern high performance fighters the potential for amplitude dependent nonlinear response is very high and should be anticipated during the experiment design. For flying qualities evaluations, identification of models characterizing the system that pilots experience while performing fine tracking maneuvers needs consideration.

REFERENCES

1. Cooper, George E., and Harper, Robert P., Jr.: The Use of Pilot Rating in the Evaluation of Aircraft Handling Qualities. NASA TND-5153. April 1969.

2. Foster, J.V.; Bundick, W. T.; Pahle, J.W.: Controls for Agility Research in the NASA High-Alpha

Technology Program. SAE TP-912148. September, 1991.

3. HARV Control Law Design Team, "Design Specification for a Thrust-Vectoring, Actuated-Nose-Strake Flight Control Law for the High-Alpha Research Vehicle", NASA Technical Memorandum 110217.

4. Murri, D. G., Shah, G. H., DiCarlo, D. J., and Trilling, T. W., "Actuated Forebody Strake Controls for the F-18 High-Alpha Research Vehicle", Journal of Aircraft, Vol. 32, May-June, 1995.

5. Bundick, W. T., Pahle, J. W., Yeager, J. C., Beissner, Jr., F. L., Design of a Mixer for the Thrust-Vectoring System on the High-Alpha Research Vehicle. NASA TM 110228. June 1996.

6. Ostroff, A. J., Proffitt, M. S., "Longitudinal-Control Design Approach for High-Angle-of-Attack Aircraft", NASA TP 3302. February 1993.

7. Murphy, P.C., Davidson, J.B., Control Design for Future Agile Fighters. Presented at AIAA Atmospheric Flight Mechanics Conference. AIAA Paper No. 91-2882. August 1991.

8. Lallman, F. J., Relative Control Effectiveness Technique With Application to Airplane Control Coordination, NASA TP 2416, April, 1985.

9. Lallman, Frederick J.: Preliminary Design Study of a Lateral-Directional Control System Using Thrust Vectoring. NASA TM-86425, November 1985.

10. Hoffler, K.D.; Brown, P.W.; Phillips, M.R.; Rivers, R.A.; Davidson, J.B.; Lallman, F.J.; Murphy, P.C.; and Ostroff, A.J.: Evaluation Maneuver and Guideline Development For High-Alpha Control Law Design Using Piloted Simulation. AIAA Paper No. 94-3512. August, 1994.

11. Davidson, J. B., Schmidt, D.K., Flight Control Synthesis for Flexible Aircraft Using Eigenspace Assignment. NASA CR-178164. June 1986.

12. Srinathkumar, S.: Modal Control Theory and Application to Aircraft Lateral Handling Qualities Design, NASA TP-1234, June 1978.

13. Mil Std 1797A, Military Standard - Flying Qualities of Piloted Aircraft, January, 1990.

14. Moorhouse, D.J.; Moran, W. A.: Flying Qualities Design Criteria For Highly Augmented Systems. IEEE National Aerospace and Electronics Conference, NAECON May 20-24, 1985.

15 Kreckler, G.C., Wilson, D.J., Riley, D.R., High Angle-of-Attack Flying Qualities Criteria. AIAA 28th Aerospace Sciences Meeting, AIAA 90-0219, Jan. 8-11, 1990.

16. Wilson, D.J., Riley, D.R., Flying Qualities Criteria Development Through Manned Simulation for 45° Angle of Attack-Final Report. Vol. 1 and 2. NASA CR 4435. April 1992.

17. Wilson, D. J. and Citurs, K. D., "High Angle-of-Attack Flying Qualities Design Guidelines," NASA

Contractor Report 4681, Volumes I and II, February, 1996.

18. Klein,V., Ratvasky, T. R., Cobleigh, B. R., Aerodynamic Parameters of HARV Estimated From Flight Data. NASA TM 102692. August, 1990.

19. Morelli, E.A.: Optimal Input Design for Closed Loop Modeling at High Angles of Attack. AIAA paper 96-3418, AIAA Atmospheric Flight Mechanics Conference. San Diego, California. July 1996.

20. Morelli, E.A.: Piloted Parameter Identification Flight Test Maneuvers for Closed Loop Modeling of the F-18 High Alpha Research Vehicle (HARV). NASA CR 198268. February 1996.

21. Morelli, E.A.: Flight Test Maneuvers for Closed Loop Lateral-Directional Modeling of the F-18 High Alpha Research Vehicle (HARV) using Forebody Strakes. NASA CR 198270. February 1996.

22. Morelli, E.A.: Parameter Identification Flight Test Maneuvers for Closed Loop Modeling of the F-18 High Alpha Research Vehicle (HARV). NASA CR 198269. February 1996.

23. Klein,V., Batterson, J.G., and Murphy, P.C.: Determination of Airplane Model Structure From Flight Data by Using Modified Stepwise Regression", NASA TP-1916, 1981.

24. Morelli, E.A., and Klein, V.: Determining the Accuracy of Maximum Likelihood Parameter Estimates with Colored Residuals. NASA CR 194893. March 1994.

25. Klein, V. "Aircraft Parameter Estimation in Frequency Domain", AIAA paper 78-1344, Atmospheric Flight Mechanics Conference, Palo Alto, CA, August 1978.
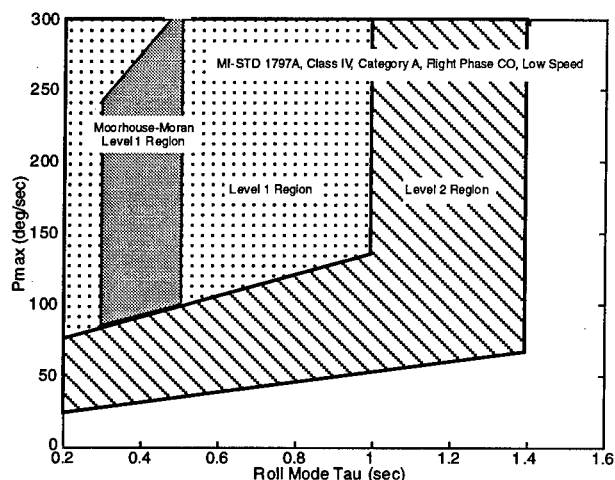
Figure 1. Roll mode specifications for low AOA.
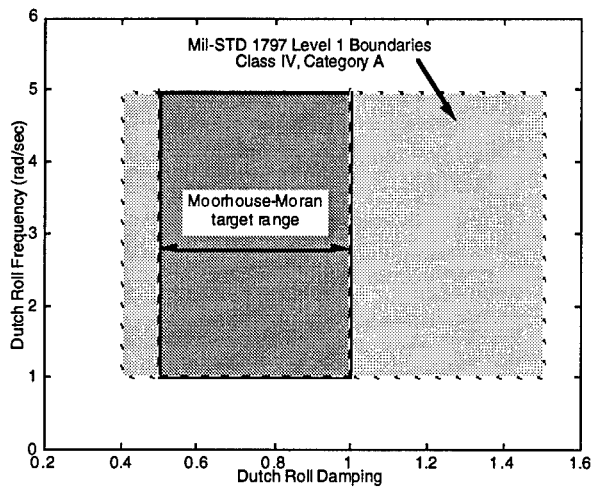
Figure 2. Dutch Roll mode specifications for low AOA.
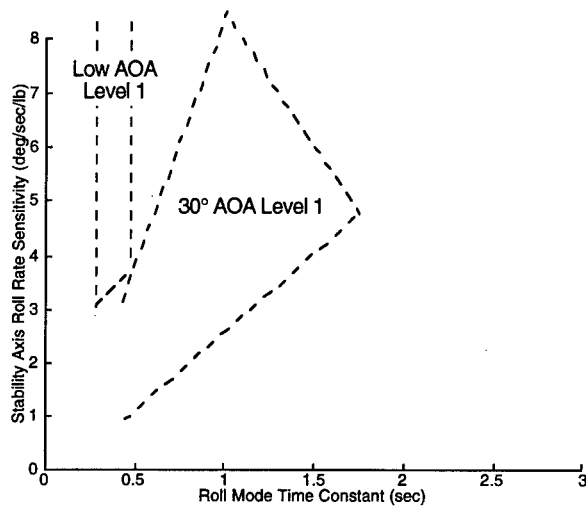
Figure 3. Roll mode specifications for fine-tracking maneuvers.
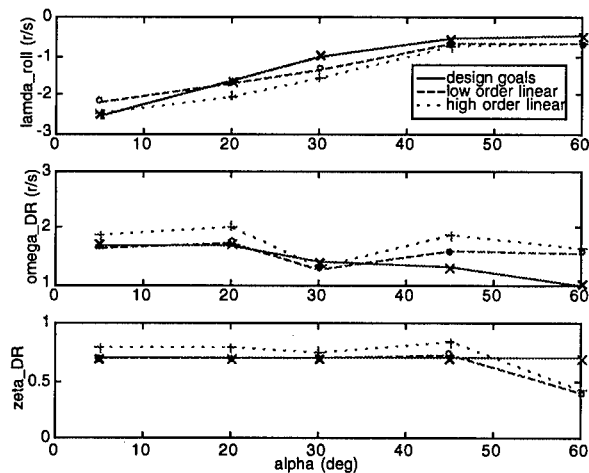
Figure 4. Rigid-body poles for design, 4th and 26th order models in TV mode.
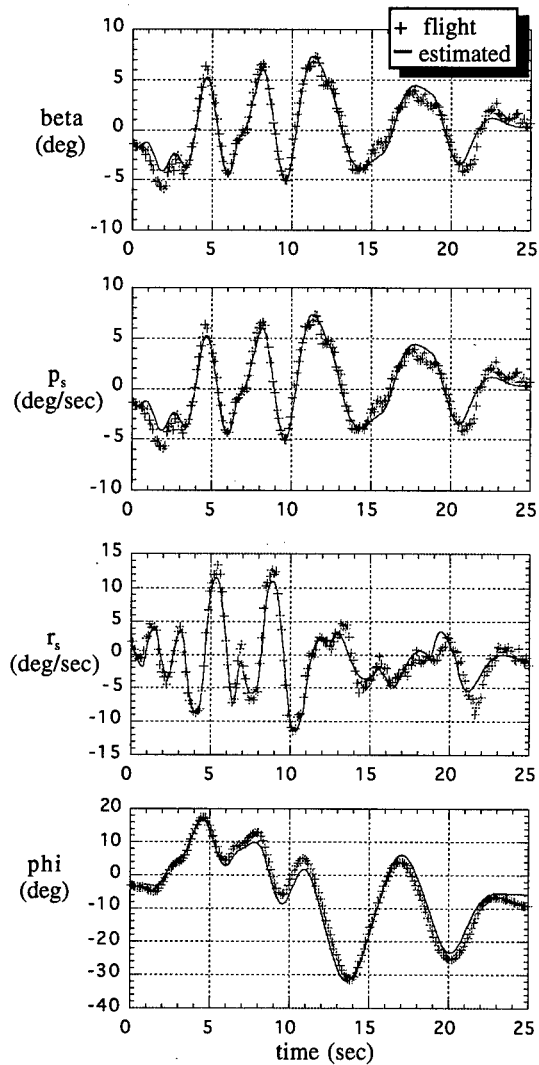
Figure 5 Sample time histories of measured and estimated responses at 45 degrees angle of attack.
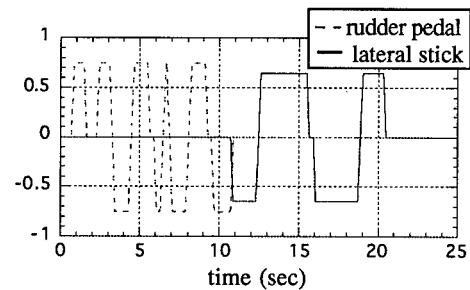
Figure 6. Sample input time histories to rudder pedal and lateral stick at 45 degrees angle of attack.
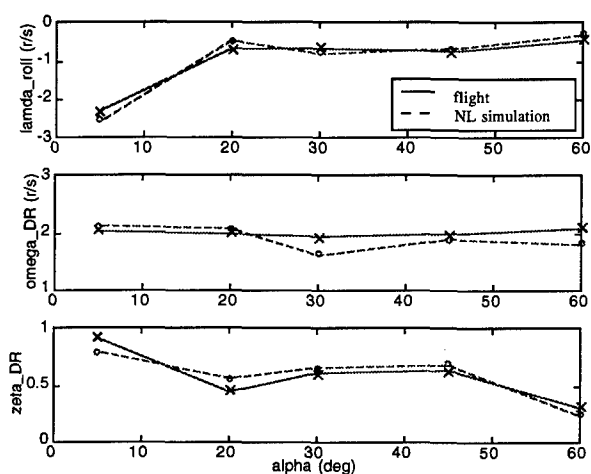
Figure 7. Rigid-body poles from SID models obtained using flight and simulation data.
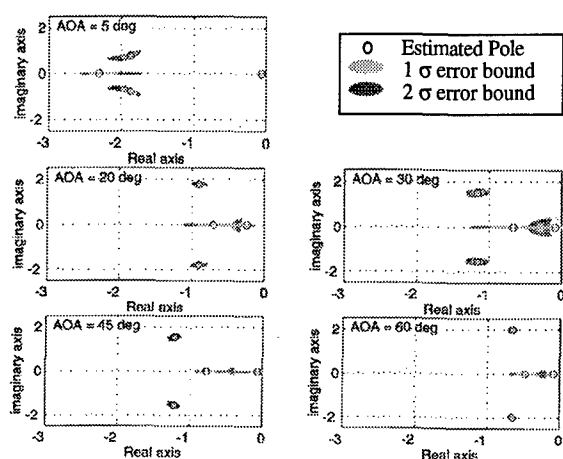
Figure 8. Flight estimated rigid-body poles with error bounds.
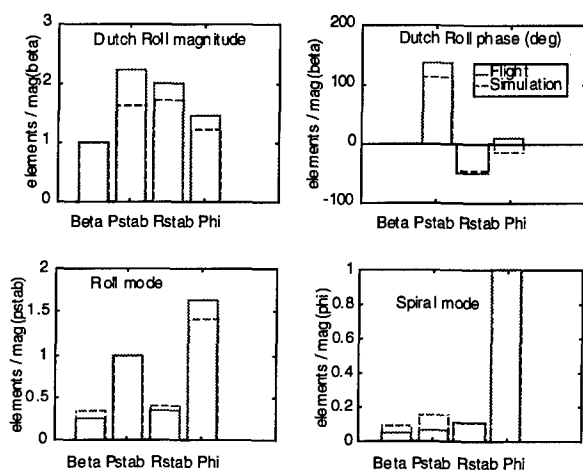
Figure 9. Stability axis eigenvectors estimated from flight and simulation SID models at 30° AOA
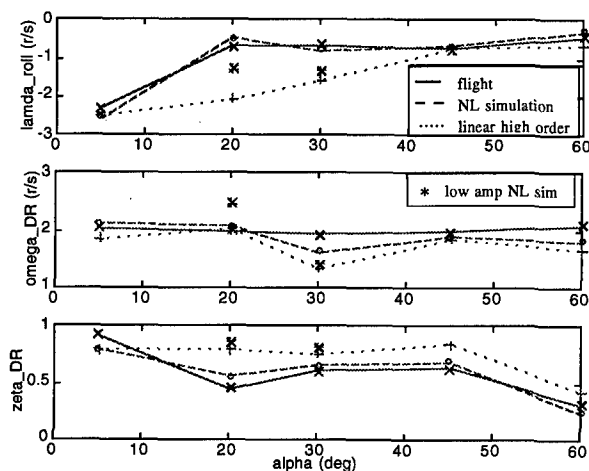
Figure 10. Rigid-body dynamics determined with large and small amplitude inputs.
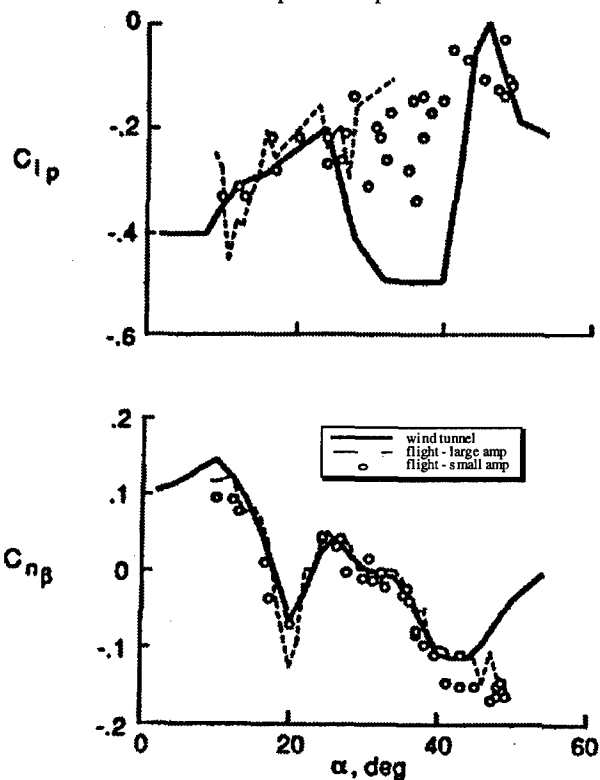
Figure 11. Aerodynamic parameters of HARV estimated from flight and wind tunnel data.
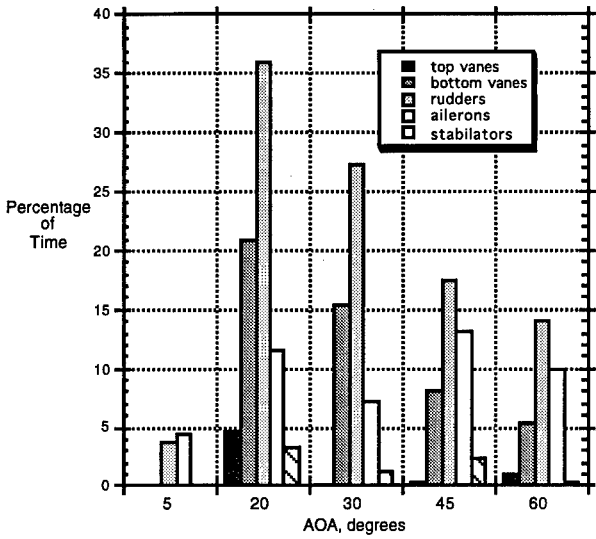
Figure 12. Percentage of time control surfaces were in rate limit during SID maneuvers.
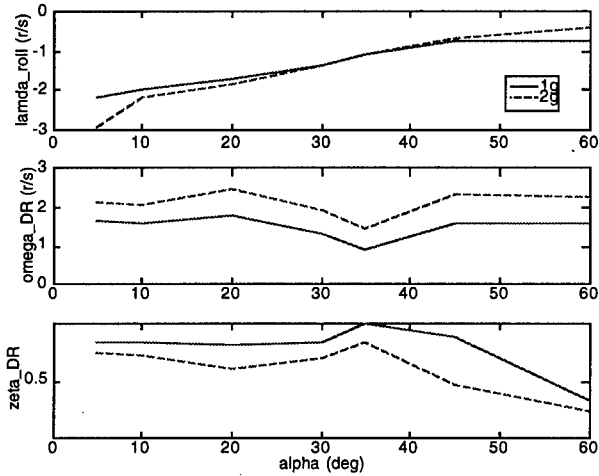
Figure 13. Variation of closed-loop rigid-body dynamics with normal acceleration.
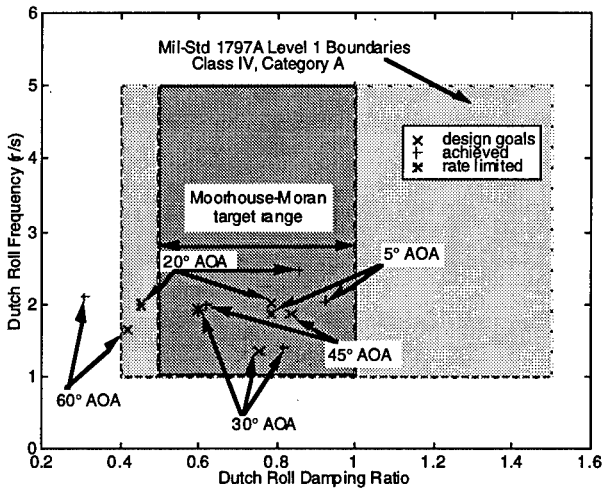
Figure 14. Dutch Roll poles with respect to flying qualities criteria.
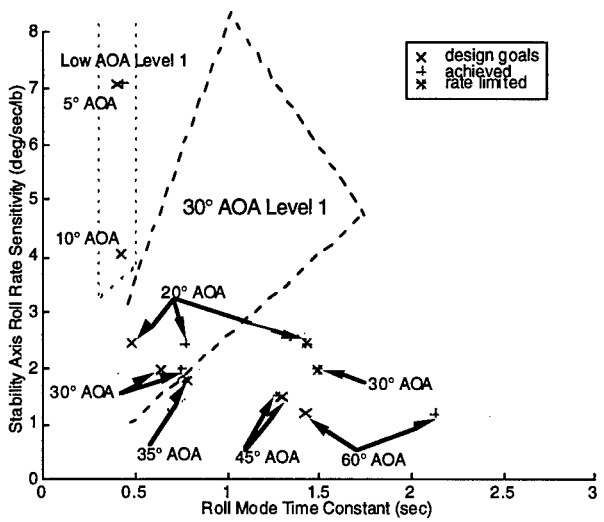
Figure 15. Roll mode poles with respect to flying qualities criteria.
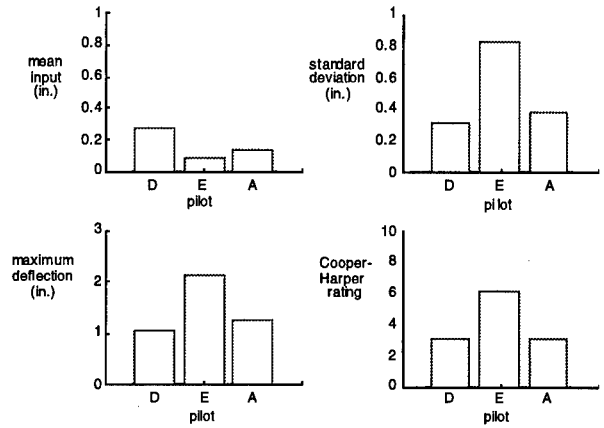
Figure 16. Pilot input characteristics during fine-tracking maneuvers at 30° AOA.
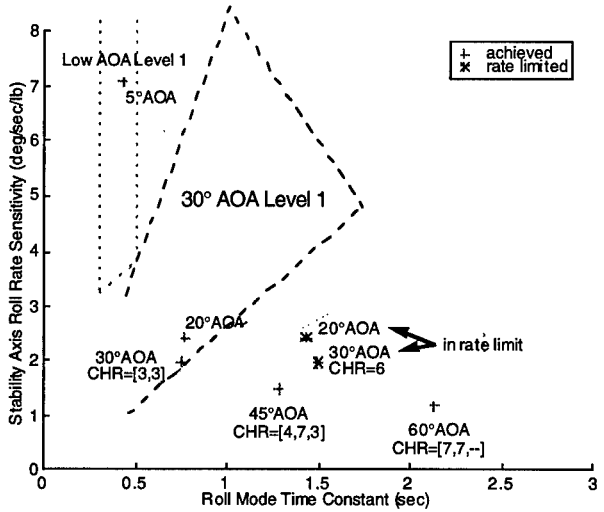
Figure 17. Pilot ratings for fine-tracking maneuvers vs flying qualities criteria.

Identification of Aircraft Stall Behavior
from Flight Test Data

D. Fischenberg and R. V. Jategaonkar

Institut für Flugmechanik
Deutsches Zentrum für Luft- und Raumfahrt (DLR)
Lilienthalplatz 7, D-38108 Braunschweig
Germany

1. SUMMARY

An unsteady 5-DoF aerodynamic model for flow separation and stall is presented. The model formulates lift, drag, and the moments in pitch, roll and yaw as a function of an internal state, namely the position of the flow separation point along the wing chord. In a quasi-steady case, this position is described as a function of the angle of attack and its rate of change, whereas in a transient case it is described in a state-space form using a first order differential equation. Using airfoil wind tunnel data, the plausibility of the model structure is discussed. In a second step, the parameters of the quasi steady and the transient model are identified for two different aircraft using stall flight test data. Validation plots demonstrate the model accuracy and it can be seen clearly that there are considerable unsteady effects at high angles of attack where flow separation occurs, which cannot be described properly using flight mechanic models for attached flow.

2. NOMENCLATURE

a_1	flow separation function coefficient
α	angle of attack
α^*	angle of attack for $x_0 = 0.5$
α_R	reference angle of attack
α_A	α-amplitude of oscillation
$\dot{\alpha}$	rate of change of angle of attack
c	reference chord
C_L	total A/C lift coefficient
$C_{L\alpha}$	lift curve slope
C_D	total A/C drag coefficient
C_m	total A/C pitching moment coefficient
Δt	time delay: r_t^*/V
Δy	effective lever arm
δ_e	elevator deflection
e	Oswald-factor
ϵ_t	downwash angle at horizontal tail
ϕ	bank angle
i_t	horizontal tail trim angle
k	reduced frequency $\omega c/V$

Λ	aspect ratio
ω	frequency
r_t	distance from CG to NP horizontal tail
r_t^*	distance from NP wing to NP horizontal tail
t	time
τ_1, τ_2	time constants
V	true airspeed
V_s	stall speed
x_0	location of steady flow separation point
x	location of unsteady flow separation point

Abbreviations:

A/C	aircraft
AoA	angle of attack
CAS	calibrated airspeed
CG	center of gravity
dyn	dynamic
FAA	Federal Aviation Administration
NP	neutral point

Subscripts:

0, st	steady
t	horizontal tail
V	vane
wb	wing-body

3. INTRODUCTION

The flight envelope of modern aircraft configurations is increasingly expanded to high angles of attack. In this region the aerodynamics is more nonlinear than in the conventional flight envelope, where the flow is completely attached to the wing surface and lift is a linear function of the angle of attack. In the high lift region different types of flow separation occur depending on airfoil shape or wing configuration. Trailing edge flow separation is the dominating effect on rough airfoils with a turbulent boundary layer. For thin airfoils, leading edge flow separation may occur additionally. Delta wing flow is often influenced by a vortex near the lead-

ing edge which separates and is transported down-stream. Generally, flow separation results in a reduction of the lift curve slope before maximum lift, whereas in the post-stall region a considerable loss of wing lift occurs. At these angles of attack, the airfoil lift cannot be described solely as a function of α, but is influenced substantially by unsteady effects.

Dynamic wind tunnel tests (e.g. ref. 1) or evaluated flight test data from highly maneuverable aircraft (e.g. ref. 2) demonstrate the lift dependency on $\alpha, \dot{\alpha}$ and the motion prehistory at high angles of attack. Recently, some models for the description of unsteady effects including flow separation were published.[3,4] These models are partly based on model formulations for unsteady helicopter rotor aerodynamics.[5,6]

The quality of those descriptions encouraged to apply them for aircraft stall modeling. Ref. 7 modified the approach of ref. 3,4 and the model parameters were identified for two different transport aircraft using flight test data. Additionally, the unsteady aerodynamic effects during stall could be demonstrated and validated with the test data.

This paper reflects ref. 7 and validates the model with airfoil wind tunnel data in order to verify its structure for unsteady aerodynamics including transient behavior and the approximation for steady stall characteristics. As a second step, the unsteady model is split into a quasi-steady formulation and a formulation including transient effects. Both models are discussed in terms of applicability for simulator models in FAA Level C/D quality[8]. Flight test data of two aircraft are used for validation: C-160 military transport aircraft and Dornier DO 328 regional transport aircraft. For these aircraft, simulator models exist that represent the aerodynamics in the conventional angle of attack range very properly.[9,10]

4. UNSTEADY FLOW SEPARATION MODEL FOR LIFT

Most wings of conventional aircraft have a rough airfoil with a turbulent boundary layer. On those airfoils, flow separation mainly begins at the trailing edge, and moves to the airfoil leading edge with increasing angle of attack. This trailing edge flow separation is the dominating effect for angle of attack rates of $\dot{\alpha} < 0.02V/c$, ref 3,5. At an assumed stall speed $V_s = 60m/s$ and a chord $c = 3.5m$ this is equivalent to $\dot{\alpha} < 20°/sec$.

For modeling of unsteady effects, a nondimensional state x is introduced, that describes the location of an idealised flow separation point on the airfoil chord ($0 \le x \le 1$), see Fig. 1. Attached flow results in $x = 1$, complete flow separation in $x = 0$. An ap-
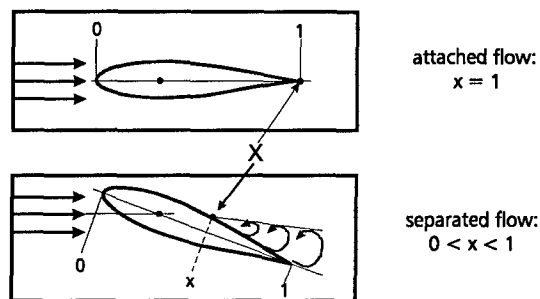
Fig. 1. Trailing edge flow separation on an airfoil

proximation of Kirchhoff's theory of flow separation from the trailing edge formulates the wing lift as a function of angle of attack and the flow separation point x:

$$C_L(\alpha, x) = C_{L\alpha} \left(\frac{1 + \sqrt{x}}{2}\right)^2 \alpha. \qquad (1)$$

The static dependency with $x = x_0(\alpha)$ can be determined from static wind tunnel data and flight test data, as will be shown later in this paper.

Unsteady conditions $\dot{\alpha} \neq 0$ with flow separation at high angles of attack cannot be modeled properly using $x_0(\alpha)$. Mathematically, unsteady effects can be divided into two categories.

1. **Quasi-steady effects.** Circulation and boundary layer effects result in a hysteresis from attached flow to flow separation and vice versa.

$$x = x_0(\alpha, \dot{\alpha}). \qquad (2)$$

The resulting delay is $\dot{\alpha}$-proportional and can be modeled by shifting the argument of x_0: The time constant τ_2 depends on airfoil shape and wing configuration and can be determined experimentally using wind tunnel or flight test data. Fig. 2 demonstrates the hysteresis
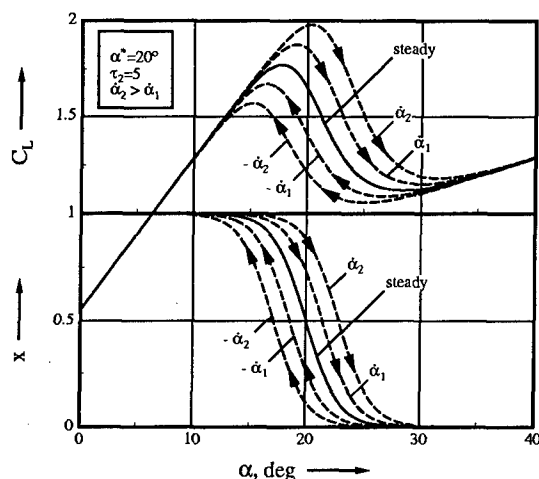

Fig. 2. Quasi-steady lift coefficient and flow separation point modeling for several constant rates of AoA
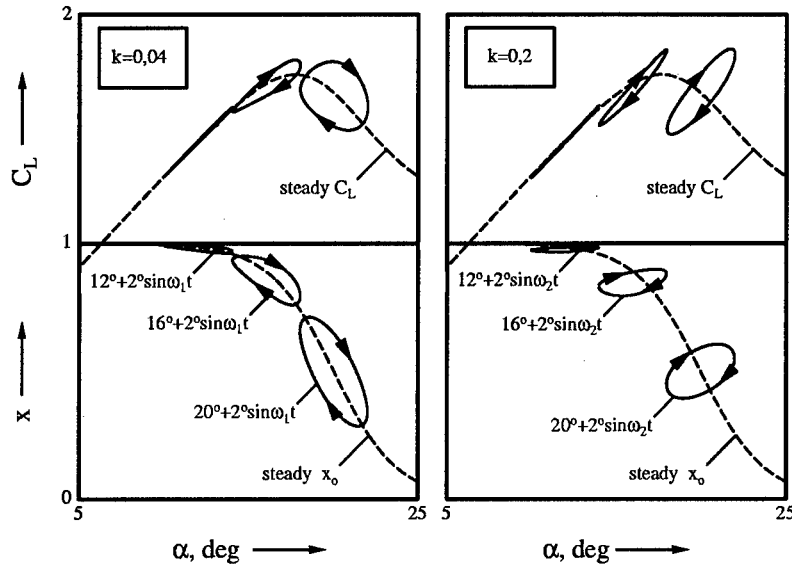
Fig. 3. Unsteady lift coefficient and flow separation point modeling (quasi-steady + transient) for various periodic oscillations

characteristics modeling of the flow separation point $x(\alpha, \dot{\alpha})$ and the corresponding lift coefficient $C_L(\alpha, x(\alpha, \dot{\alpha}))$ using a generic steady function x_0 in Eq. (2). The solid lines correspond to steady conditions $\dot{\alpha} = 0$, the dashed lines show x and C_L at different, constant rates $\dot{\alpha}$. For positive $\dot{\alpha}$ flow separation occurs at higher angles of attack, for negative $\dot{\alpha}$ the flow reattachment is delayed to smaller angles of attack compared to the steady case. Maximum lift is increased considerably for $\dot{\alpha} > 0$.

2. **Transient effects.** Unsteady aerodynamics are a function of time and describe the response of aerodynamic forces after a changed flow condition. A new flow condition can be caused by turbulence or is evident after a rapid angle of attack change. For attached flow conditions, those effects can be described using a differential equation of first order[5], which is a simple, but practical approximation of the Wagner and Theodorsen function[11,12]. For separated flow conditions, the actual position of the flow separation point is also time-dependent and can be approximated with a differential equation of first order, too.[3,4] Now Eq. (2) expands to:

$$\tau_1 \frac{dx}{dt} + x = x_0(\alpha, \tau_2 \dot{\alpha}). \tag{3}$$

The two time constants τ_1 and τ_2 characterise the transient and quasi-steady effects and can be determined using experimental data. It should be noted that the time constant τ_2 cannot be compared to that one in Eq. (2). If Eq. (2) is used for unsteady aerodynamic modeling with flow separation only, τ_2 is a substitute parameter describing both quasi-steady and transient aerodynamic behavior.

Fig. 3 shows the principal characteristics of Eq. (3) using the same generic *steady* flow separation function as depicted in *Fig. 2*. The unsteady lift (Eq. (1)) and the flow separation point (Eq. (3)) are plotted for periodic α-oscillations according to

$$\alpha = \alpha_R + \alpha_A \sin \omega t$$
$$\dot{\alpha} = \omega \alpha_A \cos \omega t. \tag{4}$$

The model response is shown for two different reduced frequencies k ($k = \omega_1 c/V = 0.04$, $k = \omega_2 c/V = 0.2$). The time constants were set to $\tau_1 = 15c/V$ and $\tau_2 = 5c/V$. It can be seen that unsteady lift is influenced essentially by: (a) the reference angle of attack α_R, and (b) the frequency of the forced oscillation. The effect of τ_1 is obvious at the maximum angles of attack ($\dot{\alpha} = 0$): in spite of the *steady* condition is $x \neq x_0$ and $C_L \neq C_{L,st}$, which heavily depends on frequency and α_R.

5. **APPROXIMATION OF THE FLOW SEPARATION FUNCTION**

The steady flow separation point is a nonlinear function of the angle of attack and is different for each airfoil and configuration. Using Eq. (1) with $x = x_0$, the function can be determined statically in wind tunnels. In ref. 6 an approximation is used that is based on two exponential functions, which can be adapted with several parameters. For identification from flight data, an alternative approximation, based on the *tanh*, is used:

$$x_0(\alpha) = \frac{1}{2} \cdot \{1 - \tanh(a_1 \cdot (\alpha - \alpha^*))\}. \tag{5}$$

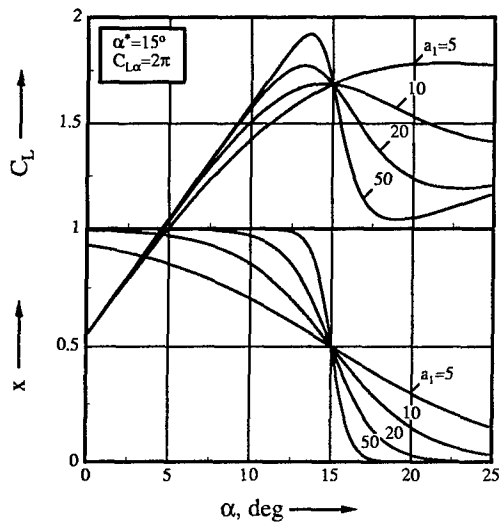This approximation is better suited for identification purposes, as only two parameters (a_1, α^*) have

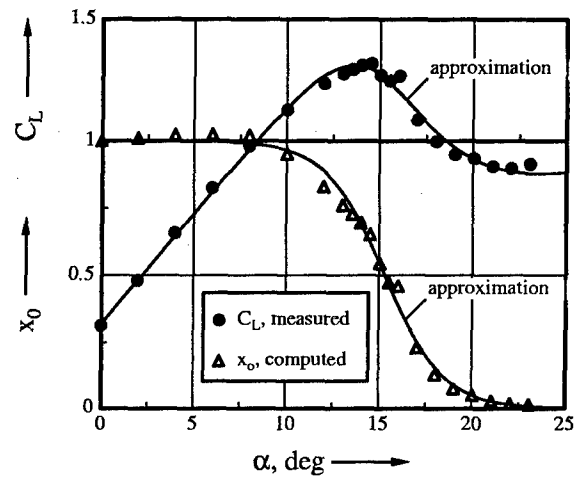Fig. 4. Parameter study (a_1) for the approximation of the flow separation function and the lift coefficient

Fig. 5. Approximation of the steady lift curve and the flow separation function of an OA213-airfoil (wind tunnel measurements)

to be determined and the tanh is a continuous function in its entire range, which is advantageous to convergence during the parameter estimation procedure.

For illustration purposes, a parameter variation of a_1 (Eq. (5)) is shown in Fig. 4 for a constant $\alpha^* = 15°$. Additionally, the corresponding lift is plotted using Eq. (1) with $x = x_0$. It is obvious that x_0 has its turning point at α^*. Variing the second parameter a^*, the steady flow separation function x_0 moves horizontally. Using this tanh-approximation, different steady airfoil stall characteristics can be approximated.

Eq. (3) can be rewritten using the approximation of Eq. (5):

$$\tau_1 \frac{dx}{dt} + x = \frac{1}{2} \cdot \{1 - \tanh(a_1 \cdot (\alpha - \tau_2\dot{\alpha} - \alpha^*))\}. \quad (6)$$

4. MODEL VERIFICATION USING WIND TUNNEL DATA

Static and dynamic wind tunnel measurements with an OA213 rotor airfoil were used in order to verify the above derived equations. As the flow separation point was not measured in the wind tunnel tests, it was computed pointwise using the inverted Kirchhoff's formulation of flow separated lift (m: measured):

$$x_0 = \left(2 \cdot \sqrt{\frac{C_{L,st}^m - C_{L0}^m}{C_{L\alpha}\alpha}} - 1\right)^2 \quad (7)$$

Fig. 5 shows the approximated measured steady OA213 lift curve und the corresponding 'measured' flow separation function using Eq. (1) and Eq. (5).

The two unknown parameters in Eq. (5) were determined to $\alpha^* = 15.3°$ and $a_1 = 17.8$. It can be
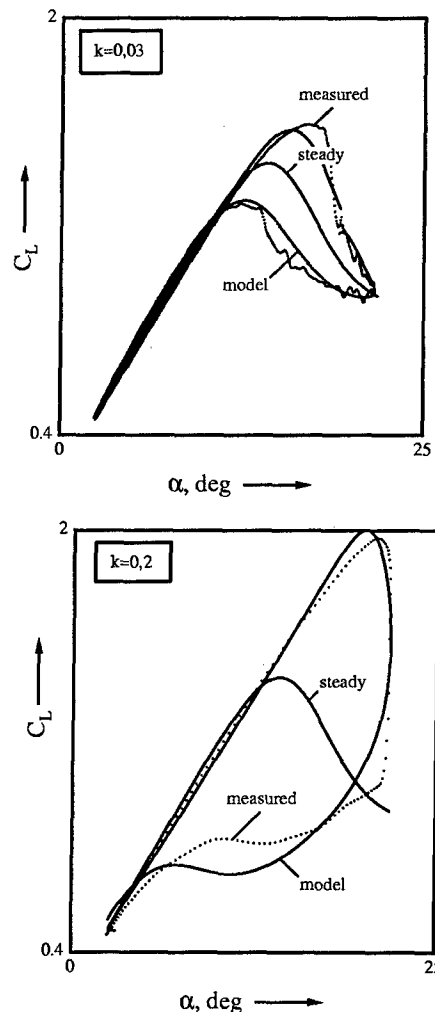
Fig. 6. Approximation of lift of an oscillating OA213-airfoil in wind tunnel at two reduced frequencies

seen that flow separation starts at $\alpha \approx 10°$ and has fully developed at $\alpha \approx 20°$. The stall characteristics are quite symmetrical to the turning point α^* (x=0.5), which is represented by the *tanh* in Eq. (5). The results show the applicability of this simple x_0-approximation to describe the steady stall characteristics of an airfoil.

As a second step the unsteady formulation of the flow separation point including transient and quasi-steady effects according to Eq. (6) is used to model lift of the OA213-airfoil oscillating in wind tunnel acc. to Eq. (1). *Fig. 6* shows the unsteady model lift compared to oscillations with reduced frequencies $k = \omega c/V = 0.03$ and $k = 0.2$. The steady curve $x_0(\alpha)$ is also presented. Unsteady aerodynamics for *attached* flow conditions are modeled with a phase delay and an effective amplitude reduction (Theodorsen[12]). The model time constants in Eq. (6) were determined to $\tau_1 = 2.37c/V$ and $\tau_2 = 3.49c/V$. The fit to the measured lift confirms the principal capability of the flow separation function to describe the unsteady lift airfoil aerodynamics for *separated* flow and different oscillation frequencies.

5. MODEL PARAMETER IDENTIFICATION FROM FLIGHT TEST DATA

5.1 Quasisteady Longitudinal Stall Modeling

Modeling decribed in this section is a practical approach, that can be recommended in two cases: (a) an additional differential equation is to be avoided for separation point modeling acc. to Eq. (3) like in real time simulators and (b) simulation of maneuvers with flow separation where transient unsteady aerodynamic effects are not as important as in highly dynamic maneuvers. Low dynamic maneuvers are e.g. stalls with a *quasi-steady* approach in contrast to stalls including a *dynamic* approach. The determination of *both* the characterising time constants τ_1 and τ_2 for unsteady aerodynamics with system identification methods is only possible using highly dynamic flight test data. Stall flight test data with quasi-steady approaches are only sufficient to determine the hysteresis time constant τ_2.

This confirms that during flow separation *hysteresis* unsteady effects are more essential than transient effects. The latter can be neglected during maneuvers with flow separation but less dynamic.

As an example stall flight test data of the Fairchild-Dornier turboprop regional aircraft 328 (*Fig. 7*) are evaluated for the purpose of a simulator model validation. The aircraft lift is modeled using Kichhoff's theory of flow separation (Eq. (1)). Drag is formulated as

$$C_D = C_{D0} + \frac{1}{e\pi\Lambda}C_L^2(\alpha, x) + \frac{\partial C_D}{\partial x}(1 - x). \quad (8)$$

The main part of unsteady drag is represented by the drag polar. Additionally, an empirical correction term $\partial C_D/\partial x$ was formulated proportional to the flow separation point x.

Pitching moment is formulated as (simplified)

$$C_m = C_{m0} + C_{m\alpha}\alpha + \frac{\partial C_m}{\partial x}(1 - x). \quad (9)$$

The flow separation point is modeled in quasi-steady form only $\alpha-$ and $\dot{\alpha}$-dependent using the steady approximation for the flow separation function:

$$x(\alpha, \dot{\alpha}) = \frac{1}{2} \cdot \{1 - \tanh(a_1 \cdot (\alpha - \tau_2\dot{\alpha} - \alpha^*))\} \quad (10)$$

Using a maximum-likelihood-identification algorithm for nonlinear systems[14], the model parameters a_1, α^*, τ_2 were identified from stall flight test data. All parameters of the basic aerodynamic model[10] were kept constant. The parameters were determined to $a_1 = 15.0$, $\alpha^* = 21.8°$, and $\tau_2 = 18.5c/V$. *Fig. 8* shows the simulation model output

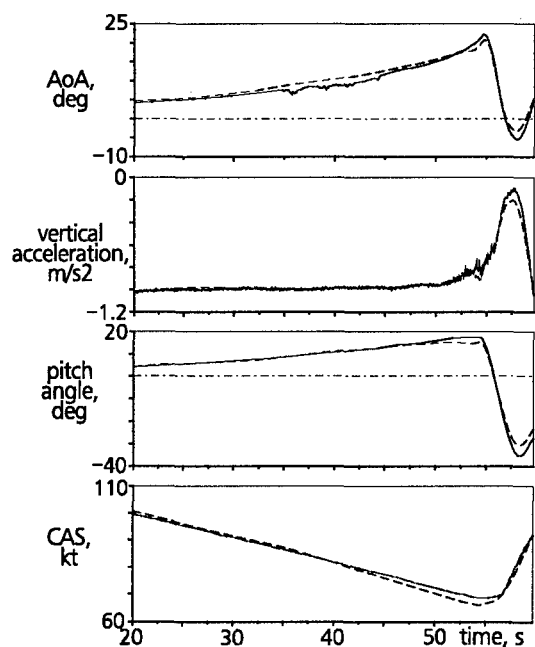*Fig. 7. DO 328 turboprop regional transport aircraft*

Fig. 8. DO 328: stall with quasi-steady approach; model output (- - -) and flight test data (———)
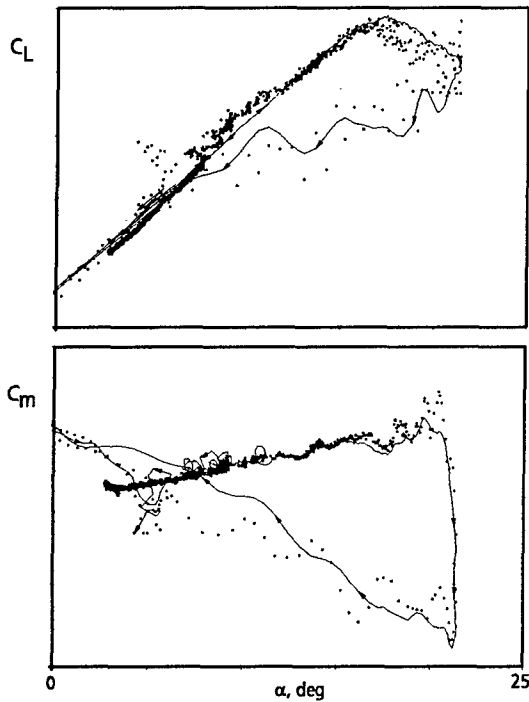
Fig. 9. DO 328: lift and pitching moment in stall approach and stall; flight test data (+ + +) and model output (——)

using these parameters compared to the stall flight test data. *Fig. 9* shows the measured total aircraft lift and pitching moment coefficients for the same stall maneuver. It is obvious, that there are strong hysteresis effects during the pitch down part of the stall. The model covers the hysteresis quite satisfactorily, only during the recovery phase some discrepancies can be seen. Summarizing, the quasi-steady stall model is a suitable solution for simulation of flow separated maneuvers with low dynamics.

5.2 Longitudinal Stall Modeling with Transient Effects

If there are stall flight test data available including highly dynamic maneuvers in the flow separated flight regime, both time constants for quasi-steady and transient unsteady aerodynamic characteristics in Eq. (3) can be identified. For simulation of those maneuvers the transient effects become more important and cannot be neglected to represent the aircraft motion properly. This will be shown using stall flight test data of the twin-turboprop military transport aircraft C-160 (*Fig. 10*).

The basic C-160 longitudinal aerodynamic model is formulated as a 2-point model[9,13], which describes the forces for wing and horizontal tail separately. Lift (for the wing) and drag is modeled as described in the section above. Pitching moment is computed alternatively in respect to the 2-point formulation using the horizontal tail lift $C_{L,t} = C_{L_{\alpha},t}\alpha_t$. The
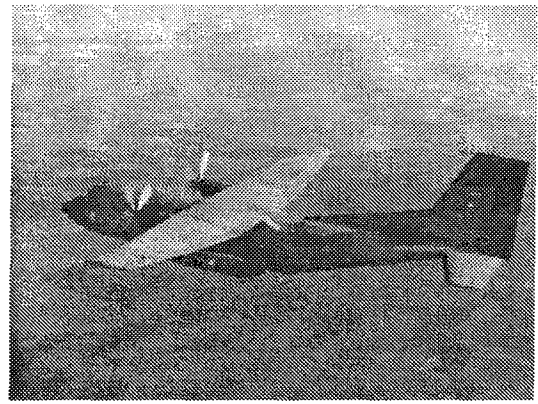
Fig. 10. C-160 turboprop military transport aircraft

effective tail angle of attack α_t is the sum of wing angle of attack α, horizontal tail trim angle i_t, the wing downwash angle at the tail ϵ_t, and the dynamic angle of attack $\alpha_{dyn} = \tan^{-1} qr_t/V$ with r_t being the distance from the aircraft's center of gravity to the horizontal tail neutral point.

$$\alpha_t = \alpha + i_t - \epsilon_t + \alpha_{dyn} \qquad (11)$$

The downwash angle ϵ_t is modeled as proportional to the wing angle of attack: $\epsilon_t = \frac{\partial \epsilon_t}{\partial \alpha}\alpha$. The 2-point aerodynamic formulation allows to consider the downwash lag from the neutral point of the wing to the neutral point of the tail: $\Delta t = r_t^*/V$. Additionally, wing flow separation influences the downwash angle at the tail, which can be modeled considering the lag effect. This reduction is as an approximation proportional to the flow separation function, which is delayed with Δt:

$$\epsilon_t = \frac{\partial \epsilon_t}{\partial \alpha}\alpha(t - \Delta t) + \frac{\partial \epsilon_t}{\partial x}\{1 - x(t - \Delta t)\}. \qquad (12)$$

Using these formulations, stall flight test data with quasi-steady and dynamic approaches were evaluated. Steady stall characteristics were determined (see Eq. (6)) to $a_1 = 25.7$ and $a^* = 20.5°$, transient unsteady characteristics to $\tau_1 = 14.5c/V$ and hysteresis effects to $\tau_2 = 3.5c/V$.

In order to validate the stall model, *Fig. 11* compares the steady model output on the left side with $x = x_o(\alpha)$ to the model output considering transient and hysteresis unsteady aerodynamics on the right side to flight test data. In both cases a time segment within the normal flight range ($\alpha < 10°$) and a segment with a strong dynamic lift overshoot ranging up into the post-stall region are presented. The left side of *Fig. 11* shows a good simulation quality in the first time segment: the angle of attack is $\alpha < 10°$. The second segment on the left side, which shows a dynamic stall approach, has obvious discrepancies to the flight test data, especially for $\alpha > \alpha_{C_{L,max}}$.

The right side of *Fig. 11* shows the same two time segments using the *unsteady* stall model. The im-
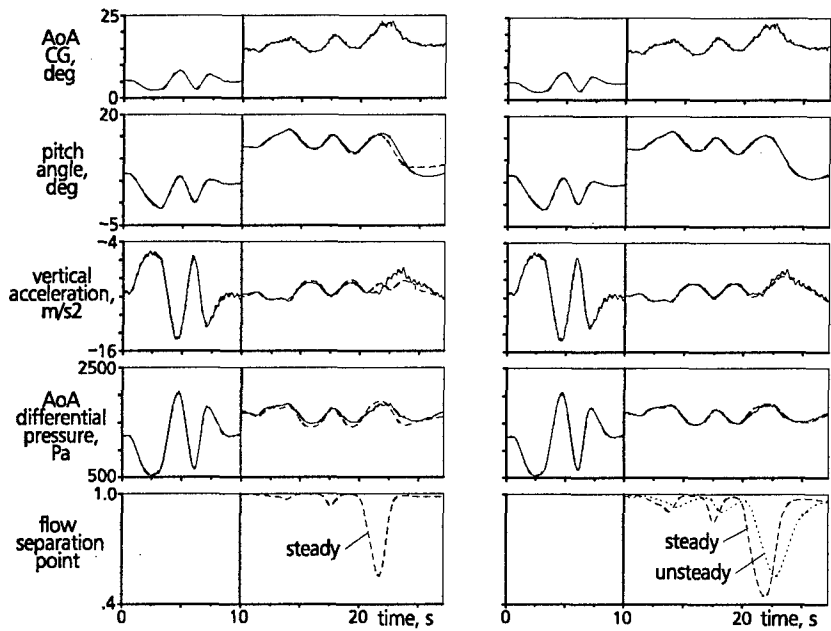
Fig. 11. C-160 model validation: (left) steady flow separation modeling, (right) unsteady flow separation modeling; model output (- - -) and flight test data (———)

provement in the second time segment is remarkable, whereas it is unchanged in the first. This improvement can only be achieved accounting for both hysteresis and transient unsteady effects. The x-time history shows a maximum flow separation of about 50%.

In order to illustrate the dynamic lift overshoot in the second time segment, *Fig. 12* presents the last 13 seconds of *Fig. 11* as a crossplot C_L and x versus wing angle of attack α. The plot shows the identified, steady $C_{L,st}(\alpha)$ and $x_0(\alpha)$ and the unsteady model outputs $C_L(t, \alpha, \dot{\alpha})$ and $x(t, \alpha, \dot{\alpha})$. It can be seen that there is a strong dynamic lift overshoot of about 12% above C_{Lmax}. The angle of attack reaches into the post-stall region. The delaying ef-

fect of τ_1 is obvious: At maximum angle of attack $\alpha \approx 21°$, the rate is $\dot{\alpha} = 0$, but $C_L \neq C_{L,st}$.

5.3 Lateral Stall Modeling

C-160 flight test data reveal substantial excursions in lateral-directional motion during stall. The pilot has to deflect considerably aileron and rudder to
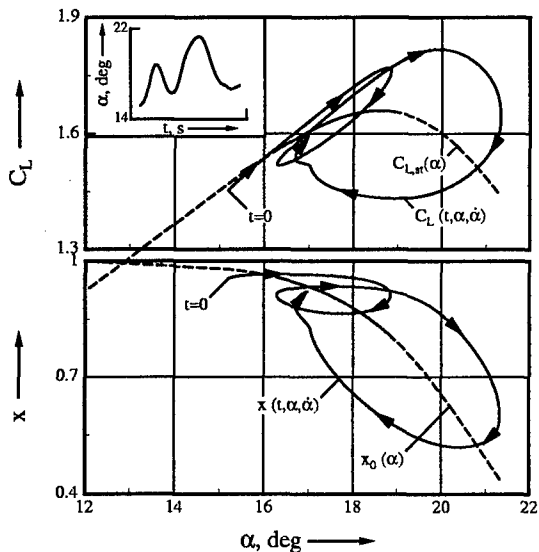
Fig. 12. Model lift coefficient and flow separation point during C-160 dynamic stall approach
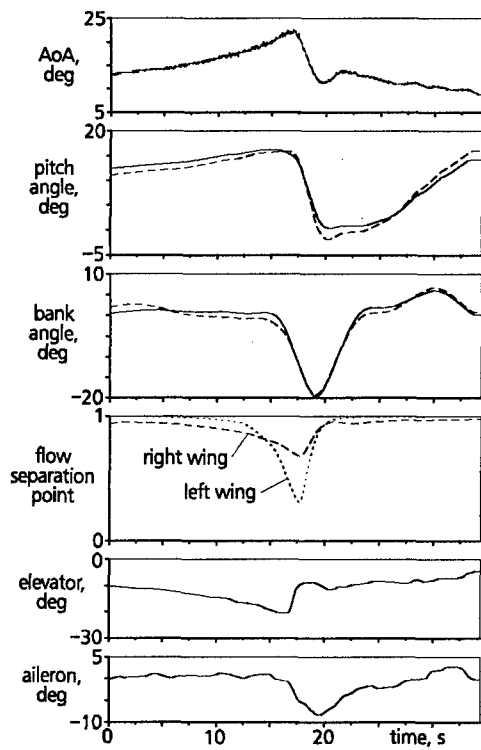
Fig. 13. Lateral excursions during C-160 stall; model output (- - -) and flight test data (———)

recover wings level.

To model those effects, the flow separation point can be formulated separately for the right and the left wing[15]. The differential lift and drag because of unsymmetrical flow separation left and right result in rolling and yawing, that can be approximated as:

$$\Delta C_l = \left(C_{L_{left}} - C_{L_{right}} \right) \Delta y$$
$$\Delta C_n = \left(C_{D_{left}} - C_{D_{right}} \right) \Delta y, \quad (13)$$

where Δy is the effective lever arm, which can be determined from flight test data.

Fig. 13 shows the model response for lateral excursions during a C-160 stall. The steady right and left wing panel flow separation is described separately as well as the hysteresis time constant τ_2. For longitudinal stall, the characteristic parameters a_1, α^* and τ_2 are the average of the left and right wing. It can be seen, that the bank angle excursion to $\phi = -20°$ is modeled properly and the longitudinal model quality in pitch is nearly unchanged.

6. CONCLUSIONS

Conventional aerodynamic modeling is not sufficient in flight conditions with flow separation on the wing surface. In this paper, a 5-DoF aerodynamic model for stall and flow separation is presented, which formulates the forces and moments as a function of an idealized flow separation point along the wing chord. The separation point modeling accounts for steady and unsteady effects.

The unsteady model divides aerodynamic flow separation effects into two categories: (a) quasi-steady circulation and boundary layer effects are modeled proportional to $\dot{\alpha}$ using a normalized time constant (hysteresis effects), and (b) unsteady transient effects are approximated by a first order differential equation (state-space representation), using a second, normalized time constant.

The model structure is first validated with steady and dynamic airfoil wind tunnel data. The model is then applied for stall representation of two different aircraft. The model parameters for steady and unsteady aerodynamic characteristics can be identified from flight test data. It is shown that flight maneuvers with quasi-steady flow separation can be modeled properly regarding only hysteresis effects, whereas in highly dynamic maneuvers with flow separation also transient unsteady effects are substantial.

7. REFERENCES

[1] E. J. Jumper, S. J. Schreck, R. L. Dimmick *Curve Characteristics for an Airfoil Pitching*

at Constant Rate. Journal of Aircraft, 1987, Vol. 24, No. 10 (1987)

[2] D. Rohlf, E. Plaetschke, S. Weiss *X-31A System Identification Applied to Post-Stall Flight - Aerodynamics & Thrust Vectoring -.* AGARD FMP Symposium 'Technologies for Highly Manoeuvrable Aircraft', Paper No. 14, Oct. 1993, Anapolis, Maryland (1993)

[3] M. Goman, A. Khrabrov *State-Space Representation of Aerodynamic Characteristics of an Aircraft at High Angle of Attack.* AIAA Conference Proceedings 92-4651 (1992)

[4] M. Goman, A. Khrabrov, S. Usoltsev *Identification of an Unsteady Aerodynamic Model of a Delta Wing at High Angle of Attack.* 10th IFAC Symposium on System Identification, Copenhagen, Denmark (1994)

[5] J. G. Leishman, K. Q. Nguyen *State-Space Representation of Unsteady Airfoil Behavior.* AIAA Journal, Vol. 28, No. 5 (1990)

[6] J. G. Leishman, T. S. Beddoes *A Semi-Empirical Model for Dynamic Stall.* Journal of the American Helicopter Society, 7/89 (1989)

[7] D. Fischenberg *Identification of an Unsteady Aerodynamic Stall Model from Flight Test Data.* AIAA Paper 95-3438-CP (1995)

[8] FAA *Airplane Simulator Qualification.* FAA Advisory Circular, AC 120-40B (1991)

[9] R. V. Jategaonkar, W. Mönnich, D. Fischenberg, B. Krag *Identification of C-160 Simulator Data Base from Flight Data* 10th IFAC Symposium on System Identification, Copenhagen, Denmark (1994)

[10] R. V. Jategaonkar, W. Mönnich *Identification of DO-328 Aerodynamic Database for a Level D Flight Simulator* AIAA Paper 97-3729-CP (1997)

[11] H. Wagner *Über die Entstehung des dynamischen Auftriebs von Tragflügeln.* Zeitschrift für angewandte Mathematik und Mechanik Vol. 5. Nr. 1 p. 17-35 (1925)

[12] T. Theodorsen *General Theory of Aerodynamic Instability and the Mechanism of Flutter.* NACA Rept. 496 (1935)

[13] W. Mönnich *Ein 2-Punkt-Aerodynamikmodell für die Identifizierung.* Symposium 'Systemidentifizierung in der Fahrzeugdynamik', DFVLR-Mitt. 87-22, Paper Nr. 3.1 (1987)

[14] R. V. Jategaonkar, E. Plaetschke *Maximum Likelihood Parameter Estimation from Flight Test Data for General Non-Linear Systems.* DLR-FB 83-14 (1983)

[15] J. Singh, R. V. Jategaonkar *Identification of Lateral-Directional Behavior in Stall from Flight Test Data.* Journal of Aircraft, Vol. 33, No. 3 (1996)

AERODYNAMIC PARAMETERS OF HIGH PERFORMANCE AIRCRAFT

ESTIMATED FROM WIND TUNNEL AND FLIGHT TEST DATA

Vladislav Klein
The George Washington University
Mail Stop 132
Hampton, Virginia 23681-0001, USA

and

Patrick C. Murphy
NASA Langley Research Center
Mail Stop 132
Hampton, Virginia 23681-0001, USA

SUMMARY

A concept of system identification applied to high performance aircraft is introduced followed by a discussion on the identification methodology. Special emphasis is given to model postulation using time invariant and time dependent aerodynamic parameters, model structure determination and parameter estimation using ordinary least squares and mixed estimation methods. At the same time problems of data collinearity detection and its assessment are discussed. These parts of methodology are demonstrated in examples using flight data of the X-29A and X-31A aircraft. In the third example wind tunnel oscillatory data of the F-16XL model are used. A strong dependence of these data on frequency led to the development of models with unsteady aerodynamic terms in the form of indicial functions. The paper is completed by concluding remarks.

NOMENCLATURE

Only the main symbols are introduced. Other symbols are explained in the body of the paper.

$\bar{c}$	mean aerodynamic chord, m
b	wing span
C_L	lift coefficient
C_ℓ, C_m, C_n	rolling-, pitching- and yawing-moment coefficient
$k = \omega \ell / V$	reduced frequency
ℓ	characteristics length, m
p, q, r	roll, pitch and yaw rate, rad/sec
R^2	coefficient of determination
V	airspeed, m/sec
α, β	angle of attack and sideslip angle, rad
η_c	control stick deflection
δ_a, δ_r	aileron and rudder deflection, rad
δ_c, δ_f, δ_s	canard, flap and strake deflection, rad
δ_{qtv}, δ_{rtv}	thrust vectoring deflection in pitch and yaw, rad
θ	unknown parameter

1. INTRODUCTION

The introduction of highly maneuverable and often inherently unstable aircraft has been presenting new challenges to aircraft identification and parameter estimation. These aircraft can perform rapid large amplitude maneuvers, often extended to the stall and poststall region where nonlinear and unsteady aerodynamic effects could be pronounced. This introduces a problem of determining how complex the model should be. Although a more complex model can be justified for more accurate description of airplane motion, it has not been clear in parameter estimation which relationship between model complexity and measurement information would be the best. If estimates for too many parameters are sought from a limited amount of data, a reduced accuracy can be expected or attempts to identify all parameters might fail. The high performance aircraft may also have more control surfaces moved through a flight control system than conventional aircraft. Such a system can introduce a close relationship between the deflections of various surfaces and at the same time can preclude maneuvers from being suitable for system identification. These characteristics can be reflected in an inability to estimate the effectiveness of individual control surfaces and to obtain accurate estimates of the remaining parameters. One of the reasons for these problems is related to the near linear relationship among several variables entering the model for various estimation techniques. This near linear relationship is often called data collinearity [1].

In recent years more attention has been given to the analysis of data obtained from dynamic wind tunnel tests. The frequency and amplitude dependency of oscillatory and ramp test data led to postulation of models with linear or nonlinear unsteady effects and subsequent parameter estimation in these models [2,3].

As follows from the above mentioned reasons and experience, a successful parameter estimation requires the

following:

a) design of an experiment for obtaining data with high accuracy, high information content and low collinearity among measured inputs and outputs;

b) determination of model structure which represents an adequate model for the aircraft under test in each maneuver analyzed;

c) introduction of techniques which reduce the adverse effect of data collinearity on parameter estimates when severe data collinearity could not be avoided by experiment design.

The purpose of this paper is to present a general approach to aircraft identification with emphasis on the above mentioned requirements for successful identification of a high performance aircraft model. The paper starts with an overview of system identification methodology followed by a discussion on data collinearity and biased estimation. In examples the flight data from experiments on X-29A and X-31A aircraft will be used. The forced oscillatory wind tunnel data on F-16XL model were selected for estimation of unsteady aerodynamic parameters. The paper is completed by concluding remarks.

2. AIRCRAFT IDENTIFICATION METHODOLOGY

When system identification is applied to an aircraft the equations governing its motion are postulated and an experiment is designed for obtaining time histories of the input and output variables. The equations of motion are formed by rigid-body force and moment equations

$$m\dot{V} + m\omega \times V = F_G + F_T + F(V,\omega,u,\theta) \qquad (1)$$
$$I\dot{\omega} + \omega \times I\omega = G(V,\omega,u,\theta)$$

and by a set of kinematic equations relating the Euler (attitude) angles and angular velocities. In eq. (1) m is the mass, I is the inertia matrix, V and ω are the linear and angular velocity vectors, and u is the control vector. The vectors F_G and F_T represent the gravity and propulsion force, F and G aerodynamic force and moment respectively, and θ is a vector of parameters which specify aerodynamic characteristics of the aircraft.

For system identification, the aircraft state equations are completed by the output and measurement equations. The complete set of all these equations can be written as

$$\dot{x} = f[x(t),u(t),\theta], \quad x(0) = x_0$$
$$y = h[x(t),u(t),\theta] \qquad (2)$$
$$z(i) = y(i) + v(i), \quad i = 1,2,...,N$$

where the state vector, x, is comprised of V, ω and Euler angles, and u is the control vector of control surface deflections. The outputs, y, are the variables defining aircraft responses. The measured outputs, z(i), are corrupted by measurement noise, v(i), and the number of data points is N.

Aircraft identification can be defined as follows: *Aircraft identification is a determination, from input and output measurements, of a structure for* F(θ) *and* G(θ) *and estimation of unknown parameters,* θ, *in* F(θ) *and* G(θ). In many practical applications, the structure of F(θ) and G(θ) is assumed to be known and aircraft identification is reduced to parameter estimation. A general approach to aircraft identification adopted at NASA Langley Research Center is shown in figure 1 in the form of a block diagram. Various steps in the procedure include model postulation, design of an experiment, data compatibility analysis, model structure determination and parameter estimation combined with collinearity diagnostic, and model validation.

Model Postulation
Model postulation is influenced by the type of selected maneuver intended for system identification and by a prior knowledge about aircraft aerodynamics. The aerodynamic forces and moments are expressed in the form of polynomials or polynomial splines as

$$C_a = C_a(0) + \sum_{j=1}^{n-1} \theta_j x_j \qquad (3)$$

where C_a is the aerodynamic coefficient, $C_a(0)$ is the value of the coefficient at initial steay-state conditions and the x_j now represents input and output variables, their combinations and/or spline terms. The postulated model is then used in model structure determination and parameter estimation. For a model with unsteady aerodynamics the forces and moments can be formulated in terms of indicial functions [4,5] as

$$C_a(t) = C_a(0) + \int_0^t C_{a\xi}(t-\tau;\xi(\tau))^T \frac{d}{d\tau}\xi(\tau)d\tau \qquad (4)$$

where ξ is a vector of aircraft state and input variables upon which the coefficient C_a depends, $C_{a\xi}(t)$ is a vector of indicial functions whose elements are the responses in C_a to unit steps in ξ. The indicial responses, $C_{a\xi}$, are functions of elapsed time $(t-\tau)$ and are continuous single-valued functions of $\xi(t)$. The indicial functions approach steady-state values with increasing values of the argument $(t-\tau)$. If the indicial response $C_{a\xi}$ is only a function of elapsed time, equations (4) is simplified as

$$C_a(t) = C_a(0) + \int_0^t C_{a\xi}(t-\tau)^T \frac{d}{d\tau} \xi(\tau)d\tau \qquad (5)$$

When analytical forms of indicial functions are specified, the aerodynamic model based on equation (4) or (5) can be used in the aircraft equations of motion for stability and control studies involving either nonlinear or linear unsteady aerodynamics, respectively. The resulting equations of motion will be represented by a set of integro-differential equations.

Design of Experiment
The most important part of the experiment design is the selection of input forms. It has been recognized that the shape of an input signal could influence the accuracy of estimated parameters from flight measurement. Attempts for obtaining parameter estimates with high accuracy led many researchers to the development of an optimal input. One of the latest techniques for optimal input design is discussed in [6].

Data Compatibility Analysis
In practice, often the measured response data, even after careful handling, can still contain bias errors. In order to verify data accuracy, a compatibility check can be applied to the measured aircraft responses. This check includes aircraft state estimation, based on known kinematics and the available sensor measurements, estimation of unknown bias errors and a comparison of reconstructed responses with those measured. The state equations are formed by kinematic relationships and the parameter vector usually contains constant offsets and scale factor errors. The estimation techniques are similar to those used in estimation of states and aerodynamic parameters.

Methods of Parameter Estimation
Model structure determination and parameter estimation combined with collinearity diagnostic form the principal part of the identification procedure. From the postulated model and measured data the model structure can be determined as explained later. When the model structure is known the parameter estimation can follow. In aeronautical application three methods, the maximum likelihood (ML), linear regression (LR) and extended Kalman filter (EKF), are the basic techniques.

The ML estimates are obtained by maximizing the conditional probability of measurement $Z=[z(1),z(2),...,z(n)]^T$ given a value of θ, i.e.

$$\hat{\theta} = \max_\theta p(Z|\theta)$$

Rather than minimize $p(Z|\theta)$, it is more convenient to minimize the negative logarithm of the likelihood function $L(\theta) = p(Z|\theta)$, called log-likelihood function,

$$\hat{\theta} = \min_\theta \{-\ell n L(\theta)\}$$

Substantial simplification to the ML estimation is obtained by assuming no external disturbances to the system and no measurement errors in input data. Then the ML estimation is reduced to the output error method with the cost function

$$J = \frac{1}{2}\sum_{i=1}^{N} v^T(i)R^{-1}v(i) + \frac{N}{2}\ell n|R| \qquad (6)$$

where $v(i)$ are the residuals, $v(i) = z(i) - y(i,\hat{\theta})$, and R is the measurement noise covariance matrix. Experience shows that a suitable technique for minimization of (6) is the Modified Newton-Raphson method. Using this technique, the step size, $\Delta\theta$, for parameter estimates is given by

$$\Delta\hat{\theta} = M^{-1}\frac{\partial \ell n L(\theta)}{\partial\theta} \qquad (7)$$

where M is the Fisher information matrix containing products and sums of the first order partials of the log-likelihood function. The expression for the information matrix is

$$M = \sum_{i=1}^{N} \left(\frac{\partial y(i)}{\partial\theta}\right)^T R^{-1}\frac{\partial y(i)}{\partial\theta} \qquad (8)$$

The information matrix provides also a lower bound on parameter covariances, i.e.

$$Cov(\hat{\theta}) = E\{(\hat{\theta}-\theta)(\hat{\theta}-\theta)^T\} \geq M^{-1} \qquad (9)$$

The inverse of M is called the Cramer-Rao lower bound and the ML estimates approach it asymptotically as N increases. Expression (8) is valid if the measurement noise is random, Gaussian and white. Numerous analyses from measured flight data showed, however, that these residuals can be far from being white.

The residuals very often contain some deterministic components. The result is colored residuals leading to new expression for parameter covariance matrix [7] in the form

$$\text{Cov}(\hat{\theta}) = M^{-1}\left[\sum_{i=1}^{N}\left(\frac{\partial y(i)}{\partial \theta}\right)^{T} R^{-1} \sum_{j=1}^{N} \Re_{vv}(i-j) R^{-1} \frac{\partial y(i)}{\partial \theta}\right] M^{-1} \quad (10)$$

where $\Re_{vv}(i-j)$ is the autocorrelation matrix for the output residual vector. It is estimated from

$$\hat{\Re}_{vv}(k) = \frac{1}{N-k}\sum_{i=1}^{N-k} v(i) v(i+k)^{T} = \hat{\Re}_{vv}(-k) \quad (11)$$

Further simplification to the ML method is obtained by assuming that both the input and states variables are measured without errors. This assumption leads to an equation error method which can be formulated as a linear regression applied to aerodynamic model equation (3). When the states, and inputs in this equation are replaced by measured values the equivalent of the general regression equation

$$y(i) = \theta_{o} + \theta_{1} x_{1}(i) + ..., \theta_{n-1} x_{n-1}(i) + \epsilon(i) \quad (12)$$

is obtained. In this equation, y now represents a dependent variable, x_1 to x_{n-1} are the regressors and ϵ is the equation error. When the regression equations are expressed as

$$Y = X\theta + \epsilon \quad (13)$$

the least squares (LS) parameter estimates are obtained as

$$\hat{\theta} = (X^{T}X)^{-1}X^{T}Y \quad (14)$$

and their covariance matrix as

$$\text{Cov}(\hat{\theta}) = \sigma^{2}(X^{T}X)^{-1} \quad (15)$$

for white noise and as

$$\text{Cov}(\hat{\theta}) = (X^{T}X)^{-1}\left[\sum_{i=1}^{N} x(i) \sum_{j=1}^{N} \Re_{ee}(i-j) x(j)^{T}\right] (X^{T}X)^{-1} \quad (16)$$

for colored noise where σ^{2} is the variance of $\epsilon(i)$

$$\hat{\Re}_{ee}(k) = \frac{1}{N-K}\sum_{i=1}^{N-K} e(i) e(i+k) = \hat{\Re}_{ee}(-k) \quad (17)$$

and

$$e(i) = y(i) - x(i)^{T}\hat{\theta} \quad (18)$$

The linear regression is a widely used estimation method for the following reasons:

a) it is a simple non-iterative method for parameter estimation;

b) the LS estimates serve as nominal starting values for the ML and EKF methods;

c) linear regression can be applied to data generated by partitioning an ensemble of data from repeated measurements with respect to one or more variables [8];

d) linear regression can be extended to a technique for model structure determination, e.g.stepwise regression;

e) formulation of a regression problem can be used for investigation of near-linear dependence (collinearity) among measured state and input variables and for the development of biased estimation techniques for dealing with highly collinear data (see Section 3).

For the development of the EKF algorithm the state vector is augmented by a parameter vector, $x_a = [x^{T} \vdots \theta^{T}]^{T}$. The vector x_a and its covariance matrix are estimated from measurements by minimizing the cost function

$$J = E\left\{[x_a(i|i-1) - x_a(i)]^{T}[x_a(i|i-1) - x_a(i)]\right\}$$

Because of inherent feed-back in the algorithm, the EKF can be easily applied to an unstable system for which the use of the output error method might be difficult or even impossible. On the other hand, the main disadvantage of the EKF method is that the initial conditions and the covariance matrices of process and measurement noise must be specified at the start of the estimation process.

Model Structure Determination

A major problem in system identification is the selection, from measured data, of an adequate (parsimonious) model. An adequate model is considered to be a model which sufficiently fits the data, facilitates the successful estimation of unknown parameters whose existence can be substantiated, and has good prediction capabilities. For model structure determination a method of stepwise regression is being used [9]. The determination of a model for the aerodynamic coefficients includes three steps: postulation of terms that might enter the model, selection of an adequate model, and validation of the model selected. After postulating the aerodynamic model equations, significant terms among the candidate variables are determined and the corresponding parameters estimated. At every step of the stepwise regression, the variables incorporated into the model in previous stages and a new variable entering the model are reexamined for their significance. Experience shows, however, that the model based only on the statistical significance of individual parameters in the model can still include too many terms and may have poor prediction capabilities. Several criteria for the selection of an adequate model have been, therefore, introduced. The most often used are:

a) The computed values of F-statistic, given as the ratio of regression mean square to residual mean square. Heuristically, the model with the maximum F-values is the "best" one for a given set of data.

b) The value of the coefficient of determination, R^2, which can be interpreted as measuring the proportion of the variation explained by the terms other than θ_0 in the model.

c) The prediction sum of squares PRESS defined for the kth subset of model parameters as

$$\text{PRESS} =$$
$$\sum_{i=1}^{N} \{y(i) - \hat{y}[i \mid x(1),...,x(i-1),x(i+1),...,x(N)]_k\}^2 \quad (19)$$

For the model to be a good predictor the value of PRESS should be minimal.

Model Validation

Model validation is the last step in the identification process and should be applied regardless of the complexity of the estimation method. The resulting model must demonstrate that its parameters have physically reasonable values and acceptable accuracy, and that the model is a good predictor. For those reasons the parameter estimates are compared with any information available about aircraft aerodynamics. Prediction capabilities of the model are checked on a set of data not used in the identification process.

3. DATA COLLLINEARITY AND BIASED ESTIMATION

As pointed out in the Introduction the augmentation of high performance aircraft very often introduces near linear relationships among the input and output variables (data collinearity). When linear regression is used in data analysis the collinearity results in an ill-conditioned $X^T X$ matrix in expression (14) for LS parameter estimates. Because of that the collinearity can cause computational problems and reduce the accuracy of estimates. Three procedures for detection of collinearity are recommended in [10] and applied to flight data. They are:

a) examination of the correlation matrix $X^{*T}X^*$ and its inverse, where the matrix X^* is formed by centered and scaled regressors;

b) eigenvalue analysis of the $X^T X$ matrix or singular value decomposition of the X matrix;

c) parameter variance decomposition into a sum of components, each corresponding to one and only one of the eigenvalues of the $X^T X$ matrix or singular values of the X matrix.

The parameter variance decomposition approach for detecting collinearity was proposed in [1]. It follows from the covariance matrix of parameter estimates $\hat{\theta}$ which can be also obtained as

$$\text{Cov}\,(\hat{\theta}) = \sigma^2 T \Lambda^{-1} T^T \quad (20)$$

where Λ is a diagonal matrix whose elements are the eigenvalues of $X^T X$ and T is a matrix whose columns are the eigenvectors of $X^T X$.

The variance of each parameter is equal to

$$\sigma^2(\hat{\theta}_j) = \sigma^2 \sum_{k=1}^{n} \frac{t_{jk}^2}{\lambda_j} = \sigma^2 \sum_{k=1}^{n} \frac{t_{jk}^2}{\mu_j^2} \quad (21)$$

where t_{jk} are the elements of eigenvector t_j associated with λ_j. Eq. (21) decomposes the variance of each parameter into a sum of components, each corresponding to one and only one of the n singular values μ_j. In (21) the singular values appear in denominator, so one or more small singular values can substantially increase the variance of θ_j. This means that an unusually high proportion of the variance of two or more coefficients for the same small singular value can provide evidence that the corresponding near dependency is causing problems. Introducing

$$\Phi_{jk} = \frac{t_{jk}^2}{\mu_j^2} \quad \text{and} \quad \Phi_j = \sum_{k=1}^{n} \Phi_{jk}$$

the j,k variance-decomposition proportion as the

proportion of the variance of the jth regression coefficient associated with the kth components of its decomposition in (21) is given as

$$\pi_{kj} = \frac{\Phi_{jk}}{\Phi_j}, \quad j,k = 1,2,...,n \qquad (22)$$

Since two or more regressors are required to create near dependency, then two or more variances will be adversely affected by high variance-decomposition proportions associated with a single singular value. Variance-decomposition proportions greater than 0.5 are recommended in [1] as a guidance for possible collinearity problems. It is also suggested that the columns of X should be scaled to unit length but not centered. Thus the role of the bias term in near-linear dependencies can be diagnosed.

If the collinearity diagnostic reveals a serious problem some way of dealing with it should be chosen. Additional data can be selected, the experiment can be redesigned, the model can be respecified or different techniques from the ordinary LS procedure can be used. Several estimation techniques which can be applied to data with severe collinearity have been developed [11]. Their development drops the requirement that the estimator of θ be unbiased. The new estimator, however, should have smaller variance than the LS estimator. By allowing the small amount of bias the parameter variance can be made small such that the mean square error of θ is less than the variance of the unbiased LS estimator. Techniques with this property belong to a class of biased estimation methods. Two of the techniques, the mixed estimation and rank reduction regression, have been introduced in [10] and used in flight data analysis. The experience with the rank reduction regression showed some difficulties in its application to aerodynamic model equations, mainly because of small number of unknown parameters in these equations. For that reason, only the mixed estimation will be introduced.

The mixed estimation (ME) is a procedure which uses prior information on parameters to augment measured data directly instead of through a prior distribution. Mixed estimation includes the usual regression model given by eq. (13) and the additional assumption that a set of prior conditions on θ can be written as

$$d = A\theta + \zeta \qquad (23)$$

In this equation, A is a matrix of known constants and ζ is a vector of random variables with $E(\zeta) = 0$ and $E(\zeta\zeta^T) = \sigma^2 W$, where W is a known weighing matrix. Combining (13) and (23) the mixed model is obtained.

For known σ^2 the application of least squares to this model results in the mixed estimator

$$\hat{\theta}_{ME} = (X^T X + A^T W^{-1} A)^{-1} (X^T Y + A^T W^{-1} d) \qquad (24)$$

It is shown in [10] that the addition of prior information to the ordinary regression results in reduction of parameter variance. In real application of the ME the *a priori* values are not known exactly therefore the resulting estimator is biased [10].

4. EXAMPLES

In the following three examples the measured data from experiments on the X-29A, X-31A and F-16XL aircraft will be used. These examples will demonstrate mainly specific problems related to identification of high performance aircraft. In addition, variations of some parameters with the angle of attack or Mach number, and their correlation with wind tunnel data and flight results from scale model will be also shown.

4.1 X-29A Aircraft

The test vehicle is a single engine, single seat fighter-type research aircraft with forward-swept wings. The aircraft has highly relaxed static longitudinal stability in subsonic and transonic regimes and near-neutral stability in supersonic regimes. For longitudinal control, deflections of canard, wing flap (flaperon), and fuselage strake are used. The lateral control is provided by the rudder and asymmetric deflection of flaperon. In addition to manual control of the aircraft, the concept of remotely augmented vehicle (RAV) could be used for the excitation of aircraft responses. The RAV arrangement employs a ground computer to augment the onboard control system. This capability is used to introduce a command to the control stick (pitch stick or roll stick command), rudder pedal, or individual control surfaces. The RAV commands, usually a pulse or doublet, are summed onto the already existing commands in order to independently move flaps, strake, canard, rudder, or differential flap. More about the RAV system can be found in [12]. A drawing of the aircraft is presented in figure 2. A more detailed description of the aircraft and its control system is contained in [13].

The following three sets of data were available for estimation of aircraft parameters:

1. longitudinal maneuvers excited by a pilot at Mach numbers from 0.5 to 1.4,

2. longitudinal and lateral maneuvers with computer generated inputs (RAV experiment) at Mach numbers from 0.6 to 1.3,

3. low speed lateral maneuvers initiated by a pilot at the angles of attack between 8^0 to 50^0.

During data analysis several problems associated with inherent instability, high augmentation and sometimes insufficient excitation of maneuvers had to be addressed. Among them were:

1. parameter estimation of an unstable vehicle,

2. data collinearity and its diagnostics,

3. adverse effect of data collinearity on parameter identifiability and accuracy.

Because of these problems, a linear regression and mixed estimation were used in data analysis.

Time histories of a typical longitudinal pilot and computer-generated input are presented in figures 3 and 4. From figure 3 close correlation among all open-loop inputs is obvious. The change in data collinearity caused by replacing the pilot by computer-generated input as a sequence of commanded flap, strake, canard and stick deflections is demonstrated in figure 4. The collinearity was assessed by comparing correlations between regressors, and corresponding, condition indexes and parameter variance proportions. The condition index is defined as the ratio of the maximum eigenvalue of the information matrix $X^T X$ to one of the remaining eigenvalues.

The correlation matrices for the two sets of data are given in tables I and II, respectively. The data with the pilot i n p u t   s h o w   c o r r e l a t i o n   b e t w e e n δ_c and $q\bar{c}/2V$ and δ_c and δ_s. The RAV data do not exhibit any significant correlation between regressors. The condition indexes and parameter variance proportions are given in tables III and IV. In this example the maximum condition index (condition number) for the set of data with pilot input is 174, in the second case 14, thus indicating reduced spread of eigenvalues where the RAV system was used. The variance proportions in table III for the largest condition index show strong collinearity among the bias term, canard and strake effectiveness. The same quantities in table IV indicate only a possibility of collinearity between the bias term and canard effectiveness.

Table V demonstrates a possibility of estimating parameters in the regression equation for the pitching-moment coefficient with sufficient accuracy. Included are the increments in coefficient of determination, ΔR^2, and t-statistics, t^*. The values of ΔR^2 represent the amount of information in the data explained by the individual terms in the model, t-statistic can be considered as a measure of significance of individual parameters. The data with the pilot input revealed that $C_{m\delta c}\delta_c$ is the highly influential term in the pitching-moment equation, that there is a limited possibility for accurate estimates of parameters $C_{m\delta f}$ and $C_{m\delta s}$, and that the significance of the $C_{mq}q\bar{c}/2V$ term is almost zero. The RAV experiment improved the identifiability of parameters $C_{m\alpha}$, $C_{m\delta f}$ and $C_{m\delta s}$, still maintaining the $C_{m\delta c}\delta_c$ as a dominant term. The chance

for accurate estimation of C_{mq} remains small.

The estimates of two parameters $C_{m\alpha}$ and $C_{m\delta c}$ which contribute the most to the pitching moment are plotted against the Mach number in figures 5 and 6 respectively and compared with the wind tunnel results. The estimates were obtained from data with pilot input using the least squares and mixed estimation, and from RAV experiment using only the least squares method. The wind tunnel values of the strake effectiveness were used as *a priori* values. The accuracies of the *a priori* values were determined from repeated test in two different wind tunnels. As can be seen from these figures, the accuracy of parameters was improved either by applying the mixed estimation to data with pilot input or by using data from the RAV experiment. Similar conclusion can be drawn from average standard errors in estimated parameters. These values are shown in table VI together with the fit error for the coefficient C_m.

The measured data from all low speed lateral maneuvers were assembled into one set with 51,200 data points which was then partitioned into 42 one-degree-α subsets and 1 three-degree-α subset. A half of the selected lateral maneuvers was analyzed as individual maneuvers using stepwise regression. The possibility of data collinearity in measured data was investigated by procedures explained in the previous examples. Application of stepwise regression to partitioned data resulted in models for the lateral aerodynamic coefficients and least squares estimates of parameters in these models. For the data subsets with $\alpha<40^0$, models with linear stability and control derivatives were adequate. For data at $\alpha>40^0$, some nonlinear and longitudinal control terms were selected by the stepwise regression. These additional terms did not provide any comprehensive information about aerodynamic nonlinearities or effects of longitudinal control setting on the lateral aerodynamic coefficients.

The estimated parameters (stability and control derivatives) from 43 subsets were plotted against the angle of attack and fitted by quadratic polynomial splines. In addition to fitted splines, the 2σ-confidence limits on the mean were computed as

$$\hat{\theta}(\alpha) \pm 2s \sqrt{x^T(X^TX)^{-1}x} \qquad (25)$$

In (25), $\hat{\theta}$ is the mean value of a parameter given by the fitted spline, s is the standard error of $\hat{\theta}$ estimated from the residuals, x is a vector of regressors. As an example, estimated values of the parameter C_{np}, fitted spline, and 2σ-confidence limits are shown in figure 7.

Stepwise regression analysis of data from single maneuvers showed that linear models for the aerodynamic coefficients were adequate within the angle-of attack range from 8^0 to 40^0. For angles of attack greater than 40^0

models for the lateral-force and yawing-moment coefficient included some of the nonlinear terms β^2, β^3, $\alpha\beta$, $\beta\delta_c$ or δ_r^3. As for the partitioned data, there was no consistent information about parameters associated with these nonlinear terms.

The least squares parameter estimates at low and moderate angles of attack were close to results from partitioned data. For $\alpha > 20^0$, however, increased scatter in the estimates and their deviation from the previous results using partitioned data were observed. This inconsistency was caused by data collinearity detected mostly among the variables pb/2V, δ_a and δ_r. In applying the mixed estimation technique, the *a priori* values were selected for parameters which were affected by collinearity. Their changes had only a small effect on aerodynamic coefficients. The *a priori* values and their uncertainty were set to the mean values and their standard errors obtained from partitioned data. An example of data collinearity is given in table VII where the eigervalues of the information matrix, condition indexes and parameter variance decompositions are included. The damaging effect of data collinearity on parameters associated with the variables pb/2V, δ_a and δ_r can be expected. Table VIII presents the parameter estimates and their standard errors in the rolling-moment equation using stepwise regression and, mixed estimation. In the last column of table VIII the parameter estimates from partitioned data are given. Large changes in the least square estimates of $C_{\ell p}$, $C_{\ell\delta a}$ and $C_{\ell\delta r}$ are visible during the model development. The final estimates of the three parameters are also quite different from those obtained from partitioned data. On the other hand, the parameters from the mixed estimation technique are close to the result from partitioned data. These estimates also have lower standard errors than the least squares results. The decrease in the fit error, $s(C_\ell)$, and squared correlation coefficient, R^2, are not substantial (see last two rows in table VIII).

Selected parameters obtained from partitined data and single maneuvers are plotted against the angle of attack in figures 8 and 9, and compared with wind tunnel data. The 2σ - confidence limits were omitted in these figures. However, the minimum and maximum values for standard errors of the estimated parameters from partitioned data are given in table IX. Both figures indicate no significant differences between the two sets of flight results. Large differences, however exist between flight and wind tunnel results in figure 8. Flight data exhibit a sudden increase in parameter values of $C_{y\beta}$ and $C_{n\beta}$ at angles of attack around 40^0 to 45^0. As indicated by wind tunnel investigations in [14], an increase of lateral force and yawing moment due to sideslip is caused by the forebody vortex assymetry. This assymetry can produce a sideforce which moves the nose into the sideslip and thus enhances directional stability. The same effect was observed in [15] during wind tunnel testing of the scaled model. The present differences between flight and wind tunnel results can be caused by different Reynolds numbers in the two experiements (0.68×10^6 in the wind tunnel; approx. 6×10^6 during the flight test) and by the effect of the nose

boom on the full scale aircraft. Positive yaw damping for $\alpha > 30^0$ is predicted by flight data whereas the wind tunnel results show low yaw damping over the whole range of angles of attack. In figure 9 three rolling moment parameters are included. The parameter $C_{\ell\beta}$ estimated from flight data agrees, in general, with wind tunnel predicitions. The roll damping decreases above $\alpha = 15^0$, from wind tunnel above $\alpha = 25^0$. Positive values of $C_{\ell p}$ from flight are about three times higher than those from wind tunnel. As mentioned in [15] and [16] the forebody aerodynamics dominates the roll-damping parameter at high angles of attack and causes the unstable damping. Therefore the differences between flight and wind tunnel results maybe attributed to different forebody aerodynamics in these two test conditions. The parameter $C_{\ell\delta a}$ is estimated with high consistency and agrees well with wind tunnel data for the angles of attack between 12^0 and 40^0. Some differences exists outside this interval. More about the parameters can be found in [17].

The results from this example lead to the following conclusions:

1. A collinearity diagnostic and a comparison of parameter estimates from flight data using the RAV experiment with those from flight data using pilot input revealed that the computer-generated deflections of individual control surfaces can substantially decrease data collinearity. A simple least squares technique can be used in estimation of all parameters in the model which also means estimation of the effectiveness of all controls used.

2. The experiment providing the data for the analysis was not properly designed. The selected input forms resulted in very small excitation of response variables. As a result some parameters were not identifiable and the identifiability of several remaining parameters was significantly reduced. These identifiability problems were apparent from the diagnostic of selected maneuvers.

3. For low speed lateral maneuvers linear aerodynamic models determined by applying stepwise regression techniques to partitioned data and single maneuvers were found to be adequate for the angles of attack less than 40^0. For angles of attack greater than 40^0, nonlinear and longitudinal control terms entered the models selected by the estimation technique. These terms, however, did not provide any comprehensive information about aerodynamic nonlinearities and the effect of longitudinal control on lateral aerodynamic coefficients. Because of data collinearity detected in single maneuvers, the data from these maneuvers were reanalyzed by using mixed estimation. No significant differences existed between parameters estimated from partitioned data and those estimated from single maneuvers.

4.2. X-31A Aircraft

The X-31A is a single engine, single seat fighter-type research aircraft with delta wing and canard. The aircraft is inherently unstable in subsonic regimes and is controllable by a digital control system. For longitudinal

control, canard and symmetrical flaperon deflections are used. The lateral control is provided by the rudder and differential flaperon. In addition to the aerodynamic control surfaces, a three-vane thrust vectoring system is mounted around the engine exhaust nozzle. This system allows thrust deflection up to 15^0 and is used for augmentation of pitch and yaw control during low speed and post-stall flights. A drawing of the aircraft is presented in figure 10.

Maneuvers from eight flights were selected for aerodynamic model structure determination and parameter estimation. These maneuvers were initiated from trim conditions at altitudes between 6,000 to 9,000 meters and angles of attack between 10^0 and 70^0. Two types of input were used, the pilot inputs and inputs generated by a flutter test box installed on one of the aircraft. The pilot inputs were either pitch command or yaw and roll commands in the form of a single doublet or a combination of doublets. The flutter test box allowed separate excitation of all aerodynamic control surfaces. These inputs were in the form of "3211" multiple signals. The surface deflection limits in the tests were 7.1^0 for the canard, 11.8^0 for the flaperons and 7.8^0 for the rudder. To ensure good excitation of aircraft motion, the longitudinal inputs were in some cases preceded by the pilot pitch doublets and the lateral inputs by pilot roll and yaw doublets. Maneuvers with pilot inputs were flown with thrust vectoring off ($\alpha < 30^0$) and on. The single surface excitation maneuvers were realized only with thrust vectoring on.

Estimated parameters from flight data were correlated with those obtained from wind tunnel data and drop model experiment. Static and dynamic wind-tunnel test were conducted at the 30 - by 60 - Foot Tunnel at NASA LaRC using a 19 - percent scale model (see [18] for some results). For a comparison with flight results presented, the parameters $C_{\ell p}$ and $C_{\ell r}$ were estimated from the oscillatory data using the techniques of [19] and [3]. More about this analysis will be presented in the third example.

In preparation for X-31A flight testing, the unpowered, 27-percent dynamically-scaled radio-controlled model of the X-31A was built and tested at NASA LaRC. During the test, the model was attached to a helicopter and lifted to an altitude between 1,500 and 3,000 m, and then released with the helicopter in forward motion. At an altitude of about 300 m the flight was terminated by deploying a large parachute. The model was controlled by a pilot on the ground but the model also had the capability to accept preprogrammed surface deflection commands. This feature was used in generating maneuvers for the purpose of parameter estimation. During the experiment, only the lateral parameters were estimated. They are presented in [20]. In this paper only estimates of four lateral parameters and two thrust vectoring parameters are presented. More results can be found in [21].

Lateral parameters:

In maneuvers with pilot inputs, high augmentation prevented sufficient excitation of sideslip angle and lateral acceleration, especially at angles of attack above 30^0, and introduced high pairwise correlation between variables p and r, δ_a and δ_r, δ_r and δ_{qtv}. The effect of limited excitation and high correlation was reflected in low accuracy of parameter estimates and, in many cases, inability to estimate some parameters at all. In the rolling-moment equation the terms with δ_a and β were predominant, explaining about 75% variation in the data of the 87% for the complete model. The main influential terms in the yawing-moment equation were those with either δ_r (for low α) or δ_{qtv} in maneuvers at high angles of attack. Their contribution represented about 85 to 96% from the overall value of 98% for the model with all terms included.

The parameter identifiability was improved, in general, by the introduction of a single surface excitation (δ_a or δ_r inputs). The above mentioned correlations were substantially reduced and the amplitude of sideslip angle increased. As a result of that, parameter identifiability in the rolling-moment equation was improved. However, the problem of accurate parameter estimation in the yawing-moment and lateral-force equations remained, with the exception of the thrust-vectoring effectiveness. Four parameters in the rolling-moment equation

$$C_\ell = \\ C_{\ell o} + C_{\ell \beta}\,\beta + C_{\ell p}\frac{pb}{2V} + C_{\ell r}\frac{rb}{2V} + C_{\ell \delta a}\delta_a + C_{\ell \delta r}\delta_r \quad (26)$$

are presented in figure 11 with their 2σ-error bounds. In this figure the results from wind tunnel and drop model tests are also included. The estimates of $C_{\ell \beta}$ are consistent with the exception of the region around $\alpha = 25^0$. There is significant departure of flight results from wind tunnel data for the angle of attack between 30 and 45^0. The reason for that has not been explained yet. Small scatter is also apparent in the estimates of $C_{\ell \delta a}$. The flight data demonstrate about 50% reduction in aileron effectiveness when compared to wind tunnel values. The estimates of $C_{\ell p}$ and $C_{\ell r}$ demonstrate the advantage of single surface excitation over pilot induced maneuvers. In the latter case, high correlation between rolling and yawing velocities, and low information content in the data prevented the estimates of both oscillatory parameters. There are no substantial differences between full-scale flight and wind tunnel estimates of these two dynamic parameters. The drop model parameter values at $30^0 < \alpha < 45^0$ are scattered with values lower than indicated by results from full-scale aircraft test.

Thrust vectoring effectiveness:

The parameter $C_{m\delta qtv}$ was estimated directly from

maneuvers with the δ_e inputs because the adequate model for the pitching moment included only variable α, δ_e and δ_{qtv}. These three regressors were not correlated. The maneuvers with δ_c inputs provided estimates of $C_{m\delta e}^*$ for $\alpha < 45^0$ and $C_{m\delta qtv}^*$ for $\alpha > 45^0$. From these estimates the thrust vectoring effectiveness was computed as

$$C_{m\delta qtv} = \left(C_{m\delta e}^* - C_{m\delta e}\right)\frac{\delta_e}{\delta_{qtv}}$$

or (27)

$$C_{m\delta qtv} = C_{m\delta qtv}^* - C_{m\delta e}\frac{\delta_e}{\delta_{qtv}}$$

where the relation δ_e / δ_{qtv} was evaluated from measured data and where the values of $C_{m\delta e}$ were obtained from maneuvers with pilot input (no thrust vectoring) and δ_e input. The values of the thrust-vectoring effectiveness, $C_{n\delta rtv}$, were estimated from the data with pilot input and single surface excitation. In the first cases, only maneuvers for $\alpha > 35^0$ were used because the effect of rudder deflection on the yawing moment was small. When necessary the final estimates were corrected for the effect of the rudder deflection by computing $C_{n\delta rtv}$ from the estimated values of $C_{n\delta rtv}^*$ as

$$C_{n\delta rtv} = C_{n\delta rtv}^* - \frac{\delta_r}{\delta_{rtv}}C_{n\delta r} \qquad (28)$$

From maneuvers excited by a single surface deflection, the parameter $C_{n\delta rtv}$ was estimated directly. Both parameters $C_{m\delta qtv}$ and $C_{n\delta rtv}$ are plotted against the thrust coefficient in figure 12 and compared with their theoretical values

$$C_{m\delta qtv} = -\frac{x_{tv}}{\bar{c}}C_T$$

(29)

$$C_{n\delta rtv} = -\frac{x_{tv}}{b}C_T$$

where x_{tv} is the distance of thrust impact point from airplane center of gravity. So far there has been no explanation for the differences between the theory and the experiment.

From the results presented here and in [22] the following conclusions can be drawn:

1. In piloted maneuvers, high correlations between input and output variables were observed. These correlations resulted in low accuracy of estimated parameters and prevented estimation of effectiveness of several control surfaces.

2. Single surface excitation reduced the above mentioned correlations. It was possible to estimate the effectiveness of all controls and increase the accuracy of estimated parameters.

3. The accuracy of parameters was also affected by their low sensitivity and small excitation of response variables, especially at high angles of attack.

4. All the influential parameters were, in general, in agreement with wind tunnel data and results from drop model tests. Some unexplained differences were, however, observed.

5. The estimated thrust vectoring effectiveness was found lower than its theoretical values.

6. The predictive capabilities of the resulting model determined from flight test data are very good for low amplitude maneuver at low to moderate angles of attack. Some deterioration in prediction was observed at high angles of attack.

4.3. F-16XL Aircraft

For better understanding of aircraft aerodynamics in large amplitude maneuvers, NASA LaRC conducted a series of wind tunnel tests on a model of the F-16XL. A sketch of the 0.10 - scale model is shown in figure 13 together with some basic model dimensions. Tests included measurement of aerodynamic forces and moments under static conditions, followed by oscillatory test about all three body axes and ramp tests in pitch. One of the reasons for the testing was to determine a mathematical model with unsteady aerodynamic terms from oscillatory data at different angles of attack and frequencies. In this paper only limited results from small amplitude ($\pm 5^0$) oscillations in pitch will be shown. More results can be found in [3] and upcoming reports.

For the following analysis of the oscillatory data it is assumed that the aerodynamic coefficients are linear functions of the angle of attack, pitching velocity and their rates. Then, for example, the increment in the lift coefficient with respect to its mean value can be formulated as

$$\Delta C_L =$$
$$C_{L\alpha}\Delta\alpha + \frac{\ell}{V}C_{L\dot\alpha}\dot\alpha + \frac{\ell}{V}C_{Lq}q + \left(\frac{\ell}{V}\right)^2 C_{L\dot q}\dot q \qquad (30)$$

then for the harmonic motion

$$\Delta C_L = \alpha_A \left(C_{L\alpha} - k^2 C_{L\dot q}\right)\sin\omega t + \alpha_A k\left(C_{L\dot\alpha} + C_{Lq}\right)\cos\omega t$$

$$= \alpha_A\left(\bar{C}_{L\alpha}\sin\omega t + k\bar{C}_{Lq}\cos\omega t\right)$$

(31)

where α_A is the amplitude, ω the angular frequency and

$$\alpha_A\bar{C}_{L\alpha} = \alpha_A\left(C_{L\alpha} - k^2 C_{L\dot q}\right)$$

$$\alpha_A k\bar{C}_{Lq} = \alpha_A k\left(C_{L\dot\alpha} + C_{Lq}\right)$$

represent the Fourier coefficients. The in-phase and out-of-phase components of $C_L (\bar{C}_{L_\alpha}$ and $\bar{C}_{L_q})$ can be obtained by integrating the time histories of ΔC_L over a selected number of cycles. The in-phase and out-of-phase components of C_L are plotted against the angle of attack in figure 14. The figure shows the effect of frequency which is especially strong on the out-of-phase components. A comparison of steady and oscillatory data is given in figure 15.

A strong dependence of wind tunnel oscillatory data on frequency lead to the development of models with unsteady aerodynamic terms, see e.g. [20] and [3]. As an example, the model for the lift increment was formulated in [20] as

$$\Delta C_L = \int_0^t C_{L\alpha}(t-\tau)\frac{d}{d\tau}\alpha\,d\tau + \frac{\ell}{V}\int_0^t C_{Lq}(t-\tau)\frac{d}{d\tau}q(\tau)d\tau \quad (32)$$

where $C_{L\alpha}(t)$ and $C_{Lq}(t)$ are the indicial functions.

For obtaining the model with limited number of parameters, it was assumed that the effect of $\dot{q}(t)$ on the lift could be neglected and the indicial function $C_{L\alpha}(t)$ can be expressed as

$$C_{L\alpha}(t) = a(1 - e^{-b_1 t}) + c \quad (33)$$

Considering the above mentioned assumptions, equation (33) is simplified as

$$\Delta C_L = \\ C_{L\alpha}(\infty)\alpha(t) - a\int_0^t e^{-b_1(t-\tau)}\frac{d}{d\tau}\alpha(\tau)d\tau + \frac{\ell}{V}C_{Lq}(\infty)q(t)$$
$$(34)$$

where $C_{L\alpha}(\infty)$ and $C_{Lq}(\infty)$ are the rates of change of C_L with α and q in steady flow. The steady form of equation (32) for harmonic changes in α is identical to that of equation (31), that is

$$\Delta C_L(t) = \alpha_A \bar{C}_{L\alpha} \sin\omega t + \alpha_A k \bar{C}_{Lq}\cos\omega t \quad (35)$$

However, with the indicial function of equation (33), the expressions for $\bar{C}_{L\alpha}$ and $\bar{C}_{Lq}$ have the form

$$\bar{C}_{L\alpha} = C_{L\alpha}(\infty) - a\frac{\tau_1^2 k^2}{1 + \tau_1^2 k^2} \quad (36)$$

$$\bar{C}_{Lq} = C_{Lq}(\infty) - a\frac{\tau_1}{1 + \tau_1^2 k^2} \quad (37)$$

where $\tau_1 = V/b_1 \ell$ is the nondimensional time constant.

From the experiment, the in-phase and out-of phase components are usually obtained for different values of the angle of attack and reduced frequency while keeping the amplitude of the oscillations constant. Then the equations (36) and (37) can be generalized as

$$\bar{u}_{ji} = u_i - a_i z_{uj} \quad (38)$$

$$\bar{v}_{ji} = v_i - a_i z_{vj} \quad (39)$$

These equation define Model I where for the lift coefficient

$$u_i = C_{L\alpha}(\alpha_i) \qquad v_i = C_{Lq}(\alpha_i)$$

$$z_{uj} = \frac{\tau_1^2 k_j^2}{1 + \tau_1^2 k_j^2} \qquad z_{vj} = \frac{\tau_1}{1 + \tau_1^2 k_j^2}$$

$$\text{for} \quad \begin{matrix} i = 1,2,...,n \\ j = 1,2,...,m \end{matrix}$$

In equations (38) and (39) there are, in general, $3n + 1$ unknown parameters: u_i, v_i, a_i and τ_1. They can be estimated from experimental data $\bar{u}_{ji}$ and $\bar{v}_{ji}$ by minimizing the cost function

$$J_I = \sum_{j=1}^{m}\sum_{i=1}^{n}\left\{\left[\bar{u}_{ji} - (u_i - a_i z_{uj})\right]^2\right\} + \left[\bar{v}_{ji} - (v_i - a_i z_{vj})\right]^2\right\}$$

In formulating airplane equations of motion it might be more convenient to obtain expressions for u, v, and a as a function of the angle of attack rather than their discrete values. For that reason the previous model was reformulated as Model II defined by the following equations:

$$\bar{u}_{ji} = u(\alpha_i) - a(\alpha_i)z_{uj} \quad (40)$$

$$\bar{v}_{ji} = v(\alpha_i) - a(\alpha_i)z_{vj} \quad (41)$$

The form of expressions for $u(\alpha_i)$, $v(\alpha_i)$ and $a(\alpha_i)$ can be either specified from the variation of estimated parameters in Model I or the form can be postulated in terms of polynomials and/or polynomial splines. In the second case adequate models for $u(\alpha), v(\alpha)$ and $a(\alpha)$ can be determined from measured data by a stepwise regression. The previously estimated value of parameter τ_1 can be used as an *a priori* value thus simplifying the parameter estimation procedure using Model II and the cost function

$$J_{II} = \sum_{j=1}^{m}\sum_{i=1}^{n}\left\{\left[\bar{u}_{ji} - (u(\alpha_i) - a(\alpha_i)z_{uj})\right]^2\right.$$
$$\left. + \left[\bar{v}_{ji} - (v(\alpha_i) - a(\alpha_i)z_{vj})\right]^2\right\}$$

Both estimation procedures were applied to oscillatory

data at four frequencies. The data for frequency $k = 0.19$ were used to demonstrate model prediction capabilities. The parameters $C_{L\alpha}(\infty)$, $C_{Lq}(\infty)$ and a in both models are plotted in figure 16. The agreement between both sets of results is very good. The parameter $C_{L\alpha}(\infty)$ agree well with that from static data. Low accuracy in $C_{Lq}(\infty)$ could result from small number of data points and small sensitivity of this parameter. The parameter a indicated smooth variation of unsteady term with the angle of attack and the largest effect of unsteady terms on the coefficient at α around 40^0. The estimated value of τ_1 was 17.2 ± 1.0, which means $b_1 = 2.71 \pm 0.16 (\text{sec})$. This result indicates that the time constant associated with the unsteady effect is about 0.4 sec. The predicted components from model eq.(40) and (41) for $k = 0.19$ are presented in figure 17 together with the corresponding measured values. This figure demonstrates that Model II is a good predictor. Similar result was obtained for Model I.

As follows from this example, a strong dependence of wind tunnel oscillatory data on frequency led to the development of model with unsteady aerodynamic terms in the form of indicial functions. These functions were postulated as simple exponentials where the unknown parameters included aerodynamic derivatives, the exponent and multiplication term.

5. CONCLUDING REMARKS

System identification applied to aircraft has proven to be a powerful tool for aircraft modeling based on experimental data. In recent years the introduction of highly maneuverable, inherently unstable and highly augmented aircraft has required high sophistication in aircraft identification methodology. At present this methodology includes basic steps: model postulation, experiment design, data compatibility analysis, model structure determination and parameter estimation combined with collinearity and identifiability diagnostics, and model validation.

The examples presented demonstrated the need for the introduction of an on-board computer generated input signals. This system and the optimal input design procedure improve identifiability of aerodynamic models and accuracy of estimated parameters. The various modifications of the ordinary least square method proved to be basic tools for model structure determination, parameter estimation and data collinearity assessment. The resulting parameters can be used as nominal values in the application of two parameter estimation techniques used in aircraft application, the maximum likelihood method (usually in the form of output error method) and the extended Kalman filter method. For meaningful information about the identified model, the parameter estimates should be completed by their covariances thus indicating the accuracy of parameters and their correlation.

In many applications of system identification methodology, only data from small excursions from trim conditions were available. By repeating the identification using data at different trim conditions, an extended model could be constructed. However, for obtaining a global model from flight data a dedicated experiment would be needed. In this experiment modeling and optimal input design would play the major role. One of the possibilities for an extension of traditional aerodynamic model is the inclusion of unsteady effects. Some initial work has already been done mostly using data from dynamic wind tunnel testing. A strong dependency of oscillatory data on frequency led to identified models with time varying terms in the form of indicial functions. Based on these experiences the extension to flight data will follow.

References

1. Belsley, D.A.; Kuh E. and Welsh, R.E.: "Regression Diagnostics: Identifying Influential Data and Sources of Collinearity", John Wiley & Sons, Inc., 1980.

2. Goman, M. and Khrabrov, A.: "State-Space Representation of Aerodynamic Characteristics of an Aircraft at High Angles of Attack", Journal of Aircraft, Vol. 31, No. 5, 1994.

3. Klein, Vladislav; Murphy, Patrick C.: Curry, Timothy J. and Brandon, Jay M.: "Analysis of Wind Tunnel Longitudinal Static and Oscillatory Data of the F-16XL Aircraft", NASA/TM-97-206276, 1997.

4. Tobak, Murray and Shiff, Lewis B.: "On the Formulation of the Aerodynamic Characteristics in Aircraft Dynamics", NASA TR R-456, 1976.

5. Klein, Vladislav and Noderer, Keith D.: "Modeling of Aircraft Unsteady Aerodynamic Characteristics. Part 1-Postulated Models", NASA TM 109120, 1994.

6. Morelli, Eugene A.: "Advances in Experiment Design for High Performance Aircraft", in "System Identification for Integrated Aircraft Development and Flight Testing", in RTA Conference Proceedings, Paper No. 8, 5-7, Madrid, Spain, May, 1998.

7. Morelli, E. A. and Klein, V.: "Accuracy of Aerodynamic Model Parameters Estimated From Flight Test Data", Journal Guidance, Control and Dynamics, Vol. 20, No. 1, 1997, pp. 74-80.

8. Batterson, J. G. and Klein, V.: "Partitioning of Flight Test Data for Aerodynamic Modeling of Aircraft at High Angles of Attack", Journal of Aircraft, Vol. 26, No. 4, 1987, pp. 334-339.

9. Klein, V.: Batterson, J. G. and Murphy, P. C.: "Determination of Airplane Model Structure From Flight Data by Using Modified Stepwise Regression", NASA TP-1916, 1981.

10. Klein, V.: "Two Biased Estimation Techniques in Linear Regression. Application to Aircraft", NASA TM-100570, 1988.

11. Hocking, R. R.; Speed, M. D. and Lynn, M. J.: "A Class of Biased Estimators in Linear Regression", Technometrcs, Vol. 18, No. 4, Nov. 1976, pp. 425-437.

12. Mackal, D. A.; Picket, M. D.; Shilling, L. J. and Wagner, C. A.: "The NASA Integrated Test Facility and its Impact on Flight Research", AIAA Paper No. 88-2095. 1988.

13. Gera, Joseph: "Dynamic and Controls Flight Testing of the X-29A Airplane", NASA TM-86803, 1986.

14. Brandon, J. M. and Nguyen, L.T.: "Experimental Study of Effects of Forebody Geometry on High Angle of Attack Static and Dynamic Stability", AIAA Paper No. 86-0331, 1986.

15. Murri, Daniel G.; Nguyen, Luat T. and Grafton, Sue B.: "Wind-Tunnel Free-Flight Investigation of A Model of a Forward-Swept-Wing Fighter Configuration", NASA TP-2230, 1984.

16. Grafton, Sue B.; Chambers, Joseph R. and Coe, Paul L. Jr.: "Wind-Tunnel Free-Flight Investigation of a Model of a Spin-Resistant Fighter Configuration", NASA TN D-7716, 1974.

17. Klein, Vladislav; Cobley, Brent R. and Noderer, Keith D.; "Lateral Aerodynamic Parameters of the X-29 Aircraft Estimated From Flight Data at Moderate to High Angles of Attack", NASA TM-104155, 1991.

18. Croom, M. A.; Fratelo, D. J.; O'Rourke, M. J. and Trilling, T. W.: "Dynamic Model Testing of the X-31A Configuration for High-Angle-of Attack Flight Dynamic Research", AIAA Paper 93-3674-CP, 1992.

19. Klein, Vladislav and Noderer, Keith D.: "Modeling of Aircraft Unsteady Aerodynamic Characteristics. Part 2-Parameters Estimated From Wind Tunnel Data", NASA TM-11016661, 1995.16

20. Klein, V. and Noderer, K. D.: "Aerodynamic Parameters of the X-31 Drop Model Estimated From Flight Data at High Angles of Attack", AIAA Paper 92-4357-CP, 1992.

21. Klein, Vladislav and Nguyen, Luong V.: "Aerodynamic and Thrust Vectoring Parameters of the X-31A Aircraft Estimated From Flight Data at Moderate to High Angles of Attack", in "High-Angle-of Attack Technology Conference", NASA Langley Research Center, September 17-19, 1996, Hampton, VA.

Table I. X^TX matrix in correlation form. Pilot input.

α	$\dfrac{q\bar{c}}{2V}$	δ_s	δ_r	δ_c
1.000	0.151	0.753	0.711	-0.795
	1.000	0.318	-0.341	-0.979
		1.000	0.643	-0.928
			1.000	-0.844
				1.000

Table II. X^TX matrix in correlation form. RAV experiment.

α	$\dfrac{q\bar{c}}{2V}$	δ_s	δ_r	δ_c
1.000	0.275	0.673	0.328	-0.772
	1.000	0.345	-0.375	-0.089
		1.000	0.098	-0.578
			1.000	-0.303
				1.000

Table III. Collinearity diagnostic. Pilot input.

Eigenvalue	Condition index	Variance proportions (scaled regressors)					
		1	α	$\dfrac{q\bar{c}}{2V}$	δ_s	δ_f	δ_c
3.3102	1	0.0000	0.0092	0.4806	0.0017	0.0006	0.0001
1.2781	3	0.0099	0.0001	0.0397	0.0720	0.0058	0.0001
1.0333	3	0.0001	0.2572	0.1604	0.0000	0.0342	0.0002
0.2613	13	0.0504	0.1140	0.0991	0.0762	0.1887	0.0245
0.0981	34	0.1220	0.6194	0.2143	0.0041	0.7123	0.0548
0.0190	174	0.8176	0.0001	0.0061	0.8460	0.0585	0.9204

Table IV. Collinearity diagnostic for RAV experiment.

Eigenvalue	Condition index	Variance proportions (scaled regressors)					
		1	α	$\dfrac{q\bar{c}}{2V}$	δ_s	δ_f	δ_c
2.5320	1	0.0003	0.0017	0.8594	0.0003	0.0000	0.0018
1.4339	2	0.0905	0.0002	0.0049	0.0008	0.0132	0.1901
1.0028	3	0.0156	0.2543	0.0098	0.1481	0.1685	0.2565
0.4745	5	0.2173	0.0355	0.0171	0.0178	0.4886	0.0172
0.3798	7	0.0460	0.6463	0.0220	0.4605	0.0094	0.0506
0.1771	14	0.6302	0.0621	0.0867	0.3724	0.4720	0.7147

Table V. Identifiability diagnostic.

Parameter	RAV		Pilot input	
	ΔR^2, %	|t*|	ΔR^2, %	|t*|
C_{m_α}	9.09	64.8	5.06	28.0
C_{m_q}	1.08	13.7	0.01	0.0
$C_{m_{\delta c}}$	75.74	99.1	91.49	12.3
$C_{m_{\delta f}}$	18.35	46.4	0.94	9.2
$C_{m_{\delta s}}$	4.46	42.7	1.00	9.2

Table VI. Average standard errors of estimated parameters.

Parameter	RAV	Pilot input	
	LS	LS	ME
$s(C_{m_\alpha})$	0.029 (0.014)	0.058 (0.075)	0.054 (0.020)
$s(C_{m_{\delta c}})$	0.017 (0.018	0.090 (0.037)	0.048 (0.020)
$s(C_m)$	0.0033 (0.0011)	0.0059 (0.0026)	0.0060 (0.0026)

Note: figures in parentheses are standard errors.

Table VII. Collinearity diagnostic.

Eigenvalue	Condition index	Variance proportions (scaled and centered regressors)				
		β	$\dfrac{pb}{2V}$	$\dfrac{rb}{2V}$	δ_a	δ_r
2.387	1.0	0.000	0.005	0.002	0.013	0.007
1.849	1.3	0.085	0.000	0.084	0.006	0.004
0.537	4.4	0.167	0.001	0.528	0.022	0.001
0.209	11.4	0.540	0.000	0.002	0.207	0.079
0.017	140.4	0.208	0.994	0.384	0.752	0.910

Table VIII. Identifiability diagnostic and parameter estimates.

Parameter	Stepwise Regression					Mixed* estimation	Partitioned data
	n = 2	n = 3	n = 4	n = 5	n = 6		
C_{l_0}	-0.0036	-0.0014	-0.0028	-0.0031	-0.0020	-0.0172	-
C_{l_β}	-0.272 (0.0080)	-0.246 (0.0072)	-0.221 (0.0070)	-0.223 (0.0064)	-0.190 (0.0057)	-0.208 (0.0056)	-0.254 (0.0087)
C_{l_p}	-	-	0.3 (0.15)	1.4 (0.13)	2.3 (0.12)	0.84 (0.050)	0.62 (0.046)
C_{l_r}	-	-	-	-	-3.3 (0.26)	-1.2 (0.22)	-1.04 (0.095)
$C_{l_{\delta a}}$	-	0.028 (0.0058)	0.049 (0.0055)	0.081 (0.0050)	0.106 (0.0046)	0.064 (0.0035)	0.064 (0.0041)
$C_{l_{\delta r}}$	-	-	-	0.031 (0.0053)	0.054 (0.0047)	0.015 (0.0010)	0.01 (0.0021)
$s(C_l)$	0.0050	0.0045	0.0043	0.0040	0.0035	0.0040	-
$R^2[\%]$	83.4	86.8	87.6	89.7	91.7	88.0	-

* a priori value $C_{l_{\delta r}} = 0.010 \pm 0.0021$

Note: figures in parentheses are standard errors

Table IX. Standard errors of estimated parameters from partitioned data.

Parameter	Standard Error	
	min	max
C_{Y_β}	0.045	0.15
C_{Y_p}	0.42	1.1
C_{Y_r}	0.78	2.3
$C_{Y_{\delta a}}$	0.026	0.060
$C_{Y_{\delta r}}$	0.016	0.053
C_{l_β}	0.0076	0.016
C_{l_p}	0.040	0.11
C_{l_r}	0.063	0.18
$C_{l_{\delta a}}$	0.0037	0.011
$C_{l_{\delta r}}$	0.0021	0.0044
C_{n_β}	0.0064	0.020
C_{n_p}	0.054	0.12
C_{n_r}	0.086	0.31
$C_{n_{\delta a}}$	0.0029	0.0070
$C_{n_{\delta r}}$	0.0013	0.0051
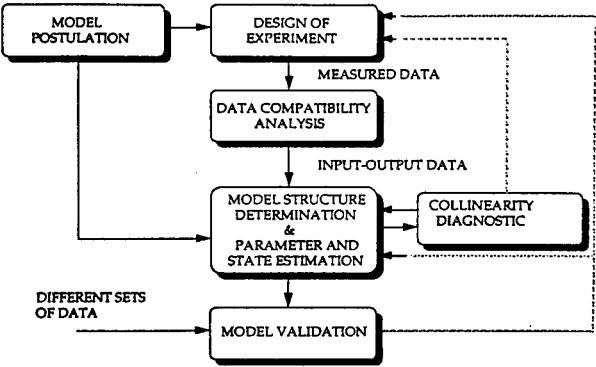
Figure 1. Block diagram of aircraft identification.
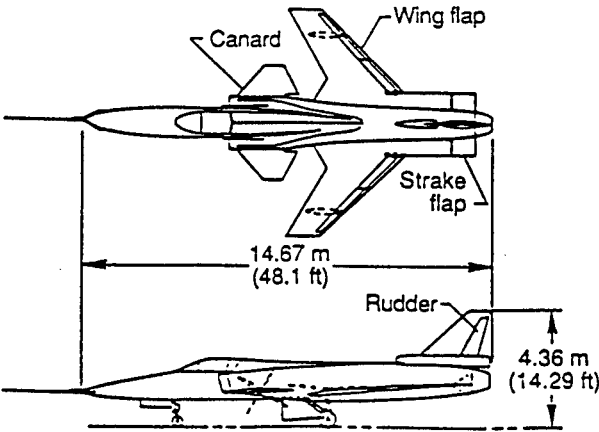
Figure 2. Drawing of X-29A aircraft.
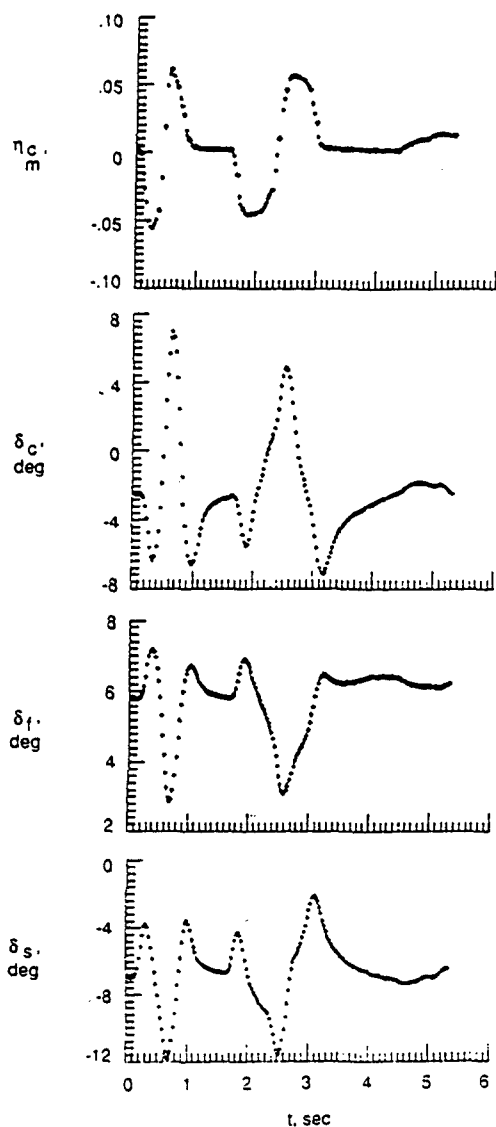
Figure 3. Time histories of measured input variables. Pilot input.
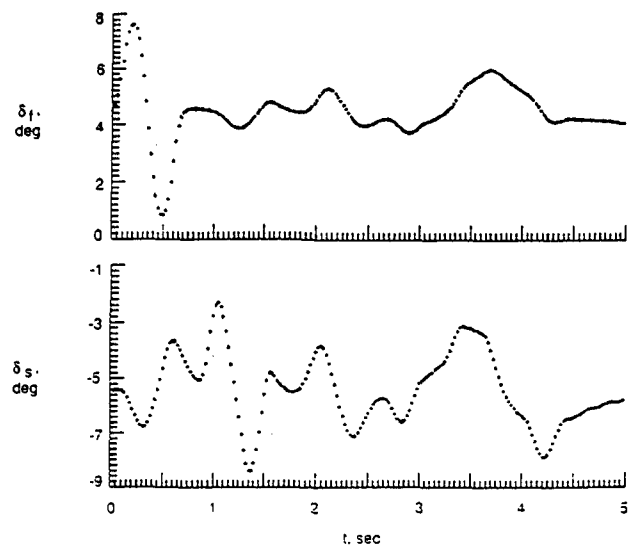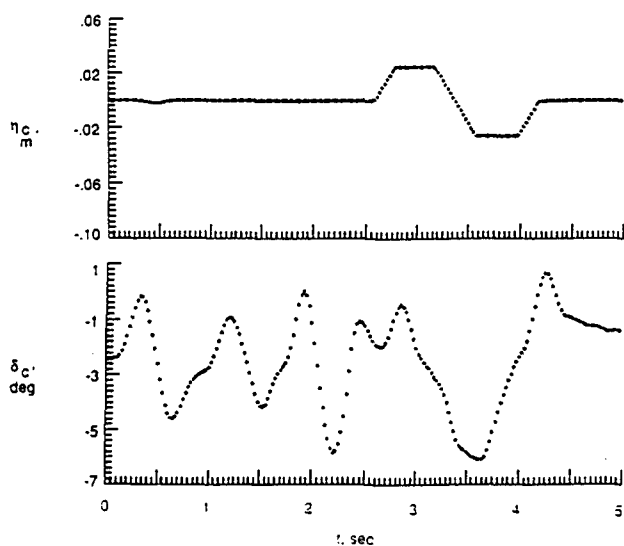
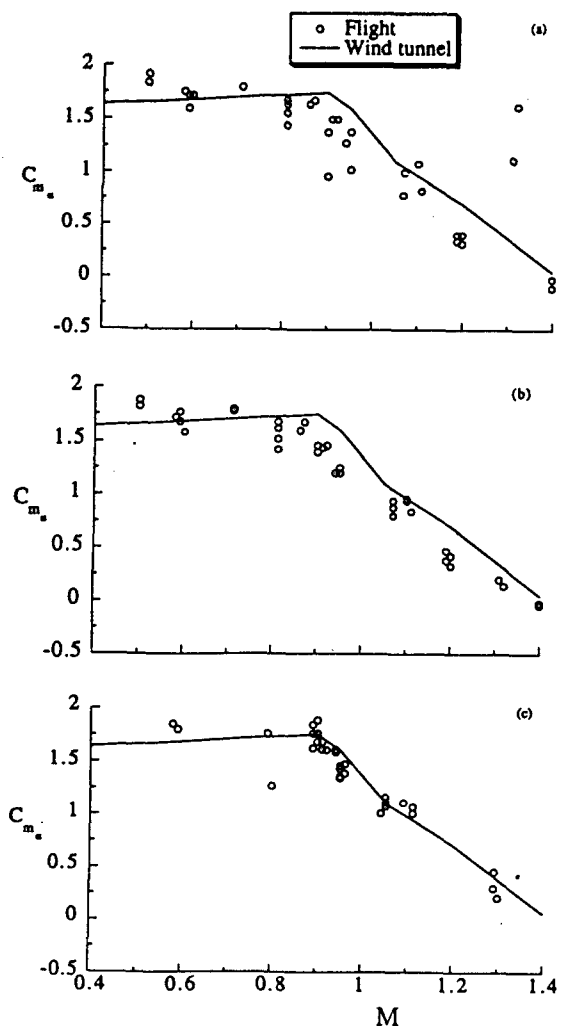Figure 4. Time histories of measured input variables. RAV experiment.

Figure 5. Static-stability parametr estimated from flight data with pilot input by using (a) least squares, (b) mixed estimation, (c) from RAV experiment.
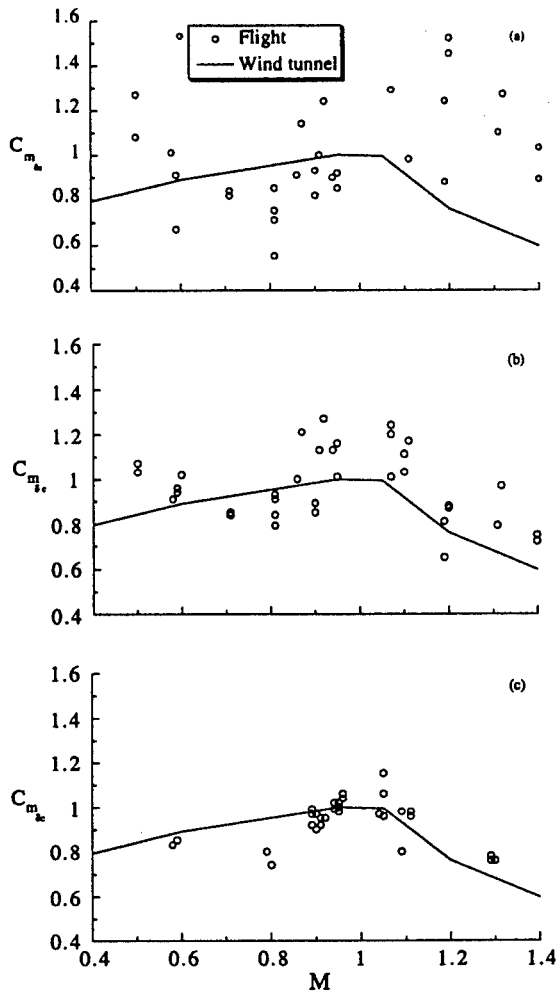
Figure 6. Canard effectiveness estimated from flight data with pilot input by using (a) least squares, (b) mixed estimation, (c) from RAV experiment.
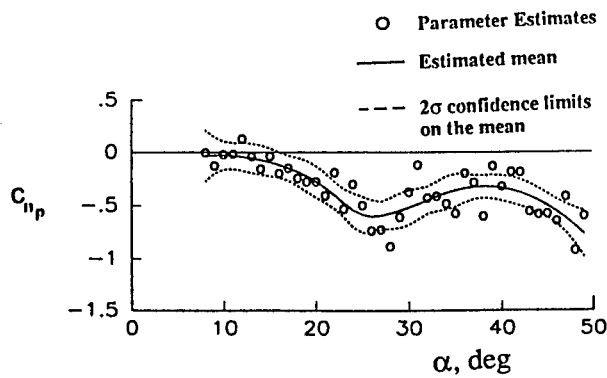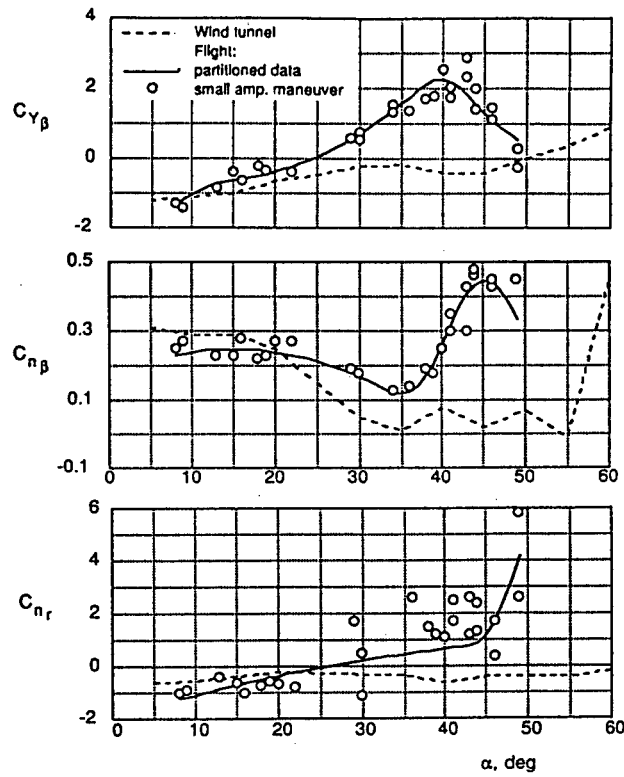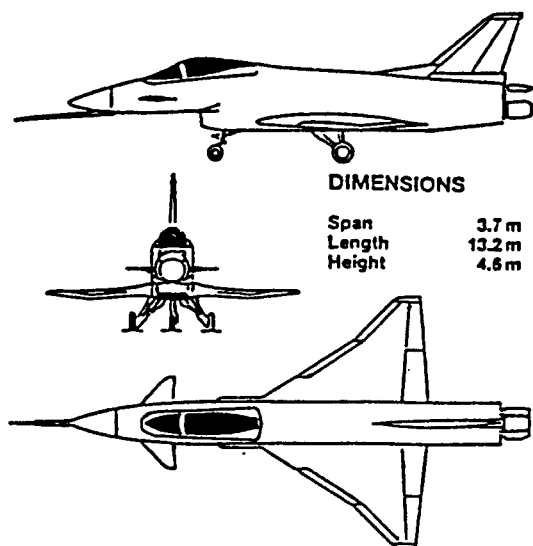

Figure 8. Comparison of lateral-force and yawing-moment parameters estimated from flight and wind-tunnel experiment.

Figure 7. Roll-rate parameter estimated from partitioned data.
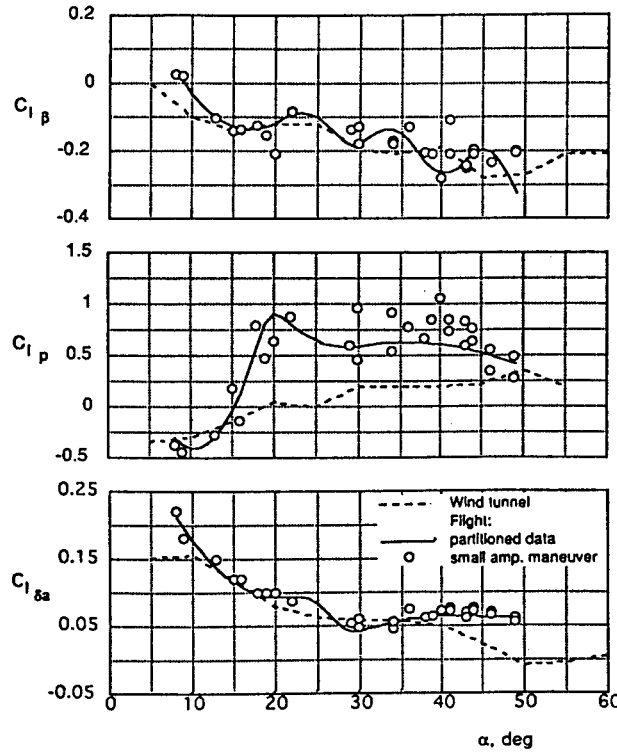
Figure 9. Comparison of rolling-moment parameters estimated from flight data and wind-tunnel experiment.

Figure 10. Drawing of X-31A aircraft.

DIMENSIONS

Span   3.7 m
Length   13.2 m
Height   4.6 m

- ○ Pilot Input
- ● Computer Input
- ▲ Drop Model
- —— Wind Tunnel
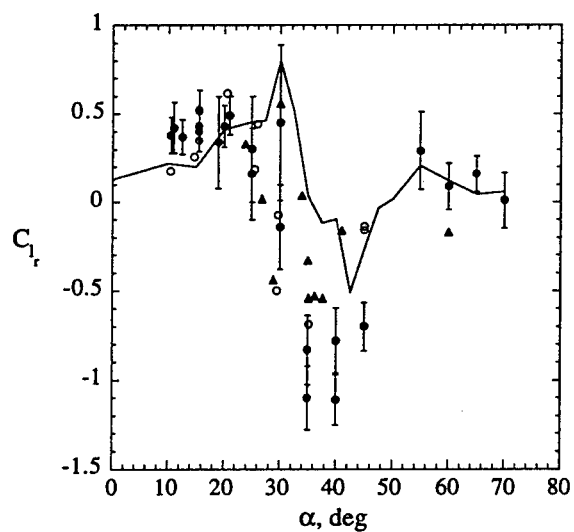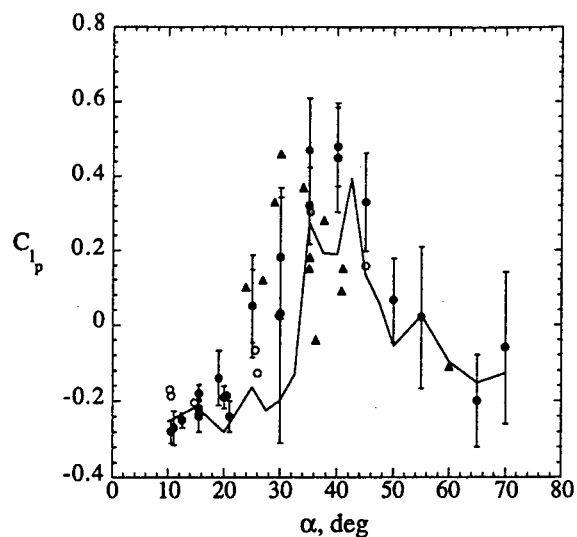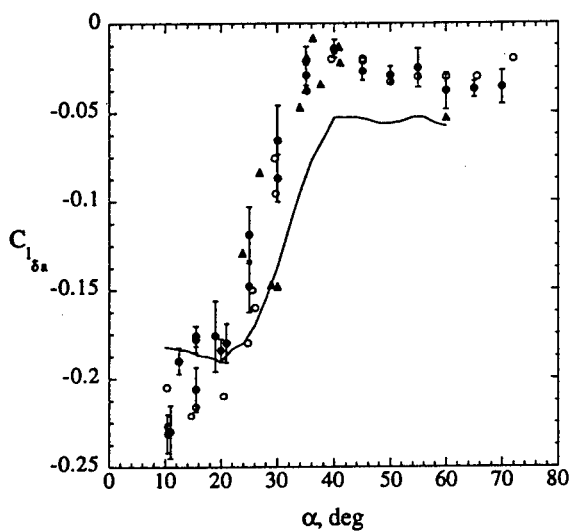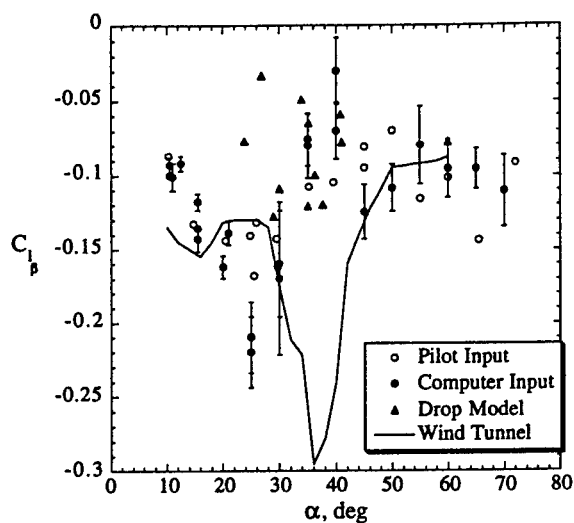
Figure 11. Comparison of rolling-moment parameters estimated from full-scale aircraft and drop model data, and wind-tunel experiment.
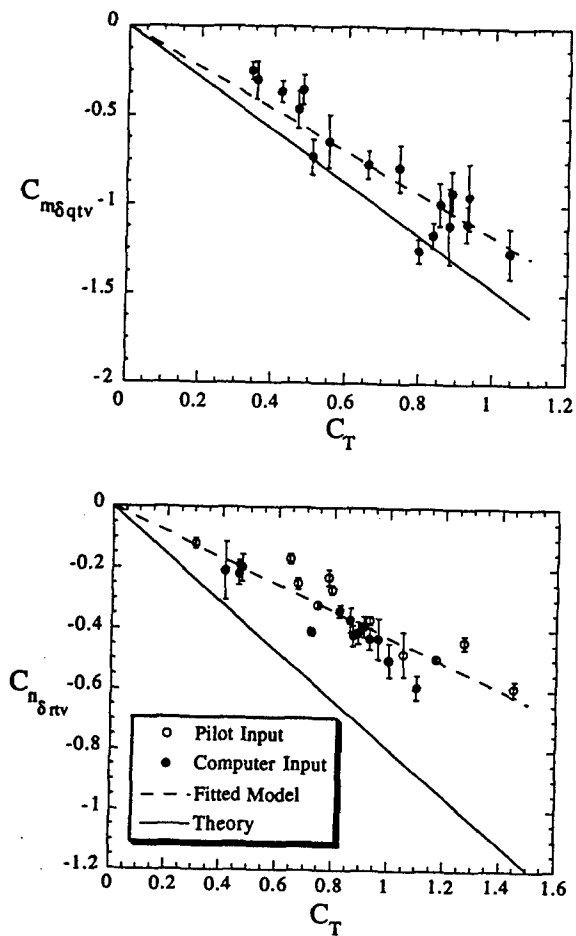
Figure 12. Comparison of estimated thrust- vectoring effectiveness and its theoretical values.
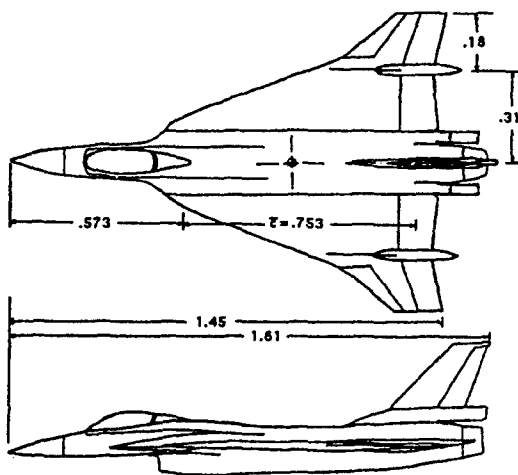

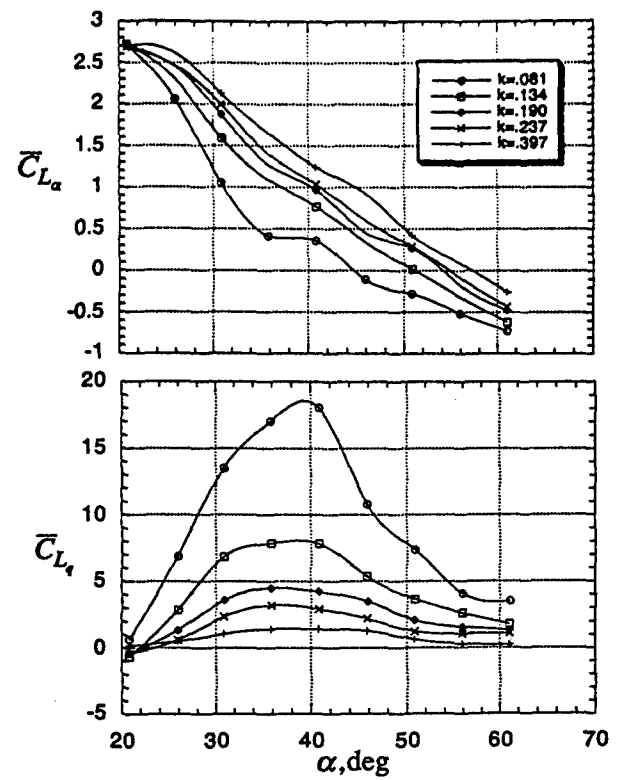Figure 13. Drawing of F-16XL model.

Figure 14. Variation of in-phase and out-of-phase components with angle of attack for different values of reduced frequency.
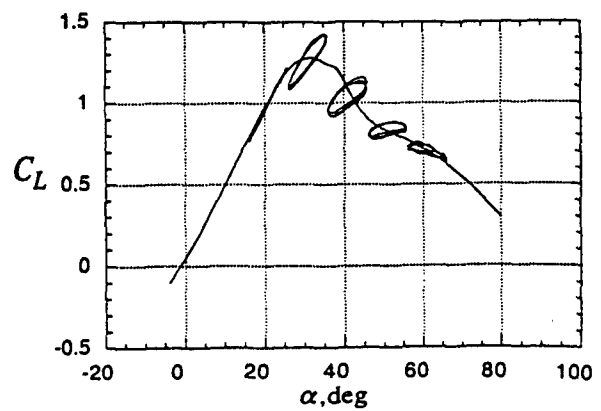

Figure 15. Lift coefficient obtained from static and oscillatory data for k=0.190.
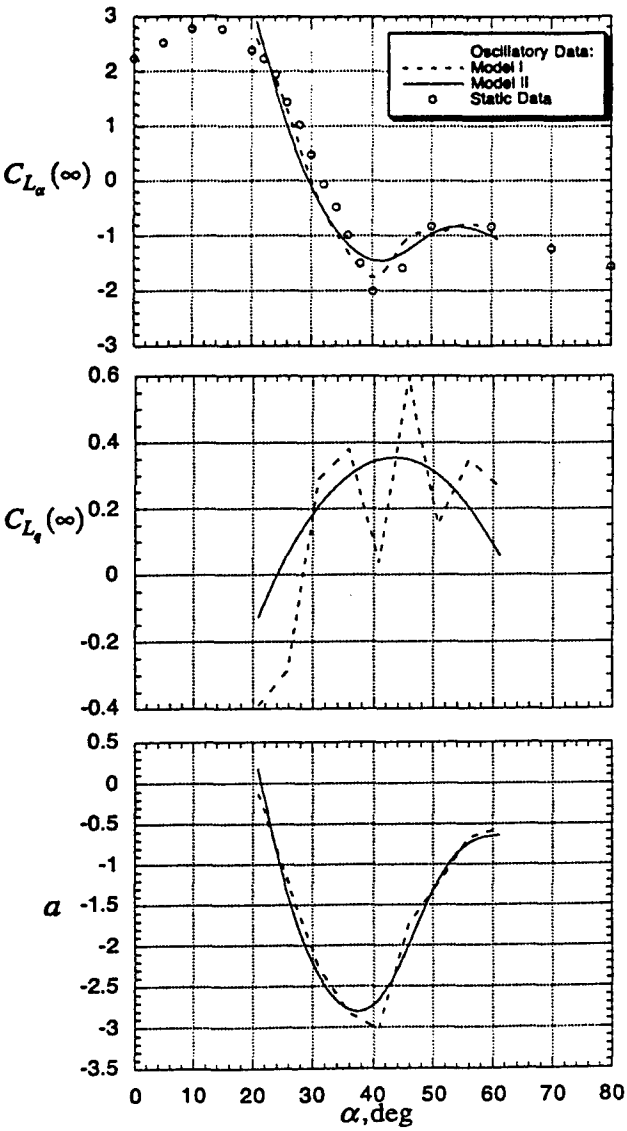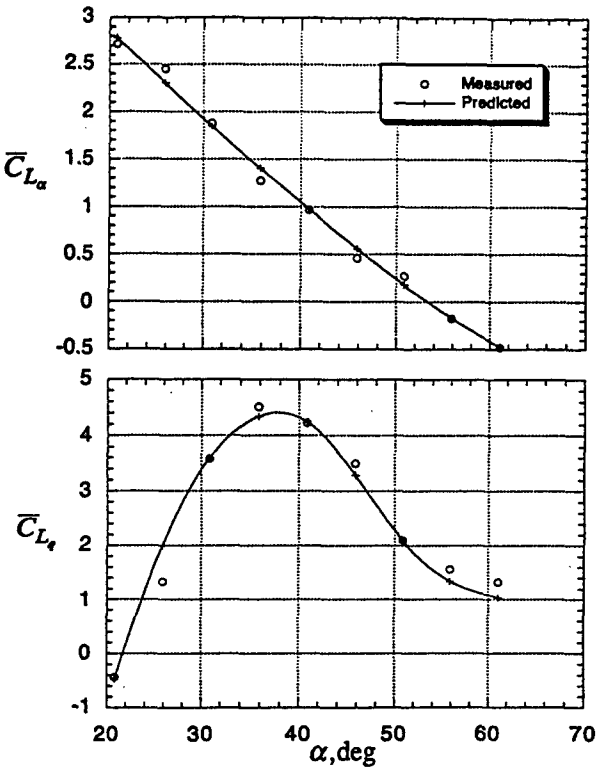
Figure 16. Estimated parameters of lift components.

Figure 17. Measured and predicted in-phase and out-of-phase components of lift coefficient. Model II, k=0.190.

AERODYNAMIC MODEL EXTENSION AND VALIDATION OF A THRUST VECTORED
DELTA-CANARD CONFIGURATION

Holger Friehmelt
DLR
Institute of Flight Mechanics
P.O. Box 32 67
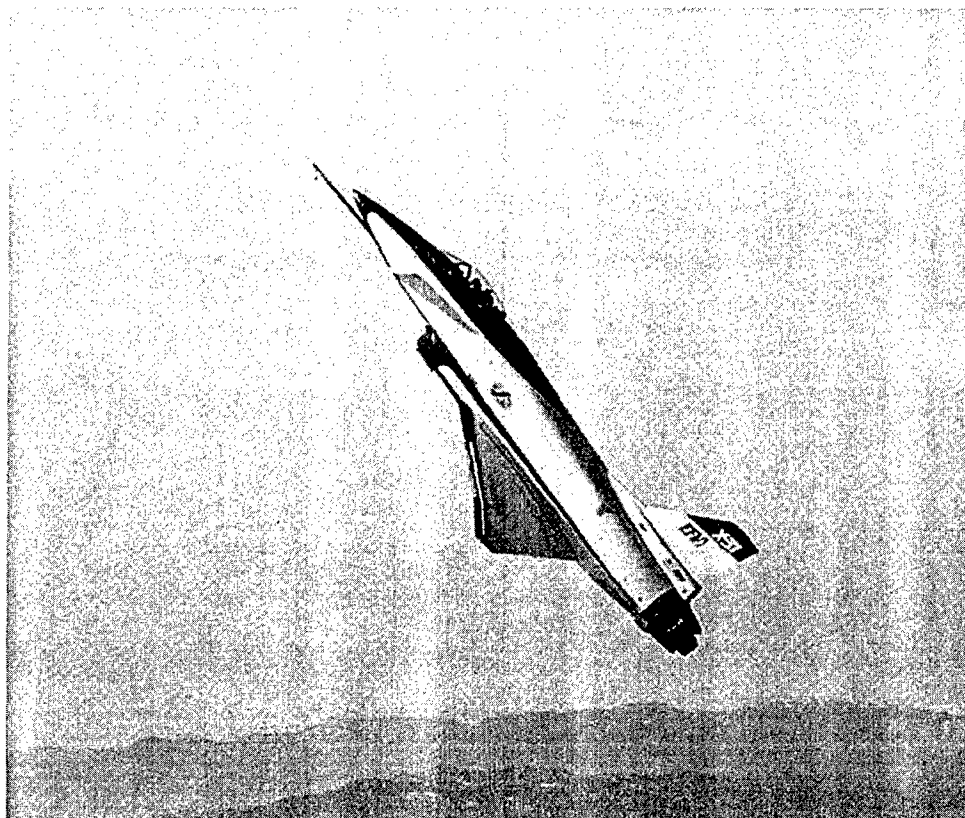D-38022 Braunschweig, Germany
eMail: Holger.Friehmelt@dlr.de

Photo Credit NASA Dryden FRC EC94-42478-16

Figure 1: X-31A Flying at 70° AoA over Edwards AFB, CA

1. ABSTRACT

Due to their advantages in aerodynamic characteristics, delta-canard configurations have experienced growing interest and have been realized in various recent aircraft designs. In addition, thrust vectoring has emerged as an efficient means of providing control power throughout the entire flight envelope. Aerodynamic modeling and identification of parameters for this kind of configurations have usually been restricted to the constant and linear terms in a Taylor series approximation of the force and moment coefficients. These modeling approaches are straight-forward and easy to handle in parameter identification processes but sometimes lack physical understanding of the flow phenomena encountered on delta-canard configuration with thrust vectoring. Interactions between aerodynamics and the thrust vectoring system, although sometimes only of secondary importance, have been omitted completely so far. The present work postulates new extended models which include nonlinear and higher order terms in order to better model thrust vector characteristics. By looking at the flow phenomena involved, model formulations are introduced which can be explained and justified by the physical understanding.

As detailed knowledge of controls effectiveness is necessary to assure proper design of the flight control system (i.e. gains) and is related to agility of aircraft, the present investigation aims at improving the modeling fidelity of thrust vector controls effectiveness.

Instead of one global, linear flaperon effectiveness, an extended model covers the directional sensitivity of flaperon deflection and a nonlinear rise in effectiveness. When the flaperon is deflected downward towards the freestream flow, its effectiveness is expected to be different than during an upstroke into the thick leeward boundary layer above the main wing and further into the region of separated flow at intermediate to high angles of attack. Results from parameter identification of these new models with actual flight test data from the X-31A aircraft (Figure 1) correlate with the physical understanding which the model extensions are based on.

The thrust vectoring system of a single engine aircraft introduces further controls in pitch and yaw. In case of the X-31A with its three aft-mounted paddles designed to deflect the engine exhaust flow, it is shown that a single linear term of thrust vector effectiveness is a very crude and only mathematically appropriate way of modeling the thrust vector effectiveness. A new model is postulated which can consider a dead-band, i.e. the lack of effectiveness of the vanes while they

are not yet emerged into the exhaust flow due to imperfect plume boundary tracking of the vanes, a deflection range of minor effectiveness as the vanes have not yet fully entered the core exhaust flow, and finally the region of high and linear effectiveness while the vanes are fully entrained by the core flow. Flight test data from the X-31A aircraft has been used to verify and validate the extended model postulations.

Parameter identification with these extended models thus yields controls effectiveness parameters which can then be interpreted by means of looking at the physical flow phenomena involved and help improve the understanding of flight dynamic characteristics of aircraft.

2. NOMENCLATURE

AFB	Air Force Base
AoA	Angle of Attack
ARPA	Advanced Research Projects Agency
Dasa	Daimler-Benz Aerospace AG
DLR	Deutsches Zentrum für Luft- und Raumfahrt e.V.
EF	EuroFighter
EFM	Enhanced Fighter Maneuverability
FMOD	Federal Ministry of Defense
ITO	International Test Organization
MBB	Messerschmidt Bölkow Blohm
NASA	National Aeronautics and Space Administration
PST	Post Stall
TKF	Taktisches Kampfflugzeug

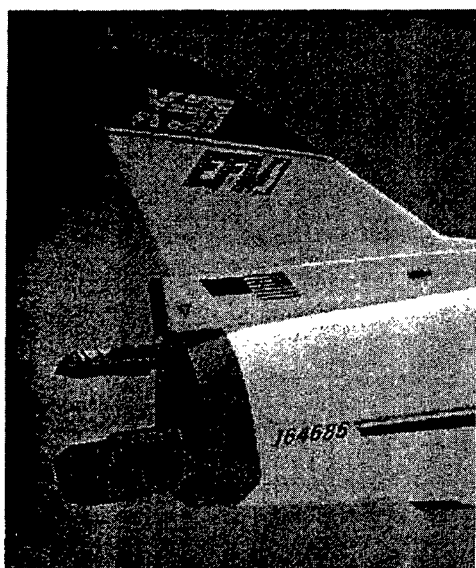|	
C_m	Lift Coefficient
g	Gravitational Acceleration
m	Mass
q	Pitch Rates
S	Wing Surface Area
T	Thrust
V	Air Speed
α	Angle of Attack
δ	Controls Deflection
ρ	Air Density
κ	Thrust Deflection Angle in Yaw
σ	Thrust Deflection Angle in Pitch

3. INTRODUCTION

Photo Credit NASA Dryden FRC EC92-04233-15

Figure 2: Thrust Vector System of the X-31A

More and more high performance fighter aircraft encompass enhanced maneuverability by means of a thrust vectoring system. The experimental aircraft X-31A [1,2] are equipped with three aft-mounted carbon-carbon paddles (Figure 2) to deflect the exhaust flow both in the vertical and horizontal plane, enabling thrust vector control both in pitch and yaw.

The X-31A comprises of a delta-canard configuration due to the aerodynamic advantages this type of wing planforms exhibit [2]. As these designs are naturally unstable configurations in the longitudinal motion, these types of aircraft can only be flown with help of sophisticated flight control systems. Design as well as verification and validation of such flight control systems require a profound knowledge of the aerodynamic and controls characteristics of the aircraft.

3.1 X-31A Configuration

The two X-31A aircraft were developed, designed, and built jointly by Rockwell International and Daimler-Benz Aerospace One design driver for the X-31A configuration was the requirement that results of X-31A flight testing should be directly transferable to a potential operational aircraft. However, no existing fighter aircraft was suitable to be retrofitted for supermaneuverability. Eventually a derivation of the German TKF (Taktisches Kampfflugzeug), a predecessor of the EF2000, was selected. Figure 3 shows a three-dimensional view of the X-31A configuration as it meets all requirements for enhanced fighter maneuverability.
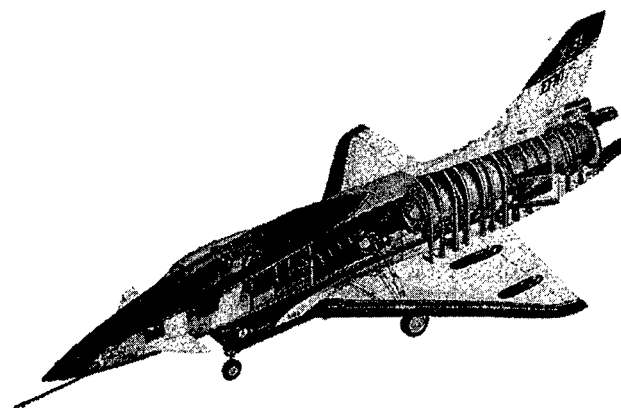

Figure 3: X-31A Configuration

The single-seat fighter-type X-31A is a delta-wing configuration with a long-coupled canard. Its take-off weight is little over 16 000 lbs. The X-31A is powered by a single General Electric F404 engine with some 17 000 lbs thrust wet. In order to reduce trim drag in supersonic flight the X-31A was designed with a center of gravity aft of the subsonic center of lift which makes it aerodynamically unstable. As the canard is commanded downward into the wind with increasing angle of attack it always maintains its control effectiveness and can be utilized for longitudinal control throughout the flight envelope. It especially guarantees adequate pitch-down control power in PST flight. Other control surfaces of the X-31A include a rudder and ailerons, i.e. trailing edge flaps which can be used both as elevator and ailerons. Unique feature of the X-31A are its three aft mounted paddles around the exhaust nozzle of the engine. These carbon-carbon paddles allow a deflection of the thrust vector in both pitch and yaw axis thus providing means of enhanced longitudinal and lateral/directional control independent from dynamic pressure and angle of attack as compared to the conventional aerodynamic control surfaces [3,4].

Summarizing the features of the X-31A configuration it is clear that the requirements for an aircraft with supermaneuverability were met:

- The thrust-to-weight ratio is in excess of 1.
- The air intake allows full power engine operation at up to 70° angle of attack by a movable intake lip.
- Aerodynamic characteristics have been tailored to enable a smooth transition into the PST regime.
- Thrust vectoring in pitch and yaw adds a vast amount of control power in those axes while the X-31A is still trimmable by conventional aerodynamic control surfaces even at PST angles of attack. Thus the thrust vectoring system is not a safety critical item in terms of recovery from a possible spin entry.

To control the X-31A a full authority, triplex, digital fly-by-wire flight control system has been developed by Dasa [5]. It includes mechanization of lateral stick inputs to roll the aircraft around the flight path at zero sideslip rather than around the familiar aircraft body axes. Thus, the so-called 'velocity vector roll' is a coordinated yaw and roll maneuver in terms of body axes. The longitudinal control features angle of attack command at low speeds and load factor command at higher speeds. One of the main tasks of the flight control system is the scheduling of control surfaces and thrust vector blend-in dependent on their control effectiveness as a function of flight condition.

3.2 System Identification

System identification [6] can be considered as postulating a suitable mathematical model and identifying the model parameters from flight test data in order to adequately model the aircraft. Whilst in the traditional approach, the model structure is already given by Taylor series expansions broken off after their linear terms and thus system identification is limited to the parameter identification of the terms in those Taylor series, the present paper focuses both on finding a suitable model which is not only mathematically feasible but which also has some physical meaning and on identifying the corresponding parameters in these models.

3.3 Traditional Modeling Approach

Basis of all aerodynamic modeling during system identification is Newton's second law of motion. It states for translational motion an equilibrium of all externally applied forces and the time rate of change of linear momentum $\bar{p}$. Simplified assuming constant mass it can be expressed by the equilibrium of external forces $\bar{F}$ and mass m multiplied by acceleration $\bar{a}$ as shown in Equation (1):

$$\bar{F} = \frac{d\bar{p}}{dt} \cong m \cdot \bar{a} \qquad (1)$$

This vector equation covers all three translational degrees of freedom. A similar fundamental expression is given by

$$\bar{M} = \frac{d\bar{H}}{dt} = \underline{\underline{I}} \cdot \frac{d\bar{\Omega}}{dt} + \frac{d\underline{\underline{I}}}{dt} \cdot \bar{\Omega} . \qquad (2)$$

for the rotational degrees of freedom. Equation (2) describes the rate of change of angular momentum $\bar{H}$ being balanced by the sum of all applied torques $\bar{M}$.

Mass properties m and moments of inertia $\underline{\underline{I}}$ can be determined before the flight test experiment and can be considered to be constant throughout the entire time slices under investigation for system identification. As maneuvers for parameter identification usually are fairly short, no changes in mass properties have to be accounted for. Only special maneuvers like during air drop require special attention [7].

A multitude of instruments aboard aircraft allows accurate measurement of translational velocities and accelerations as well as angular rates which yield angular accelerations by numerical differentiation. Thus, the right-hand sides of Equations (1) and (2) are known. Only the forces and moments in these equations remain to be modeled. After choosing a suitable reference system, all forces and moments acting on the airframe can be summed up. Figure 4 gives an example for the longitudinal motion.
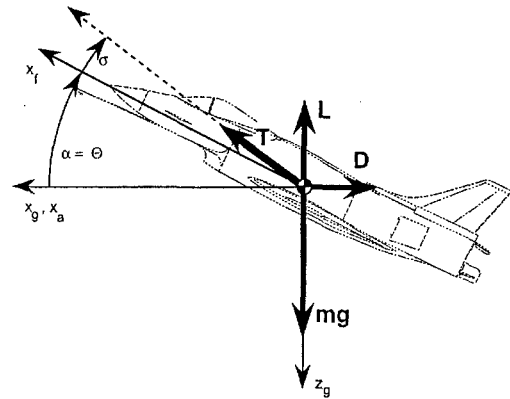

Figure 4: Longitudinal Equilibrium of Forces

When formulating the differential equations for the aircraft's motion (based on Newton's second law [Equations (1) and (2)]), the aerodynamic forces and moments are usually approximated by Taylor series expansions.

$$f(x) = \sum_{v=0}^{n} \frac{f^{(v)}(x_0)}{v!} (x - x_0)^v + R_n(x) \qquad (3)$$

with $R_n(x) \overset{def}{=} \frac{f^{(n+1)}(x_0 + \vartheta(x - x_0))}{(n+1)!} (x - x_0)^{n+1}$ $\qquad (4)$

$$\vartheta \in (0,1)$$

Traditionally, flight mechanical models are derived from a Taylor series expansions broken off after its linear terms:

$$f(x + h) \approx f(x) + hf'(x) \qquad (5)$$

As an example, the pitching moment equation is shown:

$$\frac{dq}{dt} = \frac{\bar{q}S\bar{c}}{I_y} C_m + \frac{M_{Engine}}{I_y} \quad \text{with} \qquad (6)$$

$$C_m = C_{m0} + C_{m\alpha}(\alpha - \alpha^*) + C_{mq}q\frac{\bar{c}}{2V} + C_{m\delta_e}\delta_e$$
$$+ C_{m\delta_{can}}(\delta_{can} - \delta_{can}^*) + C_{m\sigma}\sigma\frac{T}{\bar{q}S} \qquad (7)$$

q denotes pitch rate, and C_m is the pitching moment coefficient, which comprises all contributions to the pitching moment from aerodynamics (symmetric trailing edge deflection δ_e and canard deflection δ_{can}) as well as thrust deflection σ. By looking at Equation (4), the linearization around a trim point (values with an asterix as superscript) becomes obvious, and terms of higher order are deliberately omitted.

The present X-31A delta-canard configuration with its highly pronounced vortex system [4], however, displays besides various nonlinearities in aerodynamic derivatives and control effectiveness parameters also possibly nonlinear characteristics of its thrust vectoring system as it is described in the present paper.

4. MOTIVATION FOR MODEL EXTENSIONS

Before two kinds of model extensions are presented in this paper, some general considerations on the observed modeling error characteristics are introduced. Thus, the motivation for those model refinements becomes apparent.

4.1 Observed Modeling Error Characteristics

With a traditional linear model one would expect an increasing modeling error with increasing deviation from the working point as depicted in Figure 5 (difference between the solid line, representing the true value, and the dashed line, depicting the model output).

A mis-estimation of the derivative in the linear Taylor series expansion is shown by the dotted line in Figure 5. It can lead to a further increase in error with increasing deviation of the input from the point of linearization.
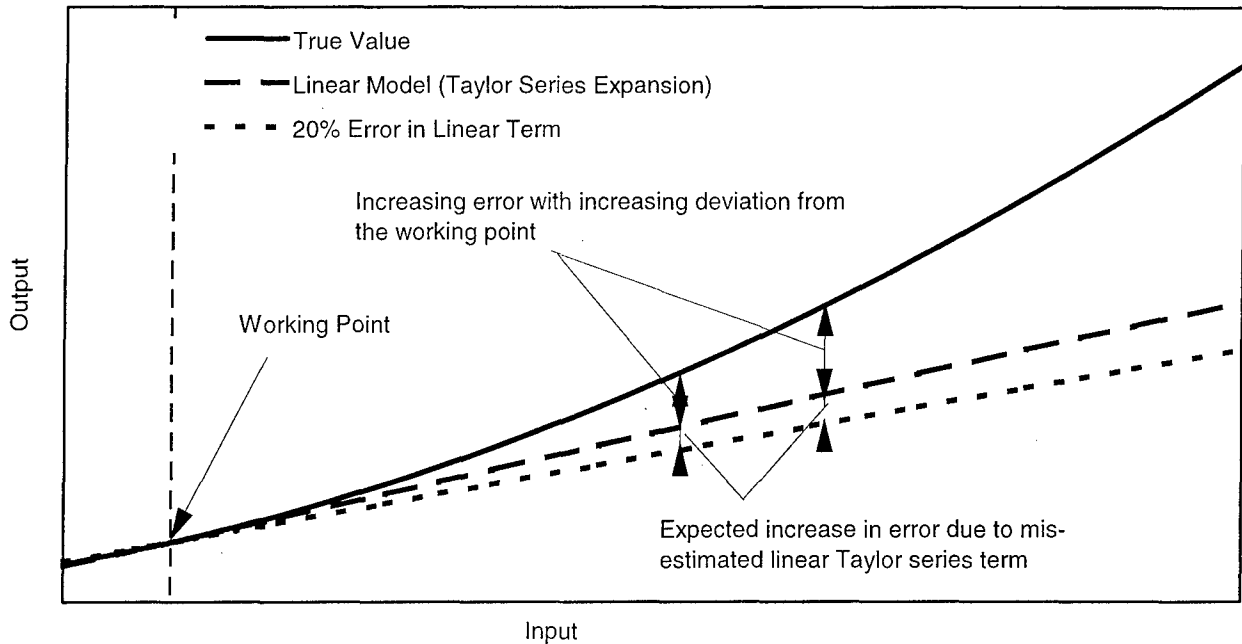

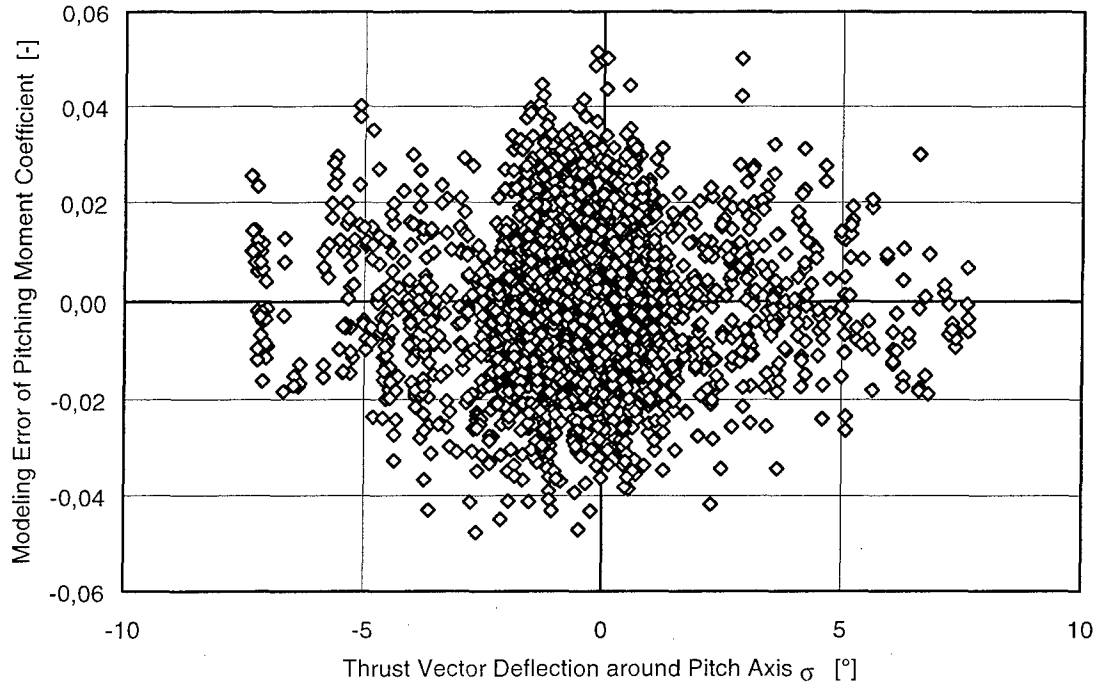Figure 5: Increase in Error for Traditional Linear Models

Figure 6: Modeling Error of Pitching Moment Coefficient vs. Thrust Deflection Angle

Actual identification results with three doublets and three 3-2-1-1 multistep inputs to individual control surfaces during so-called 'separate surface excitation' experiments [8,9] show a completely different error characteristics in pitching moment coefficient. Figure 6 shows the error in pitching moment coefficient versus the thrust deflection angle σ around the pitch axis. Thus the observed error characteristics contradict the expected error characteristics as explained above and depicted schematically in Figure 7. These model deficiencies led to a search for model extensions for the thrust vectoring characteristics during system identification based on physical understanding.
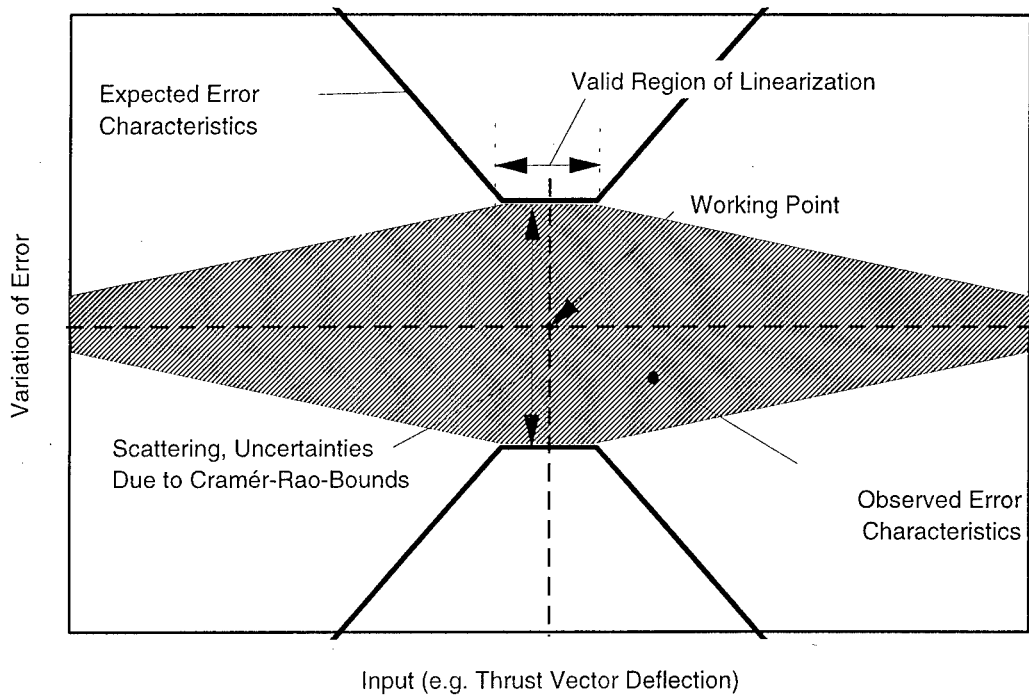
Figure 7: Comparison of Expected and Observed Error Characteristics

5. DIRECTIONAL SENSITIVITY

The thrust vectoring system of the X-31A with its three aft-mounted deflection vanes [10] is depicted in Figure 8 [11]. Considering the phenomena involved during thrust deflection can lead to a modeling refinement incorporating directional sensitivity of the thrust vector effectiveness parameter as described below.

5.1 Flow Physical Background

As it becomes obvious from Figure 8, a commanded downward thrust deflection is realized by the X-31A thrust vector system solely with the upper of the three articulated vanes. In contrast, an upward deflection involved both lower thrust deflection vanes.

Figure 8: X-31A Thrust Deflection Vanes [11]

When impinging the thrust deflection vanes into the exhaust flow of the engine, several phenomena cause thrust and deflection losses [12].

Due to the abrupt deflection of the exhaust stream when hitting the vane surface, some of the exhaust flow is not directed exactly into the desired direction.

As the vanes have to have a certain spacing in between to avoid contact in their fully deflected positions, a certain amount of the exhaust flow can leak through this gap as shown in Figure 9. (This is avoided in case of internal thrust vectoring systems e.g. with a nozzle [12].)
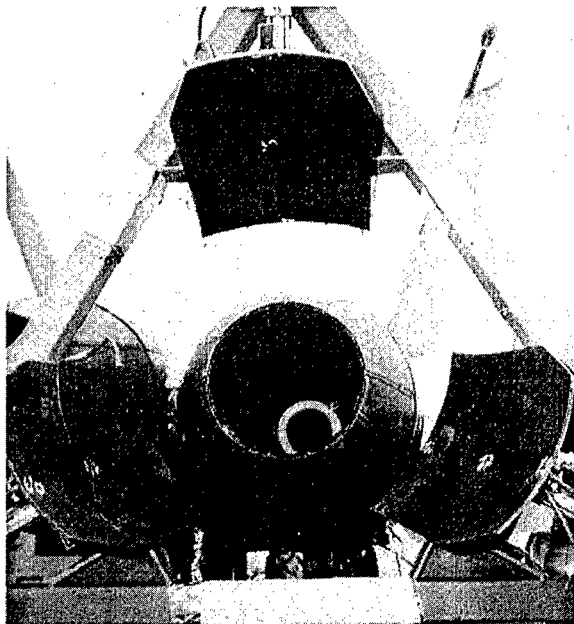

Photo Credit NASA Dryden

Figure 9: Spillage during Thrust Deflection

These considerations suggest that there might be different characteristics of the thrust vectoring system for upward and downward deflections. Thus, the introduction of a directional sensitivity of the thrust vector effectiveness parameter, i.e. allowing for a different behavior of the system when only one vane is engaged as in case of a downward deflection and when both lower vanes are active as in case of an upward deflection respectively, becomes viable. This possible directional sensitivity is schematically depicted in Figure 10.

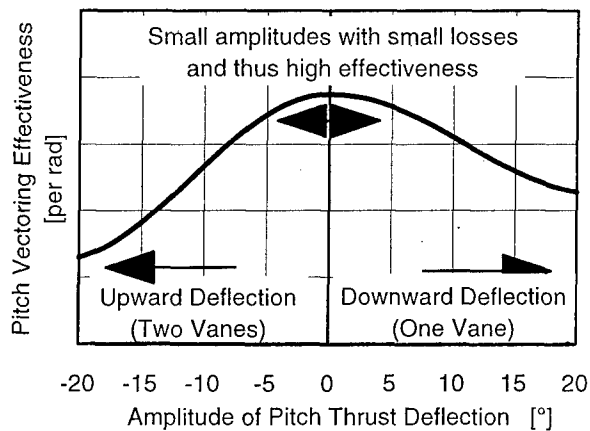Figure 10: Possible Characteristics (Schematic) of Thrust Vectoring Effectiveness with Directional Sensitivity

5.2 Model Extension

The aerodynamic model has now been extended to cope with the before mentioned possible directional sensitivity. Two new parameters for thrust vector effectiveness have been introduced (underlined in Equation 8) and the traditional thrust vector effectiveness has been omitted.

$$\overline{C}_{m\sigma-} = \left.\frac{\partial C_m}{\partial \sigma}\right|_{(\sigma-\sigma^*)<0} \cdot \frac{\frac{\rho}{2}V^2 S}{T} \text{ and } \quad (8a)$$

$$\overline{C}_{m\sigma+} = \left.\frac{\partial C_m}{\partial \sigma}\right|_{(\sigma-\sigma^*)>0} \cdot \frac{\frac{\rho}{2}V^2 S}{T}, \text{ respectively.} \quad (8b)$$

Similar expressions have been derived for the lift and drag coefficients and have been incorporated into the aerodynamic model as shown below.

$$C_m = C_{m0} + C_{m\alpha}(\alpha - \alpha^*) + C_{mq}q\frac{\overline{c}}{2V} + C_{m\delta_e}(\delta_e - \delta_e^*)$$

$$+ C_{mCAN}(\delta_{CAN} - \delta_{CAN}^*) + \overline{C}_{m\sigma}\left(\sigma - \sigma^*\right)\frac{T}{\overline{q}S}$$

$$+ \left\{ \overline{C}_{m\sigma-}(\sigma - \sigma^*)\Big|_{(\sigma-\sigma^*)<0} + \overline{C}_{m\sigma+}(\sigma - \sigma^*)\Big|_{(\sigma-\sigma^*)>0} \right\} \cdot \frac{T}{\overline{q}S} \cdot \cos\kappa \quad (9)$$

5.3 Results

This extended model has been evaluated with dedicated PID maneuvers with a so-called 'single surface excitation' [8, 9] in order to avoid the high correlations between states and controls over the entire angle of attack regime of the X-31A aircraft. The identification results for the directionally

sensitive parameters of the thrust vector effectiveness are plotted in Figure 11. The solid bars depict the identified thrust vector effectiveness from the traditional linear model as it has been described in chapter 3.3 for comparison. In all cases, the result of the linear model lies in between the two directionally sensitive effectiveness parameters.
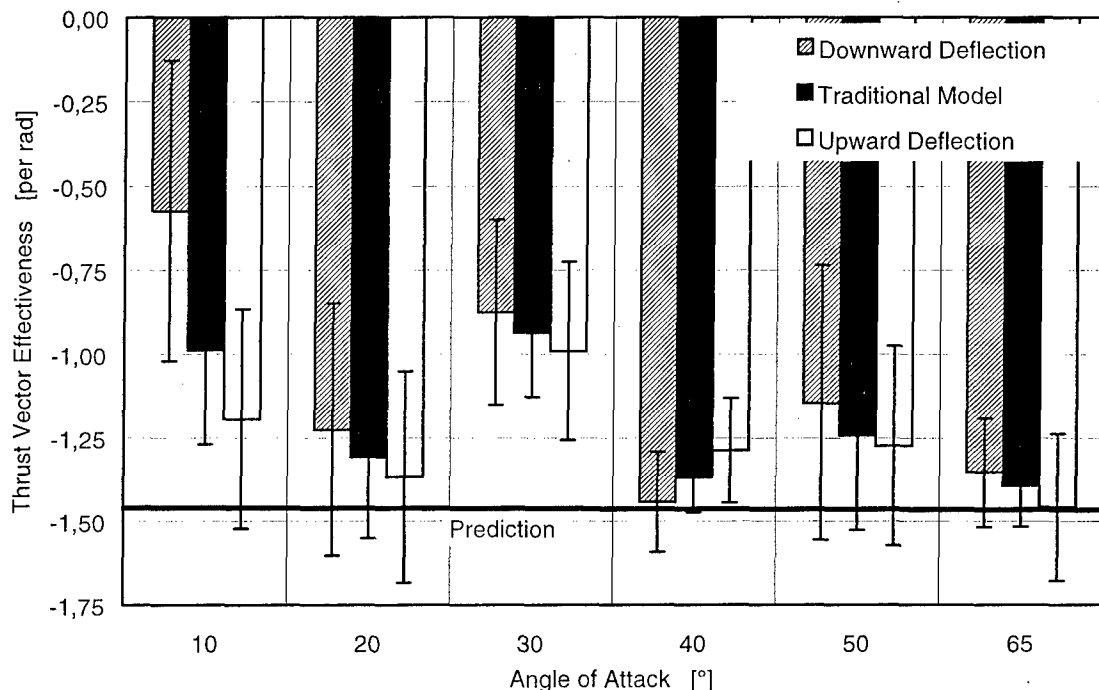
Figure 11: Identified Thrust Vector Effectiveness with Directional Sensitivity

At all angles of attack but 40° the same trend can be observed. The identified thrust vector effectiveness is of smaller magnitude in case of downward deflections. Complex interactions between the thrust vectoring system and the flow-field around the main wing and the aft fuselage may contribute

to the observed nonlinear characteristics and may even be a reason for the observed exception at 40° angle of attack. Furthermore, the asymmetry of the tables describing the thrust vector system in the flight control system may be a cause for the observed nonlinearities. Although these tables are highly

sophisticated and fairly comprehensive in their scope to describe the characteristics of the thrust vectoring system [9], small mis-matches may have an impact on the identification results through the data pre-processing before the actual parameter identification with the extended model.

6. NONLINEAR THRUST EFFECTIVENESS MODEL
Motivation of a profound investigation of the possibly nonlinear effectiveness parameters of the thrust vectoring system was derived from the following considerations.

6.1 Flow Physical Background
Nonlinearities of the thrust vectoring system can arouse due to the non-perfect 'plume boundary' tracking and the structure of the exhaust flow.

If the vanes are not perfectly following the boundary of the exhaust plume (which changes with thrust setting) a deadband can emerge before the vanes become effective (see Figure 12). Furthermore, thrust vector effectiveness could be lower in an outer region of the plume (less energetic flow) than in the core region of the exhaust plume.
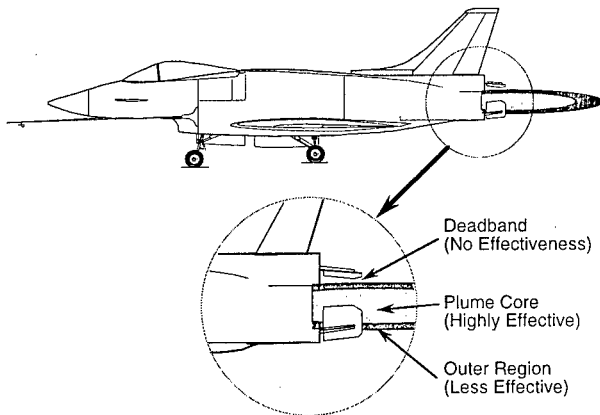

Figure 12: Schematic Drawing of Thrust Vectoring System and Exhaust Plume

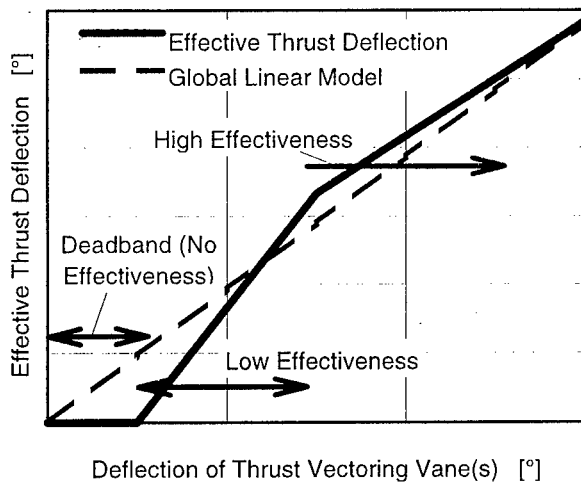Deflection of Thrust Vectoring Vane(s) [°]

Figure 13: Possible Nonlinearities in TV Effectiveness

Thus, the consideration of a dead-band and a breakpoint in the thrust vector effectiveness versus thrust vane and thrust deflection angle, respectively, as shown in Figure 13, is viable.

6.2 Model Extension
In this second approach the aerodynamic model has been extended to cover nonlinear characteristics of the thrust vectoring system directly in the model. Intervals of thrust deflection angle have been defined (Figure 14) for which linear behavior of thrust vector deflection effectiveness according to the conventional Taylor series expansion is assumed. For investigation of nonlinear thrust vector effectiveness ten intervals with a width of small thrust vector deflection $\Delta\sigma$ have been considered. These intervals are arranged symmetrically around $\sigma = 0°$ as indicated in Figure 14.

An interval width of 0.5° has proven to be most suitable for this kind of a model extension. The intervals are thus small enough to resolve the expected local characteristics and still coarse enough to assure a big enough information content of the data points to allow for a high fidelity identification process.

Contributions to the pitching moment by thrust vector deflection are assigned to a linear derivative, which in turn is assigned to the corresponding interval of thrust vector deflection angle σ. This is achieved in the regression model during the parameter identification process through staggered „If…Then…Else" statements, which are run through subsequently to determine the interval and to assign the pitching moment contribution to the corresponding parameter.
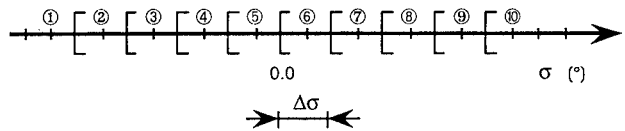
Thrust Deflection Angle

Figure 14: Intervals for Piecewise Linear Thrust Vector Effectiveness Parameters

The extended model structure is shown in Equations 10 through 12 for the example of the pitching moment coefficient. Again, new terms are underlined while the traditional parameter for the thrust vector effectiveness has been omitted. Similar expressions hold for the lift and drag coefficient in the aerodynamic model and hence are not shown here.

$$\overline{C}_m(\sigma) = \begin{cases} \overline{C}_{m\sigma1}\left(\sigma - \sigma^*\right)\Big|_{\sigma\in]-\infty;-2,0°[} \\ \overline{C}_{m\sigma2}\left(\sigma - \sigma^*\right)\Big|_{\sigma\in[-1,5°;-1,0°[} & \text{with} \\ \vdots \\ \overline{C}_{m\sigma10}\left(\sigma - \sigma^*\right)\Big|_{\sigma\in[2,00°;\infty[} \end{cases} \quad (10)$$

$$\overline{C}_{m\sigma_i} = \left.\frac{\partial C_m}{\partial\sigma}\right|_{\sigma\in[\sigma_i;\sigma_i+\Delta\sigma_{Interval\ Width}]} \cdot \frac{\frac{\rho}{2}V^2S}{T}$$

$$i = 1 \ldots 10. \quad (11)$$

$$C_m = C_{m0} + C_{m\alpha}(\alpha - \alpha^*) + C_{mq}q\frac{\overline{c}}{2V} + C_{m\delta_e}(\delta_e - \delta_e^*)$$

$$+ C_{mCAN}(\delta_{CAN} - \delta_{CAN}^*) + \overline{C}_{m\sigma}(\sigma - \sigma^*)\frac{T}{qS} + \overline{C}_m(\sigma)\cdot\frac{T}{qS}\cdot\cos\kappa \quad (12)$$
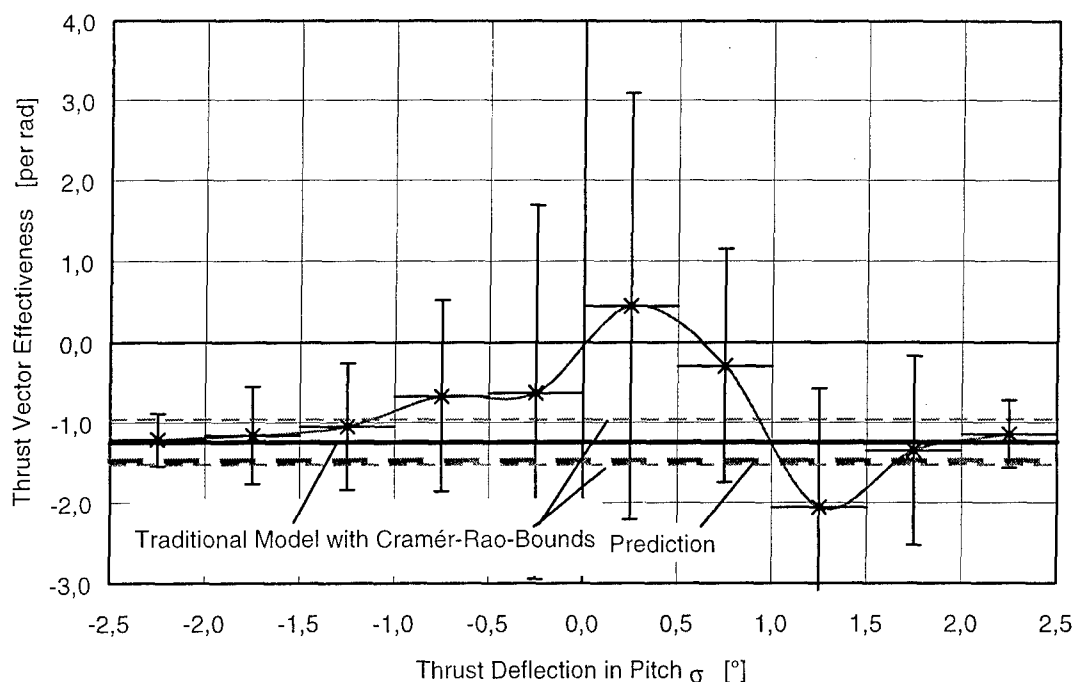
6.3 Results

Figure 15: Piecewise Linear Thrust Vector Effectiveness at 50° AoA

Selected results from representative PID maneuvers at 50° angle of attack are depicted in Figure 15. The solid line depicts the identification results for the traditional linear and globally valid parameter of thrust vector effectiveness including its Cramér-Rao uncertainty bounds for reference purposes. The dashed line represents the prediction of the aerodynamic data set, i.e. the thrust vector characteristics tables. For large pitch deflections, in the present example for amplitudes above roughly 1.5°, the local parameters of thrust vector effectiveness approach the identification value of the traditional model and exhibit similar Cramér-Rao uncertainty bounds as the linear control derivative. For small thrust deflections in pitch, a reduced thrust vector effectiveness can be observed. However, these results for amplitudes below ±1.5° are accompanied with larger Cramér-Rao uncertainty bounds.
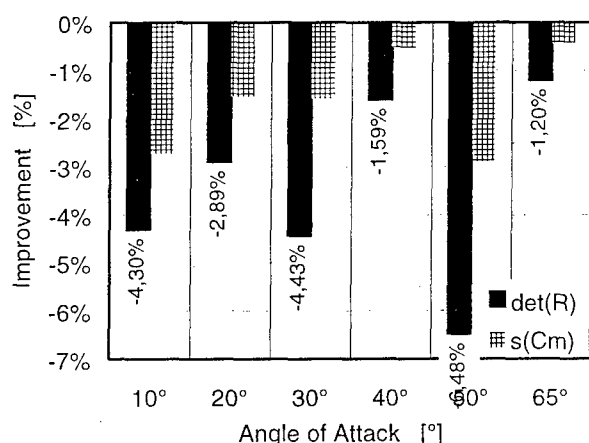

Figure 16: Improvement of Identification Fidelity by Introducing Piecewise Linear Thrust Vector Effectiveness Parameters

The limited number of data points satisfying the interval conditions and the corresponding limited information content of the data samples available somewhat hamper the identification process and its fidelity. The results nevertheless appear to be most likely and plausible.

The overall improvement of the identification fidelity of the extended model compared to the traditional ones is visualized in Figure 16 by the determinants of the estimation error covariance matrix det(R) and the standard deviations of the modeling error of the pitching moment. Similar trends can be observed for the standard deviations of the modeling errors of lift and drag coefficients although not shown here. The improvement of the determinants is in the order of some percent, normally around 5%, and thus well justifies the proposed model extensions.

7. GLOBAL HIGH-ORDER NONLINEAR MODELS

One might be tempted to address the issue of nonlinear characteristic of the thrust vector effectiveness with a globally valid nonlinear higher-order model to avoid the cumbersome model extensions aforementioned and discussed.

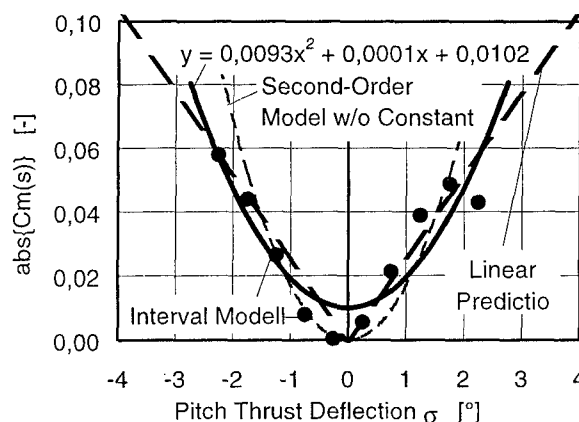That such an approach is not feasible in the present case shall be explained here.

Figure 17: Schematics of a Second-Order TV Model

Figure 17 depicts the schematics of a second-order thrust vectoring model as compared to the traditional linear one (dashed line) and a piecewise linear one of an extended model (solid dots). A full second-order model would however either mislead for very small thrust deflections by suggesting a thrust vector force even without any thrust deflection (as shown in Figure 17), or would overestimate the effectiveness at high amplitudes since the flanks of the parabola are too steep.

Another problem with such a high-order model becomes apparent when looking at the necessary aerodynamic model equations.

The constant term of the second-order thrust vector model (underlined with dashed line) is almost fully correlated to the constant pitching moment coefficient (underlined) as during typical PID maneuvers hardly any thrust variations necessary to de-couple these parameters occur.

$$C_m = \underline{C_{m0}} + C_{m\alpha}(\alpha - \alpha^*) + C_{mq}q\frac{\overline{c}}{2V} + C_{m\delta_e}(\delta_e - \delta_e^*)$$

$$+ C_{mCAN}(\delta_{CAN} - \delta_{CAN}^*) + \overline{C}_{m\sigma}\left(\sigma - \sigma^*\right)\frac{T}{qS} \quad (13)$$

$$+ \left\{\overline{C}_{m\sigma^2} \cdot \sigma^2 + \overline{C}_{m\sigma} \cdot \sigma + \underline{\overline{C}_{m\sigma_0}}\right\} \cdot \frac{T}{qS} \cdot \cos\kappa$$

Omitting this constant term in the second-order thrust vector model aggravates the problem of poor match of the parabola with the actually observed characteristics at large amplitudes due to the even steeper flanks of the parabola. The model wouldn't be valid over the necessary range of thrust deflection angles as is also visualized in Figure 17 by the dashed parabola. It can thus be concluded that the type of nonlinearity of the thrust vectoring system and the problem arising from correlation of higher-order model parameters with other aerodynamic parameters prohibit the application of global nonlinear models to account for these nonlinearities.

8. DATA PARTITIONING
Previously, such anticipated nonlinear aerodynamic and controls characteristics have been evaluated during system identification by means of a so-called 'data partitioning' technique [13,14]. The DLR parameter identification code NLMLKL program code [15] provides this kind of a performance feature allowing to extract data from time slices for specified intervals. The 'data partitioning' procedure is explained schematically in Figure 18. Depending on the investigated variable and the range of values specified, the program code cuts out automatically all time frames for a given interval from the entire maneuver and pastes these time slices together for a subsequent regression analysis. See as an example the shaded interval in Figure 18.
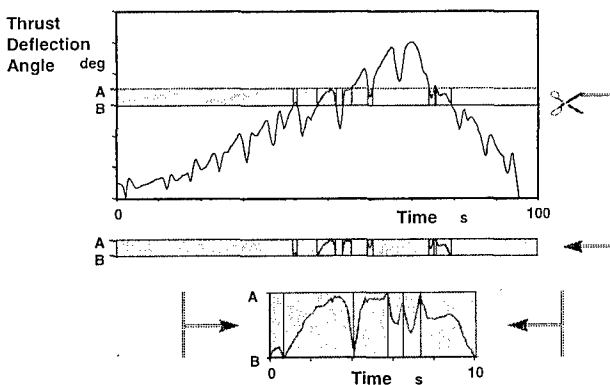

Figure 18: Schematic Explanation of 'Data Partitioning' [14]

Studies of other nonlinear phenomena during system identification however have revealed an only limited suitability of 'data partitioning' for this kind of analysis (results to be published).

Thus, data partitioning has not been utilized to analyze intervals of specified thrust deflection angle σ and only the approach to cover nonlinear characteristics of the thrust vectoring system directly in the model and not by 'externally' partitioning the flight test data has been chosen.

The advantage of this nonlinear model extension compared to analysis with conventional data partitioning is, that nonlinearities can be investigated simultaneously in one extended model, while data partitioning only allows to analyze time frames dependent on one selected variable only. Thus, the necessary information content of the time segments for parameter identification is much higher during evaluation of extended models than during data partitioning. Identification fidelity can consequently be improved.

9. CONCLUSIONS
Both qualitative and quantitative statements about nonlinear model extensions for describing the thrust vectoring system, which are justified by looking at the physical flow phenomena involved, including the examples above have been introduced in this paper. In a first step directional sensitivity of the thrust vector effectiveness parameter has been introduced as a model extension to cover the different characteristics of the thrust vectoring system with articulated vanes like in the case of the two X-31A aircraft. A further model refinement comprises of a piecewise linear description of the thrust vector effectiveness over the whole range of thrust deflection angles. With this model, a small area of reduced effectiveness associated with small deflection amplitudes has been identified from flight test data. This region can be explained as a small deadband due to imperfect plume boundary tracking. For larger thrust deflection amplitudes the results from a piecewise linear model approach the values of the traditional global linear model. Stronger nonlinearities have not been revealed since the thrust vector calibration of the X-31A has been extremely elaborate. During ground-testing and flight test analysis, detailed tables containing thrust vector characteristics including descriptions of thrust deflection angle in terms of vanes deflections have been compiled [10].

The refined models presented here considerably help understanding the identification results of thrust vector control effectiveness parameters since these can be interpreted physically and are not only a mathematical approximation of the thrust vectoring system on a delta-canard configured aircraft. These types of model extensions associated with nonlinearities can also be applied to cover local effects, nonlinear aerodynamics, as well as flow interactions of the canard and main wing.
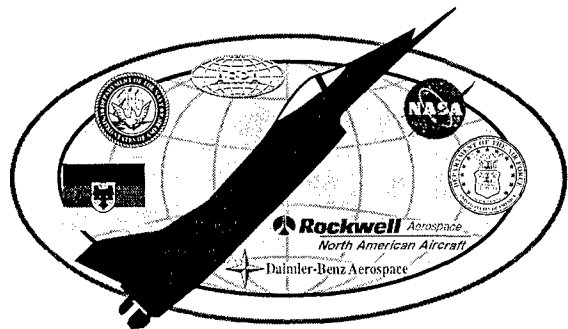
10. ACKNOWLEDGMENT

Figure 19: ITO Logo

11. REFERENCES

[1] Robinson, M.R. and Herbst, W.B.: *The X-31A and Advanced Highly Maneuverable Aircraft*. 17th ICAS Congress, Stockholm, Sweden, 1990, Proceedings Vol. I, S. LV - LXIV

[2] Francis, M.S.: *X-31: An International Success Story*. Aerospace America, Feb. 1995, pp. 22 - 27 & 32

[3] Polhamus, E.C.: *A Concept of the Vortex Lift of Sharp-Edge Delta Wings Based on a Leading-Edge-Suction Analogy*. NASA TN D-3767, 1966

[4] Howard, R.M. and O'Leary, J.F.: *Flowfield Study of a Close-Coupled Canard Configuration*. Journal of Aircraft, Vol. 31 (1994), No. 4, pp. 908 - 914

[5] Beh, H. and Hofinger, G.: *Control Law Design of the Experimental Aircraft X-31A*. 19th Congress of the International Council of the Aeronautical Sciences, AIAA, Paper ICAS 94-7.2.1, Anaheim, CA, Sep 18 - 23, 1994

[6] Hamel, P.G. and Jategaonkar, R.V.: *The Evolution of Flight Vehicle System Identification*. AGARD SMP Specialists' Meeting on 'Advanced Aeroservoelastic Testing and Data Analysis', AGARD CP-566, May 8 - 10, 1995, Rotterdam, The Netherlands, pp. 19.1 - 19.28

[7] Krag, B.; Jategaonkar, R.V.; Mönnich, W. and Fischenberg, D. (1993). Estimation of an Aerodynamic Data Base for the New C-160 'Transall' Flight Simulator from Flight Data. In: *Proc. RAeS Symposium. 'Data Issues for Flight Simulators'*, London.

[8] Weiß, S.; Friehmelt, H.; Plaetschke, E.; and Rohlf, D. (1996). *X-31A System Identification Using Single-Surface Excitation at High Angles of Attack*. Journal of Aircraft, Vol. 33 (1996), No. 3, May - June 1996, pp. 485 - 490

[9] Friehmelt, H.; Weiß, S.; Rohlf, D.; and Plaetschke, E.: *Using Single Surface Excitation for X-31 System Identification at High AoA*. 26th Annual Symposium of the Society of Flight Test Engineers (SFTE) 'Open Sky', Berlin, June 19 - 23, 1995

[10] Georg, H.-U.: *Aerodynamic Development and Effectiveness Evaluation of the X-31A Thrust Vectoring System*. 4th High Alpha Conference, NASA CP-10143, Edwards, CA, Jul 12 - 14, 1994

[11] Ross, H. and Kuny, K. (1988). *Das X-31-Programm*. Hochleistungsflugzeuge, FE-11/X-31A/PUB-002, Unternehmensbereich Flugzeuge, MBB Deutsche Aerospace, pp. 153 - 162

[12] Friehmelt, H.: *Thrust Vectoring and Tailless Aircraft Design - Review and Outlook*. AIAA Atmospheric Flight Mechanics Conference, Paper AIAA 96-3412-CP, San Diego, CA, 29. - 31. Juli 1996, pp. 420 - 430

[13] Batterson, J.G. and Klein, V.: *Partitioning of Flight Data for Aerodynamic Modeling of Aircraft at High Angles of Attack*. Journal of Aircraft, Vol. 26 (1989), No. 4, pp. 334 - 339

[14] Friehmelt, H.; Rohlf, D.; Plaetschke, E.; and Weiß, S. (1995). *X-31A Flugversuche mit unkorrelierten Steuerflächenausschlägen zur Bestimmung der aerodynamischen Derivative*. DGLR-Jahrestagung, Bonn - Bad Godesberg, 26. - 29. Sept. 1995, DGLR Vortrag 95-077 Band II, pp. 555 - 564

[15] Jategaonkar, R.V.: *User's Manual for NLMLKL, a General FORTRAN Program for Parameter Estimation in the Time Domain*, DLR IB 111-95/03, March 1995

Time Domain Identification of Helicopters – A New Perspective

T Clarke
Department of Electronics
University of York
Heslington
York
YO1 5DD
England

1. Summary

The time-domain, observer-Kalman filter/eigensystem realisation algorithm is successfully applied to the problem of generating a minimal state space model realisation from a non-linear Lynx helicopter model. A linear realisation is generated which gives a better representation of the non-linear model than that obtained using small perturbation linearisation methods. The approach can be used to extract an unstable model from the flight data of a closed-loop stabilised system, even when the feedback dynamics are not precisely known.

2. Introduction

A basic raison d'être for system identification is the generation of a mathematical description of a physical system from its available input-output data. In the state space context, *system realisation* refers to the process of constructing a state space representation directly from input and output test data. This is particularly important in aerospace engineering practice where in many cases a model is derived directly from flight test data.

This paper describes the first use of a powerful time-domain method for system realisation using a non-linear model of the Westland Lynx helicopter. The method incorporates the theory of the Observer-Kalman Filter/Eigensystem Realisation Algorithm (OKID/ERA) [1, 2, 3, 4, 5, 6, 7]. An earlier paper [9] describes a Matlab Toolbox (OKERA Toolbox) which facilitates this task. The achieved objective of this programme was to provide sufficiently accurate mathematical models for use in preliminary flight control system design. Attendant on this, the non-linear model, supplied by GKN Westland Helicopters, is deemed to be representative of the real aircraft, and must be so for controller design.

By using a non-linear simulation, it has been possible to show that this time-domain approach will be appropriate for real helicopter identification, without having to consider data harmonisation and other such issues as well.

The paper is structured as follows. Section 2 presents a brief overview of the fundamental processes involved in the OKID/ERA method. Section 3 then provides an interim result based upon a 10th order linear model of the Lynx helicopter, which was extracted from the full non-linear simulation, trimmed for 50 knots forward flight, using the standard small perturbation method. Following this, in Section 4, there is a description of the use of the OKERA Toolbox to extract linear representations of the non-linear dynamics of the helicopter. Section 5 considers some alternative time-domain techniques that have been applied to the helicopter identification problem. Finally, some overall conclusions are presented in Section 6, specifically directed at the helicopter problem, then, more

generally, at the OKID/ERA approach as a viable method for generating realisations of large-scale non-linear, unstable dynamic systems.

3. OKID/ERA Fundamentals

A review of the mathematical basis for the OKID/ERA approach is given in [9]. However, the following is a brief summary of the main results in order to support the material that follows.

3.1 Basic System Markov Parameters

Consider a discrete multivariable linear system described by:

$$x(k+1) = Ax(k) + Bu(k)$$
$$y(k) = Cx(k) + Du(k) \tag{1}$$

where $x(k) \in \Re^n$, $y(k) \in \Re^q$, $u(i) \in \Re^m$. The Markov parameters of the system are defined as the sequence: D, CB, CAB, ... , CA^iB, $CA^{i+1}B$, ... In the case of $x(0) = 0$, one can easily find the relationship between the Markov parameters and the system input and output histories:

$$\underset{q\times ml}{y} = \underset{q\times ml}{Y} \; \underset{q\times ml}{U} \tag{2}$$

where:

l is the number of data samples

$y = [y(0)\, y(1)\, y(2) \ldots y^{(l-1)}]$

$Y = [D\; CB\; CAB \ldots CA^{l-2}B]$

and

$$U = \begin{bmatrix} u(0) & u(1) & u(2) & \cdots & u(l-1) \\ & u(0) & u(1) & \cdots & u(l-2) \\ & & u(0) & \cdots & u(l-3) \\ & & & \ddots & \vdots \\ & & & & u(0) \end{bmatrix}$$

(2) has little practical use for MIMO systems where, if $m > l$, there are insufficient equations for solving, uniquely, the unknown Markov parameters.

If A is asymptotically stable, then for some sufficiently large p, $A^i \approx 0$ for all time steps $i \geq p$. Under these circumstances, (2) can be approximated as:

$$\underset{q\times m(p+1)}{y} = \underset{q\times m(p+1)}{Y} \; \underset{m(p+1)\times l}{U} \tag{3}$$

y is the same as in (2),

$Y = [D\; CB\; CAB \ldots CA^{p-1}B]$

and

$$U = \begin{bmatrix} u(0) & u(1) & u(2) & \cdots & u(p) & \cdots & u(l-1) \\ & u(0) & u(1) & \cdots & u(p-1) & \cdots & u(l-2) \\ & & u(0) & \cdots & u(p-2) & \cdots & u(l-3) \\ & & & \ddots & \vdots & \cdots & \vdots \\ & & & & u(0) & \cdots & u(l-p-1) \end{bmatrix}$$

So, for MIMO systems, when the data length l is greater than $m(p+1)$, there are enough equations to approximate the first p Markov parameters through $Y = yU^+$, where U^+ is the pseudoinverse of the matrix U.

2.2 System and Observer Markov Parameters

A fundamental problem with (3) is that for systems with lightly damped dynamic modes, the integer p and therefore the magnitude of l required to allow this approximation, make it unfeasible. The matrix U becomes too large for its pseudo-inverse to be solved numerically.

If one is able to increase the system damping artificially, truncating the Markov parameter series, the identification process is expedited. Through feedback augmentation, the observer/Kalman filter identification (OKID) algorithm was proposed in [2] in order to accomplish this.

Adding and subtracting the term $My(k)$ to the right-hand side of (1) yields:

$$\begin{aligned} x(k+1) &= \overline{A}x(k) + \overline{B}v(k) \\ y(k) &= Cx(k) + Du(k) \end{aligned} \tag{4}$$

where:

$\overline{A} = A + MC$

$\overline{B} = [B + MD, -M]$

$v(k) = [u(k)\ y(k)]'$

M is an $n \times q$ arbitrary matrix chosen to achieve the desired properties of the matrix $\overline{A}$.

By considering $x(k)$ in (4) as an observer state $\hat{x}(k)$, (4) describes the linear structure of an observer. The Markov parameters generated are therefore known as the observer Markov parameters (OMP).

It is now possible to generate the relationship:

$$\underset{q \times [(q+m)p+m]}{\overset{q \times l}{y}} = \overset{[(m+q)p+m] \times l}{\overline{Y}} V \tag{5}$$

where:

$\overline{Y} = [D\ \overline{CB}\ \overline{CAB} \cdots \overline{CA}^{p-1}\overline{B}]$

$$V = \begin{bmatrix} u(0) & u(1) & u(2) & \cdots & u(p) & \cdots & u(l-1) \\ & v(0) & v(1) & \cdots & v(p-1) & \cdots & v(l-2) \\ & & v(0) & \cdots & v(p-2) & \cdots & v(l-3) \\ & & & \ddots & \vdots & \cdots & \vdots \\ & & & & v(0) & \cdots & v(l-p-1) \\ & & & & & \ddots & \vdots \\ & & & & & & v(0) \end{bmatrix}.$$

Since M is arbitrary, one can assign the eigenvalues of $\overline{A}$ arbitrarily, to obtain a deadbeat condition, where $\overline{CA}^k\overline{B} = 0$ for $k \geq p$.

Process and Measurement Noise

For real data, including process and measurement noise, the eigenvalues are, in practice, placed such that $\overline{CA}^k\overline{B} \approx 0$ for $k \geq p$, where p is normally a sufficiently large integer. In this case:

$$\underset{q \times [(q+m)p+m]}{\overset{q \times l}{y}} = \overset{[(m+q)p+m] \times l}{\overline{Y}} V \tag{6}$$

where

$\overline{Y} = [D\ \overline{CB}\ \overline{CAB} \cdots \overline{CA}^{p-1}\overline{B}]$

$$V = \begin{bmatrix} u(0) & u(1) & u(2) & \cdots & u(p) & \cdots & u(l-1) \\ & v(0) & v(1) & \cdots & v(p-1) & \cdots & v(l-2) \\ & & v(0) & \cdots & v(p-2) & \cdots & v(l-3) \\ & & & \ddots & \vdots & \cdots & \vdots \\ & & & & v(0) & \cdots & v(l-p-1) \end{bmatrix}$$

and the first p OMP approximately satisfy $\overline{Y} = yV^+$.

The approximation error decreases as p increases.

In [6], it is shown that when the observer poles are placed at the origin of the z-plane in order to obtain a deadbeat observer of a sufficiently high order and then data containing both plant and measurement noise are used in the formulation of the desired Markov parameters, the result is the Kalman filter Markov parameters. Put another way, when seeking to achieve the Markov parameters of the fastest deterministic deadbeat observer, using noisy data results in the Markov parameters of a slower Kalman filter, which is the fastest possible observer in a stochastic environment.

2.3 The Eigensystem Realisation Algorithm (ERA)

ERA is based on the Markov parameters $Y(k) = CA^{k-1}B$. The system realisation is achieved by constructing the constant matrices $[A, B, C]$ in terms of $Y(k)$ such that the identity holds. A discussion of the processes involved is given in [9].

Knowing the OMP $\overline{Y}$, the actual system Markov parameters Y, together with a sequence of parameters for the observer gain, M, can be recovered in accordance with [9].

2.4 Extensions

Further extensions, such as working with state-feedback closed loop systems and obtaining open loop realisation, the effects of direct transmission terms (such as occurs with accelerometer data), dynamic-feedback and output-feedback closed loop systems are also summarised in [9].

3 Identification of a Linear Helicopter Model

3.1 Model Details

The first test case was a linear model, generated using small perturbation linearisation of a non-linear Lynx helicopter model which was trimmed for straight and level flight at a forward speed of 50 knots. The linear model structure is:

$$\dot{x} = A_{50}x + B_{50}U \tag{7}$$

where: the two matrices are defined at the end of this paper as equations (8) and (9).

The ten states are:

$$x^T = \begin{bmatrix} u & w & q & \theta & v & p & r & \phi & A1_s & B1_s \end{bmatrix} \quad (10)$$

the four control inputs are

$$U = \begin{bmatrix} \Theta_0 & A1 & B1 & \Theta_t \end{bmatrix} \quad (11)$$

u, v and w are, respectively, the forward, sideslip and vertical linear body velocities

p, q and r are, respectively, the roll, pitch and yaw body angular velocities

θ and ϕ are, respectively, the pitch and roll body angles

$A1_s$ and $B1_s$ represent lateral and longitudinal disc tilt, respectively

Θ_0 is main rotor collective, $A1$ is lateral cyclic, $B1$ is longitudinal cyclic and Θ_t is tail rotor collective.

Analysis of the model shows it to be statically unstable. The poles of the discrete form, sampled at 50 Hz are:

$$\lambda(A_{50})_{discrete} = \begin{bmatrix} 0.8506 \pm 0.1797i \\ 0.7878 \\ 0.9488 \\ 0.9906 \\ 0.9922 \pm 0.0220i \\ 1.0001 \\ 1.0027 \pm 0.0081i \end{bmatrix} \quad (12)$$

There are two unstable modes. One is divergent with a long time constant whilst the other exhibits low-frequency divergent oscillations.

The model was then stabilised by output feedback with the selected group of output variables:

$$y = \begin{bmatrix} \dot{h} & p & q & r & \theta & \phi \end{bmatrix}' \quad (13)$$

where $\dot{h}$ is the height change rate (positive upwards). The closed-loop discrete model then exhibited the following stable eigenvalues:

$$\lambda(A_{cl})_{discrete} = \begin{bmatrix} 0.8275 \\ 0.8468 \pm 0.3092i \\ 0.9562 \pm 0.0247i \\ 0.9766 \pm 0.0023i \\ 0.9886 \pm 0.0128i \\ 0.9986 \end{bmatrix} \quad (14)$$

3.2   Application of the OKERA Toolbox

The stimulation inputs for the four channels were separate zero-mean, uniformly-distributed, random signals. In practice, the stimuli could be bandlimited, as the high frequency components will not contribute significantly to the realisation process. The total sampling period was $t_{total}=120s$, corresponding to 6000 sample points, and standard deviations in each channel were [0.2 0.43 2.7 3.3] (equation 11)).

Using the first 3000 data points (l), equivalent to a time duration $t=60s$, with 60 Markov parameters, p, and the output set as equation (13), the resultant outputs using these control inputs were mixed with further random noise. The observer Markov parameters (YOMK) were calculated (using **omkfyu0**

[9]) followed by the real Markov parameters (YMK) (using **mkfomk** [9]). Figure 3 shows the time sequences of both YOMK and YMK.

Figure 3 shows the significant 'dead beat' feature of the observer Markov parameters. Following this, the Hankel matrices $H_{rs}(0)$ and $H_{rs}(1)$ were calculated, using YMK (and the function **hankf**, [9]). Here $mr=20$ and $nc=40$. Applying the singular-value decomposition to $H_{rs}(0)$ gave a singular-value decay pattern which yielded a cut-off point at $n=9$, suggesting a 9th order system.

The poles of this identified system are:

$$\lambda(A_{cl})_{discrete_{ERA}} = \begin{bmatrix} 0.8271 \\ 0.8468 \pm 0.3093i \\ 0.9550 \pm 0.0260i \\ 0.9784 \pm 0.0017i \\ 0.9878 \pm 0.0137i \end{bmatrix} \quad (15)$$

which are close to the first nine eigenvalues of $(A_{cl})_{discrete}$ (equation (14)).

Relative Error Norm Analysis between two sequential variables, $y_1(k)$ and $y_2(k)$, is defined as:

$$RENA(y_1(k), y_2(k)) =$$
$$\left(\frac{\|y_1(1,:) - y_2(1,:)\|_2}{\|y_1(1,:)\|_2}, \frac{\|y_1(2,:) - y_2(2,:)\|_2}{\|y_1(2,:)\|_2}, \dots \right)\% \quad (16)$$

This formula is frequently used later to evaluate the matching of data and systems.

When the second half of the input data points are applied to both the identified system model

$$[(A_{cl})_{discrete_{ERA}}, (B_{cl})_{discrete_{ERA}}, (C_{cl})_{discrete_{ERA}}, (D_{cl})_{discrete_{ERA}}]$$

and the original model

$$[(A_{cl})_{discrete}, (B_{cl})_{discrete}, (C_{cl})_{discrete}, (D_{cl})_{discrete}]$$

the outputs (y_e and y respectively) are almost identical. Applying RENA analysis to y_e and y:

$$RENA(y, y_e) =$$
$$(3\%, 0.9\%, 0.62\%, 6.7\%, 5.34\%, 15\%) \quad (17)$$

The identified system model exhibits a very close match to the true closed-loop system, based upon the chosen output variables. However, further analysis of the eigenvalues of the both models shows that the missing mode is an asymptotic slow-convergence motion mode. From the principles of the ERA approach, this is a clear indication that the observability property, resulting from the choice of y is insufficient to reveal that particular mode. Actually, if one calculates the Hankel matrix $H_{rs}(0)$ of the closed-loop system through multiplication of the observability matrix by the controllability matrix (Equation (17) in [9]), the singular value group is:

$$SV = [\ 67.6, 14.4, 5.9, 4.2, 1.3, \dots$$
$$1.0, 0.55, 0.09, 0.0142, 0.00005] \quad (18)$$

This highlights an "almost unidentified" 10th mode.

Consequently, another test was carried out, with the same conditions except that the data length was increased to l=5000 points, t=100sec. When p=60, mr=20 and nc=40, the results are slightly worse than the l=3000 case, with the singular value cut-off point still at n=9, the identified model has the eigenvalues:

$$\lambda(A_{cl})_{discrete_{ERA}} = \begin{bmatrix} 0.8263 \\ 0.8468 \pm 0.3092i \\ 0.9550 \pm 0.0263i \\ 0.9791 \pm 0.0014i \\ 0.9866 \pm 0.0145i \end{bmatrix} \quad (19)$$

and

$$RENA(y,y_{el}) = \\ (5.7\%, 1.56\%, 1.63\%, 9\%, 6.55\%, 17\%) \quad (20)$$

Since the missing identified mode is a slow convergent one, it is natural to link this mode to the forward velocity of a helicopter. If $\dot{h}$ in equation (13) is replaced with the perturbation forward velocity u, the Hankel matrix $H_{rs}(0)$ of the closed-loop system, calculated as for equation (18) shows improved observability characteristics in the slow convergent mode, with the non-zero singular values:

$$SV=[9.25, 6.12, 4.07, 2.37,... \\ 1.06, 0.58, 0.48, 0.14, 0.05, 0.00026] \quad (21)$$

Modifications were therefore made to improve the identification process. The output variable $\dot{h}$ was replaced by u and the number of sample points was increased to l=6000 and p was increased to 100.

From the new YMK, the Hankel matrix $H_{rs}(0)$ exhibited the following decay pattern in the singular values (the first 20 values are listed):

$$SV=[82.4, 7.38, 4.94, 4.71, 3.51, 3.31, 2.57, 1.12, 0.38, 0.24, \\ 0.029, 0.029, 0.028, 0.027, 0.027, 0.027, 0.026, 0.026, 0.025, \\ 0.025 ...] \quad (22)$$

The pattern shows a distinct cut-off point at n=10. From this, a system realisation gave the following modal structure:

$$\lambda(A_{cl})_{discrete_{ERA}} = \begin{bmatrix} 0.8263 \\ 0.8469 \pm 0.3092i \\ 0.9562 \pm 0.0257i \\ 0.9772 \pm 0.0022i \\ 0.9886 + 0.0126i \\ 0.9985 \end{bmatrix} \quad (23)$$

which, when compared to the target system, equation (14), shows a considerable improvement in the low damping ratio modes and overall improvement in modal accuracy.
RENA analysis using the same inputs gives:

$$RENA(y,y_e) = \\ (1\%, 1\%, 0.5\%, 2.7\%, 2.2\%, 2.34\%) \quad (24)$$

which also demonstrates an excellent match between the output variables concerned.

Since the feedback gain, K, was known, the open-loop Markov parameters for A_{d50} could be recovered using the function **mkofmkc** [9], which gave the following identified modes:

$$\lambda(A_{cl})_{discrete_{ERA}} = \begin{bmatrix} 0.7874 \\ 0.8506 \pm 0.1797i \\ 0.9488 \\ 0.9904 \\ 0.9921 \pm 0.0224i \\ 1.0001 \\ 1.0027 \pm 0.0080i \end{bmatrix} \quad (25)$$

which compare favourably with those of the target open-loop system in equation 12).

Converting to the continuous model gives the following modal parameters:

$Modes(A_{cl})_{continuous_{ERA}} =$

Eigenvalues	Frequency	Damping
-7.0002 ±10.4124i	12.55	0.56
-11.9505	11.9505	1.0
-2.6303	2.6303	1.0
-0.3814 + 1.1268i	1.19	0.32
-0.4834	0.4834	1.0
0.0027	0.0027	-1.0
0.1371 ± 0.4008i	0.424	-0.324

(26)

which, again, compare favourably with the true continuous open-loop system:

$Modes(A_{50}) =$

Eigenvalues	Frequency	Damping
-6.9965 ±10.41i	12.542	0.56
-11.924	11.924	1.0
-2.6263	2.6263	1.0
-0.378 + 1.107i	1.17	0.32
-0.4744	0.4744	1.0
0.0034	0.0034	-1.0
0.1378 ± 0.4024i	0.425	-0.324

(27)

4 Identification of a Non-Linear Helicopter Model

Based on the above evaluation with a linear model, the approach was applied to a non-linear Lynx model. This model [8] serves as a useful analytical tool for 6-degree of freedom simulation of typical non-linear helicopter dynamics. Inputs can either be pilot commands in the four standard channels, or perturbations such as gusts and noise.

The objectives of using OKID/ERA to extract linear representations of non-linear dynamics at equivalent points were twofold:
- Firstly, to show that the process provides a linear model with a better match to the unstable, non-linear plant in a 'dynamic' sense (i.e. better fit in both time and frequency domains).
- Secondly, to show that the approach can cope well with some non-linear effects through the addition of 'extra' linear modes to the final realisation.

In the case of this non-linear simulation, the signals that actually stimulate the model, are through the pilot sticks and pedals. Therefore, not only were the outputs measured, but also the control inputs within the closed-loop.

4.1 Filtered pilot inputs

Since the unaugmented helicopter model is unstable, a feedback controller was designed to provide stability (but not good handling qualities). In accordance with established helicopter engineering practice, the controller linked system outputs to a point just after the series actuators (Figure 2).

The pilot inputs in the four channel were generated as random signals, limited to a percentage of the full ambit of each effector. They were also filtered to represent true pilot handling more properly. Figure 4 shows the configuration from the pilot stick/pedal inputs to the rotor control inputs. The input limitations were ±25%, ±20%, ±20% and ±10% in collective, lateral cyclic stick, longitudinal cyclic stick and rudder pedals, respectively.

4.2 Model Realisation

The approach taken was slightly different to the linear case, but to facilitate comparison, the non-linear helicopter was trimmed at $U = 50$ knots. The output variables were chosen as

$$y = [u\ p\ q\ r\ \theta\ \phi] \qquad (28)$$

The number of Markov parameters, p, was a larger 120, and a full range of the test points, $l=6000$, were used.

A significant difference occurs in the singular values pattern of the Hankel matrix $H_{rs}(0)$. For the non-linear case, it appears that a cut-off point for the system order is difficult to find.

$$SV=$$
[95, 12, 9.8, 6.1, 4.2, 3.7, 2.9, 1.6, 0.6, 0.45, 0.42, 0.35, 0.22, 0.18, 0.15, 0.085, 0.044, 0.026, 0.022, 0.02]
...(29)

It initially appears that the only clear cut-off point is at $n=8$. However, a closer look indicates that other possible choices are $n=15$, 16 or 17.

System realisations in terms of A_e, B_e and C_e for these different orders were calculated using ERA. The results were judged by RENA analysis, where y is the non-linear system output and y_e the realised counterpart.

$n=15$:
$RENA(y,y_e) = (28.6\%, 3\%, 5\%, 18.9\%, 11.4\%, 12.2\%)$;
...(30)

$n=16$:
$RENA(y,y_e) = (10.4\%, 3\%, 5.5\%, 20.7\%, 20.3\%, 8.67\%)$;
...(31)

$n=17$:
$RENA(y,y_e) = (16.7\%, 2.7\%, 3.7\%, 18.9\%, 16.2\%, 10.7\%)$;
...(32)

A value of $n=16$ was selected to give good short and long period mode variable agreement.

Although comparison in the time domain showed that the realised linear model and the small perturbation linear model provided similar output responses to the non-linear model, frequency response analysis of the three showed quite different features. Figures 5 (a), (b) and (c) show the frequency spectra of the five angular variables for the three systems, respectively.

They indicate a good match between the realised linear model and the non-linear one in the frequency-domain, compared to the small perturbation linear model where considerable miss-match occurs, predominantly in the 2-3 Hz band of frequencies. Subsequent analysis showed this mismatch to be mainly in the roll channel.

The Markov parameters of a realised linear model of the open-loop non-linear plant were recovered. This discrete realised linear model was unstable with the following eigenvalues:

$$\lambda(A_{50})_{discrete_{ERA}} = \begin{bmatrix} 0.6617 \\ 0.6794 \\ 0.7587 \\ 0.8120 \\ 0.8519 \pm 0.1866i \\ 0.8768 \\ 0.9582 \pm 0.1726i \\ 0.9418 \\ 0.9800 \\ 0.9919 \pm 0.0253i \\ 1.0001 \\ 1.0024 \pm 0.0082i \end{bmatrix} \qquad (33)$$

Compared with the open loop modes of the linear small perturbation model in equation (12), the realised linear model includes all those eigenvalue modes seen in the linear perturbation model, together with some additional ones. Examining the continuous version of the realised linear model:

$Modes(A_{50})_{continuous_{ERA}} =$

Eigenvalues	Frequency	Damping
-20.65	20.65	1.0
-19.33	19.33	1.0
-13.81	13.81	1.0
-6.843 ±10.781i	12.77	0.54
-10.413	10.413	1.0
-1.3373 ±8.9102	9.01	0.15
-6.5735	6.5735	1.0
-3.0	3.0	1.0
-0.3924 + 1.2727i	1.332	0.295
-1.012	1.012	1.0
0.0074	0.0074	-1.0
0.12 ± 0.41i	0.428	-0.28

...(34)

it, too, shows the inclusion of all the modes of the linear small perturbation model A_{50}, equation (27), plus some extras.

5 Comparison with Other Helicopter Identification Methods

It is appropriate to compare the results of the OKID/ERA approach with other time domain methods. In [11,12], an exposition of the commonly-used output error Maximum Likelihood Techniques is presented. Alternatively, a regression analysis based equation error method is presented. The idealised situation underlying these methods is based upon

the absence of process noise and the assumption that the measurement noise is zero-mean, independent, Gaussian and with an identity covariance matrix. The objective of the first method is to adjust the values for the unknown parameters of a linear model to give the best possible fit between the measured output variables and the calculated model response. The second approach is based upon the premise that, is a sufficient number of observed variables is available to determine the state variables from the observation equations, then, if the measured variables are measured without error, the state variables can be determined without error. The application of either to the rotorcraft problem is flawed on theoretical grounds since they are unable to deliver unbiased estimates of the parameters. This is borne out by practical experience.

6   Concluding Remarks

This is thought to be the first attempt at using the OKID/ERA method for identification and modelling of helicopter dynamics. In this case, the method was applied to a representative non-linear Lynx helicopter model, supplied by GKN Westland Helicopters.

The encouraging results show the effectiveness of the method for off-line identification of large-scale linear MIMO dynamics with widely distributed and cross-coupled modes. The method generates a robust model realisation.

Since in most cases, a conventional helicopter is naturally unstable, the identification of such an unstable model is indirect and involves, firstly, feedback stabilisation of the plant dynamics, secondly, the identification of the stabilised closed-loop dynamics, and, finally, the recovery of the open-loop plant dynamics through the relationship between the Markov chains. The identification practice, described and catalogued above, shows the effectiveness of the routine.

Through careful experimental design it is possible to maximise modal observability and explicitly guarantee the presence of those modes in the open-loop plant dynamics, e.g. the unstable long-period motions, which are, to a large extent, masked by the feedback stabilisation. The results demonstrate an accurate match between the realised model and the non-linear system in the time and frequency domains. They also show that the OKID/ERA approach will produce more effective models than the 'conventional' linear models generated by the small perturbation approach.

7   Acknowledgements

8   References

[1]   Chen, C.-W., Huang, J.-K., Ohan, M. and Juang, J.-N., "Integrated System Identification and State Estimation for Control of Flexible Space Structures," *Journal of Guidance*, Vol. 15, No. 1, Jan.-Feb. 1992, pp. 88~95.

[2]   Juang, J.-N., Cooper, J.E. and Wright, J.R., "An Eigensystem Realization Algorithm Using Data Correlations (ERA/DC) for Modal Parameter Identification," *Control Theory and Advanced Technology*, Vol. 4, No. 1, March 1988, pp. 5~14.

[3]   Juang, J.-N. and Pappa, R.S., "An Eigensystem Realization Algorithm for Modal Parameter Identification and Modal Reduction," *J. Guidance*, Vol. 8, No. 5, Sept.-Oct. 1985, pp. 620~627.

[4]   Juang, J.-N. and Phan, M., "Identification of System, Observer, and Controller from Closed-Loop Experimental Data," *Journal of Guidance, Control, and Dynamics*, Vol. 17, No. 1, Jan.-Feb. 1994a, pp. 91~96.

[5]   Juang, J.-N. and Phan, M., "Linear System Identification via Backward-Time Observer Models," *Journal of Guidance, Control, and Dynamics*, Vol. 17, No. 3, May-June 1994b, pp. 505~512.

[6]   Juang, J.-N., Phan, M. Horta, L.G., and Longman, R.W., "Identification of Observer/Kalman Filter Markov Parameters: Theory and Experiments," *Journal of Guidance, Control, and Dynamics*, Vol. 16, No. 2, March-April 1993, pp. 320~329.

[7]   Phan, M., Juang, J.-N., Horta, L.G., and Longman, R.W., "System Identification from Closed-Loop Data with Known Output Feedback Dynamics," *Journal of Guidance, Control, and Dynamics*, Vol. 17, No. 4, July-August 1994, pp. 661~669.

[8]   Sun, X.-D., Clarke, T., "Robust H^∞-based Implicit Model-Following Control of Helicopters", *Proc IFAC Symposium on Robust Control Design*, Rio de Janeiro, 14-16 September, 1994

[9]   Sun, X,-D., Clarke, T. & Maiza M. A. "A Toolbox for Minimal State Space Model Realisation", *IEE Proceedings, Control Theory and Applications*, March 1996, pp. 152~158

[10]   Tischler, M.B., "System Identification Requirements for High-Bandwidth Rotorcraft Flight Control System Design," *J. Guidance*, Vol. 13, No. 5, Sept.-Oct. 1990, pp. 835~841

[11]   AGARD Advisory Report 280, Rotorcraft System Identification, AGARD, Neuilly-sur-Seine, 1991

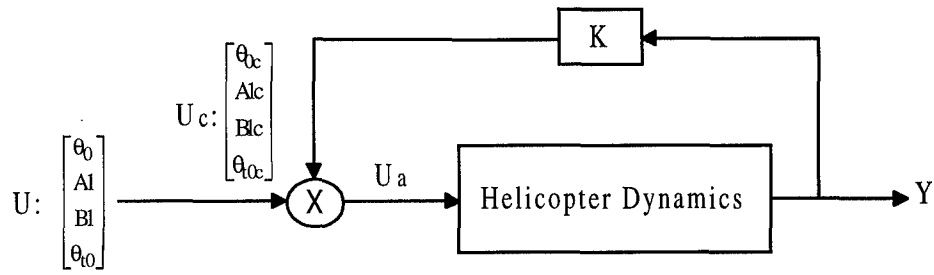[12]   AGARD Lecture Series 178, Rotorcraft System Identification, AGARD, Neuilly-sur-Seine, 1991

Figure 1 Inner Closed-Loop Identification
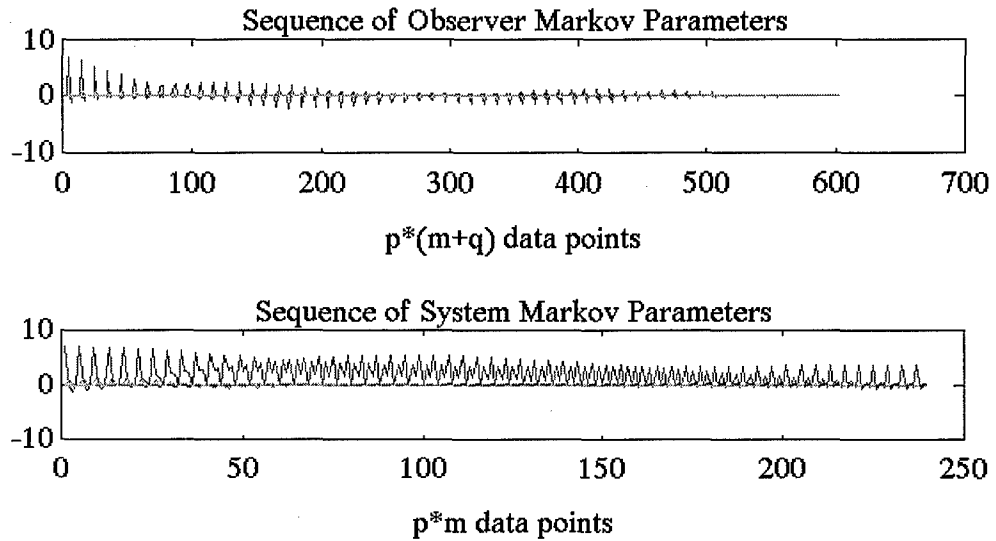where $Ua=U+Uc$.

Figure 2 Observer Markov Parameters (YOMK)
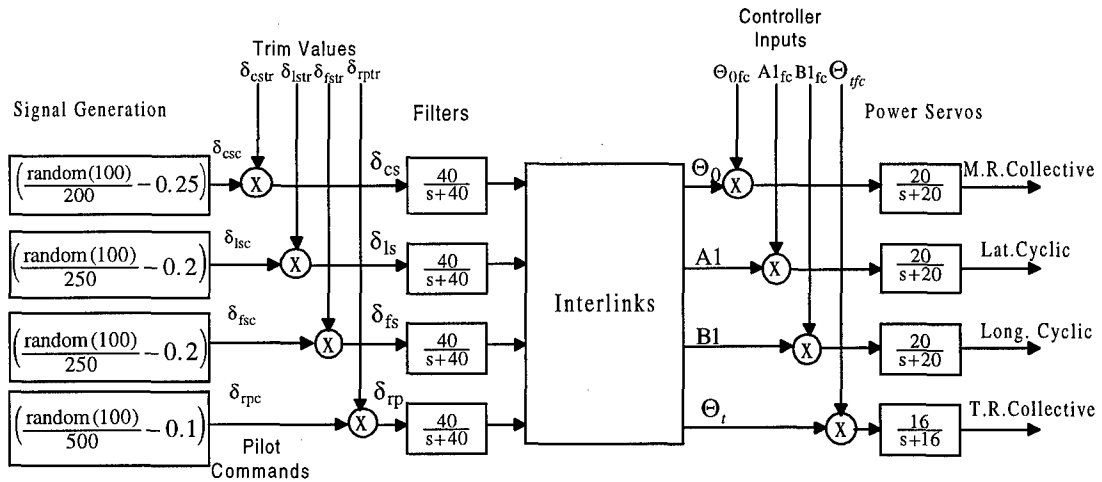and System Markov Parameters (YMK)
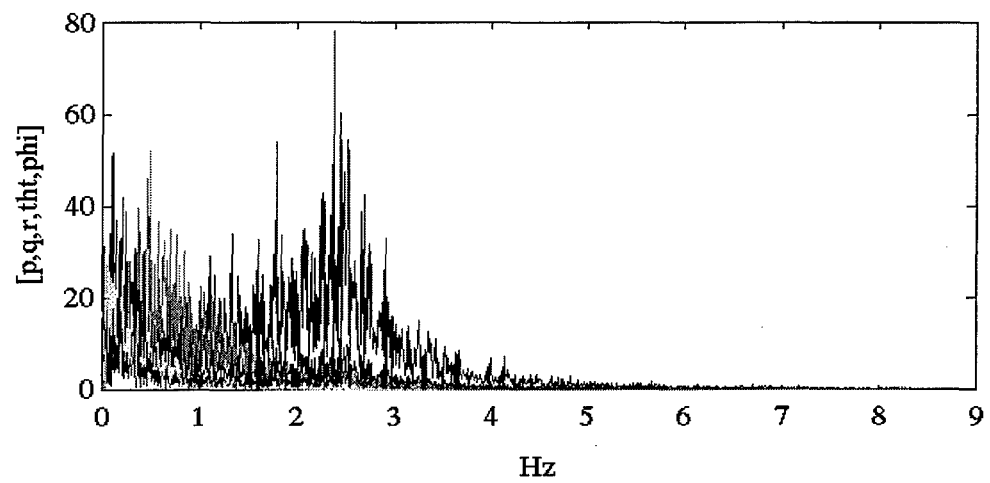

Figure 3 Input Signal Linkage Mechanism

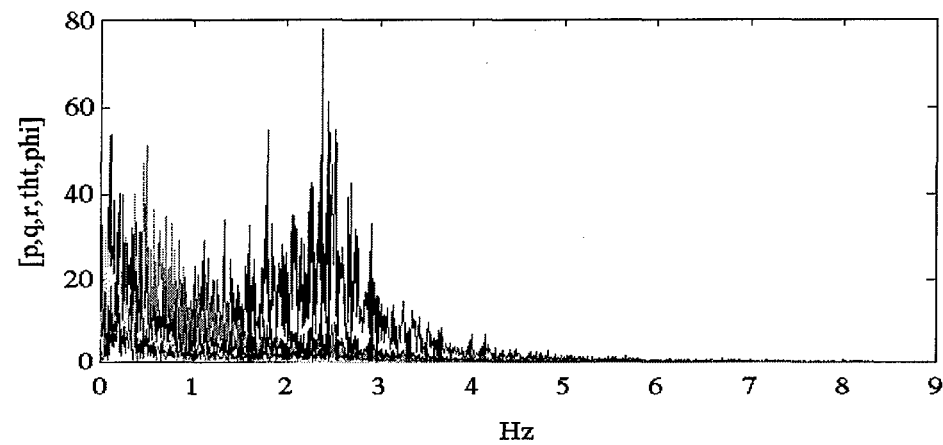Figure 4(a) Fourier transform of the non-linear y(t)

Figure 4(b) Fourier transform of the linear realised model y_e
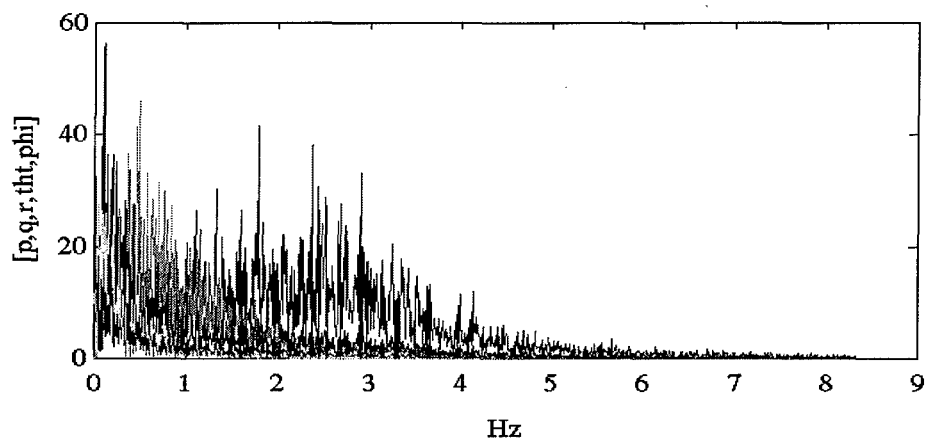

Figure 4(c) Fourier transform of the linear perturbation model y_l

$$
A_{50} = \begin{bmatrix}
-0.0133 & 0.0451 & -3.3205 & -32.1732 & 0.0006 & 0.0813 & 10.4273 & 0 & -32.1892 & 0 \\
-0.0661 & -0.7066 & 84.8104 & -1.2610 & -0.0093 & -11.6724 & 0 & 0 & -2.2471 & 0 \\
0.002 & -0.0009 & -0.0623 & 0 & -0.0001 & -1.0802 & 0 & 0 & 18.0403 & 0 \\
0 & 0 & 1.0 & 0 & 0 & 0 & 0 & 0 & 0 & 0 \\
-0.0049 & -0.0011 & 0.0563 & 0 & -0.1193 & 3.1886 & -83.872 & 32.1732 & 0 & 32.1892 \\
0.001 & -0.0058 & 7.1650 & 0 & 0.0054 & 0.016 & -0.0709 & 0 & -1.2625 & 121.115 \\
-0.0044 & -0.0062 & 1.4068 & 0 & 0.0102 & 0.084 & -0.3960 & 0 & -2.1684 & 23.1011 \\
0 & 0 & 0 & 0 & 0 & 1.0 & 0.0392 & 0 & 0 & 0 \\
0.0031 & 0.0123 & -1.2248 & 0 & 0.005 & 0.0207 & 0 & 0 & -14.0330 & -2.2795 \\
-0.0034 & 0.0125 & 0.0138 & 0 & -0.0089 & -1.2319 & 0 & 0 & 2.1637 & -14.1795
\end{bmatrix} \quad (8)
$$

$$
B_{50} = \begin{bmatrix}
22.9397 & -1.0287 & -4.0625 & 0 \\
-351.0892 & 15.7465 & 62.1819 & 0 \\
-1.6529 & 0.0911 & 0.3117 & 0 \\
0 & 0 & 0 & 0 \\
-1.7141 & 0.0764 & 0.2983 & 12.2813 \\
5.2945 & -0.2192 & -0.9177 & -1.3869 \\
9.5237 & -0.4145 & -1.6709 & -7.7443 \\
0 & 0 & 0 & 0 \\
7.4647 & 2.5864 & -16.9534 & 0 \\
3.4288 & 16.0486 & 1.8612 & 0
\end{bmatrix} \quad (9)
$$

Identification du modèle de mécanique du vol d'un hélicoptère aux basses vitesses

B.Gimonet
ONERA-CERT
Département Commande des Systèmes et Dynamique du vol
2 avenue Edouard Belin (BP 4025)
31055 Toulouse Cedex 4
France

1. RÉSUMÉ

Le Dauphin 6075 en service au Centre d'Essais en Vol (CEV) sert de support à de nombreux essais en vol sous contrat des Services Officiel Français (SPAé).

Ce dispositif expérimental a été utilisé dans le cadre de la collaboration DLR/ONERA sur le concept Smart Helicopter en ce qui concerne la modélisation de l'hélicoptère aux basses vitesses.

Ce texte décrit les travaux entrepris pour identifier un modèle linéaire. Des travaux préliminaires sur la sélection des essais valides et sur le choix de la structure du modèle sont menés. La nécessité d'introduire le premier harmonique de battement dans le modèle et, pour des travaux ultérieurs, des termes non linéaires est évoquée. Une technique classique de minimisation de l'erreur de sortie, avec sélection des paramètres significatifs, travaillant dans le domaine fréquentiel, fournit une estimation des principales dérivées de stabilité et de commande.

Une comparaison des résultats obtenus avec des modèles comportant 6 ou 9 degrés de liberté est présentée.

2. INTRODUCTION

Depuis 1992, l'ONERA et la DLR sont engagés dans un projet de recherche commun sur le concept Smart Helicopter. Il s'agit d'analyser, de modéliser et d'améliorer les qualités de vol d'un hélicoptère aux basses vitesses.

Cette tâche se subdivise en plusieurs sous-tâches dédiées à l'amélioration des modèles de simulation, à l'identification de modèles linéaires, à la mesure des qualités de vol et à la synthèse de lois de commande.

En ce qui concerne la sous tâche d'identification des modèles linéaires, deux appareils ont été choisis comme supports expérimentaux. Il s'agit du BO 105 de la DLR, pour lequel les résultats ont été publiés au 21ème Forum Européen sur les hélicoptères [1], mais également du Dauphin 6075 du Centre d'Essais en vol (CEV).

Cet appareil dédié aux recherches en vol financées par les Services Officiels Français (SPAé), a fait l'objet d'une description détaillée au 23ème Forum Européen [2].

Ce papier insiste sur la partie des installations et des travaux qui concerne plus particulièrement l'identification des modèles à basse vitesse. Les choix de méthode et de structure du modèle, de sélection des coefficients significatifs sont évoqués. Les résultats modaux et les

simulations obtenus pour un cas de vol à 60 kt de vitesse d'avancement sont présentés avec des modèles incluant ou non la dynamique du rotor.

3. CAPTEURS

Le Dauphin 6075 se caractérise par une grande redondance de mesures qui permet d'obtenir des données fiables quels que soient les aléas d'une campagne d'essais.

Deux systèmes d'acquisition différents permettent d'accéder aux données de la cellule d'une part, avec une cadence d'acquisition de 64 Hz et aux données issues du rotor d'autre part, avec une cadence d'acquisition de 1024 Hz.

Les deux listes de mesures sont synchronisées grâce à une mesure commune de la position azimutale de la pale de référence fournie par un compteur délivrant 1024 tops par tour de rotor. Les données de la cellule proviennent d'une centrale à inertie et de capteurs spécifiques cellule en ce qui concerne les mesures inertielles, d'une centrale anémométrique encore valide jusqu'à 40 kt de vitesse d'avancement et de mesures en differents points de la chaîne de commande.

En ce qui concerne l'identification proprement dite, les mesures suivantes peuvent être utilisées :

DDM1	déplacement vérin longitudinal (%)
DDL1G	déplacement vérin gauche latéral (%)
DDL1D	déplacement vérin droit latéral (%)
DDN	déplacement servo commande fenestron (°)
DDTO	déplacement levier de pas collectif (°)

Les déplacements somment les actions du pilote et les retours du pilote automatique, ils permettent d'accéder aux pas des rotors commandés.

Pour le pas latéral, on a :
$$DDL1G + DDL1D = 100\%$$
$$pas\ latéral = DDL1D - DDL1G$$

Ces mesures de pas sont complétées par des mesures de déplacements des vérins du plateau fixe codés en degrés équivalents de pas de pale :

DTA	déplacement du vérin avant (°)
DTD	déplacement du vérin droit(°)
DTG	déplacement du vérin gauche (°)

Dans le jeu de capteurs associé à la cellule nous disposons de :

NX)	
NY (	accélération dans les axes de la cellule (g)
NZ)	

P)
Q (vitesses de roulis tangage lacet (°/s)
R)

θ)
φ (angles d'Euler (°)
ψ)

V_X)
V_Y (vitesses inertielles Doppler (kt)
V_Z) dans les axes hélicoptère

La centrale ULISS fournit quant à elle les mêmes informations notées :

AXL, AYL, AZL, PL, θL, RL, QL, φ L, ψL, VXL, VYL, VZL dans un référentiel légèrement différent.

La centrale anémométrique fournit les pressions statique et dynamique et la température statique qui permettent de reconstituer la vitesse aérodynamique VA(m/s) et altitude barométrique Z(m).

La vitesse du rotor NR (t/mn) et les couples des moteurs droit et gauche COUD et COUG (mxN) sont également accessibles.

La valeur du compteur d'azimut de la pale de référence ainsi que le contenu de l'horloge codée sur 4 registres (heures, minutes, secondes, millisecondes) sont également disponibles.

L'unité d'acquisition des mesures rotor fournit outre l'azimut de la pale de référence, les angles de battements instantanés BATP1, BATP2, BATP3, BATP4 des quatre pales.

4. GESTION DES ESSAIS EN VOL

Les essais sont effectués pour une masse de 3700 kg à un altitude de 1000 pieds. Les vols ont été réalisés en boucle ouverte, pilote automatique complètement déconnecté.

L'électronique du pilote automatique a pu être utilisée pour injecter dans la chaîne de commande, de manière automatique, les signaux test nécessaires à l'identification, à condition d'utiliser un système d'augmentation de bande passante (BAVE) mis au point par le CEV. Le rôle du pilote humain est de maintenir l'hélicoptère dans des évolutions compatibles avec un modèle linéaire (10° d'écart angulaire, 5 m/s de variation de vitesse). Les signaux identificateurs sont de deux types: des séquences 3211 et des séquences binaires pseudo-aléatoires (S.B.P.A.) de 127 points de période et de largeur de commutation minimale 0,5 s.

Pour chaque cas de vol étudié et sur chaque entrée de commande plusieurs essais sont réalisés avec l'une ou l'autre des entrées test.

Pour chaque essai, l'hélicoptère est stabilisé manuellement avant de délivrer les séquences identificatrices. La durée exploitable des essais varie de 30 à 40 s, ce qui semble suffisant pour identifier le mode le plus lent (phugoïde) qui a une période de l'ordre de grandeur de 20 à 30 s. La largeur de bande des entrées a été limitée à 2 Hz pour ne pas exciter les modes de battement de traînée déclenchant un phénomène de résonance air.

5. METHODE D'IDENTIFICATION

Une technique classique d'identification paramétrique par minimisation d'erreur de sortie est utilisée. Le modèle a pour représentation d'état :

$$\dot{x} = Ax + Bu + b_x$$
$$y = Cx + D\dot{x} + Eu + b_z \qquad (1)$$

où u est le vecteur des entrées, x le vecteur d'état, y le vecteur des mesures qui dépend de l'état, de sa dérivée ou des entrées directement.

La forme choisie pour y est redondante (termes en x, $\dot{x}$, u) mais elle permet de s'adapter au mieux aux situations pratiques en jouant sur les matrices C D E en général connues.

b_x et b_z sont des termes inconnus de fermeture des équations (1) qui s'intègrent à partir des conditions initiales x(0)=0.
b_x et b_z rendent compte pour un système linéaire des biais, des conditions initiales et de la méconnaissance de l'état d'équilibre autour duquel le modèle est linéarisé.
Les paramètres estimés minimisent un critère d'écart quadratique sur les y mesurés et simulés grâce à l'algorithme de Gauss-Newton.

Dans le cas où l'état est mesuré, sa dérivée mesurée ou estimée, on peut identifier directement les coefficients des matrices A et B par moindres carrés, solution recommandée pour initialiser la recherche des paramètres.

Des termes non linéaires de structure connue peuvent être introduits dans l'équation d'état pour identifier un modèle non linéaire.

Le domaine des basses vitesses se caractérise par une grande instabilité et des difficultés à mener, les essais en vol bien sûr, mais aussi les simulations lors des évolutions du modèle dans le domaine paramétrique.

Dans ces conditions, et pour un modèle linéaire strict, il peut être utile de travailler dans le domaine fréquentiel. Avec un essai de longueur T, en remplaçant la transformée de Fourier par l'intégrale de Fourier sur [0, T], on peut écrire

$$\begin{cases} j\omega X(\omega) = AX(\omega) + BU(\omega) + x(0) - x(T) \\ Y(\omega) = [CX(\omega) + J\omega D]X(\omega) \qquad (2) \\ \qquad + D[x(T) - x(0)] + E U(\omega) \end{cases}$$

pour $\omega = k \cdot 2\pi/T$
Il suffit alors de remplacer le critère d'écart sur les y(t) par un critère portant sur les Y(ω).

Que l'on travaille dans le domaine temporel ou fréquentiel l'algorithme d'estimation des paramètres est itératif. A chaque itération k, on obtient l'estimation des paramètres α par :

$$\widehat{\alpha}_k = \widehat{\alpha}_{k-1} - J^{-1}G$$

G et J, respectivement gradient du critère et approximation du gradient second du critère, sont calculés par sommation numérique des variables de sensibilité $\dfrac{\partial y}{\partial \alpha}$ dont les équations d'état sont les dérivées analytiques de (1) et (2).

On a tout intérêt à régulariser la matrice J pour améliorer la convergence et éviter un mauvais conditionnement du à l'insensibilité de certains paramètres.

La matrice J définie positive peut se mettre sous la forme

$$J = V \Lambda V^{-1}$$

où V est une matrice unitaire et Λ une matrice diagonale de termes tous positifs.

Dans ces conditions, on peut sélectionner toutes les valeurs propres inférieures à une fraction de la valeur maximale :

$$\lambda_i \leq \mu \, \lambda_{max}$$

pour chacune de ces valeurs propres λ_i, on sélectionne les composantes des vecteurs propres V_i normalisés qui sont supérieures à V. On obtient alors une liste de paramètres réputés peu sensibles et non concernés par l'itération en cours.

V est en général fixé à 0.1 tandis que μ est piloté depuis 10^{-3} à 10^{-12} par exemple, pour éviter de mettre en recherche un trop grand nombre de paramètres peu identifiables lorsqu'on est trop loin de l'optimum.

6. STRUCTURE DES MODÈLES

D'une manière classique, on distingue les modèles à 6 degrés de liberté, n'incluant pas les modes rotor aux modèles d'ordre supérieur qui prennent en compte sa dynamique.

6.1. Modèle à 6 degrés de liberté

Pour un modèle à 6 degrés de liberté, l'état x est composé de

u	vitesse longitudinale
w	vitesse normale
q	vitesse de tangage
θ	assiette longitudinale
v	vitesse latérale
p	vitesse de roulis
r	vitesse de lacet
φ	assiette latérale

Il est possible d'introduire dans l'équation d'état des termes non linéaires bien connus.

$$\dot{x} = Ax + Bu + f(x)$$

En effet, si a_x, a_z sont les accélérations dans les axes hélicoptère, les équations classiques de la mécanique permettent d'écrire :

$$\dot{u} = a_x - g \sin \theta - qw + rv$$

$$\dot{w} = a_z + g \cos \theta \cos \varphi + qu - pv$$

$$\dot{\theta} = q + q (\cos \varphi - 1) - r \sin \varphi \qquad (3)$$

$$\dot{v} = a_y + g \cos \theta \sin \varphi + pw - ru$$

$$\dot{\varphi} = p + (q \sin \varphi + r \cos \varphi) \, tg \, \theta$$

L'expression linéaire de a_x, a_y, a_z sur les états et les commandes permet d'écrire une partie du modèle linéaire auquel il convient d'ajouter les équations en $\dot{q}$, $\dot{p}$ et $\dot{r}$.

En ce qui concerne les termes non linéaires, ils peuvent être :

- linéarisés autour de l'équilibre u_o, w_o, θ_0, v_o, φ_0
- utilisés comme tels dans le modèle qui devient non linéaire en mécanique et linéaire pour les termes de forces et moments aérodynamiques
- utilisés comme tels mais calculés à partir des variables mesurées et jouant donc le rôle d'entrées auxiliaires.

C'est cette dernière option qui sera choisie pour mettre l'accent sur la recherche des paramètres aérodynamiques.

Dans ces conditions, le modèle obtenu peut être linéarisé autour de u_o, v_o, w_o, identifiés et de $\theta_0 = 0$, $\varphi_0 = 0$. Le résultat de cette linéarisation est ajouté aux termes de A pour évaluation définitive des modes, valeurs propres de la matrice A finale.

La dynamique du rotor négligée est prise en compte grâce des retards purs sur les commandes.

6.2. Modèle à 9 degrés de liberté

Lors de l'écriture d'un modèle théorique incluant les modes rotor, il est d'usage d'introduire une équation différentielle du premier ordre sur la vitesse induite moyenne du rotor principal et des équations différentielles du second ordre sur la conicité β_0 et les battements longitudinal β_{1c} et latéral β_{1s} composantes du premier harmonique du battement.

La vitesse induite n'étant pas mesurable, il est difficile de l'introduire dans le modèle pour obtenir des coefficients d'influence réalistes par identification. Les battements cycliques sont associés à des modes dit régressifs et progressifs. Ces derniers se trouvent dans une plage de fréquence au delà de la fréquence de rotation du rotor et donc inaccessibles à notre expérience. Une modélisation du premier ordre est donc suffisante.

En ce qui concerne l'équation de conicité, l'ordre deux est souvent conservé par impossibilité physique de dédoubler les modes correspondants. Cette variable est parfois négligée, car en dehors de la plage fréquentielle de travail.

Nous avons choisi de conserver un modèle du premier ordre en conicité pour tenir compte d'un déphasage entre commandes et mouvements du rotor.

Notre modèle à 9 degrés de liberté inclut donc trois variables d'état supplémentaires β_0, β_{1c}, β_{1s} et est plutôt boite noire en ce qui concerne la partie rotor.

6.3. Détermination de la structure d'un modèle

Le choix entre plusieurs structures de modèle ainsi que la détermination des coefficients du modèle non significativement différents de 0 pourraient être le résultat d'une analyse de régression. Cependant la méconnaissance des propriétés statistiques des erreurs conduit le plus souvent à des décisions erronées.

Une simple analyse déterministe basée sur un critère d'identification par moindres carrés permet de classer les différents candidats modèle.

Sur la planche 1, on peut par exemple évaluer différentes restitutions de $\dot{q}$ en minimisant le critère :

$$C = \sum_n \left[\dot{q}(n) - \Phi^T(n) \, \alpha \right]^2$$

où α est le vecteur des paramètres inconnus et où $\Phi^T(n)$ est tout d'abord une ligne composée de mesures à l'instant n de u, w, q, v, p r, et de δ_{lon}, δ_{coll}, δ_{lat}, δ_{arr}, les pas longitudinal, collectif, latéral et le pas du rotor arrière.

Un deuxième calcul est effectué en ajoutant à Φ tous les termes bilinéaires construits à partir de la liste précédente $(uq, u\beta, \cdots)$

Le troisième modèle est linéaire et contient les termes en β_0, β_{1c}, β_{1s}.

Le quatrième introduit une forme bilinéaire sur tous ces termes.

Une analyse des simulations et des critères résiduels montre l'apport des termes de battements et des termes non linéaires.

L'identification des modèles non linéaires ne fait pas l'objet de ce papier mais elle sera sans doute nécessaire lors de développements ultérieurs.

Cette démarche a permis de rejeter les termes en $\dot{\beta}_0$ dans le modèle et d'introduire des termes nuls dans la structure prédéfinie avec un impératif de dégradation du critère de restitution de $\dot{x}$ de moins de 0,1%.

Cette analyse préliminaire du modèle ne saurait être faite avec l'identification par erreur de sortie incapable de gérer un modèle trop lourd et redondant en paramètres non significatifs.

Rappelons qu'au cours des itérations, on peut provisoirement ne pas actualiser tel ou tel paramètre grâce à l'analyse des gradients du critère selon la procédure définie en 5.

7. PRÉTRAITEMENT DES DONNEES

7.1. Reconstitution de l'état cellule

A partir des équations (3) auxquelles on a ajouté les équations en cap :

$$\dot{\psi} = (q \sin \varphi + r \cos \varphi)/tg\,\theta \qquad (4)$$

et en altitude

$$\dot{h} = u \sin \theta - v \cos \theta \sin \varphi - w \cos \theta \cos \varphi \qquad (5)$$

On peut identifier les biais et les conditions initiales d'un système non linéaire ayant

- a_x, az, θ, a_y, p, r   comme entrées
- v, w, θ, v, φ, ψ, h   comme états

Les mesures utilisées sont celles de la centrale sauf en ce qui concerne le triplet pqr de meilleure qualité sur l'hélicoptère.

Il convient alors d'estimer le calage du triplet pqr par rapport aux axes centrale. Ceci ne peut être obtenu par une identification conjointe avec les biais de mesures.

Trois calculs avec des calages de 0, 2 et 5° alors sont effectués. Une approximation parabolique sur les critères de restitution obtenus permet d'obtenir le bon calage et de corriger en conséquence les données p, q, r. Pour l'identification, les donnés a_x, a_z, θ, a_y, p, r seront utilisées, en ce qui concerne u, w θ, v, φ, ce sont les données restituées par l'analyse de cohérence qui seront utilisées et non les données de vol brutes.

7.2. Estimation des perturbations atmosphériques

Avec l'hypothèse vent géographique constant et horizontal de composantes V_{x0} et V_{y0}, on peut calculer les composantes du vent dans les axes hélicoptère grâce aux formules :

$$\begin{cases} V_{ventx} = & \cos \psi \cos \theta\, V_{x0} + \sin \psi \cos \theta\, V_{y0} \\[4pt] V_{venty} = & \left(- \sin \psi \cos \varphi + \cos \psi \sin \theta \sin \varphi\right) V_{x0} \\[4pt] & + \left(\cos \psi \cos \varphi + \sin \psi \sin \theta \sin \varphi \right) V_{y0} \qquad (6) \\[4pt] V_{ventz} = & \left(\sin \psi \cos \varphi + \cos \psi \sin \theta \sin \varphi\right) V_{x0} \\[4pt] & + \left(- \cos \psi \cos \varphi + \sin \psi \sin \theta \sin \varphi \right) V_{y0} \end{cases}$$

En appelant V_{air} le module global de la vitesse air et V_x, V_y, V_z les composantes de la vitesse inertielle dans les axes hélicoptère, on peut calculer les termes constants V_{x0} et V_{y0} qui minimisent le critère.

$$C = \sum_{mesures} \left| V_{air} - \sqrt{\left(V_x - \widehat{V}_{vent\,x}\right)^2 + \left(V_y - \widehat{V}_{vent\,y}\right)^2 + \left(V_z - \widehat{V}_{vent\,z}\right)^2} \right|^2$$

Ces estimations permettent de tester la validité de l'hypothèse vent faible et constant qui permet de mener l'identification avec les mesures inertielles.

7.3. Reconstitution des pas du rotor principal

Les informations de la chaîne de commande sont disponibles en de nombreux points de mesure. Les pas en pied de pale n'étant pas mesurables directement, on reconstitue leurs variations cycliques à partir des mesures des déplacements des vérins du plateau cyclique grâce aux relations :

$$\begin{cases} \theta_{1s} = \dfrac{DTD + DTG}{2} - DTA & \text{longitudinal} \\[8pt] \theta_{1c} = \dfrac{DTD - DTG}{2} & \text{latéral} \qquad (7) \\[8pt] \theta_0 = \dfrac{DTD + DTG}{2} & \text{collectif} \end{cases}$$

qui tient compte de la géométrie du plateau.

La validité de ce calibrage a été vérifiée grâce à des mesures de déplacements et de pas effectuées au sol. Ce sont ces valeurs reconstituées par (7) qui seront utilisées comme entrées du modèle identifié.

7.4. Calcul du battement cyclique

A partir des battements instantanés des quatre pales β_i et l'azimut ψ de la pale de référence, on peut en négligeant le battement de traînée, reconstituer :

$$\beta_o = \frac{1}{4} \sum_{i=1}^{4} \beta_i$$

$$\beta_{1c} = \frac{1}{2} \sum_{i=1}^{4} \beta_i \cos\left(\psi - i\,\frac{\pi}{2}\right) \qquad (8)$$

$$\beta_{1s} = \frac{1}{2} \sum_{i=1}^{4} \beta_i \sin\left(\psi - i\,\frac{\pi}{2}\right)$$

mais les β_i utilisés doivent être corrigés de manière à égaliser les calibrages des capteurs de battement.

Soient $\bar{\beta}$ et σ les moyenne et écart-type des battements de chaque pale. Toutes les mesures sont corrigées pour avoir les mêmes moyenne et variance que pour la pale de référence :

$$\beta_{i\,corrigé} = \left(\beta_i - \bar{\beta}_i\right)\frac{\sigma_{ref}}{\sigma_i} + \bar{\beta}_{ref}$$

8. RÉSULTATS

8.1. Structure du modèle

La planche 1 compare sur l'exemple de l'accélération de tangage $\dot{q}$ l'effet d'une modélisation par moindres carrés à partir de termes linéaires purs ou de termes bilinéaires, de termes associés à l'état cellule seulement ou de termes additifs venant l'état du rotor.

Si l'on s'en tient aux valeurs résiduelles du critère quadratique portant sur la restitution de $\dot{q}$, on constate que les apports des termes non linéaires d'une part et des termes de battement $\beta_0, \beta_{1c}, \beta_{1s}$ comme variables explicatives, sont équivalents.

Une amélioration sensible du critère est obtenue avec un modèle complet non linéaire.

Cependant dans ce dernier cas, le nombre de paramètres à identifier est trop important compte tenu de la richesse des signaux de test utilisés. La recherche d'un tel modèle fera donc l'objet d'essais et de calculs ultérieurs.

Pour la suite des calculs présentés, nous avons utilisé essentiellement un modèle linéaire à 9 degrés de liberté avec un état composé de u, w, q, θ, v, p, r, φ, β_0, β_{1c}, β_{1s}.

8.2. Identification d'un modèle à 9 ddl avec entrées auxiliaires

La planche 2 représente pour quatre essais concatenés les entrées utilisées et la comparaison modèle/mesure des variables du rotor.

Les essais sélectionnés ont été l'essai en séquences binaires pseudo-aléatoires pour la commande longitudinale, et les séquences 3 2 1 1 pour les autres commandes.

Les planches 3 et 4 permettent d'observer le comportement des variables de l'état de la cellule (modèle et mesure).

La très bonne restitution des vitesses linéaires est due en grande partie à l'introduction des entrées auxiliaires construites à partir des termes gyroscopiques et de pesanteur qui fournissent souvent la plus grande partie de l'information utile (dans le cas de $\dot{u}$ par exemple). Avec le Dauphin, nous nous sommes heurté à une grande difficulté : l'obtention d'un accord acceptable modèle-mesure à la fois sur l'axe de tangage et sur l'axe de lacet. Le résultat présenté est l'un des compromis acceptables.

8.3. Validation de l'identification

Le même modèle à 9 ddl a été validé à partir d'essais n'ayant pas servi à l'identifier. Dans ce cas, l'accord est moins bon mais tout de même acceptable sauf en ce qui concerne une basse fréquence mal modélisée particulièrement visible sur θ, φ et r .

8.4. Modèle linéaire pur

Les termes non linéaires gyroscopiques et de pesanteur sont linéarisés autour de u_0, v_0, w_0 inconnus et de $\theta_0 = 0$, $\varphi_0 = 0$. L'ensemble des coefficients du modèle est alors recalé pour minimiser le critère d'écart simulation-mesures.

Les planches 7 et 8 montrent les résultats obtenus avec quelques discordances en basse fréquence, cette fois très visibles sur les termes de vitesse linéaire.

Il y a trop peu de différence entre les simulations des modèle à 6 et 9 degrés de liberté pour qu'une comparaison graphique présente quelque intérêt.

Un nombre important de dérivées de stabilité et de commande sont peu identifiables et il est nécessaire de fournir avec chaque estimation, un intervalle de confiance associé.

Les bornes de Cramer-Rao, racines carrées des termes diagonaux de J^{-1}, fournissent une évaluation de la variance d'erreur d'estimation des paramètres. Cette information est délicate à interpréter du fait du peu de validité des hypothèses statistiques sur les bruits.

Comme pour l'analyse de régression, nous privilégions une démarche déterministe. Un développement de Taylor du critère C autour de l'estimation α_0 du vecteur des paramètres s'écrit:

$$C = C_0 + G^T(\alpha - \alpha_0) + \frac{1}{2}(\alpha - \alpha_0)^T J(\alpha - \alpha_0)$$

Au voisinage du minimum, le gradient G est nul et les variations du critère ne dépendent que de J.

Une variation de 1% du critère serait donc obtenue, pour chaque paramètre i , avec la variation:

$$\Delta\alpha_i = \sqrt{\frac{2C_0}{100 J_{ii}}}$$

Les $\Delta\alpha_i$ déterminent un hypercube de sensibilité associé à l'isocritère $1.01 C_0$.

Pour obtenir l'hypercube tangent extérieur à l'isocritère, il suffirait de remplacer les $\frac{1}{J_{ii}}$ par J_{ii}^{-1} .

Une comparaison de quelques dérivées de stabilité et des retards purs de commande, associés à leurs plages de sensibilité pour 1% du critère, est visible sur le tableau suivant:

Para-mètres	6 ddl	9 ddl
Z_w	-0.84 ± 0.04	-0.16 ± 0.06
Z_q	-5.1 ± 1.1	-4.7 ± 1.5
M_u	0.057 ± 0.002	-0.013 ± 0.001
M_w	0.081 ± 0.005	0.066 ± 0.002
M_q	-7.01 ± 0.15	-0.92 ± 0.05
M_v	-0.031 ± 0.006	0.067 ± 0.002
M_p	1.12 ± 0.18	2.50 ± 0.04
Y_v	-0.12 ± 0.03	-0.13 ± 0.03
L_q	-1.38 ± 0.56	2.29 ± 0.48
L_v	-0.11 ± 0.01	-0.046 ± 0.011
L_p	-2.65 ± 0.19	-0.79 ± 0.19
L_r	0.72 ± 0.29	0.46 ± 0.34
N_u	0.016 ± 0.002	0.023 ± 0.001
N_w	0.025 ± 0.004	-0.051 ± 0.004
N_q	-0.77 ± 0.11	-2.50 ± 0.11
N_v	0.017 ± 0.003	-0.006 ± 0.003
N_p	-0.76 ± 0.07	-0.56 ± 0.02
N_r	-0.63 ± 0.09	-0.13 ± 0.10
τ_{lon}	0.12 ± 0.14	$\varnothing$
τ_{coll}	0.16 ± 0.06	$\varnothing$
τ_{lat}	0.03 ± 0.11	$\varnothing$
τ_{an}	0.01 ± 0.26	$\varnothing$
$\beta_0\beta_0$	—	-4.2 ± 0.4
$\beta_{1c}\beta_{1c}$	—	-7.8 ± 0.36
$\beta_{1c}\beta_{1s}$	—	10 ± 0.2

La comparaison des modes, valeurs propres de la matrice A obtenus pour les deux types de modèles sont les suivants :

Modes	9ddl	6ddl
Phugoïde	0.09 ± j 0.34	0.04 ± j 0.38
Incidence	-1 ± j 0.024	-7 ; - 0.59
Roulis	- 2.78	-3.11
Roulis hollandais	-0.24 ± j 1.27	- 0.21 ± j 1.41
Spiral	-0.2	- 0.067
Conicité	- 7.8	-
Battement cyclique	-5.5 ± j 3.2	

9. CONCLUSIONS ET PERSPECTIVES

9.1. Analyse des résultats obtenus

Malgré une analyse préliminaire prometteuse, l'introduction de variables rotor dans le modèle n'a que très peu amélioré la concordance entre les mesures et la simulation du modèle. On peut sans doute incriminer la trop faible largeur de bande des signaux d'identification limitée à 2Hz pour des raisons expérimentales.

Cependant, l'utilisation d'un modèle à 9 degrés de liberté a régularisé les résultats numériques obtenus et a fourni des dérivées de stabilité et des modes plus proches de ceux physiquement attendus.

La validation du modèle sur des essais n'ayant pas servi à l'identifier a donné des résultats satisfaisants. Bien sur, l'introduction de pseudo-entrées formées à partir des termes gyroscopiques et de pesanteur mesurés s'est avérée nécessaire pour obtenir des résultats corrects, mais c'est le prix à payer pour la réalisation d'essais en boucle ouverte dans des conditions difficiles : faible amplitude des signaux d'identication, forte amplitude des signaux de contrôle du pilote humain et grande variation des vitesses à peine compatible avec les hypothèses linéaires.

En dépit de ces restrictions sur les premiers résultats, nous disposons avec le Dauphin 6075 du CEV d'un appareil dédié aux recherches avec lequel nous allons enrichir notre base de données et poursuivre nos investigations sur la mécanique du vol des basses vitesses.

9.2. Travaux futurs

Des essais au voisinage du stationnaire vont être programmés. Pour éviter les défauts des essais précédents, ils seront réalisés en boucle fermée à partir d'entrées large bande et d'amplitudes plus importantes. Le comportement en basse fréquence n'imposera plus une limitation abusive des amplitudes des signaux test.

Pour limiter la dégradation d'information apportée par la boucle fermée nous suggérons de dépouiller huit essais concatenés et non quatre.

Pour chaque entrée de commande, deux essais seront réalisés, l'un en boucle fermée avec une séquence binaire pseudo-aléatoire pouvant solliciter en toute tranquillité le comportement haute fréquence de l'appareil et l'autre en boucle ouverte avec un essai plus court et une sollicitation rustique en double créneau juste bonne à sensibiliser phugoïde ou roulis hollandais par exemple.

9.3. Applications ultérieures

Dans le cadre de nos travaux, la finalité de l'identification est d'obtenir un modèle utilisable pour la synthèse de lois de commande.

Les expériences passées montrent que la loi 1 définie sur un modèle nominal identifié en boucle ouverte donne rarement toute satisfaction.

Une deuxième identification de l'hélicoptère muni de la loi 1 fournirait un modèle sans doute biaisé mais obtenu dans des conditions plus proches de celles du fonctionnement de l'hélicoptère muni de sa loi définitive. La loi obtenue avec ce deuxième modèle est espérée plus pertinente que la première. Cette stratégie de recalage d'une loi de commande à partir d'essais en vol nous semble une voie prometteuse qui renforce le rôle de l'identification dans la démarche de synthèse d'une loi de commande.

Bibliographie

[1] J.Kaletka , B.Gimonet. Identification of extended models from BO105 - Flight Test Data for Hoover Flight Condition - 21st European Rotorcraft Forum - August 1995 - St Petersburg (Russie)

[2] D.Papiller, P.Lange, P.Bonnet, B.Gimonet, D.Heuzé The Dolphin 6075 : an helicopter dedicated to flight test research - 23st European Rotorcraft Forum

[3] B.Gimonet, J.Kaletka DLR ONERA cooperation on Smart Helicopter" Concept Status Report ont task 1.3 - Helicopter System Identification - December 1994

[4] B.Gimonet Concept Smart Helicopter - Cooperation ONERA-DLR - Rapport DRET - May 1993

[5] P.G.Hamel (Editor) Rotorcraft System Identification - AGARD AR 280, 1991

[6] J.W.Fletcher Identification of UH 60 stability derivative models in Hoover from flight test data - American Helicopter Society 49 th, Annual Forum, May 1993

[7] K.H.Fu, J.Kaletka Frequency domain identification of BO 105 derivative models with rotor degrees of freedom - 16th European Rotorcraft Forum, Glasgow UK, 1990 and Journal of the American Helicopter Society, Vol. 38, n°1, January 1993

[8] J.Kaletka, K.H.Fu Frequency domain identification of Unstable system using X-31 aircraft flight test data - AIAA Atmospheric Flight Mechanics, Monterey (USA), August 9-11, 1993

[9] K.H.Fu, J.Kaletka BO 105 system identification for Hoover flight condition - 19th European Rotorcraft Forum, Cernoblio (Italy), September 14-16, 1993

[10] Maj A.Ham, C.K.Gardner, M.B.Tischler Flight testing and frequency domain analysis for Rotorcraft handling qualities Characterics - American Helicopter Society's Specialists Meeting Conf. on Flying Qualities & Human Factors, San Francisco (USA), January 1993

[11] J.A.Schroeder, D.C.Watson, M.B.Tischler, M.M.Eshow Identification and simulation Evaluation of an AH 64 helicopter Hoover Math.Model. - AIAA Atmospheric FLight Mechanics Conference, New Orléans (USA), August 1991
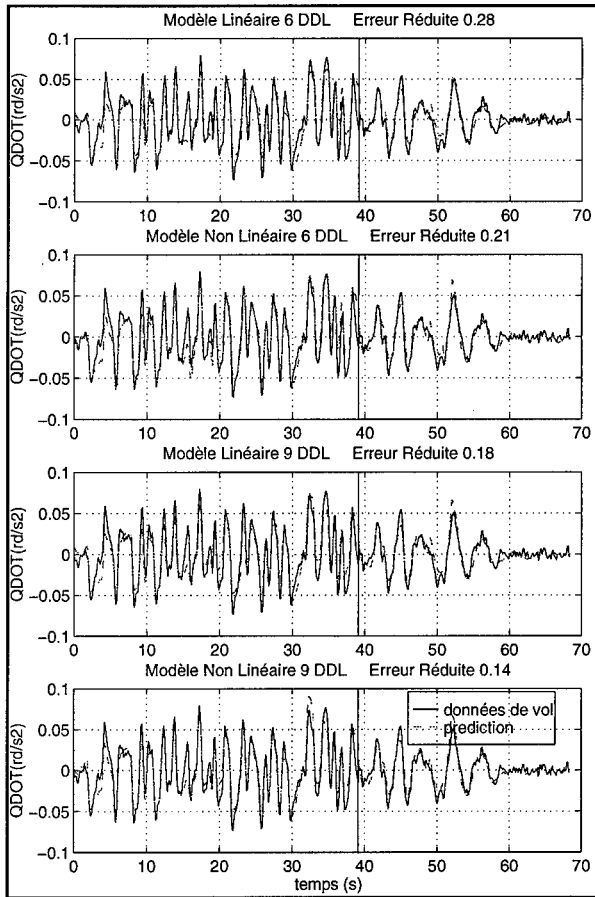
Planche 1 : Comparaison de 4 structures de modèle sur la prédiction de l'accélération de tangage
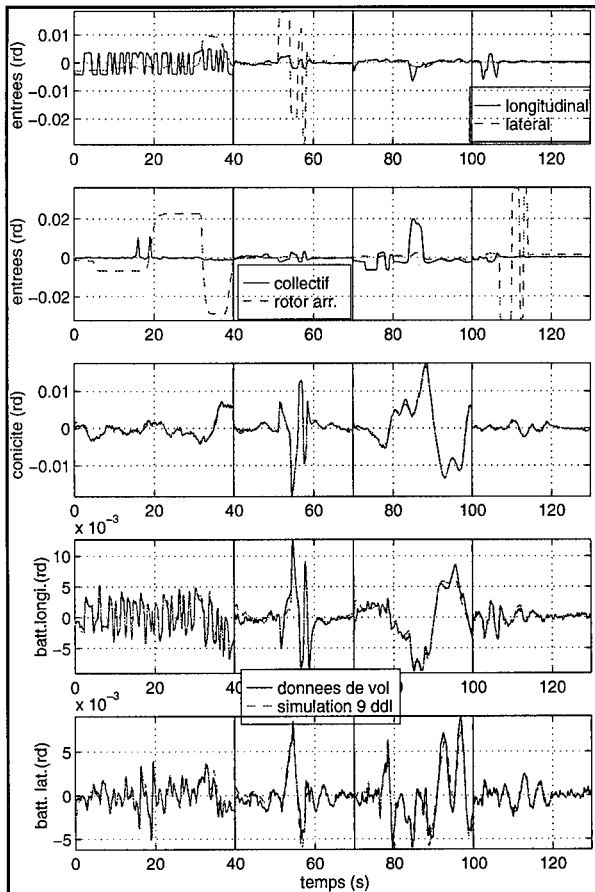

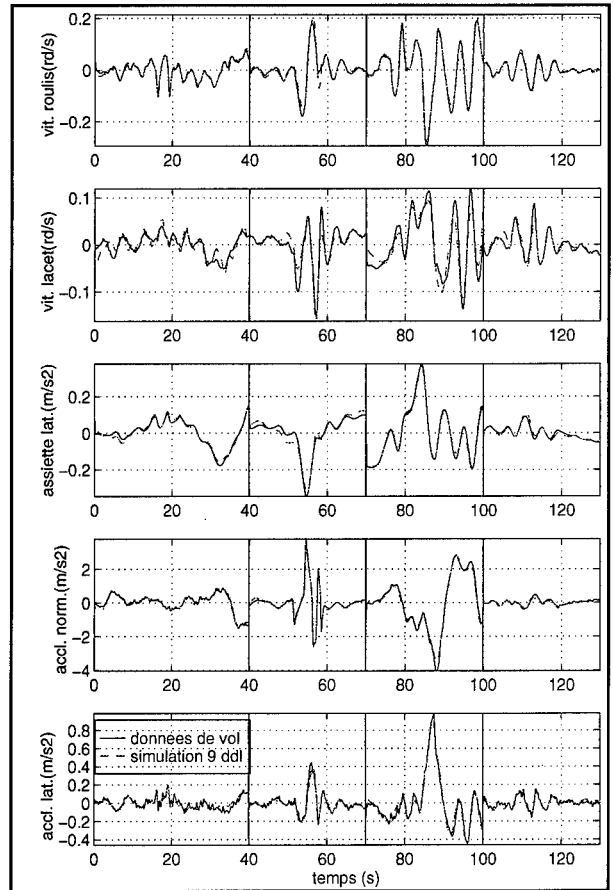Planche 3 : Identification d'un modèle à 9ddl avec entrées auxiliaires (suite)

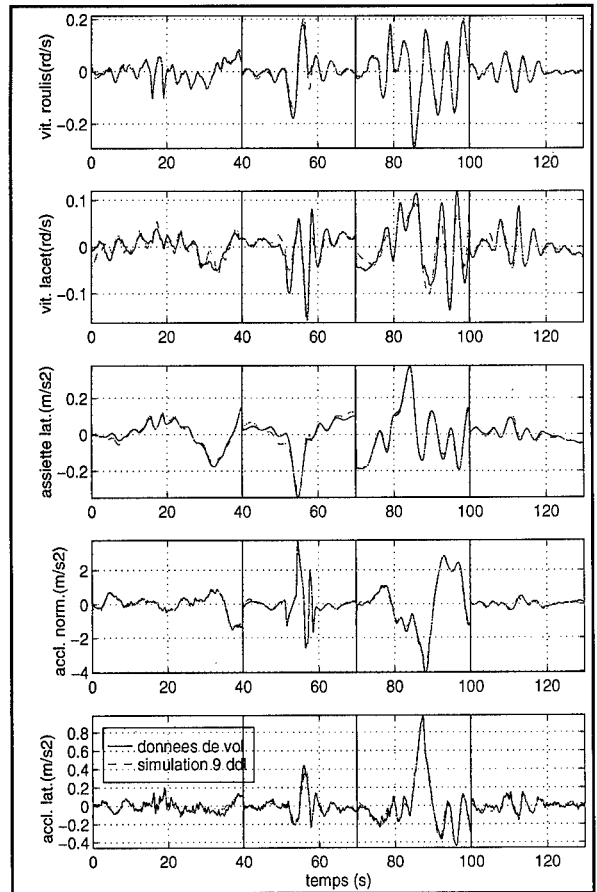Planche 2 : Identification d'un modèle à 9ddl avec entrées auxiliaires

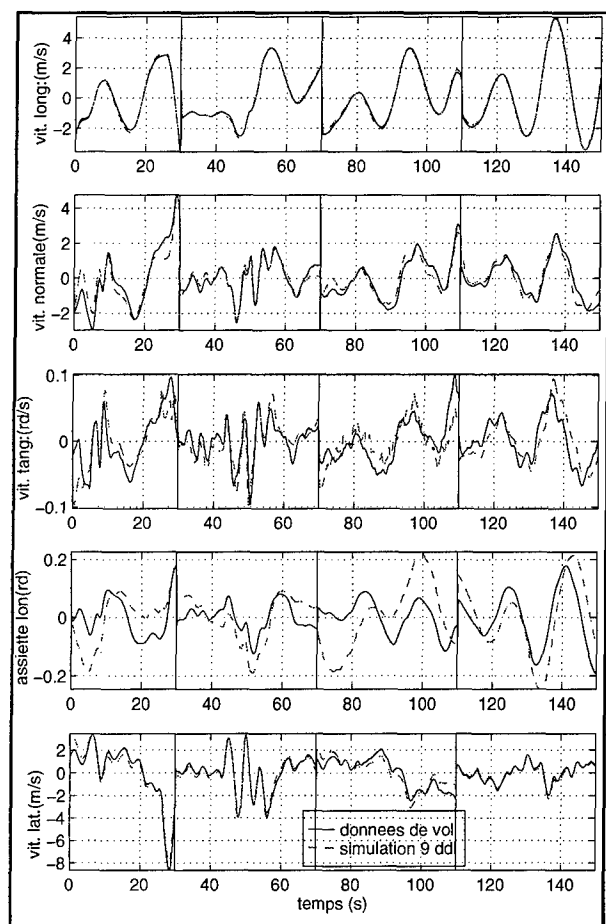Planche 4 : Identification d'un modèle à 9ddl avec entrées auxiliaires (fin)

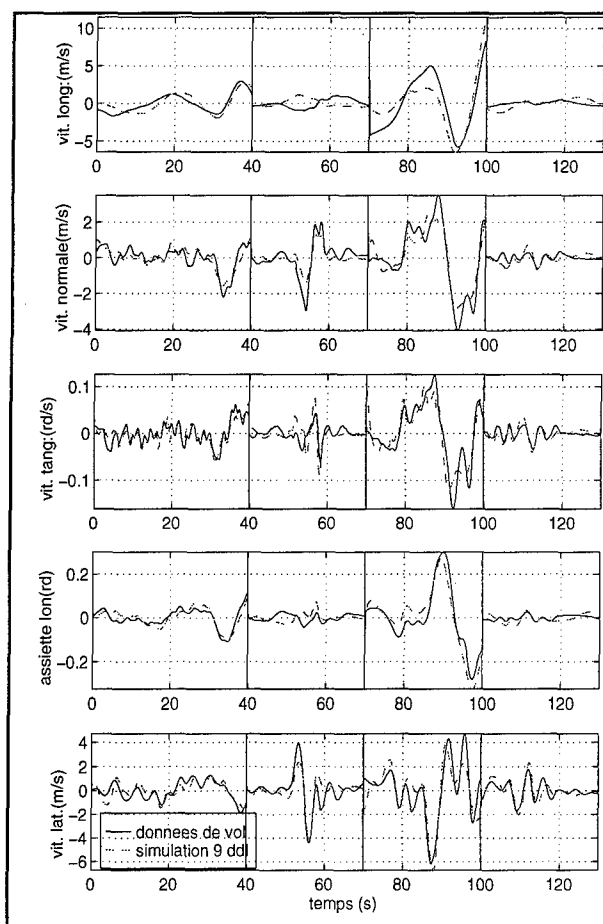Planche 5 : Validation de l'identification

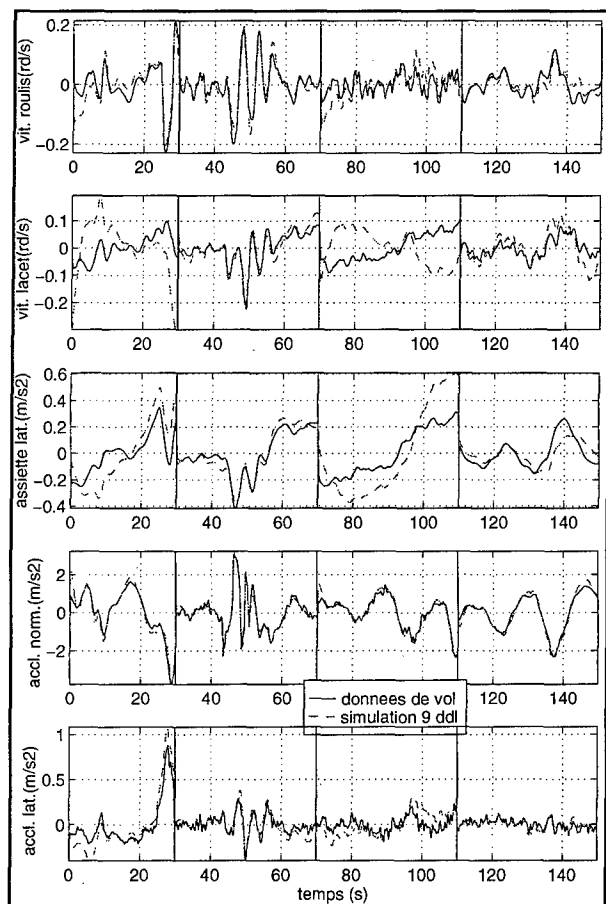Planche 7 : Identification du modèle linéaire pur

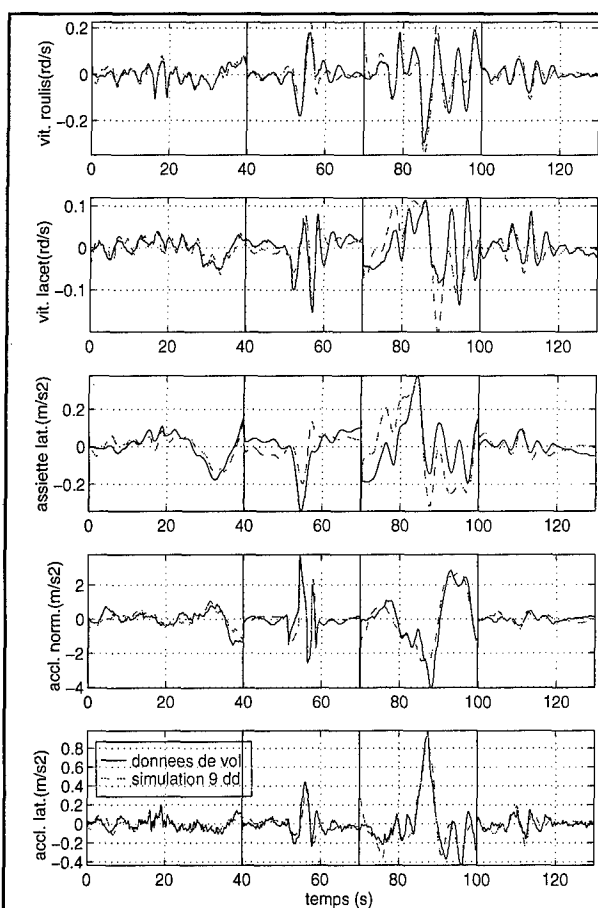Planche 6 : Validation de l'identification (fin)

Planche 8 : Identification modèle linéaire pur (fin)

Nonlinear Rotorcraft Modeling and Identification

M. Rohlfs, W. v. Grünhagen, J. Kaletka
Deutsches Zentrum für Luft- und Raumfahrt e.V. (DLR)
Institut für Flugmechanik
Lilienthalplatz, 7
D-38108 Braunschweig, Germany

1. SUMMARY

Since regulations for the evaluation of helicopter flight simulators were published in the Advisory Circular 120-63 (AC 120-63) of the Federal Aviation Administration, the need of increasing the simulation fidelity of the helicopter mathematical models becomes more and more relevant to meet the new more restricted requirements. In the Institute of Flight Mechanics mainly two approaches are used to develop helicopter mathematical models. First, linear derivative models are identified from flight test data. The second approach uses detailed vehicle characteristics for the development of a nonlinear helicopter simulation program. The paper describes the two helicopter mathematical modeling approaches and discusses their advantages and disadvantages. Finally, a third approach is introduced, which combines the advantages of both, the linear identified models and the nonlinear generically derived models. Results from all three modeling approaches are presented in both, the time and frequency domain. They are discussed with respect to some selected requirements given in the new FAA advisory circular on helicopter simulator qualification AC 120-63. Finally, conclusions are made and an outlook of future activities is given.

2. NOTATION

$\underline{\underline{A}}$	System matrix
a_x	Longitudinal acceleration
a_y	Lateral acceleration
a_z	Vertical acceleration
a_0	Coning
a_1	Longitudinal flapping
$\underline{\underline{B}}$	Control matrix
b_1	Lateral flapping
$\underline{\underline{C}}$	Output matrix
C_D	Drag coefficient
C_{D0}	Drag zero derivativ
$C_{D\alpha^2}$	Drag α^2 derivativ
C_L	Lift coefficient
C_{L0}	Lift zero derivativ
$C_{L\alpha}$	Lift α derivativ
$C_{\lambda_{0,()}}$	Zero downwash derivativ
$C_{\lambda_{c,()}}$	Cos downwash derivativ
$C_{\lambda_{s,()}}$	Sin downwash derivativ
$\underline{\underline{D}}$	Direct transmission matrix
g	acceleration due to gravity

$I_{()}$	Moments of inertia
$L_{()}$	Lateral system coefficients
$\tilde{L}_{()}$	Lateral system coefficients
L_{aero}	Aerodynamic rollmoment
$L_{inertia}$	Inertial rollmoment
m	Mass
M_{aero}	Aerodynamic pitchmoment
$M_{inertia}$	Inertial pitchmoment
N_{aero}	Aerodynamic yawmoment
$N_{inertia}$	Inertial yawmoment
p	Roll rate
q	Pitch rate
r	Yaw rate
u	Longitudinal velocity component
$\underline{u}$	Control vector
v	Lateral velocity component
w	Vertical velocity component
V_r	Rotor tip speed
$\underline{x}$	State vector
X_{aero}	Aerodynamic longitudinal force
$X_{inertia}$	Inertial longitudinal force
$\underline{y}$	Output vector
Y_{aero}	Aerodynamic lateral force
$Y_{inertia}$	Inertial lateral force
Z_{aero}	Aerodynamic vertical force
$Z_{inertia}$	Inertial vertical force
α	Angle of attack
$\delta_{control}$	Control input
λ_0	Ext. downwash velocity, zero comp.
λ_c	Ext. downwash velocity, cos comp.
λ_s	Ext. downwash velocity, sin comp.
$\lambda_{0,PP}$	Org. downwash velocity, zero comp.
$\lambda_{c,PP}$	Org. downwash velocity, cos comp.
$\lambda_{s,PP}$	Org. downwash velocity, sin comp.
Ω	Rotor angular rate
Φ	Roll angle
Θ	Pitch angle
Ψ	Yaw angle
τ_b	Time constant
$\dot{()}$	$d()/dt$
$\ddot{()}$	$d^2()/dt^2$

3. INTRODUCTION

In the Institute of Flight Mechanics mainly two approaches are used to develop helicopter mathematical models. First, linear derivative models are iden-

**High-Fidelity Simulation
State Space Models**

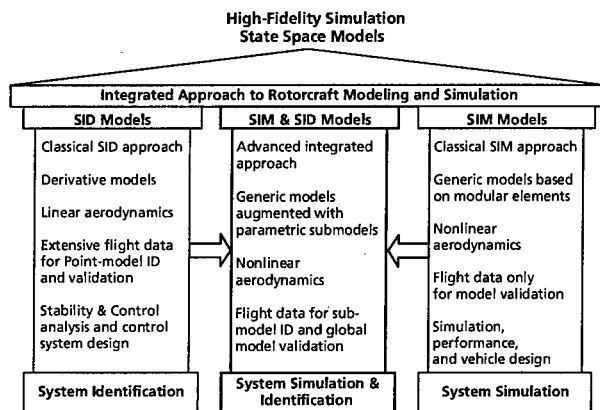| Integrated Approach to Rotorcraft Modeling and Simulation		
SID Models	**SIM & SID Models**	**SIM Models**
Classical SID approach	Advanced integrated approach	Classical SIM approach
Derivative models		Generic models based on modular elements
Linear aerodynamics	Generic models augmented with parametric submodels	
Extensive flight data for Point-model ID and validation		Nonlinear aerodynamics
	Nonlinear aerodynamics	Flight data only for model validation
Stability & Control analysis and control system design	Flight data for sub-model ID and global model validation	Simulation, performance, and vehicle design
System Identification	**System Simulation & Identification**	**System Simulation**

Figure 1: Rotorcraft modeling and validation, the three columns approach

tified from flight test data [1, 2]. This approach is represented by the left column in Fig. 1. The simulation fidelity of the obtained linear models is accurate but they are restricted by small perturbation assumptions. The second approach, represented by the right column in Fig. 1, uses detailed vehicle characteristics for the development of a nonlinear helicopter simulation program [3]. Due to recent improvements of this model [4], its fidelity now mostly fullfills the standards given in the Advisory Circular AC 120-63 on Helicopter Simulator Qualification [6] of the Federal Aviation Administration (FAA). In addition, first steps to identify more complex nonlinear helicopter models have been undertaken [7]. A third modeling approach is represented by the middle column in Fig. 1. It combines the advantages of both, the linear identified models and the nonlinear generically derived models.

4. MODELING APPROACHES

In the past in the DLR Institute of Flight Mechanics mainly two helicopter mathematical modeling approaches were used for various applications. The left and right columns in Fig. 1 describe their main characteristics. In the following these approaches are discussed.

4.1. Linear modeling and identification

In the first approach coefficients in a linear derivative model are determined using system identification methods. In this case extensive flight test data is needed for the model determination and validation. The obtained global models are mainly used for the development of the model following control system of the Institute's In-Flight-Simulator ATTHeS (Advanced Technology Testing Helicopter System) [1, 2] and for stability and control analysis. Since the structure of these models is linear, they cover only a small range of the flight envelope, namely the range around the trim condition and they are valid only for small control excitations. When a model for a larger range

within the flight envelope is needed, individual linear models at well selected flight conditions have to be determined and an interpolation between these models can be used.

4.2. Nonlinear modeling

The second method to obtain a helicopter mathematical model is a physical approach where the model is generically derived [3]. The model is modular structured and it is based on detailed vehicle characteristics. This model is mainly used for real time flight simulation tasks and it is also implemented in the Institute's helicopter ground based flight simulator. Depending on the model complexity, it also can be used during the design phase for detailed prediction and for overall performance analysis. The main advantages of this model are that it covers the whole flight envelope and that flight test data is only needed to validate the model. The modeling status and fidelity is described in [4]. It was shown that it mostly fullfills the requirements described in the FAA's AC 120-63.

4.3. System identification at DLR

In the DLR Institute of Flight Mechanics a great amount of experience exists in the area of system identification for both, rotary and fixed wing aircraft. One of the latest most challenging tasks was the identification of the model database of the Dornier DO-328 aircraft for a level D flight simulator [8]. Despite the very complex mathematical model and a high number of parameters it turned out, that the system identification methodology is well suited to determine a database which meets the stringent requirements for a level D fixed wing aircraft simulator [9]. Also and in parallel to fixed wing aircraft application, system identification activities resulted in the determination of accurate linear helicopter models from flight test data [10, 11, 12].

4.4. Nonlinear modeling and identification

In regard of this development it was considered to combine the two helicopter mathematical model development approaches. The goal is to use system identification methods to identify parametric extensions in a nonlinear generically derived helicopter model in order to overcome small perturbation assumptions and to achieve a great simulation fidelity. As the middle column of Fig. 1 shows, the model is, similar to the generic 'nonlinear modeling' approach and modular structured. In addition, parametric extensions are introduced to provide improved descriptions of inaccurately known model components. Flight test data are needed for the determination of the introduced parameters and for the validation of the model.

5. IDENTIFICATION PROCEDURE

Fig. 2 shows the principle of the parameter identification [5]. Specially designed input signals are used to excite the aircraft. Both, control inputs and air-
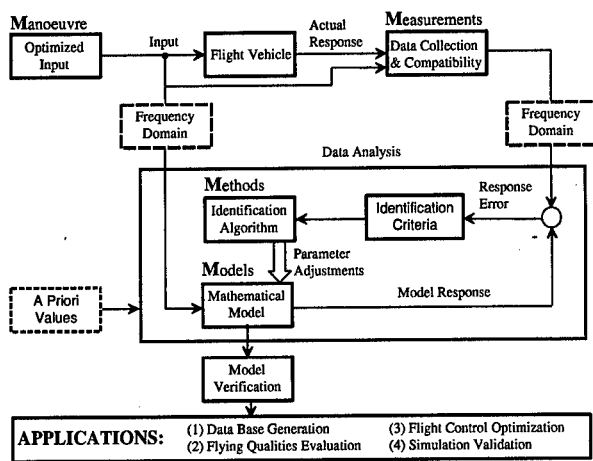
Figure 2: The principle of parameter identification

Longitudinal Handling Qualities Control Response Test		
Tolerances	Flight Conditions	Comments
Pitch Rate: ±10% or ±2 deg/s Pitch Attitude Change: ±10% or ±1.5 deg	Cruise	Step control input. Off axis response must show correct trend.

Table 1: Longitudinal Requirements

Lateral Handling Qualities Control Response Test		
Tolerances	Flight Conditions	Comments
Roll Rate: ±10% or ±3 deg/s Roll Attitude Change: ±10% or ±3 deg	Cruise	Step control input. Off axis response must show correct trend.

Table 2: Lateral Requirements

craft response are measured and recorded. The data is checked for compatibility and errors are corrected as far as possible. The identification techniques can be implemented for working either in the time or frequency domain. Consequently the measured data have the form of time histories or they are transferred into the frequency domain. The aircraft model is formulated as a set of differential equations or respectively as transfer functions. Unknown parameters in the model are adjusted using the differences between measured and computed data to obtain a better agreement. The identification process is usually an iterative process. The adjustment of the parameters is repeated until an accuracy requirement is accomplished or a certain number of iterations is reached.

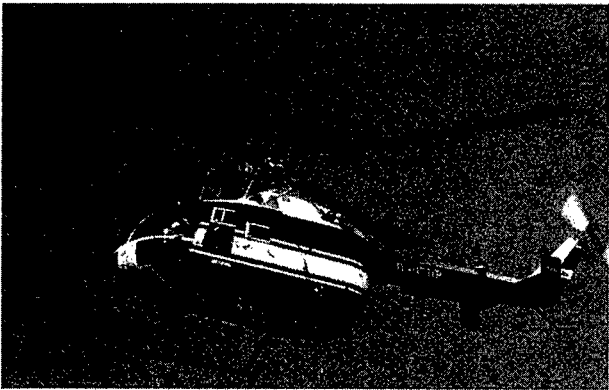| Directional Handling Qualities Control Response Test		
Tolerances	Flight Conditions	Comments
Yaw Rate: ±10% or ±2 deg/s Yaw Attitude Change: ±10% or ±2 deg	Cruise	Step control input. Off axis response must show correct trend.

Table 3: Directional Requirements

Figure 3: BO 105 research helicopter

6. SIMULATION FIDELITY REQUIRE-MENTS

For the presentation of the results, tolerances given in the Advisory Circular AC 120-63 on Helicopter Simulator Qualification [6] of the Federal Aviation Administration (FAA) will be applied. They help to give a quantitative impression about the model accuracy and needs for further improvements. The tolerances are added to the measured flight test data and the obtained range is plotted as shaded area in the time history format. (The actual measurements are right in the middle of this area). Then the calculated model response is shown as solid line, which has to stay within the error boundaries to fulfill the AC 120-63 criteria. As example Tables 1 to 3 describe the requirements for a level D simulator for cruise flight condition for the primary longitudinal, lateral and directional control responses. Error boundaries are only given for the direct, e.g. on-axis response whereas the off-axis responses must at least show a correct trend. In this paper the above FAA-boundaries are also applied to the off-axes responses.

7. FLIGHT TEST DATABASE

The flight test database used in this work originates from different flight test campaigns. The programs were conducted with the BO 105 research helicopter from DLR (Fig. 3). The flight test database consists of tests at different speeds from hover to 110 kts and different input signals like sweep, doublet and 3211 signals for all four control inputs. Before using the

data for identification and verification, its consistency was checked by performing a flight path reconstruction.

8. LINEAR MODELING AND IDENTIFICATION

For rotorcraft system identification the dynamics are modeled by a set of linear differential equations describing the external forces and moments in terms of accelerations, state and control variables, where the coefficients are stability and control derivatives. The helicopter response due to a control input is highly coupled in all degrees of freedom. Therefore, a separation into models for the longitudinal and lateral directional motions, as often used for fixed wing aircraft, is generally not appropriate. At least, a 6 degrees of freedom (DOF) rigid body model formulation is needed. As can be seen from Fig. 2, identification techniques rely on the relationship between measured inputs and the resulting helicopter response. In consequence, the flight test data must provide sufficient information about the vehicle characteristics. In general, a single test run, for helicopters often limited in time due to aircraft instabilities, cannot meet this requirement. Therefore, different individually flown test runs are concatenated in the evaluation to increase the information content. As result, one common model is obtained. This approach has become standard in helicopter system identification and is widely used.

8.1. Characteristics of identified models

Some of the major characteristics of linear rotorcraft models are summarised in Fig. 1. In analytical simulation approaches, defined helicopter components, like main and tail rotors, fuselage, etc., are modeled individually. The resulting forces and moments are transferred to the center of gravity and summarised. The obtained total forces and moments are then used to calculate the helicopter motion. In contrast to this modular model structure, system identification only provides a global model structure, without details about individual components. Linear derivative models are always based on small perturbation assumptions allowing only small deviations from a defined steady state trim condition. When a model for a larger range within the flight envelope is needed, individual linear models at well selected flight conditions have to be determined. Then, an interpolation between these models, e.g. with respect to speed can be used. However, in any case, quite extensive flight testing is necessary to provide the required flight test data for the identification and system validation procedures.

The development of identification tools, their application and progress is well documented in several AGARD publications, in particular a Lecture Series on identification in general [13] and a Working Group Report and Lecture Series on rotorcraft identification [14, 15]. A short review of the Working Group activities was also presented in [16] and [?].

8.2. 6 degree of freedom models

For linear 6 DOF models, the state equations are

$$\underline{\dot{x}} = \underline{\underline{A}}\,\underline{x} + \underline{\underline{B}}\,\underline{u}. \tag{1}$$

The output equations can be formulated as

$$\underline{y} = \underline{\underline{C}}\,\underline{x} + \underline{\underline{D}}\,\underline{u}. \tag{2}$$

With the state vector

$$\underline{x}^T = [u, v, w, p, q, r, \Phi, \Theta], \tag{3}$$

the control vector

$$\underline{u}^T = [long.\ stick,\ lat.\ stick,\ pedal,\ collective] \tag{4}$$

and the output vector

$$\underline{y}^T = [a_x, a_y, a_z, u, v, w, p, q, r, \Phi, \Theta, \dot{p}, \dot{q}, \dot{r}]. \tag{5}$$

This model is linear. When identification techniques allow nonlinear model formulations, like the Maximum Likelihood method, the kinematic and gravity terms are sometimes kept nonlinear and calculated with actual state variables.

When a control input is given to a 6 DOF model an immediate response is seen in the on-axis rotational acceleration. Measurements, however, show a delay between control inputs and rotational accelerations, caused by the dynamic characteristics of the main rotor, which are neglected in 6 DOF models. A common approach to overcome this deficit is to approximate the main rotor dynamics by equivalent time delays for the controls. Here, typical values for the BO 105 are in the order of 40 to 100 milliseconds depending on the considered control. This approach is often applied and it has been shown with different helicopters that the obtained identified models give a reliable representation of the aircraft dynamics in the lower and mid frequency range (for BO 105 up to about 1.5 Hz).

As the main rotor dynamics are only approximated by equivalent time delays a decreasing model accuracy has to be accepted for higher frequencies. In conclusion, it can be stated that 6 DOF models are appropriate and useful for applications in the lower and mid frequency range, e.g. for handling qualities evaluations and for less demanding control system designs.

For applications, where a more accurate representation of the high frequency dynamics is needed, higher order models with rotor degrees of freedom are required. This is true for high bandwidth control systems in general and, more specifically, for the design of model following control systems for helicopter in-flight-simulation, which is a major research objective at the DLR Institute of Flight Mechanics. Therefore, emphasis was placed on extending the conventional models by a more appropriate characterisation and identification of the rotor dynamics. Here, various linear model formulations were developed. Two of them are briefly described here.

8.3. Extended model with implizit 1st order approximations of the main rotor

This approach is based on the high correlation between the flapping motions of the rotor tip path plane (lateral and longitudinal flapping) and the body rotational accelerations (roll and pitch acceleration) [18]. The correlation is clearly seen for the BO105 helicopter, and here in particular for the lateral flapping and roll accelerations, and mainly exists for helicopters with rigid rotors and high hinge offsets. The relationship between these variables can be formulated as

$$\dot{p} = L_{b1} b_1 \tag{6}$$

and

$$\dot{b}_1 = -\frac{1}{\tau_b} b_1 + \frac{1}{\tau_b} \delta_{control} - p. \tag{7}$$

With differentiating Eq. 6 and then inserting Eq. 7 the conventional linear first order flapping differential equation becomes

$$\ddot{p} = \tilde{L}_{\dot{p}}\dot{p} + \tilde{L}_p p + \tilde{L}_q q + \ldots + \tilde{L}_{\delta_{control}} \delta_{control}. \tag{8}$$

When a corresponding formulation is made for the longitudinal motion, two additional second order differential equations for the rotor/body motion are obtained. The main advantage of this approach is that the extended model explicitly represents the dynamics of the rotor degrees of freedom as a first order system. However, for the identification, blade measurements, which often are not available, are not required. Rotational acceleration variables can easily and accurately be obtained by differentiating the rates.

The identified extended model is still linear and of 10th order. In comparison to the 6 DOF model it covers a wider frequency range. As rotor dynamics are now implicitly included, there is no need for any time
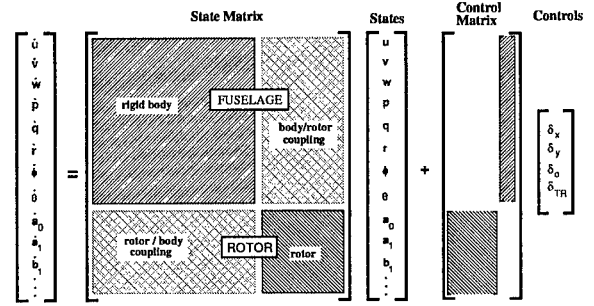

Figure 4: Extended linear model structure

delays to approximate the rotor influence. The obtained models were used for the design of the model-following control system of the DLR BO 105 In-Flight Simulator ATTHeS and extensive flight tests have proven their reliability and suitability [18].

8.4. Extended model with explizit 2nd order flapping equations for the main rotor

The basic approach for extending the conventional 6 DOF model formulation by explicit rotor degrees of freedom is illustrated in Fig. 4. Considering the blade flapping motions in the format of tip path plane variables, the state vector is extended by

$$\underline{x}^T = \left[a_1, b_1, a_0, \dot{a}_1, \dot{b}_1, \dot{a}_0 \right]. \tag{9}$$

Here, longitudinal and lateral flapping (a_1, b_1) as well as coning (a_0) are modeled as 2nd order system. The model structure consists of two sets of equations, representing the fuselage and the rotor characteristics. The individual submatrices describe rigid body and rotor behaviour and the corresponding coupling. This model structure is closer to the reality and can provide a more detailed insight into the helicopter dynamics. However, the identification needs measurements of the blade motions. Some model variations, different in the order of the rotor equations and the number of identified parameters, were applied. One of the more complex ones consisted of:

- longitudinal flapping as 2nd order system,
- lateral flapping as 2nd order system,
- coning as 2nd order system,
- an approximation of the lead/lag motion as 2nd order transfer function.

The model has 9 degrees of freedom and is of 16th order [10].

8.5. Database
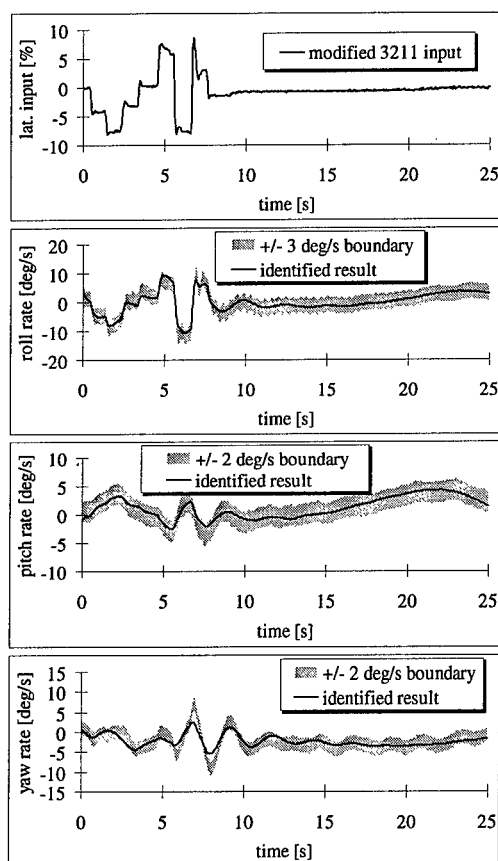For the identification a dataset at 80 kts velocity was
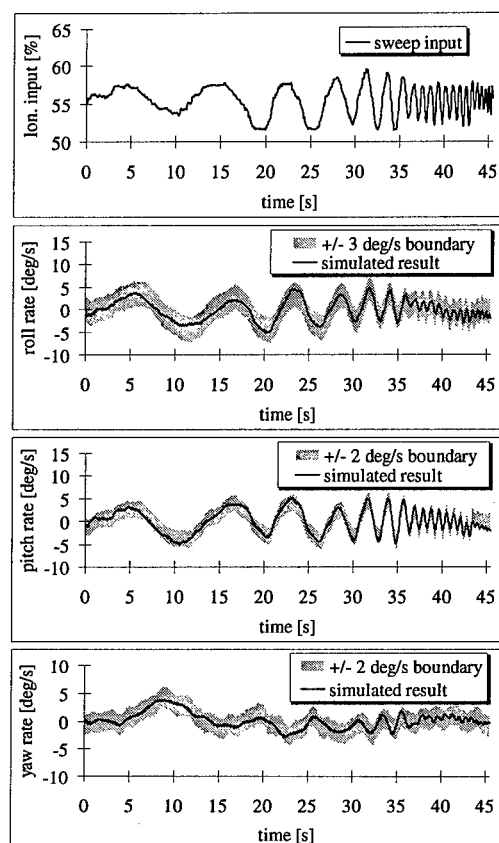
Figure 5: Lateral 3211 input

Figure 6: Lateral sweep input

used. Four runs, longitudinal, lateral, pedal and collective modified 3211 inputs of 25 seconds duration were concatenated and identified together. For the evaluation of the obtained model sweep input signals of 45 seconds duration were used for all four control inputs.

8.6. Results

In the following representative results are presented.

8.6.1. 6 DOF model identification

As an example Fig. 5 presents the comparison between measured data and the model response for a lateral stick 3211 control input. In addition, the FAA's AC 120-63 specifications are shown, too. It can be seen that the requirements for the direct response could be fullfilled. The off axis responses show the correct trend but the yaw rate is not allways within the tolerance.

8.6.2. 6 DOF model verification

To demonstrate the high predicting capability of the 6 DOF model, Fig. 6 gives a verification result, where data not used during identification were applied. Here, responses due to a frequency sweep input for the longitudinal control are shown. Again the AC 120-63 requirements are presented, too.

8.6.3. Extended model identification

To visualise the improvement of the extended model against the 6 DOF model, Fig. 7 compares the flight test data to both, the responses of the 6 DOF model and the extended model for a short data segment with a lateral stick control input. The roll acceleration responses clearly illustrate that the model without rotor DOF cannot match the peak amplitudes, occurring when the control input is reversed. This data part corresponds to the higher frequency content in the data. The extended model perfectly matches both, the roll acceleration and the measured lateral flapping. (The time histories of the roll acceleration and lateral flapping also demonstrate the high correlation, which was the prerequisite for the rotor approximation described in section 8.3.).

To allow a direct comparison of the three different models and the flight test data a presentation in the frequency domain format is used. Fig. 8 shows the Bode plot of the transfer functions roll rate due to lateral stick. All models accurately mach the measured data in the lower frequency range. But for increasing frequencies the improvement of higher order and more complex models is clearly seen.

8.7. Conclusions

At the linear identification approach the helicopter model is completly obtained from flight test data. This means that
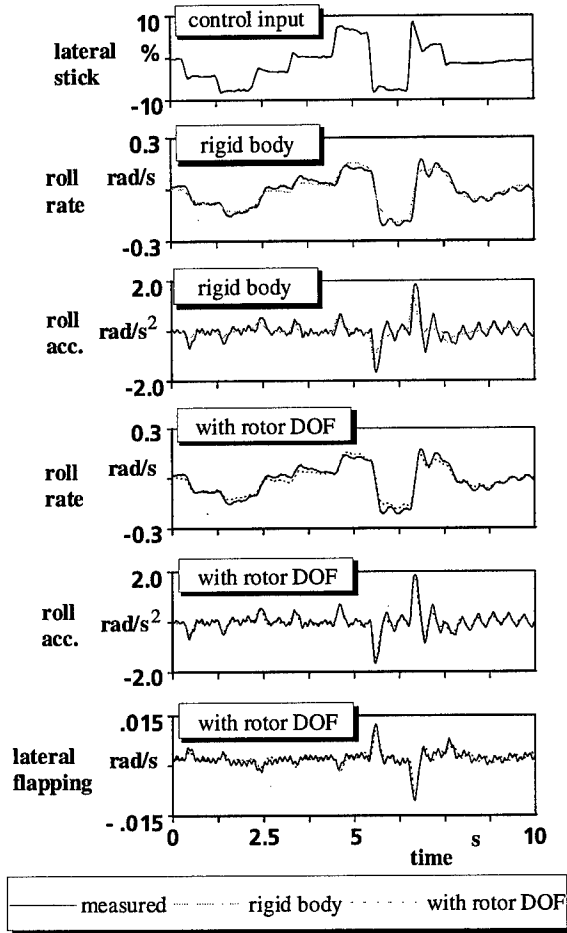
Figure 7: Identification of extended models

Figure 8: Transferfunction of different linear models

- detailed knowledge of the helicopter is not necessary for the model development,

- extensive flight test data is needed for the model identification and validation,

- the model is applicable only around its trim condition and not for the whole flight envelope.

Consequently this model can only be obtained when suitable flight test data of the actual helicopter are available. It can be used for various applications, in particular when an extrem good simulation fidelity is required or a linear model formulation is necessary.

9. NONLINEAR MODELING

The basic problem of a flight dynamics simulation program is to describe the motion of the vehicle's center of gravity in space. This description is governed by the following system of differential equations.

$$m\,(\dot{u} + qw - rv) = X_{aero} + X_{inertia}$$
$$+ mg\sin\Theta$$
$$m\,(\dot{v} + ru - pw) = Y_{aero} + Y_{inertia}$$
$$- mg\cos\Theta\sin\Phi$$

$$m\,(\dot{w} + pv - qu) = Z_{aero} + Z_{inertia}$$
$$- mg\cos\Theta\cos\Phi$$

$$I_{xx}\dot{p} - I_{xz}\dot{r} + qr\,(I_{zz} - I_{yy}) - I_{xz}pq =$$
$$L_{aero} + L_{inertia}$$
$$I_{yy}\dot{q} + pr\,(I_{xx} - I_{zz}) + I_{xz}\,(p^2 - r^2) =$$
$$M_{aero} + M_{inertia}$$
$$I_{zz}\dot{r} - I_{xz}\dot{p} + pq\,(I_{yy} - I_{xx}) + I_{xz}qr =$$
$$N_{aero} + N_{inertia} \qquad (10)$$

In a generic approach the right hand sides of these equations are filled up with physically based description of the vehicle with all components contributing to the balance of the three forces and moments. In contrast to a classical 6 degree of freedom approach for a helicopter simulation program the internal inertia forces and their internal reactions have to be described in detail.

The most common approach is a modular describtion by breaking up the vehicle into its components or modules and describing their individual contributions to the right hand side balance of the above system Eq. 10. For a helicopter these components are

- main rotor,
- tail rotor,
- fuselage,
- empennage-horizontal stabilizer and
- fin-vertical stabilizer.

The contribution of the last three components to the overall equilibrium are pure aerodynamic forces and moments whereas the first two ones include also inertia forces and moments acting onto the center of gravity. The principle structure is shown in Fig. 9 as a block diagram.

9.1. Helicopter model modules

In the following, the modules of a helicopter model will be explained in more detail.
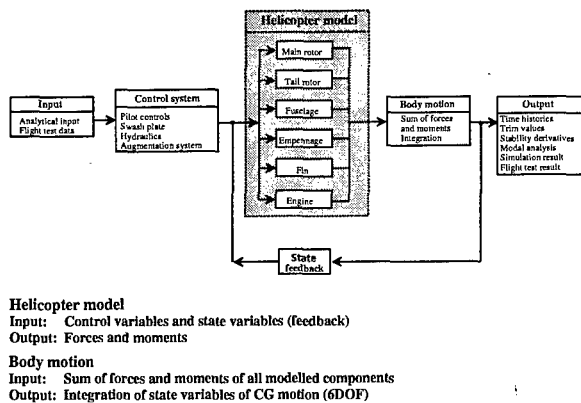
Helicopter model
Input: Control variables and state variables (feedback)
Output: Forces and moments

Body motion
Input: Sum of forces and moments of all modelled components
Output: Integration of state variables of CG motion (6DOF)

Figure 9: Principle structure of a helicopter simulation program

9.1.1. Main rotor module

The standard approach for the main rotor description is the blade element formulation. The rotor is discretisized into the individual blades which are then devided into several segments. The local aerodynamic and inertia forces are then summed up for all segments and all blades to determine the total rotor forces and moments.

9.1.2. Dynamic modeling

Depending on the application and rotor hub-blade design different model complexities are required. Three categories of model approaches can be distinguished, often referenced as

- analytical formulation,

- rigid blade formulation or

- modal formulation.

The analytical formulation is based on a linearisation procedure to get a set of formulas suitable for bladespanwise integration. In addition a multiblade summation is performed ('tip path plane approach'). The spanwise integration requires a small angle assumption for the local inflow and linearized aerodynamics to determine segmental aerodynamic forces and moments of the blade.

The rigid blade formulation neglects blade elasticity and describes the behavior of an articulated rotor. For hingeless rotors so called equivalent systems, with spring and dampers, are used for the description of the rotor dynamics, i. e. flapping and lagging degrees of freedom. The local blade aerodynamics are described in detail below.

The modal formulation tries to solve the fully coupled aeroelastic rotor problem by taking the eigenmodes of

the modal analysis and making a separation approach for the modal synthesis.

9.1.3. Aerodynamic modeling

There are several ways to determine the blade segmental aerodynamic forces and moments, depending on the above mentioned hub-blade dynamics. The determination requires the evaluation of the blade segment velocities with respect to the air. This is a fully nonlinear transformation to calculate the three components of the inflow vector with respect to the blade element profile. The aerodynamic forces and moments are then determined by 2D or 3D profile aerodynamics, the blade profile coefficients are normally taken from tables dependent of the local inflow angle and Mach number. The profile aerodynamics can be performed quasisteady, by taking into account the value of the inflow angle only or unsteady by taking into account its time derivative, too. The realization of the unsteady modeling is normally done by using appropriate filter functions. The inflow angle cannot be calculated straightforward, but only in an iterative way, due to the influence of the induced velocities.

9.1.4. Induced velocities modeling

The calculation of the distribution of the induced velocities is based on momentum theory either global or local. The basic description of using trapezoidal downwash distribution in wind axis was given by Glauert as quasisteady description. The extension to a dynamic formulation was developed by Pitt & Peters [19] using the dynamics of thrust and aerodynamic pitch and roll moments produced by the rotor. Their perturbation approach was recently extended to describe the influence of the helicopter motion onto the dynamics of the downwash shape. One of the approaches can be referenced as parametric wake distortion approach.

9.1.5. The tail rotor module

Due to the high rotational speed, the dynamic inertia forces from the tail rotor do not influence the flight dynamic response. So the model description used is normally a pure aerodynamic description, either the above mentioned analytical approach or blade element approach.

9.1.6. Fuselage, horizontal and vertical stabilizer module

The aerodynamic forces and moments are normally determined by using aerodynamic coefficient tables depending on angle of attack and sideslip and normalized for dynamic pressure. The tables are derived from model windtunnel measurements.

9.1.7. Engine module

The helicopter yaw response, when considered as coupling response, is highly influenced by the dynamic engine and drive train torque. Here the basic engine

dynamics and the behavior of the rpm governor have to be modeled.

9.1.8. *Interference aerodynamics*

In addition to the inflow caused by the unperturbed air, the disturbances caused by the downwash interference onto the individual parts have to be modeled. This can be done either in a parametric way using influence factors or in a dynamic way, for example the horizontal stabilizer entering and leaving the rotor wake during a pitch maneuver.

9.1.9. *Helicopter configuration*

From all the above mentioned helicopter components, the dynamic forces and moments with respect to the center of gravity have to be summed up to build the right hand sides of the equations Eq. 10. This is done in physical dimensions, i. e. forces in Newton and moments in Newtonmeter. To calculate these forces and moments a detailed description and knowledge of all helicopter components is necessary. This includes the pure construction details as well as the aerodynamic characterisics.

9.2. DLR simulation platform SIMH

For its various simulation activities DLR operates its simulation platform SIMH. This platform is used for most flight dynamic simulation problems and serves as a nonlinear model development and new models integration platform. It is further used as the development and definition platform for realtime codes. A special application is the realtime model to be build in to the system simulation for the new in-flight simulator and technology demonstrator ACT/FHS based on an EC 135. An overview about recent model developments and model integration results are given in [3] and [4].

9.3. Database

For the model validation two datasets at hover and 80 kts velocity were used. The 80 kts run has a duration of ten seconds. The control input here was a lateral modified 3211 input. The control input for the hover run is a longitudinal doublet input and the duration is four seconds.

9.4. Results

Here the validation results obtained with this program with reference to flight tests are shown. Two examples are given in Fig. 10 and Fig. 11. In Fig. 10 the simulation of a lateral modified 3211 input at 80 kts is shown. In addition the AC 120-63 boundaries are indicated. It can be seen that the overall achieved performance is good and the requirements could nearly always be fullfilled. Fig. 11 shows the validation result for a longitudinal doublet input at hover and the belonging boundaries. Again it can be seen that the specifications could mostly be fullfilled.
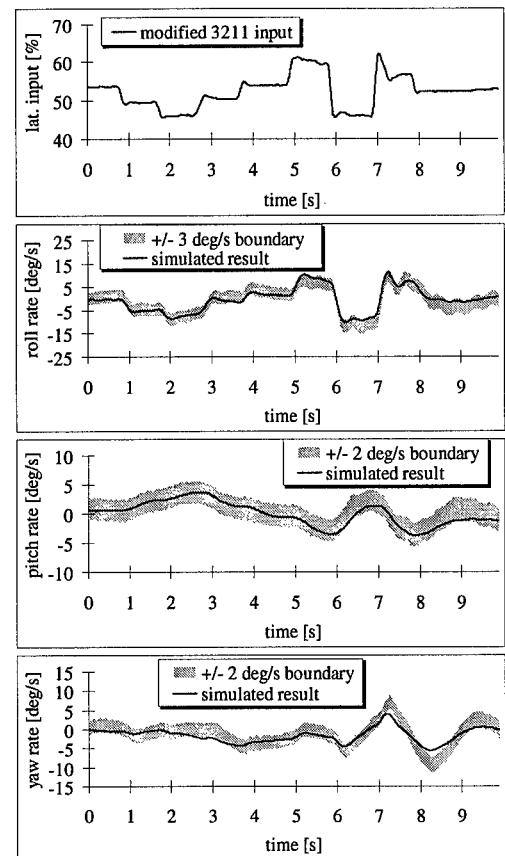

Figure 10: Lateral 3211 input

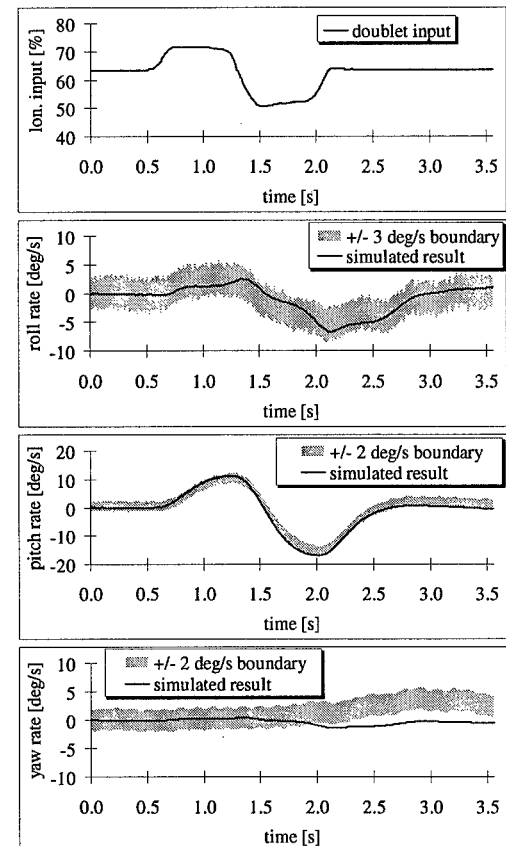Figure 11: Longitudinal doublet input

9.5. Conclusions

At the nonlinear modeling approach the helicopter model is completly generically derived. This means that

- detailed knowledge of all components of the helicopter is necessary for the model development,

- flight test data is only needed for the model validation,

- the model is applicable in the full flight envelope.

Consequently this model can be directly used during the helicopter design phase, where no flight test data are available. Later on, when flight test data become available, the model is verified and improved. The model shows good overall performance and the requirements of the AC 120-63 could nearly be fullfilled.

10. NONLINEAR MODELING AND IDENTIFICATION

The objective of this approach is to combine the advantages of the Linear Identification and the Nonlinear Modeling approaches. Information from flight test data is used to enhance the fidelity of generically derived nonlinear helicopter models. The main characteristics of the nonlinear identification approach are listed below:

- The model structure is modular.

- The model is based on vehicle characteristics with parametric extensions.

- Flight test data determine and validate the model.

- The result is valid for individual applications.

10.1 Helicopter Modeling

The formulation of the model is generically derived and very similar to analytical simulation models. It is based on the blade element theory, is completely nonlinear and modular structured. The main modules of the model are:

- Main rotor: blade element theory, including the blade flapping motion.

- Tail rotor: blade element theory.

- Main rotor dynamic downwash model: Pitt and Peters approach [19] with parametric extensions.

- Tail rotor dynamic downwash model: Pitt and Peters approach with parametric extensions.

- Fuselage and Empennage: combined parametric formulation.

- Engine: parametric formulation, including the governor.

The aerodynamic parameters of the blades and fuselage are not taken from windtunnel data tables but a derivative approach is made. In addition, the dynamic downwash approach from Pitt and Peters is extended with a derivative approach, too. In the following some important elements of the model, are described in more detail.

10.1.1. Blade Element Aerodynamics

First the modeling of the aerodynamics of a rotor blade element is described:

$$C_L = C_{L0} + C_{L\alpha}\alpha, \tag{11}$$

$$C_D = C_{D0} + C_{D\alpha^2}\alpha^2. \tag{12}$$

Eq. 11 provides the derivative formulation of the lift coefficient. Eq. 12 describes the modeling of the drag coefficient. All four derivatives, C_{L0}, $C_{L\alpha}$, C_{D0} and $C_{D\alpha^2}$ are determined in the identification process. The same aerodynamic formulation is used for the tail rotor. That leads to a total of eight parameters for the aerodynamic models of the main and tail rotor.

10.1.2. Downwash

Most of the parameters are used to extend the dynamic downwash model from Pitt and Peters mainly to improve the off axis coupling. The downwash model from Pitt and Peters is described in [19]. Nowadays it is used in most of the efficient helicopter simulation models. A proposal for extending the model is given in [20]. In this paper a more complex approach is made.

$$\begin{aligned}
\dot{\lambda}_0 &= \dot{\lambda}_{0,PP} \\
&+ C_{\lambda_0,u}\frac{u}{V_r} + C_{\lambda_0,v}\frac{v}{V_r} + C_{\lambda_0,w}\frac{w}{V_r} \\
&+ C_{\lambda_0,p}\frac{p}{\Omega} + C_{\lambda_0,q}\frac{q}{\Omega} + C_{\lambda_0,r}\frac{r}{\Omega} \\
&+ C_{\lambda_0,\dot{u}}\frac{\dot{u}}{V_r^2} + C_{\lambda_0,\dot{v}}\frac{\dot{v}}{V_r^2} + C_{\lambda_0,\dot{w}}\frac{\dot{w}}{V_r^2} \\
&+ C_{\lambda_0,\dot{p}}\frac{\dot{p}}{\Omega^2} + C_{\lambda_0,\dot{q}}\frac{\dot{q}}{\Omega^2} + C_{\lambda_0,\dot{r}}\frac{\dot{r}}{\Omega^2}
\end{aligned} \tag{13}$$

$$\begin{aligned}
\dot{\lambda}_c &= \dot{\lambda}_{c,PP} \\
&+ C_{\lambda_c,u}\frac{u}{V_r} + C_{\lambda_c,v}\frac{v}{V_r} + C_{\lambda_c,w}\frac{w}{V_r}
\end{aligned}$$

$$+ \quad C_{\lambda_c,p}\frac{p}{\Omega} + C_{\lambda_c,q}\frac{q}{\Omega} + C_{\lambda_c,r}\frac{r}{\Omega}$$

$$+ \quad C_{\lambda_c,\dot{u}}\frac{\dot{u}}{V_r^2} + C_{\lambda_c,\dot{v}}\frac{\dot{v}}{V_r^2} + C_{\lambda_c,\dot{w}}\frac{\dot{w}}{V_r^2}$$

$$+ \quad C_{\lambda_c,\dot{p}}\frac{\dot{p}}{\Omega^2} + C_{\lambda_c,\dot{q}}\frac{\dot{q}}{\Omega^2} + C_{\lambda_c,\dot{r}}\frac{\dot{r}}{\Omega^2} \qquad (14)$$

$$\dot{\lambda}_s \quad = \quad \dot{\lambda}_{s,PP}$$

$$+ \quad C_{\lambda_s,u}\frac{u}{V_r} + C_{\lambda_s,v}\frac{v}{V_r} + C_{\lambda_s,w}\frac{w}{V_r}$$

$$+ \quad C_{\lambda_s,p}\frac{p}{\Omega} + C_{\lambda_s,q}\frac{q}{\Omega} + C_{\lambda_s,r}\frac{r}{\Omega}$$

$$+ \quad C_{\lambda_s,\dot{u}}\frac{\dot{u}}{V_r^2} + C_{\lambda_s,\dot{v}}\frac{\dot{v}}{V_r^2} + C_{\lambda_s,\dot{w}}\frac{\dot{w}}{V_r^2}$$

$$+ \quad C_{\lambda_s,\dot{p}}\frac{\dot{p}}{\Omega^2} + C_{\lambda_s,\dot{q}}\frac{\dot{q}}{\Omega^2} + C_{\lambda_s,\dot{r}}\frac{\dot{r}}{\Omega^2} \qquad (15)$$

Eq. 13, Eq. 14 and Eq. 15 explain the approach. $\dot{\lambda}_{0,PP}$, $\dot{\lambda}_{c,PP}$ and $\dot{\lambda}_{s,PP}$ is the original Pitt and Peters dynamic downwash approach. The extention leads to 36 additional parameters for the main rotor downwash. In addition 12 parameters for the tail rotor downwash are estimated.

10.2. Database

For the identification a dataset at 80 kts velocity was used. Four runs, longitudinal, lateral, pedal and collective input of 15 seconds duration were evaluated together. As no data with step control inputs as required in the AC 120-63 was available, data with doublet inputs was used. However, the doublet signal consists of three steps, so it should be justified to use it instead of step signal inputs. For the evaluation of the obtained model, sweep input signals of 45 seconds duration were used for all four control inputs.

10.3. Results

In addition to the above introduced 56 parameters, five parameters for the engine model and another six parameters for the fuselage and empennage are determined. The identification is conducted with the NLMLKL program of the Institute of Flight Mechanics. This program is appropriate to identify nonlinear differential equation systems in the time domain. The negative logarithm of the Likelihood function is minimized with a modified Newton-Raphson algorithm. The four runs with doublet inputs and a total duration of 60 seconds are evaluated together.

10.3.1. Identification

As an example, Fig. 12 shows the identification results for the rate response due to a doublet lateral control input at 80 kts. Again, the grey area represents the tolerance of the AC 120-63. It can be seen that not only the direct responses are within the tolerance but also the off axis responses meet the requirements. The other three identified runs with longitudinal, collec-
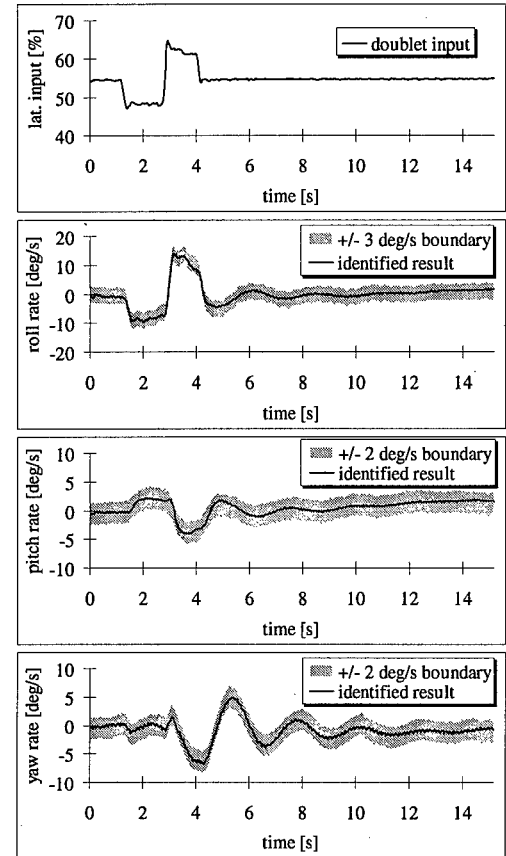
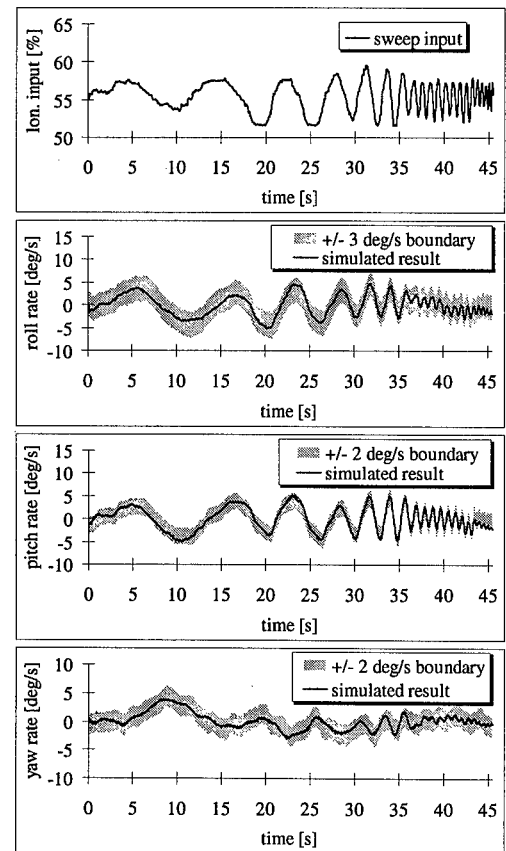Figure 12: Lateral doublet input
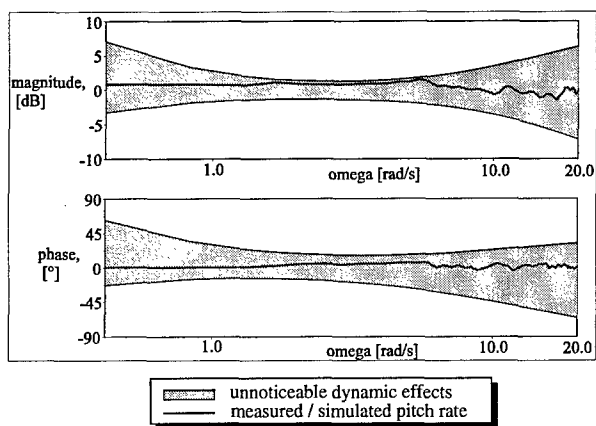
Figure 13: Longitudinal sweep input

Figure 14: Pitch rate model quality control

Figure 15: Pitch rate due to longitudinal input

tive and pedal inputs show similar results.

10.3.2. *Verification*

To validate the obtained model, a verification simulation was done with unseen data with a different input signal. To stabilise the simulation only offsets in the four control inputs and initial conditions for 8 state variables were estimated. As an example, Fig. 13 shows the rate results of the verification for a longitudinal sweep input. The duration of the verification run is 45 seconds. The AC 120-63 boundaries are shown, too. It can be seen that the achieved results meet the requirements for almost the total time length although the data was not used for identification. As a further tool for evaluating the model fidelity, a technique was independently proposed by Hamel [16] and Tischler [12]. In their proposal the relationship between a measured response variable and the corresponding model response is used. When, for example, the measured pitch rate is considered as output and the model pitch rate as input, a 'frequency response' can be calculated. Then, for an ideal model the magnitude is one and the phase angle is zero. Deviations are caused by differences between model and flight test. Using the frequency domain format, boundaries were used as defined in [21], symbolizing acceptable errors a pilot would not notice in a simulation. As an example Fig. 14 presents the frequency response for the pitch rates due to a longitudinal sweep input (direct response) and the boundaries of the so-called unnoticeable dynamic effects. It can be seen that the frequency response is within the tolerances for the interesting frequency range. Fig. 15 shows the Bode diagrams for the transfer function from pitch rate due to longitudinal sweep input. The results presented in Fig. 14 and Fig. 15 were obtained from a 45 second longitudinal sweep verification flight test run.

10.4. Conclusions

For the nonlinear modeling and identification approach the helicopter model is generically derived and parametric extensions are introduced. This means
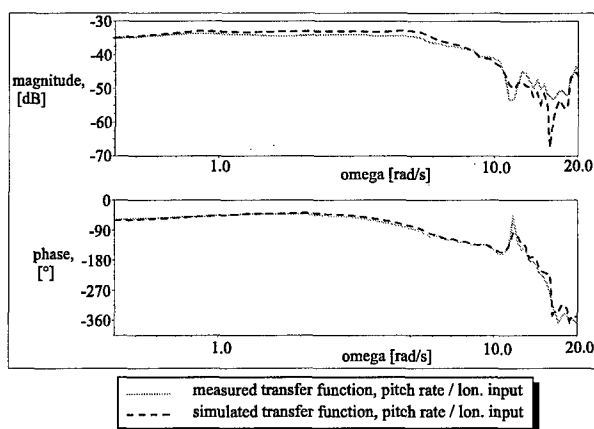
that

- knowledge of all components of the helicopter is necessary for the model development,

- flight test data is needed for the model identification and validation,

- the model is applicable in the full flight envelope.

Consequently this kind of model can only be obtained when flight test data from the actual helicopter are available. The model shows a very good overall performance and the requirements of the AC 120-63 were met. It can be used for various applications, in particular when a high simulation fidelity is required.

11. CONCLUSIONS

Based on the experiences in the field of helicopter model development and system identification at the DLR Institute of Flight Mechanics, a nonlinear modular structured helicopter model was developed. The goal was to combine the good simulation fidelity of pure identified parametric models with the advantages of generically derived nonlinear model formulations. To improve the overall performance, parametric extensions to the model were introduced. The prediction fidelity of the modeling approach was successfully optimized using system identification methods. The AC 120-63 criteria for cruise flight condition could be fullfilled by the model in all considered cases. The obtained dataset was validated using unseen data which was not used in the identification process. The simulation fidelity of the verification show similar good results.

In the future the model's applicability for a wider speed range will be further investigated.

12. REFERENCES

[1] Kaletka, J., von Grünhagen, W.: *Identification of Mathematical Models for the Design of a Model Following Control System,* American Helicopter Society 45th Annual Forum, May 1989 and Vertica, Vol. 13, No 3, 1989

[2] von Grünhagen, W., Bouwer, G., Pausder, H.-J., Henschel, F., Kaletka, J.: *A High Bandwidth Control System for a Helicopter In Flight Simulator,* International Journal of Control, Vol. 59, No. 1, 1994

[3] von Grünhagen, W.: *Nonlinear Helicopter Model Validation Applied to Realtime Simulations,* The American Helicopter Society Aeromechanics Specialist Conference 1995, Fairfield County, CT, October 1995

[4] Hamers, M., von Grünhagen, W.: *Nonlinear Helicopter Model Validation Applied to Realtime Simulations,* American Helicopter Society 53rd Annual Forum, Virginia Beach, Virginia, April 1997

[5] Hamel, P. G., Jategaonkar, R. V..: *The Evolution of Flight Vehicle System Identification,* AGARD Stuctures and Materials Panel Specialists' Meeting on ADVANCED AEROELASTIC TESTING AND DATA ANALYSIS, Rotterdam, The Netherlands, MAy 1995

[6] N.N.: *Advisory Circular AC 120-63,* U.S Department of Transportation, Federal Aviation Administration, October 1994

[7] Rohlfs, M.: *Identification of Nonlinear Derivative Models from BO 105 Flight Test Data,* 22nd European Rotorcraft Forum, Brighton, November 1996

[8] Jategaonkar, R., Mönnich, W.: *Identification Of DO328 Aerodynamic Database For A Level D Flight Simulator,* AIAA Modeling and Simulation Technologies Conference and Exhibit, New Orleans, LA, 1997

[9] N.N.: *Airplane Flight Simulator Evaluation Handbook,* The Royal Aeronautical Society, London, February 1995

[10] Fu, K.-H., Kaletka, J.: *Frequency-Domain Identification of BO 105 Derivative Models with Rotor Degrees of Freedom,* 16th European Rotorcraft Forum, Glasgow, UK, 1990 and Journal of the American Helicopter Society, Volume 38, No 1, January 1993

[11] Fletcher, J. W.: *Identification of UH-60 Stability Derivative Models in Hover from Flight Test Data,* American Helicopter Society 49th Annual Forum, May 1993

[12] Tischler, M. B.: *System Identification Methods for Aircraft Flight Control Development and Validation,* NASA TM110369, Army TR-95-A-007, October 1995

[13] Hamel, P. G. (editor): *Parameter identification,* AGARD LS-104, 1991

[14] Hamel, P. G. (editor): *Rotorcraft system identification,* AGARD AR-280, 1991

[15] Hamel, P. G. (editor): *Rotorcraft system identification,* AGARD LS-178, 1991

[16] Hamel, P. G., Kaletka, J.: *Advances in rotorcraft system identification,* AGARD CP 552, 1995

[17] Hamel, P. G., Kaletka, J.: *Advances in rotorcraft system identification,* Progress in Aerospace Sciences, Vol.33, 1997

[18] von Grünhagen, W., Bouwer, G., Pausder, H.-J., Henschel, F., Kaletka, J.: *A high bandwith control system for the helicopter in-flight simulator ATTHeS-modelling, performance and applications in Advances in Aircraft Flight Control,* Taylor & Francis, 1996, pp 73-101

[19] Pitt D. M., Peters D. A.: *Theoretical prediction of dynamic-inflow derivatives,* Vertica, 1981

[20] Curtiss Jr., H. C., Keller, J. D., Kothmann, B. D.: *On Aerodynamic Modelling for Rotorcraft Flight Dynamics,* 22nd European Rotorcraft Forum, Brighton, November 1996

[21] Hodgkinson, J., Wood, J. R.: *Equivalent System Criteria for the Flying Qualities MIL Standard,* in Fuller, S. G., Potts, D. W. Design Criteria for the Future of Flight Controls. Proceedings of the Flight Dynamics Laboratory Flying Qualities and Flight Controls Symposium, 2. - 5. March 1982. Technical Report AFWAL-TR-82-3064

The Inclusion of Higher-Order Rotor Dynamics
To Improve the Dynamic Model
Of a Single Rotor Helicopter in Hover

Kenneth Hui
Tel: (613) 998-9682   Fax: (613) 952-1704   E-mail: Ken.Hui@NRC.CA
Ramesh Srinivasan
Flight Research Laboratory, Institute for Aerospace Research, National Research Council
Ottawa, Ontario, Canada K1A0R6

1.   SUMMARY

This paper describes the development of a higher-order, rotor dynamic mathematical model of a single-rotor helicopter from flight test data, and illustrates the improvements in model fidelity realised by the inclusion of higher-order terms in the model. This model development is based on flight data gathered from "3211" and "frequency sweep" manoeuvres with the NRC Bell 412HP helicopter in hover. The data suite included the standard fuselage response parameters. This flight data was analysed using both the time domain (Maximum Likelihood Estimation or MLE) and frequency domain (*CIFER*) system identification techniques. The resulting models, from both the time and frequency domain techniques, with the various combinations of the higher-order rotor dynamic terms included, are compared to determine the improvements derived by each approach.

2.   INTRODUCTION
2.1   Background

The Flight Research Laboratory (FRL) of the Institute for Aerospace Research (IAR), National Research Council of Canada (NRC), acquired a Bell 412HP helicopter in 1993. This helicopter (Figure 1), known as the Advanced Systems Research Aircraft (ASRA), is being developed to fulfil its intended role as a Fly-By-Wire (FBW) In-flight Simulator.
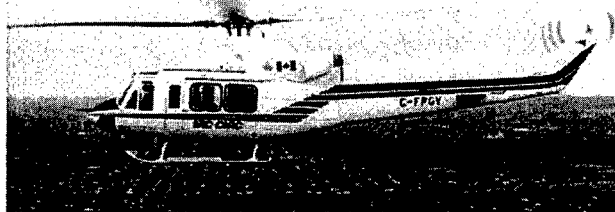
Figure 1: NRC Bell 412HP Helicopter

The NRC Bell 412HP ASRA now has an advanced data acquisition system and a full suite of state sensors, including a Litton LTN-92 Inertial Navigation System, instrumented control positions, engine torque sensors, rotor RPM tachometers and air data transducers. More recently, swashplate position transducers and fuel flow rate sensors have been added, to aid in the development of a high-fidelity Bell 412HP aircraft model. The FRL is now in the process of upgrading ASRA to include a full authority FBW flight control system. The intention is to utilize this aircraft for advanced research in the area of helicopter flight controls, currently being performed by the FRL's Bell 205A Airborne Simulator. The Bell 412HP's hingeless rotor system, characterized by higher control power and lower inherent time delays than the Bell 205A, allows for research to be performed using higher bandwidth control systems than is possible with the Bell 205A.

In order to be able to use ASRA as a research helicopter, especially as a FBW in-flight simulator, the development of an accurate mathematical model of the Bell 412HP airframe was identified as a vital prerequisite task.

Recent publications (Ref. 1, 2, 3) have shown that linear models can be developed by the use of system identification techniques applied to flight test data. These models produce higher fidelity flight simulation time histories as compared to the ones derived from numerical blade-element methods. On this basis, it was decided to use system identification methods applied to aircraft flight test data to extract mathematical models of the aircraft.

Earlier rotorcraft system identification work at the FRL had focused on modelling the Bell 205A, Bell 206 and Bell 412HP helicopters in forward flight. Previously published results (Ref. 1, 4) had indicated that both the Bell 205A and Bell 206 (helicopters with teetering rotor systems) could be modelled adequately with a conventional six degrees-of-freedom (dof) mathematical model.   The same conventional, quasi-steady formulation in six dof was used in the development of a mathematical model of the NRC Bell 412HP helicopter (Ref. 5). However, the initial conventional formulation resulted in a poor representation of the Bell 412HP (a helicopter with a "soft-in-plane" rotor system). Examining the initial responses of the aircraft to control inputs highlighted deficiencies in the initial model. These shortcomings of the conventional, six dof model formulation have also been documented by other researchers, through the examination of frequency

domain system identification results. In these cases, some on-axis responses could not be matched at higher frequencies while off-axis responses matched poorly at lower frequencies (Ref. 3).

These model deficiencies can cause significant problems in high gain feedback control systems often used in the design of flight control systems. In a particular case of a control system designed to improve the wind gust disturbance rejection features of an articulated rotor helicopter, the model errors associated with the rotor regression mode resulted in feedback gains which caused this mode to become unstable (Ref. 6). To circumvent this modeling problem, a simplified rotor dynamics formulation was devised, which was incorporated in the conventional model to form a hybrid model (Ref. 5). This hybrid model has been shown to be sufficient for most forward flight conditions.

In order to meet the stringent requirements of high bandwidth control system design, it is expected that a higher-order mathematical model will be required to represent the Bell 412HP for low speed and hover flight conditions. Initial attempts to develop a hover model using time domain MLE techniques resulted in divergent solutions in most cases. In the absence of special techniques based on major modifications of the output error method, engineering judgement and tedious iterations involving the trial and error approach were used, but did not lead to satisfactory solutions. System identification in the frequency domain was then considered to solve some of these problems. Under a bilateral agreement, the US Army gave NRC research access to their *CIFER* frequency domain systems identification software (Ref. 7), in April 1997.

2.2   Purpose and Scope
The objectives of this paper are to describe:
1. An early attempt to develop a Bell 412HP hover model, using time domain MLE (including/excluding flapping dynamics);
2. The lessons learned in developing a Bell 205A hover model, using *CIFER*;
3. The successful development of an inflow model using the Bell 205A, to support the ADS 33D ship-borne recovery project;
4. A "six dof plus inflow" model structure, to represent the Bell 412HP in hover, using CIFER;
5. How to parameterise the inflow dynamics when integrated with the fuselage model;
6. The lessons learned and the results of using *CIFER* to develop a hover model.

The paper will examine the fidelity of the various models by analysing the frequency responses and will highlight the lessons learned on improving the model fidelity.

Descriptions of the test aircraft, instrumentation system, flight test techniques and the flight data reduction processes follow.

3.   AIRCRAFT DESCRIPTION
The Bell 412HP, depicted in Figure 1, is a medium-sized twin turbo-shaft-engine (PTP6-3BE) helicopter, with an advanced design, four-bladed, soft-in-plane, flex-beam yoke rotor system, fitted with elastomeric bearings. Cyclic and collective control of the main rotor is effected through three primary servo-actuators and a swashplate. The tail rotor features collective pitch control only with a two-bladed, teetering rotor, pivoted through a single servo-actuator and swash plate. Primary control of the aircraft is accomplished with a mechanical control system and a limited authority electronic stability augmentation system (SAS). SAS inputs are directly summed with the pilot's inputs, and the total inputs are passed through a mechanical mixing box. The output from the mixing box drives the primary servos through mechanical linkages, and the tail-rotor servo through cable assemblies. Longitudinal/lateral cyclic control response coupling is reduced by a swashplate phase angle setting, which minimises steady-state off-axis rotor flapping. The main rotor is inclined forward relative to the fuselage reference line axis by five degrees and to the left by one degree.

4.   AIRCRAFT INSTRUMENTATION
ASRA is fitted with a Litton LTN-92 Inertial Navigation System (INS), mounted on the cabin floor, close to the planar centre of gravity of the aircraft. The inertial data was filtered, giving rise to a time delay of 50-100 msec, then recorded at 64 Hz. The controls were instrumented to measure the positions of the cyclic stick, collective lever and pedals. These control position signals were passed through an A/D converter, merged with the INS data (aircraft angular rates, attitudes and accelerations from ring laser gyros and an accelerometer triad), sampled at 64 Hz and recorded on a Digital Audio Tape (DAT).

State Estimation was then used to check the kinematic consistency of the inertial data set. The purpose of this was primarily to verify the accuracy of the INS's internal filtering and time delays, but also to correct the measurements to the centre of gravity and remove small biases from the INS data. Excellent internal consistency and compatibility of the inertial data set was verified.

5.   FLIGHT TEST PROGRAM
Despite very stringent time constraints dictated by ASRA's Fly-By-Wire developmental schedule, the System Identification flight test program was conducted, using ASRA, in February 1998. The frequency sweep was used as the primary test manoeuvre. Three flights were performed in calm air conditions, on three different days, at an altitude of 300 feet AGL. The takeoff weight

of the aircraft was approximately 9700 pounds. As the pilot progressed through the low-frequency portion of the sweep manoeuvre (using small magnitude control inputs), the aircraft was found to be divergent, often making it difficult to obtain low frequency content in the time histories of these manoeuvres.

A fourth flight was performed, in slightly turbulent wind conditions, to collect data for model verification purposes. The first pilot performed four doublets in one direction and the second pilot executed the same four doublets, but in the opposite direction.

5.1 Bell 205A Identification Experience

The frequency sweep technique, which has been described in Ref. 8, provides the baseline reference manual to execute a frequency sweep. Experience gained during initial modelling work on the NRC Bell 205A had showed that the standard sweep technique often needed small modifications to suit the characteristics of the individual helicopter.

During the process of determining the model structure of the Bell 205A, two important static derivatives (the roll damping term and the dihedral effect term) were estimated with the opposite sign and eventually eliminated from the model. Several additional flights were conducted, but the aircraft was found to always diverge in response to the small amplitude control inputs. An aircraft instability problem became apparent during the execution of the lateral cyclic manoeuvre. Also, significant coupling started to develop and the pilot had to rush into the higher frequency portion of the sweep. This pointed to the lack of low frequency content in the sweep time history data, which resulted in the development of a modified sweep technique, in a bid to enrich the low frequency content of the manoeuvres.

5.2 Flight Test Considerations

The NRC Bell 412HP ASRA was instrumented to measure the standard fuselage parameters, engine torque and main rotor RPM. Then, 3211 and frequency sweep manoeuvres were conducted for the out-of-ground-effect hover conditions. These manoeuvres were performed to start and end in a trim condition. Secondary control was applied in a pulse form in order to prevent large deviations in the cross-axis. Care was also taken during the frequency sweeps to ensure that the pilot did not generate large amplitude inputs at higher frequencies, where structural damage can occur. Although no strain gauges were mounted on the mast to obtain the exact structural loads, ASRA had been instrumented and cleared for structural loads below 3 Hz of control input.

Identification of the SAS-on, bare airframe model of the Bell 412HP, was considered next. The aircraft would likely be more stable for low frequency, small amplitude inputs. However, it was suspected that having the SAS on may cause a strong correlation and remove the low frequency information, thus, once again, making the identification of the static derivatives difficult. For these reasons, it was decided not to attempt the SAS-on identification at the present time.

The following modified frequency sweep technique was gradually developed, to generate slower dynamic manoeuvres, specifically for the Bell 412HP helicopter:

Pedal - The standard frequency sweep technique was used with a control input frequency range from 0.05 Hz to 2 Hz, with pulse type inputs in the cross-axis to minimise yaw rate to the left. A high yaw rate tended to cause a strong roll to the left, which then had to be countered aggressively.

Collective - The standard frequency sweep technique, with a control input frequency range from 0.05 Hz to 3 Hz, was modified slightly to prevent excitation of the engine governor dynamic mode. During the collective sweep, high descent rates caused moderate aircraft pitch-ups, which had to be countered by the pilot to avoid a tail slide. Yaw and roll coupling were found to be small.

Longitudinal - A slightly modified frequency sweep technique was used with a control input frequency range from 0.05 Hz to 2.5 Hz. The longitudinal sweep required a slight modification of the technique for periods below 12 seconds. As the aircraft accelerated through translational lift, it tended to pitch up, which required a quick forward then aft cyclic stick motion; after which the standard sweep could be continued until the aircraft accelerated aft through translational lift.

Lateral - A modified frequency sweep technique was used with a control input frequency range from 0.05 Hz to 3 Hz. The lateral sweep not only had similar problems to the longitudinal axis, associated with translational lift, but was also strongly coupled in yaw and pitch. This required the pilot to move the cyclic stick rapidly in the longitudinal axis, while trying to maintain a slow progression in the lateral axis. Compounded by the necessity for rapid control motions in the lateral axis when going through translational lift, and the cross-coupling in the yaw axis, this made it virtually impossible to obtain cycles with a period of 12 seconds, or longer.

6. MODEL STRUCTURE FORMULATION

Initially, the development of a conventional, six dof mathematical model is described and used as a baseline for all comparisons to follow. The deficiencies of this model are thoroughly identified. Subsequently, the structure of more advanced models are determined through consideration of the important dynamic modes of the Bell 412HP in the frequency range of interest for flight control applications. This more complex structure represents the fuselage rigid body six dof

dynamics, the rotor tip-path-plane flapping and lead-lag dynamics, the main rotor RPM and induced velocity dynamics, and engine gas generator and governor dynamics (Ref. 9). These dynamics are considered and included in their order of importance in the development of higher order rotor dynamics of the Bell 412HP for in-flight simulation. The model structure is investigated and adjusted to include the dynamics necessary to represent these responses.

In the model structure formulation process, decisions must be made regarding which dynamics are to be included in the model and how they are to be parameterized. This is largely determined by the desired frequency range of the model and the recorded dynamic states during the flight test. To achieve a high fidelity model, all the significant dynamics in the desired frequency range should be included. Rotor dynamic modes are often important; however, in practice, the rotor measurements are difficult to obtain. With the fuselage-based measurements only, rotor modes are difficult to identify. If over-parameterization occurs (i.e., if the model has too many degrees of freedom for the number of measurements available), then some parts of the model must be fixed at empirical values, or a simplification of the dynamics must be made.

All the model development analyses presented in this paper are based on the use of a time domain parameter estimation process called "$MMLE3$" (Ref. 10, 11) and/or a frequency domain software called "$CIFER$" (Ref. 7).

6.1 Tip-Path-Plane Flapping Mode in MLE

In the development of models of helicopters at forward speeds, in the past, the yaw-axis had presented some problems (Ref. 5). The use of simplified flapping dynamics had provided satisfactory solutions to these problems.

To perform parameter estimation using $MMLE3$ and the hybrid model formulation, the state and observation equations require rotor state information. Due to the lack of the rotor state measurements in the flight test data, a simplified theoretical model describing rotor flapping effects was used to generate the rotor flapping responses from existing measurements. The theoretical rotor-flapping model is a non-linear, total force and total moment model for a single main rotor helicopter, as presented by Peter D. Talbot et al in Ref. 12.

From Ref. 5, the final flapping equation is:

$$\begin{bmatrix} \dot{a_1} \\ \dot{b_1} \end{bmatrix} + \frac{\Omega}{\gamma/64 + 4} \begin{bmatrix} \gamma/4 & \gamma^2/64 \\ -\gamma^2/64 & \gamma/4 \end{bmatrix} \begin{bmatrix} a_1 \\ b_1 \end{bmatrix} =$$

$$\frac{\Omega}{\gamma^2/64 + 4} \begin{bmatrix} A1\,\gamma^2/64 & -B1\,\gamma/4 \\ A1\,\gamma/4 & B1\,\gamma^2/64 \end{bmatrix} - \begin{bmatrix} q \\ p \end{bmatrix}$$

where, $a1$ is the longitudinal flapping angle,

$b1$ is the lateral flapping angle,

A1 is the lateral cyclic pitch (rad),

B1 is the longitudinal cyclic pitch (rad),

both measured from the hub-plane, in the wind-hub system.

Ω is the rotor speed = 33.93 rad/s,

γ is blade Lock number = 5.537.

The longitudinal and lateral flapping angles and rates were calculated by solving the above differential equations. These calculated quantities were then used as pseudo-measurements. The corresponding flapping equation coefficient used in the MLE state equations needed to be constrained.
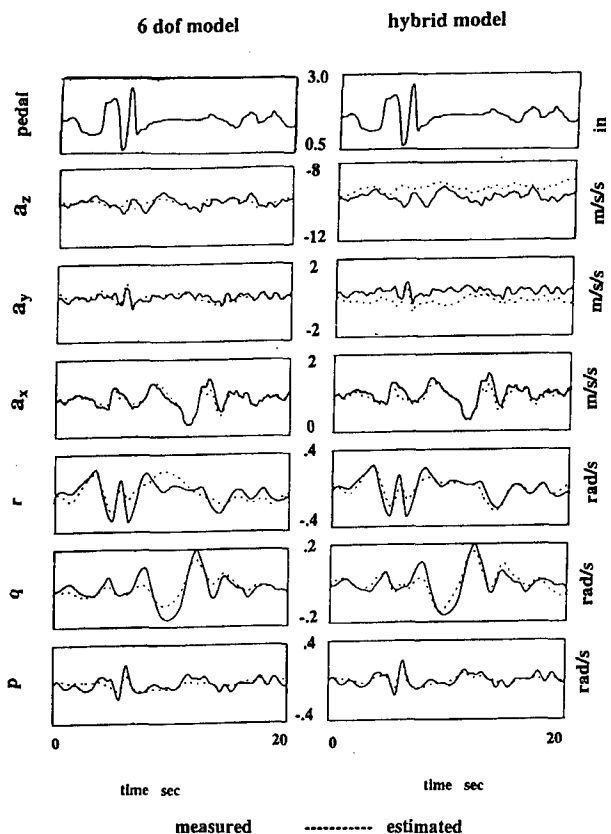

Figure 2: Verification of Flapping Mode in Hover

For low speeds, a hover model was attempted by using a conventional six dof model and a hybrid model with simplified flapping dynamics.

On comparing the flight data to the responses of the models, with and without the flapping mode included (Figure 2), it was concluded that appending the flapping mode improves the angular rate responses, but at the cost of degrading the velocity and acceleration responses.

6.2 Dynamic Inflow Effects in the Bell 205A Heave Axis Identification

The classical first-order equation describing the vertical velocity to collective transfer function (Ref. 13), neglecting inflow dynamics is:

$$w/\delta_{col} = Z_{\delta col} / (s + Z_w)$$
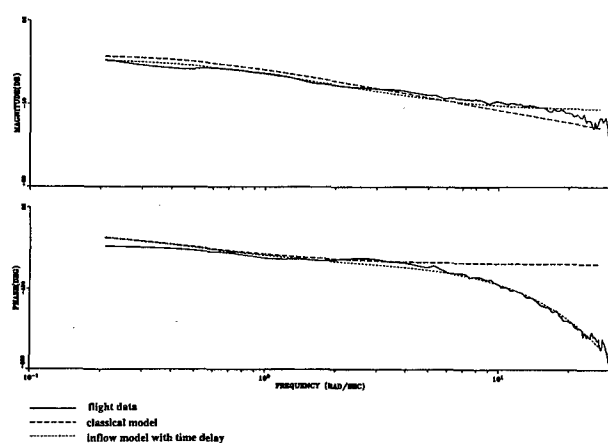
Figure 3: Dynamic Inflow Effects

In Figure 3, the long-dashed line shows that this model fits the aircraft's collective-to-vertical-velocity frequency response poorly. In particular, the model does not match the magnitude curve well.

A second model was formulated to include terms to model the dynamic inflow. The influence of dynamic inflow was approximated in the transfer function through the addition of a zero and a time delay to the first-order model of vertical- velocity-to-collective- stick:

$$w/\delta_{col} = Z_{\delta col} (s + Z_L)e^{-\tau s} / (s + Z_w)$$

The short-dashed line in Figure 3 shows that the match is significantly better than that of the model which neglects inflow dynamics.

In support of the NRC "ADS 33 Ship-borne Recovery" project, a control loop was wrapped around the heave-axis of the NRC Bell 205A. A block diagram of this system is shown in Figure 4, where a first-order transfer function is used to represent the Bell 205A.
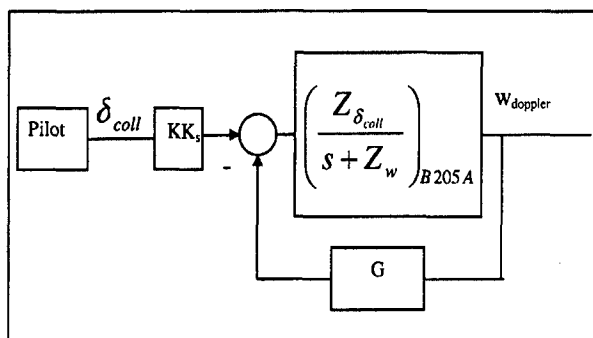

Figure 4: Bell 205A Control System Block Diagram

To change the standard Bell 205A heave damping (in the range of heave damping values between -0.1 and -0.5 sec^{-1}), the first-order control response was modified by varying the gain "G".

To determine the appropriate gain values, a series of collective frequency sweeps was conducted in the hover, out of ground effect (OGE), and in light wind conditions. The sweep time histories were analyzed using CIFER, taking into consideration, the effects of control time delay and rotor inflow (Ref. 14).

Figure 5 presents the results of the analysis in the form of heave damping achieved for various gains, with the circles representing the final gain value selected for the ADS 33 ship borne recovery trial.
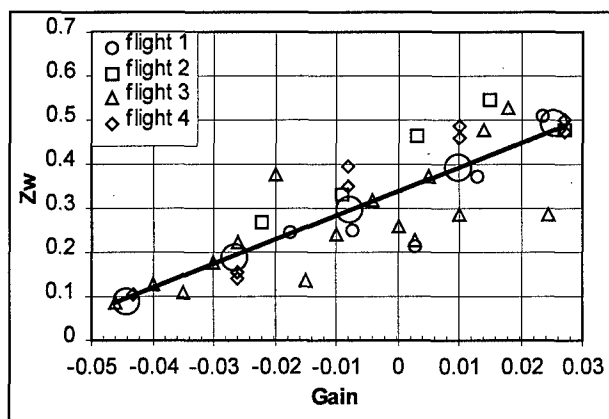

Figure 5: Results of Heave Damping Analysis

6.3 The Lead-Lag Mode

ASRA is equipped with an advanced design, four-bladed, soft-in-plane, flex-beam yoke rotor system fitted with elastomeric bearings. The elastomeric bearings, which consist of a layer of rubber, shelter the head of each rotor blade inboard of the blade grip. During flight testing, the lead-lag mode did not appear to be excited, even with excitation frequencies up to 20 rad/sec. It was not possible to go beyond 20 rad/s due to structural load constraints that limit the control inputs to 3 Hz. Since this lead-lag mode could not be excited, it was decided not to include this mode in the model structure.

6.4 ASRA Drive Train Dynamics

The Bell 412HP torque dynamic characteristics were studied by Erdos (Ref. 15). Further investigations using step and doublet inputs in the collective-axis, in hover, revealed that the rotor mast torque was under-damped with a period of about 3 seconds. This is explained further in Section 8.3.

To provide additional insight into the engine drive-train dynamics (see Figure 6 and Ref. 16), it was decided to measure more quantities associated with these dynamics. Two fuel flow rate transducers were purchased in the hope that, together with the engine torques and rotor RPM, these additional measurements would enable a simplified engine drive-train model to be developed. Unfortunately, delays in delivery, coupled with calibration problems, resulted in the fuel flow rate measurements being unavailable. Efforts to develop a simple engine drive-train dynamics model will be pursued in future studies.
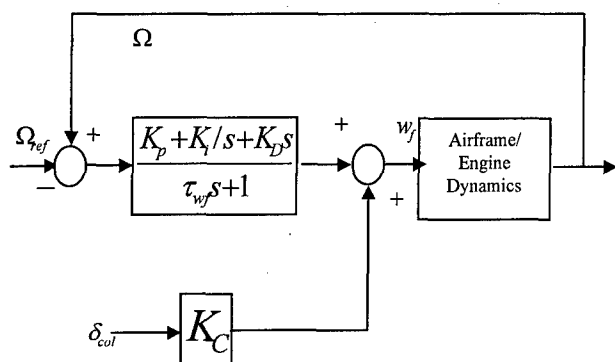
Figure 6: ASRA Drive-train Dynamics Model

7. BELL 412HP HOVER MODEL IDENTIFICATION

The initial objective of this work was to study the SAS-off, bare airframe, and identify the hover model. If the static derivatives were to prove difficult to identify, the data would be gathered with SAS on, and the swashplate measurements would be used to identify the underlying aircraft. Although it was known that the amount of correlation introduced by the SAS-on condition may degrade the identification, the aircraft would at least be more stable, allowing the pilot to put in characteristically better sweep inputs.

7.1 Model Identification Techniques

The following reviews are summarised from Ref. 2, 17:
Various mathematical model structures were examined for the improvement of model fidelity to match the various dynamic modes and the responses of the aircraft in the desired frequency range. Frequency domain system identification methods are well suited to aircraft flight control systems development, since many current design specifications, design and analysis techniques, and acceptance flight test techniques are

based in the frequency domain. The frequency domain method is band-limited to accommodate the desired model structure; i.e. the frequency domain method places adequate weighting on both the fuselage modes at lower frequency and the rotor modes at higher frequency. The frequency domain method has fewer parameter values to be determined because a determination of the initial conditions and instrumentation bias is not required.

The disadvantages of the technique are:
1) it is computationally intensive and,
2) it is less intuitive than the time domain method, in that it is more difficult to correlate the results with a physical understanding of how the state space model parameters affect the frequency responses being matched.

The time domain technique, on the other hand, provides a clearer understanding of the state space model parameters. Time domain techniques have been used routinely for fixed-wing aircraft, but due to their limited application to rotary wing aircraft to date, their use has yielded limited success for helicopters. The two approaches to modeling, where rotor dynamics effects are included or excluded from the estimation model, will be compared for the Bell 412HP at hover. Further, the resulting linear model structure applicable to identification of the Bell 412HP flight dynamics, in hover flight, without rotor state data, will be developed.

CIFER, a windows-based, user-friendly software package with several utilities for reporting and plotting, allows the user to perform simple end-to-end transfer function identification of complex state space systems. *CIFER* has been extensively developed to include:
1) frequency response analysis;
2) end-to-end input/output transfer function analysis;
3) aircraft handling qualities evaluation; and
4) state space system identification and verification.
It allows the end-user to perform sophisticated numerical computations with ease.

CIFER was used for the generation of a model based on multi-input, multi-output frequency responses. These responses were used to develop the Bell 412HP mathematical model by a "secant minimization" of the frequency response pairs by changing the time delays and the stability and control derivatives. The following process was followed:

FRESPID, MISOSA and *COMPOSITE,* the various sub-processes of *CIFER,* were used to produce high quality broad-band frequency responses from time history data.

DERIVID, another *CIFER* sub-process, was used to minimize the errors between the frequency responses of the postulated model and the flight data generated

frequency responses, by iterating the control time delay and the stability and control derivatives.

The optimum frequency range should be decided before determination of the model structure. The range of the frequency responses is governed by the applicability of the target model. A frequency response table was made by including only those response pairs with a coherence greater than 0.4. The factors that affect the coherence function are the lack of input excitation, lack of aircraft response, process noise such as gust and non-linearities in the dynamics.

The initial stability and control derivatives for this project were derived from the time domain MLE analysis. Alternatively, initial values could be obtained from simulation results or stepwise regression techniques.

Following the procedure outlined in Ref. 7, the model structure was determined by removing the more insensitive parameters and then, the parameters with high Cramer-Rao (CR) bounds, in order to produce a robust mathematical model. From previous experience, the insensitivity threshold was set at 10% and the CR% was cut off at 20%, leading to a correlation of 80%. This was done by setting the highest insensitivity parameter to 0. This process was terminated when either the total cost function increased by 1, or when the individual cost functions of several (approximately five) frequency responses exceeded 5-10.

After eliminating the parameters with the highest CR bound values, another iteration was performed, leading to a converged model. It should be noted that, when eliminating those parameters with a CR bound of 40 % or lower, the cost functions of many individual frequency responses may be elevated beyond 5-10. This would indicate that the model structure from the previous iteration should be considered as the final converged model. Despite being subjective, this approach has been used by several previous system identification researchers (Ref. 8, 11) and has been determined, through their experiences, to accurately and reliably minimize the model structure.

8. IDENTIFICATION RESULTS
8.1 Frequency Response Comparisons

Frequency responses of the identified model are compared with the flight test data in Figures 7 through 9. Excellent excitation of the aircraft dynamics has extended the bandwidth well into the 0.1 – 30 rad/sec range. The overall identification model matched well with the flight test frequency response data. The good results can be attributed to the use of high quality flight data, in the present work.

Figure 7: An excellent match was obtained between the estimated and actual, on-axis, roll rate frequency responses, while those for the cross-axis matched reasonably well too. Similar results were also seen for the pitch axis.
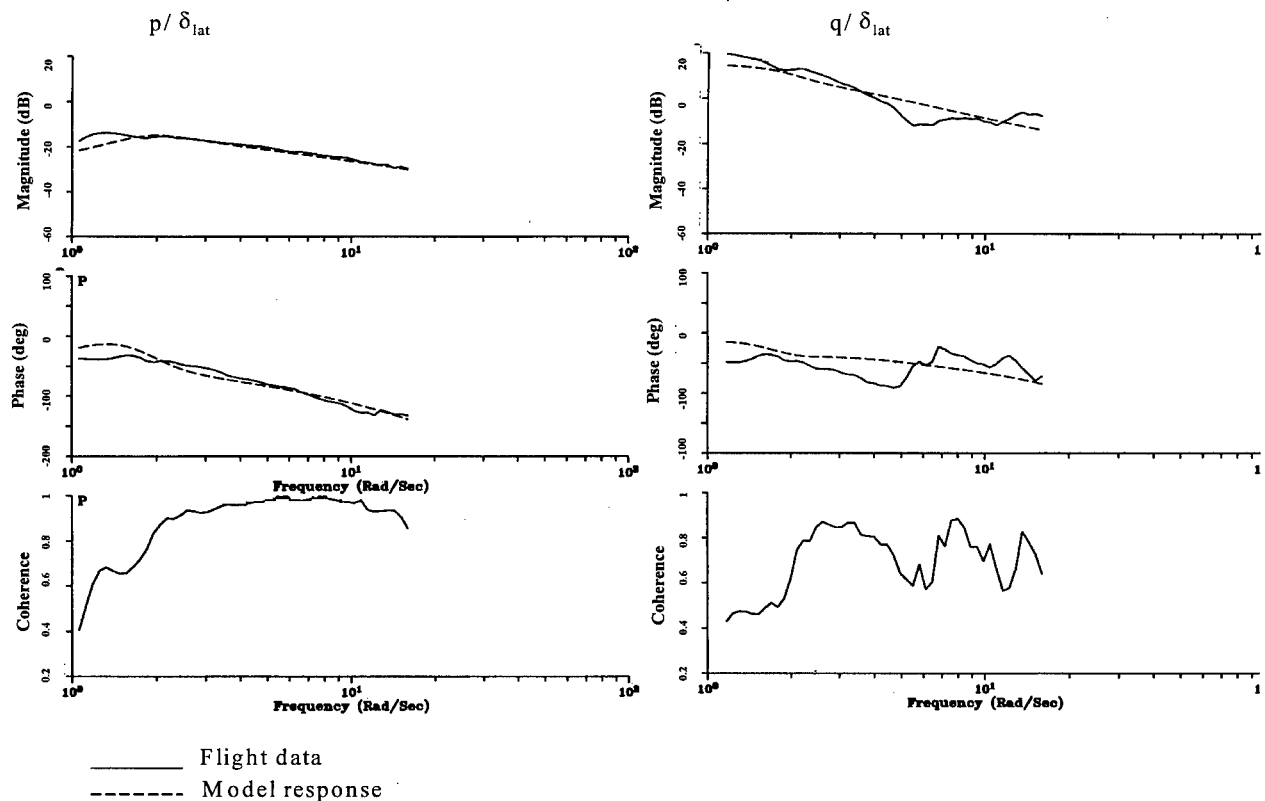

Flight data
Model response

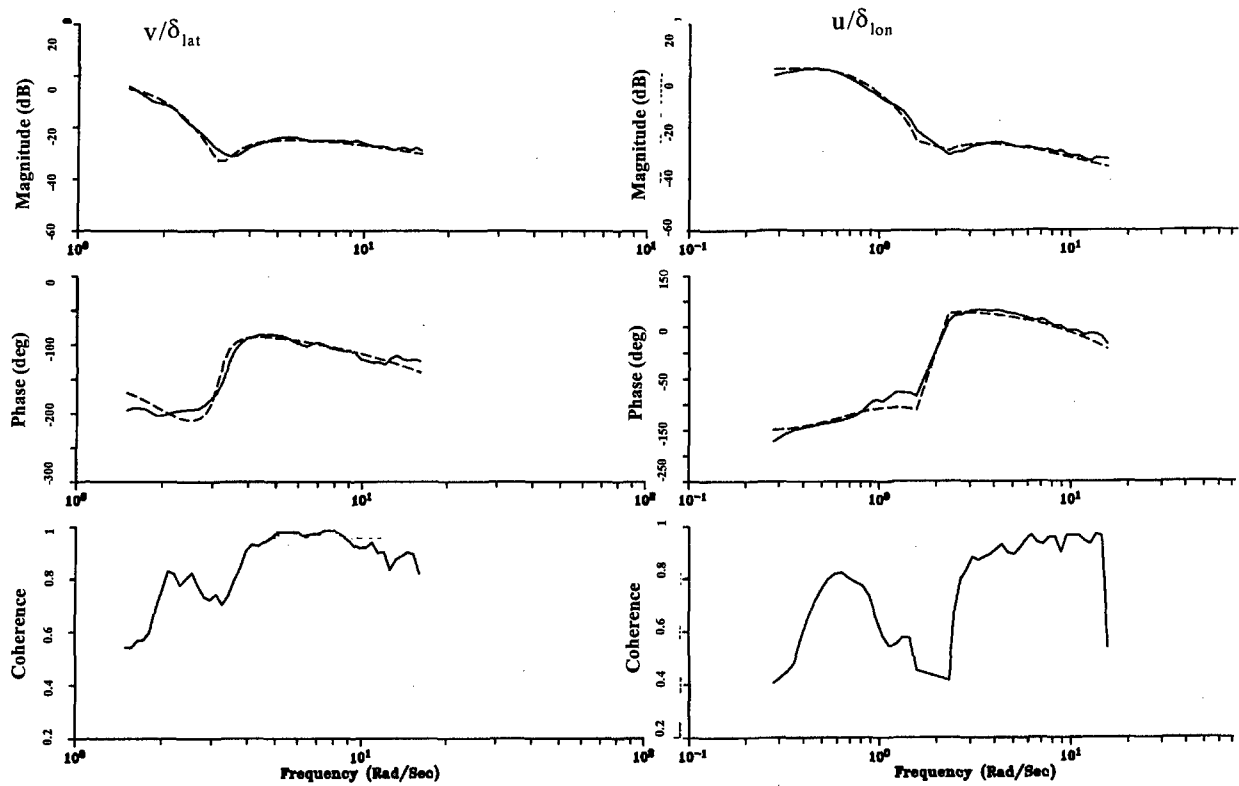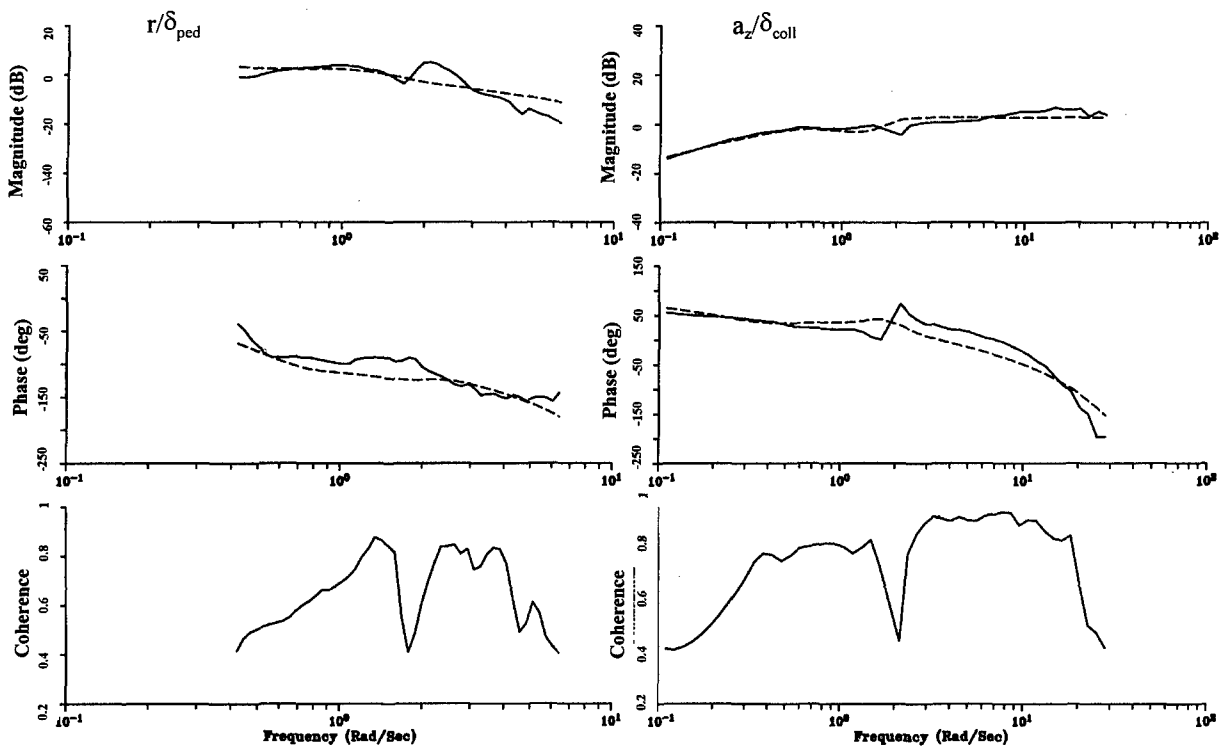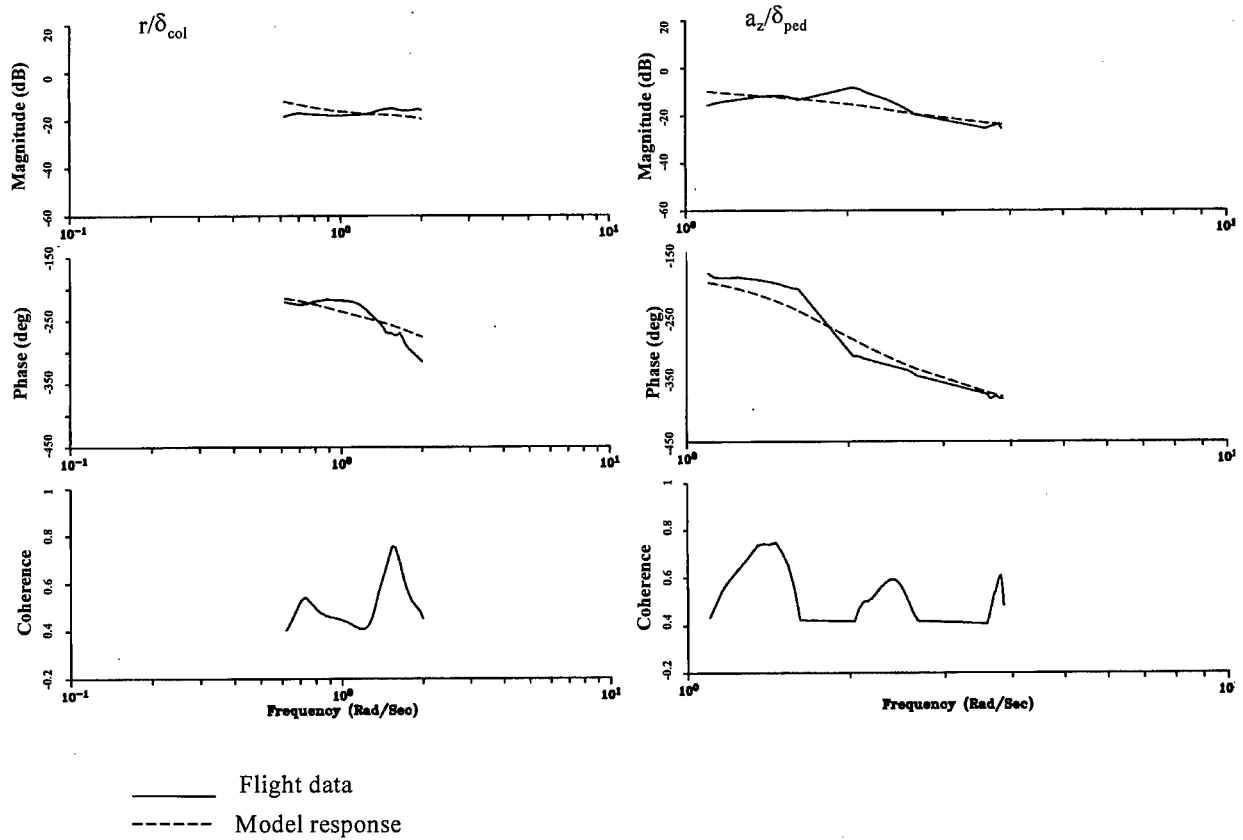**Figure 7: Angular Rate Frequency Responses**

Figure 8: Velocity Frequency Responses

Figure 8: An excellent match was obtained for the on-axis velocity frequency responses, for both, the roll and pitch axes. It should be noted that these velocity frequency responses are usually difficult to excite at low frequencies.

_____ Flight data

------ Model response

Figure 9: Haw-Heave Dynamics

Figure 9: The r/δ$_{ped}$ and the a$_z$/δ$_{col}$ frequency responses matched quite well, except in the frequency range of 1.5 - 2.5 rad/sec. This points to the presence of additional unmodelled dynamics here, which is explained in section 8.3. The yaw-heave coupling dynamics were predicted quite reasonably (as evident from the r/δ$_{col}$ and a$_z$/δ$_{ped}$ responses), despite not including engine dynamics and rotor RPM in the model.

8.2   Stability and Control Derivatives Evaluation

The identified stability and control derivatives, their Cramer-Rao bounds (in percent) and the parameter insensitivities are listed in Table-1. All parameters are below the insensitivity threshold of 10%. A few parameters are just slightly above the CR bound threshold of 20%. It was decided to freeze the model at this point, because it was anticipated that a further reduction (e.g. Z$_q$) could only be achieved at the cost of a large change in the total cost function.

Stability Derivative	Value	Cramer-Rao %	Insens %
MT$_{IN}$	-0.01 !	------	------
X$_u$	-0.1129	11.55	1.492
X$_v$	0.08752	23.41	4.188
X$_w$	0.0 +	------	------
X$_p$	0.0 +	------	------

X$_q$	0.9908	21.38	5.38
X$_r$	0.3298	13.28	2.264
Y$_u$	-0.4322	22.01	3.876
Y$_v$	-0.8281	10.42	1.888
Y$_w$	-0.5682	18.79	2.376
Y$_p$	-1.942	7.09	1.219
Y$_q$	-4.285	12.49	2.201
Y$_r$	0.0 +	------	------
G$_{CT}$	9.786 !	------	------
Z$_u$	0.0 +	------	------
Z$_v$	-1.769	6.291	1.166
Z$_w$	-1.127	9.178	1.513
Z$_p$	1.695	5.489	1.110
Z$_q$	1.6	30.7	6.286
Z$_r$	-0.5885	22.6	5.623
G$_{ST}$	-0.6843 !	------	------
L$_u$	-0.3688	17.32	0.9652
L$_v$	-0.7565	9.516	0.9046
L$_w$	-1.023	7.223	0.4116
L$_p$	-2.397	5.927	0.7691
L$_q$	-5.848	8.411	1.109
L$_r$	-0.7576	13.9	1.699
M$_u$	0.0 +	------	------
M$_v$	-0.08677	18.01	1.758
M$_w$	-0.09402	15.95	1.02
M$_p$	-0.208	12.67	3.873

Control Derivative	Value	Cramer-Rao %	Insens %
M_q	-0.9405	13.59	2.184
M_r	-0.3376	9.823	0.9844
N_u	-0.2	21.63	0.9689
N_v	-0.492	11.37	0.8003
N_w	-0.5231	12.76	0.4603
N_p	-0.6578	8.97	2.938
N_q	-4.31	7.775	1.345
N_r	-0.513	11.8	1.768
Control Derivative	**Value**	**Cramer-Rao %**	**Insens %**
$X_{\delta lat}$	0.08518	3.83	1.893
$X_{\delta col}$	-0.08332	13.32	3.437
$X_{\delta ped}$	0.0942	5.125	2.316
$X_{\delta lon}$	-0.2691	3.335	0.99
$Y_{\delta lat}$	0.5157	2.689	0.5518
$Y_{\delta col}$	0.0 +	------	------
$Y_{\delta ped}$	-0.0634	9.926	3.283
$Y_{\delta lon}$	0.1554	3.236	1.391
$Z_{\delta lat}$	-0.07496	9.584	2.423
$Z_{\delta col}$	1.34	3.711	1.409
$Z_{\delta ped}$	0.03741	16.83	5.449
$Z_{\delta lon}$	-0.287	3.173	1.157
$L_{\delta lat}$	0.5087	3.181	0.5085
$L_{\delta col}$	0.123	7.162	2.843
$L_{\delta ped}$	-0.05719	12.2	2.435
$L_{\delta lon}$	0.1491	5.302	1.725
$M_{\delta lat}$	-0.02907	8.796	3.4
$M_{\delta col}$	-0.05956	5.895	1.916
$M_{\delta ped}$	0.0 +	------	------
$M_{\delta lon}$	0.1273	3.946	0.9069
$N_{\delta lat}$	0.1102	4.298	1.636
$N_{\delta col}$	-0.0957	21.5	5.017
$N_{\delta ped}$	0.1779	5.086	1.652
$N_{\delta lon}$	0.02612	10.49	4.483
δ_{lat}	0.06399	4.015	1.696
δ_{col}	0.09627	3.407	1.557
δ_{ped}	0.2524	4.603	1.688
δ_{lon}	0.0952	3.066	1.054

+ Eliminated during model structure determination
! Constant gravity terms

Units: Derivatives   m, rad, s.
        Controls   cm, deg.

**Table 1: Bell 412HP ASRA Hover Model:
Stability and Control Derivatives**

The eigenvalues of this system are:

Real	Imaginary	Name
-0.3153	0.0	Aperiod pitch2
0.6112	0.0	Spiral
0.4584	-0.5419	Phugoid
0.4584	0.5419	Phugoid
-1.127	0.0	Aperiod pitch1
-0.7027	-1.758	Dutch roll
-0.7027	1.758	Dutch roll
-4.598	0.0	Aperiod roll

In the frequency domain analysis, the velocity derivatives proved to be more difficult to identify. This was due to the lack of low frequency information in the flight test data. The stability derivatives X_u, Y_v, Z_w and L_v (dihedral) showed the correct sign and had reasonable values, from theory. The model was insensitive to the speed derivative, M_u, resulting in its eventual elimination. It has been suggested (Ref. 13) that some of these derivatives may be better estimated from static tests and then fixed during the identification process.

The identification of all the angular rate damping derivatives was robust and consistent, in that the damping derivatives had reasonable values and correct sign, from theory. When the inflow derivative was fixed at a value of -0.01, this basically had the effect equivalent to removing the dynamics from the rotor. This effect will be explained in Section 8.3. The control equivalent time-delay values were approximately 100 msec, as expected, except the pedal time-delay, which was 250 msec. This effect too will be explained in Section 8.3.

8.3 Identification Problems

A summary of identification problems follows:
1. From Figure 8, it can be seen that the r/δ_{ped} and a_z/δ_{col} frequency responses match poorly in the range of 1.5 - 2.5 rad/sec,
2. With the derivatives for dynamic inflow fixed, the pedal equivalent time-delay value was as large 250 msec.

Extensive investigations were conducted on:
- the LTN-92 yaw rate and the data transcription process,
- the mechanical link from the pedal to the tail-rotor swashplate,
- state estimation to ensure kinematic compatibility of the yaw rate,
- pedal position compared to the actuator position,
- calibrations.
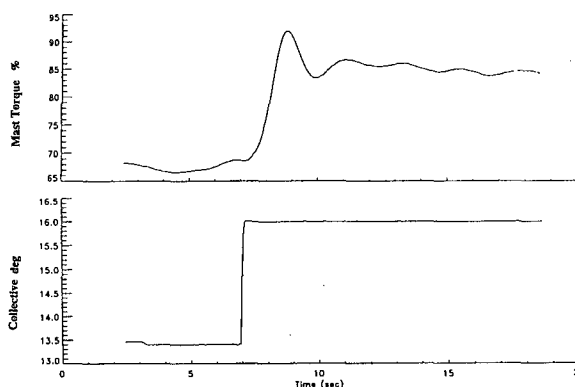
Figure 10: ASRA Mast Torque Response

None of the above investigations revealed any discrepancies, so the rotor mast torque was investigated next. The following four figures show the torque response to collective input. Figure 10 shows the rotor mast torque response to a 1-inch collective step input while the aircraft was in hover. The torque overshoot characteristics clearly denote an under-damped system with oscillations.
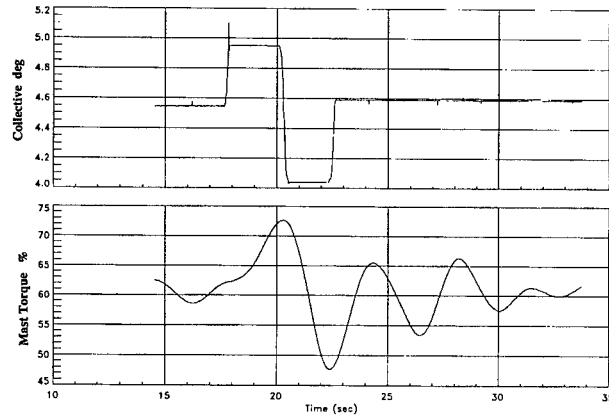

Figure 11: Collective Doublet Input

Figure 11 shows the rotor mast torque response to a doublet input. In the steady-state, the mast torque is oscillatory with weak damping and a 3-4 second period. The under-damped response characteristics of the engine governor clearly proved to be a problem. CIFER allows the effects of torque to be removed or "conditioned out" from the model, if it is used as a pseudo control input to the state space model.
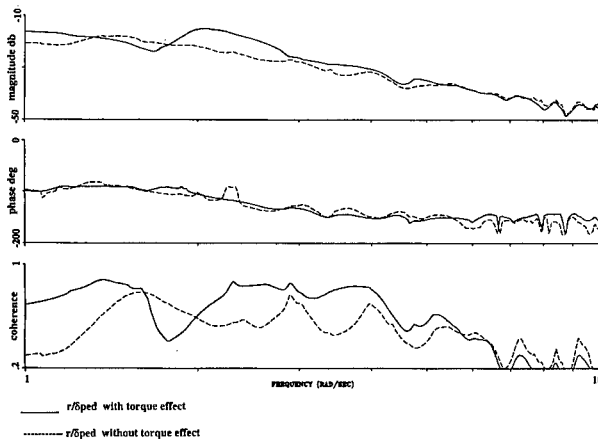

Figure 12: Mast Torque Effects

Figure 12 shows a plot of yaw rate-to-pedal response (r/δ_{ped}), in the frequency range of 1 to 10 rad/sec, with and without the mast torque dynamics included. The solid line represents the original model response while the dashed line shows the response of the model with the torque effect conditioned-out. By inspecting the magnitude plot, it is clear that the 6dB rise is removed and the coherence droop is smoothed out, above the threshold coherence of 0.4, in the frequency range of 1.5

- 3.0 rad/sec. This 6db rise is equivalent to a second-order system with a weak damping ratio.

Figure 13, which is a plot of yaw rate-to-torque response, shows that the coherence peaks at 1.5 – 3.0 rad/s and the magnitude is flat with a phase shift of 0 degrees. The torque measurement was, therefore, used as a "pseudo-control" in the state-space equation.
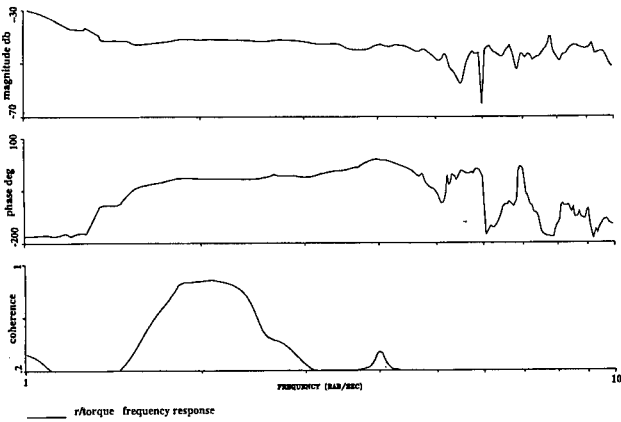

Figure 13: Yaw-rate to Torque Response

On re-inspection of Figure 12, the magnitude curve rolls off at 40 dB/decade, while the phase curve shows a -180 degrees roll-off within the 1-10 rad/sec interval. These second-order dynamic characteristics were not captured by the linear six-dof model. It can also be concluded that this was not caused by rotor torque dynamics of the Bell 412HP. This led to the suspicion of the presence of another unknown second-order yaw-axis dynamic effect. Future flight tests and analysis are required to study these yaw-axis dynamic effects. The collective axis indicated a similar observation as shown in the a_z/δ_{col} frequency response. The pitch and roll frequency responses were affected minimally by this engine governor second-order dynamics.

8.4   Model Verification

The final model was checked for robustness by using the final model structure with a different characteristic data-set of manoeuvres (i.e. one not used in the identification process), and comparing the model responses to flight test responses.

The model responses matched those of the data, well in the pitch and roll axes, but poorly in the collective and pedal axes. It can be seen from Figure 14 , that the roll rate and bank angle responses fit the data with high fidelity, those for the pitch rate and pitch attitude match well too, but yaw-rate was a poor match. This was due the unmodelled dynamics of the yaw axis. The yaw axis non-linearities were composed of the weak engine governor and the unmodelled second order effects.
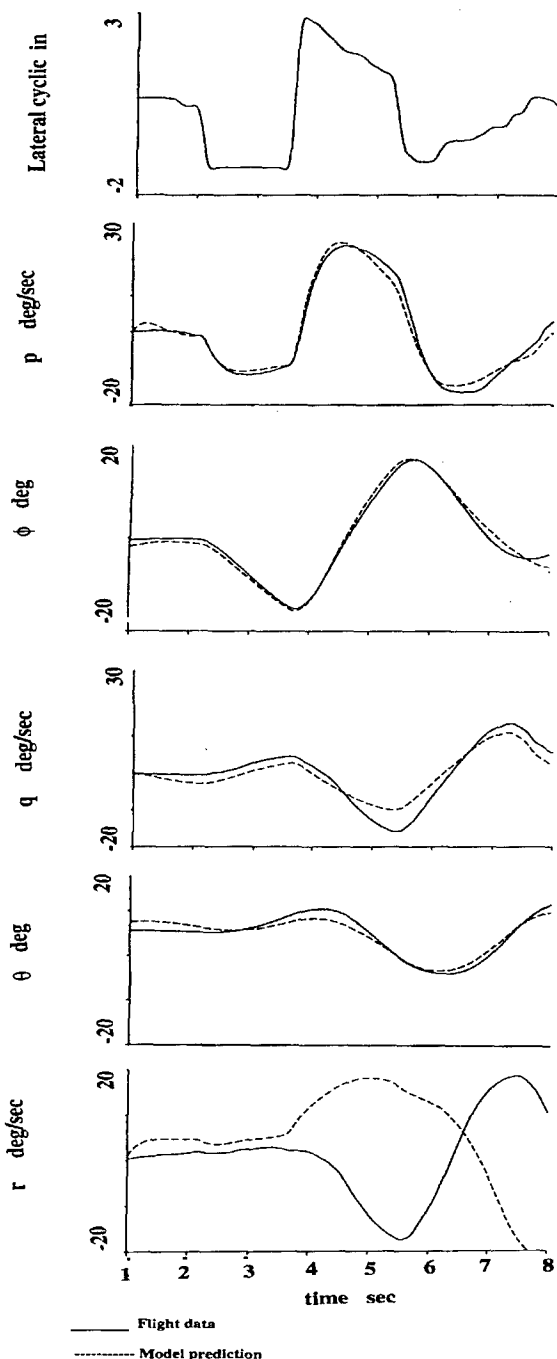
Figure 14: Lateral Cyclic Verification Results

The time response of the identified model to a lateral cyclic doublet is plotted. Once again, the response of yaw rate to pedal control input was not completely understood nor modelled; therefore, during the verification, the yaw rate response was de-weighted; It is clear from Figure 14 that the responses in the other axes were degraded by the absence of the correct yaw response. The on-axis roll attitude and roll rate matched well but responses related to the pedal input did not match well. This yaw-axis "second order dynamics" will be further examined in the second phase of this research.

9. CONCLUSIONS

The following summarises the main conclusions and lessons learned, while using the time domain MLE technique and the frequency domain *CIFER* method, to develop a mathematical model of the NRC Bell 412HP helicopter:

1. *CIFER* was found to be user-friendly, efficient and robust;
2. The identified final model represents the NRC Bell 412HP accurately in the frequency range of 0.1 to 30 rad/s;
3. The final model predicts the aircraft's pitch and roll responses very well, whereas it predicts collective and pedal responses quite poorly;
4. The engine governor was found to be under-damped giving rise to torque-RPM oscillations with a 3 second period, thus made modelling the heave and yaw axes more difficult;
5. A second order yaw-axis effect is suspected, but as yet unmodelled.

9.1 Future Work

It is clear that the second-order nature of the yaw-axis dynamics needs to be better modelled. An explicit engine model will be required to capture the collective and pedal dynamics at the frequency range of 1.5 - 3.0 rad/sec. Once the above dynamics have been adequately represented, inflow could then be characterised. It is thought that in this process, control phasing and flapping dynamics may surface as the next major effects to be modelled in the development of high-bandwidth control systems for the aircraft.

10. ACKNOWLEDGEMENTS

11. REFERENCES

1. Hui, K., Yuce M. and Chowdhury S., "Development of Parameter Estimation Technology", NAE Contractor Report NAE-CR-7, March 1990.
2. Tischler, M.B., "System Identification Methods for Aircraft Flight Control Development and Validation", NASA TM-110369, October 1995.
3. Fletcher, J.W., "Identification of UH-60 Stability Derivative Models in Hover from Flight Test Data", J. AHS, vol. 40, no. 1, 1995.
4. Hui, K., "An Improved Aerodynamic Model of a Bell 205A in Forward Flight", CAS Journal, vol. 42, no. 4, Dec. 1996.

5. Hui, K. and Baillie, S.W., "Improving Prediction: The Incorporation of Simplified Rotor Dynamics in a Mathematical Model of the Bell 412HP", CAS Journal, vol. 40, no. 4, Dec 1994,

6. Takahashi, M.D., "Rotor-State Feedback in the Design of Flight Control Laws for a Hovering Helicopter", J. Amer. Soc., Jan. 1994.

7. Tischler, M.B. and Cauffman, M.G., "Frequency-Response Method for Rotorcraft System Identification: Flight Applications to BO 105 coupled Rotor/Fuselage Dynamics" Journal of the American Helicopter Society, Vol 37, No. 3, pp. 3-17, July, 1992.

8. Williams, J.N., Ham, J.A., Tischler, M.B., "Flight Test Manual: Rotorcraft Frequency Domain Flight Testing", U.S. Army Aviation Technical Test Center, Airworthiness Qualification Test Directorate, AQTD Project No. 93-14, September 1995.

9. Fletcher, J.W., "Identification of Linear Models of the UH60 in Hover and Forward Flight", Presented at the 21st European Forum, Saint Petersburg, Russia, 29 August - 1 September, 1995.

10. Maine, R.E. and Iliff, K.W., "User's Manual for MMLE3, a General FORTRAN Program for Maximum Likelihood Parameter Estimation", NASA TP-1563, Nov. 1980.

11. Maine, R.E., "Programmer's Manual for MMLE3, a General FORTRAN Program for Maximum Likelihood Parameter Estimation", NASA TP-1690, June 1981.

12. Talbot, P.D., et al, "A Mathematical Model of a Single Rotor Helicopter for Piloted Simulation", NASA TM- 84281, Sept. 1982.

13. Ham, J.A., Gardner, C.K. and Tischler, M.B., "Flight Testing and Frequency Domain Analysis for Rotorcraft Handling Qualities Characteristics", presented at AHS Specialists' Meeting, "Pilot Vertical Flight Aircraft, A Conference on Flying Qualities and Human Factors", San Francisco, CA, January 1993.

14. Hui, K., and Miller A., "Frequency Domain Analysis of a Bell 205A Heave Axis Handling Qualities Characteristics" to be published, Lab. Memo, FRL, NRC, Canada, May,1998.

15. Erdos, R., "Torque Dynamic Characterization of the Bell 412 Helicopter", NRC, LTR-FR-139, December 1997.

16. Williams, J.N., Howard, J.M. and Fletcher, J.W., "OH-58D(I) Kiowa Warrior Transient Power-train Speed Characteristics Test in the Frequency Domain", presented at AHS 51st Annual Forum, Fort Worth, Texas, May 9-11,1995.

17. Hamel, P.G.(ed.), "Rotorcraft System Identification", Advisory Report 280, AGARD 8-AR-280,1991.

Study of a Rotor Flap-Inflow Model Including Wake Distortion Terms

Krishnamohan R. Krothapalli
J.V.R. Prasad
School of Aerospace Engineering
Georgia Institute of Technology
Atlanta, GA 30332-0150 USA

David A. Peters
School of Mechanical Engineering
Washington University
St. Louis, MO USA

SUMMARY

For many years, analysts have been puzzled by the fact that the off-axis coupling of a helicopter exhibits the opposite sign in flight tests as compared to simulations. Recently, researchers have shown that the effect may be attributable to the bending of the wake during a pitching maneuver, which introduces a fore-to-aft gradient in induced flow that can reverse the predicted sign of the roll coupling. Other research has shown that this result can also be obtained with momentum and vortex theory. There are many issues still under debate regarding the magnitude of wake distortion and its effectiveness in predicting off-axis dynamics. In the present work, a generalized dynamic wake model is augmented to include wake distortions. This model is then coupled with a flap model for simulation in low speed forward flight. Frequency responses from the simulation are collected with and without wake distortion, and these are compared with wind tunnel test data.

LIST OF SYMBOLS

C_T	thrust coefficient
C_L	aerodynamic rolling moment coefficient
C_M	aerodynamic pitching moment coefficient
C_n^m, D_n^m	coefficients of pressure potential function
K_β	hinge flap spring
K_R	wake distortion parameter (curvature)
$[L]$	matrix of inflow gains
$[M]$	apparent mass matrix for dynamic inflow
$\bar{P}_n^m, \bar{Q}_n^m$	normalized Legendre polynomials, 1st and 2nd kind
Q	number of rotor blades
R	rotor radius
R_c	wake radius of curvature
V_∞	rotor climb speed
a	lift curve slope
c	blade chord
e	blade hinge offset
r_R	blade root cutout
v^c	longitudinal inflow gradient distribution
Γ_o	bound circulation
ψ	rotor azimuth
Ω	rotor angular velocity
α_n^m, β_n^m	coefficients of inflow distribution
$\dot{\alpha}$	tip path plane angular rate
γ	blade Lock number
$\bar{\eta}, \bar{\nu}$	normalized ellipsoidal coordinates
η	flap mode shape
κ	wake curvature
λ	non-dimensional rotor climb speed
μ	non-dimensional forward flight speed
ν	non-dimensional inflow, $V_i/\Omega R$
ν_o, ν_c, ν_s	mean, longitudinal, and lateral inflow coefficients

1   INTRODUCTION

A helicopter is a very complicated dynamic system that has separate controls for the pilot to change the pitch, roll, yaw, and thrust of the vehicle. However, unlike the fixed wing aircraft, a helicopter exhibits a substantial degree of cross-coupling between the control axes. It is necessary to develop accurate simulation models of helicopter dynamic response to control inputs for such purposes as flight control design, handling qualities, acoustic analysis, and vibration analysis. The current study is focussed on the off-axis response to main rotor cyclic inputs. For many years, helicopter simulations have predicted an off-axis response in hover and low speed forward flight that is opposite in sign to the corresponding flight test data[1,2,3], a result that has confused many researchers for years.

Various attempts have been made to explain the off-axis response of the helicopter. Some of the theories and methods to explain the coupling are:

1) aerodynamic interaction between the rotor and the fuselage[4]
2) filtering of the lift and drag forces[5]
3) Theodorsen-like unsteady aerodynamic phase lag between the inputs to the two axes[6]
4) gyroscopic forces due to the angular momentum of the wake about the hub axis[7]

Some of the methods described above may produce improved results in the prediction of off-axis response, but they may not have physical meaning. Empirical modeling cannot be generalized to all rotor configurations, and significant flight-testing is required for identification and validation. A general simulation model of an arbitrary configuration that can accurately predict dynamic responses would be a valuable tool in the design phase of a helicopter.

It was proposed that the bending of the wake into a curved structure during a pitch or roll maneuver results in a gradient in the inflow at the rotor disk that could account for the sign reversal in the off-axis response. Rosen and Isser[8] showed that this effect could account for the reversal by including a distorted geometry of the rotor wake in their unsteady aerodynamic model (TEMURA). They showed that the

flapping dynamics equations for an articulated rotor with a nominal hinge offset would predict a steady state off-axis flap response that was opposite in sign to the flap response predicted without wake distortion. Keller[9] has used a vortex tube theory to model the inflow gradient effect in hover as a function of wake curvature, and captured the inflow gradient effect with a single factor called K_R. Elliptical integrals were used to calculate a value of 1.5 for K_R. Using this new model, researchers were able to show improvements in off-axis prediction[9,10,11]. Identification studies have shown that the analytical calculation of wake distortion proves to be insufficient in magnitude to correctly predict off-axis behavior in free-flight hover. The identified values for wake distortion show that an increase of 50-100% in wake curvature is needed. This could be understandable, since the wake geometry of a hovering rotor is very complicated, and inflow gradients at the rotor disk have been shown to be very sensitive to perturbations in wake geometry in hover[12].

In the present work, the generalized dynamic wake model is extended to include wake curvature using the exact result of vortex tube theory[12]. This extended wake model is then coupled to a rigid blade flap model. The frequency responses of the rotor to cyclic inputs in low speed forward flight ($\mu=0.093$) are compared to the five-bladed Sikorsky Bearingless Main Rotor (SBMR) frequency response database generated at NASA Ames Research Center[2,13,14]. It is theorized that the analytically determined wake curvature has less uncertainty for this flight condition than for hover, and this will lead to better prediction of off-axis rotor dynamics.

2 THEORETICAL BACKGROUND

2.1 Dynamic Inflow

Sissingh[15] was the first to represent the inflow at the rotor disk with both mean and first order harmonic variations in azimuth:

$$v(\psi) = v_o + v_c \cos\psi + v_s \sin\psi \qquad (1)$$

This model neglected radial variations in inflow, resulting in a discontinuity in inflow at the rotor disk. Peters[16] extended Sissingh's inflow model to include linear variations in radial position. The improved model is written as:

$$v(\bar{r},\psi) = v_o + v_c \bar{r} \cos\psi + v_s \bar{r} \sin\psi \qquad (2)$$

With this representation of the inflow at the rotor disk, the first three-state dynamic inflow model was developed. The equations are three nonlinear, first order differential equations that can be written in matrix form:

$$[M]\begin{bmatrix}\dot{v}_o \\ \dot{v}_c \\ \dot{v}_s\end{bmatrix} + [V][L]^{-1}\begin{bmatrix}v_o \\ v_c \\ v_s\end{bmatrix} = \begin{bmatrix}C_T \\ -C_M \\ C_L\end{bmatrix} \qquad (3)$$

Various theories have been used to determine the coefficients of the L and M matrices, as well as the elements of the mass-flow parameter matrix, V. A brief description of these theories is included.

2.2 Momentum Theory

The basic assumption of momentum theory is that thrust on a streamtube through the rotor disk is equal to the mass flow rate

multiplied by the total change in velocity of the air in the tube from top to bottom. Momentum theory always assumes that this total change in velocity is equal to twice the induced flow at the disk. For uniform inflow, the thrust at the rotor disk for axial flight is written:

$$T = \dot{m} * \Delta V = \rho \pi R^2 (V_\infty + v) * 2v \qquad (4)$$

This quantity can be non-dimensionalized to give a thrust coefficient:

$$C_T = \frac{T}{\rho \pi R^2 (\Omega R)^2} = 2v|\lambda + v| \qquad (5)$$

In hover, this reduces to the simple expression relating thrust and mean inflow in hover:

$$v = \sqrt{\frac{C_T}{2}} \qquad (6)$$

and for the low lift climb:

$$T = 2\rho \pi R^2 |V_\infty + v| v \cong 2\rho \pi R^2 V_\infty v \qquad (7)$$
$$C_T = 2v|\lambda + v| \cong 2v\lambda$$

For the general case where the inflow and freestream velocities vary across the disk, the thrust must be determined by integrating over the disk area. For an arbitrary flight condition with an arbitrary inflow distribution, the thrust is calculated by:

$$C_T = \int_0^1 \int_0^{2\pi} 2v(\bar{r},\psi)\sqrt{\mu^2 + (\lambda + v(r,\psi))^2}\, \bar{r}\, d\bar{r}\, d\psi \qquad (8)$$

Thrust can also be calculated from lifting line theory in axial flight if the bound circulation distribution along the blade radius is known:

$$dT = \rho\Omega r\Gamma_o dr$$
$$T = \int_0^R \rho\Omega r\Gamma_o dr \qquad (9)$$

Solving for the thrust and combining with equation (7) gives a value for mean inflow:

$$v = \frac{\Gamma_o}{4\pi\Omega R^2 V} \qquad (10)$$

Normalizing the bound circulation by $2\pi\Omega R^2$ gives:

$$v = \frac{\bar{\Gamma}_o}{2\lambda} \qquad (11)$$

The induced velocity in a low-lift climb can be predicted if the climb velocity and circulation are known.

2.3 Potential Flow Theory

Momentum theory is a good tool for predicting global aerodynamic properties of a rotor in axial or hovering flight. However, momentum theory fails to give good performance in forward flight since the only assumption on wake structure is

that induced flow doubles downstream. This does not account for the inflow variations from a skewed wake structure anticipated by a rotor in forward flight. This deficiency led to the development of the most popular and widely used dynamic inflow models by Pitt and Peters[17]. The model is derived using an acceleration potential approach. Kinner[18] was the first to show that Legendre polynomial functions in ellipsoidal coordinates can be used to model a discontinuity over a circular disk while still satisfying Laplace's equation, a concept that proved to be ideal for rotor aerodynamic analyses. The pressure potential is written in equation (12) where P and Q are associated Legendre polynomials of the first and second kinds, and C and D are arbitrary coefficients.

$$\Phi(\bar{v},\bar{\eta},\psi) = -\sum_{n=m+1}^{\infty}\sum_{m=0}^{\infty}\bar{P}_n^m(\bar{v})\bar{Q}_n^m(i\bar{\eta})\left[C_n^m\cos m\psi + D_n^m\sin m\psi\right] \quad (12)$$

The expression for the induced velocity is written in equation (13) where α_n^m and β_n^m are arbitrary coefficients for the inflow distributions.

$$v(r,\psi) = \sum_{n=m+1}^{\infty}\sum_{m=0}^{\infty}\phi_n^m(\bar{r})\left[\alpha_n^m\cos m\psi + \beta_n^m\sin m\psi\right] \quad (13)$$

where $\qquad \phi_n^m(\bar{r}) = \dfrac{\bar{P}_n^m(\bar{v})}{\bar{v}}$

This extension to the Pitt/Peters model was developed to include an arbitrary number of radial inflow shape functions for each harmonic[19].

2.4 Vortex Tube

The vortices from the rotor blade tips in a low lift climb lie on the surface of a cylindrical tube extending below the plane of the rotor disk. The vortices are a result of the lift on the blades, and they induce a velocity in the flowfield at all points. The component of induced velocity that is perpendicular to the rotor disk is particularly important, since it has a dominant role in the lift on the rotor blades. The velocity induced at an arbitrary point in space by a vortex filament can be calculated by the Biot-Savart Law:

$$d\bar{v} = \frac{\Gamma}{4\pi}\frac{d\bar{S}\times\bar{R}_p}{\left|\bar{R}_p\right|^3} \quad (14)$$

where $\bar{R}_p$ is the vector from the filament to the point of interest and $d\bar{S}$ is an incremental vector along the vortex filament.

In the limit as the number of blades increases (for ideal blades with uniform circulation distribution), the density of the vortex filaments on the cylindrical tube increases until the vorticity on this surface approaches a constant value. For this case, the vorticity is well represented mathematically by a vortex tube. The vortex tube is well suited for an analytical calculation of the induced velocity normal to the rotor disk. For a cylindrical vortex tube distorted in a circular fashion, the wake structure would form a torus if the wake were allowed to age sufficiently. Considering only a quarter of the torus beneath the rotor plane for various radii of curvature leads to the following model for the induced velocity components:

$$\frac{v_c}{v_o} = \frac{K_R}{R_c}$$
$$K_R = 1.0 \quad (15a\text{-}c)$$
$$R_c = \frac{V_T}{\dot{\alpha}R}$$

where V_T is the climb speed, $\dot{\alpha}$ is the pitch rate of the rotor plane, and R is the rotor radius used for non-dimensionalization. A full derivation of the vortex tube model used to calculate the induced velocities can be found in the literature[12]. The value of $K_R=1.0$ is less than the value of $K_R=1.5$ derived by Keller[9]. This difference is due to the constant curvature assumption in the former case.

It has been shown that the vortex lattice method[20,21] for a finite bladed rotor produces the same results seen in equation (15). This result gives the relationship between a single circulation distribution and a single inflow distribution. The single inflow distribution fails to fully capture the effect of the wake on the flap response in maneuvering flight. A study was done to investigate the effective flap moment prediction ratio for a finite-bladed rotor due to wake curvature[22]. Using the vortex lattice method for 3,4, and 5 bladed rotors, an average value for K_R-effective was found to be approximately 4/3. This value was determined by calculating the effective moment on the rotor blade rather than calculating the coefficient of the radial inflow distribution.

3   GENERALIZED DYNAMIC WAKE MODEL

3.1   Concentric Vortex Tube Formulation

The inclusion of wake curvature in the generalized dynamic wake model is considered first. From momentum theory, a circulation distribution can be related to the mean inflow distribution. When the circulation is expressed as a Legendre polynomial the radial distribution of mean inflow can be written using vortex tube theory:

$$v(\bar{r}) = \frac{\bar{P}_n^0(\bar{v})}{2\lambda}, \bar{v} = \sqrt{1-\bar{r}^2}, n = 1,3,5,\ldots \quad (16)$$

Using superposition of concentric tubes, the relationship between the mean and first harmonic radial distributions of induced flow for a pitching rotor in low-lift climb has previously been obtained as[21].

$$v^c(\bar{r}) = \frac{\dot{\alpha}}{\lambda}\bar{r}\,v(\bar{r}) = \kappa\,\bar{r}\,v(\bar{r}) \quad (17)$$

This relation does lead to a closed form model, but it also introduces significant error in the prediction of wake curvature induced inflow gradients. Therefore, equation (17) is replaced with the exact result from vortex tube theory[12] including the effective coupling term.

$$v^c(\bar{r}) = -\frac{\kappa K_{RE}}{2\lambda_o}\int_r^1\frac{d\Gamma_o}{dr_d}\frac{\bar{r}}{r_d}dr_d \quad (18)$$

where Γ_o represents the mean circulation distribution, and r_d is a dummy variable for radial integration. The derivative of the bound circulation creates numerical problems near the rotor tip, so equation (18) is rewritten using integration by parts:

$$\overline{v}^c(r) = -r\left[\frac{\Gamma_o}{r_d}\right]_r^1 + \int_r^1 \frac{\Gamma_o}{r_d^2} dr_d\right] \qquad (19)$$

where $\qquad \overline{v}^c(r) = v^c(r) * \dfrac{2\lambda_o}{\kappa K_{RE}}$

If the first harmonic inflow is expressed as a linear combination of Legendre polynomials:

$$\overline{v}^c(r) = \sum \alpha_p^1 \frac{\overline{P}_p^1(\overline{v})}{\overline{v}} \qquad (20)$$

The coefficients of the inflow distribution can be calculated:

$$\alpha_p^1 = \int_0^1 \overline{v}^c(\overline{r}) \overline{P}_p^1(\overline{v}) \overline{r}\, d\overline{r} \qquad (21)$$

In matrix form, for the case of an arbitrary radial circulation distribution:

$$\Gamma_o(\overline{v}) = \sum_k \tau_k \overline{P}_k^0(\overline{v}) \qquad (22)$$

$$\{\alpha_p^1\} = \frac{\kappa}{2\lambda_o}[C_{pk}]\{\tau_k^0\} \qquad (23)$$

where C_{pk} is calculated by assuming a circulation distribution equaling $\overline{P}_k^0(\overline{v})$, calculating the corresponding $\overline{v}^c(\overline{r})$, then determining the associated inflow coefficient, α_p^1, using equation (21).

3.2 Augmented Wake Model

The new L-matrix for an arbitrary radial circulation distribution including wake curvature is given in equation (24) using the right-hand side factorization. Since there is coupling between the first harmonic inflow and the mean inflow coefficients, it is now necessary to combine the L_c and L_s matrices into a single L-matrix padded by appropriately sized matrices of all zeros:

$$[L] = [\tilde{L}][V]^{-1} + [C][V]^{-1} \qquad (24)$$

where

$$[\tilde{L}] = \begin{bmatrix} \tilde{L}_c & 0 \\ 0 & \tilde{L}_s \end{bmatrix},$$

$$[C] = \begin{bmatrix} 0 & \frac{1}{2}C_{pk}^T\kappa_c & 0 & \frac{1}{2}C_{pk}^T\kappa_s & 0 \\ C_{pk}\kappa_c & 0 & 0 & 0 & 0 \\ 0 & 0 & 0 & 0 & 0 \\ C_{pk}\kappa_s & 0 & 0 & 0 & 0 \\ 0 & 0 & 0 & 0 & 0 \end{bmatrix},$$

$$\kappa_c = -\frac{\overset{*}{\beta}_{1c}}{V_T}, \quad \kappa_s = -\frac{\overset{*}{\beta}_{1s}}{V_T},$$

and

$$[V]^{-1} = \begin{bmatrix} \frac{1}{V_n^m} & 0 & 0 \\ 0 & \frac{1}{V_n^m} & 0 \\ 0 & 0 & \frac{1}{V_n^m} \end{bmatrix},$$

The dynamic wake equation retains its original form:

$$[K]\{\dot{\alpha}_j^r\} + [L]^{-1}\{\alpha_j^r\} = \frac{1}{2}\{\tau_n^m\} \qquad (25)$$

where K represents the diagonal apparent mass matrix associated with these inflow states. The C-matrix, given in equation (24), is shown for an inflow model including up to the 2nd harmonic. The zeros in the $\tilde{L}$-matrix and the C-matrix represent zero-matrices, with the dimension for each zero-matrix consistent with the number of radial functions for the harmonics. The right-hand factorization is preferred in equation (24) where the curvature takes the simple formula:

$$\kappa = \frac{\dot{\alpha}}{V_T} \qquad (26)$$

and the decrease in K_R by one-half is implicitly canceled by the actual doubling of the wake curvature in hover. It should be noted that K_R, though not explicitly written in the generalized dynamic wake model, is implicitly captured by the inflow states.

4   FLAP-INFLOW SIMULATION MODEL

4.1   Flapping Equations of Motion

The flap-inflow model is based on a code developed at the Florida Atlantic University for turbulence studies[23]. This model is extended to include a flap-hinge offset, a flap spring, and blade pitch inputs (collective pitch, cyclic pitch, blade twist, taper, cutout, etc.). The blade moment of inertia is defined using the normalized mode shape for a rigid blade with hinge offset, e as:

$$I_b = R^2 \int_e^1 \eta^2 m\, dr \qquad (27)$$

with the characteristic mode shape for flapping defined as:

$$\eta = \frac{r-e}{1-e} \qquad (28)$$

Using this definition, the flapping equation of motion for a single rotor blade is:

$$\ddot{\beta} + v_\beta^2 \beta = \gamma M_F \qquad (29)$$

with the rotating flap frequency defined using a uniform mass distribution along the blade span, and the Lock number defined using the blade moment of inertia:

$$v_\beta^2 = 1 + \frac{3e}{2(1-e)} + \frac{K_\beta}{I_b\Omega^2(1-e)} \qquad (30)$$

$$\gamma = \frac{\rho a c R^4}{I_b} \qquad (31)$$

The moment on a single blade is the sum of the effects of blade pitch, flapping, freestream, and the rotor wake:

$$M_F = M_\theta \theta + M_{\theta_{tw}} \theta_{tw} + M_{\dot\beta} \dot\beta + M_\beta \beta + M_{\lambda_f} \lambda_f + M_v \qquad (32)$$

The calculation of moments on the rotor blade follows Johnson[24], except for the last term, which is a summation that includes all of the wake states:

$$M_v = -\frac{1}{2} \sum_{n=m+1}^{N(m)} \sum_{m=0}^{M} \int_{r_R}^{1} M_{vr}(\bar r, n, m, q) d\bar r \qquad (33)$$

$$M_{vr}(\bar r, n, m, q) = \left(\eta\, \bar r \phi_n^m(\bar r) + \mu\eta\phi_n^m(\bar r)\sin\psi_q \right)^* \\ \left(\alpha_n^m \cos(m\psi_q) + \beta_n^m \sin(m\psi_q) \right)$$

The blade moment coefficients are numerically integrated from the root cutout (30% for SBMR) to the blade tip. These coefficients are calculated once at the beginning of the code to reduce the computational time that would be required for radial integration at each time step.

The multiblade coordinate transformations are used to transform the rotor flapping response from the rotating to the non-rotating frame.

$$\beta_0 = \frac{1}{Q} \sum_{q=1}^{Q} \beta_q$$

$$\beta_{1c} = \frac{2}{Q} \sum_{q=1}^{Q} \beta_q \cos\psi_q \qquad (34a\text{-}c)$$

$$\beta_{1s} = \frac{2}{Q} \sum_{q=1}^{Q} \beta_q \sin\psi_q$$

Additionally, the time derivatives of the cyclic flapping are needed to calculate the rotor plane angular rates for use in the wake distortion model:

$$\dot\beta_{1c} = \frac{2}{Q} \sum_{q=1}^{Q} \left(\dot\beta_q \cos\psi_q - \beta_q \sin\psi_q \right)$$

$$\dot\beta_{1s} = \frac{2}{Q} \sum_{q=1}^{Q} \left(\dot\beta_q \sin\psi_q + \beta_q \cos\psi_q \right) \qquad (35a,b)$$

4.2 Coupled Wake Equations

The pressure coefficients on the right side of equation (25) are modified to include the effect of hinge offset and root cutout in addition to blade pitch control. For a rotor with Q blades, the pressure functions are given by[23]:

$$\tau_n^{0c} = \frac{1}{2\pi} \sum_{q=1}^{Q} \int_{r_R}^{1} \bar L_q \phi_n^0(\bar r) d\bar r$$

$$\tau_n^{mc} = \frac{1}{\pi} \sum_{q=1}^{Q} \int_{r_R}^{1} \bar L_q \phi_n^m(\bar r)\cos(m\psi_q) d\bar r \qquad (36a\text{-}c)$$

$$\tau_n^{ms} = \frac{1}{\pi} \sum_{q=1}^{Q} \int_{r_R}^{1} \bar L_q \phi_n^m(\bar r)\sin(m\psi_q) d\bar r$$

with the normalized circulatory lift:

$$\bar L_q = \frac{1}{2} ac\bar V_\Omega (\bar V_\Omega \theta_q - V_\Omega \bar r \theta tw_q - \lambda - v - \beta_q \eta'\mu\cos\psi_q - \dot\beta_q \eta) \qquad (37)$$

where $\quad \bar V_\Omega = \bar r + \mu\sin\psi_q$

All radial integrals in the flapping and wake dynamics are calculated and stored before the rotor simulation begins to reduce computation time. The state derivatives are computed using linear combinations of the integral values with the control inputs, flap states, and wake states.

5   COMPARISON WITH SBMR DATA

5.1   Wind Tunnel Measured Data

The flap angle for the SBMR was measured using strain gauges near the root of the flexbeam; therefore it is assumed that rigid blade flapping is sufficient for modeling purposes. The relation between flap angle and bending strain on one blade is given using a strain calibration factor[2]:

$$(\beta_q)_\varepsilon = (SF_\beta)(\beta_q)_{rad} \qquad (38)$$

with the calibration factor equal to .102e6 for the 40kts flight condition.

The rolling and pitching moments at the rotor hub are also measured. If the spanwise loading on the blades is proportional to the selected flap mode shape, the hub moments can be exactly determined from the multiblade flap angles. This is not the case in general, but it is a good approximation since the neglected aerodynamic and inertial moments oppose each other and result in a small contribution to hub moment. The hub moments relate to the flapping as follows:

$$\gamma \frac{2C_{Mx}}{\sigma a} = (v_\beta^2 - 1)\beta_{1s}$$

$$\gamma \frac{2C_{My}}{\sigma a} = -(v_\beta^2 - 1)\beta_{1c} \qquad (39a,b)$$

$$M_{x,y} = \rho\pi R^2 (\Omega R)^2 R\, C_{Mx,y} \qquad (40)$$

5.2   Simulation Data Collection

The procedure described below is similar to the one employed by Tischler using the modified GENHEL simulation model[2,14]. The difference between the current model and the GENHEL model is the use of a generalized dynamic wake model with wake distortion in place of a 3-state dynamic inflow model. The simulation is started with the specified flight condition, and feedback loops on the swashplate controls are used to obtain the desired thrust, pitching and rolling moments used for the trim condition in the wind tunnel. When the desired conditions are reached, the trim controls are fixed, and a frequency sweep signal is added to the trim setting for each channel (one channel at a time) so that frequency response input-output pairs could be calculated using the CIFER (Comprehensive Identification from FrEquency Responses) software package[25]. The rotor

parameters of the SBMR used in the simulation can be found in Table 1.

The number of wake states chosen for the simulation was determined by choosing the radial shapes in a consistent manner up to the 5th harmonic for this 5-bladed rotor. A maximum of 8 was chosen for the highest power of r, and truncating the states beyond the 5th harmonic results in 37 wake states. It becomes necessary to include up to the 5th harmonic to ensure that the Q/rev unsteady inflow in the non-rotating system precludes the need for a tip loss effect[19].

5.3 Frequency Response Comparison

The first response examined is the coning response to collective pitch input, seen in Figure 1. The simulation response qualitatively matches the SBMR data very well, with phase characteristics within a few degrees over the frequency range of interest. Of note is the approximately 2dB overprediction of coning response magnitude over the frequency range, which corresponds to an error of about 25% in magnitude. In most of the SBMR frequency responses, the effect of the first regressive lead-lag mode is very apparent at approximately 9 rad/s. These dynamics are not modeled since there is little coupling, and the frequencies of interest are below the first lead-lag mode. Tischler[2,14] has successfully modeled the lead-lag dynamics, effectively capturing the dynamics of the first regressive lead-lad mode.

Examination of the on-axis flapping and hub moment responses for both the lateral and longitudinal stick inputs (Figures 2-5) show excellent correlation in both magnitude and phase, with the notable exception being the longitudinal flapping response to longitudinal stick input (β_{1c}/d_{lon}) in Figure 2. The simulation model fails to capture the peak in amplitude at approximately 1.5 rad/s and subsequent rolloff. The 2.5dB discrepancy and approximately 20-degree phase difference are most certainly the result of unmodeled dynamics. It is suggested that the second flap mode (which is estimated to have a frequency slightly larger than 3Ω) is excited by this input. This is supported by the fact that this peak in amplitude is not seen in the corresponding hub moment response (M_y/d_{lon}) shown in Figure 4. Since the flap angles are measured with strain gauges at the roots of the blades, the measurements are valid if only the first flap bending mode is excited.

The off-axis hub moment responses without wake distortion show a significant discrepancy in phase as compared to the SBMR data. With the inclusion of the wake distortion terms, significant improvement is seen in the off-axis phase predictions. It is noted, however, that the correction in phase for the off-axis response to the longitudinal stick input is overpredicted, while the off-axis response to the lateral stick input is underpredicted. The values for K_{RE} must be identified separately for the lateral and longitudinal rotor plane rates. These values are denoted K_{REs} and K_{REc} representing the wake curvature parameters associated with lateral and longitudinal rotor plane angular rates and massflow parameter. The identified values for these parameters for this flight condition are $K_{REs} = 1.7$ and $K_{REs} = 1.0$, in comparison to the predicted value of 1.33 for both. The off-axis, hub rolling moment frequency responses can be seen in Figures 6 and 7. The corresponding pitch moment responses can be seen in Figures 8 and 9. It should also be noted that the definition of K_R used by Keller is defined differently than the K_{RE} parameters in the current study. In the former, K_R is functionally dependent on the mass-flow parameter, while in the latter, the mass-flow parameter is contained in the wake curvature estimate.

6 CONCLUSIONS AND RECOMMENDATIONS

The augmented generalized wake model has been successfully coupled with a rigid blade flap model, and responses have shown excellent qualitative results, and good quantitative results for all but a few notable exceptions in the range of frequencies below the first lag mode. By combining the existing L_c and L_s matrices, the wake distortion terms can be added in a compact manner.

The coupled flap/inflow model shows that prediction of off-axis response is significantly improved using the wake distortion terms. The wake distortion terms show negligible effect on the on-axis frequency responses for this flight condition. The phase corrections in the off-axis moment responses indicate that the wake curvature estimates for equal longitudinal and lateral rotor plane rates are not equal in forward flight, as previously assumed. A full identification procedure using the CIFER software package is underway, where the uncertain rotor and wake parameters can be studied.

Continuation of this work involves extension of the generalized dynamic wake model with distortion for application to arbitrary flight conditions. One limitation is the loss of equivalence between circulation and lift distribution in forward flight. This approximation is valid only for hover and low speed forward flight. Another limitation is the wake geometry in transitional flight conditions where the result could be a highly distorted wake. Also, the distortion augmentation model must be expressed in closed form for the ease of application.
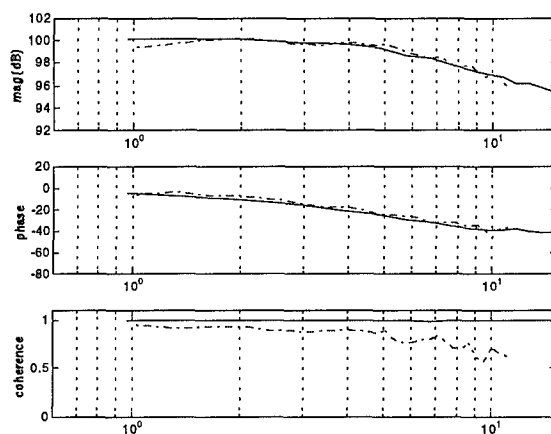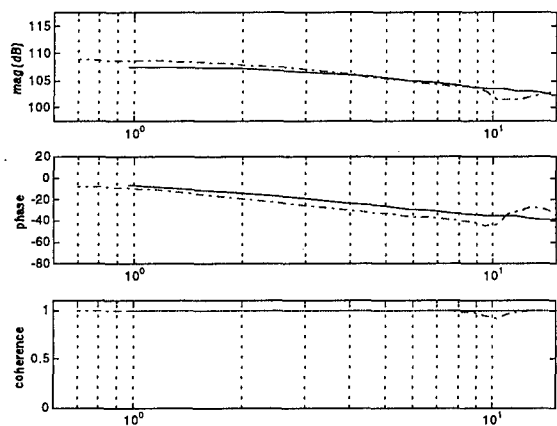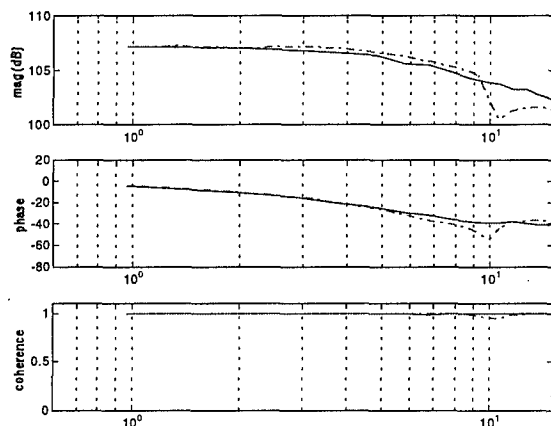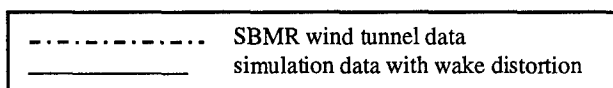
7 ACKNOWLEDGEMENT

8 REFERENCES

1. Takahashi, M.D., "A Flight-Dynamic Helicopter Mathematical Model with a Single Flap-Lag-Torsion Main Rotor," NASA TM 102267, USAAVSCOM TM 90-A-004, February 1990.

2. Tischler, M.B., Driscoll, J.T., Cauffman, M.G., and Freedman, C.J., "Study of Bearingless Main Rotor Dynamics From a Frequency-Response Wind Tunnel Test Data," Presented at the American Helicopter Society Aeromechanics Specialists Conference, San Francisco, CA, January 1994.

3. Harding, J.W., and Bass, S.M., "Validation of a Flight Simulation Model of the AH-64 Apache Attack Helicopter Against Flight Test Data," American Helicopter Society 46th Annual Forum, Washington D.C., May 1990.

4. Ballin, M.G., and Dalang-Secretan, M.A., "Validation of the Dynamic Response of a Blade-Element UH-60 Simulation Model in Hovering Flight," *Journal of the American Helicopter Society*, Vol. 36, #4, 1991.

5. Mansur, H.M., and Tischler, M.B., "An Empirical Correction Method for Improving Off-Axis Response Prediction in Component Type Flight Mechanics Helicopter Models," AGARD Flight Vehicle Integration Panel on "Advances in Rotorcraft Technology," Ottawa, Canada, May 1996.

6. Takahashi, M.D., Fletcher, J.W., and Tischler, M.B., "Development of a Model Following Control Law for Inflight Simulation Using Analytical and Identified Models," Presented at the American Helicopter Society 51st Annual Forum, Ft. Worth, TX, 1995.

7. von Grunhagen, W., "Dynamic Inflow Modeling for Helicopter Rotors and its Influence on the Prediction of Crosscoupling," AHS Aeromechanics Specialist Conference, Fairfield County, CT, October 1995.

8. Rosen, A, and Isser, A., "A New Model of Rotor Dynamics During Pitch and Roll of a Hovering Helicopter," *Journal of the American Helicopter Society*, Vol. 40, #3, July 1995.

9. Keller, J.D., "An Investigation of Helicopter Dynamic Coupling Using an Analytical Model," Presented at the 51st Annual Forum of the American Helicopter Society, Ft. Worth, TX, May 9-11 1995.

10. Arnold, U.T.P., Keller, J.D., Curtiss, H.C., and Reichert, G., "The Effect of Inflow Models on the Dynamic Response of Helicopters," 21st European Rotorcraft Forum, St. Petersburg, Russia 1995.

11. Hamers, M., and von Grunhagen, W., "Nonlinear Helicopter Model Validation Applied to Realtime Simulations," Presented at the 53rd Annual Forum of the American Helicopter Society, Virginia Beach, VA, April 29-May 1 1997.

12. Krothapalli, K.R., Prasad, J.V.R., and Peters, D.A., "Improved Wake Geometry for a Maneuvering Rotor," Presented at the American Helicopter Society Technical Specialists' Meeting for Rotorcraft Acoustics and Aerodynamics, Williamsburg, VA, October 1997.

13. Norman, T.R., Cooper, C.R., Fredrickson, A., and Herter, J.R., "Full-Scale Wind Tunnel Evaluation of the Sikorsky Five-Bladed Bearingless Main Rotor," Presented at the American Helicopter Society 49th Annual Forum, St. Louis, MO, May 1993.

14. Advances in Aircraft Flight Control, Tischler, M.B. (Ed), Taylor and Francis, 1996.

15. Sissingh, G.J., "The Effect of Induced Velocity Variation on Helicopter Rotor Damping in Pitch or Roll," Aeronautical Research Council Paper No. 101, Technical Report No. Aero 2132, November 1952.

16. Peters, D.A., "Hingeless Rotor Frequency Response with Unsteady Inflow," Presented at the AHS/NASA Ames Specialists Meeting on Rotorcraft Dynamics, NASA SP-362, February 1974.

17. Pitt, D.M., and Peters, D.A., "Theoretical Prediction of Dynamic Inflow Derivatives," *Vertica*, Vol. 5, #1, 1981.

18. Kinner, W., "Theory of Circular Wing," *Ingenieur Archiv*, Vol. 7, 1937, Translation No. 2345, Ministry of Aircraft Production, UK.

19. He, C.J., "Development and Application of a Generalized Dynamic Wake Theory for Lifting Rotors," PhD Dissertation, Department of Aerospace Engineering, Georgia Institute of Technology, 1989.

20. Barocela, E. "The Effect of Wake Distortion on Dynamic Inflow for Lifting Rotors," Masters Thesis, Dept. of Mechanical Engineering, Washington University, St. Louis, MO, May 1997.

21. Barocela, E., Peters, D.A., Krothapalli, K.R., and Prasad, J.V.R., "The Effect of Wake Distortion on Rotor Inflow Gradients and Off-Axis Coupling," Presented at the 1997 AIAA Atmospheric Flight Mechanics Conference, New Orleans, LA, August 1997.

22. Krothapalli, K.R., "Helicopter Rotor Dynamic Inflow Modeling for Maneuvering Flight," PhD Proposal, Department of Aerospace Engineering, Georgia Institute of Technology, July 1, 1997.

23. Dang, Y.Y., Subramanian, and Gaonkar, G.H., "Modeling Turbulence Seen by Multibladed Rotors for Predicting Rotorcraft Response with Three-Dimensional Wake," *Journal of the American Helicopter Society*, Vol. 42, #4, October 1997.

24. Johnson, W., Helicopter Theory, Princeton University Press, Princeton, NJ, 1980.

25. Tischler, M. B., Cauffman, M. G., "Frequency Response Method for Rotorcraft System Identification: Flight Applications to BO-105 Rotor/fuselage Identification," *Journal of the American Helicopter Society*, Vol. 37 #3, July 1992.

Parameter	Symbol	Units	Value
Blades	Q	-	5
Radius	R	ft	22
Avg chord	c	ft	1.29
Flap spring	K_β	ft-lbs/rad	2887
Rotor speed	Ω	rad/s	32.98
blade twist	Θ_{tw}	deg	-10.0
Lock number	γ	–	8.26
flap inertia	I_b	slg-ft^2	499.01
flap hinge offset	e	-	0.097
flap frequency	ν_β	per rev	1.079
pitch-flap coupling	$K_{p\beta}$	rad/rad	-0.174
control phase angle	Δ_{sp}	rad	-0.244

Table 1: Rotor Parameters
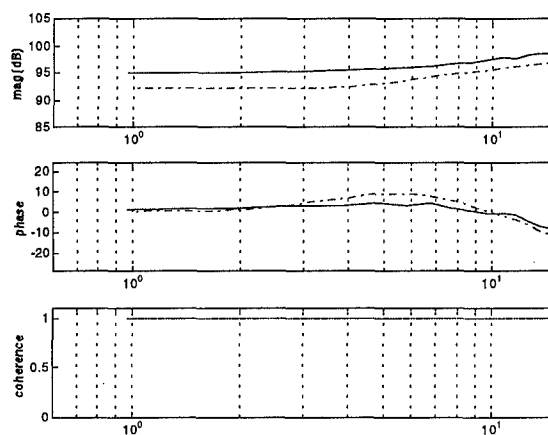
Figure 1: β_o/θ_o coning response
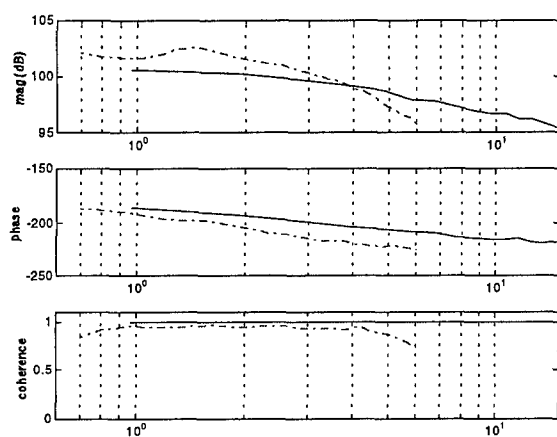
Figure 2: β_{1c}/δ_{lon} on-axis longitudinal flapping

Figure 3: β_{1s}/δ_{lat} on-axis lateral flapping

Figure 4: M_y/δ_{lon} on-axis pitching moment

Figure 5: M_x/δ_{lat} on-axis rolling moment
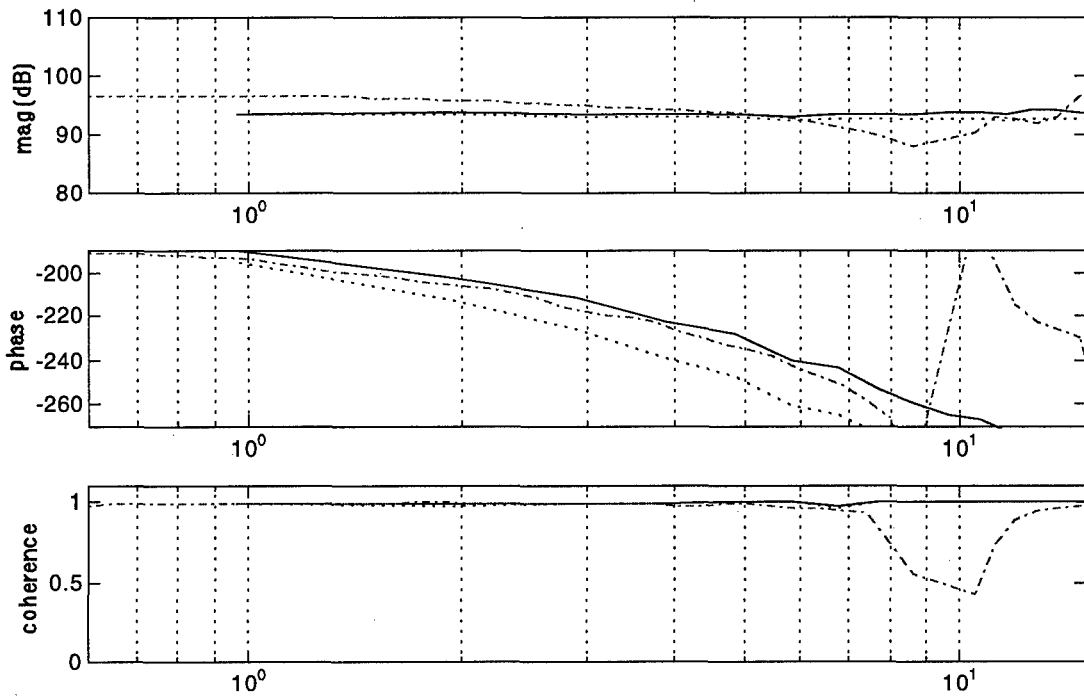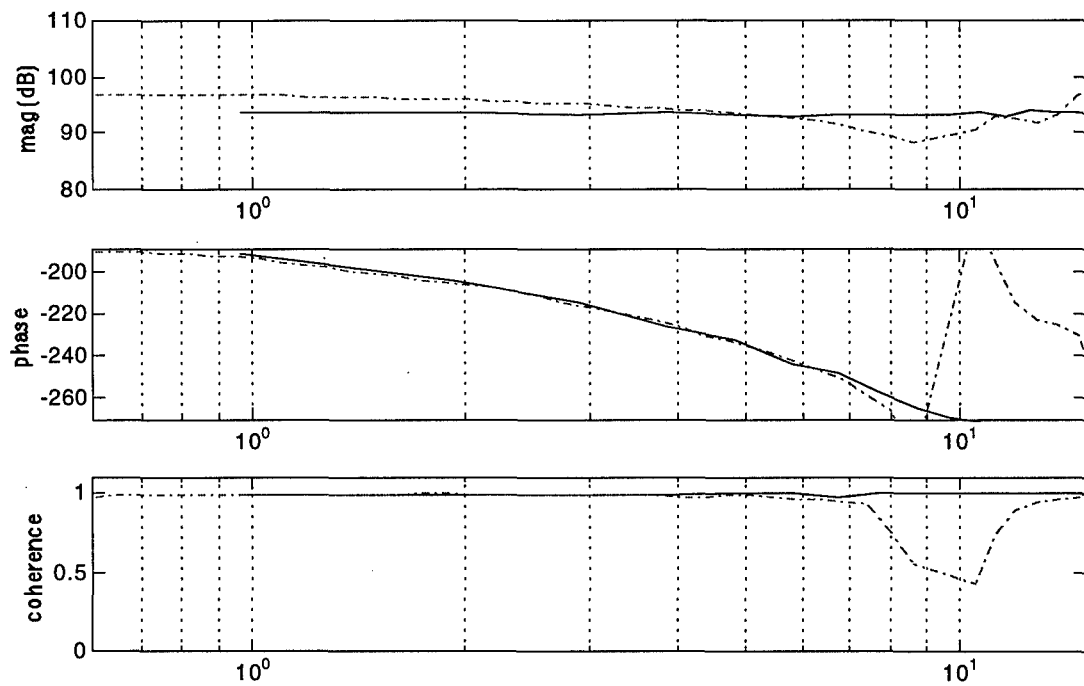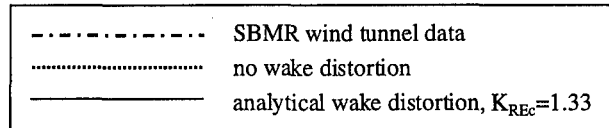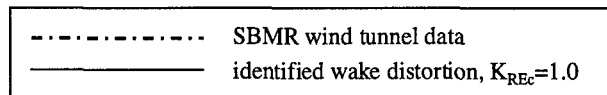

SBMR wind tunnel data
simulation data with wake distortion

Figure 6: M_x/δ_{lon}
off-axis rolling moment

- - - - - - SBMR wind tunnel data
.... no wake distortion
———— analytical wake distortion, $K_{REc}=1.33$

Figure 7: M_x/δ_{lon}
off-axis rolling moment

- - - - - - SBMR wind tunnel data
———— identified wake distortion, $K_{REc}=1.0$

Figure 8: M_y/δ_{lat}
off-axis pitching moment

─·─·─·─·─·─	SBMR wind tunnel data
····························	no wake distortion
───────	analytical wake distortion , $K_{REs}=1.33$

Figure 9: M_y/δ_{lat}
off-axis pitching moment

─·─·─·─·─·─	SBMR wind tunnel data
───────	identified wake distortion, $K_{REs}=1.7$
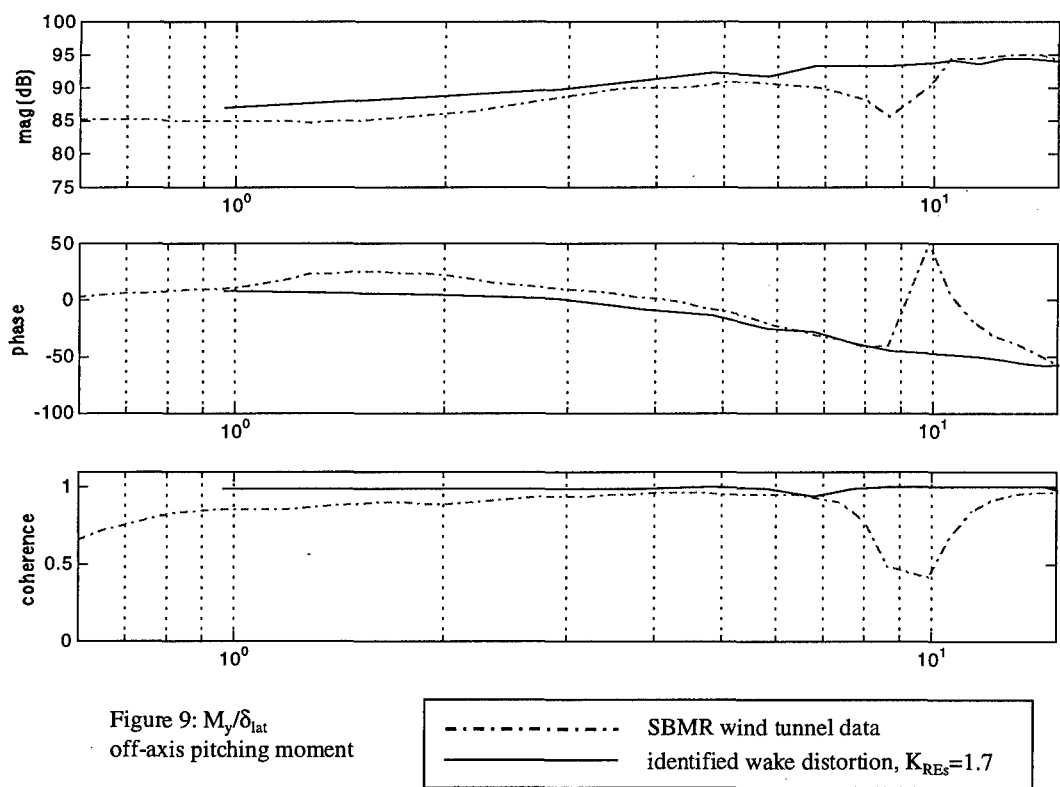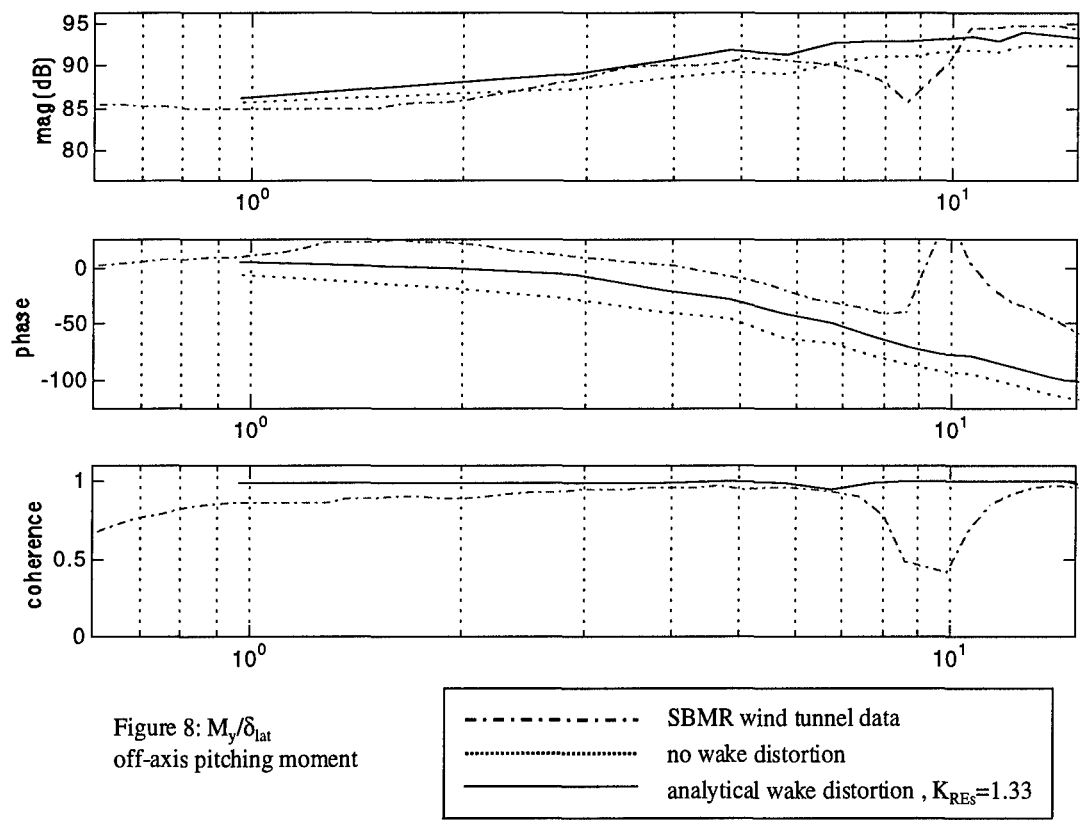
Solar Powered Stratospheric Research Aircraft - Flight Test and System Identification

Derek L. Lisoski
AeroVironment, Inc. 4685-3H Industrial St.
Simi Valley, CA, 93063, USA

Mark B. Tischler
Aeroflightdynamics Directorate, NASA Ames Research Ctr
Mail Stop N211-2
Moffett Field, CA 94035-1099, USA

1. SUMMARY

On July 7th, 1997, the NASA Pathfinder solar-powered aircraft flew to a record altitude of 71,500 feet; establishing new world altitude records for electric powered and propeller-driven aircraft. The Pathfinder platform, developed by AeroVironment for NASA's Environmental Research Aircraft and Sensor Technology (ERAST[1]) program, is an unmanned solar-powered flying wing which serves as the first of a series of technology demonstrators which are slated to include the 100,000 ft altitude Centurion and the multi-week duration Helios solar aircraft.

During the 1997 flight test deployment at the Pacific Missile Range Facility, Kauai, Hawaii, Pathfinder flew a total of six times, establishing the viability of a solar powered aircraft for scientific and commercial payload missions. During this flight test series, extensive use was made of the CIFER®[2] frequency response analysis code for initial simulation verification, in-flight real-time stability determination, and post-flight system identification to ensure flight safety. This paper presents an overview of Pathfinder and the flight test program, outlines some of the analysis techniques used, and summarizes their results.

2. INTRODUCTION

Significant progress towards the goal of long duration high altitude flight was achieved by AeroVironment on July 7th, 1997, when the first test bed for a solar-powered RPA, called "Pathfinder", achieved a record altitude of 71,500ft during a 14 hour flight at the US Navy's Pacific Missile Range Facility, Kauai, Hawaii. This altitude is higher than any previous propeller-driven or electric powered aircraft has achieved.

AeroVironment's solar electric aircraft are funded as a part of the NASA Environmental Research Aircraft and Sensor Technology (ERAST[1]) program; this program is developing advanced aircraft and sensors for environmental research in the upper atmosphere.

Solar powered aircraft are, of necessity, very efficient. Pathfinder realizes this efficiency through the use of an extremely lightweight (wing loading of 0.7 pounds per square foot) span-loaded flying wing structure, which gives the most efficient utilization of planform area for solar energy collection. This design has marginal static and dynamic stability characteristics, unique control methods, a very flexible structure, and it is dominated by unsteady aerodynamic and aeroelastic structural factors, many of which are normally neglected in traditional aircraft design.

Development of a reliable and autonomous flight control system (AFCS) for this class of aircraft is very challenging.

The CIFER®[2] frequency domain analysis code has been used since 1995 during flight tests of Pathfinder, for both real-time and post-flight analysis. System identification was used along with low altitude flight test results to obtain a reliable quasi-linear six-degree of freedom computer simulation model, which was then used for control system development, gain scheduling and high altitude stability margin prediction. During the actual high altitude flights, real-time frequency domain testing was used to obtain stability margin trends with altitude to ensure adequate margin remained as the aircraft climbed. Subsequent post-flight system identification continues to improve the simulation model and allows rapid evaluation of control system performance and design changes. In-flight analysis will again be used on future flights as new altitude records are achieved, and for very long duration flights, stability analysis will be used periodically to detect slow system degradation (such as the loss of actuators) that could not otherwise be easily detected.

3. PROJECT HISTORY

Since the late 1970s, the design development center of AeroVironment has specialized in the development of lightweight, high efficiency aircraft[3,4,5]. In July 1980, the AeroVironment Gossamer Penguin (a three-quarter-scale variant of the Gossamer Albatross, the first human-powered aircraft to fly the English Channel) was outfitted with a solar array and electric motor and flew a distance of 2 miles at Rogers Dry Lakebed, Edwards AFB, CA.

Following the Penguin, a new more rugged design, the Dupont Solar Challenger, first flew on November 15th, 1980, and eventually flew a 260-Km flight from Cergy-Pontoise, France (just outside of Paris) to RAF Manston, at Kent, England.

After successfully flying the Penguin and Solar Challenger with pilots, the feasibility of an unpiloted, solar-powered aircraft that could stay aloft on solar energy for months at a time was studied. In order to achieve low weight, efficiency, and high reliability, a unique multi-engine, span-loaded, flying wing design was selected. A proof-of-concept vehicle, HALSOL, which was one hundred feet in span and had eight motors and propellers distributed along the wing, completed a series of nine flights in the summer of 1983.

By 1992, energy storage techniques had improved enough to make very long missions feasible using solar power. In 1993 the Ballistic Missile Defense Organization (BMDO) funded a series of successful low-altitude test flights of a refurbished HALSOL, now dubbed RAPTOR Pathfinder.

In 1994, development of Pathfinder continued under the NASA ERAST program. On September 11th, 1995, Pathfinder made a successful flight to 50,500'; this represented a new altitude record almost 36,000 feet higher than any previous solar powered flight.

In early 1997, Pathfinder was shipped to the Pacific Missile Range Facility (PMRF) on the island of Kauai, in the Hawaiian Islands. This location offered good weather, a high average solar angle during the summer, and an almost ideal arrangement of restricted and military use airspace. On July 7th, 1997, Pathfinder took off at 8:34 AM, climbed to a peak altitude of 71,500 feet over the Pacific Ocean at 3:36 PM, and then descended for a smooth, night landing at Barking Sands Airfield. This altitude is over 4,000 feet higher than the first Pathfinder record flight which was flown in June, and is approximately 4,500 feet higher than any other propeller-driven aircraft has ever flown.

4. SYSTEM DESCRIPTION

4.1 General

The Pathfinder RPA system[6,7] consists of three main components: the Pathfinder aircraft itself, a Stationary Ground Control Station (GCS) from which the aircraft is flown for most of the flight, and a Mobile GCS, which is used for takeoff and landing.

The Mobile GCS is a converted passenger van that contains a pilot controller and two telemetry display computers; it is manned by the mobile pilot, flight engineer, and director who control the aircraft primarily by visual reference. Control of the Pathfinder is transferred to a Stationary GCS for flight altitudes above 1,000 feet.

The Stationary GCS is a converted Army truck that contains a pilot's controller and five telemetry display computers to navigate the aircraft and monitor the health of the aircraft's systems. It is manned by a pilot, flight engineer, stability and control engineer, communications engineer, and flight director who control the aircraft during the climb, loiter, and descent phases of the flight.

The pilot's controller includes all the switches, knobs, and sticks required for controlling the RPA. Four gain switches on the controller allow in-flight changes to be made to control system gains.

Apple Macintosh computers are used for downlink telemetry data display and stability analysis. Downlink data is displayed in many formats on several different selectable display pages, including:

- A Pilot's Display, with moving tapes and bar graphs for critical flight parameters including airspeed, altitude, angle of attack and sideslip, heading, power output, pitch rate, etc.

- A Navigation Display, which displays selectable GPS based moving maps with superimposed UAV position, range boundaries, flight termination footprint, ground track vector, wind vector, glide cone, altitude, way-point locations, and FTS fall point.

- A Diagnostics Display, which compares information from the two flight computers and triply redundant critical sensors and automatically flags discrepancies or out-of-range conditions.

4.2 Mission Description

On a typical flight day, the mission countdown starts at 05:00 hrs, when preflight and range safety systems tests are performed, after which the aircraft is towed to the main runway for takeoff. Takeoff occurs between 08:30 and 11:00 hrs when there is sufficient solar energy for a sustained climb rate and when weather conditions permit a viable flight plan. During the high altitude missions, Pathfinder spends most of the day climbing and reaches peak altitude from 15:00-16:00 hrs. Once the mission is complete, Pathfinder begins its descent in the late afternoon for a landing a few hours after sunset, usually between 22:00-23:00 hrs.

During a high altitude flight, stability and control data is collected and analyzed in near-real time. By performing pre-programmed frequency sweeps in the longitudinal and lateral axes at roughly 10,000-foot altitude increments, the stability margins and open- and closed-loop aircraft responses are established using the CIFER®[2] analysis code. Decisions are then made on any required excitation amplitude or gain changes, which are then implemented by the flight crew.

4.3 Aircraft Description

Pathfinder is a very lightweight span-loaded flying wing with a span of 99 feet and a chord of 8 feet, as shown in Figure 1. The aircraft features lightweight and strong materials used in a structurally efficient flying wing design, efficient low-Reynolds number aerodynamics, redundancy in motors, props, control surfaces, and flight control hardware, and simple, highly reliable flight control software and hardware with 'soft' failure modes. Detailed specifications are given in Table #1.

Pathfinder has six electric motors that weigh 13 pounds each and consist of a fixed-pitch 79-inch propeller, solid-state motor with internal power electronics, nacelle, and cooling fins. Differential power to two tip motors on either side is used for lateral control. There is no active roll control since the wing dihedral provides sufficient roll stability. Twenty-six elevator control surfaces are attached to the wing trailing edge to provide pitch control.

Pathfinder employs a large conformal solar array covering over 70% of the wing's upper surface to power the aircraft's electric motors and avionics. The solar array can generate approximately 8,000 watts near solar noon.
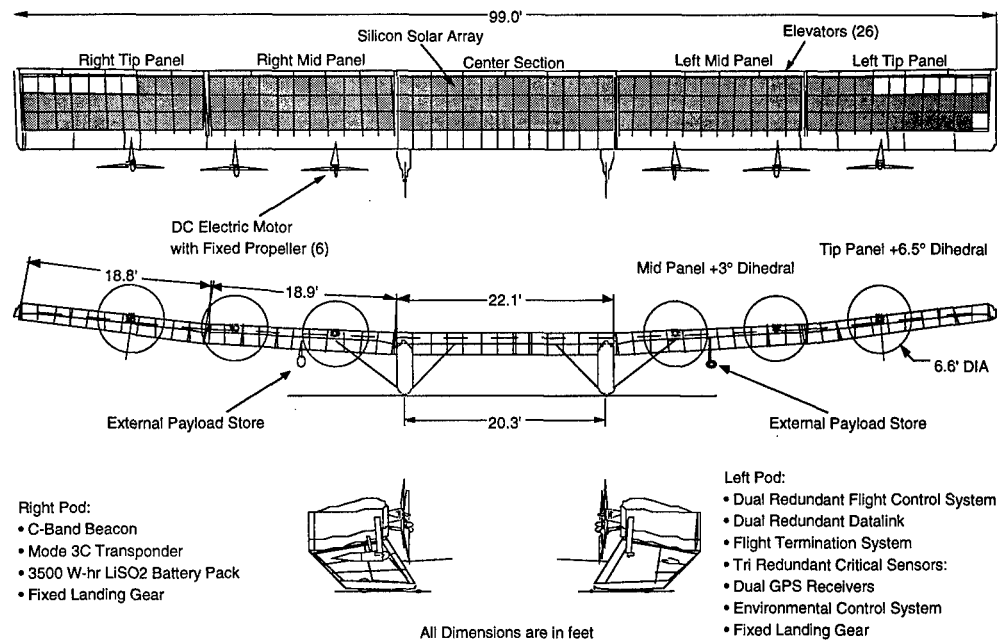
Figure #1 – Pathfinder three view drawing.

Performance Parameter	English	S I
Wingspan	99 ft	30 m
Chord	8 ft	2.4 m
Length	11 ft	3.4 m
Aircraft Weight without Payload(s)	500 lb	230 kg

Maximum Operating Altitude
   Without Payloads
   With 50lb (23kg) Payload
	
	75,000 ft
	49,000 ft
		
		23,000 m
		15,000 m

Typical Flight Speed at 70,000 ft
   Equivalent
   True
	
	28 ft/sec
	115 ft/sec
		
		8.4 m/sec
		35 m/sec

Average Vertical Climb Rate from Sea Level to 41,000 ft	Up to 200 ft/min Depending on Mission	Up to 61 m/min
"Best Glide" Sink Rate (Equivalent) Maximum Sink Rate (Equivalent)	64 ft/min. 138 ft/min.	19.4 m/min. / 0.32 m/sec 42 m/min. / 0.70 m/sec
Turn Rate (max.)	3 deg/sec @ SL 1.7 deg/sec @ 60,000ft	3 deg/sec @ SL 1.7 deg/sec @ 18,300 m
Bank Angle (max.)	5 degrees	5 degrees

Table #1 – Pathfinder technical specifications.

5. AUTOMATIC FLIGHT CONTROL SYSTEM

5.1 Stability and Control Issues

Several design features of solar electric aircraft such as Pathfinder make flight control system design very challenging. Since there is relatively little solar power available, these aircraft must be very lightweight for their size. This and the flying wing design mean a very low wing loading (0.7 psf, about the same as a small bird). Due to this lightweight, at low altitude unsteady effects due to the apparent mass of the air surrounding the aircraft are important; in heave the additional apparent mass of the air amounts to 380 pounds, a very large fraction of the aircraft gross weight of 540 pounds. The apparent mass tensor is very geometry dependent; in yaw or plunge, for example,

the apparent mass is negligible. A light wing loading also means that the aircraft flies very slowly (about 28 feet per second is a normal cruise speed). This means that wake history effects are important; and in combination with unsteady effects, aerodynamic coefficients that are normally neglected can have significant contributions.

Low speeds and high altitudes also combine to make low Reynolds number aerodynamics very important in the overall design, non-linear Reynolds number effects at high altitude contribute to unusual aerodynamic results, and are suspected of preventing a climb to higher altitudes during the record flight in 1997.

Being a lightweight structure, Pathfinder derives much of its strength and load alleviation from flexibility; the structure deflects vertically about 6 feet at the wingtips in

going from stationary on the ground to normal 1-g flight. This flexibility, along with washout in the wingtips, means that dihedral angle is a very strong function of both load factor and airspeed. Being primarily a span loader, Pathfinder is also torsionally very flexible, non-linear aero-elastic effects are therefore predominant throughout the flight envelope of the aircraft.

Power also has a large affect on the aircraft, a large percentage of the wing is in a propeller slipstream and the thrust line is high above the vertical center of gravity. In addition to throttle position, motor power is a function of solar array output. This power output is a function of the sun angle on the array (which is a function of heading, airspeed, load factor, turn rate, time of day, time of year, and latitude), the number of clouds, the Albedo of earth below, and the temperature. In short, control system design must consider many different variables that would typically not be considered important.

5.2 Control System Description

Pathfinder is remotely piloted through a dual radio frequency data link for communicating with the aircraft's automatic flight control system (AFCS) as shown in Figure 2. The dual-redundant airborne AFCS consists of two identical flight computers, uplink receivers, downlink transmitters, a triply redundant suite of sensors, and dual GPS receivers. The design objective was to allow for any single point failure and still return to base safely.

During normal flight, a "waypoint mode" outer control loop allows the AFCS to fly the RPA autonomously to any one of 100 pilot-selected waypoints using GPS position data.

A simplified block diagram of the flight control system architecture used on Pathfinder is shown in Figure 3. Fundamentally, the system uses proportional and integral (PI) feedback loops on pitch rate and airspeed in the longitudinal axis and yaw rate and heading in the lateral axis. A feedforward loop of throttle to elevator (not shown) alleviates the nose down pitching moment associated with the high thrust line.

Gains used in the AFCS are scheduled with altitude by multiplying the sea-level gain by σ^n, where σ is the density ratio at the current altitude and n is an altitude schedule predefined individually for each gain. For example, at 60,000 feet, $\sigma = 0.094$, so an altitude schedule n = -0.25 for Kui would represent a total multiplier of $0.094^{-.25} = 1.81$ (+5.2 dB) at 60k'.

A set of four, three-position gain switches on the pilot's controller are programmed prior to flight to encompass as much of the expected gain change requirements as possible.

5.3 Computer Simulation

All of the above unsteady, aerodynamic, aero-elastic, and power affects combine to make Pathfinder a difficult aircraft to reliably simulate prior to high altitude flights. A 6-degree of freedom (6DOF) quasi-non-linear numerical simulation was developed prior to the early 1995 flight test series to predict initial gains and gain scheduling and to develop and practice the in-flight frequency sweep testing technique described below.
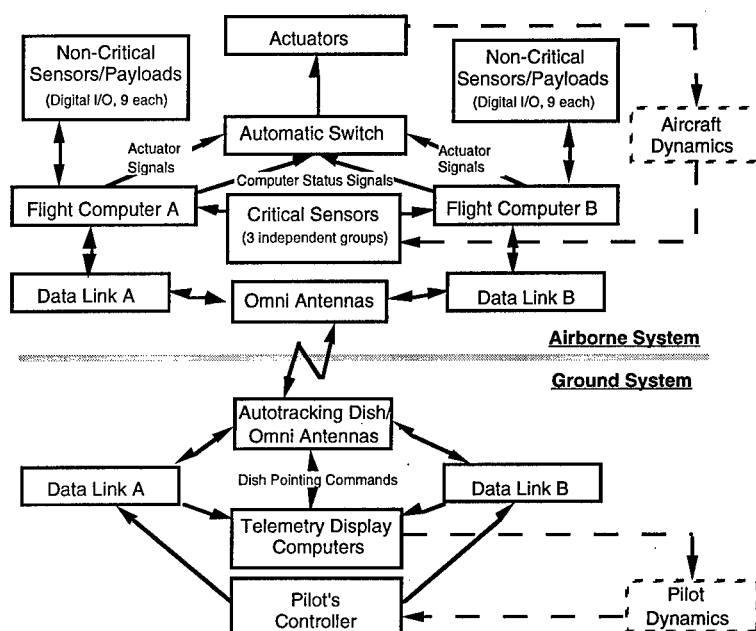

Figure #2 – Pathfinder control architecture.

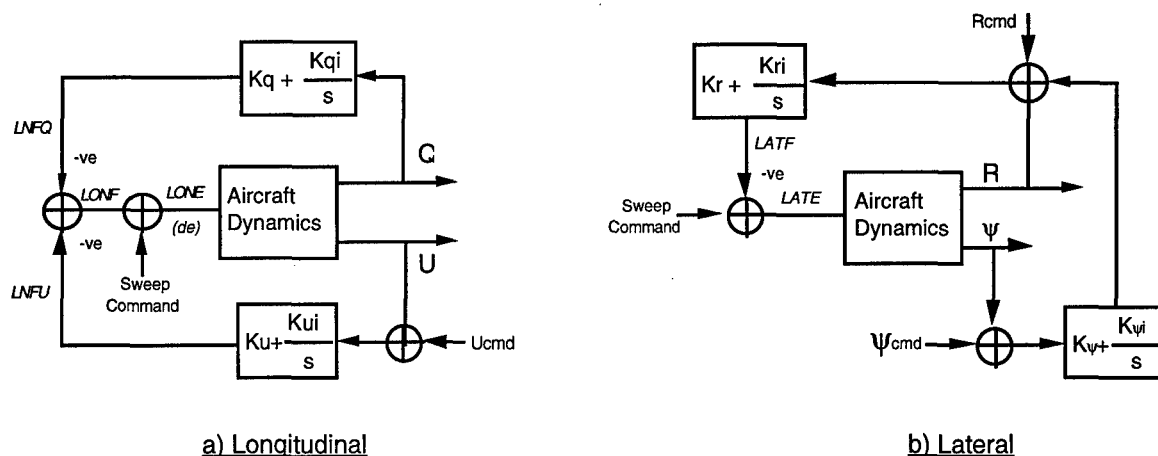a) Longitudinal   b) Lateral

Figure #3 – Pathfinder automatic flight control system architecture.

After initial low altitude flights, post-flight system identification greatly improved the accuracy and prediction capability of the simulation (See Figure #4). This prediction capability allowed gain schedules to be established with enough accuracy that the pilot's controller switches could be used to make the relatively minor gain corrections required during subsequent high altitude flights.

Currently, the simulation continues to be updated using the latest available flight test data in an attempt to better predict future flight test results, to help understand control anomalies discovered during flight testing, and to reliably assess the potential impact of developmental changes in the airframe and AFCS.

5.4 In-flight Control System Testing

To accomplish repeatable frequency sweep stability testing during flight, "Sweep Waypoints" were programmed into the AFCS prior to each flight, each waypoint number corresponding to a given type and amplitude of excitation on a given control input. Figure #5 presents a time history plot for a longitudinal frequency sweep performed during the high altitude 97-2 flight at 30,000 feet altitude and 28 fps EAS. Note the relative lack of off-axes response, and that all testing was performed with the AFCS fully active, thus the commanded and actual control positions do not correspond, due to control system feedback.

Downlinked sweep data is collected and analyzed in the stationary GCS using the CIFER®[2] analysis code running on a DEC MicroVAX computer. Results are displayed, printed out, and compared with computer simulation and predicted responses. This procedure takes about 10 to 15 minutes to complete, from the time the sweep is started to having final results available for analysis.

Normally, longitudinal and lateral frequency sweep tests are performed at about 10,000-foot altitude increments during the entire ascent phase of the flight. Flight conditions and sweeps used for these test points are kept the same (except for altitude), so that trends can be established and gain changes made before stability margins degrade to a dangerous level. For post-flight analysis and system identification, numerous additional test points are flown, each at a different condition of speed, power, altitude and excitation amplitude. On a typical flight, anywhere from 5 to 50 frequency sweeps will be performed, depending on the goal of the mission.

5.5 In-flight Stability Analysis Results

In-flight real-time stability analysis has shown itself to be a valuable tool in allowing flights to high altitude without the traditional requirement of many successively higher flights with post-flight analysis between each.

Using the data from Figure #5 and the above noted procedure, a longitudinal broken loop frequency response can be obtained. This response represents the transfer function from (for example) the LONE and LONF signals noted on Figure #3a. Such a response is shown in Figure #6 as the thin solid line. Note that the coherence is high in the crossover region for all cases, which is generally true for all frequency responses used for analysis.

From these broken loop responses we can establish the gain and phase margins in the usual way. During the climb to high altitude, longitudinal stability margins remained fairly constant, with gain margins between 5 and 7 dB (increasing with altitude), phase margins between 45 and 85 degrees (increasing with altitude), crossover frequencies between 1 and 3 rps (decreasing with altitude) and 180 degree crossover frequencies of about 4 to 6 rps (also decreasing with altitude). It appeared that some additional longitudinal gain could be added at higher altitudes, providing better control and improving the flight control systems ability to damp out increasingly unstable open-loop longitudinal dynamics.
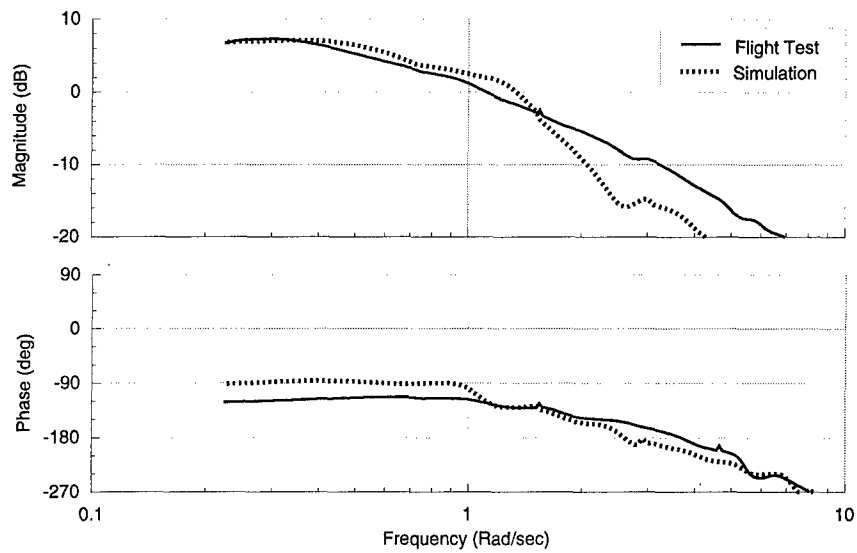
Figure #4 – Typical comparison of simulation and flight test lateral frequency response Bode plots.
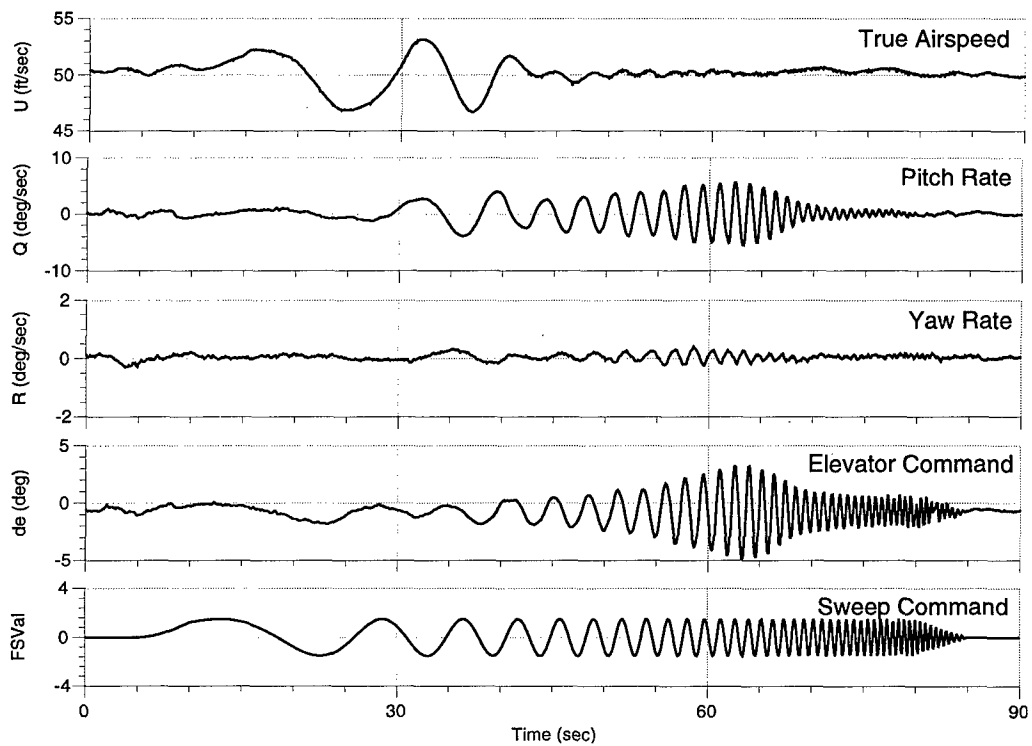

Figure #5 – Typical time response plot for elevator (longitudinal) frequency sweep.
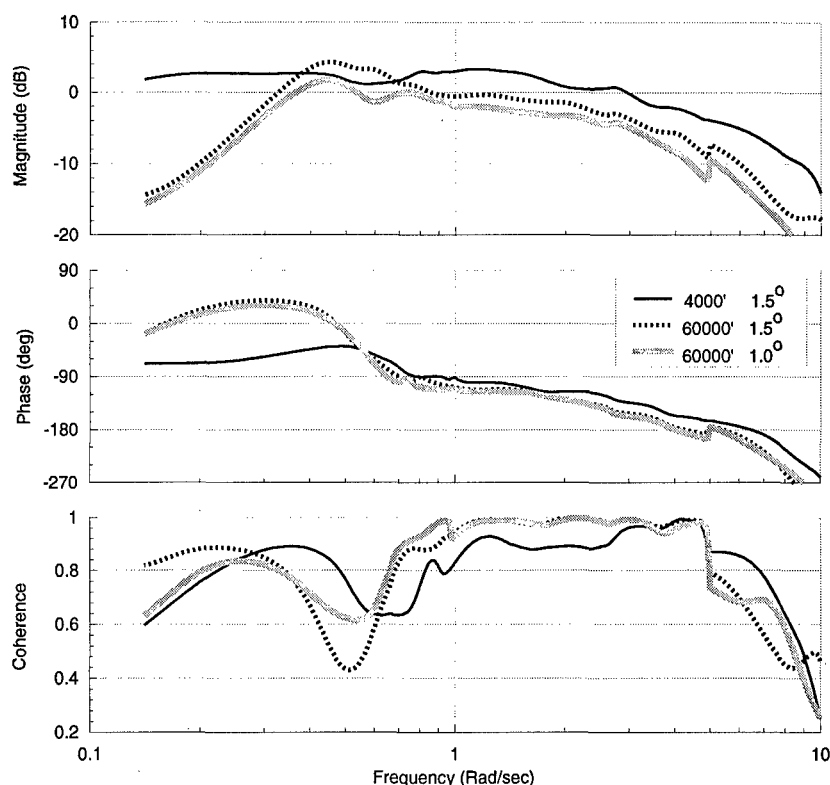
Figure #6 – Typical longitudinal broken loop (LONE-LONF) frequency responses. Note changes with altitude and excitation amplitude.

A typical lateral broken loop (LATE to LATF in Figure #3b) frequency response is shown in Figure 7. Lateral stability margins are fairly consistent; with gain margins between 15 and 16 dB (almost constant with altitude), phase margins between 45 and 65 degrees (decreasing with altitude), crossover frequencies between 0.5 and 0.8 rps (decreasing with altitude), and 180 degree crossover frequencies of about 2.3 to 3.8 rps (also decreasing with altitude). The decreasing lateral phase margin was

somewhat problematic, although it was decreasing at a slow enough rate that at 71,000 feet altitude it was not yet a problem.

Lateral gain margins are kept very high due to internal motor power electronic rate limits. It was feared that this could lead to limit cycle behavior, although due to poor handling qualities during landing, the gains have since been increased several dB at low altitude with no ill effects.
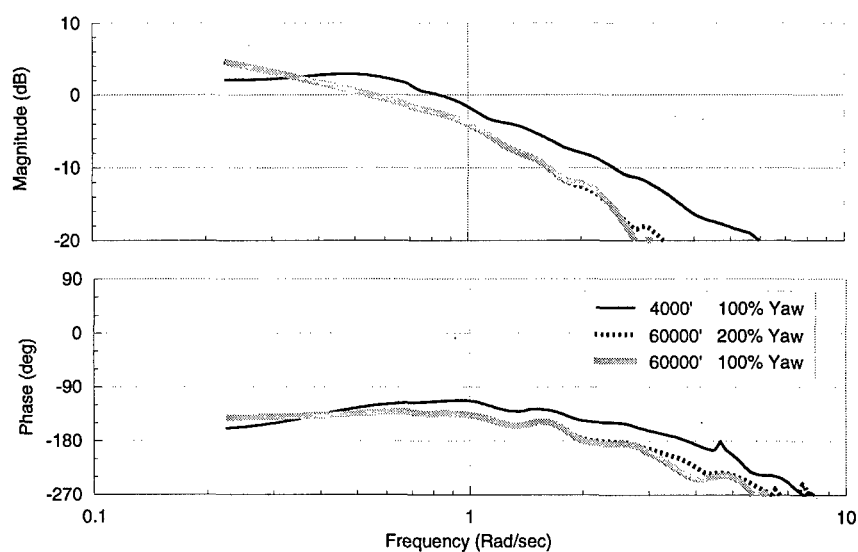

Figure #7 – Typical lateral broken loop (LATE-LATF) frequency responses. Note changes with altitude and excitation amplitude.

5.5.1 *Altitude Effects*

Typical altitude effects on the broken loop responses can also be seen in Figure #6 and Figure #7 as the wide gray line, which represents the response at an altitude of 60,000 feet. High altitude is characterized by reduced open loop damping, reduced phase margins, and a requirement for correspondingly low control system authority.

5.5.2 *Hysteresis Estimate*

To better establish the effects of non-linearity's and hysteresis inherent in the system, frequency sweeps of different excitation amplitudes can be used. Figure #6 gives a comparison of two longitudinal frequency sweeps of different amplitudes at an altitude of 60,000 feet. The difference in the magnitude response indicates about 0.5 degrees of hysteresis in the elevator system. In the lateral direction (Figure #7), there is obviously very little effect of hysteresis.

5.5.3 *Power Effects*

Pathfinder relies on differential power for lateral control. During the descent, lateral sweeps were performed at different power settings to evaluate the available lateral control authority. Results can be seen in Figure #8. Note the large change in magnitude response, with much reduced control authority at low power settings. This is obviously problematic during the descent phase, when power levels are low. Scheduling of lateral control system gains with power level has been considered, but, as noted above, power is a very strong function of sun angle (which varies with heading, for example), making this control architecture very difficult to analyze; it was feared that large dynamic transients in the lateral control system

could develop, so the gains were compromised to be suitable for both high and low power cases, with the pilot able to selectively increase or decrease gains as required.

5.5.4 *Airspeed Effects*

At higher airspeeds, Pathfinder tends to lose much of its dihedral due to the washout in the wingtips forcing the tips to blow down. Airspeed could therefore be expected to have a significant effect on lateral frequency response. Figure #9 presents a comparison of two frequency responses at the high and low ends of the airspeed envelope. It appears that power (Figure #8) has a much larger influence on lateral control than does airspeed, although there is some reduced control authority and phase margin at the higher airspeeds.

5.6 Post-flight Analysis

One of the first tasks after a high altitude flight is to assess gain changes (if any) that were required during the flight and to evaluate the as-flown stability margins. Changes to the gains, or gain re-scheduling, is then done to eliminate these changes on future flights, reducing flight crew workload.

Stability or handling qualities issues are then addressed. Handling qualities during landing became an issue when operations were switched from Edwards dry lake in California, with a 1-mile diameter landing target, to PRMF in Hawaii with a 150-foot wide runway. Post-flight analysis using CIFER®[2] indicated that more lateral gain and higher lateral rate limits could likely be tolerated at low altitudes, subsequent flights using higher gains and rates gave improved handling qualities.
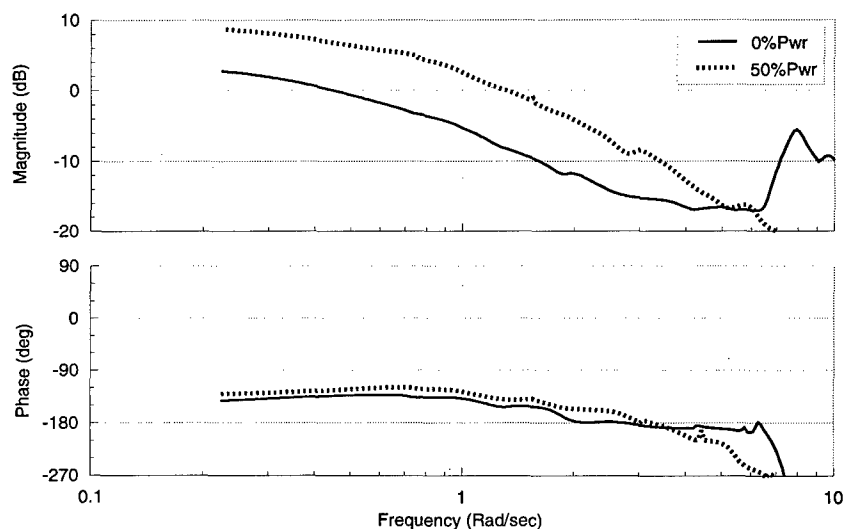

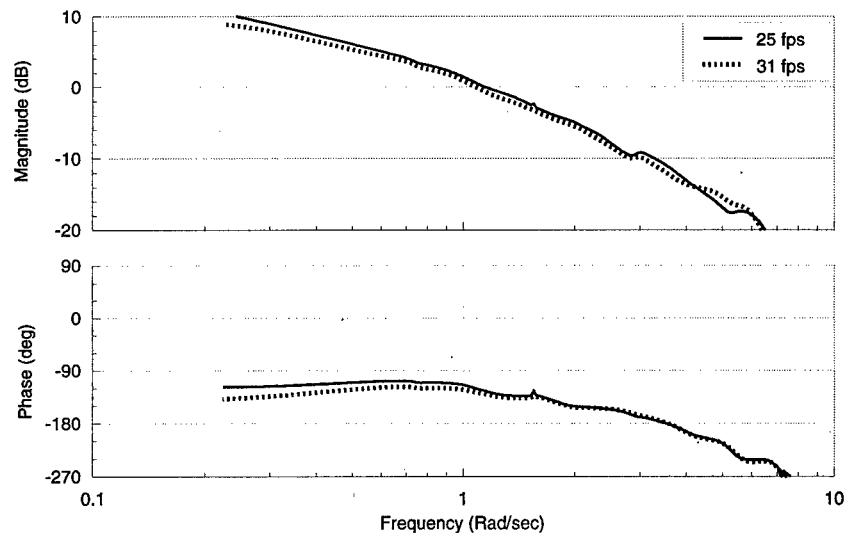Figure #8 – Effect of power setting on lateral broken loop responses.

Figure #9 – Effect of airspeed on lateral broken loop responses.

Stability problems encountered during the flights are also investigated. As an example, during the high altitude flight on July 7th, after the 180° turn, power reduction and initial descent from the peak altitude of 71,500', an uncommanded roll oscillation occurred. This was a coupled pitch/yaw/roll instability (or "wallowing" similar to a Dutch roll but with large sideslip component) of about a 20 sec period that had a maximum amplitude of about 12° roll angle. During the remainder of the 97-2 flight and in successive flights, extensive frequency sweep testing was performed to investigate the effects of altitude, gain setting, and power levels on the aircraft's lateral dynamic characteristics. Likely causes for the uncommanded oscillation near peak altitude include dynamic coupling with the magnetic compass, coupling between lateral and longitudinal axes, propeller or wing Reynolds number

nonlinear effects, motor rate limits, or propeller tip stalling at low airspeeds.

Although the aircraft was flown safely and exhibited generally excellent handling qualities in all of the 1997 flights, additional stability and control analyses are being performed in an attempt to better characterize flight test results.

Another use of in-flight frequency sweep testing is for post-flight system identification. As an example of one technique, frequency sweep results have been used to identify the open loop frequency responses LATE/R and LATE/ψ (Figure #3b), which can then be used either directly or in the 6DOF computer simulation model. Using the known control system gains in the feedback paths, the frequency responses R/LATF and ψ/Rcmd can be determined analytically and their frequency responses synthesized.
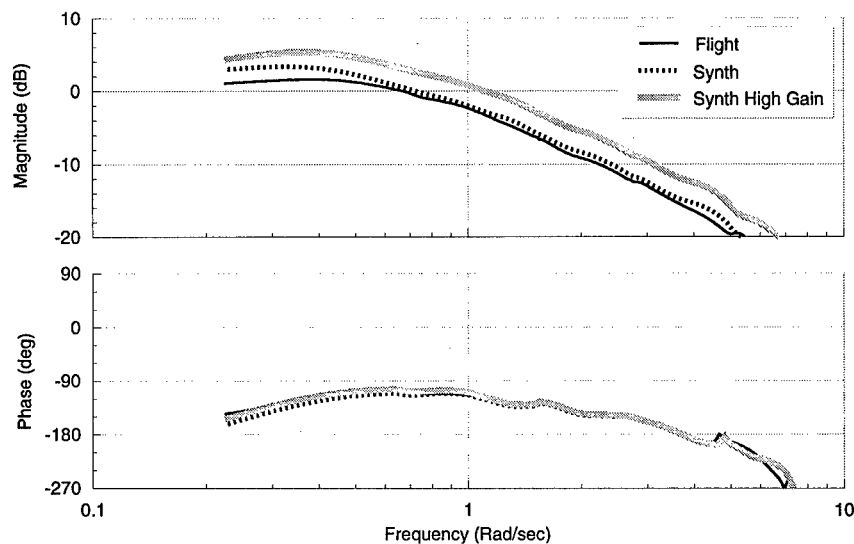

Figure #10 – Illustration of synthesized broken loop responses in comparison to flight test results.

Using the measured open loop responses and the "synthesized" control system responses, an overall analytical broken loop response can be calculated directly and compared to the flight test broken loop response, as shown in Figure 10; note that the agreement is very good in the region near crossover. The measured in-flight open loop responses, or the computer model, can then be used to test additional experimental control system configurations with different gains, gain schedules or loop architectures, as illustrated by the wide gray line in Figure #10, which represent the predicted lateral response in the high gain setting of the pilots controller. This response compares well with that obtained during flight.

7. CONCLUSIONS

Continuing changes to airframe and flight control systems require continued use and improvement of frequency response and system identification tools and techniques. During the summer of 1998, NASA and AeroVironment plan to fly an upgraded Pathfinder on several high altitude missions above 80,000 feet from the Pacific Missile Range Facility, Kauai. For this new aircraft, dubbed "PathfinderPlus", changes include replacing the center wing section with a 20-foot longer section incorporating the Centurion aircraft airfoil, new higher efficiency solar cells, and higher efficiency propellers and electric motors. Such rapid evolution necessitates the use of rapid analysis and design techniques, and makes in-flight identification and testing vital to continued flight safety.

The success of the recent Pathfinder flight test program validated many of the enabling technologies required for high altitude, long duration flight, as well as demonstrating that solar airplanes can be used for beneficial and meaningful science missions. Integral to this success, engineering models and control system analysis techniques proved capable of predicting and rapidly evaluating the performance of Pathfinder's systems to a high degree of accuracy throughout the entire flight envelope. The extensive amount of aerodynamic and control system data, system performance data, and operational experience that was gained during the 1997 deployment will aid with the development of the 100,000 foot altitude Centurion solar aircraft to be flown in 1999 and the multi-week duration Helios solar aircraft to be flown in 2002.

7. AKNOWLEDGEMENTS

7. REFERENCES

1. Baer-Riedhart, J., "NASA Environmental Research Aircraft and Sensor Technology Program," Aerospace America, January 1998.

2. Tischler, M.B. , Cauffman, M.G., "Frequency-Response Method for Rotorcraft System Identification: Flight Applications to BO-105 Coupled Rotor/Fuselage Dynamics," Journal of the American Helicopter Society, Vol 37, No 3, pgs 3-17, July 1992.

3. Cowley, M., Morgan, W.R., and MacCready, P., "Bionic Bat Stored Energy Human Powered Speed Aircraft," AIAA Paper 85-1447, AIAA 21st Joint Propulsion Conference, Monterey, California, July 1985.

4. Mitchell, D.G., and Jex, H..R., "Flight Testing the Gossamer Albatross Human-Powered Aircraft," AIAA Paper 83-2699, November 1983.

5. MacCready, P., Lissman , P., Morgan, W.R., and Burke, J.D., "Sun Powered Aircraft Design," AIAA Paper 81-0916, May 1981.

6. Brown, S., " The Eternal Airplane," Popular Science, April 1994.

7. Morgan, W. R., "Solar Electric UAV's as Atmospheric Repeater Platforms-A Lower Cost Alternative to Satellites," AIAA, 1995.

Direct Update of a Global Simulation Model with Increments via System Identification

D. Rohlf
Institut für Flugmechanik
DLR - Deutsches Zentrum für Luft- und Raumfahrt
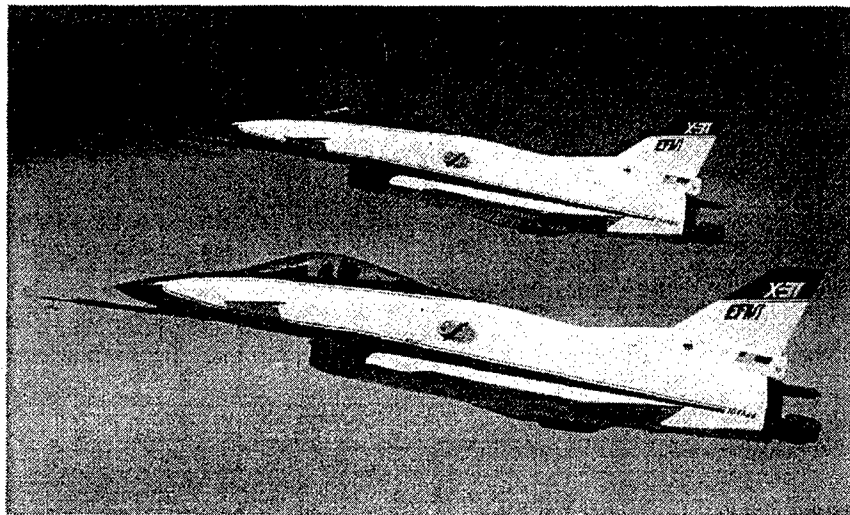Lilienthalplatz 7, 38108 Braunschweig
Germany
eMail: detlef.rohlf@dlr.de

Fig. 1   *The X-31A Twins*

1. SUMMARY

This paper describes a method using system identi-fication for a data base update where the aerody-namic coefficients derived from the original wind-tunnel data base are supplemented by increments. The model update is performed applying a regres-sion method to match the model calculated accel-erations with the in-flight measured accelerations.

The work is based on flight test data of the thrust-vectored research aircraft X-31A. Its simulation model is updated in the entire flight envelope using a representative selection from all flight maneuvers which became available in this project. More than 3000 seconds of flight test are evaluated in one identification run covering an angle of attack re-gime from about -5 deg up to 70 deg and Mach numbers from about 0.2 up to 1.25. A practice flight for the spectacular X-31A demonstration at the Paris Air Show '95 is used for model verifica-tion.

Thrust is calculated from flight measured power lever position using an existing static engine table model. A rate limited first order dynamic engine model with additional time lag to account for after-burner ignition is implemented. Thrust amount and thrust vector effectiveness are estimated separately
for after-burner on and off. Actual c.g.-location, A/C weight and inertia are taken into account based on existing weight and balance data with measured fuel quantity as input. The latter is corrected for fuel slosh impact depending on tank filling ratio and translational A/C accelerations.

2. INTRODUCTION

System identification has been proven many times to be a valuable tool for verification and update of aircraft simulation models [1]. The aerodynamic data base is usually derived from wind-tunnel measurements and supplemental calculations. If deviations of the aircraft aerodynamics from the data base predictions are obvious, they have to be incorporated into the simulation model. This might, consequently, require modifications of the flight control system gains in case of an highly augmented aircraft such as the X-31A.

The two X-31A demonstrator aircraft (Fig. 1) built by Rockwell International and Daimler-Benz Aero-space [2,3] are the first international aircraft in the famous series of 'X-Planes'. Since their maiden flight in 1990 both experimental aircraft have flown more than 500 flights. The concept of enhanced fighter maneuverability in the post stall (PST) flight

regime by utilizing thrust vectoring and the resulting tactical advantage have been demonstrated impressively. The X-31A gave one of the most spectacular flight demonstrations at the Paris Air Show 1995.

The DLR Institute of Flight Mechanics participated in the X-31 program by contract of the German Ministry of Defense / Federal Office of Defense Technology and Procurement (BMVg / BWB). Besides contributions to the analysis of handling qualities, a DLR project team focused on the identification of aerodynamic parameters from flight test data (PID). Although the X-31 flight test program was completed some years ago, precious data are waiting for detailed analysis after the work which supported the project during the flight test program.

3. BACKGROUND

3.1 The Post Stall Demonstrator X-31A

The X-31A is an aerodynamically unstable delta wing aircraft with canard. Its wing span is 7.3 m and the fuselage measures 12.8 m in length (Fig. 2). The primary control surfaces for the longitudinal axis are symmetrical trailing-edge flaps and canard. Differential trailing-edge flaps provide for roll control and a conventional rudder is used for directional control. In addition to the aerodynamic control surfaces, an unique three-paddle thrust vectoring (TV) system is mounted around the engine exhaust nozzle. The TV system augments pitch and yaw control power during low-speed and PST-flight.

The X-31A is powered by a single General Electric F404-GE-400 turbofan engine, producing 70,000 N of thrust with after-burner. A movable inlet provides adequate airflow to the engine at high angles of attack (AoA). Typical take-off weight is about 7,000 kg. Design speed is Mach 0.9 although supersonic cruise capabilities have been demonstrated. The X-31A can fly up to a maximum altitude of about 12,000 m.

3.2 PID During X-31A Envelope Expansion

Mainly during flight envelope expansion into the PST and supersonic flight regime a wide variety of pilot generated maneuvers were flown to investigate handling qualities [4,5]. These maneuvers covered the entire flight envelope up to 70° angle of attack as well as up to supersonic speeds of about Mach 1.2 as shown in Fig. 3. Additionally, some tests were flown at negative angle of attack (push-over maneuvers or inverted flights).

Due to the lack of dedicated PID maneuvers, the pilot generated maneuvers had to be used for PID purposes as well. Not all of the aerodynamic derivatives and control effectiveness parameters could be identified independently from these maneuvers [6] because of strong correlation between aircraft state and control variables. This correlation is caused by the very high flight control system feedback [7] of the basically unstable aircraft.

Later in the program, the X-31 flutter test box (FTB) was modified with a PID-card designed by DLR to separately excite the aerodynamic control surfaces bypassing the flight control system. Using this single surface excitation (SSE), all relevant parameters could be estimated with significantly reduced standard deviations [8,9]. Additionally, PID maneuvers requested by NASA Langley were flown which consisted of level decelerations from about 10° up to 70° angle of attack with randomly distributed piloted doublets to excite either the longitudinal or lateral-directional eigenmotion [10].

4. DIRECT MODEL UPDATE

4.1 Objective

The objective of A/C system identification is to isolate possible deficiencies of an existing data base and to update the simulation model accordingly. In the past, this was done mostly in three steps:

(1) identification of derivatives in linear/nonlinear models describing the aerodynamics at separate reference conditions,

(2) comparison of the results to the original data base, and

(3) update of the data base if necessary.

The now discussed *direct* model update combines these three steps into one. It can be performed progressively during flight envelope expansion estimating only the subset of model parameters already covered by flight test. Therefore, the updated model always covers the entire flight regime using the updated data base in the cleared regime and the original data base in the remainder. The model is applicable to both, small and large amplitude maneuvers. Similar approaches for an aerodynamic data set update have been presented in [11,12].

4.2 PID Procedure

As mentioned before, the X-31A is basically unstable due to its unique aerodynamic design. This instability leads to divergence or even to an overflow in the integration of the state equations when the well-known maximum likelihood (ML) output error method is applied for parameter identification.

Only time slices up to a maximum of 10-15 seconds X-31A flight time can be evaluated. The problem can be overcome by using either an estimation algorithm that stabilizes the numerical integration, or an estimation algorithm that avoids numerical integration. As it is intended to use the direct model update procedure for the evaluation of long-time large amplitude maneuvers, a regression algorithm is applied. The regression method has a second advantage, a considerable decrease of CPU-time compared e.g. to the ML-output error method. Prerequisite for regression are compatible flight test data, i.e. the data have to be checked and if necessary to be corrected for sensor calibrations such as bias and factors. This was done using a flight path reconstruction (FPR) algorithm.

It is not possible to match the aerodynamic coefficients directly as it is usually done when applying a regression method. Not only the aerodynamics, but also thrust amount, thrust vector forces, and corrections to the measured fuel quantity for A/C weight and balance calculations have to be evaluated at the same time. It is therefore necessary to use the accelerations as observation variables. In the mathematical model (Fig. 4), the accelerations are simulated by driving the original data base with flight measured inputs. Increments to the aerodynamic model are then identified together with parameters for thrust model calibration and fuel quantity correction.

4.3 Flight Test Data

For the simulation model update, a selection of flight maneuvers gathered within the X-31 test period of about 5 years is used. The flight test data from the two nearly identical aircraft show some differences due to fabrication tolerances and individual measurement system characteristics. They have to be taken into account for identification as well as the A/C modifications (aft strakes, nose strakes, and noseboom) performed for PST improvement.

To get a representative result covering nearly the entire design envelope with angle of attack from about -5 deg up to 70 deg and Mach number from about 0.2 up to 1.25, more than 3000 seconds of flight test time are gathered for one identification run (Fig. 5). The assembled 70 time slices include:

(1) single surface excitation maneuvers,

(2) deceleration maneuvers with randomly distributed pilot doublet inputs,

(3) pilot doublet inputs at supersonic speed,

(4) pilot doublet inputs with extended speed brakes,

(5) full 360° post stall roll.

As far as available, maneuvers with and without active thrust vectoring (no PST, i.e. maneuvering beyond 30° AoA, without TV) and with after-burner on and off were selected.

4.4 Model Extensions

To get a satisfactory fit for the body-fixed 6-DoF accelerations in the entire X-31 flight envelope, three model extensions were found to be necessary:

(1) correction of the measured fuel quantity for fuel slosh impact (used for subsequent A/C weight and balance data calculations),

(2) implementation and identification of a simplified dynamic engine model accounting for after-burner operation,

(3) incremental update of the aerodynamic coefficients depending on angle of attack and Mach number, performed together with thrust calibration.

These corrections and supplements to the original data base are briefly outlined in the following three chapters.

5. FUEL SLOSH IMPACT ON MEASURED FUEL QUANTITY

It is a prerequisite for aerodynamic system identification to use accurate A/C weight, inertia, and c.g.-location. The X-31A weight and balance calculations uses measured fuel quantity as input.

As shown in Fig. 6, the X-31A fuel tank is built around the engine's air intake tube. This design creates significant nonlinear fuel slosh impact on the measured fuel quantity. It is obvious that fuel slosh depends on translational A/C accelerations. In addition, it was found that the tank filling ratio itself has a nonlinear influence due to the unique fuel tank design.

The fuel slosh impact on measured fuel quantity is illustrated in Fig. 7. Steady heading sideslip (SHSS) maneuvers and deceleration maneuvers covering an entire flight from full to nearly empty fuel tank are shown. As the measured fuel flow does not account for after-burner fuel consumption, the latter is estimated as an additional constant fuel flow. The signal for after-burner operation is provided by the dynamic engine model described in the following chapter.

The sum of both, measured fuel flow and estimated after-burner consumption is numerically integrated to 'true' fuel quantity. The gap to measured fuel quantity is caused by fuel slosh. Accounting for this measurement error leads to the 'faulty' fuel quan-

tity which therefore shows a good fit. For the modeling of the fuel slosh impact, the translational accelerations are used in linear dependence on the tank filling ratio relative to an identified middle filling level.

The fuel slosh not only affects long-duration tests, e.g. deceleration maneuvers, but also short-duration tests at high angles of attack, e.g. pilot doublets for handling qualities investigations. Although the fuel slosh corrections can not be identified from these short time slices, it is necessary to use the 'true' fuel quantity, i.e. corrected fuel quantity, for subsequent weight and balance calculations.

6. ENGINE DYNAMICS AND THRUST ESTIMATION

Thrust is calculated from measured power lever position, Mach number and altitude using an existing static engine model. It had to be augmented by a simple dynamic engine model to match the flight measured longitudinal accelerations. This dynamic model is characterized by:

- *after-burner off:* 1. order dynamics with different time constants and rate limitations for thrust increase and decrease,

- *after-burner operation:* switch with time lag for after-burner on and hysteresis for after-burner on/off

For identification of this engine model, the following observation variables are used which are both, measured and provided by the static engine model:

- Fan- & Core-RPM,

- exhaust nozzle area & pressure ratio.

Fig. 8 shows the time histories of some typical flight tests without after-burner. Overall, the engine dynamics are well reproduced, only the overshoot in Fan-RPM can not be modeled correctly by the 1. order system. In addition to the engine dynamics, the calculated gross thrust contains a calibration factor which was necessary to achieve a good fit for the longitudinal acceleration.

Fig. 9 shows the time histories of a continuous level deceleration & acceleration maneuver with randomly distributed piloted pitch doublets. The after-burner is ignited during the test to provide sufficient power for post stall flight. To obtain a good fit for the longitudinal accelerations, it is necessary to implement a time delay which accounts for after-burner ignition. This time delay can clearly be seen by comparing the measured power lever to the calculated power lever signal, the latter includes the engine model dynamics.

Correction factors for calculation of thrust amount and thrust vector effectiveness are estimated separately for after-burner on and off.

7. AERODYNAMIC COEFFICIENT UPDATE

The aerodynamic data set is updated by determing increments to the original data set that depend on angle of attack and Mach number. The increments are calculated from derivative tables using non-equidistant breakpoints which are estimated together with all other model parameters:

- *Angle of attack:*

  - regime: -5° to 75°,

  - 10 breakpoints,

- *Mach number:*

  - regime: 0.25 to 1.3,

  - 5 breakpoints.

At Mach numbers below 0.25 (corresponding to AoA above about 30°), the incremental model freezes Mach effect and depends only on angle of attack.

It would not be suitable to use equidistant table breakpoints because, on one hand, the X-31A aerodynamic data set covers an extended envelope and, on the other hand, the essential changes in the coefficients are concentrated on some smaller areas. Although the start values for the breakpoints were equidistant, the final breakpoint estimates are concentrated in the areas with great changes in the aerodynamics. The estimated breakpoints show no correlation and small standard deviations.

In additional to angle of attack and Mach number, the following variables are inputs to the derivative tables for incremental model update:

- *longitudinal motion:*

  pitch rate (q), canard (δ_{CAN}), symmetrical trailing edge flap (δ_{TEsym}), and leading edge flap δ_{LE},

- *lateral-directional motion:*

  angle of sideslip (β), roll rate (r), yaw rate (p), differential trailing edge flap (δ_{TEdif}), and rudder (δ_{RUD}).

Leading edge flap deflection δ_{LE} is a function of angle of attack. Nevertheless, the leading edge flap effectiveness can be estimated uncorrelated to AoA parameters applying multi-point evaluation for the entire flight envelope. In the case of single-point

evaluation, this separation from angle of attack effects is not possible.

Speed brake and gear effects are included in the incremental model but not addressed in this paper. Two results are presented and compared to those from the PID during envelope expansion flight phase.

7.1 Results: Lift and Drag

Single-point evaluation: During X-31 envelope expansion, identification was performed using single-point evaluation (single maneuver with pilot inputs and/or single surface excitation). Fig. 10 shows the PID-results for lift and drag coefficient, CL_{trim} and CD_{trim}, compared to their predictions from the original data set. The model derivatives were estimated from the trimmed steady state conditions. The coefficients therefore contain the increments of the trimmed aerodynamic control surface deflections (TV is not used for trim). The identification was performed using thrust as calculated from the static engine model and using measured fuel quantity for the calculation of A/C weight, inertia and c.g.-location. Lift and drag coefficients are therefore affected by possible measurement and/or thrust model errors.

Multi-point evaluation: In the case of multi-point evaluation, parameters for thrust model calibration and fuel quantity correction are estimated from flight data together with the aerodynamics as described before. Fig. 11 shows the basic lift and drag coefficients (i.e. untrimmed in contrast to Fig. 10), CL_{basic} and CD_{basic}, for the original and the updated data set. The identified AoA table breakpoints are also shown. Both coefficients, for lift and drag, show generally higher values than predicted. This is mainly a result from the thrust modification described in chapter 7. The thrust modification affects both, lift and drag. Due to the transformation from body-fixed coordinates to the aerodynamic coordinate system, the effect of thrust on lift increases while the effect on drag decreases with increasing AoA.

7.2 Results: Dihedral Effect

Single-point evaluation: Fig. 12 shows the dihedral derivative $Cl\beta$ plotted versus angle of attack. The PID results from single-point evaluation are compared to $Cl\beta$ from the original data set. The PID results do not confirm the large negative values from wind-tunnel tests at angles of attack between 30 and 45°. During the envelope expansion flight phase, the aerodynamic database for the X-31 was updated for angles of attack up to 50° and the dihedral derivative was changed as shown (PID2 up-

date, 1993). This update was based on single maneuver PID only which shows relative large scatter and uncertainty levels.

Multi-point evaluation: Fig. 13 compares the results of the incremental table model identification to the original data set. Again the AoA table breakpoints are presented. When the identified increment $\Delta Cl\beta$ is added to the large negative $Cl\beta$-values from the wind-tunnel predictions, the resulting updated data set is very close to the results from single-point evaluation shown in Fig. 12. Only the peak at about 45° AoA deviates significantly. This may be caused by linear interpolation between the two relatively wide separated α-breakpoints at about 38° and 49° AoA.

8. MODEL VERIFICATION

Practice maneuvers for the Paris-Air Show are used for model verification. Fig. 14 presents flight test and identification model output for a complete 6 min. flight, which was flown at Edwards Air Force Base in California, USA. The four highlights of the flight demonstration are: (1) *PST-Loop* (loop with pull-up into PST before the vertex), (2) the *Mongoose* maneuver (like the well-known *Cobra* maneuver but with additional yawing in PST), (3) the *Herbst-Turn* (pull-up into PST followed by a small radius turn), and a second loop, (4) the *Heli-Loop* (PST-Loop with a PST-roll reversal maneuver in the recovering phase). Start and landing phases are presented only for completion; on-ground operations before lift-off and after touch-down are not yet completely implemented into the identification model.

Fig. 14 shows power lever angle (again in-flight measured pilot command and model output including engine dynamics), altitude, Mach number, and angle of attack as used as input for the simulation with the updated data base. To prove the data base quality, the accelerations characterizing the longitudinal A/C-motion are presented. Longitudinal and normal accelerations show a good fit during the entire flight. The fit of the pitch acceleration shows less quality in some flight phases caused either by aerodynamics, or by not yet modeled thrust interference. Here, more detailed investigations remain to be done.

Although, the direct model update procedure using regression has the potential for model verification it is indispensable to use simulation with numerical integration for the validation of the updated model.

9. CONCLUSIONS

The presented approach of direct simulation model update uses the original wind-tunnel based data set as a basis. Incremental aerodynamic coefficients are identified and supplemented only where necessary. The entire flight envelope is covered and can be updated step by step estimating only those parameters which correspond to the angle of attack and Mach regime covered by flight tests. Therefore, this procedure may be of special interest to the identification during the envelope expansion of a new aircraft. Direct determination of the deficiencies of the existing data base is provided. The procedure is applicable to small and large amplitude maneuvers and can also be used for model verification.

As a regression algorithm is applied, compatible flight test data are required. Evaluating X-31A aerodynamics, additional prerequisites are: (1) the correction for fuel slosh impact on measured fuel quantity to be used for weight and balance calculations and (2) the implementation of a simplified dynamic engine model which accounts for afterburner operations. Thrust amount and thrust vector effectiveness have to be evaluated together with the aerodynamic increments. The comparison of the results to those from former single-point evaluation show good corresponding results for the derivatives which are not directly affected by thrust, e.g. the dihedral derivative $Cl\beta$.

The presented results are not yet final and some improvements still remain to be done. This refers e.g. to the modeling of instationary aerodynamics including hysteresis at separated flow conditions and some deficiencies in pitch acceleration caused by not yet modeled aerodynamics, or by thrust interference effects.

10. ACKNOWLEDGMENTS

11. REFERENCES

[1] Hamel, P.G. and Jategaonkar, R.V.: *Evolution of Vehicle System Identification.* Journal of Aircraft, Vol. 33, No. 1, Jan.-Feb. 1996, pp 9-28.

[2] Robinson, M.R. and Herbst, W.B.: *The X-31A and Advanced Highly Maneuverable Aircraft.* 17th ICAS Congress, Stockholm, Sweden, 1990, Proceedings Vol. I.

[3] Ross, H.: *X-31 Enhancement of Aerodynamics for Maneuvering beyond Stall.* AGARD-CP-497, Nov. 1991, Paper No. 2.

[4] Huber, P. and Galleithner, H.: *Control Laws / Flying Qualities and Flight Test Results.* High-Angle-of-Attack Projects and Technology Conference, NASA Dryden Flight Research Center, April 21-23 1992, NASA-CP-3137, Vol. 1, pp. 171-188.

[5] Huber, P. and Schellenger, H.: *X-31 Flugeigenschaften im Hochanstellwinkelbereich.* DGLR Jahrestagung, Paper 94-C4-056, Erlangen, Oct 4 - 7, 1994, pp. 429 - 436.

[6] Weiss, S., Plaetschke, E., Rohlf, D., and Galleithner, H.: *System Identification for X-31A Project Support - Lessons Learned so far.* AGARD FMP Symposium "Flight Testing", Chania, Crete, Greece, May 11-14 1992, AGARD-CP-519, Paper No. 14.

[7] Beh, H. and Hofinger, G.: *Control Law Design of the Experimental Aircraft X-31A.* 19th Congress of the International Council of the Aeronautical Sciences, AIAA, Paper ICAS 94-7.2.1, Anaheim, CA, 18. - 23. Sept., 1994.

[8] Friehmelt, H., Weiss, S., Rohlf, D., and Plaetschke E.: *Using Single Surface Excitation for X-31 System Identification at High AoA.* Proceedings of the 26th Annual Symposium of the Society of Flight Test Engineers, Berlin, June 19.23, 1995, pp 4.51-4.62.

[9] Weiss, S., Friehmelt, H., Plaetschke, E., and Rohlf, D.: *X-31A System Identification Using Single Surface Excitation at High Angles of Attack.* Journal of Aircraft, Vol. 33, No. 3, May-June 1996, pp 485-490.

[10] Plaetschke, E., Weiss, S., Rohlf, D.: *Comparison of Parameter Identification Results from Pilot and Flutter Test Box Input Maneuvers.* DLR-IB 111-95/15, 1995.

[11] Neville, K. W. and Stephens, A. T.: *Flight Update of Aerodynamic Math Model.* AIAA Flight Simulation Technologies Conference, Paper 93-3596, Monterey, CA, Aug. 9.-11., 1993.

[12] Trankle, T. L. and Bachner, S. D.: *Identification of a Nonlinear Aerodynamic Model of the F-14 Aircraft.* Journal of Guidance, Control, and Dynamics, Vol. 18, No. 6, Nov.-Dez. 1995, pp. 1292-1297.

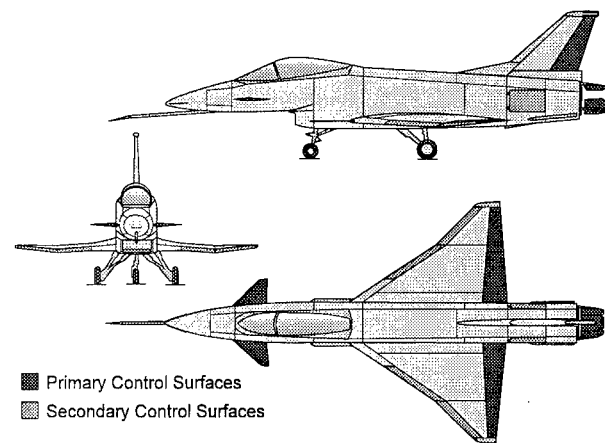## 12. FIGURES

Fig. 1 *The X-31A Twins (see front-page)*

Fig. 2 *Three-view Drawing of the X-31A*

Primary Control Surfaces
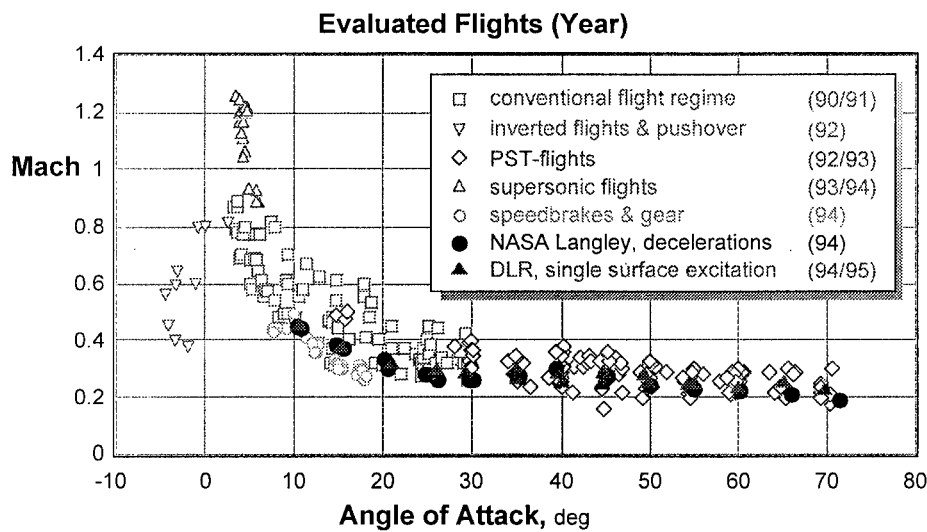Secondary Control Surfaces

Fig. 3 *X-31 Flight Tests used for Envelope Expansion PID*
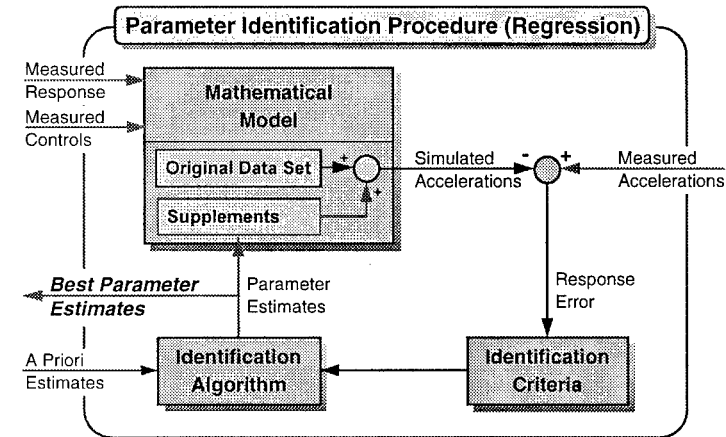
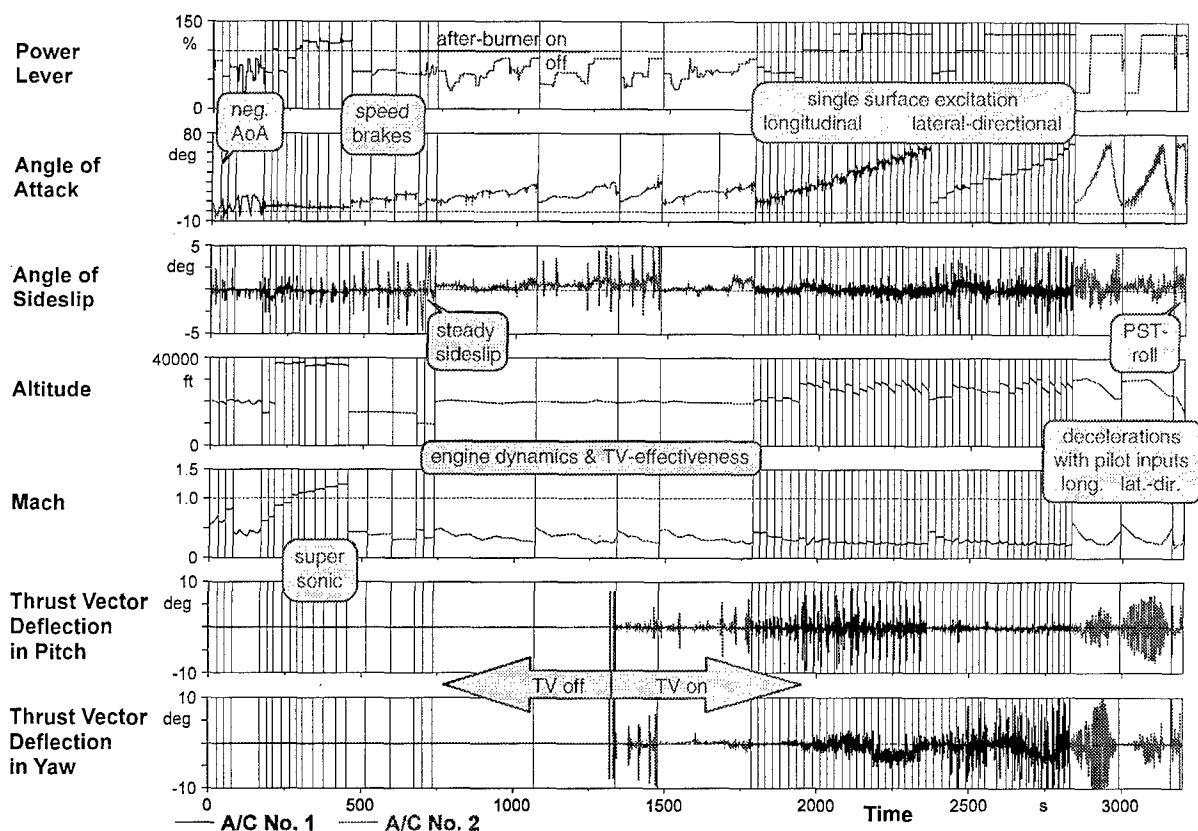**Fig. 4** *Parameter Identification Procedure for Direct Data Set Update*
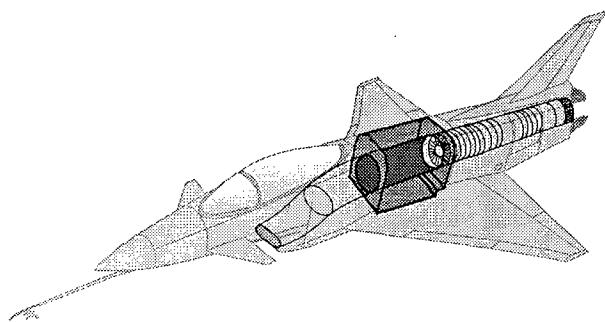
Fig. 5 *X-31 Flight Test Data for Multi-Run Evaluation*
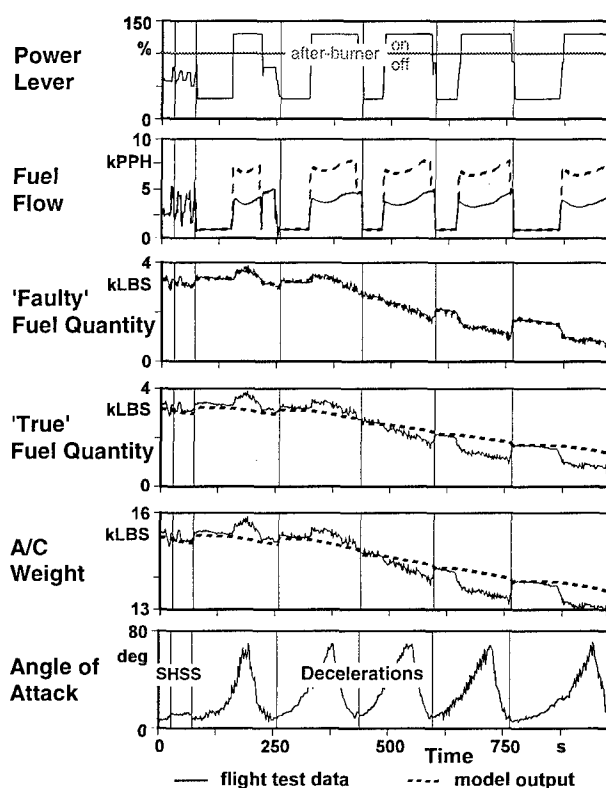

Fig. 6 *Scetch of X-31A Fuel Tank Integration*
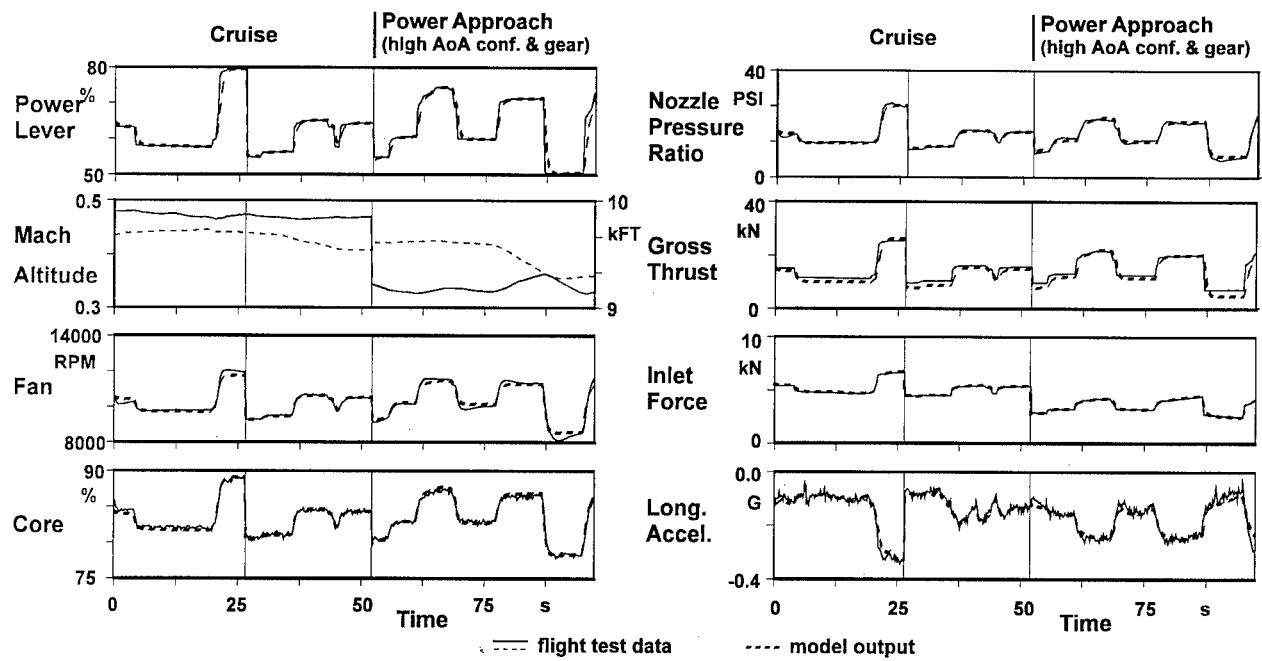

Fig. 7 *Fuel Quantity Estimation and A/C Weight Calculation*

Fig. 8 *Low Order Engine Dynamic Estimation (After-Burner off)*
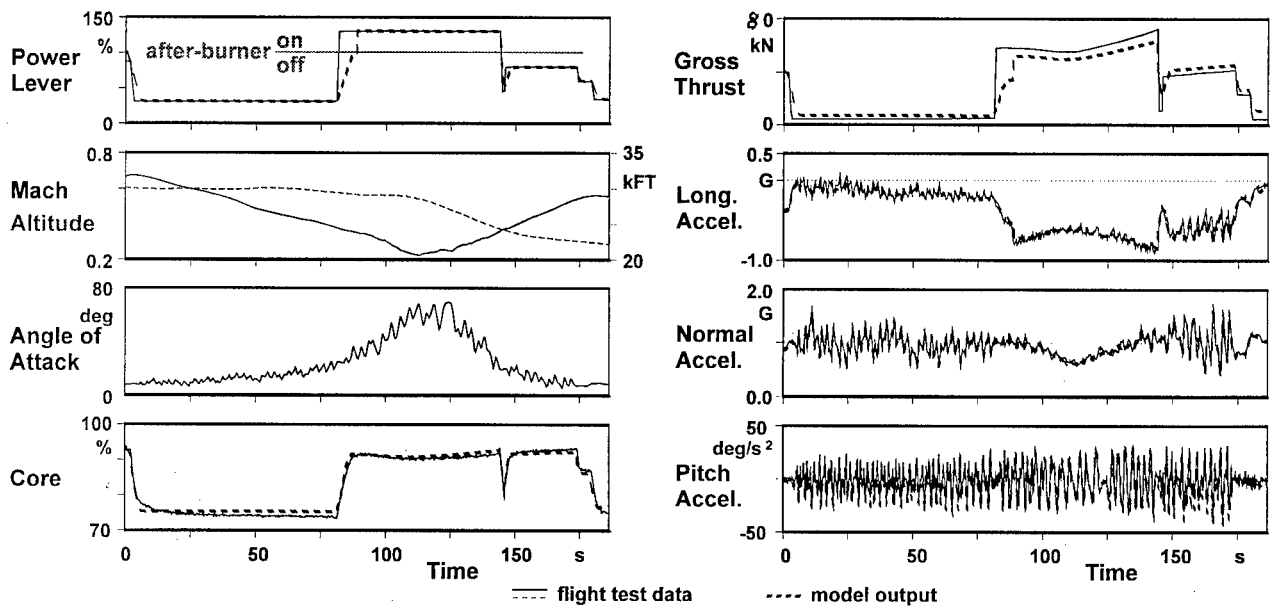
Fig. 9 *Low Order Engine Dynamic Estimation (After-Burner Operation)*
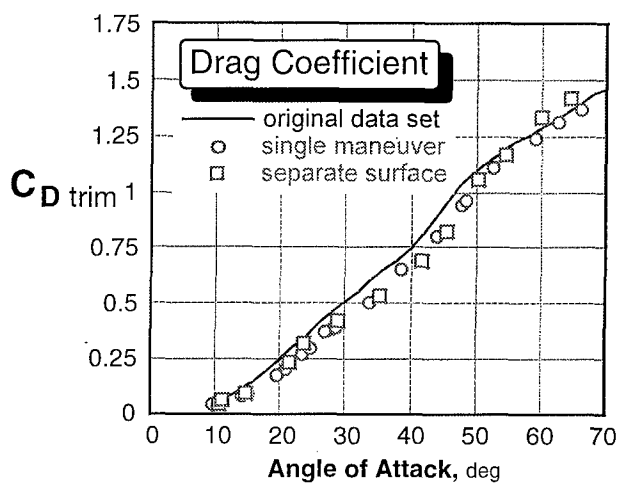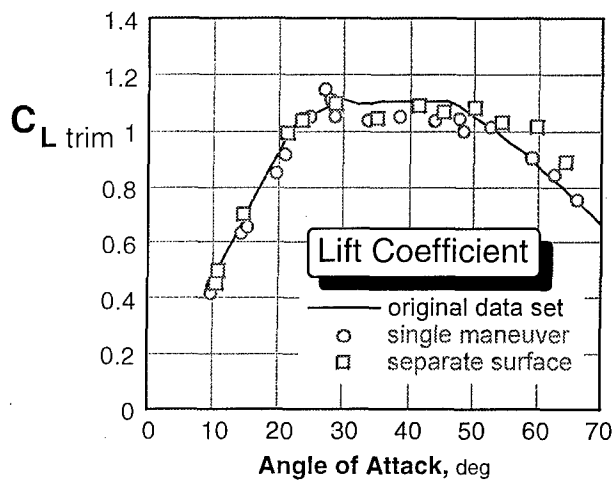
Fig. 10 *Lift and Drag from Single-Point Evaluation*
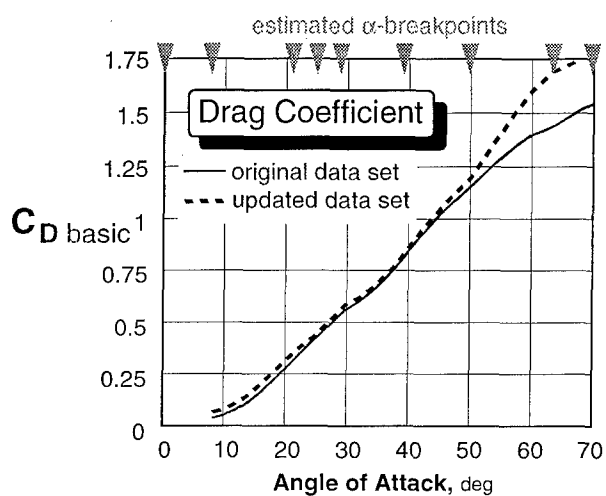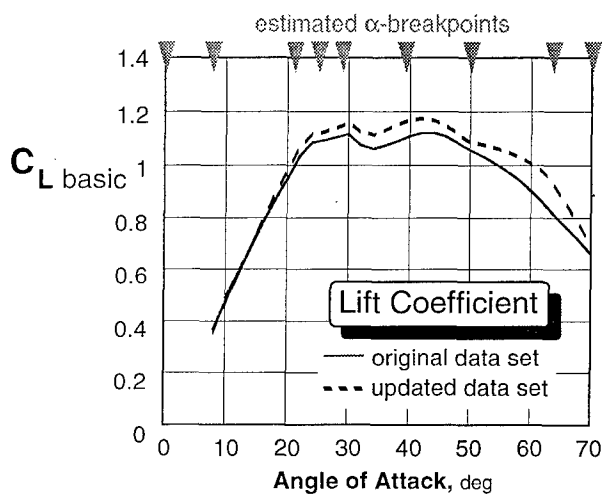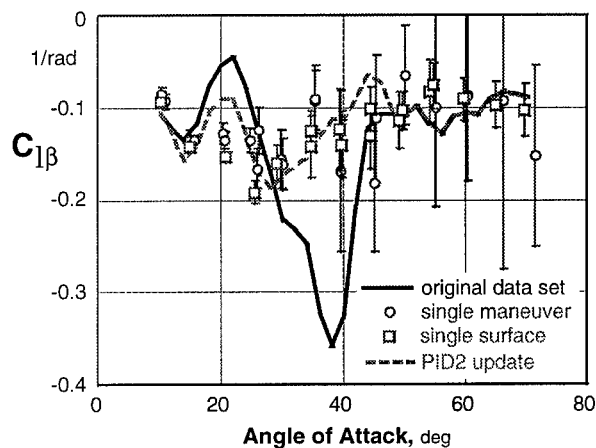

Fig. 11 *Lift and Drag from Multi-Point Evaluation*

estimated α-breakpoints

$\Delta C_{l\beta}$ (1/rad)

data set increment

$C_{l\beta}$ (1/rad)

original data set
single maneuver
single surface
PID2 update

Angle of Attack, deg

Fig. 12 *Dihedral Derivative from Single-Point Evaluation*

$C_{l\beta}$ (1/rad)

original data set
updated data set

Angle of Attack, deg
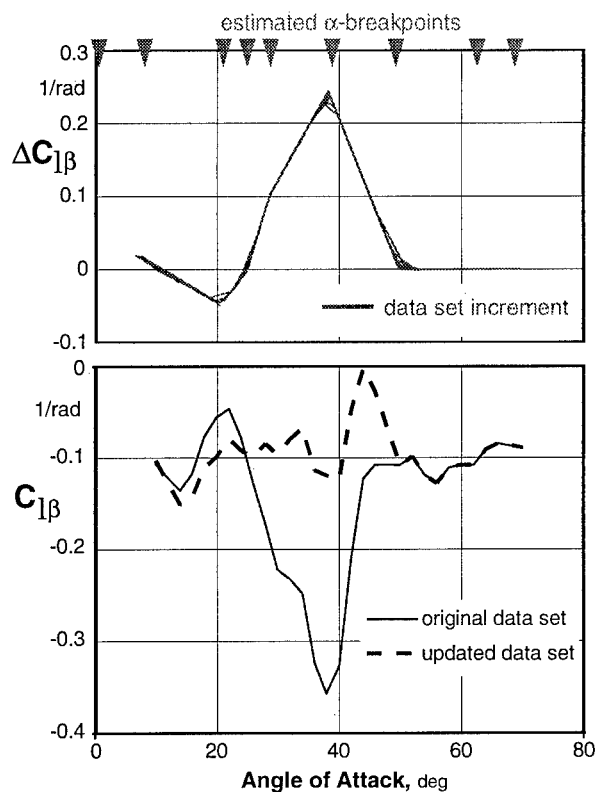
Fig. 13 *Dihedral Derivative from Multi-Point Evaluation*

Power Lever (%)

after-burner on / off

Altitude (ft)

Mach

PST-Loop   Mongoose   Herbst-Turn   Heli-Loop

Angle of Attack (deg)

lift off

touch down

Longitudinal Acceleration (g)

Normal Acceleration (g)

Pitch Acceleration (deg/s²)

Time (s)

flight test data   model output
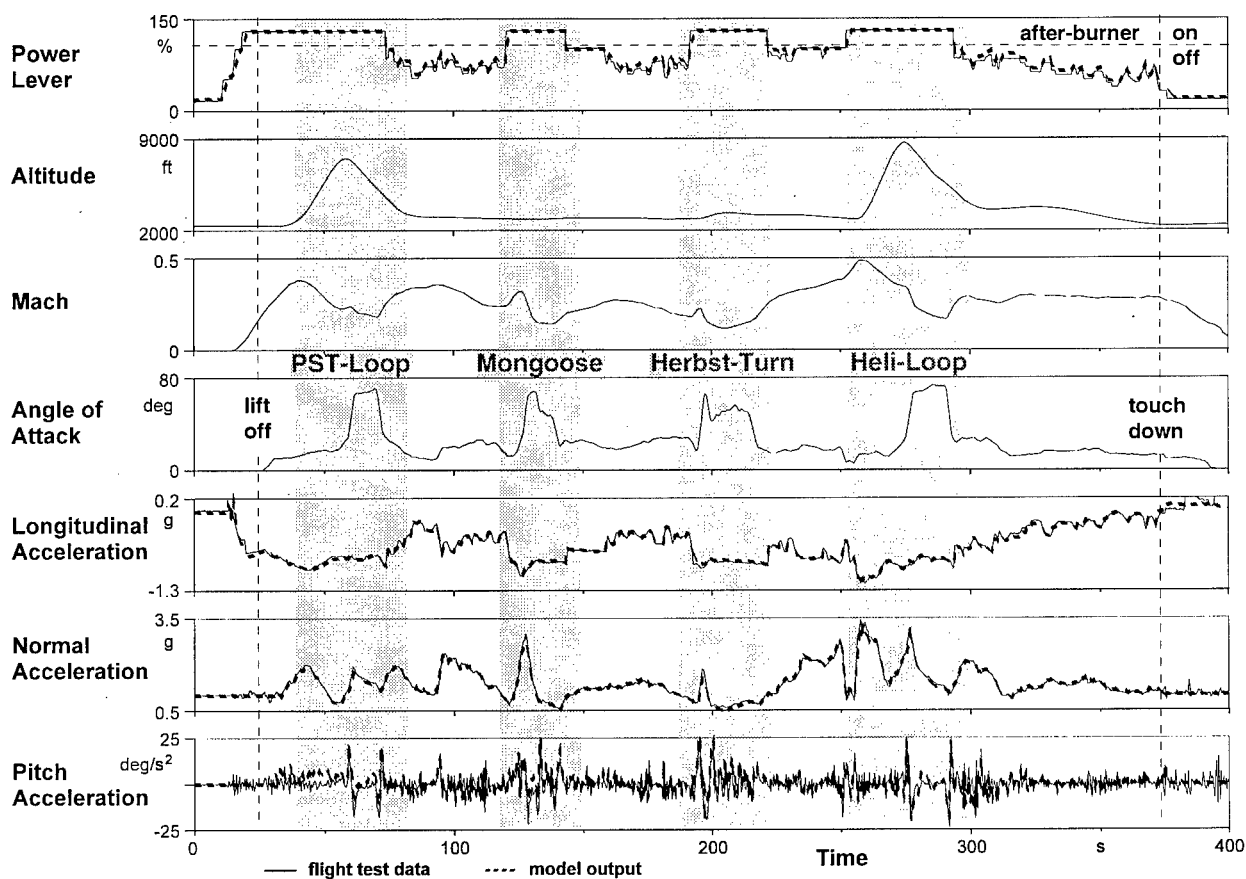
Fig. 14 *Validation of the Updated X-31 Data Base (Paris Air Show Practice Flight)*

ARMOR UAV IDENTIFICATION USING AN ADAPTIVE HYBRID GENETIC ALGORITHM

Peter D Bruce and Martin G Kellett
DAPS, Royal Military College of Science (Cranfield University),
Shrivenham, SWINDON, SN6 8LA, ENGLAND.

J R Azinheira
Instituto Superior Técnico, Lisbon, PORTUGAL

Summary

This paper presents the use of an Adaptive Hybrid Genetic Algorithm for the Maximum Likelihood identification of aircraft dynamics. The technique is compared to the conventional Modified Newton-Rhapson method and to the simplex method for the identification of a linear model of the dynamics of the ARMOR UAV. A simple example is used to illustrate the method's advantages when identifying nonlinear systems. The method has advantages over the Modified Newton-Rhapson method in that initial parameter estimates do not have to be stated, rather, a bound on the parameters is given. It also does not suffer from numerical problems sometimes evident with gradient-based optimisation techniques and it can locate the global minimum when a multi-modal cost function is present. It is also simple to incorporate initial parameter estimates if available.

Introduction

In recent years, the efficient extraction of aircraft stability and control parameters from flight test data has become more and more important as the drive to reduce the costs of bringing an aircraft into service increases. There are many techniques in the literature for such a problem, the most common of which is the Maximum Likelihood[1] (ML) method, however, there are a number of problems associated with this technique.

Numerical problems can be caused by poor initial parameter estimates, by an input signal which does not excite the system dynamics adequately or by inadequate modelling[2]. Another problem with aircraft at high angles of attack is that a small change in the dynamic parameters can lead to the aircraft becoming unstable, also leading to numerical problems.

A technique based on a Genetic Algorithm for overcoming some of these problems is proposed here.

Genetic Algorithms

A genetic algorithm (GA) is a parameter search procedure modelled on the mechanisms of biological evolution. It operates on a population of individuals, each of which is a possible solution to the problem and using a Darwinian survival of the fittest methodology, attempts to produce better solutions in succeeding generations. Because a GA evaluates multiple points in the solution space simultaneously, it has the potential to converge to the global optimum.

There is much in the literature covering GAs. (see for example, [3-5]). The basic elements of a simple GA are described and then the modifications introduced to improve convergence in this case are detailed.

Basic GA

The procedural elements of a GA are listed below:

1. Initialise population
2. Evaluate fitness of each individual
3. Select individuals for breeding and create new individuals by mating
4. Apply mutation operator
5. Delete members of old population and insert new individuals
6. If not finished, repeat from step 2.

The traditional GA codes the parameter set of the optimisation problem as a binary string. An initial population of individuals consisting of a number of these binary strings is created and an objective function is evaluated for each individual. The objective function is a measure of how good a solution to the problem that individual represents. In the case of a minimisation problem, the best individuals will have the lowest numerical value of the associated objective function. The objective function is usually transformed into a measure of relative fitness by some scaling function.

The choice of scaling function can dramatically affect the convergence performance of the GA[6]. The next stage is to select individuals to become parents. Individuals with lower objective functions will have a greater probability of being selected to reproduce. There are many methods such as Roulette-Wheel Selection (RWS) and Stochastic Universal Selection (SUS)[6].

The selection algorithms have differing performances measured by metrics described by Baker[7]. These are bias and spread. Bias is taken as an

indication of accuracy and the spread is a measure of consistency. In this study, Stochastic Universal Selection is used as it has zero bias and minimum spread, unlike the Roulette-Wheel selection methods.

Once the parents have been selected, reproduction is carried out by the crossover genetic operator. This randomly selects strings from the parents and combines them to produce new individuals. Crossover is the most dominant operator in most GAs. Mutation is also applied, which (for a binary-encoded GA) flips randomly selected bits of an individual. The main purpose of this operator is to ensure that the GA can search areas not represented in the initial population. It also acts as an insurance against the loss of good genetic material through selection and crossover. Mutation is usually applied with a low probability, typically 0.001.

Once a new population has been created through the above processes, the fitness of the new individuals is calculated. These are to be reinserted into the old population and so some members of the old population have to be deleted. This can be carried out by replacing the least fit or oldest members, or by random replacement, to name some techniques. Here, fitness-based reinsertion was used. Finally, the new population has been produced and the process can start again. Because the GA has stochastic transition rules, the population may converge to one value and remain there until the mutation operator creates a new, better individual. For this reason, it is difficult to specify convergence criteria.

Maximum Likelihood Technique

A detailed summary of the Maximum Likelihood technique for parameter identification can be found in [8], but the main elements are stated here. This method assumes a mathematical model formulated as follows:

$$x(t_0) = x_0 \qquad (1)$$

$$\dot{x}(t) = f[x(t), y(t), u(t), \theta] \qquad (2)$$

$$y(i) = g[u(i), \theta, G] \qquad (3)$$

where x is the state vector, y is the output vector, u is the input vector, θ is the vector of unknown parameters and G is a vector of uncorrelated Gaussian white noise.

Note that the output error formulation is being used here. There are other formulations of the ML method, such as filter error[9] and equation error, but the output error formulation has been applied successfully on many occasions for aircraft identification (see for example [9]).

The ML estimates of the unknown parameters are those such that the output, y is 'most likely' to occur. Stated more formally, the parameters are chosen so that

the conditional probability density function of the observation y given θ (or Likelihood function) is maximised. Most optimisation procedures minimise a function, so it is common to take the negative logarithm of the Likelihood function and call it the log-likelihood function (Equation (4)).

$$J(\theta) = \tfrac{1}{2}\sum_{i=1}^{N}[y(i) - \hat{y}(i)]^T R^{-1}[y(i) - \hat{y}(i)] \qquad (4)$$

where R is the measurement noise covariance which usually has to be estimated, N is the number of data points, $y(i)$ is the measured (or filtered) output and $\hat{y}(i)$ is the output of the identified model.

The most common method of minimising Equation (4) is to use a modified Newton-Rhapson (MNR) technique[8]. This forms the parameter update as:

$$\Delta\theta = \theta - \hat{\theta} \qquad (5)$$

$$= \left[\sum_{i=1}^{N} S(i)^T R^{-1} S(i)\right]^{-1} \sum_{i=1}^{N} S(i)^T R^{-1}[y(i) - \hat{y}(i)] \qquad (6)$$

S(i) is the sensitivity matrix defined as:

$$S(i) = \left.\frac{\partial y(i)}{\partial \theta}\right|_{\theta=\hat{\theta}} \qquad (7)$$

As part of the ML technique, the parameter Cramer-Rao bounds are obtained, which are the minimum achievable parameter variances. These are the diagonal elements of the inverse of the Information Matrix M:

$$M = \sum_{i=1}^{N} S(i)^T R^{-1} S(i) \qquad (8)$$

There are known problems with this method, however. The parameter update is calculated from Equations (5) and (6).The information matrix may be ill-conditioned due to incorrect model equations, from numerical problems in the calculation of the sensitivity matrix, or from poor excitation of the aircraft dynamics. If M becomes nearly singular, the parameter updates should be treated with suspicion.

Another problem with the above formulation is that initial parameter estimates are needed. With nonlinear model equations, the LLF may have more than one minimum. Poor initial parameter estimates can cause the solution to reach a local minimum.

Given the above problems, the standard algorithm used for estimating the parameters can fail. A genetic

algorithm has good potential for use in this situation as no sensitivities have to be calculated and GAs are claimed to be better at finding a global minimum than standard hill-climbing techniques. Another advantage is that instead of initial parameter estimates, the user defines a bound on each parameter.

Problem Description and Baseline Identification

A 4th order state-space linearised model of the Portuguese ARMOR X7 (Figure 1) fixed-wing UAV[10] was used whose parameters were known:

$$\dot{x} = Ax + Bu$$
$$y = Cx \tag{9}$$

$$A = \begin{bmatrix} 0 & 0 & 0 & 1 \\ -9.7040 & -0.0249 & 0.8080 & -3.0223 \\ -1.4382 & -0.6043 & -3.2998 & 24.5441 \\ 0 & 0.012 & -0.0819 & -10.5435 \end{bmatrix}$$

$$B = \begin{bmatrix} 0 \\ 1.3566 \\ -9.1535 \\ -55.6073 \end{bmatrix}$$

$$C = \begin{bmatrix} 1.000 & 0.0083 & -0.0562 & 0 \\ 0 & 0.9893 & 0.1456 & 0 \\ 0 & 0 & 0 & 1 \end{bmatrix} \tag{10}$$

where the input, state and output vectors are respectively;

$$u = \delta_E \quad \text{elevator angle (rad)} \tag{11}$$

$$x = \begin{cases} \theta & \text{pitch angle (rad)} \\ u & \text{forward speed (m/s)} \\ w & \text{normal speed (m/s)} \\ q & \text{pitch rate (rad/s)} \end{cases} \tag{12}$$

$$y = \begin{cases} \gamma & \text{flight path angle (rad)} \\ V & \text{total speed (m/s)} \\ q & \text{pitch rate (rad/s)} \end{cases} \tag{13}$$

One of the most important aspects of an identification experiment is the input signal used. One input signal commonly used for aircraft identification purposes is the 3-2-1-1[11].
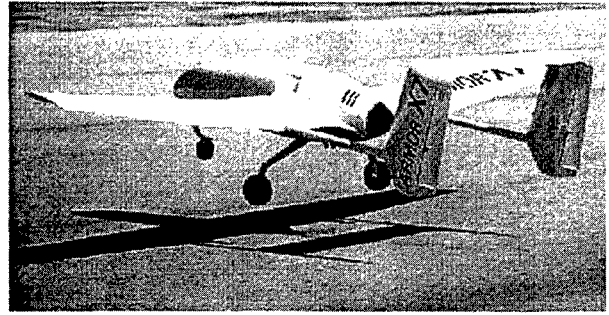

Figure 1 ARMOR Civilian UAV

The UAV was trimmed at ≈24m/s. A 3-2-1-1 input of 5 deg. amplitude and 1s time unit was applied to the elevator. The resulting outputs were recorded and used for identification. The identification technique used in each case was the output error formulation of the ML technique. The cost function to be minimised was therefore given by Equation (4). R was not identified and so was nominally fixed as the identity matrix.

A Monte Carlo simulation of 250 runs was carried out using the MNR technique with the initial parameter estimates randomly selected between the actual parameter values ±50%. The baseline identification was taken as the average of these results. More runs of the Monte Carlo simulation to improve its statistical significance would have been impractical due to the amount of time taken.

Genetic Operators

As mentioned above, it is common to use a constant mutation rate, typically 0.001. It has been found, however, that a non-uniform mutation rate can have beneficial effects on convergence. Mutation often does not play as large a role as crossover in the early stages of a GA and so it seems sensible to start with a low mutation rate, allowing crossover to extract the best genetic material from the initial population, and then, as the population converges, mutation becomes more important for later fine-tuning, so the mutation rate should increase. A large mutation rate can effectively reduce the GA to a random search of the parameter space, albeit with selection, so this increase in mutation rate with time should be coupled with a method to stop this degeneration occurring. This is where a reduction in the mutation bounds comes in.

It has been found[3] that for a binary-encoded GA, one method of improving fine local tuning is to increase the probability that a bit towards the right of the bit string gets mutated, compared with bits close to the left, as the number of generations increase. This means that the search caused by mutation is global (in the sense that it searches the space defined by the parameter bounds) at the beginning of the GA, becoming more

localised as the GA progresses. The GA used in this study used a floating-point (FP) representation, so an operator analogous to the binary one described above was needed.

The use of a binary-encoded GA uses a fixed-length bit string, effectively bounding the parameters. Similarly with a FPGA, the user specifies an upper and a lower bound on each parameter. These bounds limit the scope of the various operators so that a new individual cannot have any parameters lying outside these bounds. The simplest method of constructing a mutation operator analogous to that above is to reduce these bounds (centred on the current parameter estimates) as the GA progresses. This will increase local searching near the end of the GA. A number of different functions defining these bounds were tried. The few presented here include a linear reduction, a "raised cosine", a "raised cosine" squared and a "raised cosine" cubed (Figure 2). It was found of the various functions tried, the "raised cosine" squared gave the best performance in improving local fine tuning.
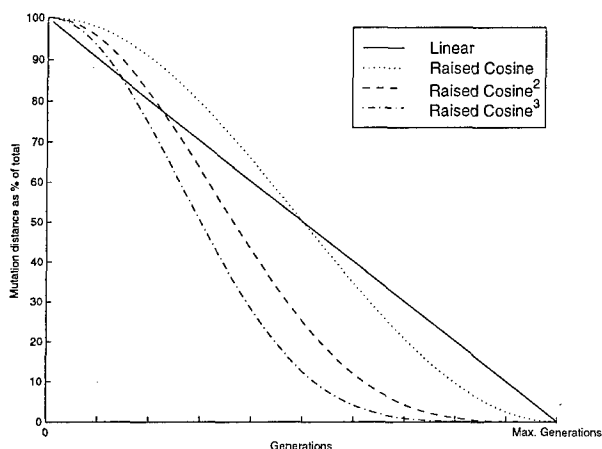
Figure 2 Variation in mutation bounds

This is a heuristic method of improving convergence which works for this example, but it would be very problem dependent. A more robust method would be to alter the mutation and crossover operators adaptively according to the current and past status of the population.

One method is presented in[12] which involves keeping track of which operator produces which offspring, and its relative fitness. Crossover and mutation probabilities are then selected according to which operator produces relatively better offspring.

A slightly simpler method is used here. The basic idea is to track the fitness value of the best individual in each generation and at times when there is little improvement, mutation rate is increased and crossover

is reduced and when there is improvement, the opposite occurs.

Specifically, the change in cost function values between the best individuals in one generation and the one before is calculated as:

$$\Delta J(\theta)_{gen} = J(\theta)_{gen} - J(\theta)_{gen-1} \qquad (14)$$

Mutation and crossover probabilities were then calculated as:

$$P_X = P_{X_{min}} + \left(P_{X_{max}} - P_{X_{min}}\right)\frac{\Delta J(\theta)_{gen}}{\Delta J(\theta)_{gen-1}} \qquad (15)$$

$$P_M = P_{M_{min}} + \left(P_{M_{max}} - P_{M_{min}}\right)\left(1 - \frac{\Delta J(\theta)_{gen}}{\Delta J(\theta)_{gen-1}}\right) \qquad (16)$$

where P_X is crossover probability, P_{Xmax} and P_{Xmin} are maximum and minimum crossover probabilities (to be defined by the user) and likewise P_M is mutation probability, P_{Mmax} and P_{Mmin} are maximum and minimum mutation probabilities (also defined by the user).

Equation (14) describes the cost function gradient between one generation and the next. It would be trivial to extend this to retain some more memory of what has happened before by increasing the number of generations over which this gradient is calculated.

Simulation Results

Evaluation of the above techniques was carried out by specifying the upper and lower bounds on the parameters as the actual parameter values ±50%. A Monte Carlo simulation of 250 runs was carried out with differing initial populations and the results averaged. Figure 3 compares the convergence of these GA methods with the MNR technique. Again, increasing the number of runs within the Monte Carlo Simulation would have taken a prohibitive amount of time
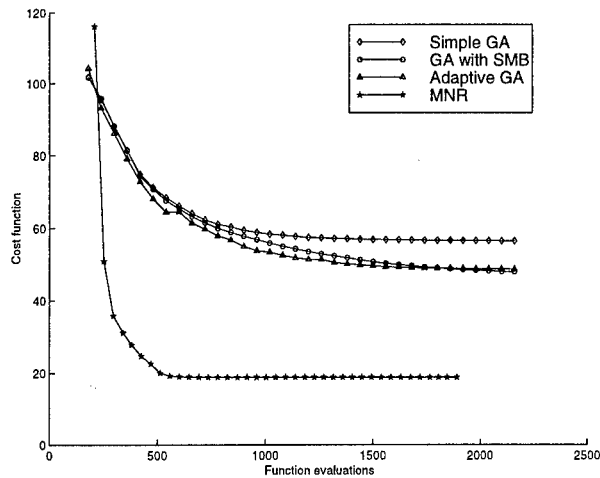
Figure 3 Convergence properties of GA techniques

From this, it shows that the modifications made to the simple GA do indeed improve convergence properties, but compared to the MNR, they still exhibit poor performance. It is interesting to note that the Simple GA did not converge to the minimum of the cost function found by the MNR technique within the time allowed, but the GA with Shrinking Mutation Bounds (SMB) and the adaptive GA converged to the same value as the MNR. The full convergence history is not shown to improve clarity.

Hybridisation

This simply means combining the GA with another technique. This method replaces the Darwinian evolutionary pattern with Lamarckian evolution[13]. This derives from the evolutionary theory of Jean Lamarck in the 19th Century, who proposed that the knowledge learned by organisms could be passed on to their offspring. In GA terms, this means that some knowledge is learned by the offspring before being returned to the population. This can be achieved by running a few iterations of a traditional optimisation technique. For initial attempts, the MNR technique was applied to the best offspring in each generation, but it was sometimes found that the approximation to the Hessian matrix (Equation (17)) was nearly singular and caused numerical problems .

$$\nabla^2_\theta J(\theta) \approx \sum_{i=1}^{N} [\nabla_\theta \hat{y}(i)]^T R^{-1} [\nabla_\theta \hat{y}(i)] \qquad (17)$$

For this reason, the simplex method was used for local optimisation within the GA. This technique requires only function evaluations, not derivatives. A description of the technique can be found in [14]. For the best

offspring in each generation the simplex method was applied with a maximum of 50 function evaluations and then fitness-based reinsertion was carried out.

Simulation Results

As above, the evaluation of the above technique was carried out by specifying the upper and lower bounds on the parameters as the actual parameter values ±50%. A Monte Carlo simulation of 250 runs was carried out with differing initial populations and the results averaged. Figure 4 compares the Hybrid technique with the MNR and simplex methods (which was evaluated in the same way as the MNR).

Convergence is much improved over the previous methods. The hybrid GA converged to the same function values as the simplex and MNR given enough time (not shown here).
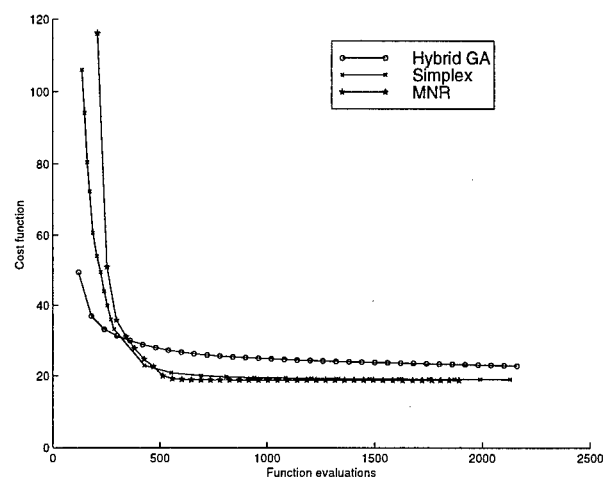

Figure 4 Convergence properties of Hybrid GA

Adaptive Hybrid GA

Given the above two methods of improving GA convergence for this problem, it seemed suitable to use a combination of the two. Operator probabilities were adapted according to Equations (15) and (16) and the simplex method was applied to the best offspring in each generation. Figure 5 shows the results of combining the adaptive GA with the hybrid using the same Monte Carlo simulation method as above.
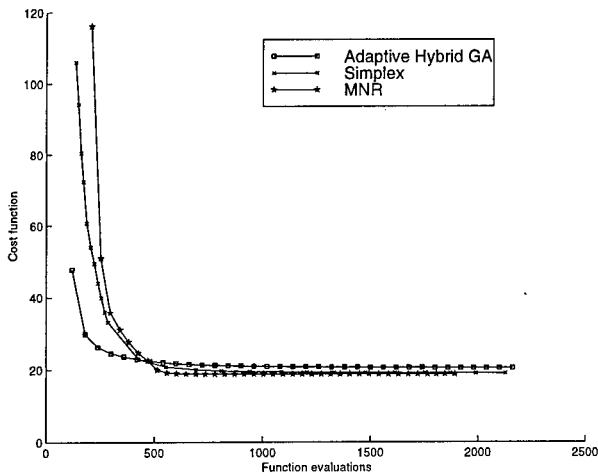
Figure 5 Convergence of Adaptive Hybrid GA

Figure 5 shows that the performance of the Adaptive Hybrid GA is now comparable to that of the Modified Newton-Rhapson method and to the simplex method.

Although the GA was hybridised with the simplex method, it is possible to combine it with any other minimiser. If a certain minimiser is known to perform well on a certain problem, then there is a good chance that that minimiser combined with the adaptive GA will outperform the original method. Further study of this is planned.

Nonlinear Identification Example

It is well known how the choice of initial parameter estimates can affect the speed of convergence of an optimisation algorithm. In addition, if the system description is a nonlinear one, the Maximum Likelihood cost function can become multi-modal and the initial parameter estimates not only affect speed of convergence, but the point to which the algorithm converges, whether that is a local or global minimum.

Generation of a nonlinear aircraft model with few enough parameters so that visualisation of the cost function is difficult to carry out, so the principle will be demonstrated using a simple nonlinear system taken from Proskawetz[2].

This nonlinear process model is of a sine wave with frequency ω_0:

$$z = \sin(\omega_0 t) \qquad (18)$$

If we model this as:

$$y = \sin(\omega t) \qquad (19)$$

then ω is the only unknown parameter and the measurement covariance matrix is known to be 1. In this case, the Maximum Likelihood cost function reduces to minimising:

$$J(\omega) = \sum_{0}^{T} [\sin(\omega_0 t_i) - \sin(\omega t_i)]^2 \qquad (20)$$

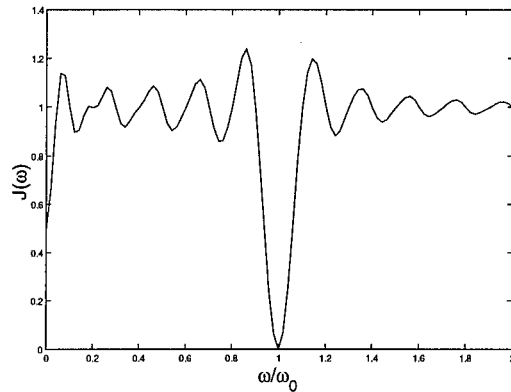The cost function for $T/T_0 = 5$ is shown in Figure 6.

Figure 6 Maximum Likelihood cost function

As can be seen, the function has one global minimum when $\omega/\omega_0 = 1$ and lots of local minima. As might be expected, application of the commonly-used MNR technique to this problem causes the results of the identification to be highly dependent on the initial estimate of ω.

Initial estimates of ω/ω_0 were specified between 0 and 2 and 100 runs of the MNR technique applied. The identified values of ω/ω_0 against the initial estimates are plotted in Figure 7.
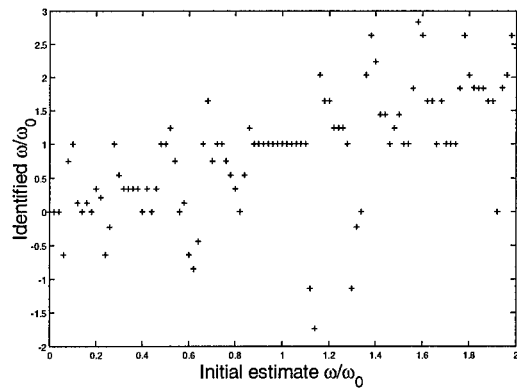

Figure 7 MNR Identified parameters against initial estimates

Out of 100 applications of the MNR technique, the global minimum was found only 26 times.

The same problem was addressed by the Adaptive Hybrid GA. The technique was applied 100 times with

ω/ω_0 bounded between 0 and 2. Since the AHGA is a population based minimiser, it does not use a single initial estimate so Figure 8 plots the identified values of ω/ω_0 against the number of run of the AHGA.
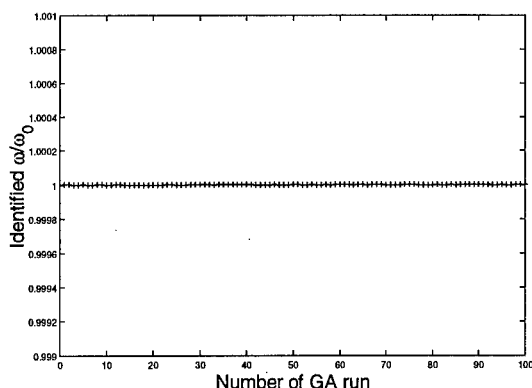

Figure 8 Identified parameters against number of AHGA run

It is clearly seen that each time, the global minimum is reached.

This is a very simple example which serves well to illustrate one of the advantages of the AHGA applied to the Maximum Likelihood identification problem.

Conclusion

An alternative search method for the Maximum Likelihood identification of aircraft dynamics from flight test data has been presented. A hybrid consisting of an adaptive Genetic Algorithm and the simplex method is used to minimise the log-likelihood function.

The technique has advantages over the conventional Modified Newton-Rhapson minimisation in that parameter bounds are specified, rather than explicit initial estimates. Sensitivity calculations are also not required and so numerical problems are avoided hence the technique should be more robust to a noisy objective function.

The method is shown for a representative linear system to perform comparably to the conventional Modified Newton-Rhapson technique and to require approximately the same number of function evaluations, which can be one of the main arguments against genetic algorithms.

It is also shown that for a nonlinear system, the Maximum Likelihood cost function can become multimodal and in this situation the Adaptive Hybrid GA performs significantly better in finding the global minimum.

Finally, prior parameter estimates can be incorporated into this technique simply by having the initial estimate as an individual in the initial population.

References

1. Maine R E & Iliff K W. *Identification of Dynamic Systems,* AGARD Flight Test Techniques Series, AGARD AG-300-Vol.2, 1985.
2. Proskawetz K O. *Robust parameter estimation of nonlinear dynamic systems.* Zeitschrift Für Flugwissenschaften und Weltraumforschung, Vol. 15, pp 12-18, 1991.
3. Michalewicz Z. *Genetic Algorithms + Data Structures = Evolution Programs,* Springer-Verlag, 1994.
4. KrishnaKumar K & Goldberg D E. *Genetic Algorithms in Control System Optimisation,* AIAA Paper 90-3488-CP, 1990.
5. Goldberg D E. *Genetic Algorithms in Search, Optimization and Machine Learning,* Addison Wesley Publishing Company, 1989.
6. Chipperfield A. *Genetic Algorithm Toolbox (for use with MATLAB) User's Guide,* Department of Automatic Control and Systems Engineering, University of Sheffield, UK.
7. Baker J E. *Reducing bias and inefficiency in the selection algorithm,* Proc. ICGA 2, pp14-21, 1987.
8. Klein V. *Estimation of Aircraft Aerodynamic Parameters from Flight Data,* Prog. Aerospace Science, Vol. 26, pp 1-77, 1989.
9. Jategaonkar R V & Plaetschke E. *Algorithms for Aircraft Parameter Estimation Accounting for Process and Measurement Noise,* J. Aircraft, Vol. 26, No. 4, pp 360-372, 1989.
10. Kellett M G et al. *Singular Value Robustness Analysis of a Remotely Piloted Vehicle,* Proc. UKACC International Conference on Control '96, Vol.2, pp 776-781, 1996.
11. Plaetschke E & Schultz G. *Practical input signal design in parameter identification,* AGARD LS-104, pp 3-1 to 3-19, 1979.
12. Davis L. *Handbook of Genetic Algorithms,* Van Nostrand Reinhold, New York, 1994.
13. Kennedy S A. *Five Ways to a Smarter Genetic Algorithm,* AI Expert, Dec. 1993.
14. Press W H et al. *Numerical Recipes,* Cambridge University Press, 1986.

Aerodynamic Data Identification Using Linear Aeroballistic Theory

Gökmen Mahmutyazıcıoğlu
Scientific and Technical Council of Turkey
Defense Industries Research and Development Institute
TÜBİTAK-SAGE
Pk. 16, 06261 Mamak, Ankara
Turkey
Prof. Dr. Bülent E. Platin
Middle East Technical University
Mechanical Engineering Department
06531 Balgat, Ankara
Turkey

SUMMARY

The history of the linear aeroballistic theory extends to 1920's to Fowler et al. It has been used widely in aeronautical studies for estimating aerodynamic parameters till 1970's when numerical and analytical methods like Chapman-Kirk Kalman filter techniques had been discovered. Today linear aeroballistic theory is still used to get an initial estimate to more complex methods. This is due to its simplicity and easiness to apply. In this paper, a new formulation, which uses the linear aeroballistic theory to estimate the aerodynamic data, will be presented. Result of the test cases obtained with this formulation will be given.

LIST OF SYMBOLS

A : reference area,

c_i : coefficients of the complex Euler angle,

d : reference diameter

d_i : coefficients of the complex swerve displacement,

i : unit imaginary number,

J : cost function,

K_0 : induced moment parameter,

K_D : drag parameter,

K_{Z_α} : normal force static stability parameter,

$K_{Z_{p_p}}$: normal force Magnus parameter,

K_{l_0} : induced roll moment parameter,

K_{l_p} : roll moment damping parameter,

K_{m_α} : pitch moment static stability parameter,

K_{m_β} : pitch moment out of plane static stability parameter,

K_{m_q} : pitch moment damping parameter,

$K_{m_{\beta_p}}$: pitch moment Magnus parameter,

k_i : complex angle of attack coefficients,

$\bar{q}$: dynamic pressure,

s : arc length along flight path,

x_g, y_g, z_g : spatial coordinates,

φ : complex swerve displacement,

η : complex Euler angle,

Λ_1, Λ_2 : eigenvalues of the complex angle of attack,

μ : complex translational angular velocity,

ρ : air density,

ζ : complex angle of attack,

ζ_c : complex angle of attack due to asymmetry,

ζ_g : complex angle of attack due to gravity.

Subscripts

i : component of a vector in the ith direction,

0 : initial condition.

Superscripts

$\sim$: states in F_n,

$\cdot$: differentiation in time domain,

$'$: differentiation in distance domain.

1. INTRODUCTION

The theory on linear aeroballistics was advanced by Fowler et al., in 1920, clarified and extended by Kent, Nielsen and Synge and McShane, Kelly and Reno, [1]. The two most outstanding names in this area are Charles H. Murphy and John D. Nicolaides. Their research work had extended to investigating the effect of the aerodynamic nonlinearities in the aerodynamic stability derivatives and nonlinear motion and developing the quasilinear theory. Murphy besides, his number of papers, reports and proceedings, the report written in 1963, named 'Free Flight Motion of Symmetric Missiles' [2] is like the Handbook of this area. The report as it can be understood from its name, explores the motion of a symmetric missile in free flight. After the derivation of the equations of motion, a detailed discussion on linear stability of rolling and nonrolling missiles is given. This is followed by the range measurement of linear and nonlinear aerodynamic coefficients and prediction of the nonlinear motion. The author divides the estimation procedure in subsections. Firstly, the estimation of the drag coefficient is investigated. This is followed by the estimation of the roll motion parameters and complex angle of attack parameters. Finally the estimation of the complex swerve displacement parameters is given. While estimating the complex swerve displacement parameters, instead of using the previously found results (complex angle of attack and complex angular rate), forcing terms are used. In this report discussion

about nonlinear aerodynamic coefficients is also given. Today this report is still cited in some of the papers.

Nicolaides has also applied similar procedure for the estimation of complex angle of attack parameters. The basic difference between the work of Nicolaides and Murphy arises in the estimation of nonlinear aerodynamic derivatives, investigation of the nonlinear motion and the quasilinear theory, which are beyond the scope of this study.

As mentioned above the study on linear aeroballistic initiated in 1920's. During the past years a number of papers on this topic were written. It is seen that the estimation of the linear aerodynamic coefficients is almost the same in most of these papers. The procedure is similar with the Murphy's formulation. The two characteristics of these procedures are complex variables and recursive solution. Recently a new study is found in the literature done by Weiss, Doherr, Schilling [3]. In this study instead of using complex variables, a different formulation is applied. The angular motion is solved defining new states, which have more simple set of differential equations. After solving the new states, solutions for the original states are also obtained. Using these solutions, the Euler angle states are solved and finally the swerve motion states are found. Similar to the previous studies a recursive solution is applied in this study. As mentioned above the basic difference is, instead of using complex variables, transformation of states is applied. Furthermore, for solving Euler angle states and swerve motion states instead of using the forcing terms on the right hand side of the differential equations, the previously obtained solutions are used. In other words, the differential equations for the Euler angles are written in terms of the angular motion states and the differential equations for the swerve motion are written in terms of the Euler angle and angular motion states.

In this study, a combined way between [2] and [3] is applied here. Similar to [2] complex variables and similar to [3] during the recursive solution previously found results will be used. This feature can be more easily understood in the next section. It is thought that the method presented here uses the advantage of the two studies mentioned: complex variables and using the previously found solutions in the next step. These features make this method very simple and practical.

2. EQUATIONS OF MOTION

In this section the derivations of the equations of motion, which will be used in the estimation procedure, will be given. The derivation of the basic flight mechanics equations can be found in any relevant literature, [4], [2]. The basic flight mechanics equations of motion in the non-rolling reference frame F_n can be written as follows:

$$m\left(\dot{\tilde{u}} + \tilde{q}\tilde{w} - \tilde{r}\tilde{w}\right) = \tilde{X} + m\tilde{g}_1, \qquad (2.1)$$

$$m\left(\dot{\tilde{v}} + \tilde{r}\tilde{u} - \hat{p}\tilde{w}\right) = \tilde{Y} + m\tilde{g}_2, \qquad (2.2)$$

$$m\left(\dot{\tilde{w}} + \hat{p}\tilde{v} - \tilde{q}\tilde{u}\right) = \tilde{Z} + m\tilde{g}_3, \qquad (2.3)$$

$$I_a\dot{\hat{p}} = \tilde{L}, \qquad (2.4)$$

$$I_t\left(\dot{\tilde{q}} + \frac{I_a}{I_t}\hat{p}\tilde{r} - \hat{p}\tilde{r}\right) = \tilde{M}, \qquad (2.5)$$

$$I_t\left(\dot{\tilde{r}} - \frac{I_a}{I_t}\hat{p}\tilde{q} + \hat{p}\tilde{q}\right) = \tilde{N}. \qquad (2.6)$$

Where, $\hat{p}$ is the first component of angular velocity of F_n with respect to earth frame F_o expressed in F_n and $\tilde{g}_1, \tilde{g}_3$ and $\tilde{g}_3$ are the components of gravitational accelerations in three directions respectively.

Besides, the equations given in F_n, the relations between these states and the corresponding ones in body fixed reference frame F_b are also required. The relations between these states can be expressed as follows.

$$\tilde{x} = x, \qquad (2.7)$$

$$\tilde{y} = y\cos(\phi) - z\sin(\phi), \qquad (2.8)$$

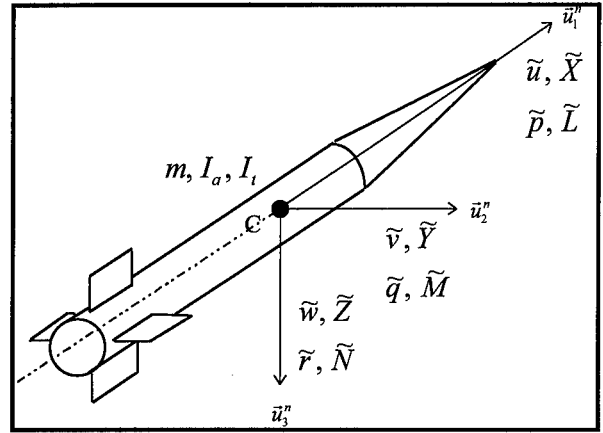$$\tilde{z} = y\sin(\phi) + z\cos(\phi). \qquad (2.9)$$

Figure 1. Unguided missile in three-dimensional flight.

Where $\tilde{x}, \tilde{y}, \tilde{z}$ denotes the states in F_n and x, y, z denotes the states in F_b in three directions respectively and ϕ denotes the roll angle.

Furthermore, one needs the kinematic relations between the translational velocities in F_n and translational positions in earth fixed coordinates in F_0 and between rotational velocities and Euler angles. These relations can be written as [5],

$$\dot{x}_g = \tilde{u}\cos(\theta)\cos(\psi) - \tilde{v}\sin(\psi) + \tilde{w}\sin(\theta)\cos(\psi), \qquad (2.10)$$

$$\dot{y}_g = \tilde{u}\cos(\theta)\sin(\psi) + \tilde{v}\cos(\psi) + \tilde{w}\sin(\theta)\sin(\psi), \qquad (2.11)$$

$$\dot{z}_g = -\tilde{u}\sin(\theta) + \tilde{w}\cos(\theta), \qquad (2.12)$$

$$\dot{\phi} = \hat{p} + \tilde{r}\tan(\theta), \qquad (2.13)$$

$$\dot{\theta} = \tilde{q}, \qquad (2.14)$$

$$\dot{\psi} = \frac{\tilde{r}}{\cos(\theta)}, \qquad (2.15)$$

$$\hat{p} = -\tilde{r}\tan(\theta). \qquad (2.16)$$

In the preceding parts the equations of motions of motion in F_n are given, besides these equations for drag analysis the translational equation in x direction of air trajectory reference frame F_w is required.

$$m\dot{V} = D. \qquad (2.17)$$

For small angle of attack and angle of sideslip axial aerodynamic force in F_b and axial aerodynamic force in F_w are assumed to be equal $(X \approx D)$.

The aerodynamic forces and moments in F_n for a symmetric and slightly asymmetric model can be written as follows:

$$\tilde{X} = -\bar{q}AC_X, \qquad (2.18)$$

$$\tilde{Y} = \bar{q}A\left(C_{Z_\alpha}\tilde{\beta} - C_{Z_{\beta_p}}\tilde{\alpha}p\frac{d}{2V}\right), \qquad (2.19)$$

$$\tilde{Z} = \bar{q}A\left(C_{Z_\alpha}\tilde{\alpha} + C_{Z_{\beta_p}}\tilde{\beta}p\frac{d}{2V}\right), \qquad (2.20)$$

$$\tilde{L} = \bar{q}Ad\left(C_{l_0} + C_{l_p}p\frac{d}{2V}\right), \qquad (2.21)$$

$$\tilde{M} = \bar{q}Ad\Big(C_{m_0}\cos(\phi) - C_{n_0}\sin(\phi) + C_{m_\alpha}\tilde{\alpha} + C_{m_\beta}\tilde{\beta},$$
$$+ C_{m_q}\tilde{q}\frac{d}{2V} + C_{m_{\beta_p}}\tilde{\beta}p\frac{d}{2V}\Big) \qquad (2.22)$$

$$\tilde{N} = \bar{q}Ad\Big(C_{m_0}\sin(\phi) + C_{n_0}\cos(\phi) - C_{m_\alpha}\tilde{\beta} + C_{m_\beta}\tilde{\alpha}.$$
$$+ C_{m_q}\tilde{r}\frac{d}{2V} + C_{m_{\beta_p}}\tilde{\alpha}p\frac{d}{2V}\Big). \qquad (2.23)$$

Where

$$\tilde{\alpha} = \frac{w\cos(\phi) + v\sin(\phi)}{u} \approx \alpha\cos(\phi) + \beta\sin(\phi),$$

$$\tilde{\beta} = \frac{v\cos(\phi) - w\sin(\phi)}{V} \approx \beta\cos(\phi) - \alpha\sin(\phi).$$

Equations of motion can be rewritten expanding aerodynamic force and moment terms,

$$\dot{V} = -\frac{\rho AV^2}{2m}C_D, \qquad (2.24)$$

$$\dot{\tilde{v}} = \frac{\rho AV^2}{2m}\left(C_{Z_\alpha}\tilde{\beta} - C_{Z_{\beta_p}}\tilde{\alpha}p\frac{d}{2V}\right) - \tilde{r}(u + \tilde{w}\tan(\theta)), \qquad (2.25)$$

$$\dot{\tilde{w}} = \frac{\rho AV^2}{2m}\left(C_{Z_\alpha}\tilde{\alpha} + C_{Z_{\beta_p}}\tilde{\beta}p\frac{d}{2V}\right) + \tilde{q}u + \tilde{r}\tilde{v}\tan(\theta),$$
$$+ g\cos(\theta), \qquad (2.26)$$

$$\dot{p} = \frac{\rho AdV^2}{2I_a}\left(C_{l_0} + C_{l_p}p\frac{d}{2V}\right), \qquad (2.27)$$

$$\dot{\tilde{q}} = \frac{\rho AdV^2}{2I_t}\Big(C_{m_0}\cos(\phi) - C_{n_0}\sin(\phi) + C_{m_\alpha}\tilde{\alpha}$$
$$+ C_{m_\beta}\tilde{\beta} + C_{m_q}\tilde{q}\frac{d}{2V} + C_{m_{\beta_p}}\tilde{\beta}p\frac{d}{2V}\Big) - \frac{I_a}{I_t}p\tilde{r} + \tilde{r}^2\tan(\theta), \qquad (2.28)$$

$$\dot{\tilde{r}} = \frac{\rho AdV^2}{2I_t}\Big(C_{m_0}\sin(\phi) + C_{n_0}\cos(\phi) - C_{m_\alpha}\tilde{\beta}$$
$$+ C_{m_\beta}\tilde{\alpha} + C_{m_q}\tilde{r}\frac{d}{2V} + C_{m_{\beta_p}}\tilde{\alpha}p\frac{d}{2V}\Big) + \frac{I_a}{I_t}p\tilde{q} - \tilde{q}\tilde{r}\tan(\theta). \qquad (2.29)$$

In order to solve the above equations, they will be transformed into distance domain for simplicity. The equations (2.24)-(2.29) can be rewritten in distance domain as,

$$V' + \frac{\rho AV}{2m}C_D = 0, \qquad (2.30)$$

$$\tilde{v}' = \frac{\rho AV}{2m}\left(C_{Z_\alpha}\tilde{\beta} - C_{Z_{\beta_p}}\tilde{\alpha}p\frac{d}{2V}\right) - \tilde{r}\left(\frac{u}{V} + \frac{\tilde{w}\tan(\theta)}{V}\right) \qquad (2.31)$$

$$\tilde{w}' = \frac{\rho AV}{2m}\left(C_{Z_\alpha}\tilde{\alpha} + C_{Z_{\beta_p}}\tilde{\beta}p\frac{d}{2V}\right) + \tilde{q}\frac{u}{V} + \frac{\tilde{v}}{V}\tilde{r}\tan(\theta)$$
$$+ \frac{g\cos(\theta)}{V}, \qquad (2.32)$$

$$p' = \frac{\rho AdV}{2I_a}\left(C_{l_0} + C_{l_p}p\frac{d}{2V}\right), \qquad (2.33)$$

$$\tilde{q}' = \frac{\rho AdV}{2I_t}\Big(C_{m_0}\cos(\phi) - C_{n_0}\sin(\phi) + C_{m_\alpha}\tilde{\alpha}$$
$$+ C_{m_\beta}\tilde{\beta} + C_{m_q}\tilde{q}\frac{d}{2V} + C_{m_{\beta_p}}\tilde{\beta}p\frac{d}{2V}\Big) - \frac{I_a}{I_t}\frac{p}{V}\tilde{r} + \frac{\tilde{r}^2\tan(\theta)}{V}, \qquad (2.34)$$

$$\tilde{r}' = \frac{\rho AdV}{2I_t}\Big(C_{m_0}\sin(\phi) + C_{n_0}\cos(\phi) - C_{m_\alpha}\tilde{\beta}$$
$$+ C_{m_\beta}\tilde{\alpha} + C_{m_q}\tilde{r}\frac{d}{2V} + C_{m_{\beta_p}}\tilde{\alpha}p\frac{d}{2V}\Big) + \frac{I_a}{I_t}\frac{p}{V}\tilde{q} - \frac{\tilde{q}\tilde{r}\tan(\theta)}{V}. \qquad (2.35)$$

Using the definition given below equation (2.24) can be written as,

$$K_D = \frac{\rho AC_D}{2m},$$

$$V' + K_D V = 0. \qquad (2.36)$$

The solution of equation (2.36) can be found as,

$$V(s) = \frac{ds}{dt} = V_0 e^{-K_D s} \qquad (2.37)$$

and,

$$t = t_0 + \frac{1}{V_0 K_D}\left(e^{K_D s} - 1\right). \qquad (2.38)$$

Using the solution for V, equation (2.27) becomes,

$$p' - K_{l_p} p = K_{l_0} V_0 e^{-K_D s} . \qquad (2.39)$$

Where

$$K_{l_p} = \frac{\rho A d^2}{4 I_a} C_{l_p} ,$$

$$K_{l_0} = \frac{\rho A d}{2 I_a} C_{l_0} .$$

The solution for this equation can be found easily using the basic ordinary differential equations knowledge as,

$$p(s) = -\frac{K_{l_0} V_0}{K_D + K_{l_p}} e^{-K_D s} + \left(p_0 + \frac{K_{l_0} V_0}{K_D + K_{l_p}} \right) e^{K_{l_p} s} . \qquad (2.40)$$

Using the solution for $p(s)$, the solution for ϕ can be found, assuming the right hand side term $\tilde{r} \tan[\theta]$ in equation (2.13) is small compared to p.

$$\phi' = \frac{p(s)}{V(s)} = -\frac{K_{l_0}}{K_D + K_{l_p}} + \left(\frac{p_0}{V_0} + \frac{K_{l_0}}{K_D + K_{l_p}} \right) e^{(K_D + K_{l_p}) s} . \qquad (2.41)$$

Using equation (2.41), the solution for $\phi(s)$ can be found as,

$$\phi(s) = \phi_0 - \frac{p_0}{V_0 (K_D + K_{l_p})} - \frac{K_{l_0}}{(K_D + K_{l_p})^2} - \frac{K_{l_0}}{K_D + K_{l_p}} s$$

$$+ \left(\frac{p_0}{V_0 (K_D + K_{l_p})} + \frac{K_{l_0}}{(K_D + K_{l_p})^2} \right) e^{(K_D + K_{l_p}) s} . \qquad (2.42)$$

Equations (2.25)-(2.26) and (2.28)-(2.29) can be put into much simpler form by using the following complex variables:

$$\tilde{\zeta} = \frac{\tilde{v} + i\tilde{w}}{V} \cong \tilde{\beta} + i\tilde{\alpha} , \qquad (2.43)$$

$$\tilde{\mu} = \frac{\tilde{q} + i\tilde{r}}{2V} . \qquad (2.44)$$

Multiplying equation (2.26) with the unit imaginary number i and adding this to equation (2.25) one obtains,

$$\tilde{v}' + i\tilde{w}' = \frac{\rho A V}{2m} \left(C_{Z_\alpha} \tilde{\zeta} + C_{Z_{\beta_p}} (i\tilde{\beta} - \tilde{\alpha}) p \frac{d}{2V} \right) + \frac{(i\tilde{q} - \tilde{r}) u}{V}$$

$$+ (i\tilde{\beta} - \tilde{\alpha}) \tilde{r} \tan(\theta) + i \frac{g \cos(\theta)}{V} . \qquad (2.45)$$

In the above equation, the ratio of u/V is assumed approximately equal to 1. Using equations (2.41), (2.42) and the below given definitions, equation (2.47) can be simplified as:

$$(\tilde{v}' + i\tilde{w}') = \tilde{\zeta} V - K_D \tilde{\zeta} V , \qquad (2.46)$$

$$i\tilde{q} - \tilde{r} = i2\tilde{\mu} V , \qquad (2.47)$$

$$i\tilde{\beta} - \tilde{\alpha} = i\tilde{\zeta} , \qquad (2.48)$$

$$K_{Z_\alpha} = \frac{\rho A}{2m} C_{Z_\alpha} ,$$

$$K_{Z_{\beta_p}} = \frac{\rho A d}{4m} C_{Z_{\beta_p}} ,$$

$$\tilde{\zeta}' = \left(K_D + K_{Z_\alpha} + K_{Z_{\beta_p}} i \frac{p}{V} + i \frac{\tilde{r} \tan(\theta)}{V} \right) \tilde{\zeta} + i2\tilde{\mu} + i \frac{g \cos(\theta)}{V^2} . \qquad (2.49)$$

In equation (2.49), the right hand-side term $i \frac{\tilde{r} \tan(\theta)}{V} \tilde{\zeta}$ is small compared to the other terms, so it can be neglected.

$$\tilde{\zeta}' = \left(K_D + K_{Z_\alpha} + K_{Z_{\beta_p}} i \frac{p}{V} \right) \tilde{\zeta} + i2\tilde{\mu} + i \frac{g \cos(\theta)}{V^2} . \qquad (2.50)$$

Similarly multiplying equation (2.29) with the unit imaginary number i and adding to equation (2.28) one obtains,

$$\tilde{q}' + i\tilde{r}' = \frac{\rho A d V}{2 I_t} \left((C_{m_0} + i C_{n_0}) e^{i\phi} - i C_{m_\alpha} \tilde{\zeta} + C_{m_\beta} \tilde{\zeta} \right)$$

$$+ C_{m_q} \tilde{\mu} d + C_{m_{\beta_p}} \tilde{\zeta} p \frac{d}{2V} + i2\tilde{\mu} \left(\frac{I_a}{I_t} p - \tilde{r} \tan(\theta) \right) . \qquad (2.51)$$

The left-hand side term can be found in terms of $\tilde{\mu}$ as:

$$(\tilde{q}' + i\tilde{r}') = 2V (\tilde{\mu}' - K_D \tilde{\mu}) . \qquad (2.52)$$

Inserting equation (2.52) into (2.51) and making the below given definitions complex angular rate equation is derived as follows,

$$K_0 = \frac{\rho A d}{2 I_t} (C_{m_0} + i C_{n_0}) ,$$

$$K_{m_\alpha} = \frac{\rho A d}{2 I_t} C_{m_\alpha} ,$$

$$K_{m_\beta} = \frac{\rho A d}{2 I_t} C_{m_\beta} ,$$

$$K_{m_q} = \frac{\rho A d^2}{4 I_t} C_{m_q} ,$$

$$K_{m_{\beta_p}} = \frac{\rho A d^2}{4 I_t} C_{m_{\beta_p}} ,$$

$$\tilde{\mu}' = \frac{1}{2} K_0 e^{i\phi} + \frac{1}{2} \left(K_{m_\beta} + K_{m_{\beta_p}} \frac{p}{V} - i K_{m_\alpha} \right) \tilde{\zeta}$$

$$+ \left(K_D + K_{m_q} + i \frac{I_a}{I_t} \frac{p}{V} - i \frac{\tilde{r}}{V} \tan(\theta) \right) \tilde{\mu} . \qquad (2.53)$$

Similar to the complex angle of attack equation the right hand side term $i \frac{\tilde{r}}{V} \tan(\theta) \tilde{\mu}$ is small compared to the other terms, so it can be neglected.

$$\tilde{\mu}' = \frac{1}{2}\left[K_0 e^{i\phi} + \left(K_{m_\beta} + K_{m_{\beta_p}} \frac{p}{V} - iK_{m_\alpha} \right)\tilde{\zeta} \right]$$
$$+ \left(K_D + K_{m_q} + i\frac{I_a}{I_t}\frac{p}{V} \right)\tilde{\mu} . \qquad (2.54)$$

Equations (2.50) and (2.54) are coupled equations, in order to solve them they have to be decoupled. In order to decouple these equations, first step is to differentiate equation (2.50) with respect to distance:

$$\tilde{\zeta}'' = \left(K_D + K_{z_\alpha} + K_{z_{\beta_p}} i\frac{p}{V} \right)\tilde{\zeta}' + i2\tilde{\mu}' + i\frac{2K_D g\cos(\theta)}{V^2} . \quad (2.55)$$

In the above equation differentiation and in the following parts, p/V term will be assumed constant. Inserting equation (2.54) into (2.55) one gets,

$$\tilde{\zeta}'' - \left(K_D + K_{z_\alpha} + K_{z_{\beta_p}} i\frac{p}{V} \right)\tilde{\zeta}' - \left(K_{m_\alpha} + iK_{m_\beta} + iK_{m_{\beta_p}} \frac{p}{V} \right)\tilde{\zeta}$$
$$= K_0 e^{i(\phi + \pi/2)} + i2\left(K_D + K_{m_q} + i\frac{I_a}{I_t}\frac{p}{V} \right)\tilde{\mu} + i\frac{2K_D g\cos(\theta)}{V^2} .$$

$$(2.56)$$

$\tilde{\mu}$ term in equation (2.56) can be eliminated using equation (2.50) as,

$$\tilde{\mu} = \frac{1}{i2}\left[\tilde{\zeta}' - \left(K_D + K_{z_\alpha} + K_{z_{\beta_p}} i\frac{p}{V} \right)\tilde{\zeta} - i\frac{g\cos(\theta)}{V^2} \right] ,$$

$$(2.57)$$

$$\tilde{\zeta}'' - \left(2K_D + K_{z_\alpha} + i\frac{p}{V}\left(K_{z_{\beta_p}} + \frac{I_a}{I_t} \right) + K_{m_q} \right)\tilde{\zeta}'$$
$$+ \left(K_{m_\alpha} + iK_{m_\beta} + iK_{m_{\beta_p}} \frac{p}{V} \right.$$
$$\left. - \left(K_D + K_{m_q} + i\frac{I_a}{I_t}\frac{p}{V} \right)\left(K_D + K_{z_\alpha} + iK_{z_{\beta_p}} \frac{p}{V} \right) \right)\tilde{\zeta}$$
$$= K_0 e^{i(\phi + \pi/2)} + i\frac{g\cos(\theta)}{V^2}\left(K_D - K_{m_q} - i\frac{I_a}{I_t}\frac{p}{V} \right) . \quad (2.58)$$

Equation (2.58) can be simplified making the following definitions:

$$b = 2K_D + K_{z_\alpha} + i\frac{p}{V}\left(K_{z_{\beta_p}} + \frac{I_a}{I_t} \right) + K_{m_q} ,$$

$$c = K_{m_\alpha} + iK_{m_\beta} + iK_{m_{\beta_p}} \frac{p}{V}$$
$$- \left(K_D + K_{m_q} + i\frac{I_a}{I_t}\frac{p}{V} \right)\left(K_D + K_{z_\alpha} + iK_{z_{\beta_p}} \frac{p}{V} \right) ,$$

$$d = K_0 e^{i(\phi + \pi/2)} + i\frac{g\cos(\theta)}{V^2}\left(K_D - K_{m_q} - i\frac{I_a}{I_t}\frac{p}{V} \right) ,$$

$$\tilde{\zeta}'' - b\tilde{\zeta}' - c\tilde{\zeta} = d . \qquad (2.59)$$

For the solution of $\tilde{\zeta}$, $e^{i(\phi + \pi/2)}$ term will be expanded in terms of p/V as,

$$\phi(s) = \phi_0 + \frac{p}{V}s ,$$

$$e^{i(\phi + \pi/2)} = e^{i\left(\phi_0 + \pi/2 + \frac{p}{V}s \right)} .$$

Inserting solution for V and the above expansion, d becomes,

$$d = K_0 e^{i(\phi_0 + \pi/2)}e^{i\frac{p}{V}s} + i\frac{g\cos(\theta)}{V_0^2}\left(K_D - K_{m_q} - i\frac{I_a}{I_t}\frac{p}{V} \right)e^{2K_D s} .$$

Using the ordinary differential equation knowledge, the homogeneous, partial and total solutions for $\tilde{\zeta}$ can be found as,

$$\tilde{\zeta}_h(s) = k_1 e^{\Lambda_1 s} + k_2 e^{\Lambda_2 s} , \qquad (2.60)$$

$$\tilde{\zeta}_p(s) = \tilde{\zeta}_g e^{2K_D s} + \tilde{\zeta}_c e^{i\frac{p}{V}s} , \qquad (2.61)$$

$$\tilde{\zeta}(s) = k_1 e^{\Lambda_1 s} + k_2 e^{\Lambda_2 s} + \tilde{\zeta}_g e^{2K_D s} + \tilde{\zeta}_c e^{i\frac{p}{V}s} \qquad (2.62)$$

Where Λ_1 and Λ_2 are the eigenvalues of the system. $\tilde{\zeta}_g$ and $\tilde{\zeta}_c$ can be found inserting the partial solution into equation (2.59),

$$\tilde{\zeta}_g = i\frac{g\cos(\theta)}{V_0^2}\frac{\left(K_D - K_{m_q} - i\frac{I_a}{I_t}\frac{p}{V} \right)}{4K_D^2 - 2K_D b - c} , \qquad (2.63)$$

$$\tilde{\zeta}_c = -\frac{K_0 e^{i(\phi_0 + \pi/2)}}{\left(\frac{p}{V} \right)^2 + ib\frac{p}{V} + c} . \qquad (2.64)$$

k_1 and k_2 can be found using the initial conditions $\tilde{\zeta}(0)$ and $\tilde{\zeta}'(0)$:

$$\tilde{\zeta}(0) = \tilde{\zeta}_0 = k_1 + k_2 + \tilde{\zeta}_g + \tilde{\zeta}_c , \qquad (2.65)$$

$$\tilde{\zeta}'(0) = \tilde{\zeta}_0' = k_1\Lambda_1 + k_2\Lambda_2 + 2\tilde{\zeta}_g K_D + i\tilde{\zeta}_c \frac{p}{V} . \quad (2.66)$$

Using equations (2.65) and (2.66), k_1 and k_2 can be evaluated as:

$$k_1 = \frac{\left(\tilde{\zeta}_0 - \tilde{\zeta}_g - \tilde{\zeta}_c \right)\Lambda_2 - \tilde{\zeta}_0' + 2K_D\tilde{\zeta}_g + i\frac{p}{V}\tilde{\zeta}_c}{\Lambda_2 - \Lambda_1} ,$$

$$(2.67)$$

$$k_2 = \frac{\tilde{\zeta}_0' - 2K_D\tilde{\zeta}_g - i\frac{p}{V}\tilde{\zeta}_c - \left(\tilde{\zeta}_0 - \tilde{\zeta}_g - \tilde{\zeta}_c \right)\Lambda_1}{\Lambda_2 - \Lambda_1} .$$

$$(2.68)$$

Finding the solution for $\tilde{\zeta}$, the next step is to find the solution for $\tilde{\mu}$. This can be done using equation (2.57):

$$\tilde{\mu} = \frac{1}{i2}\left[\left(\Lambda_1 - \left(K_D + K_{z_\alpha} + K_{z_{\beta_p}} i\frac{p}{V}\right)\right)k_1 e^{\Lambda_1 s}\right.$$
$$+ \left(\Lambda_2 - \left(K_D + K_{z_\alpha} + K_{z_{\beta_p}} i\frac{p}{V}\right)\right)k_2 e^{\Lambda_2 s}\right]$$
$$+ e^{2K_D s}\left[\frac{\tilde{\zeta}_g}{i2}\left(K_D - K_{z_\alpha} - K_{z_{\beta_p}} i\frac{p}{V}\right) - \frac{g\cos(\theta)}{2V_0^2}\right]$$
$$+ \left(i\frac{p}{V} - \frac{1}{i2}\left(K_D + K_{z_\alpha} + K_{z_{\beta_p}} i\frac{p}{V}\right)\right)\tilde{\zeta}_c e^{i p/V s}. \qquad (2.69)$$

Solving the differential equations for $\tilde{\zeta}$ and $\tilde{\mu}$, the next step is to find the solution for Euler angles θ and ψ. The solution procedure is similar with the previous one; first, the differential equations (2.14) and (2.15) will be transformed into distance domain and then a complex Euler angle will be defined arranging two equations.

$$\theta'V = \tilde{q}, \qquad (2.70)$$

$$\psi'V = \frac{\tilde{r}}{\cos(\theta)} \cong \tilde{r}, \qquad (2.71)$$

$$V(\theta' + i\psi') = \tilde{q} + i\tilde{r}, \qquad (2.72)$$

$$\eta' = (\theta' + i\psi') = 2\tilde{\mu}. \qquad (2.73)$$

Solution for η can be found using equation (2.69):

$$\eta_h(s) = c_1, \qquad (2.74)$$

$$\eta_p(s) = c_2 e^{i p/V s} + c_3 e^{2K_D s} + c_4 e^{\Lambda_1 s} + c_5 e^{\Lambda_2 s}, \qquad (2.75)$$

$$\eta(s) = c_1 + c_2 e^{i p/V s} + c_3 e^{2K_D s} + c_4 e^{\Lambda_1 s} + c_5 e^{\Lambda_2 s}. \qquad (2.76)$$

Constants c_2, c_3, c_4 and c_5 can be found substituting (2.69) into (2.73):

$$c_2 = \left(2 + iK_{z_{\beta_p}} + \frac{(K_D + K_{z_\alpha})}{p/V}\right)\tilde{\zeta}_c, \qquad (2.77)$$

$$c_3 = \frac{1}{2K_D}\left[i\tilde{\zeta}_g\left(K_{z_\alpha} + K_{z_{\beta_p}} i\frac{p}{V} - K_D\right) - \frac{g\cos(\theta)}{V_0^2}\right], \qquad (2.78)$$

$$c_4 = i\frac{k_1}{\Lambda_1}\left(\left(K_D + K_{z_\alpha} + K_{z_{\beta_p}} i\frac{p}{V}\right) - \Lambda_1\right), \qquad (2.79)$$

$$c_5 = i\frac{k_2}{\Lambda_2}\left(\left(K_D + K_{z_\alpha} + K_{z_{\beta_p}} i\frac{p}{V}\right) - \Lambda_2\right). \qquad (2.80)$$

c_1 is evaluated using the initial condition η_0.

$$c_1 = \eta_0 - c_2 - c_3 - c_4 - c_5. \qquad (2.81)$$

Finally the last step is to find the solution for swerving motion y_g and z_g. Similar procedure will be applied here also. The first step is to transform equations (2.11) and (2.12) into distance domain.

$$y_g' = \frac{u}{V}\cos(\theta)\sin(\psi) + \frac{\tilde{v}}{V}\cos(\psi) + \frac{\tilde{w}}{V}\sin(\theta)\sin(\psi), \qquad (2.82)$$

$$z_g' = -\frac{u}{V}\sin(\theta) + \frac{\tilde{w}}{V}\cos(\theta). \qquad (2.83)$$

Assuming small angles, the following simplifications are made,

$$\cos(\theta) \cong \cos(\psi) \cong 1,$$

$$\sin(\theta) \cong \theta,$$

$$\sin(\psi) \cong \psi,$$

$$\sin(\theta)\sin(\psi) \cong 0.$$

Using these simplifications equations (2.82) and (2.83) will become,

$$y_g' \cong \psi + \tilde{\beta}, \qquad (2.84)$$

$$z_g' \cong -\theta + \tilde{\alpha}. \qquad (2.85)$$

Arranging the two equations under the complex swerve displacement φ, one gets,

$$\varphi' = (y_g' + iz_g') = \zeta - i\eta, \qquad (2.86)$$

$$\varphi' = \tilde{\zeta}_c e^{i p/V s} + \tilde{\zeta}_g e^{2K_D s} + k_1 e^{\Lambda_1 s} + k_2 e^{\Lambda_2 s}$$
$$- i\left(c_1 + c_2 e^{i p/V s} + c_3 e^{2K_D s} + c_4 e^{\Lambda_1 s} + c_5 e^{\Lambda_2 s}\right). \qquad (2.87)$$

Solution for φ can be found using the solutions for ζ and η:

$$\varphi_p(s) = d_1, \qquad (2.88)$$

$$\varphi_p(s) = d_2 s + d_3 e^{i p/V s} + d_4 e^{2K_D s} + d_5 e^{\Lambda_1 s} + d_6 e^{\Lambda_2 s}. \qquad (2.89)$$

$$\varphi(s) = d_1 + d_2 s + d_3 e^{i p/V s} + d_4 e^{2K_D s} + d_5 e^{\Lambda_1 s} + d_6 e^{\Lambda_2 s} \qquad (2.90)$$

The constants d_1, d_2, d_3, d_4, d_5 and d_6 are evaluated as,

$$d_1 = \varphi_0 - d_3 - d_4 - d_5 - d_6, \qquad (2.91)$$

$$d_2 = -ic_1, \qquad (2.92)$$

$$d_3 = \frac{\tilde{\zeta}_c - ic_2}{i \, {}^{P}\!/_{V}}, \qquad (2.93)$$

$$d_4 = \frac{1}{2K_D}\left(\tilde{\zeta}_g - ic_3\right), \qquad (2.94)$$

$$d_5 = \frac{1}{\Lambda_1}\left(k_1 - ic_4\right), \qquad (2.95)$$

$$d_6 = \frac{1}{\Lambda_2}\left(k_2 - ic_5\right). \qquad (2.96)$$

3. ESTIMATION OF PARAMETERS

In this section, estimation procedures will be defined. Similar to the derivation of the analytical solutions of motion, the estimation procedure will be done step by step. First the drag parameter K_D will be estimated, and then the roll coefficients, and so on.

3.1. Estimation of The Drag Parameter

For the estimation of the drag parameter K_D, initial velocity V_0 and initial time t_0, equation (2.38) will be used. Since this equation is not linear in terms of the parameters a nonlinear least squares procedure will be applied. Before going on estimation procedure equation (2.38) has to be linearized using Taylor series expansion:

$$t(s) = \left[t(s) + \frac{\partial t(s)}{\partial K_D}\Delta K_D + \frac{\partial t(s)}{\partial V_0}\Delta V_0 + \frac{\partial t(s)}{\partial t_0}\Delta t_0\right]_0. \qquad (3.1)$$

Using equation (2.38), the gradients $\dfrac{\partial t(s)}{\partial K_D}$, $\dfrac{\partial t(s)}{\partial V_0}$ and $\dfrac{\partial t(s)}{\partial t_0}$ can be derived as given below:

$$\frac{\partial t(s)}{\partial K_D} = \frac{K_D{}^2 e^{K_D s} - \left(e^{K_D s} - 1\right)}{V_0 K_D{}^2}, \qquad (3.2)$$

$$\frac{\partial t(s)}{\partial V_0} = -\frac{1}{V_0{}^2 K_D}\left(e^{K_D s} - 1\right), \qquad (3.3)$$

$$\frac{\partial t(s)}{\partial t_0} = 1. \qquad (3.4)$$

Using the linearized equation and least squares cost function, parameters K_D, V_0 and t_0 can be estimated. In this study, matrix equations are solved by *Singular Value Decomposition* method [6]. This method is selected since it can handle ill-conditioned problems and it is especially suggested for identification of parameters due this property.

3.2. Estimation of The Roll Angle Parameters

For the estimation of roll damping parameter K_{l_p}, induced roll moment parameter K_{l_0}, initial roll rate p_0 and initial roll angle ϕ_0, equation (2.44) will be used. Different from the drag coefficient estimation, this equation can not linearized in terms of the three parameters, so a nonlinear least squares procedure will be applied. Equation (2.44) can be linearized

using the Taylor series expansion, taking the first gradients only:

$$\phi(s) \cong \left[\phi(s) + \frac{\partial \phi(s)}{\partial K_{l_p}}\Delta K_{l_p} + \frac{\partial \phi(s)}{\partial K_{l_0}}\Delta K_{l_0}\right.$$
$$\left. + \frac{\partial \phi(s)}{\partial p_0}\Delta p_0 + \frac{\partial \phi(s)}{\partial \phi_0}\Delta \phi_0\right]_0. \qquad (3.5)$$

Using equation (2.44), the gradients $\dfrac{\partial \phi(s)}{\partial K_{l_p}}$, $\dfrac{\partial \phi(s)}{\partial K_{l_0}}$, $\dfrac{\partial \phi(s)}{\partial p_0}$ and $\dfrac{\partial \phi(s)}{\partial \phi_0}$ can be derived as given below:

$$\frac{\partial \phi(s)}{\partial K_{l_p}} = \frac{p_0}{V_0\left(K_D + K_{l_p}\right)^2} + \frac{2K_{l_0}}{\left(K_D + K_{l_p}\right)^3} + \frac{K_{l_0}}{\left(K_D + K_{l_p}\right)^2}s$$
$$-\left(\frac{p_0}{V_0\left(K_D + K_{l_p}\right)^2} + \frac{2K_{l_0}}{\left(K_D + K_{l_p}\right)^3}\right.$$
$$\left. - \frac{p_0}{V_0\left(K_D + K_{l_p}\right)}s - \frac{K_{l_0}}{\left(K_D + K_{l_p}\right)^2}s\right)e^{\left(K_D + K_{l_p}\right)s}, \qquad (3.6)$$

$$\frac{\partial \phi(s)}{\partial K_{l_0}} = \frac{1}{\left(K_D + K_{l_p}\right)^2}\left[e^{\left(K_D + K_{l_p}\right)s} - 1\right] - \frac{1}{\left(K_D + K_{l_p}\right)}s, \qquad (3.7)$$

$$\frac{\partial \phi(s)}{\partial p_0} = \frac{1}{V_0\left(K_D + K_{l_p}\right)}\left(-1 + e^{\left(K_D + K_{l_p}\right)s}\right), \qquad (3.8)$$

$$\frac{\partial \phi(s)}{\partial \phi_0} = 1. \qquad (3.9)$$

Similarly, using the linearized equation and least squares cost function parameters K_{l_p}, K_{l_0}, p_0 and ϕ_0 can be estimated.

3.3. Estimation of The Complex Angle of Attack Parameters

In this section, estimation of the two eigenvalues Λ_1 and Λ_2, initial conditions $\tilde{\zeta}_0$ and $\tilde{\zeta}_0'$, complex angle of attack due to gravity $\tilde{\zeta}_g$ and complex of angle of attack due to asymmetry $\tilde{\zeta}_c$ will be presented. The aerodynamic parameters pitch moment static stability parameter K_{m_α}, pitch moment out of plane static stability parameter K_{m_β}, pitch moment damping stability parameter K_{m_q} will be evaluated using the estimated eigenvalues and induced moment parameter K_0 will be evaluated using the $\tilde{\zeta}_c$. This problem is also nonlinear in terms of the above-mentioned parameters, therefore a nonlinear least squares procedure will be applied. The Taylor series expansion for the equation (2.62) can be written as follows:

$$\tilde{\zeta}(s) \cong \left[\tilde{\zeta}(s) + \frac{\partial \tilde{\zeta}(s)}{\partial \Lambda_1} \Delta \Lambda_1 + \frac{\partial \tilde{\zeta}(s)}{\partial \Lambda_2} \Delta \Lambda_2 + \frac{\partial \tilde{\zeta}(s)}{\partial \tilde{\zeta}_0} \Delta \tilde{\zeta}_0 \right.$$
$$\left. + \frac{\partial \tilde{\zeta}(s)}{\partial \tilde{\zeta}_0'} \Delta \tilde{\zeta}_0' + \frac{\partial \tilde{\zeta}(s)}{\partial \tilde{\zeta}_g} \Delta \tilde{\zeta}_g + \frac{\partial \tilde{\zeta}(s)}{\partial \tilde{\zeta}_c} \Delta \tilde{\zeta}_c \right]_0 \quad (3.10)$$

The gradients with respect to $\Lambda_1, \Lambda_2, \tilde{\zeta}_0, \tilde{\zeta}_0', \tilde{\zeta}_g$ and $\tilde{\zeta}_c$ will be,

$$\frac{\partial \tilde{\zeta}(s)}{\partial \Lambda_1} = \frac{\partial k_1}{\partial \Lambda_1} e^{\Lambda_1 s} + k_1 e^{\Lambda_1 s} s + \frac{\partial k_2}{\partial \Lambda_1} e^{\Lambda_2 s} + \frac{\partial \tilde{\zeta}_g}{\partial \Lambda_1} e^{2K_D s}$$
$$+ 2 \tilde{\zeta}_g \frac{\partial K_D}{\partial \Lambda_1} e^{2K_D s} s + \frac{\partial \tilde{\zeta}_c}{\partial \Lambda_1} e^{iP/V s}, \quad (3.11)$$

$$\frac{\partial \tilde{\zeta}(s)}{\partial \Lambda_2} = \frac{\partial k_1}{\partial \Lambda_2} e^{\Lambda_1 s} + \frac{\partial k_2}{\partial \Lambda_2} e^{\Lambda_2 s} + k_2 e^{\Lambda_2 s} s + \frac{\partial \tilde{\zeta}_g}{\partial \Lambda_2} e^{2K_D s}$$
$$+ 2 \tilde{\zeta}_g \frac{\partial K_D}{\partial \Lambda_2} e^{2K_D s} s + \frac{\partial \tilde{\zeta}_c}{\partial \Lambda_2} e^{iP/V s}, \quad (3.12)$$

$$\frac{\partial \tilde{\zeta}(s)}{\partial \tilde{\zeta}_0} = \frac{\partial k_1}{\partial \tilde{\zeta}_0} e^{\Lambda_1 s} + \frac{\partial k_2}{\partial \tilde{\zeta}_0} e^{\Lambda_2 s}, \quad (3.13)$$

$$\frac{\partial \tilde{\zeta}(s)}{\partial \tilde{\zeta}_0'} = \frac{\partial k_1}{\partial \tilde{\zeta}_0'} e^{\Lambda_1 s} + \frac{\partial k_2}{\partial \tilde{\zeta}_0'} e^{\Lambda_2 s}, \quad (3.14)$$

$$\frac{\partial \tilde{\zeta}(s)}{\partial \tilde{\zeta}_g} = \frac{\partial k_1}{\partial \tilde{\zeta}_g} e^{\Lambda_1 s} + \frac{\partial k_2}{\partial \tilde{\zeta}_g} e^{\Lambda_2 s} + e^{2K_D s}, \quad (3.15)$$

$$\frac{\partial \tilde{\zeta}(s)}{\partial \tilde{\zeta}_c} = \frac{\partial k_1}{\partial \tilde{\zeta}_c} e^{\Lambda_1 s} + \frac{\partial k_2}{\partial \tilde{\zeta}_c} e^{\Lambda_2 s} + e^{iP/V s}. \quad (3.16)$$

In the equations, (3.11) and (3.12) the gradients of $\tilde{\zeta}_g, \tilde{\zeta}_c$ and K_D with respect to the eigenvalues are assumed to be zero, since there is no explicit dependence between them. In order to evaluate the above gradients, the gradients of k_1 and k_2 with respect to $\Lambda_1, \Lambda_2, \tilde{\zeta}_0, \tilde{\zeta}_0', \tilde{\zeta}_g$ and $\tilde{\zeta}_c$ are required. These gradients can be found using equations (2.67) and (2.68):

$$\frac{\partial k_1}{\partial \Lambda_1} = \frac{\left(\tilde{\zeta}_0 - \tilde{\zeta}_g - \tilde{\zeta}_c\right)\Lambda_2 - \tilde{\zeta}_0' + 2K_D \tilde{\zeta}_g + iP/V \tilde{\zeta}_c}{\left(\Lambda_2 - \Lambda_1\right)^2}, \quad (3.17)$$

$$\frac{\partial k_2}{\partial \Lambda_1} = \frac{\tilde{\zeta}_0' - 2K_D \tilde{\zeta}_g - iP/V \tilde{\zeta}_c - \left(\tilde{\zeta}_0 - \tilde{\zeta}_g - \tilde{\zeta}_c\right)\Lambda_2}{\left(\Lambda_2 - \Lambda_1\right)^2}, \quad (3.18)$$

$$\frac{\partial k_1}{\partial \Lambda_2} = \frac{\tilde{\zeta}_0' - 2K_D \tilde{\zeta}_g - iP/V \tilde{\zeta}_c - \left(\tilde{\zeta}_0 - \tilde{\zeta}_g - \tilde{\zeta}_c\right)\Lambda_1}{\left(\Lambda_2 - \Lambda_1\right)^2}, \quad (3.19)$$

$$\frac{\partial k_2}{\partial \Lambda_2} = \frac{\left(\tilde{\zeta}_0 - \tilde{\zeta}_g - \tilde{\zeta}_c\right)\Lambda_1 - \tilde{\zeta}_0' + 2K_D \tilde{\zeta}_g + iP/V \tilde{\zeta}_c}{\left(\Lambda_2 - \Lambda_1\right)^2}, \quad (3.20)$$

$$\frac{\partial k_1}{\partial \tilde{\zeta}_0} = \frac{\Lambda_2}{\Lambda_2 - \Lambda_1}, \quad (3.21)$$

$$\frac{\partial k_2}{\partial \tilde{\zeta}_0} = \frac{-\Lambda_1}{\Lambda_2 - \Lambda_1}, \quad (3.22)$$

$$\frac{\partial k_1}{\partial \tilde{\zeta}_0'} = \frac{-1}{\Lambda_2 - \Lambda_1}, \quad (3.23)$$

$$\frac{\partial k_2}{\partial \tilde{\zeta}_0'} = \frac{1}{\Lambda_2 - \Lambda_1}, \quad (3.24)$$

$$\frac{\partial k_1}{\partial \tilde{\zeta}_g} = \frac{2K_D - \Lambda_2}{\Lambda_2 - \Lambda_1}, \quad (3.25)$$

$$\frac{\partial k_2}{\partial \tilde{\zeta}_g} = \frac{\Lambda_1 - 2K_D}{\Lambda_2 - \Lambda_1}, \quad (3.26)$$

$$\frac{\partial k_1}{\partial \tilde{\zeta}_c} = \frac{iP/V - \Lambda_2}{\Lambda_2 - \Lambda_1}, \quad (3.27)$$

$$\frac{\partial k_2}{\partial \tilde{\zeta}_c} = \frac{\Lambda_1 - iP/V}{\Lambda_2 - \Lambda_1}. \quad (3.28)$$

After finding the parameters of the differential equation, aerodynamic coefficients can be evaluated using the eigenvalues Λ_1 and Λ_2. Using the fact that, the characteristic equation with these eigenvalues will be,

$$\left(s - \Lambda_1\right)\left(s - \Lambda_2\right) = 0,$$

$$s^2 - \left(\Lambda_1 + \Lambda_2\right)s - \Lambda_1 \Lambda_2 = 0. \quad (3.29)$$

Equating this equation to the characteristic equation of (2.61), one can find the following equalities:

$$\Lambda_1 + \Lambda_2 = b = 2K_D + K_{Z_\alpha} + i\frac{p}{V}\left(K_{Z_{\beta_p}} + \frac{I_a}{I_t}\right) + K_{m_q},$$

$$-\Lambda_1 \Lambda_2 = c = \left(K_{m_\alpha} + iK_{m_\beta} + iK_{m_{\beta_p}}\right)$$
$$-\left(K_D + K_{m_q} + i\frac{I_a}{I_t}\frac{p}{V}\right)\left(K_D + K_{Z_\alpha} + iK_{Z_{\beta_p}}\frac{p}{V}\right).$$

Using the above equalities, aerodynamic derivatives can be found, assuming K_D and K_{Z_α} are known,

$$K_{m_q} = \text{Re}\left(\Lambda_1 + \Lambda_2\right) - 2K_D - K_{Z_\alpha}, \quad (3.30)$$

$$K_{Z_{\beta_p}} = \text{Im}\left(\Lambda_1 + \Lambda_2\right)\frac{V}{p} - \frac{I_a}{I_t}, \quad (3.31)$$

$$K_{m_\alpha} = \text{Re}\left(-\Lambda_1\Lambda_2\right) + \left(K_D + K_{m_q}\right)\left(K_D + K_{z_\alpha}\right) - \frac{I_a}{I_t}K_{z_{\beta_p}}\left(\frac{p}{V}\right)^2 ,$$

(3.32)

$$K_{m_\beta} + K_{m_{\beta_p}}\frac{p}{V} = \text{Im}\left(-\Lambda_1\Lambda_2\right) + \frac{I_a}{I_t}\frac{p}{V}\left(K_D + K_{z_\alpha}\right)$$

$$+ K_{z_{\beta_p}}\frac{p}{V}\left(K_D + K_{m_q}\right).$$

(3.33)

Note that, the out of plane stability derivatives K_{m_β} and $K_{m_{\beta_p}}$ can not be discritized. Using the definition for $\tilde{\zeta}_c$, K_0 can be found as:

$$K_0 = -\tilde{\zeta}_c c e^{-i\left(\phi_0 + \pi/2\right)}.$$

(3.34)

This completes the discussion for estimating complex angle of attack parameters. Note that during the evaluation of the aerodynamic parameters, K_{z_α} is assumed to be known, although it has not yet estimated. These calculations are carried out with the initial estimate of K_{z_α} and after evaluating it, the calculations for complex angle of attack parameters are revised.

3.4. Estimation of The Complex Euler Angle Parameters

The next step in the estimation procedure is the evaluation of the complex Euler angle of parameters, c_2, c_3, c_4, c_5 and η_0 Using c_4 and c_5 normal force static stability parameter K_{z_α} will be found. Similar to the previous cases, a nonlinear least squares procedure will be applied here. The Taylor series expanded form of complex Euler angle will be:

$$\eta(s) \cong \left[\eta(s) + \frac{\partial\eta(s)}{\partial c_2}\Delta c_2 + \frac{\partial\eta(s)}{\partial c_3}\Delta c_3\right.$$

$$\left. + \frac{\partial\eta(s)}{\partial c_4}\Delta c_4 + \frac{\partial\eta(s)}{\partial c_5}\Delta c_5 + \frac{\partial\eta(s)}{\partial\eta_0}\Delta\eta_0\right]_0 .$$

(3.35)

Note that in the above equation c_1 is omitted, this is due to that this parameter can be written in terms of others and the initial condition. The gradients of $\eta(s)$ with respect to the parameters can be found as:

$$\frac{\partial\eta(s)}{\partial c_2} = e^{ip/\nu s} - 1 ,$$

(3.36)

$$\frac{\partial\eta(s)}{\partial c_3} = e^{2K_D s} - 1 ,$$

(3.37)

$$\frac{\partial\eta(s)}{\partial c_4} = e^{\Lambda_1 s} - 1 ,$$

(3.38)

$$\frac{\partial\eta(s)}{\partial c_5} = e^{\Lambda_2 s} - 1 ,$$

(3.39)

$$\frac{\partial\eta(s)}{\partial\eta_0} = 1 .$$

(3.40)

Obtaining parameters c_4 and c_5, K_{z_α} can be found:

$$K_{z_\alpha} = \frac{-ic_4\Lambda_1}{k_1} + \Lambda_1 - K_D - K_{z_{\beta_p}}i\frac{p}{V} ,$$

(3.41)

$$K_{z_\alpha} = \frac{-ic_5\Lambda_2}{k_2} + \Lambda_2 - K_D - K_{z_{\beta_p}}i\frac{p}{V}$$

(3.42)

Although K_{z_α} is a real variable the estimated values using (3.41) and (3.42) came out to be complex. The real and imaginary parts of the estimations are nearly the same in magnitude but the imaginary parts have the opposite sign. Taking the mean of the two estimations eliminates the complex part and gives a better result.

3.5. Estimation of The Complex Swerve Displacement Parameters

Final step is the estimation of complex swerve displacement parameters d_2, d_3, d_4, d_5, d_6 and φ_0 The Taylor series expanded form of the complex swerve displacement will be:

$$\varphi(s) \cong \left[\varphi(s) + \frac{\partial\varphi(s)}{\partial d_2}\Delta d_2 + \frac{\partial\varphi(s)}{\partial d_3}\Delta d_3 + \frac{\partial\varphi(s)}{\partial d_4}\Delta d_4\right.$$

$$\left. + \frac{\partial\varphi(s)}{\partial d_5}\Delta d_5 + \frac{\partial\varphi(s)}{\partial d_6}\Delta d_6 + \frac{\partial\varphi(s)}{\partial\varphi_0}\Delta\varphi_0\right]_0 .$$

(3.43)

The gradients of $\varphi(s)$ with respect to the parameters are,

$$\frac{\partial\varphi(s)}{\partial d_2} = s ,$$

(3.44)

$$\frac{\partial\varphi(s)}{\partial d_3} = e^{ip/\nu s} - 1 ,$$

(3.45)

$$\frac{\partial\varphi(s)}{\partial d_4} = e^{2K_D s} - 1 ,$$

(3.46)

$$\frac{\partial\varphi(s)}{\partial d_5} = e^{\Lambda_1 s} - 1 ,$$

(3.47)

$$\frac{\partial\varphi(s)}{\partial d_6} = e^{\Lambda_2 s} - 1 ,$$

(3.48)

$$\frac{\partial\varphi(s)}{\partial\varphi_0} = 1 .$$

(3.49)

Similar to the Euler angle case K_{z_α} can be found using the differential equation parameters d_5 and d_6 .

$$K_{z_\alpha} = \frac{d_5\Lambda_1^2}{k_1} - K_D - K_{z_{\beta_p}}i\frac{p}{V} ,$$

(3.50)

$$K_{z_\alpha} = \frac{d_6\Lambda_2^2}{k_2} - K_D - K_{z_{\beta_p}}i\frac{p}{V} .$$

(3.51)

Similar to the complex Euler angle case the two estimations came out to be approximately complex conjugates, so the

mean of the two is taken. Two K_{Z_α} estimates are found, in complex Euler angle and complex swerve displacement, it is seen that the K_{Z_α} value found using the complex swerve displacement solution comes out to be more close to the exact data. The K_{Z_α} value found from the swerve motion solution is taken as the final estimate, complex Euler angle solution is recalculated using this estimate.

4. RESULTS

In this section, result of test cases with simulation data, will be presented. The simulation data is generated by a computer code, which uses 6 degree of freedom flight mechanics equations of motion.

In Figure 2-Figure 5 simulated and estimated motion data are presented. The simulation data is generated using the values given in Table 1. The error of the states is plotted in Figure 6-Figure 9. The estimation results, seems to be very good. This can be verified from the mean error values given in Table 2. Furthermore, the estimation quality can be investigated from the estimated values of the parameters, presented in Table 3. Investigating this table, it can be seen that all of the parameters have an accuracy better that 1 %.

Table 1. Simulation parameters.

C_D	0.87
C_{Z_α}	-12.1
C_{l_0}	-1.0×10^{-3}
C_{l_p}	-1.0
C_{m_α}	-27.4
C_{m_q}	-544.0
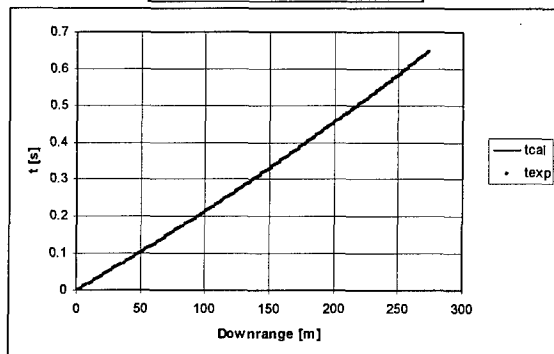
Figure 2. Simulated and estimated variation of velocity.
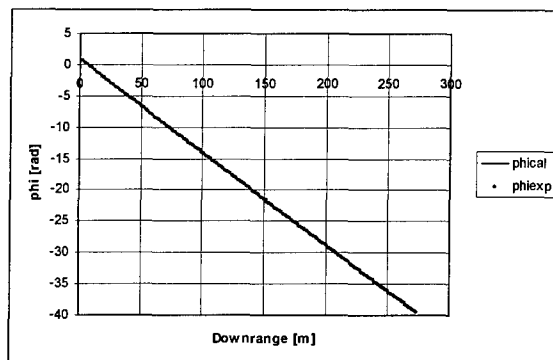
Figure 3. Simulated and estimated variation of roll angle.
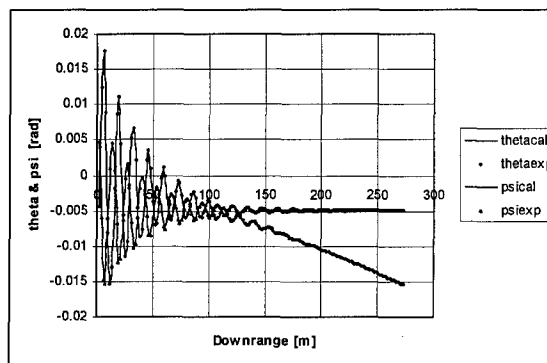
Figure 4. Simulated and estimated variation of pitch and yaw angle.
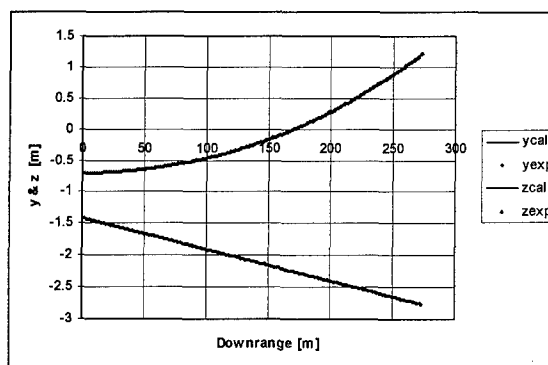
Figure 5. Simulated and estimated variation of crossrange and altitude.
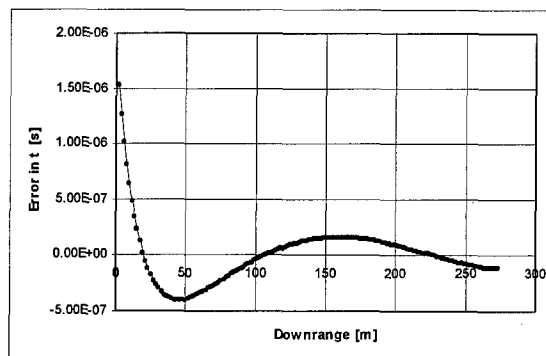
Figure 6. Variation of error in velocity.
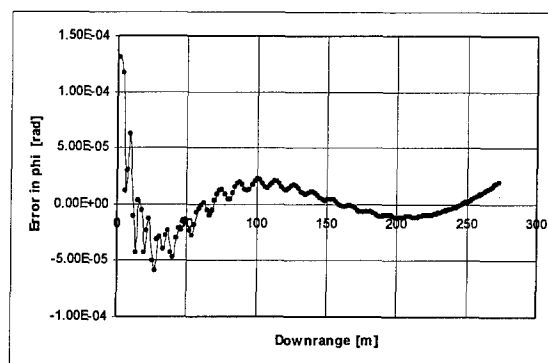
Figure 7. Variation of error in roll angle.
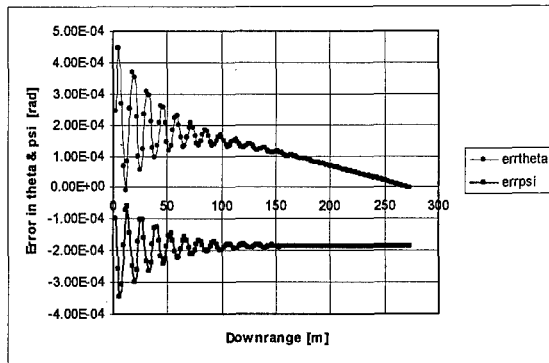
Figure 8. Variation of error in pitch and yaw angle.
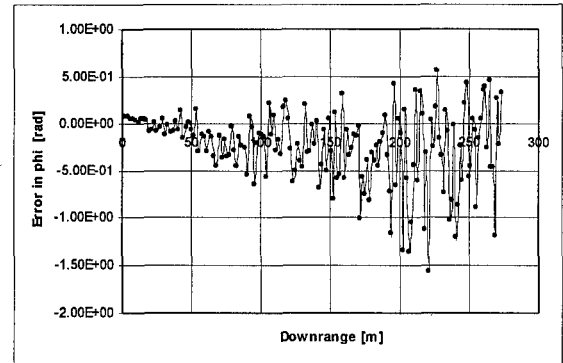
Figure 10. Variation of error in roll angle.
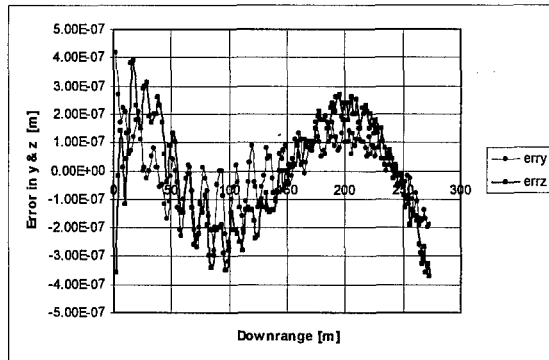
Figure 9. Variation of error in crossrange and altitude.

Figure 11. Variation of error in pitch angle.

Table 2. Mean errors of the states.

$t\ [s]$	2.599×10^{-7}
$\phi\ [rad]$	2.148×10^{-5}
$y - z\ [m]$	1.559×10^{-7}
$\theta - \psi\ [rad]$	2.666×10^{-4}

Table 3. Exact and estimated parameters.

	Exact	Estimation	Error	% Error
C_D	0.87	0.87007	7.0×10^{-5}	8.05×10^{-3}
C_{Z_α}	-12.1	-12.249	0.149	1.23
C_{l_0}	-1.0×10^{-3}	1.007×10^{-3}	7.0×10^{-6}	0.70
C_{l_p}	-1.0	-1.0055	5.5×10^{-3}	0.55
C_{m_α}	-27.4	-27.4015	1.5×10^{-3}	5.47×10^{-3}
C_{m_q}	-544.0	-541.123	2.877	0.53
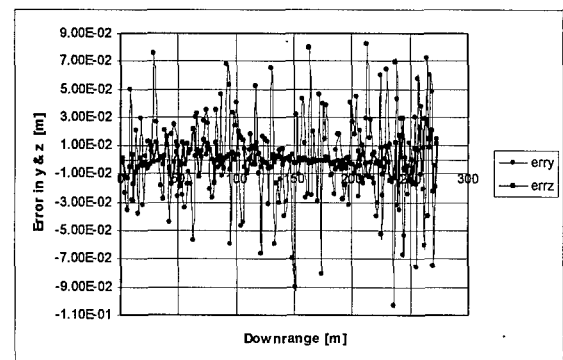
Figure 12. Variation of error in crossrange.

Table 4. Mean errors of the states.

$t\ [s]$	2.599×10^{-7}
$\phi\ [rad]$	0.451
$y - z\ [m]$	2.624×10^{-2}
$\theta - \psi\ [rad]$	4.579×10^{-3}

Table 5. Exact and estimated parameters.

	Exact	Estimation	Error	% Error
C_D	0.87	0.87007	7.0×10^{-5}	8.05×10^{-3}
C_{Z_α}	-12.1	-33.118	21.018	173.70
C_{l_0}	-1.0×10^{-3}	1.088×10^{-3}	8.8×10^{-5}	8.80
C_{l_p}	-1.0	-1.035	3.5×10^{-2}	3.50
C_{m_α}	-27.40	-28.73	1.33	4.85
C_{m_q}	-544.0	-549.637	5.637	1.04

In the preceding part, the test results of the programs with the ideal data were presented. In the real life experiences, the data will always include noise terms coming from the measurement devices. This will degrade the estimation accuracy. The second test is made with a data containing data. The data is generated with the same aerodynamic parameters but 5 % noise is added to output states except x. No noise is added to x, since x depends on the position of the measurement station, which can be known accurately. In the following part the test results obtained using the test, results will be presented (Figure 10-Figure 12).

Comparing the results for the ideal case (Table 2) and the noisy case (Table 4), the loss of accuracy can be easily pointed

out. Besides, this decrease in accuracy some of the estimated parameters are very close to the exact ones, C_{m_α}, C_{l_p} and C_{l_0}. This feature is very important for the real tests. Although the error of the drag coefficient C_D is very small, no comment on this parameter is made since the data for this parameter does not include noise. It is known that the drag coefficient has the same feature.

5.CONCLUSION

The aim of this study was to understand the nature of the linear aeroballistic data identification technique and to build an initial estimator for the complex estimators. During this study a modified formulation is developed which uses the advantages of the existing methods. For this purpose, a mathematical model is build and then computer codes are prepared. The written codes are tested using simulation data. It is seen that in the absence of noise, the estimation accuracy is very good and this degrades for the noisy case.

Although the estimation accuracy degrades in the case of noise, it is observed that some basic parameters C_D, C_{l_p}, C_{m_α} and C_{l_0} came out to be close to the exact parameters, which is believed to be an important property.

REFERENCES

[1]. C. W. INGRAM, J. D. NICOLAIDES, ' Obtaining Nonlinear Aerodynamic Stability Coefficients from Free-Angular Motion of Rigid Bodies,' Journal of Spacecraft and Rockets, Vol. 8 No. 4, April 1971.

[2]. MURPHY C. H., 'Free Flight Motion of Symmetric Missiles,' Report No. 1216, Ballistic Research Laboratories, Aberdeen Proving Ground, Maryland, 1963.

[3]. WEISS S., DOHERR K-F., SCHILING H., 'Analytical Solution and Parameter Estimation of Projectile Dynamics,' Journal of Spacecraft and Rockets, Vol. 32, No. 1, January-February, 1995.

[4]. TANRIKULU Ö., 'Linear Stability Analysis of Symmetric and Slightly Asymmetric Rolling and Non-rolling Unguided Missiles in Free Flight,' TÜBİTAK-SAGE Report, March 1993.

[5]. ETKIN, B., 'Dynamics of Atmospheric Flight,' Wiley, 1972.

[6]. PRESS W., FLANNERY B. P., TEUKOLSKY S. A., VETTERLING W. T., ' Numerical Recipes,' Cambridge University Press, 1990.

[7]. WHYTE R. H., HATHAWAY W. H., 'Aeroballistic Range Data Reduction Technique Utilizing Numerical Integration,' Technical Report AFATL-TR-74-41, February 1974.

[8]. MAHMUTYAZICIOĞLU G., 'Aerodynamic Data Identification Using Linear Aeroballistic Theory,' TÜBİTAK-SAGE Report, SAGE-A06-RA-MS-0109, April 1997.

Identification of Gyroplane Stability and Control Characteristics

S. Houston, D. Thomson
Dept. of Aerospace Engineering
University of Glasgow
Glasgow
Scotland
G12 8QQ

1　Summary

This Paper presents an analysis of test data recorded during flight trials of a gyroplane. This class of rotary-wing aircraft has found limited application in areas other than sport or recreational flying. However, the accident rate is such that a study of the configuration's stability and control characteristics is timely, and in addition substantive data is required for a new airworthiness and design standard that is under development. The Paper discusses the special nature of the application of system identification tools to the gyroplane problem, particularly in the context of lack of *a priori* knowledge of the type's dynamic characteristics, design of installation and experiments, and data analysis.

2　Nomenclature

A, B	state-space system and control matrices
i	imaginary operator
L_v, L_p, etc	rolling acceleration derivatives, 1/(ms), 1/s etc.
M_u, M_q, etc	pitching moment derivatives, 1/(ms), 1/s etc.
N	number of points in time series
N_v, N_p, etc	yawing acceleration derivatives, 1/(ms), 1/s etc.
p, q, r	angular velocity components about x, y, z body axes, rad/s
Q_u, Q_w, etc	rotor torque derivatives, rev/min/(m)
R	correlation coefficient
$Re[], Im[]$	real and imaginary components of []
V_f	airspeed, m/s
u, v, w	velocity component along lateral body axis, m/s
$u_{probe}, v_{probe}, w_{probe}$	velocity component along lateral air data probe axis, m/s
$\underline{x}, \underline{u}$	state and control vectors
$\underline{x}(\omega), \underline{u}(\omega)$	Fourier-transformed state and control vectors
$x_{vane}, y_{vane}, z_{vane}$	sideslip vane location in body axes, m
x_{cg}, y_{cg}, z_{cg}	aircraft centre-of-mass position in body axes, m
X_u, X_q, etc	longitudinal body axis acceleration derivatives, 1/s, m/(rad s), etc.
Y_v, Y_p, etc	lateral body axis acceleration derivatives, 1/s, m/(rad s), etc.
Z_u, Z_q, etc	vertical body axis acceleration derivatives, 1/s, m/(rad s), etc.
$\alpha_{vane}, \beta_{vane}$	angle of attack and sideslip measured at vane location, rad
Δf	frequency increment, rad/s
Δt	time increment, s
η_c	lateral stick position, % (0% fully left)
η_{ped}	rudder pedal position, % (0% fully left)
η_s	longitudinal stick position, % (0% fully forward)
ω	frequency, rad/s
$'$	perturbation quantities

3　Introduction

There is a wide range of configurations in the class of aircraft known as rotorcraft. The helicopter is the most common type, finding widespread application in commercial and military aviation. The gyroplane (or autogyro), however, is an increasingly popular machine in sport and recreational flying, having found no practical application in contemporary commercial or military roles.

Currently, most if not all types of gyroplane are in the homebuilt, or experimental category. The study of the configuration's flight mechanics is timely, given the accident rate suffered by the aircraft, e.g. Ref. 1. This, together with the increase in light gyroplane flying in the U.K., has heightened interest in this class of aircraft, and a new airworthiness and design standard (BCAR Section T) has been published by the U.K. Civil Aviation Authority, Ref. 2.

The gyroplane presents a particular challenge, in addition to those normally met with helicopter system identification. The aircraft is light, which can place stringent limits on atmospheric conditions during the tests. Solo operation of this aircraft was essential due to the mass and space restrictions imposed by the instrumentation system. This placed particular demands on the test pilot's flying skills in order that the quality of test input was not compromised. The gyroplane also constituted a special application of system identification and parameter estimation tools, as there are no contemporary flight test analyses in the open literature, to provide a base of *a priori* knowledge.

4　Background

The gyroplane helped to pave the way for the development of the helicopter, introducing cyclic pitch control and blades attached to the rotor hub by means of a hinge. However, it is only recently that stability and control issues have been addressed in the literature, Refs. 3 and 4. This work separately considered longitudinal, and lateral directional, stability and control. It has shown that gyroplanes can exhibit conventional stability and control characteristics, although the rotorspeed degree of freedom couples strongly with the classical short-period and phugoid modes of motion. Prior to that work, the literature on gyroplanes nonetheless is considerable, Refs. 5-15 for example. However, in a contemporary context, this work is now largely of historical significance. It provides the basis of the understanding of gyroplane flight, but does not address the issues of stability and control. Examination of the literature shows a logical development of the study of gyroplanes, from the elementary theory of gyroplane flight, to an analysis of aerodynamics and performance and ultimately rotor

behaviour, but only for steady flight. Interest then apparently waned and the next logical stage in the study of the gyroplane i.e. stability and control, was not examined. For example, the work of Glauert includes the derivation of simple expressions for rotorspeed as a function of loading and axial velocity, Ref. 5. Wheatley, Ref. 11 derived expressions for the flapping angles required for equilibrium flight, presenting results that show how coning, longitudinal and lateral flap angles vary with flight condition. Nowadays, these analyses would be recognisable as classical rotary-wing theory and analogous to that found in helicopter text books. Wheatley even examined higher harmonic components of blade flapping behaviour, Ref. 13.

5   Data Analysis and Model Synthesis

The model structure for which coefficients are to be identified, is of conventional state-space form, i.e.

$$\dot{\underline{x}} = A\underline{x} + B\underline{u} \tag{1}$$

The lateral/directional and longitudinal motions were treated separately. For the former, the A and B matrices are given by

$$A = \begin{bmatrix} Y_v & Y_p & Y_\phi & Y_r & 0 \\ L_v & L_p & 0 & L_r & 0 \\ 0 & 1 & 0 & 0 & 0 \\ N_v & N_p & 0 & N_r & 0 \\ 0 & 0 & 0 & 1 & 0 \end{bmatrix} , \quad B = \begin{bmatrix} Y_{\eta_c} & Y_{\eta_{ped}} \\ L_{\eta_c} & L_{\eta_{ped}} \\ 0 & 0 \\ N_{\eta_c} & N_{\eta_{ped}} \\ 0 & 0 \end{bmatrix} \tag{2}$$

with

$$\underline{x} = \begin{bmatrix} v' & p' & \phi' & r' & \psi' \end{bmatrix}^T, \quad \underline{u} = \begin{bmatrix} \eta_c' & \eta_{ped}' \end{bmatrix}^T \tag{3}$$

For the latter, the A and B matrices are given by

$$A = \begin{bmatrix} X_u & X_w & X_q & X_\theta & X_\Omega \\ Z_u & Z_w & Z_q & Z_\theta & Z_\Omega \\ M_u & M_w & M_q & M_\theta & M_\Omega \\ 0 & 0 & 1 & 0 & 0 \\ Q_u & Q_w & Q_q & Q_\theta & Q_\Omega \end{bmatrix} , \quad B = \begin{bmatrix} X_{\eta_s} \\ Z_{\eta_s} \\ M_{\eta_s} \\ 0 \\ Q_{\eta_s} \end{bmatrix} \tag{4}$$

with

$$\underline{x} = \begin{bmatrix} u' & w' & q' & \theta' & \Omega' \end{bmatrix}^T, \quad \underline{u} = \begin{bmatrix} \eta_s' \end{bmatrix} \tag{5}$$

The rigid body states are taken to be with respect to the usual mutually orthogonal, right-handed frame of reference whose origin is at the centre of mass.

The angular quantities in the state vector, and the control positions, are all measured directly. The translational velocities u, v, w are obtained from airspeed, sideslip and angle of attack data measured at the nose-mounted boom, as follows.

$$u = u_{probe} - q(z_{vane} - z_{cg}) + r(y_{vane} - y_{cg})$$

$$v = v_{probe} + p(z_{vane} - z_{cg}) - r(x_{vane} - x_{cg}) \tag{6}$$

$$w = w_{probe} - p(y_{vane} - y_{cg}) + q(x_{vane} - x_{cg})$$

and

$$u_{probe} = \frac{V_f \cos\beta_{vane}}{\sqrt{1 + \tan^2\alpha_{vane}}} \quad ;$$

$$v_{probe} = V_f \sin\beta_{vane} \quad ; \tag{7}$$

$$w_{probe} = u_{probe} \tan\alpha_{probe}$$

The time histories of each variable were then converted into frequency domain information using a Discrete Fourier Transform, Ref. 21, given by

$$X(k\Delta f) = \Delta t \sum_{n=0}^{N-1} x_n e^{-i2\pi(kn)/N}; \quad k = 0,1,2,\ldots,N-1 \tag{8}$$

which gives real and imaginary parts of X ,

$$\text{Re}[X(k\Delta f)] = \Delta t \sum_{n=0}^{N-1} x_n \cos(2\pi(kn)/N)$$

$$\tag{9}$$

$$\text{Im}[X(k\Delta f)] = -\Delta t \sum_{n=0}^{N-1} x_n \sin(2\pi(kn)/N)$$

where

$$\Delta f = \frac{2\pi}{N\Delta t} \tag{10}$$

The quality of these frequency domain data can be enhanced by standard processing techniques such as applying overlapped and tapered windows to the data, as recommended by Tischler, Ref. 21.

Each degree of freedom can then be treated separately, and formulation as a linear regression problem allows estimation of the coefficients. The state-space description is converted to the frequency domain, i.e.

$$i\omega\,\underline{x}(\omega) = A\underline{x}(\omega) + B\underline{u}(\omega) \tag{11}$$

Note that this assumes that any process noise is zero. The real parts on each side can be equated, as can the imaginary parts, to give two matrix equations that the A and B coefficients must satisfy, viz.

$$-\omega\,\text{Im}[\underline{x}(\omega)] = A(\text{Re}[\underline{x}(\omega)]) + B(\text{Re}[\underline{u}(\omega)])$$

$$\omega\,\text{Re}[\underline{x}(\omega)] = A(\text{Im}[\underline{x}(\omega)]) + B(\text{Im}[\underline{u}(\omega)]) \tag{12}$$

The rolling moment equation for example, is then expressed as the two equations

$$-\omega\,\text{Im}[p(\omega)] = L_v\,\text{Re}[v(\omega)] + L_p\,\text{Re}[p(\omega)]$$

$$+ L_r\,\text{Re}[r(\omega)] + L_{\eta_c}\,\text{Re}[\eta_c(\omega)]$$

$$+ L_{\eta_{ped}}\,\text{Re}[\eta_{ped}(\omega)]$$

$$\omega\,\text{Re}[p(\omega)] = L_v\,\text{Im}[v(\omega)] + L_p\,\text{Im}[p(\omega)] \tag{13}$$

$$+ L_r\,\text{Im}[r(\omega)] + L_{\eta_c}\,\text{Im}[\eta_c(\omega)]$$

$$+ L_{\eta_{ped}}\,\text{Im}[\eta_{ped}(\omega)]$$

The other degrees of freedom are in a similar form.

The equation-error formulation is especially useful in circumstances where not all the degrees of freedom in the model structure can be identified from a single event. In such cases the rolling moment, for example, identified

from one flight or event can be incorporated in the state-space model structure with the sideforce or yawing moment equations identified from another. Such flexibility proved necessary in the analysis of this gyroplane's lateral/directional characteristics.

6   Aircraft and Experimental Installation

The aircraft used in this study was the VPM M16 gyroplane, Figure 1. It is of Italian origin, produced in kit form for assembly by the owner. The maximum all-up mass is 450 kg. The aircraft is powered by a four-cylinder two-stroke engine driving a three-bladed fixed pitch propeller. For helicopter engineers not familiar with gyroplanes, the rotor system is of an interesting configuration, typical of this class of aircraft. The two main rotor blades are bolted to a teeter bar, suspended from a teeter bolt. The blades are untwisted, and no cyclic pitch can be applied. This hub assembly is mounted on a spindle, about 200mm long, and this spindle pivots about its lower end to tilt the entire rotor fore and aft and laterally to effect pitch and roll control, respectively. In this regard, the aircraft could be classed as a tilt-rotor. The rotor system is linked mechanically by rods to the pilot's control column, and a conventional rudder is operated by a cable assembly from foot pedals.
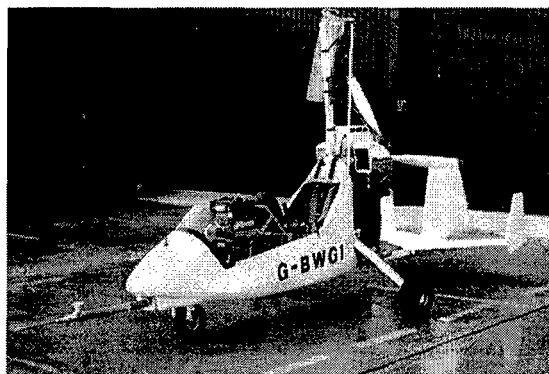
Figure 1 VPM M16 gyroplane instrumented for flight trials

The experimental installation consisted of a digital on-board recording system, operating at 10 Hz. A nose-mounted air data probe containing sideslip and angle of attack vanes was fitted, and an inertial unit measured angular velocities about three axes, and linear accelerations along these axes. A separate unit was used to measure roll and pitch angles. Pilot control positions were measured using potentiometers. Rotorspeed was also recorded. The front seat and flight controls were removed to accommodate the system.

7   Results

An important aspect in any system identification study is the *identifiability* of the estimated parameters, Refs. 22, 23. This is particularly germane to the equation error approach. *Robust* estimates of the derivatives are those whose values can be judged to be invariant with the event, input type, estimation method or frequency range used, and for which a low standard error is calculated. *Verification* of the appropriateness of the identified model is usually achieved by confirming that it will predict the response to a dissimilar control input to that used in the identification. Refs. 3 and 4 address these issues, and the results are summarised here. As stated previously, until the results in Refs. 3 and 4 had been published, there had

been no contemporary literature on gyroplane flight testing, rendereing the issue of identifiability particularly germane to the autogyro problem.

7.1   Longitudinal dynamics

The test points were nominal airspeeds of 30, 50 and 70 mph. At each of these speeds, a doublet-type input was used to excite the short-term response, and the standard technique of displacing the stick to provoke a speed change before returning it to trim was used to excite any phugoid. Frequency sweep inputs were conducted only at the 70 mph test point. Figure 2 illustrates a typical frequency sweep.
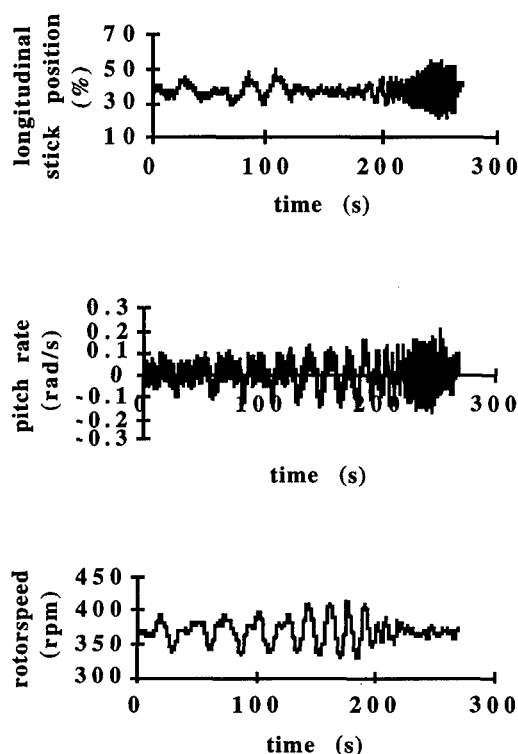

Figure 2 Response during frequency sweep test at 70 mph

This type of test proved difficult to perform at 30 and 50 mph due to the ineffectiveness of the trim system on the aircraft at airspeeds less than 70 mph. The consequent out-of-trim stick force proved distracting and difficult to compensate for during the conduct of a sweep. Estimation of derivatives was therefore made using spectral estimates from concatenated doublet and phugoid tests.

7.2   Verification of longitudinal models

Figure 3a shows verification of a model identified from frequency sweep data. The model is driven by a doublet-type input made at the same nominal flight condition of 70 mph. The doublet-type input was used specifically to excite the short-term response, where the dominant variables were observed to be pitch rate and rotorspeed. The identified model provides a very good representation of the response, but displays a feature common to verification with other runs, in that any mismatch between identified model and measurement is associated with reduction in rotorspeed.
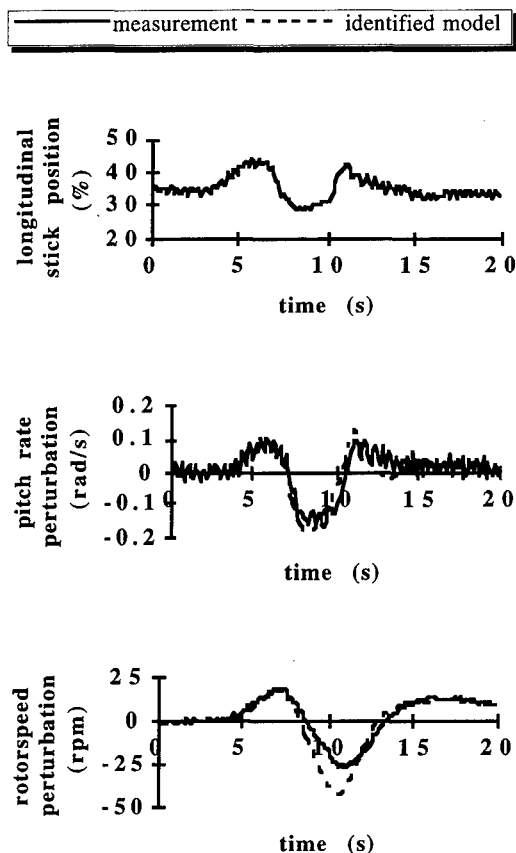
31-4

Figure 3a Identified model verification, 70 mph, short-term response

Figure 3b Identified model verification, 70 mph, long-term response

Figure 3b shows the model's ability to simulate measured behaviour during a phugoid test. Amplitude and phase of the u velocity and rotorspeed components of the phugoid mode are well represented by the identified model. The slight mismatch in the long-period response is the result of the model result being shifted in time by about 2 s relative to the measured response. This is perhaps not surprising for two reasons. First, the correlation coefficients shown previously indicate that the model structure may only approximate observed behaviour. Second, the input required for this test input produced a very substantial reduction in airspeed, which may take the identified model out of its limit of applicability. Notwithstanding this, the model does capture the substantial reduction in airspeed and rotorspeed before the control is returned to trim.

Unlike the 70 mph test point, the doublet-type input is sufficient to excite longer-term as well as short-term responses at 30 mph. This is shown in Figure 4 which compares the response predicted by the identified model for 30 mph. This model captures the salient features of the response, giving added confidence that concatenated doublet/phugoid test inputs can be used for identification.

Figure 5 presents the 95% confidence, 95% probability bounds of those identified derivatives that tend to determine fundamentally the dynamic characteristics. The

Figure 4 Identified model verification, 30mph
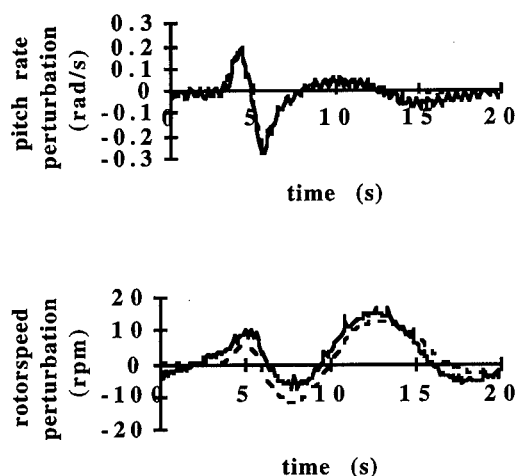
Figure 4 (conc.) Identified model verification, 30 mph

relatively wide boundaries associated with X_u, and the small or even positive identified values are probably due to the fact that the propeller speed variations are not included in the model structure. The other derivative estimates all exhibit much narrower bounds. The aircraft exhibits "classical" static stability characteristics ($M_u > 0$, $M_w < 0$, $M_q < 0$) across the speed range, and not just at 70 mph as noted previously. The derivative unique to the autogyro is M_Ω, and being negative, will tend to be stabilising. This is because an increase in rotorspeed will result in a nose-down moment, tending to reduce the axial flow through the rotor, and hence tending to reduce the original rotorspeed disturbance.

M_u is an indication of the speed stability of the aircraft, and the exhibited trend is consistent with the measured longitudinal stick position in trimmed flight. Unmodelled propeller speed and hence thrust variations may very well have a role to play in this derivative, quite apart from the usual rotor and tailplane contributions. M_w is the angle of attack stability, and unusually for a rotorcraft, is negative throughout the speed range. This is an important derivative as it holds the clue to a general understanding of autogyro flight dynamics. Unaugmented rotorcraft generally rely on a horizontal tailplane to provide $M_w < 0$. This is because the natural tendency of the rotor (and hence thrust vector) is to flap back with angle of attack, or w disturbances. Since rotor thrust also increases with w, and the thrust line usually passes close to the centre-of-mass in undisturbed flight, then both effects sum to produce $M_w > 0$, Ref. 25. However, the profile of M_u and M_q with speed would tend to suggest that the tailplane on this autogyro is somewhat ineffective, despite its relatively large size. This is consistent with wind tunnel tests on this configuration, Ref. 26. Pusher propeller configurations will tend to produce a stabilising contribution to M_w as a consequence of the propeller normal force increasing with angle of attack disturbances. However, the relatively low power of the engine would suggest that this effect is small, and if considered with the very unclean aerodynamic environment in which the propeller operates, renders this phenomenon difficult to quantify.
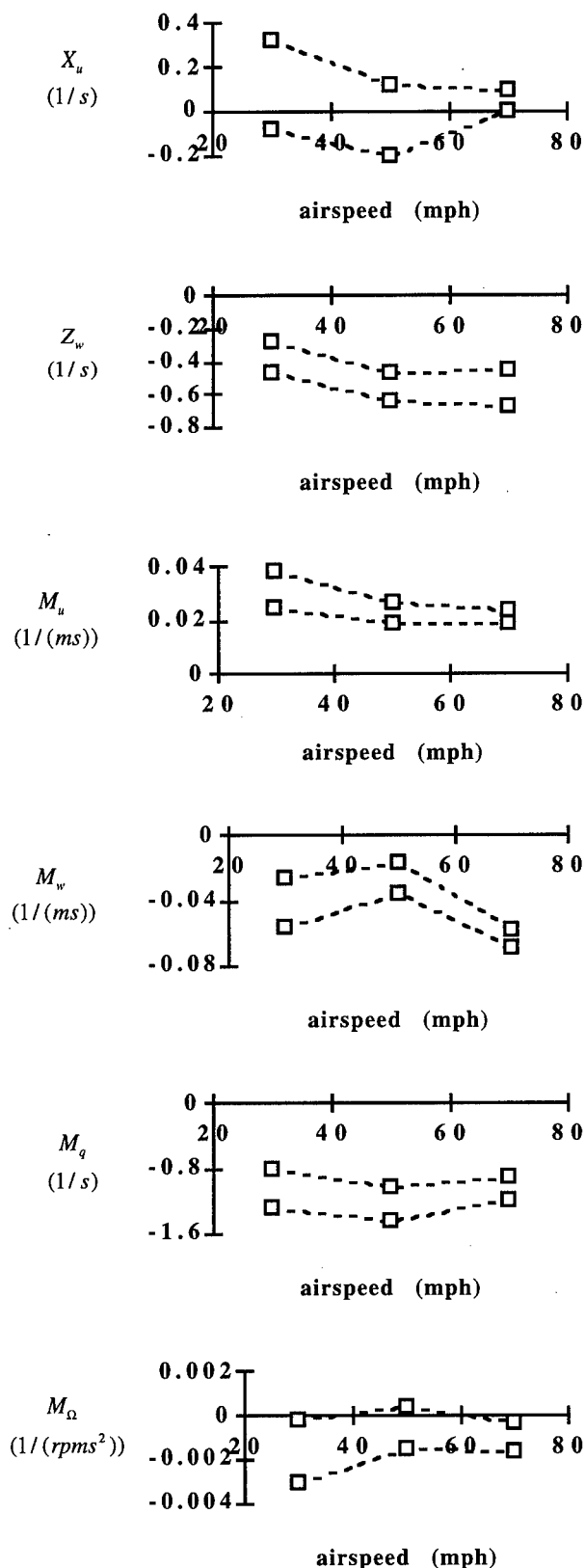

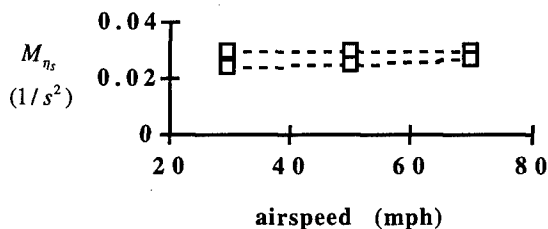Figure 5 Key identified force and pitching moment derivatives

M_{η_s} $(1/s^2)$

Figure 5 (concl.) Key identified force and pitching moment derivatives

Ref. 3 discusses this result in M_w fully, and attributes it to a propeller thrust line below the aircraft centre of mass. Such a configuration would require the resulting nose-up moment to be balanced in equilibrium flight by having the main rotor thrust line placed behind the centre of mass, tending to produce $M_w < 0$.
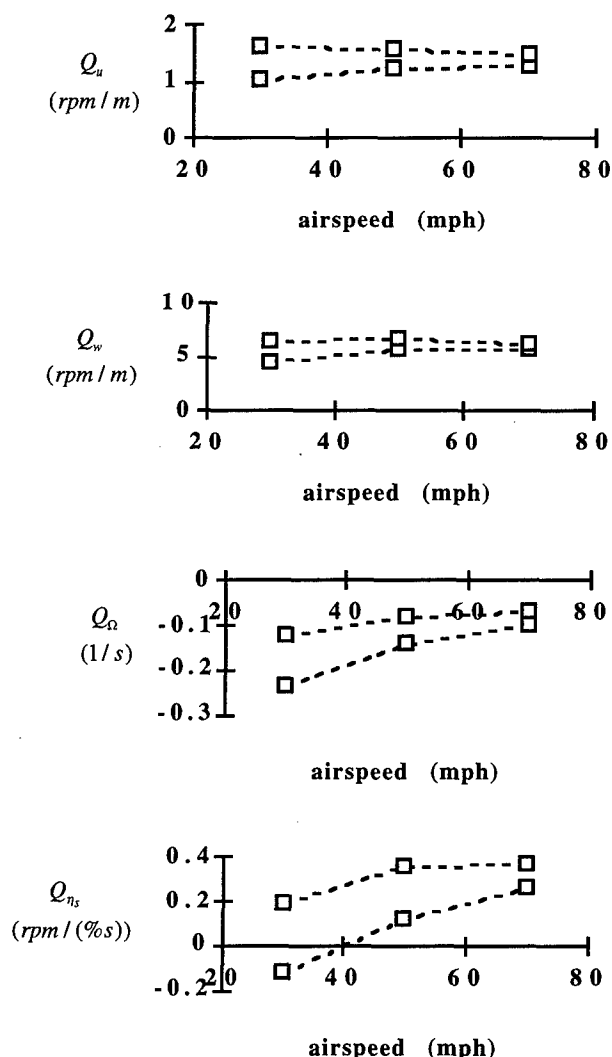
Figure 6 shows the identified derivatives in the rotor

Q_u (rpm/m)

Q_w (rpm/m)

Q_Ω $(1/s)$

Q_{η_s} $(rpm/(\%s))$

Figure 6 Rotor torque derivatives

torque equation. It is impossible to relate these to any previous quantitative work. However, qualitatively Q_u and Q_w are consistent with Glauert's seminal work, Ref. 5 in that an increase in airspeed and axial velocity will both tend to increase rotorspeed ($Q_u > 0$, $Q_w > 0$). Although the primary damping term Q_Ω decreases with airspeed, the rotorspeed mode itself exhibits the opposite trend, Figure 7. This indicates the extent of inter-modal coupling between the rotorspeed and body degrees of freedom. Finally, the control derivative Q_{η_s} shows that the rotorspeed response will become increasingly sensitive to control application with airspeed.

Longitudinal characteristics are summarised in Figure 7, which shows the eigenvalues of the synthesised models at 30 and 70 mph. The arrows indicate the progression from low to high speed. The two oscillatory modes are consistent with the frequency and damping of classical fixed-wing aircraft short-period and phugoid oscillations. The aperiodic mode is that of the rotorspeed degree of freedom. Assessment of the eigenvectors of the identified A matrices indicates that rotorspeed also features significantly in the rigid-body modes. The phugoid mode is relatively insensitive to changes in airspeed. The time to half amplitude is about 30-40 sec, its period 12-15 sec. The short-period mode is less than critically-damped throughout the speed range, with a damped natural frequency of between 0.1 and 0.25 Hz. The rotorspeed mode time to half amplitude lies between 1-4 sec.
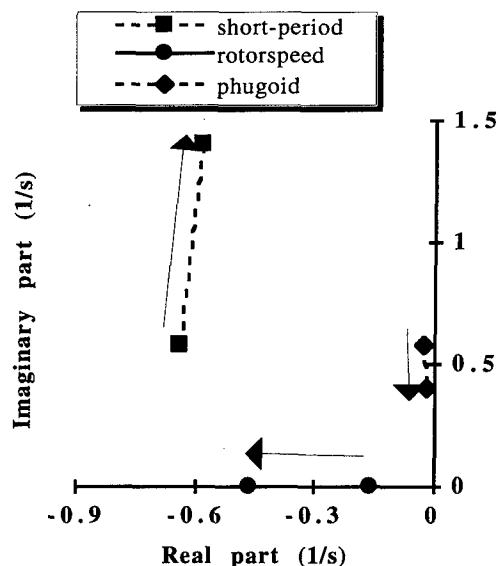

Figure 7 Longitudinal modes of motion

7.3 Lateral/directional dynamics

Frequency sweep inputs were performed on rudder and lateral stick controls at a nominal airspeed of 70 mph. These data were used for identifying the stability and control derivatives. Doublet inputs were also applied to these controls to provide dissimilar data for checking the veracity of the identified models. The analysis here focusses on the upper end of the speed range, since lateral/directional characteristics are significantly affected by airframe aerodynamics, which it is reasonable to assume increase in importance with dynamic pressure.

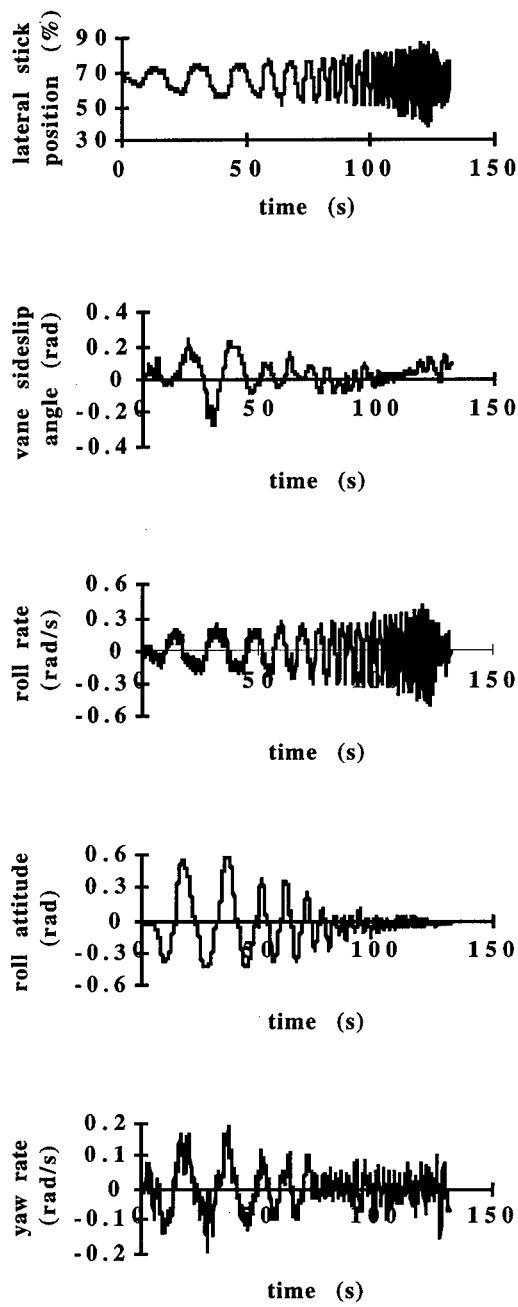Figure 8 illustrates a typical frequency sweep performed with lateral stick.

Figure 8 Response during frequency sweep test at 70 mph

It is instructive to consider these data qualitatively before any processing is carried out. Other than at very low frequencies, the lateral stick input produces small yaw rates in relation to the roll rate generated. This subjective assessment is quantified in Figure 9, which shows frequency domain comparisons of the roll and yaw rate response during a lateral stick input. (Correspondingly, rudder input produced sideslip and yaw rate response, but an insignificant level of coherent response in the roll degree of freedom).
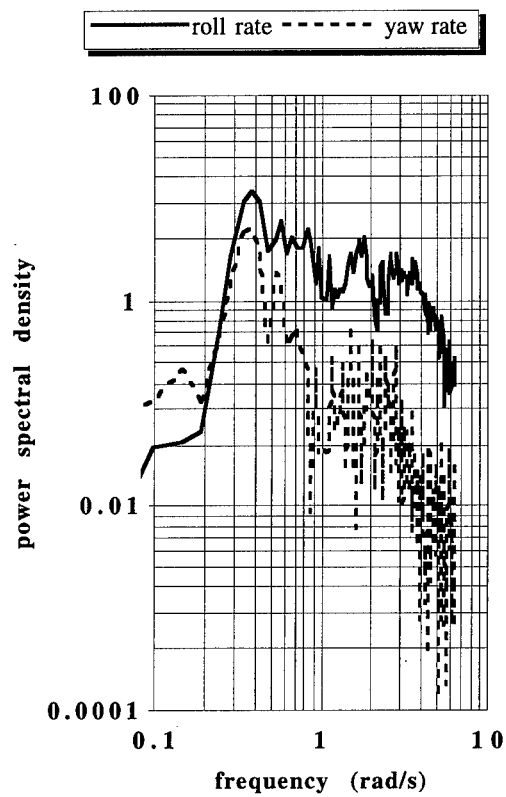
Figure 9 Frequency domain comparison of roll and yaw rate during lateral sweep

These characteristics required engineering judgement to extract and fully understand the lateral/directional characteristics, as issues of identifiabilty were raised due to the information content (or lack of it) in the responses to secondary controls. These issues are discussed fully in Ref. 4, and are illustrated here by example.

Estimates of the rolling moment derivatives obtained from lateral stick inputs, are compared with those obtained from rudder in Table 1. The standard error

Table 1 rolling moment derivative comparison - dissimilar input types

parameter	lateral stick input	rudder pedal input
R^2	0.882	0.060
L_v	0.047 (0.010)	-0.001 (0.003)
L_p	-2.407 (0.090)	-0.144 (0.206)
L_r	0.169 (0.252)	-0.112 (0.111)
L_{η_c}	0.069 (0.002)	-0.001 (0.002)
$L_{\eta_{ped}}$	-0.003 (0.005)	0.005 (0.003)

associated with each derivative is given in parentheses. The rudder pedal sweep data is clearly inappropriate, in several respects. The correlation coefficient is too small, indicating a poor model structure for these data; the standard error for each parameter is very large in relation to the parameter estimates; and inspection of the data in time or frequncy domain format showed that rudder inputs produce insignificant amounts of roll response.

By contrast, the lateral stick frequency sweep data gives derivatives with a very low standard error, with the exception of L_r and $L_{\eta_{ped}}$. In the latter case this is due to the fact that there is an insignificant level of rudder activity during the lateral sweep, while in the former it is because there is little yaw response to lateral stick displacement, as seen in Figures 8 and 9.

These results suggest that the roll moment model structure should be modified to neglect L_r and $L_{\eta_{ped}}$. Table 2 shows the result. The very small standard error relative to the corresponding derivative estimate is a measure of the high degree of confidence in the estimated values.

Table 2 rolling moment derivative estimates from lateral stick frequency sweep - revised model structure

parameter	estimate
R^2	0.882
L_v	0.050 (0.004)
L_p	-2.438 (0.082)
L_{η_c}	0.069 (0.002)

Follwing a similar analysis of rudder pedal sweep data, sideforce and yaw moment equations were obtained, and combined with the rolling moment equation from lateral stick data to give

$$
\begin{bmatrix} \dot{v}' \\ \dot{p}' \\ \dot{\phi}' \\ \dot{r}' \\ \dot{\psi}' \end{bmatrix} = \begin{bmatrix} -0.089 & 0 & 9.80665 & -32.212 & 0 \\ 0.034 & -2.582 & 0 & 0 & 0 \\ 0 & 1 & 0 & 0 & 0 \\ 0.059 & 0 & 0 & -0.904 & 0 \\ 0 & 0 & 0 & 1 & 0 \end{bmatrix} \begin{bmatrix} v' \\ p' \\ \phi' \\ r' \\ \psi' \end{bmatrix}
$$
$$
+ \begin{bmatrix} 0 & 0.035 \\ 0.063 & 0 \\ 0 & 0 \\ 0 & 0.031 \\ 0 & 0 \end{bmatrix} \begin{bmatrix} \eta_c' \\ \eta_{ped}' \end{bmatrix} \quad (14)
$$

Note that in the sideforce equation, the derivatives Y_ϕ and Y_r are either dominated by, or are exclusively made up of, non-aerodynamic contributions. For example, the former is exclusively the acceleration due to gravity, while the latter is dominated by a kinematic acceleration that is proportional to flight speed. The identified value of Y_ϕ was 11.111, close to the physically-correct value of 9.80665. The identified value of Y_r is very close in magnitude to the nominal airspeed. These results serve to give additional confidence in the identification of the sideforce equation, although the physically correct value of Y_ϕ was substituted in Equation 14.

The eigenvalues or stability roots of the system are given in Table 3, and are recognisable as roll subsidence, dutch roll and spiral modes of motion.

Table 3 identified lateral/directional model stability roots

mode	eigenvalue
roll	-2.546
dutch roll	-0.544±1.301i
spiral	0.060

7.4 Verification of lateral/directional model

Figure 10 shows verification of the model given as Equation 14. The model is driven by a doublet-type input made with lateral stick displacements at the same nominal flight condition. The identified model provides a very good representation of the overall response. Note that this input appears not to excite the unstable spiral mode. Analysis of the eigenstructure of the system matrix above using a simple test for modal controllability, Ref. 27, does confirm that lateral stick inputs will have little impact on excitation of the spiral mode.
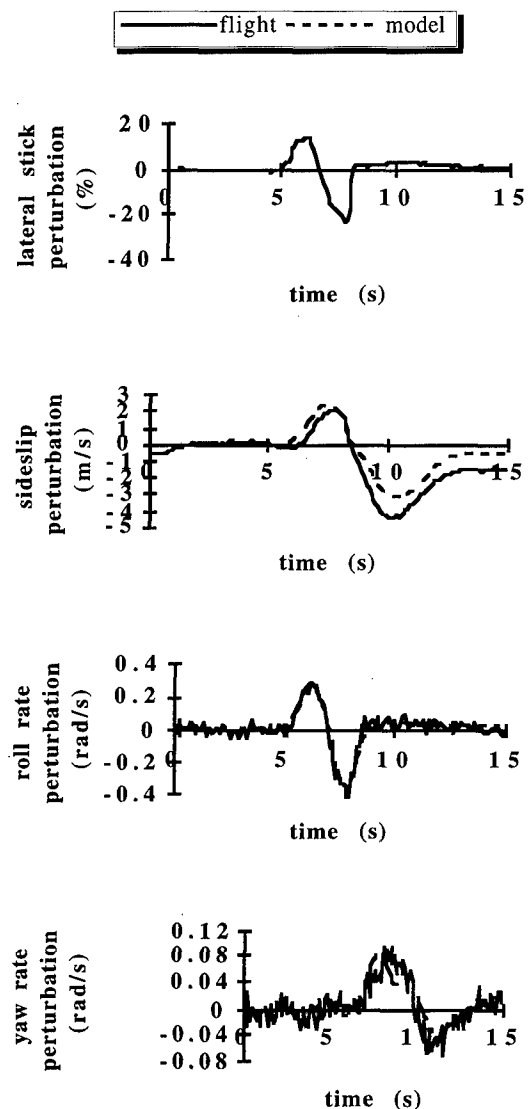
Figure 10 Verification of lateral/directional model - lateral stick input

Figure 11 shows verification of the model for rudder inputs. The identified model provides a very good representation of the short- to medium-term response, i.e.

that dominated by roll subsidence and dutch roll. The influence of the unstable spiral mode is clear in this case however, with the longer term response of the model diverging from the flight measurements.
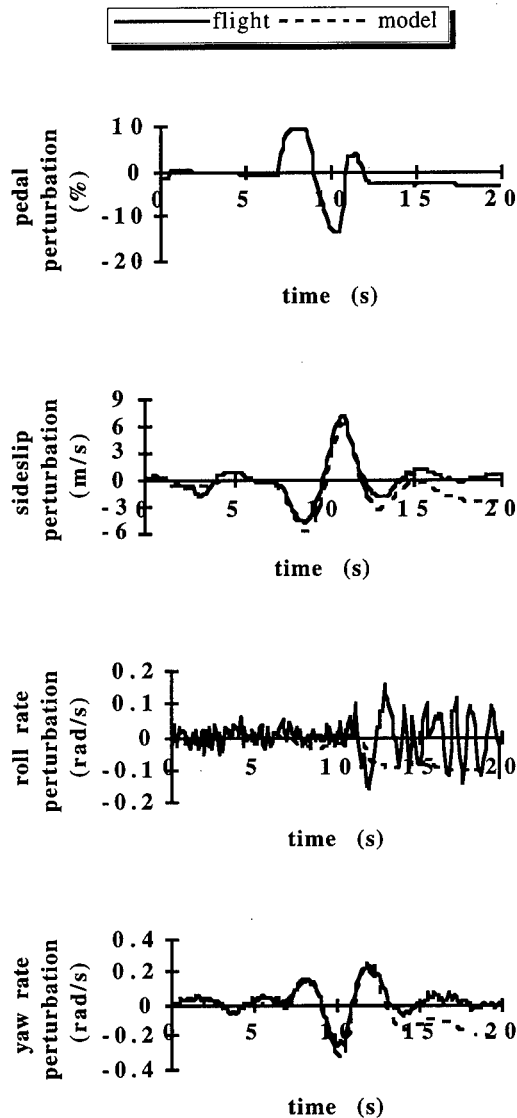

flight ------ model

Figure 11 Verification of lateral/directional model - rudder pedal input

7.5 Analysis of spiral mode characteristics

The unstable spiral mode is inconsistent with the observed behaviour in any response data from rudder or lateral stick inputs, which shows no divergent tendency. Padfield, Ref. 28, presents an approximation to the spiral mode which shows that it is influenced by all of the lateral and directional stability derivatives. For $L_r = 0$ and $N_p = 0$, it reduces to

$$\lambda_{spiral} = \frac{g(L_v N_r)}{V_f(L_p N_v + gL_v / V_f)} \qquad (15)$$

This approximation can be used to examine the nature of spiral mode, as it gives $\lambda_{spiral} = 0.061$, i.e. very close to the identified value in Table 3. Inspection of the approximation above shows that the stability of this

mode is determined by the dihedral effect, L_v. Positive dihedral effect, $L_v < 0$ will tend to stabilise the spiral mode. Here, $L_v > 0$. Simple numerical sensitivity analysis using the identified state-space model confirms that reducing the magnitude of L_v reduces the magnitude of λ_{spiral}.

There could be three reasons for absence of an unstable divergence in the aircraft response to rudder inputs: firstly, the real aircraft may indeed have an unstable spiral mode but either it is not excited by the control inputs applied, or the pilot may be unintentionally stabilising the mode; secondly, the identified (linear) model is an incomplete description of behaviour, and slight non-linearity or coupling with other degrees of freedom is stabilising the spiral mode; thirdly, L_v could be poorly identified. The latter is highly unlikely, as the standard error associated with the estimates is very small, indicating high confidence in the result. Similar values have been obtained from other events, Table 4.

Table 4 multi-run consistency in estimates of L_v

flight/event	estimate
flight 10/event 4	0.034 (0.003)
flight 10/event 11	0.041 (0.005)
flight 10/event 14	0.048 (0.004)

Data from steady heading sideslip tests is given in Figure 12, which shows lateral stick variation with sideslip angle at 70 mph, together with a best-fit through the measured data. The slope of the latter is -0.23 %/deg, or -0.30 %/deg if the measurement at 15 deg sideslip is discarded. From the rolling moment equation the rate of change of lateral stick with sideslip is given by

$$-\frac{L_v}{L_{\eta_c}}V_f \qquad (16)$$

Substituting the identified values of L_v and L_{η_c} gives a value for the stick position versus sideslip gradient of -0.30 %/deg. These data serve to confirm further that L_v has been correctly identified. Since $L_v > 0$ is the reason for the unstable spiral mode in the identified model, the absence of unstable long-term behaviour in the flight data is most probably due to one or more of the three reasons outlined above. Padfield, Ref. 25, does highlight the difficulty in identifying spiral mode characteristics, which he suggests are probably better identified, in part, by steady manoeuvres.

8 Discussion

The application of system identification and parameter estimation methods to the gyroplane is special for a variety of reasons. First, the lack of *a priori* information, data or experience in the literature, means that great care was required in the design of the experiments, collection of data, selection of analysis method and interpretation of results. Second, this particular test campaign utilised a private, standard aircraft and not a dedicated flight research vehicle that could be used repeatedly, i.e. the flight experiments had to be right first time, as this was the only opportunity available. Thirdly, the gyroplane proved to have special characteristics for a rotorcraft.

The successful outcome of this exercise is testimony to the maturity of system identification and parameter estimation, and serves as a positive example to help consolidate the position of these methods as powerful tools for solving real engineering problems.
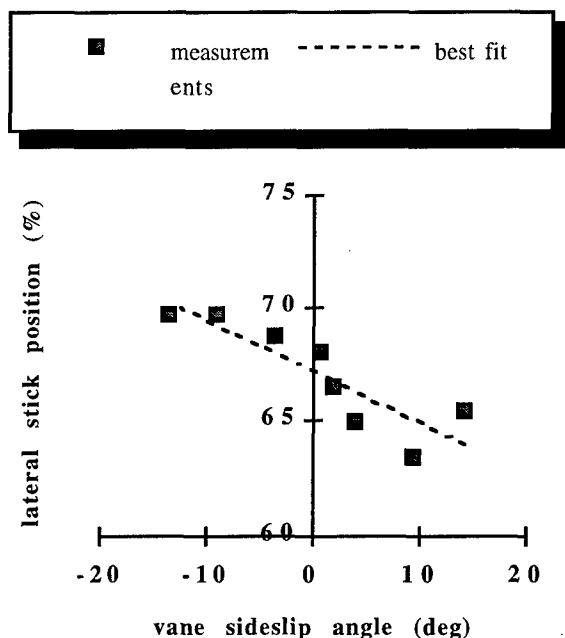

Figure 12 Lateral stick position with sideslip

9   Conclusions

Robust identification of autogyro longitudinal stability and control derivatives has been possible using relatively straightforward frequency-domain parameter estimation tools.

Unusually for rotorcraft in general, the type examined displays "classical" longitudinal dynamic stability characteristics, and is stable throughout the speed range. However, rotorspeed is an important variable and is closely coupled with the conventional rigid-body degrees of freedom. Interpretation of the identified stability derivatives indicates that the vertical position of the centre of mass in relation to the propeller thrust line may have an important role to play in autogyro longitudinal stability.

Spiral mode characteristics proved difficult to identify, but this is consistent with previous helicopter experience. Concern that dihedral effect (which dominates spiral mode stability) has been incorrectly identified, is dispelled by verifying the result obtained from dynamic tests · with steady heading sideslip data. The lateral/directional results indicate that the basic design configuration of the contemporary light gyroplane does not compromise lateral/directional characteristics, although greater dihedral effect is possibly desirable.

The results contribute directly to the development of the UK autogyro airworthiness and design standard, BCAR Section T in the important areas of dynamic stability, and weight and balance.

References
1) Anon, "Airworthiness Review of Air Command Gyroplanes", Air Accidents Investigation Branch Report, Sept. 1991.
2). Anon, "British Civil Airworthiness Requirements, Section T, Light Gyroplane Design Requirements" Civil Aviation Authority Paper No. T 860 Issue 2, Jul. 1993.
3). Houston, S. S., "Identification of Autogyro Longitudinal Stability and Control Characteristics", Journal of Guidance, Control and Dynamics, Vol. 21, No. 3, pp. 1-9, 1998.
4). Houston, S. S., "Identification of Gyroplane Lateral/Directional Stability and Control Characteristics from Flight Test", University of Glasgow Dept. of Aerospace Engineering Report No. 9710, 1997.
5). Glauert, H., "A General Theory of the Autogyro", Aeronautical Research Committee Reports and Memoranda No. 1111, Nov. 1926.
6). Lock, C. N. H., "Further Development of Autogyro Theory Parts I and II", Aeronautical Research Committee Reports and Memoranda No. 1127, Mar. 1927.
7). Glauert, H., "Lift and Torque of an Autogyro on the Ground", Aeronautical Research Committee Reports and Memoranda No. 1131, Jul. 1927.
8). Lock, C. N. H., Townend, H. C. H., "Wind Tunnel Experiments on a Model Autogyro at Small Angles of Incidence", Aeronautical Research Committee Reports and Memoranda No. 1154, Mar. 1927.
9). Glauert, H., Lock, C. N. H., "A Summary of the Experimental and Theoretical Investigations of the Characteristics of an Autogyro", Aeronautical Research Committee Reports and Memoranda No. 1162, Apr. 1928.
10). Wheatley, J. B., "Wing Pressure Distribution and Rotor-Blade Motion of an Autogyro as Determined in Flight", NACA TR 475, 1933.
11). Wheatley, J. B., "An Aerodynamic Analysis of the Autogyro Rotor with a Comparison Between Calculated and Experimental Results", NACA TR 487, 1934.
12). Wheatley, J. B., Hood, M. J., "Full-Scale Wind-Tunnel Tests of a PCA-2 Autogyro Rotor", NACA TR 515, 1935.
13). Wheatley, J. B., "An Analytical and Experimental Study of the Effect of Periodic Blade Twist on the Thrust, Torque and Flapping Motion of an Autogyro Rotor", NACA TR 591, 1937.
14). Schad, J. L., "Small Autogyro Performance", Journal of the American Helicopter Society, Vol.10, No. 3, 1965, pp. 39-43.
15). McKillip, R. M., Chih, M. H., "Instrumented Blade Experiments Using a Light Autogyro", Proceedings of the 16th. European Rotorcraft Forum, Glasgow, Scotland, Sept. 1990.
16). Fu, K.-H., Marchand, M., "Helicopter System Identification in the Frequency Domain", Proceedings of the 9th. European Rotorcraft Forum, Stresa, Italy, Sept. 1983.
17). Tischler, M. B., et al, "Demonstration of Frequency-Sweep Testing Technique using a Bell 214-ST Helicopter", NASA TM-89422, April 1987.
18). Tischler, M. B., "Frequency-Response Identification of XV-15 Tilt-Rotor Aircraft Dynamics", NASA TM-89428, May 1987.

19). de Leeuw, J. H., "Identification Techniques, Model Structure and Time Domain Methods", AGARD LS178, pp. 5-1 to 5-9, October 1991.

20). Kaletka, J., "Instrumentation and Data Processing", AGARD LS178, pp. 3-1 to 3-18, October 1991.

21). Tischler, M. B., "Identification Techniques, Frequency Domain Methods", AGARD LS178, pp. 6-1 to 6-4, October 1991.

22). Houston, S. S., Black, C. G., "On the Identifiability of Helicopter Models Incorporating Higher Order Dynamics", *AIAA Journal of Guidance, Control and Dynamics*, Vol. 14, No. 4, July-August 1991, pp. 840-847.

23). Murray-Smith, D. J., "Modelling Aspects and Robustness Issues in Rotorcraft System Identification", AGARD LS178, pp. 6-1 to 6-4, October 1991.

24). Padfield, G. D., "On the Use of Approximate Models in Helicopter Flight Mechanics", *Vertica*, Vol. 5, No. 3, 1981, pp. 243-259..

25). Bramwell, A. R. S., "Helicopter Dynamics", Arnold, London, 1976, pp. 199-200.

26). Coton, F., et. al., "Aerodynamic Characteristics of a Gyroplane Configuration", *Journal of Aircraft*, Vol. 35, No.2, 1998, pp. 274-279.

27). Richards, R. J., "An Introduction to Dynamics and Control",Longman, London 1979, pp. 312-313.

28). Padfield, G. D., "SA330 Puma Identification Results", AGARD LS178, pp. 10-1 to 10-38, October 1991.

SEPARATION DE CHARGE SOUS AVION D'ARMES
DE LA MODELISATION THEORIQUE A LA VALIDATION EN VOL

D. Fleygnac, P. Bariant, M. Rapuc

Direction Générale Technique / Direction Technique Aéronef
DASSAULT AVIATION
78, Quai Marcel Dassault, 92210 SAINT-CLOUD
FRANCE

1- INTRODUCTION

La polyvalence d'un avion d'armes moderne passe, notamment, par sa capacité à emporter des charges multiples et variées capables d'assurer l'ensemble des missions qui lui sont confiées: bombes, missiles pilotés, réservoirs largables... La prise en compte de cette exigence dès le stade de la conception permet sur un avion de nouvelle génération tel que RAFALE d'offrir une capacité d'emports très étendue et ouverte vis à vis d'armements futurs.

Pour autant, l'intégration d'un emport nouveau est un problème complexe et multidisciplinaire, tant pour ce qui concerne son intégration fonctionnelle dans le Système de Navigation et d'Attaque, que sur le plan aéro-mécanique par:
- l'étude de la mise en place de la charge, sous voilure ou sous fuselage, et le respect de contraintes d'aménagement pouvant conduire au développement de dispositifs spécifiques d'accrochage, notamment dans le cas d'emports multiples.
- l'étude du vol en emport où la stabilité et les performances de l'avion muni de son Système de Commandes de Vol doivent être vérifiées en tenant compte des modifications aérodynamiques et structurales notables qui résultent de la présence de la charge. De même, le respect des efforts structuraux admissibles doit être démontré.
- enfin, l'étude du largage en vol.

Plusieurs raisons motivent les concepteurs d'avions de combat, comme DASSAULT AVIATION, à se doter des moyens d'étudier le largage d'emports. D'une part, le besoin opérationnel nécessite un domaine d'utilisation de plus en plus étendu comme le largage en conditions Très Basse Altitude ou en régime transsonique. Ensuite, la complexité croissante des charges peut rendre leur séparation particulièrement critique vis à vis de la sécurité du porteur. Enfin, les dynamiques du vol de l'avion et de la charge à la séparation sont fortement couplées et peuvent devoir être prises en compte dans la conception même du Système de Commandes de Vol.

C'est ce qui a conduit DASSAULT AVIATION à mettre en place, dans le domaine du largage d'emports, une méthodologie et les outils associés, notamment dans le domaine de la modélisation et de la simulation, lui permettant d'assurer, en coopération avec ses partenaires industriels, sa responsabilité de l'intégration, en particulier pour ce qui concerne les aspects relatifs à la sécurité avion.

2- METHODOLOGIE GENERALE

2.1- Objectifs

La définition d'un domaine de largage en vol admissible est le résultat d'un compromis entre des contraintes:
- de sécurité, d'une part, caractérisée par les risques de collision avion-emport dans les premiers instants de la séparation, mais aussi par les efforts induits dans la structure au moment de la séparation ainsi que les éventuels mouvements avion qui en résultent.
- de performances, d'autre part, dans le cas d'armements pour lesquels la réussite de la mission impose de rester dans un certain domaine d'attitudes en phase de séparation.

L'étude de la séparation a pour but de définir les réglages qui autoriseront le domaine de tir opérationnel le plus large possible tout en respectant ces contraintes antagonistes. Pour un emport en cours de conception ou de développement, ces réglages peuvent aller jusqu'à des propositions d'évolution de forme ou de définition. En revanche, pour un emport existant, ils concerneront, selon le type d'engin:
-le choix du point d'accrochage sous avion,
-la mise en place: type de liaison, calage
-le précalage de gouvernes de la charge
-la définition et le réglage des dispositifs d'éjection...

Au cours de ces dernières années, une nouvelle génération d'armements est apparue dont la conception prend en compte de façon plus poussée les contraintes géométriques de discrétion, d'intégrations multiples sous différents porteurs et de manoeuvrabilité. Il en résulte que les caractéristiques

aérodynamiques de ces armements, en phase de séparation, sont telles que l'on peut rencontrer des domaines de stabilité aérodynamique réduite. Le missilier est alors amené à développer un système de pilotage de l'engin qui, étant mis en service dès les premiers instants de la séparation, permet la stabilisation de l'arme et, par la suite, la réussite du tir. Les trajectoires de ce type d'armement sont, alors, très sensibles aux conditions initiales, en particulier dans le cas de tirs où l'on cherche simplement à se séparer de l'arme et pour lesquels le pilotage n'est pas actif. Par ailleurs si la fonction pilotage n'est pas suffisamment fiabilisée, il faudra démontrer que l'occurrence d'une panne ne remet pas en cause la sécurité de l'avion.

On comprend, alors, que l'étude de la séparation dans un vaste domaine de Mach, altitude, facteur de charge, requiert l'analyse d'un très grand nombre de trajectoires.

De par son coût l'approche expérimentale consistant en largages en soufflerie puis essais en vol n'est plus adaptée à ce type d'armement. En outre, l'utilisation d'emports de grande taille installés sous voilure est de nature à induire, à la séparation, un mouvement avion important dont la prévision et la prise en compte ne peut être acquise par des moyens d'essais sol.

Une nouvelle méthodologie a donc été développée; elle fait appel pour une large part à la modélisation et la simulation, en complément aux outils traditionnels d'expérimentation. L'identification des modèles et leur validation par l'expérience constituent, alors, un élément essentiel de cette méthodologie.

2.2- Méthodologie

La méthodologie générale, présentée ci-dessous, s'appuie sur un processus itératif à trois niveaux:
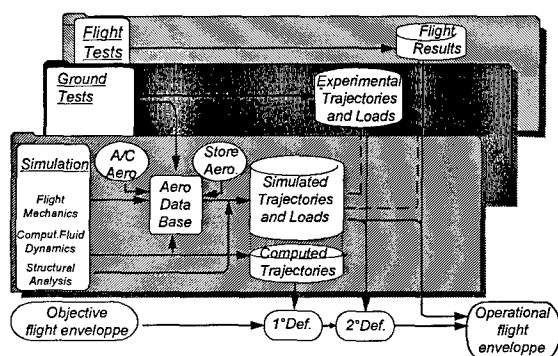
- la simulation qui regroupe les calculs aérodynamiques et les simulations de trajectoires à partir de bases de données aérodynamiques ainsi que les calculs structuraux,

- les essais sol: essais de soufflerie et mesures d'efforts par des éjections au portique ou sous avion,
- les essais en vol.

Chaque niveau contribue de manière différente à l'objectif final qui est la définition du domaine de tir opérationnel.

Au premier niveau, la simulation, elle-même fondée sur des modélisations théoriques ou expérimentales, permet, par des balayages systématiques, de proposer des réglages visant à satisfaire le domaine de tir objectif. La prise en compte, dans les balayages, d'incertitudes sur les différents paramètres du système permet de couvrir les imprécisions de modélisation ainsi que les dispersions attendues sur les conditions de fonctionnement.
Les essais sol permettent de consolider cette définition et fournissent les éléments d'un premier recalage des modèles.
Puis les essais en vol fournissent une validation globale et permettent, par un retour à la simulation, de définir le domaine de tir opérationnel.

Il convient de souligner que cette méthodologie générale qui fédère l'ensemble des moyens d'étude disponibles ne se décline pas de la même manière selon les emports considérés. Le recours à tel ou tel moyen doit être envisagé dans une perspective d'amélioration du rapport efficacité/coût. En outre, chaque niveau implique une coopération, avec les partenaires industriels qui participent aux travaux de simulation et d'étude, ainsi qu'avec les organismes étatiques responsables des moyens d'essais.

Le chapitre suivant présente les principaux outils et moyens associés à cette méthodologie. Dans le cadre de ce congrès, l'accent est plus particulièrement mis sur les moyens relevant de l'aérodynamique et de la mécanique du vol.

3. OUTILS ET MOYENS ASSOCIES

3.1- Outil de simulation de mécanique du vol

3.1.1- *Architecture de la simulation*

Le largage d'emports est une phase particulièrement dynamique au cours de laquelle les comportements en vol de l'avion et de la charge interagissent fortement au travers:
- des dispositifs d'éjection,
- des interactions aérodynamiques en champ proche.
  Il convient de souligner que dans le cas d'emports de grande taille ces interactions peuvent avoir un effet significatif sur le comportement avion comme cela sera illustré par les applications présentées plus loin.

C'est ce qui a conduit DASSAULT AVIATION à mettre en place un ensemble de simulation complet du composite avion-emport à la séparation dont la structure est présentée ci-après.
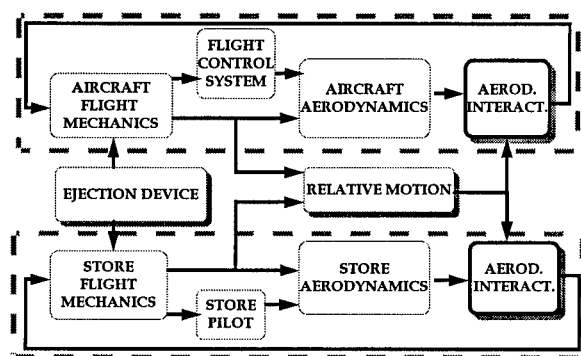
La simulation comporte, de manière symétrique, une représentation de l'avion, muni de son Système de Commandes de Vol, et de la charge munie, le cas échéant, de son système de pilotage; le modèle du pilotage constituant, alors, une fourniture de la part du missilier.

La prise en compte, dans la simulation, de l'avion muni de son Système de Commandes de Vol (SCV) est de nature à permettre de:
- prévoir le mouvement avion à la séparation et en tenir compte dans les études relatives à la séparation. En particulier, dans le cas d'armements tirés en salve, la dynamique de la réaction avion peut être un paramètre dimensionnant de la séquence de tir, voire imposer des adaptations spécifiques des lois du SCV.
- prendre en compte ce mouvement dans le calcul des trajectoires relatives avion-charge à la séparation,
- disposer de l'évolution dynamique, au cours du largage, des braquages de gouvernes avion dont l'effet sur les interactions avion/charge, et donc sur la trajectoire de la charge, peut être très significatif.

3.1.2- Modèles aérodynamiques

Dans le but de permettre une utilisation intensive de la simulation, dans le cadre de balayages systématiques sur les conditions de vol et/ou les incertitudes de modélisation, les modèles aérodynamiques utilisés sont constitués de bases de coefficients globaux tabulés, fonction des conditions de vol, configuration aérodynamique, positions...

La structure de modélisation retenue généralement consiste, tant pour l'avion que l'emport, en un modèle aérodynamique hors interactions appelé usuellement 'champ libre' et un modèle des interactions.

L'identification du champ libre se fonde, classiquement, sur des données expérimentales de soufflerie, éventuellement complétées par le calcul, puis un recalage/validation sur des résultats de vol. L'identification des interactions est un problème complexe dans la mesure où celles-ci dépendent d'un grand nombre de paramètres: conditions de vol, positions relatives, configurations aérodynamiques respectives. Selon le problème traité, cette identification se fonde sur des résultats de calculs théoriques (cf §3.2) et/ou des résultats de mesures de soufflerie (cf §3.3).

En outre, un couplage de la simulation avec des calculs théoriques peut permettre l'obtention de trajectoires 'tout numérique' pour des cas ponctuels d'analyse et de compréhension des phénomènes. Cette possibilité sera présentée au §3.2.

3.1.3- Modèles mécaniques

Durant la phase d'éjection proprement dite (durée typique 0.1 seconde), les dispositifs d'éjection induisent, tant sur le porteur que sur la charge, des efforts importants qui doivent être pris en compte dans le cadre des analyses structurales et du dimensionnement avion. En résultat de ces travaux, un modèle simplifié représentatif des performances des éjecteurs installés sur avion, et des conditions initiales de vol qui en résultent, peut être constitué et introduit dans la simulation de mécanique du vol. Cette approche facilite, en outre, l'introduction d'incertitudes globales sur le fonctionnement des dispositifs d'éjection comme cela sera repris au §3.1.5.

Dans la plupart des cas, pour la simulation des trajectoires de séparation, l'avion et l'emport sont supposés rigides. Cette hypothèse parait adaptée dans la mesure où les déformations structurales ne sont pas de nature à influer sensiblement le comportement en vol des deux objets. Dans le cadre d'analyses fines des phénomènes, un couplage de la simulation avec les outils de modélisation structurale peut être envisagé.

3.1.4- Post-traitement

En sortie de la simulation, un grand nombre de trajectoires relatives avion-emport peut être produit. Le couplage avec une fonction de post-traitement développée autour du logiciel CATIA permet:
- de visualiser les mouvements parfois complexes des deux objets et de fournir une aide à leur interprétation,
- d'évaluer les distances relatives et de vérifier, ainsi, le respect de distances minimales de passage qui constituent un paramètre essentiel de la sécurité du porteur au largage,

- de traiter, de manière automatique, un très grand nombre de résultats dans le cadre d'études systématiques d'influences et de recherche de comportement enveloppe.

Les exemples d'application présentés au §4 fourniront une illustration de l'utilisation de cet outil de post-traitement.

3.1.5- *Protocole d'utilisation*

Comme indiqué au §2.2 relatif à la méthodologie générale, la simulation intervient tout au long du processus, les modèles aérodynamiques et mécaniques étant progressivement enrichis par les résultats de calculs ou d'essais disponibles.

L'effort de prévision et de simulation des trajectoires relatives de séparation se heurte toutefois:
- d'une part, à la très grande sensibilité de ces trajectoires aux conditions initiales de séparation et aux dispersions probables de fabrication et de fonctionnement des différents systèmes tels que les dispositifs d'éjection,
- d'autre part, à la difficulté de modélisation et notamment aux incertitudes relatives à la connaissance des caractéristiques aérodynamiques de la charge en champ proche,
- enfin, à l'effet éventuel de certains éléments non-modélisés.

Ces quelques constats conduisent à introduire, pour un point de tir et une configuration donnés, la notion d''enveloppe de séparation', elle-même résultat d'un vaste ensemble de simulations incluant la prise en compte, de manière systématique ou aléatoire, de dispersions sur les différentes caractéristiques aérodynamiques et mécaniques et sur les conditions de vol.

En conséquence, chaque modèle impliqué dans la simulation est caractérisé par:
-ses paramètres nominaux, ou de référence,
-le modèle d'incertitudes associé,
la disponibilité de résultats d'essais pouvant conduire aussi bien à adapter les caractéristiques nominales et/ou à modifier la bande d'incertitudes.

Cette démarche soulève un certain nombre de difficultés relatives à l'estimation des niveaux d'incertitudes à prendre en compte: recours à l'expérience acquise ou à des analyses de sensibilité permettant de privilégier les paramètres de modélisation dimensionnants.

Elle présente, en revanche, l'avantage d'assurer, dès les pré-études d'intégration, un certain niveau de robustesse aux solutions proposées, qui réduit le risque de modification des réglages après validation en vol.

Les niveaux d'incertitudes, qui peuvent évoluer au fur et à mesure de l'avancement des travaux et de la connaissance des phénomènes doivent être choisis pour assurer un compromis entre:
- la robustesse des solutions qui réduit le risque d'itérations coûteuses,
- la faisabilité de ces solutions qui peut être mise en cause par une exigence trop forte de robustesse.

Les deux paragraphes suivants présentent les moyens disponibles pour l'identification, avant vol, des modèles aérodynamiques: calcul théorique et essais en soufflerie.

3.2- Calculs aérodynamiques

Les progrès des méthodes numériques et l'accroissement de puissance des ordinateurs, a permis une avancée notable des calculs numériques qui permettent maintenant de calculer des écoulements non linéaires autour de géométries complexes et plus particulièrement les configurations d'avion avec charges, que ce soit en phase d'emport ou en phase de séparation.

Depuis une vingtaine d'années, DASSAULT AVIATION développe ses propres outils de calcul et dispose de toute une panoplie de logiciels de maillage et de résolution des équations de la Mécanique des Fluides.

Dans le cadre des études de séparation de charges sous avion, les calculs numériques sont utilisés principalement pour:
- l'identification des modèles aérodynamiques impliqués dans la simulation de mécanique du vol
- la réalisation de trajectoires 'tout numérique' par couplage des modules aérodynamiques au module de mécanique du vol.

Pour cela, une structure regroupant des outils de mécanique des fluides a été développée pour permettre le calcul automatique d'une série de positions discrètes de la charge sous avion:
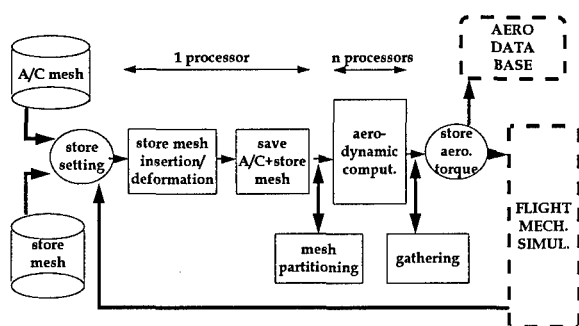
Cette structure a été conçue pour être utilisée d'une manière industrielle et doit répondre à des critères de modularité, permettant de l'enrichir très facilement et d'augmenter ses possibilités d'évolution pour mieux prendre en compte certains phénomènes complexes d'aérodynamique, ainsi que de portabilité, de façon à pouvoir être utilisée sur différents types d'ordinateurs, séquentiels et/ou parallèles. Afin d'obtenir des calculs aérodynamiques dans un délai raisonnable, ces logiciels ont été implantés en environnement parallèle.

Afin de calculer plus facilement des écoulements autour de géométries complexes, DASSAULT AVIATION a fait le choix de discrétiser l'espace de manière non structurée. Ce choix, fait il y a déjà de nombreuses années, a permis d'acquérir une forte expérience dans la réalisation de maillages non structurés de qualité. Cette expérience a permis de surmonter un obstacle majeur dans la réalisation de cette chaîne aérodynamique, à savoir la difficulté d'automatisation indispensable à la simulation de trajectoire de largage.

3.2.1- Maillage

La souplesse de la description non structurée des maillages qui sont employés ainsi que leur bonne adaptation aux géométries les plus complexes ont conduit à envisager, pour les différentes positions relatives de la charge par rapport à l'avion, de régénérer un maillage conforme, géométriquement et topologiquement correct.

De ce point de vue, les deux principales difficultés consistaient à ce que cette étape de la chaîne soit la moins coûteuse possible en temps de calcul et à ce que le processus de recréation automatique du maillage final ait une probabilité de réussite maximale (ce qui conduit, notamment en champ proche avion, à une gestion relativement complexe de la précision géométrique du maillage).
Un pré-traitement suppose la génération d'un maillage avion et d'un maillage charge indépendants l'un de l'autre, mais destinés à être combinés.

L'algorithme mis en oeuvre peut se décomposer de la manière suivante :
* aménagement dans le maillage avion de base de l'espace nécessaire à l'accueil du maillage charge à insérer,
* construction explicite du raccord topologique entre les deux domaines,
* assemblage de toutes les parties pour aboutir à une description unique de l'ensemble,
* homogénéisation du maillage après insertion permettant d'obtenir des solutions aérodynamiques de meilleure qualité et consommant un temps de calcul moindre.
* vérification de la validité du maillage final et optimisation de celui-ci au sens de critères géométriques et topologiques.
Une illustration de cet algorithme est donnée ci-après:
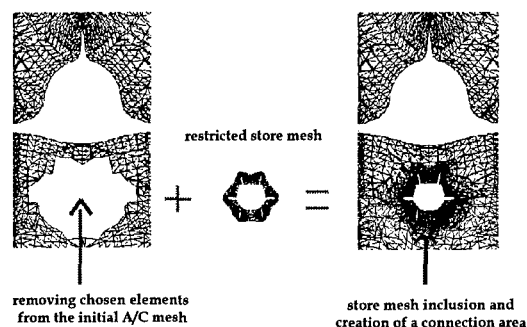
On voit que le maillage final est la réunion de trois parties préalablement conditionnées pour que leur assemblage permette la discrétisation exacte adaptée à la position relative considérée. Dans le cas de positions très proches, le maillage de la charge est, si nécessaire, automatiquement réduit jusqu'à la surface facettée limitée à la peau de la charge.

Les principaux avantages de cette technique sont:
* l'insertion possible de la charge en champ très proche avion, avec la possibilité de raccord géométrique et topologique des deux maillages,
* le temps de création très faible du maillage à chaque étape de largage (de l'ordre de la minute sur station de travail IBM RS6000),
* l'obtention d'une représentation conforme à tout instant.

3.2.2- Logiciel aérodynamique

La composante aérodynamique est constituée du logiciel EUGENIE développé chez DASSAULT AVIATION et utilisé couramment pour optimiser les formes d'avion.

Pour répondre à cet objectif de calcul, divers solveurs des équations de la Mécanique des Fluides ont été intégrés dans ce logiciel, ce qui lui donne les caractéristiques suivantes:

- résolution des équations du potentiel complet ou des équations d'Euler avec schémas centré ou décentré, implicite ou explicite,
- formulation non structurée multi-élément (tétraèdres, hexaèdres, prismes, pyramides),
- calcul de l'avion complet avec différentes conditions aux limites (uniforme, entrée d'air, tuyère ...),
- prise en compte d'effets visqueux par couplage avec méthodes intégrales de calcul de couche limite,
- raffinement automatique local de maillage selon divers critères géométriques, numériques (résidus...) ou aérodynamiques (Mach, pression, entropie...).
- prise en compte du mouvement relatif d'un corps par rapport à un autre par la modification des conditions aux limites aux différents corps. Dans le cas présent cela permet de prendre en compte les vitesses relatives de la charge par rapport à l'avion dans le calcul aérodynamique.

Ce logiciel a été intégré sans aucune modification dans sa version industrielle actuelle; ce qui a permis d'abord de minimiser les coûts de développement et aussi de profiter de sa robustesse et de sa fiabilité et ensuite de bénéficier immédiatement et automatiquement de toute amélioration ou évolution de la composante aérodynamique.

3.2.3- *Fonctionnement en environnement parallèle*

Comme il a été évoqué précédemment, un pré-traitement produit un maillage autour de l'avion et un autre maillage autour de la charge destinée à être larguée. Ces deux maillages constituent les seules entrées géométriques de cette structure. Les autres données sont la position d'emport, les conditions initiales d'éjection, un pas de temps et les conditions nécessaires au calcul aérodynamique dans le cas du calcul d'une trajectoire numérique, et une liste de positions et attitudes relatives de la charge par rapport à l'avion dans le cas de calcul de points de grilles.

Un premier module positionne le maillage de la charge dans les références du maillage avion pour les conditions d'emport. Ensuite, l'insertion de ce maillage de la charge est automatiquement réalisée suivant la technique décrite au §3.2.1.
Un processeur de l'ordinateur parallèle à mémoire distribuée est dédié aux modules d'insertion de maillage et de positionnement relatif.
Les autres processeurs de l'ordinateur parallèle sont réservés pour le calcul aérodynamique. Pour utiliser la composante aérodynamique sur ordinateurs parallèles, une technique de décomposition de domaines a été employée pour paralléliser ce logiciel. Cette technique impose l'introduction dans la chaîne d'un découpeur automatique de maillage non structuré (mesh partitioner) développé en collaboration avec l'ONERA. Le maillage est décomposé en sous-domaines à nombre d'éléments pratiquement constants, distribués sur les processeurs alloués au calcul aérodynamique. Au cours de l'algorithme itératif de résolution des équations de la mécanique des fluides, les processeurs vont échanger des informations relatives aux interfaces entre domaines voisins.

Les solutions de chaque domaine sont regroupées en une solution unique stockée sur le fichier du maillage global avion +charge. A partir de cette solution, le module d'intégration permet de définir le torseur d'efforts s'appliquant sur la charge et sur l'avion.

3.2.4- *Utilisation*

Le torseur d'efforts issu du calcul théorique sert:
- soit à l'établissement de bases de données aérodynamiques pour des positions prédéfinies
- soit d'entrée au module de mécanique du vol dans le cas du calcul d'une trajectoire numérique. Le processus itératif mis en place dans cette structure, permet de déterminer pas à pas la trajectoire de la charge.

3.3- Essais en soufflerie

Les essais en soufflerie ont toujours représenté une étape importante, préalable aux essais en vol, dans le processus de développement de l'intégration des emports. Les essais relatifs à la séparation visent, selon l'étape du développement, soit à l'identification de caractéristiques aérodynamiques en champ proche soit à des validations partielles ou globales.

On distingue principalement deux grandes familles d'essais en soufflerie:
- les essais de largage libre
- les essais utilisant les Systèmes de Trajectographie Captive (STC).

DASSAULT AVIATION de par son métier de constructeur d'avion d'armes a une longue tradition d'essais en soufflerie réalisés en étroite collaboration avec les responsables étatiques des moyens d'essais:
- l'ONERA pour les souffleries S1 et S2 de Modane en grande vitesse
- le CEAT pour la soufflerie S5 de Toulouse en basse vitesse.

3.3.1- *Largage libre*

Dans le cas du largage libre, on laisse tomber la charge dans la soufflerie après lui avoir communiqué par l'intermédiaire d'éjecteurs des conditions initiales réputées respecter la similitude avion.

Le mouvement de la charge est filmé sous plusieurs angles de vue par des caméras. Le dépouillement de ces films permet d'obtenir la position du centre de gravité et les attitudes de la charge en fonction du temps.

Le facteur de charge au moment du tir n'est représenté que par l'incidence et l'avion n'est animé d'aucun mouvement au cours de la trajectoire.

La maquette de la charge se doit de respecter différentes règles de conception (masse, inertie) qui dépendent de la similitude utilisée:
- similitude de Froude à basse vitesse (respect du rapport des accélérations entre vol et soufflerie),
- similitude de Mach (respect du nombre de Mach) en grande vitesse.

Si ces techniques présentent l'avantage que l'écoulement aérodynamique autour de la charge n'est pas perturbé par les supports et que les effets dynamiques sont présents, elles restent limitées sur plusieurs plans:
- les maquettes sont détruites à chaque tir,
- aucun effort aérodynamique n'est mesuré,
- pour des tirs à facteur de charge différent de 1, l'absence de mouvement relatif entre l'avion (qui ne bouge pas) et la charge dégrade la qualité du résultat.

Les essais en largage libre sont aujourd'hui réservés à des cas spécifiques de validation pour lesquels on cherche une réponse en tout ou rien telle que:
- le largage en détresse au décollage en cas de panne moteur que l'on se doit de couvrir afin d'autoriser le vol des nouvelles configurations,
- le tir dans un domaine limité en facteur de charge d'une arme dont le développement est terminé,
- la séparation des réservoirs largables du fait de l'existence d'une liaison mécanique (lors de la phase initiale de la séparation) entre le réservoir et l'avion difficile à modéliser (cf §3.3.2).

3.3.2-*Système de Trajectographie Captive (STC)*

Devant les inconvénients du largage libre, rappelés ci-dessus, l'ONERA a développé des systèmes de trajectographie à six degrés de liberté. Ces dispositifs permettent de positionner une charge sous l'avion tout en mesurant les six composantes du torseur aérodynamique auquel elle est soumise grâce à une balance située dans la charge.

Par un couplage à un logiciel de mécanique du vol, il est alors possible de réaliser des trajectoires à partir de conditions initiales en intégrant pas à pas les efforts subis par la charge. La trajectoire ainsi obtenue est plus riche que celle du largage libre puisque l'on dispose ici de l'historique des efforts aérodynamiques qui permet d'analyser et de comprendre le mouvement.

Une photo du montage de la soufflerie S2MA de l'ONERA lors d'un essai RAFALE est présentée ci-après.
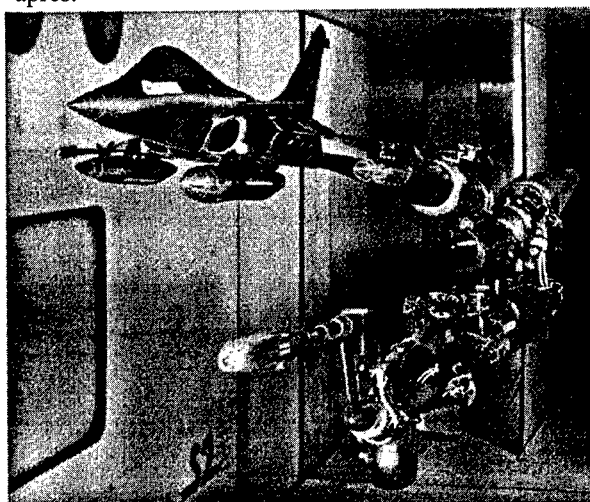
Dans cette soufflerie, des maquettes au 1/15 peuvent être testées en transsonique et supersonique. Pour les charges qui ne dépassent pas M=0.9, un moyen similaire est disponible dans la grande soufflerie S1Modane de l'ONERA, l'échelle étant environ 1/6.

On comprend alors que ce type d'essais est bien adapté aux armements en cours de développement pour lesquels une compréhension fine du comportement est nécessaire afin de pouvoir faire éventuellement évoluer la définition de la charge.

L'essai commence par une identification de la maquette de la charge en champ libre, dans le but d'évaluer, ensuite, les termes d'interaction à partir des mesures en champ proche.

Au cours de la trajectoire, entre deux pas de calcul, les positions relatives avion-charge sont réajustées de façon à tenir compte des effets liés à des facteurs de charge différents de 1. L'avion est ici supposé suivre une trajectoire à facteur de charge constant égal à celui du tir.

On peut ainsi simuler différents point de tir. Cependant, le nombre de trajectoires nécessaires pour couvrir le domaine de tir de façon raisonnablement complète devient très vite prohibitif si on introduit des

incertitudes sur les coefficients aérodynamiques de la charge. De plus une trajectoire ne vaut que par les hypothèses et les conditions initiales qui ont permis de la réaliser, il n'est donc pas nécessaire d'en réaliser beaucoup à un stade trop amont.

Dans les phases amonts, on procède alors généralement à la mesure des coefficients aérodynamiques d'interaction entre l'avion et la charge au travers de 'grilles'. Une grille représente un ensemble de mesure au cours duquel un degré de liberté varie alors que les autres sont fixés à des valeurs de consignes. La base de résultats ainsi constituée permet d'identifier les modèles aérodynamiques de perturbation impliqués dans la simulation de mécanique du vol (cf §3.1).

En cours de développement, une fois les meilleurs réglages proposés sur la base des simulations, on peut, si le cas est relativement éloigné des cas initialement essayés, retourner en soufflerie pour une petite campagne de vérification avant essais en vol, l'avantage de la soufflerie étant alors essentiellement l'absence d'interpolation dans les différents modèles.

Ces dispositifs STC sont très performants et ils fournissent une grande quantité d'information; ils sont donc préférentiellement utilisés. Cependant ils présentent trois difficultés:

- les limitations mécaniques des montages ne permettent pas de couvrir les trajectoires extrêmes, en particulier celles des cas dégradés (des améliorations constantes sur ce point sont réalisées),
- les termes dynamiques ne sont pas physiquement présents, la qualité de la simulation pour les cas à très forte dynamique n'est donc pas assurée,
- toutes les interactions mécaniques avion-charge doivent être modélisées, ce qui rend difficile le cas de liaisons complexes.

L'analyse des caractéristiques de ces différents moyens montre qu'une réflexion doit être conduite en amont pour que la stratégie des essais proposée soit adaptée au problème posé et qu'elle puisse améliorer le rapport efficacité/coût.

3.4- Essais en vol

Les essais en vol représentent une étape incontournable dans le développement de l'intégration d'un emport car ils permettent de prendre en compte l'ensemble des phénomènes physiques. Au-delà des aspects aéromécaniques, ils mettent en jeu l'ensemble des systèmes dans une validation globale.

Les moyens d'acquisition sont constitués de diverses caméras filmant la trajectoire de la charge et, dans le cas de charge instrumentée, de capteurs permettant d'accéder aux efforts aérodynamiques.

La comparaison vol-prévision est d'abord globale. Elle permet de situer l'essai par rapport à l'enveloppe de comportement issue des simulations préparatoires avec prise en compte d'incertitudes sur les différents éléments de modélisation. Compte-tenu de la complexité des phénomènes et du nombre élevé des paramètres de modélisation, l'identification de ceux-ci peut s'avérer délicate. L'exploitation du vol peut en fait conduire soit à des recalages de modélisation, soit à des adaptations des modèles d'incertitudes.
L'essai en vol permet donc de confirmer (ou d'infirmer) les choix réalisés en amont. Pour qu'il soit totalement efficace il ne faut pas qu'il intervienne uniquement en fin de parcours car alors les risques deviennent trop importants. Il est souhaitable, qu'au cours du développement, des séparations puissent intervenir à un stade où une remise en cause du système n'ait pas de trop graves conséquences et à l'inverse où une confirmation en vol puisse soit permettre d'accélérer le développement soit de rassurer sur les choix effectués.

Pour ces essais en vol intermédiaires, au lieu d'utiliser les réglages finaux, on pourra s'appuyer sur des propositions plus sécurisantes qui rempliront tout autant leur rôle de recalage et de progression de la connaissance.

Bien sûr, c'est ensuite l'essai en vol final qui permettra de statuer sur l'ouverture du domaine de tir. Ce ou ces essais en vol qui permettent de conclure doivent être choisis avec grand soin car leur nombre reste forcement limité. Il faudra les choisir tels que :

- les phénomènes sensibles (Mach, badin,...) soient présents,
- la sécurité du porteur soit assurée.

En effet pour être profitables ces essais doivent être représentatifs des points les plus critiques. Et on s'appuiera pour les choisir sur la simulation en y intégrant les différentes études de robustesses, comme l'illustre le premier exemple d'application ci-après.

Seuls les cas nominaux ou possibles au cours de la vie opérationnelle sont essayés en vol. Il n'apparaît en effet pas nécessaire d'essayer les cas dégradés en vol. Ceux-ci sont traités par simulations en ayant soin de démontrer l'exhaustivité de l'étude pour convaincre sur la fiabilité du résultat.

4. EXEMPLES D'APPLICATIONS

4.1- Préparation d'un tir de développement APACHE ventral sous Mirage 2000

4.1.1- *Contexte*

Dans le cadre de l'intégration du missile APACHE sous Mirage 2000, la méthodologie précédemment décrite est appliquée au titre d'un partenariat industriel entre l'avionneur et le missilier.

Des campagnes d'essais en soufflerie, utilisant le Système de Trajectographie Captive (cf §3.3) ont permis d'identifier les caractéristiques du missile en champ proche et de constituer des modèles de simulation.

Les tirs en vol de développement visent, alors, à qualifier les réglages proposés et à valider l'ensemble de la séquence de séparation. C'est à ce titre qu'a été réalisé, en Mars 1998, un tir de maquette inerte (sans pilotage) au point de vol :

$$M=0.9 \qquad h=5000 \text{ ft} \qquad n=0.9$$

En complément des travaux réalisés par le missilier pour la préparation de ce tir, DASSAULT AVIATION a réalisé un parcours, fondé sur la simulation, et dont la présentation ci-après fournit une illustration de la méthode décrite au §3.1.5.

4.1.2- *Simulations préparatoires du tir*

Dans le but d'assurer la sécurité du tir, un ensemble de simulations de séparation a été réalisé dans les conditions de vol prévues. Conformément au protocole décrit au §3.1.5, ces simulations tiennent compte d'incertitudes relatives :
-aux caractéristiques aérodynamiques de la charge, longitudinales et transversales
-au fonctionnement des éjecteurs
-au point de vol

Une illustration est fournie ci-dessous par le faisceau des trajectoires, au point de vol du tir, résultant de la prise en compte des incertitudes aérodynamiques et des dispersions d'éjecteurs. Pour les deux trajectoires 'enveloppe', la silhouette de la charge est représentée. Cette illustration est obtenue grâce à l'outil de post-traitement présenté au §3.1.4.

300 ms

500 ms

800 ms
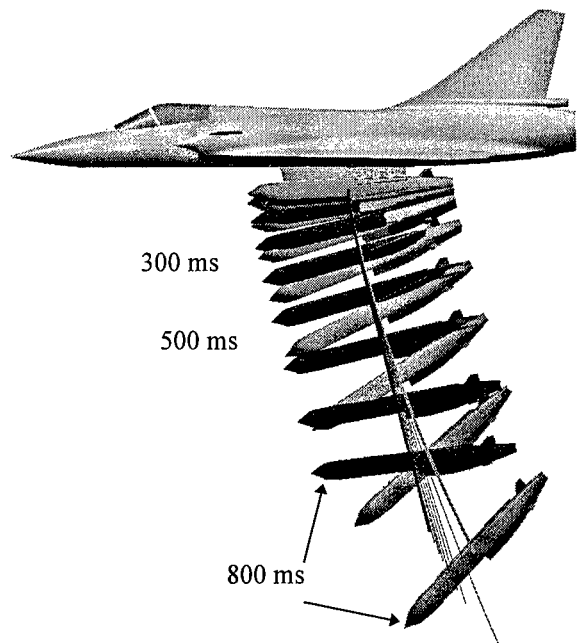
Cet ensemble de résultats fait apparaître que:
- la prise en compte des incertitudes peut conduire, compte-tenu des caractéristiques de la charge, à une forte dispersion sur le comportement angulaire.
- pour autant, le point de tir choisi, et les réglages adoptés (éjecteurs, précalage des empennages) assurent, vis-à-vis de la trajectoire à la séparation, une relative robustesse illustrée par la faible dispersion des trajectoires obtenues.

Cet ensemble de résultats permet d'engager le tir d'essai avec le niveau de confiance suffisant.

4.1.2- *Résultats après vol*

Le dépouillement des résultats du vol permet de situer le comportement dynamique de la charge par rapport à l'enveloppe des prévisions. Le résultat est présenté ci-dessous par le tracé superposé du pinceau de trajectoires précédemment établi, par les simulations préparatoires avec prise en compte d'incertitudes, et la trajectoire du vol. En outre, pour la trajectoire du vol la silhouette de la charge est représentée.
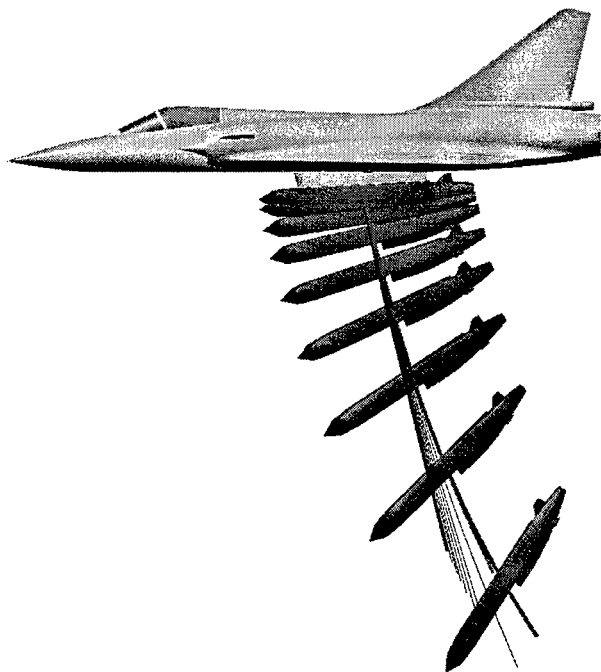
On observe que la trajectoire du vol se situe à l'intérieur de l'enveloppe des prévisions, du côté des incertitudes maximales à piquer. Un tel constat va dans le sens de la sécurité vis à vis des risques de collision.

Ce résultat est relativement satisfaisant dans la mesure où:
- il ne remet pas en cause les hypothèses de modélisation et les niveaux d'incertitudes retenus;
- en conséquence, il conforte les choix de conception et de réglages définis, par simulation, pour assurer le domaine de tir objectif.

Un dépouillement plus complet du vol par exploitation des capteurs embarqués dans le missile pourra permettre, en accord avec le missilier, de procéder à quelques recalages de modélisation, en particulier sur les caractéristiques 'champ libre'. Une telle opération reste toutefois délicate compte-tenu, rappelons-le, de la complexité des phénomènes et de la multiplicité des paramètres de modélisation et ne doit être entreprise qu'après confirmation des résultats sur plusieurs tirs d'essai.

4.1.3- *Commentaires*

L'exemple qui vient d'être présenté est représentatif de la méthodologie suivie pour l'étude de la sécurité du largage d'emports et, en particulier, de la prise en compte de facteurs de robustesse.

Cette approche, délicate sur le plan de la modélisation dans la mesure où elle impose de définir des domaines d'incertitudes autour des paramètres critiques de modélisation, permet, en revanche, d'assurer les tirs de développement puis de définir le domaine

opérationnel d'emploi avec le niveau requis de sécurité.

4.2- Comportement avion au largage de réservoirs sous voilure du RAFALE

4.2.1- *Contexte*

Les essais récents de largage de réservoirs de 1250 l sous voilure du RAFALE fournissent une illustration du caractère parfois fortement couplé des dynamiques de l'avion et de la charge en phase de séparation.

Les réservoirs largables étant des charges perdues, leur trajectoire ne répond à aucune autre exigence que celle de ne pas interférer avec le porteur. C'est ce qui a conduit, pour ce type de charges, à concevoir un dispositif de séparation constitué, outre les éjecteurs en partie médiane, d'un système de retenue arrière qui impose un mouvement à piquer et une désolidarisation pour des valeurs d'assiette relative supérieures à 20 degrés.

Ce dispositif est tout à fait efficace pour assurer la sécurité du largage. Les assiettes relatives pratiquées induisent, en revanche, une forte interaction aérodynamique appliquée à l'avion dont l'analyse a fait l'objet des travaux présentés ci-après.

4.2.2- *Etude du mouvement avion à la séparation*

La figure ci-après illustre les comportements dynamiques de l'avion et de la charge observés au cours d'un largage réservoir plein à M=0.9 à t=0, 0.2, 0.4 et 1 seconde.
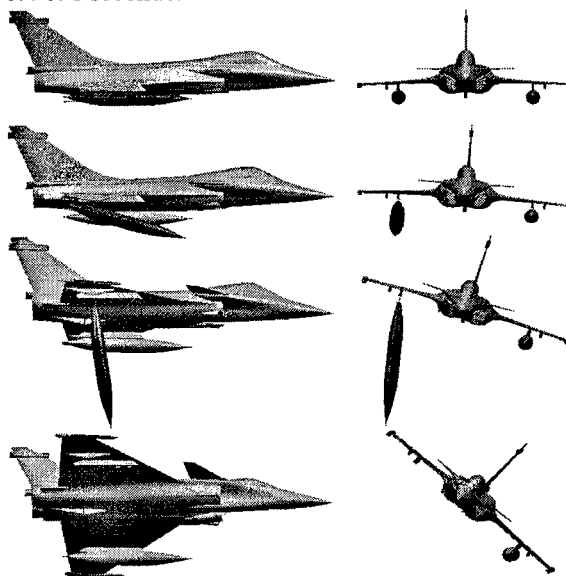
Ce mouvement est dû, essentiellement, à trois effets conjugués:
- la variation massique et inertielle du porteur à la séparation

- l'effet des forces d'éjection et de retenue arrière par le principe d'action-réaction
- l'interaction aérodynamique du réservoir sur l'avion susceptible d'être importante compte-tenu des assiettes relatives des deux corps en champ proche

Le dépouillement du vol permet d'identifier cette interaction au cours du temps par traitement des capteurs gyrométriques et accélérométriques embarqués.

La simulation décrite au §3.1 permet, alors, d'évaluer la contribution des différents termes expliquant le mouvement avion. Les résultats sont présentés ci-dessous par les historiques, au largage, de la vitesse de roulis avion.
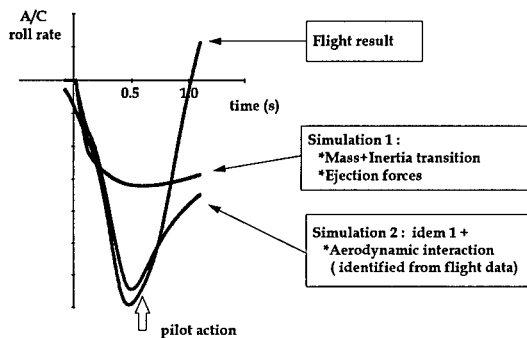
Les simulations sont réalisées sans action pilote ce qui explique les différences de comportement vol/simulation au-delà de t=0.6s. Les tracés comparés du vol et de la simulation mettent en évidence que:

- les effets 'mécaniques' (effets massiques, poussées d'éjecteurs et dispositif de retenue arrière) expliquent pour moitié la valeur maximale de roulis avion au point de vol étudié
- l'interaction aérodynamique explique la seconde part du mouvement. Ce résultat, qui souligne le caractère éventuellement très important des interactions aérodynamiques sur le mouvement avion, a pu être confirmé par le calcul théorique.

4.2.3- Analyse par le calcul théorique

Le dépouillement du vol a permis, comme indiqué ci-dessus, d'identifier la perturbation aérodynamique induite sur l'avion au cours du largage de réservoirs. Dans le but d'analyser ce résultat, et de valider les moyens de prévision, un certain nombre de calculs théoriques ont été réalisés dans les conditions du vol pour plusieurs positions relatives réservoir/avion. Une illustration en est fournie ci-après par un champ de pression pour une assiette relative réservoir/avion intermédiaire.
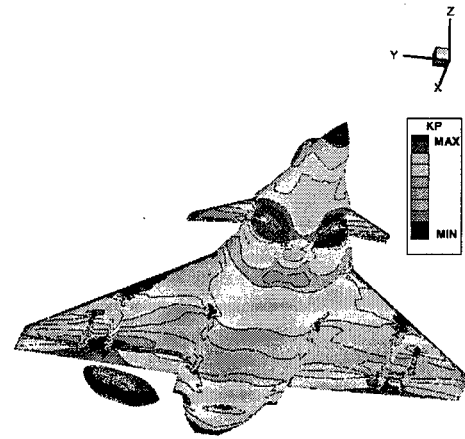
Le calcul montre la dissymétrie des pressions entre la partie gauche de l'avion et la partie droite. Cette modification des pressions affecte la plus grande partie de l'intrados voilure ce qui conduit à la modification du Cl de l'avion.

Les résultats comparés essai/calcul sont présentés ci-dessous.
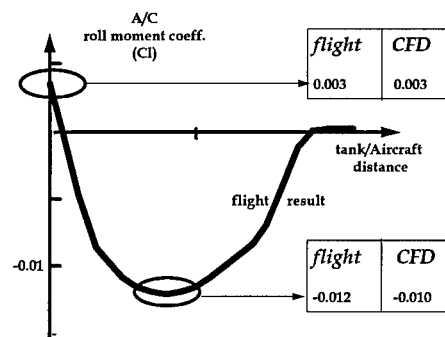
L'interaction identifiée en vol est tracée fonction de la distance réservoir-avion. La valeur à l'origine représente l'écart de Cl en emport par rapport à la valeur charge larguée. L'évolution de l'interaction avec la position relative du réservoir n'est pas monotone mais fait apparaître un fort dépassement pour des positions intermédiaires correspondant à une assiette relative du réservoir de l'ordre de 45 degrés. Ce dépassement explique le résultat observé sur le comportement avion en roulis vu au §4.2.2.

Les calculs théoriques effectués pour plusieurs positions relatives rendent bien compte de ce phénomène. En particulier on observe, sur la figure ci-dessus, un bon recoupement sur la valeur d'interaction en emport ainsi que sur le niveau du dépassement pour des attitudes intermédiaires.

4.2.4- *Commentaires*

L'analyse des largages de réservoirs sous voilure qui vient d'être présentée est illustrative:
- des forts couplages aérodynamiques qui peuvent être observés au largage d'emports et de leur effet sur le mouvement avion
- de l'apport du calcul théorique dans le processus d'identification et de compréhension des résultats du vol. Au-delà le calcul fournit des éléments de transposition et de prévision

Il convient de souligner l'importance de ce résultat dans la mesure où le mouvement avion à la séparation, s'il n'est pas critique du strict point de vue de la sécurité du porteur peut en revanche l'être en termes de performances dans le cas de largages de missiles pilotés pour lesquels les conditions initiales de vol conditionnent la réussite de la mission.

6. CONCLUSION

La présentation qui vient d'être faite illustre la complexité des problèmes posés par l'étude de la séparation d'un emport sous avion d'armes:
- complexité des armements
- couplage des dynamiques avion/charge
- multiplicité des points d'emports
- domaines opérationnels étendus...

L'engagement sur un domaine opérationnel d'utilisation est de la responsabilité de l'avionneur, en partenariat avec les industriels impliqués et les Organismes Etatiques. Pour assurer cette responsabilité, DASSAULT AVIATION a mis en place, et utilise aujourd'hui, une méthodologie et les outils associés permettant notamment de maîtriser la sécurité du porteur et les conditions d'un tir réussi.

Cette méthodologie est largement fondée sur la simulation et la prise en compte, dès les premières études, de facteurs de robustesse permettant de réduire les risques d'itérations coûteuses. L'identification des modèles impliqués dans la simulation fait appel de manière complémentaire:
- au calcul théorique dont l'automatisation permet aujourd'hui de produire des trajectoires complètes de séparation
- à la soufflerie qui par des dispositifs originaux mis en place par l'ONERA permet d'identifier les caractéristiques aérodynamiques en champ proche
- au vol, qui fournit une validation globale et doit, à ce titre, intervenir le plus tôt possible dans le développement.

A terme, la mise en commun et le couplage des moyens d'étude avec ceux développés par les concepteurs d'emports doivent être envisagés dans le cadre de Centres Communs de Calcul ou de Simulation.

Aujourd'hui, les progrès réalisés en termes de modélisation et d'identification des phénomènes permettent, par une approche fondée sur la simulation et les différents moyens d'essai, de relever les défis techniques posés par l'intégration d'emports dans un contexte exigeant de maîtrise des coûts et des délais.

ON-LINE LEARNING HARDWARE-BASED NEURAL NETWORKS: APPLICATIONS TO ADAPTIVE CONTROLS AND FAILURE IDENTIFICATION

Marcello R. Napolitano
Department of Mechanical and Aerospace Engineering
West Virginia University
Morgantown, WV 26506-6106, USA

Mario Innocenti, Giovanni Silvestri
Department of Electrical Systems and Automation
University of Pisa, Pisa 56126, Italy

1. SUMMARY

Neural Networks have shown to be a very attractive alternative to classic adaptation methods for identification and control of non-linear dynamic systems. The purpose of this paper is to show the improvements in neural network applications achievable through the use of a learning algorithm more efficient than the classic Back-Propagation and through the implementation of the neural schemes in parallel hardware. In addition, applications to failure detection and identification of control loop components will be addressed.

The paper illustrates dynamic simulations relative to examples of identification and control of non-linear unknown systems with on-line learning for the hardware-based neural architectures performed with both the classic and the Extended Back-Propagation algorithm. The latter algorithm has shown remarkable improvements with respect to the classic algorithm in terms of learning speed, accuracy, and local minimum problems. The neural schemes are implemented in a set of parallel transputer modules with appealing flexibility for on-line applications.

2. INTRODUCTION

The previous decade has witnessed a dramatic increase in neural networks (NN's) research, mostly induced by the introduction of the Back-Propagation algorithm for feed-forward NN's with supervised learning. During the initial stage of this growth NN's have been applied to pattern recognition and classification, which can be classified as static problems. Within a later trend NN's have been proposed for identification and control of dynamic systems of both linear and non-linear nature. The reason behind this application lies in the fact that, despite progresses were made in adaptive control theory for linear systems, a solution for the identification and control of a non-linear uncertain system has yet to be formulated.

A complete review on NN theoretical principles is available in [25], and [19]. In general, a neural network is defined as an architecture featuring input and output parameters interconnected through one or more layers of neurons, also called processing elements, which provide a non-linear activation.

The operations at each neuron consist of adding the total weighted sum of all the input signals of the preceding layer, with the option of adding a threshold value; this total sum becomes then the argument of a non-linear function, which provides the activation, to generate an output signal. For the neurons of the hidden layer(s) these output signals become the input signal for the processing elements of the above layer of the neural architecture. During learning, the weights and the thresholds of the architecture are updated, typically with a gradient based method, with the goal of minimizing a cost function associated with an identification or a control task. A block diagram of a typical three layer NN (one input, one hidden and one output layer) is shown in Figure 1. Reference [15] and, to a greater extent, [10] provided a substantial background work for several NN applications, clearly stated the necessary theoretical assumptions in order to have well formulated problems.

This paper concentrates on the application of NNs for identification and control of unknown non-linear systems. Particularly, the paper presents studies relative to the implementation of neural networks to some of the non-linear systems reported in [15]. It is intended to be a more application-oriented paper in that it has the objectives of emphasizing the advantages of a particular learning algorithm more efficient than the Back-Propagation for on-line applications. An additional goal is to show that, due to the inherent parallel nature of the neural computations, the implementation of neural schemes in microprocessors, in lieu of software-based neural computations, can be an attractive solution for practical applications.

From a more general perspective, the main objective of this paper is to build an ideal bridge for those in the technical community, who are considering practical implementations of neural networks, but are not quite convinced about the feasibility of hardware-based neural computations and, at the same time, have reservations about the performance of the Back-Propagation algorithm.

3. BASIC CONCEPTS IN IDENTIFICATION, AND CONTROL

A generic multi-input/multi-output (MIMO) discrete-time system with n states, m inputs and l measurable outputs can be represented by:

$$x(k + 1) = \Phi[x(k), u(k)] \tag{1}$$

$$y(k) = \Psi[x(k)] \tag{2}$$

where $x(k)=[x_1(k), x_2(k), \ldots, x_n(k)]^T$
  $u(k)=[u_1(k), u_2(k), \ldots, u_m(k)]^T$
  $y(k)=[y_1(k), y_2(k), \ldots, y_l(k)]^T$

Furthermore, for the control task at non-linear conditions, there is a lack of control schemes regardless whether Φ, Ψ are known or unknown. Adaptive control of uncertain systems is feasible in the linear case. In particular, within this direction, SISO adaptive systems tracking a desired dynamics have been extensively analyzed with the Model Reference Adaptive Control (MRAC) method, shown in [1], and [27], being one of the most representative approaches.
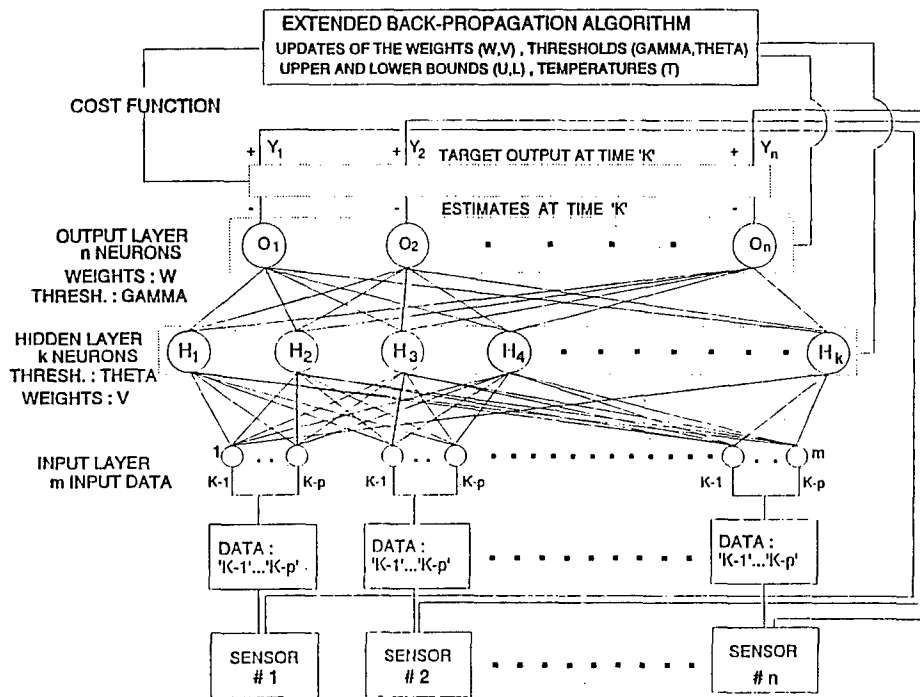
Figure 1. 3 Layer Neural Network

If the system is linear and time-invariant then equations (1), and (2) take on the well-known form:

$$x(k+1) = Ax(k) + Bu(k) \tag{3}$$

$$y(k) = C[x(k)] \tag{4}$$

where A_{nxn}, B_{nxm} and C_{nxl} are the traditional state, control and output matrices. The relative system will then defined through the set of matrices (A,B,C).

Reference [20] shows that, if the system is linear and known, controllability of the system can be asserted and different feedback control strategies, either of classic compensation type or from modern control theory, can be introduced to meet different specifications. For the identification task at linear conditions, that is if the system is linear and (A,B,C) are unknown, the problem of identifying (A,B,C) can be clearly formulated and solved. However, if the system is non-linear and Φ, Ψ are unknown, the identification problem is quite more complicated.

Let us specifically consider the problem of identification and control of SISO non-linear unknown systems. There are four discrete-time models, which can be used to describe this type of systems:

$$Model\ I: y(k + 1) = f[y(k), .., y(k - n)] + \sum_{i=0}^{m} b_i u(k - i) \tag{5}$$

$$Model\ II: y(k + 1) = f[y(k), ..., y(k - n)] + \sum_{i=0}^{m} b_i u(k - i) \tag{6}$$

$$Model\ III: y(k + 1) = f[y(k), ..., y(k - n)] + g[u(k), ..., u(k - m)] \tag{7}$$

$$Model\ IV: y(k + 1) = f[y(k), ..., y(k - n), u(k), ..., u(k - m)] \tag{8}$$

There has been a large variety of studies related to observability, controllability for these systems as well as for designing controllers and observers for them. References [24], [8], and [11] describe the results of some

References [24], [8], and [11] describe the results of some of these investigations. Despite these efforts, solutions to these problems on the same line as the ones for the linear systems have yet to be formulated. In this paper we will refer to multi-layer feed-forward NNs with supervised learning performed with gradient based algorithms. The suitability of a NN approach to the general identification and control task becomes somewhat immediate if one considers the following properties.

Applicability to non-linear systems. The applicability of NNs to non-linear systems originates from their mapping capabilities. [6], and [9] have shown that a feed-forward NN with at least one hidden layer is capable of approximating any non-linear function once enough training is provided. This property can be extremely useful when the input/output data are related to a non-linear time-varying system.

Parallel processing and hardware implementation. NNs have an inherent parallel architecture, which, leads naturally to parallel hardware implementations. These implementation have also the advantages of having, in general, high degree of fault-tolerance and high processing speed, due to the simplicity of the computations (additions, subtractions, multiplications). These advantages have been magnified by the introduction of digital microprocessors with ever increasing performance.

Multivariable systems. NNs, by definition, are multi-input, multi-output (MIMO) entities and this, naturally, leads to their application to multivariable systems.

Learning and adaptation. NNs can be trained using past recorded data or simulated data (off-line training) or current data (on-line learning). Furthermore, among the learning capabilities of a NN, one must differentiate between local and global learning capabilities. Local learning leads to adaptation capabilities to new dynamic conditions while global learning leads to memorization capabilities from previously presented data.

While the learning capabilities above are undoubtedly very attractive, the implementation of neural schemes for adaptive identification and control must be analyzed very carefully. In fact, a key issue is the selection of an on-line learning vs. off-line training working mode. On-line learning implies that the NN has the capability of changing the values of the numerical components, which make up its architecture, in real-time. Off-line training implies that the NN operating on-line had been previously trained and it has a frozen numerical architecture. For on-line learning points of particular concern are:
-the amount of time needed to acquire a substantial learning level;
-the complexity of the neural architectures.

3.1. Identification of a Nonlinear SISO System via Neural Networks

Consider a generic SISO non-linear unknown system

described by any of the four models in the previous section. The objective is to provide a NN-based identification scheme for the functions 'f' and/or 'g'.

A necessary assumption for a well-posed approach is that the system have a bounded response for any bounded set of input data (that is, it is a BIBO stable system). This, in turn, implies that the neural identifier will also need to be BIBO stable. Extensive research efforts are undergoing at this time for the analysis and the proof of stability properties of multi-layer neural networks

Another assumption is that the neural identifier will have to be of series-parallel type meaning that the actual system output $y(k)$, rather than its estimate, is used as input by the identification scheme during and after the training. The alternative is to use a parallel-type identifier, meaning that the estimate of $y(k)$ from the neural identifier is obtained using as input estimates of $y(k)$ at previous time steps. It should be underlined that the stability for this type of identifiers has yet to be proved even for simple linear systems. The selection of a series-parallel mode instead of a parallel model is mainly due to the fact that, since the system is assumed to be BIBO and stable, all the input to the NN's are bounded. However, once the neural identifier has been sufficiently trained and the estimation error has converged to a sufficiently low asymptotic value, the series-parallel mode may be replaced by the parallel-working mode.

With these working assumptions in place, the next issue to be addressed is related to the selection of the training algorithm for the neural identifiers. To date, the majority of the training for neural networks is being performed with the Back-Propagation (BP) algorithm, a gradient-based optimization method.

Slow learning, especially for large order systems, and local minima are "classical" well documented problems of the BP. Unfortunately, these two problems are known to be mutually related and interactive. For example, it has been shown that the learning speed can be improved by setting a proper learning rate. However, this also increases the possibility for the BP to be trapped in a local minimum or to oscillate around the global minimum.

To solve these problems, several alternatives to the BP have been proposed by many researchers. Most of the work has been concentrated on introducing different activation functions or particular procedures for selecting the initial weights. Within this stream of investigations, the authors have used an approach based on the introduction of an heterogeneous network, described in [4].

In an heterogeneous network each neuron in the hidden and output layers has its own capability of updating some new parameters giving the overall architecture increased mapping and adaptation performance. Specifically, in a heterogeneous network each neuron is able to change its

heterogeneous network each neuron is able to change its output range (upper and lower bounds: U, L) and the slope of the sigmoid activation function (temperature: T). The new non-linear activation function will be given by:

$$f(x_{ij}, U_{ij}, L_{ij}, T_{ij}) = \frac{U_{ij} - L_{ij}}{1 + e^{-x_{ij}/T_{ij}}} + L_{ij} \qquad (9)$$

where i,j are the indices for the generic neurons of the hidden and output layers and 'x' is the argument of the classic sigmoid function of the BPA. This function is implemented at each processing element of the hidden layer(s) and output layer. The gradient is calculated to perform the steepest descent as in the BP. The only difference is that the gradient descent will be found with respect to each of the independent variables 'x','U','L','T', as opposed to 'x' only. The training algorithm associated with this heterogeneous network is named Extended Back-Propagation (EBP) and is described with details in [4], and [13].

The design of on-line learning neural controllers, and neural identifiers can be complicated by the large number of degrees of freedom (number of hidden layers, number of neurons per hidden layer, size of input data window, magnitude of the learning rate and momentum coefficients) in the selection of the neural architectures. This issue has been addressed in [2], and [7]. Previous work coordinated by the first author provided the following guidelines for the selection of suitable neural architectures :
- on-line learning neural controllers and neural identifiers are generally very robust to different number of neurons per hidden layer and a different input data window;
- medium-high learning rates, either constant or slowly decreasing with time, performed better for on-line learning neural controllers while low learning rates perform better for on-line learning neural identifiers;
- simple single hidden layer architectures perform as well or better than more complicated and more computationally intensive multiple hidden layers architectures;
- a proper selection of the data to be presented as input and an appropriate choice of the performance indices to be minimized are, by far, the most effective degrees of freedom in the selection of neural architectures.

These parametric studies are better described in [3], [16], and [18]. However, these guidelines, originated in a study related to on-line learning neural identifiers and controllers for flight control applications, were arbitrarily neglected in the first part of the work. In fact, one of the goals was to show improvements achievable with the EBP algorithm with respect to the BP algorithm using the same architectures of the neural networks used in [15] and, therefore, without any attempt to optimize the learning process.

Next, neural identifiers will be introduced using both BP and EBP algorithms. Consider a different SISO unknown non-linear system described by :

$$y(k + 1) = \frac{y(k)}{1 + [y(k)]^2} + [u(k)]^3 \qquad (10)$$

representing a Model III system. In this case a neural network based identification scheme will consist of two neural identifiers, that is an identifier N_f for the function:

$$f[y(k)] = \frac{y(k)}{1 + [y(k)]^2} \qquad (11)$$

and an identifier N_g for the function:

$$g[u(k)] = [u(k)]^3 \qquad (12)$$

such that the estimation dynamics can be expressed as:

$$\hat{y}(k + 1) = N_f[y(k)] + N_g[u(k)] \qquad (13)$$

The simulation of the unknown system is performed within a Simulink™ environment with the user having the possibility to select for the neural computations to be performed by either a C++ code or by customized neural hardware to be described later in the section.

As in [15], a two hidden layer architecture was selected : both neural identifiers are of the type $N_{1,20,10,1}$. The study involved two different phases, that is an initial training phase followed by a testing phase. During the training phase two sets of two similar $N_{1,20,10,1}$ architectures (one using the BP and the other using the EBP) were trained for 100,000 steps with u(k) being a random number uniformly distributed between [-2,2] and using a 0.25 learning rate. The range for u(k) implies that the estimate of g will span between [-8,8] while the estimate of f will span between [-10,10]. During this phase the identifier is working in a series-parallel mode, that is the actual system outputs at previous time steps are used by the identifier to provide an estimate at the present time step.

The training performances associated with the two algorithms were evaluated every 2,000 steps during the 100,000 steps simulation for a total of 50 test points. At each test point the performance of the neural identifier were analyzed using a 100 steps simulation. Classical statistical parameters, that is mean, mean square and variance, were introduced to monitor the estimation errors for 'f' and 'g' and given by

$$M_{EE} = \sum_{i=1}^{100} \frac{[\hat{y}(i) - y(i)]}{100} = \sum_{i=1}^{100} \frac{e(i)}{100} \qquad (14)$$

$$MS_{EE} = \sum_{i=1}^{100} \frac{[\hat{y}(i) - y(i)]^2}{100} = \sum_{i=1}^{100} \frac{e(i)^2}{100} \qquad (15)$$

$$V_{EE} = \sum_{i=1}^{100} \frac{[e(i) - M_{EE}]^2}{100} \qquad (16)$$

In terms of complexity and required computational effort for the neural architectures, the number of parameters to be updated at each time is 354 using the EBP and 261 using the BP. Therefore, there is a 35% increase in complexity using the EBP due to the additional parameters U,L, and T.

The statistical results are shown in Figure 2 for the identification of the function 'f', similar results are available for function 'g'. The trends for M_{EE}, MS_{EE} and V_{EE} show that the EBP clearly outperforms the BP. In particular, it can be seen that the estimates using BP exhibit a bias most likely caused by the BP algorithm getting stuck in a local minimum point. Efforts were made in repeating the training phase with the BP several times; however, local minimum points problems seemed always to be present to a certain extent. The bias problem for the BP is even more clear in Figure 3, showing estimates of 'f' following the training phase.

After the 100,000 steps training phase the two combined neural identifiers, working in a parallel mode, providing an estimate for y(k+1) are tested for 1000 steps with the control sequence u(k)=sin(2πk/25)+sin(2πk/10). The results are reported in Figure 4 and Table I indicating better performance of the EBP algorithm.

Figure 3. Testing Phase, Estimate of Function 'f'

Table I. Statistics of Estimation Error: Testing Phase

	BP Algorithm	EBP Algorithm
Time	100,001-100,100	100,001-100,100
Mee	-.0277	-.0154
Msee	.0017	.000518
Vee	.000945	.000750
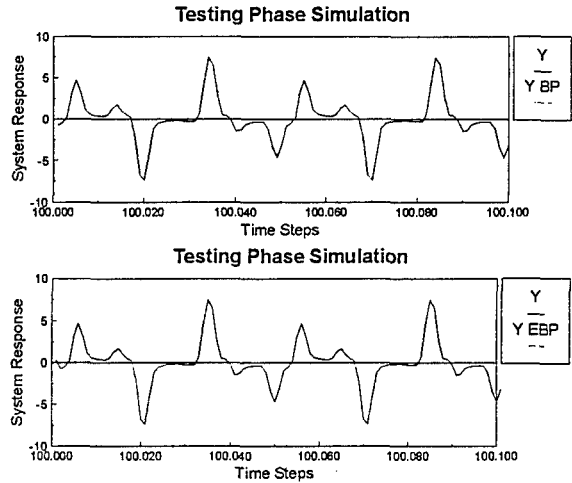
Figure 4. Testing Phase: Simulation

Figure 2. Statistics of Training Phase for Function 'f'

The reason for the improved performance of the EBP vs. the BP algorithm has to be searched in the different learning characteristics. The EBP has more degrees of freedom in the learning through the use in the gradient method of the following partial derivatives :

$$\frac{\partial f[x_{ij}, U_{ij}, L_{ij}, T_{ij}]}{\partial x_{ij}} = -\frac{(O_{ij} - U_{ij})(O_{ij} - L_{ij})}{T_{ij}(U_{ij} - L_{ij})} \quad (17)$$

$$\frac{\partial f[x_{ij}, U_{ij}, L_{ij}, T_{ij}]}{\partial U_{ij}} = \frac{1}{1 + e^{-x_{ij}/T_{ij}}} \qquad (18)$$

$$\frac{\partial f[x_{ij}, U_{ij}, L_{ij}, T_{ij}]}{\partial L_{ij}} = 1 - \frac{1}{1 + e^{-x_{ij}/T_{ij}}} \qquad (19)$$

$$\frac{\partial f[x_{ij}, U_{ij}, L_{ij}, T_{ij}]}{\partial T_{ij}} = \frac{x_{ij}(O_{ij} - U_{ij})(O_{ij} - L_{ij})}{T_{ij}^2(U_{ij} - L_{ij})} \qquad (20)$$

as opposed to the derivative

$$\frac{\partial f[x_{ij}]}{\partial x_{ij}} = \frac{e^{-x_{ij}}}{\left(1 + e^{-x_{ij}}\right)^2} \qquad (21)$$

in the BP algorithm. In the above equations, O_{ij} represents the generic output of a neuron at the hidden layer(s), and at the output layer respectively.

3.2. Identification and Control of a Nonlinear SISO System via Neural Networks

The previous study has illustrated successful applications of neural identifiers. Next, the problem of adaptive control via NN's is considered. The problem of controlling a generic dynamic system can be divided into a regulation or a tracking problem. In a regulation problem the goal is to achieve, through an appropriate feedback control law, an equilibrium condition around a certain set point. In the tracking problem the objective is instead to achieve, through the feedback control law, an accurate following of a reference model response. The control part of this paper is related to the tracking problem for an unknown non-linear SISO system.

It is known that most of adaptive control theory is based on the Model Reference Adaptive Control (MRAC) relative to linear time-invariant systems. Particularly, Reference [14] shows two different approaches, that is the direct and the indirect approaches. It should be emphasized that the closed-loop dynamics with the adaptive control scheme, both in the direct and indirect form, will be non-linear even if the open-loop system is linear and time-invariant.

In a direct adaptive control scheme the parameters of the control scheme are adjusted on-line to satisfy some control specifications. In indirect adaptive control scheme instead the parameter identification scheme is first implemented providing estimates of the actual system parameters with the parameters of the controller calculated assuming these estimates of the system parameters.

There is a well known problem in using a neural network approach for a direct adaptive control of a non-linear system. In fact, the neural network controller output error, which is used to update the weights and the thresholds of the neural controller, is not directly available. The only available information is the tracking error between the desired and the actual response, which is only a function of the error at the neural controller output. Several methods have been proposed in the literature to overcome this problem and tested on non-linear SISO systems. Reference [21] suggests a method where the system dynamics are treated as not modifiable layer of the neural controller and the tracking error is back-propagated through the dynamics. In [5] another approach is

suggested, where the tracking error is transformed into the neural controller error using the dynamics inverse transfer matrix. Reference [12] presents a third method where a feedback gain is introduced to generate a transformed error signal used to update the architecture of the neural controller. Finally in [26] a scheme is introduced, where the architecture of the neural controller is updated using the tracking error with the addition of an extra single layer gain between the neural controller and the system.

This section, however, describes results related to indirect adaptive control with a neural approach. In the absence of well formulated stability and robustness criteria a natural approach for non-linear systems can be given by trying to extend some results relative to linear adaptive control theory. For example, in linear adaptive control theory it was concluded that adaptive control laws for a stable closed-loop system can be found if some "a priori" knowledge of the system was available. Similarly, the probability of success of the adaptive control of a non-linear SISO system can be assumed to be a strong function of the amount of "a priori" information on the unknown system.

A safer and more conservative set-up of the problem is to apply adaptive control, in order to achieve tracking of a desired system response using an indirect approach. That is only after the non-linear system has been identified within a desirable level of accuracy. It should be underlined, however, that even this conservative approach does not guarantee closed-loop stability and acceptable tracking performance, even in the case of a BIBO stable system, since the adaptive control law can lead to an unstable system during the transient. It can be speculated that fast on-line learning capabilities of the neural controllers, which are direct function of the selected learning algorithm, are critical for this purpose.

On the other side, closed-loop stability, and possibly good tracking performance are only a remote possibility if adaptive control using neural identifiers and neural controllers is attempted with a direct approach, that is without any "a priori" identification phase. In the following, the tracking capabilities and the robustness of a NN-based indirect adaptive control scheme are evaluated.

Consider the same unknown SISO non-linear system described in equation (10), representing a Model III system. This time the objective is to find an adaptive control law u(k) such that the actual system response y(k) tracks a desired model response y_m(k), with the dynamics for the reference model given by:

$$y_m(k+1) = 0.6 y_m(k) + r(k) \qquad (22)$$

recall that previously we had:

$$\hat{y}(k+1) = N_f[y(k)] + N_g[u(k)] = \hat{f}[y(k)] + \hat{g}[u(k)]$$
(23)

Following the training phase we had that the estimates of y(k) were converging to the actual y(k) response. For the actual system to track the desired model response we would have

$$\hat{f}[y(k)] + \hat{g}[u(k)] = 0.6y_m(k) + r(k)$$
(24)

isolating $\hat{g}[u(k)]$ yields:

$$u(k) = \hat{g}^{-1}\{0.6y_m(k) + r(k) - \hat{f}[y(k)]\} = \hat{g}^{-1}[z(k)]$$
(25)

The tracking problem is solved by introducing a neural adaptive controller N_c for the on-line determination of u(k). Particularly, two neural controllers, trained using EBP and BP respectively, are introduced. Both of them will have architecture $N_{1,20,10,1}$ with input z(k) with a learning rate of 0.01.

The closed-loop system will therefore include :
- 2 neural identifiers ($N_f N_g$);
- 1 neural controller (N_c).

Again, there is an initial training phase and a testing phase. During the training phase two similar sets (one using BP and the other using EBP) of 3 neural architectures ($N_f N_g N_c$) were trained for 100,000 steps using the same random input u(k) between [-2,2] used previously. The training performance are evaluated every 2,000 steps for a total of 50 test points. The statistical results for the identification of 'f' and 'g' were very similar to the ones obtained previously, while the results for the identification of the inverse function of 'g' are shown in Figure 5.

The tracking capabilities of the closed-loop system are then evaluated with a 5000 steps simulation. The results are summarized in Figure 6; in particular Figure 6 shows 2 different 100 steps simulation starting respectively at instants 1, and 4,901. The superior performance of the EBP algorithm are once again confirmed by the statistical data on the tracking error shown in Table II. It can be seen that the EBP neural estimate is practically unbiased and has a variance approximately 4.25 times smaller than the correspondent BP variance.

Statistics of the Training Phase for Nc
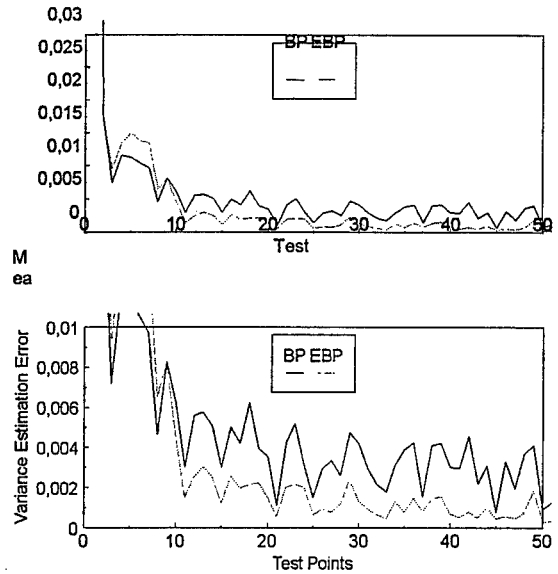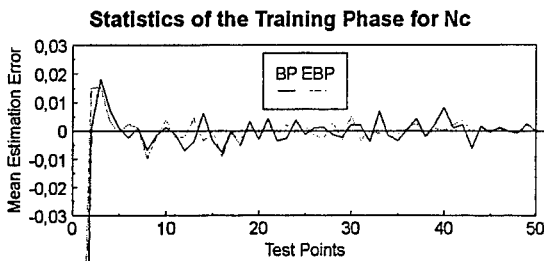
Figure 5. Statistics of the Training Phase for "g-inverse"
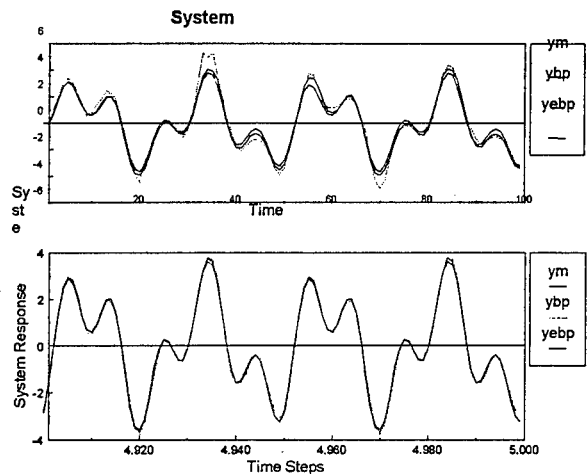
Figure 6. Testing Phase: Simulation

Table II. Statistics of the Tracking Error: Testing Phase

	BP Algorithm		
Time	1-1,000	2,501-2,600	4,901-5000
Mte	-0.0237	.0004	-.0003
MSte	.2743	.0139	.0148
Vte	.2765	.014	.0149
	EBP Algorithm		
Time	1-1,000	2,501-2,600	4,901-5000
Mte	.0707	.0005	.0002
MSte	.0720	.0042	.0035
Vte	.0677	.0042	.0035

The next objective of this study is to evaluate the robustness of the neural-based tracking to a time-varying system. For this purpose the original non-linear SISO system described by equation (22) is simulated to change instantaneously, starting at the 5,000-th step, to 3 different arbitrarily selected configurations before returning to the original configuration. At each configuration a 5,000 steps simulation is performed using both the EBP and the

steps simulation is performed using both the EBP and the BP algorithms. The different configurations are shown below:

For k=5,000-9,999, Config. 1

$$y(k+1) = \frac{y(k)}{1+y^2(k)} + [1.5u(k)]^3 + 2 \qquad (27)$$

For k=10,000-14,999, Config. 2

$$y(k+1) = \frac{2y(k)+2}{0.5+y^2(k)} + [1+u(k)]^3 - 1 \qquad (28)$$

For k=15,000-19,999, Config. 3

$$y(k+1) = \frac{2y(k)+2}{0.5+y^2(k)} + [1+u(k)]^3 - 1 \qquad (29)$$

For k=20,000-24,999, Config. 4

$$y(k+1) = \frac{y(k)}{1+y^2(k)} + [u(k)]^3 \qquad (30)$$

Several 100 steps simulations time histories of the reference model along with the closed-loop system response using both EBP and BP algorithms are shown in Figures 7-11 for different points of the 5,000 step simulation. For the tracking problem the statistics are expressed in terms of the tracking error, defined as:

$$M_{TE} = \sum_{i=1}^{100} \frac{[y(i)-y_m(i)]}{100} = \sum_{i=1}^{100} \frac{e(i)}{100} \qquad (31)$$

$$MS_{TE} = \sum_{i=1}^{100} \frac{[y(i)-y_m(i)]^2}{100} = \sum_{i=1}^{100} \frac{e(i)^2}{100} \qquad (32)$$

$$V_{TE} = \sum_{i=1}^{100} \frac{[e(i)-M_{TE}(i)]^2}{100} \qquad (33)$$

From the plots and the statistical results, it can be seen that the tracking performance associated with the EBP algorithm are somewhat worse than the correspondent BP performance only during the transient phase of the transition of the system between different configurations. Once this transient phase is past, the closed-loop system with EBP trained neural identifiers and controller clearly outperforms the BP version.

Figure 8. Simulation Comparison to Config. 1
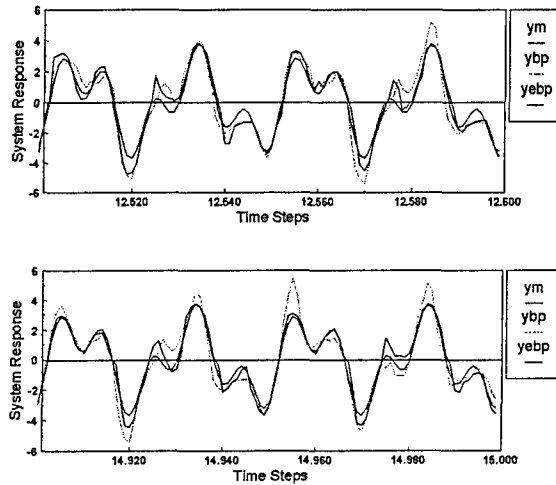
Figure 9. Simulation Comparison to Config. 2

Figure 7. Simulation Comparison Original System
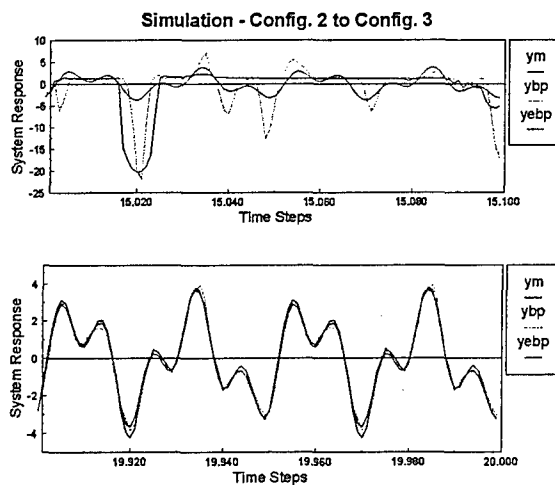
Figure 10. Simulation Comparison to Config. 3
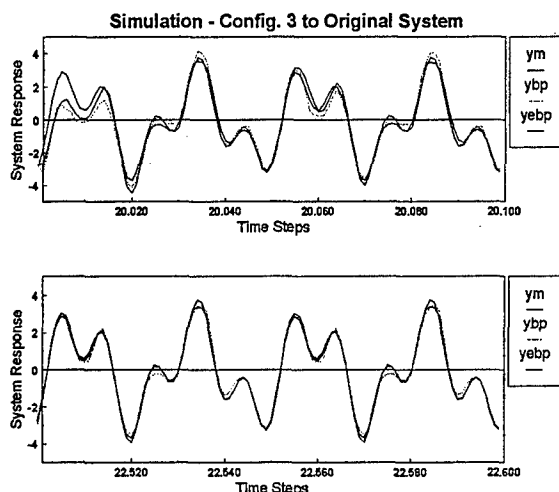
Figure 11. Simulation Comparison to Original System

3.3. Hardware Implementation

The on-line learning neural architectures for the studies previously presented were implemented on transputer modules mounted on an INMOS B008 IBM PC motherboard, which can be considered as "old technology" by today's standards. Two different types of modules were used. The first type is an INMOS B404. This module features an Inmos T800 floating point transputer with 32 Kbytes of no-wait state static RAM and 2 Mbytes of one-wait-state dynamic RAM. The B404 is directly interfaced with the PC-ISA bus and contains a de-multiplexing process to properly distribute the inputs to the other 2 modules. One B404, occupying 2 of the 10 slots on the PC motherboard, was used. The second type of module is an INMOS B420 VecTram. This module features, again, an Inmos T800 floating point transputer, with 1 Mbyte dynamic RAM, connected with a high performance vector/signal processing co-processor. The two processors can handshake via interrupts and can operate concurrently, using separate dynamic and static memory blocks. The vector/signal processor is normally operated as a slave to the T800 transputer which can read and write to the static RAM (256 Kbytes). Two B420s VecTram, occupying the remaining 8 of the 10 slots on the motherboard, were used.

The assembled B008 IBM PC motherboard, with 1 B404 and 2 B420 modules, was then inserted in a PC-ISA bus in a Pentium based PC. A comprehensive set of software libraries in C language supports the implementation of these modules. Hardware parallel simulations were performed using C-MEX files for interfacing Simulink schemes to the neural software coded in the 3 T-800 modules.

The selected equipment was not the most powerful available on the market; it was, however, very cost effective. It must be emphasized that the underlying idea of this study is to show the potentials of on-line learning

parallel hardware-based neural architectures rather than to demonstrate the performance of the latest in microprocessor technology. In general, the selection of the equipment to be used is problem-dependent [33].

In terms of hardware-setup for the two studies we had the following configurations:
1st STUDY : 2 neural identifiers (N_f, N_g), implemented in two B420 modules;
2nd STUDY : 2 neural identifiers (N_f, N_g) and 1 neural controller (N_c) implemented in the two B420 modules and in the B404 respectively.

4. FAILURE DETECTION USING NEURAL NETWORKS

Failure detection (FD) is a widely investigated problem in current flight control research, due to the ever-increasing complexity, and interconnectivity of the system at end. Generally speaking, FD implies some sort of continuous monitoring of the measurable outputs of the system. Under nominal conditions, these variable tend to follow rather well established patterns, within the uncertainty due to process disturbances, such as atmospheric turbulence, sensor noise, and actuator biases.

A failure to any component of the FCS will produce deviations from nominal and somewhat predictable trajectories. Spotting a deviation between nominal and failed trajectory is usually the basis of any FD technique. The knowledge of the system's behavior by the flight control system at any operating point needs then to be available at a very heavy computational and storage costs, limiting the prediction to linear time invariant, low order, and white noise-based models of predicted trajectory behavior.

Neural network architectures have been primary candidates to maintaining the same level of, or improving FD capability without increasing computational burden [30], [31]. The mapping property of a NN architecture can be extremely attractive when the input-output data are related to completely or partially unknown dynamics.

Several factors must be taken into account however, when considering the implementation of NN estimators. A key issue in the design of a NN based state estimator is the selection of on-line learning vs. off-line learning. Of course in an off-line situation all training has been performed beforehand, and the network has a frozen architecture. Due to the variability of the dynamics and failure conditions, however, the potential of on-line architectures was studied in the present work because of its inherent added flexibility. In the following, we refer to an on-line structure of feed-forward type with interlayer connections schematically shown in Figure 1 as implemented by a three-layer NN. More details on the architecture can be found in [32].

4.1. Sensor Failure Detection

The overall sensor failure detection, identification, and accommodation (SFDIA) problem is addressed in the context of aircraft dynamics, by using multiple architectures consisting of a centralized structure (MNN), and a set of 'n' decentralized structures (DNN), where 'n' is the number of non-redundant sensors. Figure 12 shows a diagram of the layout of the main neural network. A similar one, but with a single output, can be obtained for the n DNN's which, after sensor failure, will provide accommodation. Figure 12 shows the flow of the SFDIA process in a three-sensor case, with a simulated failure for sensor #2. A more detailed description of the process can be found in [32], [35].

the absolute value of the estimation error of the ith DNN

$$E_{DNN}^{ID} = |E_j| \qquad (35)$$

Identification is again assumed if the error in equation (35) is greater than a specified level.

The procedure outlined above consists of two steps, thus reducing the chance of false alarm. Failure accommodation is then performed by replacing the value of the data coming from the failed sensor, with the estimate of the corresponding DNN, which stops the learning process and "freezes" its architecture at this point.
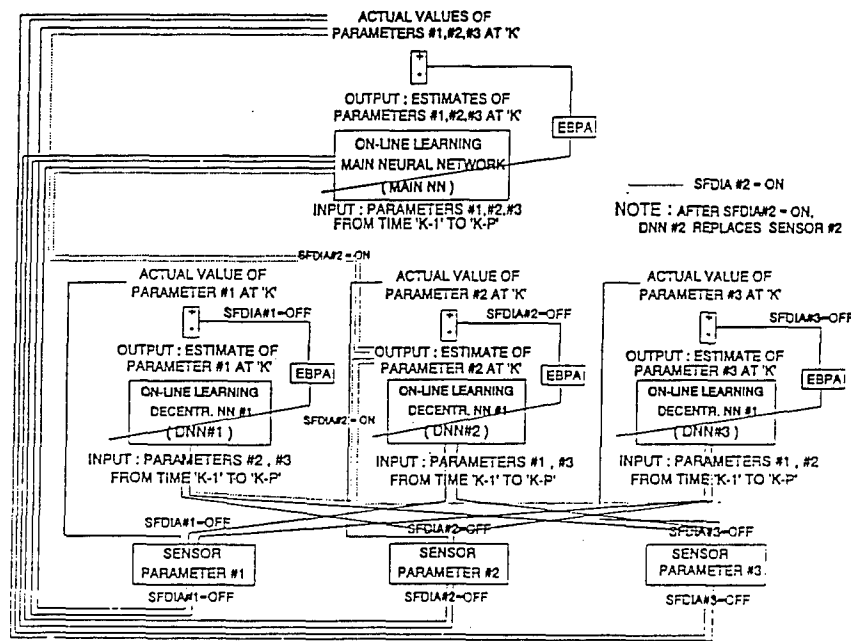
Figure 12. SFDIA Diagram, Sensor #2 failed [Ref. 34]

The main network MNN receives the input from control commands and the vector of measurements y, providing the estimate y^E of the same measurements as output. The EBPA updates MNN based on the error, and the learning process is monitored by a quadratic error parameter

$$E_{MNN} = \sum_{i=1}^{outputs} \left(y^E - y \right)^2 \qquad (34)$$

Each ith DNN receives the input form the control and n-1 sensors, where the missing signal is relative to the corresponding measurement. The training procedure is similar to that of MNN, until failure is detected. Upon failure of the ith sensor, detection can be accomplished by the value of E_{MNN} exceeding a given threshold. When this occurs, identification can be achieved by monitoring

Figure 1 with a single output describes therefore the accommodation procedure as well, whereas the entire SFDIA is described in Figure 12, noting that DNN's update is performed at each step, at the frequency of the sensors. References [34], [35] present several applications simulating soft and hard failures in the dynamic behavior of a full-envelope nonlinear aircraft model representative of a high performance twin engine flight vehicle. The system has 11 sensors and 5 actuators.

As an example, we consider the case of a soft failure (the sensor does not fail completely) representative for instance of added bias in the instrument readings. The sensor considered here is the roll-rate gyro, which is one of the primary measurements in the lateral-directional motion of the aircraft. Figure 13 shows the time history of the error in the MNN with a detection spike at 1700 seconds, while the measured variable, roll rate is plotted in Figure 14.
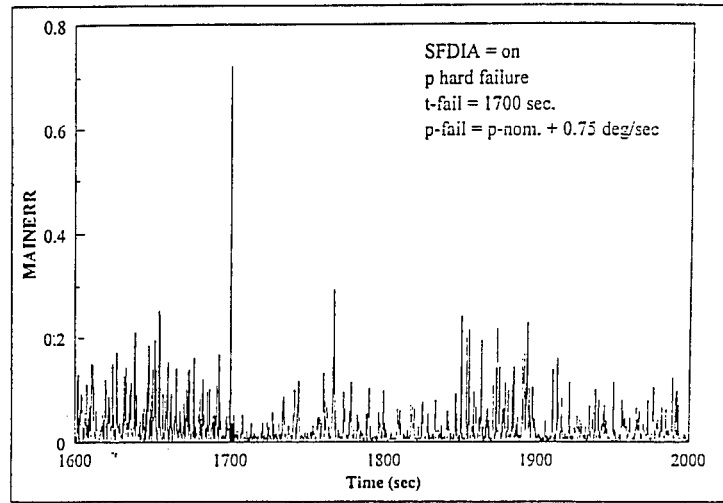
Figure 13. Roll Rate Gyro Failure, NN Estimation Error SFDIA On
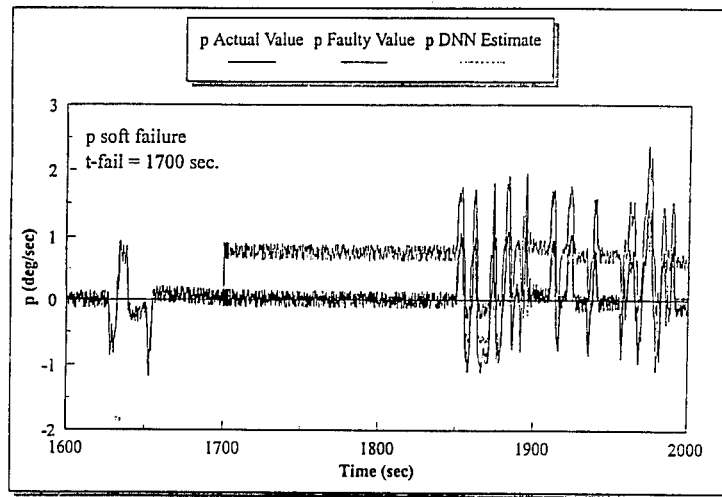
Figure 14. roll Rate Gyro Failure, Time Histories

the measured variable, roll rate is plotted in Figure 14. From that figure, the time history of the roll rate DNN follows the actual roll rate in a satisfactory manner.

4.2. Actuator Failure Detection

During the operation of a flight vehicle, actuator failures can occur for reasons internal to the system, as well as for external causes such as battle damage for military aircraft. Dealing properly with actuator failure is usually critical in that reduced controllability and even loss of controllability may happen with heavy financial losses as well life-threatening situations.

The same dynamic system described in the previous section is considered here, which is modeled by a full nonlinear simulation code, and a FCS consisting of five aerodynamic control surfaces providing control moments on the three axes (pitch, roll, and yaw). The simulation is related to a typical high maneuverability task with

simultaneous commands on the actuators, plus the appropriate thrust setting. Several actuator failures have been studied involving a fault in the hinge moment capability, and percent loss of control effectiveness. These failures require extensive analysis of the modified aerodynamic effects on the aircraft, in order to have a realistic simulation capability and were part of a concerted research effort [35].

The measurement data are all fed into the neural network, which is training on-line, and the process is monitored by evaluating the difference between the estimated and actual angular velocity in terms of body axes components at each instant k as

$$\Omega_{err}(k) =$$

$$\frac{1}{2}\left[\left(p(k) - p^{est}(k)\right)^2 + \left(q(k) - q^{est}(k)\right)^2 + \left(r(k) - r^{est}(k)\right)^2\right]$$

(36)

It must be noted that in this case, unlike SFDIA, the

network must be able to separate sudden variations in the actuator time histories due to pilot maneuvering commands, from failures, therefore training plays a much more critical role here.

induces a variation in $\Omega_{err}(k)$, interpreted as failure detection as shown in Figure 16. Note that a different parameter could have been chosen in the failure detection
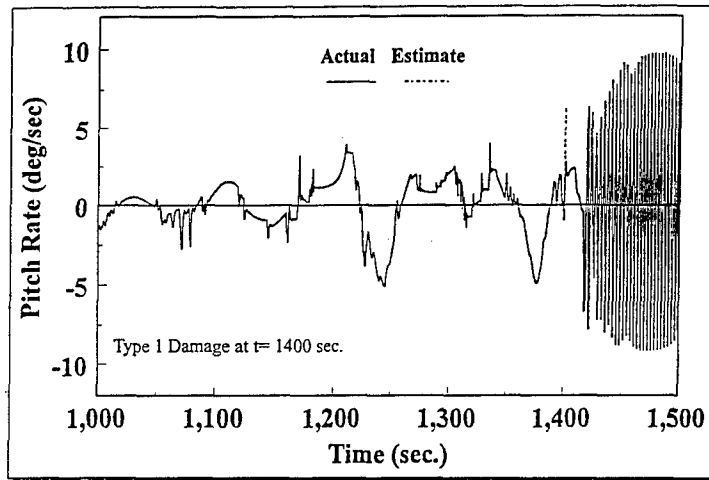
Figure 15. True and Estimated Pitch Rate after Damage
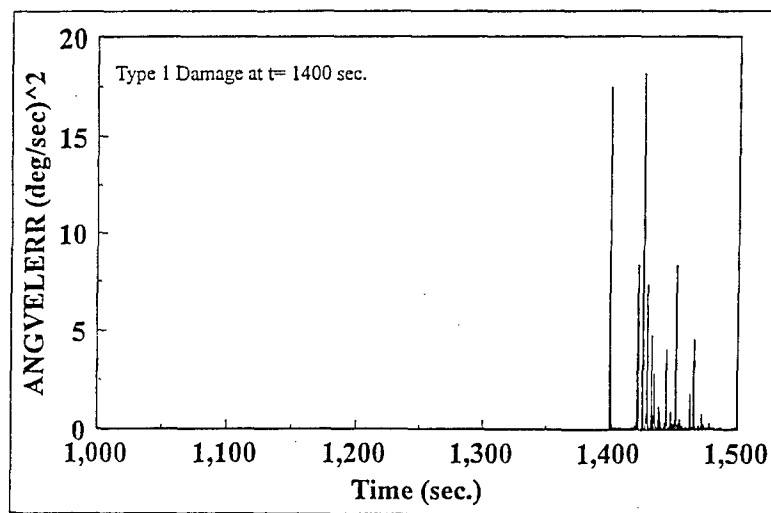
Figue 16. Actuator Failure Detection using Angular Velocity Error

A parametric analysis was carried out [35] to determine the most appropriate failure detection and identification scheme keeping in mind a compromise between NN architecture complexity and on-line computational requirements. The results indicated a structure consisting of 9 inputs 2 patterns, 18 input data, 1 hidden layer, 10 P.E. in the hidden layer, and 3 P.E. in the output layer.

Figure 15 gives an example of pitch rate (q) time history following a damage of the left stabilator of the aircraft at t=1400 sec (control surface stuck at 20 degrees, and 50% loss of control effectiveness).

The change in behavior of q, which is coupled with similar changes in the other components of angular velocity,

scheme. Choice of $\Omega_{err}(k)$ was preferred since it contains variables directly affected by the aircraft dynamics, and dimensionally consistent.

Following the detection of failure, sensor data must be interpreted in order to identify the damage location. The identification procedure relies on on-line evaluation of the cross-correlation function between key variables, which is then stored in temporary memory on the FCS computer. In the above example of a damaged stabilator, since both pitch and roll rate are involved, the cross-correlation function used is given by

$$\Sigma\left|R_{pq}^{coef}(k-1)\right| - \Sigma\left|R_{pq}^{coef}(k-2)\right| > \varepsilon_{FI}^{Thres} \qquad (36)$$

and similarly for the other actuators. The behavior of

equation (36) is shown in Figure 17 taken with a time window of 7 instances. Although the presence of false alarms is not avoided, especially at the detection level, the use of equation (36) has proven very effective in terms of false alarm rate of the entire failure detection and identification process [35].

linearized model of the system itself, and relative to angular velocity rate gyros.

The structure of the KF-based scheme is taken at first as specular of that relative to the neural network SFDIA of
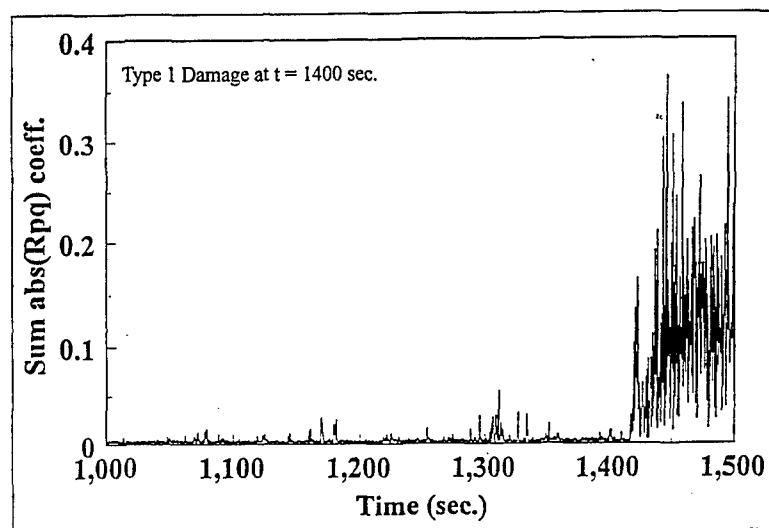
Figure 17. Pitch and Rol Rates Cross Correlation as Failure Identification Parameter

5. Comparison with Standard Methods

One of the techniques traditionally used is the failure detection problem is based on the application of a Kalman filter both in its linear (KF) and nonlinear (EKF) versions.

section 4. This implies a main Kalman filter block (MKF), plus a number n of decentralized blocks (DKFs) corresponding to the number of on board sensors (three sensors in this application). Several types of failures were considered ranging from instantaneous biases of different
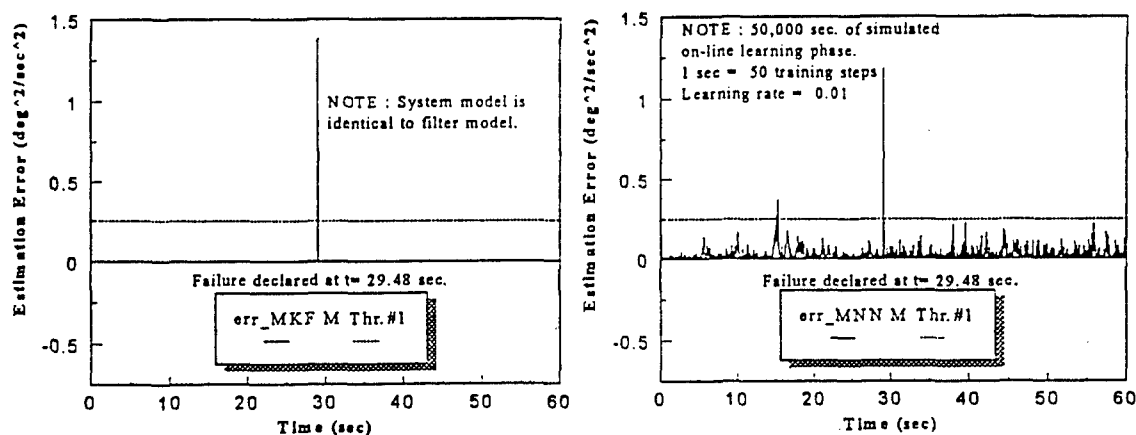
Figure 18. Estimation Error between KF and NN (no Model Discrepancy)

Valuable contribution of Kalman filtering relies heavily on the particular structure of the dynamic system, that is its linearity or linearization properties. In this section, a preliminary comparison between the neural network approach presented in section 4 and the application of KF is presented. The material is taken mostly from the work presented in references [37], and [38]. The dynamic system considered is representative of a high altitude unmanned aircraft used for scientific missions, sensor failure detection and identification is analyzed, based on a

amplitude, to biases entered with ramp transients. Different system's configurations were also studied, from nominal model and system dynamics and noise, to discrepancies in the dynamics and noise statistics.

Figure 18 shows the estimation error comparison in the case of step bias (1.2 deg/sec) in the pitch rate gyro, when there is no discrepancy between system and filter models. Figure 19 shows the failure of the Kalman filter scheme to recognize a 2.4 deg/sec bias entering as a ramp as

supposed to the NN scheme, when system and filter models have discrepancies in the dynamics and noise statistics.

1.2 deg/sec biases entering as a ramp, with system and filter models having dynamic and noise discrepancies.
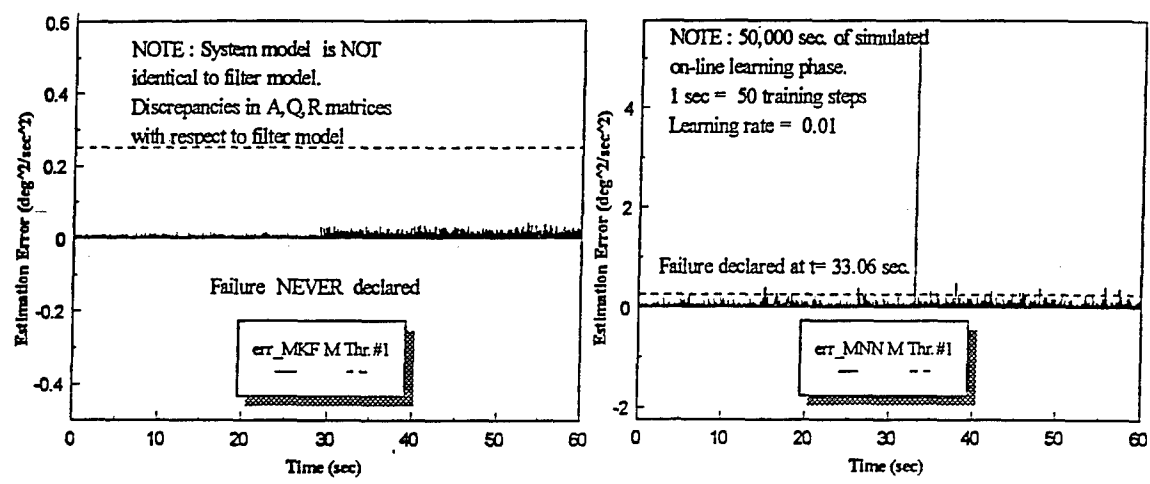
Figure 19. Estimation Error between KF and NN (withModel Discrepancy)

If we use a different structure for the Kalman filter failure detection scheme [38], results may change however. In the reference, the failure detection algorithm consists of an EKF block generating analytical redundancy on an augmented system state vector (system states plus additional states, which must detect failure), and an identification block which localizes, and quantifies the failure.

In this case the failure is detected after about 3 seconds, as opposed to 49.48 seconds of the NN scheme described previously [37].

The above examples indicate that both methods have advantages and disadvantages, and should be used appropriately. Clearly a KF-based structure, so dependent
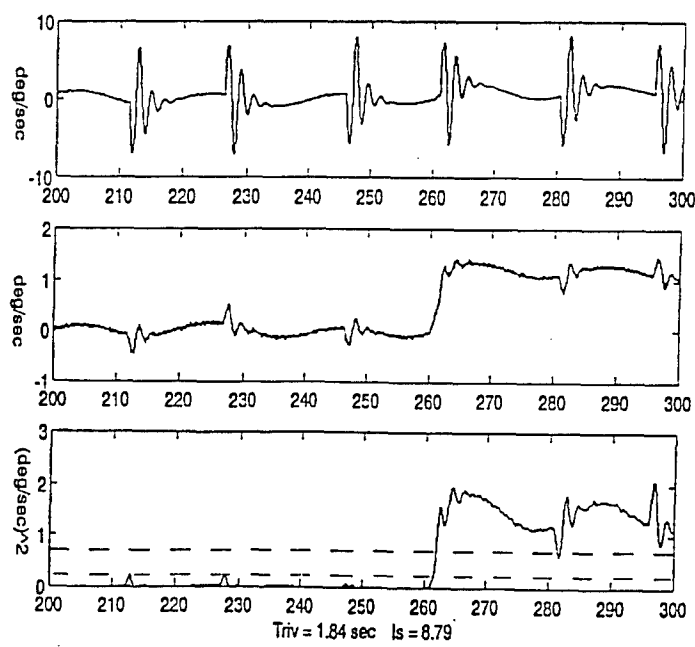
Figue 20. Failure Detection time History using EKF on Augmented Plant

As an example, figure 20 shows the time history for a pitch rate gyro failure (measured output, failure variable, and mean square error respectively), when the failure is a

on the knowledge of the system, requires an architecture that takes advantage of that, a NN-based approach, especially if learning continues, appears more appropriate

when the nonlinearity of the plant is difficult to cast in a modeling structure.

6. Conclusions

This paper has presented the results of a study undertaken with the goal of showing the potential of on-line learning parallel neural networks for adaptive control at non-linear conditions. Particularly the paper has shown successful simulations of identification and (identification + control) using an indirect approach for non-linear SISO systems. The first objective was to emphasize the superior learning performance of the Extended Back-Propagation algorithm, derived from the classic Back-Propagation algorithm through a modification of its activation function.

This algorithm allows a substantial improvement in the speed and the accuracy of the learning for a reasonable increase in the required computational effort. The second objective was to show the feasibility of hardware-based parallel neural computations. This can increase flexibility for practical applications where software-based neural computations may be too intensive to be housed in existing computational units.

The paper presented also some issues related to the use of neural architectures in the area of sensor and actuator failure detection and identification. The main focus of the work was the problem of achieving satisfactory performance for on-line learning, and subsequent potential for on-board implementation on flight vehicles having low and/or no physical redundancy. To this end standard gradient-based neural networks were considered and adapted to the above constraints.

Current research is addressing the improvement of the hardware used for parallel processing of the methods, using DSP boards much faster than the transputer technology described in the paper. Finally, the general problem of control system reconfiguration is being sought.

7. References

1. Astrom, K.J, Wittenmark, 1989, "*Adaptive Control*", Addison-Wesley Publishing Co.
2. Barnard, E.,1992 "Optimization for Training Neural Nets", *IEEE Transactions on Neural Networks*, Volume 3, Number 3, pg. 232
3. Casdorph, V.A., 1994 "Detection and Identification of Battle Damage and/or Generic Failure Using On-Line Learning Neural Networks and Cross Correlation Functions", Master Thesis, West Virginia University, USA.
4. Chen, C.L., Nutter, R.S., 1992 "An Extended Back-Propagation Learning Algorithm by Using Heterogeneous Processing Units", IJCNN92, Baltimore, Md, USA.
5. Chen, V.C., Pao, Y.H., 1989, "Learning Control with Neural Networks", Proceedings of the International Conference on Robotics and Automation.
6. Cybenko, G. , 1989, "Approximation by Superposition of Sigmoidal Functions", *Mathematics of Control Signals and Systems*, Vol.2, No.4, pg. 303.
7. De Villiers,J., Barnard, E., 1993, "Back-Propagation Neural Nets with One and Two Hidden Layers", *IEEE Transactions on Neural Networks*, Volume 4, Number 1, pg. 136.
8. Freund, E., 1975, "The Structure of Decoupled Non-Linear Systems", *International Journal of Control*, Vol. 21, pg.651.
9. Hornik, K., Stinchcomb, M., and White, H., 1989, "Multilayer Feedforward Networks Are Universal Approximators", *Neural Networks*, Vol.2, pg.359.
10. Hunt, K.J., Sbarbaro, D., Zbikowski, R., and Gawtrhop, P.J., 1992 "Neural Networks for Control Systems - A Survey", *Automatica*, Vol. 28, No. 6, pg.1083.
11. Isidori, et al., A., 1981, "Non-Linear Decoupling Via Feedback : a Differential Geometric Approach", *IEEE Transactions on Automatic Controls*, Vol. AC-26, pg.341.
12. Kawato, M., Furukawa, F., and Suzuki, R., 1987, "A Hierarchical Neural Network Model for Control and Learning of Voluntary Movement", *Biological Cybernetics*, Vol.57, pg.169.
13. Napolitano, M.R., Chen, C.I., and Naylor, S., 1993, "Aircraft Failure Detection and Identification Using Neural Networks", *AIAA Journal of Guidance, Control and Dynamics*, Volume 16, Number 6, pg. 999.
14. Narendra, K.S., Monopoli, R.V., 1980 "*Applications of Adaptive Control*", New York Academic Press.
15. Narendra, K.S., Partasarathy, K., 1990, "Identification and Control of Dynamical Systems Using Neural Networks", *IEEE Transactions on Neural Networks*, Vol.1, No.1.
16. Naylor, S.M., 1994, "On-Line Learning Non-Linear Neural Controllers for Restructurable Flight Control Systems", Master Thesis, West Virginia University, Morgantown, WV, USA.
18. Neppach, C.D., 1994, "Application of Neural Networks in Sensor Failure Detection, Identification and Accommodation in a System Without Sensor Redundancy", Master Thesis, West Virginia University, Morgantown, WV, USA.
19. Nielsen, R.H., 1991, "*Neurocomputing*", Addison Wesley Publishing Company.
20. Ogata, K., 1987, "*Discrete-Time Control Systems*", Prentice-Hall, Inc.
21. Psaltis, D., Sideris, A., and Yamamura, A., 1988, "A Multilayered Neural Network Controller", *IEEE Control Systems Magazine*, Vol. 4, pg.17.
22. Sastry, S.S., Isidori, A., 1989 "Adaptive Control of Linearizable Systems", *IEEE Transactions on Automatic Controls*, Vol. 34, No.11, pg.1123.
23. Simpson, P.K., 1990, "*Artificial Neural Systems*", Pergamon Press Inc., Fairview Park, NY.
24. Singh, S.N., and Rugh, W.J., 1972, "Decoupling in a Class of Non-Linear Systems by State Variable Feedback", *ASME Transactions*, Vol. 94, pg.323.

25. Rumelhart, D. and McClelland, J., 1986, "*Parallel Distributed Processing*", MIT Press, Cambridge, MA,USA.

26. Venugopal, K.P., et al., 1994 "An Improved Scheme for Direct Adaptive Control of Dynamical Systems Using Backpropagation Neural Networks", accepted for publication to be published in "*Journal of Circuits, Systems and Signal Processing*".

27. Widrow, B., and Stearns, S.D., 1985, "*Adaptive Signal Processing*", Prentice Hall, Inc.

28. NASA, 1993,"Cooperative Agreement Award No. NCCW-0051", with West Virginia University.

29. ASI, 1995-1997, "Sviluppo di Architetture Neurali Software e Hardware per la Identificazione in Linea di Guasti in Sensori e Attuatori di Veicoli Aerospaziali", Contratto di Ricerca Agenzia Spaziale Italiana-Consorzio Pisa Ricerche.

30. Willsky, A.S., 1976, "A Survey of several Failure Detection Methods", *Automatica*, Vol. 12, No. 6.

31. Guo, T., Nurre, J., 1991, "Sensor Failure Detection Recovery using Neural Networks", *Proc. of the IJCNN '91*.

32. Napolitano, M.R., Innocenti, M., et. al, 1994, "Sensor Failure Detection, Identification, and Accomodation using a Neural Network based Approach", *Proc. of the AIAA Guidance, Navigation, and Control Conference*, Scottsdale, AZ, August.

33. Silvestri, G., 1995, "Implementazione real-time di reti neurali in applicazioni di identificazione e di controllo in presenza di malfunzionamento sui sensori", Ph.D. dissertation, University of Pisa, Italy.

34. Napolitano, M.R., Innocenti, M., et. al., 1995, "Neural-Network-Based Scheme for Sensor Failure Detection, Identification, and Accomodation", *AIAA Journal of Guidance, Control, and Dynamics*, Vol. 18, No. 6.

35. Napolitano, M.R., Casdorph, V., Neppach, C., Naylor, S., Innocenti, M., Silvestri, G, 1996, "Online Learning Neural Architectures and Cross-Correlation Analysis for Acutator Failure Detection, and Identification", *International Journal of Control*, January.

36. Napolitano, M.R., Casdorph, V., Neppach, C., Naylor, S., Innocenti, M., Silvestri, G, 1994, "Implementation of Hardware-Based On-Line Neural Architectures for Sensor Failure Detection, Identification, and Accomodation", submitted for publication to the *AIAA Journal of Guidance, Control, and Dynamics*, October.

37. Napolitano, M.R.m Windon, D., Casanova, J., Innocenti, M., 1996, "A Comparison between Kalman Filter and Neural Network Approaches for Sensor Validation", AIAA-96-3894, Guidance and Control Conference, San Diego, California, August.

38. Del Gobbo, D., 1996, "Tecniche avanzate per la Rilevazione di Malfunzionamenti", Master thesis, Universita' di Pisa, Italy.

REPORT DOCUMENTATION PAGE

1. Recipient's Reference	2. Originator's References	3. Further Reference	4. Security Classification of Document
	RTO-MP-11 AC/323(SCI)TP/7	ISBN 92-837-0006-6	UNCLASSIFIED/ UNLIMITED

5. Originator Research and Technology Organization
North Atlantic Treaty Organization
BP 25, 7 rue Ancelle, F-92201 Neuilly-sur-Seine Cedex, France

6. Title
System Identification for Integrated Aircraft Development and Flight Testing

7. Presented at/sponsored by
the Systems Concepts and Integration Panel (SCI) Symposium held in Madrid, Spain, 5-7 May 1998.

8. Author(s)/Editor(s)	9. Date
Multiple	March 1999

10. Author's/Editor's Address	11. Pages
Multiple	412

12. Distribution Statement There are no restrictions on the distribution of this document. Information about the availability of this and other RTO unclassified publications is given on the back cover.

13. Keywords/Descriptors

Identifying	Mathematical models
Aircraft	Control equipment
Helicopters	Flight simulators
Operational effectiveness	Defense economics
Flight tests	Computerized simulation
Evaluation	Experimental design
Systems engineering	Stability
Aerodynamics	

14. Abstract

The NATO RTO symposium focused on the use of system identification as a "technology integrator". The symposium was organized in seven sessions covering an overview of recent aircraft programs, identification methodologies, flight test techniques, fixed-wing applications, rotary-wing applications, special vehicle applications (including UAVs) and a session comprising short papers covering "up-to-the-minute" flight test results. A final session presented prepared remarks from experts and concluded with an open discussion format to consider the key lessons learned in the application of system identification, and areas of needed future work.

Copies of papers presented at the Systems Concepts and Integration Panel Symposium held in Madrid, Spain, 5-7 May 1998.

NORTH ATLANTIC TREATY ORGANIZATION

RT

RESEARCH AND TECHNOLOGY ORGANIZATION

BP 25 • 7 RUE ANCELLE

F-92201 NEUILLY-SUR-SEINE CEDEX • FRANCE

Télécopie 0(1)55.61.22.99 • Télex 610 176

DIFFUSION DES PUBLICATIONS

RTO NON CLASSIFIEES

L'Organisation pour la recherche et la technologie de l'OTAN (RTO), détient un stock limité de certaines de ses publications récentes, ainsi que de celles de l'ancien AGARD (Groupe consultatif pour la recherche et les réalisations aérospatiales de l'OTAN). Celles-ci pourront éventuellement être obtenues sous forme de copie papier. Pour de plus amples renseignements concernant l'achat de ces ouvrages, adressez-vous par lettre ou par télécopie à l'adresse indiquée ci-dessus. Veuillez ne pas téléphoner.

Des exemplaires supplémentaires peuvent parfois être obtenus auprès des centres nationaux de distribution indiqués ci-dessous. Si vous souhaitez recevoir toutes les publications de la RTO, ou simplement celles qui concernent certains Panels, vous pouvez demander d'être inclus sur la liste d'envoi de l'un de ces centres.

Les publications de la RTO et de l'AGARD sont en vente auprès des agences de vente indiquées ci-dessous, sous forme de photocopie ou de microfiche. Certains originaux peuvent également être obtenus auprès de CASI.

CENTRES DE DIFFUSION NATIONAUX

ALLEMAGNE
Fachinformationszentrum Karlsruhe
D-76344 Eggenstein-Leopoldshafen 2

BELGIQUE
Coordinateur RTO - VSL/RTO
Etat-Major de la Force Aérienne
Quartier Reine Elisabeth
Rue d'Evere, B-1140 Bruxelles

CANADA
Directeur - Gestion de l'information
(Recherche et développement) - DRDGI 3
Ministère de la Défense nationale
Ottawa, Ontario K1A 0K2

DANEMARK
Danish Defence Research Establishment
Ryvangs Allé 1
P.O. Box 2715
DK-2100 Copenhagen Ø

ESPAGNE
INTA (RTO/AGARD Publications)
Carretera de Torrejón a Ajalvir, Pk.4
28850 Torrejón de Ardoz - Madrid

ETATS-UNIS
NASA Center for AeroSpace Information (CASI)
Parkway Center, 7121 Standard Drive
Hanover, MD 21076-1320

FRANCE
O.N.E.R.A. (Direction)
29, Avenue de la Division Leclerc
92322 Châtillon Cedex

GRECE
Hellenic Air Force
Air War College
Scientific and Technical Library
Dekelia Air Force Base
Dekelia, Athens TGA 1010

ISLANDE
Director of Aviation
c/o Flugrad
Reykjavik

ITALIE
Aeronautica Militare
Ufficio Stralcio RTO/AGARD
Aeroporto Pratica di Mare
00040 Pomezia (Roma)

LUXEMBOURG
Voir Belgique

NORVEGE
Norwegian Defence Research Establishment
Attn: Biblioteket
P.O. Box 25
N-2007 Kjeller

PAYS-BAS
NDRCC
DGM/DWOO
P.O. Box 20701
2500 ES Den Haag

PORTUGAL
Estado Maior da Força Aérea
SDFA - Centro de Documentação
Alfragide
P-2720 Amadora

ROYAUME-UNI
Defence Research Information Centre
Kentigern House
65 Brown Street
Glasgow G2 8EX

TURQUIE
Millî Savunma Başkanliği (MSB)
ARGE Dairesi Başkanliği (MSB)
06650 Bakanliklar - Ankara

AGENCES DE VENTE

**NASA Center for AeroSpace
Information (CASI)**
Parkway Center
7121 Standard Drive
Hanover, MD 21076-1320
Etats-Unis

**The British Library Document
Supply Centre**
Boston Spa, Wetherby
West Yorkshire LS23 7BQ
Royaume-Uni

**Canada Institute for Scientific and
Technical Information (CISTI)**
National Research Council
Document Delivery,
Montreal Road, Building M-55
Ottawa K1A 0S2
Canada

Les demandes de documents RTO ou AGARD doivent comporter la dénomination "RTO" ou "AGARD" selon le cas, suivie du numéro de série (par exemple AGARD-AG-315). Des informations analogues, telles que le titre et la date de publication sont souhaitables. Des références bibliographiques complètes ainsi que des résumés des publications RTO et AGARD figurent dans les journaux suivants:
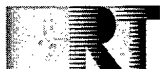
Scientific and Technical Aerospace Reports (STAR)
STAR peut être consulté en ligne au localisateur de ressources uniformes (URL) suivant:
http://www.sti.nasa.gov/Pubs/star/Star.html
STAR est édité par CASI dans le cadre du programme
NASA d'information scientifique et technique (STI)
STI Program Office, MS 157A
NASA Langley Research Center
Hampton, Virginia 23681-0001
Etats-Unis

Government Reports Announcements & Index (GRA&I)
publié par le National Technical Information Service
Springfield
Virginia 2216
Etats-Unis
(accessible également en mode interactif dans la base de données bibliographiques en ligne du NTIS, et sur CD-ROM)

Imprimé par le Groupe Communication Canada Inc.
(membre de la Corporation St-Joseph)
45, boul. Sacré-Cœur, Hull (Québec), Canada K1A 0S7

NORTH ATLANTIC TREATY ORGANIZATION

RT

RESEARCH AND TECHNOLOGY ORGANIZATION
BP 25 • 7 RUE ANCELLE
F-92201 NEUILLY-SUR-SEINE CEDEX • FRANCE
Telefax 0(1)55.61.22.99 • Telex 610 176

DISTRIBUTION OF UNCLASSIFIED
RTO PUBLICATIONS

NATO's Research and Technology Organization (RTO) holds limited quantities of some of its recent publications and those of the former AGARD (Advisory Group for Aerospace Research & Development of NATO), and these may be available for purchase in hard copy form. For more information, write or send a telefax to the address given above. **Please do not telephone**.

Further copies are sometimes available from the National Distribution Centres listed below. If you wish to receive all RTO publications, or just those relating to one or more specific RTO Panels, they may be willing to include you (or your organisation) in their distribution.

RTO and AGARD publications may be purchased from the Sales Agencies listed below, in photocopy or microfiche form. Original copies of some publications may be available from CASI.

NATIONAL DISTRIBUTION CENTRES

BELGIUM
Coordinateur RTO - VSL/RTO
Etat-Major de la Force Aérienne
Quartier Reine Elisabeth
Rue d'Evere, B-1140 Bruxelles

CANADA
Director Research & Development
Information Management - DRDIM 3
Dept of National Defence
Ottawa, Ontario K1A 0K2

DENMARK
Danish Defence Research Establishment
Ryvangs Allé 1
P.O. Box 2715
DK-2100 Copenhagen Ø

FRANCE
O.N.E.R.A. (Direction)
29 Avenue de la Division Leclerc
92322 Châtillon Cedex

GERMANY
Fachinformationszentrum Karlsruhe
D-76344 Eggenstein-Leopoldshafen 2

GREECE
Hellenic Air Force
Air War College
Scientific and Technical Library
Dekelia Air Force Base
Dekelia, Athens TGA 1010

ICELAND
Director of Aviation
c/o Flugrad
Reykjavik

ITALY
Aeronautica Militare
Ufficio Stralcio RTO/AGARD
Aeroporto Pratica di Mare
00040 Pomezia (Roma)

LUXEMBOURG
See Belgium

NETHERLANDS
NDRCC
DGM/DWOO
P.O. Box 20701
2500 ES Den Haag

NORWAY
Norwegian Defence Research Establishment
Attn: Biblioteket
P.O. Box 25
N-2007 Kjeller

PORTUGAL
Estado Maior da Força Aérea
SDFA - Centro de Documentação
Alfragide
P-2720 Amadora

SPAIN
INTA (RTO/AGARD Publications)
Carretera de Torrejón a Ajalvir, Pk.4
28850 Torrejón de Ardoz - Madrid

TURKEY
Millî Savunma Başkanliği (MSB)
ARGE Dairesi Başkanliği (MSB)
06650 Bakanliklar - Ankara

UNITED KINGDOM
Defence Research Information Centre
Kentigern House
65 Brown Street
Glasgow G2 8EX

UNITED STATES
NASA Center for AeroSpace Information (CASI)
Parkway Center, 7121 Standard Drive
Hanover, MD 21076-1320

SALES AGENCIES

NASA Center for AeroSpace Information (CASI)
Parkway Center
7121 Standard Drive
Hanover, MD 21076-1320
United States

The British Library Document Supply Centre
Boston Spa, Wetherby
West Yorkshire LS23 7BQ
United Kingdom

Canada Institute for Scientific and Technical Information (CISTI)
National Research Council
Document Delivery,
Montreal Road, Building M-55
Ottawa K1A 0S2
Canada

Requests for RTO or AGARD documents should include the word 'RTO' or 'AGARD', as appropriate, followed by the serial number (for example AGARD-AG-315). Collateral information such as title and publication date is desirable. Full bibliographical references and abstracts of RTO and AGARD publications are given in the following journals:

Scientific and Technical Aerospace Reports (STAR)
STAR is available on-line at the following uniform resource locator:
http://www.sti.nasa.gov/Pubs/star/Star.html
STAR is published by CASI for the NASA Scientific and Technical Information (STI) Program
STI Program Office, MS 157A
NASA Langley Research Center
Hampton, Virginia 23681-0001
United States

Government Reports Announcements & Index (GRA&I)
published by the National Technical Information Service
Springfield
Virginia 22161
United States
(also available online in the NTIS Bibliographic Database or on CD-ROM)

Printed by Canada Communication Group Inc.
(A St. Joseph Corporation Company)
45 Sacré-Cœur Blvd., Hull (Québec), Canada K1A 0S7

ISBN 92-837-0006-6